

Contents Volume 2

5 TET in Linear Continuous Systems with Single- and Multi-DOF NESs	1
5.1 Beam of Finite Length with SDOF NES	1
5.1.1 Formulation of the Problem and Computational Procedure	1
5.1.2 Parametric Study of TET	6
5.2 Rod of Finite Length with SDOF NES	10
5.2.1 Formulation of the Problem, Computational Procedure and Post-Processing Algorithms	13
5.2.2 Computational Study of TET	23
5.2.3 Damped Transitions on the Hamiltonian FEP	44
5.3 Rod of Semi-Infinite Length with SDOF NES	70
5.3.1 Reduction to Integro-differential Form	72
5.3.2 Numerical Study of Damped Transitions	79
5.3.3 Analytical Study	91
5.4 Rod of Finite Length with MDOF NES	103
5.4.1 Formulation of the Problem and FEPs	104
5.4.2 Computational Study of TET	114
5.4.3 Multi-Modal Damped Transitions and Multi-Scale Analysis	122
5.5 Plate with SDOF and MDOF NESs	139
5.5.1 Case of a SDOF NES	147
5.5.2 Case of Multiple SDOF NESs	152
5.5.3 Case of a MDOF NES	155
5.5.4 Comparative Study with Linear Tuned Mass Damper	158
6 Targeted Energy Transfer in Systems with Periodic Excitations	167
6.1 Steady State Responses and Generic Bifurcations	168
6.1.1 Analysis of Steady State Motions	168
6.1.2 Numerical Verification of the Analytical Results	181
6.2 Strongly Modulated Responses (SMRs)	183
6.2.1 General Formulation and Invariant Manifold Approach	183
6.2.2 Reduction to One-Dimensional Maps and Existence Conditions for SMRs	193
6.2.3 Numerical Simulations	200
6.3 NESs as Strongly Nonlinear Absorbers for Vibration Isolation	208
6.3.1 Co-existent Response Regimes	208

6.3.2	Efficiency and Broadband Features of the Vibration Isolation	210
6.3.3	Passive Self-tuning Capacity of the NES	220
7	NESs with Non-Smooth Stiffness Characteristics	235
7.1	System with Multiple NESs Possessing Clearance Nonlinearities	235
7.1.1	Problem Description	236
7.1.2	Numerical Results	239
7.2	Vibro-Impact (VI) NESs as Shock Absorbers	247
7.2.1	Passive TET to VI NESs	248
7.2.2	Shock Isolation	257
7.3	SDOF Linear Oscillator with a VI NES	265
7.3.1	Periodic Orbits for Elastic Vibro-Impacts Represented on the FEP	266
7.3.2	Vibro-Impact Transitions in the Dissipative Case: VI TET	285
8	Experimental Verification of Targeted Energy Transfer	317
8.1	TET to Ungrounded SDOF NES (Configuration II)	317
8.1.1	System Identification	318
8.1.2	Experimental Measurements	320
8.2	TET to Grounded SDOF NES (Configuration I)	326
8.2.1	Experimental Fixture	328
8.2.2	Results and Discussion	330
8.3	Experimental Demonstration of 1:1 TRCs Leading to TET	336
8.3.1	Experimental Fixture	337
8.3.2	Experimental TRCs	339
8.4	Steady State TET Under Harmonic Excitation	348
8.4.1	System Configuration and Theoretical Analysis	350
8.4.2	Experimental Study	353
9	Suppression of Aeroelastic Instabilities through Passive Targeted Energy Transfer	359
9.1	Suppression of Limit-Cycle Oscillations in the van der Pol Oscillator	359
9.1.1	VDP Oscillator and NES Configurations	361
9.1.2	Transient Dynamics	365
9.1.3	Steady State Dynamics and Bifurcation Analysis	387
9.1.4	Summary of Results	400
9.2	Triggering Mechanism for Aeroelastic Instability of an In-Flow Wing	403
9.2.1	The Two-DOF Aeroelastic Model	405
9.2.2	Slow Flow Dynamics	408
9.2.3	LCO Triggering Mechanism	434
9.2.4	Concluding Remarks	453
9.3	Suppressing Aeroelastic Instability of an In-Flow Wing Using a SDOF NES	459
9.3.1	Preliminary Numerical Study	459
9.3.2	Study of LCO Suppression Mechanisms	469

9.3.3	Robustness of LCO Suppression	493
9.3.4	Concluding Remarks	505
9.4	Experimental Validation of TET-Based, Passive LCO Suppression	508
9.4.1	Experimental Apparatus and Procedures	508
9.4.2	Results and Discussion	514
9.5	Suppressing Aeroelastic Instability of an In-Flow Wing Using a MDOF NES	526
9.5.1	Revisiting the SDOF NES Design	526
9.5.2	Configuration of a Wing with an Attached MDOF NES	538
9.5.3	Robustness of LCO Suppression – Bifurcation Analysis	542
9.6	Preliminary Results on LCO Suppression in a Wing in Unsteady Flow	565
10	Seismic Mitigation by Targeted Energy Transfer	577
10.1	The Two-DOF Linear Primary System with VI NES	578
10.1.1	System Description	578
10.1.2	Simulation and Optimization	580
10.1.3	Computational Results	582
10.2	Scaled Three-Story Steel Frame Structure with NESs	587
10.2.1	Characterization of the Three-Story Linear Frame Structure	588
10.2.2	Simulation and Optimization of the Frame-Single VI NES System	591
10.2.3	Simulation and Optimization of the Frame-VI NES-Smooth NES System	601
10.3	Experimental Verification	609
10.3.1	System Incorporating the Single-VI NES	612
10.3.2	System Incorporating both VI and Smooth NESs	615
10.4	Observations, Summary and Conclusions	621
11	Suppression of Instabilities in Drilling Operations through TET	625
11.1	Problem Description	626
11.2	Instability in the Drill-String Model	631
11.3	Suppression of Friction-Induced Limit Cycles by TET	633
11.3.1	Addition of an NES to the Drill-String System	635
11.3.2	Parametric Study for Determining the NES Parameters	636
11.4	Detailed Analysis of the Drill-String with NES Attached	639
11.4.1	NES Efficacy	640
11.4.2	Robustness of LCO Suppression	643
11.4.3	Transient Resonance Captures	645
11.5	Concluding Remarks	646
12	Postscript	651
	Index	655

Chapter 5

Targeted Energy Transfer in Linear Continuous Systems with Single- and Multi-DOF NESs

Up to now we have considered passive targeted energy transfer from linear discrete systems of coupled oscillators to attached SDOF and MDOF NESs. In this chapter we extend the study of TET dynamics to linear elastic continua possessing attached NESs attached to their boundaries. Our study builds on the formulations, methodologies and results discussed in previous Chapters, in an effort to demonstrate that appropriately designed and placed essentially nonlinear local attachments may affect the *global* dynamics of the elastic systems to which they are attached. More importantly, we show that such nonlinear attachments can passively absorb and locally dissipate significant portions of shock-induced energy inputs from directly excited linear continua. This paves the way for the practical implementation of TET and the concept of NES to flexible systems encountered in engineering practice.

5.1 Beam of Finite Length with SDOF NES

The first class of elastic systems considered is composed of linear beams with attached NESs, with general configuration depicted in Figure 5.1 (Georgiades, 2006; Georgiades et al., 2007). Specifically, we consider an impulsively forced, simply supported, damped linear beam, with an attached essentially nonlinear, damped SDOF oscillator (the NES). As in the case of discrete oscillators considered in Chapters 3 and 4, we will show that the NES can passively and irreversibly absorb a major portion of the impulsive energy of the beam. Moreover, TET from the linear beam to the NES can be optimized by appropriate design and placement of the attachment.

5.1.1 Formulation of the Problem and Computational Procedure

Assuming that the beam dynamics is governed by linear Bernoulli–Euler theory, the equations of motion of the integrated system are given by

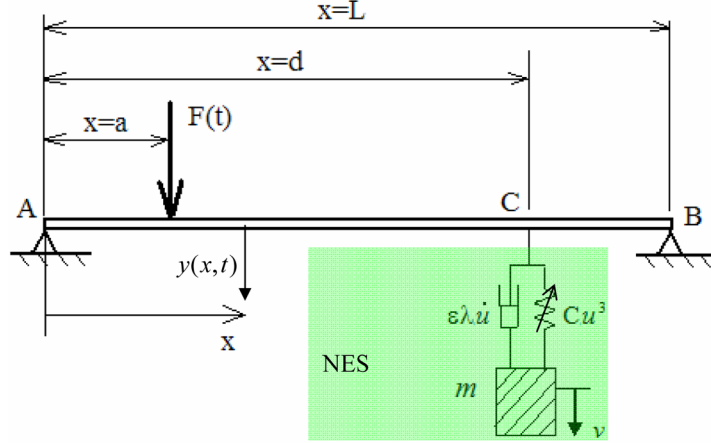


Fig. 5.1 Linear beam with attached SDOF NES.

$$\begin{aligned}
 & EI y_{xxxx}(x, t) + \varepsilon \lambda y_t(x, t) + m y_{tt}(x, t) \\
 & + \{C[y(d, t) - v(t)]^3 + \varepsilon \lambda [y_t(d, t) - \dot{v}(t)]\} \delta(x - d) = F(t) \delta(x - a) \\
 & \varepsilon \ddot{v}(t) + C[(v(t) - y(d, t))]^3 + \varepsilon \lambda [\dot{v}(t) - y_t(d, t)] = 0
 \end{aligned} \tag{5.1}$$

with zero initial conditions. In (5.1), E is the Young's modulus, I the moment of inertia of the cross section, and m the mass per unit length of the beam; moreover, proportional distributed viscous damping is assumed for the beam, and the short-hand notation for partial differentiation is enforced, e.g., $(\cdot)_{xx} \equiv \partial^2(\cdot)/\partial x^2$, $(\cdot)_t \equiv \partial(\cdot)/\partial t$, \dots . By adopting the usual assumption $0 < \varepsilon \ll 1$, the system is assumed to possess weak viscous damping, and the NES is assumed to be lightweight compared to the mass of the beam. Clearly, this last assumption is important for the practical implementation of this design, since in practical engineering applications one requires that the NES does not add significant new weight or modify considerably the overall structural configuration. In addition, we assume that the attachment possesses essential cubic stiffness nonlinearity, which, together with viscous dissipation are prerequisites for the realization of TET.

We now discuss certain aspects of the computational study of the transient dynamics of the essentially nonlinear damped system (5.1). First, we consider the set of linear normal modes of the simply supported beam with no damping, external forcing, or NES attached. This is given by

$$\begin{aligned}
 \phi_r(x) &= (2/mL)^{1/2} \sin(r\pi x/L), \\
 \omega_r &= (r\pi)^2 (EI/mL^4)^{1/2}, \quad r = 1, 2, \dots
 \end{aligned} \tag{5.2}$$

where $\phi_r(x)$ and ω_r are the mode shape and natural frequency of the mode, respectively. Since these modes are solutions of a Sturm–Liouville eigenvalue problem

they satisfy the following orthonormality relations:

$$\int_0^L m\phi_r\phi_s dx = \delta_{rs} \quad \text{and} \quad \int_0^L EI \frac{\partial^2 \phi_r}{\partial x^2} \frac{\partial^2 \phi_s}{\partial x^2} dx = \omega_r^2 \delta_{rs}, \quad r, s = 1, 2, \dots$$

Considering now the integrated damped beam-NES system, its transient response is numerically computed by projecting the dynamics of the partial differential equation (with attached NES) in the functional space defined by the complete and orthonormal base of normal modes (5.2). To this end, we non-dimensionalize the system (5.1) by introducing the following new normalized parameters and variables:

$$\tau = t \frac{EI}{m}, \quad \varepsilon_1 = \frac{\varepsilon}{m}, \quad c = \frac{C}{EI}, \quad \lambda_1 = \frac{\varepsilon \lambda}{m}, \quad Q(x, \tau) = \frac{F(x, \tau)}{EI m}$$

which bring (5.1) into the following non-dimensional form:

$$\begin{aligned} & y_{xxxx}(x, \tau) + \lambda_1 y_\tau(x, \tau) + y_{\tau\tau}(x, \tau) \\ & + \{c[y(d, \tau) - v(\tau)]^3 + \lambda_1[y_\tau(d, \tau) - \dot{v}(\tau)]\} \delta(x - d) = Q(\tau) \delta(x - a) \\ & \varepsilon_1 \ddot{v}(\tau) + c[v(\tau) - y(d, \tau)]^3 + \lambda_1[\dot{v}(\tau) - y_\tau(d, \tau)] = 0 \end{aligned} \quad (5.3)$$

In (5.3) dots denote differentiation with respect to the scaled time variable τ .

To project the dynamics of (5.3) in the infinite-dimensional base of orthonormal normal modes (5.2) we express the transverse displacement field $y(x, t)$ in the series form

$$y(x, \tau) = \sum_{r=1}^{\infty} a_r(\tau) \phi_r(x) \quad (5.4)$$

Substituting (5.4) into (5.3), leads to

$$\begin{aligned} & \sum_{r=1}^{\infty} a_r(\tau) \frac{d^4 \phi_r(x)}{dx^4} + \lambda_1 \sum_{r=1}^{\infty} \dot{a}_r(\tau) \phi_r(x) + \sum_{r=1}^{\infty} \ddot{a}_r(\tau) \phi_r(x) \\ & + \left\{ c \left[\sum_{r=1}^{\infty} a_r(\tau) \phi_r(d) - v(\tau) \right]^3 + \lambda_1 \left[\sum_{r=1}^{\infty} \dot{a}_r(\tau) \phi_r(d) - \dot{v}(\tau) \right] \right\} \delta(x - d) \\ & = F(\tau) \delta(x - a) \\ & \varepsilon_1 \ddot{v}(\tau) - c \left[\sum_{r=1}^{\infty} a_r(\tau) \phi_r(d) - v(\tau) \right]^3 - \lambda_1 \left[\sum_{r=1}^{\infty} \dot{a}_r(\tau) \phi_r(d) - \dot{v}(\tau) \right] = 0 \end{aligned} \quad (5.5)$$

By multiplying (5.5) by an arbitrary modeshape $\phi_p(x)$, integrating with respect to x from 0 to L , and enforcing the orthonormality conditions satisfied by the normal modes, yields the following set of coupled nonlinear ordinary differential equations governing the modal amplitudes $a_p(\tau)$, $p = 1, 2, \dots$:

$$\begin{aligned}
& \ddot{a}_p(\tau) + \omega_p^2 a_p(\tau) + \varepsilon_1 \dot{a}_p(\tau) \\
& + \left\{ c \left[\sum_{r=1}^{\infty} a_r(\tau) \phi_r(d) - v(\tau) \right]^3 + \lambda_1 \left[\sum_{r=1}^{\infty} \dot{a}_r(\tau) \phi_r(d) - \dot{v}(\tau) \right] \right\} \phi_p(d) \\
& = q(\tau) \phi_p(a) \\
& \varepsilon_1 \ddot{v}(\tau) + c \left[v(\tau) - \sum_{r=1}^{\infty} a_r(\tau) \phi_r(d) \right]^3 + \lambda_1 \left[\dot{v}(\tau) - \sum_{r=1}^{\infty} \dot{a}_r(\tau) \phi_r(d) \right] = 0
\end{aligned} \tag{5.6}$$

We note that the essential nonlinearity and the damping term of the NES couples all modes through the infinite summation terms, whereas, the linear part of the system decouples completely by the projection to the orthonormal basis of normal modes of the uncoupled linear beam. It follows that *although the NES is local and lightweight it introduces global effects in the dynamics of the integrated system*. This is due, of course, to the essential (strong) stiffness nonlinearity of the system.

As in Chapters 3 and 4, a quantitative measure of TET (that is, a measure of the effectiveness of the NES to passively absorb and locally dissipate energy from the directly forced beam) is given by the energy dissipation measure (EDM) which quantifies the instantaneous portion of impulsive energy of the beam that is dissipated by the damper of the NES:

$$E_{\text{NES}}(\tau) \equiv \frac{\int_0^\tau \lambda_1 \left[\dot{v}(u) - \sum_{r=1}^{\infty} \dot{a}_r(u) \phi_r(d) \right]^2 du}{\int_0^T F(\tau) \sum_{r=1}^{\infty} \dot{a}_r(\tau) \phi_r(a) d\tau} \tag{5.7}$$

In this passive system, the EDM (5.7) reaches an asymptotic limit denoted by $E_{\text{NES}, \tau \gg 1} \equiv \lim_{\tau \gg 1} E_{\text{NES}}(\tau)$, which quantifies the portion of impulsive energy that is eventually dissipated by the NES over the entire duration of the decaying motion.

In the numerical simulations the infinite series (5.4) was truncated to include only a finite number of modes; this is equivalent to performing an approximate projection of the dynamics to a finite-dimensional basis of orthonormal normal modes. The dimensionality of the truncated space that is required for accurate numerical simulations is determined by performing a convergence study. It was found that $N = 5$ modes were sufficient for accurately computing the transient dynamics. Representative examples of typical convergence results are depicted in Figures 5.2a, b, where we depict the EDM $E_{\text{NES}, \tau \gg 1} \approx E_{\text{NES}}(\tau = 150)$ as function of the nonlinear coefficient c and the position d of the NES, respectively. For these simulations the impulsive force was selected as a half sine pulse,

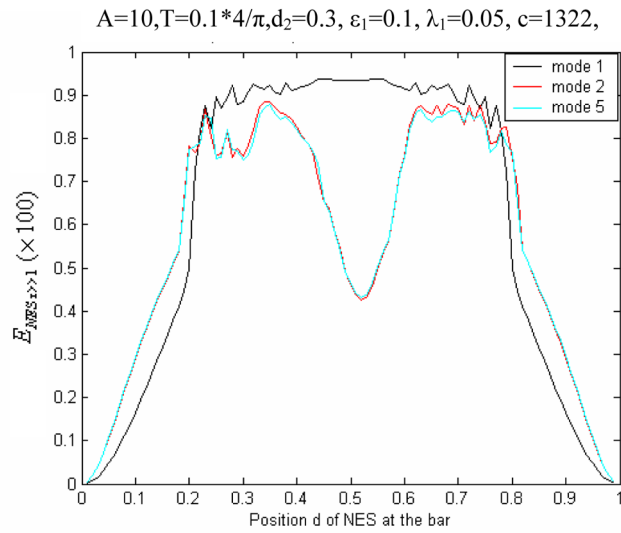
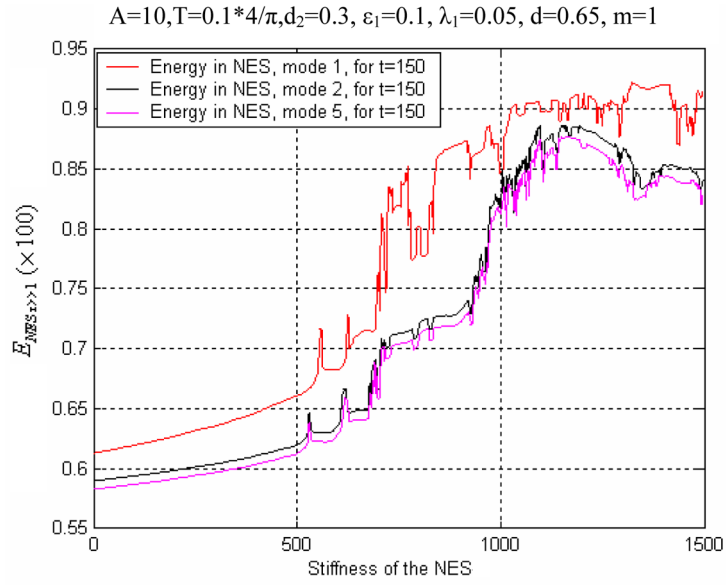


Fig. 5.2 Convergence study of the EDM $E_{NES, \tau \gg 1}$ for the truncated system with $N = 1, 2$ and 5 modes as function of (a) NES stiffness C and (b) NES position d .

$$q(t) = \begin{cases} A \sin(2\pi\tau/T), & 0 \leq \tau \leq T/2 \\ 0, & t > T/2 \end{cases} \quad (5.8)$$

with $A = 10.0$ and $T = 0.4/\pi$. Moreover, the system parameters were assigned the numerical values: $EI = 1.0$, $m = 1.0$, $L = 1.0$, $\varepsilon_1 = 0.1$, $a = 0.3$, $\lambda_1 = 0.05$, with $d = 0.65$ for the convergence plot of Figure 5.2a, and $c = 1.322 \times 10^3$ for that depicted in Figure 5.2b. Studying the plots of Figures 5.2a, b we note convergence of the results for $N = 5$ modes, justifying the mode truncation implemented in the following results.

Considering the dependence of the EDM $E_{\text{NES}, \tau \gg 1}$, on the nonlinear coefficient c of the NES (see Figure 5.2a), we note that for c of $O(10^3)$ the EDM is significant, reaching values above 80%; this indicates that strong TET is realized in this case. Considering the dependence of $E_{\text{NES}, \tau \gg 1}$ on the NES position (Figure 5.2b), we note two regions of strong TET (with the EDM reaching values of the order of 80%), corresponding to placement of the NES between the boundaries and the center of the beam. On the contrary, significantly weaker TET is realized when the NES is placed near the center of the beam (where the second and fourth normal modes of the uncoupled beam possess nodes), or near the boundaries of the beam where the response of the beam is small.

These results indicate that an appropriately designed and placed NES can passively absorb and locally dissipate a major portion of the energy induced to the beam by the external shock; moreover, this passive energy absorption is broadband and irreversible (on the average), as verified by the significant levels of energy eventually dissipated by the damper of the NES. In the following section we present the results of a parametric study of TET in the system, in an effort to optimize TET from the beam to the NES. Although an optimization study of TET should address not only maximization of the EDM $E_{\text{NES}, \tau \gg 1}$, but also the issue of the time scale governing the energy transfer, in this section we only focus on the former issue, leaving the discussion of the later issue (i.e., of the time scale of TET) for Chapters 7, 9 and 10.

5.1.2 Parametric Study of TET

The following simulations are performed for the half-sine shock excitation (5.8) with $A = 10.0$, $T = 0.4/\pi$ and system parameters, $EI = 1.0$, $m = 1.0$, $L = 1.0$, $\varepsilon_1 = 0.1$, $a = 0.3$ and $\lambda_1 = 0.05$. In addition, by the results of the convergence study we truncate the discretized set of equations (5.6) to $N = 5$ terms, which corresponds to a strongly nonlinear set of five coupled modal oscillators. In the first parametric study we keep the (light) mass of the NES fixed and compute the asymptotic EDM $E_{\text{NES}, \tau \gg 1}$ as function of the nonlinear coefficient c and the position d of the NES. Viewed in context, the plots of Figure 5.2 for $N = 5$ modes can be regarded as different ‘slices’ of the three-dimensional plot of Figure 5.3a.

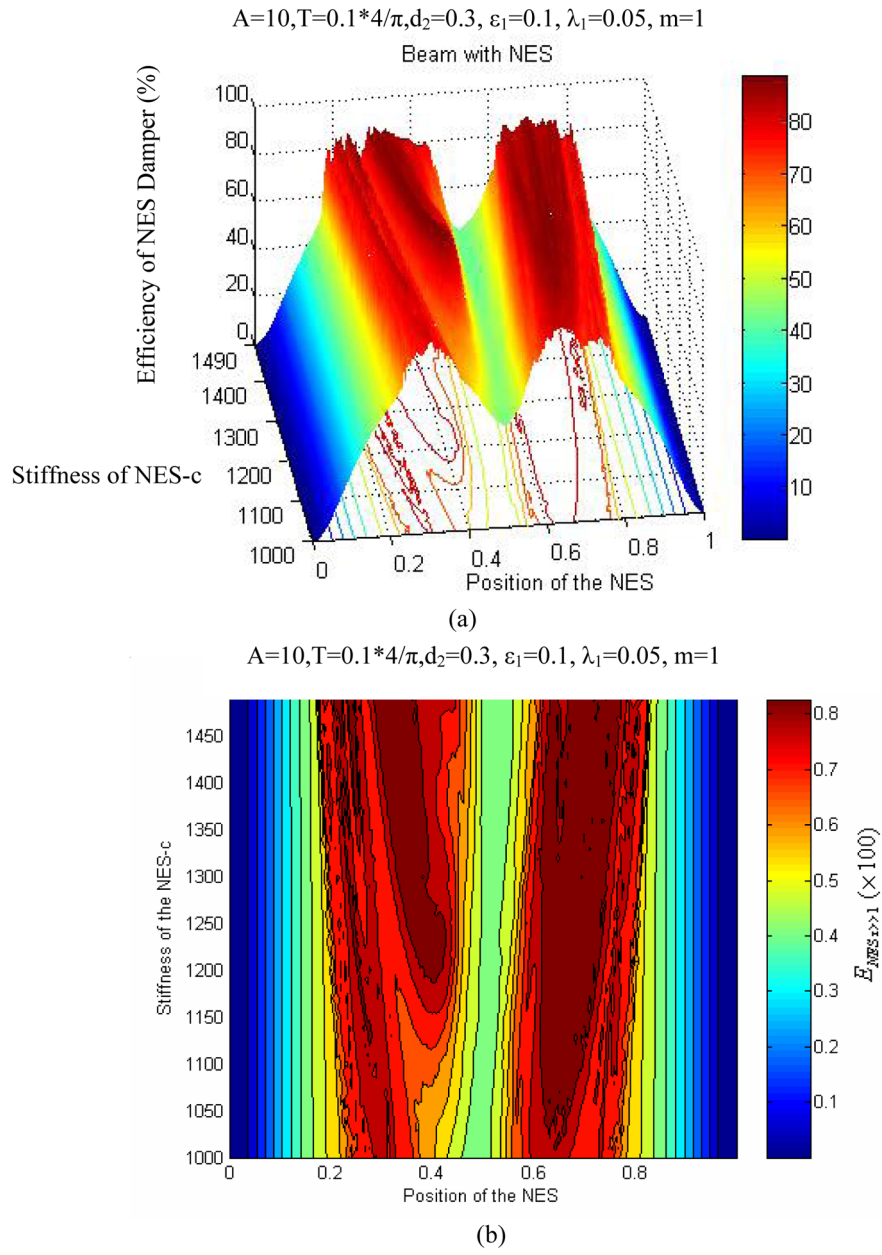


Fig. 5.3 EDM $E_{NES, \tau \gg 1}$ as function of the NES c and the position d : (a) three-dimensional plot, (b) contour projection in the (c, d) plane.

There are two regions of strong TET in the (c, d) plane realized for $c = 1.32 \times 10^3$ and $d = 0.348$, with optimal NES energy dissipation reaching the level of 83.3%. Moreover, for c of $O(10^3)$ the effectiveness of the NES appears to be robust in variations of the nonlinear coefficient c ; this is indicated by the two distinct ‘strips’ of sustained high values of energy dissipation in the plots of Figure 5.3. Moreover, the plots of Figure 5.3 reveal a strong dependence of TET on NES position d . This should be expected, given that by placing the NES closer to the center of the beam, the NES is hindered from interacting with half of the beam modes that possess nodes near that position.

A general conclusion drawn from the plots in Figure 5.3 is that a lightweight, essentially nonlinear NES can be designed and appropriately placed to passively absorb a major portion (of the order of 80%) of shock energy induced in the beam. The described energy absorption is broadband (as it involves shock excitation and multi-modal beam response), and is realized over a wide frequency range. This observation highlights the advantage of the proposed NES design compared to existing designs based on linear vibration absorbers: this is the capacity of the NES to absorb effectively broadband energy over wide ranges of frequencies and system parameters, in contrast to the linear absorber whose action is narrowband. As we discussed in Chapters 3 and 4, the main reason behind the capacity of the NES for broadband passive vibration absorption is its essentially nonlinearity (and the corresponding absence of preferential resonance frequencies), which enables it to engage in transient resonance captures (TRCs) or resonance capture cascades (RCCs) with isolated or sets of structural modes on arbitrary frequency ranges.

To demonstrate the significant reduction in amplitude of the beam vibrations achieved due to passive TET, in Figure 5.4 we depict the transient responses of the NES, of the point of attachment of the beam and of another point of the beam at position $x = 0.8$. The system parameters for these simulations were fixed to the values $c = 1.322 \times 10^3$ and $d = 0.65$; by the results depicted in Figure 5.3 this corresponds to a case of strong TET with $E_{\text{NES}, \tau \gg 1} \approx 83\%$; for comparison purposes we also depict the corresponding responses of the beam with no NES attached. We note the drastic reduction in the envelope of oscillation of the transient responses of the beam when the NES is attached, due to the rapid absorption and local dissipation of impulsive energy by the NES. The multi-frequency content clearly evidenced in the NES transient response indicates broadband absorption of vibration energy by the NES from different structural modes of the beam, and demonstrates clearly the capacity of the NES to absorb and dissipate broadband energy from the beam. We note, especially, the early high frequency transients resembling a nonlinear beat (i.e., a transient ‘bridging’ orbit) followed by the transition of the dynamics towards lower frequencies – and resonance capture – as time progresses.

In the plots in Figure 5.5 we depict the transient responses for the system for parameters $c = 2$ and $d = 0.65$ where TET is much weaker, corresponding to EDM $E_{\text{NES}, \tau \gg 1} \approx 58\%$. In this case, we note a much smaller reduction of the envelope of the beam responses when the NES is attached; moreover, the reduction of the envelope occurs over a longer time scale compared to the case of efficient TET of Figure 5.4. In addition, in this case the response of NES is of much smaller

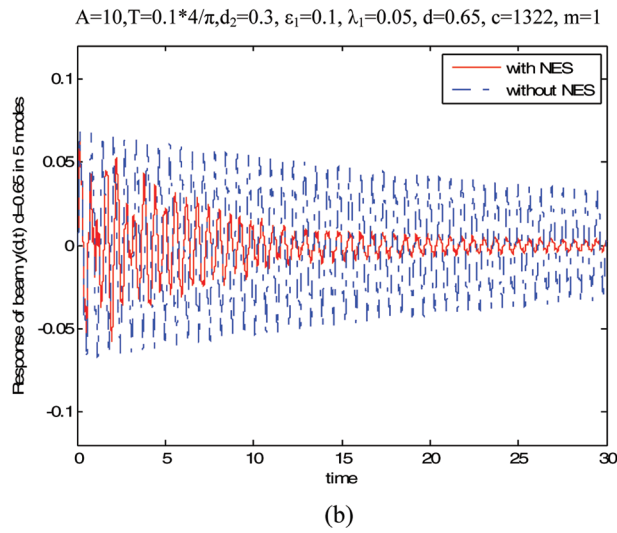
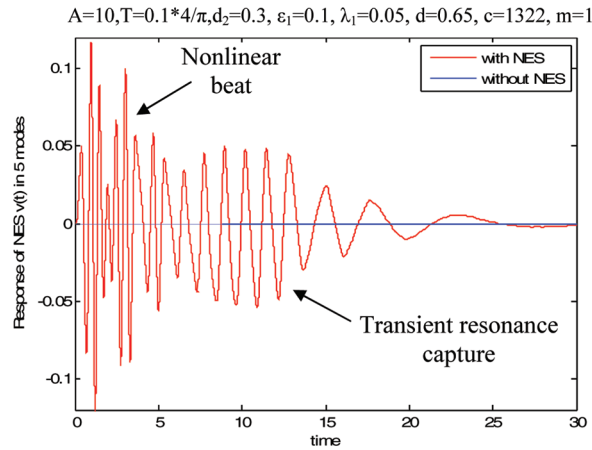


Fig. 5.4 Case of strong TET to the NES, transient responses of the system with and without NES attached: (a) NES response, (b) beam response at the point of attachment.

amplitude than the beam response, which indicates the inability of the NES to absorb and dissipate a major part of the impulsive energy of the beam.

These results highlight the usefulness of the parametric plots of Figure 5.3. Indeed, using such plots one can determine optimal NES parameters for which strong and *robust* TET from the beam to the NES takes place. Moreover, these plots can form the basis for practical NES designs, capable of significantly reducing the level of unwanted vibration of flexible structural components forced by external shocks.

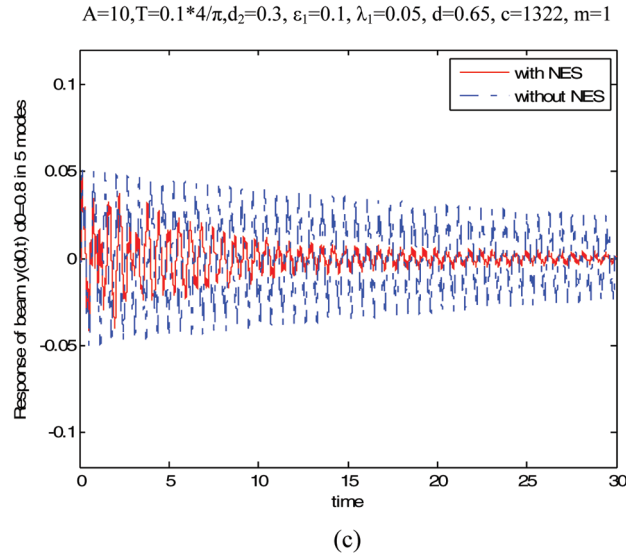


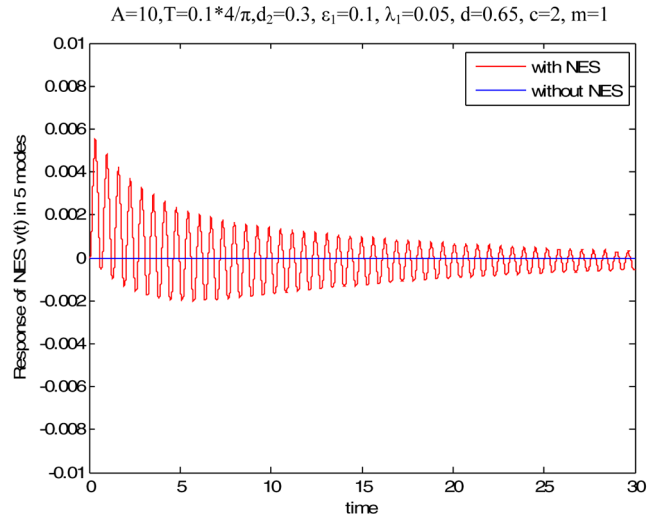
Fig. 5.4 Case of strong TET to the NES, transient responses of the system with and without NES attached: (c) beam response at $x = 0.65$.

To be able to better study the robustness of TET, one needs to extend the present parametric study to include changes in initial conditions and system parameters of the linear structure (in this case the beam). This addresses the need of studying how the effectiveness of the NES is affected by changes due to structural degradation, and the initial state of the system.

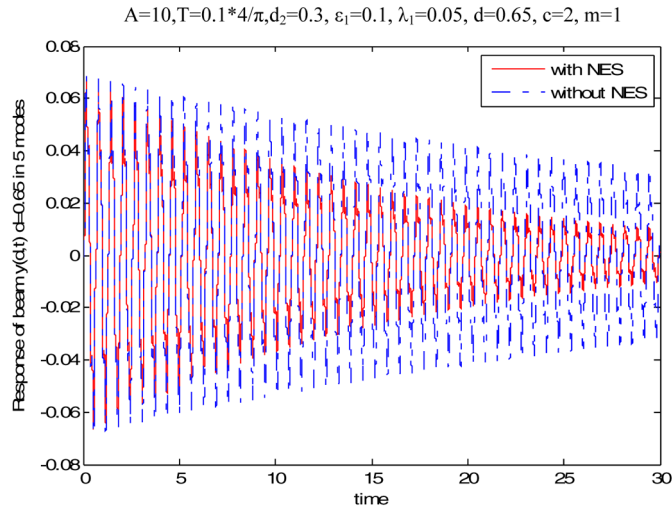
The results of this section provide a first evidence of TET from a linear elastic continuum to an attached NES. In contrast to our study of TET in discrete systems carried out thus far, to address passive energy transfers in the beam-NES configuration we needed to carefully study the effect that the location of the NES had on TET efficiency. This is due to the fact that if the NES is attached close to a node of a structural mode of the flexible system, its capacity to passively absorb and dissipate energy from that mode is drastically diminished so TET deteriorates. In this respect, the performance of parametric studies similar to the one presented in this section can help us determine optimal placements of NESs to structural assemblies.

5.2 Rod of Finite Length with SDOF NES

In an effort to extend our study of TET from linear elastic continua to attached NESs we now consider an impulsively forced (dispersive) rod of finite length that rests on a linear elastic foundation and possesses a SDOF NES attached to its end. The results reported in this section are drawn from the works by Georgiades (2006),



(a)



(b)

Fig. 5.5 Case of weak TET to the NES, transient responses of the system with and without NES attached: (a) NES response, (b) beam response at the point of attachment.

Tsakirtzis (2006), Tsakirtzis et al. (2007a) and Panagopoulos et al. (2007), which should be consulted for more details. We mention that a new feature of the analysis presented in this section is the detailed post-processing of the time series of

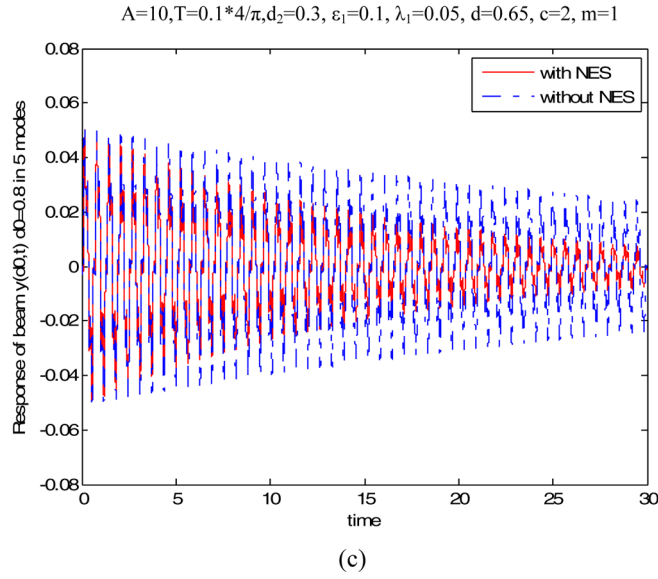


Fig. 5.5 Case of weak TET to the NES, transient responses of the system with and without NES attached: (c) beam response at $x = 0.65$.

the nonlinear dynamical interaction between the NES and the elastic continuum through a combination of numerical wavelet transforms (WTs) and Empirical Mode Decompositions (EMDs). It will be shown that the combination of these numerical transforms will enable us to study in detail the mechanisms governing the strongly nonlinear dynamical interactions and energy exchanges between the rod and the NES. This task will be performed by computing the evolutions of the dominant harmonic components of the corresponding time series, ultimately yielding multi-scale analysis of the transient nonlinear dynamics, and identification of the principal resonance modal interactions that occur between the continuum and the NES that are responsible for TET (or lack of it).

In the following exposition we systematically study passive broadband TET from the linear dispersive rod to the attached ungrounded, strongly (essentially) nonlinear SDOF NES. What distinguishes (and complicates) the present study compared to our studies of discrete oscillators discussed in Chapters 3 and 4, is the fact that due to the essentially nonlinear coupling between the continuum and the NES *there occurs simultaneous nonlinear coupling between the NES and the infinity of modes of the rod*, opening the possibility for transient nonlinear modal interactions of increased complexity. It is precisely this type of complicated nonlinear modal interactions, however, that give rise to TET in the system under consideration.

In the previous section we considered a beam with an attached NES, and demonstrated that strong TET was possible in that system. Moreover, in Vakakis et al. (2004a) the different types of dynamic interactions of a semi-infinite dispersive rod

with a grounded essentially nonlinear attachment were analytically and numerically studied, but no attempt to systematically study TET was undertaken. In that work (which will be reviewed in Section 5.2) it was shown that the attachment initially engages in nonlinear resonance with incoming traveling elastic waves; as the energy of the attachment decreases due to damping and radiation of energy back to the rod, the attachment engages in 1:1 transient resonance capture (TRC) with the in-phase mode of the dispersive rod, leading to TET from the rod to the attachment; further decrease of energy of the NES leads to escape of the dynamics from TRC and appearance of the linearized regime of the motion. No study of the efficiency of TET, however, was undertaken in that work. Nevertheless, the computational and analytical results reported in Vakakis et al. (2004a) reveal that resonant interactions of elastic continua with local essentially nonlinear attachments can give rise to complex resonant phenomena; this can be justified by the observation that *local* essentially nonlinear attachments may introduce *global* changes in the dynamics of the elastic continua to which they are attached.

5.2.1 Formulation of the Problem, Computational Procedure and Post-Processing Algorithms

The system under consideration consists of a linear elastic rod of mass distribution M and length L resting on a linear elastic foundation with distributed stiffness k and distributed viscous damping δ . At its right boundary the rod is coupled to an ungrounded, lightweight end attachment of mass $m \ll M$ by means of an essentially nonlinear cubic stiffness of constant C in parallel to a viscous damper $\varepsilon\lambda$ (see Figure 5.6). The elastic foundation renders the dynamics of the rod *dispersive* and introduces a cut-off frequency; in the frequency spectrum of the corresponding rod of infinite length this frequency separates traveling waves from attenuating waves. As the constant of the elastic foundation tends to zero this cut-off frequency also tends to zero, and the dynamics of the rod become *non-dispersive*. It is assumed that the left boundary of the rod is clamped, that an impulsive force (shock) $F(t)$ is applied at position $x = d$ (where x is measured from the left clamped end of the rod), and that the entire system is initially at rest.

Under these assumptions, the governing equations of motion of the system are expressed as follows:

$$\begin{aligned} EA \frac{\partial^2 u(x, t)}{\partial x^2} - ku(x, t) - \delta \frac{\partial u(x, t)}{\partial t} + F(t)\delta(x - d) \\ - C[u(L, t) - v(t)]^3 \delta(x - L) - \varepsilon\lambda \left[\frac{\partial u(L, t)}{\partial t} - \dot{v}(t) \right] \delta(x - L) \\ = M \frac{\partial^2 u(x, t)}{\partial t^2}, \quad 0 \leq x \leq L \end{aligned}$$

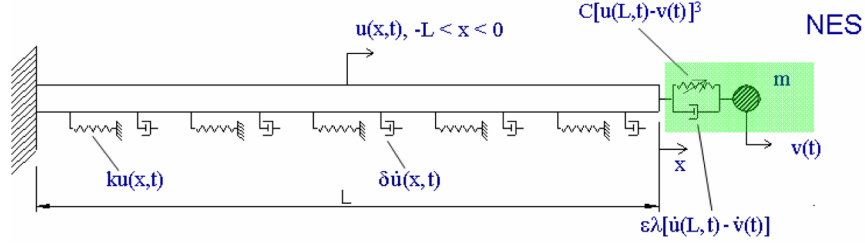


Fig. 5.6 Linear dispersive rod with attached SDOF NES.

Table 5.1 Leading eigenfrequencies of the uncoupled undamped rod ($k = 1$).

Normal Mode	1	2	3	4	5	6	7	8
Eigenfrequency (Hz)	0.29	0.77	1.26	1.76	2.26	2.75	3.25	3.75

$$\begin{aligned}
 u(0, t) &= 0, & C[u(L, t) - v(t)]^3 + \varepsilon\lambda \left[\frac{\partial u(L, t)}{\partial t} - \dot{v}(t) \right] &= m\ddot{v}(t) \\
 u(x, 0) &= 0, & \frac{\partial u(x, 0)}{\partial t} &= 0, & v(0) &= 0, & \dot{v}(0) &= 0
 \end{aligned} \tag{5.9}$$

This an initial value (Cauchy) problem governed by a set of coupled partial and ordinary differential equations, with an essentially nonlinear local element. Clearly, (5.9) represents a well-posed mathematical problem, but no analytic solution for the transient dynamics is possible; hence, one must resort to numerical methods for its solution.

It is emphasized that of interest in this work is the study of the transient nonlinear dynamics of the system, especially, at the initial stage of the motion (i.e., immediately after the imposition of the external shock) where the energy of the system is at its highest and strong nonlinear dynamical interactions between the rod and the NES are anticipated. It is precisely, these strongly nonlinear dynamical interactions that we aim to analyze in detail in this section. In the following numerical simulations the transient dynamics was computed by performing a finite element (FE) discretization of the equations of motion (5.9). The methodology was developed in the thesis by Georgiades (2006) and is reproduced here.

First we mention that the eigenfrequencies of the linear rod on an elastic foundation with no damping and forcing terms, and no NES attached, are given by (in rad/s):

$$\omega_q = \sqrt{(2q - 1)^2 \frac{\pi^2}{4L^2} \frac{EA}{M} + \frac{k}{M}}, \quad q = 1, 2, \dots \tag{5.10}$$

In Table 5.1 we present the leading eigenfrequencies of the uncoupled and undamped rod [with NES detached – expression (5.10)] for parameters $L = 1$, $EA = 1.0$, $M = 1.0$, $\delta = 0.05$, $m = 0.1$, $\varepsilon = 0.1$, $\lambda = 0.5$, and elastic foundation equal to $k = 1$.

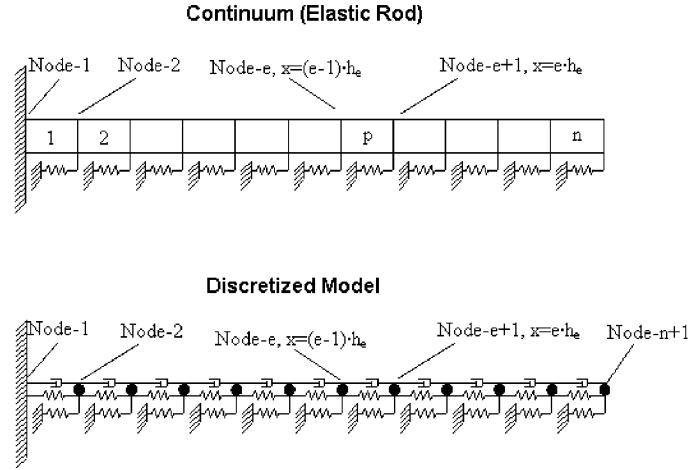


Fig. 5.7 FE discretization of the rod.

To construct the FE model of (5.9) it is necessary to perform the discretization of the continuous part of the system, i.e., the elastic rod this means that the governing partial differential equation of the rod will be approximated by a discrete equation using shape functions. Let us consider that the rod is divided into n elements, each of length h_e (see Figure 5.7); then the displacement field in the p -th element with edges at coordinates x_e and x_{e+1} (with $x_{e+1} - x_e = h_e$) is interpolated by the following formula:

$$u_p(x, t) = \sum_{j=1}^2 u_j(t) \psi_j(x) \quad (5.11)$$

In (5.11), $u_j(t)$ is the axial displacement at each end of the element, and $\psi_j(x)$ are the shape functions (or interpolating functions) of the element. The determination of the shape functions can be performed by assuming that the displacement, although a function of time at each time step of the numerical integration, can be regarded as a constant, and, moreover, that the axial stiffness is constant over the element; then the axial displacement $u_p(x, t)$ is determined by the following procedure. First, the equation satisfied by the axial displacements is given by

$$EA \frac{d^2 u_p(x, t)}{dx^2} = 0, \quad x_e < x < x_{e+1} \quad (5.12)$$

which by double integration leads to

$$u_p(x, t) = c_1(t) + c_2(t)x \quad (5.13)$$

where $c_1(t)$ and $c_2(t)$ are constants of integration (with respect to x). Imposing the boundary conditions at the two end of the element, we obtain the following system

of equations:

$$\begin{aligned} u_p(x_e, t) &= c_1(t) + c_2(t)x_e = e_e(t) \\ u_p(x_{e+1}, t) &= c_1(t) + c_2(t)x_{e+1} = u_{e+1}(t) \end{aligned} \quad (5.14)$$

with solutions

$$c_1(t) = \frac{u_e(t)x_{e+1} - u_{e+1}(t)x_e}{h_e}, \quad c_2(t) = \frac{u_{e+1}(t) - u_e(t)}{h_e} \quad (5.15)$$

These lead to the following expression for (5.13):

$$u_p(x, t) = u_e \left(\frac{x_{e+1} - x}{h_e} \right) + u_{e+1} \left(\frac{x - x_e}{h_e} \right) \quad (5.16)$$

Combining the expressions (5.16) and (5.11), we obtain the following expressions for the shape functions:

$$\psi_1 = \frac{x_{e+1} - x}{x_{e+1} - x_e} = \frac{x_{e+1} - x}{h_e}, \quad \psi_2 = \frac{x - x_e}{x_{e+1} - x_e} = \frac{x - x_e}{h_e} \quad (5.17a)$$

with

$$\frac{d\psi_1}{dx} = -\frac{1}{x_{e+1} - x_e} = -\frac{1}{h_e}, \quad \frac{d\psi_2}{dx} = \frac{1}{x_{e+1} - x_e} = \frac{1}{h_e} \quad (5.17b)$$

There are different ways for discretizing system (5.9), and in the following formulation we use the variational formulation. This method consists in multiplying equation (5.1) with the previous shape functions, and integrating the resulting residual over one element. The overall residual (resulting by superposing the residuals at all nodes in the problem domain) is then assembled and set equal to zero in order to establish the system equation for the entire system (Reddy, 1993; Liu and Quek, 2003).

We start by constructing a local discretized model for the p -th element, by applying the afore-mentioned procedure in the interval $x_e < x < x_{e+1}$:

$$\begin{aligned} EA \frac{\partial^2 u}{\partial x^2} - ku - \delta \frac{\partial u}{\partial t} + F(t)\delta(x - d) &= M \frac{\partial^2 u}{\partial t^2} \\ \Leftrightarrow \int_{x_e}^{x_{e+1}} \begin{bmatrix} \psi_1 \\ \psi_2 \end{bmatrix} \left\{ EA \frac{\partial}{\partial x^2} [\psi_1 \ \psi_2] \begin{bmatrix} u_e \\ u_{e+1} \end{bmatrix} - k [\psi_1 \ \psi_2] \begin{bmatrix} u_e \\ u_{e+1} \end{bmatrix} \right. \\ &\quad \left. - \delta [\psi_1 \ \psi_2] \frac{\partial}{\partial t} \begin{bmatrix} u_e \\ u_{e+1} \end{bmatrix} \right\} \\ &+ \int_{x_e}^{x_{e+1}} \begin{bmatrix} \psi_1 \\ \psi_2 \end{bmatrix} \left\{ F(t)\delta(x - d) - \delta [\psi_1 \ \psi_2] \frac{\partial}{\partial t} \begin{bmatrix} u_e \\ u_{e+1} \end{bmatrix} \right\} \end{aligned}$$

$$- M[\psi_1 \ \psi_2] \frac{\partial^2}{\partial t^2} \begin{bmatrix} u_e \\ u_{e+1} \end{bmatrix} \Bigg\} dx = 0 \quad (5.18)$$

Integrating by parts,

$$\begin{aligned} & \int_{x_e}^{x_{e+1}} \begin{bmatrix} \psi_1 \\ \psi_2 \end{bmatrix} EA \frac{\partial^2}{\partial x^2} EA \frac{\partial^2}{\partial x^2} [\psi_1 \ \psi_2] \begin{bmatrix} u_e \\ u_{e+1} \end{bmatrix} dx \\ &= - \int_{x_e}^{x_{e+1}} EA \frac{\partial}{\partial x} [\psi_1 \ \psi_2] \frac{\partial}{\partial x} [\psi_1 \ \psi_2] \begin{bmatrix} u_e \\ u_{e+1} \end{bmatrix} dx \\ &+ \left[EA \frac{\partial}{\partial x} [\psi_1 \ \psi_2] \begin{bmatrix} u_e \\ u_{e+1} \end{bmatrix} \right]_{x_e}^{x_{e+1}} \end{aligned}$$

and noting that the second term in the above expression vanishes due to (5.17b), the discretized equation assumes the form:

$$\begin{aligned} & \int_{x_e}^{x_{e+1}} \left\{ EA \frac{\partial}{\partial x} \begin{bmatrix} \psi_1 \\ \psi_2 \end{bmatrix} \frac{\partial}{\partial x} [\psi_1 \ \psi_2] \begin{bmatrix} u_e \\ u_{e+1} \end{bmatrix} + k \begin{bmatrix} \psi_1 \\ \psi_2 \end{bmatrix} [\psi_1 \ \psi_2] \begin{bmatrix} u_e \\ u_{e+1} \end{bmatrix} \right. \\ &+ \delta \begin{bmatrix} \psi_1 \\ \psi_2 \end{bmatrix} [\psi_1 \ \psi_2] \frac{\partial}{\partial t} \begin{bmatrix} u_e \\ u_{e+1} \end{bmatrix} \Bigg\} dx \\ &+ \int_{x_e}^{x_{e+1}} \left\{ \delta \begin{bmatrix} \psi_1 \\ \psi_2 \end{bmatrix} [\psi_1 \ \psi_2] \frac{\partial}{\partial t} \begin{bmatrix} u_e \\ u_{e+1} \end{bmatrix} - \begin{bmatrix} \psi_1 \\ \psi_2 \end{bmatrix} F(t) \delta(x-d) \right. \\ &+ M \begin{bmatrix} \psi_1 \\ \psi_2 \end{bmatrix} [\psi_1 \ \psi_2] \frac{\partial^2}{\partial t^2} \begin{bmatrix} u_e \\ u_{e+1} \end{bmatrix} \Bigg\} dx = 0 \quad (5.19) \end{aligned}$$

This leads to the following discrete model for a single element of the linear rod in axial vibration:

$$(K_{el}^1 + K_{el}^2) \begin{Bmatrix} u_e \\ u_{e+1} \end{Bmatrix} + D_{el}^1 \begin{Bmatrix} \dot{u}_e \\ \dot{u}_{e+1} \end{Bmatrix} + M_{el} \begin{Bmatrix} \ddot{u}_e \\ \ddot{u}_{e+1} \end{Bmatrix} = F \quad (5.20)$$

where the elementary structural matrices are defined by:

$$\begin{aligned} K_{el}^1 &= \int_{x_e}^{x_{e+1}} EA \frac{d}{dx} \begin{bmatrix} \psi_1 \\ \psi_2 \end{bmatrix} \frac{d}{dx} [\psi_1 \ \psi_2] dx = \frac{EA}{h_e} \begin{bmatrix} 1 & -1 \\ -1 & 1 \end{bmatrix} \\ K_{el}^2 &= k \int_{x_e}^{x_{e+1}} \frac{d}{dx} \begin{bmatrix} \psi_1 \\ \psi_2 \end{bmatrix} [\psi_1 \ \psi_2] dx = \frac{kh_e}{6} \begin{bmatrix} 2 & 1 \\ 1 & 2 \end{bmatrix} \\ M_{el} &= M \int_{x_e}^{x_{e+1}} \begin{bmatrix} \psi_1 \\ \psi_2 \end{bmatrix} [\psi_1 \ \psi_2] dx = \frac{Mh_e}{6} \begin{bmatrix} 2 & 1 \\ 1 & 2 \end{bmatrix} \end{aligned}$$

$$D_{\text{el}}^1 = \delta \int_{x_e}^{x_{e+1}} \begin{bmatrix} \psi_1 \\ \psi_2 \end{bmatrix} [\psi_1 \ \psi_2] dx = \frac{\delta h_e}{6} \begin{bmatrix} 2 & 1 \\ 1 & 2 \end{bmatrix}, \quad F = F(t) \begin{bmatrix} \delta(x-d) \\ \delta(x-d) \end{bmatrix}$$

These elementary structural matrices are assembled into an integrated model, which, when the NES is added, leads to the following global discretized model of system (5.9):

$$(K^1 + K^2) \begin{Bmatrix} u \\ v \end{Bmatrix} + D \begin{Bmatrix} \dot{u} \\ \dot{v} \end{Bmatrix} + M \begin{Bmatrix} \ddot{u} \\ \ddot{v} \end{Bmatrix} + F_{\text{NES}} = F \quad (5.21)$$

Considering n discrete elements for the clamped-free rod, the response vectors u , \dot{u} and \ddot{u} are $(n-1) \times 1$ vectors containing the displacements, velocities and accelerations of the nodes of the rod, respectively; v denotes the (scalar) displacement of the NES; and the global system matrices in (5.21) with NES attached at the free end of rod are given by

$$K^1 = \frac{EA}{h_e} \begin{bmatrix} 2 & -1 & 0 & \cdot & \cdot & \cdot & 0 \\ -1 & 2 & -1 & 0 & & & \cdot \\ 0 & -1 & \cdot & & & & \cdot \\ \cdot & 0 & \cdot & & & & \cdot \\ \cdot & & & & -1 & 0 & \\ \cdot & & & & -1 & 1 & 0 \\ 0 & \cdot & \cdot & \cdot & 0 & 0 & 0 \end{bmatrix}_{(n \times n)} \quad (5.22a)$$

$$K^2 = \frac{kh_e}{6} \begin{bmatrix} 4 & 1 & 0 & \cdot & \cdot & \cdot & 0 \\ 1 & 4 & 1 & 0 & & & \cdot \\ 0 & 1 & \cdot & & & & \cdot \\ \cdot & 0 & \cdot & & & & \cdot \\ \cdot & & & & 1 & 0 & \\ \cdot & & & & 1 & 2 & 0 \\ 0 & \cdot & \cdot & \cdot & 0 & 0 & 0 \end{bmatrix}_{(n \times n)} \quad (5.22b)$$

$$M = \frac{Mh_e}{6} \begin{bmatrix} 4 & 1 & 0 & \cdot & \cdot & \cdot & 0 \\ 1 & 4 & 1 & 0 & & & \cdot \\ 0 & 1 & \cdot & & & & \cdot \\ \cdot & 0 & \cdot & & & & \cdot \\ \cdot & & & & 1 & 0 & \\ \cdot & & & & 2 & 0 & \\ 0 & \cdot & \cdot & \cdot & 0 & 0 & 0 \end{bmatrix}_{(n \times n)} + \begin{bmatrix} 0 & \cdot & \cdot & \cdot & 0 \\ \cdot & \cdot & \cdot & \cdot & \cdot \\ \cdot & \cdot & \cdot & \cdot & \cdot \\ \cdot & \cdot & 0 & 0 & \\ 0 & \cdot & \cdot & 0 & m_{\text{NES}} \end{bmatrix}_{(n \times n)} \quad (5.22c)$$

$$D = \frac{\partial h_e}{6} \begin{bmatrix} 4 & 1 & 0 & \dots & \dots & 0 \\ 1 & 4 & 1 & 0 & & \\ 0 & 1 & \dots & & & \\ \dots & 0 & \dots & & & \\ \dots & & & & 2 & 0 \\ 0 & \dots & \dots & 0 & 0 & 0 \end{bmatrix}_{(n \times n)} + \varepsilon \lambda \begin{bmatrix} 0 & 0 & 0 & \dots & \dots & 0 \\ 0 & 0 & 0 & 0 & & \\ 0 & 0 & \dots & & & \\ \dots & 0 & \dots & & & \\ \dots & & & & & 0 \\ \dots & & & & 1 & -1 \\ 0 & \dots & \dots & 0 & -1 & 1 \end{bmatrix}_{(n \times n)} \quad (5.22d)$$

The coupling of the NES with the rod is incorporated in the global model with the following vector,

$$F_{\text{NES}} = \begin{bmatrix} 0 & \dots & 0 & 0 \\ 0 & \dots & & \\ \dots & \dots & & \\ \dots & \dots & & \\ \dots & \dots & 0 & C & 0 \\ 0 & \dots & 0 & -C \end{bmatrix}_{(n \times n)} \begin{Bmatrix} 0 \\ \dots \\ \dots \\ (u_{n-1} - v)^3 \\ (u_{n-1} - v)^3 \end{Bmatrix}_{(n \times 1) \times 1} \quad (5.22e)$$

and, since the excitation is a point force applied at $x = d$ corresponding to the k -th node of the FE discretization, the excitation vector in (5.21) is given by:

$$F = \begin{bmatrix} 0 & \dots & 0 & \underbrace{F(t)}_{k\text{-th position}} & 0 & \dots & 0 \end{bmatrix}_{(n-1) \times 1}^T \quad (5.22f)$$

The discrete equation (5.21) has been integrated using the adaptive Newmark Algorithm (Geradin and Rixen, 1997). As an excitation of the rod, the following impulsive half-sine pulse is considered:

$$F(t) = \begin{cases} A \sin(2\pi \tau / T), & 0 \leq \tau \leq T/2 \\ 0, & t > T/2 \end{cases} \quad (5.23)$$

with varying amplitude A and period $T = 0.1T_1$, where T_1 is the period of the first mode of the linear rod with no NES attached; this assures that the impulsive excitation is of sufficiently small duration compared to the characteristic time scale of the system T_1 . The shock is applied at position $d = 0.3$ on the rod (see Figure 5.6), and the system parameters were assigned the numerical values,

$$L = 1, \quad EA = 1.0, \quad M = 1.0, \quad \delta = 0.05, \quad m = 0.1, \quad \varepsilon = 0.1, \quad \lambda = 0.5$$

In the performed simulations the results are post-processed by computing a set of energy measures, in order to study the energy absorbed and dissipated in the NES attachment, as well as the energy exchanges between the NES and the rod during their transient nonlinear interaction. Post-processing of the numerically computed

time series of the rod and the NES was performed in two different ways. First, we perform a spectral analysis of the computed time series by employing numerical Wavelet Transforms (WTs), and constructing numerical WT spectra of the responses. As explained in Section 2.5, WT spectra enable one to determine accurately the dominant frequency components in the transient responses, and, in addition, to study the evolutions of these dominant harmonic components in time. Such wavelet spectra enable one to better understand the ‘slow flow’ dynamics of the studied rod-NES interactions.

In an alternative approach, the time series were analyzed by Empirical Mode Decomposition (EMD) (see Section 2.5). Through this numerical algorithm one decomposes the computed time series (signals) in terms of intrinsic mode functions (IMFs) which can be regarded as oscillatory modes embedded in the signal. By construction, the superposition of all IMFs regenerates the signal. Further analyzing the IMFs by means of the Hilbert Transform one determines the dominant frequency components of the IMFs, which, when compared to the corresponding WT spectra, enables one to examine in detail the resonant dynamic interactions that occur between the rod and the NES. The nonlinearity and the non-stationarity of the computed transient signals force us to combine both mentioned techniques for post-processing of the data.

The initial step of the post-processing analysis, however, is to introduce certain energy measures. These were first introduced by Georgiades (2006). Certain of these measures help us assess the accuracy of the numerical simulations: indeed, the total energy of the system – including the energy dissipated by the dampers – should be approximately preserved, not only at each time step of the numerical integration, but also for the entire time window of the numerical simulation. Additional energy measures enable us to study carefully the energy exchanges that occur between the rod and the NES; as shown below, by constructing energy transaction histories between the rod and the NES, we are able to identify the distinct dynamical mechanisms that govern TET (i.e., nonlinear beats, irreversible, one-way TET, or a combination of the two). It is interesting to note that the aforementioned energy exchange mechanisms can be eventually related to the results of WT and EMD of the computed time series of the rod and NES responses.

The normalized energy dissipated by the damper of the NES at time t , is computed by the following EDM,

$$E_{\text{NES}(t)} = \frac{\varepsilon \lambda \int_0^t [\dot{u}(L, \tau) - \dot{v}(\tau)]^2 d\tau}{\frac{1}{2} \int_0^t F(t) \dot{u}(d, t) dt} \times 100 \quad (5.24)$$

which is the percentage of impulsive energy applied to the rod that is dissipated by the damper of the NES up to time t . For the passive system considered here this EDM reaches a definitive asymptotic limit with increasing time, $E_{\text{NES}, t \gg 1} = \lim_{t \gg 1} E_{\text{NES}}(t)$. This represents the percentage of impulsive energy that is eventually dissipated by the NES during the entire duration of the motion.

For each simulation we estimate the normalized total dissipated energy over the entire duration of the motion, which, to ensure accuracy of the FE simulation, should be approximately equal to unity:

$$\eta_{\text{total}}(t) \equiv \lim_{t \gg 1} \frac{E_{\text{damp,NES}}(t) + E_{\text{damp,rod}}(t)}{E_{\text{in}}} \approx 1 \quad (5.25)$$

In (5.25), $E_{\text{damp,NES}}(t)$ and $E_{\text{damp,rod}}(t)$ are the energies dissipated by the NES and the rod up to time t , respectively, whereas E_{in} is the input impulsive energy. By ensuring that this ratio assumes numerical values close to unity, we also ensure that the FE simulation is performed for a sufficiently large time interval, so that no essential transient dynamics is omitted from the time window of the numerical study. Additional energy measures utilized to check the accuracy of the simulations are discussed in Georgiades (1996).

An additional important energy measure computes the instantaneous transaction of energy between the rod and the NES. Assuming that the NES is an open system that exchanges continuously energy with the rod (through energy absorption from incoming waves or energy backscattering to the rod), one defines the following Energy Transaction Measure (ETM), E_{Trans} , between the NES and the rod:

$$E_{\text{Trans}} = \Delta E_{k,\text{NES}} + \Delta E_{d,\text{NES}} + \Delta E_{\text{damp,NES}} \quad (5.26)$$

In the above relation Δ denotes the corresponding energy difference between two subsequent time steps; $E_{k,\text{NES}}(t) = (1/2)m\dot{v}^2(t)$ is the instantaneous kinetic energy and $E_{d,\text{NES}}(t) = (1/4)C[u(L, t) - v(t)]^4$ the instantaneous potential energy of the NES; whereas

$$E_{\text{damp,NES}}(t) = \varepsilon\lambda \int_0^t [\dot{u}(L, \tau) - \dot{v}(\tau)]^2 d\tau$$

is the energy dissipated by the damper of the NES up to the time instant t . The ETM is an important energy measure from a physical point of view, since it helps one identify instantaneous inflow or outflow of energy from the rod to the NES or vice versa; in particular, when there is inflow from the rod to the NES, it holds that $E_{\text{Trans}} > 0$, whereas, negative values of the ETM ($E_{\text{Trans}} < 0$) correspond to backscattering of energy from the NES to the rod. Moreover, in the limit when the time step Δt of the numerical simulation tends to zero, the ratio $E_{\text{Trans}}/\Delta t$ represents the instantaneous power inflow to or outflow between the rod and the NES.

Clearly, *efficient TET from the rod to the NES is signified by strong positive energy transactions ($E_{\text{Trans}} > 0$) throughout the transient response of the system, but especially in the initial regime of the motion (i.e., immediately after the imposition of the external shock), when the energy of the system is at its highest level.* In cases where there are only positive spikes of the ETM, there occurs irreversible energy transfer from the rod to the NES, that is, energy is continuously transferred from the rod to the NES where it is eventually dissipated by viscous damping. This optimal scenario for TET will be designated as *irreversible TET*.

As shown below, there are alternative, non-optimal TET scenarios corresponding to different types of energy transactions between the rod and the NES. For example, it is possible to obtain *TET through nonlinear beats*, corresponding to alternating series of positive and negative spikes in the energy transaction between the rod and the NES. This indicates that energy flows back and forth from the rod to the NES, with the overall average of the ETM E_{Trans} being positive; in this case the NES backscatters significant portions of energy back to the rod, but, on the average, it absorbs and dissipates a certain portion of the input energy of the rod. Finally, it is possible to obtain a combination of the aforementioned energy transaction scenarios, i.e., an initial stage of irreversible TET, followed by a regime of TET through nonlinear beats.

Finally, we make some remarks concerning the post-processing of the numerical results through WT and EMD. In the following numerical simulations we will be interested mainly in the high-energy transient dynamics at the early stage of the response, i.e., immediately after the imposition of the external shock. Therefore, in certain cases we will need to divide the time series into early and late parts, since, as the amplitudes of the responses get smaller due to damping dissipation the corresponding numerical wavelet traces are too light to be tracable. As in Chapters 3 and 4, the WT spectra will be employed to study the temporal evolutions of the dominant frequency components of the time series, as well as the nonlinear modal interactions occurring between the rod and the NES. One disadvantage of the WT compared to the EMD is its ineffectiveness to detect complex details of the time series, such as, intrawaves in the nonlinear signals, i.e., oscillatory components of the time series possessing frequency components that vary rapidly within a characteristic period. This is one of the reasons that EMD is employed as an alternative tool for the post-processing the numerical time series.

As discussed in Section 2.5, EMD provides the characteristic time scales of the dominant nonlinear dynamics of the rod-NES interaction. Moreover, by adopting this analysis one can identify and analyze the most important nonlinear resonance interactions between the rod and the NES which are responsible for the nonlinear energy exchanges between these two subsystems. To this end, we say that a *k:m transient resonance capture* (TRC) occurs between the IMF $c_1(t)$ of the rod, and the IMF $c_2(t)$ of the NES (with corresponding phases $\varphi_1(t)$ and $\varphi_2(t)$, respectively), whenever their instantaneous frequencies satisfy the following approximate relation:

$$k\dot{\varphi}_1(t) - m\dot{\varphi}_2(t) \approx \text{const}, \quad \text{for } t \in [T_1, T_2]$$

The time interval $[T_1, T_2]$ defines the duration of the said TRC. A more complete picture of the TRC between the two mentioned IMFs can be gained by constructing appropriate phase plots that involve the phase difference $\Delta\varphi_{12}(t) \approx \varphi_1(t) - \varphi_2(t)$ and its time derivative. More specifically, a TRC is signified by the existence of a small loop in the phase plot of $\Delta\varphi_{12}(t)$ versus $\Delta\dot{\varphi}_{12}(t)$; whereas absence of (or escape from) TRC is signified by time-like (that is, monotonically varying) behavior of $\Delta\varphi_{12}(t)$ and $\Delta\dot{\varphi}_{12}(t)$. In addition, the ratio of instantaneous frequencies of the IMFs, $\dot{\varphi}_1(t)/\dot{\varphi}_2(t)$, provides a confirmation of the order of the *k:m* TRC.

It is precisely these features that make EMD useful for studying the strongly nonlinear transient problem considered in this section. Indeed, the decomposition of the rod and NES transient responses in terms of their oscillatory components (the IMFs), and the subsequent computation of their instantaneous frequencies, provide a useful tool for studying nonlinear resonant interactions between the NES and the modes of the rod. In what follows we provide results of this analysis.

5.2.2 Computational Study of TET

In Georgiades (1996) four main sets of FE simulations were performed for the system parameters and the half-sine applied external shock defined in the previous section. What distinguished the first and second sets of FE simulations was the different parameter values for the elastic foundation of the rod, k , the NES stiffness, C , and the magnitude of the applied shock, A . Specifically, the first set of simulations was performed for a dispersive rod with fixed distributed elastic foundation $k = 1.0$, for 22 values of the nonlinear characteristic in the range $C \in [0.001, 20]$, and 15 values of the shock amplitude in the range $A \in [0, 500]$. This gave a total of $22 \times 15 = 330$ possible pairs (C, A) , all of which were simulated in the first series. Similarly, the second set of numerical simulations involved the same 330 numerical simulations but for an elastic foundation with $k = 0$, corresponding to a non-dispersive rod. Each of the transient simulations of the first two series was performed for a sufficiently large time interval, so that at the end of the simulation at least 99% of the input shock energy was damped by the distributed viscous damping of the rod and the discrete viscous damper of the NES.

The numerical study has multiple objectives. The first objective is to study the ranges of parameters for which the NES is capable of passively absorbing and locally dissipating a significant portion of the shock energy applied to the rod, and, in addition, to investigate robustness of the NES performance to certain parameter variations. The second objective is to study the dynamical mechanisms that influence TET from the rod to the NES, and in the way, to determine the most favorable conditions for the realization of strong TET. An additional objective is to analyze in detail the TRCs between the NES and the rod responsible for TET (and the characteristic time scales of these interactions) through the use of WTs and EMD.

In Figure 5.8 we depict the contour plot of the EDM $E_{NES, t \gg 1}$, as function of the parameters C and A for the FE simulations corresponding to the dispersive rod, $k = 1$ (the results corresponding to the non-dispersive rod $k = 0$ can be found in Georgiades (2006) and Georgiades et al. (2007)). In the remainder of this work, whenever we mention ‘the EDM’, we will be referring to the asymptotic value $E_{NES, t \gg 1}$. Regions of the plot where the EDM is relatively large correspond to strong TET from the rod to the NES, indicating that a significant percentage of the shock energy of the rod is eventually absorbed and dissipated by the NES. These numerical results reveal that when strong shocks are applied, enhanced TET occurs (with more than 75% of shock energy eventually dissipated by the NES) when the essential

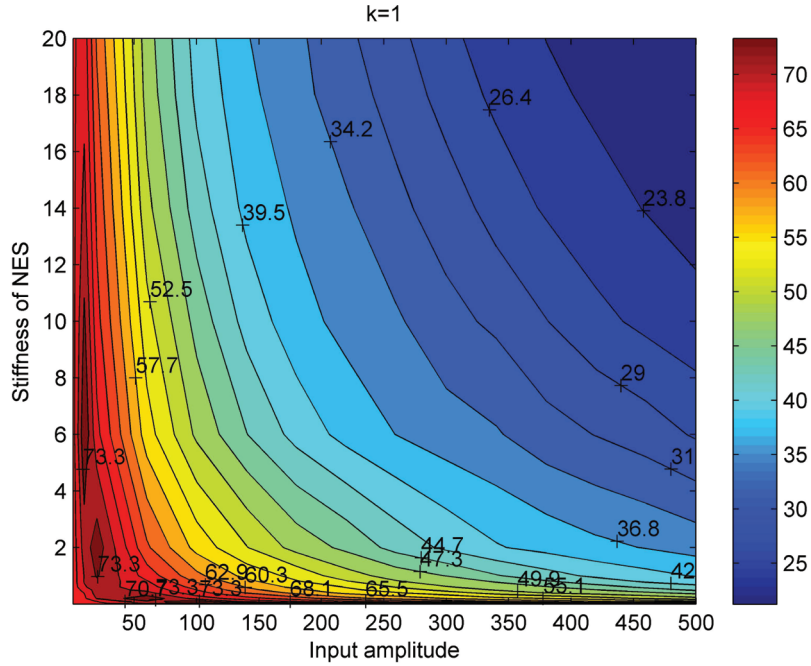


Fig. 5.8 Contour plot of the percentage of shock energy eventually dissipated by the NES, $E_{NES, t \gg 1}$, as function of the nonlinear stiffness, C , and the shock amplitude, A , for a dispersive rod ($k = 1$).

stiffness nonlinearity is relatively weak. By contrast, when smaller shocks are applied, strong TET occurs (corresponding to $E_{NES, t \gg 1} > 75\%$) over a wide range of values of the essentially nonlinear stiffness of the NES. This should be expected, since when the energy is high, a stiff essential nonlinearity amounts to a near-rigid connection between the rod and the NES, yielding small relative velocities across the NES damper, and, hence, small energy dissipation by the NES.

In an additional set of FE simulations four distinct values of the nonlinear stiffness of the NES are considered, namely, $C = 0.004, 0.01, 2.0, 10.0$, for varying mass of the NES in the range $m \in [0.01, 0.1]$ (for a total of 11 values), and shock amplitude in the range $A \in [1, 420]$ (for a total of 13 values). Therefore for each value of C there were $11 \times 13 = 143$ possible pairs (m, A) , all of which were realized in the numerical simulations. Again, to ensure that the numerical integration was of sufficient duration, an additional requirement was imposed, namely that at least 99% of the shock energy should be dissipated at the end of each of FE simulation. In Figure 5.9 we depict the EDM as function of the NES mass m and the shock amplitude A for four chosen values of the nonlinear stiffness characteristic ($C = 0.004, 0.01, 2.0, 10.0$), and a dispersive rod ($k = 1$). As in Figure 5.8, we deduce that there are parameter regions where strong TET from the rod to the NES

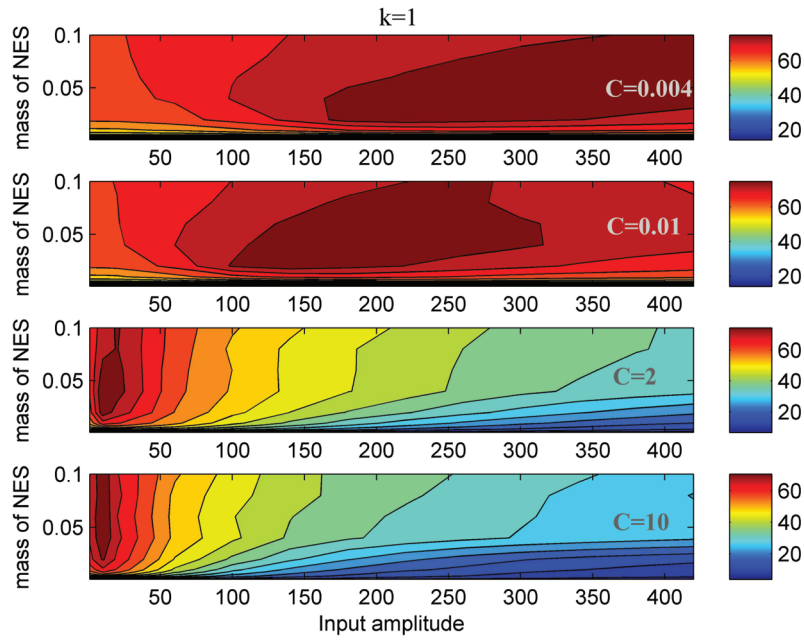


Fig. 5.9 Contour plots of the percentage of shock energy eventually dissipated by the NES, $E_{NES,t>1}$, as function of the NES mass m , and the shock amplitude A for four different values of the nonlinear stiffness C , and a dispersive rod ($k = 1$).

is realized. Moreover, as the value of the nonlinear stiffness characteristic increases the region of strong TET shifts to smaller shock amplitudes and becomes narrower. In addition, in parameter ranges where relatively strong TET occurs there appears to be nearly negligible dependence of the EDM on the NES mass for values of $m > 0.02$.

These results indicate that the NES can be designed to passively absorb and locally dissipate a significant portion of the applied (broadband) shock energy of the rod. Moreover, the NES can be designed so that the passive TET from the rod to the NES is *both strong and robust* to small changes in the impulsive energy and the system parameters. These results demonstrate the efficacy of using lightweight essentially nonlinear local attachments as passive absorbers and local energy dissipaters of broadband energy from elastic continua. This result extends the results reported in previous chapters where discrete linear oscillators with local essentially nonlinear attachments were studied.

We now proceed to a detailed analysis of the dynamics governing TET from the rod to the NES in the system of Figure 5.6. Considering the dispersive rod with $k = 1$, 21 FE simulations [termed from now on ‘Applications’ (Georgiades, 2006)] were considered for the system whose TET plot is depicted in Figure 5.8. In Table 5.2 we present the system parameters used for each application, together with

Table 5.2 FE simulations of the system whose TET plot appears in Figure 5.8.

FE Simulation – Application No.	Phenomena	Group	C	A	$E_{\text{NES}, t \gg 1}$ (%)
1	B	b	0.02	180	76
2	B-I	b	0.004	180	72
3	B	a	6	10	76
4	B	a	9	10	74
5	B	a	2	20	75
6	B	c	5	50	60
7	B	c	5	100	51
8	I	a	0.01	20	67
9	B	b	0.01	260	76
10	B	b	0.005	400	75
11	B	b	0.02	200	75
12	B	b	0.06	100	76
13	B	c	0.08	420	60
14	B	b	0.09	100	74
15	B	b	0.1	60	74
16	B	c	0.2	460	52
17	B-I	a	0.8	10	71
18	B	c	0.8	180	56
19	B-I	a	5	3	69
20	I	a	0.2	5	67
21	B	c	20	500	21

the corresponding EDMs and the characterization of the corresponding dynamical phenomena. ‘B’ indicates the occurrence of *nonlinear beat phenomena* in the transient responses of the rod and the NES. ‘I’ indicates irreversible (one-way) energy transfer from the rod to the NES; we note, however, even in these cases there exists an initial region, albeit small, where very early nonlinear beat phenomena occur, so we may designate the phenomenon as being *predominantly irreversible energy transfer*. Finally, the designation ‘B-I’ indicates early nonlinear beat phenomena in the transient dynamics, followed by irreversible energy transfer from the rod to the NES. These designations refer to the previous discussion regarding energy transactions between the linear and nonlinear components of the system considered.

A simple comparison of the different applications listed in Table 5.2 reveals that, with the exception of Applications 7, 16, and 21, all applications correspond to rather strong TET, since a major part of the input (broadband) vibration energy in the rod is passively absorbed and dissipated by the NES. This observation is in itself interesting since it shows that strong TET in the system under consideration occurs over wide combinations of input energy and system parameters. It follows that comparisons of TET efficiency between different applications can only be performed on a *relative* basis, and in that context the EDM can only be considered as a relative indicator of TET efficiency. Specific examples for all three types of the afore-mentioned dynamical mechanisms (‘B’, ‘B-I’ and ‘I’) are discussed below.

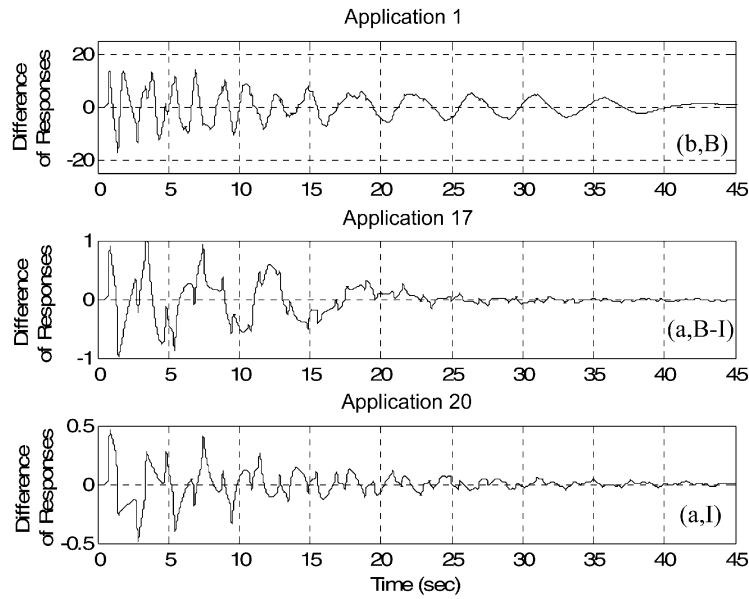


Fig. 5.10 Relative responses between the end of the rod and the NES for Applications 1, 17, 20 (see Table 5.2).

The applications listed in Table 5.2 are partitioned into three main groups. Group (a) consists of Applications 3, 4, 5, 8, 17, 19 and 20 with relatively strong TET from the rod to the NES, corresponding to relatively small input energies (shocks). All three dynamical mechanisms (B, I, and B-I) are realized in the applications of Group (a). The second group of Applications 1, 2, 9, 10, 11, 12, 14 and 15 [labeled as Group (b)] is again characterized by relatively strong TET, but corresponds to higher levels of input energy; these applications involve the dynamical mechanisms B and B-I. Finally, Group (c) consists of Applications 6, 7, 13, 16, 18 and 21 with relatively weak energy transfers, and higher levels of input energy; all applications in this group are characterized by persistent nonlinear beat phenomena (mechanism B), involving continuous energy exchanges between the rod and the NES.

Typical transient relative displacements of the NES with respect to the edge of the rod are presented in Figures 5.10 and 5.11. In each of these plots (as in the ones that follow), each application is characterized by its group and the governing dynamical mechanism; for example, in Figure 5.10 Application 1 is labeled by (b, B), and so on. The measure of relative displacement between the NES and the edge of the rod affects directly the efficiency of TET, since the capacity of the NES to dissipate energy transferred from the rod is directly related to the relative velocity across its viscous damper. It follows that enhanced energy dissipation by the NES is realized when this relative displacement (and its time derivative) attains large magnitudes, especially in the critical initial regime of the motion where the energy is still relatively large (and energy dissipation due to damping in the rod is still small).

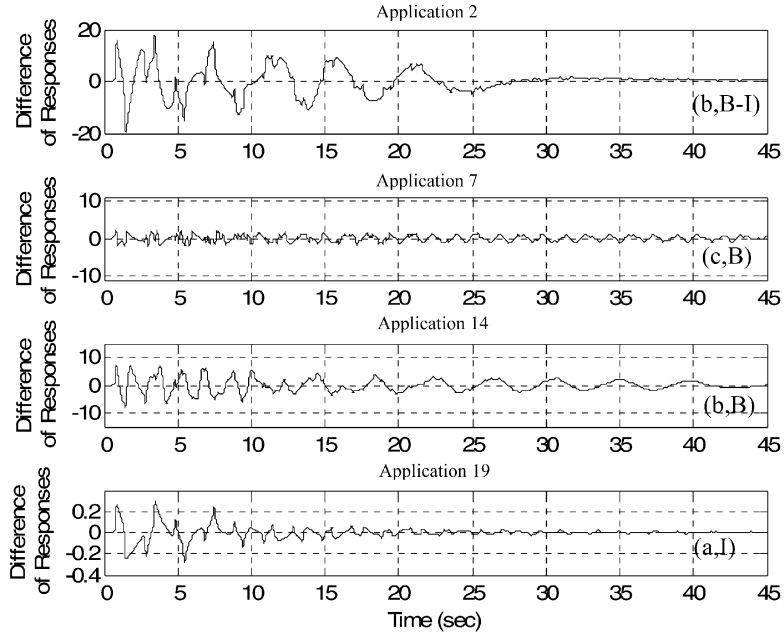


Fig. 5.11 Relative responses between the end of the rod and the NES for Applications 2, 7, 14, 19 (see Table 5.2).

Examples of cases where large, early relative displacement between the rod and the NES occur are Applications 1 (Figure 5.10) and 2 (see Figure 5.11) with corresponding dissipation measures $E_{\text{NES}, t \gg 1} = 76\%$ and 72% , respectively; whereas an example where small relative displacement occurs is Application 7 (Figure 5.11) corresponding to $E_{\text{NES}, t \gg 1} = 51\%$.

An interesting feature of the NES is its capacity to interact with more than one structural modes of the rod (this is done sequentially through resonance capture cascades – RCCs, see below). Indeed, due to the essential coupling nonlinearity, the NES is simultaneously ‘coupled’ to all modes of the rod [as can be realized from the differential equations (5.9)], so it has the capacity to nonlinearly resonate with structural modes over wide frequency ranges, provided, of course, that the initial conditions are appropriate. Such multi-modal and multi-frequency interactions of the NES with the rod may lead to multi-frequency energy pumping and complex dynamic phenomena, such as, abrupt transitions between different dynamical regimes. These interactions become apparent in the WT spectra of the dynamics, although in some cases they may be visible in the time series themselves. For instance, in Figure 5.10 – Application 1 the frequency content of the NES is rich, and the RCC is evident; this is also the case in Figure 5.11 – Application 14.

A useful computational tool for studying the nonlinear dynamic interaction between the rod and the NES is the study of the transient energy transaction history

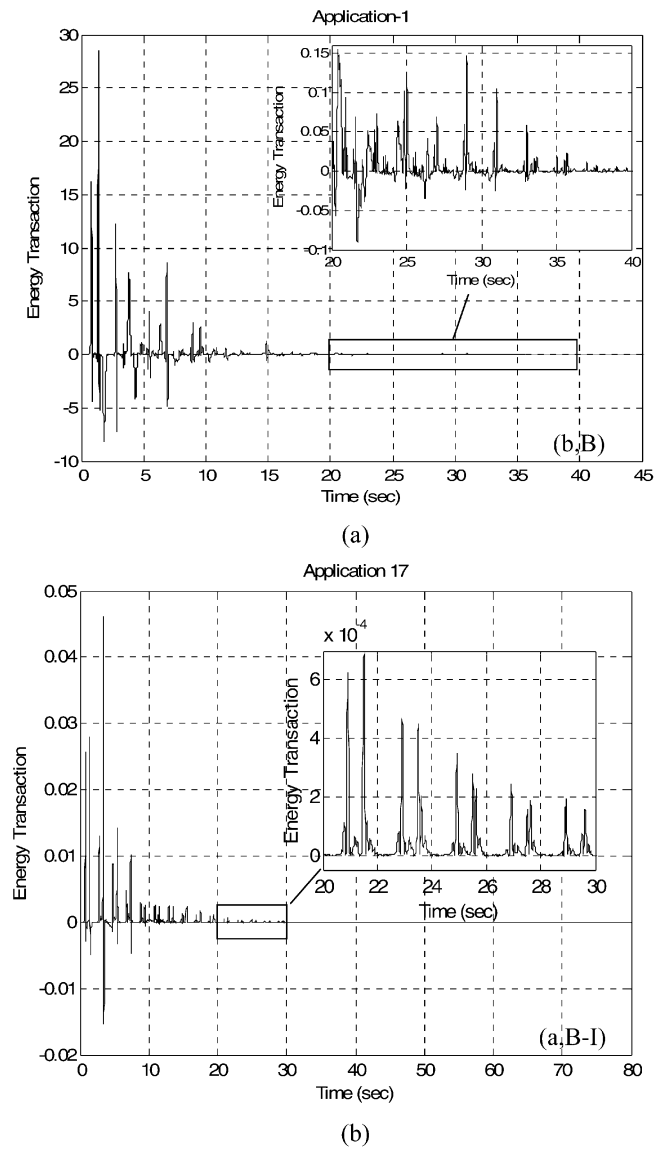


Fig. 5.12 Case of strong TET, ETMs between the rod and the NES for (a) Application 1 (case 'B', nonlinear beats); (b) Application 17 (case 'B-I', initial nonlinear beats followed by irreversible energy transfer).

between these two subsystems. In Figures 5.12a, b we depict the energy transaction histories between the NES and the rod for Applications 1 and 17, where strong TET from the rod to the NES occurs (76% of shock energy dissipated by the NES in Ap-

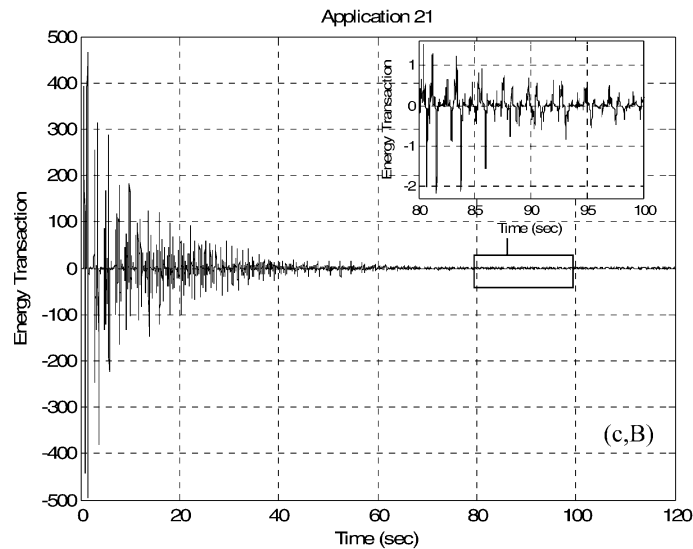
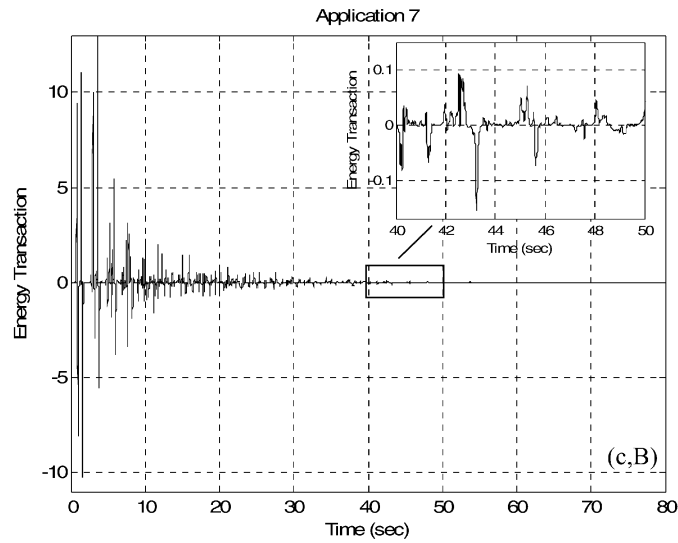


Fig. 5.13 Case of weak TET, ETMs between the rod and the NES for (a) Application 7 (case 'B', nonlinear beats); (b) Application 21 (case 'B', nonlinear beats).

plication 1, and 71% in Application 17) (Georgiades, 2006). In these plots we note the strong positive spikes of energy transmission from the rod to the NES and the small negative spikes of energy backscattered from the NES to the rod; this explains

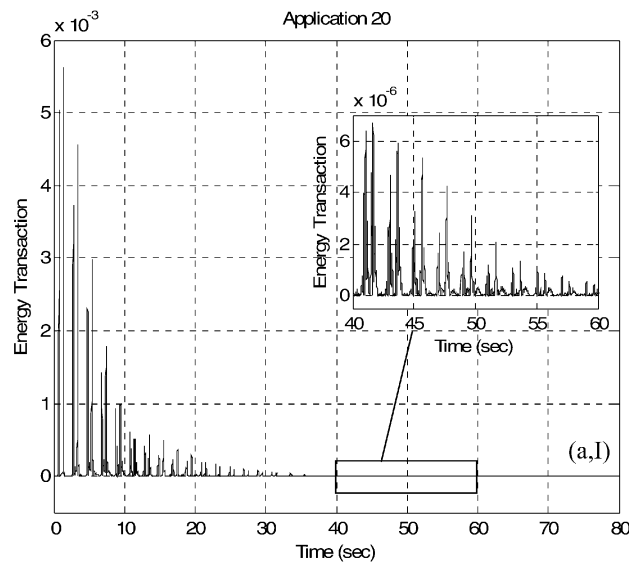


Fig. 5.14 Case of strong TET, ETMs between the rod and the NES for Application 21 (case ‘I’, irreversible energy transfer).

the relatively high values of the EDM realized in these applications. In addition, in both applications there is a positive net balance of energy transferred from the rod to the NES during the critical early regime of the response where the overall energy of the motion is relatively high. In Figures 5.13a, b we depict the energy transaction histories for two applications (7 and 21) corresponding to relatively weak TET (51% of shock energy eventually dissipated by the NES in Application 7, and 21% in Application 21); in these simulations we note that strong backscattering of energy from the NES to the rod occurs, which explains the corresponding weaker energy transfers.

An alternating series of positive and negative spikes of energy transfers is an indication that nonlinear beat phenomena between the rod and the NES occur (dynamical mechanism ‘B’ in Table 5.2). This is especially evident in the energy transaction history of Application 1 (see Figure 5.12a), where nonlinear beat phenomena with strong positive spikes are clearly detected. In Application 17 (see Figure 5.12b) the series of strong initial nonlinear beats is followed by irreversible (one-way) energy transfer (dynamical mechanism I in Table 5.2) from the rod to the NES, as evidenced by the late series of positive – only energy spikes. Similar persisting nonlinear beats are observed in the energy transaction histories depicted in Figures 5.13a, b where applications with relatively weaker TET are depicted. The distinctive feature of the beats in these cases is that the negative and positive energy spikes are of comparable magnitudes, preventing strong ‘flow of energy’ from the rod to the NES. In Figure 5.14 we depict the energy transaction for Application 20 where irreversible

energy transfer from the rod to the NES occurs right from the beginning of the dynamics, and nonlinear beat phenomena are completely absent; indeed, in Applications 8 and 20 there is only irreversible ‘flow of energy’ from rod to the NES, where the energy is localized to the NES and dissipated by the NES damper. The resulting TET is relatively strong in this case, and comparable to the strong TET realized in applications governed by the dynamical mechanisms B and B-I.

In all considered simulations, the energy exchanges between the rod and the NES are realized in the form of spikes, which reflects the fact that the external excitation itself is in the form of a spike (short pulse); this generates forward- and backward-propagating pulses in the rod which are either reflected at the left (clamped) boundary of the rod, or are partially reflected and transmitted into the NES at its right boundary. Numerical plots such as the ones depicted in Figures 5.12–5.14 enable one to study in detail the transient energy exchanges between the rod and the NES, and, more importantly, to determine the dynamical mechanisms that govern these energy exchanges. In addition, it is possible to deduce the precise time windows of the dynamics where, either strong TET to the rod, or backscattering of energy from the NES back to the rod take place. In the following study we relate the previous energy transaction histories to the TRCs that take place due to nonlinear modal interactions between the rod and the NES.

In Figure 5.15 we depict the WT spectra of the relative transient responses between the edge of the rod (from now referred to as ‘the rod’) and the NES, for four cases where either strong TET occurs [cases (a, B-I) – Application 17; (a, B) – Application 1; and (a, I) – Application 20] or weaker TET is realized [case (c, B) – Application 7]. The WT spectra reveal the dominant frequency components of the corresponding responses, as well as their temporal evolutions with decreasing energy due to damping dissipation. Considering Application 17 [case (a, B-I)] where strong TET from the rod to the NES occurs (see Figure 5.15c), we observe early (i.e., high energy) transient resonant interactions of the NES with predominantly the first and second modes of the rod, as well as a weaker early NES resonant interaction with the third mode of the rod; all these early interactions are realized in the form of nonlinear beats. Moreover, we observe a nonlinear transient capture of the dominant frequency component of the dynamics by a nonlinear mode whose frequency shifts below the first linearized mode of the rod. During this low-frequency transition the dynamics localizes gradually to the NES with decreasing energy; similar transitions were detected in previous chapters (see also Lee et al., (2005; Kerschen et al., 2005) in the dynamics of discrete linear oscillators coupled to NESs. The aforementioned early resonant interactions explain the nonlinear beats observed in the early response regime (mechanism ‘B’), whereas the low frequency transition of the dominant harmonic yields one-way irreversible energy transfers from the rod to the NES (mechanism ‘I’) in this application.

Similar transient capture of the dynamics by a nonlinear mode is deduced in the WT spectrum of Figure 5.15a [Application 1 – (a, B)], however, in this case the frequency variation of the nonlinear mode (dominant harmonic) takes place in between the first and second eigenfrequencies of the rod. Similarly to Application 17 (Figure 5.15c) this transition yields strong TET from the rod to the NES. Additional

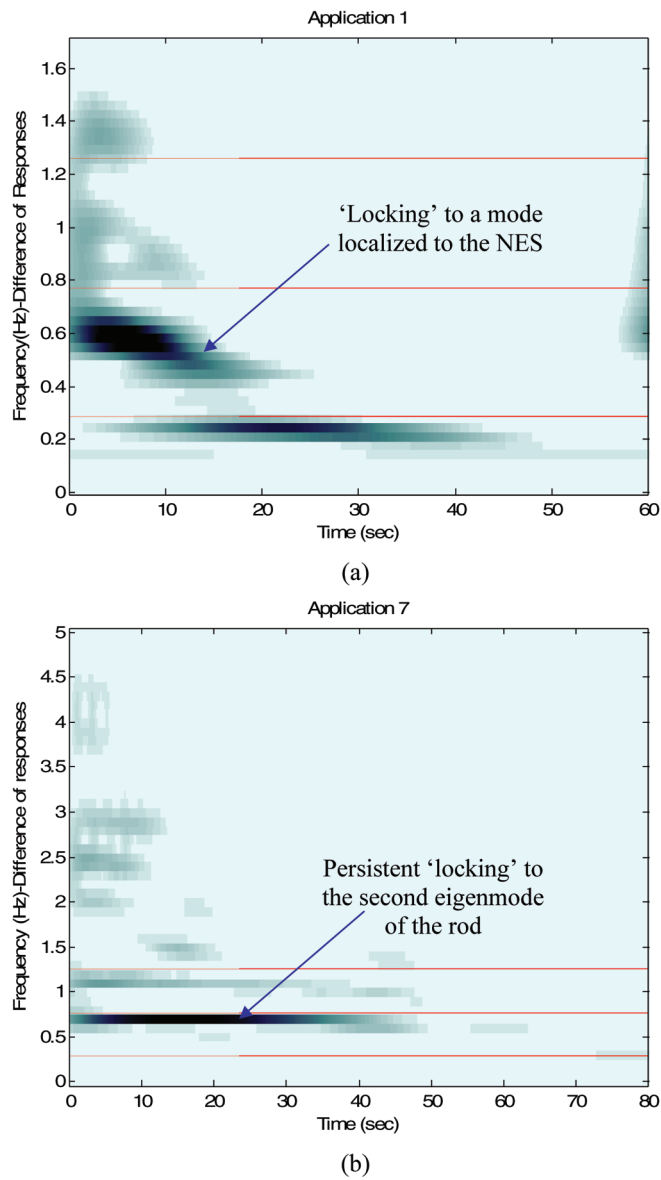


Fig. 5.15 WT spectrum of the relative motion of the NES with respect to the edge of the rod: (a) Application 1 – case 'B'; (b) Application 7 – case 'B'.

early beats between the NES and the second and third modes of the rod take place (mechanism 'B', as in Application 17); more importantly, however, there occurs a secondary late transition of the dynamics from the nonlinear mode to the first rod

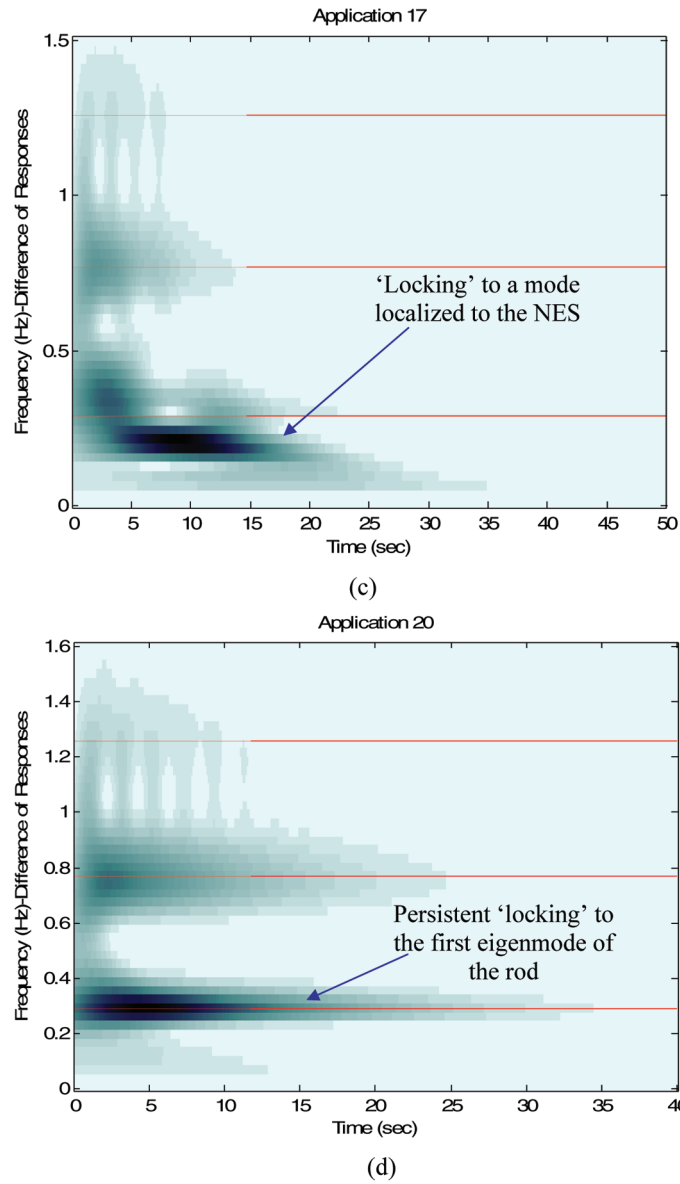


Fig. 5.15 WT spectrum of the relative motion of the NES with respect to the edge of the rod: (c) Application 17 – case ‘B-I’; (d) Application 20 – case ‘I’; the first three eigenfrequencies of the uncoupled linear rod are indicated.

mode, after which additional persistent beats between the NES and the first rod mode are realized (mechanism ‘B’). This late transition is qualitatively different from the dynamics depicted in Figure 5.15c.

No such low frequency transitions occur in the WT spectra of the relative transient responses of Applications 7 [case (c, B) – weaker TET from the rod to the NES], and 20 [case (a, I) – strong TET], that are presented in Figures 5.15b, d, respectively. In the case of weaker TET (Figure 5.15b) we observe strong and persistent resonance locking of the relative response at the frequency of the second linearized mode of the rod, which explains the corresponding persistent nonlinear beats observed in the transient response. It is interesting to note that in this case there is complete absence of resonance interactions between the relative response and the first mode of the rod. In the case of stronger TET in Application 20 (see Figure 5.15d) there is similar resonance locking of the relative response at the first linearized mode of the rod, which, however, is not as persistent as in the WT spectrum of Figure 5.15b. In both cases, there is the absence of transient capture of the early (high energy) relative motion by a nonlinear mode localized at the NES (as in Figures 5.15a, c).

Finally, we note clearly the multi-modal content of the dynamics of the rod-NES interaction, reaffirming our previous comment with regard to the capacity of the NES to sequentially interact with a set of linearized modes of the rod. In general, such multi-modal resonant interactions enhance the effectiveness of nonlinear TET in the system, and lead to complex dynamical phenomena such as resonance capture cascades (RCCs). The WT spectra, when combined with empirical mode decomposition (EMD) of the transient responses of the rod and the NES form a powerful computational tool that can be utilized to reveal additional dynamical features of the resonance interactions occurring between the rod and the NES. This is discussed in what follows.

For a more detailed study of the nonlinear resonance interactions between the rod and the NES two representative cases of EMD analysis concerning Applications 7 and 17 are considered (Georgiades et al., 2007). To increase the accuracy of the analysis, the early and late transient responses of Application 7 are analyzed separately, whereas, no such separation was deemed necessary for Application 17. In each case we analyze through EMD the transient responses of the edge of the rod and of the NES. Examination of the IMFs of these transient responses and their instantaneous frequencies provides insightful information concerning the resonance interactions that occur between the rod and the NES. Indeed, the computation of the instantaneous frequencies of the IMFs, combined with the previous WT spectra provide us with the opportunity to interpret the WT results in terms of resonance interactions between specific IMFs of the rod and the NES. In what follows we will apply this methodology to examine in detail resonance interactions in Applications 17 [case (a, B-D)] and 7 [case (c, B)].

In Figure 5.16a we present IMF-based reconstructions of the transient responses of the edge of the rod and the NES for Application 17; complete agreement between numerical simulation and IMF-based reconstruction is observed, proving the validity of the EMD analysis for decomposing the transient nonlinear responses through

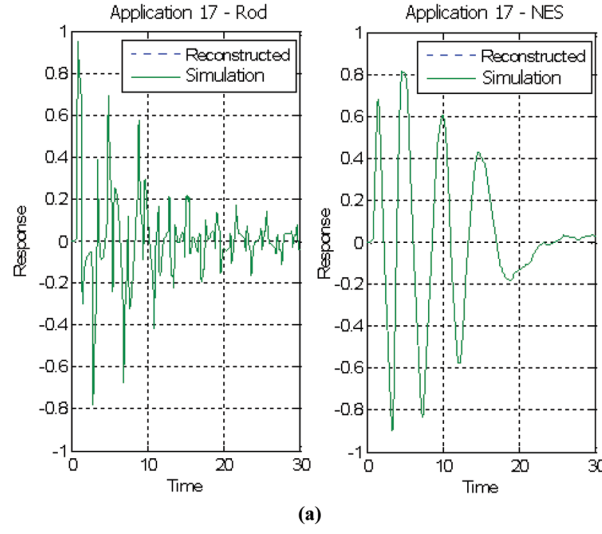


Fig. 5.16 EMD analysis of Application 17 – case ‘B-I’: (a) IMF-based reconstructed transient response of the edge of the rod and the NES compared to numerical simulations.

IMFs. Representative IMFs are depicted in Figure 5.16b. Next, decompositions of the IMFs in terms of their instantaneous amplitudes and phases were performed in order to examine their individual frequency contents. This information should be analyzed together with the corresponding WT spectrum of the relative transient response between the edge of the rod and the NES (see Figure 5.15a); from that plot it is clearly observed that in this case strong nonlinear TET is associated with low frequency ‘locking’ of the dynamics to a nonlinear mode below the first eigenfrequency of the rod (at 0.29 Hz). In Figure 5.17a we depict the transient evolutions of the IMF frequency components of the rod and the NES, i.e., the instantaneous frequencies $\dot{\phi}_{2\text{NES}}(t)$ and $\dot{\phi}_{9\text{Rod}}(t)$, respectively, superimposed to the WT spectra of the respective numerical time series.

The following conclusions are drawn from these results. It is clear that the 2nd IMF of the NES and the 9th IMF of the rod possess nearly constant instantaneous frequencies precisely at the low frequency range of the nonlinear mode of the WT spectrum of Figure 5.15a; hence, these IMFs engage in 1:1 TRC in the initial (high energy) stage of the transient dynamics. This 1:1 TRC becomes apparent by considering the corresponding phase plot of the phase difference $\phi_{2\text{NES}}(t) - \phi_{9\text{Rod}}(t)$ in the early time window where the 1:1 TRC occurs (see Figure 5.17b). Indeed, resonance capture between two IMFs is indicated by the non-time-like, ‘slow’ evolution of the difference between their corresponding phase difference, so that the averaging theorem cannot be applied with respect to that phase difference and preventing averaging out of the dynamics. It is precisely such resonance captures that lead to passive TET from the rod to the NES, as quantified by the EDM. Moreover, the fact that the mentioned 1:1 TRC takes place in the early stage of the dynamics where

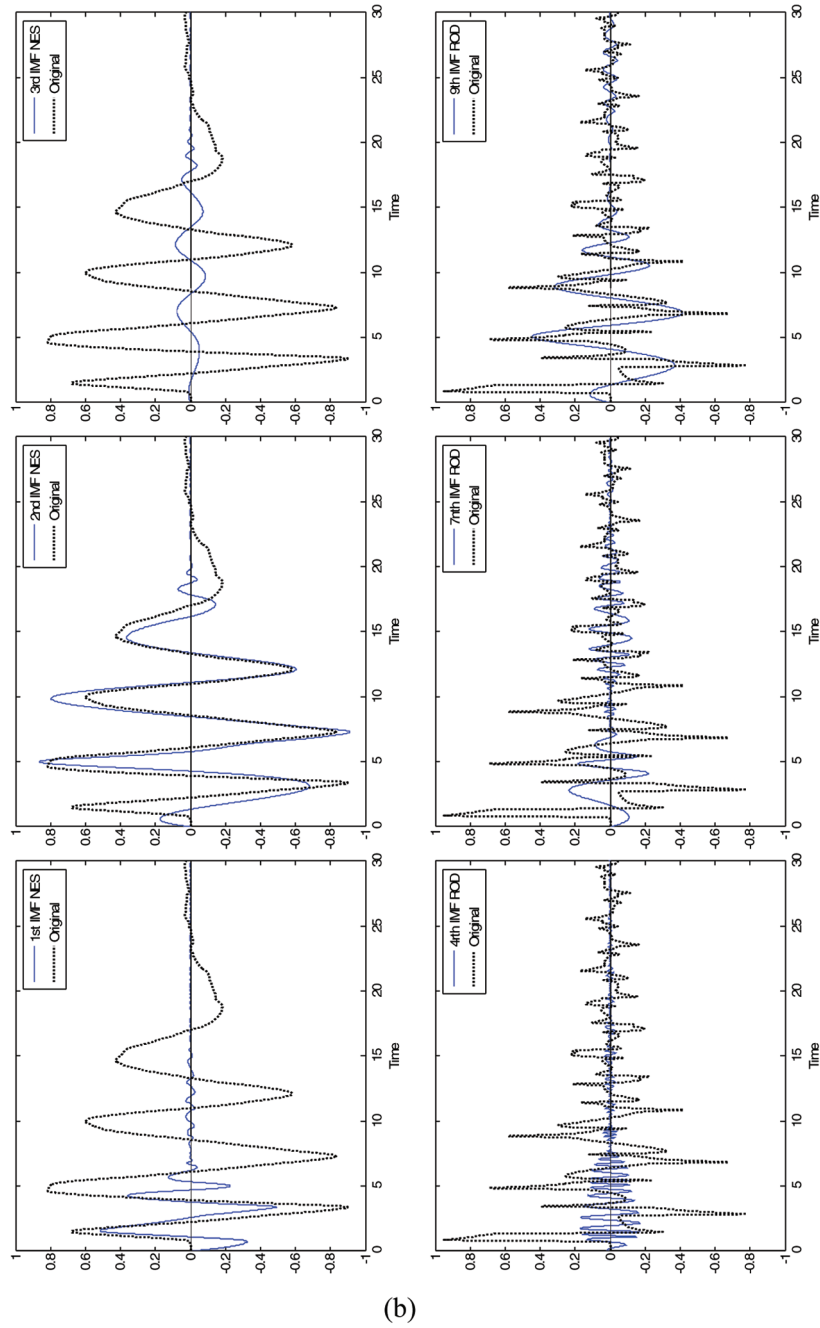


Fig. 5.16 EMD analysis of Application 17 – case ‘B-I’: (b) IMFs of the transient response of the edge of the rod and the NES.

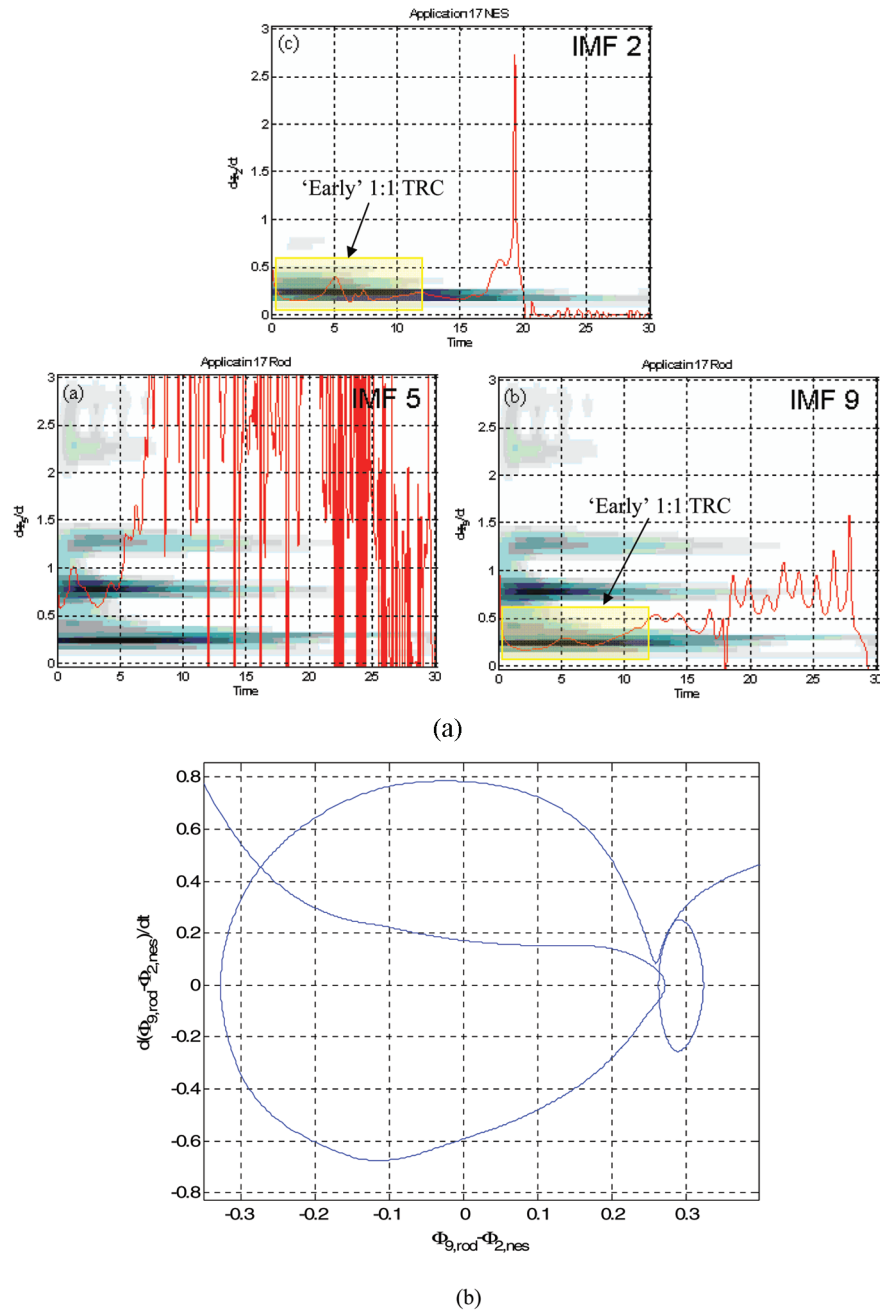


Fig. 5.17 Nonlinear 1:1 TRC in Application 17 between the 2nd IMF of the NES and the 9th IMF of the edge of the rod: (a) instantaneous frequencies of the two IMFs; (b) phase plot of the phase difference indicating the 1:1 TRC.

the energy of the system is at its highest level, explains the strong TET observed in this application. In this resonance capture regime, the 2nd (dominant) IMF of the rod coincides in frequency with the dominant harmonic component of the transient response of the NES, whereas the 9th IMF of the rod coincides with the lowest of the dominant harmonic components of the transient response of the edge of the rod.

These results (together the ones presented below) demonstrate the capacity of the combined EMD-WT analysis to accurately identify the oscillatory components of the rod and NES time series that engage in TRC, and, are ultimately responsible for passive TET phenomena from the rod to the NES.

In Figure 5.18a we depict the exact and IMF-based reconstructed responses for Application 7 [case (c, B) – weaker TET], from which again complete agreement between simulations and IMF reconstructions is observed. Representative IMFs of the early (high energy) responses of the edge of the rod and the NES are depicted in Figure 5.18b. Consideration of the resonance interactions between the IMFs of the rod and the NES reveals the reason that weak TET is realized in this application. Referring to the WT spectrum of the relative response between the edge of the rod and the NES for this application (see Figure 5.15c), we established ‘locking’ of the dynamics in the vicinity of the second linearized eigenfrequency of the rod (close to 0.77 Hz). Examining the temporal evolutions of the instantaneous frequencies of the IMFs of the early transient responses of the edge of the rod and the NES (see Figure 5.19a), we note that the 1st IMF of the NES and the 5th IMF of the rod develop *delayed* frequency ‘plateaus’ close to 0.77 Hz for $t > 12$. Moreover, examining the phase plot of the phase difference $\phi_{1\text{NES}}(t) - \phi_{5\text{Rod}}(t)$ over the time window where the frequency plateaus are realized, we note the characteristic loops that are indicative of 1:1 resonance capture between these two IMFs (see Figure 5.19b). However, since this TRC occurs at a *late stage of the response* (i.e., at the stage where a significant portion of the initial energy of the system has already been dissipated due to damping), the resulting TET from the rod to the NES is not as strong as in the previously discussed Application 17, where the corresponding TRC takes place at the early highly energetic stage of the dynamics. In Figure 5.19 we also show that in Application 7 there occurs an additional ‘delayed’ 1:1 TRC between the 2nd IMF of the NES and the 6th IMF of the edge of the rod at a frequency near the first eigenfrequency of the rod (0.29 Hz), which, however, does not lead to significant energy transfer from the rod to the NES. Finally, from the plots of Figure 5.19a we note that, by superimposing the instantaneous frequencies of the IMFs to the WT spectra of the respective numerical time series, we infer that the 1st and 2nd IMFs of the NES coincide with the higher and lower dominant harmonics, respectively, of the time series of the NES, but only during the later, low-energy stage of the motion. Similar conclusions can be drawn with regard to the 5th and 6th IMFs of the rod.

Summarizing, it appears that *strong TET in the system under consideration is associated with TRCs between IMFs of the NES and rod responses at specific frequency ranges and during the critical early stage of the motion where the energy of the system is at high levels; delayed TRCs between IMFs of the rod and the NES that occur at diminished energy levels result in weaker TET from the rod to the NES*. In terms of the corresponding WT spectra, strong energy exchanges and early (high-

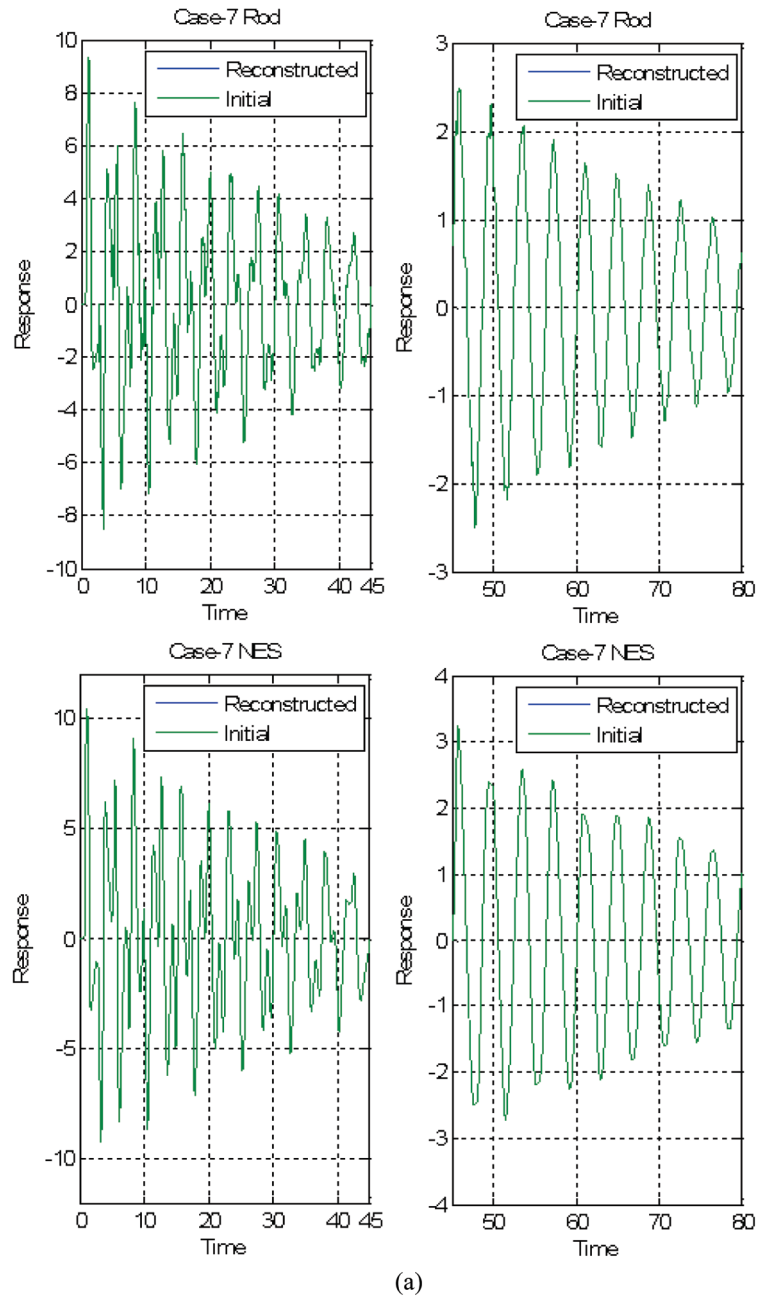
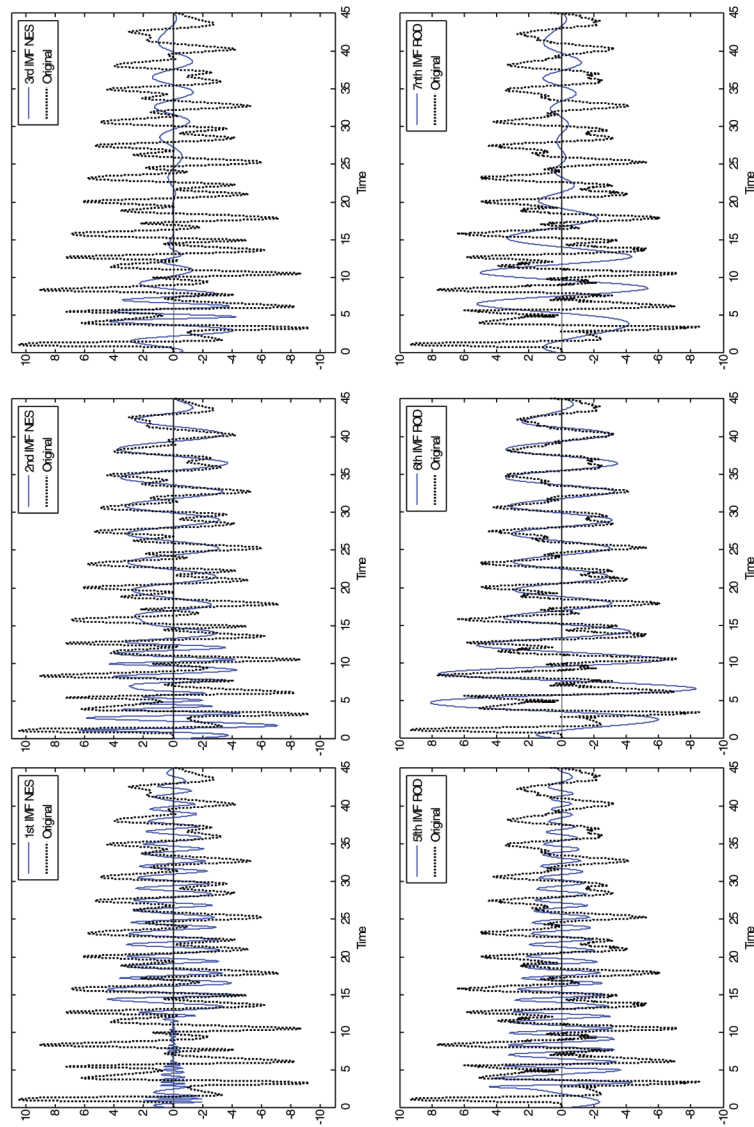


Fig. 5.18 EMD analysis of Application 17 – case ‘B’: (a) IMF-based reconstructed transient responses of the edge of the rod and the NES versus numerical simulations – early and late responses are treated separately.



(b)

Fig. 5.18 EMD analysis of Application 17 – case ‘B’: (b) IMFs of the early transient responses of the edge of the rod and the NES.

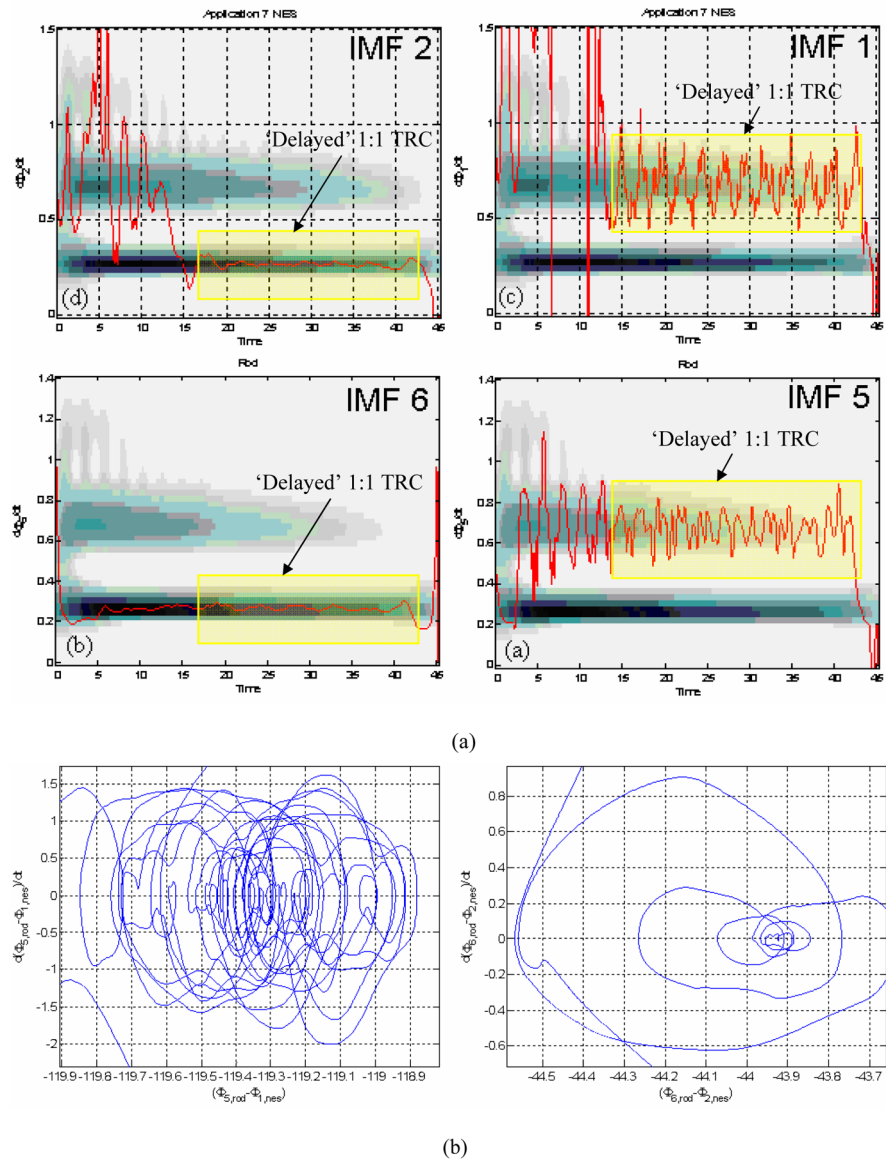


Fig. 5.19 Nonlinear 1:1 TRCs in Application 7 between the 1st IMF of the NES and the 5th IMF of the edge of the rod, and the 2nd IMF of the NES and the 6th IMF of the rod: (a) instantaneous frequencies of the IMFs of the NES and the edge of the rod; (b) phase plots of the phase differences indicating the two 1:1 TRCs.

energy regime) TRCs between IMFs are associated with ‘locking’ of the dynamics with nonlinear normal modes that localize to the NES as the energy of the system diminishes due to damping dissipation.

The results of this section demonstrate the efficacy of using lightweight essentially nonlinear attachments – NESs as passive absorbers of broadband (shock) energy from elastic structures. The resulting irreversible TET of shock energy from the rod to the NESs, eliminate in an effective way unwanted structural disturbances. Hence, the proposed design can be regarded as a new paradigm for passive shock isolation of elastic structures. An interesting (and appealing) feature of the NES concept is that, *although an NES represents a local alteration of the physical configuration of a structure, it can affect the global structural dynamics*. The reason behind this seemingly paradoxical finding (and also being the basic feature that distinguishes the NES from previous absorber designs mentioned in the literature), is the essential stiffness nonlinearity of the NES, which enables it to resonantly interact (i.e., to engage in resonance captures) with structural modes at arbitrary frequency ranges, provided, of course, that its point of attachment is not close to nodes of the structural modes of interest.

A new feature of the study of TET carried out in this section is the use of combined Wavelet Transforms (WTs) and Empirical Mode Decomposition (EMD) as a tool for identifying the specific TRCs responsible for nonlinear modal interactions between the NES and the structure to which it is attached. It was found that there exist at least three distinct dynamical mechanisms governing the NES-rod nonlinear resonance interactions; namely, nonlinear beat phenomena (mechanism ‘B’), direct one-way irreversible energy transfers from the rod to the NES (mechanism ‘I’), or a combination of the two (mechanism ‘B-I’). Although no direct association of any one of these three mechanisms to the strength of TET to the NES can be discerned based on the results presented, some interesting observations based on the previous computational findings can still be made.

Indeed, relatively strong TET is associated with the occurrence of early nonlinear beats in the response (cases ‘B’ and ‘B-I’); this is not to say, however, that nonlinear beats *always* give rise to relatively strong TET (counterexamples are Applications 7, 16, 18 and 21 in Table 5.2). These observations regarding early nonlinear beats are consistent with results reported in Sections 3.3 and 3.4 (see also Kerschen et al., 2005), where it was found that the most efficient mechanism for TET in the two-DOF system considered there is the excitation of early nonlinear beats (or, of stable IOs close to the 1:1 resonance manifold of the dynamics).

Returning to the results reported in this section and motivated by the previous discussion, we conjecture that strong TET in the rod-NES configuration is similarly ‘triggered’ by early nonlinear beat phenomena occurring in the neighborhood of the 1:1 resonance manifold of the frequency-energy plot (FEP) of the underlying Hamiltonian system (i.e., of the undamped rod with undamped attached NES). To prove this conjecture one needs to follow a methodology similar to the one developed in Sections 3.3 and 3.4 for the two-DOF system. First, we need to construct the nonlinear FEP of the periodic (and quasi-periodic) orbits of the underlying Hamiltonian system (a challenging task in itself). Then, we need to compute periodic and

quasi-periodic orbits with initial conditions that ‘trigger’ strong TET; finally, by superimposing the computed FEP to WT spectra of the numerical transient responses of the damped system we wish to prove that transient responses producing strong TET are ‘triggered’ by periodic or quasi-periodic nonlinear beats in the FEP. In the following section we provide some preliminary results towards interpreting damped transitions of the finite rod-NES system in terms of the FEP of the underlying Hamiltonian system.

5.2.3 Damped Transitions on the Hamiltonian FEP

In this section we follow an alternative approach in our study of multi-frequency transitions in the transient dynamics of the viscously damped dispersive finite rod with the NES (see Figure 5.6). First, we will compute the periodic orbits of the underlying Hamiltonian system with no damping and external forcing and depict them in a frequency-energy plot (FEP); this will be similar to the plots constructed for the Hamiltonian dynamics of the discrete systems examined in the previous chapters. As shown in Section 3.3 this representation enables one to clearly distinguish between the different types of periodic motions in terms of backbone curves, subharmonic tongues and manifolds of impulsive orbits (IOs).

Then, the dynamics of the damped and forced system will be considered and the corresponding WT spectra will be depicted in the FEP in an effort to interpret complex damped multi-frequency responses in terms of transitions between different branches of periodic solutions on the FEP. Finally, the damped dynamics will be decomposed by EMD, that is, the computed time series will be decomposed in terms of intrinsic mode functions (IMFs) at different characteristic time (or frequency) scales. Comparisons of the evolutions of the instantaneous frequencies of the IMFs with the WT spectra of the corresponding time series, will enable us to identify the dominant IMFs of the signals and the time scales at which the dominant dynamics evolve at different time windows of the responses. Moreover, by superimposing the WT spectra of the damped responses to the FEP of the underlying Hamiltonian system, will be able to clearly relate multi-scaled transitions occurring in the transient damped dynamics, to transitions between different solution branches in the FEP. As a result, we aim to develop a physics-based, multi-scaled approach and provide the necessary computational tools for multi-scaled analysis of complex multi-frequency transitions occurring in the dynamics of essentially nonlinear dynamical systems (Tsakirtzis, 2006; Panagopoulos et al., 2007).

The first step in our computational approach is to study the Hamiltonian system derived by omitting damping and forcing terms from the equations of motion (5.1). The reason for studying the Hamiltonian dynamics, is that, as shown in Chapters 3 and 4, for sufficiently weak damping the transient damped dynamics of system (5.1) is expected to approximately trace the branches of periodic or quasi-periodic solutions of the corresponding Hamiltonian system. To this end, we rewrite the equations of motion (5.8) in normalized form, omitting the forcing terms and adding general

initial conditions for the rod and the NES:

$$\begin{aligned}
& -\frac{\partial^2 u(x, t)}{\partial x^2} + \omega_0^2 u(x, t) + \varepsilon \lambda_1 \frac{\partial u(x, t)}{\partial t} + \frac{\partial^2 u(x, t)}{\partial t^2} = 0, \quad 0 \leq x \leq L \\
& \frac{\partial u(L, t)}{\partial x} = -\varepsilon \ddot{v}(t), \quad u(0, t) = 0 \\
& C[u(L, t) - v(t)]^3 + \varepsilon \lambda_2 \left[\frac{\partial u(L, t)}{\partial t} - \dot{v}(t) \right] = \varepsilon \ddot{v}(t) \\
& u(x, 0) = r(x), \quad \frac{\partial u(x, 0)}{\partial t} = s(x), \quad v(0) = v_0, \quad \dot{v}(0) = \dot{v}_0 \quad (5.27)
\end{aligned}$$

In addition, we explicitly denote the lightweightness of the NES by the small parameter $0 < \varepsilon \ll 1$, and allow for different damping coefficients for the rod and the NES.

Setting $\lambda_1 = \lambda_2 = 0$ we derive the following Hamiltonian system:

$$\begin{aligned}
& \frac{\partial^2 u(x, t)}{\partial t^2} + \omega_0^2 u(x, t) - \frac{\partial^2 u(x, t)}{\partial x^2} = 0, \quad 0 \leq x \leq L \\
& \varepsilon \ddot{v}(t) + C[v(t) - u(L, t)]^3 = 0, \quad u(0, t) = 0, \quad \frac{\partial u(L, t)}{\partial x} = -\varepsilon \ddot{v}(t) \quad (5.28)
\end{aligned}$$

Initial conditions are omitted from (5.28) since the problem of computing the undamped periodic orbits of the Hamiltonian system constitutes a nonlinear boundary value problem (NLBVP); this is in contrast to problems (5.8) and (5.27) which are formulated as Cauchy (initial value) problems. To compute T -periodic solutions of system (5.28) the displacements of the rod and the NES are expressed in the following series forms (Panagopoulos et al., 2007):

$$\begin{aligned}
u(x, t) &= \sum_{k=1}^{\infty} C_k(x) \cos[(2k-1)\Omega t] + \sum_{k=1}^{\infty} S_k(x) \sin[(2k-1)\Omega t] \\
v(t) &= \sum_{k=1}^{\infty} V_{c,k} \cos[(2k-1)\Omega t] + \sum_{k=1}^{\infty} V_{s,k} \sin[(2k-1)\Omega t] \quad (5.29)
\end{aligned}$$

where by $\Omega = 2\pi/T$ we denote the basic frequency of the time-periodic motion. We note that the above infinite series expressions represent exact periodic solutions of the NLBVP (5.28), as they are, in essence, the Fourier series expansions of the sought solutions. Approximations in the computations will be made when the infinite series are truncated for computational purposes.

Substituting (5.29) into the (linear) partial differential equation in (5.28) and taking into account the imposed boundary conditions, the following series of linear boundary value problems (BVPs) are obtained, governing the evolutions in space of the distributions $C_k(x)$ and $S_k(x)$, $k = 1, 2, \dots$:

$$\begin{aligned}
\frac{d^2 C_k(x)}{dx^2} + [(2k-1)^2 \Omega^2 - \omega_0^2] C_k(x) &= 0 \\
\frac{d^2 S_k(x)}{dx^2} + [(2k-1)^2 \Omega^2 - \omega_0^2] S_k(x) &= 0 \\
C_k(0) = S_k(0) = 0, \quad \frac{dC_k(L)}{dx} &= \varepsilon(2k-1)^2 \Omega^2 V_{c,k}, \\
\frac{dS_k(L)}{dx} &= \varepsilon(2k-1)^2 \Omega^2 V_{s,k}
\end{aligned} \tag{5.30}$$

The general solutions of the first two linear ordinary differential equations in (5.30) are expressed as

$$\begin{aligned}
C_k(x) &= \hat{C}_k \in \left[x \sqrt{(2k-1)^2 \Omega^2 - \omega_0^2} \right] \\
S_k(x) &= \hat{S}_k \in \left[x \sqrt{(2k-1)^2 \Omega^2 - \omega_0^2} \right]
\end{aligned} \tag{5.31}$$

where

$$\begin{aligned}
\hat{C}_k &= \frac{\varepsilon(2k-1)^2 \Omega^2 V_{c,k}}{\cos \left[L \sqrt{(2k-1)^2 \Omega^2 - \omega_0^2} \right] \sqrt{(2k-1)^2 \Omega^2 - \omega_0^2}} \\
\hat{S}_k &= \frac{\varepsilon(2k-1)^2 \Omega^2 V_{s,k}}{\cos \left[L \sqrt{(2k-1)^2 \Omega^2 - \omega_0^2} \right] \sqrt{(2k-1)^2 \Omega^2 - \omega_0^2}}
\end{aligned}$$

The expressions (5.31) are valid over the entire frequency range $\Omega \in [0, \infty)$, i.e., for harmonics with frequencies in both the propagation zone (PZ) and attenuation zone (AZ) of the uncoupled linear rod of infinite length. However, depending on the value of the frequency Ω , the solutions (5.31) may change qualitatively assuming the form of traveling waves or attenuating standing waves. Indeed, for values of the fundamental frequency Ω satisfying $(2k-1)^2 \Omega^2 - \omega_0^2 < 0$ for some $k \in N^+$ (inside the AZ of the dispersive rod), the following well-known relations can be employed:

$$\sin(j\alpha) = j \sinh(\alpha), \quad \cos(j\alpha) = \cosh(\alpha) \quad \text{with } j = \sqrt{-1}$$

then expressions (5.31) yield time-periodic standing waves with attenuating spatial envelopes. On the contrary, time-periodic solutions satisfying the condition $(2k-1)^2 \Omega^2 - \omega_0^2 > 0$ for some $k \in N^+$ (inside the PZ of the rod), correspond to time-periodic traveling waves of constant amplitude that propagate freely in the rod until they reach either one of its boundaries where they scatter. We note that resonances (standing waves) in the rod can only occur inside the PZ of the corresponding infinite rod, as they result from positive interference of left- and right-going traveling waves.

Expressions (5.31) are derived in terms of the amplitudes $V_{s,k}$ and $V_{c,k}$ of the harmonics of the NES. These are computed by substituting (5.29) and (5.31) into the nonlinear ordinary differential equation in (5.28), yielding the following algebraic expression in terms of an infinite series with respect to the index k (Panagopoulos et al., 2007):

$$\begin{aligned}
& -\varepsilon \left\{ \sum_{k=1}^{\infty} (2k-1)^2 \Omega^2 \left(V_{c,k} \cos[(2k-1)\Omega t] + V_{s,k} \sin[(2k-1)\Omega t] \right) \right\} \\
& + C \left\{ \sum_{k=1}^{\infty} \left(1 - \varepsilon(2k-1)^2 \Omega^2 [(2k-1)^2 \Omega^2 - \omega_0^2]^{-1/2} \tan \left(L \sqrt{(2k-1)^2 \Omega^2 - \omega_0^2} \right) \right) \right. \\
& \left. \times \left(V_{c,k} \cos[(2k-1)\Omega t] + V_{s,k} \sin[(2k-1)\Omega t] \right) \right\}^3 = 0 \tag{5.32}
\end{aligned}$$

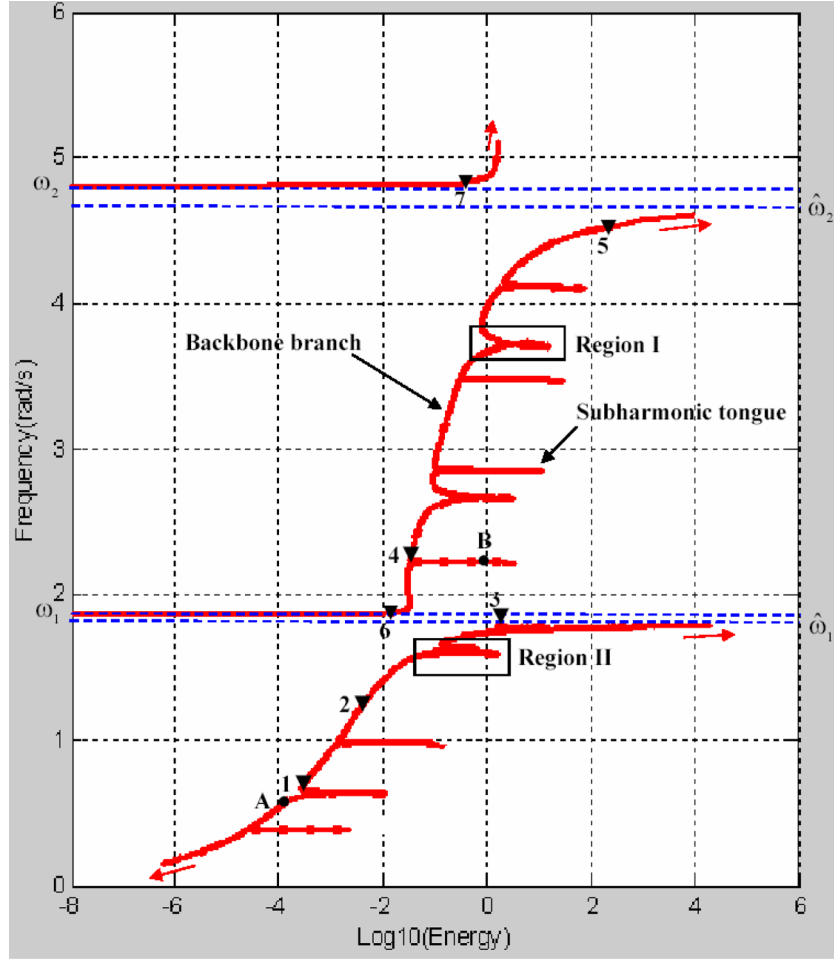
Expanding the cubic power in (5.32), and setting the resulting coefficients of the trigonometric functions $\cos[(2k-1)\Omega t]$ and $\sin[(2k-1)\Omega t]$, $k = 1, 2, \dots$ separately equal to zero, one derives an infinite set of nonlinear algebraic equations for the amplitudes $V_{s,k}$ and $V_{c,k}$, whose solution completely determines the time-periodic solutions of the Hamiltonian system (5.28).

In the numerical computations the infinite set of nonlinear algebraic equations resulting from (5.32) was truncated by considering terms only up to the fifth harmonic (i.e., $k = 1, 2, 3$), and omitting higher harmonics. The resulting truncated set of six nonlinear algebraic equations was then numerically solved for the amplitudes $V_{s,k}$ and $V_{c,k}$, which also determined approximately the time-periodic response of the rod through relations (5.29) and (5.31).

In Figure 5.20 we depict the approximate branches of time-periodic solutions of the Hamiltonian system in the FEP; specifically we employ the previously derived truncated system to compute the approximate amplitude of the relative displacement $[v(t) - u(L, t)]$ of the truncated system (for $k = 1, 2, 3$) for varying values of the fundamental frequency Ω and fixed parameters $\varepsilon = 0.05$, $\omega_0 = 1.0$, $C = 1.0$, $L = 1.0$ and $\lambda_1 = \lambda_2 = 0$. Only the frequency range covering the two leading modes of the uncoupled linear rod is considered in the FEP, which depicts the logarithm of the energy of a periodic orbit, $\log_{10}(E)$, as function of the fundamental frequency Ω (in rad/s) of that orbit. The (conserved) energy E of the periodic orbit is computed by the following expression:

$$\begin{aligned}
E &= \frac{1}{2} \int_0^L \left[\frac{\partial u(x, t)}{\partial t} \right]^2 dx + \frac{1}{2} \int_0^L \left[\frac{\partial u(x, t)}{\partial x} \right]^2 dx + \frac{1}{2} \omega_0^2 \int_0^L u^2(x, t) dx \\
&+ \frac{1}{2} \varepsilon v^2(t) + \frac{1}{4} C [v(t) - u(L, t)]^4 \tag{5.33}
\end{aligned}$$

Considering the FEP of Figure 5.20, we discern the existence of two low-frequency asymptotes. These correspond to the two leading modes of the linear



(a)

Fig. 5.20 FEP of the Hamiltonian system (5.28) based on the truncated system (5.31, 5.32) with $k = 1, 2, 3$: (a) backbone branches of periodic motions and tongues of subharmonic motions.

uncoupled rod,

$$\omega_n = \sqrt{\omega_0^2 + \frac{(2n-1)^2\pi^2}{4L^2}}, \quad n = 1, 2 \quad (5.34)$$

where for the chosen parameters these are given by $\omega_1 = 1.8621$ rad/s and $\omega_2 = 4.8173$ rad/s. In addition, there exist two high-frequency asymptotes at frequencies $\hat{\omega}_1$ and $\hat{\omega}_2$. Noting that at high energies and finite frequencies the essentially nonlinear stiffness of system (5.28) behaves as a massless rigid link, the high-frequency asymptotes are computed as the eigenfrequencies of the following

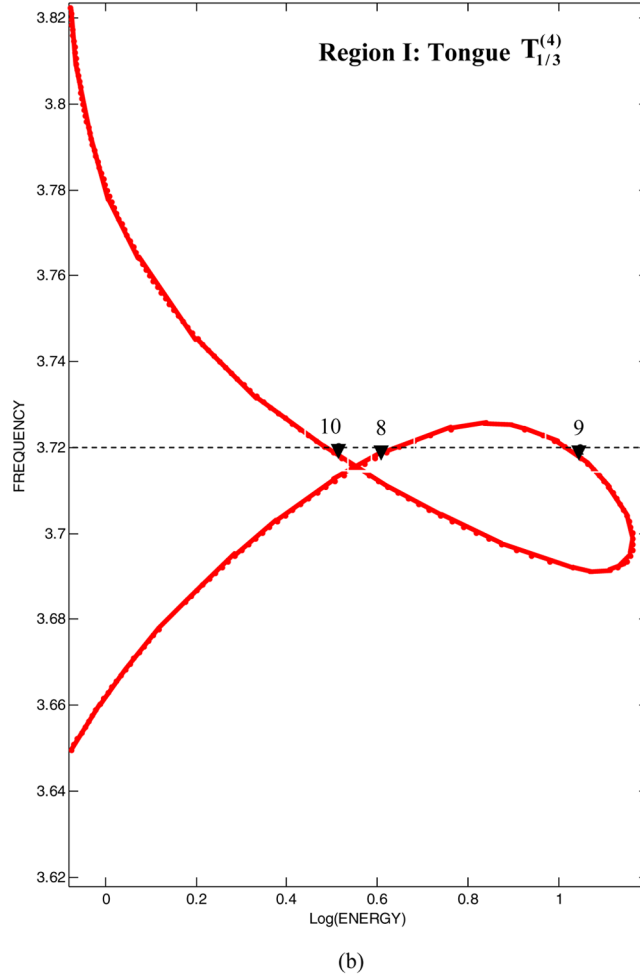


Fig. 5.20 FEP of the Hamiltonian system (5.28) based on the truncated system (5.31, 5.32) with $k = 1, 2, 3$: (b) details of regions I and II; numbers (▼) correspond to the periodic orbits depicted in Figures 5.21 and 5.22, and letters (●) to the numerical simulations of damped transitions.

alternative limiting linear system:

$$\begin{aligned} \frac{\partial^2 u(x, t)}{\partial t^2} + \omega_0^2 u(x, t) - \frac{\partial^2 u(x, t)}{\partial x^2} &= 0, \quad 0 \leq x \leq L \\ u(0, t) &= 0, \quad \frac{\partial u(L, t)}{\partial x} = -\varepsilon \frac{\partial^2 u(L, t)}{\partial t^2} \end{aligned} \quad (5.35)$$

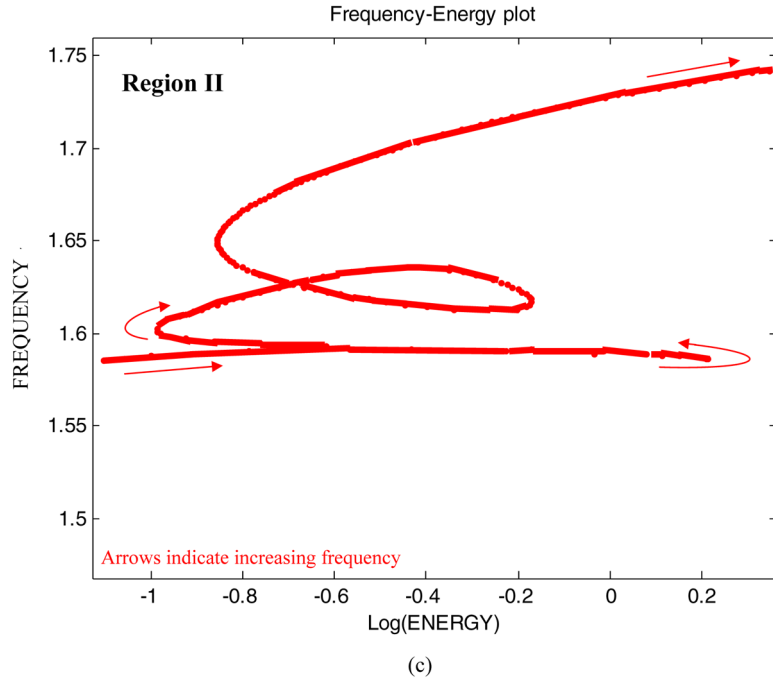


Fig. 5.20 FEP of the Hamiltonian system (5.28) based on the truncated system (5.31, 5.32) with $k = 1, 2, 3$: (c) details of regions I and II; numbers (▼) correspond to the periodic orbits depicted in Figures 5.21 and 5.22, and letters (●) to the numerical simulations of damped transitions.

i.e., of the dispersive rod with a mass ε attached to its right end. The eigenfrequencies of this limiting system are computed by solving the following transcendental equation,

$$\tan \left[L \sqrt{\hat{\omega}^2 - \omega_0^2} \right] = \frac{\sqrt{\hat{\omega}^2 - \omega_0^2}}{\varepsilon \hat{\omega}^2} \quad (5.36)$$

which for the chosen parameters are given by $\hat{\omega}_1 = 1.7728$ rad/s and $\hat{\omega}_2 = 4.5916$ rad/s.

Since the principal aim for constructing the FEP is to interpret the (weakly) damped dynamics of system (5.27) in terms of the topological structure of the periodic solutions of the underlying Hamiltonian system, it is necessary to discuss certain qualitative features of this plot. A first observation concerns the complexity of the FEP. For comparison purposes, we note that for the system where the attachment is connected by means of a linear stiffness, the FEP consists of straight horizontal lines corresponding to the countable infinity of linear vibration modes whose mode shapes and frequencies do not depend on the energy of the vibration. It follows that *all curves in the FEP deviating from the horizontal direction represent essentially nonlinear periodic motions of the nonlinear system, having no counterparts in linear theory and localizing mainly to the nonlinear attachment*. By the same token,

branches of solutions that are nearly horizontal represent weakly nonlinear motions, as they can be regarded as mere perturbations of linearized vibration modes; these solutions are mainly confined to the elastic rod. *That the addition of a single, light-weight essentially nonlinear NES introduces such drastic, strongly nonlinear effects in the FEP (occurring over wide frequency and energy ranges), proves that the addition of the local NES induces global effects on the dynamics of the system.* This is caused by the fact that, due to its essential nonlinearity, the NES is capable of interacting with any of the modes of the rod over arbitrary frequency ranges.

Proceeding to discuss the specific details of the FEP of Figure 5.20, there exist two types of branches of periodic motions, namely *backbone (global) branches* and *subharmonic tongues (local) tongues*. These are similar to the corresponding branches and tongues of the FEP of the two-DOF discussed in Section 3.3.1.2 (see Figure 3.20). Backbone branches consist of nearly monochromatic time-periodic solutions possessing dominant harmonic components and higher harmonics at integer multiples of the dominant harmonics. These branches are defined over extended frequency and energy ranges, and typically are composed of strongly nonlinear periodic solutions that are mainly localized at the nonlinear attachment. Exceptions are in neighborhoods of the linearized eigenfrequencies of the rod, $\omega_1, \omega_2, \dots$, where the spatial distributions of the periodic motions resemble those of the corresponding rod mode shapes and are localized at the rod; and in neighborhoods of the high-energy asymptotes $\hat{\omega}_1, \hat{\omega}_2, \dots$, where the relative displacements between the nonlinear attachment and the rod end tend to zero (i.e., the nonlinear coupling stiffness is nearly unstretched) and, as a result, the nonlinear effects are nearly negligible. In these energy ranges the corresponding segments of the backbone branch in the FEP appear as nearly horizontal segments.

In the plots depicted in Figure 5.21 some representative periodic motions on the backbone branch are depicted. These solutions are regarded as *analytically predicted* time-periodic solutions of the system, since their initial conditions are determined by solving the truncated system (5.32) with the index assuming the values $k = 1, 2, 3$. The accuracy of these solutions is confirmed by comparing them to direct numerical simulations of the equations of motion (Tsakirtzis, 2006; Panagopoulos et al., 2007).

An additional set of periodic solutions of the FEP of Figure 5.20 are realized on *subharmonic tongues (local branches)*; these are multi-frequency time-periodic motions, with frequencies being approximately equal to rational multiples of the eigenfrequencies ω_n of the uncoupled rod. Each tongue is defined over a finite energy range and is composed of two distinct branches of subharmonic solutions. At a critical energy level the two branches coalesce in a bifurcation that signifies the end of that particular tongue and the elimination of the corresponding subharmonic motions at higher energy values. It can be proven that there exists a countable infinity of tongues emanating from the backbone branches at frequencies being in rational relation with respect to the eigenfrequencies of the uncoupled linear rod, ω_n . On a given subharmonic tongue the responses at any point of the rod and of the attachment resemble those of two linear oscillators, albeit possessing different (but rationally related) eigenfrequencies. *Hence, the interesting (and paradoxical)*

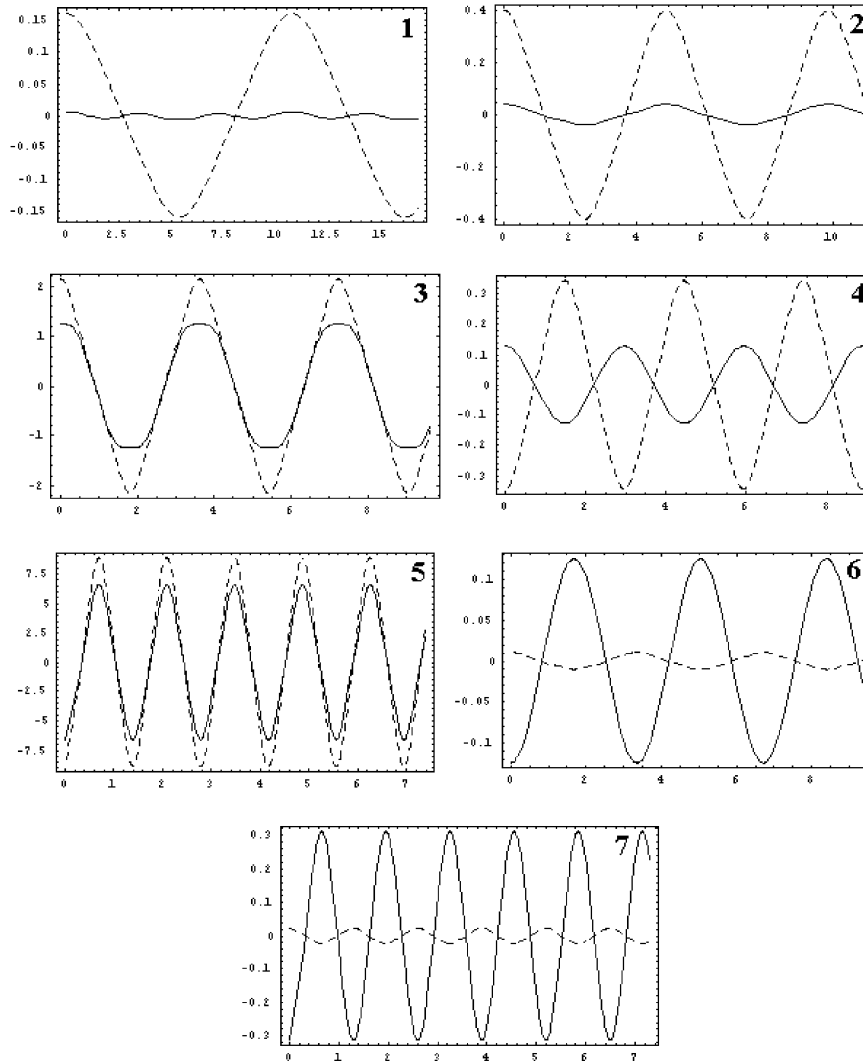


Fig. 5.21 Periodic orbits on backbone branches of the FEP: (1) $\Omega = 0.6$ rad/s, (2) $\Omega = 1.3$ rad/s, (3) $\Omega = 1.75$ rad/s, (4) $\Omega = 2.3$ rad/s, (5) $\Omega = 4.5$ rad/s, (6) $\Omega = 1.87$ rad/s, (7) $\Omega = 4.83$ rad/s; — rod end, - - - NES.

observation can be drawn, that on the essentially nonlinear subharmonic tongues (they are characterized as such since they exist due to the strong stiffness nonlinearity of the system) the rod-attachment system behaves nearly as an equivalent two-frequency linear system. This observation, which is similar to what was found for the subharmonic orbits of the two-DOF system studied in Section 3.3.1.2 [also

see Kerschen et al. (2005)] provides a hint on the rich and complex dynamics of the system considered herein.

In the FEP of Figure 5.20, we depict only a subset of leading subharmonic tongues. For example, the tongue depicted in Region I (see Figure 5.21b) is in the vicinity of $\omega_4/3$; it follows that subharmonic motions on this tongue correspond to responses where the nonlinear attachment possesses a dominant harmonic with frequency $\omega_4/3$ (and a minor harmonic at ω_4), whereas the response of the rod end possesses a dominant harmonic at frequency ω_4 (and a minor harmonic at $\omega_4/3$). In the following exposition a tongue labeled as $T_{p/q}^{(n)}$ will denote the branch of subharmonic motions where the frequency of the dominant harmonic component of the nonlinear attachment is nearly equal to $(p/q)\omega_n$, whereas that of the rod end equals ω_n . It follows that the relative displacement $[v(t) - u(L, t)]$ during a subharmonic motion on tongue $T_{p/q}^{(n)}$ possesses two main harmonics at frequencies ω_n and $(p/q)\omega_n$. Using this notation, the subharmonic tongue depicted in Figure 5.21b is labeled as $T_{1/3}^{(4)}$. In Figure 5.22 three subharmonic orbits on the tongue $T_{1/3}^{(4)}$ of the FEP are depicted in the neighborhood of frequency $\omega_4/3$. We mention that although all these subharmonic orbits coexist, i.e., they possess the same fundamental frequency Ω , they correspond to qualitatively different dynamics.

We now focus on the damped dynamics of system (5.27). This study was performed through direct simulations of the governing equations of motion and post-processing of the computed time series. The transient responses of the rod-attachment system with viscous dissipation are computed by a finite element code developed for Matlab[®]. This code is different from the FE code discussed in Section 5.2.1 and will be employed also in Section 5.3 to model a rod of infinite length; comparison of the results given by this code with the results obtained by the FE code described in Section 5.2.1 was also performed in order to ensure convergence and accuracy of the results. For these computations the rod was discretized into 200 finite elements, which ensured a five-digit convergence regarding the computation of the three leading modes of the rod. This was deemed to be sufficient for the computations presented herein, as we will be interested only in a frequency range encompassing the first three linearized modes of the rod.

Regarding the numerical integrations of the equations of motion (5.27), the Newmark algorithm was utilized with parameters chosen to ensure unconditional stability of the numerical algorithm. The sampling frequency was such that the eigenfrequencies of the leading three modes of the rod were less than 6% of the sampling frequency. Regarding viscous dissipation, proportional damping in the rod was assumed, by expressing the damping matrix in the form $D = a_1M + a_2K$, where M and K are the mass and stiffness matrices of the rod. The parameters used for the FE computations were chosen as $\varepsilon = 0.05$, $C = 1.0$, $L = 1.0$, $\omega_0 = 1.0$, $\lambda_2 = 0.02$, $\alpha_1 = 0.001$, and $\alpha_2 = 0.0$, and the damped responses were initiated with different sets of initial conditions of the rod and the NES.

The first numerical simulation is performed with initial conditions corresponding to point A on the main backbone branch of the FEP at frequency $\Omega = 0.6$ rad/s (see Figure 5.20a). These initial conditions for the rod and the nonlinear attachment are approximately computed as follows:

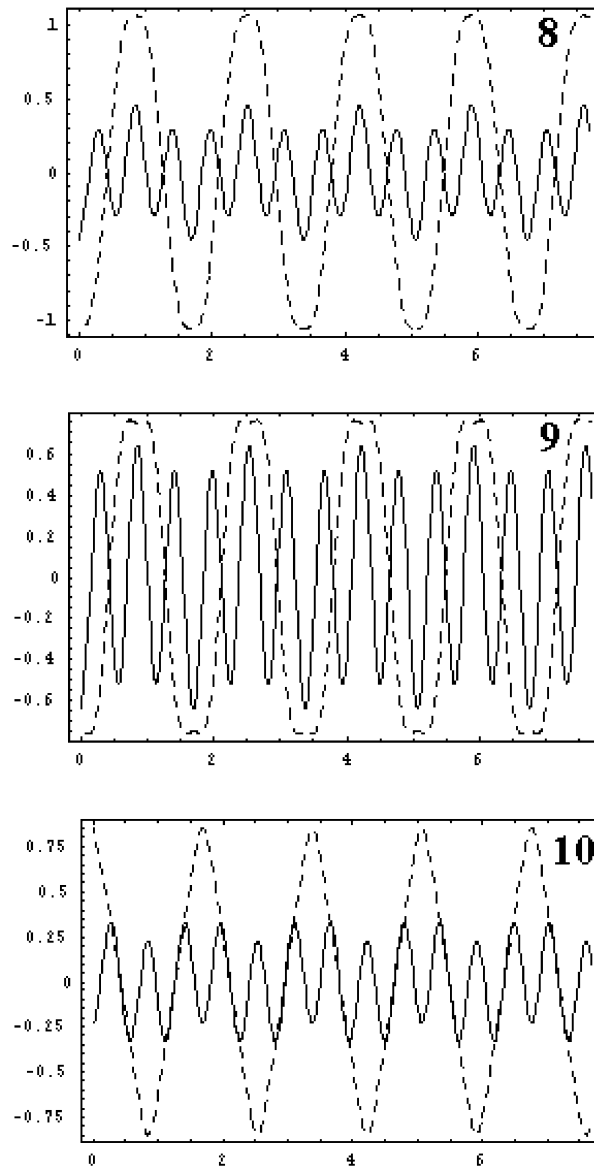


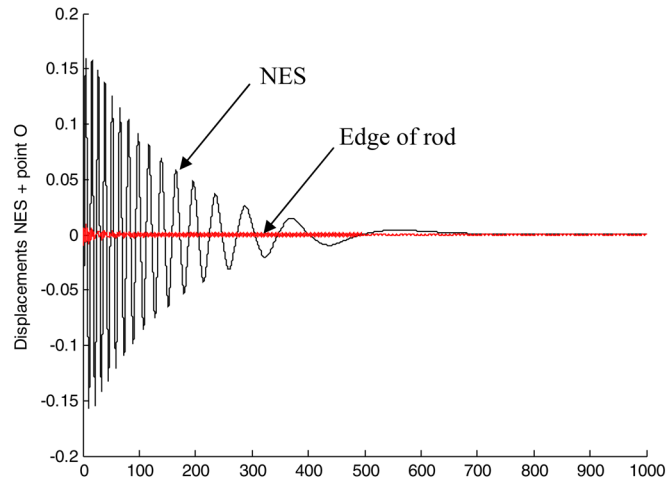
Fig. 5.22 Periodic orbits on the subharmonic tongue $T_{1/3}^{(4)}$ (Region I, Figure 5.20b): (8) $\Omega = 3.72$ rad/s, $\log(\text{Energy}) = 0.645$; (9) $\Omega = 3.72$ rad/s, $\log(\text{Energy}) = 1.015$; (10) $\Omega = 3.72$ rad/s, $\log(\text{Energy}) = 0.48$; — rod end, - - - NES.

$$\begin{aligned}
v(0) &\approx \{V_{c,1} \cos(\omega t) + V_{c,2} \cos(3\omega t) + V_{c,3} \cos(5\omega t)\}_{t=0} \Rightarrow \\
u(x, 0) &\approx \left\{ \hat{C}_1 \sin\left(\sqrt{\omega^2 - \omega_0^2}\right) \cos(\omega t) + \hat{C}_2 \sin\left(x\sqrt{9\omega^2 - \omega_0^2}\right) \cos(3\omega t) \right. \\
&\quad \left. + \hat{C}_3 \sin\left(x\sqrt{25\omega^2 - \omega_0^2}\right) \cos(5\omega t) \right\}_{t=0} \Rightarrow \\
u(0, 0) &\approx -0.0052
\end{aligned} \tag{5.37}$$

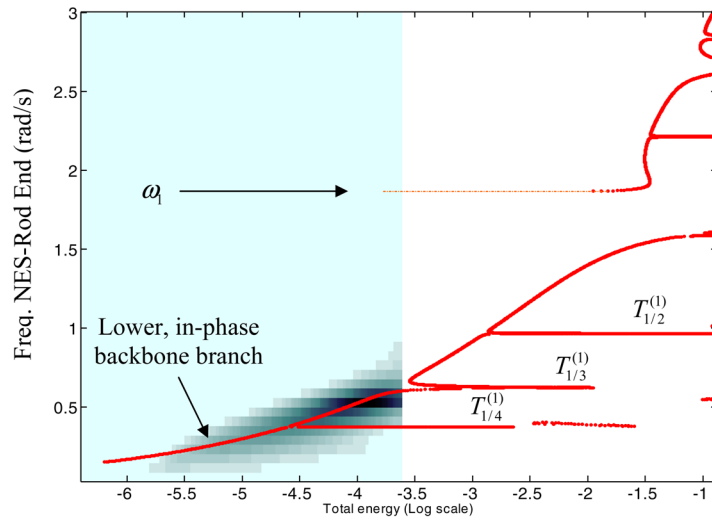
with $V_{c1} = -0.1597$, $V_{c2} = -0.054$, $V_{c3} = 0.0001$, and $\hat{C}_1 = 0.0027$, $\hat{C}_2 = -0.0079$ and $\hat{C}_3 = -0.00002$. In the undamped system these initial conditions correspond to a periodic motion that is predominantly localized to the nonlinear attachment (the NES). In Figure 5.23 we depict the damped responses of the NES and the point of its connection to the rod, together with the wavelet transform spectrum of the damped relative motion $[v(t) - u(L, t)]$ superimposed to the FEP of the Hamiltonian system. We observe that as energy decreases due to damping dissipation the motion appears to trace closely the lower, in-phase backbone branch of the corresponding Hamiltonian system. This observation confirms that for sufficiently weak damping the damped response lies close to the dynamics of the underlying Hamiltonian system (in fact, as discussed in Chapters 3 and 4 the damped motion takes place on the damped invariant NNM manifold lying on the neighborhood of the corresponding NNM manifold of the Hamiltonian system). The nonlinear dynamic interaction between the rod and the NES during this damped transition is now examined in more detail.

In this particular application the damped motion is initiated close to the subharmonic tongue $T_{1/3}^{(1)}$ (see Figure 5.23b), so a weak 1:3 TRC occurs at least in the beginning of the motion; indeed, in that early response regime both the rod end and the NES execute in-phase oscillations, with the rod oscillating nearly three times faster than the NES. Since there is a countable infinity of low subharmonic orbits emanating from the lower in-phase backbone branch of the FEP with decreasing energy, the damped dynamics passes through a sequence of TRCs of increasing order; hence, as energy decreases the rod oscillates increasingly faster compared to the NES. Moreover, since the lower in-phase backbone branch of the FEP does not undergo any major topological changes with decreasing energy – apart from the minor topological changes related to the bifurcations that generate the countable infinities of low-energy subharmonic tongues – the damped transition is also smooth and does not undergo major sudden transitions in frequency.

The transient energy transaction measure (ETM) [defined by relation (5.26)] between the rod and the NES is depicted in Figure 5.24. It indicates the presence of (weak) nonlinear beat phenomena between the rod and the NES, with continuous energy being exchanged between them. We note that in the damped transition of Figure 5.23 the motion is predominantly localized to the nonlinear attachment throughout the motion, so that only weak energy exchanges occur between the two subsystems. As shown in Section 5.2.2 [but also in Georgiades et al. (2007)] for different sets of initial conditions stronger energy exchanges may occur, resulting in strong TET from the rod to the NES. There we showed that TET may be real-



(a)



(b)

Fig. 5.23 Damped response initiated at point A of the FEP of Figure 5.20a: (a) transient responses $v(t)$ and $u(L, t)$; (b) WT spectrum of the relative response $[v(t) - u(L, t)]$ superimposed to the FEP of the Hamiltonian system.

ized through either nonlinear beats, one-way energy transfers from the rod to the attachment (evidenced by a series of positive-only spikes in the ETM plot), or a combination of both these mechanisms.

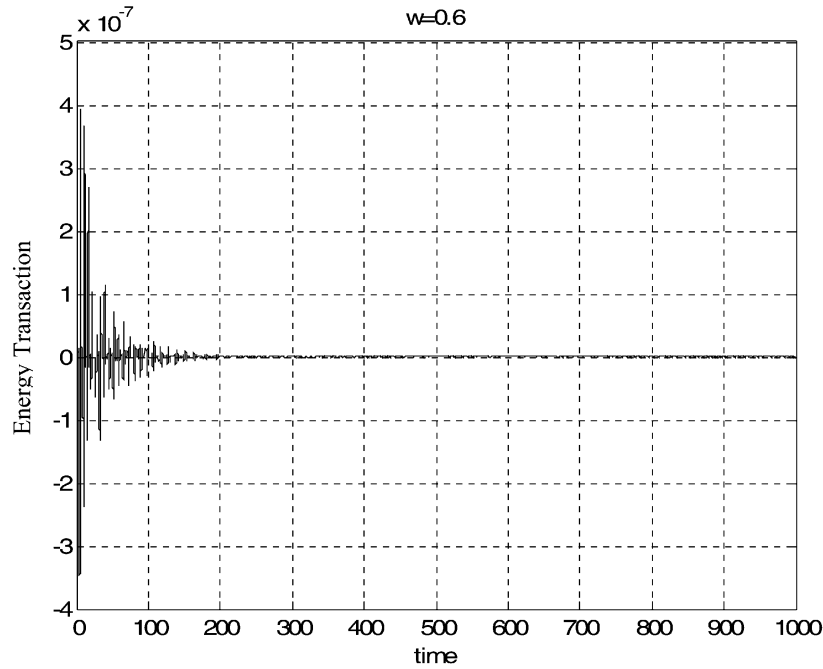
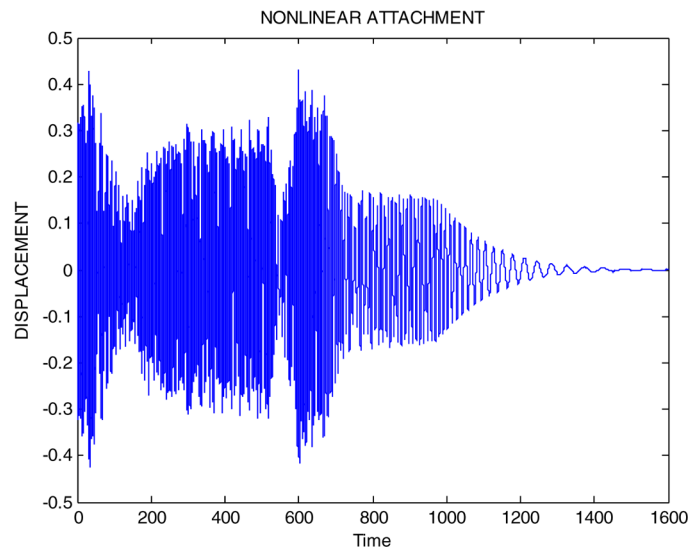


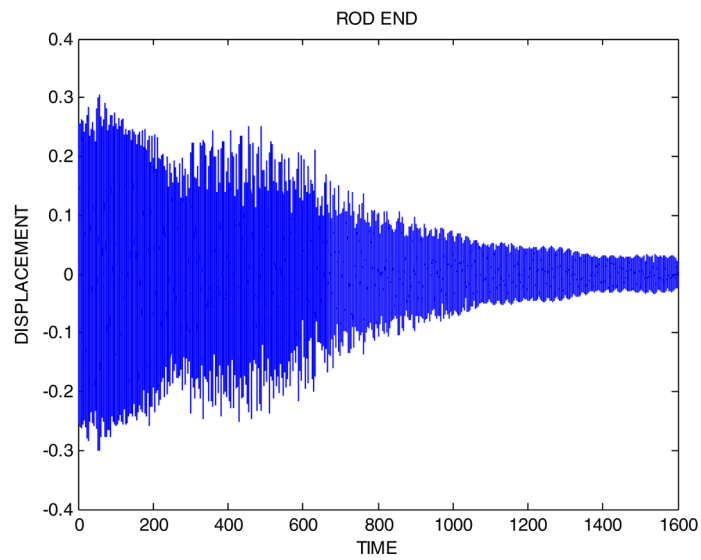
Fig. 5.24 ETM between the rod and the NES for damped responses depicted in Figure 5.23.

Summarizing, with decreasing energy the damped transition traces the lower in-phase backbone branch of the FEP. Since the damped orbit is initiated in the neighborhood of the subharmonic tongue $T_{1/3}^{(1)}$, the rod and the NES are initially locked into 1:3 TRC, with the rod oscillating nearly three times as fast as the NES, albeit with much smaller amplitude. As energy decreases due to damping dissipation the oscillation of the rod becomes increasingly faster than the NES (with ever decreasing amplitude), as the damped dynamics visits neighborhoods of higher-order tongues $T_{(1/n)}^{(1)}$, $n > 3$ lying along the lower in-phase backbone branch (see Figure 5.23b). As a result, the dynamics engages in increasingly higher-order in-phase TRCs, which, however, are realized at increasingly smaller time intervals. Since the lower backbone branch of the FEP does not undergo any major topological changes, no major (abrupt) transitions occur in the damped dynamics for this particular simulation.

An interesting series of nonlinear transitions is observed in the second numerical simulation of the damped dynamics depicted in Figures 5.25–5.27, and corresponding to initial condition of the system at point B on the subharmonic tongue $T_{1/5}^{(4)}$ of the FEP. That is, the motion is initiated on an undamped subharmonic orbit with dominant frequencies $\Omega = 2.214 \text{ rad/s} \approx \omega_4/5$ and ω_4 , see Figure 5.20a. Transitions in the damped dynamics are clearly evidenced by the irregular amplitude modulations of the time series (especially the one corresponding to the nonlinear



(a)



(b)

Fig. 5.25 Damped response initiated at point B of the FEP of Figure 5.20a. Transient responses $v(t)$ and $u(L, t)$.

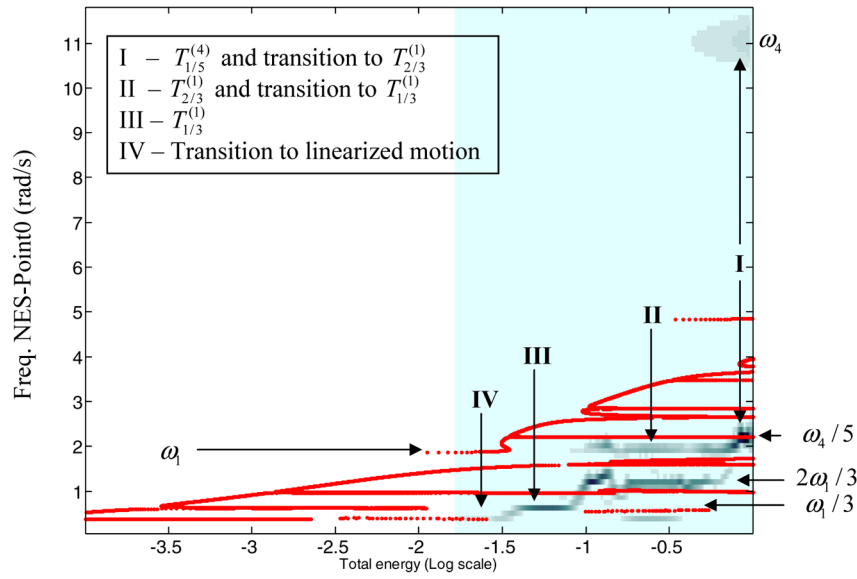


Fig. 5.26 Damped response initiated at point B of the FEP of Figure 5.20a. WT spectrum of the relative response $[v(t) - u(L, t)]$ superimposed to the FEP of the Hamiltonian system.

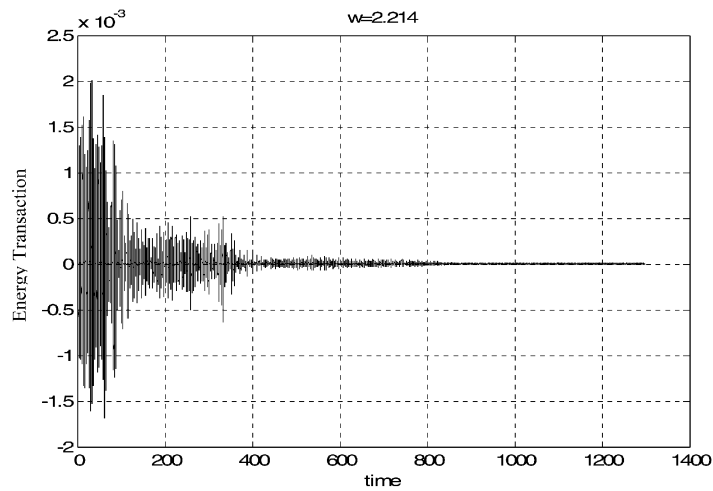


Fig. 5.27 ETM between the rod and the NES for the damped responses depicted in Figures 5.25 and 5.26.

attachment), or equivalently, by their multi-frequency contents. A better representation of the transitions in the damped dynamics is achieved by superimposing the WT spectrum of the relative motion $[v(t) - u(L, t)]$ to the FEP of the undamped sys-

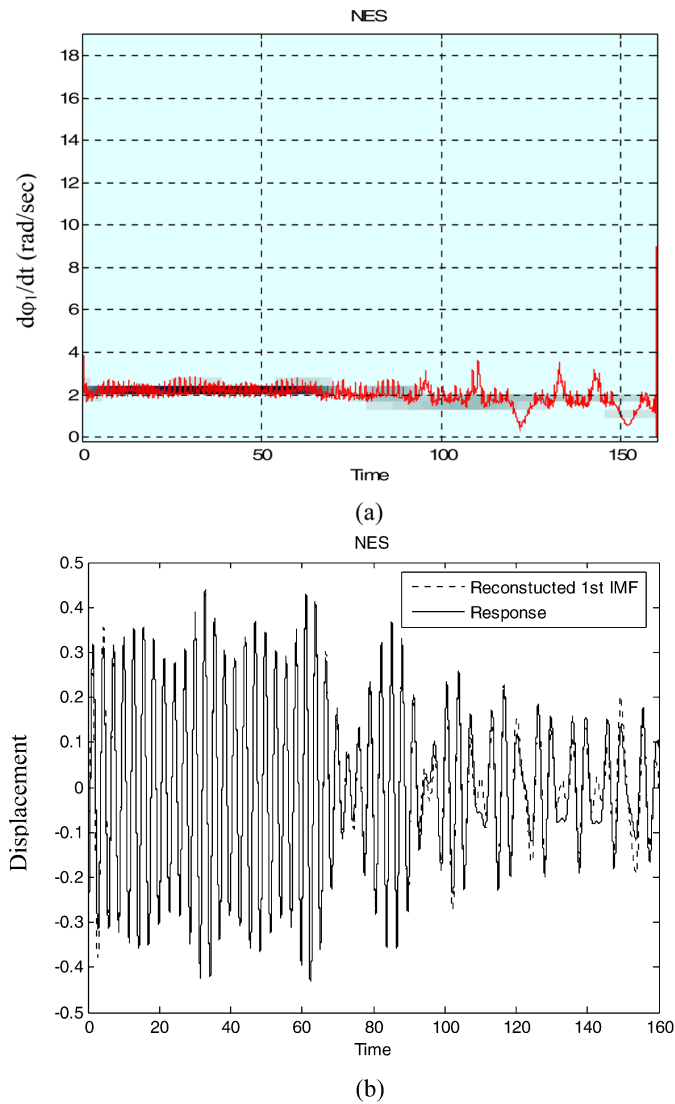


Fig. 5.28 EMD analysis of the NES response at Stage 1 of the damped transition of Figure 5.26: (a) instantaneous frequency of the 1st IMF superimposed to the WT spectrum of the transient response; (b) reconstruction of the transient response using the 1st IMF.

tem (see Figure 5.26). The following transitions are then discerned with decreasing energy of the motion:

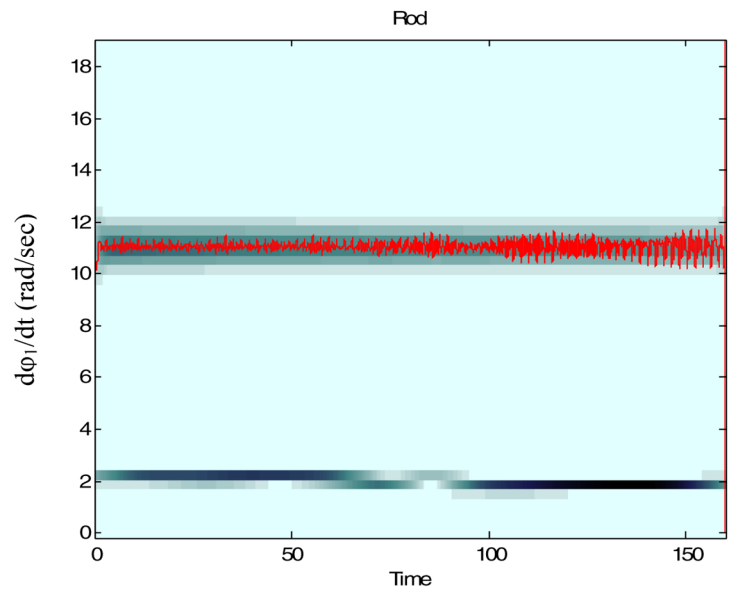
- I. Initial high energy transition from the subharmonic tongue $T_{1/5}^{(4)}$ (where the motion is initiated) to tongue $T_{2/3}^{(1)}$; two dominant harmonics appear at frequencies ω_4 and $\omega_4/5$ during this early stage of the response;
- II. Subharmonic transient resonance capture (TRC) on $T_{2/3}^{(1)}$ with the nonlinear attachment possessing a nearly constant dominant harmonic component at frequency $2\omega_1/3$ and a minor harmonic at frequency ω_1 ;
- III. Transition from tongue $T_{2/3}^{(1)}$ to tongue $T_{1/3}^{(1)}$ and subharmonic TRC on $T_{1/3}^{(1)}$; this secondary TRC is signified by the strong harmonic at frequency $\omega_1/3$ and the weaker harmonic at frequency ω_1 ;
- IV. Final low-energy transition to the linearized (low-amplitude) state, where the response of the nonlinear attachment is nearly zero and the dynamics is dominated by the response of the linear rod; the motion ends up being confined predominantly to the linear rod as its response decays to zero.

These complex transitions are caused by the fact that the essentially nonlinear attachment lacks a preferential frequency of oscillation (since it possesses zero linearized stiffness), which enables it to engage in fundamental or subharmonic TRCs with different modes of the linear rod over broad frequency ranges. Equivalently, the essential stiffness nonlinearity of the attachment generates a series of resonance capture cascades (RCCs) between the NES and the rod. As discussed in Section 3.5 such RCCs may lead to strong, multi-frequency TET.

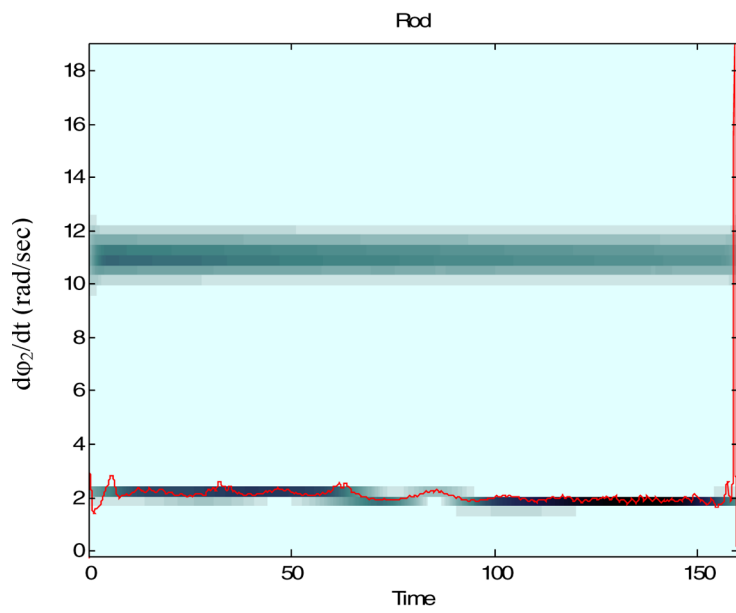
The WT spectra of the relative responses superimposed to the FEP provide a clear picture of the TRCs occurring in the damped transitions (see Figures 5.23b and 5.26). Even in cases where complex, multi-scale transitions take place, the depiction of WT spectra against appropriate FEPs provides a clear explanation and interpretation of the damped transitions. Hence, the methodology followed in this work can be extended to other applications where post-processing analysis of complex multi-frequency signals is performed.

We now proceed to the multi-scale analysis of the damped transition initiated on the subharmonic tongue $T_{1/5}^{(4)}$ (depicted in Figure 5.25) by applying EMD. Each of the four transitions I–IV identified in Figure 5.26 will be examined separately, with the aim to model the dynamics during each transition and determine the characteristic time scales where the nonlinear resonance interactions between the rod and the nonlinear attachment (or NES) take place.

Starting with the initial high-energy transition from tongue $T_{1/5}^{(4)}$ (where the motion is initiated) to tongue $T_{2/3}^{(1)}$ (Stage I, $0 < t < 160$ s), EMD analysis indicates that the NES response is dominated by its 1st IMF (see Figure 5.28), whereas, the rod end response is approximately modeled by two dominant IMFs, namely, its 1st and 2nd IMFs (see Figure 5.29). Proceeding to the analysis of the instantaneous frequencies of the dominant IMFs of the NES and rod end responses, we notice that these coincide with dominant harmonic components of the corresponding transient responses; hence, one concludes that the nonlinear dynamics of *the rod-NES transient interaction during Stage I of the damped transition is low-dimensional*, with the dynamics of the NES resembling the response of a single-DOF oscillator



(a)



(b)

Fig. 5.29 EMD analysis of the rod end response during Stage I of the damped transition of Figure 5.26: (a, b) instantaneous frequencies of the 1st and 2nd IMFs superimposed to the WT spectrum of the corresponding transient response.

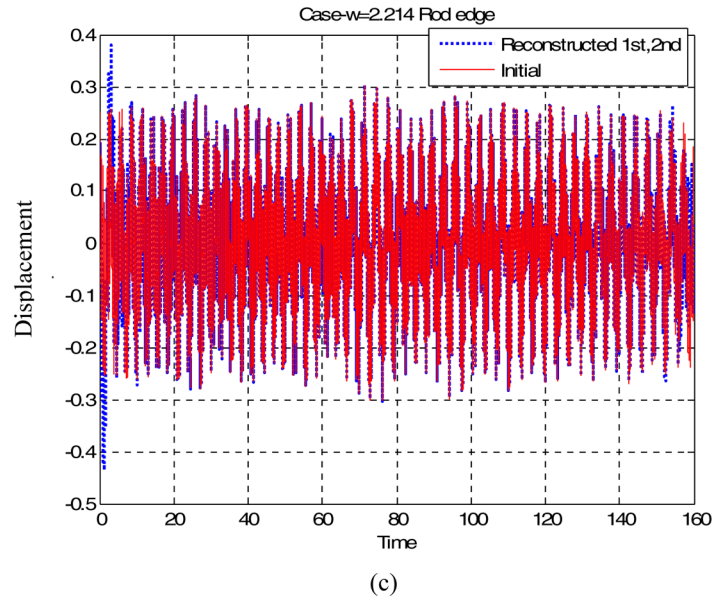


Fig. 5.29 EMD analysis of the rod end response during Stage I of the damped transition of Figure 5.26: (c) reconstruction of the transient response using the 1st and 2nd IMF.

with frequency being approximately equal to $\omega_4/5 \approx 2.214$ rad/s, and the dynamics of the rod end resembling the superposition of two single-DOF oscillators with frequencies ω_4 and $\omega_4/5$, respectively.

Hence, the EMD analysis indicates there is one dominant time scale in the transient dynamics of the NES and two dominant time scales in the dynamics of the rod end. These results are confirmed by the time series reconstructions depicted in Figures 5.28b and 5.29c, which prove the low-dimensionality of the NES-rod end nonlinear interaction during this initial (and highly energetic) stage of the motion. Moreover, during Stage I it is observed that the 1st IMF of the NES response is in near 1:5 resonance with the 1st IMF of the rod end response, and in near 1:1 resonance with 2nd IMF of the rod end response. These IMF TRCs are responsible for the energy exchanges that occur between the rod and the NES during Stage I of the transition.

Proceeding now to the more complicated damped transition occurring during Stage II ($160 < t < 420$ s – where the dynamics is captured on tongue $T_{2/3}^{(1)}$), the NES response appears to be dominated (and modeled) by its two leading IMFs (see Figure 5.30), which indicates that in this case the NES responds like a two-DOF oscillator. Considering the rod end response one establishes the existence of three dominant IMFs (the leading three IMFs depicted in Figure 5.31), with the instantaneous frequency of the 1st IMF executing modulated oscillations, and that of the 2nd IMF suffering sudden transitions (jumps) with increasing time. This type of com-

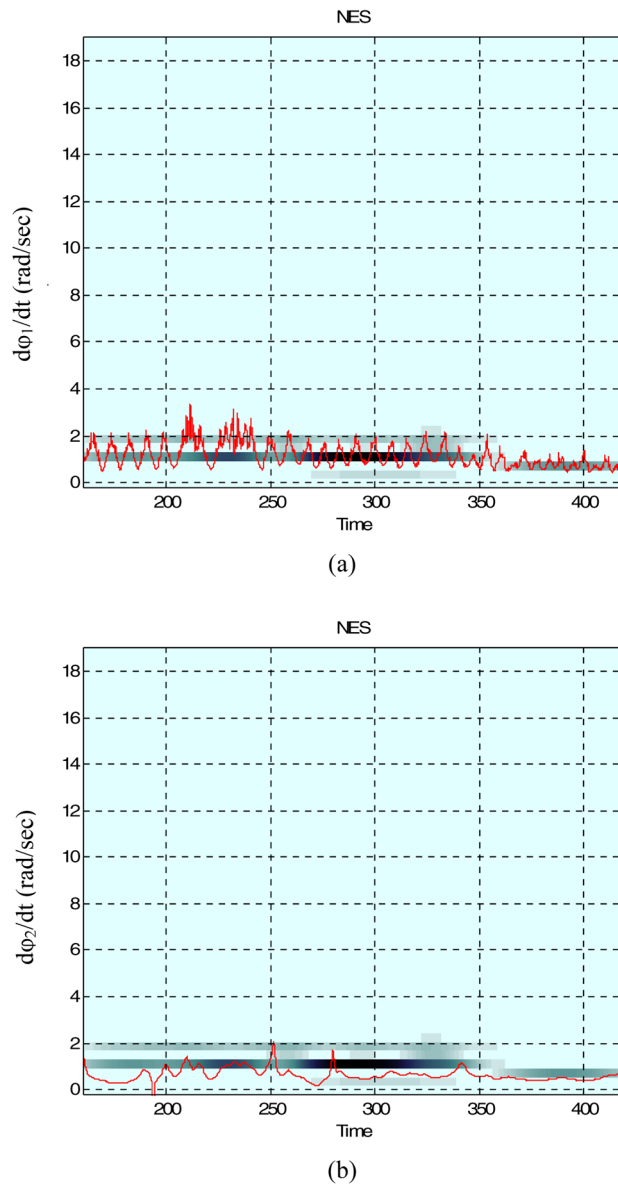


Fig. 5.30 EMD analysis of the NES response in Stage II of the damped transition of Figure 5.26: (a, b) instantaneous frequencies on the 1st and 2nd IMFS superimposed to the WT spectrum of the corresponding transient response.

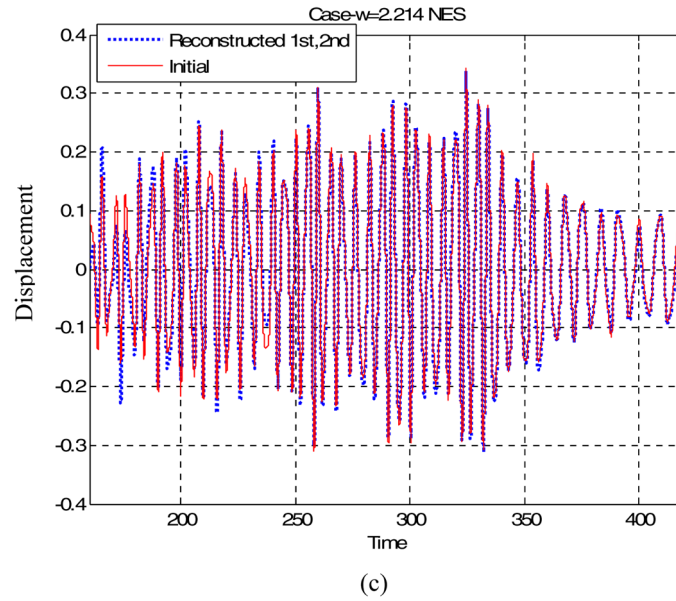
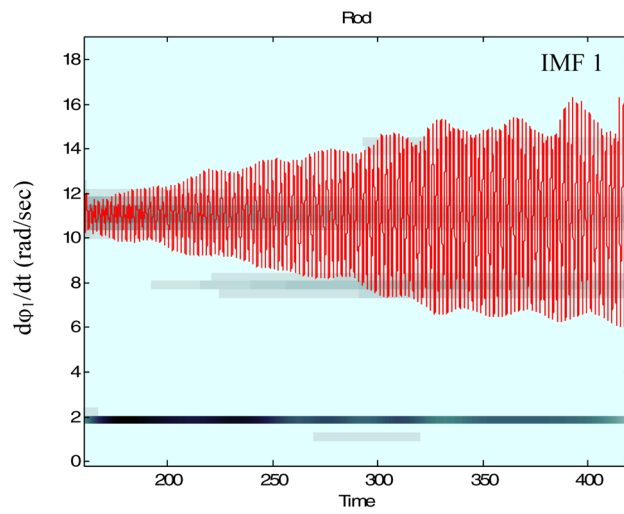


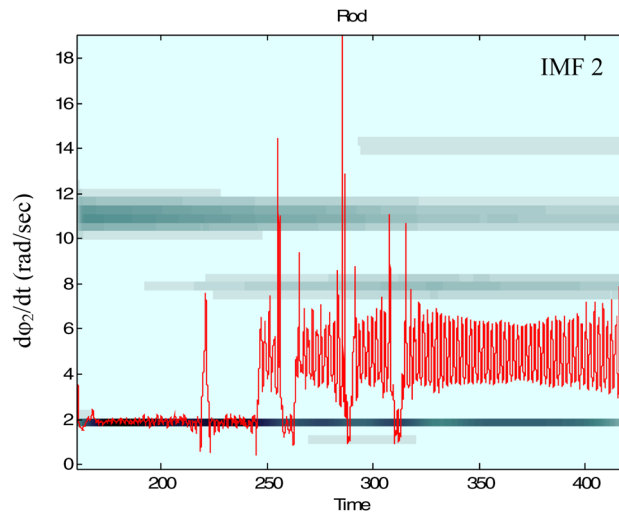
Fig. 5.30 EMD analysis of the NES response in Stage II of the damped transition of Figure 5.26: (c) reconstruction of the transient response using the 1st and 2nd IMF.

plex behavior of the IMFs is distinctly different from what was observed in Stage I and is characteristic of *intrawaves* in the time series. The existence of intrawaves in oscillatory modes (IMFs) is one of the nonlinear effects detected in typical nonlinear systems, such as the forced Duffing oscillator, the Lorenz system and the Rossler chaotic attractor, with the WT spectra not being able to detect them; as mentioned in Huang et al. (1998), ‘... in fact such an instantaneous frequency presentation actually reveals more details of the system: it reveals the variation of the frequency within one period, a view never seen before ...’. The time series reconstructions depicted in Figures 5.30b and 5.31b confirm that the superposition of the dominant IMFs accurately models the damped transition during this Stage of the motion. Note that the higher dimensionality of the NES and rod end responses observed in this case, signifies that the complexity of the dynamics increases compared to Stage I.

Considering the resonance interactions between the IMFs of the NES and the rod end responses during Stage II of the damped response, the 1st IMF of the NES is in near 2:3 internal resonance with the 2nd IMF of the rod end in the time interval $160 < t < 250$ s, and with the 3rd IMF of the rod end in the interval $250 < t < 350$ s. Moreover, there appears to be 1:1 internal resonance between the 1st IMF of the NES and the 3rd IMF of the rod end in the time interval $160 < t < 250$ s. The transition of the dynamics from tongue $T_{2/3}^{(1)}$ to tongue $T_{1/3}^{(1)}$ is signified by the decrease of the instantaneous frequency of the 1st IMF of the NES in the interval $t < 350$ s. The 1st IMF of the rod end possesses an oscillatory instantaneous frequency close to ω_4 in the interval $160 < t < 300$ s, and between ω_3 and ω_4 in the interval

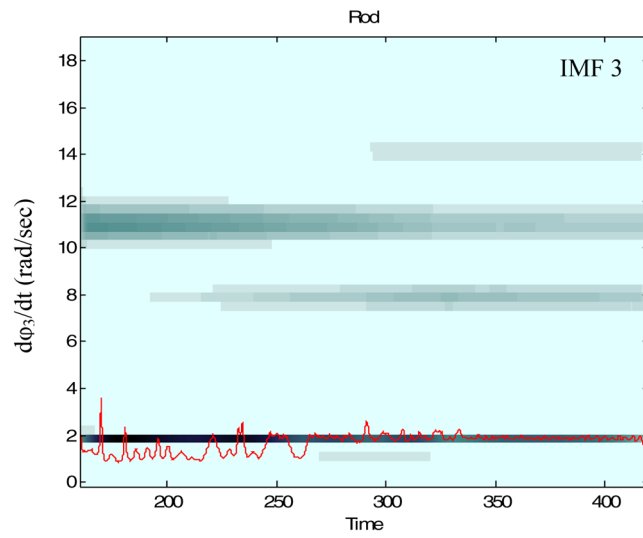


(a)

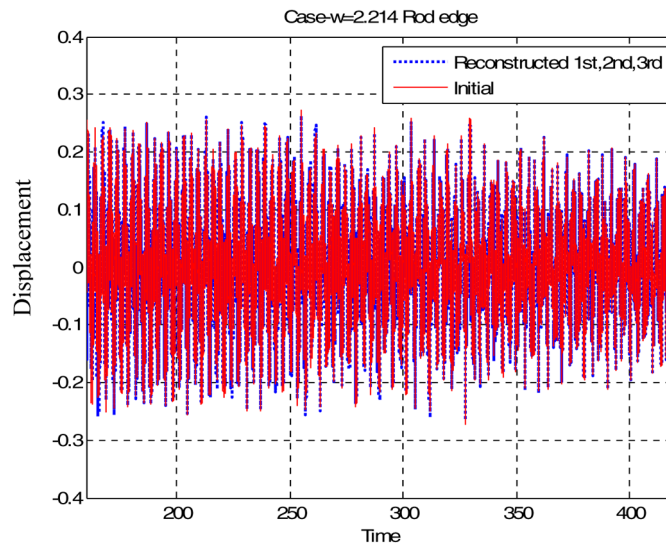


(b)

Fig. 5.31 EMD analysis of the rod end response in Stage II of the damped transition of Figure 5.26: (a, b) instantaneous frequencies of the 1st and 2nd IMFs superimposed to the WT spectrum of the corresponding transient response.



(c)



(d)

Fig. 5.31 EMD analysis of the rod end response in Stage II of the damped transition of Figure 5.26: (c) instantaneous frequencies of the 3rd IMFs superimposed to the WT spectrum of the corresponding transient response; (d) reconstruction of the transient response using the 1st, 2nd and 3rd IMF.

$300 < t < 420$ s (due to intrawaves, as discussed above). This EMD result agrees qualitatively with the late excitation of the 3rd linear mode of the rod, as indicated by the WT spectrum of the time series. The 2nd IMF of the rod end possesses an instantaneous frequency that is approximately equal to ω_1 for $160 < t < 250$ s, and is oscillatory about ω_2 for $250 < t < 350$ s; note that the WT spectrum of the time series of the rod end response does not indicate any excitation of the second mode of the rod during Stage II (which demonstrates the clear advantage of using EMD when analyzing complex signals, compared to the WT).

In Figures 5.32–5.34 the results of the EMD analysis of the damped response in Stages III and IV ($t > 420$ s) are depicted. In this case the NES response possesses three dominant IMFs, whereas the response of the rod end possesses four. Resonance capture of the dynamics on tongue $T_{1/3}^{(1)}$ is signified by the fact that the instantaneous frequency of the 3rd IMF of the NES response (which is dominant) is approximately equal to $\omega_1/3$ in the time interval $420 < t < 820$ s (with the exception of a ‘high frequency burst’ in the neighborhood of $t = 500$ s, which, however is of no practical significance as it corresponds to small amplitude of the IMF and is noise dominated); whereas, the transition from $T_{1/3}^{(1)}$ to the linearized regime is signified by the decrease of the instantaneous frequency of the same IMF for $t > 820$ s. It is interesting to note that in the time interval where the ‘high frequency burst’ of the 3rd IMF of the NES occurs, the 4th IMF of the NES ‘locks’ to the value $\omega_1/3$, and, hence, through superposition provides the necessary correction in the reconstruction of the overall time series in that time interval. Moreover, by studying the waveform of the 5th IMF of the NES one notes that this IMF dominates the transition from $T_{1/3}^{(1)}$ to the linearized regime occurring for $t > 800$ s. Considering the IMFs of the rod end response, one notes intrawaves centered at the linearized eigenfrequencies of the rod, $\omega_1, \dots, \omega_4$, similarly to those observed in the EMD analysis of the response in Stage II.

These results demonstrate the usefulness of EMD as a computational tool for post-processing transient nonlinear responses that involve multiple resonance captures and escapes. In fact, the previous results indicate that the EMD can capture delicate features of the dynamics (such as intrawave effects or participation of modes) that are not evident in the corresponding WT spectra. Nevertheless, the presented computational analysis shows that the combination of EMD and WT forms a powerful computational methodology for post-processing and modeling of complex nonlinear transient responses of practical structural systems.

In summary, damped nonlinear transitions of system (5.27) can be analyzed by a combination of numerical WT and EMD. These post-processing algorithms are capable of analyzing even complex nonlinear transitions, by providing the dominant frequency components (or equivalently the time scales) where the nonlinear phenomena take place. In addition, the EMD can detect delicate features of the dynamics, such as intrawaves – i.e., IMFs with modulated instantaneous frequencies, which the WTs cannot accurately sense. More importantly, the superposition of the dominant IMFs of the signal accurately reconstructs the signal, and, hence, these dominant IMFs may be interpreted in terms of outputs of intrinsic modal oscillators. It follows, that the determination of the dominant IMFs of a complex nonlinear signal,

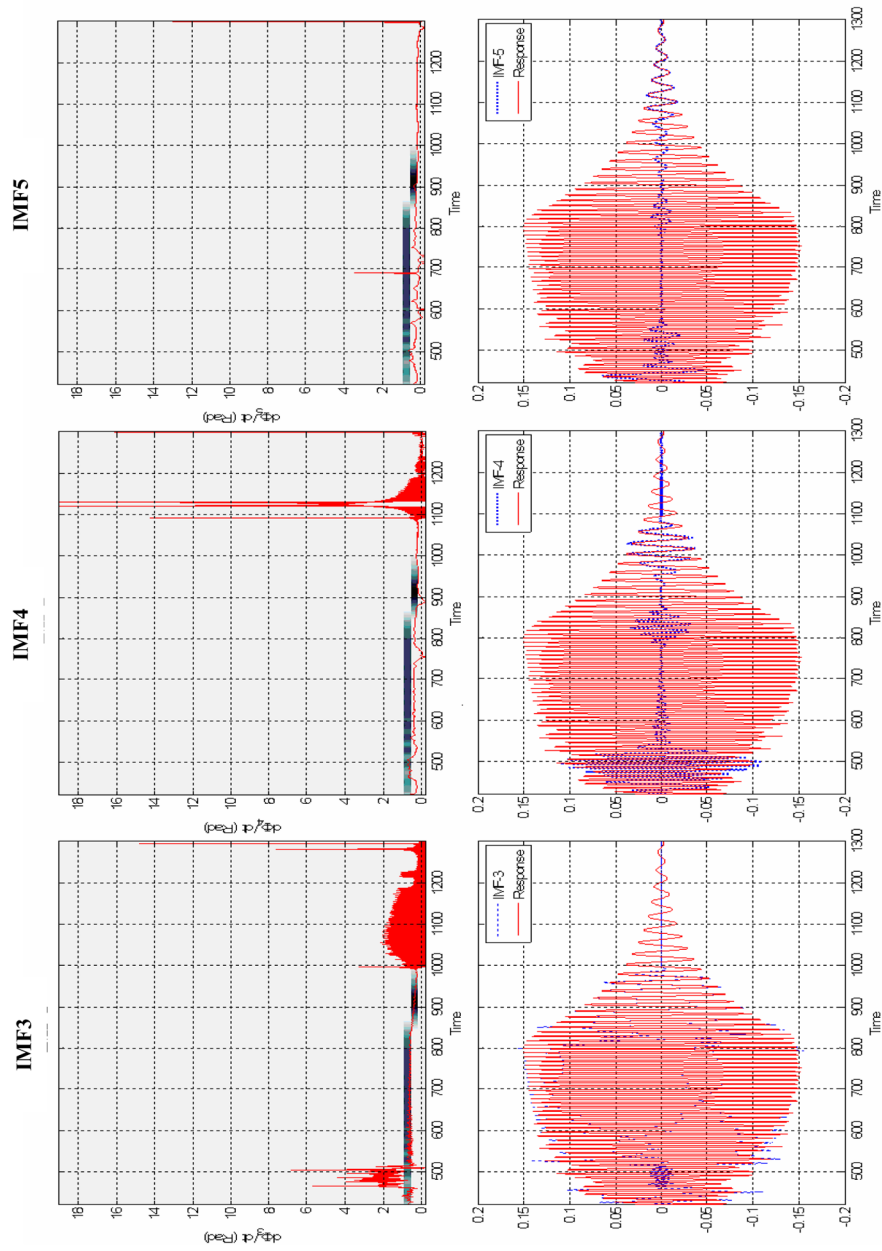


Fig. 5.32 EMD analysis of the NES response in Stages III–IV of the damped transition of Figure 5.26: instantaneous frequencies (superimposed on the wavelet transform of the response), and time series of the (dominant) 3rd, 4th and 5th IMFs.

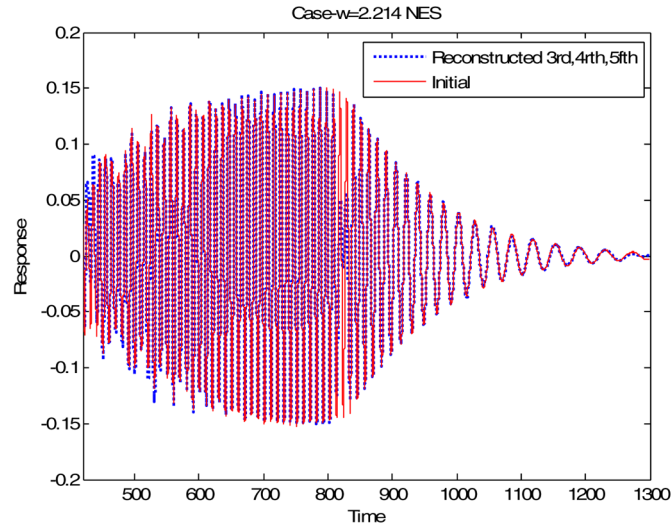


Fig. 5.33 EMD analysis of the NES response in Stages III–IV of the damped transition of Figure 5.26. Reconstruction of the response by superposing the three dominant IMFs.

paves the way for modeling this signal as a superposition of the responses of intrinsic modal oscillators, for determining the dimensionality of the governing dynamics, and for ultimately performing multi-scaled system identification of the underlying dynamics of the system.

5.3 Rod of Semi-Infinite Length with SDOF NES

We now extend our study of strongly nonlinear dynamic interactions and TET in elastic continua with strongly nonlinear end attachments, by analyzing the damped dynamics of a semi-infinite linear dispersive rod possessing a local essentially nonlinear end attachment. We study resonant interactions of the attachment with incident traveling waves from the rod, as well as 1:1 TRCs of the nonlinear attachment with an in-phase mode at the bounding frequency between the PZ and AZ of the rod. This study can be considered as extension of the study of finite rod-NES dynamics carried out in Section 5.2, and of the analysis of semi-infinite linear chain-NES dynamic interaction studied in Section 3.5.2.

As pointed out by Goodman et al. (2002), the interaction of incident traveling solitary waves with a local defect can lead to various dynamic phenomena, such as, speed up or slow down of the traveling wave; scattering of the wave to multiple independent wavepackets; or even trapping of the wave at the point of defect in the form of a localized mode (standing wave). Goodman et al. (2002) investigated in detail the complicated dynamics resulting from soliton – local impurity interaction for the

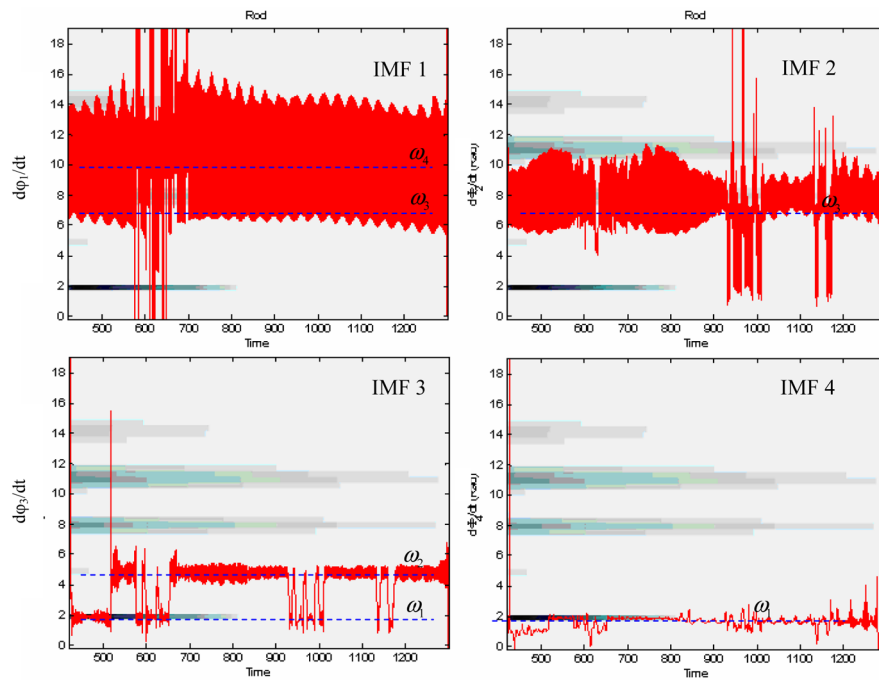


Fig. 5.34 EMD analysis of the rod end response in Stages III–IV of the damped transition of Figure 5.26. Instantaneous frequencies (superimposed on the WT spectrum of the response) of the (dominant) 1st, 2nd, 3rd and 4th IMF.

case of the sine – Gordon equation. If the local nonlinear attachment considered in this section is regarded as a type of ‘defect’, the dynamical phenomena considered are similar, but in the context of linear wave-guide/local nonlinear defect interaction. Additional studies on soliton-defect dynamic interactions were performed in Cao and Malomed (1995), Zei et al. (1992), Goodman and Haberman (2004) and in references therein.

In other related works, localized modes in a multi-coupled periodic system of infinite extent with a single nonlinear disorder were analyzed by Cai et al. (2000); symmetric, anti-symmetric and asymmetric localized modes were computed, and their stability was analyzed in that work. Komech (1995) studied the dynamics of an infinite string with an attached nonlinear oscillator and showed that each finite-energy solution of the integrated system tends to a stationary solution as $t \rightarrow \pm\infty$. Trapped (localized) modes in stop bands (AZs) of two-dimensional waveguides with obstacles were discussed in Linton et al. (2002) and in a series of works referenced therein. In a more applied work (Qu, 2002), order reduction techniques for engineering systems with local nonlinearities were discussed. In related works, Kotousov (1996) studied wave propagation in elastic continua with local nonlinearities; El-Khatib et al. (2005) studied suppression of bending waves in a beam by means

of a tuned vibration absorber; and Komech and Komech (2006) studied long-term asymptotics of finite-energy solutions of a Klein–Gordon equation with a local oscillator attachment.

5.3.1 Reduction to Integro-differential Form

We consider a general linear undamped elastic waveguide (designated as the primary system), coupled to an essentially nonlinear attachment (the NES) by means of a weak linear stiffness. The local attachment is grounded, and possesses unit mass, viscous damping and nonlinearizable stiffness nonlinearity of the third degree. Denoting by $v(t)$ the displacement of the NES, and by $u(\underline{x}_O, t)$ the displacement of the primary system at the point of attachment O in the direction of $v(t)$, we obtain the following governing differential equation for motion of the attachment (see Figure 5.35):

$$\ddot{v}(t) + \lambda \dot{v}(t) + \varepsilon v(t) + Cv^3(t) = \varepsilon u(\underline{x}_O, t) \quad (5.38)$$

In (5.38) the small parameter $0 < \varepsilon \ll 1$ scales the weak coupling, λ denotes the viscous damping coefficient, and C the coefficient of the stiffness nonlinearity; the spatial coordinate \underline{x} parametrizes the undeformed configuration of the primary system in its configuration space. Assuming that the primary system is initially at rest and that an external force $F(\underline{x}_A, t)$ is applied at point A at $t = 0$ (see Figure 5.35), we express its response at the point of attachment O, $u(\underline{x}_O, t)$, in terms of its corresponding Green's functions g_{OO} and g_{OA} :

$$u(\underline{x}_O, t) = \int_{-\infty}^t F(\underline{x}_A, \tau) g_{OA}(t - \tau) d\tau - \int_{-\infty}^t \varepsilon [u(\underline{x}_O, \tau) - v(\tau)] g_{OO}(t - \tau) d\tau \quad (5.39)$$

The Green's function g_{OO} denotes the displacement at point O of the primary system in the direction of $v(t)$ due to a unit impulse applied at the same point and the same direction; whereas g_{OA} denotes the displacement at point O of the primary system in the direction of $v(t)$, due to a unit impulse applied at point A in the direction of the external force.

Substituting (5.39) into (5.38) and iterating repeatedly the previous procedure in order to express $u(\underline{x}_O, t)$ on the right-hand side in terms of the afore-mentioned Green's functions and the NES displacement $v(t)$, we obtain the following general integro-differential equation governing the oscillation of the nonlinear attachment

$$\begin{aligned} \ddot{v}(t) + \lambda \dot{v}(t) + \varepsilon v(t) + Cv^3(t) &= \varepsilon [F(\underline{x}_A, t) * g_{OA}(t)] \\ &+ \varepsilon^2 [-F(\underline{x}_A, t) * g_{OA}(t) * g_{OO}(t) + v(t) * g_{OO}(t)] + \dots \\ &+ \varepsilon^n \left[(-1)^{n-1} F(\underline{x}_A, t) * g_{OA}(t) * \underbrace{g_{OO}(t) * \dots * g_{OO}(t)}_{(n-1) \text{ terms}} \right] \end{aligned}$$

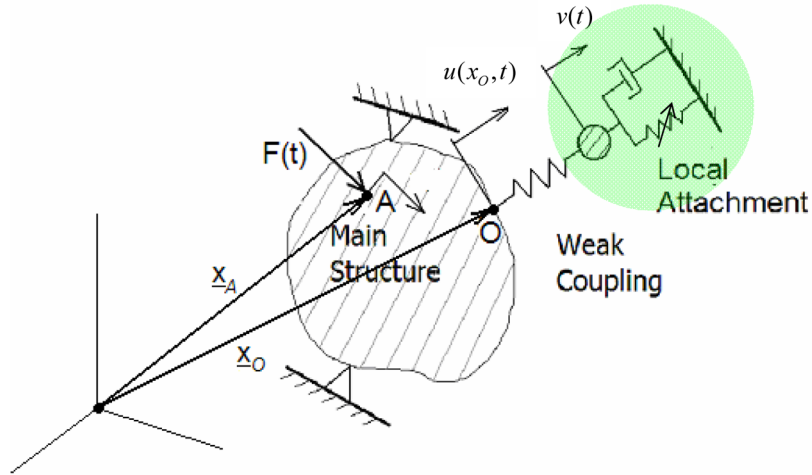


Fig. 5.35 Elastic wave guide with a weakly coupled grounded NES.

$$+ (-1)^n v(t) * \underbrace{g_{OO}(t) * \dots * g_{OO}(t)}_{(n-1) \text{ terms}} \Big] + \dots \quad (5.40)$$

where (*) denotes the convolution operator. What makes possible the reduction of the governing equations of motion to integro-differential form is the assumption of linearity of the primary system (i.e., the elastic waveguide). Terms on the right-hand side of (5.40) containing only the external excitation $F(\underline{x}_A, t)$ represent non-homogeneous ‘forcing’ terms of the above dynamical system, and govern, in essence, the dynamics of the attachment predominantly influenced by the external excitation. Similarly, terms on the right-hand side that contain integrals in terms of $v(t)$ represent the dynamics of the attachment predominantly influenced by its complex nonlinear dynamic interaction with the primary system, including scattering of waves from the NES back to the waveguide and targeted energy transfer effects. We conclude that the representation (5.40) leads to a natural partition of the dynamics of the attachment.

In the remainder of this section we employ the general expression (5.40) to study the nonlinear dynamic interaction of a dispersive linear rod of infinite spatial extent resting on a continuous elastic foundation (the primary system), with an essentially nonlinear grounded attachment that is weakly coupled to its right boundary. This system can be regarded as the semi-infinite extension as $L \rightarrow \infty$ of the rod-NES system depicted in Figure 5.6 (but with a grounded instead of an ungrounded NES). The analysis follows closely (Vakakis et al., 2004).

Depending on the specific initial conditions and the external forces considered, we distinguish between two systems, and label them as *Systems I* and *II*. System I is forced by an impulsive excitation applied to a single point of the semi-infinite rod,

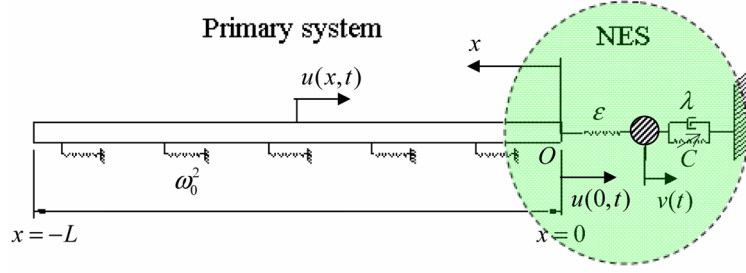


Fig. 5.36 Rod on elastic foundation with weakly coupled grounded NES.

with all initial conditions of the primary system and the local attachment being assumed as zero. System II is unforced with the excitation being provided by an initial displacement of the rod in the form of a finite unit step, with all other initial conditions being set equal to zero. After providing detailed mathematical descriptions of the two systems, a study of the different regimes of the rod-attachment interaction is carried out using computational and analytical tools.

5.3.1.1 System I: Impulsive Excitation

Assuming for the moment that the primary system is an undamped linearly elastic rod of finite length L resting on a continuous linear elastic foundation, the dynamics become one-dimensional with governing equations of motion given by

$$\begin{aligned}
 -\frac{\partial^2 u(x, t)}{\partial x^2} + \omega_0^2 u(x, t) + \frac{\partial^2 u(x, t)}{\partial t^2} &= F\delta(x + e)\delta(t), \quad -L \leq x \leq 0 \\
 \ddot{v}(t) &= \lambda \dot{v}(t) + Cv^3(t) + \varepsilon[v(t) - u(0, t)] = 0 \\
 \frac{\partial u(0, t)}{\partial x} + \varepsilon[v(t) - u(0, t)] &= 0, \quad u(-L, t) = 0 \\
 u(x, 0) = \frac{\partial u(x, 0)}{\partial t} &= v(0) = \dot{v}(0) = 0
 \end{aligned} \tag{5.41}$$

The point of attachment is situated at $x = 0$, normalized material properties for the rod are used, and the normalized stiffness of the elastic foundation is denoted by ω_0^2 ; in addition, all geometric and material properties of the rod are assumed to be uniform. It is assumed that an impulse of magnitude F is applied at $x = -e > -L$ at $t = 0$.

Taking the limit $L = \infty$ one obtains a semi-infinite, impulsively loaded dispersive rod. The rod of infinite length possesses a PZ corresponding to $\omega > \omega_0$, where traveling wave solutions exist, and an AZ for $0 < \omega < \omega_0$ where localized standing waves (near-field) solutions are realized. At the bounding frequency $\omega_b = \omega_0$

(separating the AZ and the PZ) the rod oscillates in an ‘in-phase’ normal mode with all points executing an identical synchronous time-periodic oscillation of constant amplitude.

The Green’s function of the rod of infinite length describing the response of the rod at position x and time t due to a unit impulse applied at point \bar{x} and time instant \bar{t} is given by

$$g_1(x - \bar{x}, t - \bar{t}) = J_0 \left[\omega_0 \sqrt{(t - \bar{t})^2 - (x - \bar{x})^2} \right] H(t - \bar{t} - x + \bar{x}) \quad (5.42)$$

where $J_0(\cdot)$ denotes the Bessel function of zero-th order and first kind, and $H(\cdot)$ Heaviside’s function. Then, in terms of the general expression (5.40), the two Green’s functions g_{OO} and g_{OA} are expressed as follows:

$$\begin{aligned} g_{OO}(t) &= g_1(0, t) = J_0(\omega_0 t) H(t) \\ g_{OA}(t) &= g_1(0 + e, t) = J_0 \left[\omega_0 \sqrt{t^2 - (0 + e)^2} \right] H(t - 0 - e) \end{aligned} \quad (5.43)$$

Substituting (5.43) into (5.40), we obtain the following governing integro-differential equation for the nonlinear attachment for System I (Vakakis et al., 2004):

$$\begin{aligned} \ddot{v}(t) + \lambda \dot{v}(t) + Cv^3(t) + \varepsilon v(t) - \varepsilon^2 \int_0^t v(\tau) J_0[\omega_0(t - \tau)] d\tau \\ = \varepsilon F J_0 \left[\omega_0 \sqrt{t^2 - e^2} \right] H(t - e) \\ - \varepsilon^2 F \int_0^t J_0 \left[\omega_0 \sqrt{\tau^2 - e^2} \right] H(\tau - e) J_0[\omega_0(t - \tau)] d\tau + O(\varepsilon^3) \\ \equiv \varepsilon F_1(t) + \varepsilon^2 F_2(t) + O(\varepsilon^3) \\ v(0) = \dot{v}(0) = 0, \quad L \rightarrow \infty \quad (\text{System I}) \end{aligned} \quad (5.44)$$

Hence, System I is an impulsively loaded semi-infinite dispersive rod with an essentially nonlinear end attachment. The two expressions on the right-hand side are pure non-homogeneous terms and represent the leading-order ‘direct forcing’ of the nonlinear attachment due to the impulsive excitation. The integral term on the left-hand side models the leading-order interaction of the NES with the dispersive rod, including energy radiation from the NES back to the rod and energy entrapment by the NES in the form of localized vibrations. These effects will be studied in more detail in the following exposition. Note, however, that the system (5.44) provides only an approximation to the dynamics since it omits $O(\varepsilon^3)$ and higher-order terms; it follows, that the derived results can only be asymptotically valid in the limit of weak coupling as $\varepsilon \rightarrow 0$.

For the case of *finite rod* the above dynamical system must be modified to account for wave effects due to reflections at the boundaries of the rod. The modifications of (5.44) due to finiteness of the dispersive rod can be analytically studied by applying

Laplace transform with respect to the temporal variable directly to the system of equations (5.41) for $0 > x > -L > -\infty$. To this end, we Laplace-transform the corresponding equations of motion (5.41) and solve the first equation to obtain

$$\begin{aligned} Y''(x, s) - (s^2 + \omega_0^2)Y(x, s) &= F\delta(x + e) \Rightarrow \\ Y(x, s) &= A \cosh[(s^2 + \omega_0^2)^{1/2}(L + x)] + B \sinh[(s^2 + \omega_0^2)^{1/2}(L + x)] \\ &+ \int_0^{-L} F\delta(\xi + e)h(x - \xi, s)d\xi \end{aligned} \quad (5.45)$$

where $Y(x, s) = \Lambda[u(x, t)]$ is the Laplace transform of $u(x, t)$, s the Laplace variable, and $h(x, s) = \alpha^{-1} \sinh \alpha x$, $\alpha = \alpha(s) = \sqrt{s^2 + \omega_0^2}$.

The unknowns A and B in (5.45) are computed by imposing the transformed boundary conditions [the third of relations (5.41)]. Evaluating the resulting expression at $x = 0$ we obtain the following expression for the Laplace-transformed displacement of the point of connection of the rod with the nonlinear attachment,

$$\begin{aligned} Y(0, x) &= \Phi(s) \cosh \alpha L \\ &+ [\alpha \coth \alpha L + \varepsilon]^{-1} \{ \varepsilon V(s) - \varepsilon \Phi(s) \coth \alpha L - \Phi(s) \alpha \sinh \alpha L \} \end{aligned} \quad (5.46)$$

where $V(s)$ is the Laplace transform of $v(t)$, and $\Phi(s)$ is computed as

$$\Phi(s) = \int_{-L}^0 F\delta(x + e)h(-L - x, s)dx = h(-L + e, s)$$

For $\varepsilon \ll 1$ we expand (5.46) in ascending powers of the small parameter to obtain the following final approximate expression for $Y(0, s)$,

$$\begin{aligned} Y(0, s) &= F\alpha^{-1}(-\tanh \alpha L \cosh \alpha e + \sinh \alpha e)[1 - \varepsilon\alpha^{-1} \tanh \alpha L] \\ &+ \varepsilon\alpha^{-1}V(s) \tanh \alpha L + O(\varepsilon^2) \end{aligned} \quad (5.47)$$

with $a = a(s) = \sqrt{s^2 + \omega_0^2}$, and $x = -e$ being the point of application of the impulsive load.

The Laplace inversion of relation (5.47) can be expressed in terms of left- and right-going waves propagating in the finite rod (Caughey, 1987). Since this approach can add to our physical insight of the early-time nonlinear dynamic interactions occurring in System I we proceed to discuss it briefly. To this end, we express the hyperbolic functions in (5.47) in terms of exponentials as follows:

$$\begin{aligned} \tanh \alpha L &= 1 - 2e^{-2\alpha L} + 2e^{-4\alpha L} - 2e^{-6\alpha L} + \dots \\ \sinh \alpha e &= \frac{e^{\alpha e} - e^{-\alpha e}}{2}, \quad \cosh \alpha e = \frac{e^{\alpha e} + e^{-\alpha e}}{2} \end{aligned}$$

Substituting these expressions into (5.47) we obtain the following approximate expression approximating the early-time dynamics of the point of connection of the rod to the NES:

$$\begin{aligned} Y(0, s) = & F\alpha^{-1}[-e^{-\alpha e} + e^{\alpha(-2L+e)} + e^{\alpha(-2L-e)} + \dots] \\ & - \varepsilon F\alpha^{-2}[-e^{-\alpha e} + e^{\alpha(-2L+e)} + e^{\alpha(-2L-e)} + \dots] \\ & + \varepsilon\alpha^{-1}V(s)[1 - 2e^{-2\alpha L} + \dots] + O(\varepsilon^2) \end{aligned} \quad (5.48)$$

The exponentials in (5.48) represent arrivals of individual longitudinal waves at the point of attachment O of the rod, caused either due to the impulsive excitation or due to reflections from the boundaries of the finite rod. The advantage of considering the Laplace-transformed response in the form (5.48) instead of (5.47) is that the former can be directly inverted to yield an approximation of the early-time transient dynamics of the system. Indeed, applying inverse Laplace transform to (5.48) we obtain the following early-time approximation of the dynamics of the connecting point, $u(0, t) = \Lambda^{-1}[Y(0, s)]$, in the form of left- and right-going traveling waves:

$$\begin{aligned} u(0, t) = & - F \left\{ J_0 \left[\omega_0 \sqrt{t^2 - e^2} \right] H(t - e) J_0 \left[\omega_0 \sqrt{t^2 - (2L - e)^2} \right] H(t - (2L - e)) + \dots \right\} \\ & + \varepsilon F \left\{ \int_0^t J_0[\omega_0(t - \tau)] J_0 \left[\omega_2 \sqrt{\tau^2 - e^2} \right] H(\tau - e) d\tau \right. \\ & \left. - \int_0^t J_0[\omega_0(t - \tau)] J_0 \left[\omega_0 \sqrt{\tau^2 - (2L - e)^2} \right] H(\tau - (2L - e)) d\tau - \dots \right\} \\ & + \varepsilon \left\{ \int_0^t v(\tau) J_0[\omega_0(t - \tau)] d\tau - 2 \int_0^t v(t - \tau) J_0 \left[\omega_0 \sqrt{\tau^2 - (2L)^2} \right] H(\tau - 2L) d\tau + \dots \right\} \\ & + O(\varepsilon^2) \end{aligned} \quad (5.49)$$

Terms in the above expression multiplied by the Heaviside function $H(t - e)$ are waves arriving at the nonlinear attachment after propagating through a length equal to e , i.e., they originate at the point of forcing directly after application of the impulsive load; terms multiplied by $H(t - 2L)$ are waves arriving at the nonlinear attachment after traveling through the entire length of the rod and after being reflected from the fixed boundary at $x = -L$, and so on. Hence, expression (5.49) enables us to study in detail the early-time dynamic interaction of the nonlinear attachment with individual incoming wavepackets propagating through the dispersive rod.

Substituting (5.49) into the second of relations (5.41) we obtain a model for the early time dynamics of the nonlinear attachment; this model is in the form of incident and reflected traveling waves. Hence, one is able to study the early-time nonlinear dynamic interaction of the nonlinear attachment with the leading incoming

wavepackets from the rod generated by the impulse. In the limit of the semi-infinite rod, $L = \infty$, we recover System I [equation (5.44)]. A similar wave-based early-time analysis can be applied to the dynamics of System II, which we now proceed to examine.

5.3.1.2 System II: Initial Step Displacement Distribution

Considering again the finite rod-NES configuration, we assume that there is no external excitation, and that a finite-step initial displacement distribution is imposed. This leads to the following system of governing equations:

$$\begin{aligned}
\frac{\partial^2 u(x, t)}{\partial t^2} + \omega_0^2 u(x, t) - \frac{\partial^2 u(x, t)}{\partial x^2} &= 0, \quad -L < x < 0 \\
\ddot{v}(t) + \lambda \dot{v}(t) + Cv^3(t) + \varepsilon[v(t) - u(0, t)] &= 0 \\
\frac{\partial u(0, t)}{\partial x} + \varepsilon[v(t) - u(0, t)] &= 0, \quad u(-L, t) = 0 \\
u(x, 0) &= D[H(x + d_1) - H(x + d_2)], \quad -L \leq -d_2 < -d_1 \leq 0 \\
\frac{\partial u(x, 0)}{\partial t} = v(0) = \dot{v}(0) &= 0
\end{aligned} \tag{5.50}$$

where $d_2 - d_1 = d > 0$, D denotes the magnitude of the step of the initial displacement, and L the length of the rod. In this case, we need to modify the previous Green's function formulation in order to compute the transient response. Indeed, an initial rod displacement $u(x_0, t_0)$ produces the equivalent force distribution $u(x_0, t_0)\delta'(t_0)$ (Morse and Feshbach, 1953), where prime denotes generalized differentiation (Richtmyer, 1985) of the delta function with respect to its argument.

Following the methodology of Section 5.3.1.1 and letting $L \rightarrow \infty$ we obtain the following approximate integro-differential equation governing the dynamics of the nonlinear attachment:

$$\begin{aligned}
&\ddot{v}(t) + \lambda \dot{v}(t) + \varepsilon v(t) + Cv^3(t) \\
&= \left\{ \varepsilon \int_0^t \int_{-\infty}^0 u(\xi, 0)\delta'(\tau)g_1(x - \xi, t - \tau)d\xi d\tau \right. \\
&\quad \left. - \varepsilon^2 \int_0^t \left[\int_0^\tau \int_{-\infty}^0 u(\xi, 0)\delta'(\tau)g_1(x - \xi, t - \lambda)d\xi d\lambda \right] g_1(0, t - \tau)d\tau \right. \\
&\quad \left. + \varepsilon^2 \int_0^1 v(t - \tau)g_1(0, \tau)d\tau \right\}_{x=0} + O(\varepsilon^3)
\end{aligned} \tag{5.51}$$

Performing manipulations on the right-hand side of the above equation we derive the following integro-differential equation governing the nonlinear dynamics of System II:

$$\begin{aligned}
& \ddot{v}(t) + \lambda \dot{v}(t) + Cv^3(t) + \varepsilon v(t) - \varepsilon^2 \int_0^t v(\tau) J_0[\omega_0(t - \tau)] d\tau \\
&= \varepsilon D \left\{ H(t - d_1) - H(t - d - 2) - t\omega_0 \int_{-d_2}^{-d_1} \frac{H(t + \xi)}{\sqrt{t^2 - \xi^2}} J_1 \left[\omega_0 \sqrt{t^2 - \xi^2} \right] d\xi \right\} \\
&- \varepsilon^2 D \int_0^t \left\{ H(\tau - d_1) - H(\tau - d_2) - \tau\omega_2 \int_{-d_2}^{-d_1} \frac{H(\tau + \xi)}{\sqrt{\tau^2 - \xi^2}} J_1 \left[\omega_0 \sqrt{\tau^2 - \xi^2} \right] d\xi \right\} \\
&\times J_0[\omega_0(t - \tau)] H(t - \tau) d\tau + O(\varepsilon^3) \\
&\equiv \varepsilon F_1(t) + \varepsilon^2 F_2(t) + O(\varepsilon^3) \\
&v(0) = \dot{v}(0) = 0, \quad L \rightarrow \infty \quad (\text{System II})
\end{aligned} \tag{5.52}$$

As for System I, this asymptotic model is approximate [since terms of $O(\varepsilon^3)$ or of higher order are omitted], and converges to the exact system in the limit of weak coupling $\varepsilon \rightarrow 0$. In summary, System II models a semi-infinite, unforced dispersive rod with a finite-step initial displacement distribution, zero initial velocity, and an essentially nonlinear end attachment to its free end. Similarly to System I the two integrals on the right-hand side of equation (5.52) are pure non-homogeneous terms representing the leading-order ‘direct forcing’ of the nonlinear attachment due to the initial step displacement distribution of the rod. The integral term on the left-hand side models the leading-order interaction between the attachment and the dispersive rod and is identical to the corresponding term for System I. Moreover, one can develop expressions analogous to (5.48) and (5.49) to study the early time dynamic interaction of the nonlinear attachment with incoming waves propagating through the dispersive finite rod.

In the following section we perform computational simulations of Systems I and II to study the nonlinear dynamical interaction of the semi-infinite rod with the nonlinear attachment (the NES). Two computational models will be considered. The first model utilizes Neumann expansions to replace the integrals on the left-hand sides of Systems I and II by an infinite set of first-order ordinary differential equations; the second model is based on finite element simulations of the original equations of motion.

5.3.2 Numerical Study of Damped Transitions

To study damped transitions in Systems I and II it is necessary to numerically integrate the corresponding governing equations of motion (5.44) and (5.52). Both

systems can be reduced to the following compact form:

$$\begin{aligned}
& \ddot{v}(t) + \lambda \dot{v}(t) + Cv^3(t) + \varepsilon v(t) - \varepsilon^2 \int_0^t v(\tau) J_0[\omega_0(t - \tau)] d\tau \\
& = \varepsilon F_1(t) + \varepsilon^2 F_2(t) + O(\varepsilon^3) \\
& v(0) = \dot{v}(0) = 0
\end{aligned} \tag{5.53}$$

which, as we proceed to show can be expressed as an infinite set of ordinary differential equations. To perform this operation we take into account the property of the Bessel function of zero-th order (Watson, 1980),

$$J_0[\omega_0(t - \tau)] = \sum_{k=-\infty}^{\infty} J_k(\omega_0 t) J_k(\omega_0 \tau) \tag{5.54}$$

which upon substitution into (5.53) leads to the following alternative representation of Systems I and II in terms of infinite sets of ordinary differential equations:

$$\begin{aligned}
& \ddot{v}(t) + \lambda \dot{v}(t) + Cv^3(t) + \varepsilon v(t) - \varepsilon^2 \left[\overbrace{J_0(\omega_0 t) \varphi_0(t) + 2 \sum_{k=1}^{\infty} J_k(\omega_0 t) \varphi_k(t)}^{\text{Neumann Series Expansion}} \right] \\
& = \varepsilon F_1(t) + \varepsilon^2 F_2(t) + O(\varepsilon^3) \\
& \dot{\varphi}_k(t) = J_k(\omega_0 t) v(t), \quad k = 0, 1, 2, \dots \\
& v(0) = \dot{v}(0) = 0, \quad \varphi_k(0) = 0, \quad k = 0, 1, 2, \dots
\end{aligned} \tag{5.55a}$$

In essence, the $O(\varepsilon^2)$ integral term in relation (5.53) was expressed as a Neumann series expansion. It is interesting to note that the set (5.55a) presents a clear representation of the effects of dispersion of the linear medium on the dynamics; indeed, in the limit $\omega_0 \rightarrow 0$ (i.e., in the limit of no elastic foundation and a non-dispersive semi-infinite rod) only the zero-th amplitude $\varphi_0(t)$ survives in (5.55a), and the infinite set degenerates to the following set of two ordinary differential equations:

$$\begin{aligned}
& \ddot{v}(t) + \lambda \dot{v}(t) + Cv^3 + \varepsilon v(t) - \varepsilon^2 \varphi_0(t) = \varepsilon F_1(t) + \varepsilon^2 F_2(t) + O(\varepsilon^3) \\
& \dot{\varphi}_0(t) = v(t) \\
& v(0) = \dot{v}(0) = 0, \quad \varphi_0(0) = 0 \quad (\text{Non-dispersive limit})
\end{aligned} \tag{5.55b}$$

It follows that non-zero amplitudes $\varphi_k(t)$, $k = 1, 2, \dots$ represent the dispersive effects on the dynamics. From a mathematical point of view the amplitudes $\varphi_k(t)$ in (5.55a) are the coefficients of the Neumann expansion (Watson, 1980) of the integral

term

$$\int_0^t v(\tau) J_0[\omega_0(t - \tau)] d\tau$$

in (5.53), following the Neumann expansion of the Bessel function in expression (5.54). As mentioned previously, this integral term models the leading-order dynamical interaction of the nonlinear attachment with the rod, including energy exchanges between these two subsystems.

It will be shown below that a disadvantage of the described Neumann series-based model (5.55a) is that it fails to converge for $t \gg 1$, since high-order terms of the infinite summation on the left-hand side grow to finite values as time increases, and $J_k(u) \approx O(1/\sqrt{u})$ as $t \gg 1$ independently of the order k . No such convergence problem is encountered, however, in the simpler non-dispersive model (5.55b). Nevertheless, as we shall see, the representation (5.55a) is still valid for *early time prediction* of the transient interaction between the rod and the nonlinear attachment.

In Figure 5.37 we present numerical simulations for System I [equations (5.55a)] with parameters $\varepsilon = 0.1$, $\omega_0 = \sqrt{0.9}$, $C = 5.0$, $F = -10$, $\lambda = 0.5$, $e = 1$ and 11 amplitudes, $\varphi_0(t), \dots, \varphi_{10}(t)$, being taken into account. In Figures 5.55a, b we depict the forcing functions $\varepsilon F_1(t)$ and $\varepsilon^2 F_2(t)$ as defined by equations (5.44), and in Figure 5.37c we present the response $v(t)$ of the nonlinear attachment computed using the Neumann series-based model (5.55a).

The response of the same system computed by the finite element (FE) approach is presented in Figure 5.37d. For the FE computations, we consider directly the original System I, relations (5.41), with the length of the rod being chosen sufficiently long ($L = 400$) to avoid numerical pollution of the results by reflected waves originating from the free right boundary. The number of elements used in the simulations ensured a five-digit convergence of the leading modes of the rod. In the case of impulse excitation (System I), the delta function in equation (5.41) was modeled using a half-sine pulse whose area was equal to the amplitude F of the delta function. The frequency of the pulse was set to 10 Hz (higher frequency pulses were also considered but it was found that above 10 Hz, the response was no longer influenced by the pulse frequency). Regarding the FE numerical integration of the equations of motion (5.41), the Newmark algorithm (Geradin and Rixen, 1994) was considered with parameters chosen to ensure unconditional stability of the algorithm (the same FE model was employed for the simulations carried out in Section 5.2.3 to discretize the finite rod). In some cases, slight numerical damping was added to ensure stability of the numerical results. Finally, in the FE simulations the sampling frequency was such that the distance travelled by the waves in one time step never exceeded the distance between two successive nodes (so the Courant condition was satisfied).

Comparing the Neumann series-based and FE simulations (Figures 5.37c and 5.37d), good agreement is obtained in the early time (highly nonlinear) phase of the motion, approximately up to $t = 20$ s. After that early time regime the predictive capability of the Neumann representation deteriorates, and there is disagreement between the two computations. The reason for the lack of convergence of the Neumann series as time increases can be understood by examining the behavior of the

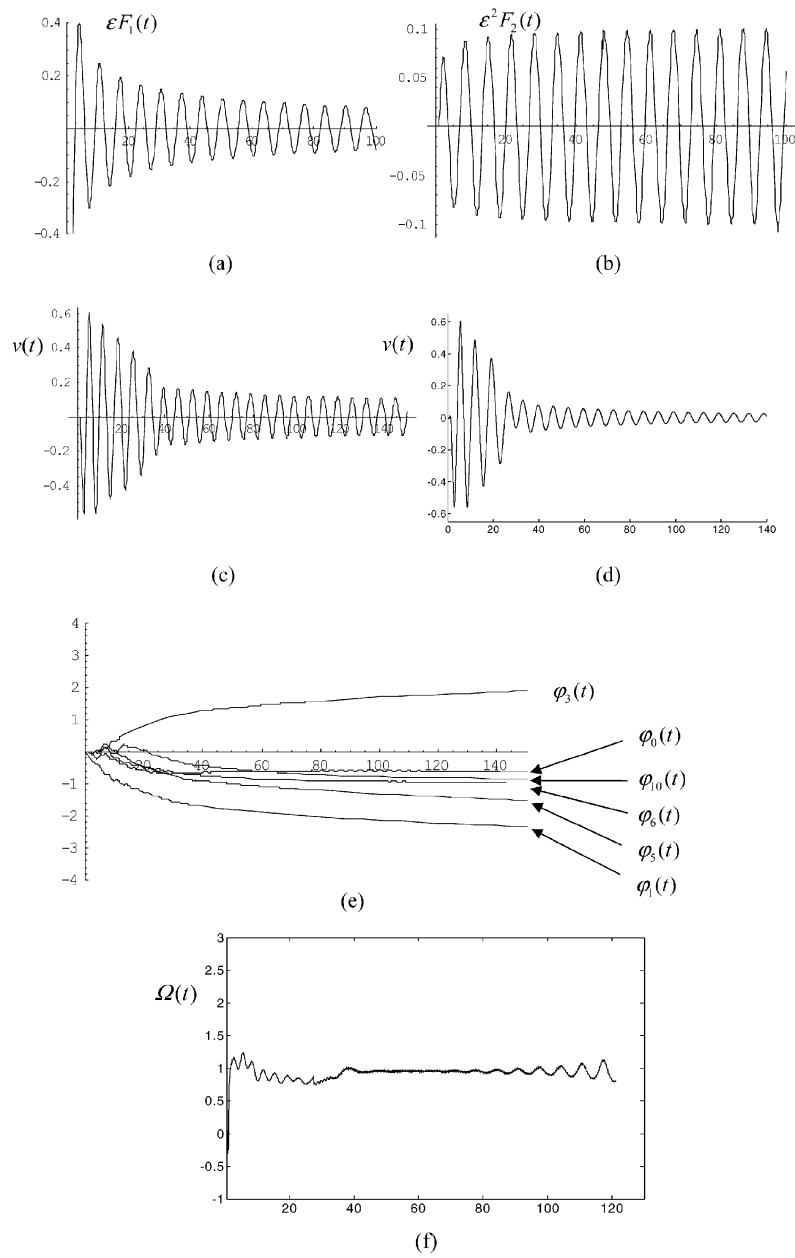


Fig. 5.37 Damped response of System I with forcing $F = -10$: (a) $\varepsilon F_1(t)$; (b) $\varepsilon^2 F_2(t)$; (c) NES response $v(t)$, model (5.55a) based on Neumann series expansions; (d) NES response $v(t)$ based on FE computations; (e) leading amplitudes $\varphi_k(t)$, $k = 0, 1, \dots, 10$; (f) instantaneous NES frequency of $v(t)$.

time series of the amplitudes $\varphi_k(t)$, as depicted in Figure 5.37e. We conclude that the participation of the high-order amplitudes is no longer negligible with increasing time. As a result, the Neumann expansion,

$$\varepsilon^2 \left[J_0(\omega_0 t) \varphi_0(t) + 2 \sum_{k=1}^{\infty} J_k(\omega_0 t) \varphi_k(t) \right]$$

[which replaces the integral in the integro-differential equation (5.53)] no longer converges with increasing time as more terms are added to the summation.

We note at this point that the Bessel functions of the first kind behave asymptotically as follows, $J_k(\omega_0 t) \sim O(\omega_0^{-1/2} t^{-1/2})$, $t \gg 1$ irrespective of the order $k = 0, 1, \dots$. It is concluded, therefore, that the model (5.55a) based on Neumann series expansions is valid only in the early-time dynamics [this does not apply, however, for the non-dispersive model (5.55b) as discussed previously]. The Neumann series-based model, however, has the advantage not to possess any integral term and to directly depict the effects of dispersion through the amplitudes $\varphi_p(t)$, $p = 1, 2, \dots$.

In Figure 5.37f we present the time evolution of the instantaneous frequency $\Omega(t)$ of the nonlinear attachment, computed by applying a numerical Hilbert transform to the exact (FE) time series depicted in Figure 5.37d [but see also the work by Chandre et al. (2003) for alternative methods of frequency extraction from a time series]. Such instantaneous frequency plots will be useful in what follows, in our study of transitions of the damped dynamics between different dynamical regimes. From Figure 5.37f we conclude that the transient response takes place in the neighborhood of the cut-off frequency $\omega = \omega_0 = 1$ that separates the attenuation and propagation zones of the dispersive rod of infinite spatial extent.

To demonstrate that the described rod-attachment dynamics is caused by the essential stiffness nonlinearity of the attachment, in Figure 5.38 we depict the response of System I with the essential nonlinearity replaced by a linear stiffness of constant $C = 5.0$, and all other parameters being left unchanged. We note the low retention of energy by the linear attachment and the nearly negligible amplitudes $\varphi_k(t)$, $k = 0, 1, \dots, 10$ in this case.

We now proceed to study the different regimes of the rod-nonlinear attachment dynamic interaction through FE computations. This investigation reveals the main regimes of the transient dynamics, and the mechanisms that govern the energy exchanges between the rod and the NES during different stages of the damped transient motion. To study the different regimes of the motion, we analyze the effect that the variation of the magnitude of the excitation has on the rod-nonlinear attachment dynamics. Specifically, the response $v(t)$ and the instantaneous frequency $\Omega(t)$ of the nonlinear attachment are computed using FE computations for System II with parameters, $\varepsilon = 0.1$, $\omega_0 = \sqrt{0.9}$, $C = 5.0$, $\lambda = 0.05$, $d_1 = -6.0$, $d_2 = -8.0$, $d = 2.0$ and varying magnitude D . In the following discussion we only consider FE computations, although as mentioned previously the Neumann series-based models (5.55a, b) can also be used to study the early-time nonlinear response.

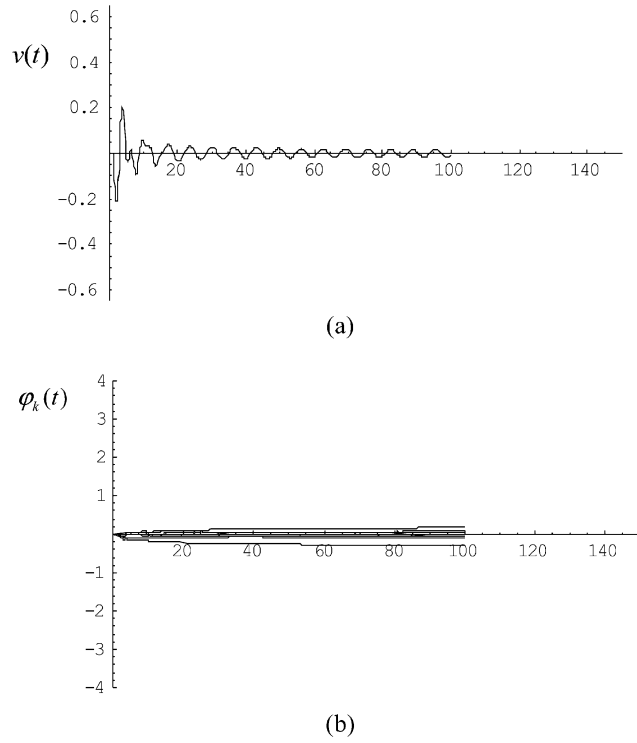


Fig. 5.38 System I with linear attachment and forcing $F = -10$: (a) attachment response $v(t)$ based on the model (5.55a) with Neumann series expansion; (b) leading amplitudes $\varphi_k(t)$, $k = 0, 1, \dots, 10$.

Different amplitudes D will be considered and start our study by examining the case $D = 4.5$. In Figure 5.39 we depict the transient responses of System II, from which we deduce the presence of three different regimes of motion labeled as Regimes 1 (0–100 s), 2 (100–300 s) and 3 (470–800 s). Moreover, the Regimes 2 and 3 are separated by a relatively large transition period (300–470 s). We make the following remarks concerning these Regimes of the motion.

In the early-time, high-frequency Regime 1 (see Figures 5.39b, c) the nonlinear attachment (NES) interacts with incoming travelling wavepackets possessing frequencies inside the PZ of the dispersive rod (i.e., with $\omega > \omega_0$). As a result, the instantaneous frequency of the attachment also is situated inside the PZ $\Omega(t) > \omega_0$. Considering the transitions of the damped dynamics of the nonlinear attachment, after an early amplitude build up to a maximum level, the dynamics makes a transition to a weakly modulated oscillation (Regime 2 in Figures 5.39b, c) caused by wave radiation from the nonlinear attachment back to the rod. This regime of weakly modulated, nearly time-periodic oscillation of the NES possesses a (fast) frequency nearly equal to ω_0 , which is the bounding frequency between the AZ and PZ of the

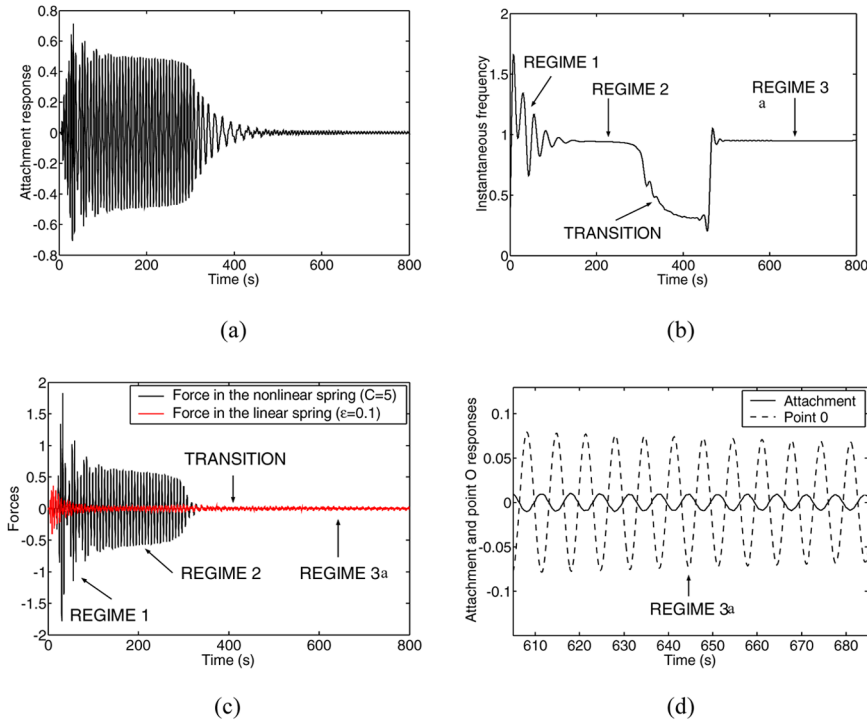
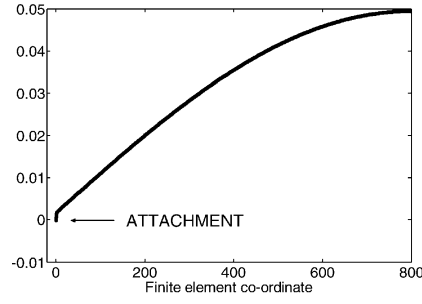


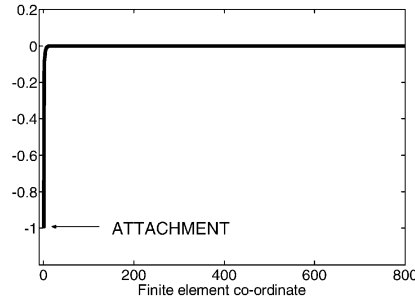
Fig. 5.39 FE simulations for System II with $D = 4.5$: (a) NES response $v(t)$; (b) NES instantaneous frequency $\Omega(t)$; (c) forces in the linear and nonlinear springs; (d) responses $v(t)$ — and $u(0, t)$ - - - for $t \gg 1$ (Regime 3a).

rod; this frequency is also the frequency of the in-phase mode of the rod. Such a weakly modulated motion of the NES possessing a single fast-frequency is typical in fundamental TET regimes (see for example, the discussion in Section 3.4.2.1). Hence, during Regime 2, the NES engages in 1:1 TRC with the in-phase normal mode of the dispersive rod at frequency ω_0 , which yields nonlinear passive extraction of energy from that mode.

As the energy of the NES decreases due to energy radiation and damping dissipation the dynamics can no longer sustain the 1:1 TRC, so escape from TRC follows; hence, energy is radiated back to the rod and the instantaneous frequency of the NES decreases until it reaches the low level $\Omega(t) = O(\epsilon^{1/2})$ [a discussion regarding the linearized motion occurring at this frequency is given below (Panagopoulos et al., 2004)]. At the end of this transition the dynamics becomes almost linear (see Figures 3.39b, c, d) and Regime 3 of the motion is reached. In actuality there are two alternative possibilities for the evolution of the dynamics of the integrated rod-NES system after escape from TRC (Regime 2); these will be denoted as Regimes 3a and 3b from here on. Both Regimes correspond to low-amplitude linearized oscillations of the system.



(a)



(b)

Fig. 5.40 System II, shape of the rod for $t \gg 1$: (a) case $D = 4.5$ (Regime 3a); (b) case $D = 10.0$ (Regime 3b).

Regime 3a (see Figures 3.39b, c, d) consists of weakly modulated periodic motions in the neighborhood of $\Omega(t) \approx \omega_0$. The in-phase mode of the rod is excited, and the NES vibrates in an out-of-phase fashion and with much smaller amplitude than the rod. These assertions can be proved analytically in this case, due to the nearly linear nature of the dynamics (Panagopoulos et al., 2004). Following the analysis in that work, for sufficiently small amplitudes of oscillation of the NES and ignoring damping for the moment, it can be shown that the response of System II in Regime 3a can be approximated as

$$\begin{aligned}
 u(x, t) &\approx \left(\frac{\varepsilon \omega_0^2 x}{\varepsilon - \omega_0^2} + 1 \right) Y e^{j\omega_0 t} + \text{cc}, \quad x \leq 0 \\
 v(t) &\approx V e^{j\omega_0 t} + \text{cc} = \frac{\varepsilon Y e^{j\omega_0 t}}{\varepsilon - \omega_0^2} + \text{cc}
 \end{aligned} \tag{5.56}$$

where ‘cc’ denotes the complex conjugate. Taking into account the actual numerical values of the parameters used for the simulations, we obtain the analytical estimate

$V/Y = -0.125$, which is in satisfactory agreement with the FE numerical simulation of Figure 3.39d. The mode shape of the rod in Regime 3a computed through FE computations is depicted in Figure 3.40a; it is noted that it is not exactly a straight line [as predicted by the analytical expression (5.56)], a discrepancy attributed to the finiteness of the rod in the FE simulations and to higher-order terms that were neglected from the above simplified linearized approximation.

This type of linearized motion with approximate frequency ω_0 is not the only possible long-time settling response of System II. The numerical confirmation of this assertion is given in Figure 5.41 which corresponds to amplitude $D = 10.0$ with parameters as defined above and damping added to the rod. We note that until the long-time Regime of the motion is reached, the dynamics is qualitatively similar to the undamped case presented in Figure 5.39. However, after escape from 1:1 TRC the NES settles into Regime 3b, consisting of low-frequency, weakly modulated oscillations of the system well inside the AZ of the dispersive rod; moreover, from the mode shape of the assembly depicted in Figure 5.40b, we conclude that this low-frequency motion is strongly localized to the NES, with the rod undergoing small amplitude, near-field oscillations close to the point of connection. This type of localized motion is similar to the localized modes studied inside AZs of discrete linear chains with essentially nonlinear attachments [we recall the results reported in Section 3.5.2 and in Manevitch et al. (2003)]. The frequency of this localized motion into which the system settles was analytically approximated in Panagopoulos et al. (2004) for the case of a discrete linear chain with a nonlinear end attachment, as $\omega_{\text{esc}} = O(\sqrt{\varepsilon})$. In addition, as shown in Figure 3.41c, in Regime 3b the attachment and the point of connection of the rod execute nearly in-phase motions. Following Panagopoulos et al. (2004), the response of the system in this linearized regime is approximated as follows:

$$\begin{aligned} u(x, t) &\approx Y(x)e^{j\omega t} + \text{cc} \\ &= \left[A \exp\left(-\sqrt{\omega_0^2 + \omega^2}x\right) + B \exp\left(\sqrt{\omega_0^2 - \omega^2}x\right) \right] e^{j\omega t} + \text{cc}, \quad \omega < \omega_0, \quad x \leq 0 \\ v(t) &\approx V e^{j\omega t} + \text{cc} \end{aligned} \quad (5.57a)$$

with the frequency ω computed by solving

$$\left(\frac{\varepsilon\omega^2}{\varepsilon - \omega^2} - \sqrt{\omega_0^2 + \omega^2} \right) \exp\left(-2L\sqrt{\omega_0^2 - \omega^2}\right) = -\frac{\varepsilon\omega^2}{\varepsilon - \omega^2} - \sqrt{\omega_0^2 - \omega^2} \quad (5.57b)$$

For $\varepsilon = 0.1$, $\omega_0^2 = 0.9$ and $L = 400$ we compute the frequency of the localized mode as $\omega = 0.3 \text{ rad/s} = O(\sqrt{\varepsilon})$, which agrees with the corresponding values derived from the numerical simulations of Figure 5.41. Moreover, the same approximate analysis estimates the steady state localized mode shape as $V/Y(0) \approx [1 - (\omega^2/\varepsilon)]^{-1}$, which confirms that when $\omega = O(\sqrt{\varepsilon})$ it holds that $V \gg Y(0)$. Hence, the linearized motion is localized to the nonlinear attachment, which oscillates in an in-phase fashion with respect to the rod end.

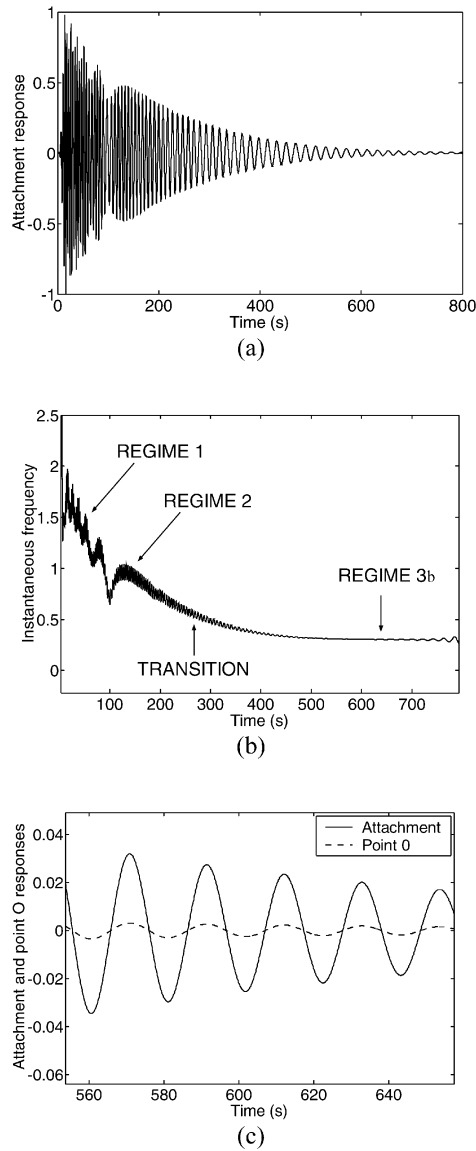


Fig. 5.41 FE simulations for System II with $D = 10.0$; (a) NES response $v(t)$; (b) NES instantaneous frequency $\Omega(t)$; (c) response $v(t)$ — and $u(0, t)$ - - - for $t \gg 1$ (Regime 3b).

In Figure 5.42 we examine the dynamics of System II for amplitudes $D = 2$ and $D = 8$. For the weakest excitation (Figure 5.42a), Regime 1 is of short duration, whereas Regime 2 (1:1 TRC) cannot be realized since the excitation is not sufficiently strong; as a result, the entire motion takes place entirely in Regime 3a, i.e., it

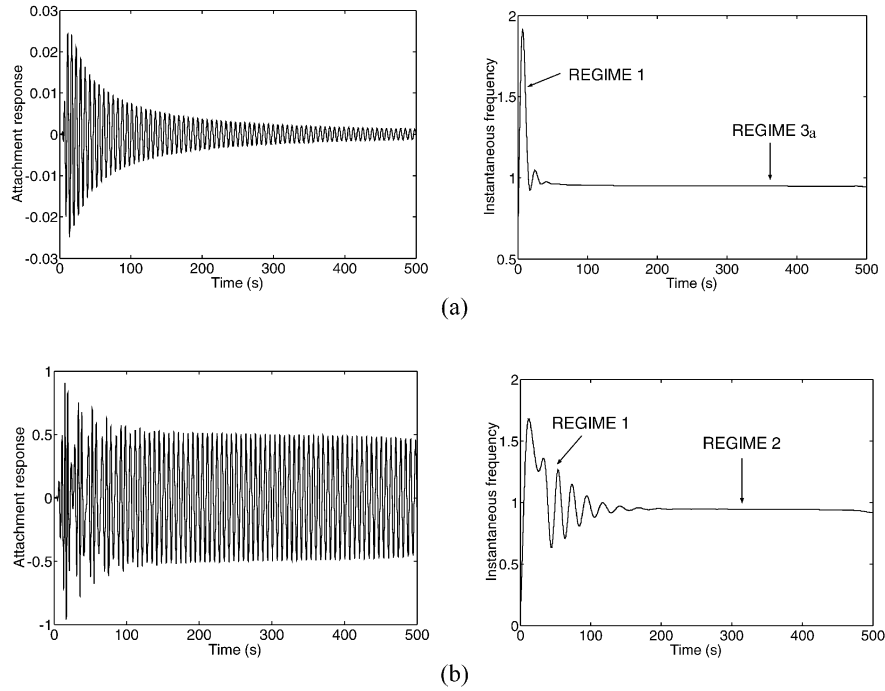


Fig. 5.42 FE simulations for System II with (a) $D = 2.0$ and (b) $D = 8.0$.

is nearly linear. Since no 1:1 TRC takes place in the neighborhood of the frequency ω_0 , the strength of TET is minimal in this case. For the case of strongest excitation (Figure 5.42b), Regimes 1 and 2 can clearly be deduced, whereas, the eventual transition to Regime 3a is not depicted in the time window considered for the numerical simulations.

Similar dynamics is noted in the FE numerical simulations of System I. In Figure 5.43 we depict the response of System I with parameters identical to System II and $F = -10$, $\varepsilon = 0.1$, $\omega_0 = \sqrt{0.9}$, $C = 5.0$, $\lambda = 0.05$. The response of the nonlinear attachment $v(t)$ is presented in Figure 5.43a, whereas the corresponding instantaneous frequency $\Omega(t)$ is shown in Figure 5.43b. After early time transients due to dynamic interaction of the nonlinear attachment with incoming travelling waves (Regime 1), the response settles into a weakly modulated periodic oscillation with frequency near ω_0 (Regime 2). For $t > 200$ s, escape from TRC occurs, and from $t > 400$ s, the nearly linear Regime 3a is reached. By adding damping to the rod, the localized mode can also be excited (i.e., Regime 3b) as in the case of System II. Hence, the dynamics is qualitatively similar to what is depicted in Figure 5.39.

The previous numerical results are in agreement with the TET scenario outlined in Section 3.5.2 for the semi-infinite chain with an essentially nonlinear end attachment. That is, that there is an initial dynamic interaction during which wave

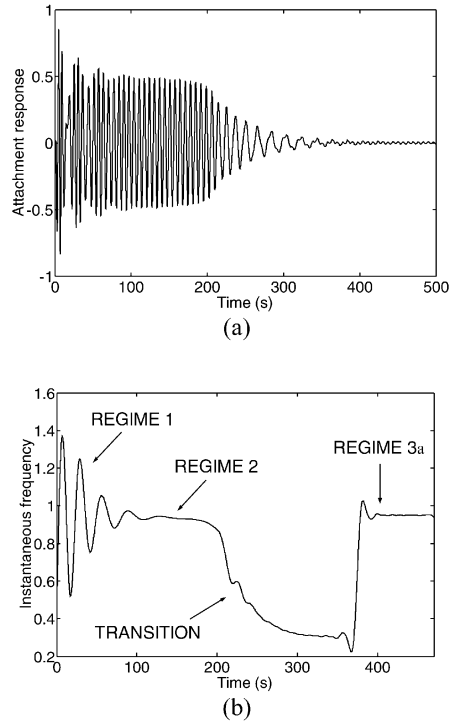


Fig. 5.43 FE simulations for System I with $F = -10.0$: (a) NES response $v(t)$; (b) NES instantaneous frequency $\Omega(t)$.

radiation from the nonlinear attachment to the semi-infinite chain is realized. This is followed by TET due to 1:1 TRC of the NES with the in-phase mode of the chain at the lower bounding frequency $\omega_{b1} = \omega_0$, followed by escape from TRC, and eventual transition to nearly linear motion. A similar scenario is realized in the continuous system examined in this section, but now the 1:1 TRC occurs between the normal mode of the rod at the bounding frequency $\omega_b = \omega_0$ of the rod of infinite extent (note that in this case a single bounding frequency exists, whereas in the semi-infinite chain considered in Section 3.5.2 there were two such bounding frequencies). This shows the robustness of the TET phenomenon, as it is realized in the two semi-infinite systems with different configurations. In the following section we perform an analytical study of the different regimes of the transient response of System I, in order to gain more insight into the underlying nonlinear dynamical mechanisms governing the nonlinear attachment-rod interaction. The analysis can be extended also for System II and for more general classes of transient excitations.

5.3.3 Analytical Study

In this section we will analyze dynamic interactions of the NES with impeding traveling waves possessing frequencies inside the PZ of the rod of infinite length (that is, nonlinear interactions in Regime 1 of the dynamics). In addition, we will study analytically weakly modulated responses of the NES possessing fast frequencies close to the bounding frequency ω_b , under conditions of 1:1 TRC; this will correspond to Regime 2 of the dynamics (Vakakis et al., 2004).

We initiate our analytical study by examining the dynamic interaction of the essentially nonlinear attachment with incoming traveling waves with frequencies inside the PZ ($\omega > \omega_0$) of the dispersive rod of infinite spatial extent. To this end, we analyze the dynamics of the NES forced by a single monochromatic incident wave, $Ae^{j(\omega t - kx)}$, with $j = (-1)^{1/2}$ and k being the wavenumber. If, to a first approximation, we neglect higher-frequency components in the reflected wave (that are generated by the essential stiffness nonlinearity of the NES), and consider only wave components at the basic frequency of the incident wave, we can express the rod response as follows:

$$u(x, t) = Ae^{j(\omega t - kx)} + Be^{j(\omega t + kx)} + \text{cc} \quad (5.58a)$$

that is, as a superposition of the incident and reflected waves. In (5.58a), B is the amplitude of the reflected wave, the (prescribed) amplitude of the incident wave, and ‘cc’ denotes complex conjugate. Substituting (5.58a) into the governing linear partial differential equation of the rod with no NES attached, we compute the wavenumber k by the following dispersion relation (which also defines the PZ of the rod of infinite length):

$$k = (\omega^2 - \omega_0^2)^{1/2}, \quad \omega \leq \omega_0 \quad (5.58b)$$

We now make the basic assumption that the NES engages in resonance with the incoming wave. This resonance interaction may be regarded as analog of the resonance interaction of the NES with nonlinear normal modes (NNMs) of the discrete chain of particles, inside the PZ of that system (Vakakis et al., 2003). Assuming that the nonlinear attachment possesses no damping ($\lambda = 0$), and that (approximately) oscillates with frequency ω (i.e., the frequency of the incident wave), we express its response as:

$$v(t) = Ze^{j\omega t} + \text{cc} \quad (5.58c)$$

Clearly, this *ansatz* is only an approximation, as it omits higher harmonics generated by the essential nonlinearity. Substituting (5.58c) together with (5.58a, b) into the governing differential equations (5.41) (with $F = 0$), we obtain the following approximate algebraic relationships for the complex amplitudes A , B and Z ,

$$\begin{aligned} (-jk + \varepsilon)B &\approx \varepsilon Z - (jk + \varepsilon)A \\ -\omega^2 Z + 3CZ^2 Z^* - \varepsilon(A + B - Z) &\approx 0 \end{aligned} \quad (5.59)$$

where (*) denotes complex conjugate. Combining these two equations, expressing the complex amplitude of the attachment in polar form, $Z = |Z|e^{j\phi}$, and setting separately equal to zero the real and imaginary parts of the resulting complex equation we obtain the following relations in terms of real variables:

$$\begin{aligned} (-m - \omega_0^2 + 3C|Z|^2 + \varepsilon)|Z| \cos \phi + \varepsilon^2 m^{-1/2} |Z| \sin \phi &= 2\varepsilon A \\ (-m - \omega_0^2 + 3C|Z|^2 + \varepsilon)|Z| \sin \phi - \varepsilon^2 m^{-1/2} |Z| \cos \phi &= -2\varepsilon^2 A m^{-1/2} \end{aligned} \quad (5.60)$$

where $m = \omega^2 - \omega_0^2 > 0$, and without loss of generality we assume that the prescribed amplitude A is a real number. Eliminating ϕ from this set of equations we derive the following frequency-amplitude relationship between $|Z|$ and m , that computes the approximate steady state response of the nonlinear attachment caused by the incident monochromatic traveling wave of amplitude A (Vakakis et al., 2004),

$$\begin{aligned} m^3 + 2(\omega_0^2 - 3C|Z|^2 - \varepsilon)m^2 + [(\omega_0^2 - 3C|Z|^2 - \varepsilon)^2 - 4\varepsilon^2(A/|Z|)^2]m \\ + [\varepsilon^4 - 4\varepsilon^4(A/|Z|)^2] \approx 0 \end{aligned} \quad (5.61)$$

with m assumed to be an $O(1)$ quantity. Once a solution $m = m(|Z|)$ is computed, the corresponding phase ϕ is obtained by either one of equations (5.60), as follows:

$$\begin{aligned} \tan(\phi/2) &\approx (1/2)(m + \omega_0^2 - 3C|Z|^2 - \varepsilon - 2\varepsilon A/|Z|)^{-1} \\ &\times \left\{ -2\varepsilon^2 m^{-1/2} \pm [4\varepsilon^4 m^{-1} - 4(m + \omega_0^2 - 3C|Z|^2 - \varepsilon - 2\varepsilon A/|Z|) \right. \\ &\left. \times (-m - \omega_0^2 + 3C|Z|^2 + \varepsilon - 2\varepsilon A/|Z|)]^{1/2} \right\} \end{aligned} \quad (5.62)$$

For the considered system parameters equation (5.61) possesses always two or three real roots for m as functions of $|Z|$. However, if we take into account that due to our previous assumptions we seek solutions only inside the PZ of the rod we must pose the additional inequality constraints, $m > 0$ and $\omega_0^2 - 3C|Z|^2 < 0$, which restrict the solution to a single branch $m = m(|Z|)$. This branch is depicted in Figure 5.44a for system parameters $\omega_0^2 = 1.0$, $C = 3.0$, $\varepsilon = 0.1$, $A = 5.0$; the corresponding phase ϕ is presented in Figure 5.44b. We note that in the neighborhood of the bounding frequency $\omega_b = \omega_0$ the incoming traveling wave degenerates into a standing wave, i.e., the in-phase normal mode, and so the previous analysis is not valid in that region. The inapplicability of the presented analysis close to $\omega_b = \omega_0$ is manifested in Figure 5.44a by the elimination of the single-validness of the solution branch $m = m(|Z|)$ in the neighborhood of point O; this is an indication that bifurcations take place as the bounding frequency is approached from above, but these cannot be analytically studied by the simplified analysis considered herein. In fact, this series of bifurcations can be studied analytically by considering the solutions of equation (5.61) in the neighborhood of the bounding frequency $\omega_b = \omega_0$, through appropriate rescaling of the frequency variable and modification of the *ansatz* for the sought analytical solution.

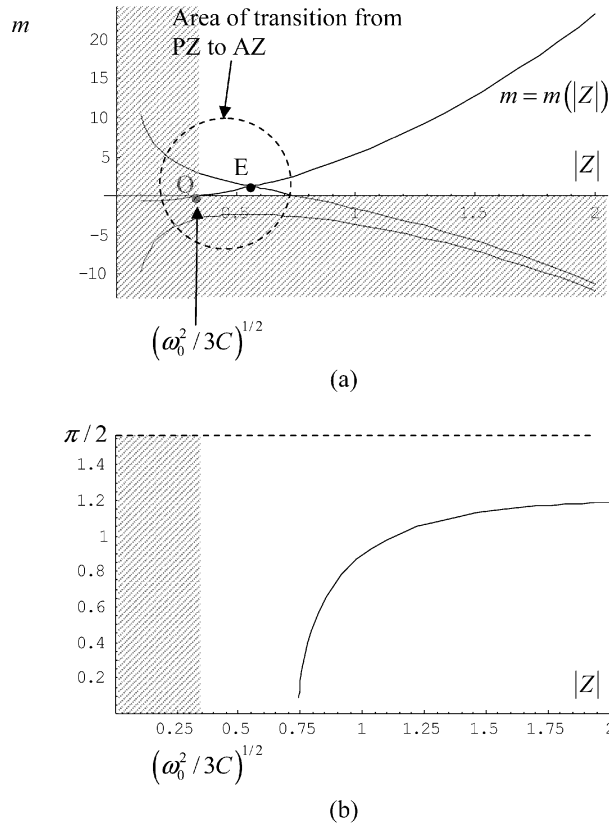


Fig. 5.44 Resonance interaction of the NES traveling with amplitude $A = 5.0$: (a) NES amplitude $|Z|$ as function of the frequency variable m ; (b) NES phase ϕ as function of amplitude $|Z|$; shaded regions denote inadmissible ranges of solutions.

Regarding the plot of the phase depicted in Figure 5.44b, we note that as the amplitude $|Z|$ of the NES increases the phase ϕ reaches the limit $\pi/2$. Moreover, we make the observation that in the limit $A \rightarrow 0$, i.e., for small-amplitude incoming waves, the point of crossing of solutions E tends to O and there is single-validness of the solution $m = m(|Z|)$ over the entire permissible region of the plot of Figure 5.44a.

In Figure 5.45 we verify the analytically predicted dynamic interactions in the PZ of the dispersive rod by performing direct numerical simulations for System I with parameters $\omega_0^2 = 1.0$, $C = 3.0$, $\varepsilon = 0.1$, $\lambda = 0$, $F = -40$, $e = 1.0$ and 11 terms considered in the Neumann expansion [expressions (5.44) and (5.55a)]. In this case the undamped nonlinear attachment undergoes a steady state periodic oscillation with amplitude approximately equal to 1.5 and frequency equal to 2 rad/s; clearly, this represents a resonance of the nonlinear attachment inside the PZ of the dispersive rod, which, although differing from the case of single incident wave

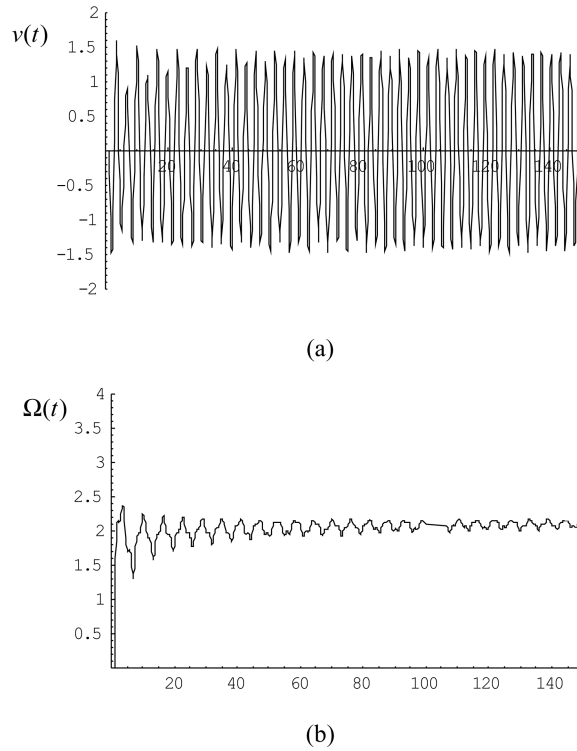


Fig. 5.45 Resonance interaction of the NES in the PZ of the dispersive rod: (a) NES response $v(t)$; (b) instantaneous NES frequency $\Omega(t)$.

(since in the numerical simulation the excitation of the attachment is in the form of an incident wave packet), nevertheless it reveals a frequency-amplitude dependence that agrees with the resonance plot of Figure 5.44a.

The nonlinear dynamic interactions of the NES with incident traveling waves are responsible for the built up of the NES response during Regime 1 of the motion, as depicted in the FE simulations of Figures 5.39 and 5.41–5.43. As the frequency of the NES decreases due to damping dissipation and energy radiation (backscattering) to the rod, the dynamics of the NES enters into the regime of 1:1 TRC with the in-phase normal mode of the rod at the bounding frequency $\omega_b = \omega_0$ (that is, Regime 2 of the motion). Then the NES executes slowly modulated oscillations with fast frequency which can be analytically studied by applying the complexification-averaging (CX-A) technique (Manevitch, 2001) discussed in Section 2.4 and applied in Chapter 3.

To study the transition of the damped dynamics from Regime 1 to Regime 2 of the motion, we will apply an order reduction methodology based on CX-A by assuming that the dynamics possesses a single fast frequency in the neighborhood

of the bounding frequency ω_b . To this end, we reconsider System I with $e = 1$, $\omega_0 = 1$ and weak viscous damping:

$$\begin{aligned}
& \ddot{v}(t) + \varepsilon\lambda\dot{v}(t) + Cv^3(t) + \varepsilon v(t) - \varepsilon^2 \left[J_0(t)\varphi_0(t) + 2 \sum_{k=1}^{\infty} J_k(t)\varphi_k(t) \right] \\
&= \varepsilon F J_0 \left[\sqrt{t^2 - e^2} \right] H(t - e) \\
& - \varepsilon^2 F \int_0^t J_0 \left[\sqrt{\tau^2 - e^2} \right] H(\tau - e) J_0(t - \tau) d\tau + O(\varepsilon^3) \\
&\equiv \varepsilon F_1(t) + \varepsilon^2 F_2(t) + O(\varepsilon^3) \\
& \dot{\varphi}_k(t) = J_k(t)v(t), \quad k = 0, 1, 2, \dots \\
& v(0) = \dot{v}(0) = 0, \quad \varphi_k(0) = 0, \quad k = 0, 1, 2, \dots
\end{aligned} \tag{5.63}$$

Since we aim to study the transient dynamics of this system under condition of 1:1 TRC, we express the NES response $v(t)$ in the form of a weakly modulated fast oscillation with frequency $\omega_b = \omega_0$, and the amplitudes $\varphi_k(t)$ as slowly varying functions. Without loss of generality we assume from this point on that $\omega_0 = 1$.

Hence, we will introduce a slow-fast partition of the dynamics of (5.63) that will enable us to focus on the slow dynamics of the system, and thus study the transition of the damped dynamics towards 1:1 TRC. To perform this task we introduce the new complex variables,

$$\begin{aligned}
z_k(t) &= \dot{\varphi}_k(t) + j\varphi_k(t), \quad k = 0, 1, \dots \\
\psi(t) &= \dot{v}(t) + jv(t)
\end{aligned} \tag{5.64}$$

where $j = (-1)^{1/2}$, and express (5.63) as the following set of complex ordinary differential equations,

$$\begin{aligned}
& \dot{\psi}(t) - \frac{j}{2}[\psi(t) + \psi^*(t)] + \frac{\varepsilon\lambda}{2}[\psi(t) + \psi^*(t)] \\
& + \frac{jC}{8}[\psi(t) - \psi^*(t)]^3 + \varepsilon \left\{ -\frac{j}{2}[\psi(t) - \psi^*(t)] \right. \\
& \left. + \frac{\varepsilon j}{2} J_0(t)[z_0(t) - z_0^*(t)] + \varepsilon j \sum_{k=1}^{\infty} J_k(t)[z_k(t) - z_k^*(t)] + O(\varepsilon^2) \right\} \\
& \equiv \varepsilon F_1(t) + \varepsilon^2 F_2(t) + O(\varepsilon^3) \\
& z_k(t) + z_k^*(t) = -j J_k(t)[\psi(t) - \psi^*(t)], \quad k = 0, 1, 2, \dots
\end{aligned} \tag{5.65}$$

where (*) denotes the complex conjugate. These equations are *exact*, since they involve no simplifications compared to the original System I [relation (5.63)]. We

now introduce the slow-fast partition of the dynamics by adopting the following representations for the dependent complex variables in (5.65),

$$\begin{aligned} z_k(t) &\approx B_k(t), \quad k = 0, 1, 2, \dots \\ \psi(t) &\approx A(t)e^{jt} \end{aligned} \quad (5.66)$$

where $A(t)$ and $B(t)$ are slowly varying complex amplitudes. By these representations we approximate $\psi(t)$ as a slowly modulated time-periodic oscillation with fast frequency $\omega_0 = 1$, and $z_k(t)$ as slowly varying complex functions. These expressions are expected to be valid only in the regime of 1:1 TRC, i.e., in Regime 2.

Before we substitute the approximations (5.66) into (5.65), we need to represent the Bessel functions and the forcing functions $\varepsilon F_1(t)$ and $\varepsilon^2 F_2(t)$ in terms of complex slow-fast partitions, in a way compatible to our CX-A analysis. One way to perform this task is by means of two-point quasi-fractional approximants as shown in Guerrero and Martin (1988), Martin and Baker (1991) and Chalbaud and Martin (1992). Indeed, employing the results of Guerrero and Martin (1988), we can approximately partition the leading-order Bessel functions of the first kind in terms of ‘slow’ and ‘fast’ components as follows:

$$\begin{aligned} J_n(t) &\approx (1+t)^{-1/2} w_n(t) e^{jt} + \text{cc} \equiv O_n(t) e^{jt} + \text{cc}, \quad n = 0, 1 \\ w_n(t) &= \frac{1}{2} [u_n(t) - jv_n(t)], \quad u_n(t) \approx \frac{\sum_{i=0}^N P_i t^i}{\sum_{j=0}^N q_j t^j}, \quad v_n(t) \approx \frac{\sum_{i=0}^N P_i t^i}{\sum_{j=0}^N q_j t^j} \end{aligned} \quad (5.67)$$

where ‘cc’ denotes complex conjugate. Hence, the two leading-order Bessel functions are expressed in terms of a fast oscillation e^{jt} modulated by the slowly varying functions $O_n(t)$. Choosing $q_0 = 1$, the remaining $(3N + 2)$ parameters are determined by solving the equations

$$\begin{aligned} \left(\sum_{s=0}^N q_s t^s \right) \left(\sum_{k=0}^{\infty} a_k t^k \right) &= \left(\sum_{i=0}^N P_i t^i \right) \left(\sum_{k=0}^{\infty} (-1)^k \frac{t^{2k}}{(2k)!} \right) \\ &+ \left(\sum_{i=0}^N p_i t^i \right) \left(\sum_{k=0}^{\infty} (-1)^k \frac{t^{2k+1}}{(2k+1)!} \right) \\ \left(\sum_{s=0}^N q_{N-s} t^{-s} \right) \left(\sum_{k=0}^{\infty} B_k t^{-k} \right) &= \sum_{i=0}^N P_{N-i} t^{-i} \\ \left(\sum_{s=0}^N q_{N-s} t^{-s} \right) \left(\sum_{k=0}^{\infty} b_k t^{-k} \right) &= \sum_{i=0}^N p_{N-i} t^{-i} \end{aligned} \quad (5.68a)$$

where

$$a_k = 2^{-n} \sum_{p=0}^{(k/2)} \binom{n+1/2}{k-2p} \frac{(-1)^p}{2^{2p} p! \Gamma(p+n+1)},$$

$$B_k = 2\text{Re}(\beta_k), \quad b_k = -2\text{Im}(\beta_k),$$

$$\beta_k = \frac{(-j)^n}{\sqrt{\pi}(1+j)} \left\{ \binom{1/2}{k} + \sum_{p=1}^k \binom{1/2}{k-p} \frac{(-j)^p}{2^p p!} \prod_{s=1}^p \left[s(s-1) + \frac{1}{4} - n^2 \right] \right\},$$

$$j = (-1)^{1/2} \quad (5.68b)$$

In Guerrero and Martin (1988) the numerical values for the coefficients q_i , p_i and P_i in the above expressions are provided for $N \leq 5$. Our numerical computations showed that the quasi-fractional approximations (5.67) and (5.68) provide approximations to the leading-order Bessel functions of the first kind, $J_0(t)$ and $J_1(t)$, that are virtually indistinguishable from the exact values of these functions. Moreover, we may use these relations to approximate higher-order Bessel functions of the first kind using the following recursive formula:

$$J_{p-1}(t) + J_{p+1}(t) = \frac{2p}{t} J_p(t) \Rightarrow$$

$$J_{p+1}(t) = \frac{2p}{t} J_p(t) - J_{p-1}(t), \quad p = 1, 2, \dots \quad (5.69)$$

Our numerical computations indicate that as the order of the Bessel function increases we need to consider increasingly more terms in the quasi-fractional approximations (5.67) (i.e., we must increase N) in order to achieve good agreement with the exact solutions as $t \rightarrow 0$. However, except for a small neighborhood of $t = 0$, there is complete agreement of the quasi-fractional approximations with the exact solutions when $N \leq 5$.

Considering now the forcing functions $\varepsilon F_1(t)$ and $\varepsilon^2 F_2(t)$, we will apply the slow-fast partition (5.67) to represent these functions in terms of slow and fast complex components. Considering first the forcing function $\varepsilon F_1(t)$, we can express it in the following form:

$$\varepsilon F_1(t) \approx \underbrace{\varepsilon F O_0 \left(\sqrt{u^2 + 2eu} \right) e^{j(\sqrt{u^2 + 2eu} - u) e^{-je} H(u)}}_{\text{Slow component}} \underbrace{e^{jt}}_{\text{Fast component}} + \text{cc}$$

$$\equiv \varepsilon W_1(u) H(u) e^{jt} + \text{cc}, \quad u = t - e \quad (5.70)$$

where $W_1(u)$ denotes the ‘slow’ modulation of the ‘fast’ oscillation with frequency $\omega_0 = 1$. Similarly, the second-order forcing function $\varepsilon^2 F_2(t)$ can be approximately partitioned in terms of slow and fast dynamics, by introducing the new variable $s = \tau = -e$:

$$\begin{aligned}
\varepsilon^2 F_2(t) &\approx \\
&\underbrace{-\varepsilon^2 F H(u) e^{-je} \int_0^u O_0(u-s) O_0\left(\sqrt{s^2+2es}\right) e^{j(\sqrt{s^2+2es}-s)} ds}_{\text{Slow component}} \underbrace{e^{jt}}_{\text{Fast component}} + \text{cc} \\
&\equiv \varepsilon^2 W_2(u) H(u) e^{jt} + \text{cc}, \quad u = t - e
\end{aligned} \tag{5.71}$$

Returning now to the equations of motion (5.65), we substitute into them the slow-fast partitions (5.66), (5.67), (5.70) and (5.71), and retain only fast terms of frequency $\omega_0 = 1$ (or equivalently, we average out harmonic components with fast frequencies higher than unity). This yields the following set of approximate modulation equations governing the slow evolutions of the complex amplitudes $A(t)$ and $B_k(t)$, $k = 0, 1, \dots$:

$$\begin{aligned}
\dot{A} + \left(\frac{j}{2} + \frac{\varepsilon\lambda}{2}\right) A + \frac{3jC}{8} |A|^2 A \\
+ \varepsilon \left[-\frac{j}{2} A + \frac{j\varepsilon}{2} O_0(B_0 - B_0^*) + j\varepsilon \sum_{k=1}^{\infty} O_k(B_k - B_k^*) + O(\varepsilon^2) \right] \\
= \varepsilon W_1(t - e) H(t - e) + \varepsilon^2 W_2(t - e) H(t - e) + O(\varepsilon^3) \\
B_k = -jA O_k^*, \quad k = 0, 1, 2, \dots
\end{aligned} \tag{5.72}$$

Substituting the infinite set of algebraic equations governing the slowly varying functions $B_k(t)$ into the first of differential equations (5.72), this set can be reduced to a single complex differential equation governing the slow evolution of the amplitude $A(t)$:

$$\begin{aligned}
\dot{A} + \left(\frac{j}{2} + \frac{\varepsilon\lambda}{2}\right) A + \frac{3jC}{8} |A|^2 A + \varepsilon \left\{ -\frac{j}{2} A + \frac{j\varepsilon}{2} O_0[-jA O_0^* - (-jA O_0^*)^*] \right. \\
\left. + j\varepsilon \sum_{k=1}^{\infty} O_k[-jA O_k^* - (-jA O_k^*)^*] + O(\varepsilon^2) \right\} \\
= \varepsilon W_1(t - e) H(t - e) + \varepsilon^2 W_2(t - e) H(t - e) + O(\varepsilon^3)
\end{aligned} \tag{5.73}$$

Hence, *the slow flow nonlinear dynamic interaction between the dispersive rod and the nonlinear attachment in the 1:1 TRC regime (Regime 2) is approximately governed by the reduced complex modulation equation (5.73)*. This means that the slow flow dynamics can be reduced to a set of two first-order real amplitude and phase modulations for the motion of the attachment. These are determined by expressing the complex amplitudes in polar form:

$$A = ae^{jb}, \quad O_k = \gamma_k e^{j\delta_k}, \quad k = 0, 1, 2, \dots$$

$$W_i = \zeta_i e^{j\sigma_i}, \quad i = 1, 2 \quad (5.74)$$

which when substituted into (5.73) and upon separation of real and imaginary parts, leads to the following set of real (slow flow) modulation equations:

$$\begin{aligned} & \dot{a}(t) + (\varepsilon\lambda/2)a(t) \\ & + \varepsilon^2 \left\{ (1/2)a(t)\gamma_0^2(t) \sin 2[b(t) - \delta_0(t)] + \sum_{k=1}^{\infty} a(t)\gamma_k^2(t) \sin 2[b(t) - \delta_k(t)] + O(\varepsilon) \right\} \\ & = \left\{ \varepsilon\zeta_1(t-e) \cos[\sigma_1(t-e) - b(t)] + \varepsilon^2\zeta_2(t-e) \cos[\sigma_2(t-e) - b(t)] + O(\varepsilon^3) \right\} H(t-e) \\ \dot{b}(t) + (1/2) - (3C/8)a^2(t) \\ & + \varepsilon \left\{ (-1/2) + \varepsilon\gamma_0^2(t) \sin^2[b(t) - \delta_0(t)] + 2\varepsilon \sum_{k=1}^{\infty} \gamma_k^2(t) \sin^2[b(t) - \delta_k(t)] + O(\varepsilon^2) \right\} \\ & = \left\{ \varepsilon[\zeta_1(t-e)/a(t)] \sin[\sigma_1(t-e) - b(t)] \right. \\ & \left. + \varepsilon^2[\zeta_2(t-e)/a(t)] \sin[\sigma_2(t-e) - b(t)] + O(\varepsilon^3) \right\} H(t-e) \end{aligned} \quad (5.75)$$

An inspection of the reduced slow flow (5.75) indicates that the condition of slow amplitude modulation is always satisfied, since $\dot{a}(t) = O(\varepsilon)$. In order to get a similar condition for the slow modulation for the phase as well, we impose the following additional restriction:

$$\dot{b}(t) = O(\varepsilon) \Rightarrow (1/2) - (3C/8)a^2(t) = O(\varepsilon) \quad (5.76)$$

Provided that this condition is satisfied, the solution of (5.75) provides the following analytic approximation for the NES-rod nonlinear interaction in Regime 2 of the motion

$$\begin{aligned} v(t) &= \frac{\psi(t) - \psi^*(t)}{2j} \approx a(t) \sin[t + b(t)] \\ \dot{v}(t) &= \frac{\dot{\psi}(t) + \dot{\psi}^*(t)}{2j} \approx a(t) \cos[t + b(t)] \end{aligned} \quad (5.77)$$

with approximate frequency of the NES given approximately by $\Omega(t) \approx 1 + \dot{b}(t) = 1 + O(\varepsilon)$.

Numerical integrations of system (5.75) were performed and compared to exact solutions derived by direct numerical simulations of System I [relations (5.63)]. Provided that the assumptions of the analysis were satisfied, satisfactory agreement between analysis and numerics was noted; a representative result is depicted in Figure 5.46 for System I with parameters $\varepsilon = 0.1$, $\omega_0 = 1.0$, $C = 5.0$, $F = -15.0$, $e = 1.0$, $\lambda = 3$, and 11 terms taken into account in the Neumann expansion. We

note that, except for the early stage $t < 10$ where the frequency correction $\dot{b}(t)$ is not of $O(\varepsilon)$, the analytical approximation for $v(t)$ is close to the exact numerical simulation. In the early regime $t < 10$ the amplitude modulation is not small, and hence it may not be studied by the analytical model (5.75); this regime of the motion (Regime 1 in the computational simulations of Section 5.3.2) represents interaction of the NES with impeding traveling waves from the rod, and, hence, is away from the 1:1 resonance manifold of the system (and so conditions for 1:1 TRC are not met). It follows that the NES response in Regime 1 cannot be studied by the simple *ansatz* (5.64–5.66) (but refer to the previous analysis in this section leading to expressions (5.61) and (5.62)). From Figure 5.46a we note that the analytical approximation predicts accurately the slow amplitude decrease of the oscillation of the NES due to damping dissipation in Regime 2 of the motion.

Since the low-order analytical model (5.75–5.76) results from the Neumann series-based model (5.55a), its validity is restricted only to the early-time response of the system, i.e., during the transition from Regime 1 to the regime of 1:1 TRC, that is, Regime 2. The analytical model, however, is not valid in the regime of escape from TRC when the transition of the dynamics to the linearized Regimes 3a or 3b is realized (this is discussed in Section 5.3.2). This becomes clear when we consider the FE simulation of the dynamics of System I with system parameters as set above (see Figure 5.46d), where divergence from the Neumann series-based numerical solution is noted with progressing time. However, the derived low-order analytical model accurately models the dynamics in the transition towards, and during the Regime 2, i.e., at least up to $t = 40$ s.

The analytical approach presented can be used to analyze alternative rod-NES configurations. For example, one can prove that the unforced and undamped non-dispersive rod-attachment system with $\omega_0 = 0$ cannot sustain 1:1 TRC and, hence, no Regime 2 can occur in its transient dynamics. This should be expected as in the non-dispersive case the bounding frequency is zero ($\omega_b = 0$) and the rod of infinite extent does not possess an AZ; in this case the rod of infinite extent supports traveling waves with every possible frequency. In this case the dynamics is governed by the set of equations (5.55b) with no forcing and damping terms,

$$\begin{aligned} \ddot{v}(t) + Cv^3(t) + \varepsilon[v(t) - \varepsilon\varphi_0(t) + O(\varepsilon^2)] &= 0, \quad v(0) \neq 0, \quad \dot{v}(0) = 0 \\ \dot{\varphi}_0(t) = v(t), \quad \varphi_0(0) &= 0 \end{aligned} \quad (5.78)$$

where an initial displacement for the nonlinear attachment is assumed, and all other initial conditions are set to zero. Introducing the variables $z_0(t) = \dot{\varphi}_0(t) + j\varphi_0(t)$, and $\psi(t) = \dot{v}(t) + jv(t)$, and expressing these into the polar forms, $\psi(t) \approx a(t)e^{jb(t)}e^{j\omega t}$ and $z_0(t) \approx B_0(t)$, we derive the following set of amplitude and phase modulation equations [that are analogous to relations (5.75)]:

$$\begin{aligned} \dot{a}(t) + \varepsilon^2 a(t)[1 - \cos 2b(t)] + O(\varepsilon^3) &= 0 \\ \dot{b}(t) + [\omega - (1/2) - (3C/8)a^2(t)] - \varepsilon/2(\varepsilon^2/2) \sin 2b(t) + O(\varepsilon^3) &= 0 \end{aligned} \quad (5.79)$$

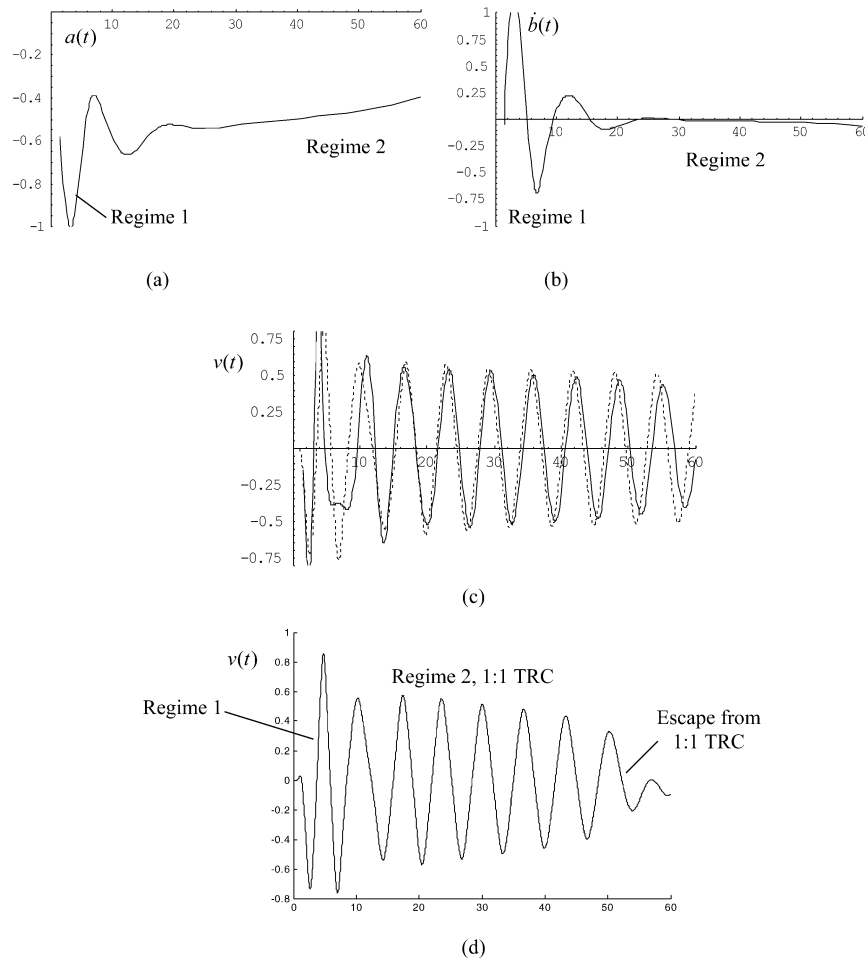


Fig. 5.46 Transition from Regime 1 to 2, System I: (a, b) evolutions of amplitude $a(t)$ and of the frequency correction $\dot{b}(t)$; (c) analytical - - - and (Neumann series-based) numerical — solutions for $v(t)$; (d) FE numerical solution for $v(t)$.

where ω being an arbitrary reference frequency. Due to the lack of a bounding frequency (in view of the non-dispersiveness of the rod), by varying the reference frequency ω the analytical model (5.79) is valid during the entire decaying motion of the attachment. Indeed, imposing the condition that the quantity $\omega - 1/2 - (3C/8)a^2(t)$ in the second of equations (5.79) is a quantity of $O(\varepsilon)$, one guarantees that the frequency correction $\dot{b}(t)$ is also of $O(\varepsilon)$, and the relations (5.79) describe slow-varying modulations. As a result, the entire decaying motion of the nonlinear attachment consists of a single regime, that is, a decaying oscillation with energy being continuously radiated to the rod in the form of traveling waves.

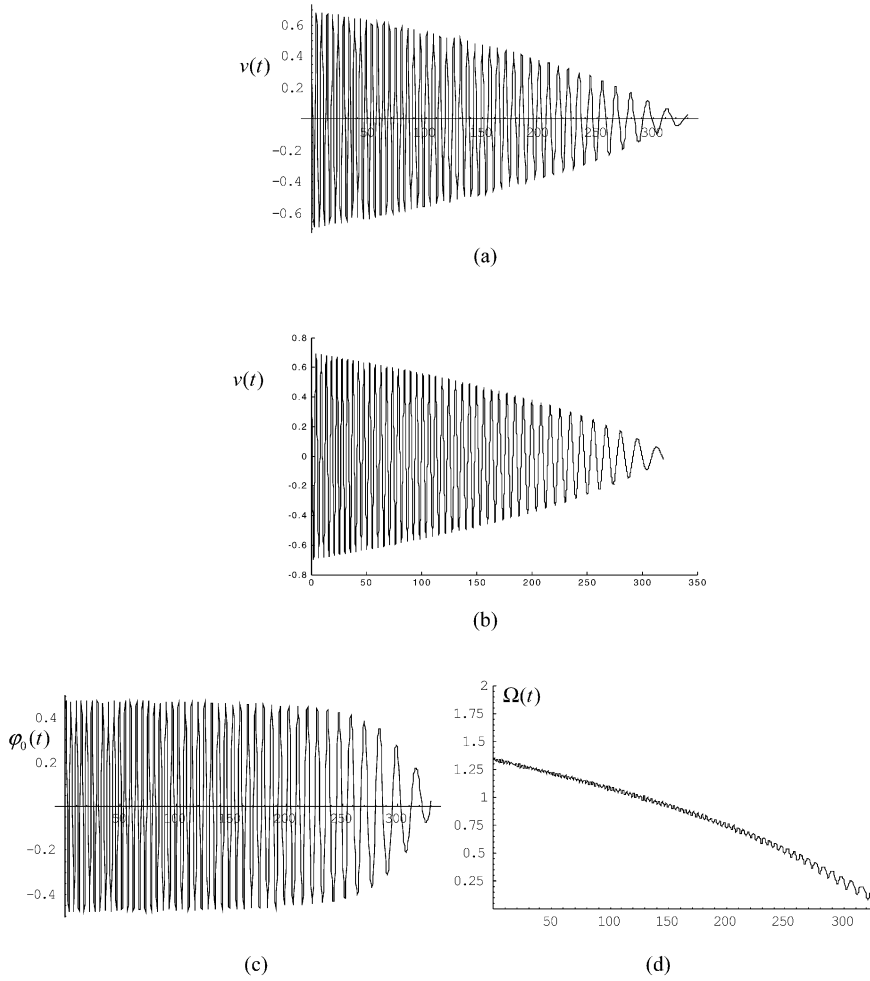


Fig. 5.47 Non-dispersive semi-infinite rod with nonlinear attachment: (a) Neumann series-based response of the attachment $v(t)$; (b) FE response $v(t)$; (c) amplitude $\varphi_0(t)$; (d) instantaneous frequency of the attachment $\Omega(t)$.

This analytical prediction is confirmed by the numerical simulation of equations (5.78) depicted in Figure 5.47; this numerical simulation is performed for system parameters $\varepsilon = 0.1$, $\omega_0 = 0$, $C = 5.0$, $\lambda = 0$, and initial condition $v(0) = 0.7$. We note that in agreement with our previous discussion, the response of the attachment $v(t)$ is composed of a single regime, that is, of a continuously decaying oscillation. The decay of the NES oscillation is due to radiation of energy to the rod during the entire regime of the motion; this is confirmed by the nearly-constant oscillation of the amplitude $\varphi_0(t)$, which decays only after the motion of the NES reaches a sufficiently low level and the level of radiated energy from the attachment to the rod

also diminishes. This result indicates that the dispersiveness of the rod dynamics influences in an essential way the qualitative dynamics of the rod-nonlinear attachment interaction. Moreover, in contrast to the dispersive case we note good agreement between the Neumann series-based and FE simulations (Figures 5.47a, b) of the transient dynamics. This should be expected, since, as discussed previously, the cause of non-convergence of the Neumann series-based numerical solution is the non-negligible contributions to the response from high-order terms of the Neumann series expansion in (5.55a) with increasing time. These non-converging terms, however, are completely missing in the non-dispersive case since only the leading amplitude $\varphi_0(t)$ survives from the infinite series of amplitudes $\varphi_i(t)$, see expression (5.55b).

This concludes our examination of the nonlinear dynamics of the semi-infinite dispersive rod possessing an end nonlinear attachment (NES). The lack of a linear part in the NES stiffness nonlinearity enables the NES to engage in resonance interactions not only with incident traveling waves from the rod, but also with the in-phase standing wave (normal mode) of the semi-infinite rod at the bounding frequency separating its propagation and attenuation zones. Relating the results of this section to the previous results of this work, resonance interactions of the NES with traveling waves in the PZ of the linear continuous medium can be considered as the ‘continuum limit’ of resonance capture cascades (RCCs) occurring between normal modes of finite-DOF discrete oscillators with attached NESs (Panagopoulos et al., 2004). Viewed in that context, the complicated resonance interactions occurring in Regime 1 of the NES response can be viewed as resonance interactions of the NES with traveling waves in the continuous spectrum of frequencies in the PZ of the linear elastic medium.

As the energy of the NES decreases due to damping dissipation and energy radiation back to the rod in the form of traveling waves is realized, the instantaneous frequency of the NES continuously decreases and approaches the bounding frequency $\omega_b = \omega_0$ from above. Then, the nonlinear attachment engages in 1:1 TRC with the in-phase mode of the rod, in similarity to TRCs studied in previous sections. This TRC can only occur due to the dispersion property of the linear medium [hence, termed by Manevitch (2003) as *apotheosis of dispersion!*], and provides conditions for the realization of passive TET from the linear medium to the NES.

5.4 Rod of Finite Length with MDOF NES

In this section we reconsider the finite dispersive rod and study its complex nonlinear dynamic interactions with a multi-DOF essentially nonlinear end attachment (a MDOF NES). This can be considered as extension of our studies of the discrete linear oscillator with an attached MDOF NES of Chapter 4, and of the finite rod with an end SDOF NES of Section 5.2. We will make use of frequency energy-plots (FEPs) for depicting and interpreting essentially nonlinear damped transitions in terms of the undamped dynamics, and, additionally, of Empirical Mode Decom-

position (EMD) for decomposing the transient dynamics in terms of multi-scaled intrinsic mode functions (IMFs). This will enable us to perform multi-scale identification of the dominant nonlinear resonant interactions that occur between the rod and the MDOF NES, and to formulate an integrated physics-based, multi-scale method for analyzing and modeling strongly nonlinear, complex dynamical interactions. The analysis of this section closely follows the works by Tsakirtzis (2006) and Tsakirtzis et al. (2007a), which should be consulted for further details.

5.4.1 Formulation of the Problem and FEPs

We consider a finite, dispersive linear rod on an elastic foundation clamped at its left end, and coupled at its right end to an essentially nonlinear MDOF ungrounded attachment (the NES). The MDOF NES possesses three small masses coupled by means of essentially nonlinear (nonlinearizable) stiffnesses situated in parallel to weak viscous dampers (see Figure 5.48). Moreover, the masses of the NES are assumed to be small, so that their summation is equal to the mass of the SDOF NES considered in Section 5.2, i.e., $m_1 + m_2 + m_3 = 0.1$. This will enable us to make direct comparisons of the performances of the SDOF and MDOF NESs without considering added mass effects in the dynamics. In addition, viscous damping in the system is assumed to be weak by setting $\lambda \ll 1$.

Assuming unidirectional vibration of the system, and denoting by $v_1(t)$, $v_2(t)$ and $v_3(t)$ the displacements of the three masses of the NES, and by $u(x, t)$ the distributed displacement of the rod at position x , we obtain the following governing differential equations for the rod:

$$\begin{aligned} \frac{\partial^2 u(x, t)}{\partial t^2} + \omega_0^2 u(x, t) + \lambda_1 \frac{\partial u(x, t)}{\partial t} - \frac{\partial^2 u(x, t)}{\partial x^2} &= F(t)\delta(x - d), \quad 0 \leq x \leq L \\ u(0, t) = 0, \quad \frac{\partial u(L, t)}{\partial x} &= \varepsilon[v_1(t) - u(L, t)], \quad u(x, 0) = 0, \quad \frac{\partial u(x, 0)}{\partial x} = 0 \end{aligned} \quad (5.80a)$$

and the MDOF NES:

$$\begin{aligned} m_1 \ddot{v}_1(t) + \varepsilon[v_1(t) - u(L, t)] + C_1[v_1(t) - v_2(t)]^3 + \lambda[\dot{v}_1(t) - \dot{v}_2(t)] &= 0 \\ v_1(0) = \dot{v}_1(0) &= 0 \\ m_2 \ddot{v}_2(t) + C_1[v_2(t) - v_1(t)]^3 + C_2[v_2(t) - v_3(t)]^3 \\ + \lambda[\dot{v}_2(t) - \dot{v}_1(t)] + \lambda[\dot{v}_2(t) - \dot{v}_3(t)] &= 0 \\ v_2(0) = \dot{v}_2(0) &= 0 \\ m_3 \ddot{v}_3(t) + C_2[v_3(t) - v_2(t)]^3 + \lambda[\dot{v}_3(t) - \dot{v}_2(t)] &= 0 \end{aligned}$$

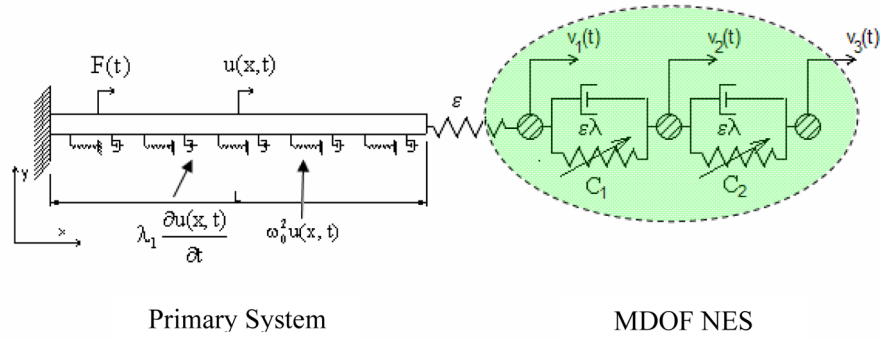


Fig. 5.48 Linear dispersive elastic rod with an attached MDOF NES.

$$v_3(0) = \dot{v}_3(0) = 0 \quad (5.80b)$$

Hence, we assume that the system is initially at rest, and that a shock is applied at position $x = d$ of the rod. In the above equations ϵ is the constant of the linear coupling stiffness between the rod and the MDOF NES, and, depending on its value there is either weak or strong coupling between the rod and the NES; in fact, one of the aims of this computational study is to investigate the effect of the coupling term on the TET performance. In (5.80) λ_1 and λ denote the viscous damping coefficients of the rod and the NES, respectively, and C_1, C_2 the coefficients of the essential stiffness nonlinearities of the MDOF NES (see Figure 5.48). Moreover, in the following analysis the length of the rod is normalized to $L = 1$. The frequency ω_0 is the non-dimensional distributed elastic support of the rod and introduces dispersive effects in its dynamics; as discussed in previous sections this frequency represents the cut-off frequency in the spectrum of the dynamics of the uncoupled, infinite dispersive rod; that is, the bounding frequency separating the attenuation ($0 < \omega < \omega_0$) and propagation zones ($\omega > \omega_0$) of the rod on the elastic foundation.

For prescribed excitation the equations of motion (5.80a, 5.80b) were solved numerically using the Matlab[®] FE code described in Section 5.2.1, employing an implicit time integration scheme based on the adapted Newmark algorithm (Gerandin and Rixen, 1997). At each time step of the numerical integration the total energy balance was computed in order to ensure that the relative energy error between subsequent steps of the computation was kept less than 0.001%, and that the total accumulative energy error throughout the entire computation was kept less than 1%.

Strong coupling between the clamped rod and the NES is a prerequisite for the occurrence of strong nonlinear modal interactions between the linear and nonlinear subsystems. The reason is that weak coupling would not excite sufficiently the NES, so insignificant nonlinear effects in the damped responses would be realized. We point out that this holds due to the clamped condition at the left boundary of the rod, which restricts the rod response to low amplitudes. We note, however, that for different boundary conditions (e.g., free left boundary) the rod response might

Table 5.3 The leading eigenfrequencies of the uncoupled dispersive rod ($\omega_0 = 1, L = 1.0$).

Normal Mode	1	2	3	4	5	6	7	8	9	10
Eigenfrequency (rad/sec)	1.8621	4.8178	7.9194	11.046	14.184	17.329	20.48	23.638	26.802	29.973

attain higher amplitudes for the shock excitation, so that strong nonlinear modal interactions might be realized even for weak coupling with the NES (see, for example, the discrete system of Figure 4.2).

In Table 5.3 we present the leading eigenfrequencies of the uncoupled clamped rod (with MDOF NES detached) on an elastic foundation with $\omega_0 = 1$. The first step of our study is to construct the FEP of the corresponding undamped and unforced Hamiltonian system with $\lambda = \lambda_1 = 0$ and $F(t) = 0$ in (5.80a, 5.80b). Then, as shown in our previous studies, the FEP can help us understand and interpret damped transitions involving strongly nonlinear modal interactions between the rod and the NES. To this end, we consider the following Hamiltonian system:

$$\begin{aligned}
& \frac{\partial^2 u(x, t)}{\partial t^2} + \omega_0^2 u(x, t) - \frac{\partial^2 u(x, t)}{\partial x^2} = 0, \quad 0 \leq x \leq L = 1 \\
& u(0, t) = 0, \quad \frac{\partial u(L, t)}{\partial x} = \varepsilon[v_1(t) - u(L, t)] \\
& m_1 \ddot{v}_1(t) + \varepsilon[v_1(t) - u(L, t)] + C_1[v_1(t) - v_2(t)]^3 = 0 \\
& m_2 \ddot{v}_2(t) + C_1[v_2(t) - v_1(t)]^3 + C_2[v_2(t) - v_3(t)]^3 = 0 \\
& m_3 \ddot{v}_3(t) + C_2[v_3(t) - v_2(t)]^3 = 0
\end{aligned} \tag{5.81}$$

We omit initial conditions at this point since we will examine the *nonlinear boundary value problem* (NLBVP) governing the periodic orbits of this system; in contrast, the original problem (5.80a, 5.80b) is formulated as an *initial value (Cauchy) problem*.

Analytical approximations of the T -periodic orbits are sought in the form of the following Fourier series:

$$\begin{aligned}
u(x, t) &= \sum_{k=1}^{\infty} C_k(x) \cos[(2k-1)\Omega t], & v_1(t) &= \sum_{k=1}^{\infty} V_{1,k} \cos[(2k-1)\Omega t] \\
v_2(t) &= \sum_{k=1}^{\infty} V_{2,k} \cos[(2k-1)\Omega t], & v_3(t) &= \sum_{k=1}^{\infty} V_{3,k} \cos[(2k-1)\Omega t]
\end{aligned} \tag{5.82}$$

where $\Omega = 2\pi/T$ denotes the basic frequency of the periodic motion. Substituting (5.82) into the differential equations (5.81) and taking account the imposed boundary conditions for the rod, we obtain the following series of linear BVPs governing the spatial distributions $C_k(x)$ of the rod:

$$\begin{aligned}
& - \sum_{k=1}^{\infty} [(2k-1)\Omega]^2 C_k(x) \cos[(2k-1)\Omega t] \\
& + \omega_0^2 \sum_{k=1}^{\infty} C_k(x) \cos[(2k-1)\Omega t] - \sum_{k=1}^{\infty} C_k''(x) \cos[(2k-1)\Omega t] = 0 \\
& \Rightarrow -C_k''(x) + [\omega_0^2 - (2k-1)\Omega^2] C_k(x) = 0 \\
& C_k(0) = 0, \quad \frac{dC_k(L)}{dx} = \varepsilon [v_{1k} - C_k(L)] \tag{5.83}
\end{aligned}$$

An explicit solution of (5.83) provides the following analytical expression for $C_k(x)$, $k = 1, 2, 3, \dots$, in terms of the corresponding coefficients V_{1k} of the NES:

$$C_k(x) = \hat{C}_k \sin \left[x \sqrt{(2k-1)^2 \Omega^2 - \omega_0^2} \right] \tag{5.84}$$

$$\hat{C}_k = \frac{\varepsilon V_{1k}}{\sqrt{(2k-1)^2 \Omega^2 - \omega_0^2} \cos \left[L \sqrt{(2k-1)^2 \Omega^2 - \omega_0^2} \right] + \varepsilon \sin \left[L \sqrt{(2k-1)^2 \Omega^2 - \omega_0^2} \right]}$$

For example, taking into account only the three leading terms in the series of $u(x, t)$, we derive the following expression for the displacement at the end of the rod during the time-periodic motion:

$$\begin{aligned}
u(L, t) \approx & \frac{\varepsilon V_{11} \cos \Omega t}{\sqrt{\Omega^2 - \omega_0^2} \cot \left[L \sqrt{\Omega^2 - \omega_0^2} \right] + \varepsilon} \\
& + \frac{\varepsilon V_{13} \cos 3\Omega t}{\sqrt{9\Omega^2 - \omega_0^2} \cot \left[L \sqrt{9\Omega^2 - \omega_0^2} \right] + \varepsilon} \\
& + \frac{\varepsilon V_{15} \cos 5\Omega t}{\sqrt{25\Omega^2 - \omega_0^2} \cot \left[L \sqrt{25\Omega^2 - \omega_0^2} \right] + \varepsilon}
\end{aligned}$$

Clearly, this expression holds only as long as

$$(2k-1)^2 \Omega^2 - \omega_0^2 \leq 0 \Rightarrow \Omega^2 \geq \omega_0^2 (2k-1)^{-2}, \quad k = 1, 2, 3, \dots$$

i.e., only when Ω lies in the PZ of the k -th harmonic; this requirement is satisfied for *all* harmonics if $\Omega^2 \geq \omega_0^2$, i.e., for periodic orbits with basic frequency in the PZ of the rod of infinite extent). In that case the solution of the rod response is spatially extended (non-localized) in the form of traveling waves, whose positive interference produces the vibration modes evidenced in the transient dynamics.

However, if $(2\tilde{k} - 1)^2\Omega^2 - \omega_0^2 < 0$ for some \tilde{k} , then, for $k \geq \tilde{k}$ the trigonometric functions in expressions (5.83) and (5.84) should be replaced by hyperbolic ones, and the spatial distributions of the \tilde{k} -th and higher harmonics of the rod response $u(x, t)$ become spatially localized (representing near-field solutions with exponentially decaying envelopes). In that case the corresponding time-periodic motion of the rod possesses a set of harmonics (starting from the \tilde{k} -th harmonic and higher) in the form of spatially decaying standing waves, or near-field solutions localized close to the boundaries of the rod. The qualitative changes in the time-periodic motion of the rod (that is, from spatially extended harmonics to spatially decaying ones) due to changes in the frequency of oscillation, are caused by the dispersion effects introduced by its elastic foundation.

Assuming that $\Omega^2 \geq \omega_0^2$, i.e., that the basic harmonic of the response is situated inside the PZ of the rod (a similar procedure holds if a harmonic lies inside the AZ), the corresponding amplitudes, $V_{1,k}$, $V_{2,k}$ and $V_{3,k}$, $k = 1, 2, 3, \dots$, of the corresponding harmonics of MDOF NES are computed by substituting the relations (5.84) into the last three nonlinear differential equations of the set (5.81). Expanding the powers of the resulting trigonometric expressions, and setting the coefficients of the resulting trigonometric functions $\cos[(2k - 1)\Omega t]$, $k = 1, 2, \dots$, equal to zero, we derive an infinite set of coupled nonlinear algebraic relations in terms of the amplitudes $V_{1,k}$, $V_{2,k}$ and $V_{3,k}$ governing the time-periodic response of the MDOF NES with basic frequency Ω . For computational reasons, this infinite set of algebraic equations must be truncated by considering terms only up to the fifth harmonic (i.e., $k = 1, 2, 3$ only), and omitting higher harmonics. The resulting truncated set of nine nonlinear algebraic equations is then numerically solved for the amplitudes $V_{1,k}$, $V_{2,k}$ and $V_{3,k}$, which completes the analytic approximation of the periodic motion of the system through relations (5.82) and (5.84). The set of nine equations is too lengthy to be reproduced here and can be found in the thesis by Tsakirtzis (2006).

In the following numerical results we consider two configurations of MDOF NESs, which are principally distinguished by the strength of the coupling stiffness ε , and the magnitudes of the nonlinear coefficients C_1 and C_2 . Indeed, our aim is to study the influence of the coupling stiffness and the coefficients of the essential nonlinear stiffnesses of the MDOF NES on TET. The first configuration considered (referred to from now on as ‘System I’) consists of a highly asymmetric MDOF NES, in the sense that it possesses strongly dissimilar nonlinear stiffness coefficients. The parameters of System I are listed below:

$$\begin{aligned} C_1 &= 1.0, & C_2 &= 0.001, & \varepsilon &= 6.6, & \lambda &= \lambda_1 = 0, \\ L &= 1.0, & \omega_0 &= 1.0, & m_1 &= m_2 = m_3 &= 0.1/3 \quad (\text{System I}) \end{aligned}$$

In Figure 5.49 we depict the FEP of System I, computed by the previously outlined analytical approximation. The FEP of Figure 5.49 depicts the dependence of the basic frequency Ω in rad/s of the time-periodic oscillation on the (conserved) logarithm of the energy of this oscillation, $\log_{10}(E)$. Only the frequency range covering the two leading modes of the uncoupled linear rod is considered in the FEP of Figure 5.49. The energy E of the periodic orbit is computed by the expression

$$\begin{aligned}
E = & \frac{1}{2} \int_0^L \left[\frac{\partial u(x, t)}{\partial t} \right]^2 dx + \frac{1}{2} \int_0^L \left[\frac{\partial u(x, t)}{\partial x} \right]^2 dx + \frac{1}{2} \omega_0^2 \int_0^L u^2(x, t) dx \\
& + \frac{1}{4} \varepsilon [v_1(t) - u(L, t)]^2 + \frac{1}{2} m_1 v_1^2(t) + \frac{1}{2} m_2 v_2^2(t) + \frac{1}{2} m_3 v_3^2(t) \\
& + \frac{1}{4} C_1 [v_2(t) - v_1(t)]^4 + \frac{1}{4} C_2 [v_3(t) - v_2(t)]^4
\end{aligned} \tag{5.85}$$

In Figure 5.50 some representative periodic orbits on different branches of the FEP are depicted. Comparisons of these results with direct FE simulations of the equations of motion (5.81) (computed for the initial conditions predicted by the analytical model) confirmed their accuracy (Tsakirtzis, 2006).

Considering the FEP depicted in Figure 5.49 one discerns two low-frequency asymptotes, which correspond to the two leading modes of the linear uncoupled rod with eigenfrequencies given by:

$$\omega_n = \sqrt{\omega_0^2 + \frac{(2n-1)^2 \pi^2}{4L^2}}, \quad n = 1, 2 \quad (\text{Low-energy asymptotes}) \tag{5.86}$$

For the parameters corresponding to System I these are computed as, $\omega_1 = 1.8621$ rad/s and $\omega_2 = 4.8173$ rad/s. In the limit of high energies there exist additional frequency asymptotes, denoted by $\hat{\omega}_i$, $i = 1, 2, \dots$, corresponding to the eigenfrequencies of the system with rigid connections between the rod and the MDOF NES. High-energy periodic orbits close to these asymptotes are weakly nonlinear motions that predominantly localize to the rod. These high-frequency asymptotes are computed as the eigenfrequencies of the dispersive rod with a mass equal to $m_1 + m_2 + m_3 = 0.1$ attached to its right end.

As in the FEPs considered in Sections 3.3 and 4.2, the FEP of Figure 5.49 possesses (global) backbone branches of periodic orbits and (local) subharmonic tongues. Backbone branches consist of nearly monochromatic periodic solutions possessing a dominant harmonic component and higher harmonics at integer multiples of the dominant harmonic; these branches are defined over extended frequency and energy ranges and are composed of periodic solutions mainly localized to the MDOF NES, except in neighborhoods of the linearized eigenfrequencies of the rod (see Figure 5.50). Subharmonic tongues are composed of multi-frequency periodic motions with frequencies at rational multiples of the eigenfrequencies ω_n of the uncoupled rod. Each tongue is defined over a finite energy range, and is composed of two distinct branches of subharmonic solutions, which, at a critical energy level, coalesce in a bifurcation that signifies the end of that particular tongue and the elimination of the corresponding subharmonic motions for higher energies. In this non-integrable dynamical system there exist countable infinite subharmonic tongues emanating from backbone branches at frequencies in rational multiples of the eigenfrequencies of the uncoupled linear rod.

To study the effect on the FEP of strong coupling between the rod and the MDOF NES and of stronger essential nonlinearity C_2 we consider a second set of parame-

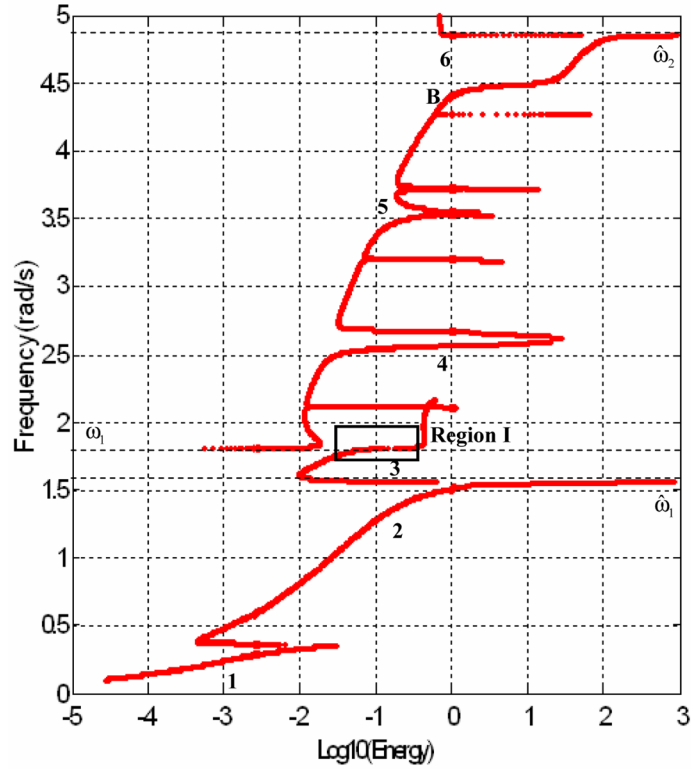


Fig. 5.49 FEP of System I based on the truncated system (5.82) and (5.84) with $k = 1, 2, 3$: digits (▼) correspond to the periodic orbits depicted in Figure 5.50; the low- and high-energy asymptotes close to the first mode of the rod are shown in dashed lines; point A (■) refers to the numerical simulations, and WT analysis of Section 5.4.3.

ters and label the corresponding system as ‘System II’:

$$C_1 = 1.0, \quad C_2 = 0.01, \quad \varepsilon = 9.0, \quad \lambda = \lambda_1 = 0,$$

$$L = 1.0, \quad \omega_0 = 1.0, \quad m_1 = m_2 = m_3 = 0.1/3 \quad (\text{System II})$$

The FEP of System II is depicted in Figure 5.51. Except in the neighborhoods of the low- and high-energy asymptotes ω_i and $\hat{\omega}_i$, $i = 1, 2, \dots$, the branches of periodic solutions are essentially nonlinear, as indicated by their high curvatures and strong dependencies on energy. The fact that all subharmonic tongues in the FEP are nearly horizontal does not mean that the dynamics are weakly nonlinear; on the contrary, the dynamics on the subharmonic tongues is essentially nonlinear. As explained in Section 3.3 and in Lee et al. (2005), on a subharmonic tongue, the strongly nonlinear system (5.81) oscillates approximately as a system of uncoupled linear oscillators, albeit with different frequencies, say ω_p and $(m/n)\omega_p$, where ω_p

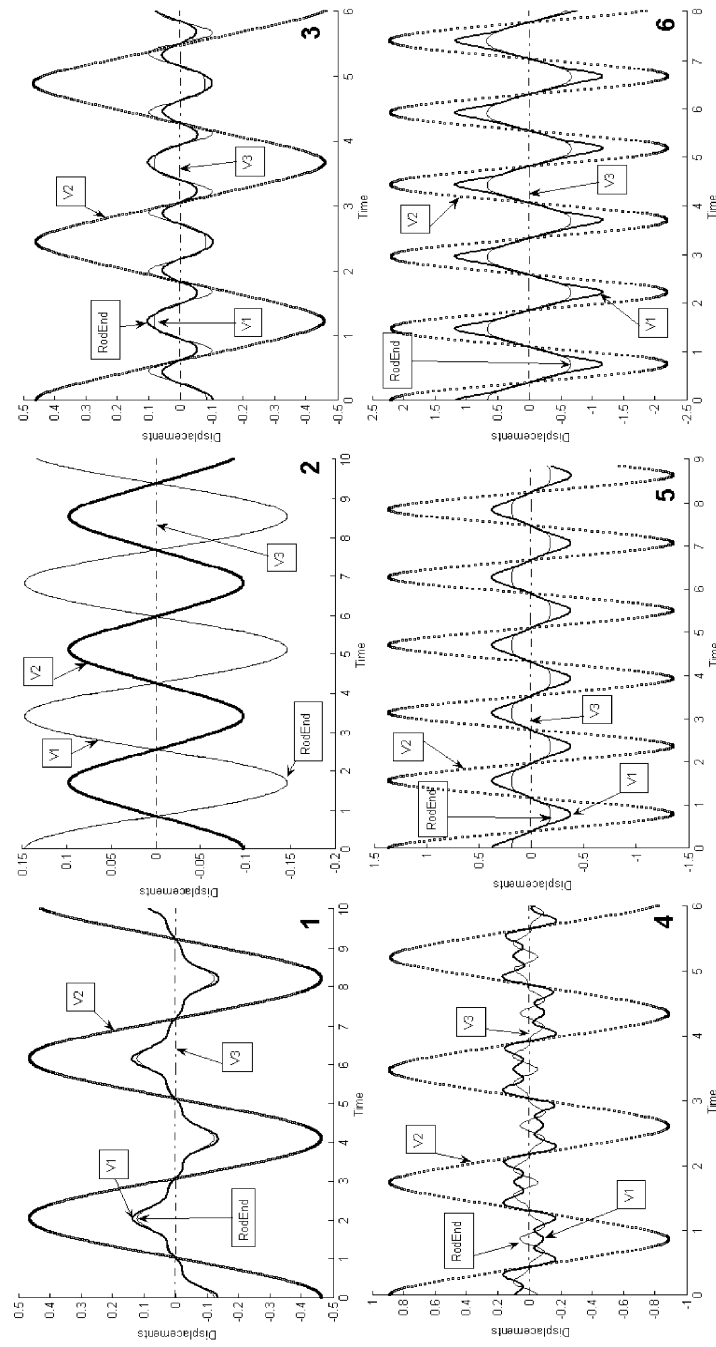


Fig. 5.50 Representative periodic orbits of the FEP of System I.

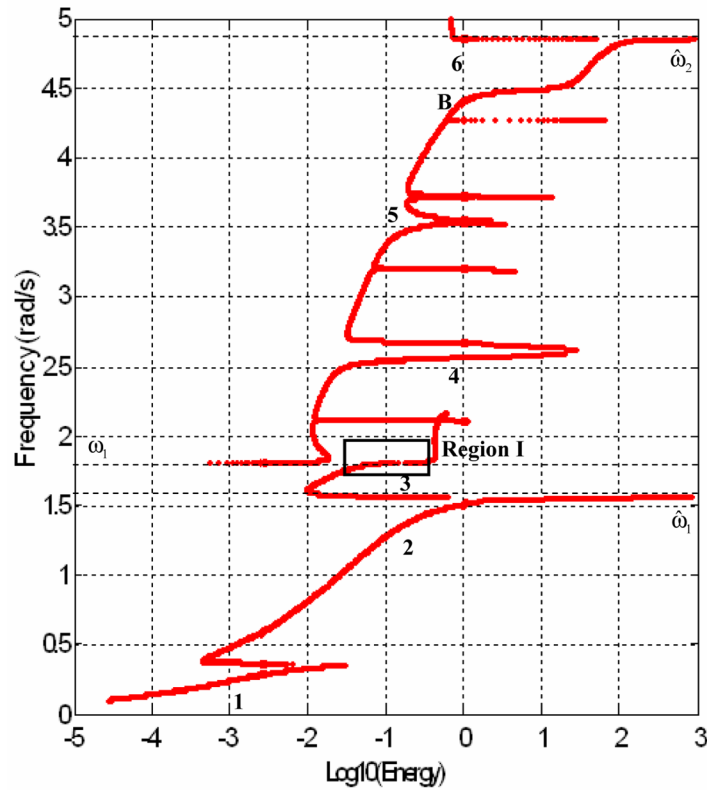


Fig. 5.51 FEP of System II based on the truncated system (5.82) and (5.84) with $k = 1, 2, 3$; digits (▼) correspond to the periodic orbits depicted in Figure 5.52; the low- and high-energy asymptotes close to the first mode of the rod are shown in dashed lines; point B (■) refers to the numerical simulations, WTs and EMD analysis of Section 5.4.3.

is the p -th eigenfrequency of the uncoupled rod and (m/n) is rational; as a result, the strongly nonlinear regimes on the subharmonic tongues resemble the dynamics of coupled linear oscillators with rationally related frequencies.

The high-energy asymptotes of the FEP of System II (in similarity to System I), indicate – as expected – that at sufficiently high energies System II resembles a rod with a concentrated end mass equal to $m_1 + m_2 + m_3 = 0.1$. This means that the dynamics of System II close to these high-energy asymptotes is weakly nonlinear, with the corresponding oscillations being predominantly localized to the rod. Hence, high-energy, weakly nonlinear dynamics may occur in System II (as in System I). Moreover, there is a region of the FEP (labeled as ‘Region I’ in Figure 5.51), where the responses of all NES masses and the rod end possess nearly identical amplitudes. In Figure 5.52 representative periodic motions lying on backbone branches of the FEP of System II are depicted.

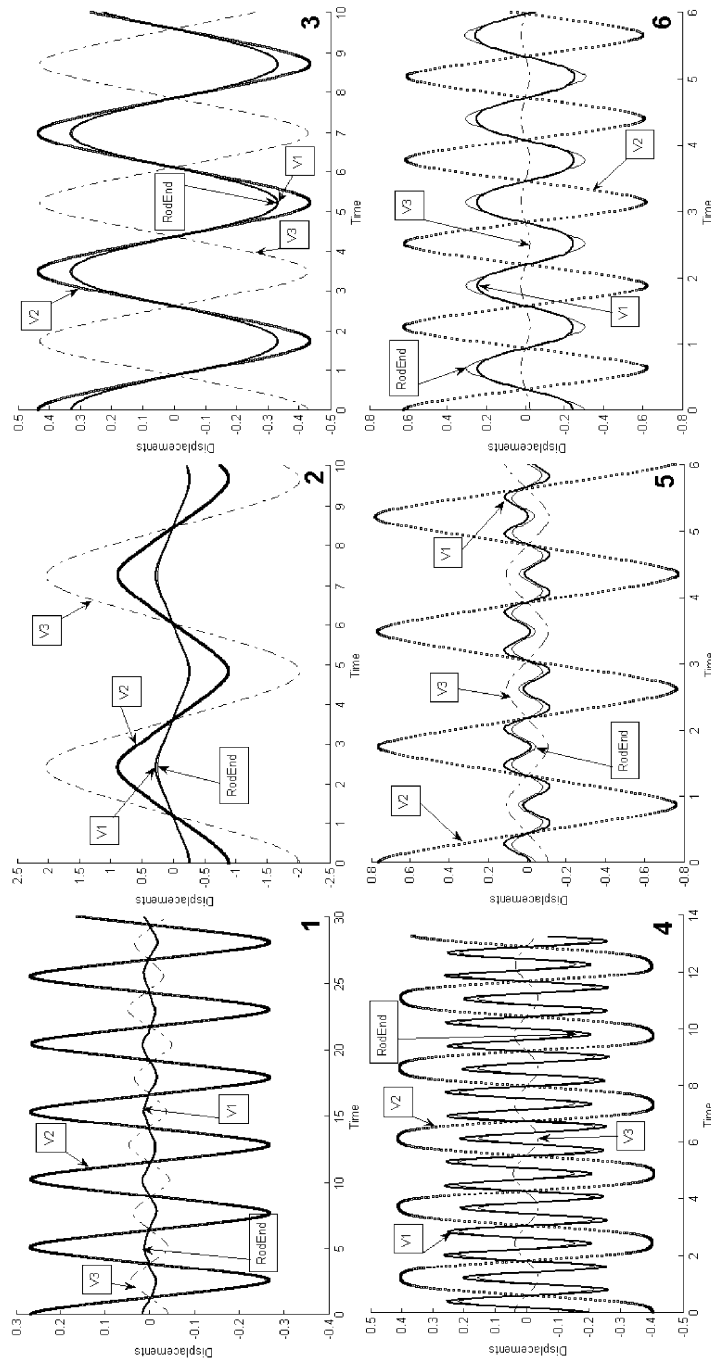


Fig. 5.52 Representative periodic orbits of the FEP of System II.

5.4.2 Computational Study of TET

We now study passive TET from the finite rod to the MDOF NES, by studying numerically the damped dynamics of system (5.80a, 5.80b). Indeed, we will examine the efficacy of using a MDOF NES as passive absorber and efficient dissipater of broadband energy from the elastic rod under shock excitation. Given that the examined NESs are lightweight, local and in modular forms (i.e., they can be attached to existing elastic structures with minimal structural modifications and added mass), our TET study can pave the way for applying the concept of NES to shock isolation of practical flexible systems. An additional aim of the following study is to show that weakly damped, nonlinear transitions in the system examined can be interpreted and understood by means of the FEP of the underlying Hamiltonian system; in that context, complex, multi-frequency dynamical transitions of the weakly damped system may be interpreted as transitions between branches of periodic solutions (NNMs) on the FEP. The same conclusion was drawn from our previous studies of damped transitions and TET in Sections 3.4, 4.3.2, and 5.2.3. Finally, we will perform multi-scale analysis of the damped responses by the combined WT-EMD methodology discussed in Section 5.2.3; this will enable us to study the strongly nonlinear modal interactions that occur between the rod and the MDOF NES and give rise to TET.

We study TET in the system depicted in Figure 5.48 by computing the asymptotic values of the corresponding energy dissipation measures (EDMs), i.e., of the percentages of shock energy of the rod that are (eventually) dissipated by the dampers of the MDOF-NES, when system parameters vary. The following parametric study is performed by numerically integrating the governing equations of motion (5.80a, 5.80b) using the previously described FE discretization. The numerical simulations are performed for a shock of the form

$$F(t) = \begin{cases} A \sin(2\pi t/T), & 0 < t \leq T/2 \\ 0, & t > T/2 \end{cases} \quad (5.87)$$

where $T = 0.1T_1$, where T_1 is the period of the first mode of the linear rod. Moreover, we assume that the shock is applied at position $d = 0.2$ from the clamped (left) end of the rod. Although the form of the applied shock is kept fixed throughout the following parametric study of TET, the shock magnitude A is varied to investigate the effect of the level of shock energy input on TET (Tsakirtzis, 2006; Tsakirtzis et al., 2007a).

The finite rod with $L = 1.0$ and $\omega_0 = 1$ was discretized into 200 finite elements, which ensured a five-digit convergence of the eigenfrequencies and shapes of its leading modes. In the simulations weak damping for the rod was assumed, modeled by a damping matrix which was expressed as linear superposition of mass and stiffness matrices, i.e., $D = a_1M + a_2K$ with $a_1 = 0$ and $a_2 = 0.01$. The leading eigenfrequencies of the uncoupled rod (with the MDOF NES detached) are listed in Table 5.3, whereas the corresponding modal critical viscous damping ratios are presented in Table 5.4. The FE model was integrated by the Newmark algorithm.

Table 5.4 The leading modal critical viscous damping ratios of the uncoupled dispersive rod ($\omega_0 = 1, L = 1.0$).

Normal Mode	1	2	3	4	5	6	7	8	9	10
Modal critical viscous ratio	0.2685	0.1038	0.0631	0.0453	0.0352	0.0289	0.0244	0.0211	0.0187	0.0166

Finally, the sampling frequency was chosen as less than 6% of the eigenfrequencies of the excited modes (i.e., the leading three modes) of the rod.

In the following parametric study (Tsakirtzis, 2006; Tsakirtzis et al., 2007a) we vary the coupling stiffness ε (which ends up as being a critical parameter for TET efficiency), and the magnitude A of the applied shock, for five different sets of nonlinear coefficients C_1 and C_2 . Moreover, we wish to study the effect of NES asymmetry on TET, that is, the effect of asymmetric nonlinear oscillator pairs on the capacity of the MDOF NES to passively absorb and dissipate shock energy from the rod. To this end, we consider the following five pairs of nonlinear stiffnesses of the MDOF NES:

Application I:	$(C_1, C_2 = (1.0, 0.001))$
Application II:	$(C_1, C_2 = (1.0, 0.01))$
Application III:	$(C_1, C_2 = (1.0, 0.1))$
Application IV:	$(C_1, C_2 = (1.0, 1.0))$
Application V:	$(C_1, C_2 = (1.0, 10.0))$

In Application I the essential stiffness nonlinearity of the pair of NES oscillators that lies the furthest from the rod was chosen to be much weaker than the corresponding nonlinearity of the pair that is directly connected to the rod through the coupling linear stiffness ε (see Figure 5.48). As we proceed from Application I to V this asymmetry decreases, until it is completely eliminated in Application III (which corresponds to a ‘symmetric’ NES), and reversed in Applications IV and V. The rationale for studying this asymmetry is that TET efficiency (i.e., the capacity of the MDOF NES to passively absorb and locally dissipate shock energy from the rod) depends, in essence, on the capacity of the pairs of NES oscillators (or at least one of these pairs) to execute large-amplitude relative (internal) oscillations, since only then the dampers of the NES can dissipate major portions of the shock energy transferred from the rod. Hence, we wish to examine if a relatively weak essential nonlinearity in at least one pair of the NES oscillators affects the capacity of the NES to execute large-amplitude relative motions and yield effective TET. On the other hand, it is clear that in the other extreme, where both essential stiffnesses of the NES are weak, we should expect deterioration of TET, as this would hinder the capacity of the MDOF NES to engage in simultaneous multi-modal nonlinear interactions with the rod (see for example the results of Chapter 4). Hence, it is necessary to

carefully examine how the asymmetry of the MDOF NES, and, specifically, *weak essential nonlinearity in a pair of NES oscillators* affects TET in this system.

In each of the above five applications the FE simulations are performed for parameters $L = 1.0$, $\lambda = 0.01/2$, $m_1 = m_2 = m_3 = 0.1/3$, $\omega_0 = 1.0$ and nonlinear stiffnesses as listed above. Zero initial conditions for the system are applied. In the series of numerical simulations performed for each application we consider coupling stiffness values in the range $\varepsilon \in [0.1, 10]$ with a step of $\Delta\varepsilon = 0.1$ for a total of 100 values; in addition, we consider amplitudes of the applied shock in the range $A \in [10, 200]$ with a step $\Delta A = 10$ for a total of 20 values. Hence, to each application corresponds a total of $20 \times 100 = 2000$ pairs (ε, A) all of which are realized in the parametric study.

The computational procedure for studying TET efficiency in each of the five applications is as follows. For each pair (ε, A) we integrate numerically the FE model of the system (5.80a, 5.80b) for a sufficiently large time interval so that at least 99.5% of the input shock energy is eventually damped during the simulation; this ensures that no essential dynamics is missed in the transient simulations due to inappropriate selection of the time interval of integration. Then, we assess TET efficiency from the rod to the MDOF NES by computing the following EDM:

$$E_{\text{NES}, t \gg 1} = \lim_{t \gg 1} \frac{\int_0^L \varepsilon \lambda \{[\dot{v}_2(\tau) - \dot{v}_1(\tau)]^2 + [\dot{v}_3(\tau) - \dot{v}_2(\tau)]^2\} d\tau}{\int_0^T F(\tau) \frac{\partial u(d, \tau)}{\partial \tau} d\tau} \times 100 \quad (5.88)$$

i.e., the percentage of shock energy of the rod that is eventually dissipated by the MDOF NES; high values of $E_{\text{NES}, t \gg 1}$ indicates strong TET. As mentioned previously, the EDM (5.88) does not provide any information regarding the time scale of the TET dynamics, i.e., on *how fast energy from the rod is passively absorbed and dissipated by the MDOF NES*. Instead, we will focus only on the percentage of input energy dissipated by the NES, and postpone the discussion of how rapid the realization of TET is for Chapters 8, 9 and 10.

In Figure 5.53 we depict contour plots of the EDM $E_{\text{NES}, t \gg 1}$ as function of the parameters ε and A for Application I, i.e., for the highly asymmetric MDOF NES. We note that there is a wide region of strong TET corresponding to relatively strong coupling ($\varepsilon > 4$) and moderate to large amplitudes of input shock ($A > 70$); in this region the MDOF NES is highly efficient and dissipates a major portion of input shock ($E_{\text{NES}, t \gg 1} > 75\%$); what is even more significant from a practical point of view is that this high TET efficiency is robust to variations in the system parameters considered. However, we should note that these results correspond to zero initial conditions of the system, so there can be no assurance regarding robustness of NES efficiency with respect to different sets of initial conditions. In summary, for strong linear coupling there occurs strong TET from the rod to the MDOF NES over a wide range of initial shocks. Moreover, the weaker the applied shock is, the stronger the coupling stiffness should be for strong TET to occur.

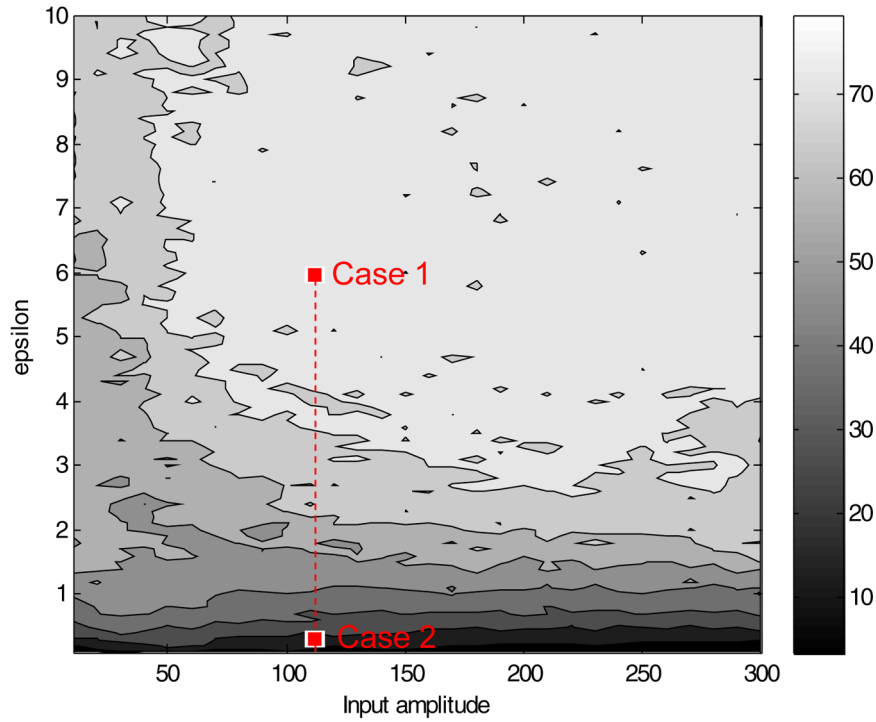


Fig. 5.53 Application I – contour plots of EDM $E_{NES,t \gg 1}$, as a function of linear coupling stiffness ϵ , and the shock amplitude A ; Cases 1 and 2 (■) refer to the simulations depicted in Figures 5.54 and 5.55.

An additional conclusion drawn from the plot of Figure 5.53 is that, compared to the SDOF NES examined in previous chapters, strong TET in the MDOF NES occurs over wider ranges of input energies (shocks). Indeed, in Chapter 3 where SDOF NESs were considered, it was found that TET was sensitive to the level input energy, in the sense that optimal TET was achieved for specific levels of input energy and that away from these levels TET deteriorated markedly (see for example the results depicted Figures 3.4 and 3.44). On the contrary, the results depicted in Figure 5.53 indicate that the MDOF NES provides better and more robust TET performance, since strong TET is maintained over wider ranges of input energy. This result is important from a practical point of view, since in engineering applications requiring effective shock absorption the demand would be for strong TET performance over a wide range of shock energies.

In order to study in more detail the damped dynamics governing TET from the rod to the MDOF NES we examined in detail two specific cases, labeled as Cases 1 and 2 in the contour plot of Figure 5.53. Case 1 (see Figure 5.54) corresponds to strong coupling, moderate applied shock, $(\epsilon, A) = (6, 110)$, and strong TET, $E_{NES,t \gg 1} = 81.15\%$; Case 2 (see Figure 5.55) corresponds to weak coupling, mod-

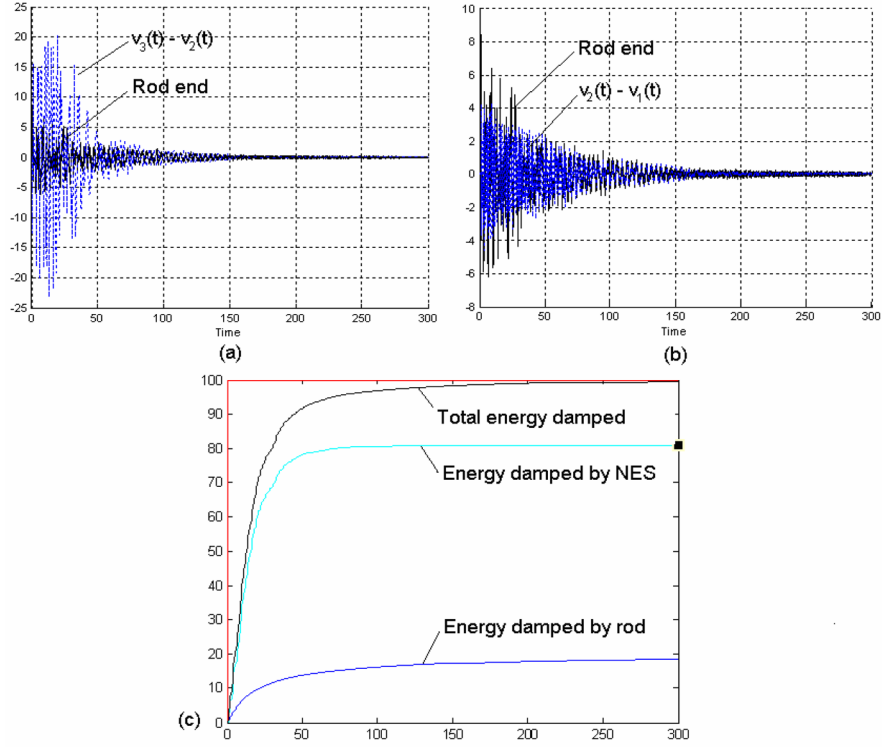


Fig. 5.54 Application I – Case 1; (a, b) NES displacements $[v_2(t) - v_1(t)]$ and $[v_3(t) - v_2(t)]$ superimposed to the response of the right end of the rod; (c) transient energy measures.

erate applied shock, $(\varepsilon, A) = (0.2, 110)$, and weak TET $E_{NES, t \gg 1} = 11.89\%$. Hence, we aim to relate the damped dynamics to the strong or weak NES efficiency of the MDOF NES for these two cases. It should be clear that the enhanced performance of the MDOF NES in Case 1 is mainly due to the large-amplitude relative displacement $[v_3(t) - v_2(t)]$, which exceeds that of the rod end especially in the early stage of the dynamics (i.e., in the most highly energetic regime of the dynamics); this, in turn, leads to a large-amplitude relative velocity $[\dot{v}_3(t) - \dot{v}_2(t)]$ and to strong shock energy dissipation by the damper of the second pair of NES oscillators. This is reflected in the plots of transient damped energies (see Figure 5.54c), where it is deduced that the NES dampens a significant portion of input energy during the early (highly energetic) stage of the response. The large amplitude of the relative displacement $[v_3(t) - v_2(t)]$ in this case (which is mainly due to the weak nonlinear coupling stiffness C_2) explains the large amount of energy damped by the viscous damper of the second pair of oscillators of the MDOF NES. It follows that *the high asymmetry of the NES in Application I proves to be beneficial for TET*. An investi-

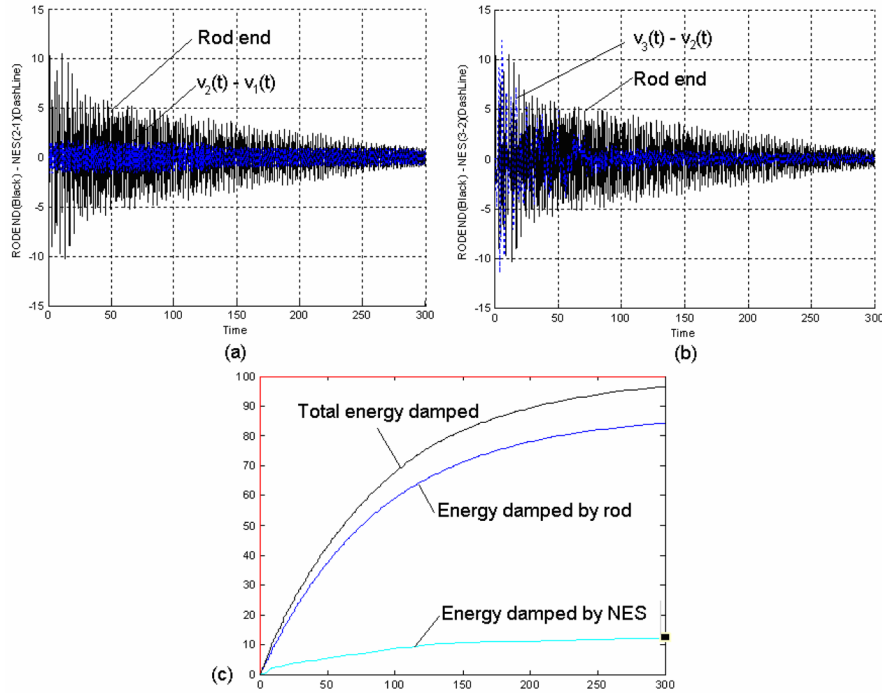


Fig. 5.55 Application I – Case 2; (a, b) NES displacements $[v_2(t) - v_1(t)]$ and $[v_3(t) - v_2(t)]$ superimposed to the response of the right end of the rod; (c) transient energy measures.

gation of the nonlinear modal (resonance) interactions giving rise to strong TET in cases like this one will be carried out in Section 5.4.3.

In Figure 5.56 we present the TET efficiency plot for Application II, i.e., for reduced NES asymmetry compared to Application I. The computational procedure outlined for Application I was also applied to Application II, that is, we varied the linear coupling stiffness in the range $\varepsilon \in [0.1, 10]$ for a total of 100 values, and the shock amplitude in the range $A \in [10, 200]$ for a total of 20 values. This gave a total of $20 \times 100 = 2000$ possible pairs (ε, A) , all of which were realized for constructing the NES efficiency plot of Figure 5.56. Similarly to Application I, we ensured that each of the numerical simulations was performed for a sufficiently long time interval, so that at least 99.5% of the input shock energy was damped in the time window considered in the simulations. In Application II (as in Application I) there is a wide region of the plot where strong TET occurs and the EDM exceeds 75%. However, we note that the region of strong TET is slightly diminished compared to Application I (see Figure 5.53). This implies that reducing NES asymmetry, reduces (even slightly) the capacity of the NES to dissipate a significant portion of the shock energy of the rod.

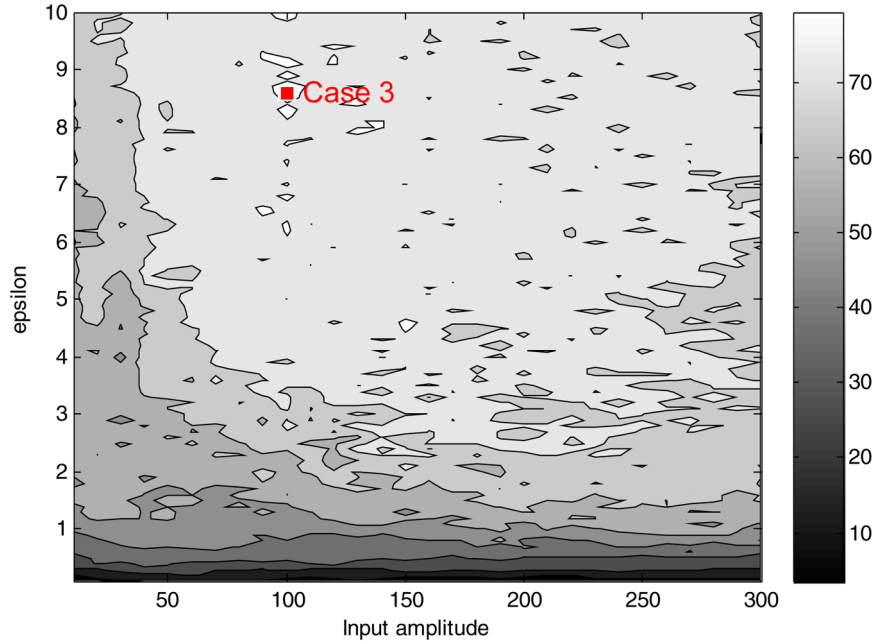


Fig. 5.56 Application II – contour plot of EDM $E_{NES, t \gg 1}$ as a function of linear coupling stiffness ϵ , and the shock amplitude A ; Case 3 (■) refers to the simulation depicted in Figure 5.57.

As in Application I strong TET occurs for stiff coupling and moderate to large amplitudes of applied shock (i.e., at moderate to high energy levels). In addition, there are small regions in the range $A \in [100, 120]$ and $\epsilon \in [8, 9]$ where strong TET from the rod to the NES ($E_{NES, t \gg 1} > 80\%$) take place; in one of these regions we have the global optimal value $E_{NES, t \gg 1} \approx 84.11\%$. In Figure 5.57 we consider the simulations corresponding to $\epsilon = 8.6$ and $A = 100$ (labeled as Case 3). We note the rapid dissipation of shock energy by the NES in the early (highly energetic) regime of the motion; this is primarily due to the high-amplitudes of the relative displacement $[v_3(t) - v_2(t)]$. Moreover, judging from the waveforms of the rod end response and the relative displacements of the MDOF NES we infer that the efficient dissipation of energy by the NES is caused by a series of transient resonance captures (TRCs) occurring in the transient dynamics.

Three additional series of numerical simulations corresponding to Applications III–V are depicted in Figures 5.58–5.60. As the NES asymmetry reverses, the region of efficient dissipation of energy by the NES also diminishes. This means that NES asymmetry by itself is insufficient to improve NES efficiency: for effective TET to occur the NES asymmetry must be related to strong nonlinear characteristic C_1 and weak nonlinear characteristic C_2 . This is an interesting conclusion from the practical (design) point of view of MDOF NESs as passive shock absorbers.

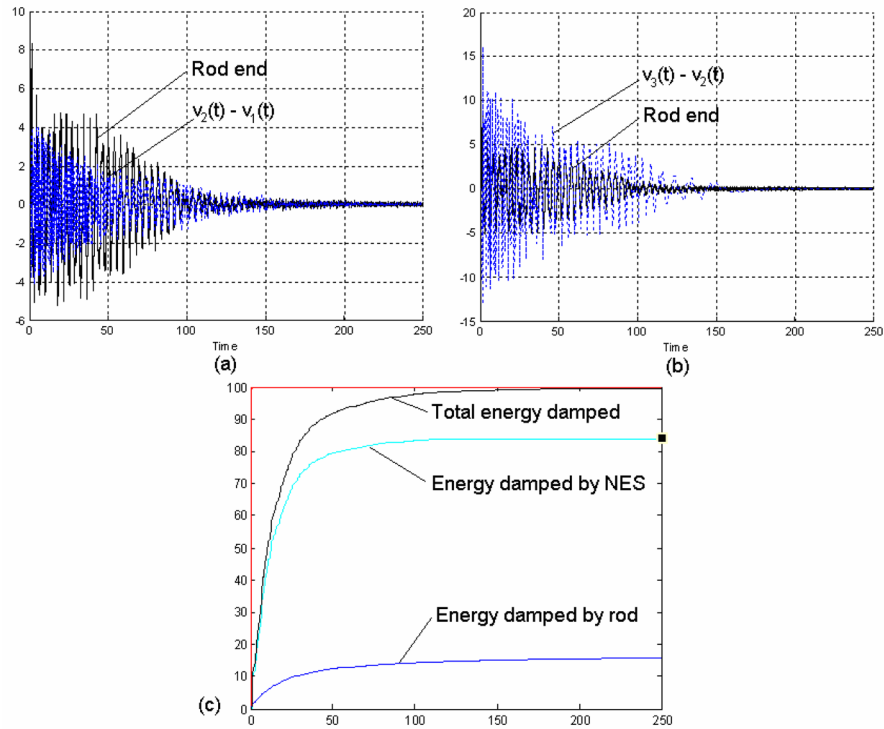


Fig. 5.57 Application II – Case 3; (a, b) NES displacements $[v_2(t) - v_1(t)]$ and $[v_3(t) - v_2(t)]$ superimposed to the response of the right end of the rod; (c) transient energy measures.

Summarizing these observations, we conclude that strong and robust TET in the system of Figure 5.48 is realized for strong linear coupling between the rod and the MDOF NES, weak coupling in the second oscillator pair of the NES (composed of the coupled masses m_2 and m_3), and strong coupling in the first oscillator pair (composed of the coupled masses m_1 and m_2). In addition, strong TET is realized for strong to moderate amplitudes of the applied shock. It appears that strong coupling between the rod and the NES and strong nonlinear stiffness C_1 yield strong transfer of shock energy from the rod to the MDOF NES; whereas, weak nonlinear stiffness C_2 yields effective dissipation of the transferred shock energy as it leads to large-amplitude relative response $[v_3(t) - v_2(t)]$. Moreover, in all cases considered the passive absorption of energy by the MDOF NES is *broadband*, contrary to conventional linear designs (based on linear vibration absorbers) where energy absorption is narrowband. This feature makes the proposed design novel and applicable to a diverse range of practical applications.

To better understand the nonlinear modal interactions between the rod and the MDOF NES and the associated TRCs leading to TET, in the next section we analyze two representative numerical simulations by combined numerical wavelet

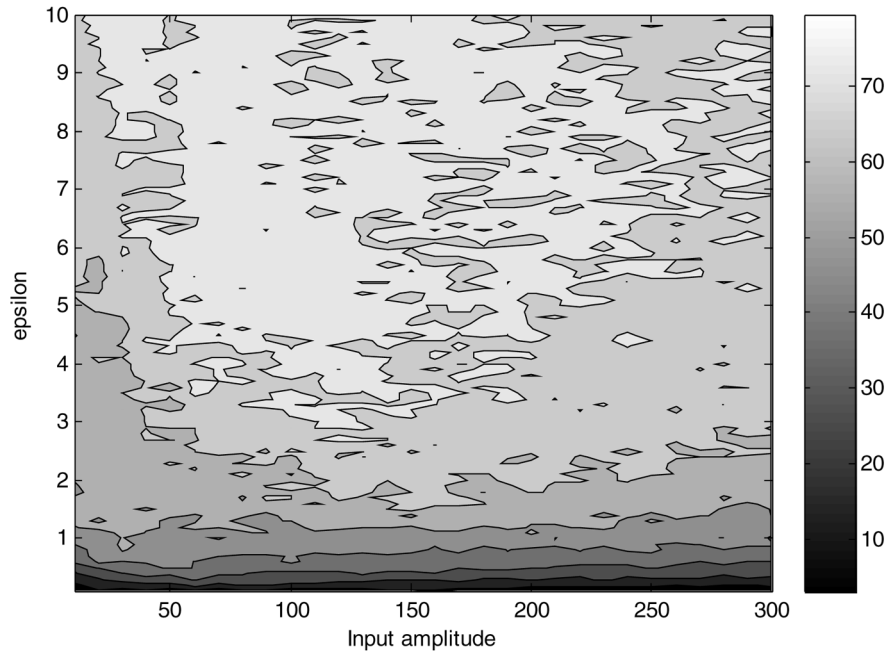


Fig. 5.58 Application III – contour plot of EDM $E_{NES, t \gg 1}$, as a function of linear coupling stiffness ε , and the shock amplitude A .

transforms (WTs) and empirical mode decomposition (EMD). We show that by superimposing the WT spectra of the responses to the corresponding Hamiltonian FEPs, and studying TRCs between individual IMFs of the rod and NES responses, we can study the nonlinear modal interactions occurring in the transient nonlinear dynamics of the system under consideration.

5.4.3 Multi-Modal Damped Transitions and Multi-Scale Analysis

The aim of this section is to study multi-modal interactions in the transient damped dynamics of the rod-MDOF NES system. This is performed through the use of numerical WTs and EMDs, which yields the identification of the dominant TRCs in the rod-MDOF nonlinear dynamic interaction, and paves the way for multi-scale analysis of the transient dynamics. The numerical simulations considered are computed utilizing the FE model described in the previous sections, but with no applied shock excitation. Instead, each of the examined damped motions is initialized with initial conditions corresponding to a specific point of the backbone branch of the corresponding FEP of the Hamiltonian system (studied in Section 5.4.1). We then wavelet-transform each of the relative transient responses $[v_1(t) - u(L, t)]$,

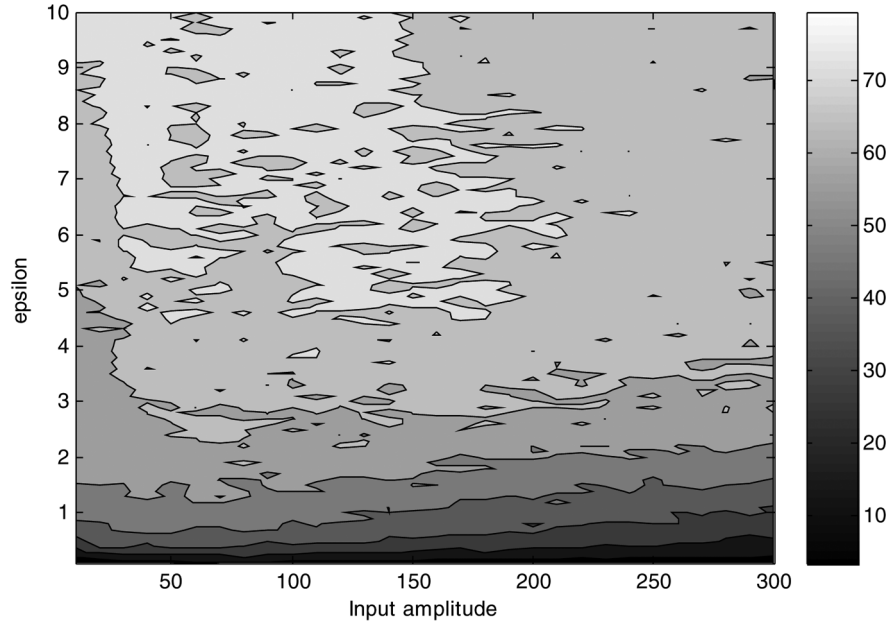


Fig. 5.59 Application IV – contour plot of EDM $E_{NES, t \gg 1}$, as a function of linear coupling stiffness ε , and the shock amplitude A .

$[v_1(t) - v_2(t)]$ and $[v_2(t) - v_3(t)]$, superimpose the resulting WT spectra to the Hamiltonian FEP, and, finally, analyze the time series by EMD. This post-processing program helps us to clearly identify the entire sequence of multi-frequency, multi-modal nonlinear transitions that occur in the damped nonlinear dynamics.

The first numerical simulation is performed for System I, i.e., for the system with parameters, $C_1 = 1.0$, $C_2 = 0.001$, $\varepsilon = 6.6$, $\lambda = 0.01/2$, $L = 1.0$, $\omega_0 = 1.0$, $m_1 = m_2 = m_3 = 0.1/3$, and initial conditions corresponding to point A on the backbone branch of the FEP of Figure 5.49. In the undamped system, this initial condition corresponds to a periodic motion (NNM) that is predominantly localized to the NES, with both the rod and the NES performing oscillations with an identical basic frequencies equal to $\Omega = 3.4$ rad/s. The specific initial conditions for the rod and the nonlinear attachment are approximately computed using the analytical method of Section 4.3 (with three terms in the truncated series) as follows:

$$U(x, 0) = \alpha_1 \sin \left[x \sqrt{\Omega^2 - \omega_0^2} \right] \\ + \alpha_3 \sin \left[x \sqrt{9\Omega^2 - \omega_0^2} \right] + \alpha_5 \sin \left[x \sqrt{25\Omega^2 - \omega_0^2} \right]$$

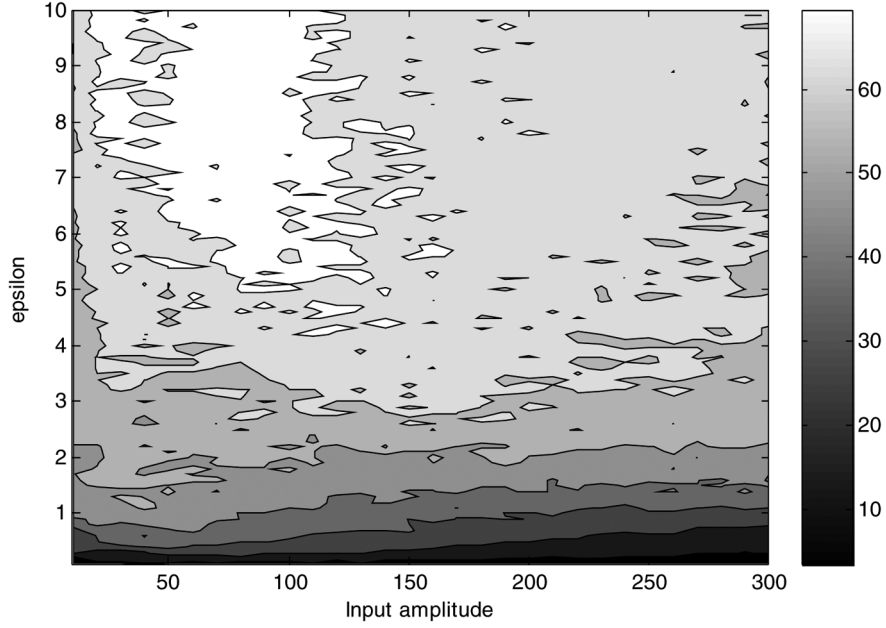


Fig. 5.60 Application V – contour plot of EDM $E_{NES, t \gg 1}$, as a function of linear coupling stiffness ε , and the shock amplitude A .

$$v_1(0) = \sum_{k=1}^{\infty} V_{1,k}, \quad v_2(0) = \sum_{k=1}^{\infty} V_{2,k}, \quad v_3(0) = \sum_{k=1}^{\infty} V_{3,k}$$

with

$$\begin{aligned} \alpha_1 &= -0.107074, & \alpha_3 &= -0.0430936, & \alpha_5 &= -0.00285114 \\ V_{11} &= 0.0639564, & V_{13} &= 0.0781734, & V_{15} &= 0.00494063 \\ V_{21} &= 0.835016, & V_{23} &= 0.0162039, & V_{25} &= -0.00341636 \\ V_{31} &= -0.00116088, & V_{33} &= -0.0000465294, & V_{35} &= -5.29816 \times 10^{-7} \end{aligned}$$

In Figures 5.61a–d we depict the relative responses of the system, together with their WT spectra superimposed to the FEP of Figure 5.49. As energy decreases due to damping dissipation the motion makes a damped transition that traces closely the main backbone branch of the FEP. This observation confirms once again that for sufficiently weak damping the damped response is dominated by the dynamics of the underlying Hamiltonian system. The nonlinear dynamic interaction between the rod and the NES during this damped transition is now examined in more detail. In the following exposition we adopt the notation regarding subharmonic tongues first introduced in Section 5.2.3; namely, a subharmonic tongue labeled as, $T_{p/q}^{(n)}$ denotes

the branch of subharmonic motions where the frequency of the dominant harmonic component of the NES response is nearly equal to $(p/q)\omega_n$, whereas that of the rod end is equal to ω_n (the n -th linearized eigenfrequency of the rod). It follows that for a subharmonic motion initiated on tongue $T_{p/q}^{(n)}$, the relative displacement between the rod and an NES mass, or the relative displacements between NES masses possess two main harmonics at frequencies ω_n and $(p/q)\omega_n$. In the present simulation, the motion starts at the point of main backbone with frequency $\Omega = 3.4$ rad/s. From Figures 5.61b–d we deduce that the WT spectra of the relative displacements initially trace the main backbone, as energy decreases. Then, the dynamics makes transitions along a series of subharmonic tongues, such as $T_{1/5}^{(4)}$, $T_{2/3}^{(2)}$, $T_{1/3}^{(3)}$, $T_{2/3}^{(1)}$, and $T_{1/2}^{(1)}$ (the tongues $T_{2/3}^{(1)}$ and $T_{1/2}^{(1)}$ are not depicted in the FEP of Figure 5.49).

Specifically, considering the response $[v_2(t) - v_3(t)]$ (see Figure 5.61b), following its initialization at point A of the backbone curve, its frequency content is *broadband*, as there is (weak) excitation of tongues in the range 2–4.5 rad/s, and also of the lower-frequency tongues $T_{2/3}^{(1)}$, $T_{1/2}^{(1)}$ and $T_{1/5}^{(1)}$. At the late, low-energy regime of the motion the response possesses low-frequency content. Considering next the response $[v_1(t) - v_2(t)]$ (see Figure 5.61c), we note that stronger frequency components exist compared to the response $[v_2(t) - v_3(t)]$. Indeed the frequency content is broadband in the range 2–5 rad/s, and after the initiation of the motion on the Hamiltonian backbone branch, subharmonic tongues, such as $T_{2/3}^{(2)}$, $T_{1/3}^{(3)}$, $T_{1/5}^{(4)}$, $T_{2/3}^{(1)}$ and $T_{1/2}^{(1)}$, are traced, which indicates that *there occur simultaneous TRCs of the MDOF NES with the 1st, 2nd, 3rd and 4th modes of the rod*. This can be explained by observing that the relative response $[v_1(t) - v_2(t)]$ corresponds to the deformation of the (stiffer) nonlinear stiffness C_1 which belongs to the part of the MDOF NES that interacts directly with the rod through the (stiff) coupling stiffness ε . At the later (low-energy) stage of the motion the response $[v_1(t) - v_2(t)]$ makes a final transition back to the backbone curve, tracing the weakly nonlinear mode close to the first eigenfrequency of the rod, ω_1 ; this contrasts to the low-frequency content of the relative response $[v_2(t) - v_3(t)]$ in the low-energy regime. Hence, we note *strongly broadband frequency content* for $[v_1(t) - v_2(t)]$ reflecting *the simultaneous transient resonance interaction (TRCs) of the MDOF NES with as many as four modes of the rod*.

Similar broadband content is observed in the WT spectrum of the relative response $[v_1(t) - u(L, t)]$ (see Figure 5.61d), which corresponds to the deformation of the linear coupling stiffness ε . However, in this case the frequency content of the signal is in the range 2.5–5 rad/s, with additional excitation of the lower-frequency subharmonic tongue $T_{1/5}^{(4)}$. There is weak excitation of the low-frequency tongues $T_{2/3}^{(1)}$ and $T_{1/2}^{(1)}$, and in the late, low-energy stage of the motion the response possesses higher frequency content compared to the relative displacements of the NES masses.

Summarizing, the nonlinear dynamical interaction between the rod and the MDOF NES is broadband, with as many as four modes of the rod participating

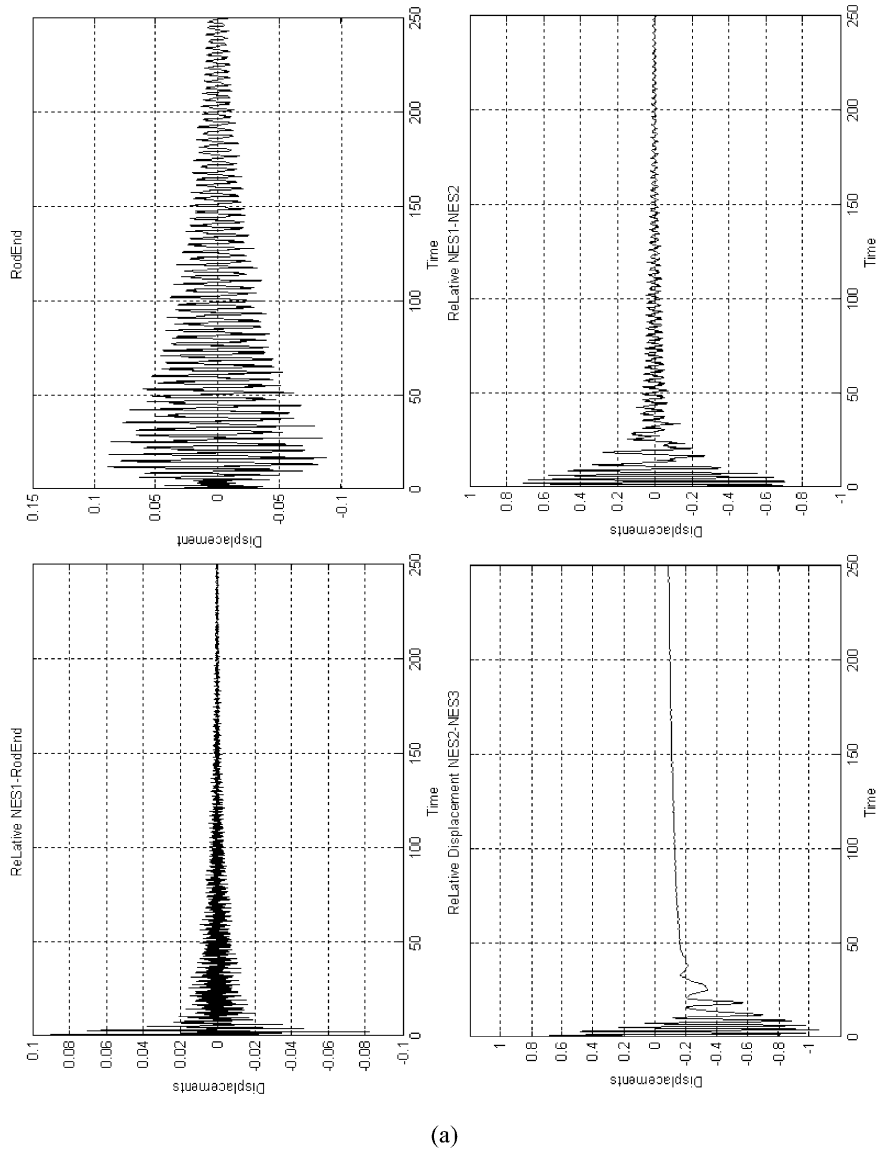
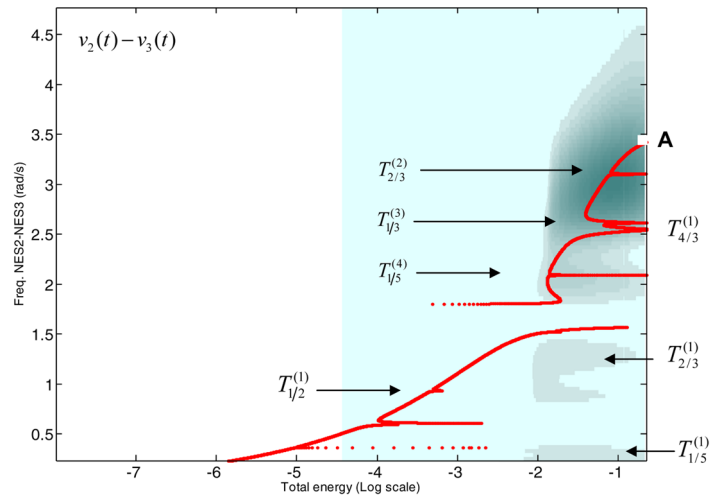
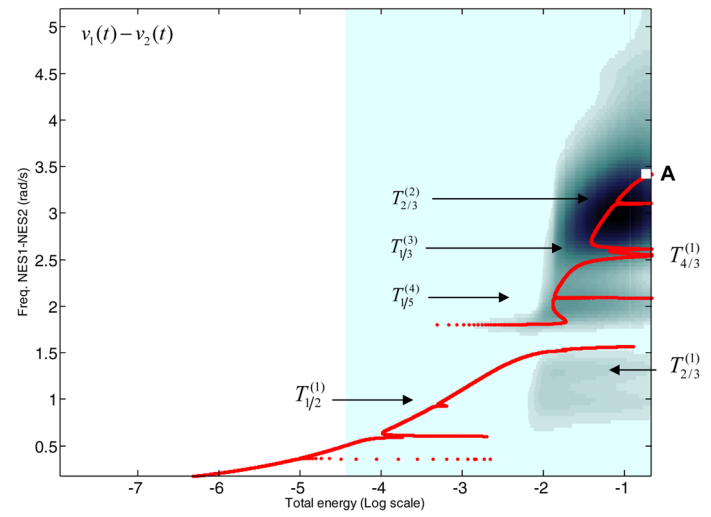


Fig. 5.61 Relative responses of System I for initial condition at point A of the FEP of Figure 5.49 ($\Omega = 3.4$ rad/s): (a) time series.



(b)



(c)

Fig. 5.61 Relative responses of System I for initial condition at point A of the FEP of Figure 5.49 ($\Omega = 3.4$ rad/s): (b, c) WT spectra superimposed to the FEP.

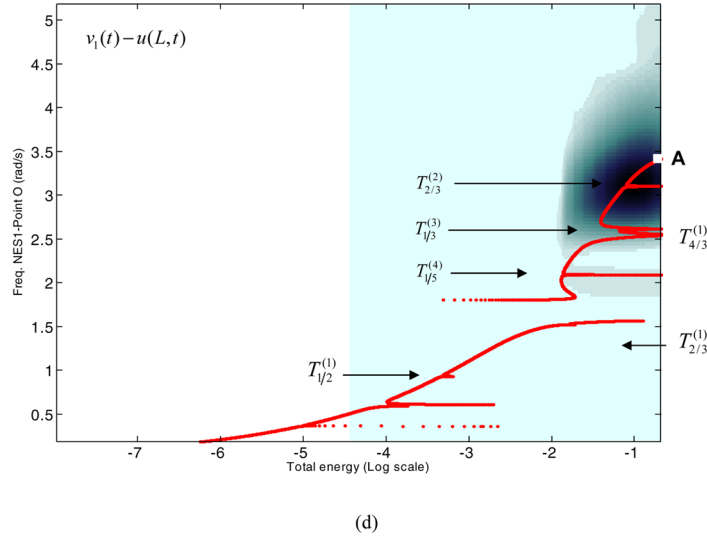


Fig. 5.61 Relative responses of System I for initial condition at point A of the FEP of Figure 5.49 ($\Omega = 3.4$ rad/s): (d) WT spectra superimposed to the FEP.

simultaneously in these resonance interactions. Moreover, the dynamics seem to occur in the neighborhoods of subharmonic tongues of the FEP.

A second numerical simulation was performed for System II, with parameters $C_1 = 1.0$, $C_2 = 0.1$, $\varepsilon = 9.0$, $\lambda = 0.01/2$, $L = 1.0$, $\omega_0 = 1.0$, $m_1 = m_2 = m_3 = 0.1/3$, and initial condition at point B on the backbone branch of the FEP of Figure 5.51. In the undamped system this initial condition gives rise to a periodic oscillation (NNM) predominantly localized to the NES, with both the rod and the NES performing oscillations with identical basic frequencies equal to $\Omega = 4.4$ rad/s. The specific initial conditions for the rod and the nonlinear attachment are approximately computed as follows:

$$\begin{aligned}
 U(x, 0) &= \alpha_1 \sin \left[x \sqrt{\Omega^2 - \omega_0^2} \right] + \alpha_3 \sin \left[x \sqrt{9\Omega^2 - \omega_0^2} \right] \\
 &\quad + \alpha_5 \sin \left[x + \sqrt{25\Omega^2 - \omega_0^2} \right] \\
 v_1(0) &= \sum_{k=1}^{\infty} V_{1,k}, \quad v_2(0) = \sum_{k=1}^{\infty} V_{2,k}, \quad v_3(0) = \sum_{k=1}^{\infty} V_{3,k}
 \end{aligned}$$

with

$$\alpha_1 = -0.30063, \quad \alpha_3 = 0.06949, \quad \alpha_5 = -0.00229$$

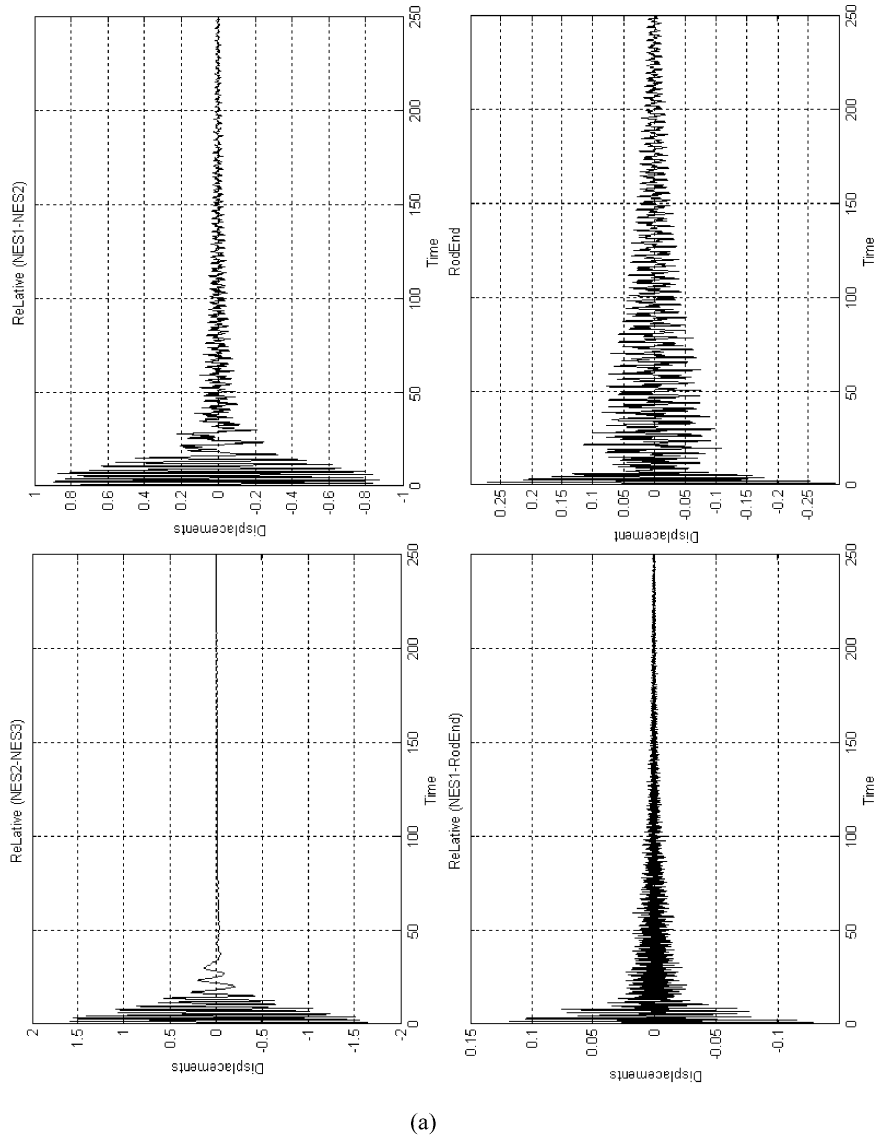
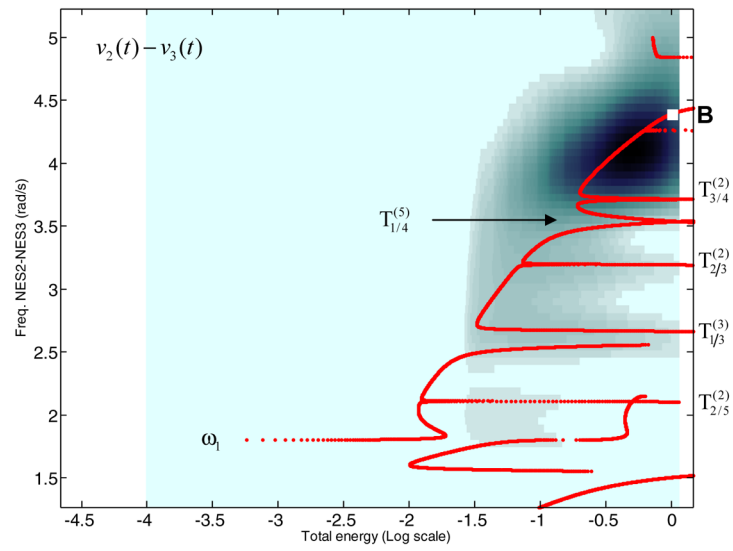
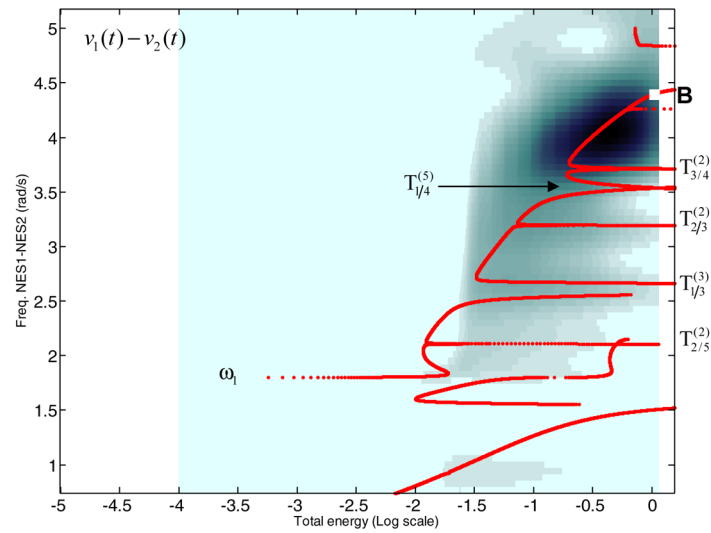


Fig. 5.62 Relative responses of System II for initial condition at point A of the FEP of Figure 5.51 ($\Omega = 4.4$ rad/s): (a) time series.



(b)



(c)

Fig. 5.62 Relative responses of System II for initial condition at point A of the FEP of Figure 5.51 ($\Omega = 4.4$ rad/s): (b, c) WT spectra superimposed to the FEP.

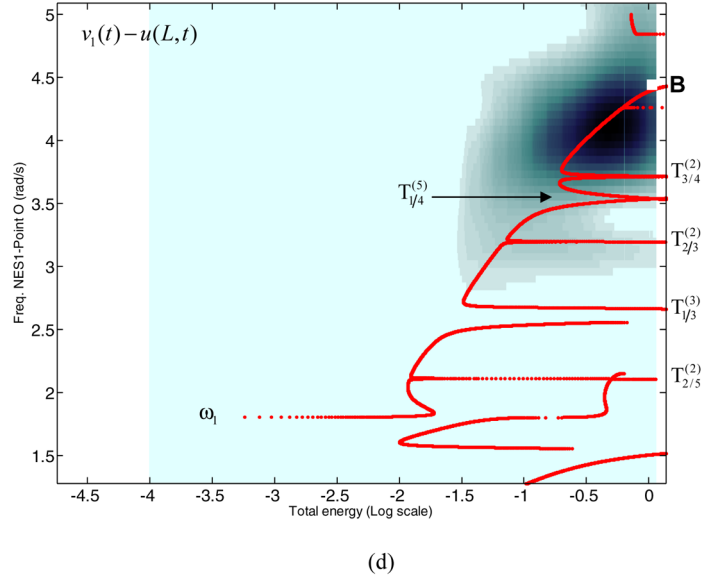
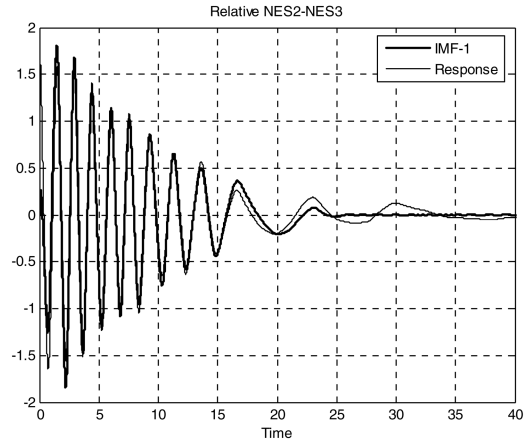


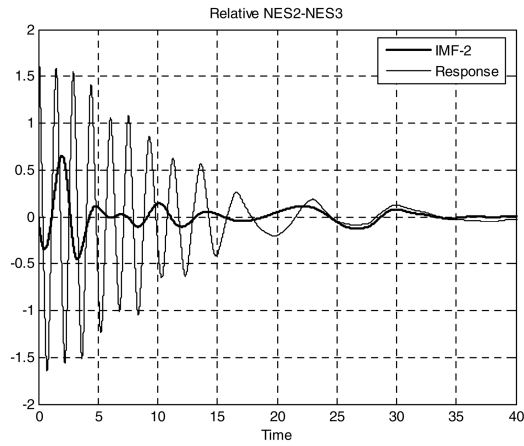
Fig. 5.62 Relative responses of System II for initial condition at point A of the FEP of Figure 5.51 ($\Omega = 4.4$ rad/s): (d) WT spectra superimposed to the FEP.

$$\begin{aligned}
 V_{11} &= 0.3329, & V_{13} &= 0.115, & V_{15} &= 0.005565 \\
 V_{21} &= 1.1067, & V_{23} &= 0.0331, & V_{25} &= -0.001618 \\
 V_{31} &= -0.6119, & V_{33} &= -0.0263, & V_{35} &= -0.00082
 \end{aligned}$$

In Figures 5.62a–d we depict the three transient relative displacements of this system, together with the WT spectra of these responses superimposed to the FEP of Figure 5.51. As in the previous numerical simulation, there occurs a series of nonlinear multi-frequency transitions in the dynamics. In this case, the motion is initiated at point B of the main backbone (with frequency $\Omega = 4.4$ rad/s); during the initial regime of the motion the damped dynamics traces the main backbone of the FEP for decreasing energy. Then, there occurs a series of TRCs involving a set of modes of the rod over broad frequency ranges. Specifically, a study of the WT spectrum of the relative response $[(v_2(t) - v_3(t))]$ (see Figure 5.62b) indicates that there occur broadband resonance interactions between the second pair of oscillators of the MDOF NES and the 1st, 2nd, 3rd and 5th modes (but not with the 4th mode) of the rod, as the subharmonic tongues $T_{1/4}^{(5)}$, $T_{1/3}^{(3)}$, $T_{3/4}^{(2)}$ and $T_{2/3}^{(2)}$ are traced by the damped dynamics for decreasing energy. Stronger modal interactions are noted in the spectrum of $[v_1(t) - v_2(t)]$ in the same broadband range above ω_1 ; this was expected, since this response represents the deformation of the stiffer nonlinear spring C_1 which belongs to the pair of oscillators of the NES that is directly connected to the rod. Moreover, in the late, low-energy regime of the motion the dynamics traces



(a)



(b)

Fig. 5.63 Relative response $[v_2(t) - v_3(t)]$ of System II initiated at point B of the FEP of Figure 5.51 ($\Omega = 4.4$ rad/s: (a, b) time series of 1st and 2nd (dominant) IMFs superimposed to the transient response.

the weakly localized nonlinear mode on the backbone curve close to the first rod eigenfrequency, ω_1 . Higher frequency components are noted in the spectrum of the relative response $[v_1(t) - u(L, t)]$, with its broadband content being in the range above 3 rad/s. It is interesting to note that these findings are confirmed by the EMD analysis performed below.

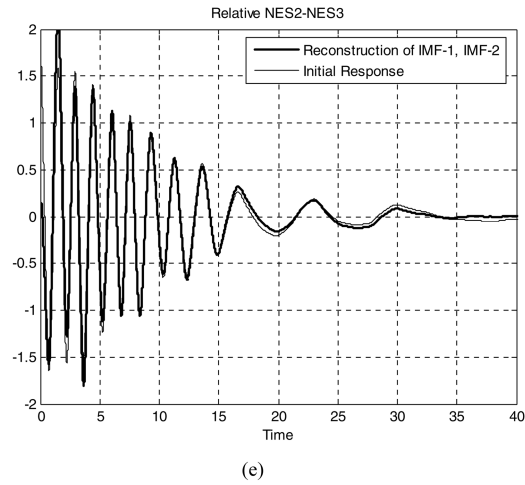
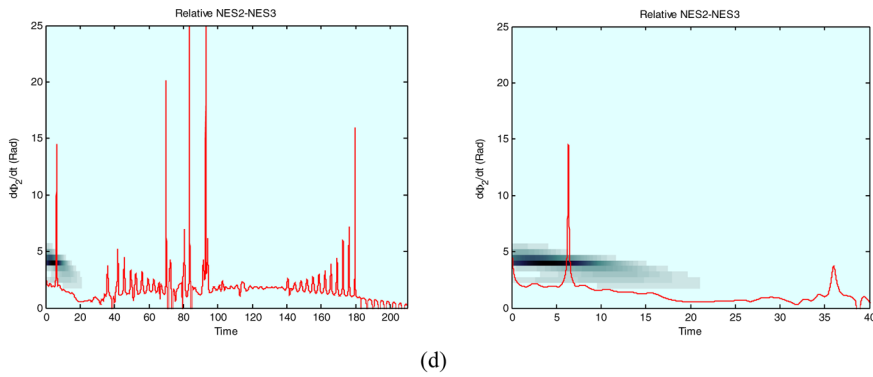
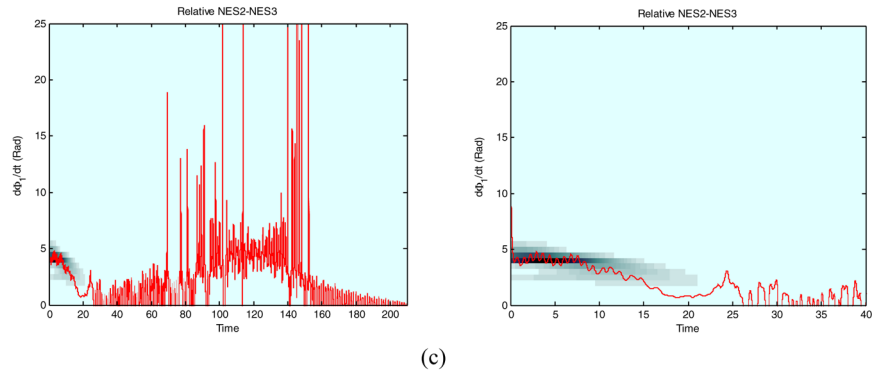
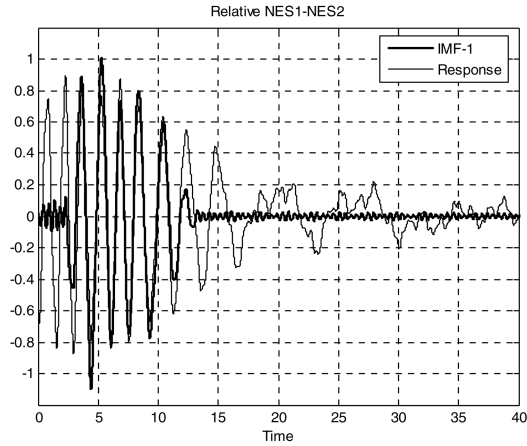
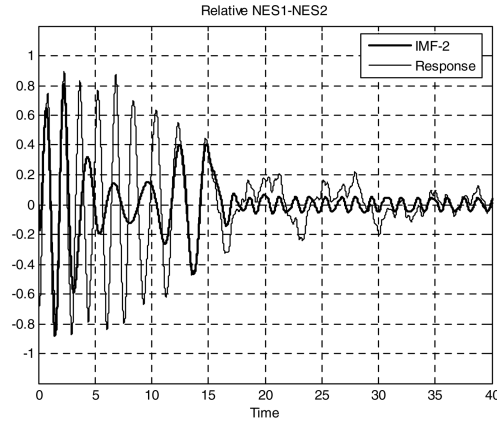


Fig. 5.63 Relative response $[v_2(t) - v_3(t)]$ of System II initiated at point B of the FEP of Figure 5.51 ($\Omega = 4.4$ rad/s: (c, d) instantaneous frequencies of the dominant IMFs superimposed to the WT spectrum of $[v_2(t) - v_3(t)]$ (early time zoomed plots are also included). (e) signal reconstruction of the response using the superposition of the two dominant IMFs.



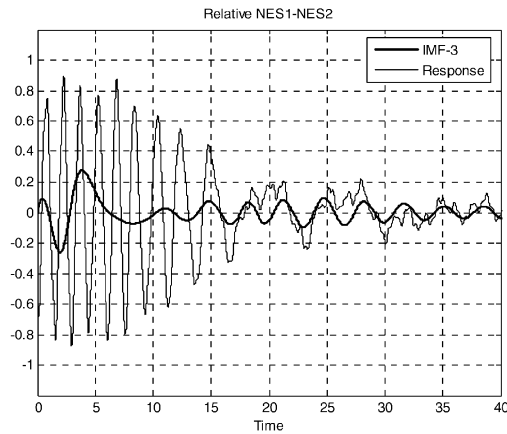
(a)



(b)

Fig. 5.64 Relative response $[v_1(t) - v_2(t)]$ of System II initiated at point B of the FEP of Figure 5.51 ($\Omega = 4.4$ rad/s): (a, b, c) time series of 1st, 2nd and 3rd (dominant) IMFs superimposed to the transient response; (d, e, f) instantaneous frequencies of the dominant IMFs superimposed to the wavelet spectrum of $[v_1(t) - v_2(t)]$ (early time zoomed plots are also included); (g) signal reconstruction of the response using the superposition of the three dominant IMFs.

Compared to the previous numerical simulations of System I (see Figure 5.61), we conclude that in System II there occur stronger nonlinear multi-modal interactions between the rod and the MDOF NES (since it possesses stiffer rod-NES coupling), over higher and broader frequency ranges. This should be expected, since the strong coupling between the rod and the MDOF NES excites higher frequency



(c)

Fig. 5.64 Continued.

modes of the rod, compared to System I, and yields higher frequency nonlinear modal interactions between the rod and the MDOF NES.

We now analyze the numerical simulations of Figure 5.62 of System II by EMD, in our effort to identify the dominant resonance interactions that occur between the rod and the MDOF NES, as well as the time scales (or frequencies) at which these resonance interactions are realized. A more detailed presentation of this analysis, together with the full EMD study of the numerical simulations of Figure 5.61 for System I can be found in Tsakirtzis (2006) and Tsakirtzis et al. (2007a). As in Section 5.2.3 the dominant IMFs of a time series are designated as the IMFs whose instantaneous frequencies coincide with dominant harmonics of the corresponding WT spectrum. Hence, *the EMD is a multi-scale analysis with the potential to identify the ‘essential’ dynamics (resonance interactions) embedded in the measured responses of coupled systems.*

The results of EMD analysis of the transient responses of System II are depicted in Figures 5.63–5.65. The EMD of the relative response provided six IMFs, of $[v_1(t) - v_2(t)]$ eight IMFs, of $[v_1(t) - u(L, t)]$ nine IMFs, and of the rod-end response nine IMFs. As mentioned previously, the IMFs are oscillatory components possessing different time scales (or frequencies) embedded in the time series, and their superposition reconstructs the measured time series. However, since the IMFs are constructed in an *ad hoc* fashion (see Section 2.5), only a subset of IMFs are expected to be *dominant*, i.e., to capture the essential dynamics embedded of the signals. Moreover, the dominant IMFs have usually a physical interpretation in terms of the characteristic time scales of the signal, whereas the ‘artificial’ (unimportant) IMFs represent artificial (non-physical) oscillating modes in the data.

Comparisons of the instantaneous frequencies of the IMFs to the corresponding WT spectra indicates that the relative response $[v_2(t) - v_3(t)]$ is dominated by its

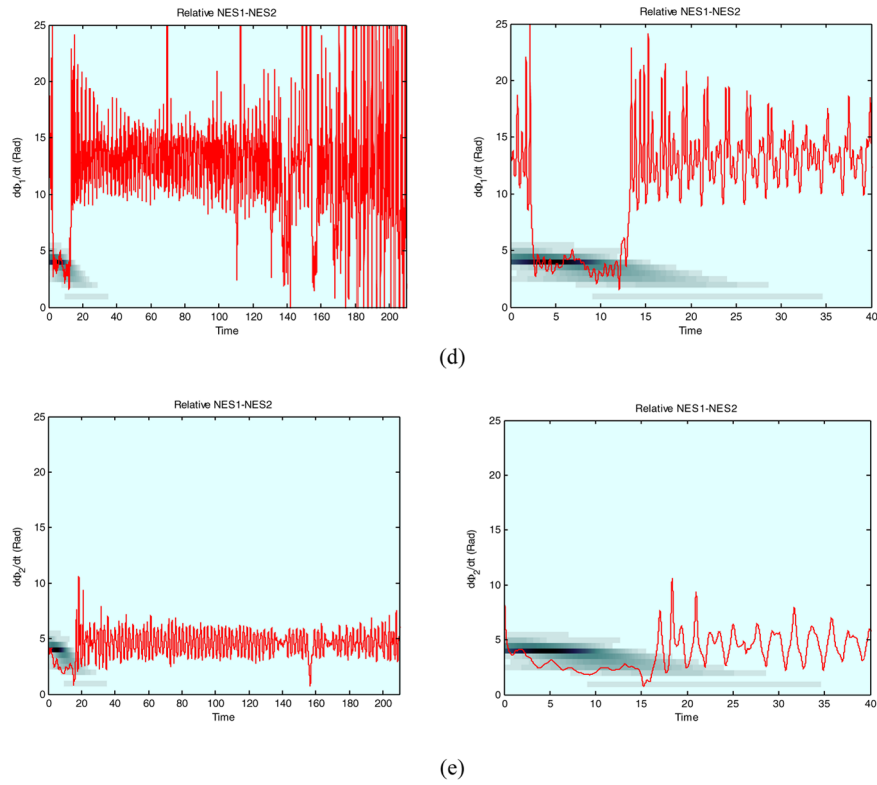
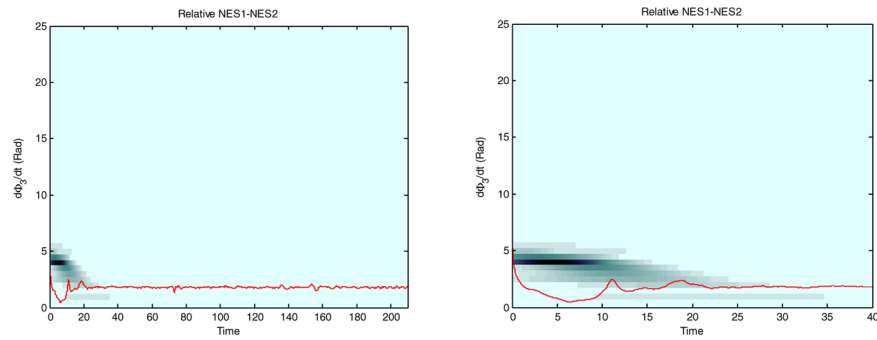


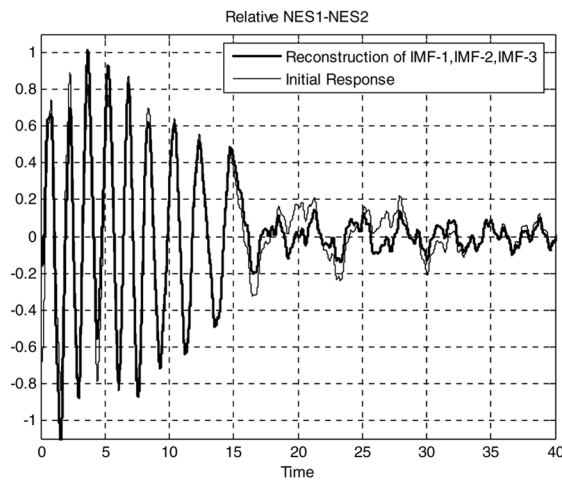
Fig. 5.64 Continued.

1st and 2nd IMFs (see Figures 5.63c, d); the relative response $[v_1(t) - v_2(t)]$ by its 1st, 2nd and 3rd IMFs (see Figures 5.64d–f); and the rod end response $u(L, t)$ by its 1st, 2nd and 3rd IMFs (see Figures 5.65d–f). These results are confirmed by the signal reconstructions depicted in Figures 5.63e, 5.64g and 5.65g which prove that the nonlinear interaction between the rod and MDOF NES is low dimensional, occurring, at most, over four time (frequency) scales.

By studying the instantaneous frequencies of the dominant IMFs of these responses we infer that the damped transitions possess four dominant time scales, corresponding to the 1st, 2nd, 3rd and 5th linearized eigenfrequencies of the rod. Hence, we confirm the results of the previous section, namely, that the MDOF NES engages in nonlinear interactions [or transient resonance captures (TRCs)] with four modes of the rod, so that energy exchanges between the two subsystems occur at four dominant time scales. It is interesting to note that no nonlinear modal interactions between the 4th mode of the rod and the NES were observed, even though the NES does interact with the 3rd and 5th rod modes; this result is in agreement with the WT analysis of the same simulation discussed previously. The specific TRCs that occur between the IMFs of the relative displacements of the NES masses and



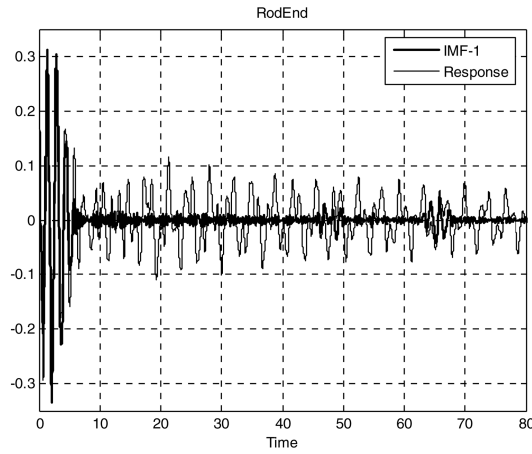
(f)



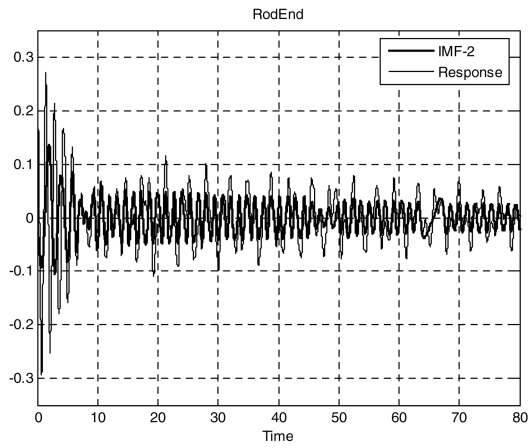
(g)

Fig. 5.64 Continued.

the rod end response can be studied in detail by considering the plots of instantaneous IMF frequencies in Figures 5.63c, d, 5.64d–f and 5.65d–f. A synopsis of these TRCs is given in Table 5.5. The numerous TRCs listed in Table 5.5 provide an indication of the complexity of the broadband nonlinear modal interactions occurring between the rod and the MDOF NES; these TRCs can be clearly detected and systematically categorized by analyzing the corresponding time series by EMD. Judging from the complex nonlinear TRCs occurring between the IMFs of the rod end response and the IMFs of the relative responses of the MDOF NES, we conclude that the increase of the DOF of the NES increases its capacity to resonantly interact with multiple modes of the linear continuum, compared to the SDOF NES



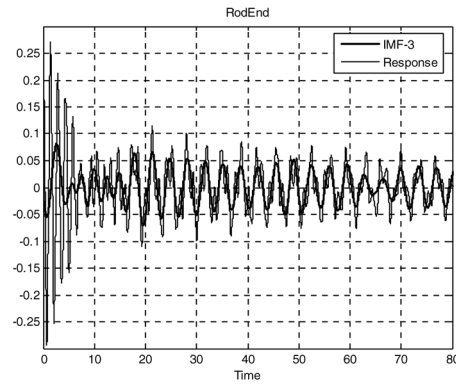
(a)



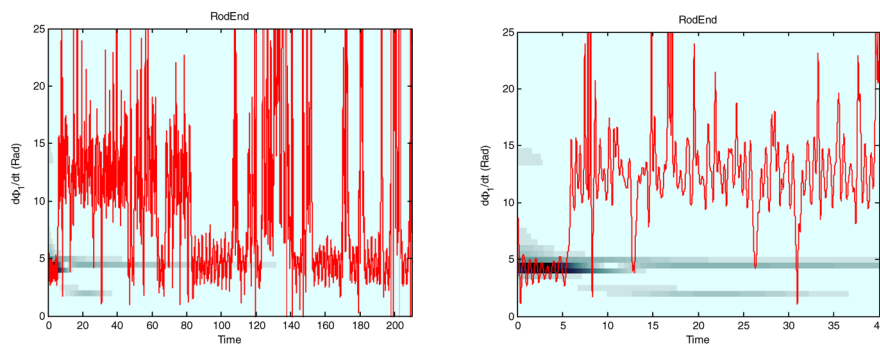
(b)

Fig. 5.65 Rod end response $u(L, t)$ of System II initiated at point B of the FEP of Figure 5.51 ($\Omega = 4.4$ rad/s): (a, b, c) time series of 1st, 2nd and 3rd (dominant) IMFs superimposed to the transient response; (d, e, f) instantaneous frequencies of the dominant IMFs superimposed to the wavelet spectrum of $u(L, t)$ (early time zoomed plots are also included); (g) signal reconstruction of the response using the superposition of the three dominant IMFs.

case. This yields a wider range of modal interactions between the rod and the MDOF NES, and enhanced broadband TET.



(c)



(d)

Fig. 5.65 Continued

5.5 Plate with SDOF and MDOF NESs

In our final study of TET in elastic systems we consider a more complicated system, namely, a thin plate lying on an elastic foundation with SDOF or MDOF NESs attached to it. This study is discussed in more detail in the thesis by Georgiades (2006) and in the paper by Georgiades and Vakakis (2008), so here we will only present a synopsis of the main results. In addition to broadband TET, we study the strongly nonlinear modal interactions in the damped dynamics by employing the combined WT-EMD post-processing technique outlined previously. The following NES configurations will be considered in this section: (i) a single ungrounded, essentially nonlinear SDOF NES; (ii) a set of two SDOF NESs attached at different points of the plate; and (iii) a single MDOF NES with multiple essential stiffness nonlinearities. We will examine in detail the underlying dynamical mechanisms governing

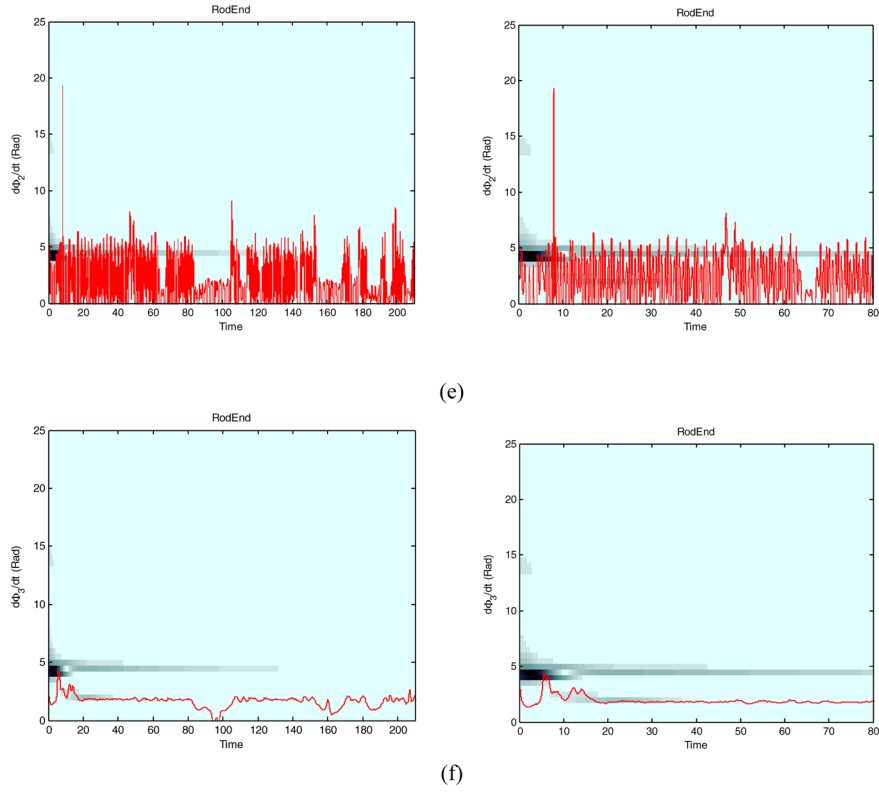


Fig. 5.65 Continued

TET in these cases by detecting the dominant TRCs that occur between the plate modes and the NESs. Moreover, we will perform comparative studies of the performance of the three considered NES configurations to the case of single or multiple linear Tuned-Mass-Dampers (TMDs).

The plate on the linear elastic foundation is depicted in Figure 5.66. It consists of a linear isotropic elastic plate with mass distribution per unit area equal to M , width W , length L , thickness h , and distributed proportional viscous damping per unit area equal to d . The plate is clamped on one edge only, with all other edges remaining traction-free, and is resting on a distributed elastic foundation with stiffness per unit area equal to k . The plate is assumed to be sufficiently thin, so that to a first approximation its shear deformation may be neglected (the so-called Kirchhoff assumptions).

Hence, the governing partial differential equation of motion and the associated boundary conditions are given by (assuming that the plate is initially at rest)

$$D\nabla^4 w + M \frac{\partial^2 w}{\partial t^2} + d \frac{\partial w}{\partial t} + kw = F(t)\delta(x - b_x, y - b_y)$$

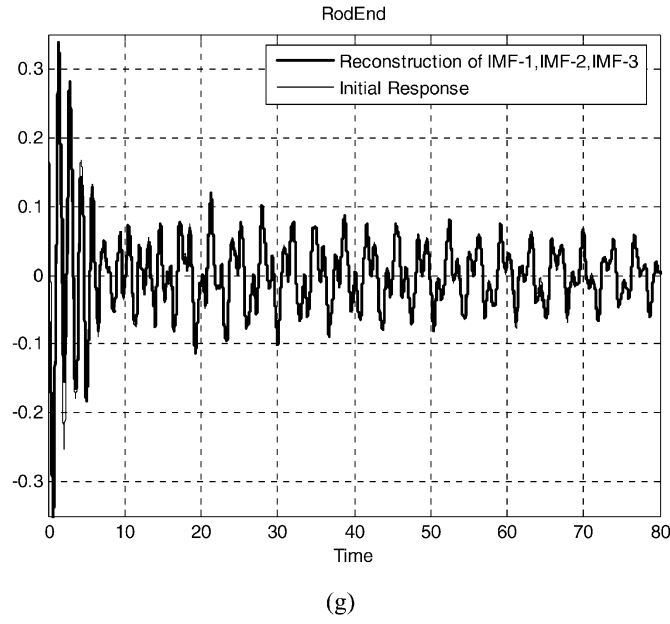


Fig. 5.65 Continued

$$\begin{aligned}
 w(x, 0, t) = 0, \quad \frac{\partial w(x, 0, t)}{\partial x} = 0, \quad w(x, y, 0) = 0, \quad \frac{\partial w(x, y, 0)}{\partial t} = 0 \\
 M_y(0, y) = M_y(W, y) = M_y(x, L) = 0 \\
 Q_y(0, y) = Q_y(W, y) = Q_y(x, L) = 0
 \end{aligned} \tag{5.89}$$

where $F(t)$ is the applied external excitation, $\delta(\cdot, \cdot)$ is Dirac's generalized function, and the differential operator ∇ applies to both x and y directions. In (5.89) the variables $M_y(\cdot, \cdot)$ and $Q_y(\cdot, \cdot)$ denote the internal bending moments about the y -axis and the shear forces along the y -axis of the plate, respectively (see Figure 5.66). Moreover, the flexibility D in the equation of the plate is defined as

$$D = \frac{Eh^3}{12(1 - \nu^2)}$$

where E is the modulus of elasticity and ν Poisson's ratio for the material of the plate (Leissa, 1993). The problem (5.89) is non-dimensionalized, with the following numerical values assigned for the plate parameters:

$$W = L = 1, \quad h = 0.01, \quad M = 1, \quad D = 1, \quad \nu = 0.3, \quad k = 100 \tag{5.90}$$

which are in accordance to the assumptions of thin plate theory; in the following simulations the damping coefficient is assigned the value $d = 10$ for the case of a

Table 5.5 Main TRCs and multimodal interactions in the transient responses of System II (see Figures 5.63–5.65).

Response	Dominant IMF No.	Time Window and Frequency of Nonlinear Interaction	TRCs
<i>Relative displacement</i> $v_1(t) - u(L, t)$	1	$0 < t < 8$ (13.9 rad/sec)	TRC with 5 th mode of Rod
		$2 < t < 7$ (4.7 rad/s)	TRC with 2 nd mode of Rod
	2	$15 < t < 36$ (7.9 rad/s)	TRC with 3 rd mode of Rod
		$40.5 < t < 48.5$ (7.9 rad/s)	TRC with 3 rd mode of Rod
		$81.5 < t < 89$ (7.9 rad/s)	TRC with 3 rd mode of Rod
		$97 < t < 103$ (7.9 rad/s)	TRC with 3 rd mode of Rod
	3	$43 < t < 92$ (4.8 rad/s)	TRC with 2 nd mode of Rod
		$136 < t < 156$ (4.8 rad/s)	TRC with 2 nd mode of Rod
	4	$95 < t < 112$ (4.8 rad/s)	TRC with 2 nd mode of Rod
		$147 < t < 164$ (4.8 rad/s)	TRC with 2 nd mode of Rod
	5	$110 < t < 135$ (1.8 rad/s)	TRC with 1 st mode of Rod
		$146 < t < 153$ (1.8 rad/s)	TRC with 1 st mode of Rod
<i>Relative displacement</i> $v_1(t) - v_2(t)$	1	$30 < t < 110$ (14 rad/s)	TRC with 5 th mode of Rod
	2	$20 < t < 210$ (4.81 rad/s)	TRC with 2 nd mode of Rod
	3	$21 < t < 210$ (1.86 rad/s)	TRC with 1 st mode of Rod
<i>Relative displacement</i> $v_2(t) - v_3(t)$	1	$0 < t < 8$ (4.8 rad/s)	TRC with 2 nd mode of Rod
		$105 < t < 140$ (4.8 rad/s)	TRC with 2 nd mode of Rod
	2	$40 < t < 67$ (1.86 rad/s)	TRC with 1 st mode of Rod
		$90 < t < 170$ (1.86 rad/s)	TRC with 1 st mode of Rod

single force (shock) applied to the plate, and $d = 15$ for the case of multiple forces applied to the plate.

We assume that at $t = 0$ a single or multiple transient forces (shocks) are applied to the plate. Each shock has the form of a half sine pulse:

$$F(t) = \begin{cases} A \sin(2\pi t/T), & 0 \leq t \leq T/2 \\ 0, & t > T/2 \end{cases} \quad (5.91)$$

In the case of a single applied shock, its position on the plate is given by, $(b_x, b_y) = (1, 1)$; whereas, in the case of multiple applied shocks, their positions on the plate are given by $(b_{x1}, b_{y1}) = (0.6, 0.5)$ (for shock 1), $(b_{x2}, b_{y2}) = (0.5, 0.5)$ (for shock 2) and $(b_{x3}, b_{y3}) = (0.4, 0.5)$ (for shock 3). Unless otherwise stated, in single shock simulations the shock amplitude is taken as $A = 100$ and its period as $T = 0.1T_5$ where T_5 is the period of the fifth mode of the linear plate no attachment. This requirement ensures that the applied shock has sufficiently small duration to directly excite at least the leading five modes of the plate; this enables us to study the capacity of the NES(s) to passively absorb broadband vibration energy from multiple plate modes. In multiple shock simulations, the shock amplitudes are taken as $A_1 = 25$, $A_2 = -100$ and $A_3 = 25$, and the shocks are assumed to possess a common period equal to $T = 0.1T_5$.

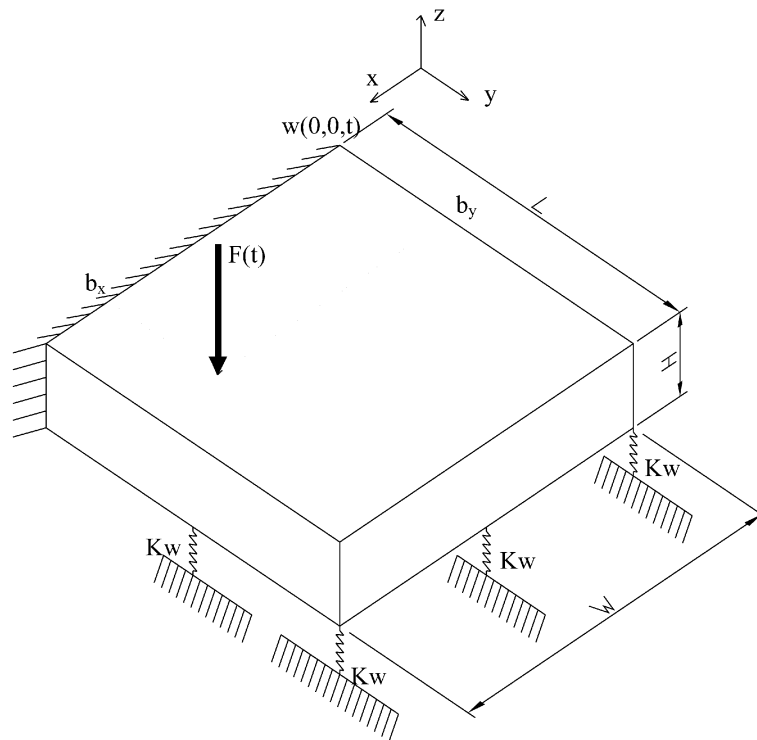
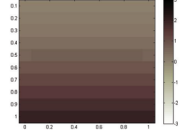
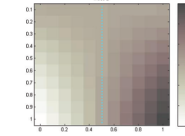
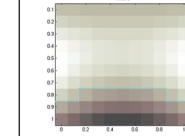
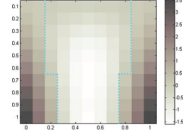
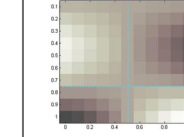


Fig. 5.66 Linear cantilever plate on elastic foundation.

The partial differential equation in (5.89) was discretized using 4-node quadrilateral elements, and non-conforming shape functions with corner nodes (with 12 degrees of freedom) (Zienkiewicz and Taylor, 2000; Liu and Quek, 2003). In each node, the transverse displacement s and the rotations about the x - and y -axes were considered. For this specific finite element, the explicit forms of the matrix of shape functions was derived by Melosh (1963), and expressed simply in terms of local normalized coordinates at each node. The FE discretization is described in detail in the thesis by Georgiades (2006), based on the energy approach, i.e., on the estimation of the energies of a single finite element from Kirchoff's plate theory and based on this estimate on the derivation of the corresponding FE mass matrices and FE displacements. Using a connection matrix that indicates which nodes correspond to adjacent elements, the full structural matrices of the plate were constructed (Georgiades, 2006). Then, the discrete system was solved numerically using the Newmark Algorithm [for details, see (Geradin and Rixen, 1997)]. In Table 5.6 the leading natural frequencies and corresponding mode shapes of the unforced and undamped plate estimated using the FE simulation, are presented. A sensitivity analysis was performed to find the required number of discrete elements for convergence of the

Table 5.6 FE computation of the leading modes of the plate on elastic foundation ($k = 100$) with no NES attached.

Mode No.	1	2	3
Eigenfrequency (Hz)	1.685	2.090	3.750
Eigenshapes- Nodal Lines (.....)			

Mode No.	4	5
Eigenfrequency (Hz)	4.607	5.179
Eigenshapes- Nodal Lines (.....)		

results; it was determined that a total of 10×10 elements (10 in each direction) were sufficient for accurate transient numerical simulations. The verification of the accuracy of the natural frequencies was performed for the case of the plate with no elastic foundation ($k = 0$) using a model in ANSYS[®], and, also by comparing with the results reported in Leissa (1993).

We now assume that a single ungrounded NES is attached at position $(x, y) = (d_x, d_y)$ of the plate. The NES is assumed to be lightweight – of mass $\varepsilon \ll 1$ – and to possess an essentially nonlinear (nonlinearizable) cubic stiffness with characteristic C , in parallel to a viscous damper λ . With the addition of the NES the modified equations of motion together with the boundary and initial conditions take the form:

$$\begin{aligned}
& D\nabla^4 w + M \frac{\partial^2 w}{\partial t^2} + d \frac{\partial w}{\partial t} + kw \\
& + \{C[w(d_x, d_y) - v(t)]^3 + \lambda[\dot{w}(d_x, d_y) - \dot{v}(t)]\} \delta(x - d_x, y - d_y) \\
& = F(t) \delta(x - b_x, y - b_y) \\
& \varepsilon \ddot{v}(t) + C[v(t) - w(d_x, d_y)]^3 + \lambda[\dot{v}(t) - \dot{w}(d_x, d_y)] = 0 \\
& w(x, 0, t) = 0, \quad \frac{\partial w(x, 0, t)}{\partial x} = 0 \\
& M_y(0, y) = M_y(W, y) = M_y(x, L) = 0 \\
& Q_y(0, y) = Q_y(W, y) = Q_y(x, L) = 0
\end{aligned}$$

$$w(x, y, 0) = 0, \quad \frac{\partial w(x, y, 0)}{\partial t} = 0, \quad v(0) = 0, \quad \dot{v}(0) = 0 \quad (5.92)$$

The dynamics of the NES is incorporated into the discretized FE equations of motion by expanding accordingly the system matrices, and adding a nonlinear stiffness component (due to the essential cubic nonlinearity) (Georgiades, 2006).

The TET capacity of the NES is studied by estimating the following energy dissipation measure (EDM):

$$E_{\text{NES}}(t) = \frac{\lambda \int_0^t [\dot{w}(d_x, d_y, \tau) - \dot{v}(\tau)]^2 d\tau}{\int_0^t F(\tau) \dot{w}(b_x, b_y, \tau) d\tau} \times 100 \quad (5.93)$$

This represents the percentage of shock energy of the plate dissipated by the damper of the NES up to time t . It is clear that with increasing time the EDM reaches an asymptotic limit, $E_{\text{NES}, t \gg 1} = \lim_{t \gg 1} E_{\text{NES}}(t)$, which represents the portion of the shock energy of the plate that is *eventually* dissipated by the NES by the end of the oscillation. The percentage of input shock energy dissipated by the distributed viscous damping of the plate up to time instant t is computed by:

$$E_{\text{plate}}(t) = \frac{\frac{1}{2} \int_0^L \int_0^W \int_0^t d \left[\frac{\partial w(x, \tau)}{\partial t} \right]^2 d\tau dx dy}{\int_0^t F(\tau) \dot{w}(b_x, b_y, \tau) d\tau} \times 100 \quad (5.94)$$

Combining (5.93) and (5.94), the percentage of input shock energy dissipated by the plate-NES system up to time instant t is computed as follows:

$$E_{\text{total}}(t) = E_{\text{NES}}(t) + E_{\text{plate}}(t) \quad (5.95)$$

Similar formulations hold when multiple SDOF NESs, MDOF NESs or linear tuned mass dampers (TDMs) are attached to the plate. We only mention that for the case of single MDOF NES attached to the plate the equations of motion are given by:

$$\begin{aligned} D\nabla^4 w + M \frac{\partial^2 w}{\partial t^2} + d \frac{\partial w}{\partial t} + kw \\ + \{C_0[w(d_x, d_y) - v(t)]\} \delta(x - d_x, y - d_y) = F(t) \delta(x - b_x, y - b_y) \\ m_1 \ddot{v}(t) + C_0[v(t) - w(d_x, d_y)] + \lambda[\dot{v}(t) - \dot{u}(t)] + C_1[v(t) - u(t)]^3 = 0 \\ m_2 \ddot{u}(t) + \lambda[\dot{u}(t) - \dot{v}(t)] + C_1[u(t) - v(t)]^3 \\ + \lambda[\dot{u}(t) - \dot{s}(t)] + C_2[u(t) - s(t)]^3 = 0 \\ m_3 \ddot{s}(t) + \lambda[\dot{s}(t) - \dot{u}(t)] + C_2[s(t) - u(t)]^3 = 0 \end{aligned}$$

$$\begin{aligned}
w(x, 0, t) &= 0, & \frac{\partial w(x, 0, t)}{\partial x} &= 0 \\
M_y(0, y) &= M_y(W, y) = M_y(x, L) = 0 \\
Q_y(0, y) &= Q_y(W, y) = Q_y(x, L) = 0 \\
w(x, y, 0) &= 0, & \frac{\partial w(x, y, 0)}{\partial t} &= 0 \\
v(0) &= 0, & \dot{v}(0) &= 0, & u(0) &= 0, & \dot{u}(0) &= 0, & s(0) &= 0, & \dot{s}(0) &= 0 \quad (5.96)
\end{aligned}$$

Details of the FE formulation and the corresponding structural matrices of the integrated system can be found in Georgiades (2006). The effectiveness of the NES to passively absorb and locally dissipate the shock energy of the plate (i.e., the TET efficiency) is studied by computing the following energy dissipation measures (EMDs):

$$\begin{aligned}
E_{\text{NES } 1}(t) &= \frac{\lambda \int_0^t [\dot{u}(\tau) - \dot{v}(\tau)]^2 d\tau}{\int_0^t F(\tau) \dot{w}(b_x, b_y, \tau) d\tau} \times 100 \\
E_{\text{NES } 2}(t) &= \frac{\lambda \int_0^t [\dot{s}(\tau) - \dot{u}(\tau)]^2 d\tau}{\int_0^t F(\tau) \dot{w}(b_x, b_y, \tau) d\tau} \times 100 \quad (5.97)
\end{aligned}$$

i.e., the percentage of shock energy dissipated by each of the two dampers of the MDOF NES up to time t . The summation of these two EMDs provides a measure of the TET efficiency of the MDOF NES. It should be clear that the two EMDs reach definite asymptotic limits $E_{\text{NES } 1,2,t \gg 1} = \lim_{t \gg 1} E_{\text{NES } 1,2}(t)$ as time progresses.

The results of the simulations are post-processed using numerical WTs and EMD. In addition, we examine the portion of shock energy dissipated by each of the two subsystems, i.e., the plate and the NES(s); moreover, in certain simulations we examine the energy transaction measure (ETM) E_{Trans} , as defined by relation (5.26) in Section 5.2.1. The ETM is an important energy measure from a physics point of view, since it helps us identify inflow or outflow of energy from the plate to the NES or vice versa; in particular, when there is inflow from the plate to the NES it holds that $E_{\text{Trans}} > 0$, whereas, negative values of the ETM correspond to backscattering of energy from the NES to the plate. We recall that the ratio $E_{\text{Trans}}/\Delta t$ where Δt tends to zero represents the power flow from the plate to the attachment and vice versa.

In the following sections all simulations are performed for a sufficiently long time window so that at least 96.5% of the energy of the system is been eventually dissipated by damping. This ensures that no essential dynamics is missed in the transient simulations due to insufficient time of numerical integration. All sets of simulations with SDOF nonlinear attachments are performed with using a $(10 \times$

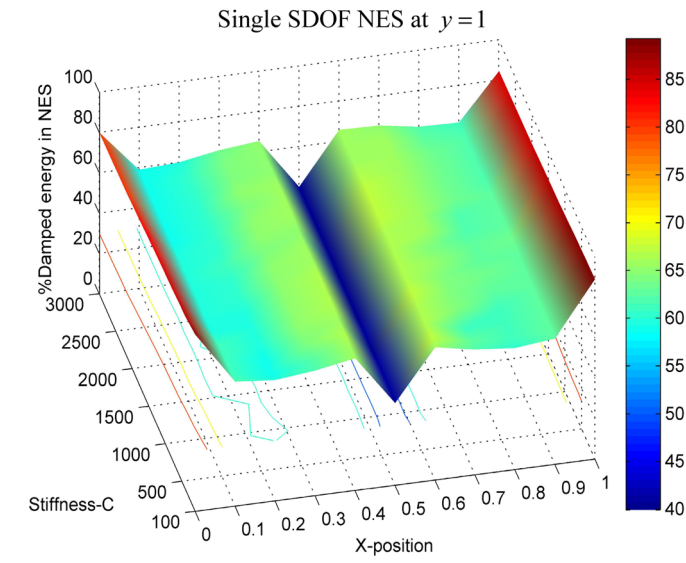
10) FE mesh for the plate. To better depict the results we divide the plate into ‘y-slices’ corresponding to fixed values of y . The parametric studies of the plate with an attached MDOF NES are performed with the NES located at all x -positions on three ‘y-slices’, namely, $y = 1.0, 0.7$ and 0.3 , again using a (10×10) FE mesh.

5.5.1 Case of a SDOF NES

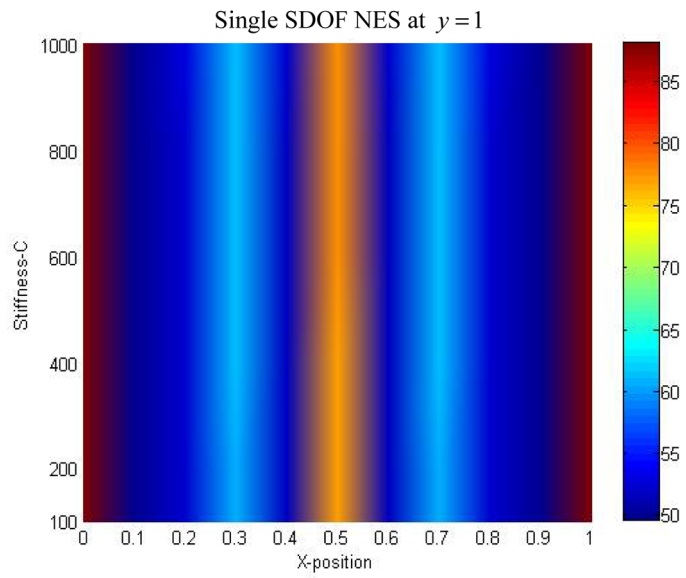
In the first parametric study we examine TET in a plate forced by single or multiple shocks, possessing a single SDOF NES attachment. We perform four main sets of FE simulations, and examine the influence of the variation of the NES parameters and input energy on TET from the plate to the NES, using as criterion the portion of total energy eventually dissipated by the NES, $E_{\text{NES}, t \gg 1} = \lim_{t \gg 1} E_{\text{NES}}(t)$. Unless otherwise stated, the mass of the NES is taken as $\varepsilon = 0.05$, the nonlinear stiffness characteristic as $C = 10^3$, and the damping coefficient as $\lambda = 0.1$.

In the first set of simulations we examined the influence of the nonlinear stiffness coefficient C and the NES position on TET. In Figure 5.67 we depict the asymptotic limit of EDM $E_{\text{NES}, t \gg 1}$, as function of C and the x -position of the NES on the ‘slice’ $y = 1$. In Figure 5.67a (corresponding to C in the range $[100, 3000]$) we depict the results for single shock excitation, whereas in Figure 5.67b (with $C \in [100, 1000]$) we depict the corresponding results for multi-shock excitation; for the simulations depicted in Figure 5.67b the mass of NES is fixed to the smaller value $\varepsilon = 0.005$.

We conclude that for a fixed x -position of the NES, TET is robust in variations of C when C is in the range $O(10^2) - O(10^3)$. Moreover, the variation of the x -position of the NES on a fixed ‘y-slice’ affects strongly TET; this sensitivity can be explained by the fact that certain locations of the NES may be close to nodal curves of the different modes of the plate, where the capacity of the NES to passively absorb and dissipate energy from these particular modes is hindered. This becomes clear when we depict TET efficiency as function of the position of the NES for fixed values of C (see Figure 5.68). The maximum efficiency of the NES occurs when it is positioned at the corners of the plate, with maximum values of the EDM $E_{\text{NES}, t \gg 1}$ reaching levels of 87.72% and 89.28%, for NES positions $(x, y) = (0, 1)$ and $(1, 1)$, respectively. The interpretation of the results depicted in Figure 5.68 (corresponding to single shock excitation) must be performed in conjunction with the results of Table 5.6, which depicts the nodal curves of the five leading modes of the linear cantilever plate (with no NES attached). The strips close to the ‘y-slices’ $y = 0.8$ and $y = 0.9$ are close to the free edge of the plate and the nodal lines of the 3rd and 5th plate modes; as a result, the NES efficiency is low in these regions. Similarly, in strips close to $x = 0.2, 0.3, 0.7$ and 0.8 , the NES efficiency is relatively low (of the order of 40%); again, this can be interpreted by the fact that these strips are in neighborhoods of nodal curves of the 4th mode of the plate. Finally, there is a strip in the middle of the plate, $x = 0.5$, where the lowest value of TET is noted; this is due to the fact that this region is in the neighborhood of nodes of the 2nd



(a)



(b)

Fig. 5.67 Parametric study of TET as function of NES stiffness C , and x -position on the plate for the 'y-slice' $y = 1$: (a) single shock excitation with NES mass, and (b) multiple shock excitation.

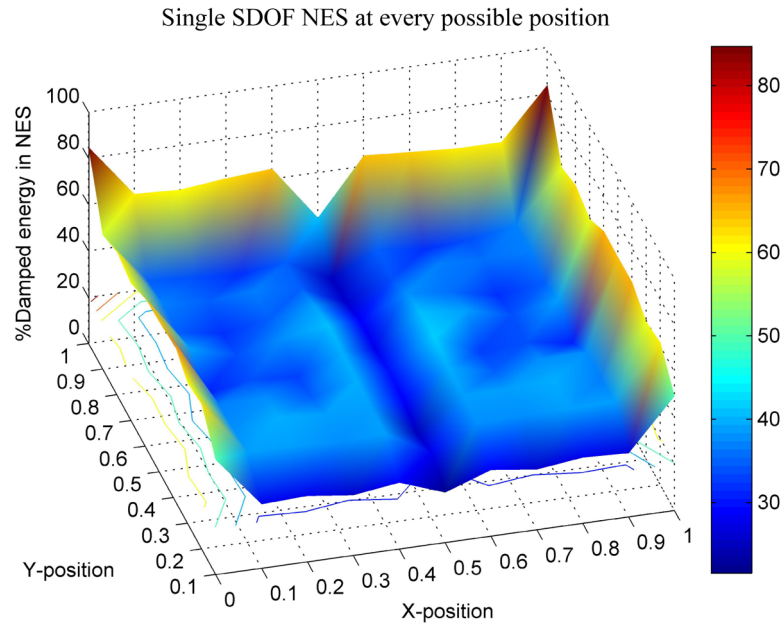


Fig. 5.68 Parametric study for TET efficiency as function of NES position on the plate for $C = 10^3$ and NES mass $\varepsilon = 0.005$; the clamped edge is at $y = 0$.

and 5th modes of the plate. Moreover, as depicted in Figure 5.68 the efficiency of the NES decreases when the NES is located closer to the clamped end where the displacements of the plate are reduced and the nonlinear effects are negligible.

In the second set of numerical simulations, we consider single shock excitation and examine the influence of the damping coefficient λ on TET, with the NES attached at every possible position on the plate. In Figure 5.69 we depict the asymptotic EDM $E_{NES, t \gg 1}$, as function of the NES damping coefficient λ in the range $\lambda \in [0.01, 0.5]$, and the x -position of the NES for a representative ‘y-slice’, $y = 1$. We note a deterioration of NES efficiency with decreasing damping coefficient. This trend, however, does not necessarily mean that by indefinitely increasing NES damping we will achieve continuous enhancement of NES efficiency. Indeed, for sufficiently large values of NES damping the *relative motion* between the NES and the plate is expected to significantly decrease (as the connection between the plate and the NES becomes more rigid); this, in turn, will result to decrease of the relative motion across the damper of the NES, and, hence, to the deterioration of the capacity of the NES damper to dissipate shock energy.

In the final set of simulations of this series, we examine the influence of the input energy and the nonlinear stiffness characteristic on TET, when the NES is located at position $(x, y) = (0, 1)$. We assume that a single shock is applied to the plate, and examine shock amplitudes in the range $A \in [0.001, 100]$. In Figure 5.70 we depict the results of this parametric study. We note the strong dependence of TET

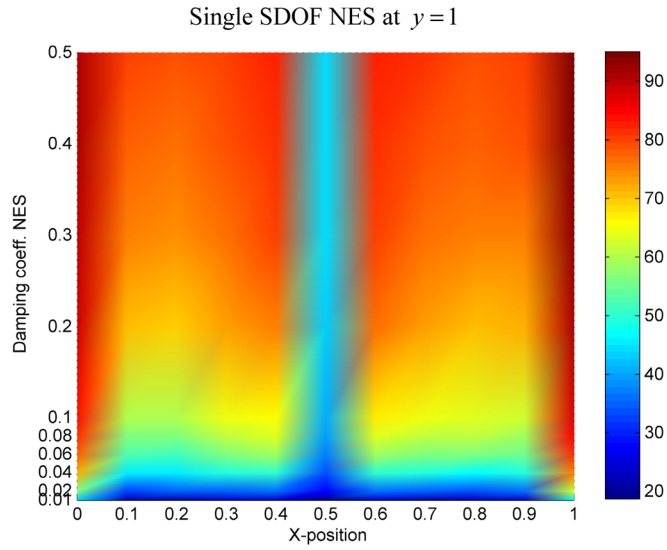


Fig. 5.69 Parametric study of TET as function of the damping coefficient λ and the x -position of the NES on the plate, for fixed $y = 1$.

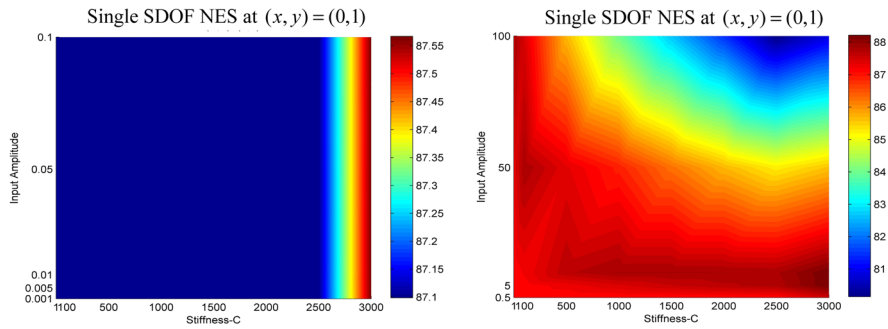


Fig. 5.70 Parametric study of TET as a function of the shock magnitude (input energy) and stiffness C , for NES position at $(x, y) = (0, 1)$.

efficiency on the magnitude of the shock: for low shock magnitudes and irrespective of the values of C TET is of the order of 87%; however, for increasing shock magnitudes and nonlinear stiffness characteristics, TET efficiency decreases within a small range, of the order of 7%.

A conclusion from this first parametric study is that strong TET can be realized from the plate to a SDOF NES, especially when the NES is located at points of the plate corresponding to antinodes of energetically high plate modes. Indeed, it is possible to passively transfer from the plate and locally dissipate at the NES as much as 87% of the shock energy of the plate. Moreover, the integrated plate-NES system can be designed for robust TET.

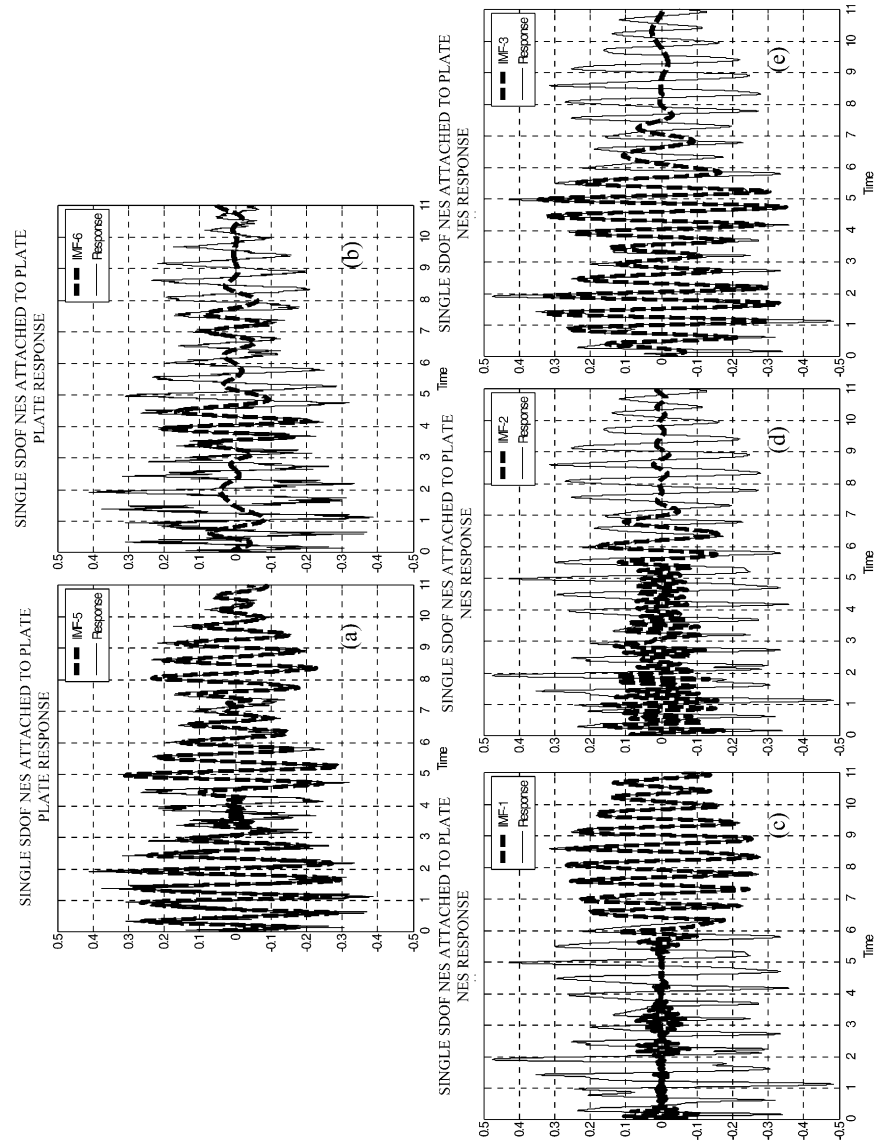


Fig. 5.71 Dominant IMFs of the response of the SDOF NES and of the plate at the point of attachment, superimposed to the corresponding time series.

To study in more detail the nonlinear modal interactions that give rise to TET in the plate-SDOF NES system, we isolate a specific case corresponding to a plate with parameters as specified previously, and the SDOF NES attached at $(x, y) = (0, 0.5)$, with parameters $C = 3 \times 10^3$, $\lambda = 0.1$ and $\varepsilon = 0.05$. We assume that there is a single applied shock in the form of a half-sine applied at $(x, y) = (1, 1)$, i.e., at one of the free corners of the plate. In this specific case 64.35% of the shock energy of the plate gets eventually transferred to and locally dissipated by the NES. We examine the transient nonlinear resonance interactions (TRCs) occurring between the plate response at the point of attachment to the NES, and the NES response, and focus mainly in the highly energetic, early stage of the response where the nonlinear effects are expected to be more profound. Specifically we wish to analyze nonlinear modal interactions and TRCs in the dynamics in the early time interval $0 < t < 5$, where more than 75% of the shock energy is been dissipated. Following the post-processing methodology outlined in previous sections, the damped responses of the plate and the NES are analyzed by numerical WTs and then decomposed in terms of Intrinsic Mode Functions (IMFs) using EMD (Georgiades, 2006). By superimposing the instantaneous frequencies of the IMFs to the corresponding WT spectra of the transient responses we can deduce the dominant IMFs of the responses, as depicted in Figures 5.71a–e. Following our post-processing methodology, the determination of the dominant IMFs of the plate and NES responses enables us to detect the dominant TRCs that govern TET in this case.

Considering the plate response, the 5th and 6th IMFs are dominant (see Figures 5.72a, b), whereas the 1st, 2nd and 3rd IMF of the NES response are also dominant (see Figures 5.72c–e). By computing the ratios of the instantaneous frequencies of the dominant IMFs of the plate and the NES responses we can identify the possible types of $k:m$ TRCs that occur in the transient dynamics, as well as, the corresponding time intervals where these TRCs occur. Considering the instantaneous frequency plots depicted in Figure 5.72 we deduce 1:1 TRCs between (a) the 5th IMF of the plate and the 3rd IMF of the NES at frequency close to 1.9 Hz in the time interval $0.25 < t < 3.25$ (TRC I); (b) the 5th IMF of the plate and the 1st IMF of the NES close to 1.9 Hz in the time interval $6 < t < 12$ (TRC II); and (c) the 6th IMF of the plate and the 2nd IMF of the NES close to 1.9 Hz in the time interval $8 < t < 14$ (TRC III). These TRCs are responsible for passive TET in this specific case, and this post-processing analysis enables us to identify the corresponding nonlinear resonance interactions between the embedded oscillatory modes in the plate and NES responses.

5.5.2 Case of Multiple SDOF NESs

The parametric study of TET efficiency in terms of NES location carried out in the previous section revealed locations where TET is weak, and alternative locations where TET is strong (with corresponding asymptotic EDM of the order of more than 70%). The computational study carried out in this section aims to investigate possi-

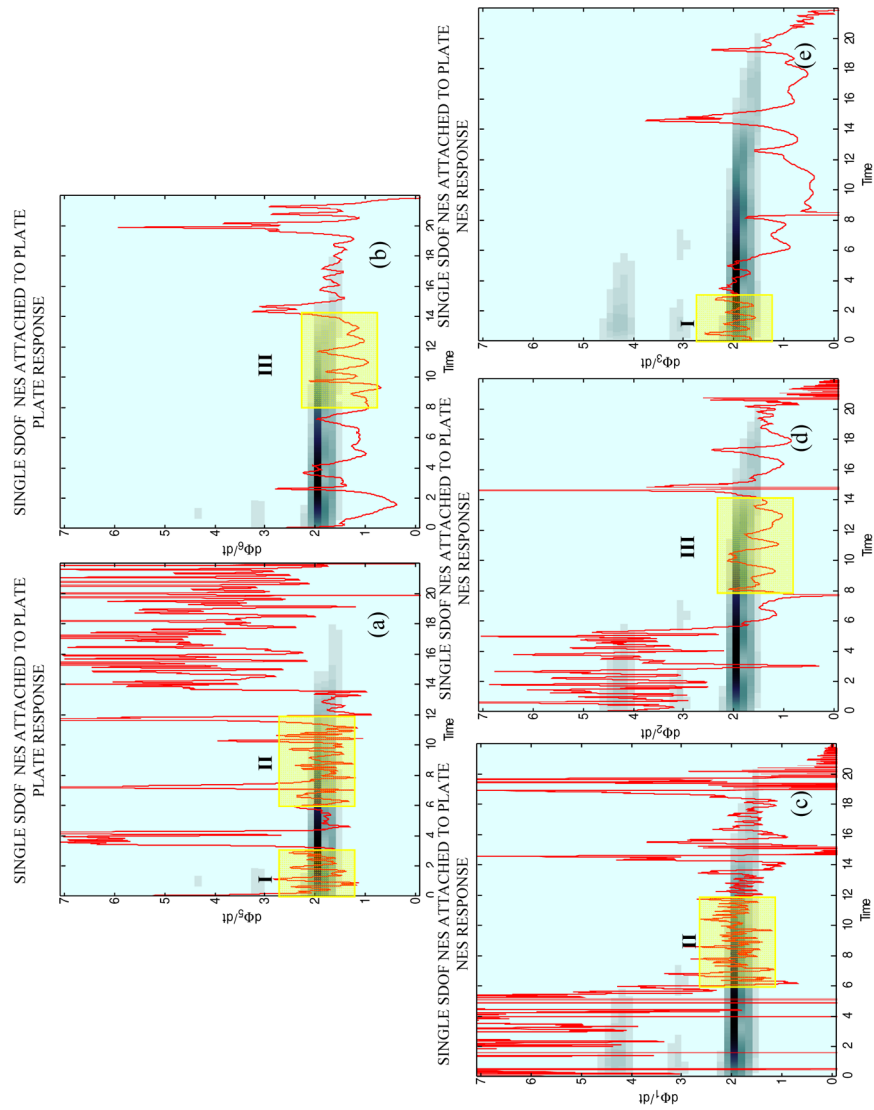


Fig. 5.72 Instantaneous frequencies of the dominant IMFs superimposed to the WT spectra of the corresponding responses: (a, b) 6th and 7th IMF of the plate response; (c, d, e, f) 1st, 2nd, 3rd and 4th IMF of the SDOF NES response; dominant 1:1 TRCs between IMFs are indicated by I, II and III.

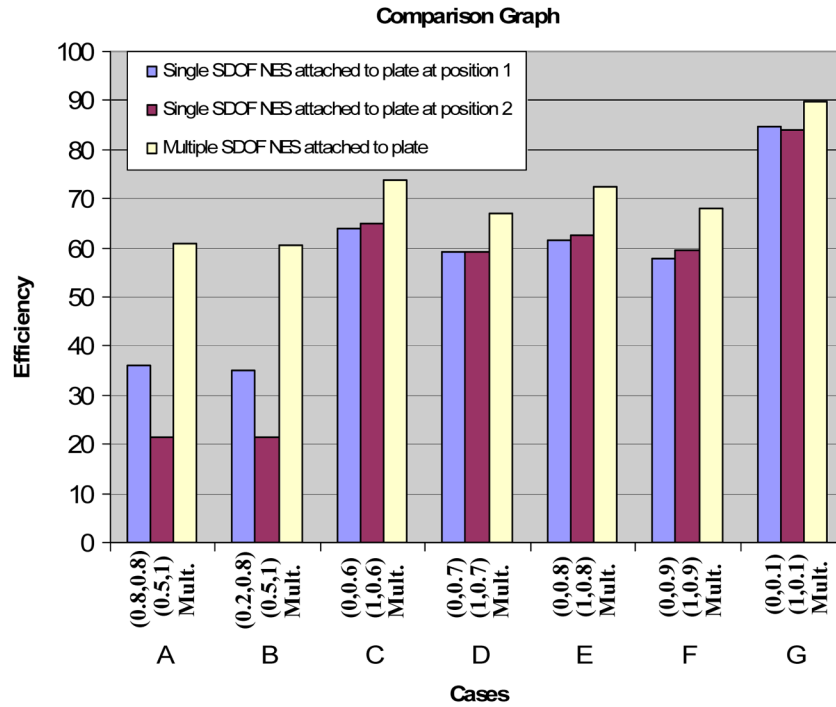


Fig. 5.73 Comparative study of TET efficiency when using two single NESs, and a set of two NESs; single shock excitation is considered.

ble enhancement of TET through the use of multiple SDOF NESs. The parameters used for the plate and the applied shock in the following numerical simulations are identical to those employed in the simulations of Section 5.5.1. In this case, however, we consider two SDOF NES attached to the plate, with each NES possessing mass $\varepsilon = 0.005$ (i.e., 0.5% of the total mass of the plate), stiffness $C = 10^3$, and damping coefficient $\lambda = 0.1$. A single shock excitation is applied to the plate, of the same form and position as in the previous section.

In the following numerical simulations we examine seven specific cases (designated as Cases A–G) where two SDOF NESs are located at various positions on the plate. Of specific interest are cases where the NESs are located at nodal curves of plate modes. In Figure 5.73 we depict a bar diagram depicting NES efficiencies for all seven cases considered. In that diagram we compare the efficiencies of single NESs attached separately to either one of the two locations occupied by the set of two NESs, to the efficiency of the set of two NESs when they are both simultaneously attached to the plate. In each case we indicate the position of the two NESs. For case A TET corresponding to attaching separately the two NESs is 36.13% and 21.58%, respectively, but this number increases to 61.02% when both NESs are attached simultaneously to the same locations; we note that the later number exceeds

the sum of the previous two, i.e., the synergetic TET achieved by the set of two NESs is enhanced compared to the sum of TETs when each of the two NESs is applied separately. This demonstrates a positive synergy effect of the set of two NESs, which, however, is not expected to persist in the other cases where NES locations more favourable to TET are considered.

In case B, the first NES is located at position $(x, y) = (0.2, 0.8)$, which is a crossing point of the nodal curves of the 3rd and 4th plate modes, and the second NES at $(x, y) = (0.5, 1.0)$, which is the location corresponding to weakest TET when a single NES is used. Again, in this case synergetic TET for the set of two NESs increases significantly to 60.4%, which exceeds the sum of the individual TETs achieved when the NESs are applied separately at the same locations. Hence, TET is again improved by positive synergy of the set of NESs in this case.

To further investigate synergetic NES effects on TET, in cases C, D, E and F we consider the set of NESs at positions on the plate where high individual TETs are achieved for a single SDOF NES (between 60–70% – such locations are at the edges of the plate, $x = 0, 1$). For cases C, D, E and F we place the NESs at the edges of the plate $x = 0, 1$, with $y = 0.6, 0.7, 0.8$ and 0.9 , respectively. For these cases we note a slight improvement (about 10%) of the synergetic efficiency of the set of two NESs (see Figure 5.73). Finally, there are two locations where the efficiency of the single SDOF NES is very high (more than 80%); these are the two free corners of the plate. The numerical simulations indicate that by attaching the two NESs simultaneously to these locations (case G), we obtain a combined TET efficiency of 89.9%, which can be considered as the optimal synergetic TET efficiency that can be achieved by the set of two NESs on the plate. We note, however, only marginal improvement in TET efficiency compared to using the two NESs in isolation at the same locations.

In conclusion, the use of the set of two NESs improves TET efficiency in regions where the use of single (isolated) NESs leads to poor TET performance. In such regions there occur positive synergisms between the two NESs of the set, which leads to TET efficiencies that exceed the sum of the efficiencies of single NESs when these are used in isolation. The use of multiple NESs, however, improves only marginally TET efficiency in locations where the isolated NESs already yield good TET performance.

5.5.3 Case of a MDOF NES

We now consider TET from the plate to a single MDOF NES. The equations of motion of this system are given by (5.96), and TET efficiency is judged by the energy dissipation measures (5.97) and their long-time asymptotic values. The first set of numerical simulations of this series was performed in order to examine the effect of the linear coupling stiffness on TET. The plate parameters are identical to the ones used for the case of SDOF NES attachment, and the applied shock is the half-sine excitation used in previous simulations, defined by relation (5.91); the duration of the applied shock was selected sufficiently small to *directly* excite at

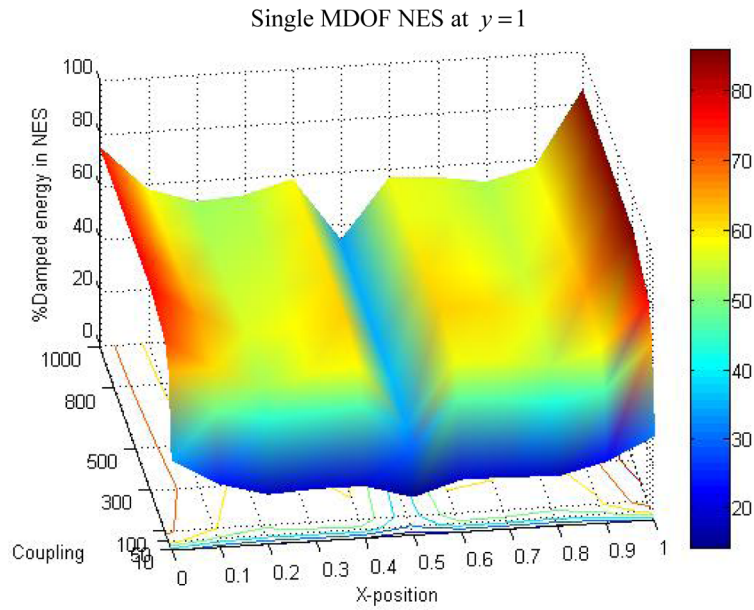


Fig. 5.74 Parametric study of TET for a MDOF NES located at every possible x -position on the ‘slice’ $y = 1$, for coupling stiffness $C_0 = 300$.

least the leading five modes of the plate – however, additional plate modes may be indirectly excited through nonlinear coupling provided by the MDOF NES. The three masses of the MDOF NES are assumed to be small, $m_1 = m_2 = m_3 = 0.005/3$, with the total mass of the MDOF NES being equal to the smallest mass of the SDOF NES used in the parametric study of the previous section. In this way we wish to perform a comparative study of the SDOF and MDOF NESs, *without any effects due to added mass*. The two nonlinear stiffnesses of the NES are selected as $C_1 = 5.0$ and $C_2 = 0.1$, whereas the two dampers of the NES possess identical damping coefficients $\lambda = 0.1$.

In Figure 5.74 we depict the long-time asymptotic value of the combined EDM $E_{NES 1, t \gg 1} + E_{NES 2, t \gg 1} = \lim_{t \gg 1} [E_{NES 1}(t) + E_{NES 2}(t)]$, which represents the portion of shock energy of the plate eventually dissipated by the two dampers of the MDOF NES, as function of the coupling stiffness C_0 (in the range $[10, 1000]$), and the x -position of the NES for the representative ‘ y -slice’ $y = 1$. A conclusion from these numerical results is that TET appears to be robust for varying C_0 provided that this is above the threshold $C_0 = 100$, and for every possible x -position of the NES (as depicted in Figure 5.74). Moreover, strong TET from the plate to the MDOF NES is realized for relatively stiff coupling stiffnesses. The levels of optimal TET values attained by using MDOF NESs reaches levels of 80%, which are comparable to the ones attained by using SDOF NESs. Similarly to the case of the SDOF NES (see Section 5.5.1), the variation of the position of the MDOF NES appears to strongly

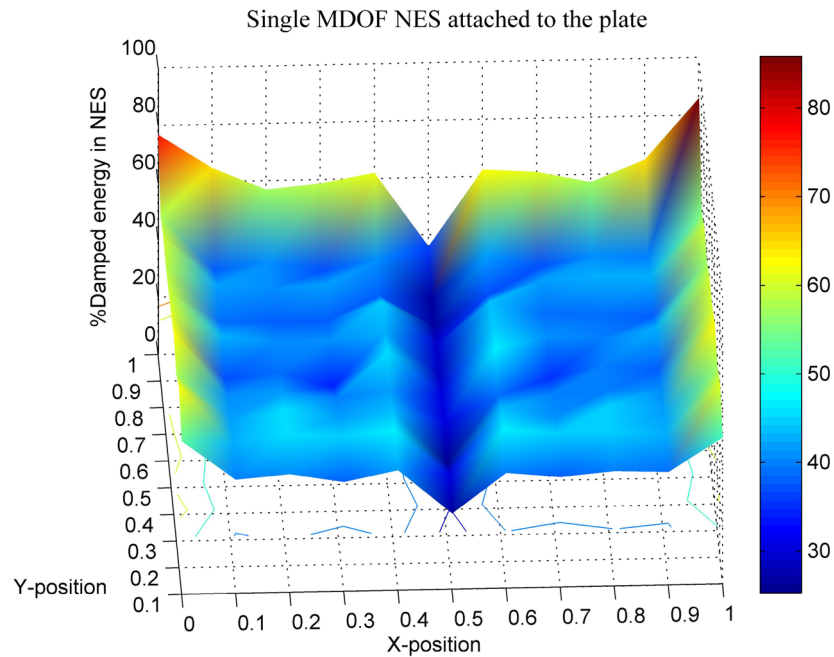


Fig. 5.75 Parametric study of TET for a MDOF NES located at every possible position on the plate, for coupling stiffness $C_0 = 300$.

affect TET, as depicted in Figure 5.74; however, this will be more evident in the second set of simulations that we now proceed to discuss.

In the second set of simulations we examine the influence of the position of the MDOF NES on TET; for this, we examine MDOF NES placement at every possible position on the plate, and apply the same NES parameters as in the previous set of simulations. In addition, we fix the coupling stiffness to $C_0 = 300$. In Figure 5.75 we depict TET as function of the NES position. Predictably, the highest values of TET are obtained when the MDOF NES is situated at the free corners of the plate, reaching 85.85% for NES position at $(x, y) = (1, 1)$, and 76.67% at $(0, 1)$. At these positions the MDOF NES can interact with all plate modes, as no nodal curves of low-order modes are located nearby. Similarly to the case of the SDOF NES, the interpretation of the results depicted in Figure 5.75 should be carried out in conjunction with Table 5.6, which depicts the nodal curves of the leading five modes of the uncoupled plate with no elastic support (labeled from hereon as the ‘plate modes’).

From Figure 5.75 we deduce that the efficiency of the NES decreases when it is located closer to the clamped end, where the displacements of the plate are small and the nonlinear effects are less profound. Since passive TET is the result of nonlinear resonance interactions (TRCs) between the plate and the NES, it is reasonable to expect that in low-amplitude regimes the effectiveness of the MDOF should de-

teriorate. As demonstrated, however, in Section 4.1.2 and in Tsakirtzis (2006) and Tsakirtzis et al. (2007b) it is possible (under certain forcing conditions and at definite ranges of NES parameters) to achieve efficient TET from a directly forced linear system to a MDOF NES, even at low amplitude regimes; such a case, however, was not realized in the simulations considered herein. An additional set of numerical simulations examining the influence on TET efficiency of the magnitude of the applied shock and the (linear) coupling stiffness C_0 is reported in Georgiades (2006) and Georgiades and Vakakis (2008). It was found that TET does not depend significantly on the variation of shock input.

The analysis of the complex nonlinear modal interactions and the corresponding TRCs that govern TET in this system can be performed by applying the combined Wavelet/EMD post-processing methodology. As the analysis becomes quite involved (since each of the transient responses of all three masses of the NES that must be considered in this case) we do not present any results here, and refer the reader to the thesis by Georgiades (2006) for a detailed presentation. In the next section we conclude our study of TET in the plate-NES system by performing a comparative study of energy absorption performance with the linear vibration absorber (or tuned mass damper – TMD); this study will demonstrate the qualitative differences in the dynamics and superior shock absorption performance of the nonlinear designs compared to conventional linear ones.

5.5.4 Comparative Study with Linear Tuned Mass Damper

We now present the results of a parametric study of the plate with a linear TMD attached. We will assess the capacity of the TMD to absorb and locally dissipate shock energy from the plate by varying the TMD parameters and its position on the plate. Then we will compare the results with the corresponding ones derived when applying SDOF or MDOF NESs to the plate. We perform a series of simulations considering single and multiple shock excitations applied to the plate. In each of these sets, the efficiency of the TMD to passively absorb and locally dissipate shock energy from the plate is estimated by the following asymptotic limit:

$$E_{\text{TMD}, t \gg 1} = \lim_{t \gg 1} E_{\text{TMD}}(t), \quad E_{\text{TMD}}(t) = \frac{\lambda \int_0^t [\dot{w}(d_x, d_y, \tau) - \dot{v}(\tau)]^2 d\tau}{\int_0^t F(\tau) \dot{w}(b_x, b_y, \tau) d\tau} \times 100 \quad (5.98)$$

where $v(t)$ is the response of the TMD. This represents the portion of the shock energy of the plate that is eventually dissipated by the damper of the TMD, and is similar to the EDMs defined in previous sections to assess the TET capacity of SDOF and MDOF NESs.

In the first set of these simulations we examine the potential of the TMD to absorb and dissipate shock energy by varying its stiffness and its location on the

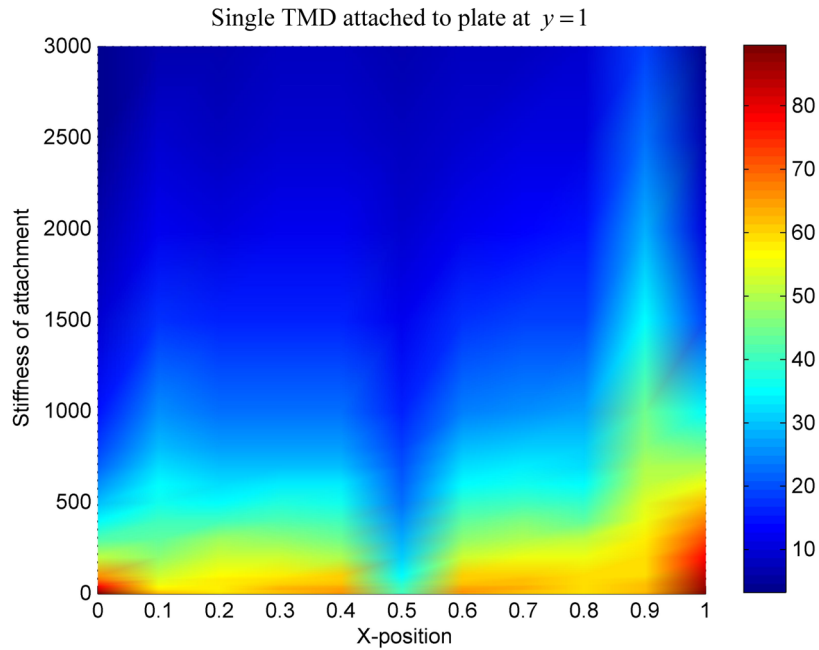


Fig. 5.76 Efficiency $E_{\text{TMD}, t \gg 1}$ of the linear TMD as a function of its stiffness and its x -position on the plate for the ‘ y -slice’ $y = 1$, for single shock excitation.

plate, for single shock excitation. The system parameters of the plate were defined in Section 5.5.1, the TMD mass is selected as $\varepsilon = 0.05$, and its damping coefficient as $\lambda = 0.1$; these are identical to the parameters used for the simulations with the SDOF NES attachment in Section 5.5.1, so the two sets of simulations can be directly compared. In Figure 5.76 we depict the efficiency of the TMD, $E_{\text{TMD}, t \gg 1}$, as function of its stiffness and x -position on the plate, for the fixed ‘ y -slice’ $y = 1$ (i.e., at the free edge of the cantilever plate). This result should be compared to the plot of Figure 5.67a for the SDOF NES. We note that the variation of the location of the TMD strongly affects its efficiency, in a manner similar to the SDOF and MDOF NES attachments examined previously. Indeed, when the TMD is located at positions close to nodal lines of the plate, the TMD can not interact with the corresponding plate modes, and therefore the absorption of shock energy from the plate deteriorates. Moreover, when the TMD is ‘tuned’ to the i -th plate mode, i.e., when its stiffness is equal to $k_{\text{In}} = \omega_i^2 \varepsilon$, where ω_i is the i -th natural frequency of the (uncoupled and linear) plate, its efficiency in extracting energy from that mode is high. However, for relatively high stiffness values of the TMD, i.e., when it is ‘detuned’ from the leading plate modes, its efficiency deteriorates, as expected. Comparing to the plot of Figure 5.67a we note that the TET efficiency for the case of SDOF NES does not show such dependence on stiffness, and hence, its performance is more robust to stiffness variations.

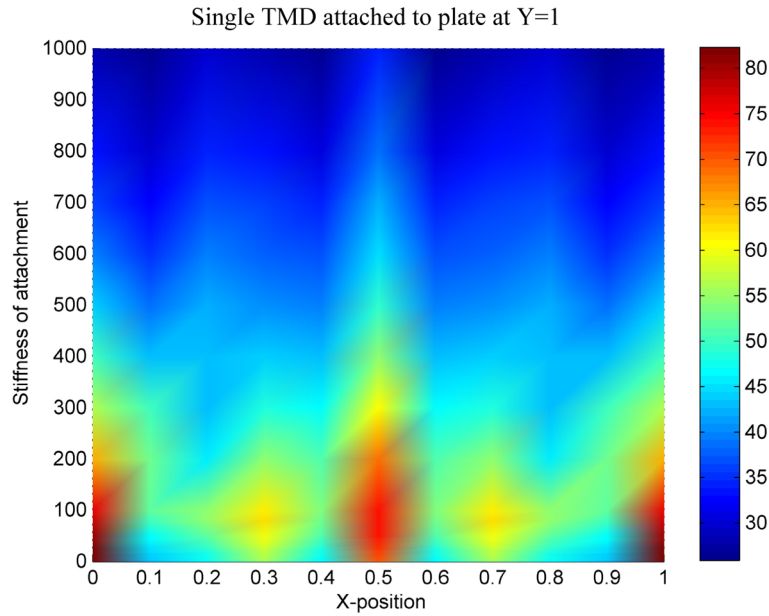


Fig. 5.77 Efficiency $E_{\text{TMD}, t \gg 1}$ of the linear TMD as a function of its stiffness and its x -position on the plate for the ‘ y -slice’ $y = 1$, for multiple shock excitation.

In the second set of simulations we examine the effectiveness of the TMD for variation of its stiffness and its location, for the case of multiple applied shocks. The parameters used are identical to the first set of simulations presented above, but the damping coefficient of the plate was selected as $d = 15$, and the TMD mass as $\varepsilon = 0.005$; these system parameters are identical to the ones used in Section 5.5.1, where the efficiency of the SDOF NES for multiple shock excitations was examined. In Figure 5.77 we present the results for this set of simulations. Again, the stiffness and position of the TMD appear to strongly affect its efficiency. Comparing these results to the plot of Figure 5.67b we note again the insensitivity of the performance of the SDOF NES to stiffness variations for the case of multiple shock excitation.

In order to compare the relative performance of the various nonlinear and linear absorber configurations considered, we performed an additional set of simulations for fixed attachment placement at $(x, y) = (0, 1)$, away from the source of the single applied shock at $(b_x, b_y) = (1, 1)$. For this set of simulations the plate parameters are defined as in Section 5.5.1, and all SDOF attachments considered possess mass $\varepsilon = 0.005$ (or 0.005% of the plate mass), and viscous damper coefficients $\lambda = 0.1$. For the simulations corresponding to a MDOF NES, each of the three NES masses was chosen equal to $0.005/3$, and the two viscous damping coefficients were set to $\lambda = 0.1$; hence no added mass effects were introduced. For simulations where the coupling stiffness C_0 varies the two nonlinear stiffness coefficients of the NES are selected as $C_1 = 5.0$ and $C_2 = 0.1$; when the stiffness C_1 varies the other stiffness

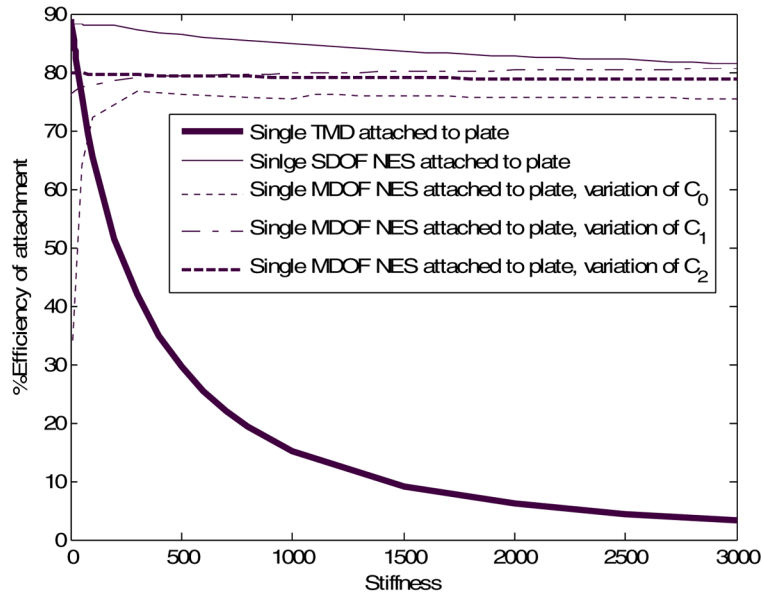


Fig. 5.78 Comparison of TET efficiency of the different nonlinear and linear attachments for varying coupling stiffness.

coefficients are selected as $C_0 = 10^3$ and $C_2 = 0.1$; whereas when C_2 varies the other stiffness coefficients are given by $C_0 = C_1 = 10^3$. In Figure 5.78 we depict the results for this set of simulations, from which we deduce that the strongest and most robust TET is achieved for the case of SDOF NES. As expected, the TMD is effective only when it is ‘tuned’ to energetically strong plate modes, and its performance rapidly deteriorates when ‘detuning’ occurs. In contrast, *the essentially nonlinear SDOF and MDOF NESs possess no such detuning limitations as they lack preferential ‘tuning’ frequencies*; hence, these NESs are capable of engaging in transient resonance (TRC) with plate modes at arbitrary frequency ranges, with the only controlling parameter determining the resulting sequence of TRCs being their instantaneous energies which ‘tune’ accordingly their instantaneous frequencies.

Finally, we examine in more detail the performances of the optimal configurations of the SDOF NES and the TMD, in order to compare their corresponding rates of TET from the plate. For this final set of simulations we considered multiple shock excitations with plate parameters defined in Section 5.5.1 and distributed damping coefficient $d = 15$. The attachments are located at one of the free corners of the plate, $(x, y) = (0, 1)$, and their parameters are given as $\varepsilon = 0.005$, $\lambda = 0.1$, $C = 100$ for the SDOF NES, and k_{ln} for the TMD (i.e., it is tuned to the 4th natural frequency of the uncoupled linear plate). For the specific optimal configurations considered, the corresponding TET efficiencies are 88.94% for the SDOF NES, and 82.24% for the TMD. Although the percentages of shock energy eventually dissipated by these two configurations are comparable, the corresponding rates of TET

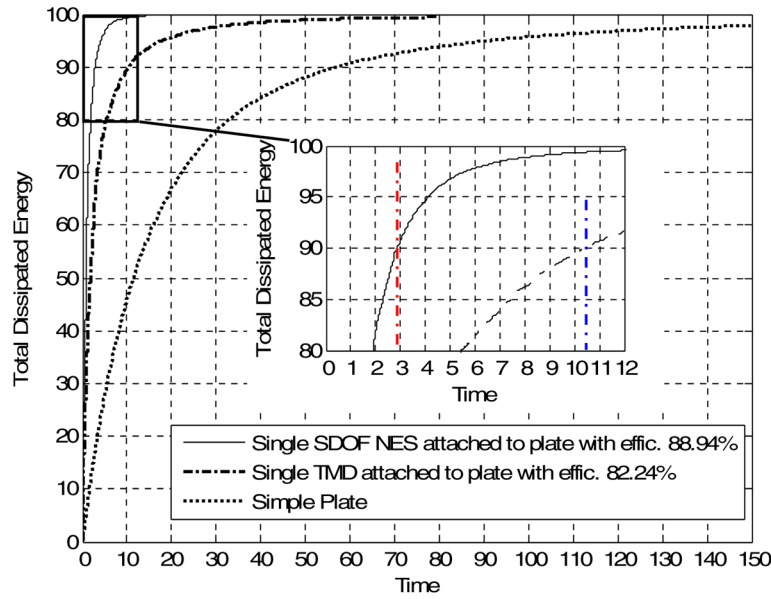


Fig. 5.79 Transient energy dissipated for single shock excitation for a plate with or without attachments; the optimal configurations for the SDOF NES and the TMD are considered.

differ drastically. The rates of shock energy dissipation can be deduced from the plots of Figure 5.79, where the total energy dissipation measure $E_{\text{total}}(t)$ [see relation (5.95)] is depicted as a function of time; for comparison purposes the rate of energy dissipation in the plate with no attachment is also depicted. We note that for multi-shock excitation the required time for the integrated plate-TMD system to dissipate 90% of the applied shock energy is approximately $t \approx 10.5$, whereas the corresponding time for the integrated plate-SDOF NES system is less than $t = 3$ (these results, of course, hold only for this multiple excitation case where three linear modes are excited with almost equal energy). Hence, *nonlinear dissipation of shock energy occurs on a faster time scale*, a result which is in agreement with the findings of previous works; actually, as shown in the thesis by Georgiades (2006), the rate of nonlinear energy dissipation can be further increased by employing NESs with non-smooth stiffness characteristics, a feature which has already been explored in seismic mitigation designs (Nucera et al., 2007). The issue of vibro-impact NESs will be studied in detail in Chapter 7, whereas their application to seismic mitigation will be studied in Chapter 10. In conclusion, apart from the lack of robustness of TET in the case of the TMD for changes of parameters, the corresponding rate of shock energy absorption and dissipation in the linear design is smaller compared to the nonlinear design.

In conclusion, this comparative study demonstrates the improved robustness of the considered NES designs, as well as the faster rate of nonlinear shock energy

dissipation when essentially nonlinear attachments are used. This is an expected finding, given that the NESs do not possess the single-tuning-frequency limitation of the TMD; instead, since they possess no preferential set of resonance frequencies they are capable of engaging in TRC with any plate mode (provided that the mode has no node close to the point of attachment to the NES), over wide frequency ranges. *It is this capacity for broadband energy absorption that renders the NES an efficient and adaptive passive boundary controller.* From a practical point of view, it is often encountered in engineering practice the situation that due to fatigue or joint degradation the natural frequencies of a structure may gradually change, detuning attached TMDs and rendering them inefficient; in such situations NES-based designs should be able to still remain ‘tuned’ to structural modes and thus maintain the efficiency of passive shock mitigation, with no further structural or design modifications required.

References

*ReferencesReferencesReferences

- Cai, C.W., Chan, H.C., Cheung, Y.K., Localized modes in a two-degree-coupling periodic system with a nonlinear disordered subsystem, *Chaos, Solit. Fract.* **11**, 1481–1492, 2000.
- Cao, X.D., Malomed, B.A., 1995, Soliton-defect collisions in the nonlinear Schrödinger equation, *Phys. Lett. A* **206**, 177–182, 1995.
- Caughey, T.K., Personal communication to AFV, 1987.
- Chalbaud, E., Martin, P., Two-point quasifractional approximant in physics: Method improvement and application to $J_\nu(x)$, *J. Math. Phys.* **33**(7), 2483–2486, 1992.
- Chandre, C., Wiggins, S., Uzer, T., Time frequency analysis of chaotic systems, *Physica D* **181**, 171–196, 2003.
- El-Khatib, H.M., Mace, B.R., Brennan, M.J., Suppression of bending waves in a beam using a tuned vibration absorber, *J. Sound Vib.* **288**, 1157–1175, 2005.
- Georgiades, F., *Nonlinear Localization and Targeted Energy Transfer Phenomena in Vibrating Systems with Smooth and Non-smooth Stiffness Nonlinearities*, PhD Thesis, National Technical University of Athens, Athens, Greece, 2006.
- Georgiades, F., Vakakis, A.F., Dynamics of a linear beam with an attached local nonlinear energy sink, *Comm. Nonl. Sc. Num. Sim.* **12**(5), 643–561, 2007.
- Georgiades, F., Vakakis, A.F., Passive targeted energy transfers and strong modal interactions in the dynamics of a thin plate with strongly nonlinear end attachments, *J. Comp. Nonl. Dyn.*, 2008 (under review).
- Georgiades, A.F., Vakakis, A.F., Kerschen, G., Broadband passive targeted energy transfer from a linear dispersive rod to a lightweight essentially nonlinear end attachment, *Int. J. Nonlinear Mech.* **42**, 773–788, 2007.
- Gerardin, M., Rixen, D., *Mechanical Vibrations, Theory and Application to Structural Dynamics*, John Willey & Sons, New York, 1997.
- Goodman, R.H., Haberman, R., Interaction of sine-Gordon kinks with defects: The two-bounce resonance, *Physica D* **195**, 303–323, 2004.
- Goodman, R.H., Holmes, P.J., Weinstein, M.I., Interaction of sine-Gordon kinks with defects: Phase space transport in a two-mode model, *Physica D* **161**, 21–44, 2002.
- Guerrero, A.L., Martin, P., Higher order two-point quasi-fractional approximations to the Bessel Functions $J_0(x)$ and $J_1(x)$, *J. Comp. Phys.* **77**, 276–281, 1988.

- Huang, N.E., Shen, Z., Long, S.R., Wu, M.C., Shih, H.H., Zheng, Q., Yen, N.C., Tung, C.C., Liu, H.H., The empirical mode decomposition and the hilbert spectrum for nonlinear and non-stationary time series analysis, *Proc. Royal Soc. London, Ser. A* **454**, 903–995, 1998.
- Kerschen, G., Lee, Y.S., Vakakis, A.F., McFarland, D.M., Bergman, L.A., Irreversible passive energy transfer in coupled oscillators with essential nonlinearity, *SIAM J. Appl. Math.* **66**(2), 648–679, 2005.
- Komech, A.I., On stabilization of string – nonlinear oscillator interaction, *J. Math. Anal. Appl.* **196**, 384–409, 1995.
- Komech, A.I., Komech, A.A., 2006, On the global attraction to solitary waves for the Klein–Gordon equation coupled to a nonlinear oscillator, *C. R. Acad. Sci. Paris, Ser. I* **343**, 111–114, 2006.
- Kotousov, A.G., Integral estimates in nonlinear oscillatory systems, *J. Appl. Math. Mech.* **60**(2), 333–336, 1996.
- Lee, Y.S., Kerschen, G., Vakakis, A.F., Panagopoulos, P.N., Bergman, L.A., McFarland, D.M., Complicated dynamics of a linear oscillator with a light, essentially nonlinear attachment, *Physica D* **204**(1–2), 41–69, 2005.
- Leissa, A., *Vibration of Plates*, Acoustical Society of America Publication, 1993.
- Linton, C.M., Melver, M., Melver, P., Ratcliffe, K., Zhang, J., Trapped modes for off-centre structures in guides, *Wave Motion* **36**, 67–85, 2002.
- Liu, G.R., Quek, S.S., *The Finite Element Method: A Practical Course*, Butterworth-Heinemann, Oxford, 2003.
- Manevitch, L.I., Description of localized normal modes in the chain of nonlinear coupled oscillators using complex variables, *Nonl. Dyn.* **25**(1–3), 95–109, 2001.
- Manevitch, L.I., Personal communication to AFV, 2003.
- Manevitch, L.I., Gendelman, O., Musienko, A., Vakakis, A.F., Bergman, L.A., Dynamic interaction of a semi-infinite linear chain of coupled oscillators with a strongly nonlinear end attachment, *Physica D* **178**(1–2), 1–18, 2003.
- Martin, P., Baker, G.A., Two-point quasifractional approximant in physics. Truncation error, *J. Math. Phys.* **32**(6), 1470–1477, 1991.
- Melosh, R.J., Structural analysis of solids, *ASCE Str. J.* **4**, 205–223, 1963.
- Morse, P.M., Feshbach, H., *Methods of Theoretical Physics*, McGraw-Hill, New York, 1953.
- Nucera, F., Vakakis, A.F., McFarland, D.M., Bergman, L.A., Kerschen, G., Targeted energy transfers in vibro-impact oscillators for seismic mitigation, *Nonl. Dyn.* (Special Issue on ‘Discontinuous Dynamical Systems’) **50**, 651–677, 2007.
- Panagopoulos, P.N., Vakakis, A.F., Tsakirtzis, S., Transient resonant interactions of linear chains with essentially nonlinear end attachments leading to passive energy pumping, *Int. J. Solids Str.* **41**(22–23), 6505–6528, 2004.
- Panagopoulos, P.N., Georgiades, F., Tsakirtzis, S., Vakakis, A.F., Bergman, L.A., Multi-scaled analysis of the damped dynamics of an elastic continuum with an essentially nonlinear end attachment, *Int. J. Solids Str.* **44**, 6256–6278, 2007.
- Qu, Zu-Qing, Model reduction for dynamical systems with local nonlinearities, *AIAA J.* **40**(2), 327–333, 2002.
- Reddy, J., *An Introduction to the Finite Element Method*, McGraw-Hill, New York, 1984.
- Richtmyer, R.D., *Principles of Advanced Mathematical Physics, Vol. I*, Springer Verlag, Berlin/New York, 1985.
- Tsakirtzis S., *Passive Targeted Energy Transfers From Elastic Continua to Essentially Nonlinear Attachments for Suppressing Dynamical Disturbances*, PhD Thesis, National Technical University of Athens, Athens, Greece, 2006.
- Tsakirtzis, S., Vakakis, A.F., Panagopoulos, S., Broadband energy exchanges between a dissipative elastic rod and a multi-degree-of-freedom dissipative, essentially nonlinear attachment, *Int. J. Nonlinear Mech.* (Special Issue on ‘Dissipative Nonlinear Systems’) **42**(1), 36–57, 2007a.
- Tsakirtzis, S., Panagopoulos, P.N., Kerschen, G., Gendelman, O., Vakakis, A.F., Bergman, L.A., Complex dynamics and targeted energy transfer in systems of linear oscillators coupled to multi-degree-of-freedom essentially nonlinear attachments, *Nonl. Dyn.* **48**, 285–318, 2007b.

- Vakakis, A.F., Manevitch, L.I., Gendelman, O., Bergman, L.A., Dynamics of linear discrete systems connected to local essentially nonlinear attachments, *J. Sound Vib.* **264**, 559–577, 2003.
- Vakakis, A.F., Manevitch, L.I., Musienko, A., Kerschen, G., Bergman, L.A., Transient dynamics of a dispersive elastic wave guide weakly coupled to an essentially nonlinear end attachment, *Wave Motion* **41**(2), 109–132, 2004.
- Watson, G.N., *A Treatise on the Theory of Bessel Functions*, Cambridge University Press, UK, 1980.
- Zei, Z., Kivshar, Y.S., Vazquez, L., Resonant kink-impurity interactions in the sine-Gordon model, *Phys. Rev. A* **45**, 6019–6030, 1992.
- Zienkiewicz, O.C., Taylor, R.L., *The Finite Element Method, Volume 2: Solid Mechanics*, Butterworth-Heinemann, Oxford, 2000.

Chapter 6

Targeted Energy Transfer in Systems with Periodic Excitations

Previous chapters demonstrated that the addition of a relatively lightweight strongly nonlinear attachment to a primary (discrete or continuous) linear structure under shock excitation can drastically modify its transient dynamic response and bring about the TET phenomenon. Hence, it is not unreasonable to expect that similar salient dynamical behavior will be revealed also for the case of external periodic excitation. The transition from shock (broadband) to periodic (narrowband) excitation, however, is not trivial, and the application of nonlinear energy sinks (NESs) to structures under narrowband excitation deserves special consideration. For, example, it is not obvious that the capacity for TET of an NES under conditions of shock excitation of a primary structure can be extended to the case of periodic excitation. This chapter treats exactly this problem.

We aim to demonstrate that the steady state response of a primary system under harmonic excitation with an attached NES exhibits not only common steady state and weakly modulated responses, but also a very special type of responses characterized by large modulations of the resulting oscillations; this response type is referred to as *Strongly Modulated Response (SMR)*, and may be regarded as the extension of the TET phenomenon to structures under periodic (narrowband) excitation. Moreover, we demonstrate that SMRs are related to relaxation oscillations of the corresponding averaged dynamical flows (the slow flows of the dynamics), and in fact, one can regard SMRs as a form of repetitive TETs under the action of persisting periodic forcing. The possible application of NESs as strongly nonlinear vibration absorbers for vibration isolation of harmonically forced single- and multi-DOF primary subsystems is then discussed, and it is shown that under certain conditions, the efficiency of the NESs as vibration isolators can far exceed that of properly tuned linear absorbers (or tuned mass dampers – TMDs).

6.1 Steady State Responses and Generic Bifurcations

6.1.1 Analysis of Steady State Motions

We initiate our study by considering a primary SDOF linear oscillator under harmonic external excitation with an ungrounded, lightweight and essentially nonlinear NES attached (Gendelman et al., 2006; Gendelman and Starosvetsky, 2007; Gendelman et al., 2008; Starosvetsky and Gendelman, 2008). This system is described by the following set of equations,

$$\begin{aligned} \ddot{y}_1 + \varepsilon\lambda(\dot{y}_1 - \dot{y}_2) + (1 + \varepsilon\sigma)y_1 + \frac{4}{3}\varepsilon(y_1 - y_2)^3 &= \varepsilon A \cos t \\ \varepsilon\ddot{y}_2 + \varepsilon\lambda(\dot{y}_2 - \dot{y}_1) + \frac{4}{3}\varepsilon(y_2 - y_1)^3 &= 0 \end{aligned} \quad (6.1)$$

where y_1 and y_2 are the displacements of the linear oscillator and the attachment respectively, $\varepsilon\lambda$ the damping coefficient, εA the amplitude of the external force, and $\varepsilon\sigma$ a frequency detuning parameter. The parameter $\varepsilon \ll 1$ is the small parameter of the problem which scales the coupling between the two oscillators, the damping forces, the amplitude of the external force, the detuning parameter, and the mass of the NES. The coefficients A, λ, σ are adopted to be of $O(1)$. The coefficient of the nonlinear term can be modified by proper rescaling of the dependent variables and the forcing amplitude; the value $(4\varepsilon/3)$ is chosen for the sake of convenience.

We will analyze the steady state periodic responses of (6.1) by the complexification-averaging (CX-A) methodology introduced in previous chapters. To this end, we apply the following coordinate transformations, denoting the center-of-mass and relative displacements of the system,

$$\begin{aligned} v &= y_1 + \varepsilon y_2 \\ w &= y_1 - y_2 \end{aligned} \quad (6.2)$$

and then switch the analysis to complex variables:

$$\begin{aligned} \varphi_1 \exp(jt) &= \dot{v} + jv \\ \varphi_2 \exp(jt) &= \dot{w} + jw \end{aligned} \quad (6.3)$$

By (6.3) we partition the dynamics into slow and fast components, and make the additional *ansatz* that the sought steady state responses are in the form of fast oscillations $\exp(jt)$ modulated by slowly-varying complex amplitudes $\varphi_i(t)$. Moreover, it is clear that we seek periodic solutions of (6.1) with dominant frequencies identical to the frequency of the external periodic force, and approximately equal to the eigenfrequency of the linear oscillator (that is, the frequency detuning $\varepsilon\sigma$ provides a slight frequency mismatch). Hence, we will be interested in *fundamental nonlinear resonances* of system (6.1).

After substitution of (6.2) and (6.3) into (6.1) and subsequent averaging over the fast oscillations of frequency unity, we obtain the following slow flow (complex modulation) equations:

$$\begin{aligned} \dot{\varphi} + \frac{j\varepsilon}{2(1+\varepsilon)}(\varphi_1 - \varphi_2) - \frac{j\varepsilon\sigma(\varphi_1 + \varepsilon\varphi_2)}{2(1+\varepsilon)} &= \frac{\varepsilon A}{2} \\ \dot{\varphi}_2 + \lambda(1+\varepsilon)\frac{\varphi_2}{2} + \frac{j}{2(1+\varepsilon)}(\varphi_2 - \varphi_1) \\ - \frac{j\varepsilon\sigma(\varphi_1 + \varepsilon\varphi_2)}{2(1+\varepsilon)} - \frac{j(1+\varepsilon)}{2}|\varphi_2|^2\varphi_2 &= \frac{\varepsilon A}{2} \end{aligned} \quad (6.4)$$

The system of equations (6.4) has a complicated structure and cannot be solved analytically. The first step towards analyzing its steady state solutions is to perform local analysis of its equilibrium (fixed points). Such analysis is of significant physical interest, since these points correspond to periodic responses of the system described by equation (6.1). To find the fixed points we equate the time derivatives of (6.4) to zero ($\dot{\varphi}_1 = \dot{\varphi}_2 = 0$) thus obtaining the following complex algebraic relations:

$$\begin{aligned} \frac{j\varepsilon}{2(1+\varepsilon)}(\varphi_{10} - \varphi_{20}) - \frac{j\varepsilon\sigma(\varphi_{10} + \varepsilon\varphi_{20})}{2(1+\varepsilon)} &= \frac{\varepsilon A}{2} \\ \lambda(1+\varepsilon)\frac{\varphi_{20}}{2} + \frac{j}{2(1+\varepsilon)}(\varphi_{20} - \varphi_{10}) \\ - \frac{j\varepsilon\sigma(\varphi_{10} + \varepsilon\varphi_{20})}{2(1+\varepsilon)} - \frac{j(1+\varepsilon)}{2}|\varphi_{20}|^2\varphi_{20} &= \frac{\varepsilon A}{2} \end{aligned} \quad (6.5)$$

By simple algebraic manipulations system (6.5) may be reduced to the following more convenient form:

$$\begin{aligned} \left[\lambda^2 + \frac{\sigma^2}{(1-\sigma)^2} \right] |\varphi_{20}|^2 + \frac{2\sigma}{1-\sigma} |\varphi_{20}|^4 + |\varphi_{20}|^6 &= \frac{A^2}{(1-\sigma)^2} \\ \theta_{20} &= \text{sign}(1-\sigma) \tan^{-1} \left[\frac{\sigma}{\lambda(1-\sigma)} + \frac{|\varphi_{20}|^2}{\lambda} \right] \\ \varphi_{10} = \frac{(1+\varepsilon\sigma)\varphi_2 - j(1+\varepsilon)A}{1-\sigma} &\Rightarrow |\varphi_{10}| = \left(\frac{1+\varepsilon\sigma}{1-\sigma} \right) \frac{|\varphi_{20}| \cos \theta_{20}}{\cos \theta_{10}} \\ \theta_{10} &= \text{sgn}(1-\sigma) \tan^{-1} \left[\tan \theta_{20} - \frac{(1+\varepsilon)A}{(1+\varepsilon\sigma)|\varphi_{20}| \cos \theta_{20}} \right] \end{aligned} \quad (6.6)$$

The polynomial in the first of equations (6.6) can be brought into the following compact form,

$$\alpha_1 Z + \alpha_2 Z^2 + \alpha_3 Z^3 + \alpha_4 = 0 \quad (6.7)$$

where

$$\begin{aligned}
|\varphi_{20}|^2 = Z, \quad \alpha_1 = \lambda^2 + \frac{\sigma^2}{(1-\sigma)^2}, \\
\alpha_2 = \frac{2\sigma}{(1-\sigma)}\alpha_3 = 1, \quad \alpha_4 = \frac{-A^2}{(1-\sigma)^2}
\end{aligned} \tag{6.8}$$

Depending on the system parameters and the coefficients (6.8), the generic polynomial (6.7) can have one or three positive (real) solutions. Therefore, due to continuity one expects generically that at certain special critical values of the parameters A, λ and σ two of these solutions will coalesce, yielding bifurcations of steady state periodic solutions; generically, these will be saddle-node (SN) bifurcations (although, as we will see later generic Hopf bifurcations can also be realized). At points of bifurcation, both the polynomial (6.7) and its derivative with respect to Z should be equal to zero:

$$3\alpha_3 Z^2 + 2\alpha_2 Z + \alpha_1 = 0 \tag{6.9}$$

It follows that to compute the bifurcation points we need to satisfy simultaneously the set of equations (6.7) and (6.9); this yields the bifurcation curve in parameter space (A, λ, σ) where SN bifurcations occur. Quite remarkably, the positions of fixed points of the slow flow do not depend on the value of the NES mass ε , as indicated by the following relation which yields the SN bifurcation points in parameter space:

$$\begin{aligned}
3\alpha_3(\alpha_1\alpha_2 - 9\alpha_3\alpha_4)^2 + 2\alpha_2(\alpha_1\alpha_2 - 9\alpha_3\alpha_4)(6\alpha_1\alpha_3 - 2\alpha_2^2) \\
+ \alpha_2(6\alpha_1\alpha_3 - 2\alpha_2^2)^2 = 0
\end{aligned} \tag{6.10}$$

The projections of the solutions of (6.10) to the two-dimensional plane of parameters (A, λ) for $\sigma = 3$ are presented in Figure 6.1. Additional projections for various positive and negative detuning values σ are presented in Figures 6.2 and 6.3. The three-dimensional surface of the SN bifurcation boundary is presented in Figures 6.4 and 6.5. The plot depicted in Figure 6.4 is related to positive values of the detuning parameter, whereas the plot of Figure 6.5 corresponds to negative values of the detuning parameter.

In addition to SN bifurcations, where a stable steady state solution of the slow flow simply disappears when it coalesces with an unstable one, there exists one additional generic bifurcation scenario for loss of stability, namely, the realization of Hopf bifurcations (Guckenheimer and Holmes, 1983; Wiggins, 1990). In order to study this type of bifurcations of the slow flow (6.4), we should explore the conditions for stability of the steady state solutions. To this end, we reconsider the equations of the slow flow (6.4) and introduce the small (complex) perturbations $\delta_i(t)$, $i = 1, 2$ of the fixed points in the following form:

$$\begin{aligned}
\varphi_1 = \varphi_{10} + \delta_1, \quad |\delta_1| \ll 1 \\
\varphi_2 = \varphi_{20} + \delta_2, \quad |\delta_2| \ll 1
\end{aligned} \tag{6.11}$$

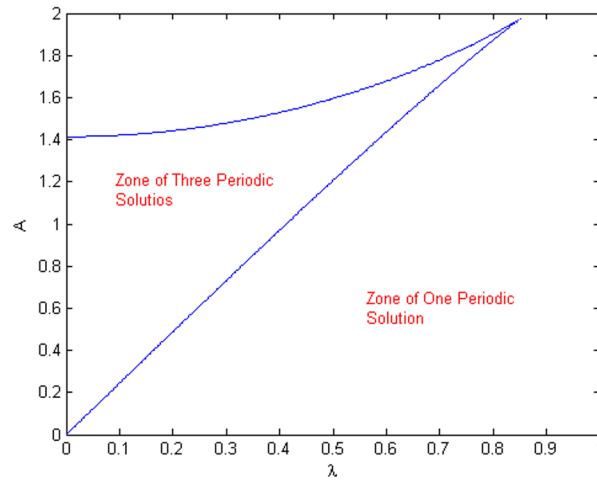


Fig. 6.1 Curves of SN bifurcations for $\sigma = 3$.

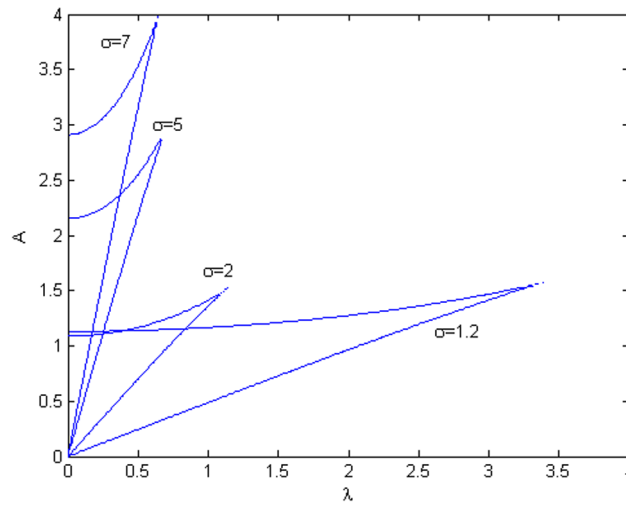


Fig. 6.2 Curves of SN bifurcations for fixed positive detuning σ .

Substituting (6.11) into (6.4) and keeping only linear terms with respect to δ_i , $i = 1, 2$ in the resulting variational equations we obtain the following linearized system of equations in terms of the perturbations,

$$\dot{\delta}_1 = -\frac{j\varepsilon}{2(1+\varepsilon)}(\delta_1 - \delta_2) + \frac{j\varepsilon\sigma(\delta_1 + \varepsilon\delta_2)}{2(1+\varepsilon)}$$

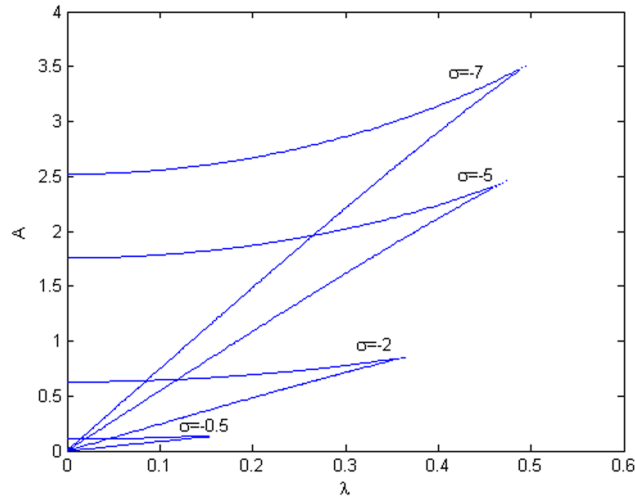


Fig. 6.3 Curves of SN bifurcations for fixed negative detuning σ .

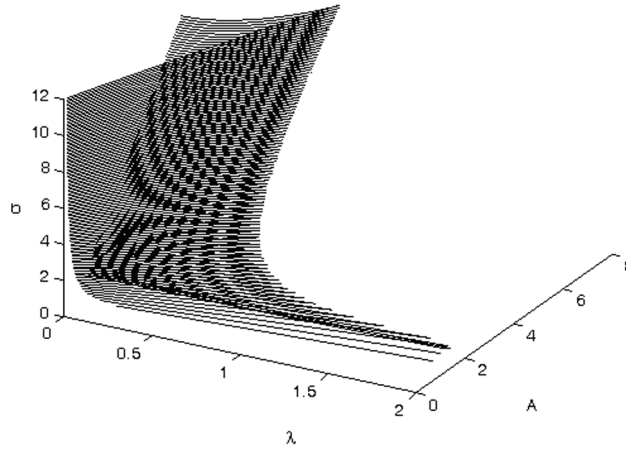


Fig. 6.4 Surface of the SN bifurcations for positive values of detuning σ .

$$\begin{aligned}\dot{\delta}_1^* &= \frac{j\varepsilon}{2(1+\varepsilon)}(\delta_1^* - \delta_2^*) - \frac{j\varepsilon\sigma(\delta_1^* + \varepsilon\delta_2^*)}{2(1+\varepsilon)} \\ \dot{\delta}_2^* &= \frac{-\lambda(1+\varepsilon)\delta_2}{2} - \frac{j(\delta_2 - \delta_1)}{2(1+\varepsilon)} + \frac{j\varepsilon\sigma(\delta_1 + \varepsilon\delta_2)}{2(1+\varepsilon)} \\ &\quad + j(1+\varepsilon)|\varphi_{20}|^2\delta_2 + \frac{j(1+\varepsilon)}{2}\varphi_{20}^2\delta_2^*\end{aligned}$$

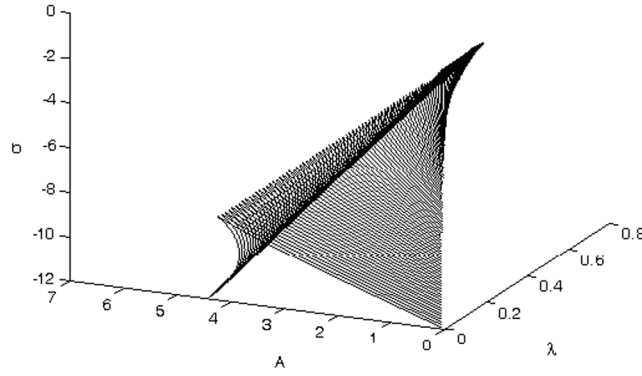


Fig. 6.5 Surface of the SN bifurcations for negative values of detuning σ .

$$\begin{aligned} \dot{\delta}_2^* = & \frac{-\lambda(1+\varepsilon)\delta_2^*}{2} + \frac{j(\delta_2^* - \delta_1^*)}{2(1+\varepsilon)} - \frac{j\varepsilon\sigma(\delta_1^* + \varepsilon\delta_2^*)}{2(1+\varepsilon)} \\ & - j(1+\varepsilon)|\varphi_{20}|^2\delta_2^* - \frac{j(1+\varepsilon)}{2}\varphi_{20}^{*2}\delta_2 \end{aligned} \quad (6.12)$$

where asterisk denotes complex conjugate. The characteristic polynomial of the linearized system (6.12) is given by

$$\mu^4 + \gamma_1\mu^3 + \gamma_2\mu^2 + \gamma_3\mu + \gamma_4 = 0 \quad (6.13)$$

with

$$\begin{aligned} |\varphi_{20}| = N_{20}, \quad \gamma_1 = \lambda(1+\varepsilon), \quad \gamma_3 = \lambda\varepsilon(\varepsilon\sigma^2 + 1)/4, \\ \gamma_2 = \left(\frac{3\varepsilon}{2} + \frac{3}{4} + \frac{3\varepsilon^3}{4} \right) N_{20}^4 + (\varepsilon^2\sigma - 1)N_{20}^2 + \frac{(\varepsilon + 1)^2\lambda^2 + (\varepsilon^2\sigma^2 + 1)}{4}, \\ \gamma_4 = \frac{3\varepsilon^2(1-\sigma)^2}{16}N_{20}^4 + \frac{\varepsilon^2\sigma(1-\sigma)}{4}N_{20}^2 + \frac{\varepsilon^2[(1-\sigma)^2\lambda^2 + \sigma^2]}{16} \end{aligned} \quad (6.14)$$

We note that the amplitude N_{20} provides the first-order approximation for the amplitude of steady state periodic oscillation of the relative response $w = y_1 - y_2$ [i.e., the displacement between the linear oscillator and the NES – see equations (6.1)]. *This amplitude is directly related to the efficiency of steady state TET* in the system considered, since as discussed in previous chapters the capacity of the NES to passively absorb and locally dissipate a significant portion of the energy of the linear oscillator is directly tied to the relative response w attaining large amplitudes. Indeed, large amplitudes of the relative response w signifies resonance interaction of the NES with the linear oscillator (which is a prerequisite for TET), and, in addition, it guarantees that the damping element coupling the NES to the linear oscillator strongly dissipates vibration energy at steady state.

Returning now to the variational system (6.12), a generic Hopf bifurcation in the slow flow (6.4) occurs at points where the characteristic polynomial possesses a pair of pure imaginary roots,

$$\mu = \pm j\Omega \quad (6.15)$$

where Ω is scalar denoting approximately the characteristic frequency of the periodic orbit that is generated from the bifurcating fixed point. Clearly, this periodic orbit of the slow flow modulations (6.4) corresponds to a torus of the full dynamical system (6.1). Before proceeding to study the occurrence of Hopf bifurcations in the slow flow we mention that the linearized variational equations (6.12–6.14) can also be employed to recover the previous boundaries for SN bifurcations in parameter space. Indeed, SN bifurcations of fixed points of the slow flow (6.4) correspond to points where roots of the characteristic polynomial (6.13) are real and change sign from negative to positive as the system parameters change. This provides an alternative way for studying SN bifurcations in the steady state dynamics.

Returning now to our study of Hopf bifurcations, substituting (6.15) into the characteristic polynomial (6.13) and splitting the resulting expression into real and imaginary parts, we obtain expressions for the boundary of Hopf bifurcation in parameter space and for estimating the characteristic frequency Ω :

$$\begin{aligned} \gamma_3^2 - \gamma_2\gamma_3\gamma_1 + \gamma_4\gamma_1^2 &= 0 \\ \Omega^2 = \frac{\gamma_3}{\gamma_1} &\Rightarrow \Omega = \pm \frac{1}{2} \left(\frac{\varepsilon^2\sigma^2 + \varepsilon}{1 + \varepsilon} \right)^{1/2} \end{aligned} \quad (6.16)$$

Additional algebraic manipulations reduce the first of expressions (6.16) in the following simpler form, in terms of the amplitude $Z = N_{20}^2$,

$$v_1 Z^2 + v_2 Z + v_3 = 0 \quad (6.17)$$

where the coefficients in (6.17) are given by

$$\begin{aligned} v_1 &= -\frac{3}{8}\varepsilon^4\sigma^2\lambda^2 - \frac{3}{8}\varepsilon^2\sigma\lambda^2 - \frac{3}{4}\varepsilon^3\sigma\lambda^2 - \frac{3}{16}\lambda^2\varepsilon^5\sigma^2 - \frac{3}{16}\lambda^2\varepsilon^3 \\ &\quad - \frac{3}{8}\varepsilon^4\sigma\lambda^2 - \frac{3}{16}\lambda^2\varepsilon - \frac{3}{8}\lambda^2\varepsilon^2 - \frac{3}{16}\varepsilon^3\sigma^2\lambda^2 \\ v_2 &= \frac{1}{4}\lambda^2\varepsilon - \frac{1}{4}\lambda^2\varepsilon^4\sigma^3 - \frac{1}{4}\varepsilon^4\sigma^2\lambda^2 + \frac{1}{4}\varepsilon^2\sigma\lambda^2 + \frac{1}{4}\varepsilon^3\sigma\lambda^2 \\ &\quad - \frac{1}{4}\lambda^2\varepsilon^5\sigma^3 + \frac{1}{4}\lambda^2\varepsilon^2 - \frac{1}{4}\varepsilon^3\sigma^2\lambda^2 \\ v_3 &= \frac{1}{8}\varepsilon^3\sigma^2\lambda^2 - \frac{1}{16}\lambda^2\varepsilon - \frac{1}{8}\lambda^4\varepsilon^4\sigma - \frac{1}{16}\lambda^4\varepsilon^3 - \frac{1}{16}\lambda^4\varepsilon \\ &\quad - \frac{1}{8}\lambda^4\varepsilon^2 - \frac{1}{16}\lambda^2\varepsilon^5\sigma^4 - \frac{1}{8}\lambda^4\varepsilon^4\sigma^2 - \frac{1}{16}\lambda^4\varepsilon^5\sigma^2 - \frac{1}{16}\lambda^4\varepsilon^3\sigma^2 \end{aligned}$$

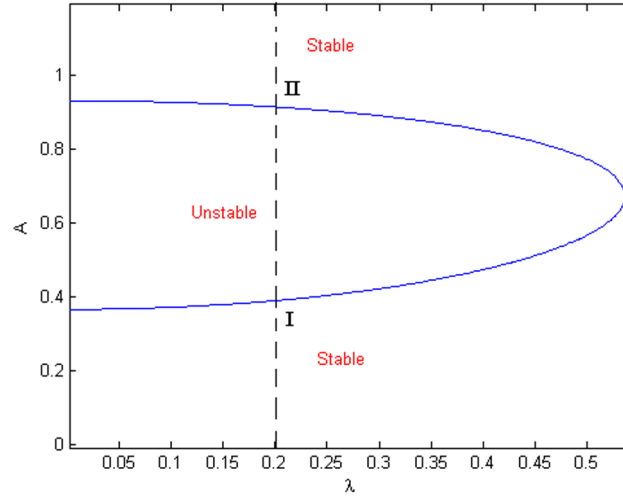


Fig. 6.6 Curves of Hopf bifurcations for $\sigma = 0.5$ and $\varepsilon = 0.05$ (no SN bifurcations exist for the parameter values chosen); points I and II refer to the bifurcation points of Figure 6.7.

$$-\frac{1}{8}\lambda^4\varepsilon^2\sigma - \frac{1}{4}\lambda^4\varepsilon^3\sigma$$

In addition to (6.17), the amplitude Z should also satisfy (6.7). Eliminating Z from these two equations, we obtain the following Hopf bifurcation boundaries in parameter space, which also provide the boundaries of stability exchange of the fixed points of the slow flow (6.4):

$$\begin{aligned}\alpha_1 Z_1 + \alpha_2 Z_1^2 + \alpha_3 Z_1^3 + \alpha_4 &= 0 \\ \alpha_1 Z_2 + \alpha_2 Z_2^2 + \alpha_3 Z_2^3 + \alpha_4 &= 0\end{aligned}\quad (6.18)$$

At points where Hopf bifurcations are realized the bifurcating fixed points are computed by the expression:

$$Z_{1,2} = \frac{(-v_2 \mp \sqrt{v_2^2 - 4v_3v_1})}{2v_1}\quad (6.19)$$

The region in parameter space of unstable fixed points of the slow flow (6.4) is bounded by the two boundaries given by (6.18). In Figure 6.6 we depict the projection of the stability boundary (or boundary of Hopf bifurcations) to the (λ, A) parameter plane for fixed values of σ and ε .

By now we have established the boundaries in three-dimensional parameter space (A, λ, σ) where SN and Hopf bifurcations of the slow flow (6.4) are realized. However in cases where more than one periodic solutions co-exist for the same set of system parameters some uncertainty remains, as to which of these solutions under-

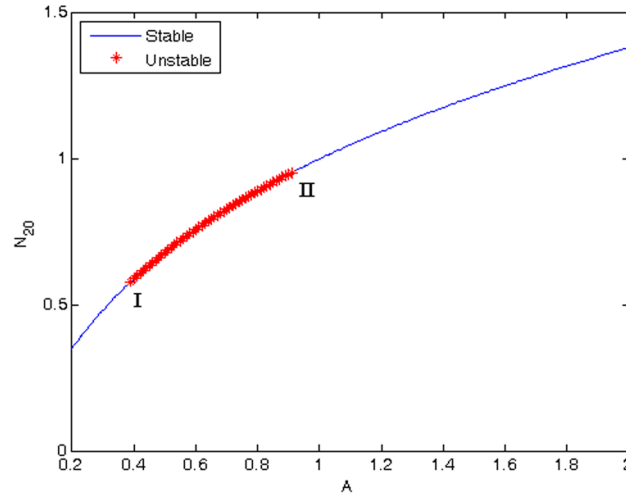


Fig. 6.7 Hopf bifurcations for the case of a single periodic solution of (6.4), for $\lambda = 0.2, \sigma = 0.5$, $\varepsilon = 0.05$; no SN bifurcations exist for these parameter values.

goes the bifurcation. In order to address this issue and thus complete the analysis, we need to combine the previously computed bifurcation results in a single plot. One way to present these results is the plot of Figure 6.7, where the amplitude of the periodic solution $N_{20} = \sqrt{Z}$ is depicted as function of the amplitude of the external harmonic excitation A for fixed values of the detuning σ , the damping λ and the NES mass ε . An alternative way is the combined bifurcation diagram of Figure 6.8 [which also depicts the boundaries of stability of the steady state periodic solution of (6.1)] where the SN and Hopf bifurcation curves are presented in the parameter plane (A, λ) for fixed values of the detuning σ and the NES mass ε . Additional bifurcation results for several parameter values are depicted in Figures 6.8–6.11.

The bifurcation results presented at Figures 6.6–6.11 require some further discussion. Considering the bifurcation diagram of Figure 6.6, the region within the boundaries of Hopf bifurcations relates to the unstable periodic solutions of the slow flow (6.4), whereas the region outside these boundaries relates to stable ones. The bifurcation diagram presented in Figure 6.7 depicts Hopf bifurcations for the case where there exists a single branch of periodic solutions of the slow flow (6.4), and corresponds to the ‘slice’ for $\lambda = 0.2$ of the diagram of Figure 6.6. Considering now the boundaries for Hopf bifurcation depicted in Figure 6.8, we note that they lie inside the region where three periodic solutions exist due to SN bifurcations. In order to determine which of these periodic solutions exhibits Hopf bifurcations we construct the bifurcation diagram of Figure 6.9, from which it becomes clear that it is the low-amplitude branch of the periodic solutions. Indeed, the resulting unstable region of the low branch of solutions refers to the internal region of the Hopf bifurcation boundary presented in Figure 6.8 for damping value $\lambda = 0.2$. The interior instability region between two SN bifurcation boundaries of Figure 6.8

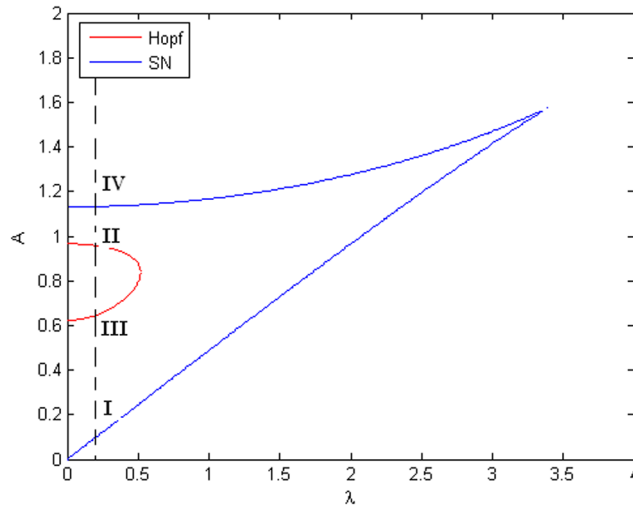


Fig. 6.8 Curves of Hopf and SN bifurcations on the plane (λ, A) for $\sigma = 1.2$ and $\varepsilon = 0.05$; points I–IV refer to the bifurcation points of Figure 6.9.

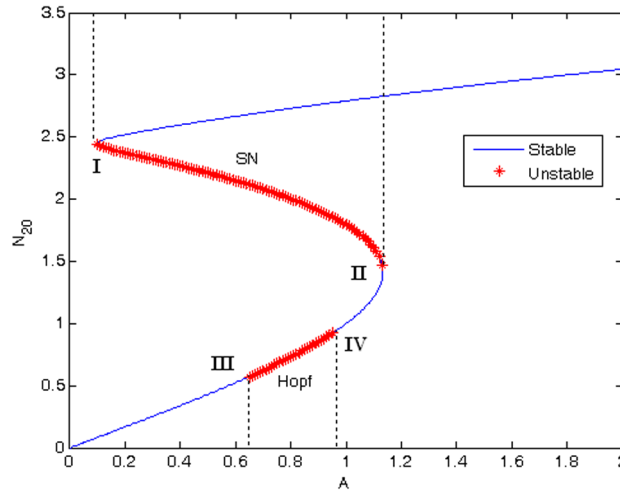


Fig. 6.9 Hopf and SN bifurcations for the case of co-existing periodic solutions of (6.4), for $\lambda = 0.2$, $\sigma = 1.2$, $\varepsilon = 0.05$.

corresponds to the instability region of the middle-amplitude solution branch in Figure 6.9 for the same value of the damping. It should be mentioned that for $\lambda = 0.2$ the large-amplitude branch of periodic solutions remains always stable for the parameter ranges considered in the plot.

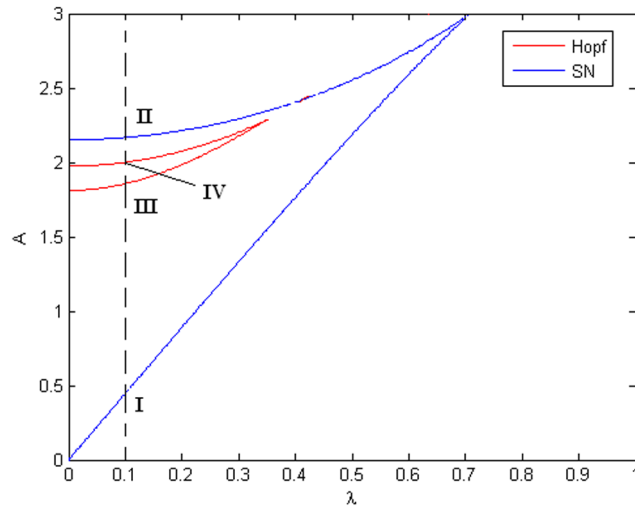


Fig. 6.10 Curves of Hopf and SN bifurcations on the plane (λ, A) for $\sigma = 5$ and $\varepsilon = 0.05$; points I–IV refer to the bifurcation points of Figure 6.11.

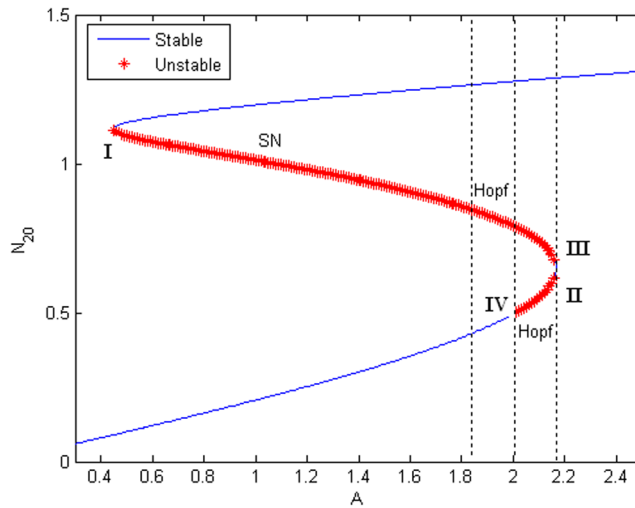


Fig. 6.11 Hopf and SN bifurcations for the case of co-existing periodic solutions of (6.4), for $\lambda = 0.1$, $\sigma = 5$, $\varepsilon = 0.05$.

The last set of bifurcation diagrams (Figures 6.10 and 6.11) for $\sigma = 0.5$ is qualitatively different from the previous cases, since in this case both the low- and middle-amplitude branches of periodic solutions undergo Hopf bifurcations. Indeed the Hopf bifurcations in this case bring a qualitatively new kind of loss of stability as predicted by the stability boundaries of Figure 6.10. Thus, the lower boundary

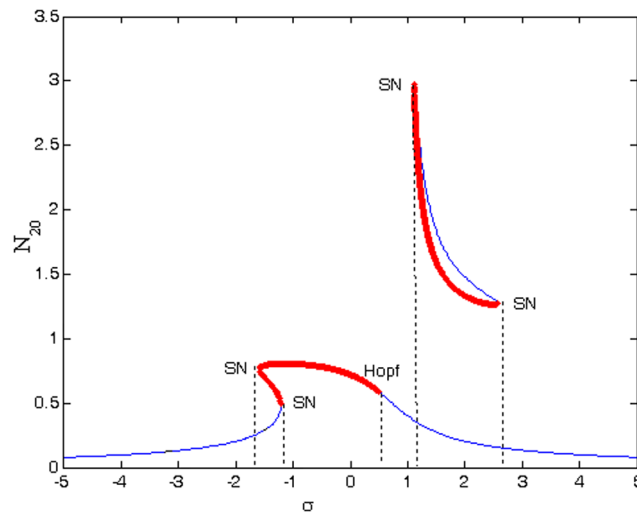


Fig. 6.12 Frequency response diagram (fundamental resonance plot) for $A = 0.4$, $\lambda = 0.2$ and $\varepsilon = 0.01$; bold lines refer to unstable regions of periodic solutions, and thin lines to stable regions (SN and Hopf bifurcations are also noted).

of Hopf bifurcations in Figure 6.10 corresponds to Hopf bifurcations of the middle branch of periodic solutions of the slow flow, whereas the upper boundary in Figure 6.10 is related to bifurcations of the lower branch of periodic solutions. It is essential to note that the both branches coalesce at the fold point ($A\ddot{Y}2.18$ for $\sigma = 0.5$).

Additional important information concerning the local bifurcations of the periodic solutions of the slow flow (6.4) may be obtained by constructing *frequency response diagrams*; these depict the amplitude $N_{20} = \sqrt{Z}$ of the steady state periodic solution as function of the detuning parameter σ , for fixed values of the amplitude of external forcing A , damping λ , and NES mass ε . In Figure 6.12 we present a representative frequency response diagram, with bifurcation points and stability types of branches of solutions also marked in that diagram. Recalling the assumptions of the analysis, the depicted frequency response provides an *approximate fundamental resonance plot* of system (6.1). Although plots of this type do not convey much new information compared to the previously considered bifurcation diagrams, they are directly applicable to the problem of vibration isolation since they depict the amplitudes of steady state responses in the frequency domain. We postpone discussion of the issue of vibration isolation until Section 6.3. Regarding the frequency response of Figure 6.12 we only mention at this point that there exists an upper stable branch of steady state periodic solutions, corresponding to large-amplitude stable periodic oscillations of the NES relative to the linear oscillator; this branch co-exists with a stable low-amplitude branch of periodic responses corresponding to low-amplitude relative oscillations. Additional examples of frequency response diagrams are presented in later sections.

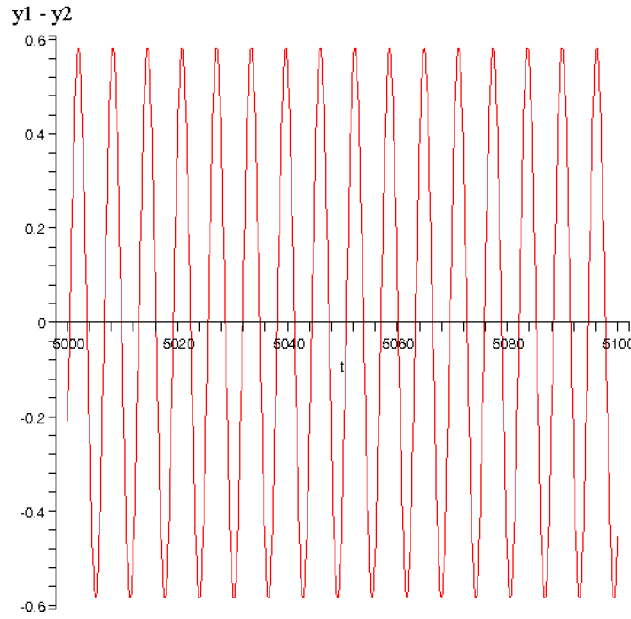


Fig. 6.13 Relative response $y_1(t) - y_2(t)$ of system (6.1) for $A = 0.225$, $\lambda = 0.2$, $\varepsilon = 0.05$ and $\sigma = 0$; initial conditions are $y_1(0) = 0.29$, $\dot{y}_1(0) = 0.25$, $y_2(0) = 0$, and $\dot{y}_2(0) = -0.15$.

Summarizing, the presented analysis indicates that there exist four types of bifurcations of equilibrium points of the slow flow (6.4); namely, SN bifurcations in the domain of existence of three equilibrium points; Hopf bifurcations in the domain of existence of a single equilibrium point; Hopf bifurcation of one equilibrium point in the domain of existence of three equilibrium points; and Hopf bifurcations of two equilibrium points in the domain of existence of three equilibrium points. Of course, all these scenarios are different combinations of the two generic co-dimension 1 bifurcations, namely SN and Hopf bifurcations. We note that equilibrium points of the slow flow (6.4) correspond to periodic solutions of the original dynamical system (6.1), whereas periodic orbits generated (or eliminated) by Hopf bifurcations of equilibrium points of the slow flow correspond to periodic or quasi-periodic oscillations on two-tori of the original system. A periodic or quasi-periodic oscillation on a bifurcating two-torus corresponds to rational or irrational ratio, respectively, of the frequency of the bifurcating periodic solution of the slow flow and the basic ‘fast’ frequency – taken as unity, see *ansatz* (6.3) – of the dynamics.

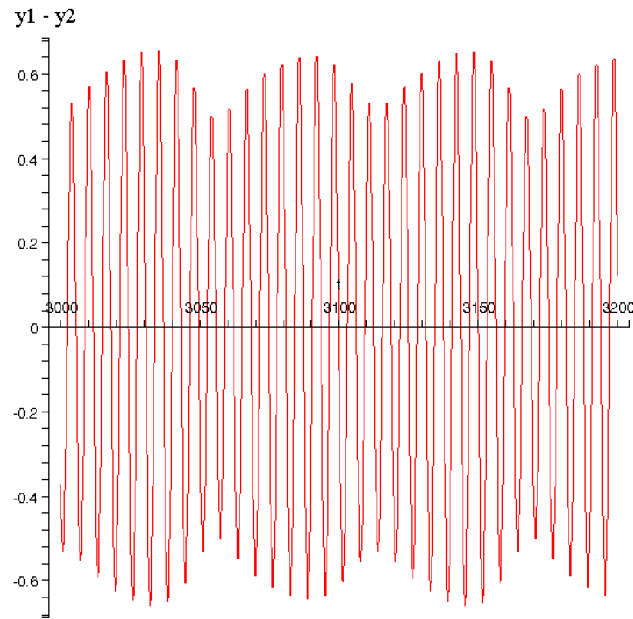


Fig. 6.14 Relative response $y_1(t) - y_2(t)$ of system (6.1) for $A = 0.24$, $\lambda = 0.2$, $\varepsilon = 0.05$ and $\sigma = 0$; initial conditions are $y_1(0) = 0.29$, $\dot{y}_1(0) = 0.25$, $y_2(0) = 0$, and $\dot{y}_2(0) = -0.15$.

6.1.2 Numerical Verification of the Analytical Results

As explained in detail in Section 2.4, the use of the CX-A approach for the analytical treatment of essentially nonlinear systems assumes that the approximation (which is formally justified only for weakly nonlinear systems), will remain correct in the limit when the small parameter of the problem becomes of order unity. This assumption requires additional verification. In order to achieve this goal, we perform direct numerical simulations of the initial system (6.1) and verify independently the predictions of the analysis. The response regimes for certain sets of parameters are presented in Figures 6.13 and 6.14.

For the parameter values used for the numerical simulations of Figure 6.13, equation (6.8) reduces to the simple form $0.04Z + Z^3 = 0.224^2$, which yields the single real solution $N_{20} = \sqrt{Z} = 0.577$. This value is in agreement with the amplitude of the numerical solution depicted in Figure 6.13. Moreover, the conditions (6.17) suggest that the combination of the parameters used for this particular simulation corresponds to a stable periodic solution [i.e., to a stable fixed point of the slow flow equations (6.4)], which again is in agreement with the findings of the numerical simulation.

The parameters for the simulation depicted in Figure 6.14 were selected in order to study the response in the zone where the analysis predicts that the periodic so-

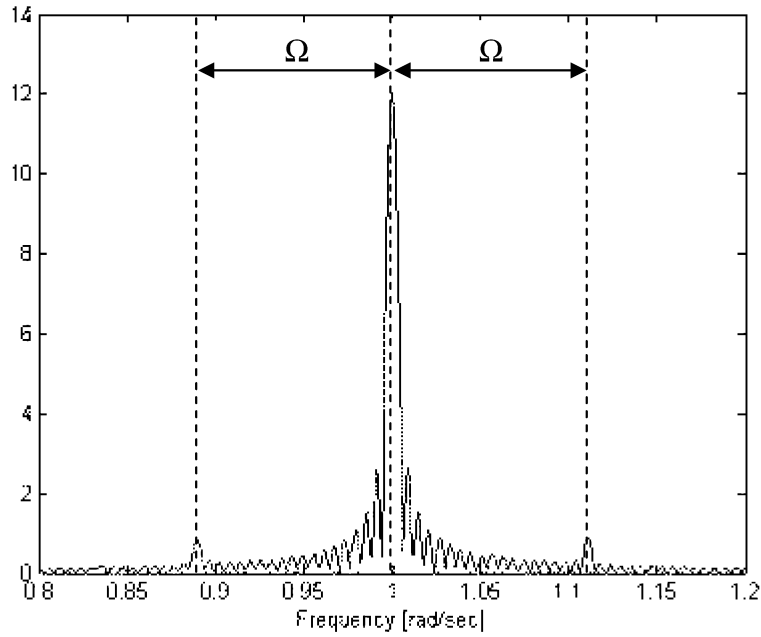


Fig. 6.15 Fast Fourier Transform of the response depicted in Figure 6.14.

lution is unstable. Indeed, the numerical solution is in the form of a quasi-periodic oscillation, as evidenced by the slowly modulated fast oscillation of Figure 6.14. For this particular simulation the corresponding point in parameter space is rather close to the boundary of stability; therefore it is reasonable to suggest that the modulation frequency should be close to the characteristic frequency Ω at the point of Hopf bifurcation. According to the second of relations (6.16), this value is predicted as $\Omega = 0.109$. In order to measure this frequency numerically, we perform Fast Fourier Transform (FFT) of the response presented in Figure 6.14 and obtain the frequency spectrum depicted in Figure 6.15. We deduce that, in addition to the main peak corresponding to the response at the excitation frequency (i.e., the ‘fast’ oscillation equal to unity), the FFT spectrum possesses a pair of secondary peaks which are symmetric with respect to the main peak. The distance between each of the two secondary peaks and the main peak corresponds to the modulation frequency. Direct measurement yields the value 0.11, which is in near agreement with the theoretical prediction.

We conclude that the analytic approach presented above yields reliable predictions of the behavior of original forced system (6.1). Moreover, the approach is rather sensitive, since the only difference between the plots of Figures 6.13 and 6.14 is an 8% difference in the forcing amplitude A . Still, this difference brings about qualitatively different responses and the analytic approach succeeds to capture this fact. So, the results of the CX-A technique are reliable and valid, at least in the

regime of fundamental nonlinear resonances, and as long as the slow-fast partition of the dynamics (6.3) (which was a basic assumption of the analysis) is justified.

Still, we should pay attention to the special sets of initial conditions used for producing the responses of Figures 6.13 and 6.14. The reason is that the response under consideration should be close enough to the fixed point of the slow flow, since the analysis presented above is only local. It follows that if the initial conditions are not specially tailored, the flow could be well attracted to alternative response regimes which do not satisfy the assumptions of the analysis, and hence, are not predicted by it. Indeed, it is a well known feature of (forced or unforced) nonlinear dynamical systems that they may possess qualitatively different co-existing solutions; in fact Guckenheimer and Holmes (1983) present examples where chaotic solutions co-exist with arbitrarily many stable or unstable periodic solutions [see discussion on Newhouse sinks and also refer to (Newhouse, 1974)]. It is true that in many harmonically excited systems (especially weakly nonlinear ones) steady state responses such as the ones discussed above (that is, either stable or Hopf-modulated) may be the only types of steady state motions that can be possibly realized by these systems. For the essentially nonlinear system (6.1), however, this is not the case as we proceed to discuss below.

6.2 Strongly Modulated Responses (SMRs)

6.2.1 General Formulation and Invariant Manifold Approach

The last claim made in the previous section is substantiated by performing numerical simulations of the original system (6.1) for the same parameter values used to generate the transient responses depicted in Figures 6.13 and 6.14, but now with zero initial conditions. The results are presented in Figures 6.16 and 6.17, respectively. In both plots we can see a qualitatively new type of response regime involving a *strongly modulated, nearly periodic oscillation*. In the beginning of each cycle the amplitudes of both responses $v = y_1 + \varepsilon y_2$ and $w = y_1 - y_2$ grow slowly. Then, after a certain amplitude threshold is reached, the amplitude of the motion of the center of mass v abruptly decreases, whereas the relative response between the NES and the linear oscillator, w , is excited with subsequent characteristic decay. This process appears to be similar to transient TET realized in an impulsively forced oscillator coupled to an NES, as discussed in Chapter 3; indeed, one form of TET in this type of impulsively forced oscillators was realized through modulated fast oscillations of the relative response between the NES and the linear oscillator. In this case, however, we deal with steady state (periodic) TET caused by periodic external forcing applied to the linear oscillator.

Qualitatively, the regimes of the strongly modulated responses of Figures 6.16 and 6.17 appear to be similar. Still, quantitative differences regarding the envelopes of the responses and the frequencies of the modulations can be discerned, despite the

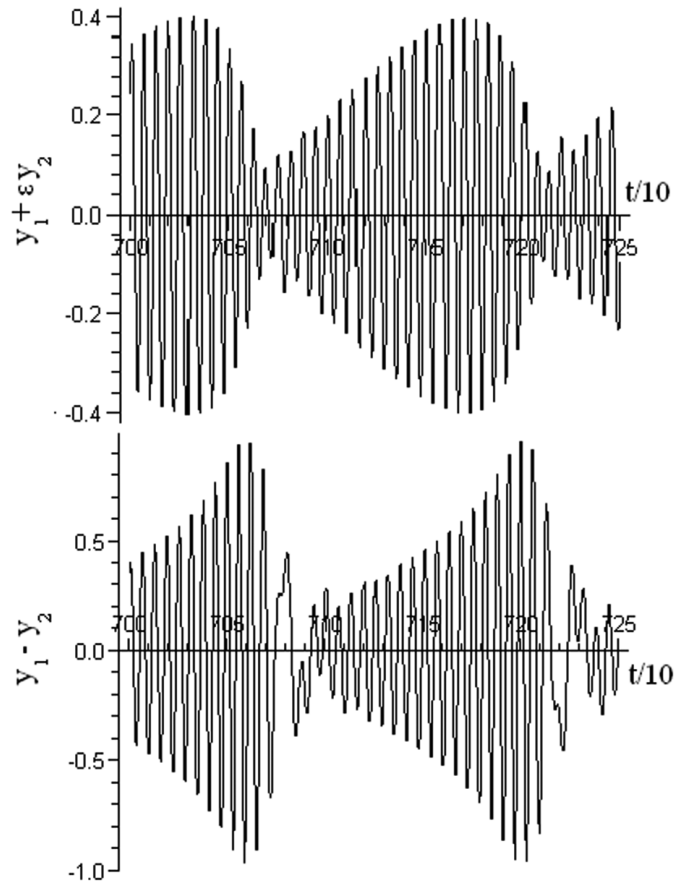


Fig. 6.16 Strongly modulated responses (SMRs) of system (6.1) for $A = 0.225$, $\lambda = 0.2$, $\varepsilon = 0.05$, $\sigma = 0$ and zero initial conditions.

minor differences between the system parameters of the two simulations. Moreover, in the simulations used for computations of responses at Figs. 6.13 and 6.14 the detuning parameter σ was chosen to be zero. From (6.7) it immediately follows that the averaged flow has only one fixed point in both cases, and the responses presented at 6.13 and 6.14 correspond to exactly these fixed points. The results depicted in Figures 6.16 and 6.17 are very different indeed. This means that the system can exhibit steady state response regimes (such as the presented strongly modulated ones) which in principle *can not be captured by local analysis of the fixed points of the averaged flow*.

In order to distinguish this type of steady state response from those derived by the local analysis of the previous sections and related to the fixed (equilibrium) points of the slow flow (6.4), we denote it as a *Strongly Modulated Response (SMR)*. The

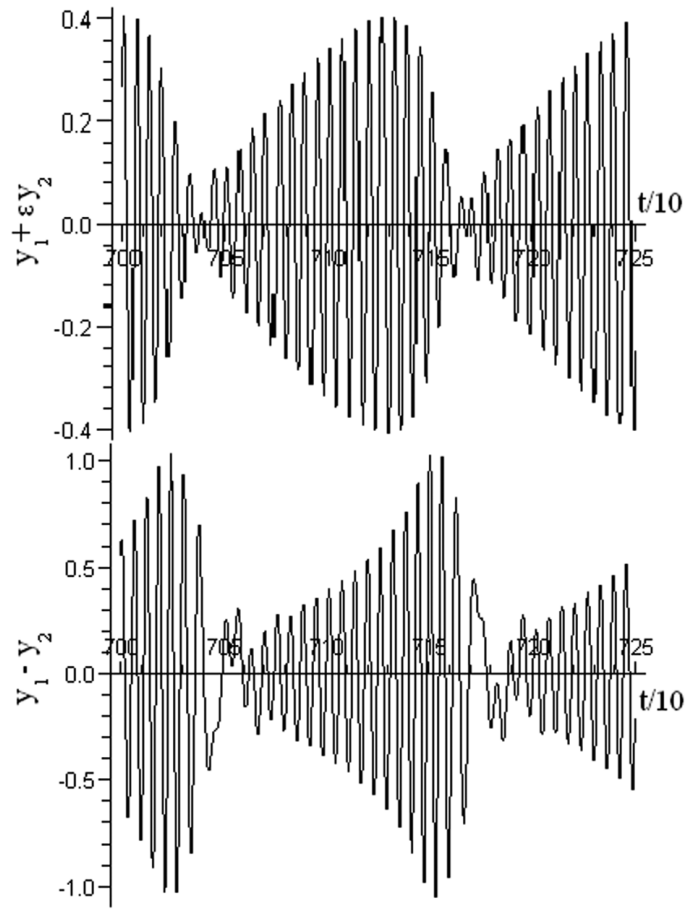


Fig. 6.17 Strongly modulated responses of system (6.1) for $A = 0.24$, $\lambda = 0.2$, $\varepsilon = 0.05$, $\sigma = 0$ and zero initial conditions.

width of the amplitude modulation is equal to the response amplitude, and the analytical treatment of such responses poses distinct challenges. Indeed, as discussed above in order to analyze SMRs local analysis of the slow flow equations (6.4) is insufficient, and, rather *global analysis* of the dynamics is required. In general, such a challenging analytical problem is hardly solvable, since the slow flow (6.4) is essentially nonlinear and evolves in four-dimensional phase space. Still, assuming that the mass ε [which can also be regarded as a mass ratio in the normalized equations (6.1)] is sufficiently small, it may be used as a small parameter for performing singular perturbation analysis. Then, the invariant manifold approach may be applied to analyze SMRs, rather similarly to the procedure outlined in Section ?? Author, Section 3.4.4 does not exist for the unforced case. It should be mentioned that

in the local analysis of the previous sections the smallness of ε was not required and not assumed.

We begin the analysis of SMRs by combining the two first-order equations of the slow flow system (6.4) through simple manipulations, and reducing the slow flow to the following single second-order complex ordinary differential equation:

$$\begin{aligned} \frac{d^2\varphi_2}{dt^2} + \frac{d}{dt} \left[\alpha\varphi_2 - \frac{j(1+\varepsilon)}{2} |\varphi_2|^2 \varphi_2 + \frac{j\varepsilon(1-\sigma)}{2(1+\varepsilon)} \varphi_2 \right] \\ + \frac{j\varepsilon(1-\sigma)}{2(1+\varepsilon)} \left[\alpha\varphi_2 - \frac{j(1+\varepsilon)}{2} |\varphi_2|^2 \varphi_2 - \frac{\varepsilon A}{2} \right] - \frac{j\varepsilon\beta(1+\varepsilon\sigma)}{2(1+\varepsilon)} \varphi_2 = \frac{\varepsilon A\beta}{2} \end{aligned} \quad (6.20)$$

where

$$\alpha = \frac{\lambda(1+\varepsilon)^2 + j(1-\varepsilon^2\sigma)}{2(1+\varepsilon)} \quad \beta = \frac{j(1+\varepsilon\sigma)}{2(1+\varepsilon)}$$

In the sequence, we perform a multiple scales analysis of the response of (6.20) by introducing the new independent time scales $\tau_k = \varepsilon^k t$, $k = 0, 1, \dots$ (where τ_0 is the leading-order time scale, and τ_1, τ_2, \dots are slow scales of increasing order), and expressing the response and the time derivatives in (6.20) as follows:

$$\begin{aligned} \varphi_2 = \varphi_2(\tau_0, \tau_1, \dots) \\ \frac{d}{dt} = \frac{\partial}{\partial \tau_0} + \varepsilon \frac{\partial}{\partial \tau_1} + \dots, \quad \frac{d^2}{dt^2} = \frac{\partial^2}{\partial \tau_0^2} + 2\varepsilon \frac{\partial^2}{\partial \tau_0 \partial \tau_1} + \dots \end{aligned} \quad (6.21)$$

Substituting (6.21) into (6.20) and setting equal to zero the coefficients of powers of ε , we derive the following hierarchy of problems at successive orders of approximation:

$$O(\varepsilon^0) : \frac{\partial^2 \varphi_2}{\partial \tau_0^2} + \frac{\partial}{\partial \tau_0} \left[\frac{\lambda \varphi_2}{2} + \frac{j \varphi_2}{2} - \frac{j}{2} |\varphi_2|^2 \varphi_2 \right] = 0 \quad (6.22a)$$

$$\begin{aligned} O(\varepsilon^1) : 2 \frac{\partial^2 \varphi_2}{\partial \tau_0 \partial \tau_1} + \frac{\partial}{\partial \tau_1} \left[\frac{\lambda \varphi_2}{2} + \frac{j \varphi_2}{2} - \frac{j}{2} |\varphi_2|^2 \varphi_2 \right] + \frac{(1-\sigma)}{4} |\varphi_2|^2 \varphi_2 \\ + \frac{\partial}{\partial \tau_0} \left[\frac{\lambda \varphi_2}{2} + \frac{j(1-\sigma)\varphi_2}{2} - \frac{j}{2} |\varphi_2|^2 \varphi_2 \right] + \left[\frac{\sigma}{4} + \frac{j\lambda(1-\sigma)}{4} \right] \varphi_2 - \frac{jA}{4} = 0 \\ \bullet \quad \bullet \quad \bullet \end{aligned} \quad (6.22b)$$

Equation (6.22a) describes the leading-order approximation of the evolution of the slow flow (averaged) dynamics. This equation can be trivially integrated,

$$\frac{\partial}{\partial \tau_0} \varphi_2 + \left(\frac{j}{2} \varphi_2 + \frac{\lambda}{2} \varphi_2 - \frac{j}{2} |\varphi_2|^2 \varphi_2 \right) = C(\tau_1, \tau_2, \dots) \quad (6.23)$$

where $C(\tau_1, \tau_2, \dots)$ is an arbitrary function of higher-order time scales. Higher-order time scales are not considered in the current analysis, since as shown below the dynamical phenomena in question are captured by the leading-order approximations (6.22a,b); hence, for the sake of brevity only the dependences on the time scales τ_0 and τ_1 will be denoted explicitly in the following analysis. It follows that the fixed (equilibrium) points of (6.23) with respect to the time scale τ_0 are denoted by and obey the following algebraic equation:

$$\frac{j}{2}\Phi(\tau_1) + \frac{\lambda}{2}\Phi(\tau_1) - \frac{j}{2}|\Phi(\tau_1)|^2\Phi(\tau_1) = C(\tau_1) \quad (6.24)$$

Equation (6.24) can be solved in closed form by expressing the fixed points in polar form, i.e., $\Phi(\tau_1) = N(\tau_1)\exp[j\theta(\tau_1)]$, and substituting in (6.24) to derive the following real equation for the amplitude of the fixed point:

$$\lambda^2 N^4(\tau_1) + [N^2(\tau_1) - N^4(\tau_1)]^2 = 4|C(\tau_1)|^2 N^2(\tau_1) \quad (6.25a)$$

Introducing the new variable $Z(\tau_1) = N^2(\tau_1)$, (6.25a) is expressed in the form

$$\lambda^2 Z(\tau_1) + Z(\tau_1)[1 - Z(\tau_1)]^2 = 4|C(\tau_1)|^2 \quad (6.25b)$$

which is a cubic polynomial amenable to explicit solutions. Once $Z(\tau_1)$ is computed, the corresponding phase $\theta(\tau_1)$ of the fixed point is evaluated by the following expression:

$$\theta(\tau_1) = \arg C(\tau_1) - \tan^{-1} \left[\frac{1 - Z(\tau_1)}{\lambda} \right] \quad (6.26)$$

The number of real and positive solutions of the cubic equation (6.25b) depends on the values of the ‘parameters’ $|C(\tau_1)|$ and λ . The homogeneous part of equation (6.25b) can be either monotonous or it may possess a maximum and a minimum. In the former case the variation of $|C(\tau_1)|$ has no effect on the number of solutions, and equation (6.25b) possesses a single positive solution. In the latter case, however, the variation of $|C(\tau_1)|$ will generate a saddle-node (SN) bifurcation of fixed points, where a new stable-unstable pair of positive fixed points is generated. In order to distinguish between these two cases we should check whether the derivative of the homogeneous part of (6.25b) with respect of Z has any real roots:

$$\frac{\partial}{\partial Z} [\lambda^2 Z + Z[1 - Z]^2] = 0 \Rightarrow Z_{1,2} = \frac{2 \mp \sqrt{1 - 3\lambda^2}}{3} \quad (6.27)$$

From this result it follows that for $\lambda < 1/\sqrt{3}$ (i.e., for relatively weak damping) two roots of the homogeneous problem are generated through a SN bifurcation; at the critical value $\lambda = 1/\sqrt{3}$ these roots coalesce, and are non-existent for $\lambda > 1/\sqrt{3}$. This is the typical structure of a cusp, with the value $\lambda = 1/\sqrt{3}$ representing the critical damping value. Of course, the results of the present analysis at $O(1)$ are similar to those reported in Section 3.4.2.4 – the only difference being that the external forcing terms appear at higher orders of approximation.

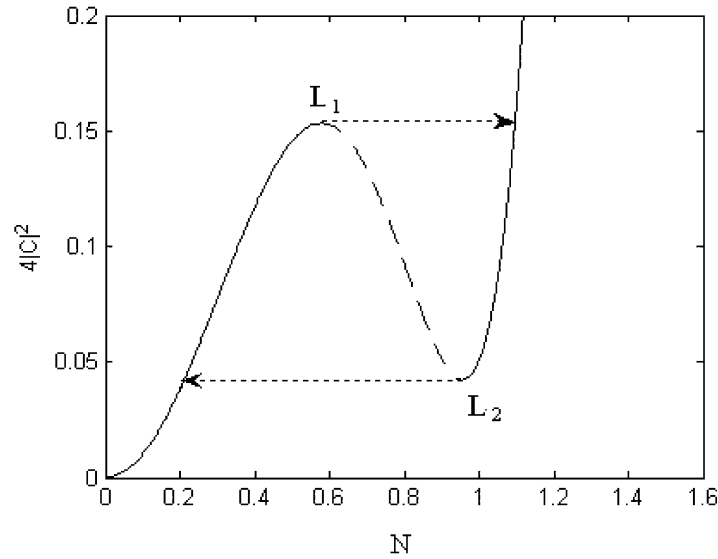


Fig. 6.18 Projection of the slow invariant manifold of the system (SIM) for $\lambda = 0.2$; the unstable branch is denoted by dashed line, and arrows denote hypothetical transitions (jumps) in the regime of relaxation oscillations.

It is easy to show through equation (6.23) that if a single fixed point of (6.25b) exists, it is stable (in the form of a node) with respect to the leading-order time scale τ_0 . If there are three fixed points, two of them are stable (nodes) and one is unstable (a saddle point). Therefore at the leading-order approximation governed by the time scale τ_0 the dynamics of the slow flow (6.4) will be attracted to either one of these nodes. In fact, equation (6.24) defines a two-dimensional *slow invariant manifold (SIM)* of the dynamics. In the case $\lambda < 1/\sqrt{3}$ the fold lines $L_{1,2} = \{N(\tau_1) = \sqrt{Z_{1,2}}, \theta(\tau_1) \in [0, 2\pi)\}$ divide the stable and unstable branches of the SIM. In Figure 6.18 we depict the projection of the two-dimensional SIM on the plane (N, C) ; the fold lines correspond to the local maximum and minimum points of the SIM.

It is well-known (Arnold et al., 1994; Guckenheimer et al., 2005; Guckenheimer et al., 2006) that such a folding structure of the SIM may give rise to *relaxation-type oscillations*, characterized by sudden transitions (jumps) of the response during each cycle (the hypothetic sudden transitions between the two stable branches are denoted by arrows at Figure 6.18). *We conjecture that such relaxation oscillations occur in the SMRs described above.* Still, such motions may be possible only if the dynamical flow can reach the fold lines $L_{1,2}$, while following the two branches of the SIM with respect to the slow time scale τ_1 .

In order to assess this possibility one should investigate the behavior of the flow on the SIM given by $\Phi(\tau_1)$. To this end, we consider the $O(\varepsilon)$ supproblem (6.22b) derived by the multiple scales expansion. In particular, we are interested in the be-

havior of the solution on the stable branches of the SIM in the limit at the fast time scale τ_0 tends to infinity, i.e., the limit $\Phi(\tau_1) = \lim_{\tau_0 \rightarrow +\infty} \varphi_2(\tau_0, \tau_1)$. Considering equation (6.22b) in the limit $\tau_0 \rightarrow +\infty$, and taking into account the asymptotic stability of points on the stable branches with respect to time scale τ_0 , we obtain the following equation for motion *on* the SIM governed by the slow time scale τ_1 :

$$\frac{\partial}{\partial \tau_1} \left[\frac{\lambda \Phi}{2} + \frac{i \Phi}{2} - \frac{j}{2} |\Phi|^2 \Phi \right] + \frac{(1-\sigma)}{4} |\Phi|^2 \Phi + \left[\frac{\sigma}{4} + \frac{j\lambda(1-\sigma)}{4} \right] \Phi - \frac{jA}{4} = 0 \quad (6.28)$$

Equation (6.28) can be written in compact form as follows:

$$\begin{aligned} \left[\frac{\lambda}{2} - \frac{j}{2} + j |\Phi|^2 \right] \frac{\partial \Phi}{\partial \tau_1} - \frac{j}{2} \frac{\partial \Phi}{\partial \tau_1} \Phi^2 &= G \\ G &= -\frac{1-\sigma}{4} |\Phi|^2 \Phi - \left[\frac{\sigma}{4} + \frac{j\lambda(1-\sigma)}{4} \right] \Phi + \frac{jA}{4} \end{aligned} \quad (6.29)$$

Adding to (6.29) its complex conjugate and performing the necessary algebraic manipulations it is possible to extract the following closed form expression for the evolution of the slow dynamics on the SIM with respect to the slow time scale τ_1 :

$$\frac{\partial \Phi}{\partial \tau_1} = \frac{2 [(\lambda - j + 2j |\Phi|^2) G + j \Phi^2 G^*]}{\lambda^2 + 1 - 4 |\Phi|^2 + 3 |\Phi|^4} \quad (6.30)$$

We note that for the particular case of no applied external harmonic force, $A = 0$, the above expression corresponds to TET in the corresponding impulsively forced or unforced system studied by the method of invariant manifolds (up to an insignificant frequency shift – see Section 3.4.2.4). This observation provides further evidence of the relationship between SMRs in the harmonically forced system and TET in the impulsively forced or unforced one. Returning now to relation (6.30) for the harmonically forced system, it is possible to reduce it to the following form:

$$\frac{\partial \Phi}{\partial \tau_1} = \frac{-\lambda \Phi + j \Phi [(1-4\sigma) |\Phi|^2 + \sigma - \lambda^2(1-\sigma) - 3(1-\sigma) |\Phi|^4]}{2 (\lambda^2 + 1 - 4 |\Phi|^2 + 3 |\Phi|^4)} \quad (6.31)$$

Expressing this complex relation in terms of its modulus and phase through the polar transformation $\Phi(\tau_1) = N(\tau_1) \exp[j\theta(\tau_1)]$, we obtain the following dynamical system on the cylinder $(N, \theta) \in (R^+ \times S^1)$ governing the slow evolution on the SIM at time scale τ_1 :

$$\begin{aligned} \frac{\partial N}{\partial \tau_1} &= \frac{-\lambda N}{2 (\lambda^2 + 1 - 4N^2 + 3N^4)} \\ \frac{\partial \theta}{\partial \tau_1} &= \frac{(1-4\sigma)N^2 + \sigma - \lambda^2(1-\sigma) - 3(1-\sigma)N^4}{2 (\lambda^2 + 1 - 4N^2 + 3N^4)} \end{aligned} \quad (6.32)$$

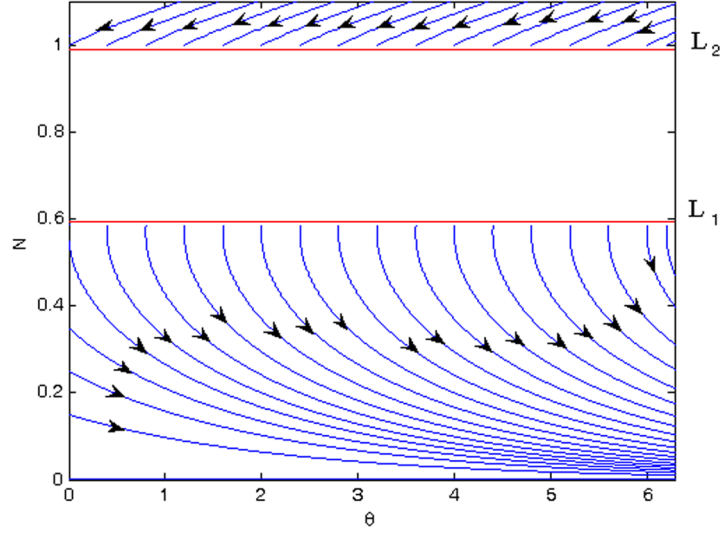


Fig. 6.19 Phase portrait of the slow evolution of the SIM for the case of no external harmonic excitation, $A = 0$.

The phase portrait of system (6.32) is presented at Figure 6.19. It is clear from the first equation of (6.32) that the phase trajectories on the upper stable branch slowly evolve directed towards the fold line L_2 , whereas the trajectories on the lower stable branch are not able to reach the fold line L_1 . This means that although the dynamics can make a sudden transition (jump) from the upper stable branch of the SIM to the lower one, it cannot make a similar transition back. Actually, this ends up as a rather trivial observation since in the absence of external harmonic forcing the dynamics cannot reach a non-trivial steady state regime, as it is damped out by dissipation towards the state of trivial (zero) equilibrium.

In order to allow for jumps from the lower stable branch of the SIM back to the upper one (and, therefore, to provide the necessary condition for the occurrence of relaxation oscillations) the slow flow in the vicinity of L_1 should undergo bifurcation. That is, at some subset of L_1 the orbits of the slow flow lines on the lower branch of the SIM should become tangent to L_1 . Such points correspond to fixed points of a *desingularized* slow flow (Guckenheimer et al., 2006), where the numerator of equation (6.30) vanishes. In order to investigate these special points, one should compute the fixed points of the slow flow equation (6.30) for arbitrary amplitudes of the external harmonic function A . The appropriate condition reads

$$(\lambda - j + 2j|\Phi|^2)G + j\Phi^2 G^* = 0 \quad (6.33)$$

and possesses two sets of solutions (fixed points). The first set is trivial and is computed by setting $G = 0$; this solution corresponds to fixed points of the initial equa-

tion (6.20), i.e., to fixed points of the global flow that (quite naturally) lie on the SIM.

The other set of solutions of (6.33) satisfies the following conditions:

$$\begin{aligned} 3|\Phi|^4 - 4|\Phi|^2 + 1 + \lambda^2 &= 0 \\ \exp(2j \arg G) &= \frac{-j\Phi^2}{\lambda + j(2|\Phi|^2 - 1)} \end{aligned} \quad (6.34)$$

The first equation in (6.34) coincides with the equation for the fold lines; therefore, as expected, the solutions of this type describe the folded singularities of the slow flow. Bifurcations of such singularities correspond to violations of the transversality condition and, therefore, yield qualitative changes of the flow in the vicinity of the fold line. Specifically, these bifurcations result in a switch of the directions of the flow lines and therefore provide the necessary conditions for relaxation oscillations. What is even more interesting is that equations (6.34) may be solved in closed form. Indeed, introducing again the polar transformation $\Phi(\tau_1) = N(\tau_1) \exp[j\theta(\tau_1)]$, (6.34) yields the following solutions for the positions of the singularities on the fold lines L_1 and L_2 :

$$\begin{aligned} L_1 : \quad N_1 &= Z_1^{1/2}, \quad \theta = \Theta_{1,2} \equiv \gamma_{01} \pm \cos^{-1} \left[\frac{\lambda N_1}{A \sqrt{(1 - N_1^2)^2 + \lambda^2}} \right] \\ L_2 : \quad N_2 &= Z_2^{1/2}, \quad \theta = \Theta_{3,4} \equiv \gamma_{02} \pm \cos^{-1} \left[\frac{\lambda N_2}{A \sqrt{(1 - N_2^2)^2 + \lambda^2}} \right] \\ N_{1,2} &= (4/3) \pm [(4/3)^2 - 4(1 + \lambda^2)/3]^{1/2} \\ \gamma_{0k} &= \sin^{-1} \left[\frac{\lambda}{\sqrt{(1 - N_k^2)^2 + \lambda^2}} \right], \quad k = 1, 2 \end{aligned} \quad (6.35)$$

We conclude that for sufficiently weak external harmonic excitations, that is, for amplitudes of the harmonic excitation below the first critical threshold,

$$A < A_{1 \text{ crit}} = \frac{\lambda N_1}{\sqrt{(1 - N_1^2)^2 + \lambda^2}} \quad (6.36a)$$

no bifurcation close to the lower fold line L_1 can occur. Then, the slow flow in the vicinity of both fold lines of the SIM remains qualitatively similar to that depicted in Figure 6.19, providing no possibility for the occurrence of relaxation oscillations (and thus of SMRs) in the slow flow (6.4). As the forcing amplitude approaches the value $A \rightarrow A_{1 \text{ crit}}$ from below, a SN bifurcation occurs at L_1 , as $\theta \rightarrow \gamma_{01}$, and a pair of singularities is formed; in the interval between these points, the flow in the

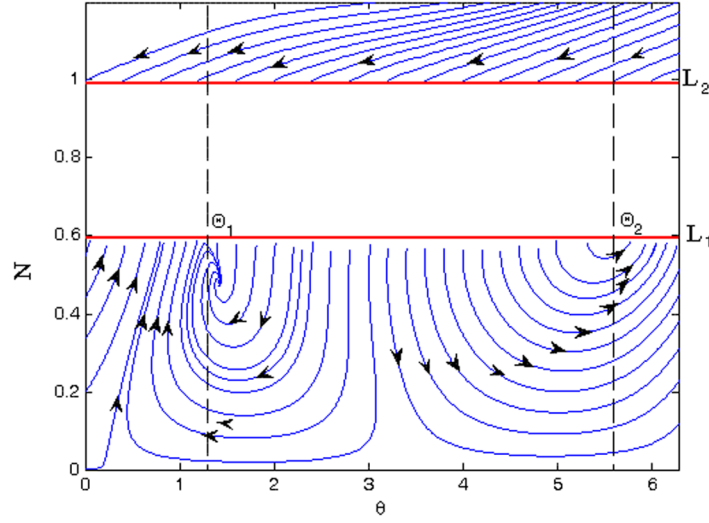


Fig. 6.20 Phase portrait of the slow evolution of the SIM for the case when $A_{1\text{crit}} < A < A_{2\text{crit}}$ and $\sigma = 0.5$; only the stable branches of the SIM are depicted.

vicinity of L_1 reverses direction. A similar SN bifurcation occurs in the neighborhood of the higher fold line L_2 as the amplitude of the external force reaches the second (higher) critical threshold,

$$A \rightarrow A_{2\text{crit}} = \frac{\lambda N_2}{\sqrt{(1 - N_2^2)^2 + \lambda^2}} \quad (6.36b)$$

again from below. The representative phase portrait describing the evolution of the slow flow on the SIM for the amplitude of the external harmonic force in the range $A_{1\text{crit}} < A < A_{2\text{crit}}$ is presented in Figure 6.20. In Figure 6.21 we present the corresponding phase portrait for the case $A > A_{2\text{crit}}$.

From the plots of Figures 6.20 and 6.21 we deduce that after the occurrence of the SN bifurcations close to the fold lines L_1 and L_2 , there exists a subset of orbits on the SIM that carry the flow to L_1 , thus providing the possibility for a jump to the upper stable branch of the SIM, and, hence, to relaxation oscillations. Indeed, the flow can reach the fold L_2 and then jump down again to L_1 , thus closing the loop of the relaxation oscillation and giving rise to the SMRs of the slow flow depicted in Figures 6.16 and 6.17.

It is interesting to note that the previously derived critical thresholds for the amplitude of the harmonic excitation, $A_{1\text{crit}}$ and $A_{2\text{crit}}$, do not depend on the detuning parameter σ . Still one cannot conclude that the SMRs are robust to changes in the detuning parameter, since the condition $A > A_{1\text{crit}}$ is *necessary*, but by no means *sufficient* for the occurrence of SMRs in the slow flow (6.40). In other terms, if this condition is valid then sudden transitions (jumps) between the stable branches of

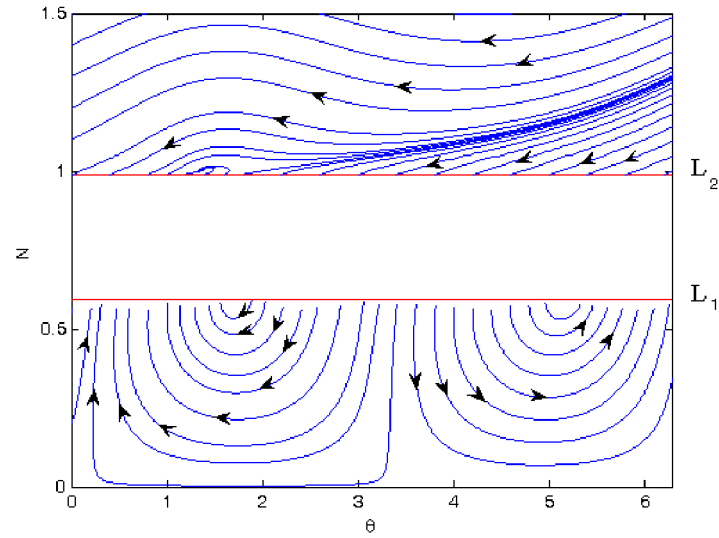


Fig. 6.21 Phase portrait of the slow evolution of the SIM for the case when $A > A_{2\text{crit}}$ and $\sigma = 0.5$; only the stable branches of the SIM are depicted.

the SIM *may occur*, but there is no guarantee that the series of these transitions will accumulate to stable attractors of the slow dynamics in the form of SMRs. In order to obtain the missing sufficient conditions for the occurrence of SMRs one should investigate more delicate aspects of the slow flow dynamics (6.4). This is performed in the next section.

6.2.2 Reduction to One-Dimensional Maps and Existence Conditions for SMRs

Studying carefully the phase portrait depicted in Figure 6.20 we deduce that there exists an interval of θ , namely, $\Theta_1 < \theta < \Theta_2$, where all orbits on the SIM arrive to the fold line L_1 and then depart from it. In the regime of relaxation oscillations, an orbit in the previously constructed phase cylinder $(N, \theta) \in (R^+ \times S^1)$ initially jumps from a point of this interval on L_1 to the upper branch of the SIM; then it slowly evolves following an orbit of the slow flow towards the upper fold line L_2 , before jumping back to the lower stable branch of the SIM; following an orbit of the slow flow it moves towards the lower fold line L_1 reaches it in one of the points of the interval $\theta \in [\Theta_1, \Theta_2]$; following this the orbit jumps up to the upper branch of the SIM and the cycle of the relaxation oscillation (SMR) continues indefinitely.

Therefore, it is natural to consider this relaxation regime in terms of a one-dimensional Poincaré map P of the interval $[\Theta_1, \Theta_2]$ of the fold line L_1 into itself:

$$P : [\Theta_1, \Theta_2] \xrightarrow{P} [\Theta_1, \Theta_2], \theta \rightarrow P(\theta)$$

In the regime of relaxation oscillations (SMRs) this map takes a point on the fold line L_1 of the cylinder $(N, \theta) \in (R^+ \times S^1)$ and maps it into L_1 under the action of the slow flow (6.30). Clearly, a stable SMR will correspond to an attractor of this map (for example, a period- k fixed point), so the conditions for existence of this attractor will provide the necessary and sufficient conditions for existence of the corresponding SMR in the slow flow (6.4), and, hence, also in the original dynamical system (6.1) for NES masse sufficiently small.

In order to construct the one-dimensional map P , we should consider separately its ‘slow’ and ‘fast’ components during a cycle of the relaxation oscillation. As far as the slow components of the map are concerned, these correspond to the parts of the relaxation cycle spent on the lower and the upper stable branches of the SIM. Hence, we may use equations (6.30) and directly connect the ‘exit’ and ‘landing’ points on the fold lines L_1 and L_2 . Due to complexity of the associated expressions, in the following developments the ‘slow’ components of the map P are evaluated numerically.

As for the ‘fast components of the map, it is clear that the function φ_2 should be continuous at the points of transition between the ‘fast’ and the ‘slow’ components. Therefore, to model the jumps which provide the ‘fast’ components of the map we should define appropriately the complex invariant $C(\tau_1)$ defined by equation (6.24). If the value of $C(\tau_1)$ is known at the point of start of the jump (the ‘exit’ point) between the two fold lines, it is possible to compute the amplitude N and phase θ corresponding to the point of ‘landing’ of the jump unambiguously, and thus to complete the definition of the map P . The procedure of numerical integration should be performed twice, however, one for each of the two stable (upper and lower) branches of the SIM; hence, two values for the invariant $C(\tau_1)$ should be computed for each of the two ‘fast’ components of the map in order to determine the ‘landing’ points of the jumps in L_1 and L_2 .

These two fast components correspond to the two jumps between fold lines during each cycle of the relaxation oscillation. Fortunately, these fast elements of the mapping cycle can be written down in closed form. For example, if one knows the values of N and θ at the ‘exit’ point of the jump on the fold line L_1 , say (N_1, θ_{01}) , and denotes the ‘landing’ point on the upper stable branch of the SIM by (N_u, θ_u) , one may compute the value of N_u from the polynomial (6.25b) by exploiting the invariance of $C(\tau_1)$ on the fast component of the jump,

$$\begin{aligned} \lambda^2 Z_1 + Z_1 (1 - Z_1)^2 &= \lambda^2 Z_u + Z_u (1 - Z_u)^2 = \\ &= \frac{2}{27} \left(1 + \sqrt{1 - 3\lambda^2}\right) + \frac{2\lambda^2}{9} \left(3 - \sqrt{1 - 3\lambda^2}\right) \Rightarrow \\ Z_u = N_u^2 &= \frac{2}{3} \left(1 + \sqrt{1 - 3\lambda^2}\right) \end{aligned} \quad (6.37)$$

where $Z_1 = N_1^2$. Then, combining (6.24) and (6.37), one obtains the following explicit expression for the phase variable at the ‘landing’ point of the jump:

$$\begin{aligned}\theta_u &= \tan^{-1} \left[\frac{(N_u^2 - N_1^2) \lambda}{\lambda^2 - (1 - N_1^2)(N_u^2 - 1)} \right] + \theta_{01} \\ &= \theta_{01} + \tan^{-1} \left[\frac{9\lambda\sqrt{1 - 3\lambda^2}}{-1 + 15\lambda^2 - \sqrt{1 - 3\lambda^2}} \right]\end{aligned}\quad (6.38a)$$

Hence, the part of map which corresponds to the jump from the lower fold line L_1 to the upper stable branch of the SIM, is very simple – the amplitude switches to N_u and the phase rotates by a constant angle.

Similarly, the jump from an ‘exit’ point (N_2, θ_{02}) on the upper fold line L_2 to the point (N_d, θ_d) on the lower stable branch of the SIM is described by the following map:

$$\begin{aligned}N_2 &\rightarrow N_d = \sqrt{\frac{2}{3} \left(1 - \sqrt{1 - 3\lambda^2} \right)} \\ \theta_{02} &\rightarrow \theta_d = \tan^{-1} \left[\frac{(N_d^2 - N_2^2) \lambda}{\lambda^2 - (1 - N_d^2)(N_2^2 - 1)} \right] + \theta_{02} \\ &= \theta_{02} - \tan^{-1} \left[\frac{9\lambda\sqrt{1 - 3\lambda^2}}{-1 + 15\lambda^2 + \sqrt{1 - 3\lambda^2}} \right]\end{aligned}\quad (6.38b)$$

It should be stressed that for each point of the interval $[\Theta_1, \Theta_2]$ only one computation is required for a single cycle of the map. The outlined construction of the one-dimensional Poincaré map P is somewhat similar to the procedure developed in Guckenheimer et al. (2006) for analyzing chaotic attractors in regimes of relaxation oscillations occurring in low-dimensional phase spaces. Clearly, not every orbit which starts from the lower fold line L_1 of the SIM will land within the interval $[\Theta_1, \Theta_2]$, since it may be attracted to alternative attractors lying either on the upper or lower stable branches of the SIM. Of course, only those points which are mapped into this interval can carry sustained relaxation oscillations and yield SMRs.

Representative examples of return maps are illustrated in Figures 6.22 and 6.23. The map depicted in Figure 6.22 is defined for all points of the interval $\theta \in [\Theta_1, \Theta_2]$, since all of these points are mapped into the same interval under the action of the map, which is clearly contracting. Therefore applying the contracting map theorem one proves the existence of a stable attractor of the map in the interval $[\Theta_1, \Theta_2]$, which corresponds to a sustained regime of relaxation oscillations and thus to an SMR of the slow flow (6.4). In this case, the attractor is the stable period-one fixed point $\theta_e \approx 0.51$.

By increasing the detuning parameter value (with the values of the forcing amplitude and the damping parameters remaining unchanged) we notice qualitative changes in the return map P (see Figure 6.23). As it becomes clear from the plot of

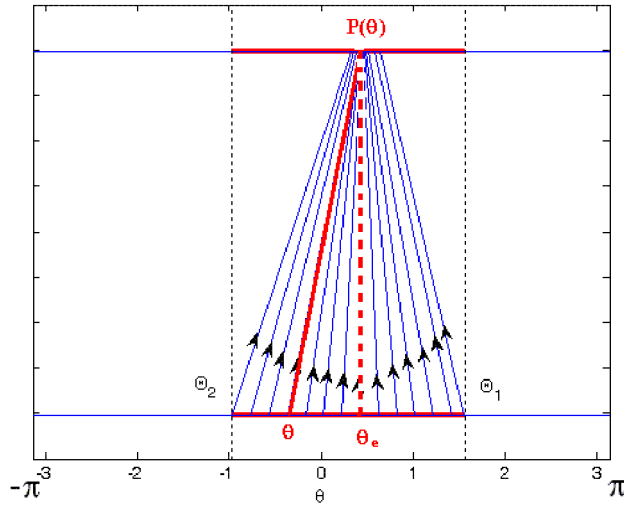


Fig. 6.22 One-dimensional map P for $A = 0.6$, $\lambda = 0.2$ and $\sigma = 1$; the stable attractor of the map is denoted by dashed line.

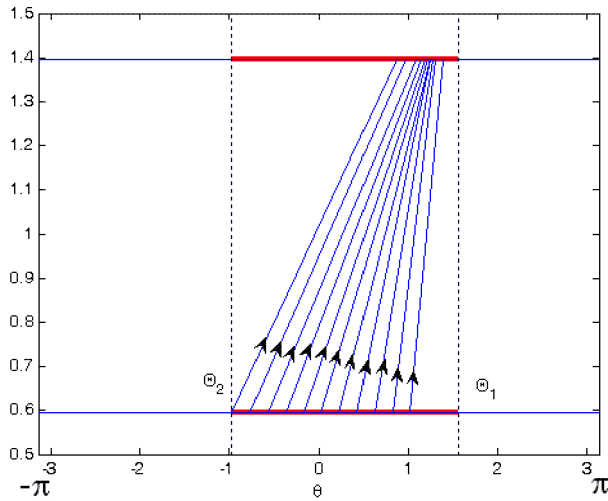


Fig. 6.23 One-dimensional map P for $A = 0.6$, $\lambda = 0.2$ and $\sigma = 2.9$.

Figure 6.23 all orbits of the map are inclined and not all points originating from the interval $[\Theta_1, \Theta_2]$ on the lower fold line L_1 land inside the corresponding interval on L_2 . Indeed, there is a region of the interval on L_1 which results in unsustainable cycles of relaxation oscillations, since orbits in the phase cylinder originating in that region are getting attracted by a stable attractor of the SIM before they can reach L_2 .

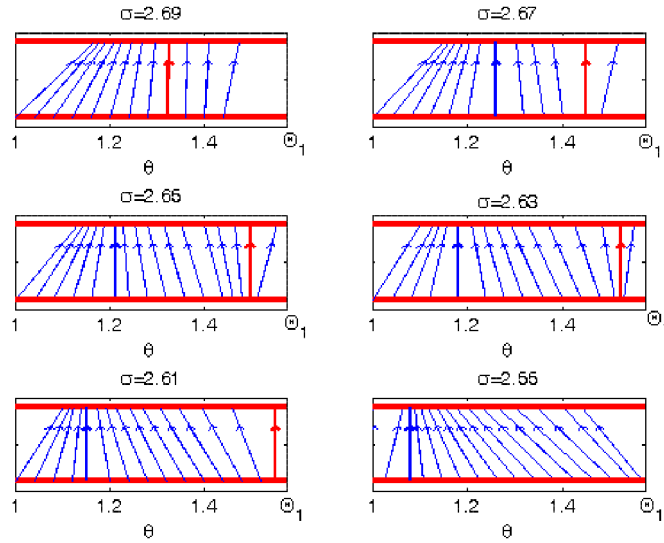


Fig. 6.24 Sequence of maps in the region $1 < \theta < \Theta_1$ close to the upper critical detuning $\sigma = \sigma_R = 2.69$; the positions of the stable and unstable period-one fixed points (SMRs) are marked by bold dashed and solid lines, respectively.

In addition, it is clear that in this case the map possesses no period- k fixed points, so that no SMRs can exist. Indeed, every orbit initiated in the interval $[\Theta_1, \Theta_2]$ on the lower fold line L_1 escapes this interval after a sufficiently large number of cycles of relaxation oscillations and settles into one of the regimes of stable steady state motions studied by the local analysis of Section 6.1.1. It follows that in this case the system can exhibit *transient relaxation oscillations* but not sustained ones, so no SMRs are possible.

From the discussion above we conclude that for higher values of the detuning parameter σ the stable period-one fixed point of the map corresponding to an SMR of the slow flow disappears. By varying the detuning parameter and by carefully studying the structure of the map, we may determine the value of σ for which the period-one attractor of the map disappears, and thus investigate the dynamical mechanism responsible for its appearance. Hence, we obtain an analytical tool for determining the frequency region of existence of SMRs. For the system considered with $A = 0.6$ and $\lambda = 0.2$, the boundaries of the detuning parameter within which the SMR exists are determined as $\sigma_R = 2.69 > \sigma > \sigma_L = -2.0546$. Considering the transformations relating the slow flow to the exact equations of motion (6.1), we conclude that SMRs in system (6.1) exists in an $O(\varepsilon)$ neighborhood of the exact resonance.

Our next goal is to investigate the mechanism that generates the limit cycles related to SMRs when the detuning parameter passes into the range of existence $\sigma \in (\sigma_L, \sigma_R)$ of these motions. In Figure 6.24 we depict a sequence of maps close to the upper critical value of the detuning parameter $\sigma = \sigma_R = 2.69$. At the criti-

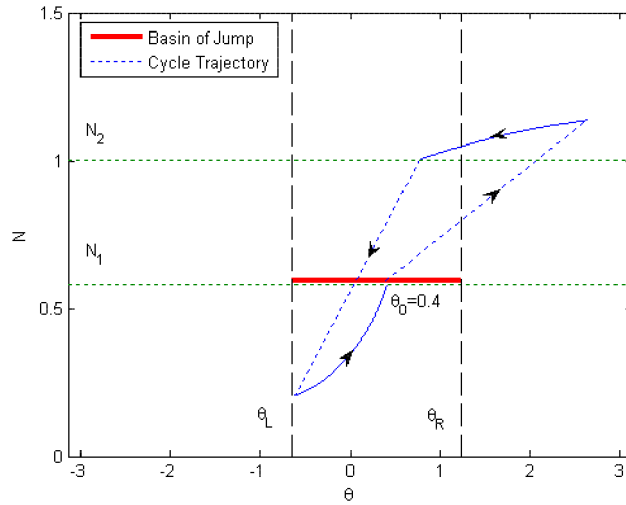


Fig. 6.25 Projection of the stable LCO corresponding to a SMR for $A = 0.3$, $\lambda = 0.2$ and $\sigma = 0.5$: dashed lines refer to ‘fast’ jumps between the two stable branches of the SIM; solid lines refer to ‘slow’ evolutions on the stable branches of the SIM.

cal value $\sigma = \sigma_R$ a SN bifurcation occurs, and for decreasing values of detuning a stable-unstable pair of period-one fixed points is generated. Interpreting this result in terms of the averaged problem (6.4) in four-dimensional phase space, this bifurcation generates a stable-unstable pair of limit cycle oscillations (LCOs); moving one step further, these LCOs correspond to motions on stable and unstable two-tori, i.e., SMRs, in the dynamics of the original system (6.1). We note that depending on the *rotation numbers* (Guckenheimer and Holmes, 1983; Wiggins, 1990) of the orbits on these two-tori, these can be either periodic (for rational rotation numbers) or quasi-periodic (for irrational rotation numbers); in turn, these lead to periodic or quasi-periodic SMRs in the original system (6.1). This global bifurcation is not related to the behavior of fixed points or of homoclinic orbits of the slow flow (6.4) (the latter are absent in this generic case), and may not be addressed by local analysis. Still, the presence of the small parameter ε (that characterizes the smallness of the NES mass compared to the mass of the linear oscillator) allows us to reduce the global flow to the one-dimensional nonlinear map P and thus to demonstrate this *global bifurcation* of the slow flow in terms of a *local bifurcation* of the map.

The previous global analysis of the dynamics identified the mechanism of creation and annihilation of the stable and unstable periodic orbits (LCOs) of the slow flow in the neighborhood of the upper boundary $\sigma = \sigma_R$ of the frequency detuning range of existence of SMRs. A projection of a representative stable LCO (SMR) on the phase cylinder $(N, \theta) \in (\mathbb{R}^+ \times S^1)$ is presented at Figure 6.25. This orbit clearly depicts the slow evolution of the dynamics on the upper and lower stable branches of the SIM (denoted by solid lines), and the fast transitions (jumps – denoted by dashed lines) when the orbit reaches the fold lines L_1 and L_2 .

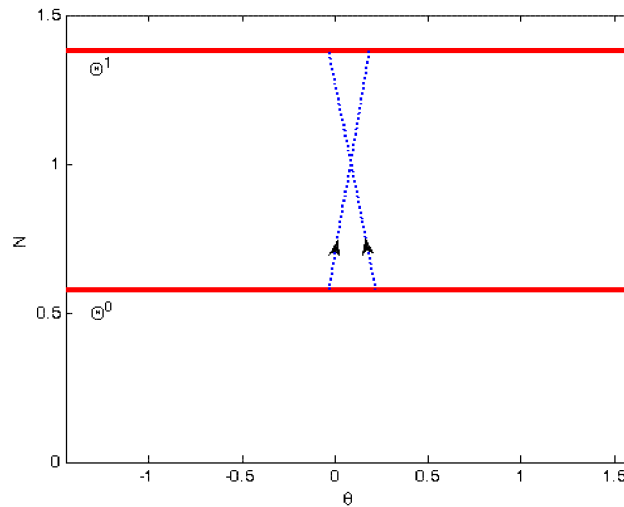


Fig. 6.26 A stable period-two periodic orbit of the one-dimensional map P .

Once the dynamics is reduced to the one-dimensional map P , one expects that the system will exhibit generic bifurcations that occur in general classes of this type of dynamical systems (Guckenheimer and Holmes, 1983). Indeed, period-doubling bifurcations of the map P are expected to occur at certain parameter values. For example, for $A = 1.0$, $\lambda = 0.05$ and $\sigma = 0$ the map possesses a stable period-two fixed point [or a period-two periodic orbit of the averaged slow flow (6.4)], as depicted in Figure 6.27. No additional period doubling bifurcations (i.e. from period-two to fixed points of higher order) were observed in the map, however, so that period doublings in this map appear to be rather ubiquitous. In Figure 6.2.2 the zones where period-two fixed points exist are depicted in the (λ, A) plane for $\sigma = 0$.

It should be mentioned that the analytical approach developed in this section is valid only in the limit $\varepsilon \rightarrow 0$, i.e., only for the case of lightweight NESs. The study of SMRs in the slow flow for finite values of ε requires the computation of higher-order expansions for equation (6.20) and the study of higher-order subproblems in the hierarchy (6.22). Clearly, this is a rather cumbersome task. Moreover, the value of such an endeavor is questionable anyway, since the obtained refinement in the analytical results will be of the order of the error introduced by the averaging procedure. Hence, in the following section we content ourselves to comparing the derived analytical predictions with direct numerical simulations of the original system (6.1) and of the averaged slow flow (6.4).

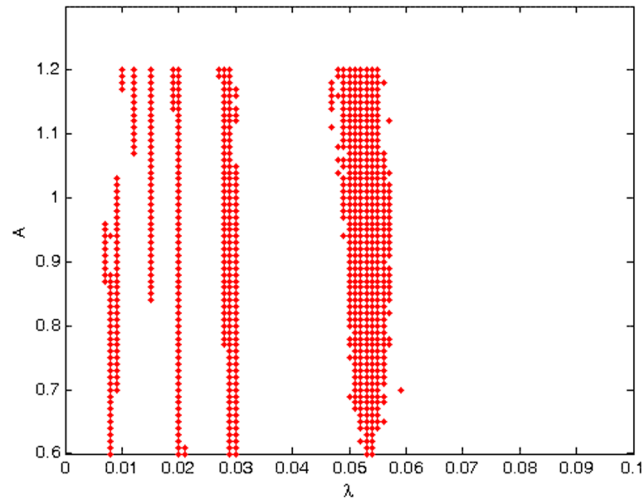


Fig. 6.27 Zones of stable period-two fixed points of the map P (for $\sigma = 0$).

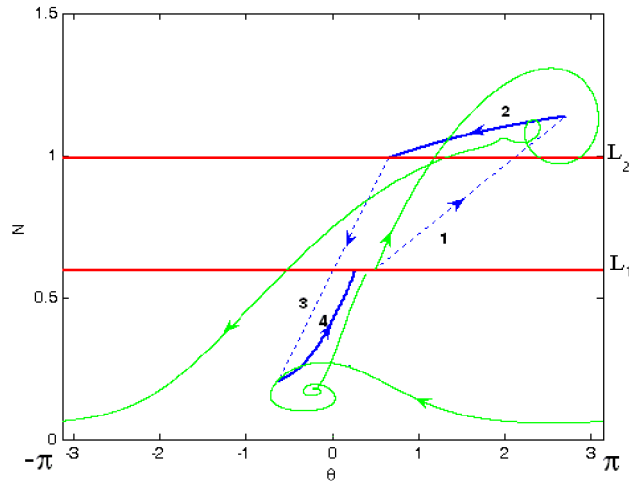


Fig. 6.28 Comparison between analytical prediction (thick line) and numerical simulation of (6.4) (thin line) for $\varepsilon = 0.01$, $\sigma = 0$; initial condition is denoted by (\bullet) , and the 'fast' components of the analytical map are denoted by dashed lines.

6.2.3 Numerical Simulations

Our next goal is to verify numerically the analytical prediction of the existence of the SMR attractors described in the previous section. In Figures 6.28–6.30 the analytical predictions obtained by employing the one-dimensional map reduction is

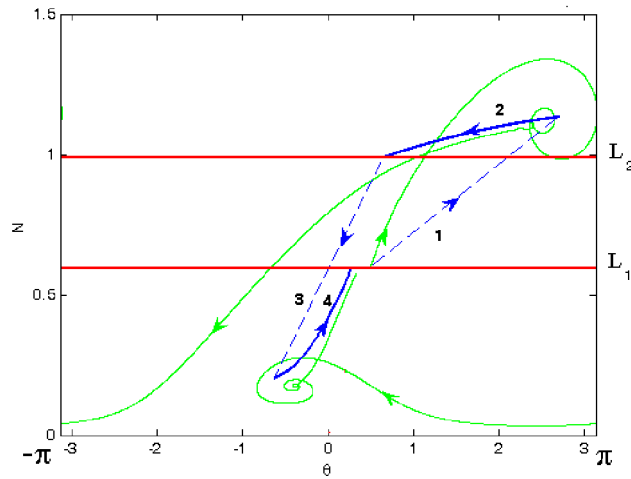


Fig. 6.29 Comparison between analytical prediction (thick line) and numerical simulation of (6.4) (thin line) for $\varepsilon = 0.005$, $\sigma = 0$; initial condition is denoted by (\bullet) , and the ‘fast’ components of the analytical map are denoted by dashed lines.

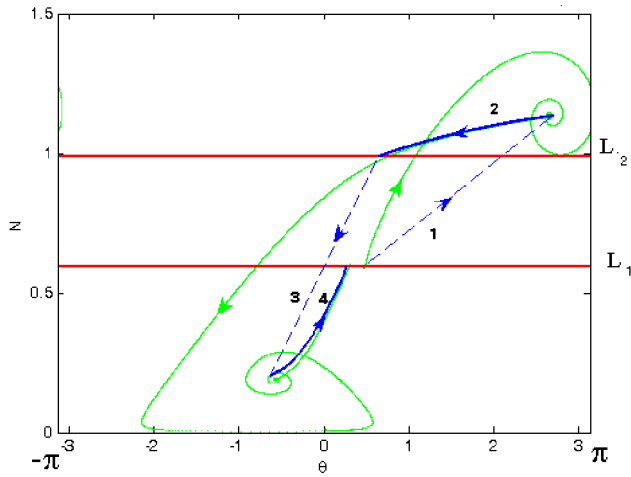


Fig. 6.30 Comparison between analytical prediction (thick line) and numerical simulation of (6.4) (thin line) for $\varepsilon = 0.001$, $\sigma = 0$; initial condition is denoted by (\bullet) , and the ‘fast’ components of the analytical map are denoted by dashed lines.

compared to direct numerical solutions of the slow flow (6.4) for identical initial conditions and varying small parameter ε . ‘Fast’ components of the analytical solutions (based on the one-dimensional map) are computed from the invariant (6.24) and, therefore, are not related to the corresponding numerical orbits (which spiral around the slow manifold due to the pair of complex conjugate eigenvalues of the

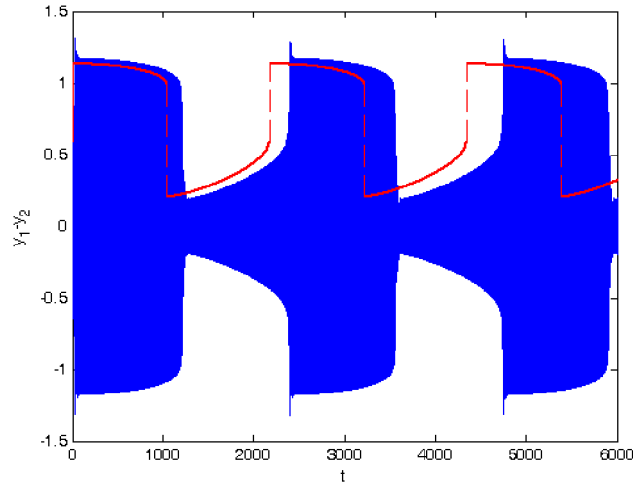


Fig. 6.31 SMR computed by direct numerical simulation of (6.1) (black line) compared to the analytical prediction based on the one-dimensional map (grey line), for $A = 0.6$, $\lambda = 0.2$, $\sigma = 1.0$ and $\varepsilon = 0.01$.

corresponding Jacobian). So, only the ‘slow’ components of the analytical solutions should be compared with the numerical simulations. It is clear from these plots that the actual orbits of the slow flow (6.4) only slightly deviate from the analytically predicted orbits; however, deviations between analytical predictions and numerical simulations increase with increasing ε , as expected. Indeed, as discussed above for moderate values of ε analytical results may not be used for quantitative predictions.

To get an estimate of the accuracy of the analytical solution based on the one-dimensional map reduction, in Figure 6.31 we compare the analytical prediction with direct numerical simulation of the original system (6.1) with initial conditions constrained to be on the SIM and for identical parameters to the ones used for constructing the plot of Figure 6.22. The range of frequency detuning for existence of the SMR attractor is computed by the analytical solution as $-0.9 < \sigma < 1$; whereas the corresponding interval computed from direct numerical simulations of system (6.1) for $\varepsilon = 0.01$ is given by $-0.9 < \sigma < 0.9$. It is essential to note that we expect the accuracy of the analytical prediction to improve with decreasing ε , in agreement with the asymptotic analysis of the previous section. From this result and the comparison depicted in Figure 6.31 we conclude that the analytical predictions are in agreement with the direct numerical simulations of the SMRs.

An additional use of the one-dimensional mapping technique discussed in the previous section has to do with its capacity to predict peculiar transient behavior in the response. Indeed, we showed analytically in the previous section that the slow flow dynamics may exhibit a few cycles of relaxation oscillations before the dynamics is eventually attracted to a stable (unmodulated) periodic response. In order to verify this analytical prediction we consider a case where no stable SMR attractor

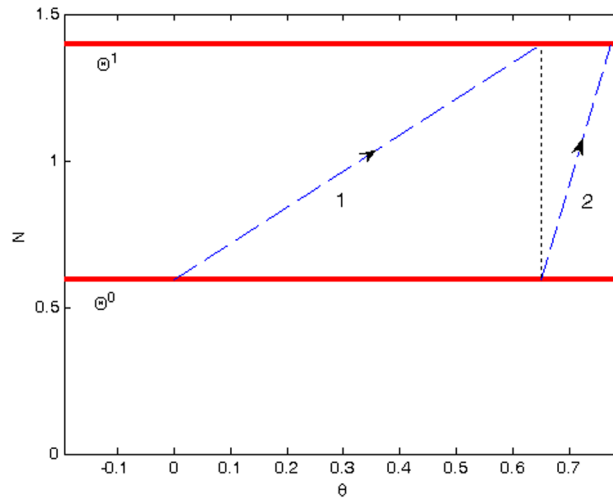


Fig. 6.32 The analytical map diagram in the absence of a stable SMR.

exists in the slow flow (6.4); hence, we consider a system with parameters $A = 0.2$, $\lambda = 0.2$ and $\sigma = 0.35$. By picking the initial value of phase angle as $\theta(0) = 0$ on the lower fold line L_1 and plotting the map, we obtain the response depicted in Figure 6.32; in this case the number of cycles of the map is equal to two. In order to check this analytical prediction, in Figure 6.33 we depict the corresponding direct numerical simulation of the original system (6.1) with identical initial conditions. From the transient response of Figure 6.33 it is clear that before the dynamics settles into the stable periodic response, it exhibits two cycles of relaxation oscillations, exactly as predicted by the analytical model. It should be mentioned, however, that in order to get such coincidence, the parameter ε needed to be picked as small. The latter requirement reflects the fact that the regime of transient relaxation oscillations occurs in close proximity to the bifurcation of the stable–unstable pair of LCOs that generates the regime of SMRs in the system; hence, the structure of the dynamical flow structure of this particular system is expected to be sensitive to changes of parameters.

The next direct numerical simulation is related to the analytical prediction of period doubling bifurcation of SMRs (see the plot of Figure 6.2.2). To this end, we performed simulations of system (6.1) for parameters in the analytically predicted zone of period doubling bifurcations, e.g., $A = 0.8$ and $\lambda = 0.053$ (Figure 6.34), as well as in the zone where a stable period-one solution of the analytical map is predicted to exist very close to the point of the period doubling bifurcation, e.g., $A = 0.7$ and $\lambda = 0.065$ (Figure 6.35). For these simulations the remaining parameters of the problem are chosen as $\varepsilon = 0.005$ and $\sigma = 0$. The numerical results are presented in two forms: (i) in terms of direct time series, and, (ii) in terms of two-dimensional Poincaré maps $\Pi: \Sigma \xrightarrow{\Pi} \Sigma, (w, \dot{w}) \rightarrow \Pi(w, \dot{w})$ on the two-

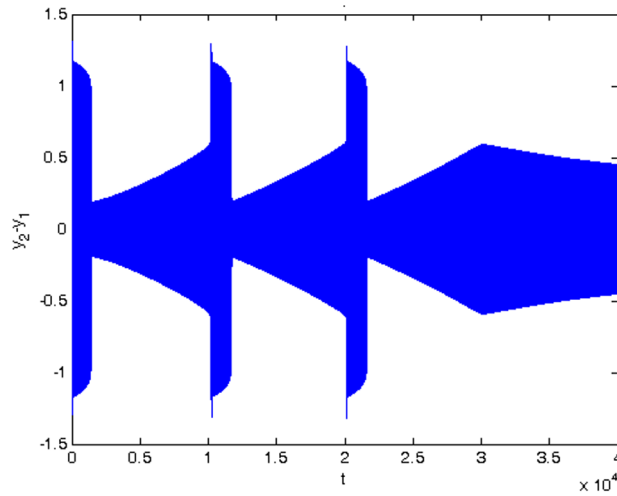


Fig. 6.33 Transient response of system (6.1) with parameters and initial conditions identical to those of the one-dimensional map of Figure 6.32), $A = 0.3$, $\lambda = 0.2$, $\sigma = 1.1$ and $\varepsilon = 0.0005$.

dimensional ‘cut section’ $\Sigma = \{(v, w, \dot{v}, \dot{w}) \in R^4, v = 0, \dot{v} \geq 0\}$ [here we employ the transformed variables (6.2)]. It is interesting to note that the numerical simulation of Figure 6.34 reveals clearly the period doubling bifurcation of the SMR. As far as the computed Poincaré maps Π are concerned, they demonstrate that in actuality both responses are chaotic-like at a time scale of $O(1/\varepsilon^2)$. Of course, the analytical treatment presented in the previous section can not be used to make any statement regarding the dynamics of the system governed by this time scale [as it is restricted to $O(\varepsilon)$ terms].

It is instructive at this point to analyze the frequency contents of a typical SMR. The analysis is performed with the help of Hilbert transform and Hilbert Vibration Decomposition (Feldman, 2006), i.e., by EMD. The harmonic components of the SMR for a case of low-amplitude harmonic excitation are presented in Figure 6.36. As expected, during most of the SMR cycle the instantaneous frequency of the dominant harmonic component of the response (i.e., of the dominant IMF) is identical to the forcing frequency, whereas the instantaneous frequency of the secondary harmonic component (the secondary IMF) is a three times multiple of that of the dominant component; this is clearly due to the essential cubic stiffness nonlinearity of system (6.1). Still, it should be mentioned that in the regions of fast transitions from high to low frequencies, the frequency of the dominant harmonic component decreases in a rather essential manner and the 1:3 TRC with the secondary component is also destroyed. This means that in these regions the dynamics escapes 1:1 fundamental TRC with the external force and is recaptured again into resonance after dissipation of energy has occurred.

A similar phenomenon of breakdown of 1:1 fundamental resonance during ‘jump down’ fast-scale frequency transitions is revealed in the strongly modulated quasi-

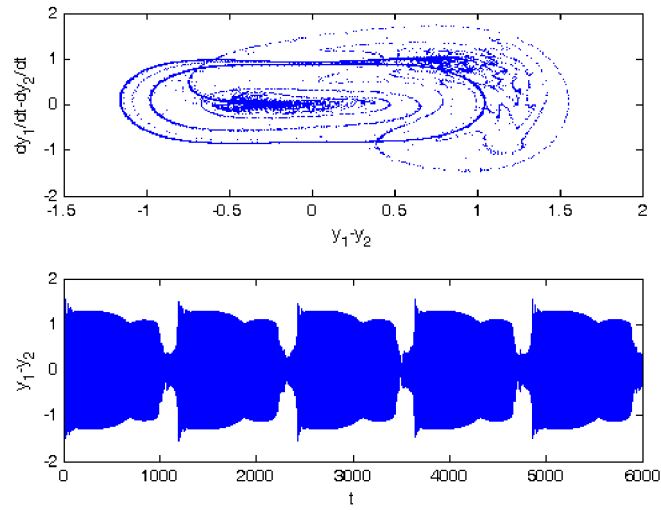


Fig. 6.34 Poincaré map $\Pi: \Sigma \xrightarrow{\Pi} \Sigma, (w, \dot{w}) \rightarrow \Pi(w, \dot{w})$, and corresponding time series of (6.1) in the analytically predicted zone of SMR period doubling.

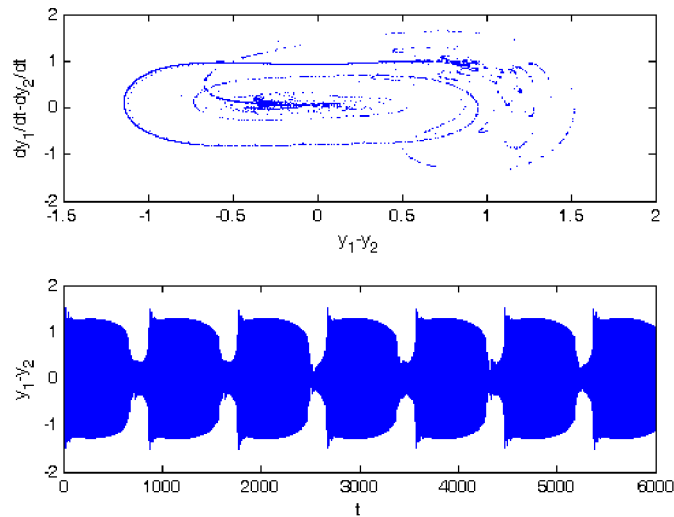


Fig. 6.35 Poincaré map $\Pi: \Sigma \xrightarrow{\Pi} \Sigma, (w, \dot{w}) \rightarrow \Pi(w, \dot{w})$, and corresponding time series of (6.1) for an SMR close to the point of period doubling bifurcation.

periodic response (SMR) corresponding to large-amplitude external harmonic excitation (see Figure 6.37). In this case the frequency of the dominant harmonic component overshoots *above* unity when the fast ‘jump down’ takes place. The secondary component behaves in an even more complicated manner, as its instan-

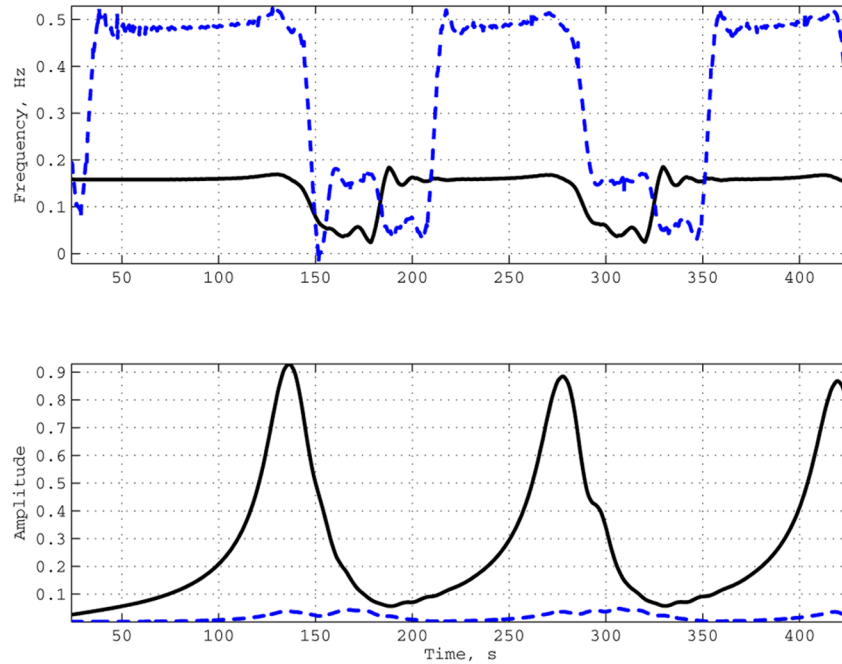


Fig. 6.36 Hilbert decomposition of the $w(t)$ component of the SMR: instantaneous frequency and amplitudes of the dominant and secondary harmonic components (IMFs) of the response for $A = 0.2$, $\lambda = 0.2$ and $\varepsilon = 0.05$; dominant IMF — solid line, secondary IMF - - - dashed line.

taneous frequency varies essentially when the frequency of the first component is almost constant; hence, no clear TRC occurs in this case. One may conjecture that the secondary harmonic component passes through a number of resonances with the dominant one, but the simulation can not clearly confirm this conjecture.

Based on the above theoretical consideration and analysis of the frequency content of SMRs, the relationship between SMRs in the periodically forced system and TET in the impulsively forced one is revealed. Viewed in the context of TRC-governed TET discussed in previous chapters, *SMRs are governed by a similar underlying mechanism, namely, repeated (periodic or quasi-periodic) series of TRCs of the steady state dynamics during the ‘slow’ components of the SMRs, with subsequent escapes during the ‘fast’ components of the SMRs, followed by recaptures.* The series of TRCs are related to increased TET from the linear oscillator (LO) to the NES and dissipation of vibration energy by the NES damper.

It was shown in this section that for the case of small NES mass ε , both TET in impulsively forced oscillators and SMRs in periodically forced ones, may be successfully treated with the help of asymptotic approaches based on singular perturbations and invariant manifold considerations. The only difference between these two cases is that in the case of TET there is a single fast transition (jump) of the transient

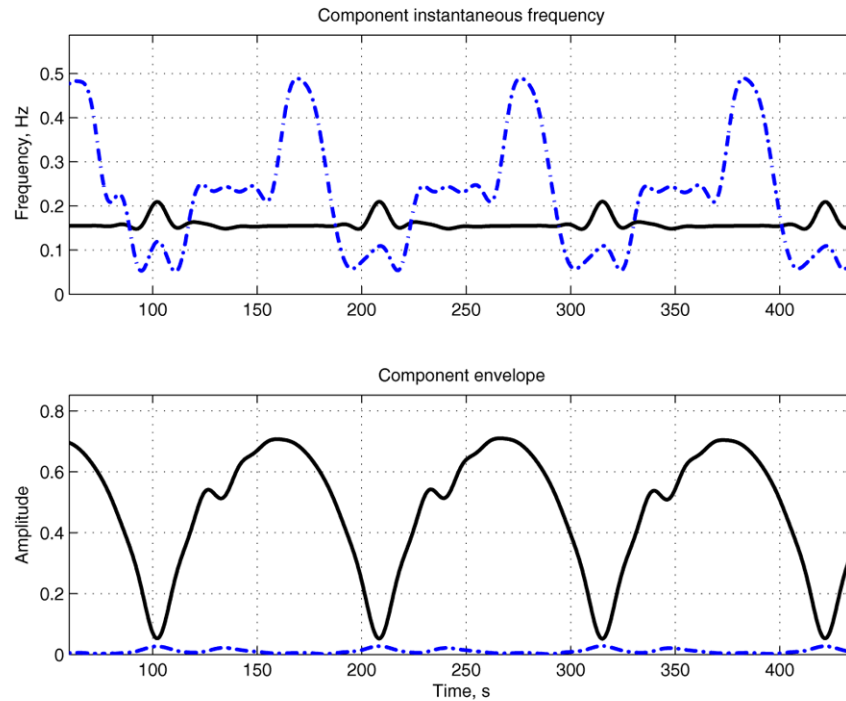


Fig. 6.37 Hilbert decomposition of the $w(t)$ component of the SMR: instantaneous frequencies and amplitudes of the dominant and secondary harmonic components (IMFs) of the response for $A = 1.4$, $\lambda = 0.2$ and $\varepsilon = 0.05$; dominant IMF — solid line, secondary IMF - - - dashed line.

dynamics from the breakdown point of the SIM; whereas for SMRs such jumps occur periodically or quasi-periodically. In addition, there occur reverse jumps during which fast frequency increases take place in the steady state dynamics. These reverse jumps occur due to energy inputs provided by the exciting force, and are consistent with the fact that during an SMR there occurs an energy balance between the input energy provided by the external harmonic excitation and the energy dissipated by the dampers of the NES and the LO. Thus, the relationship between transient TET and steady state SMRs is clear, both from the mathematical and physical points of view: *the SMRs can be viewed, in essence, as periodic or quasi-periodic versions of transient TET*. Still, the fact that the periodic (or quasi-periodic) sequence of TETs noted in the SMRs occurs under the action of constant-amplitude harmonic excitations, is still somewhat puzzling. One may conjecture that an SMR represents a non-trivial consequence of the interaction of external (fundamental) and subharmonic TRCs occurring in the essentially nonlinear system (6.1). In the following section we examine the use of NESs as vibration absorbers of steady state motions of harmonically forced oscillators.

6.3 NESs as Strongly Nonlinear Absorbers for Vibration Isolation

The most popular current solution in passive vibration isolation designs is the linear vibration absorber or tuned mass damper (TMD), where an additional linear SDOF oscillator is added to an existing linear or weakly nonlinear structure for the purpose of attenuating vibration over a narrow frequency range centered at the natural frequency of the absorber (Frahm, 1991; Ormondroyd and Den Hartog, 1928). The effective bandwidth of the TMD is governed by the damping of the absorber, and a trade-off exists between attenuation efficiency and bandwidth (Ormondroyd and Den Hartog, 1928; Bykhovsky, 1980). However the use of a linear absorber poses distinct problems when the excitation frequency is not fixed, and the frequency response in the neighborhood of structural resonances outside the narrowband action of the TMD can be adversely affected, to the extent that resonant peaks can become very steep (Roberson, 1952). To achieve linear broadband vibration absorption, multi-absorber designs have been considered both theoretically (Carcattera et al., 2005, 2006; Koç et al., 2005; Carcattera and Akay, 2007) and experimentally (Akay et al., 2005). In addition, adaptive tuned mass dampers have also been considered towards this goal (Bonello et al., 2005; Brennan, 2006).

Alternative designs employed vibration absorbers with nonlinear stiffness elements; Carella et al. (2007a, 2007b), Virgin and Davies (2003) and Virgin et al. (2007) considered buckled struts and absorbers with geometrically nonlinear stiffnesses and studied their vibration isolation capacities; their approaches, however, differ from the approach considered in this work, as no targeted energy transfer was considered. In a separate series of studies, nonlinear vibration absorbers with linearized stiffness characteristics were studied (Shaw et al., 1989; Natsiavas, 1992, 1993a,b,c; Rice and McCraith, 1987), but the case of the strong (essential) stiffness nonlinearity received less attention.

The methods and results presented in the previous sections of this chapter enable one to investigate the variety of response regimes exhibited by the NES attached to a primary SDOF linear oscillator under external harmonic excitation, and on the condition of 1:1 fundamental resonance. Therefore, it is possible to employ the previously developed techniques and the derived results in order to assess the performance of the NES as strongly nonlinear vibration absorber. Moreover, the followed approach can be generalized to the more general class of discrete or continuous primary linear systems with more degrees of freedom possessing SDOF or MDOF essentially nonlinear attachments.

6.3.1 Co-existent Response Regimes

The treatment presented in the previous sections allowed us to figure out two main types of the steady state *regular* response regimes of system (6.1); namely, time-

periodic or weakly modulated steady state responses [corresponding to equilibrium points or LCOs generated through SN or Hopf local bifurcations of the slow flow (6.4)], and *strongly modulated responses (SMRs)* [due to relaxation-type oscillations generated from global bifurcations in the slow flow (6.4)]. Moreover, for this essentially nonlinear system one can expect ever more complicated *irregular* steady state responses, involving high-order resonances or even chaotic orbits, although such responses are typically realized for relatively large values of forcing amplitudes A .

In this section we will restrict our consideration only to cases where 1:1 fundamental resonances occur, i.e., when the primary system and the NES oscillate with frequencies that are nearly identical to the forcing frequency. Consequently, the two types of regular steady state responses mentioned above are the only possible responses for the system. In order to assess the efficiency of the NES as nonlinear vibration absorber, one should in principle describe all possible responses realized at the ranges of system parameters of interest, since by omitting any co-existing stable steady state regimes we may jeopardize the efficiency and robustness of the our vibration isolation designs. Then, it is possible to decide whether in the worst case scenario we get satisfactory conditions of vibration isolation, excluding the possibility of transitions to other unfavorable response regimes for small changes of the system parameters or initial conditions.

So, it is of considerable importance to be able to predict the co-existence of the possible response regimes over the frequency and parameter ranges considered in the vibration isolation design. Not less important task is a prediction of domains of attraction for every response regime that can be realized in the forced system. This problem is of special interest due to the multiplicity of possible steady state responses. Even if some of these responses are not favorable and compatible to the vibration isolation objective, and one cannot eliminate these regimes by appropriate choice of parameters, it may be still possible to reduce their domains of attraction in the space of initial conditions. It is clear that every practical system is expected to work only in certain finite range of possible initial conditions and the designer should be able to estimate this region. If one can design the system in a way that these realistic initial conditions will never lead the dynamics to undesired response regimes, then the problem of vibration isolation can still be solved despite theoretical possibility of problematic responses.

In this section, we present certain examples of co-existence of different time-periodic or weakly modulated steady state responses and SMRs. For the sake of convenience, we make use of the frequency response diagrams described in Section 6.1, and for each diagram we indicate the zone of existence of SMRs as well. Representative frequency response diagrams corresponding to different topologies of branches of responses are depicted in Figures 6.38–6.40. These results should be viewed from the point of view that increased values of the amplitude N correspond to large relative oscillations between the LO and the NES, and, hence, are expected to yield enhanced steady state dissipation of vibration energy by the damper of the NES. It is reasonable then to conclude that *large-amplitude branches of the frequency response plots of Figures 6.38–6.40 correspond to strong steady state TET from the LO to the NES, and yield to enhanced local dissipation of vibration energy*

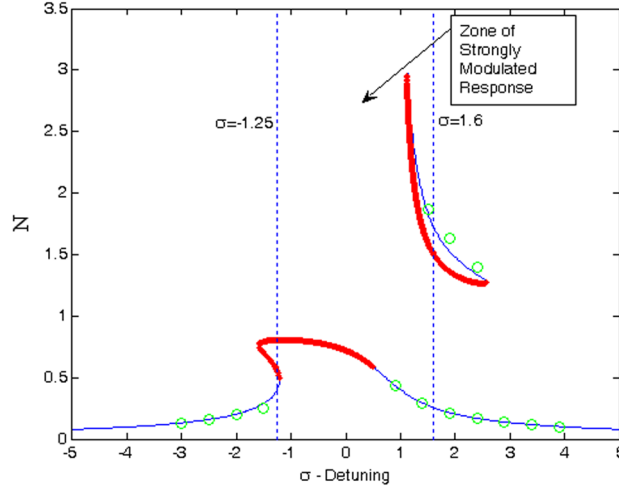


Fig. 6.38 Numerical verification of the frequency response diagram for $A = 0.4$, $\lambda = 0.2$ and $\varepsilon = 0.01$: (O) numerical integration; bold (thin) line indicates unstable (stable) periodic response.

by the NES; therefore, large-amplitude branches are favorable towards vibration isolation. In addition, as will be discussed below, co-existing regimes of stable SMRs can also provide favorable conditions for steady state TET. This should not be surprising given that SMRs can be viewed as periodic or quasi-periodic versions of TET realized in transiently forced oscillators (see our previous discussion in Section 6.2).

These results suggest a satisfactory agreement between the analytically predicted and numerically obtained periodic steady state response amplitudes. In order to verify numerically the co-existence of the various system regimes predicted in the previous section, we have picked the most interesting cases which reveal the existence of three distinct regimes for the same set of parameters but for different initial conditions. The selected cases relate to the frequency response diagrams presented in Figures 6.38–6.40, and a representative result of three co-existent steady state responses is depicted in Figure 6.41.

6.3.2 Efficiency and Broadband Features of the Vibration Isolation

The first task that needs to be addressed in order to use the NES as a vibration absorber is its tuning, so we initiate our study of nonlinear vibration isolation from this task. To this end, we reconsider the harmonically forced system (6.1) and expressed it in the following slightly modified form:

$$\ddot{y}_1 + \varepsilon\lambda(\dot{y}_1 - \dot{y}_2) + y_1 + \varepsilon k(y_1 - y_2)^3 = \varepsilon A \cos \omega t$$

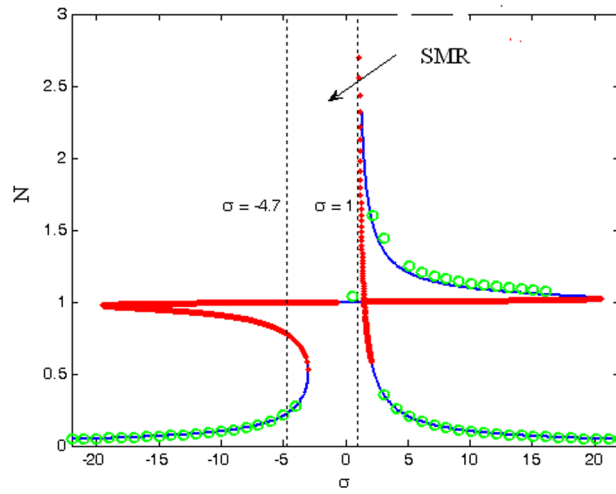


Fig. 6.39 Numerical verification of the frequency response diagram for $A = 1.0$, $\lambda = 0.05$ and $\varepsilon = 0.01$: (O) numerical integration; bold (thin) line indicates unstable (stable) periodic response.

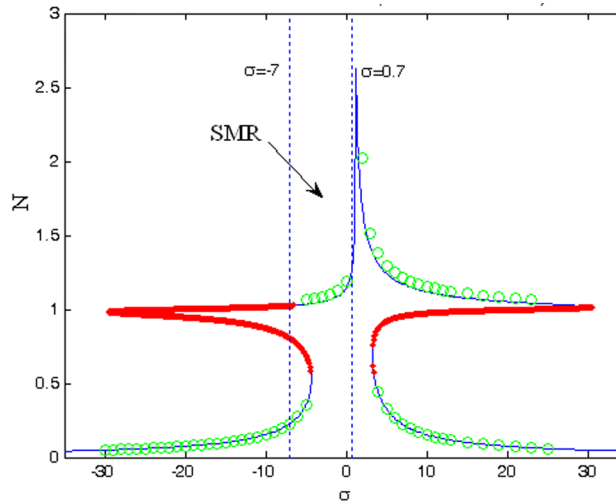


Fig. 6.40 Numerical verification of the frequency response diagram for $A = 1.5$, $\lambda = 0.05$ and $\varepsilon = 0.01$: (O) numerical integration; bold (thin) line indicates unstable (stable) periodic response.

$$\varepsilon \ddot{y}_2 + \varepsilon \lambda (\dot{y}_2 - \dot{y}_1) + \varepsilon k (y_2 - y_1)^3 = 0 \tag{6.39}$$

We note that only the primary LO possesses damping, whereas the NES is considered to be undamped. Since we consider the regime of fundamental resonance of this system we suppose that the forcing frequency is close to unity, $\omega \approx 1$, and introduce the parameter k of the NES which needs to be tuned for optimal vibra-

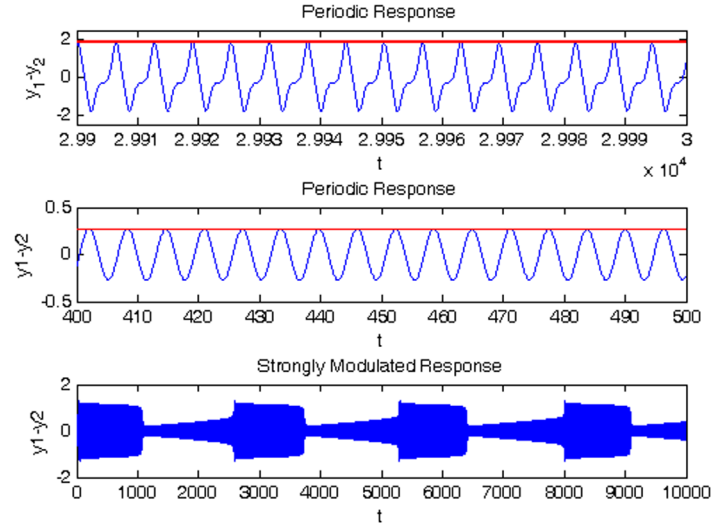


Fig. 6.41 Co-existence of three response regimes corresponding to different initial conditions for the system with parameters $A = 0.4$, $\lambda = 0.2$, $\sigma = 1.5$ and $\varepsilon = 0.001$.

tion isolation performance (as defined by the energy criteria defined below). For the case of the classical linear vibration absorber (i.e., with linear coupling stiffness between the LO and the secondary system), the tuning of parameter k is performed by equating the frequency of the absorber to the resonance frequency of the LO. In the essentially nonlinear case considered herein, however, the tuning procedure is more complicated.

Direct application of the analytical procedure outlined in previous sections enables one to estimate the co-existing steady state responses of system (6.39) over the frequency range of interest, and, therefore, to optimize the target function selected as criterion for the vibration isolation. We select two such possible energy criteria. First, the total energy of system (6.39) defined as

$$E_{\text{tot}} = \frac{\dot{y}_1^2}{2} + \varepsilon \frac{\dot{y}_2^2}{2} + \frac{y_1^2}{2} + \varepsilon k \frac{(y_1 - y_2)^4}{4} \quad (6.40a)$$

and, second, the kinetic energy of the primary LO to be isolated:

$$E_{\text{kin}} = \frac{\dot{y}_1^2}{2} \quad (6.40b)$$

Moreover, since the above energy criteria are time dependent due to the time-varying external forcing and damping terms, the corresponding averages of these quantities are considered instead.

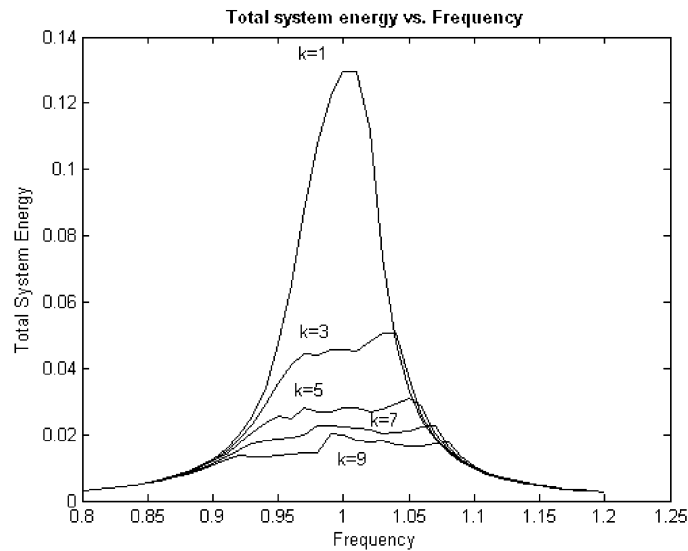


Fig. 6.42 Averaged total system energy frequency response in the regime of 1:1 fundamental resonance.

A typical frequency response plot depicting the dependence of the average of the total energy of the system E_{tot} on frequency is depicted in Figure 6.42, for $A = 0.3$, $\lambda = 0.4$ and $\varepsilon = 0.1$, and varying values of the tuning parameter k . From this plot we conclude that the average total energy in the system can be efficiently reduced by varying the parameter k , while keeping all other parameters fixed; moreover, for relatively high values of k this reduction is made robust over a wide frequency range. It should be mentioned that further increase of k above the values considered in Figure 6.42, causes the appearance of a co-existing large-amplitude steady state response regime (similar to one presented in Figure 6.41), and, following the reasoning of the previous section, this leads to deterioration of vibration isolation. In addition, the non-monotonic dependence of the averaged total energy on frequency is attributed to SMRs that exist precisely at the regimes of non-monotonicity. So, the enhanced energy reduction and absorption for the system with high value of k is related to this specific response regime.

At this stage it is important to emphasize that there is definitely the possibility for additional co-existing stable steady state regimes at certain frequency detuning ranges, $\sigma > 0$. However in the vicinity of the 1:1 fundamental resonance there is a region where a single stable periodic attractor and a stable strongly quasi-periodic (SMR) attractor co-exist. In this co-existence region the optimization carried out in this section is valid. Additional co-existing steady state attractors are in the form of periodic lower-amplitude regimes, which may improve even more the efficiency of vibration isolation compared to the regime of SMRs. The previous discussion dictates the establishment of a performance criterion according to which the vibra-

tion isolation capacity of the optimally tuned nonlinear absorber (NES) considered herein can be compared to that of the corresponding optimally tuned classical linear vibration absorber (TMD) with identical parameters A , λ and ε . This will enable us to judge the improvement achieved in the proposed vibration isolation design based on the use of essential stiffness nonlinearities.

Before we proceed with a particular tuning, some classical results concerning the tuning of the damped, forced linear absorber (Den Hartog, 1956) are reviewed at this point. Here we consider only the main results that will assist us in our discussion on tuning that follows. To this end, we write the system treated by Den Hartog (1956) as follows:

$$\begin{aligned} M\ddot{y}_1 + c(\dot{y}_1 - \dot{y}_2) + y_1 + k_{\text{LIN}}(y_1 - y_2) &= P_0 \cos(\omega t) \\ m\ddot{y}_2 + c(\dot{y}_2 - \dot{y}_1) + k_{\text{LIN}}(y_2 - y_1) &= 0 \end{aligned}$$

The main goal of the tuning process outlined by Den Hartog was to reduce the displacement of the primary LO, based on the steady state action of the attached damped linear absorber. The following normalized quantities are introduced: mass ratio, $\mu = m/M$; natural frequency of the absorber, $\omega_a^2 = k_{\text{LIN}}/m$; natural frequency of the primary LO, $\Omega_n^2 = K/M$; ratio of natural frequencies, $f = \omega_a/\Omega_n$; and forced frequency ratio, $g = \omega/\Omega_n$.

A frequency response plot depicting the steady state response $|y_1|$ of the primary LO for varying damping parameters is depicted in Figure 6.43. All plots pass through the *fixed points* of intersection P and Q, which, therefore, are invariant to variations of the damping parameter. By varying the ratio of natural frequencies f these fixed points can be shifted up and down. Thus the tuning process followed by Den Hartog was based on the requirement that P and Q lie at equal heights, and then, the adjustment of the damping parameter to render the frequency response curve to pass through these fixed points with horizontal (or near horizontal) tangent. Equal-height fixed points P and Q correspond to Den Hartog (1956):

$$f = \frac{1}{1 + \mu} \quad (6.41)$$

Then, the adjustment of the damping parameter was performed according to an analytic expression developed by Den Hartog (1956) which is not reproduced here.

To translate these tuning results in terms of the system parameters of (6.37), we set $M = 1$, $c = \varepsilon\lambda$, $P_0 = \varepsilon A$ and $m = \varepsilon$. Then, according to the previous results we obtain the following expression for optimal tuning of the linear vibration absorber:

$$k_{\text{LIN}} = \frac{\varepsilon}{(1 + \varepsilon)^2} \quad (6.42)$$

It can be proved (Den Hartog, 1956) that due to the linearity of the problem, similar tuning holds for the optimization of the total energy stored in the system.

The criterion for comparing the vibration isolation performances of the NES and the tuned linear absorber is now formulated. Specifically, defining as optimization

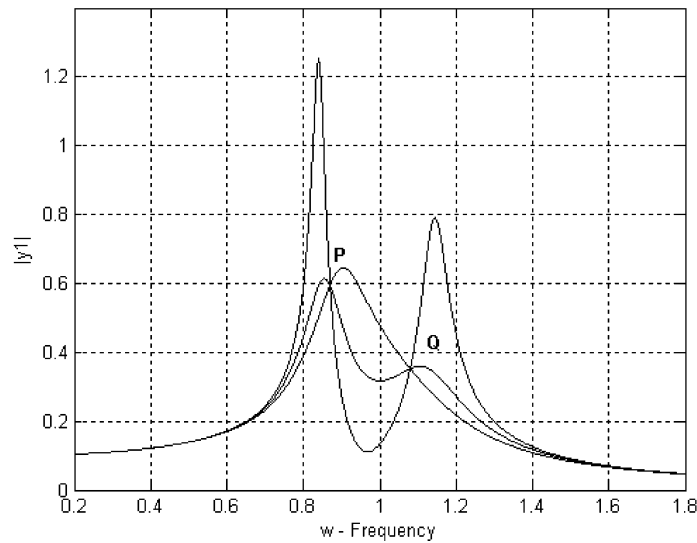


Fig. 6.43 Linear vibration absorber, frequency response plot of the primary LO for varying damping values; the points of intersection P,Q are denoted.

criterion for our vibration isolation study the minimization of the highest peak of the averaged total system energy (labeled as *critical energy peak – CEP*) over the frequency range of interest, the performance of the linear and nonlinear designs will be compared by comparing the corresponding CEPs.

The rules according to which these two absorbers are to be compared are formulated as follows: (i) the mass, damping, external forcing amplitude and frequency of the primary LO are to remain fixed for a particular study; and (ii) the linear and nonlinear vibration absorbers will possess identical masses but their stiffness parameters k and k_{LIN} will be optimized (tuned) independently. The averaged total energy criterion will be used for the comparison, since, as discussed in previous sections there exists the possibility that the steady state responses of the nonlinear system will be strongly amplitude-modulated (of the beating type); in that case the averaged criterion can be applied for assessing the efficacy and effectiveness of the nonlinear vibration isolation design over a period of the strong modulation (beating). Of course, this doesn't rule out the possibility that undesired isolated amplitude peaks might occur within a cycle of the response, but the alternative criterion of reducing the maximum absolute peak amplitude will not be considered herein.

A typical comparison study of the performances of the linear and nonlinear absorbers under the previously specified conditions is presented in Figure 6.44, for $A = 0.2$, $\lambda = 0.1$ and $\varepsilon = 0.1$. Clearly, the optimally tuned nonlinear absorber is more effective and its performance is more robust to frequency variations compared the optimally-tuned linear absorber for the considered set of system parameters. Although the linear absorber provides better isolation in the narrowband region close to

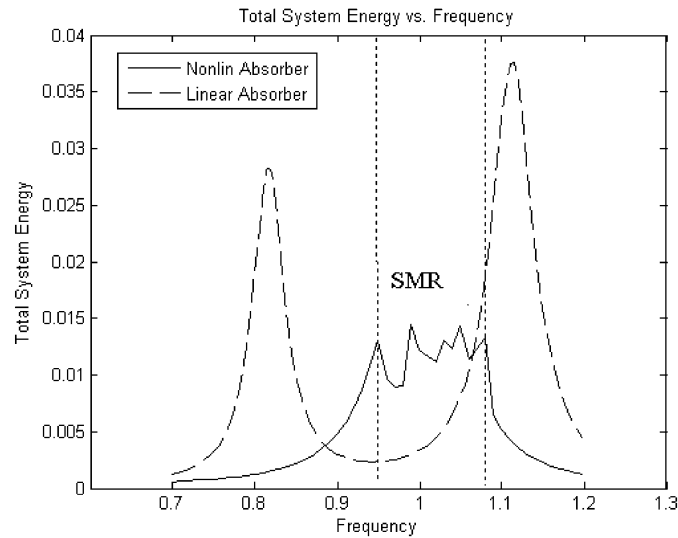


Fig. 6.44 Averaged total system energy frequency responses for linear and nonlinear vibration absorbers; the zone of existence of SMRs is indicated.

its tuning frequency, the NES provides consistent reduction of the averaged energy peaks over the entire frequency range of interest, and, hence, better performance over a wider frequency range compared to the linear absorber.

The frequency response plot at Figure 6.44 is somewhat unusual – the response curve exhibits a number of discontinuities (range of non-monotonicity) in the zone where the SMR regime exists, and it appears to be rather smooth outside this region. This result has been obtained as a result of numerical simulations, and one may conjecture that for different values of the frequency the dynamical flow in that zone might be attracted to either one of multiple co-existing stable steady state regimes; that is, either to a stationary (or weakly quasi-periodic) response, or, alternatively, to an SMR. It follows that when designing the essentially nonlinear vibration absorber for optimal vibration isolation, one should care about the regimes to which the flow is attracted, since some of these might be rather undesirable. Therefore, *a study of the effect of the initial conditions on nonlinear vibration isolation is required*. From the persistence point of view, such an obstacle could undermine the entire endeavor, since rather often the domains of attraction of different response regimes are mixed, and, in addition, in some cases the boundaries of domains of attraction might even be of fractal nature (Jackson, 1991). Still, as mentioned previously, if one can demonstrate that at certain ranges of initial conditions the dynamics of the system is not attracted to problematic attractors, then the design of the NES as nonlinear absorber can still be deemed as satisfactory.

In order to illustrate this point, we performed Monte Carlo simulations of the steady state dynamics for different values of randomly picked initial conditions. The parameters used are identical to those of Figure 6.38, but with $\varepsilon = 0.001$. It should

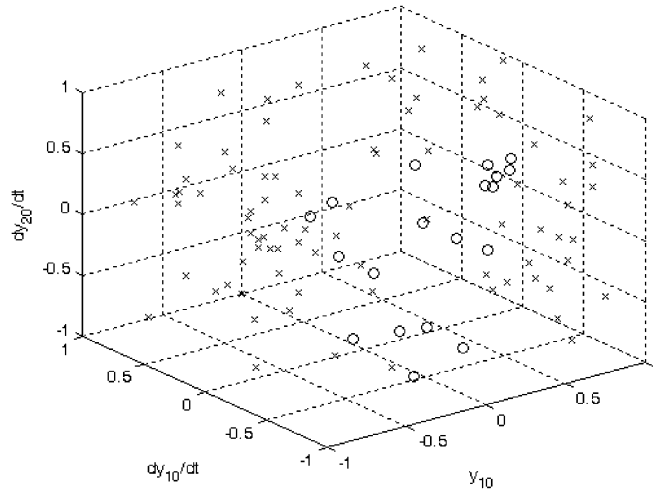


Fig. 6.45 Monte Carlo simulations of steady state attractors of the dynamics for randomly varying initial conditions, $A = 0.4$, $\lambda = 0.2$, $\sigma = 1.5$, $\varepsilon = 0.001$ and $y_{20} = 0$; the SMR attractor is denoted by (o), the low-amplitude stationary attractor by (x), and the high-amplitude (undesirable) stationary attractor by (•).

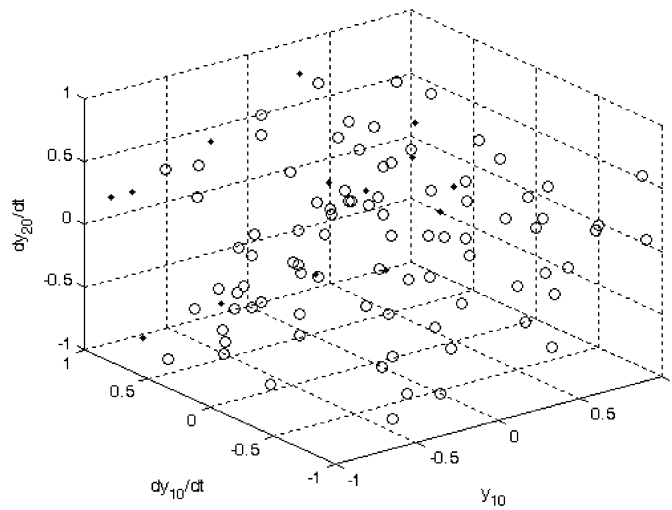


Fig. 6.46 Monte Carlo simulations of steady state attractors of the dynamics for randomly varying initial conditions, $A = 0.4$, $\lambda = 0.2$, $\sigma = 2.0$, $\varepsilon = 0.001$ and $y_{20} = 0$; the SMR attractor is denoted by (o), the low-amplitude stationary attractor by (x), and the high-amplitude (undesirable) stationary attractor by (•).

be mentioned that the shape of the frequency response plot does not depend on the value of ε in the framework of the approximations used in the previous analysis. We

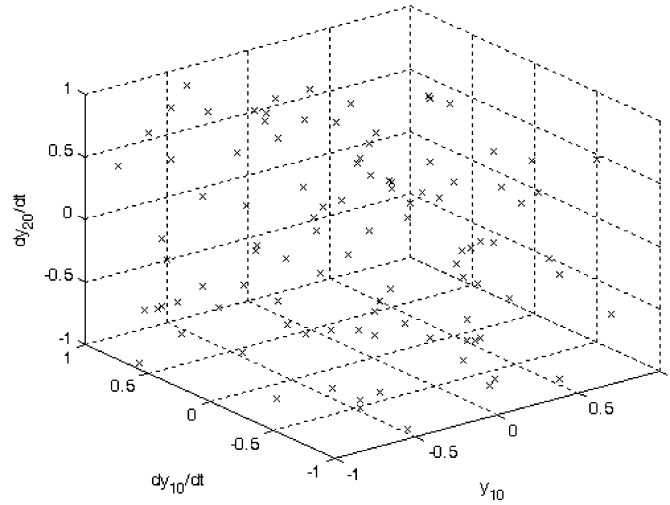


Fig. 6.47 Monte Carlo simulations of steady state attractors of the dynamics for randomly varying initial conditions, $A = 0.4$, $\lambda = 0.2$, $\sigma = 0.5$, $\varepsilon = 0.05$ and $y_{20} = 0$; the SMR attractor is denoted by (\circ) , the low-amplitude stationary attractor by (\circ) , and the high-amplitude (undesirable) stationary attractor by (\bullet) .

explore two different values of the detuning parameter, namely, $\sigma = 1.5$ (a regime of co-existence of desirable SMRs with periodic or weakly modulated stationary solutions) and $\sigma = 2.0$ (a regime where no SMRs exist). For both selected values of the detuning parameter there exist two stationary responses, namely, a (desirable) low-amplitude solution, and an (undesirable) high-amplitude one.

The results of the Monte Carlo simulations are presented at Figures 6.45 and 6.46. One can see that for $\sigma = 1.5$ no trajectory is attracted to the undesirable high-amplitude stationary response which is unfavorable for vibration isolation; instead, trajectories are attracted by, either the low-amplitude stationary steady state solution or the SMR. Both of these stable solutions are favorable to vibration isolation, with the SMR solution being preferable since, as discussed previously, it represents a version of steady state TET. On the contrary, by increasing the detuning parameter to $\sigma = 2.0$ we reach a regime where no SMRs exist, and, as a result, a subset of initial conditions leads to attraction of the dynamics by the undesirable high-amplitude stationary stable response. From these simulations it appears that the regime of SMRs represents a rather strong attractor, since it prevents the dynamical flow from being attracted by the undesirable high-amplitude stationary response. This result, however, is only based on this specific series of Monte Carlo simulations and is not based on any rigorous analytical proof.

Moreover, the above example may be regarded as of little practical significance, since it corresponds to a very small (and hence impractical) value of the mass ratio ε ; indeed, for this value of the mass ratio the previously developed theoretical asymptotic analysis is expected to yield satisfactory quantitative predictions. However,

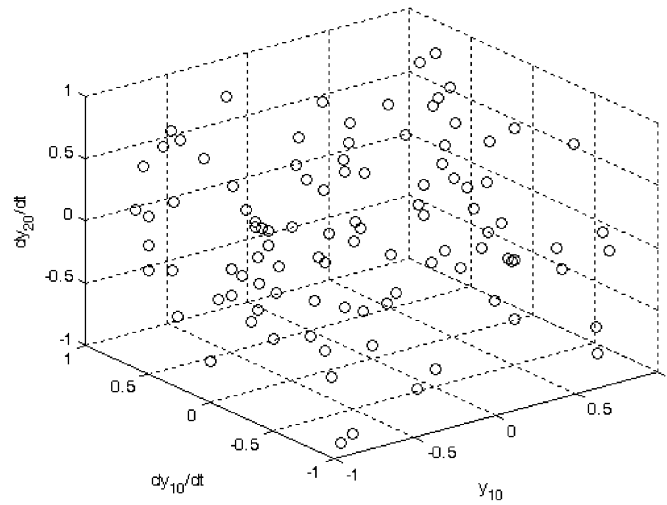


Fig. 6.48 Monte Carlo simulations of steady state attractors of the dynamics for randomly varying initial conditions, $A = 0.4$, $\lambda = 0.2$, $\sigma = 1.0$, $\varepsilon = 0.05$ and $y_{20} = 0$; the SMR attractor is denoted by (\bullet) , the low-amplitude stationary attractor by (\circ) , and the high-amplitude (undesirable) stationary attractor by (\bullet) .

qualitatively similar results can be obtained for cases of more practical significance, which, however, are beyond the range of validity of our previous analytical approximations. This is demonstrated in Figures 6.47–6.49, which correspond to increased mass ratio $\varepsilon = 0.05$ and varying detuning parameter σ . In all three cases shown and for all values of randomly chosen initial conditions considered, the absorber dynamics are not attracted by an undesirable high-amplitude stationary response. Rather its steady state response is either an SMR or a low-amplitude stationary solution, which ensures robust vibration isolation for all initial conditions considered in the Monte-Carlo simulation. Although a more detailed investigation may be required to proceed into final and analytically rigorous conclusions, the presented results indicate robustness of nonlinear vibration isolation by the considered NES design.

The nonlinear absorber has an additional feature which justifies its use: it possesses a self-tuning capacity to variations of the external frequency, and thus can be applied for the case of linear primary systems with many degrees of freedom. The reason behind this self-tuning capacity of the NES is its essential nonlinearity which, in contrast to the linear vibration absorber, prevents the existence of a preferential resonance frequency. This extends the capacity of the NES to engage in resonance interaction with multiple modes of the linear primary system to which it is attached (and, hence, to provide multi-modal passive vibration isolation). The next section provides a demonstrative example of this feature of the NES.

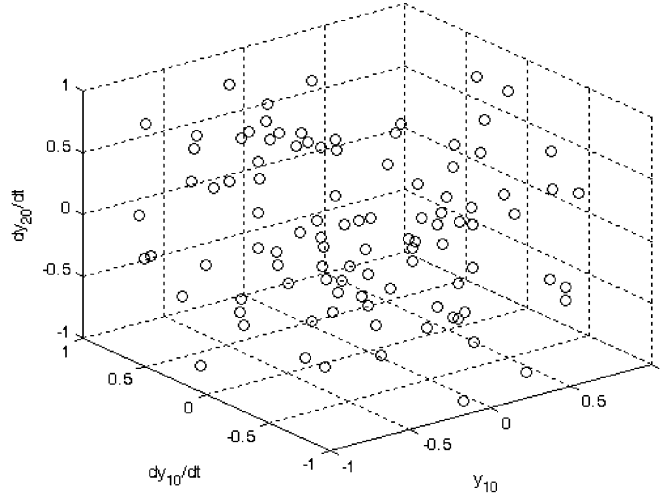


Fig. 6.49 Monte Carlo simulations of steady state attractors of the dynamics for randomly varying initial conditions, $A = 0.4$, $\lambda = 0.2$, $\sigma = 1.5$, $\varepsilon = 0.05$ and $y_{20} = 0$; the SMR attractor is denoted by (\circ) , the low-amplitude stationary attractor by (\bullet) , and the high-amplitude (undesirable) stationary attractor by (\bullet) .

6.3.3 Passive Self-tuning Capacity of the NES

To study the vibration isolation properties of the NES when applied to a MDOF system, we consider a harmonically excited two-DOF system of linear coupled oscillators (the primary linear system) with a nonlinear energy sink (NES) attached to it. The masses of the linear oscillators are assumed to be identical (and taken as equal to unity without loss of generality). The system is described by the following equations,

$$\begin{aligned} \ddot{y}_2 + k_2 y_2 + k_1 (y_2 - y_1) &= \varepsilon F_2 \cos \omega t \\ \ddot{y}_1 + k_2 y_1 + k_1 (y_1 - y_2) + \varepsilon k_v (y_1 - v)^3 + \varepsilon \lambda (\dot{y}_1 - \dot{v}) &= \varepsilon F_1 \cos \omega t \\ \varepsilon \ddot{v} + \varepsilon k_v (v - y_1)^3 + \varepsilon \lambda (\dot{v} - \dot{y}_1) &= 0 \end{aligned} \quad (6.43)$$

where y_1 , y_2 and v are the displacements of the linear oscillators and the NES, respectively; $\varepsilon \lambda$ is the damping coefficient; and εF_i , $i = 1, 2$ are the amplitudes of the weak excitations applied to each of the linear oscillators. The system (6.43) may be rescaled by introducing the following normalized variables and parameters:

$$t = \sqrt{k_1} \tau, \quad \tilde{k}_2 = \frac{k_2}{k_1}, \quad \tilde{\lambda} = \frac{\lambda}{\sqrt{k_1}}, \quad \tilde{F}_1 = \frac{F_1}{k_1}, \quad \tilde{F}_2 = \frac{F_2}{k_1}, \quad \tilde{k}_v = \frac{k_v}{k_1} \quad (6.44)$$

Substitution of (6.44) into (6.43) yields the following rescaled system:

$$\begin{aligned}
y_2'' + (\tilde{k}_2 + 1)y_2 - y_1 &= \varepsilon \tilde{F}_2 \cos \omega \tau \\
y_1'' + (\tilde{k}_2 + 1)y_1 - y_2 &= \varepsilon \tilde{F}_1 \cos \omega \tau - \varepsilon \tilde{k}_v (y_1 - v)^3 - \varepsilon \tilde{\lambda} (y_1' - v') \\
\varepsilon v'' + \varepsilon \tilde{k}_v (v - y_1)^3 + \varepsilon \tilde{\lambda} (v' - y_1') &= 0
\end{aligned} \tag{6.45}$$

where primes denote differentiation with respect to the normalized independent variable τ . The two natural frequencies of the primary linear system are assumed to be of the same order of magnitude, incommensurate and well separated [i.e., their difference is of $O(1)$]. It follows that the normalized coupling stiffness \tilde{k}_2 is selected in a way to provide two distinct incommensurate natural frequencies for the primary linear system; e.g., $\tilde{k}_2 = 1$ yields the natural frequencies $\omega_2 = \sqrt{3}$ and $\omega_1 = 1$. Although the assignment of numerical values may seem rather restrictive, it will become clear from the following development that the particular values of the natural frequencies are of no significance for the analysis, as long, of course, as the previous assumptions are enforced. Indeed, the only significant restriction is the absence of beats in the linear primary system, that is, the requirement of well separated natural frequencies. For cases where the natural frequencies of the primary system are closely spaced a separate asymptotic analysis must be performed.

At this point we transform the dynamical system (6.45) in terms of modal coordinates of the primary system,

$$\begin{aligned}
y_1 &= (x_1 + x_2) / \sqrt{2} \\
y_2 &= (x_1 - x_2) / \sqrt{2}
\end{aligned} \tag{6.46}$$

yielding the following transformed system of equations:

$$\begin{aligned}
x_2'' + 3x_2 &= -\frac{\varepsilon \tilde{A}_2}{\sqrt{2}} \cos \omega \tau - \frac{\varepsilon \tilde{k}_v}{\sqrt{2}} \left[\frac{(x_1 + x_2)}{\sqrt{2}} - v \right]^3 - \frac{\varepsilon \tilde{\lambda}}{\sqrt{2}} \left[\frac{(x_1' + x_2')}{\sqrt{2}} - v' \right] \\
x_1'' + x_1 &= \frac{\varepsilon \tilde{A}_1}{\sqrt{2}} \cos \omega \tau - \frac{\varepsilon \tilde{k}_v}{\sqrt{2}} \left[\frac{(x_1 + x_2)}{\sqrt{2}} - v \right]^3 - \frac{\varepsilon \tilde{\lambda}}{\sqrt{2}} \left[\frac{(x_1' + x_2')}{\sqrt{2}} - v' \right] \\
\varepsilon v'' + \varepsilon \tilde{k}_v \left[v - \frac{(x_1 + x_2)}{\sqrt{2}} \right]^3 + \varepsilon \tilde{\lambda} \left[v' - \frac{(x_1' + x_2')}{\sqrt{2}} \right] &= 0
\end{aligned} \tag{6.47}$$

Note that the introduced modal transformation decouples the left-hand-sides of the linear oscillators of the primary system but there is still $O(\varepsilon)$ coupling between the two linear modes through the nonlinear and damping terms on the right-hand-sides. In (6.47), we have introduced the notations $\tilde{A}_1 = \tilde{F}_1 + \tilde{F}_2$ and $\tilde{A}_2 = \tilde{F}_1 - \tilde{F}_2$, which represent the modal harmonic excitations of the two linear modes. The additional rescalings,

$$\tilde{x}_1 = \frac{x_1}{\sqrt{2}}; \quad \tilde{x}_2 = \frac{x_2}{\sqrt{2}}; \quad \tilde{\varepsilon} = \frac{\varepsilon}{2} \tag{6.48}$$

bring the system to the following simpler form:

$$\begin{aligned}
\tilde{x}_2'' + 3\tilde{x}_2 &= -\tilde{\varepsilon}\tilde{A}_2 \cos \omega\tau - \tilde{\varepsilon}\tilde{k}_v (\tilde{x}_1 + \tilde{x}_2 - v)^3 - \tilde{\varepsilon}\tilde{\lambda}(\tilde{x}_1' + \tilde{x}_2' - v') \\
\tilde{x}_1'' + \tilde{x}_1 &= \tilde{\varepsilon}\tilde{A}_1 \cos \omega\tau - \tilde{\varepsilon}\tilde{k}_v (\tilde{x}_1 + \tilde{x}_2 - v)^3 - \tilde{\varepsilon}\tilde{\lambda}(\tilde{x}_1' + \tilde{x}_2' - v') \\
\tilde{\varepsilon}v'' + \tilde{\varepsilon}\tilde{k}_v (v - \tilde{x}_1 + \tilde{x}_2)^3 + \tilde{\varepsilon}\tilde{\lambda}(v' - \tilde{x}_1' + \tilde{x}_2') &= 0
\end{aligned} \tag{6.49}$$

For the sake of notational convenience the tildes in the variables will be omitted from now on in the analysis. From the rescaled dynamical system (6.49) we note that *due to its essential stiffness nonlinearity the NES is directly coupled to both modes of the primary system, so it may engage in resonance interactions with both.*

The steady state solutions of system (6.49) will be analyzed using the CX-A method. Before we perform the direct calculation of the periodic steady state responses it is convenient to perform a final coordinate transformation that will bring the rescaled dynamical system (6.49) into its final form. To this end, leaving the first two equations of (6.49) unchanged we replace the third equation (governing the response of the NES) by adding the first two equations of (6.49) and then subtracting from the sum the third equation. Defining the new variable w according to,

$$w \equiv x_1 + x_2 - v \tag{6.50}$$

system (6.49) is rewritten in the following final form:

$$\begin{aligned}
x_2'' + 3x_2 &= -\varepsilon A_2 \cos \omega\tau - \varepsilon k_v w^3 - \varepsilon \lambda w' \\
x_1'' + x_1 &= \varepsilon A_1 \cos \omega\tau - \varepsilon k_v w^3 - \varepsilon \lambda w' \\
w'' + 3x_2 + x_1 &= \varepsilon (A_1 - A_2) \cos \omega\tau - (1 + 2\varepsilon)k_v w^3 - (1 + 2\varepsilon)\lambda w'
\end{aligned} \tag{6.51}$$

which will be the basis of the following analysis.

We begin our treatment by considering harmonic excitations with frequencies close to the first natural frequency of the primary system; hence, we consider direct harmonic excitation of the lower linear mode only. We will refer to this resonance as *in-phase fundamental resonance*. To this end, we introduce the weak frequency detuning $\varepsilon\sigma$ defined as

$$\omega = 1 + \varepsilon\sigma \tag{6.52}$$

which measures the closeness of the excitation frequency ω to the first natural frequency. To apply the CX-A methodology we introduce the following new complex variables,

$$\begin{aligned}
x_1' + ix_1 &= \varphi_1 \exp[j(1 + \varepsilon\sigma)\tau] \\
x_2' + ix_2 &= \varphi_2 \exp[j(1 + \varepsilon\sigma)\tau] \\
w' + iw &= \varphi_w \exp[j(1 + \varepsilon\sigma)\tau]
\end{aligned} \tag{6.53}$$

where $\varphi_1, \varphi_2, \varphi_w$ are assumed to be slowly evolving complex modulations of a fast oscillation at the frequency of the external excitation. By the slow-fast partition in the *ansatz* (6.53) we seek steady state solutions possessing a single fast frequency

equal to the first natural frequency of the primary system. Introducing (6.53) into (6.51) and averaging over one period of the external excitation we obtain the following slow flow dynamical system, which governs the slow evolutions of the modulations φ_1 , φ_2 and φ_w in the neighborhood of the first linear mode:

$$\begin{aligned}\dot{\varphi}_2 + j(\varepsilon\sigma - 1)\varphi_2 &= \frac{-\varepsilon A_2}{2} + \frac{3j\varepsilon k_v}{8} |\varphi_w|^2 \varphi_w - \frac{\varepsilon\lambda}{2} \varphi_w \\ \dot{\varphi}_1 + j\varepsilon\sigma\varphi_1 &= \frac{\varepsilon A_1}{2} + \frac{3j\varepsilon k_v}{8} |\varphi_w|^2 \varphi_w - \frac{\varepsilon\lambda}{2} \varphi_w \\ \dot{\varphi}_w + j\left(\frac{1}{2} + \varepsilon\sigma\right)\varphi_w - \frac{3j}{2}\varphi_2 - \frac{j}{2}\varphi_1 \\ &= \frac{\varepsilon(A_1 - A_2)}{2} + \frac{3j(1 + 2\varepsilon)k_v}{8} |\varphi_w|^2 \varphi_w - \frac{\lambda(1 + 2\varepsilon)}{2} \varphi_w\end{aligned}\quad (6.54)$$

In order to analytically estimate the periodic responses of the system we consider the fixed points of (6.54) by setting $\dot{\varphi}_1 = \dot{\varphi}_2 = \dot{\varphi}_w = 0$. This yields the following system of nonlinear algebraic equations,

$$\begin{aligned}j(\varepsilon\sigma - 1)\varphi_{20} &= \frac{-\varepsilon A_2}{2} + \frac{3\varepsilon j k_v}{8} |\varphi_{w0}|^2 \varphi_{w0} - \frac{\varepsilon\lambda}{2} \varphi_{w0} \\ j\varepsilon\sigma\varphi_{10} &= \frac{\varepsilon A_1}{2} + \frac{3\varepsilon j k_v}{8} |\varphi_{w0}|^2 \varphi_{w0} - \frac{\varepsilon\lambda}{2} \varphi_{w0} \\ j\left(\frac{1}{2} + \varepsilon\sigma\right)\varphi_{w0} - \frac{3j}{2}\varphi_{20} - \frac{j}{2}\varphi_{10} \\ &= \frac{\varepsilon(A_1 - A_2)}{2} + \frac{3(1 + 2\varepsilon)j k_v}{8} |\varphi_{w0}|^2 \varphi_{w0} - (1 + 2\varepsilon)\frac{\lambda}{2}\varphi_{w0}\end{aligned}\quad (6.55)$$

where subscript '0' denotes the value of the corresponding modulation at the fixed point. The solutions of (6.55) can be calculated by simple algebraic manipulations. Indeed, we may reduce the computation to a single third-order inhomogeneous polynomial in terms of the modulus of the complex amplitude φ_{w0} , by recognizing that the system (6.55) can be manipulated to yield,

$$\alpha_2 \bar{\alpha}_2 |\varphi_{w0}|^6 + (\alpha_2 \bar{\alpha}_1 + \alpha_1 \bar{\alpha}_2) |\varphi_{w0}|^4 + \alpha_1 \bar{\alpha}_1 |\varphi_{w0}|^2 = \alpha_3 \bar{\alpha}_3 \quad (6.56)$$

where

$$\begin{aligned}\alpha_1 &= j\left(\varepsilon\sigma + \frac{1}{2}\right) + \frac{3\varepsilon\lambda}{4(\varepsilon\sigma - 1)} + \frac{\lambda}{4\sigma} + \frac{\lambda(1 + 2\varepsilon)}{2} \\ \alpha_2 &= -\left[\frac{9j\varepsilon k_v}{16(\varepsilon\sigma - 1)} + \frac{3jk_v}{16\sigma} + \frac{3jk_v(1 + 2\varepsilon)}{8}\right] \\ \alpha_3 &= \frac{3\varepsilon A_2}{4(\varepsilon\sigma - 1)} - \frac{A_1}{4\sigma} - \frac{\varepsilon(A_1 - A_2)}{2}\end{aligned}$$

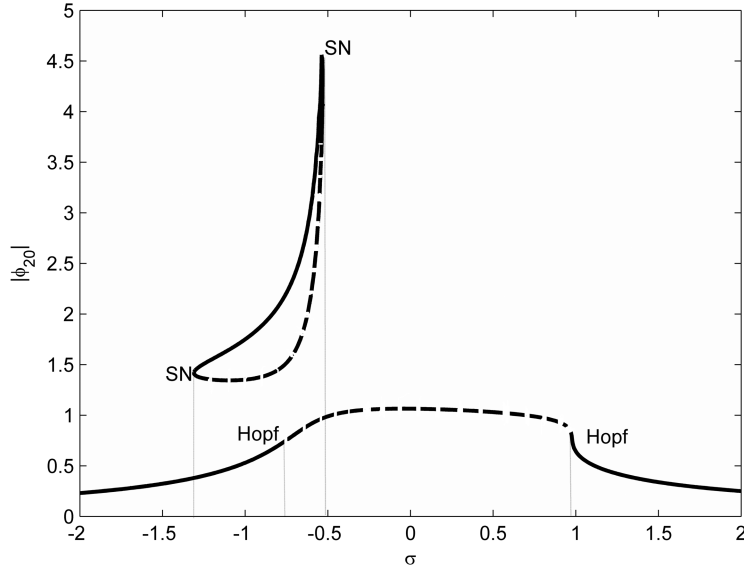


Fig. 6.50 Steady state frequency response for in-phase fundamental resonance (for $\omega \approx 1.0$); dashed lines refer to unstable periodic solutions and solid lines to stable ones.

and overbar denotes complex conjugate. The phase of φ_{w0} and the remaining two amplitudes are then computed through the relations,

$$\begin{aligned}\varphi_{w0} &= \frac{-\alpha_3}{\alpha_1 + \alpha_2 |\varphi_{w0}|^2} \\ \varphi_{20} &= \frac{j\varepsilon A_2}{2(\varepsilon\sigma - 1)} + \frac{3\varepsilon k_v}{8(\varepsilon\sigma - 1)} |\varphi_{w0}|^2 \varphi_{w0} + \frac{j\varepsilon\lambda}{2(\varepsilon\sigma - 1)} \varphi_{w0} \\ \varphi_{10} &= -\frac{jA_1}{2\sigma} + \frac{3k_v}{8\sigma} |\varphi_{w0}|^2 \varphi_{w0} + \frac{j\lambda}{2\sigma} \varphi_{w0}\end{aligned}\quad (6.57)$$

In Figure 6.50 we depict the frequency response plot for this type of excitation. SN and Hopf bifurcations can be analytically studied by performing a stability analysis of the computed fixed points, in accordance to the procedure developed in Section 6.1. Points of bifurcation are indicated in the plot of Figure 6.45. In similarity to previous sections, large values of $|\varphi_{w0}|$ indicate strong steady state TET from the forced primary system to the NES, and, hence, enhanced vibration isolation.

Considering now the *out-of-phase fundamental resonance* of the system by assuming an excitation with frequency close to the second eigenfrequency of the primary system,

$$\omega = \sqrt{3} + \varepsilon\sigma \quad (6.58)$$

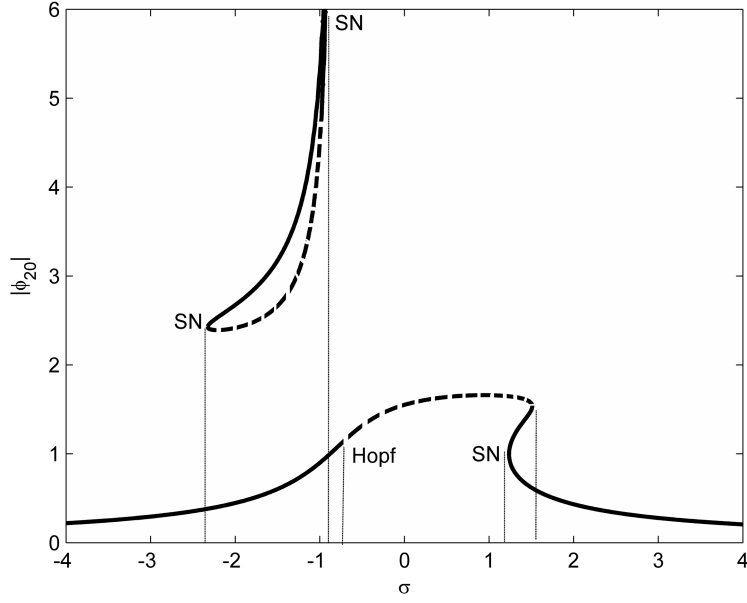


Fig. 6.51 Steady state frequency response plot for out-of-phase fundamental resonance (for $\omega \approx 1.732$); dashed lines refer to unstable periodic solutions and solid lines to stable ones.

we follow a similar CX-A procedure to derive the approximate frequency response plot of Figure 6.51. In similarity to the plot depicted in Figure 6.50, this frequency response plot is based on the analysis of the slow flow dynamics.

It is rather reasonable to expect that SMRs will exist for system (6.49) as well. As in a case of periodic or weakly modulated steady state regimes (generated by Hopf bifurcations), analytical treatment of SMRs must be carried out separately for the cases of in-phase and out-of-phase fundamental resonances. Such reduction is possible in the case of sufficiently small NES mass ε . To this end, we reconsider the original equations (6.49) in slightly modified form, for excitation frequencies close to the first natural frequency of the linear primary system (that is, for the case of in-phase fundamental resonance):

$$\begin{aligned}
 x_2'' + 3x_2 &= -\varepsilon A_2 \cos[(1 + \varepsilon\sigma)\tau] - \varepsilon k_v (x_1 + \varepsilon x_2 - v)^3 - \varepsilon \lambda (x_1' + \varepsilon x_2' - v') \\
 x_1'' + x_1 &= \varepsilon A_1 \cos[(1 + \varepsilon\sigma)\tau] - \varepsilon k_v (x_1 + \varepsilon x_2 - v)^3 - \varepsilon \lambda (x_1' + \varepsilon x_2' - v') \\
 \varepsilon v'' + k_v (v - x_1 - \varepsilon x_2)^3 + \lambda (v' - x_1' - \varepsilon x_2') &= 0
 \end{aligned} \tag{6.59}$$

In this case the ordering of terms with respect to the small parameter ε can only be balanced if we assume that $x_1 \sim O(1)$, $v \sim O(1)$ (under condition of 1:1 resonance) and $x_2 \sim O(\varepsilon)$. If this is the case, then terms related to x_2 in the last two equations of (6.59) bring about corrections of at most $O(\varepsilon^2)$ and can be neglected in lower-order approximations. Following this argument the three-DOF

system (6.59) can be trivially reduced to a two-DOF system similar to (6.1) with appropriate notational accommodation. Thus, the treatment of SMRs in this case may be accomplished similarly to the process described in Section 6.2 and does not need any further analytical consideration. We note, however, that this reduction can only be made due to our assumption of well-separated linear modes of the primary system. When primary systems with closely-spaced modes are considered then coupling (beat phenomena) between linear modes occur and the above reduction to a two-DOF can not be accomplished. In that case a global analysis of the slow flow dynamics of the original, full three-DOF system (6.45) must be performed to study the regimes of SMRs (this raises interesting questions concerning the form of the necessary Poincaré map reduction that needs to be developed to study relaxation oscillations – SMRs in the corresponding higher-dimensional slow flow, and the corresponding bifurcations of that map).

The case of out-of-phase fundamental resonances of (6.59), i.e., of SMRs in the vicinity of the second natural frequency can be treated similarly, and the associated problem can be reduced to a two-DOF problem as well. It should be mentioned that SMRs are expected to exist in an $O(\varepsilon)$ -neighborhood of the exact resonance. As mentioned above, since the two natural frequencies of the primary system of (6.59) are well separated, no overlap of in-phase and out-of-phase SMRs is expected in the system under consideration. The open question, of course, that merits further investigation is the interaction of these two types of SMRs when the primary system has closely spaced modes; however, this interesting question is not dealt with in this work.

Motivated by the previously outlined tuning procedure for the case of SDOF linear primary system (see Section 6.3.2), the principal aim of the tuning procedure for selecting the coupling stiffness k_v and the coupling damper λ in the three-DOF system (6.45), should be to allow excitation of in-phase or out-of-phase SMRs for fixed NES mass. We will demonstrate this tuning procedure by means of a demonstrative example. Specifically, we consider the following values for the amplitudes of the excitation and the NES mass, $A_1 = 1$, $A_2 = 3$, and $\varepsilon = 0.01$. We need to select the NES parameters (k_v, λ) in such a way as to allow excitation of SMRs in the neighborhood of each mode of the linear primary system. In order to determine these values, in the neighborhood of each excited mode we vary the NES parameters (k_v, λ) with a small step, and for each pair we construct the corresponding one-dimensional Poincaré maps that we introduced in Section 6.2 for studying relaxation oscillations. Then, we obtain the frequency ranges of existence of in-phase and out-of-phase SMRs (as the stable fixed points of the corresponding one-dimensional maps) in the neighborhood of each excited mode. By ensuring that for the selected pair (k_v, λ) there exist both stable in-phase and out-of-phase SMRs in the frequency ranges of interest (in the neighborhoods of the two linear modes) we satisfy the basic requirement of the tuning procedure.

Suppose that the described procedure yields a pair of NES parameters $k_v = 1$, $\lambda = 0.2$ that allows SMRs in the neighborhood of each of the modes of the primary system. For this NES parameter pair we plot the corresponding in-phase and out-of-phase fundamental frequency response diagrams as in Figure 6.52; these

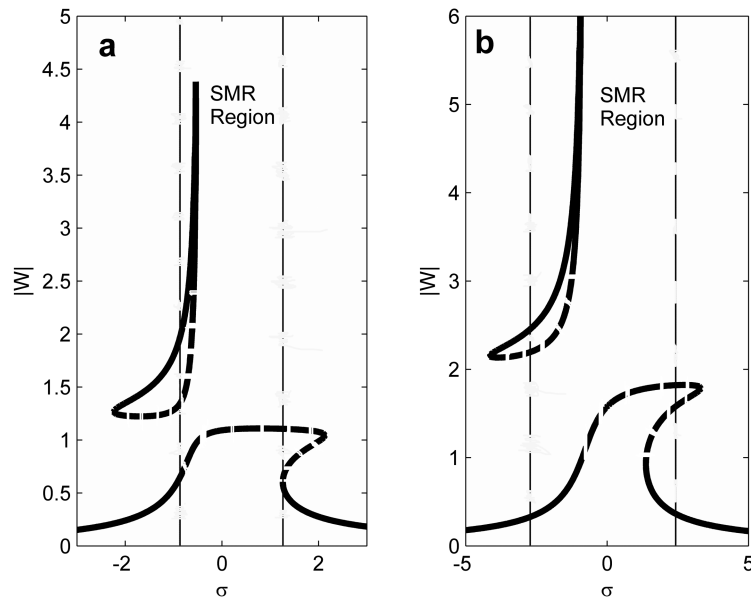


Fig. 6.52 Fundamental resonance plots: (a) in-phase, (b) out-of-phase; dashed lines refer to unstable periodic solutions and solid lines to stable ones; the domains of existence of SMRs are indicated; in the shaded region undesirable conditions for vibration isolation develop.

diagrams possess branches of stable periodic oscillations that co-exist with regimes of stable SMRs (computed as outlined above). Despite the excitation of SMRs in the vicinity of each mode we note that an undesirable situation has developed in the neighborhood of the left bound of the domain of existence of SMRs for the case of in-phase fundamental resonances (see Figure 6.52a). Indeed, observing the diagram of Figure 6.52b we can see that the lower-frequency Hopf bifurcation (point A) occurs on the lower stable branch of periodic solutions slightly before the lower (left) boundary of the domain of existence of SMRs. This bifurcation causes an undesirable effect on the system response since the loss of stability of the lower branch may be accompanied by the jump of the dynamics to the upper stable branch which yields large-amplitude vibrations; clearly this is an unfavorable scenario for vibration isolation. In order to avoid this effect our design should be to translate the lower Hopf bifurcation of the lower branch into the domain of existence of SMRs, in order to ensure the transition from the lower stable branch of periodic solutions into the regime of SMRs with increasing frequency detuning, thus avoiding potential undesirable jumps to the larger-amplitude stable branch of solutions. This can be achieved easily by appropriate design of the system parameters, e.g., by increasing the damping parameter from $\lambda = 0.2$ to $\lambda = 0.4$, as depicted in Figure 6.53 where the corresponding frequency response plots of the redesigned system are depicted.

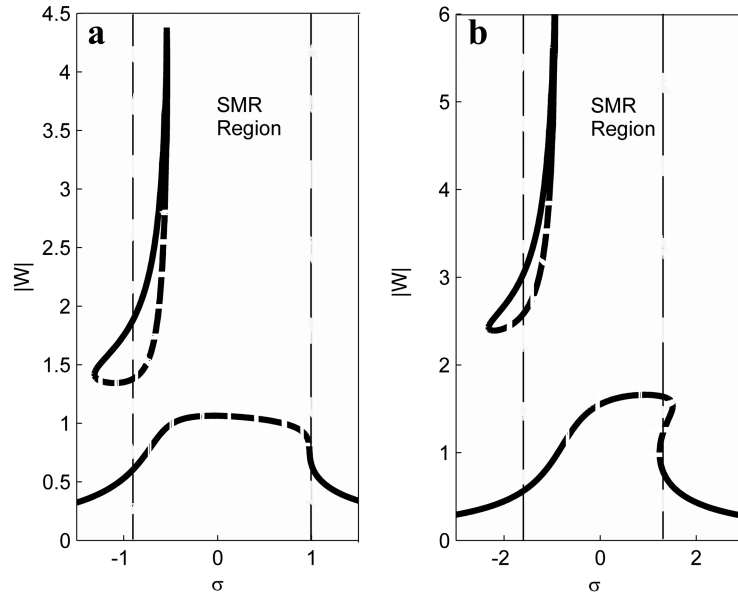


Fig. 6.53 Transition of the Hopf bifurcation point on the lower stable branches of periodic solutions of fundamental, (a) in-phase and (b) out-of-phase resonance plots by increasing the damping λ ; dashed lines refer to unstable periodic solutions and solid lines to stable ones; the domains of existence of SMRs are indicated.

The frequency response diagrams presented in Figure 6.53 suggest that by increasing the frequency detuning there is the possibility of transitions from the lower stable branch of periodic solutions to the regime of SMRs for both the in-phase and out-of-phase modes. The following direct numerical simulations carried out for this system in the entire frequency range under study (including both modes) and zero initial conditions, reveal that no undesirable transitions (jumps) to the upper branches of periodic solutions are realized. It is essential to note that there still exists the possibility of transitions of the dynamics to the upper stable branches for different (non-zero sets of initial conditions. These regimes may be excited, for example, by relatively large initial displacements; e.g., this is the case when strong non-harmonic or even non-periodic but repeated excitations – in the form of impulses or trains of pulses – are applied, which are capable of inducing transitions of the dynamics to the high-amplitude stable solution branches, and thus affect adversely the vibration isolation design. Such excitations are not considered in this work, however, and investigation of their effects on the steady state dynamics of systems with attached NES is left as an open problem.

Summarizing the results of the example provided above, we have seen that it is not enough to excite in-phase or out-of-phase SMRs for achieving satisfactory vibration isolation performance; what is also important is to design the system so that low-frequency Hopf bifurcation points on the lower stable branches of periodic so-

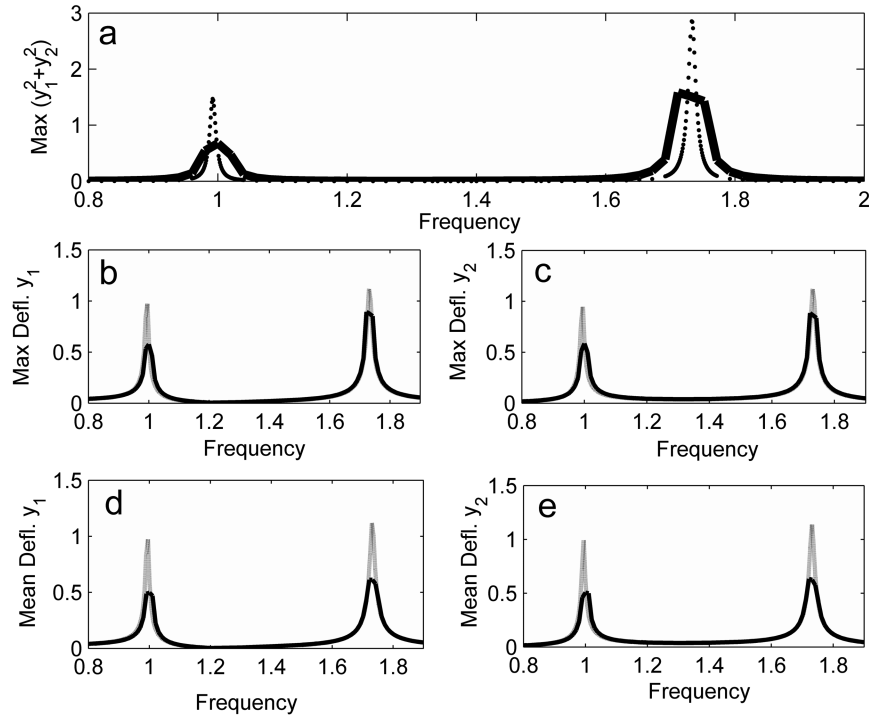


Fig. 6.54 Numerical frequency responses: (a) $\max(y_1^2 + y_2^2)$; (b) $\max(y_1)$; (c) $\max(y_2)$; (d) mean amplitude of $y_1(t)$; (e) mean amplitude of $y_2(t)$; superimposed to each plot is the corresponding frequency response of the optimally tuned linear absorber (dotted lines).

lutions occur well inside the domain of existence of SMRs. Indeed, by shifting these bifurcation points on the lower branches of periodic responses into the domain of existence of SMRs, we ensure effective and robust vibration isolation by application of the NES.

In order to study more systematically the vibration mitigation performance of the NES, we construct numerical frequency response plots for zero initial conditions over the entire frequency range of interest that include both natural frequencies of the linear primary system. Referring to system (6.43), in the considered frequency response plots we depict the variations of the following quantities for varying excitation frequency ω : (i) $\max(y_1^2 + y_2^2)$ (see Figure 6.54a); (ii) $\max(y_1)$ and $\max(y_2)$ (see Figures 6.54b, c); and (iii) mean amplitudes of $y_1(t)$ and $y_2(t)$ (see Figures 6.54d, e). For comparison, on the same plots we also depict the corresponding frequency responses of the optimally tuned linear absorber; the linear absorber was tuned numerically by minimizing the summation of the two resonant peaks of the corresponding frequency response curve. For these simulations the parameters of the problem were selected as $A_1 = 1$, $A_2 = 3$, $k_v = 1$, $\lambda = 0.4$ and $\varepsilon = 0.01$.

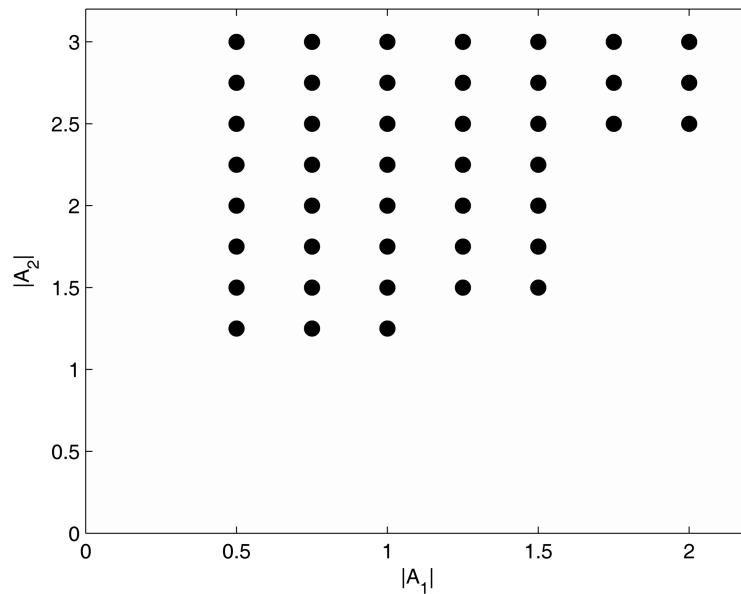


Fig. 6.55 Comparisons of linear and nonlinear designs in the (A_1, A_2) plane; dots indicate better performance of the SMR-based nonlinear design.

We now perform a numerical parametric study of the amplitudes of the external excitations for which SMRs in the nonlinear design provide better vibration isolation performance than the optimally tuned absorber in the linear design. It should be noted that both linear and nonlinear vibration absorbers are tuned according to the same criteria discussed above (that is, minimal sum of resonant peaks of the maximal response deflection). In Figure 6.55 we depict schematically the zone on the (A_1, A_2) plane for which the SMR-based nonlinear vibration isolation is preferable.

From the results presented in Figure 6.55 we note that better performance of SMR-based nonlinear vibration isolation is realized for relatively high amplitudes of external excitations. This result is not surprising since the analytical model predicts that the upper branch of the SIM does not depend on the amplitude of excitation; it follows that for some low excitation amplitudes SMRs may be already excited, however, the system response will be rather high compared to the one realized when a linear absorber is applied. In the case of high amplitude excitation, the response of the system with linear absorber attached will overcome the SMRs. This is due to the fact that SMRs are weakly affected by the increase of the excitation amplitudes; this is contrary to the case when the linear absorber is attached.

In order to demonstrate the robustness of the nonlinear vibration isolation achieved by excitation of either the lower branch of stable periodic responses or the regime of SMRs, we have performed a series of direct numerical integrations of the original dynamical system (6.47) for random sets of initial conditions. Specifically, we randomly picked 300 triplets of initial displacements in the ranges

$-0.5 \leq x_i(0) \leq 0.5$, $i = 1, 2$ and $-0.5 \leq v(0) \leq 0.5$, and zero initial velocities, under conditions of in-phase or out-of-phase fundamental resonances. Two frequency detuning values were selected for each type of fundamental resonance. Referring to the previously discussed frequency response diagrams of the system with NES attached [see Figures 6.50–6.53], the first value of frequency detuning refers to the region of two co-existing stable periodic regimes, and is out of the domain of existence of stable SMRs; while for the second detuning value there is co-existence of the regime of stable SMRs and the upper branch of stable periodic responses. Hence, the frequencies of external excitation are defined as follows: for the in-phase fundamental resonances, $\omega = 1 + \varepsilon\sigma$, with $\sigma = -0.8, -1.0$; for the out-of-phase fundamental resonances, $\omega = \sqrt{3} + \varepsilon\sigma$, with $\sigma = -1.2, -1.5$. The system parameters are selected as $A_1 = 1$, $A_2 = 3$, $\varepsilon = 0.01$, $\lambda = 0.4$ and $k_v = 1$.

The results of these simulations are depicted in Figure 6.56. The attractor reached in each of the numerical simulations (corresponding to a triplet of initial conditions chosen from the random set) is marked by a diamond when the attractor is a stable SMR, or by a circle when the attractor is on the upper branch of stable periodic solutions. It is clear from these results that for values of the frequency detuning in the regime of co-existence of two branches of stable periodic motions, all simulations are attracted by the periodic solution on the lower branch. For values of frequency detuning in the regime of co-existence of SMRs and stable periodic responses, all numerical simulations are attracted by a stable SMR. These results provide additional confirmation of the robustness of the steady state regimes related to the lower stable branch of periodic solutions and the regime of stable SMRs. Both these regimes are favorable to the objective of vibration isolation. It is essential to note that the considered initial displacements possess much larger magnitudes than the amplitudes of the external excitations.

The results presented in this chapter indicate that there are some major differences between commonly used designs based on linear vibration absorbers (TMDs) and the essentially nonlinear absorber (NES) designs proposed herein. First, the performance of the NES-based design depends on the amplitude of the external excitation, i.e., it works properly only for specific ranges of forcing amplitudes. The TMD, at least in theory, is free of this drawback as the dynamics is purely linear and hence energy-independent; however, in practice too high amplitudes of the external forcing are also problematic in the linear design, as they yield prohibitively large displacements of the damper which either leads to degeneration of the system due to fatigue or drives the dynamics out of the linear regime. On the other side, if the excitation is small enough, no protection is required in the first place. From this viewpoint, the NES may be plausible despite its limitations concerning the permissible range of external excitation amplitudes.

The nonlinear absorber has two main advantages compared to the TMD. The first is based on the fact that, simply, it is more effective – it yields better vibration isolation performance. However, with this comes the possible drawback that alternative undesirable response regimes might co-exist with the ones that are favorable for vibration isolation. Still, as demonstrated in the previous study, proper design of the NES will guarantee that for certain ranges of initial conditions these problem-

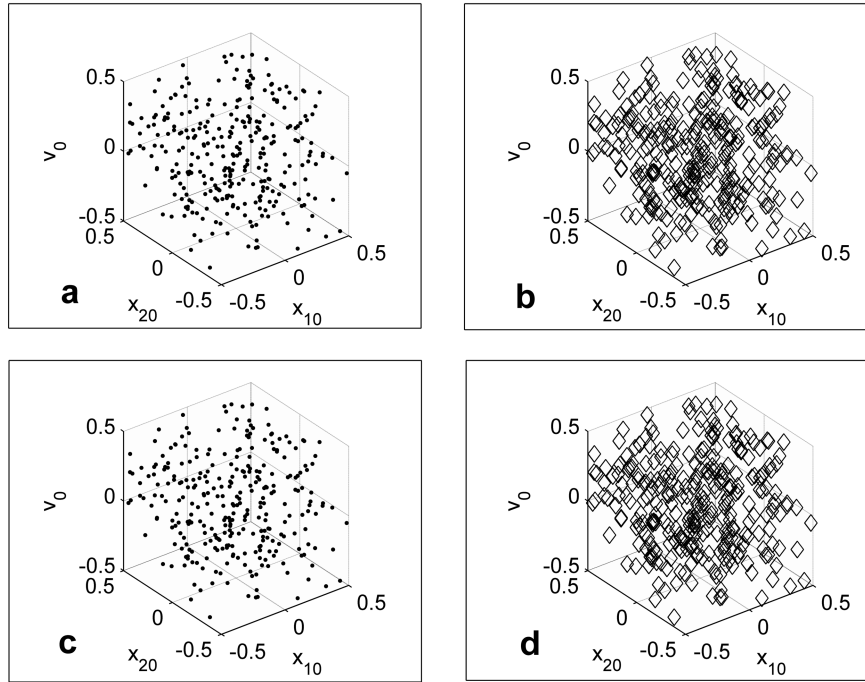


Fig. 6.56 Attractors of the dynamics for random sets of the initial conditions: (a) in-phase fundamental resonance, $\sigma = -1$; (b) in-phase fundamental resonance, $\sigma = -0.8$; (c) out-of-phase fundamental resonance, $\sigma = -1.5$, (d) out-of-phase fundamental resonance, $\sigma = -1.2$; dots denote the lower stable branch of periodic orbits, and diamonds denote the regime of stable SMRs.

atic responses are not excited at all. The regime of SMRs greatly facilitates robust vibration absorption, since through its extended domain of attraction it is capable of deferring the dynamical flow from the undesired dynamic attractors. Consequently, the regime of SMRs is a rather desirable response regime for effective vibration mitigation. This conclusion is a bit unexpected in the sense that normally, quasi-periodic responses are rather undesirable in engineering systems. Yet, this counter-intuitive conclusion is perhaps in line with the overall theme of this work, which is the consideration of essentially nonlinear designs in engineering practice. This contrasts with the view that nonlinearities in engineering are counterproductive and hence should be avoided at all cost.

The second major advantage of the proposed essentially nonlinear absorber is its capability to work over broad frequency bands. While connected to a two-DOF primary system, the NES demonstrates much better performance than a properly tuned TMD. To achieve comparable broadband performance by means of linear vibration absorbers, one should design them to possess more degrees of freedom.

These advantageous properties of the strongly nonlinear vibration absorbers were revealed by means of theoretical analysis and numeric simulation; experimental ver-

ifications on the subject are few and incomplete. Hence, there is the need for further experimental study and validation of the proposed NES designs. Moreover, the study of applying SDOF or MDOF NESs for vibration isolation of periodically forced continuous elastic systems can be carried out by extending the methodologies and optimization procedures developed in this chapter. In the context of applying such designs to practical engineering problems, a systematic and rigorous study of the issue of robustness of nonlinear vibration isolation in the presence of co-existing unfavorable response regimes deserves further investigation.

References

*ReferencesReferencesReferences

- Akay, A., Xu, Z., Experiments on vibration absorption using energy sinks, *J. Acoust. Soc. Am.* **118**(5), 3043–3049, 2005.
- Arnold, V.I., Afrajmovich, V.S., Il'yashenko, Yu.S., Shil'nikov, L.P., *Dynamical Systems V*. Encyclopedia of Mathematical Sciences, Springer-Verlag, Berlin/New York, 1994.
- Bonello, P., Brennan, M.J., Elliot, S.J., Vincent, J.F.V., Jeronimidis, G., Designs for an adaptive tuned vibration absorber with variable shape stiffness element, *Proc. Roy. Soc. A* **461** (2064), 3955–3976, 2005.
- Brennan, M.J., Some recent developments in adaptive tuned vibration absorbers/neutralizers, *Shock Vib.* **13**(4–5), 531–543, 2006.
- Bykhovsky, I.I., *Fundamentals of Vibration Engineering*, Robert E. Krieger, New York, 1980.
- Carcattera, A., Akay, A., Koç, I.M., Near-irreversibility in a conservative linear structure with singularity points in its modal density, *J. Acoust. Soc. Am.* **119**(4), 2141–2149, 2006.
- Carcattera, A., Akay, A., Koç, I.M., Theoretical foundations of apparent-damping phenomena and nearly irreversible energy exchange in linear conservative systems, *J. Acoust. Soc. Am.* **121**(4), 1971–1982, 2007.
- Carrella, A., Brennan, M.J., Waters, T.P., Static analysis of a passive vibration isolator with quasi-zero-stiffness characteristic, *J. Sound Vib.* **301**(3–5), 678–689, 2007a.
- Carrella, A., Brennan, M.J., Waters, T.P., Optimization of a quasi-zero-stiffness isolator, *J. Mech. Sc. Tech.* **21**(6), 946–949, 2007b.
- Den Hartog, J.P., *Mechanical Vibrations*, McGraw-Hill, New York, 1956.
- Feldman, M., Time-varying vibration decomposition and analysis based on the Hilbert transform, *J. Sound Vib.* **295**, 518–530, 2006.
- Frahm, H., Device for damping vibrations of bodies, U.S. Patent 989,958, 1911.
- Gendelman, O.V., Starosvetsky, Y., Quasi-periodic response regimes of linear oscillator coupled to nonlinear energy sink under periodic forcing, *J. Appl. Mech.* **74**, 325–331, 2007.
- Gendelman, O.V., Gourdon, E., Lamarque, C.-H., Quasi-periodic energy pumping in coupled oscillators under periodic forcing, *J. Sound Vib.* **294**, 651–662, 2006.
- Gendelman, O.V., Starosvetsky, Y., Feldman, M., Attractors of harmonically forced linear oscillator with attached nonlinear energy sink I: Description of response regimes, *Nonl. Dyn.* **51**, 31–46, 2008.
- Guckenheimer, J., Holmes, P., *Nonlinear Oscillations, Dynamical System, and Bifurcation of Vector Fields*, Springer-Verlag, New York, 1983.
- Guckenheimer, J., Hoffman, K., Weckesser, W., Bifurcations of relaxation oscillations near folded saddles, *Int. J. Bif. Chaos* **15**, 3411–3421, 2005.
- Guckenheimer, J., Wechselberger, M., Young, L.-S., Chaotic attractors of relaxation oscillators, *Nonlinearity* **19**, 701–720, 2006.
- Jackson, E.A., *Perspectives of Nonlinear Dynamics*, Vol. 1, Cambridge University Press, 1991.

- Koç, I.M., Carcaterra, A., Xu Z., Akay, A., Energy sinks: Vibration absorption by an optimal set of undamped oscillators, *J. Acoust. Soc. Am.* **118**(5), 3031–2042, 2005.
- Natsiavas, S., Steady state oscillations and stability of non-linear dynamic vibration absorbers, *J. Sound Vib.* **156**, 227–245, 1992.
- Natsiavas, S., Dynamics of multiple degree-of-freedom oscillators with colliding components, *J. Sound Vib.* **165**, 439–453, 1993a.
- Natsiavas, S., Vibration absorbers for a class of self-excited mechanical systems, *J. Appl. Mech.* **60**, 382–387, 1993b.
- Natsiavas, S., Mode localization and frequency veering in a damped system with dissimilar components, *J. Sound Vib.* **165**, 137–147, 1993c.
- Newhouse, S.E., Diffeomorphisms with infinitely many sinks, *Topology* **13**, 9–18, 1974.
- Ormondroyd, J., Den Hartog, J.P., The theory of the dynamic vibration absorber, *Trans. ASME* **50**, A9–A22, 1928.
- Rice, H.J., McCraith, J.R., Practical non-linear vibration absorber design, *J. Sound Vib.* **116**, 545–559, 1987.
- Roberson, R.E., Synthesis of a nonlinear dynamic vibration absorber, *J. Franklin Inst.* **254**, 205–220, 1952.
- Shaw, J., Shaw, S.W., Haddow, A.G., On the response of the nonlinear vibration absorber, *Int. J. Nonlinear Mech.* **24**, 281–293, 1989.
- Starosvetsky, Y., Gendelman, O.V., Attractors of harmonically forced linear oscillator with attached nonlinear energy sink II: Optimization of a nonlinear vibration absorber, *Nonl. Dyn.* **51**, 47–57, 2008.
- Szmolyan, P., Wechselberger, M., Relaxation oscillations in R^3 , *J. Diff. Eq.* **200**, 69–104, 2004.
- Virgin, L.N., Davis, R.B., Vibration isolation using buckled struts, *J. Sound Vib.* **260**, 965–973, 2003.
- Virgin, L.N., Santillan, S.T., Plaut, R.H., Vibration isolation using extreme geometric nonlinearity, in *Proceedings Euromech Colloquium 483 on Geometrically Nonlinear Vibrations of Structures*, July 9–11, FEUP, Porto, Portugal, 2007.
- Wiggins, S., *Introduction to Applied Nonlinear Dynamical Systems and Chaos*, Springer-Verlag, New York, 1990.

Chapter 7

NESs with Non-Smooth Stiffness Characteristics

In this chapter we consider NESs with non-smooth stiffness nonlinearities, such as, clearances and vibro-impacts. Apart from their interesting nonlinear dynamics, the additional motivation for studying this class of nonlinear attachments is their capacity to absorb shock energy at fast time scales. The consequence of this capacity for rapid passive energy absorption is that this type of NESs are good candidates for applications where the targeted energy transfer (TET) from the directly forced primary structure to the NES(s) must be accomplished at the very early stage of the motion, that is, immediately after the application of the external shock where the energy is at its highest level; examples are, structures under seismic excitation or cars during collision.

We will provide a theoretical basis for assessing the capacity of NESs with non-smooth nonlinearities for TET at fast time scales, and postpone until Chapter 10 the discussion of the application of NESs with vibro-impact nonlinearities to the important problem of passive seismic mitigation of structures. For works on the mechanics of systems with non-smooth stiffness or damping nonlinearities we refer to the monographs by Babitsky (1998), Persson (1998), Brogliato (1999), Wiercigroch and de Kraker (2000), Babitsky and Krupenin (2001), Glocker (2001), Awrejcewicz and Lamarque (2003) and references therein. In the first two sections we provide numerical evidence of the capacity for shock isolation of NESs with non-smooth stiffnesses. In the following sections we will be focusing on systems with NESs possessing clearance or vibro-impact nonlinearities, in an effort to study certain aspects of the complex dynamics of these systems and related them to TET.

7.1 System with Multiple NESs Possessing Clearance Nonlinearities

We initiate the study of TET in coupled mechanical oscillators with NESs possessing non-smooth stiffness characteristics (referred to from now on as *non-smooth NESs* – *NS NESs*) by studying the shock isolation properties of a system of two

coupled non-conservative linear oscillators with NESs possessing clearance nonlinearities (Georgiades, 2006; Georgiades et al., 2005). Apart from the fact that such non-smooth stiffness elements introduce strong nonlinearities to the system, they are rather easy to implement in practical settings since they can be realized by means of assemblies of linear stiffnesses. This renders the proposed designs practical in their implementation, and convenient to study experimentally under realistic forcing conditions (e.g., refer to the experimental work reported in Chapter 10).

7.1.1 Problem Description

The system considered in this section is depicted in Figure 7.1. The primary system is composed of two weakly coupled, viscously damped linear oscillators (LOs – referred to as LO 1 and 2), where the small parameter of the problem, $0 < \varepsilon \ll 1$, scales the weak coupling. To each of the two LOs there is an attached NS NES (labeled as NES 1 or 2 – see Figure 7.1) through a weak linear stiffness; each NES possesses viscous damping and an internal restoring linear spring which acts in parallel to a linear stiffness with clearance. We assume that an external shock $F(t)$ is applied to LO 1, and wish to examine the capacity of the two NS NESs to passively and *rapidly* extract shock energy from (and thus isolate from shock) the primary system. That is, *we aim to study the capacity of the NS NESs to absorb shock energy from the primary system at a sufficiently fast time scale and reduce the level of vibration of the primary system at the initial stage of the motion where the energy is at its highest level.*

Note that this objective is more demanding than similar objectives for TET posed in previous Chapters, where effectiveness of TET was judged primarily based on asymptotic energy dissipation measures (EDMs), i.e., by studying the capacity of a ('smooth') NES to absorb significant portions of the energy induced in a primary system, without paying much attention on the time scale of TET (i.e., on how rapid TET is). In addition, contrary to our studies of NESs with smooth stiffness characteristics carried out in previous chapters, in the present study we do not make any assumption regarding the smallness of the NES masses m_1, \dots, m_4 , allowing them to be $O(1)$ quantities.

Hence, we aim to show that appropriately designed NS NESs can rapidly absorb significant fractions of the broadband shock energy of the primary system through passive TET, and locally dissipate this energy without 'spreading it back' to the primary system. If this type of TET can occur at a sufficiently fast time scale, then this should result in drastic reduction of the level of vibration of the primary system at the critical initial stage of the motion (that is, immediately after the shock has been applied), and, hence, to effective passive shock isolation. As shown below, *the non-smooth stiffness characteristics of the NESs can, indeed, yield broadband TET on a fast time scale.*

Returning to the system of Figure 7.1, the non-smooth stiffnesses of the two NS NESs are piecewise linear, and expressed as

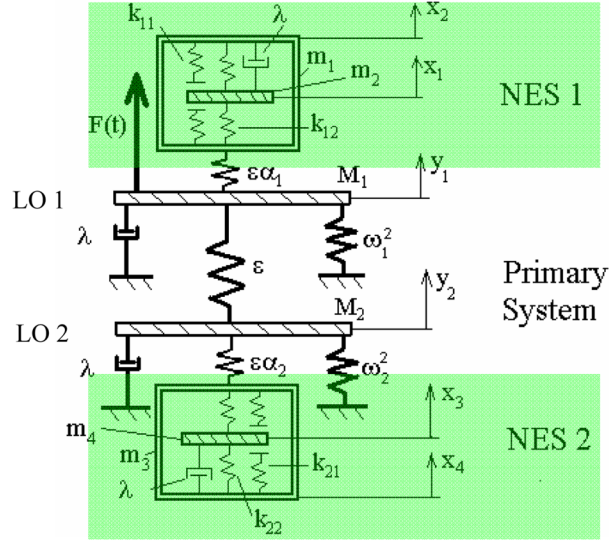


Fig. 7.1 Primary system with multiple NES with clearance nonlinearities.

$$G_1(v_1) = \begin{cases} k_{12}v_1 + k_{11}(v_1 + e_1), & v_1 \leq -e_1 \\ k_{12}v_1, & -e_1 < v_1 < e_1 \\ k_{12}v_1 + k_{11}(v_1 - e_1), & v_1 \geq e_1 \end{cases} \quad (7.1a)$$

and

$$G_2(v_2) = \begin{cases} k_{22}v_2 + k_{21}(v_2 + e_2), & v_2 \leq -e_2 \\ k_{22}v_2, & -e_2 < v_2 < e_2 \\ k_{22}v_2 + k_{21}(v_2 - e_2), & v_2 \geq e_2 \end{cases} \quad (7.1b)$$

where $v_1 = x_2 - x_1$, $v_2 = x_4 - x_3$, and e_1, e_2 denote the clearances at the upper and lower NESs, respectively. We note that in the limits $k_{11}, k_{21} \rightarrow \infty$, the clearance nonlinearities approach vibro-impact (VI) limits, so the NS NES design considered herein can be extended to the VI case as well. As mentioned above, the considered non-smooth stiffness nonlinearities represent strong forms of stiffness nonlinearities. This can be easily inferred from the VI limit, where each vibro-impact represents an impulsive (pseudo) excitation of the system, and, as a result, excites modes of the system over a broad frequency range. Therefore, we anticipate that the dynamic interactions in the system of Figure 7.1 will be broadband.

We introduce at this point the following coordinate transformations:

$$u_1 = (x_1 + x_2)/2, \quad v_1 = x_2 - x_1, \quad u_2 = (x_3 + x_4)/2, \quad v_2 = x_4 - x_3 \quad (7.2)$$

In physical terms, variables v_1 and v_2 are the relative displacements of the internal masses m_2 and m_4 of the two NESs with respect to their frames, whereas, u_1 and u_2 are related to the motions of their centers of mass. Using these new coordinates the

equations of motion of the system are expressed as follows:

$$\begin{aligned}
\ddot{u}_1 + \varepsilon\alpha_1(v_1/2 + u_1 - y_1)^3 &= 0 \\
\ddot{v}_1 + 2\varepsilon\alpha_1(v_1/2 + u_1 - y_1)^3 + 4G_1(v_1) + 4\lambda\dot{v}_1 &= 0 \\
\ddot{y}_1 + \lambda\dot{y}_1 + \omega_1^2 y_1 + \varepsilon\alpha_1(-v_1/2 - u_1 + y_1)^3 + \varepsilon(y_1 - y_2) &= F(t) \\
\ddot{y}_2 + \lambda\dot{y}_2 + \omega_2^2 y_2 + \varepsilon\alpha_2(-v_2/2 - u_2 + y_2)^3 + \varepsilon(y_2 - y_1) &= 0 \\
\ddot{u}_2 + \varepsilon\alpha_2(v_2/2 + u_2 - y_2)^3 &= 0 \\
\ddot{v}_2 + 2\varepsilon\alpha_2(v_2/2 + u_2 - y_2)^3 + 4G_2(v_2) + 4\lambda\dot{v}_2 &= 0
\end{aligned} \tag{7.3}$$

with zero initial conditions. Unless otherwise noted, in the following exposition the masses of the system are assigned the values $M_1 = M_2 = 1$ and $m_1 = m_2 = m_3 = m_4 = 1/2$.

The system of equations (7.3) is solved numerically in Matlab[®] (Georgiades, 2006; Georgiades et al., 2005). The accuracy of the numerical computations is ensured by computing the overall instantaneous energy of the system at each step of the computation, as well as the amount of energy dissipated up to that time instant by the dampers of the system; it is checked that the summation of these two energy measures is identical (within a small numerical round-off error) to the energy input to the system provided by the external shock. A first quantitative assessment of TET efficiency in the system is performed by defining appropriate energy dissipation measures (EDMs), i.e., by computing the percentage of shock energy dissipated by each NES up to a specified time instant (as discussed in previous chapters). To this end the following two EDMs are introduced,

$$E_{\text{NES } i}(t) = \frac{\lambda \int_0^t \dot{v}_i^2(\xi) d\xi}{\int_0^T F(\tau) \dot{y}_1(\tau) d\tau} \times 100, \quad i = 1, 2 \tag{7.4}$$

where T is the duration of the external shock.

An additional quantitative measure to study the efficacy of utilizing the non-smooth NESs for shock isolation is the computation of *nonlinear shock spectra*; in this study these will be plots of the maximum level of vibration attained by the LO 2 for varying grounding stiffness ω_1^2 (see Figure 7.1) and fixed shock and fixed system parameters. The use of shock spectra is a standard technique for designing *linear* shock isolation systems. Although in the nonlinear case the use of such spectra is limited by their dependence on the magnitude of the excitation (or the energy of the motion), nevertheless, as reported below they can provide useful information for judging the effectiveness of the NESs when the *relative duration* of the shock with regard to a characteristic time scale of the problem varies; such a characteristic time scale can be chosen as being equal to either one of the characteristic periods of the linear primary system, $T_i = 2\pi/\omega_i$, $i = 1, 2$. Moreover, one can compare the

nonlinear spectra with reference linear spectra corresponding to systems of similar designs but with no NESs attached in order to assess and compare the effect of TET on shock isolation.

Finally, we note that since the system of Figure 7.1 possesses a symmetrical design, it is capable of *dual-mode shock isolation*, i.e., of preventing transient disturbances of either one of the LOs of the primary system from being transmitted to the other. Clearly, the underlying dynamical mechanism governing this type of shock isolation is passive nonlinear TET.

7.1.2 Numerical Results

In the following series of numerical simulations we consider finite half-sine external excitations of the form:

$$F(t) = \begin{cases} A \sin\left(\frac{2\pi t}{T}\right), & 0 \leq t \leq T \\ 0, & t > 0 \end{cases} \quad (7.5)$$

In Figure 7.2 we depict the portion of shock energy dissipated by the dampers of the two NESs for varying clearance e_1 of NES 1. For this series of simulations the characteristics of the force were set equal to $A = 10^4$ and $T = 10^{-4}$, whereas the other parameters of the system were assigned the following values:

$$\begin{aligned} \varepsilon = 0.27, \quad \lambda = 0.1, \quad \omega_1^2 = \omega_2^2 = 0.5, \quad e_2 = 0.05, \quad k_{12} = k_{22} = 0, \\ k_{11} = 10^2, \quad k_{21} = 10, \quad \alpha_1 = \alpha_2 = 85 \end{aligned}$$

To obtain these results we integrated the equations of motion and computed the transient EDMs (7.4). The plot of Figure 7.2 depicts the asymptotic limit $E_{\text{NES}, t \gg 1} \equiv \lim_{t \gg 1} \{E_{\text{NES } 1}(t) + E_{\text{NES } 2}(t)\}$, which represents the percentage of shock energy that is *eventually* dissipated by the two NESs during the entire duration of the motion. From the plot of Figure 7.2 we conclude that the maximum value of $E_{\text{NES}, t \gg 1}$ is approximately 75% and occurs for $e_1 \approx 0.23$. For clearances greater than this optimal value the internal mass of NES 1 does not possess enough amplitude to overcome the clearance, and the nonlinear effects in the dynamics of NES 1 are eliminated. Note that even above this optimal clearance the damper of NES 1 still dissipates about 42% of shock energy, but this amount is not affected by the clearance e_1 anymore. For $e_1 > 0.23$, however, there are still nonlinear clearance effects in the dynamics of NES 2, as this NES possesses sufficiently large relative amplitude $|v_2|$ to overcome the clearance e_2 .

Referring to the plot of Figure 7.2, we note that in the range of small clearances $e - 1$ there is an almost linear increase of $E_{\text{NES}, t \gg 1}$ as function of clearance. The ineffectiveness of NES 1 for small clearances can be explained by noting that the internal restoring stiffness k_{11} used in these particular simulations is rather strong; it follows that at low clearances the motion x_1 of the internal mass m_2 of NES 1

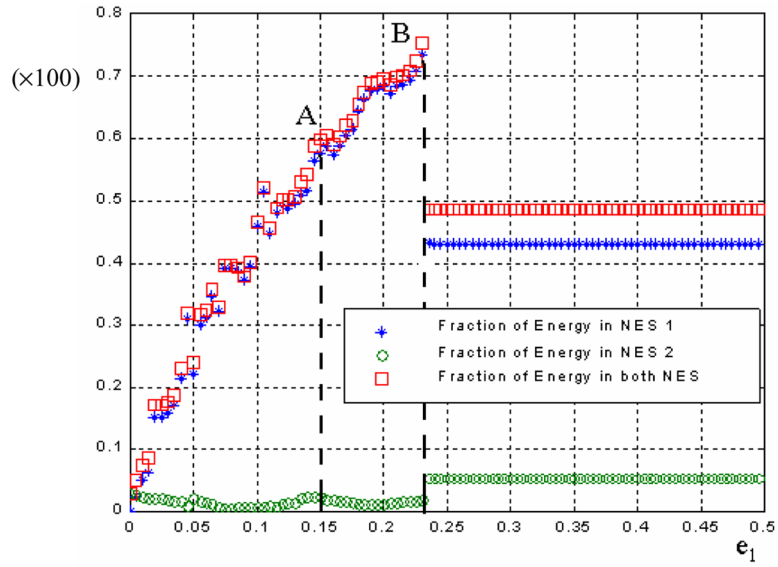


Fig. 7.2 Percentage of shock energy, $E_{NES,t \gg 1}$, eventually dissipated by the two NESs as a function of clearance e_1 , for $A = 10^4$ and $T = 10^{-4}$; points A and B correspond to the plots of Figures 7.4 and 7.5, respectively.

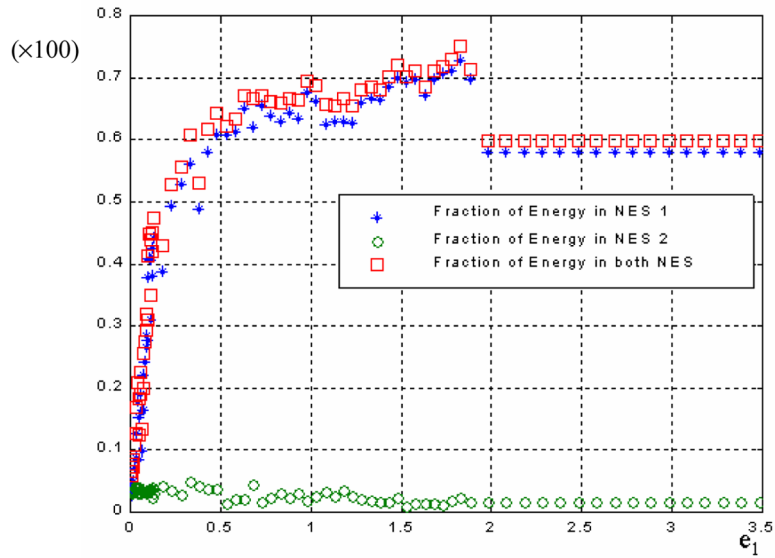


Fig. 7.3 Percentage of shock energy, $E_{NES,t \gg 1}$, eventually dissipated by the two NESs as a function of clearance e_1 , for $A = 10^5$ and $T = 10^{-4}$.

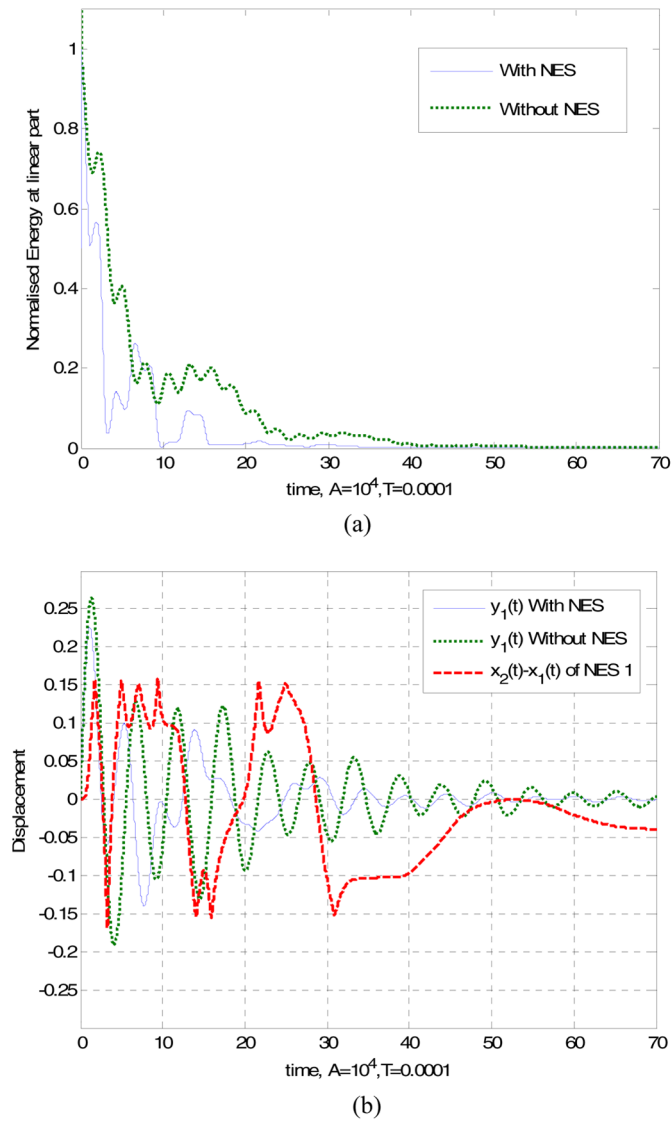


Fig. 7.4 Transient responses corresponding to point A of Figure 7.2: (a) instantaneous normalized energy in the primary system; (b) transient responses of LO 1 and NES 1.

is heavily constrained by its restoring stiffness k_{11} , yielding small relative displacement v_1 . As a result, only a small fraction of the total external energy ends up being dissipated by the internal damper of NES 1.

With increasing clearance, the displacement of the internal mass of NES 1 also increases, which is reflected on the corresponding increase of $E_{NES, t \gg 1}$ in Fig-

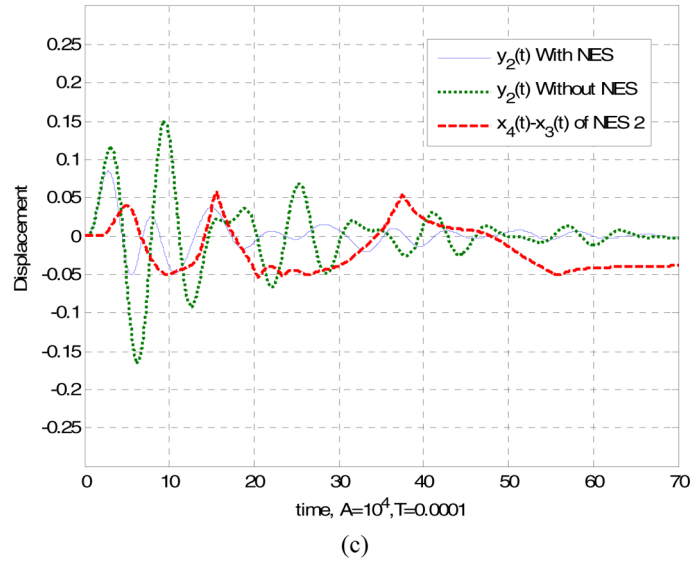


Fig. 7.4 Transient responses corresponding to point A of Figure 7.2: (c) transient responses of LO 2 and NES 2.

ure 7.2. With increasing clearance e_1 one expects the percentage of shock energy dissipated by NES 1 to reach a maximum before settling to a linear motion when the clearance is large enough to eliminate the nonlinear effects in that NES. A similar phenomenon was observed in the dynamics of a vibro-impacting beam (Azeez and Vakakis, 2001) where proper orthogonal decomposition was used to quantitatively identify regions of maximum nonlinear vibro-impact interaction between the beam and the rigid constraints which caused the vibro-impacts.

The effect of increasing the shock amplitude on $E_{NES, t \gg 1}$ is investigated in the plot of Figure 7.3, corresponding to force characteristics $A = 10^5$ and $T = 10^{-4}$, and all other parameters held fixed. We note that since the system under consideration is nonlinear one expects that the dynamics will change qualitatively (and obviously quantitatively) with increasing energy input. In this case the maximum portion of energy dissipated by the two NESs again reaches levels up to nearly 75% (yielding an optimal clearance of $e_1 \approx 1.83$). For sufficiently low clearances, again there is a nearly linear increase of $E_{NES, t \gg 1}$ as function of e_1 ; however, as the clearance increases a saturation-like effect is noted regarding TET efficiency.

To study the time scale of TET in this system we study the diminishing of the energy stored in the primary system in time. In Figures 7.4 and 7.5 we depict representative plots of the instantaneous normalized energy (with respect to the shock energy) of the primary linear system for simulations corresponding to points A ($e_1 = 0.15$) and B ($e_1 = 0.23$) of the plot of Figure 7.2. For comparison purposes the corresponding plots for systems with no NESs attached are also shown. Note the significant reduction of the normalized energy when the NESs are attached

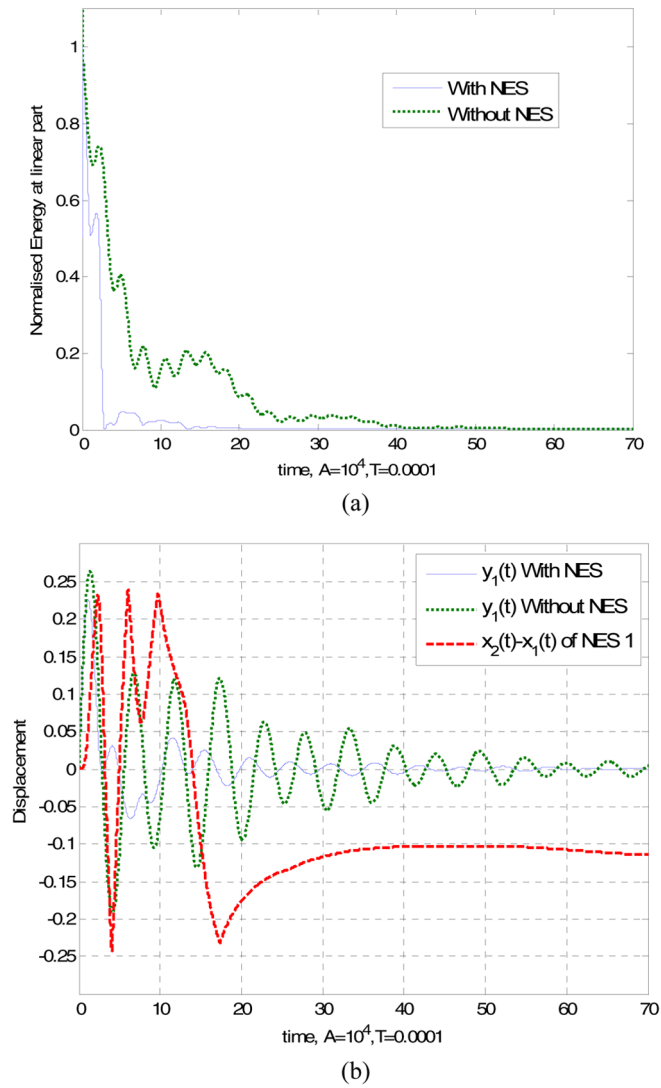


Fig. 7.5 Transient responses corresponding to point B of Figure 7.2: (a) instantaneous normalized energy in the primary system; (b) transient responses of LO 1 and NES 1.

(see Figures 7.4a and 7.5a); also note the significant reduction (nearly 40%) of the corresponding maximum amplitude of $y_2(t)$ (see Figures 7.4c and 7.5c). Clearly, the energy absorbed and dissipated by the NESs results in enhanced shock isolation of the primary system.

A special note is appropriate at this point, with regard to the fast time scale of energy dissipation in the system when NESs are attached. This yields considerable

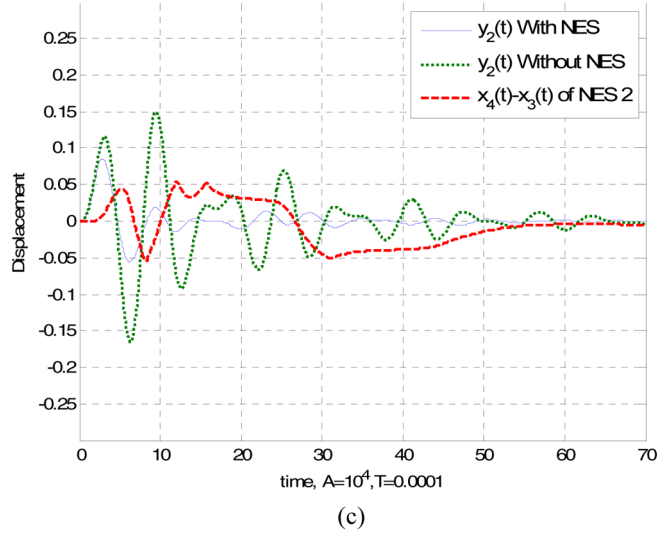


Fig. 7.5 Transient responses corresponding to point B of Figure 7.2: (c) transient responses of LO 2 and NES 2.

energy transfer from the primary system to the NESs right from the beginning of the motion (i.e., during the energetically high regime of the dynamics). The capacity of the NESs to rapidly absorb shock energy in the initial highly energetic regime is critical to their role as shock isolators, and is evidenced by the drastic reduction of the initial peaks in the transient responses of the LOs 1 and 2, occurring immediately after the application of the external shock (see Figures 7.4b, c and 7.5b, c).

We now construct nonlinear shock spectra of the response of the system of Figure 7.1. For fixed external shock, these spectra depict the maximum amplitude reached by the LO 2 of the primary system as function of the grounding stiffness ω_1^2 . In essence, we investigate the maximum amplitude of $y_2(t)$ by varying the duration T of the shock with respect to the period of free oscillation of the LO 1 of the primary system. For comparison purposes we also compute the linear shock spectra of the following two reference systems: (i) the linear primary system with no NESs attached, and, (ii) the primary system with no NESs attached, but possessing masses $M_1 = M_2 = 2$ (that is, when the mass of each of the removed NESs is integrated into the corresponding mass of the LO to which it was originally attached). The second reference system is considered in order to cancel any missing mass effects from the comparisons of the shock spectra of the linear and nonlinear systems.

In Figure 7.6 we depict the nonlinear spectrum for the system with parameters

$$\begin{aligned} \varepsilon = 0.27, \quad \lambda = 0.1, \quad \omega_2^2 = 5.0, \quad e_2 = 0, \quad e_1 = 0.9, \quad k_{12} = k_{22} = 0, \\ k_{11} = k_{21} = 5 \times 10^2, \quad \alpha_1 = \alpha_2 = 85 \end{aligned}$$

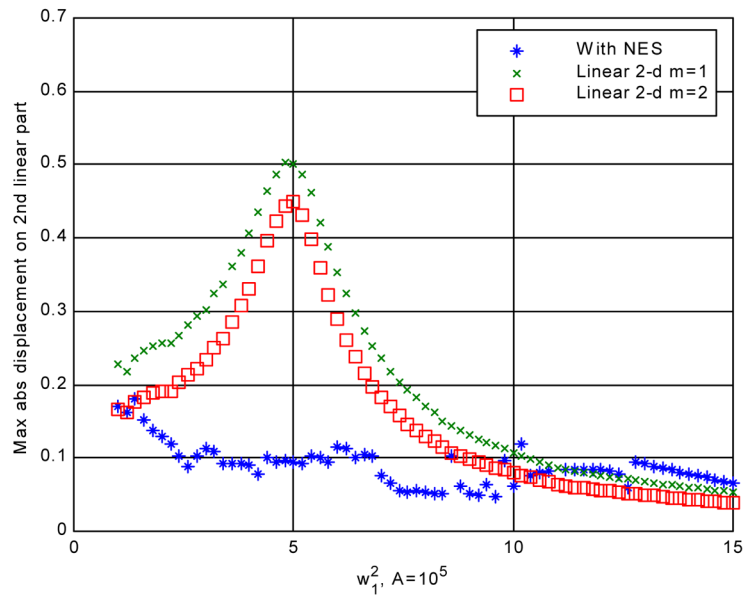


Fig. 7.6 Nonlinear shock spectra of the system with NESs attached, and the two linear reference systems, for $A = 10^5$ and $T = 10^{-4}$.

and shock characteristics $A = 5 \times 10^5$ and $T = 10^{-4}$. Referring to the nonlinear spectrum we note that by adding the NESs we are able to reduce the maximum of $y_2(t)$ by as much as 80% (for $\omega_1^2 \approx 5$); in addition, we are able to nearly eliminate the resonance of the linear spectra in the neighborhood of $\omega_1^2 = 5$. These results demonstrate the drastic effect of broadband TET from the primary system to the NESs on the shock isolation of the primary system. However, since the system under consideration is nonlinear the depicted nonlinear spectrum is energy dependent, and as such, it will vary when the forcing level varies.

Similar conclusions can be drawn by examining the nonlinear spectrum of Figure 7.7 corresponding to $e_1 = 0.51$, force characteristics $A = 5 \times 10^4$ and $T = 10^{-4}$, and all other parameters held fixed. For this weaker shock excitation, there is again significant reduction of the amplitude of the nonlinear system compared to the two linear reference systems. Again, we note the near complete elimination of the linear resonance close to $\omega_1^2 = 5$ from the nonlinear spectrum.

Additional results reported in Georgiades (2006) demonstrate the insensitivity of the EDM with respect to variations of the clearance stiffnesses k_{11} and k_{21} , indicating that the capacities for TET of the NESs do not change significantly in the vibro-impact limit, i.e., for $k_{11}, k_{21} \rightarrow \infty$.

The results reported in this section provide numerical evidence of the capacity of NS NESs for TET at a fast scale, and demonstrate the efficacy of using NS NESs in shock isolation designs. The significance of using NS NESs lies in the fact that they can rapidly absorb a major portion of the shock energy of the primary system, during

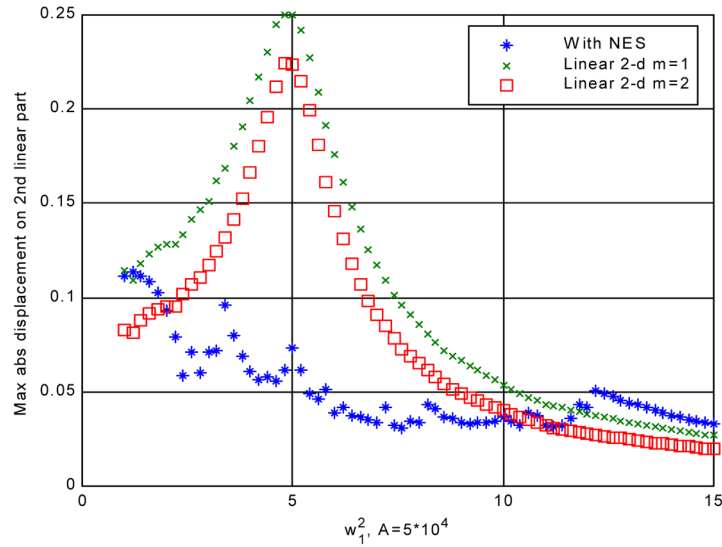


Fig. 7.7 Nonlinear shock spectra of the system with NESs attached, and the two linear reference systems, for $A = 5 \times 10^4$ and $T = 10^{-4}$.

the critical initial (highly energetic) stage of the dynamics, that is, immediately after the external shock is applied. Moreover, the clearance nonlinearities utilized herein are easily implementable in practical settings, since they are realized by means of assemblies of *linear* stiffness elements. In the limits of large clearance stiffnesses the nonlinearities approach VI limits. The numerical simulations performed in the VI limits indicate that the capacities for TET of the NESs are not significantly altered. Indeed, results similar to those reported in this section hold in the VI case as well, provided, of course, that the vibro-impacts occur elastically, i.e., that they do not introduce additional sources of dissipation in the system [for a discussion of the effects of inelastic impacts on vibro-impact dynamics of elastic systems, the reader is referred to Emaci et al. (1997)]. Hence, the afore-mentioned conclusions are expected to hold also for the VI case.

Finally, we point out that the attached NS NESs affect the global dynamics of the integrated system in a time-varying fashion. This is evidenced by the capacity of the NS NESs to passively absorb shock energy from the primary system early on, that is, right at the initiation of the motion when the energy is at its highest (and damage due to shock is expected typically to occur). As the overall energy level decreases due to damping dissipation, the nonlinear effects of the NS NESs on the dynamics gradually decrease, and the system settles into linearized motion regimes. It follows that *the effects of the NS NESs on the system dynamics are expected to be significant only in the highly energetic initial stages of the shock-induced motion*, i.e., at precisely the regime where fast and efficient energy dissipation should be achieved in order to effectively isolate the primary system.

7.2 Vibro-Impact (VI) NESs as Shock Absorbers

We now provide a second application of a non-smooth NES, by studying a SDOF LO (the primary system) with an ungrounded vibro-impact (VI) NES. We aim to study the use of the VI NES as shock absorber. Then, by considering different configurations of primary LOs with VI attachments we will investigate the capacity of this type of attachments to rapidly absorb and dissipate significant portions of shock energy applied to the primary systems. In addition, we will perform parametric studies to determine the dependence of energy dissipation by the VI attachment on the system parameters. To perform these tasks we will employ nonlinear shock spectra similar to the ones considered in the previous section in order to demonstrate that a properly designed VI attachment can significantly reduce the maximum level of shock response of primary systems (over wide frequency ranges) through fast-time broadband TET. This is in contrast to classical linear vibration absorbers, whose actions are restricted to be narrowband. As in the previous section we will show that VI attachments can significantly reduce or even completely eliminate resonances from the corresponding shock spectra, thus providing strong, robust and broadband shock protection to the primary structures to which they are attached.

The regular and chaotic dynamics and bifurcations of vibro-impact (VI) oscillators have been studied extensively in the literature (Shaw and Rand, 1998; Babitsky, 1998; Brogliato, 1999; Kryzhevich and Pliss, 2005; Thota et al., 2006; Thota and Dankowicz, 2006). In an additional series of papers (Masri and Caughey, 1966; Masri and Ibrahim, 1973; Filippov, 1998; Pfeiffer and Glocker, 2000; Blazejczyk-Okolewska, 2001; Leine and Nijmeijer, 2004; Peterka and Blazejczyk-Okolewska, 2005; Sun and Luo, 2006), VI dampers were considered for reducing the vibration levels of structures under periodic or stochastic excitation. Shaw and Holmes (1982, 1983), Shaw (1985) and Shaw and Shaw (1989) applied methods from the geometrical theory of nonlinear dynamics to analyze the dynamics of free and forced dynamics of systems with piece-wise nonlinearities, including systems undergoing vibro-impacts.

In additional recent works, Gorelyshev and Neishtadt (2006) discussed the extension of adiabatic perturbation theory to VI systems; Mikhlin et al. (1998), Leine et al. (2000), Czolczynski and Kapitaniak (2004), Wen et al. (2004), Kryzhevich and Pliss (2005), Dupac and Marghitu (2006), Leine (2006), Lin et al. (2006), Halse et al. (2007), Luo et al. (2007) studied periodic orbits, bifurcations and chaos in discrete and continuous oscillators with clearance or vibro-impact nonlinearities; Ivanov (1993, 2003, 2004) analyzed singularities of the dynamics of systems with bilateral and unilateral constraints and discussed properties of the solutions of systems with Coulomb friction; Zhuravlev (1976, 1977) investigated vibro-impact oscillations using non-smooth coordinate transformations [for an additional application of this method, see also Azeez et al. (1999)], and Pilipchuk (1985, 1988, 2001, 2002) extended this approach by considering non-smooth transformations of the dependent (temporal) variable of the problem; in a recent work Thomsen and Fidlin (2007) developed an analytical methodology for analyzing the dynamics of systems undergoing near-elastic vibro-impacts, by extending the method of discontinuous

transformations in conjunction with an extended averaging principle; Pinnington (2003) analyzed energy exchange and dissipation due to collisions in a line of coupled oscillators; (Valente et al., 2003) provided a geometrical analysis of the dynamics of a vibro-impacting two-DOF system; Salapaka et al. (2001) studied the dynamics of a linear oscillator impacting with a vibrating platform; Quinn (2005) investigated the oscillations of two parametrically excited pendula undergoing vibro-impacts; Li and Darby reported experimental work on the effect of an impact damper on a MDOF system; Zhao and Dankowicz (2006) analyzed degenerate grazing dynamics of impact microactuators using analytical and numerical techniques; Lancioni and Lenci (2007) studied the forced dynamics of a semi-infinite beam on unilateral elastic springs, and Murphy and Morrison (2002) studied computationally and experimentally instabilities and bifurcations of a vibro-impacting string; Hu and Schiehlen (2003) discussed multi-scale simulation of impact responses with applications ranging from wave propagation to rigid body dynamics; Sampaio and Soize (2007) formulated measures that quantify nonlinear effects for uncertain systems, whereas Azeez and Vakakis (2001) approached the issue of quantification of nonlinear effects in the dynamics of vibro-impacting systems by means of the method of proper orthogonal decomposition.

Vedenova and Manevitch (1981), Vedenova et al. (1985), Gendelman (2006) and (Meimukhlin and Gendelman, 2007) examined modeling inelastic impacts with smooth, essentially nonlinear stiffness functions of high degree; Nayeri et al. (2007) investigated the action of multi-unit impact dampers in systems under stochastic excitation, and Namachchivaya and Park (2005) developed an analytical approach based on averaging for studying the dynamics of VI systems under stochastic excitation; Wagg (2007) used energy balance analysis to examine multi-modal systems undergoing vibro-impacts, and studied effective restitution coefficients; Shaw and Pierre (2006) applied tuned impact dampers to rotating structural components and assessed their performance; and Veprik and Babitsky (2001) investigated vibration isolation of a SDOF linear oscillator with a dynamic vibration absorber with motion-limiting constraints.

7.2.1 Passive TET to VI NESs

Following Karayannis et al. (2008), we consider the system depicted in Figure 7.8 consisting of a SDOF LO with mass m coupled to an attachment with vibro-impact (VI) nonlinearity. Apart from the weak restoring stiffness k_1 , it is assumed that the nonlinear attachment undergoes two-sided inelastic impacts when it reaches the left and right limits of the clearance $2e$. We assume that the LO is forced by a half-sine shock $F(t)$ of magnitude A and duration T ,

$$F(t) = \begin{cases} A \sin \frac{2\pi t}{T}, & 0 \leq t \leq \frac{T}{2} \\ 0, & t \geq \frac{T}{2} \end{cases} \quad (7.6)$$

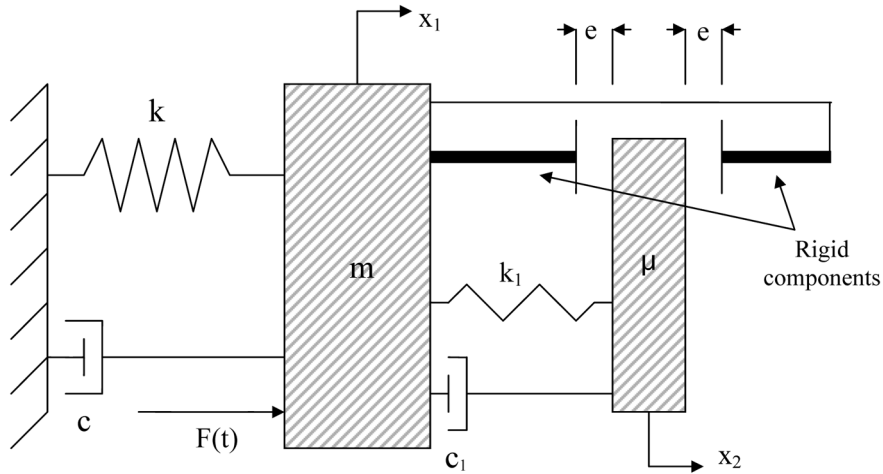


Fig. 7.8 SDOF LO with vibro-impact (VI) NES.

and that the system has zero initial conditions. The system possesses two viscous dampers with characteristics c and c_1 , with additional passive energy dissipation resulting from the inelastic collisions of the attachment mass μ . We model inelastic impacts by introducing the coefficient of restitution rc , defined by the relation

$$rc = -\frac{\dot{x}_1^+ - \dot{x}_2^+}{\dot{x}_1^- - \dot{x}_2^-} \quad (7.7)$$

where the superscripts (\pm) refer to velocities before and after impacts, respectively. Clearly, the coefficient of restitution assumes values in the range $0 < rc < 1$, with unity corresponding to perfectly elastic, and zero to purely plastic impacts. Although the coefficient of restitution depends on the composition of the impacting bodies and surfaces, and on the magnitudes of the velocities of the bodies during impact, in this study it is assumed to remain constant during each individual numerical simulation.

For sufficiently large clearances no vibro-impacts occur, and the system becomes linear (in effect we obtain a LO with a classical linear vibration absorber attached to it). It follows that by increasing the clearance to sufficiently large values we will be able to compare the dynamics of the linear and VI-systems, and, hence, assess the effects of vibro-impacts on the transient dynamics and on shock isolation. We wish to study passive TETs from the directly forced LO to the VI NES, leading to passive shock isolation of the LO. We note that even though the VI system under consideration is strongly nonlinear, in intervals between impacts it behaves in a purely linear fashion. Hence, in time windows in between vibro-impacts the non-dimensionalized equations of motion are expressed as the following linear set:

$$\ddot{x}_1 + \omega_n^2 x_1 + \lambda \dot{x}_1 - \lambda_1 (\dot{x}_2 - \dot{x}_1) - \Omega^2 (x_2 - x_1) = N(t)$$

$$\varepsilon \ddot{x}_2 + \Omega^2(x_2 - x_1) + \lambda_1(\dot{x}_2 - \dot{x}_1) = 0 \quad (7.8)$$

where $\omega_n^2 = k/m$, $\Omega^2 = k_1/m$, $\lambda = c/m$, $\lambda_1 = c_1/m$, $\varepsilon = \mu/m$, $N(t) = F(t)/m$. This linear system of equations is numerically integrated until the condition of impact $|x_2 - x_1| = e$ is realized. At that time instant the two conditions of continuity of displacements and discontinuity of (jump in) velocities are imposed, according to the following formulas:

$$\dot{x}_1^+ = \frac{\dot{x}_1^-(1 - \varepsilon rc) + \varepsilon \dot{x}_2^-(rc + 1)}{1 + \varepsilon}, \quad \dot{x}_2^+ = \frac{\dot{x}_1^-(1 + rc) + \dot{x}_2^-(\varepsilon - rc)}{1 + \varepsilon} \quad (7.9)$$

Then, the system (7.8) is numerically integrated subject to the new initial conditions following the impact, until the impact condition is met again and the previous procedure is repeated. It follows that a precise computation of the time instants of vibro-impacts is crucial for the correct numerical integration of the transient dynamics of the considered two-DOF system.

The transient VI dynamics is simulated utilizing a Matlab[®] code which computes precisely the time instants where impacts occur. This class of VI dynamical problems is especially challenging from the analysis and computational point of view, since the time instants where the vibro-impacts occur are determined by the solution itself, so they cannot be determined *a priori*, i.e., before solving the problem. Moreover, the essential (strong) nonlinearity of the system is generated precisely at these time instants (due to the impulsive excitations applied to the integrated system); in addition, at exactly these time instants significant portions of energy are dissipated due to inelastic collisions between the attachment mass and the mass of the linear oscillator (due to the fact that $rc < 1$). It follows that in order to computationally model this class of problems correctly one must pay special attention to the accurate computation of the time instants of vibro-impacts, as well as the energy dissipated during each impact. In the numerical code the accuracy of the transient computation was evaluated by checking that at each time instant of the simulation the total initial energy of the system (provided by the external shock) equaled the sum of instantaneous kinetic and potential energies of the system, as well as the energy dissipated by the two viscous dampers and the inelastic vibro-impacts up to that time instant.

The efficiency of the VI NES to passively absorb and locally dissipate shock energy from the LO is evaluated by computing the instantaneous energy dissipation measure (EDM) and its asymptotic limit, i.e., of the percentage of shock energy that is *eventually* dissipated by the NES damper and by the inelastic vibro-impacts:

$$E_{\text{VI NES}, t \gg 1} = \lim_{t \gg 1} E_{\text{VI NES}}(t),$$

$$E_{\text{VI NES}}(t) = \frac{\int_0^t c_1 [\dot{x}_1(\tau) - \dot{x}_2(\tau)]^2 d\tau + \sum_{p=1}^{P_t} \Delta_p}{\int_0^T f(\tau) \dot{x}_1(\tau) d\tau} \times 100 \quad (7.10)$$

The EDM $E_{\text{VI NES}}(t)$ represents the percentage of shock energy dissipated up to time instant t ; Δ_p , $p = 1, \dots, P_t$, the amount of energy dissipated during the p -th vibro-impact; and P_t the number of vibro-impacts that occur during the decaying motion up to time instant t .

We perform a series of parametric studies for the following system parameters, $m = 1$, $\omega_n^2 = 1$, $\lambda = \lambda_1 = 0.1$, $A = 10$, $T = 0.1(2\pi/\omega_n)$, $rc = 0.6$; in the simulations we varied the mass ratio of the VI NES ε , the coupling frequency squared Ω^2 , and the clearance e . In Figure 7.9 we depict contour plots of the asymptotic EDM $E_{\text{VI NES}, t \gg 1}$ for fixed clearance and varying mass ratio and coupling frequency squared; whereas in Figure 7.10 we present the corresponding contour plot for the linear system with relatively large clearance ($e \approx 2.0$) so that no vibro-impacts occur during the entire decaying motion. Considering first the linear case (see Figure 7.10), we note that the asymptotic EDM assumes high values (reaching a maximum of 73.7%) on a narrow zone corresponding to linear resonance of the attachment with the primary system. Away from this zone the EDM deteriorates to less than 50%. This is expected, as the effectiveness of the linear attachment as shock absorber is *narrowband* and, as a result, its performance deteriorates away from the condition of linear resonance with the primary system. By contrast, the performance of the VI attachment is *broadband*, so its effectiveness to passively absorb and dissipate shock energy is expected to extend over wider parameter ranges.

Regarding the performance of the VI NES (see Figure 7.9), we note the existence of two regions in each of the EDM contour plots, corresponding to weak and stiff coupling frequency Ω , respectively, compared to the grounding frequency ω_n of the primary system. In the region of weak coupling frequency, an increase of the clearance up to the value of 1.25 results in an increase of the EDM and, hence, enhancement of TET; above this clearance value, however, we note deterioration of the EDM. In contrast, in the region of stiff coupling frequency, increasing the clearance results in an increase of the EDM, and, hence, enhances the performance of the VI NES as shock absorber. As expected, for relatively large values of the clearance, the EDM contour plot of the VI system approaches the linear plot of Figure 7.10, as fewer or no vibro-impacts occur during the decaying motion.

Clearly, the number and timings of vibro-impacts are expected to affect significantly TET from the primary LO to the NES, and, hence, the effectiveness of the VI NES as shock absorber. To study in more detail the dependence of TET on the occurring vibro-impacts, we examined the differences in the asymptotic EDM contour plots between the VI and linear systems, and attempted to relate these differences to the number of vibro-impacts occurring in the corresponding nonlinear responses. In Figure 7.11 we depict representative results that address this issue; positive (negative) differences in the asymptotic EDM correspond to surplus (deficit) of energy dissipated by the VI NES when compared to the linear vibration absorber.

From these plots we infer that the number of vibro-impacts plays an important role in the enhancement of the asymptotic EDM in the VI case. By increasing the clearance, the number of vibro-impacts diminishes (as expected), but this does not necessarily imply that the effectiveness of the VI NES as shock isolator deteriorates. For example, for clearance $e = 0.25$ (not shown in Figure 7.11) although the num-

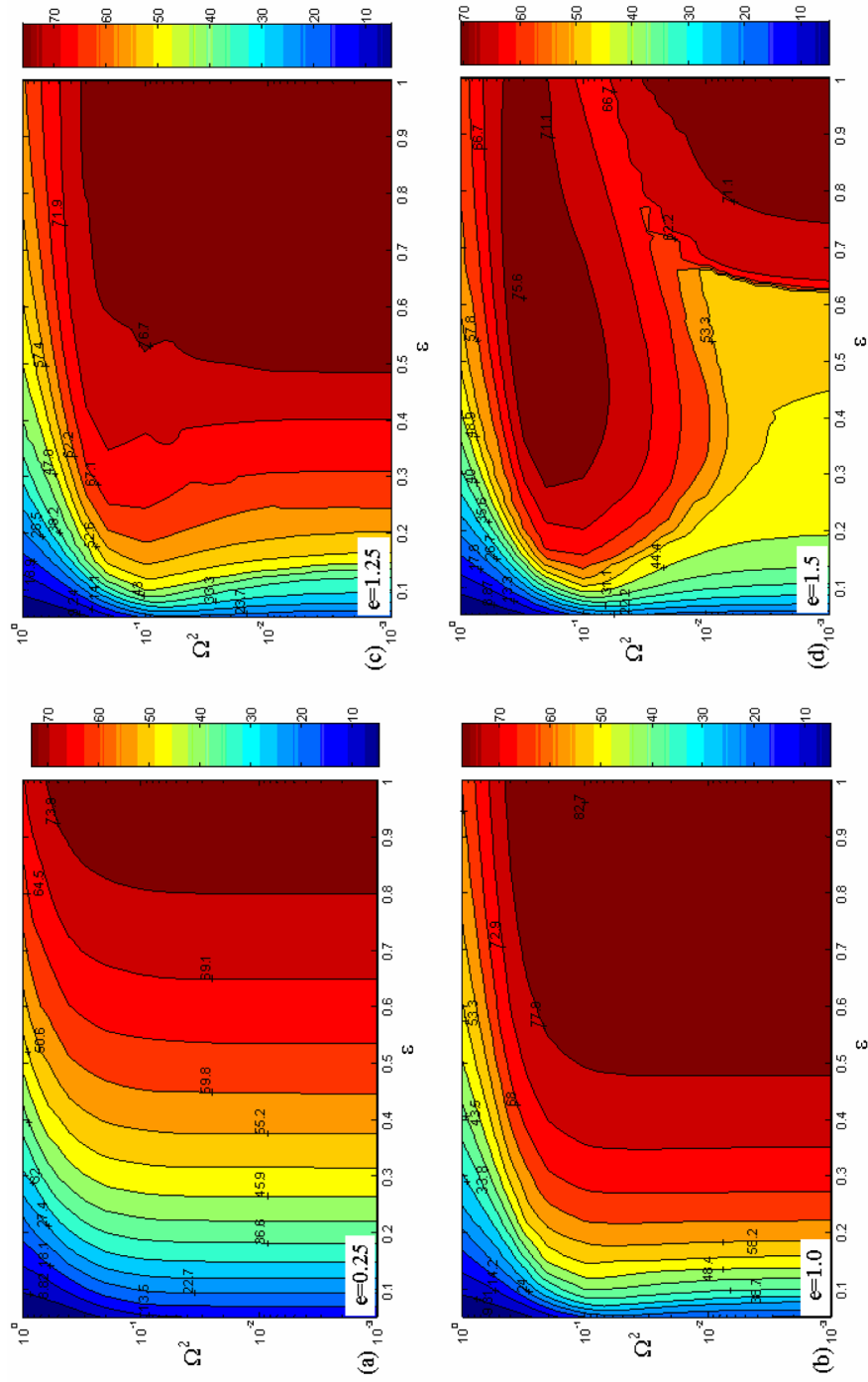


Fig. 7.9 Contour plots of the energy dissipation measure $E_{VI NES, t \gg 1}$ for varying Ω^2 and mass ratio ϵ : (a) $e = 0.25$; (b) $e = 1.00$; (c) $e = 1.25$; (d) $e = 1.50$.

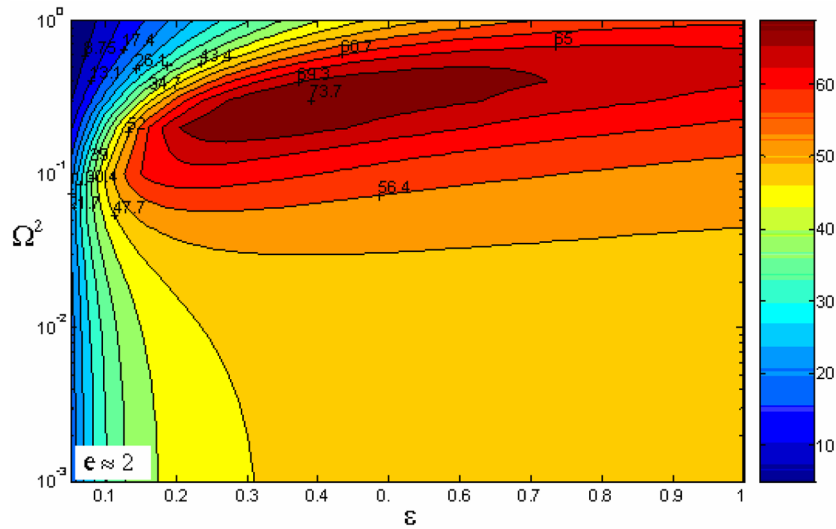


Fig. 7.10 Contour plots of the energy dissipation measure $E_{VI NES, t \gg 1}$ for the linear system (no vibro-impacts, $e \approx 2.0$), for varying Ω^2 and mass ratio ϵ .

ber of vibro-impacts is of the order of 6000, the performance of the VI NES is not significantly enhanced compared to cases with larger clearances (see Figure 7.10); on the other hand, for $e = 1.50$ there occur at most 3 vibro-impacts (and in most of the contour plot of Figure 7.11b no vibro-impacts occur at all), yet the VI NES shows as much as 18% better EDM efficiency compared to the linear absorber in this case. This can be explained by noting that for small clearances and mass ratios the relative displacements and velocities across the viscous damper c_1 of the VI NES are expected to be small, so that relatively small amounts of shock energy are dissipated by that damper (these results agree with the findings reported in the previous section). In addition, if vibro-impacts start immediately after or even during the application of the external shock, for small mass ratios the attachment is prevented from attaining sufficient acceleration and velocity, and as a result, the exchange of momentum between the LO and the NES and the amount of shock energy dissipated due to vibro-impacts may be small even if a large total number of vibro-impacts occurs. From the plots of Figure 7.11a we note that by increasing the mass ratio, we can achieve enhanced EDM; moreover, the regions of intense vibro-impacts coincide with the regions of enhanced nonlinear shock absorption efficiency. Of course, in regions where no vibro-impacts occur the performance of the VI attachment converges to that of the linear absorber. It follows that *efficient shock absorption efficiency of the vibro-impact NES can be achieved even for small number of occurring vibro-impacts*.

These findings should be considered in conjunction with the fact that in the two limits $e \rightarrow 0$ and $e \approx 2$ the two-DOF system of Figure 7.8 degenerates into two different linear systems: either a SDOF linear oscillator with mass equal to $(m + \mu)$,

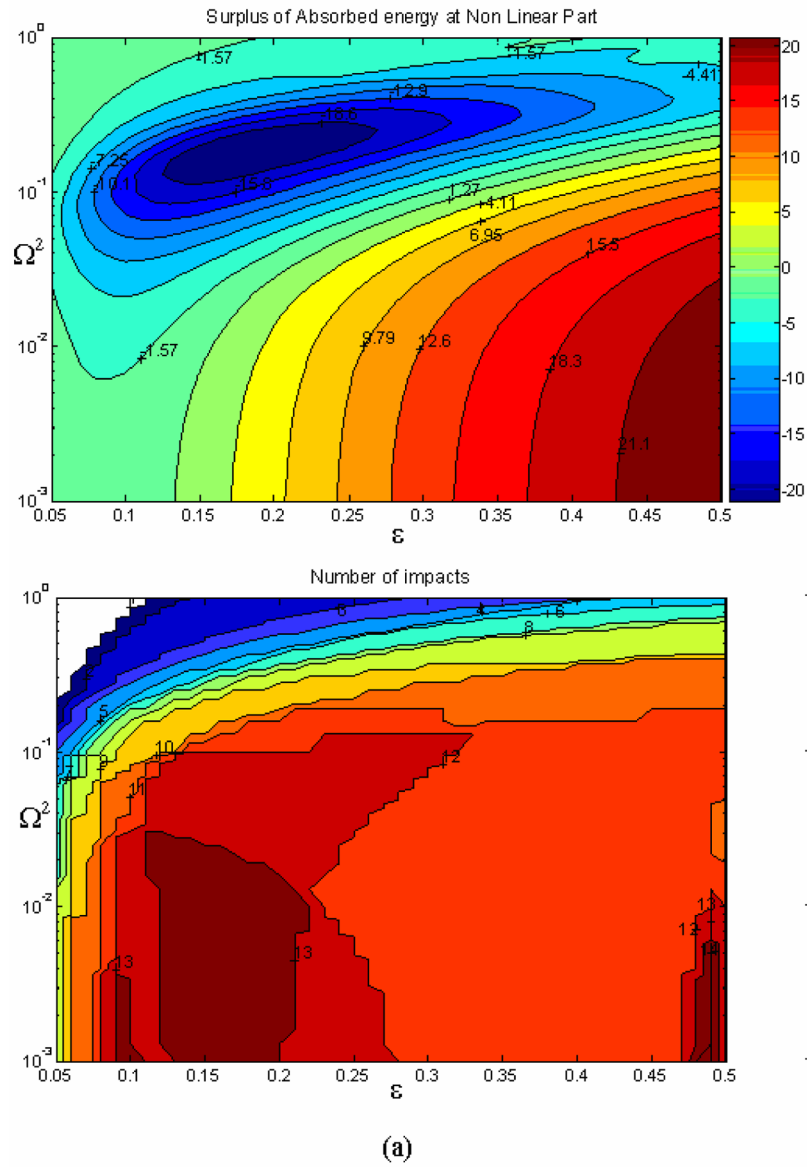


Fig. 7.11 Difference of asymptotic EDM contour plots between the VI and linear systems and corresponding number of vibro-impacts: (a) $e = 0.50$; positive (negative) values correspond to surplus (deficit) of energy dissipated by the VI NES.

or a linear oscillator of mass m with an attached linear vibration absorber of mass μ . For intermediate values of e and small values of Ω^2 , the response of the system is strongly nonlinear, and there exist extensive regions in the parameter plane (ε, Ω^2)

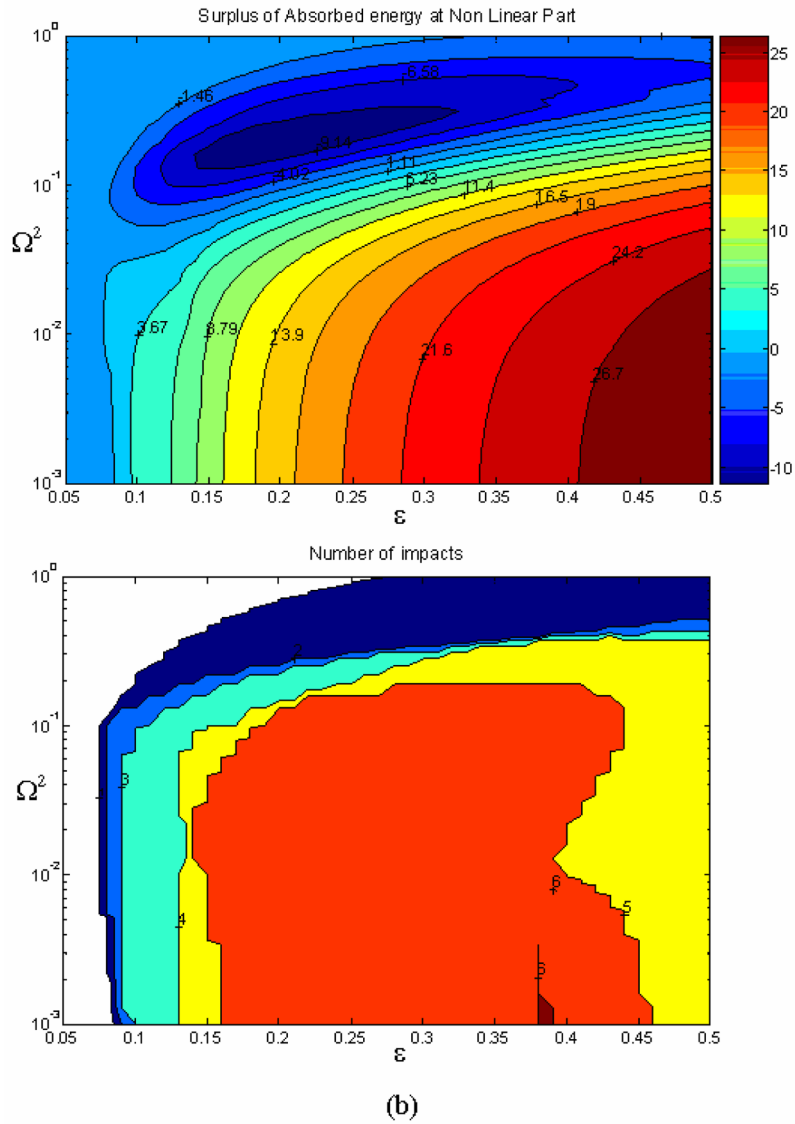


Fig. 7.11 Difference of asymptotic EDM contour plots between the VI and linear systems and corresponding number of vibro-impacts: (b) $e = 1.00$; positive (negative) values correspond to surplus (deficit) of energy dissipated by the VI NES.

where the efficiency of the VI NES exceeds that of the linear absorber by as much as 29% (for a clearance $e \approx 1$). In terms of the asymptotic EDM, for mass ratios in the range $0.2 < \epsilon < 0.5$ the VI NES eventually absorbs and locally dissipates 60–80%

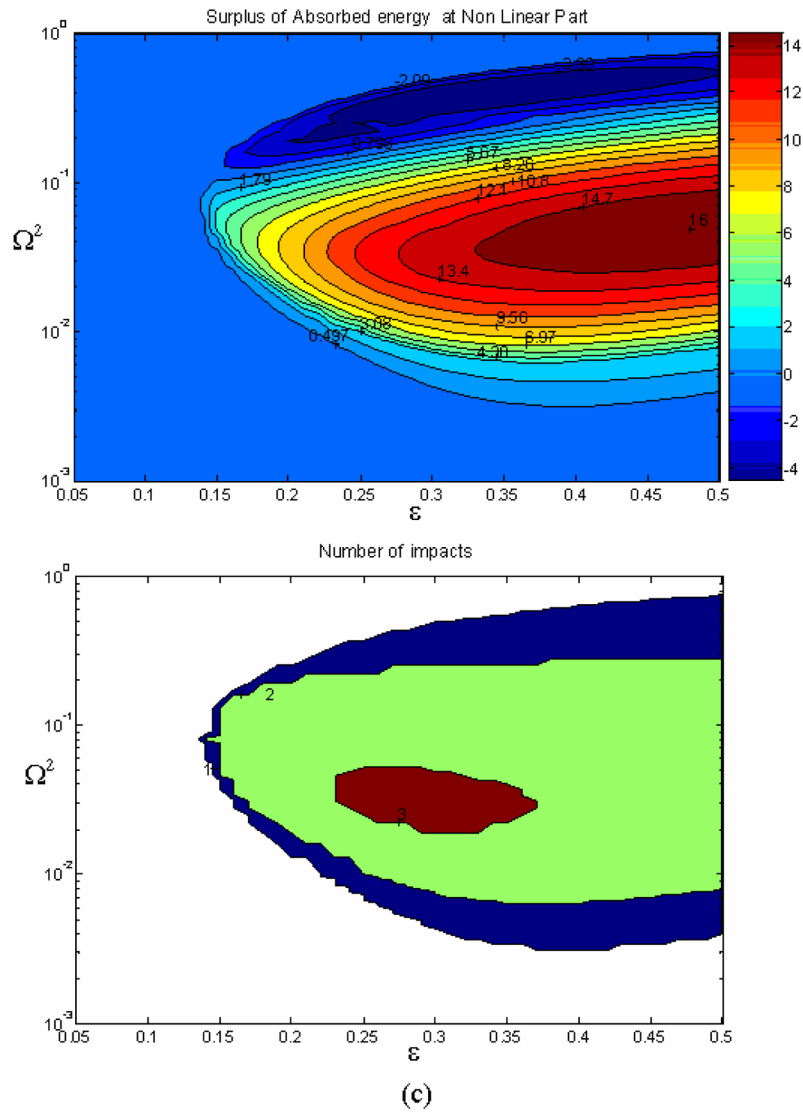


Fig. 7.11 Difference of asymptotic EDM contour plots between the VI and linear systems and corresponding number of vibro-impacts: (c) $e = 1.50$; positive (negative) values correspond to surplus (deficit) of energy dissipated by the VI NES.

of the shock energy, even for a relatively small number of total vibro-impacts (from 2 to 6).

In Figure 7.12 we depict the asymptotic EDM $E_{VI NES, t \gg 1}$ as function of clearance e for a VI NES with $\Omega^2 = 0.005$ and mass ratio $\epsilon = 0.3$. For this small value

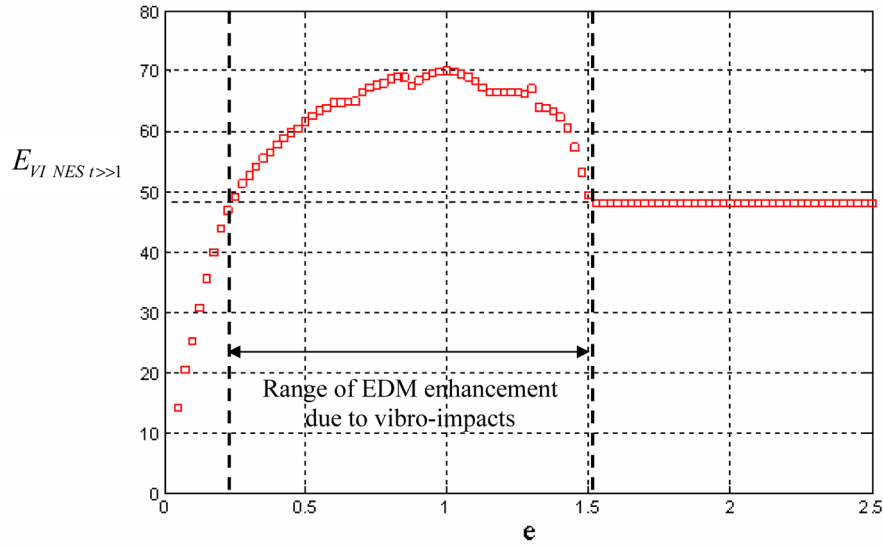


Fig. 7.12 Asymptotic EDM $E_{VI NES, t \gg 1}$ as a function of clearance e for $\Omega^2 = 0.005$ and $\varepsilon = 0.3$.

of coupling frequency, there is a nearly linear variation of $E_{VI NES, t \gg 1}$ for small clearances. However, for increasing clearance we note saturation in the plot of the asymptotic EDM yielding to an optimal value of this measure. Further increase of results in deterioration of the asymptotic EDM, until the linear regime is reached, where no vibro-impacts occur and the EDM becomes independent of clearance [the constant level of EDM in that regime is due to the percentage of shock energy dissipated by the coupling viscous damper c_1 (see Figure 7.8)].

In conclusion, superior shock absorption by the VI NES compared to the linear absorber is attained for intermediate clearances (i.e., away from the two limiting linear systems corresponding to zero or large clearances), small coupling frequencies Ω^2 , and large mass ratios ε . Moreover, high shock absorption efficiencies may be attained for even small total number of vibro-impacts, provided that conditions for sufficient momentum and energy exchanges between the primary system and the NES during vibro-impacts are realized. In the next section we examine the shock isolation properties of VI NES-based designs by constructing nonlinear shock spectra and comparing these to reference linear spectra.

7.2.2 Shock Isolation

To study the capacity for shock isolation of the VI NES we consider the system of Figure 7.13a consisting of a two-DOF linear primary system with an attached VI

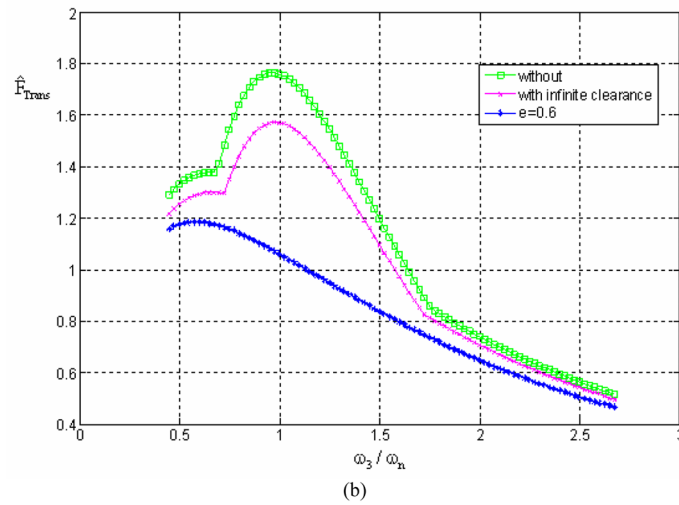
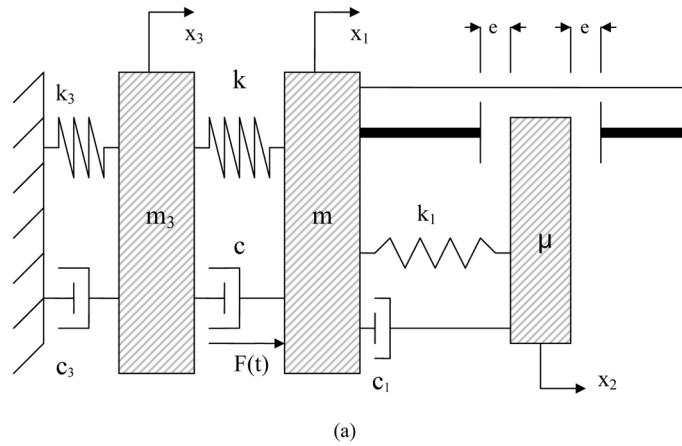


Fig. 7.13 Primary structure on foundation with VI NES attached: (a) system configuration; (b) spectra depicting maximum normalized force transmitted to ground as a function of normalized frequency ratio.

NES. As with the study of the previous section, the following exposition follows closely (Karayannis et al., 2008). The mass m represents the primary structure to be isolated, resting on an elastic foundation of mass m_3 . An external half-sine shock (7.6) is applied to the primary structure, and our aim is to assess the capacity for shock isolation of a VI NES-based design. The computational study of this system is performed for the following parameter values:

$$m = 1, \quad m_3/m = 5, \quad \omega_3^2 = k_3/m_3, \quad \omega_n^2 = k/m = 5, \quad \lambda = c/m = 0.1,$$

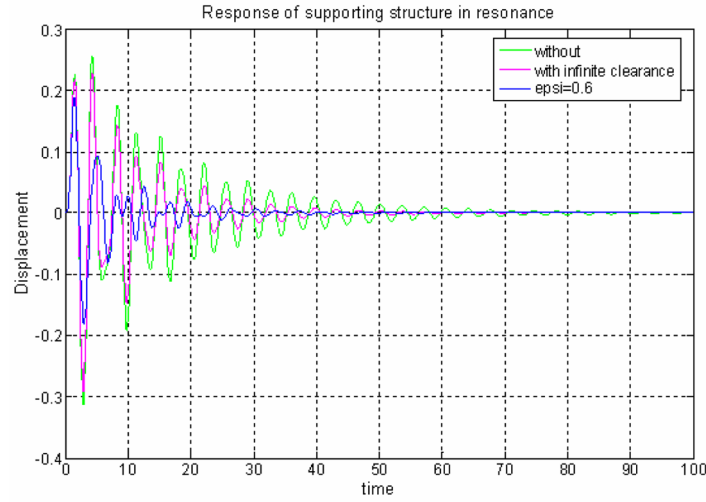


Fig. 7.14 Transient response x_3 of the foundation under resonance, $\omega_3/\omega_n = 1$.

$$\lambda_1 = c_1/m = 0.1, \quad \lambda_3 = c_3/m_3 = 0.1\omega_3, \quad e = 0.6, \quad A = 10, \quad k_1 = 0.005, \\ rc = 0.6, \quad \mu = 0.35, \quad T = 0.2\pi$$

In Figure 7.13b we depict the nonlinear shock spectrum for the vibro-impacting system. For comparison purposes, we present also two additional reference shock spectra of the following two limiting linear systems: the system obtained in the limit of large clearances when no vibro-impacts occur (i.e., when the system degenerates to a primary system attached to a linear vibration absorber); and the system obtained in the limit of zero NES mass (that is, the primary system with no NES attached). In each shock spectrum we depict the maximum value of normalized forced transmitted to ground, $\hat{F}_{\text{Trans}} = \max\{c_3\dot{x}_3 + m_3\omega_3^2 x_3\}/(J\omega_3)$, as a function of the non-dimensional frequency ratio (ω_3/ω_n). The parameter J in the denominator of the normalized transmitted force \hat{F}_{Trans} represents the shock impulse defined by

$$J = \int_0^T F(t)dt \quad (7.11)$$

From the results depicted in Figure 7.13b we infer that due to TET of shock energy from the primary structure to the VI NES there is significant reduction of the normalized transmitted force; in the resonance region $\omega_3 \approx \omega_n$, \hat{F}_{Trans} reaches levels which are 40% less compared to the reference linear system with no attachment, and 32% less compared to the reference system with linear absorber attached. Moreover, in the VI system complete elimination of the resonance in the shock spectrum is realized, so effective shock isolation is provided over a broad frequency range. Hence, in contrast to the *narrowband* action of the linear vibration absorber, the VI

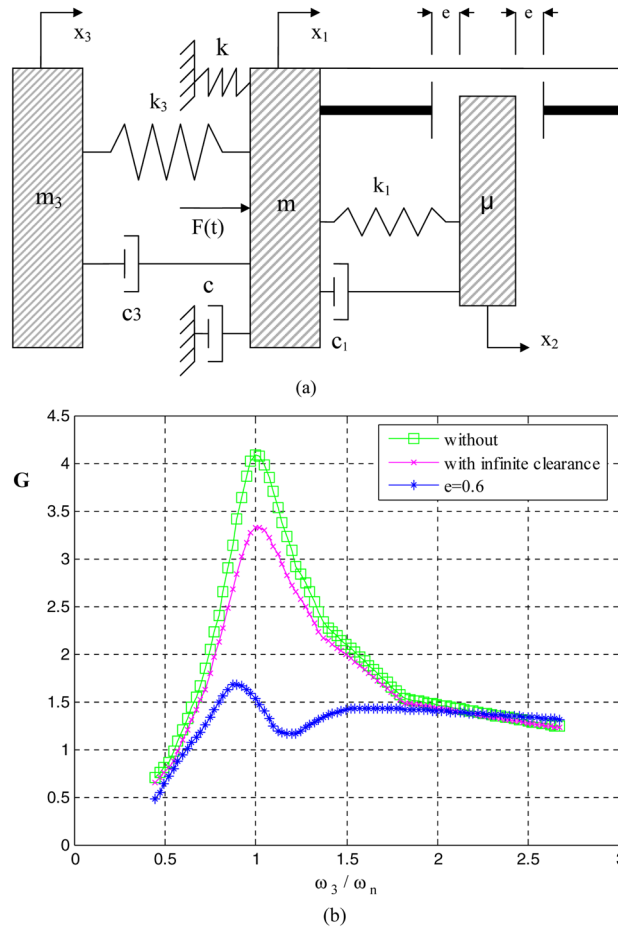


Fig. 7.15 Primary structure with sensitive component and VI NES: (a) system configuration; (b) spectra of maximum normalized acceleration of the sensitive component as function of non-dimensional frequency ratio.

NES provides effective *broadband* shock isolation. In Figure 7.14 we present the response x_3 of the foundation under resonance, $\omega_3 / \omega_n = 1$, for the nonlinear and reference linear configurations discussed previously. Note the significant suppression of the maximum response of the foundation in the case of VI NES, signified by the rapid decay of the corresponding transient motion.

The second system considered in our shock isolation study is depicted in Figure 7.15a (Karayannis et al., 2008). We wish to study the transmission of shock-induced vibrations from the directly forced primary structure to a sensitive component (denoted by the mass m_3) that is connected to the mass of the primary system m . A vibro-impact NES is attached to the primary system, which itself is excited by

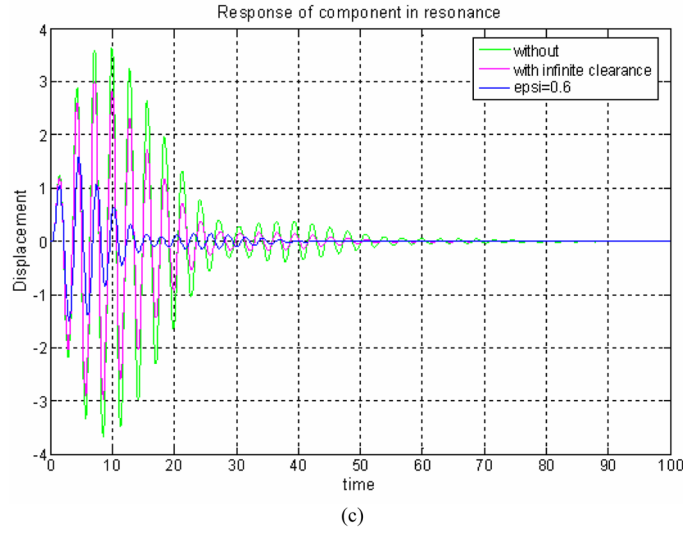


Fig. 7.15 Primary structure with sensitive component and VI NES: (c) transient response x_3 of the sensitive component under linear resonance, $\omega_3/\omega_n = 1$.

the half-sine shock (7.6). This shock isolation study is performed for the following parameter values:

$$\begin{aligned} m &= 1, & m_3/m &= 0.01, & \omega_3^2 &= k_3/m_3, & \omega_n^2 &= k/m = 5, & \lambda &= c/m = 0.1, \\ \lambda_1 &= c_1/m = 0.1, & \lambda_3 &= c_3/m_3 = 0.1\omega_3, & e &= 0.6, & A &= 10, & k_1 &= 0.005, \\ rc &= 0.6, & \mu &= 0.35, & T &= 0.2\pi \end{aligned}$$

In Figure 7.15b we depict the nonlinear shock spectrum of this system, and compare it to two reference spectra, corresponding to linear systems with, either no VI attachment, or a linear vibration absorber attached instead of an VI NES. These spectra are computed by depicting the maximum normalized acceleration of the sensitive component, $G = \max\{\ddot{x}_3/(\dot{u}_m\omega_3)\}$, as a function of the non-dimensional frequency ratio (ω_3/ω_n) . The velocity \dot{u}_m in the denominator of the normalized acceleration G is computed by the following relation:

$$\dot{u}_m = \frac{J}{m}, \quad J = \int_0^T F(t)dt \quad (7.12)$$

From these results we deduce that the VI attachment provides effective shock isolation of the sensitive component over a broad range of frequency ratios, by significantly reducing the maximum normalized acceleration G . Moreover, in the critical resonance region $\omega_3 \approx \omega_n$ the reduction in acceleration due to TET of shock energy to the VI NES is significant compared to the reference linear systems; in

fact, in the nonlinear spectrum the linear resonance close to $\omega_3/\omega_n = 1$ is almost completely suppressed. In Figure 7.15c we depict the transient response x_3 of the sensitive component for the nonlinear and reference linear systems under resonance, $\omega_3/\omega_n = 1$. We note the drastic reduction of the level vibration due to TET of shock energy to the VI NES.

To study the robustness of the shock isolation performance of the VI NES we performed a final series of numerical simulations, where for fixed impulsive excitation ($A = 10$, $T = 0.2\pi$) and linear system parameters as defined above, we varied the parameters of the VI NES and computed shock spectra similar to that depicted in Figure 7.15b; we then compared these nonlinear spectra to the ones of the corresponding linear systems with infinite clearance (i.e., primary systems with linear absorbers attached) in order to judge the effect that vibro-impacts have on the shock isolation. In each of these plots, the system parameters that are not varied are assigned the numerical values defined above. The results are depicted in Figure 7.16.

In Figure 7.16a we depict the comparison between the nonlinear and linear spectra for five values of VI NES mass, $\mu = 0.1, 0.2, 0.35, 0.4$ and 0.5 , keeping all other NES parameters fixed. We note that the larger the VI NES mass is, the better the relative performance of the VI NES becomes with respect to the linear absorber design; therefore, we conclude that the mass of the VI NES is an important parameter for shock isolation (this was to be expected, since as mentioned previously, the mass of the VI NES affects its momentum exchange with the linear oscillator during vibro-impacts). In Figure 7.16b we examine the effect of varying the clearance e on shock isolation, by considering nonlinear spectra for four different clearances, $e = 0.1, 0.2, 0.4$ and 0.6 and all other NES parameters being kept fixed. We note that for decreasing clearance the linear and nonlinear spectra converge, and that better relative shock isolation performance of the VI NES is achieved for larger clearances.

In Figure 7.16c we examine the effect of varying the viscous damping coefficient of the VI NES, by considering five different damping values, namely, $\lambda_1 = 0.01, 0.05, 0.2, 0.3$ and 0.4 . From these results we conclude that the variation of viscous damping of the VI NES does not affect significantly its effectiveness. Similarly, the variation of the coefficient of restitution of the vibro-impacts from the value $rc = 0.6$ (this series of plots is not shown here) has a marginal effect on the performance of the VI NES. Finally, in Figure 7.16d we depict the effect on the nonlinear shock spectra of the variation of the restoring linear stiffness k_1 of the VI NES. In that study we considered five different values of linear stiffness, namely, $k_1 = 5 \times 10^{-3}, 1 \times 10^{-2}, 0.1, 0.5$ and 1.0 ; by comparing the nonlinear shock spectra with the corresponding linear ones, we note that there is robustness of shock elimination within the examined range of stiffness values. By further increasing the stiffness ($k > 5.0$), no vibro-impacts occur and the response of the system becomes purely linear. The results presented in Figure 7.16 demonstrate robustness of the shock isolation provided by the VI NES for changes of its parameters.

Summarizing, we studied alternative shock isolation designs of primary structures with attached VI NESs. We showed that VI NESs can be designed as effective shock isolators, providing significant reduction of maximum responses of the primary systems over broad frequency ranges. Hence, appropriately designed VI

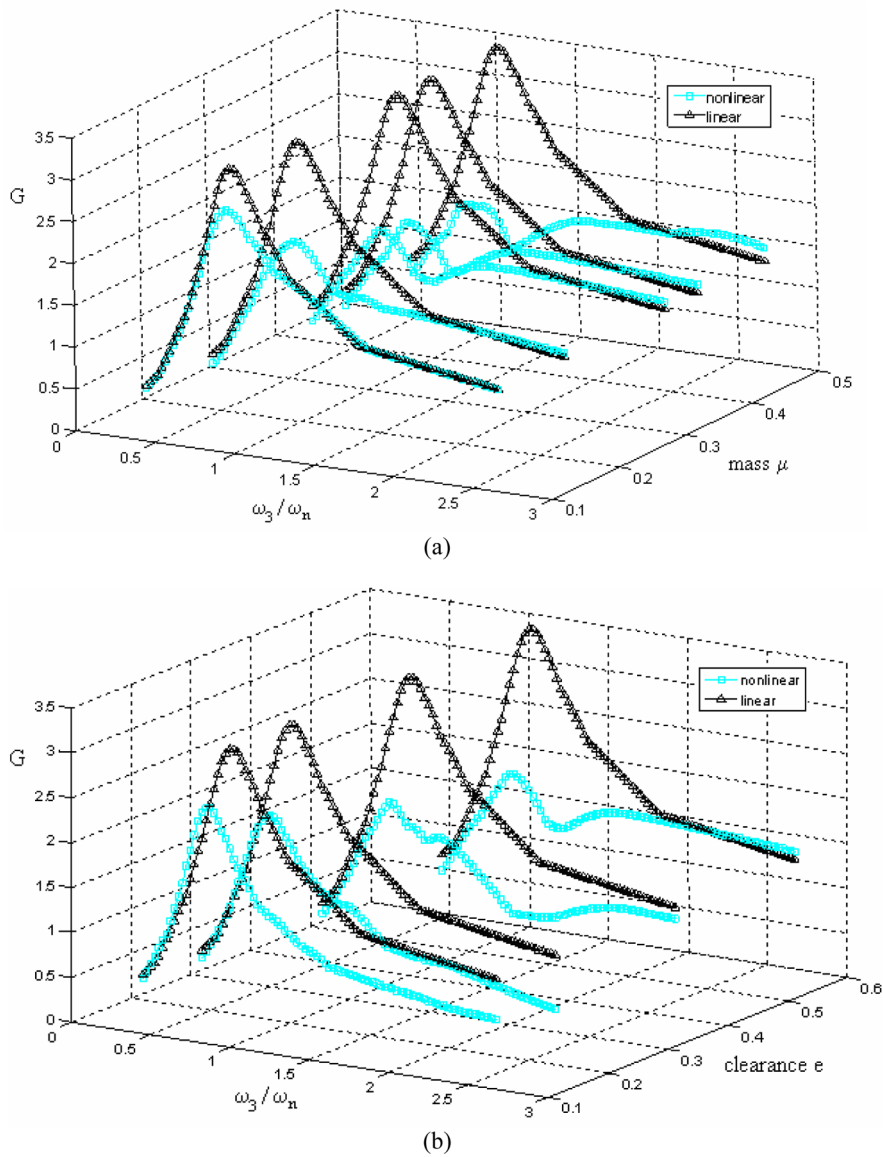


Fig. 7.16 Parametric study of shock spectra of maximum normalized acceleration of the sensitive component as function of ω_3/ω_n and (a) the VI NES mass μ ; (b) the clearance e ; for comparison, the corresponding linear spectra of systems with infinite clearances (e.g., with linear vibration absorbers attached) are also depicted.

NESs can act as broadband, passive shock isolators, which may significantly reduce or even completely eliminate resonances from shock spectra. The results presented

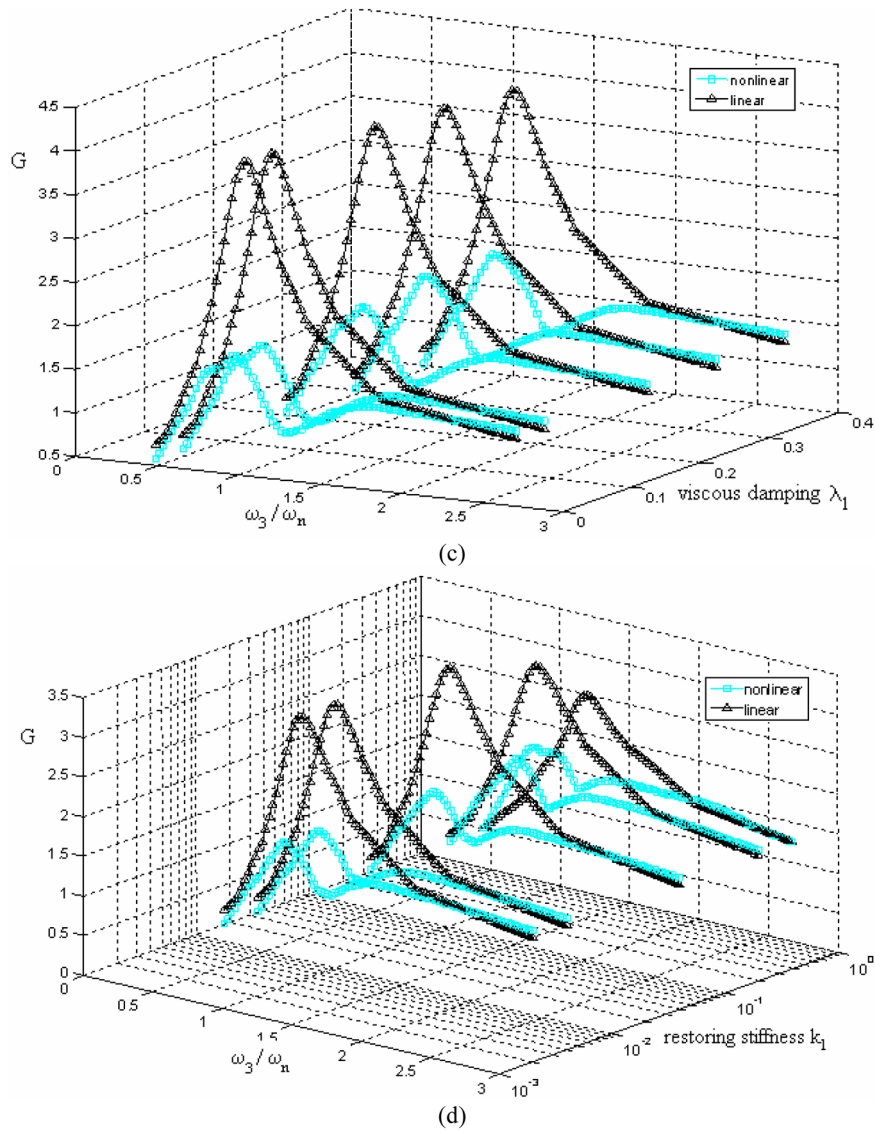


Fig. 7.16 Parametric study of shock spectra of maximum normalized acceleration of the sensitive component as function of ω_3/ω_n and (c) the VI NES viscous damping λ_1 ; and (d) the restoring stiffness k_1 ; for comparison, the corresponding linear spectra of systems with infinite clearances (e.g., with linear vibration absorbers attached) are also depicted.

indicate that, in designing VI NESs as shock isolators, important design parameters that should be taken into account are the clearances, the coupling stiffnesses and the NES masses. The parametric studies performed in this section indicate that

depending on the application and the types of applied shocks, there is a range of clearances for which effective shock energy absorption and dissipation occurs; outside this range, smaller or larger clearances result in deterioration of shock absorption, as the vibro-impacting systems approach linear limiting systems. Moreover, better vibro-impact shock absorption is anticipated for weak coupling stiffness between the primary systems and the attached NESs, and relatively large values of NES masses compared to the masses of the corresponding primary systems. These results are in agreement with findings of Section 7.1.

7.3 SDOF Linear Oscillator with a VI NES

In Section 7.2 we provided numerical evidence of the potential of vibro-impact (VI) attachments as passive shock absorbers. In this section we study in more detail the unforced dynamics of a SDOF linear primary system with a VI attachment, in an effort to explore the richness and complexity of the vibro-impact dynamics and relate it to TET. Our methodology will be similar to that followed in Sections 3.3 and 3.4 for the analogous system with ungrounded NES with smooth nonlinear stiffness characteristics.

First, we will explore the rich structure of periodic orbits (and impulsive orbits – IOs) of the VI dynamics in a frequency-energy plot (FEP) of the Hamiltonian system undergoing purely elastic vibro-impacts; our aim will be to study if the FEP of the Hamiltonian VI system possesses a structure of backbone curves, subharmonic tongues and impulsive orbits, similar to the one of the system with ‘smooth’ NES. Then, we will study damped transitions in the dynamics of the VI system undergoing inelastic vibro-impacts, by superimposing the wavelet transform (WT) spectra of transient damped responses to the Hamiltonian FEP; our effort will be to demonstrate schematically that such representations contribute to the identification and interpretation of complex resonance captures and multi-modal transitions occurring in these damped transitions. Finally, we will proceed to make some preliminary remarks and conjectures regarding the mechanisms for TET in the VI system.

Overall, our aim will be to demonstrate that vibro-impacts in oscillators with even small clearances can introduce great complexity in the unforced dynamics of the two-DOF system considered. Our exposition will follow the results of Nucera et al. (2007) and Lee et al. (2008), which should be consulted for additional results on this topic. Application of VI NESs to the problem of seismic mitigation was studied by Nucera et al. (2007a, b), and the results of these works will be discussed in Chapter 10.

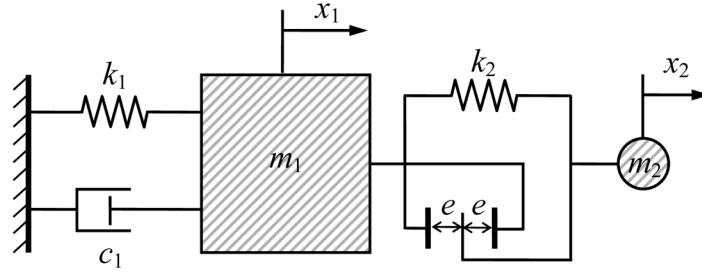


Fig. 7.17 SDOF LO with VI NES.

7.3.1 Periodic Orbits for Elastic Vibro-Impacts Represented on the FEP

To study the underlying dynamical mechanisms and associated TRCs that generate passive TET in systems with attached VI NESs, and in order to demonstrate the complexity that a single VI NES (with even small clearance) can introduce to the dynamics, we consider the simplest possible primary system – VI NES configuration, namely a SDOF LO coupled to a VI NES (see Figure 7.17). As in the case of the NES with smooth essential nonlinearities we will show that a clear interpretation of damped VI transitions governing TET in the shock-excited system may be gained by depicting the WT spectra of these motions in a FEP of the underlying VI Hamiltonian system (i.e., for the system with purely elastic impacts and no viscous damping elements).

As in the case of the NES with smooth nonlinearities we will demonstrate that *for sufficiently weak dissipation, damped VI transitions take place near branches of periodic or quasi-periodic motions of the corresponding undamped system*. Hence, by studying the structure of periodic orbits of the Hamiltonian system, we should be able to gain an understanding of the governing dynamics of the weakly damped dynamics, and to be able to clearly identify complex multi-frequency transitions and resonance captures producing strong energy exchanges and TET in the weakly damped VI system.

We initiate our study by constructing the FEP of the Hamiltonian VI system with no viscous damping dissipation and purely elastic vibro-impacts. We consider the VI model introduced in Section 7.2.1. In time intervals between vibro-impacts the equations of motion are purely linear and given by (with an alternative notation being adopted for the system parameters compared to Section 7.2.1),

$$\begin{aligned} m_1 \ddot{x}_1 + k_1 x_1 + c_1 \dot{x}_1 + k_2(x_1 - x_2) &= 0 \\ m_2 \ddot{x}_2 + k_2(x_2 - x_1) &= 0 \end{aligned} \quad (7.13)$$

or in non-dimensional form:

$$\begin{aligned}x_1'' + x_1 + \lambda x_1' + \sigma(x_1 - x_2) &= 0 \\ \varepsilon x_2'' + \sigma(x_2 - x_1) &= 0\end{aligned}\quad (7.14)$$

In the normalized equations (7.14) primes denote differentiation with respect to the transformed temporal variable $\xi = (k_1/m_1)^{1/2}t$, and $\lambda = c_1/(k_1m_1)^{1/2}$, $\varepsilon = m_2/m_1$, $\sigma = k_2/k_1$ are dimensionless damping, mass and stiffness parameters, respectively. Moreover, in (7.14) we consider normalized displacements defined by the rescalings $x_i \rightarrow x_i/e$, $i = 1, 2$, so in terms of these normalized displacements vibro-impacts occur when $|x_1 - x_2| = 1$. As in Section 7.2 the mass m_2 of the NES is not necessarily small compared to the mass m_1 of the LO, so the ratio ε is assumed to be an $O(1)$ quantity.

Assuming zero viscous damping, $\lambda = 0$, and considering purely elastic impacts (corresponding to restitution coefficient $\rho = 1$), the VI system becomes Hamiltonian. The velocities of the LO and the NES after an impact (denoted by superscripts +) are computed in terms of the corresponding velocities before impact (denoted by superscripts -) as follows:

$$x_1^{'+} = \frac{x_1'^{-}(1 - \varepsilon) + 2\varepsilon x_2'^{-}}{1 + \varepsilon}, \quad x_2^{'+} = \frac{2x_1'^{-} + (\varepsilon - 1)x_2'^{-}}{1 + \varepsilon}\quad (7.15)$$

In the numerical algorithm used for our computational study the linear equations (7.14) are integrated as long as the no-impact condition $|x_1 - x_2| < 1$ is satisfied. When $|x_1 - x_2| = 1$ a (purely elastic) impact occurs and discontinuities in the velocities take place, whereas the displacements remain continuous through the vibro-impact process; the velocities immediately after the impact are computed by relations (7.15), and the numerical integration of the linear system (7.14) resumes with the new initial conditions until the next vibro-impact occurs and the outlined procedure is iterated.

As discussed in Section 7.2.1 and Nucera et al. (2007), the precise computation of the time instants of vibro-impacts is essential for the accuracy of the numerical simulations. This accuracy was checked by recording the total energy of the VI motion, ensuring its conservation throughout the entire interval of the simulation. The total (conserved) energy of the normalized Hamiltonian system $H(x_1, x_1', x_2, x_2')$ is computed in terms of the initial conditions of the normalized system (7.14) as follows:

$$H(x_1, x_1', x_2, x_2') = \frac{\varepsilon x_2'^2(0) + x_1'^2(0)}{2} + \frac{\sigma[x_2(0) - x_1(0)]^2 + x_1^2(0)}{2} = h \quad (7.16)$$

Assuming zero initial velocities, the critical threshold below which no vibro-impacts can occur is computed as $k_{\text{crit}} = \sigma/2$. Throughout this section the normalized mass and stiffness parameters are taken as $\varepsilon = 0.1$ and $\sigma = 0.1$, respectively.

The periodic solutions of the Hamiltonian vibro-impacting system were computed by employing the method of non-smooth transformations first introduced by Pilipchuk (1985) and Pilipchuk et al. (1997), and applied in Section 3.3.1.1 for computing the periodic orbits (NNMs) of the corresponding system with smooth essen-

tial nonlinearity (i.e., with a ‘smooth’ NES). To this end, we introduce the following coordinate transformations:

$$x_1(\xi) = e(\xi/\alpha)y_1(\tau(\xi/\alpha)), \quad x_2(\xi) = e(\xi/\alpha)y_2(\tau(\xi/\alpha)) \quad (7.17)$$

where $\alpha = T/4$ represents the quarter period of the periodic motion, and the non-smooth functions $\tau(\cdot)$ and $e(\cdot)$ are defined according to expressions (3.9). Then, we obtain the following NLBVP in terms of the variables $y_1, y_2, y_3 = y_1'$ and $y_4 = y_2'$, in analogy to system (3.10) of Section 3.3.1.1:

$$\begin{aligned} y_1' &= y_3 \\ y_2' &= y_4 \\ y_3' &= -\alpha^2 y_1 - \sigma \alpha^2 (y_1 - y_2) \\ y_4' &= -(\sigma \alpha^2 / \varepsilon)(y_2 - y_2) \\ y_1(\pm 1) &= 0, \quad y_2(\pm 1) = 0 \end{aligned} \quad (7.18)$$

In system (7.18) primes denote differentiations with respect to the non-smooth variable τ , and the periodic orbits are computed subject to zero initial velocities. Vibro-impacts occur when $|y_1 - y_2| = 1$, where discontinuity conditions in the velocities are imposed, in similarity to conditions (7.15). The solution of the NLBVP (7.18) computes the VI periodic orbit over half its period $T = 4\alpha$ (i.e., for $-1 \leq \tau \leq 1 \Rightarrow -\alpha \leq \xi \leq \alpha$); to extend this orbit over the entire period of the oscillation we take into account the form of the non-smooth transformations (7.17) (see also related discussion in Section 3.3.1.1). Moreover, taking into account the transformations (7.17), the conserved energy of the VI periodic orbit is expressed as

$$h = \frac{1}{2\alpha^2}[\varepsilon y_2^2(-1) + y_1^2(-1)] \quad (7.19)$$

The NLBVP (7.18) is solved by a shooting algorithm in the bounded domain $-1 \leq \tau \leq 1$. However, unlike the shooting method employed for the case of the NES with smooth nonlinearity (Lee et al., 2005), matching at $\tau = 0$ of the two solutions initiated from the left and right boundaries ($\tau = \pm 1$) is not helpful in the present VI problem. This is due to the fact that symmetric VI periodic orbits are expected to exhibit vibro-impacts at $\tau = 0$, so matching solutions at this point is meaningless. Therefore, for the VI problem the following matching procedure is adopted (Lee et al., 2008): for fixed quarter period α the set of equations of the NLBVP is solved as an initial value problem with initial conditions defined at the left boundary, $y_i(-1) = 0, y_i'(-1) \neq 0, i = 1, 2$; then we perform matching of the solution of the initial value problem at the right boundary through the inequalities, $|y_i(+1)| < \text{tol} \ll 1, i = 1, 2$, where the tolerance is taken as $\text{tol} \sim O(10^{-5}) - O(10^{-6})$. This procedure ensures that the NLBVP (7.18) is approximately solved (that is, within the prescribed numerical tolerance).

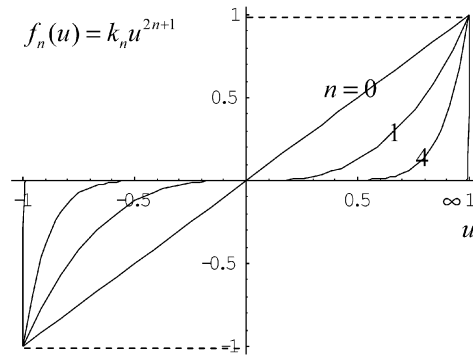


Fig. 7.18 Vibro-impact nonlinearity as limiting case of a family of smooth, essentially nonlinear stiffnesses.

It is anticipated that the seemingly simple VI system of Figure 7.17 will possess a very complicated structure of periodic orbits in the FEP. This expectation is justified when considering that vibro-impact nonlinearity represents a very strong (and degenerate) form of nonlinearity. A way to view this is by considering the following family of odd essentially nonlinear stiffnesses,

$$f_n(u) = k_n u^{2n+1}, \quad n = 0, 1, 2, \dots \quad (7.20)$$

where the coefficient k_n depends on the exponent and is selected so that the normalization condition $f_n(\pm 1) = 1$, $n = 0, 1, 2, \dots$ is satisfied. Then, the vibro-impact nonlinearity corresponding to purely elastic impacts is obtained as the (degenerate) discontinuous limit $f_\infty(u) = \lim_{n \rightarrow \infty} f_n(u)$ (Vedenova et al., 1985; Manevitch et al., 1989). Viewed in this context, *vibro-impact nonlinearity can be considered as the 'strongest possible' stiffness nonlinearity of the family (7.20)*. Following this reasoning, Pilipchuk (1985, 1988, 1996) developed an asymptotic methodology based on non-smooth transformations and non-smooth generating functions, that is applicable to strongly nonlinear regimes (Pilipchuk et al., 1997, 1998; Salenger and Vakakis, 1998). In fact, it is interesting to note that Pilipchuk's technique is not applicable to weakly nonlinear regimes, where conventional perturbation methods of the dynamical systems theory based on harmonic generating functions are applicable! For more information of this method we refer to the above-mentioned works by Pilipchuk and to (Vakakis et al., 1996).

The anticipated high complexity of the structure VI periodic orbits dictates the use of careful notation for their representation in the FEP (Lee et al., 2008). In principle, the basic notation introduced in Section 3.3.1.1 for the FEP of the dynamics of the Hamiltonian system with 'smooth' NES is followed, with an additional index being introduced characterizing the pattern of the occurring vibro-impacts. To this end, we employ the following notation for depicting the various types of VI periodic orbits in the FEP.

Symmetric VI periodic orbits are denoted as $SmnE(O)pp\pm$, and satisfy the conditions $x_i(t) = \pm x_i(\xi + T/2)$, $\forall t \in R$, $i = 1, 2$, where T is the period of the motion. Similarly to the case of ‘smooth’ NES, symmetric VI orbits correspond to synchronous oscillations of the LO and the VI NES, and typically are represented by curves in the configuration plane (x_1, x_2) . *Unsymmetric VI periodic orbits* labeled as $Umnppq\pm$, do not satisfy the conditions of the symmetric ones (for notational simplicity, whenever $p = q$ we will adopt the convention, $Umnpp\pm \equiv Umn\pm$). These orbits correspond to asynchronous motions of the two oscillators and are represented by open or closed (Lissajous) curves in the configuration plane (x_1, x_2) . The integer index m denotes the number of half-waves in the VI NES response within a half-period, whereas, the integer index n denotes the corresponding number of half-waves in the LO response; clearly, the ratio $(m:n)$ indicates the order of nonlinear resonance that occurs between the VI NES and the LO on the given VI periodic orbit. The index E or O denotes the symmetry pattern of the vibro-impacts, and has meaning only for symmetric VI orbits: $E(O)$ denotes an even (odd) symmetry of occurring vibro-impacts within a half-period; it follows that the notation $E(O)$ implies that a vibro-impact occurs (does not occur) at quarter-period $\xi = \alpha \equiv T/4$. The integer indices p and q denote the number of vibro-impacts that occur in the first and second quarter-period, respectively, of a given VI periodic orbit; it follows that for symmetric orbits it holds that $p = q$. Finally, the $(+)$ sign corresponds to *in-phase* VI periodic motions, where, for zero initial displacements the initial velocities of the LO and the NES possess identical signs at the beginning of both the first and second half-periods of the periodic motion; otherwise, the VI periodic motion is deemed to be *out-of-phase* and the $(-)$ sign is used. Finally, the two in-phase and out-of-phase linear modes of the system with zero clearance ($e = 0$) are denoted by $Lmm\pm$, and are, in fact, equivalent to $L11\pm$.

The FEP of the Hamiltonian VI system for $\varepsilon = 0.1$, $\sigma = 0.1$ and $e = 0.1$ is depicted in Figure 7.19, with some representative VI periodic orbits presented in Figure 7.20. The complexity of the bifurcations that generate the VI periodic orbits can be inferred from the bifurcation diagrams of Figure 7.21 where the initial velocities of the LO and the VI NES (for zero initial displacements) are depicted as functions of the total energy h . This complexity was anticipated in view of the degenerate vibro-impact nonlinearity of this system.

Note that the FEP in Figure 7.19 is obtained for system (7.14) with all displacements being normalized with respect to the clearance e , so that vibro-impacts occur whenever the absolute value of the relative displacement between the two particles becomes equal to unity in magnitude. Considering the original system (7.13) with clearance e , its Hamiltonian is expressed as, $\hat{H} = e^2 H$ where H is the normalized Hamiltonian defined by (7.16). This implies that, for fixed system parameters, $\varepsilon = 0.1$ and $\sigma = 0.1$, the Hamiltonian structure of the original (non-normalized) system will be identical to that of Figure 7.19; it follows that for a larger (smaller) clearance, the entire structure of VI periodic orbits will be preserved by just shifted towards higher (lower) energy regimes. So, the introduced normalization allows us to study all possible VI responses of the original system by considering a single ‘normalized’ FEP for fixed mass and coupling stiffness ratios. It is interesting to

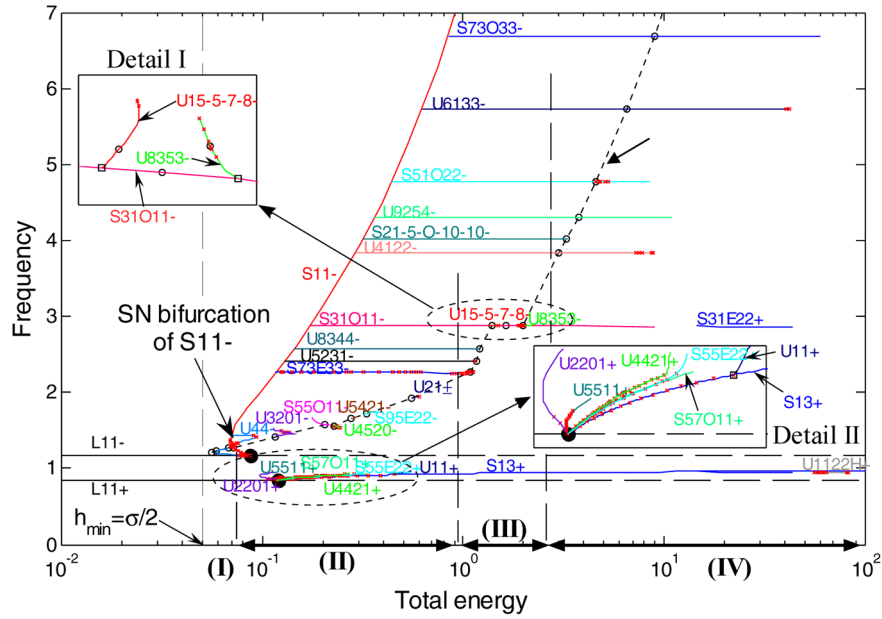


Fig. 7.19 Fep of periodic orbits of the Hamiltonian system with VI NES for $\varepsilon = \sigma = 0.1$; the manifold of VI IOs is indicated by the dashed line (---), whereas the thresholds for vibro-impacts for the in-phase and out-of-phase modes are denoted by bullets (•); unstable branches are denoted by crosses, and energy regimes I–IV referred to in Section 7.3.2.2 are indicated.

note that this normalization does not hold for the system with smooth stiffness nonlinearity (i.e., the ‘smooth’ NES); this can be easily deduced when noting that the introduced normalizations change the form of the system with smooth nonlinearities. Indeed, as we recall from the discussion of Chapter 3, the topological structure of the FEP of the system with ‘smooth’ NES (and the corresponding bifurcation structure of the Hamiltonian periodic orbits) is affected by both the mass ratio and the essentially stiffness nonlinearity of the NES.

We now make some comments and remarks regarding the ‘normalized’ FEP of Figure 7.19. First, we note that the two dots indicate the critical energy thresholds below which oscillations without vibro-impacts occur, and the dynamics of the two-DOF system is purely linear. Clearly, only the in-phase and out-of-phase linear modes $L11\pm$ exist below these energy thresholds. As we increase the energy the motion above these energy thresholds vibro-impacts start occurring, giving rise to two main branches of symmetric periodic VI NNMs: the branch of out-of-phase symmetric VI NNMs $SmmO11-$, which bifurcates from the out-of-phase linear mode $L11-$, after which this mode becomes unstable; and the branch of symmetric in-phase VI NNMs $S13O11+$ which bifurcates out of the in-phase linear mode $L11+$, after which this linear mode also becomes unstable. For convenience, from hereon the shortened notations, $SmmO11- \equiv S11-$ and $S13O11+ \equiv S13+$,

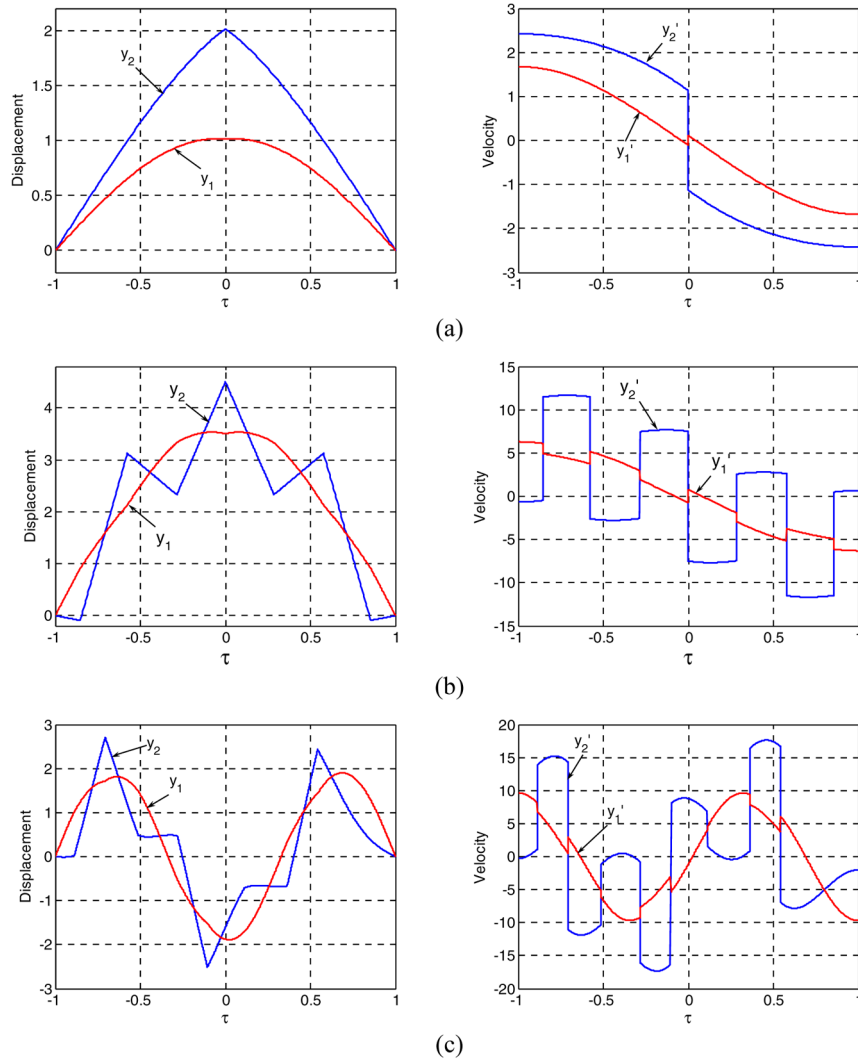


Fig. 7.20 Solutions of the NLBVP (7.18) for $\varepsilon = \sigma = 0.1$: (a) symmetric VI periodic orbit on the backbone $S13O00+ \equiv S13+$, $\alpha = 1.7$, $h = 0.58875$; (b) symmetric VI periodic orbit $S73O33-$, $\alpha = 1.6459$, $h = 7.3348$; (c) unsymmetric VI periodic orbit $U8353-$, $\alpha = 4.9065$, $h = 1.9458$.

will be adopted for these two main backbone branches, which will be referred to as *backbone (global) branches* of the FEP. Both backbone branches exist over broad frequency and energy ranges, and, except for the neighborhoods of the bifurcation points with $L11\pm$, they correspond to oscillations that are mainly localized to the VI NES. A basic bifurcation in the VI FEP is the saddle node (SN) bifurcation of the two backbone branches $S11-$ (at $h \approx 0.06$), which signifies the elimination of

the unstable branch $S11-$ that bifurcates out of $L11-$; the stable branch $S11-$ that is generated after this SN bifurcation maintains its stability for increasing energies. As shown below, this SN bifurcation of the backbone branch $S11-$ affects the capacity of the VI NES for TET. The additional in-phase backbone branch $S13+$ that bifurcates out of the in-phase linear mode $L11+$ is stable until high energies where zones of instability appear.

In Figure 7.20a we depict a typical stable VI orbit on the in-phase backbone branch $S13+$. We note that in the corresponding FEP of the system with ‘smooth’ NES studied in Section 3.3 (see Figure 3.20), there exist two backbone branches $S11\pm$. As indicated by the time series of Figure 7.20a, however, on the in-phase VI backbone branch $S13+$ three sign changes for the LO velocity within half a period are realized, compared to only one for the NES velocity (Lee et al., 2008); this high-frequency component becomes more prominent at higher energies (in addition, as shown in the next section, a 3:1 TRC occurs in the neighborhood of this branch when weak damping is added to the system).

A different class of VI periodic solutions of the FEP lies on *subharmonic tongues* (*local branches*); these are multi-frequency periodic motions, possessing frequencies that are rational multiples of one of the linearized eigenfrequencies of the system. In similarity to the FEP of the system with ‘smooth’ NES (see Figure 3.20), each subharmonic tongue is defined over a finite energy range, and is composed of a pair of branches of in- and out-of-phase subharmonic oscillations. Depending on the behavior of these VI subharmonic tongues with varying energy, the FEP is portioned into four main Regimes, which are labeled as *Regimes I–IV* in Figure 7.19.

In the highest energy Regime IV, out-of-phase VI subharmonic orbits (both symmetric and unsymmetric) bifurcate out of the backbone branch $S11-$. With increasing energy they form subharmonic tongues of out-of-phase motions with almost constant frequencies, until they reach the manifold of VI IOs (see discussion below) after which they change to in-phase motions until they coalesce with the in-phase backbone branch $S13+$ at specific energy levels; this signifies the end of these tongues and the elimination of the corresponding subharmonic motions for higher energy values. This is similar to what was observed in the FEP of the system with ‘smooth’ NES. Unlike, however, that case, the unsymmetric subharmonic tongues do not fold on themselves to reach back the out-of-phase backbone branch $S11-$.

In Regime III of the FEP the bifurcation behavior of subharmonic tongues is similar to Regime IV. The apparent difference is that the manifold of VI IOs undergoes a discontinuous transition on branch $S31O11-$, caused by the two bifurcations of that branch with the unsymmetric subharmonic branches $U(15)578-$ and $U8353-$ in that region (see Detail I in Figure 7.19).

The subharmonic orbits in Regime II exhibit different bifurcation behavior than in Regimes IV and III. In fact, there appear to be no subharmonic tongues bifurcating from $S11-$; instead, small subharmonic tongues appear to lie along the manifold of VI IOs, and eventually merge with the in-phase backbone branch $S13+$ with decreasing energy. For example, the in-phase unsymmetric branch $U21+$ bifurcates from $S13+$ and turns into the out-of-phase unsymmetric branch $U21-$ after it crosses the manifold of VI IOs. In addition, for frequencies in between the

two linearized frequencies ω_1 and ω_2 there exist multiple subharmonic branches bifurcating in a degenerate (higher co-dimensional) bifurcation from the in-phase linear mode $L11+$ (see Detail II in the FEP of Figure 7.19). These subharmonic branches coexist with the in-phase backbone branch $S13+$, which is unstable in most of Regime II. Examples of this type of subharmonic branches are $U2201+$, $U5511+$, $U4421+$, ... in the FEP of Figure 7.19.

Finally, the lowest energy Regime I of the FEP is defined for energies below the bifurcation point of the linear mode $L11-$. The manifold of VI IOs meets the stable out-of-phase linear mode $L11-$ at a bifurcation point that coincides with the critical energy level $h_{\text{crit}} = \sigma/2$; we recall that for $h < h_{\text{crit}}$ no vibro-impacts are possible and the dynamics of the system is completely linear.

As in the case of the system with ‘smooth’ NES there exists a countable infinity of subharmonic tongues, corresponding to symmetric or unsymmetric VI subharmonic motions with different patterns of vibro-impacts during a cycle of the oscillation. As in the case of smooth nonlinearity (see Figure 3.20), unsymmetric VI periodic orbits are represented by closed (Lissajous) curves in the configuration plane of the system. In Figures 7.20b, c we depict two representative symmetric and unsymmetric VI orbits on two subharmonic branches of the FEP.

Finally, there exists a third class of VI motions in the FEP, which are denoted as *VI impulsive orbits* (VI IOs). These are VI periodic solutions corresponding to zero initial conditions of the system, except for the initial velocity of the LO. As discussed in Section 3.3 a VI IO represents, in essence, the response of the system being initially at rest and forced by a single impulse applied to the LO at time $t = 0+$. Apart from the clear similarity of a VI IO to the Green’s function defined for the corresponding linear system, the importance of studying this class of orbits stems from their essential role regarding passive TET from the linear oscillator to the NES [see Section 3.4.2 and Lee et al. (2005), Kerschen et al. (2005, 2006, 2008)]. Indeed, in the case of the NES with smooth nonlinearities, IOs (which, under some conditions are in the forms of nonlinear beats) play the role of *bridging orbits* occurring in the initial phase of TET and ‘channeling’ a significant portion of the applied impulsive energy from the linear primary system (in this case the LO) to the NES at a relatively fast time scale; as discussed in Section 3.4.2 this represents the most efficient scenario for passive TET (i.e., TET through nonlinear beats – see Sections 3.4.2.4 and 3.4.2.5). Although the aforementioned results refer to damped impulsive orbits, the dynamics of the underlying Hamiltonian system determines, in essence, the dynamics of the damped system as well, provided that damping is sufficiently small. It follows that the IOs of the VI Hamiltonian system govern, in essence, the initial phase of TET from the LO to the NES. The numerical results show that VI periodic and quasi-periodic IOs form a manifold in the FEP, containing a countable infinity of periodic IOs, and an uncountable infinity of quasi-periodic IOs.

For the system under consideration the approximation of the manifold of VI IOs was computed numerically, and in Figure 7.19 is superimposed to the FEP; in general, the manifold resembles a smooth curve, with the exception of a number of outliers, which are due to the adopted convention for the frequency index in the FEP (Lee et al., 2008). On a VI subharmonic tongue, a VI IO is realized when-

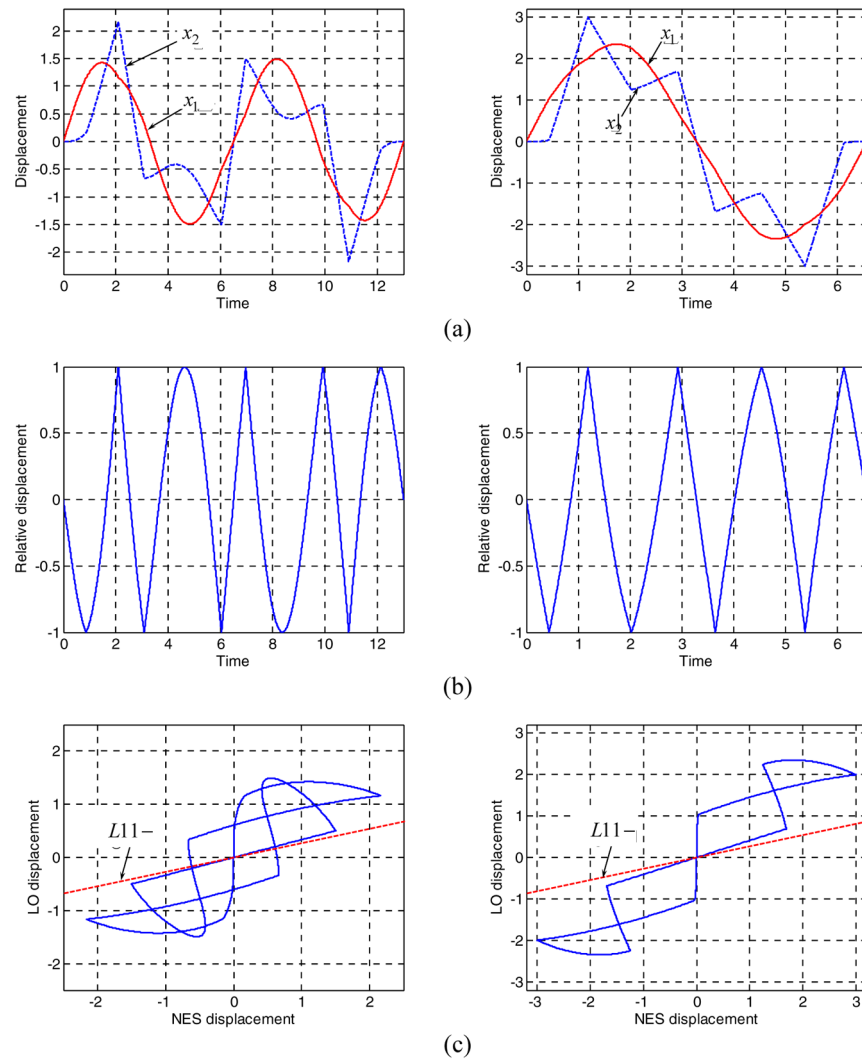


Fig. 7.22 Two representative VI IOs for $\varepsilon = \sigma = 0.1$ (left $U5231-$, right $U4122-$): 9a) unnormalized responses $x_1(t)$ (LO) and $x_2(t)$ (VI NES); (b) relative responses $x_2(t) - x_1(t)$; (c) representation in the configuration plane (x_2, x_1) .

ever the relative motion between that LO and the VI NES changes from in-phase to out-of-phase. Representative VI IOs are depicted in Figure 7.22. In general, the IOs become increasingly more localized to the VI NES as their energy decreases, a result which is in agreement with previous results for NESs with smooth essential nonlinearities (Kerschen et al., 2008a). As energy increases, the VI IOs tend towards the in-phase mode, i.e., their plot in the configuration plane (x_2, x_1) tends

to a straight line of slope 0.084π [since the eigenvector for $L11+$ on the (x_2, x_1) plane is equal to $(3.702, 1)$]. Moreover, we note there is no critical energy threshold for the appearance of VI IOs since there are no low-energy VI motions (the system is linear for low energy levels), and that the dominant frequency of a VI IO depends on the clearance e (i.e., on the energy regime where the VI periodic orbits exist).

Due to the degenerate VI nonlinearity of this system, it is expected that higher-dimensional bifurcations will occur in the dynamics. One case of indication of such degenerate bifurcations is presented in the Detail II of the FEP of Figure 7.19, where multiple branches of symmetric and unsymmetric VI periodic orbits (branches $S95E22-$, $U5421-$, $U4520-$, $S55O11-$, $U3201-$, ...) are noted to bifurcate from the in-phase linear mode $L11+$ at the point of generation of the in-phase backbone branch $S13+$. In addition, VI periodic orbits below the branch $S73E33-$ appear to lie along the VI IO manifold, for example, tongues $U21\pm$, $S95E22-$, $U5421-$, $U4520-$, $S55O11-$, $U3401-$ and $U44-$ in the FEP of Figure 7.19.

It is interesting to note that the complexity of the FEP is solely due to the clearance e that gives rise to vibro-impacts. *Indeed, in the limit of no clearance, $e \rightarrow 0$, the entire structure of VI orbits depicted in the FEP of Figure 7.19 collapses to two horizontal lines corresponding to the linear modes $L11\pm$.* We conclude that, due to the degeneracy of the VI dynamics, even a small clearance can generate significant complexity, including chaotic orbits, as discussed below.

The global dynamics of the Hamiltonian VI system (7.14–7.15) was studied by constructing Poincaré maps resulting from the projection of the isoenergetic dynamics (i.e., of the dynamical flow corresponding to fixed value of h) on the two-dimensional ‘cut section’,

$$\Sigma = \{(x_1, x'_1, x_2, x'_2) \in R^4 / H(x_1, x'_1, x_2, x'_2) = h, \quad x_1 = 0, \quad \dot{x}_1 > 0\}$$

which is transverse to the flow except at points where $\dot{x}_1 = 0$. Similar Poincaré map constructions for vibro-impact dynamics were considered in Mikhlin et al. (1998), and for the VI system under consideration are depicted in Figure 7.23. Below the energy level $h = h_{\text{crit}} = \sigma/2 = 0.05$ no vibro-impacts occur (see Figure 7.23a), and the only possible periodic solutions are the linear stable modes $L11+$.

At energy levels above this critical threshold (see Figures 7.23b–h), vibro-impacts occur (at $|x_2 - x_1| = 1$), and generate a countable infinity of subharmonic VI orbits that replace the two linear modes $L11\pm$; this complex structure of orbits is a direct consequence of the non-integrability of the Hamiltonian VI dynamics. When vibro-impacts occur, the sections of the Poincaré maps corresponding to $|x_2| > 1$ are cut-off from the Poincaré maps, and the last bounding points that are included in the map are those for which the conditions $\{x_1 = 0 \text{ and } |x_2| = 1\}$ hold. For increasing energies, the ‘stochastic seas’ (i.e., the regions of chaotic motions in the Poincaré maps diminish, and the domains of regular motion expand.

An additional use of the Poincaré map is that it can help us identify or infer the existence of global features of the dynamics, such as homoclinic and heteroclinic loops. For example, at the energy level $h = 0.06$ (see Figure 7.23c) we identify

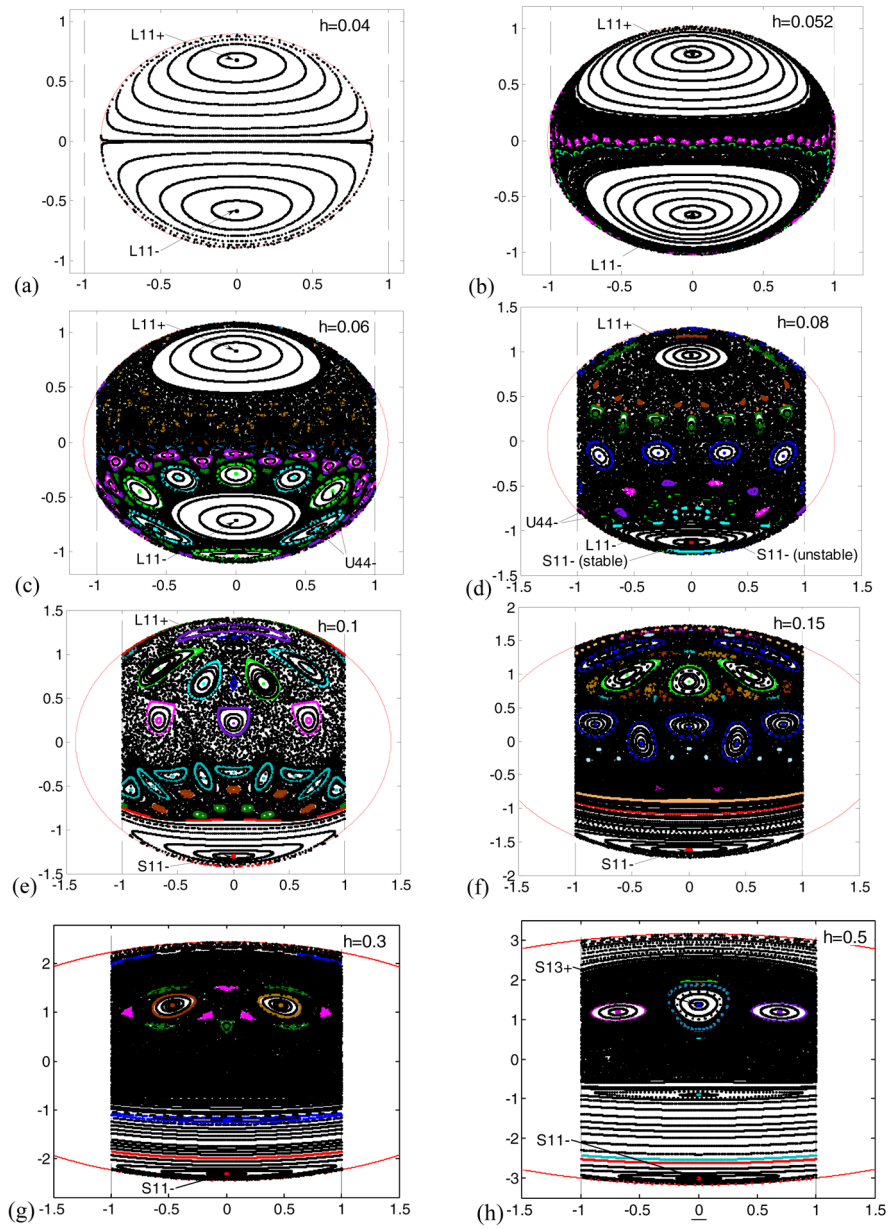


Fig. 7.23 Poincaré maps of VI dynamics for $\sigma = \varepsilon = 1$ and varying energy.

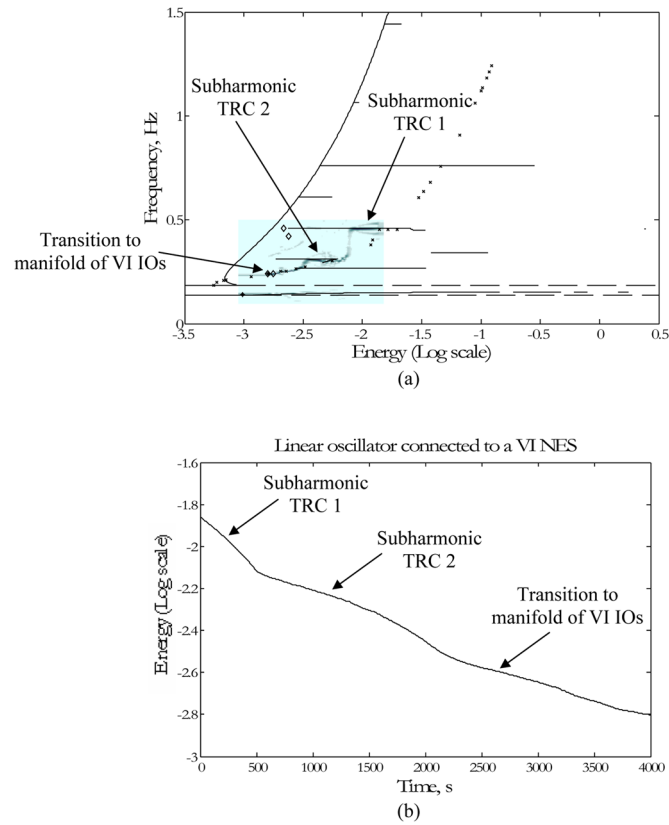


Fig. 7.24 Damped transition for no viscous dissipation and weakly inelastic impacts: (a) WT spectrum of the relative response $x_2 - x_1$ superimposed to the FEP; (b) logarithm of instantaneous energy versus time.

stable and unstable VI periodic orbits $U44-$ in the neighborhood of the linear mode $L11-$ and the unstable NNM $S11-$ (see also the location of this branch in the FEP of Figure 7.19). This infers the existence of a homoclinic loop that connects the unstable periodic orbit $S11-$. The topologies of VI IOs on branches such as $U44-$ (which lie in the neighborhood of the SN bifurcation of $S11-$) are greatly influenced by the family of homoclinic orbits of the unstable branch $S11-$ and affect significantly the efficiency of TET from the LO to the NES. This is similar to what occurs for the case of smooth nonlinearity (see discussion in Section 3.4.2.5), where it was found that close to this family of homoclinic orbits conditions for optimal TET are realized. Indeed, as shown in the next section, excitation of stable VI IOs in the neighborhood of the family of homoclinic orbits of $S11-$ provides conditions for optimal VI TET, since large-amplitude relative displacements between the LO

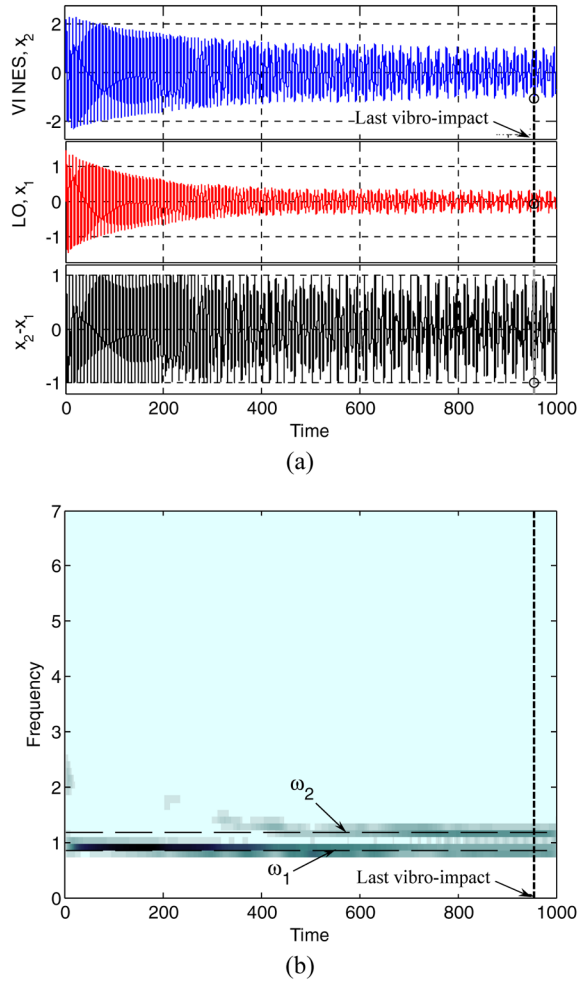


Fig. 7.25 Damped transition for $\rho = 0.7$, $\lambda = 0$: (a) time series; (b) WT spectrum of the relative response $x_2 - x_1$.

and the VI NES are realized in that region and the time scale of the resulting TET is affected as well.

Apart from the compact representation of VI periodic motions, the FEP is a valuable tool for understanding the nonlinear resonant interactions (transient resonance captures – TRCs) that govern energy exchanges and TET during damped transitions in the weakly dissipative VI system. This is due to the fact that for sufficiently weak dissipation (caused by inelastic vibro-impacts, viscous damping or both), the damped VI dynamics is expected to be realized in neighborhoods of branches in the FEP of the underlying VI Hamiltonian system. This is demonstrated in Figure 7.24

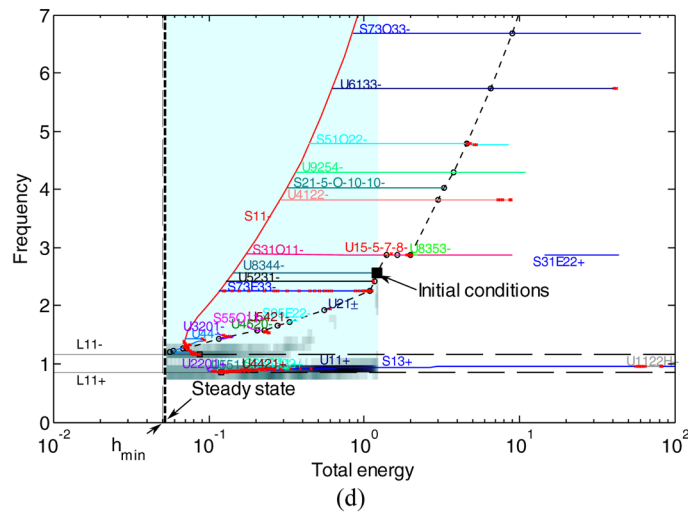
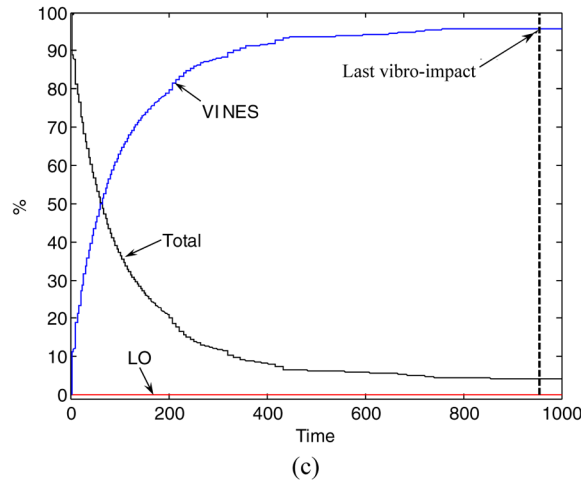


Fig. 7.25 Damped transition for $\rho = 0.7$, $\lambda = 0$: (c) percentages of total energy dissipated by the LO and the VINES; (d) WT spectrum of the relative response $x_2 - x_1$ superimposed to the FEP.

where we depict the wavelet transform (WT) spectra of the damped response of the system with $\varepsilon = \sigma = 0.1$, $\lambda = 0$ and $\rho = 0.95$ superimposed to the Hamiltonian FEP [in this particular simulation the unnormalized responses of the system are depicted (Nucera et al., 2007)]. The motion is initiated on a subharmonic tongue, and we may distinguish three distinct stages in the resulting damped VI transition. In an initial stage, the motion remains in the neighborhood of the subharmonic tongue where it is generated, yielding an initial persistent subharmonic TRC. As a result, subharmonic VI TET takes place from the LO to the NES, and efficient energy dis-

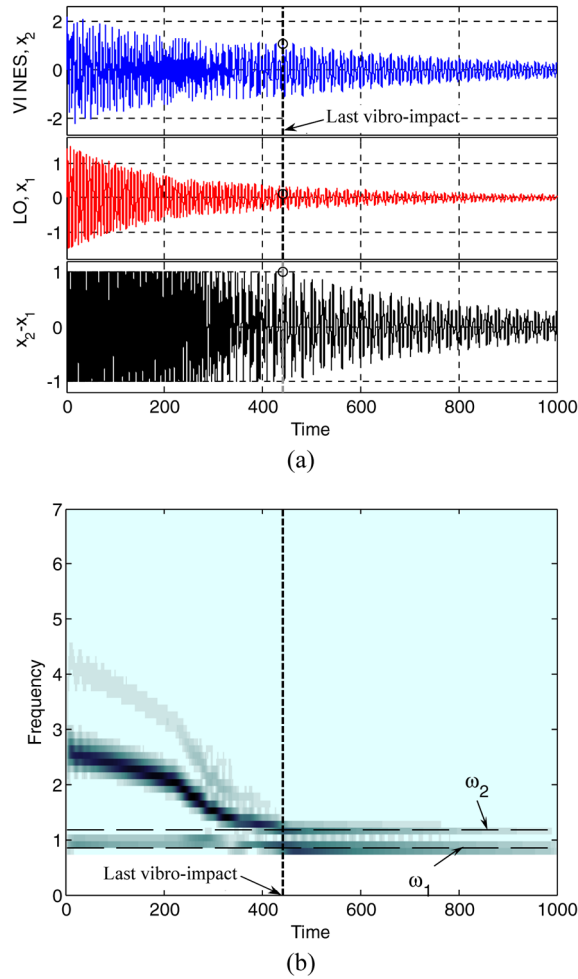


Fig. 7.26 Damped transition for $\rho = 1.0$, $\lambda = 0.005\lambda_{\text{crit}}$: (a) time series; (b) WT spectrum of the relative response $x_2 - x_1$.

sipation occurs, as evidenced by the energy dissipation plot of Figure 7.24b. In the second stage of the damped motion the dynamics makes a transition to a different lower energy subharmonic tongue, which signifies the occurrence of a different subharmonic TRC (and subharmonic TET) in the damped dynamics. Escape from this second TRC regimes leads to a transition of the dynamics to the manifold of VI IOs during the third stage of the motion, before the dynamics becomes linear, and undergoes a final transition to the linear mode $L11+$ (the final stage of the response).

It will be shown in the next section that the transition of the damped dynamics along the manifold of VI IOs during the third stage of the motion is associated with a complex series of multiple TRCs with subharmonic tongues existing in the vicinity

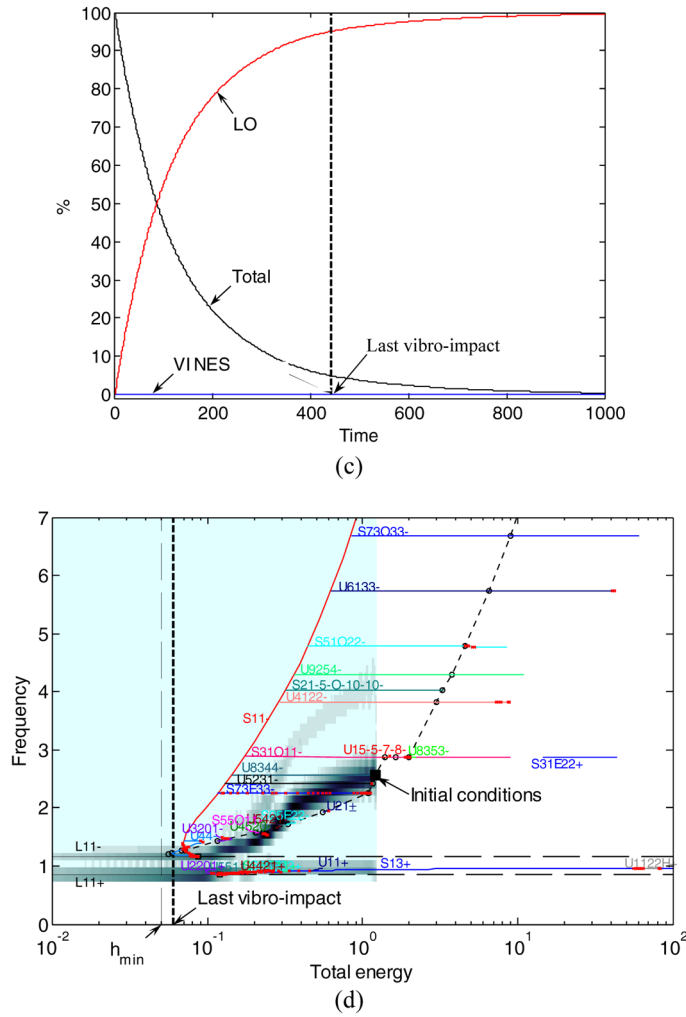


Fig. 7.26 Damped transition for $\rho = 1.0$, $\lambda = 0.005\lambda_{crit}$: (c) percentages of total energy dissipated by the LO and the VINES; (d) WT spectrum of the relative response $x_2 - x_1$ superimposed to the FEP.

of this manifold. It follows, that by studying VI transitions in the FEP and relating them to rates of energy dissipation by the VINES, we should be able to identify the most effective damped transitions from a TET point of view. In a more general context, in the next section we will perform a systematic study of the dynamics of TET in the two-DOF system of Figure 7.17 by assuming inelastic impacts and viscous dissipation in the LO, and analyzing the resulting transient responses and viscous dissipation in the LO, and analyzing the resulting transient responses by numerical WTs. Then, we will superimpose the resulting WT spectra to the FEP of Figure 7.19

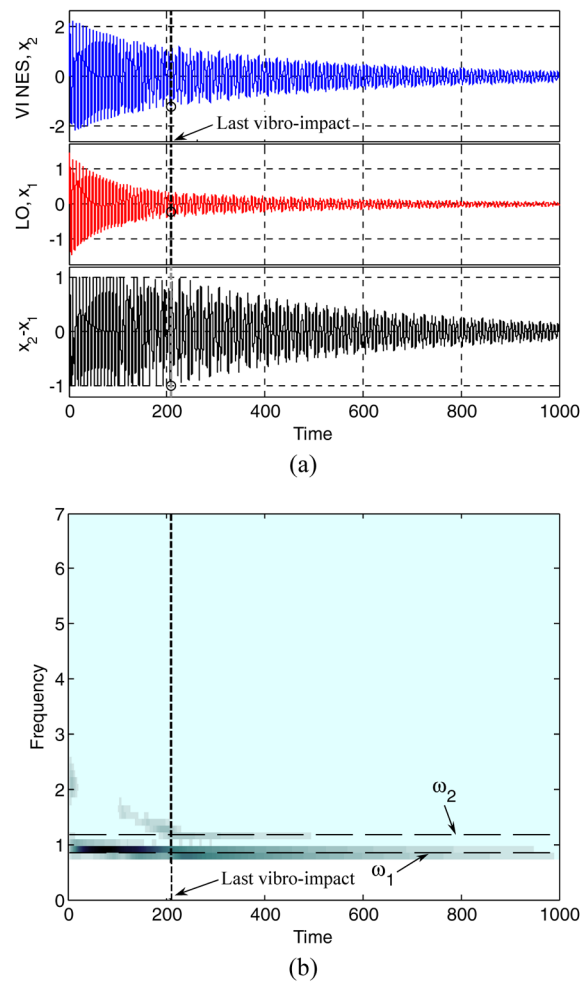


Fig. 7.27 Damped transition for $\rho = 0.7$, $\lambda = 0.05\lambda_{\text{crit}}$: (a) time series; (b) WT spectrum of the relative response $x_2 - x_1$.

(similarly to Figure 7.24), in an effort to interpret the damped transitions in terms of the underlying Hamiltonian dynamics, and to identify the governing dynamical mechanisms for VI TET.

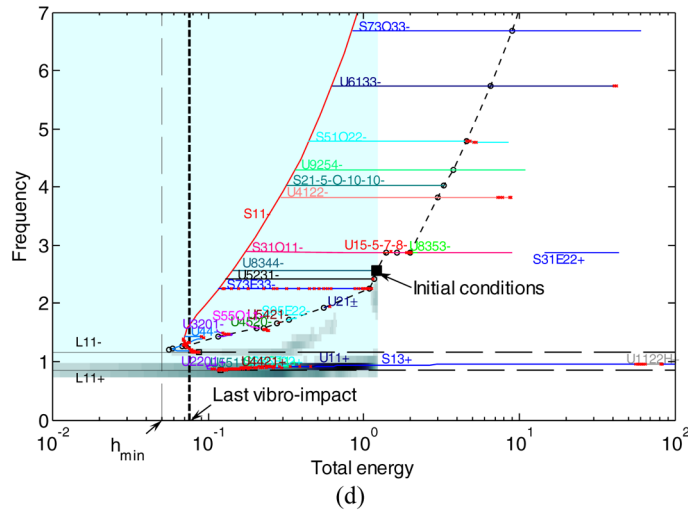
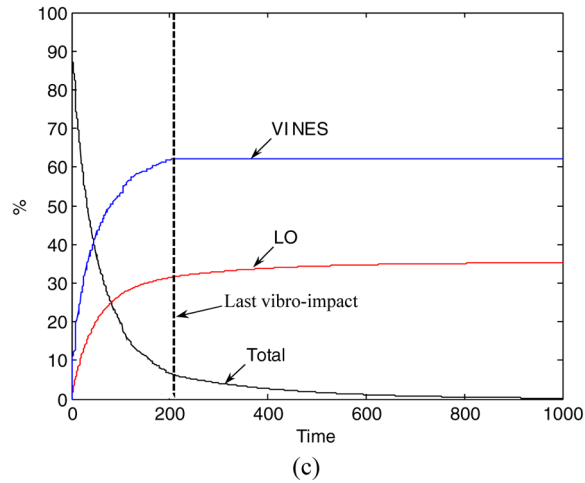


Fig. 7.27 Damped transition for $\rho = 0.7$, $\lambda = 0.05\lambda_{crit}$: (c) percentages of total energy dissipated by the LO and the VI NES; (d) WT spectrum of the relative response $x_2 - x_1$ superimposed to the FEP.

7.3.2 Vibro-Impact Transitions in the Dissipative Case: VI TET

We now consider the weakly dissipative normalized system (7.14) with $\lambda \neq 0$ and inelastic impacts. Then, the relations (7.15) computing the normalized velocities of the LO and the VI NES immediately after an impact in terms of the corresponding velocities before impact, are replaced by the following expressions:

$$x_1'^+ = \frac{(1 - \varepsilon\rho)x_1'^- + \varepsilon(1 + \rho)x_2'^-}{1 + \varepsilon}, \quad x_2'^+ = \frac{(1 + \rho)x_1'^- + (\varepsilon - \rho)\dot{x}_2'^-}{1 + \varepsilon} \quad (7.21)$$

where $0 < \rho \leq 1$ is the coefficient of restitution. Through the numerical simulations of this section, and unless otherwise noted, we assume that $\varepsilon = 0.1$, $\sigma = 0.1$, $e = 0.1$, $\rho = 0.7$ and $\lambda = 0.005\lambda_{\text{crit}}$, where $\lambda_{\text{crit}} = 2$ is the value of critical viscous damping for the LO (hence, weak viscous damping is assumed) (Lee et al., 2008).

Before we proceed to analyze damped transitions, we investigate the competition between the two energy dissipation sources present in the system, namely, viscous dissipation in the LO and inelastic impacts in the VI NES. For this purpose, the damped motion was initiated on the stable VI IO lying on the subharmonic tongue $U8344-$. In Figures 7.25–7.27 we depict the damped responses for the following cases: (a) for no viscous dissipation in the LO and inelastic impacts ($\rho = 0.7$, $\lambda = 0$ – Figure 7.25); (b) for viscous dissipation $\lambda = 0.005\lambda_{\text{crit}}$ and purely elastic impacts ($\rho = 1.0$, $\lambda = 0.005\lambda_{\text{crit}}$ – Figure 7.26); and (c) for a combination of viscous dissipation and inelastic impacts ($\rho = 0.7$, $\lambda = 0.005\lambda_{\text{crit}}$ – Figure 7.27). Comparing the WT spectra of Figures 7.25b, d and 7.26b, d, we note distinct patterns of energy exchange and dissipation in the damped transient dynamics. For purely elastic impacts the response is linear and the WT spectra lie along the two linear modes $L11\pm$; when inelastic impacts occur, there occurs a strongly nonlinear transition of the VI dynamics along strongly nonlinear subharmonic tongues and the in-phase backbone branch $S13+$, until, at the later stage of the response, the dynamics settles into linearized motion along the modes $L11\pm$. A similar, albeit weaker, nonlinear transition is noted for the case of combined inelastic impacts and viscous dissipation (see Figures 7.27b, d), where the damped dynamics traces, primarily the backbone branch $S13+$ (i.e., there occurs an immediate 1:1 TRC of the dynamics of the NES and the in-phase mode $L11+$ right from the beginning of the motion), and, secondarily, higher frequency subharmonic tongues. *We conclude that the addition of weak viscous dissipation in the LO does not affect significantly the VI damped transitions.*

We focus now in the study of the mechanisms that govern VI TET by fixing $\rho = 0.7$ and $\lambda = 0.005\lambda_{\text{crit}}$, in order to compare the dynamical mechanisms for VI TET to the corresponding mechanisms for the case of ‘smooth’ NES discussed in Chapter 3. As discussed in Section 3.4.2, in the smooth case the following three mechanisms for TET were established: (a) fundamental TET, where the damped in-phase NNM invariant manifold $S11+$ is excited; (b) subharmonic TET, where a low-frequency subharmonic tongue is excited; and (c) TET through nonlinear beats, where an IO close to the 1:1 resonance manifold of the dynamics is excited. Our study of TET in the VI case will follow similar lines, by considering energy exchanges between the LO and the NES for alternative types of initial excitation of the system. In particular, we will study VI TET when in-phase or out-of-phase periodic orbits lying on backbone and subharmonic tongues are excited, as well as, when the damped motion is initiated by exciting VI IOs at various energy levels. In what follows we examine each of these cases separately.

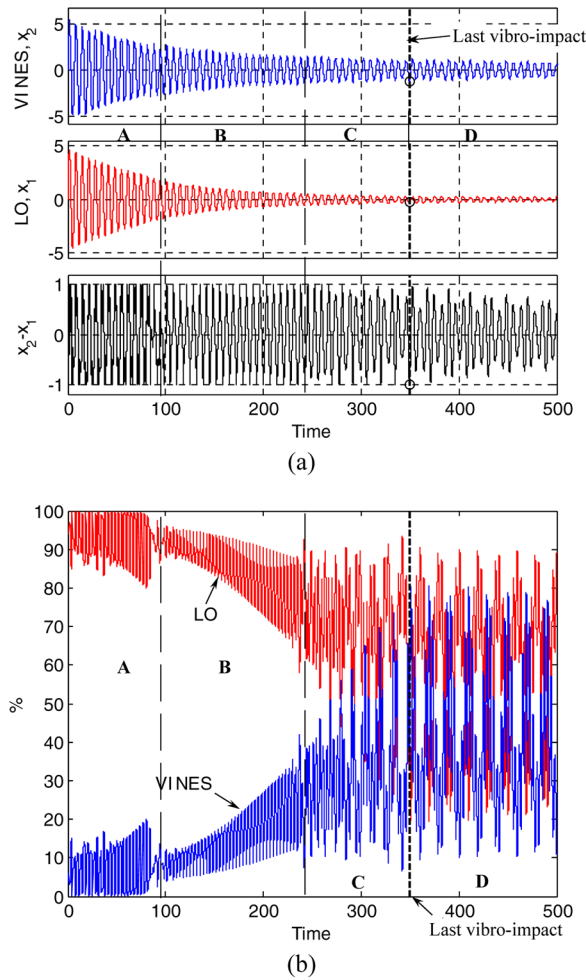


Fig. 7.28 Damped transition initiated on $S13+$: (a) time series; (b) percentages of total instantaneous energy in the LO and the VINES; Stages A–D of the damped transition are indicated.

7.3.2.1 Fundamental VI TET

In Figure 7.28 we present the damped response of the system for initial conditions on the in-phase backbone branch $S13+$ and initial normalized energy $h \approx 10.0$. There are four distinct stages in the damped response, which are denoted as Stages A–D in Figure 7.28. In the highly energetic initial Stage A there occurs a 1:1 TRC in the dynamics, with the response possessing a strong harmonic at the frequency of the in-phase linear mode and a weaker harmonic at $3\omega_1$. This is evident by examining the detailed plot depicted in Figures 7.29a, where it is clear that the relative transient

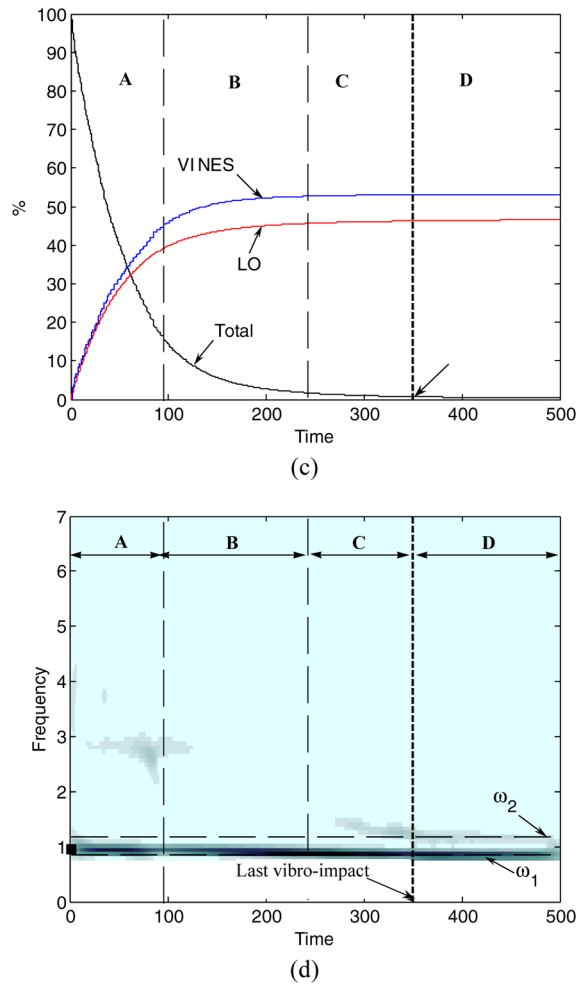


Fig. 7.28 Damped transition initiated on $S13+$: (c) percentages of total energy dissipated by the LO and the VINES; (d) WT spectrum of the relative response $x_2 - x_1$; Stages A–D of the damped transition are indicated.

response $x_2 - x_1$ in Stage A possesses a third harmonic component; moreover, in the detailed plot of Figure 7.30a it is noted that the WT spectrum of the relative response possesses two clear components, a main one at frequency ω_1 , and a secondary one at $3\omega_1$ on the subharmonic branch $S31O11-$. This leads to fundamental VI TET from the LO to the VINES, with almost 85% of the initial energy (nearly 45% by the LO and 40% by the VINES) being dissipated during this initial stage of the motion. The nonlinear modal interactions that lead to fundamental VI TET will be examined in more detail later by EMD, where the governing 1:1 TRC will be more clearly identified.

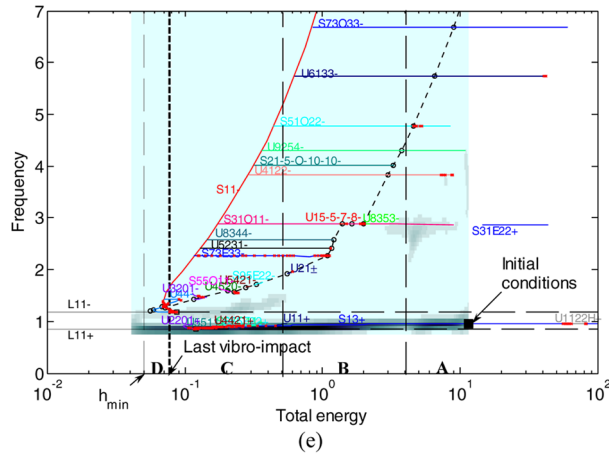


Fig. 7.28 Damped transition initiated on $S13+$: (e) WT spectrum of the relative response $x_2 - x_1$ superimposed to the FEP; Stages A–D of the damped transition are indicated.

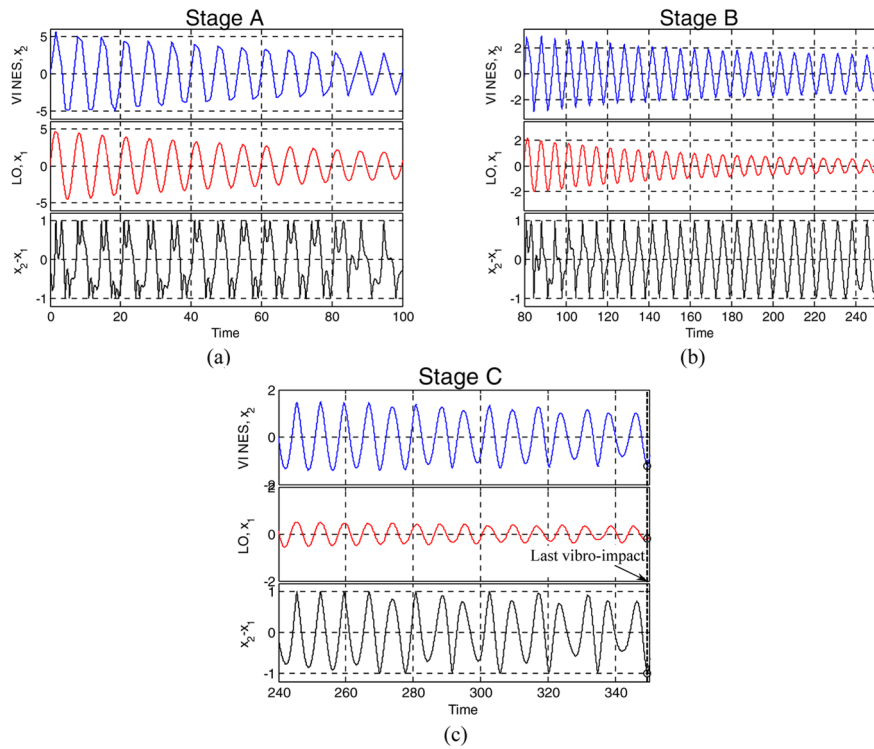


Fig. 7.29 Damped transition initiated on $S13+$, time series of responses: (a) Stage A, (b) Stage B, (c) Stage C.

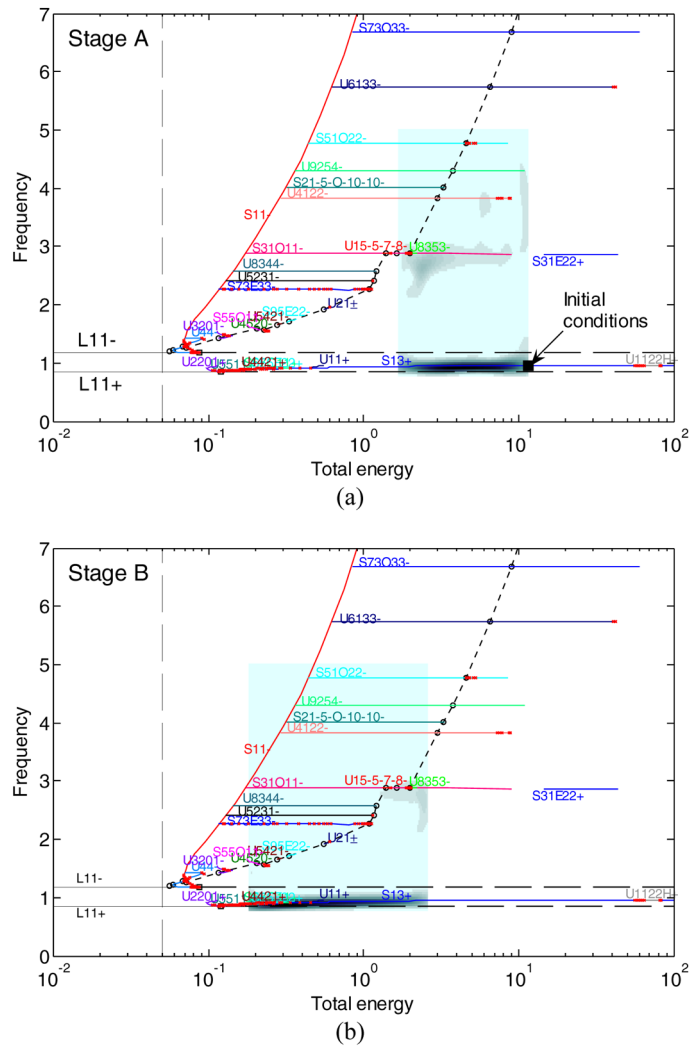


Fig. 7.30 Damped transition initiated on $S13+$, WT spectrum of the relative response $x_2 - x_1$ superimposed to the FEP: (a) Stage A, (b) Stage B.

Stage B (see Figures 7.29b and 7.30b) corresponds to a regime of pure 1:1 TRC as the third harmonic component is nearly eliminated, and the LO and the VI NES execute in-phase oscillations with frequencies approximately equal to ω_1 . It is clear that the weakly damped dynamics follows approximately the in-phase backbone branch $S13+$ until this branch becomes unstable (i.e., at the bifurcation point where the subharmonic branches $U11+$ and $U21\pm$ bifurcate out of this branch – see Fig-

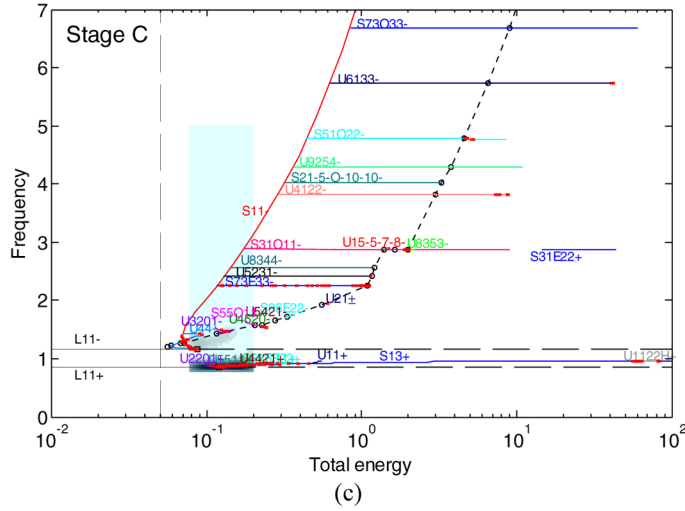


Fig. 7.30 Damped transition initiated on $S13+$, WT spectrum of the relative response $x_2 - x_1$ superimposed to the FEP: (c) Stage C.

ure 7.19). This provides further evidence of the connection between the weakly damped dynamics and the dynamics of the underlying Hamiltonian system.

During Stage C of the damped motion there occurs a series of TRCs along subharmonic tongues on the FEP, whereas in the low-energy Stage D vibro-impacts cease to occur, the motion is purely linear, and energy dissipation is solely due to viscous damping of the LO. As expected, the linear dynamics consist of a combination of the damped analogs of the linear in-phase and out-of-phase modes $L11\pm$, with mode $L11+$ being more dominant in the response.

We conclude that in this numerical simulation there occurs *fundamental VI TET* due to 1:1 TRC of the dynamics of the VI NES at frequency ω_1 . Recalling that ω_1 is the natural frequency of the in-phase linear mode $L11+$, we conclude that *during fundamental VI TET the LO and the VI NES engage in in-phase 1:1 resonance capture*. This VI TET mechanism is analogous to fundamental TET discussed in the case of smooth nonlinearity (see Section 3.4.2.1).

The next simulation examines the damped response of the system for initial conditions on the out-of-phase backbone branch $S11-$ at $h \approx 0.8$ (see Figure 7.31). There is insignificant TET from the LO to the NES in this case, since (as in the case of smooth nonlinearity) the initial energy of the motion localizes predominantly to the VI NES right from the beginning of the motion; then, localization to the VI NES is maintained throughout, as the damped VI motion approximately traces the backbone branch $S11-$. In fact, in this case vibro-impacts occur only during a short initial stage of the motion (i.e., for $\xi < 10$ – see Figure 7.31a), where almost 90% of total energy is dissipated. In the purely linear regime where no vibro-impacts occur (for $\xi > 10$) the response is mainly composed of the damped analogue of the out-

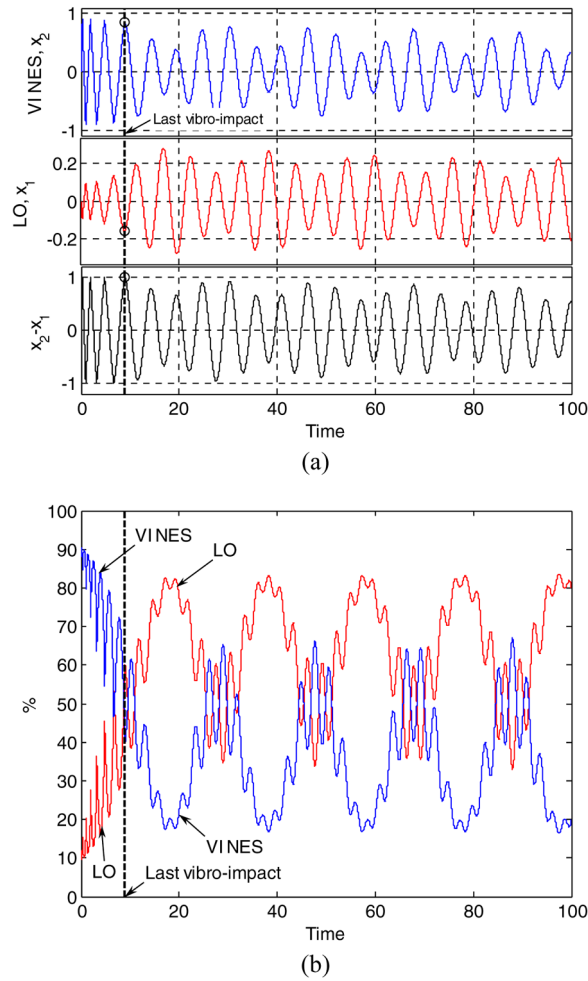


Fig. 7.31 Damped transition initiated on $S11-$: (a) time series; (b) percentages of total instantaneous energy in the LO and the VINEs.

of-phase linear mode $L11-$, with a weaker participation of the in-phase damped mode $L11+$. The participation of these closely spaced modes in the linear response produces a beat phenomenon, which is evidenced by the strong energy exchange noted in the plot of Figure 7.31b.

We conclude that there is immediate escape of the transient damped dynamics from the initially excited out-of-phase backbone branch $S11-$, followed by settlement of the response in alternative response regimes. This is a general conclusion drawn from the performed numerical simulations (Lee et al., 2008), and holds for motions that are initiated on all branches and tongues of the FEP other than the in-

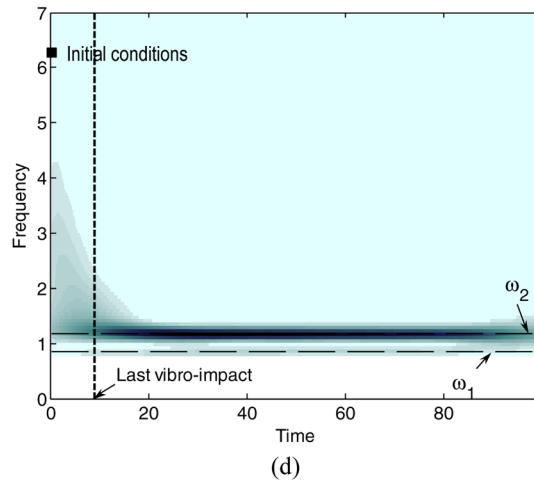
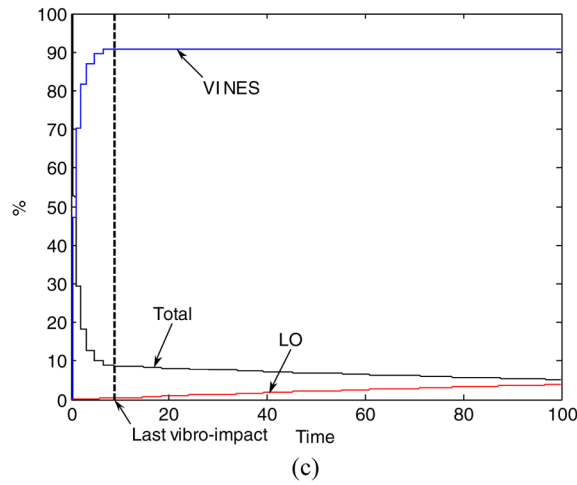


Fig. 7.31 Damped transition initiated on $S11$ —: (c) percentage of total energy dissipated by the LO and the VINES; (d) WT spectrum of the relative response $x_2 - x_1$.

phase backbone branch (we recall that this was also the case for the case of smooth nonlinearity, see Section 3.4).

7.3.2.2 VI TET through Excitation of VI IOs

Having established the mechanism of fundamental TET in the system with VINES, we now consider the possibility of alternative mechanisms for VI TET based on the excitation of VI IOs. As shown in Section 3.4.2 excitation of IOs on certain energy

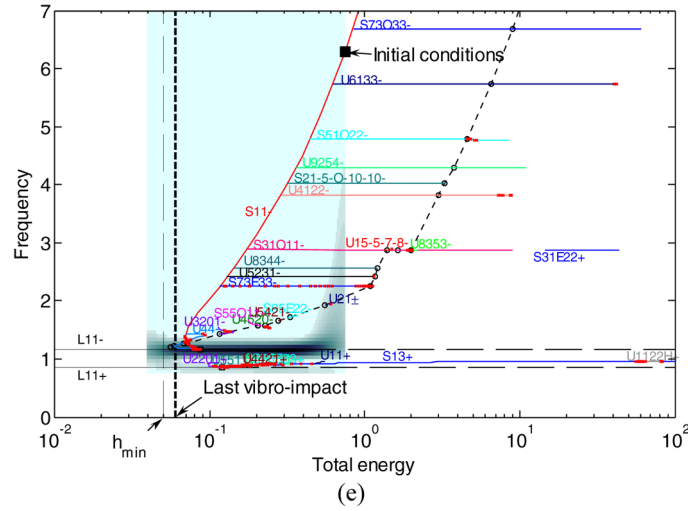


Fig. 7.31 Damped transition initiated on $S11-$: (e) WT spectrum of the relative response $x_2 - x_1$ superimposed to the FEP.

ranges provides the mechanism for most efficient TET in the system with NES with smooth nonlinearity.

In the following study we study efficiency of TET from the LO to the NES when VI IOs are excited in the four previously defined Regimes I–IV of the FEP. We recall from the case of NES with smooth nonlinearity that IOs play an important role as far as TET is concerned; this holds especially for IOs lying in the neighborhood of the family of homoclinic orbits of the unstable in-phase damped NNMs $S11+$, close to the 1:1 resonance manifold of the damped dynamics (see discussion in Section 3.4.2.5).

In Figure 7.32 we depict the damped response of the system when a VI IO in Regime I is excited. Since the initial energy of the motion is relatively low, vibro-impacts occur only during the short-duration initial stage of the dynamics, and afterwards the dynamics become completely linear, involving continuous energy exchanges between the two linear modes of the system (with no vibro-impacts) with frequencies ω_1 and ω_2 . Due to the closely spaced linear natural frequencies, a linear beat develops and energy is predominantly dissipated by viscous dissipation in the LO. In this case insignificant TET from the LO to the VI NES occurs.

The damped responses for initial excitation of the VI IO on the subharmonic tongue $S95E22-$ in Regime II of the FEP are depicted in Figure 7.33. In this case the dynamics cannot exhibit a 1:1 TRC, since the in-phase backbone branch $S13+$ is unstable at the specific initial energy level considered in this simulation. As a result, the damped dynamics may be divided into four distinct stages, labeled A–D in Figure 7.33. Stages A–C are strongly nonlinear, whereas, the low-energy Stage D is linear with no vibro-impacts occurring in that late stage of the response. In Stage

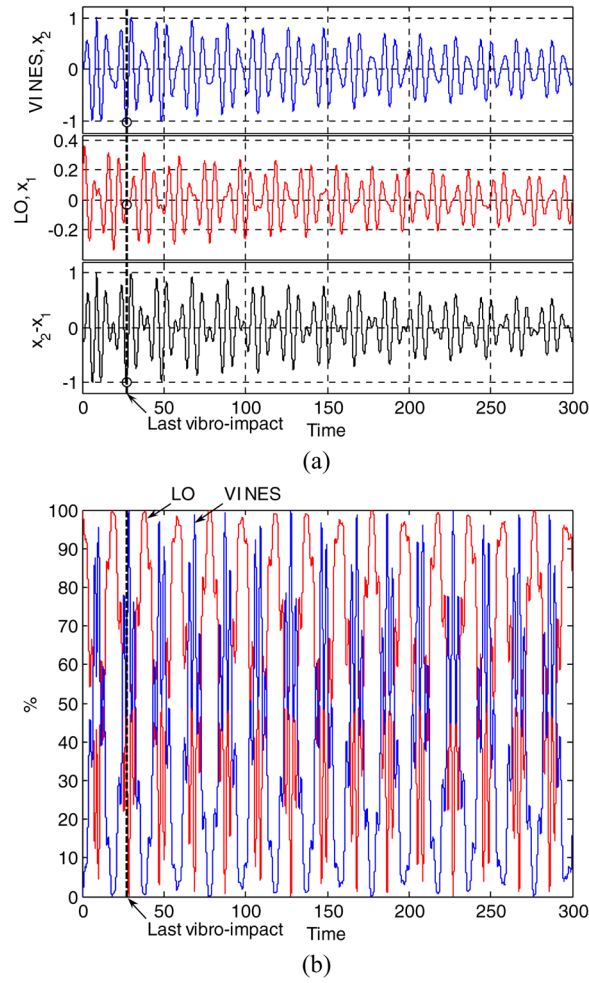


Fig. 7.32 Damped transition initiated on a VI IO in regime I: (a) time series; (b) percentages of total instantaneous energy in the LO and the VINES.

At the damped dynamics follows approximately the tongue $S95E22-$ (where the motion is initiated) with decreasing energy. Nearly 50% of the total initial energy is dissipated during this stage of the response, with 33% of total energy being dissipated due to TET from the LO to the VINES. The damped dynamics in Stages B and C is complex, as it undergoes transitions along subharmonic tongues such as $U5421-$, $U4520-$, $S55O11-$ and $U3201-$ lying close to the manifold of IO. Finally, when sufficient energy is dissipated and no additional vibro-impacts can occur the dynamics settles into the linear Stage D, where predominant contribution of mode $L11+$ is realized.

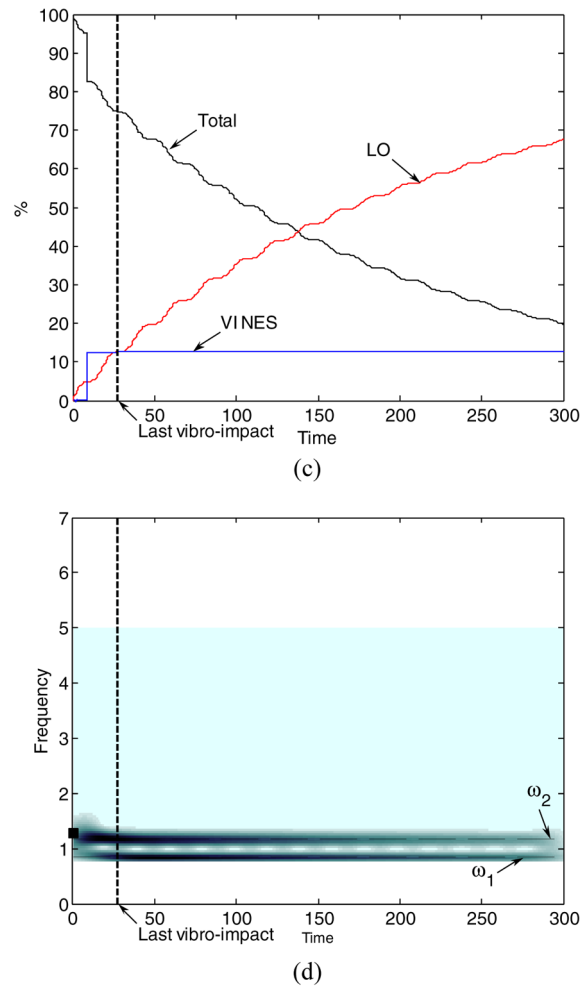


Fig. 7.32 Damped transition initiated on a VI IO in regime I: (c) percentages of total energy dissipated by the LO and the VI NES; (d) WT spectrum of the relative response $x_2 - x_1$.

In Figure 7.34 the damped dynamics for excitation of the VI IO on the subharmonic tongue $S32O11$ in Regime III of the FEP is presented. For the selected initial energy level for this simulation 1:1 TRC is possible (since the backbone branch $S13+$ is stable at the initial energy level considered), and five distinct stages of the damped motion (labeled as A–E in Figure 7.34) are inferred. In Stage A the damped motion follows the subharmonic tongue $S31O11$ — which acts as bridging orbit for the dynamics to make the transition for its initial state to 1:1 TRC (which is realized in Stage B). In Stage B there occurs a 1:1 TRC as the stable in-phase backbone branch $S13+$ is excited; as a result, fundamental TET from the LO to the VI NES is realized, so that nearly 50% of the total initial energy is dissipated by the VI NES by

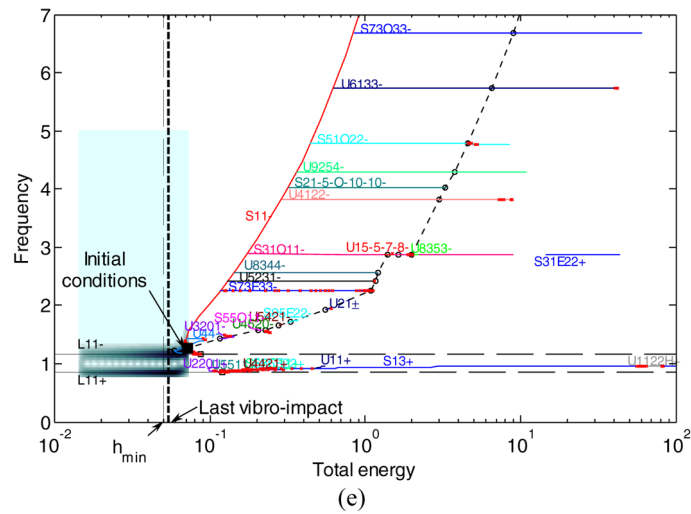


Fig. 7.32 Damped transition initiated on a VI IO in regime I: (e) WT spectrum of the relative response superimposed to the FEP.

the end of this stage of the motion. As energy decreases due to viscous dissipation and inelastic impacts, the in-phase backbone branch $S13+$ becomes unstable and the damped dynamics makes a transition to Stages C and D; these stages are similar to those occurring in Regime II of the FEP, and the dynamics follows complex transitions along subharmonic tongues, similar to the ones depicted in Figure 7.33. At the later, low-energy Stage E the dynamics is linear and dominated by mode $L11+$. We conclude that by exciting VI IOs lying in Regime III of the FEP the ‘bridging orbit’ scenario is realized (as in the case of the system with ‘smooth’ NES), leading eventually to fundamental VI TET. This scenario yields efficient TET from the LO to the VI NES.

Finally, when IOs in the high-energy Regime IV of the FEP are excited (see Figure 7.35) the damped transitions are similar to those realized in Regime III, with TET efficiency at the end of fundamental VI TET reaching levels of nearly 55%.

In conclusion, we identify two mechanisms for VI TET, namely, *fundamental VI TET due to 1:1 TRC*, and *VI TET through excitation of a VI IO leading eventually to fundamental VI TET*. These are similar to the corresponding TET mechanisms for the case of ‘smooth’ NES. No subharmonic VI TET (caused by TRC of the dynamics on an isolated VI subharmonic tongue) could be realized in the numerical simulations of the dynamics of the VI system under consideration, as the VI dynamics seem to engage in series of TRCs involving multiple subharmonic tongues (instead of an isolated one) lying close to the manifold of VI IOs. However, as shown in the simulations of Figure 7.24, subharmonic VI TET is indeed possible in the VI system of Figure 7.17. We conjecture, therefore, that, *probably, subharmonic VI TET is a mechanism for TET in systems with very weak viscous damping and*

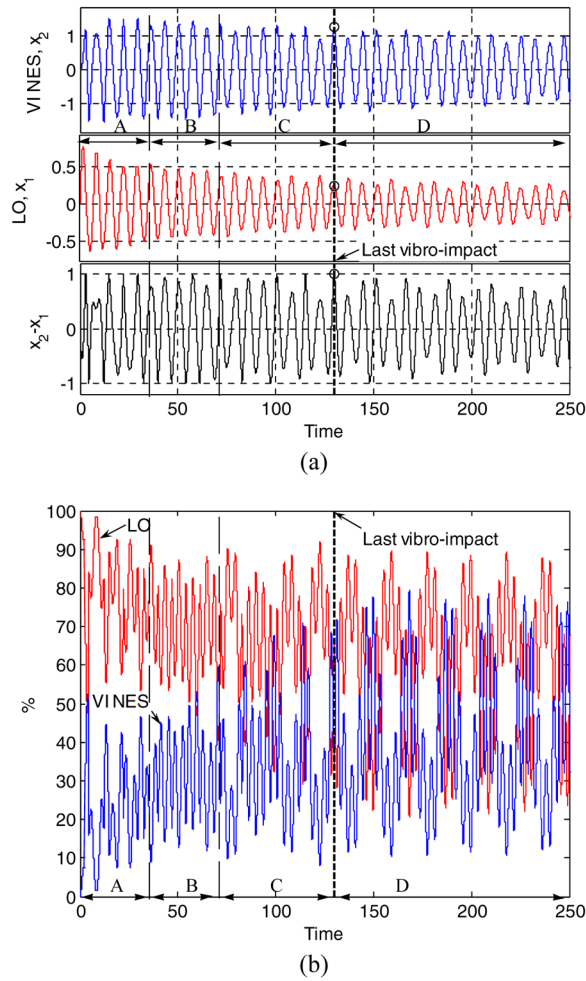


Fig. 7.33 Damped transition initiated on a VI IO in regime II: (a) time series; (b) percentages of total instantaneous energy in the LO and the VINES.

weakly inelastic impacts. A final conclusion drawn from the previous simulations is that lack of fundamental TET in Regimes I and II of the FEP can be attributed to the instability of the in-phase backbone branch $S13+$ in the corresponding energy ranges. This is an additional indication of the strong relation that exists between the Hamiltonian dynamics and the weakly damped transitions.

The specific nonlinear resonance interactions leading to TET in the VI system can be further analyzed by post-processing the corresponding time series by Empirical Mode Decomposition (EMD). We demonstrate this by analyzing in detail the mechanism for fundamental VI TET and showing that it corresponds to a 1:1 TRC.

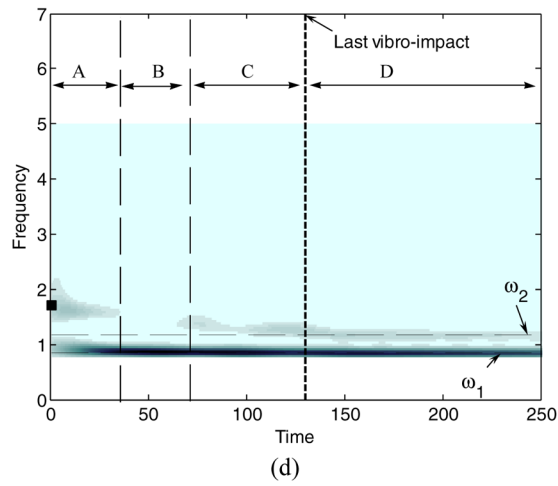
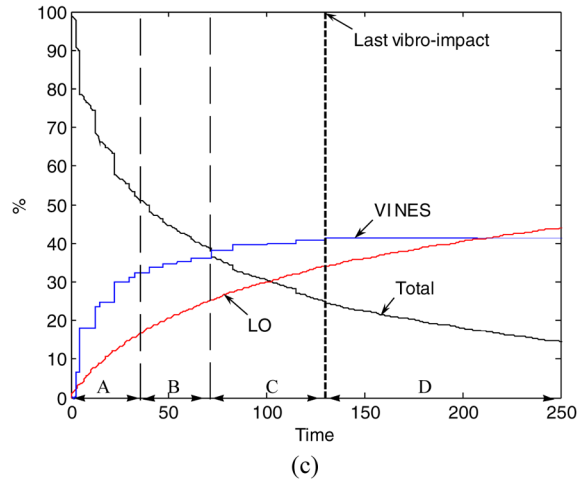


Fig. 7.33 Damped transition initiated on a VI IO in regime II: (c) percentages of total energy dissipated by the LO and the VINES; (d) WT spectrum of the relative response $x_2 - x_1$.

To this end, we analyze the high-energy damped transition depicted in Figure 7.28 for motion initiated on the in-phase backbone branch. As shown in previous chapters, decomposition of nonlinear damped transitions by EMD leads to multi-scale nonlinear system identification of the governing dynamics, and provides the means for identifying nonlinear resonance (modal) interactions between substructures, as well as the time (of frequency) scales where these modal interactions occur.

In Figure 7.36 we depict the results of EMD analysis, from which we conclude that the response of the VINES possesses a single dominant IMF [the leading one – denoted by c_1 (NES)], whereas, the LO response possesses two dominant IMFs [the

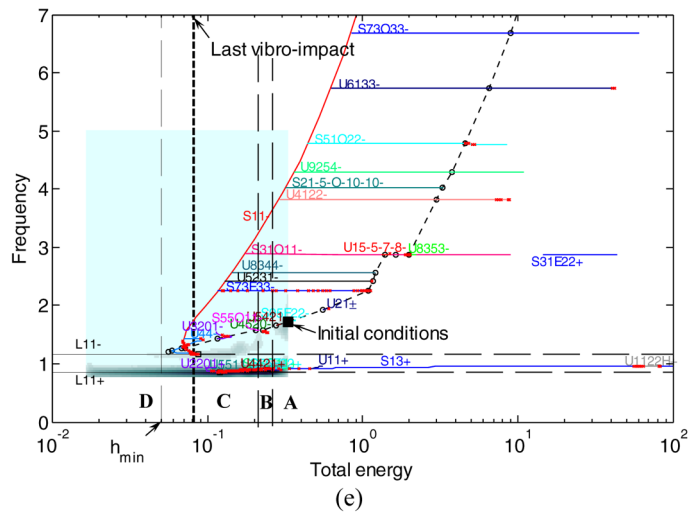


Fig. 7.33 Damped transition initiated on a VI IO in regime II: (e) WT spectrum of the relative response superimposed to the FEP.

first and second ones – denoted by $c_1(\text{LO})$ and $c_2(\text{LO})$]. Denoting by the instantaneous phase of the dominant IMF $c_1(\text{NES})$ computed by the numerical Hilbert transform, and by ϕ_{21} and ϕ_{22} the corresponding phases of $c_1(\text{LO})$ and $c_2(\text{LO})$, and computing the phase differences $\theta_1 = \phi_{11} - \phi_{21}$ and $\theta_2 = \phi_{11} - \phi_{22}$, TRCs occurring between IMFs can be studied in detail. Indeed, as discussed in previous Chapters, when a specific phase difference exhibits time- like (i.e., monotonic with time) behavior over a specified time interval, it may be regarded as a ‘fast’ angle, and, hence, may be averaged out of the dynamics; this eliminates the possibility of resonance interaction between the corresponding IMFs. On the contrary, non-time-like behavior of a phase difference precludes the direct application of the averaging theorem with respect to that angle, and the possibility for resonance interaction between the corresponding IMFs.

In Figure 7.36d we note non-time-like behavior of the phase difference θ_1 during Stage A of the damped motion, which indicates that a 1:1 TRC between the dominant IMF of the VI NES and the first dominant IMF of the LO is realized (denoted as RC1 in Figure 7.36d). Escape from this resonance capture is signified by the time-like behavior of θ_1 in Stage B, followed by an additional 1:1 TRC (RC3) in the weakly nonlinear Stage C, and by the purely linear Stage D. This delayed low-energy TRC signifies the excitation of the in-phase linear mode $L11+$ towards the end of the damped transition. An additional 1:1 TRC (RC2) between the dominant IMF of the VI NES and the second dominant IMF of the LO is revealed by the non-time-like behavior of the phase difference θ_2 in stage B of the decaying response. As discussed previously, this corresponds to the regime of pure 1:1 TRC between the VI NES and the LO, which leads to fundamental TET.

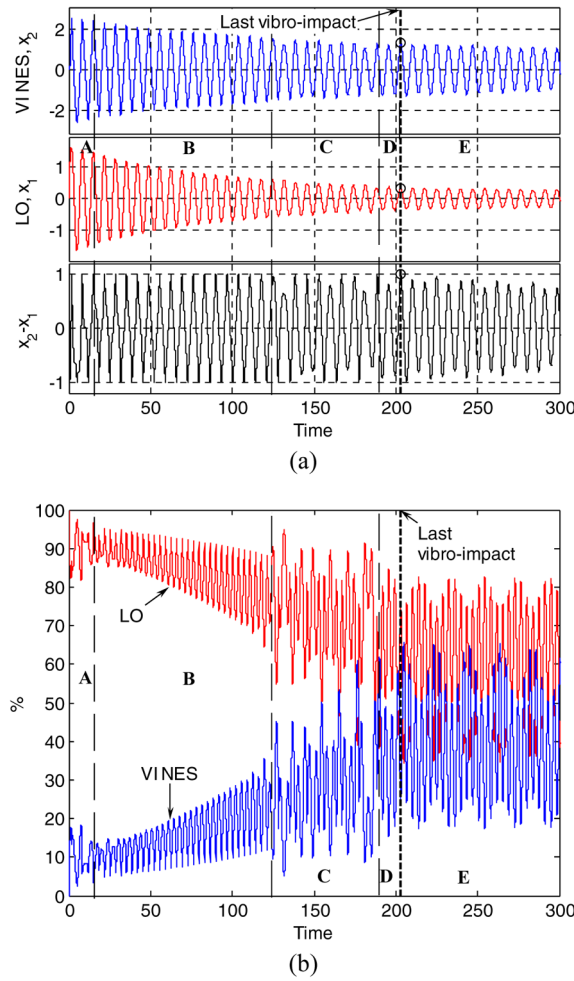


Fig. 7.34 Damped transition initiated on a VI IO in regime III: (a) time series; (b) percentages of total instantaneous energy in the LO and the VINES.

It is interesting to note that the aforementioned partitioning of the phase evolution plot of Figure 7.36d in terms of distinct stages, coincides with the corresponding partitioning introduced previously in the plots of Figure 7.28 (see, especially the energy exchange plot of Figure 7.28b). This demonstrates that *the EMD technique although applied (by construction) in an ad hoc manner, can still lead to physically relevant results*. Efforts towards a rigorous physical interpretation of EMD results in terms of the slow flow dynamics of a system, and application of EMD in the context of nonlinear, non-parametric system identification are undertaken currently (Kerschen et al., 2008b).

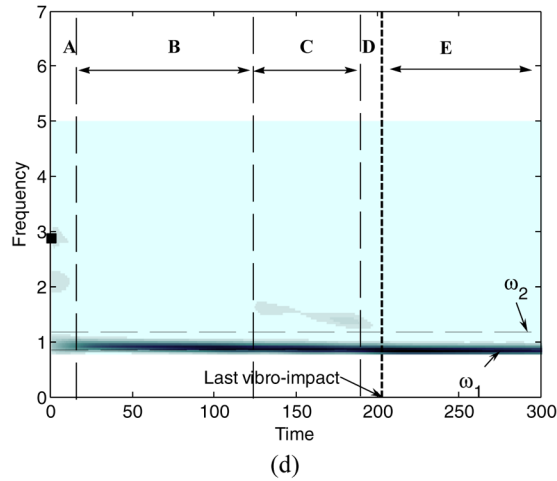
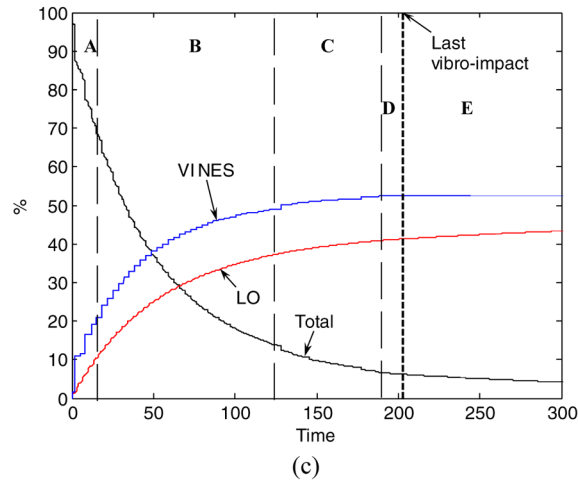


Fig. 7.34 Damped transition initiated on a VI IO in regime III: (c) percentages of total energy dissipated by the LO and the VINES; (d) WT spectrum of the relative response $x_2 - x_1$.

We end this section by mentioning that the presented VI TET results are by no means optimized, that is, higher TET efficiencies may be achieved when alternative sets of initial conditions are considered. This leads us naturally to the discussion of TET efficiency in the system with VI NES carried out in the next section.

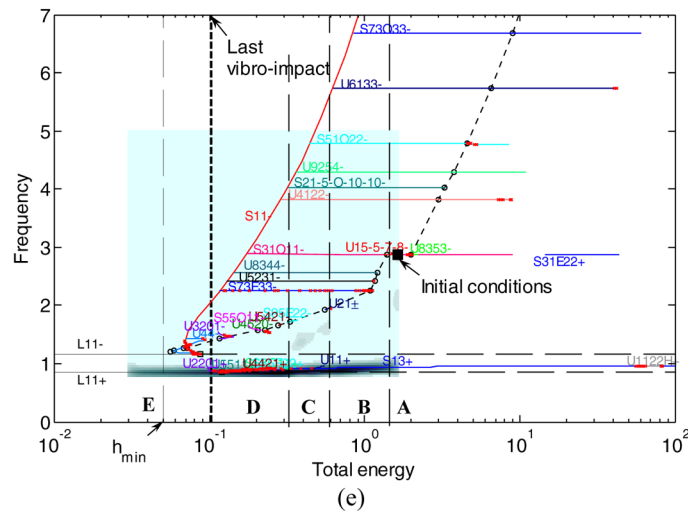


Fig. 7.34 Damped transition initiated on a VI IO in regime III: (e) WT spectrum of the relative response superimposed to the FEP.

7.3.2.3 Efficiency of VI TET

We aim to study the efficiency of VI TET in the system of Figure 7.17 by introducing certain definitions related to the capacity of the VI NES to passively absorb and dissipate vibration energy from the LO, as well as the time required for this VI dissipation to occur. Specifically, we denote by ξ_{LI} the normalized time instant when the last vibro-impact in a given simulation occurs (that is, for $\xi > \xi_{LI}$ the transient response is purely linear); by $\xi_{95\%}$ the time required for 95% of the initial energy of the system to get dissipated by viscous dissipation and inelastic vibro-impacts; and by $E_{VI\ NES}$ the percentage of initial energy that is eventually dissipated by the VI NES due to inelastic vibro-impacts (i.e., during the entire duration of the damped motion). In this context, the ratio $E_{VI\ NES}/\xi_{LI}$ represents the average measure of the percentage of energy dissipated by the VI NES per unit time, whereas, the ratio $95/\xi_{95\%}$ the average percentage of energy dissipated per unit time until 95% of total energy is dissipated. The ratio $E_{VI\ NES}/\xi_{LI}$ provides a measure of VI TET efficiency per unit time as long as vibro-impacts occur (i.e., for $\xi \leq \xi_{LI}$), and is used as a means of judging the rate (time scale) of energy dissipation (efficiency) by the VI NES only; on the contrary, the measure $95/\xi_{95\%}$ is used to study the overall rate of energy dissipation in the system (including the combined the effects of inelastic vibro- impacts and viscous damping dissipation).

Clearly, higher values of the energy measure $E_{VI\ NES}$, and/or lower values of the time measure $\xi_{95\%}$, result in more efficient VI TET in the system under consideration. Moreover, if there are no other sources of dissipation, higher values of the average rate $E_{VI\ NES}/\xi_{LI}$ indicate high VI TET efficiency in the nonlinear regime of

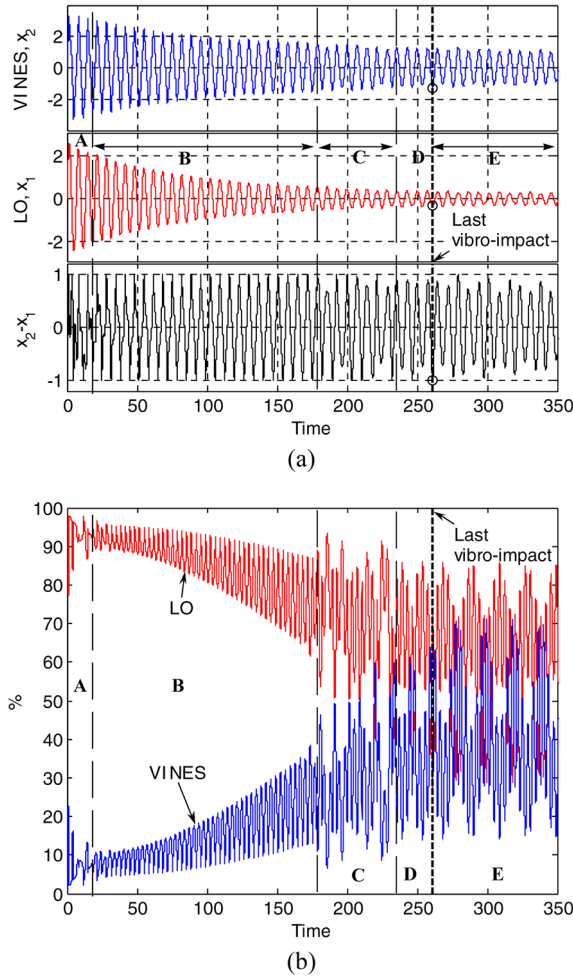


Fig. 7.35 Damped transition initiated on a VI IO in regime IV: (a) time series; (b) percentages of total instantaneous energy in the LO and the VINES.

the damped response, i.e., in the regime where vibro-impacts are realized. However, in the presence of additional viscous damping dissipation in the LO, the average rate $95/\xi_{95\%}$ provides a better indicator of the overall efficiency of TET to dissipate a significant portion of the total initial energy of the system throughout the damped motion.

In Figure 7.37 we depict the measures ξ_{LI} , $\xi_{95\%}$, E_{VINES} and the average rates E_{VINES}/ξ_{LI} , $95/\xi_{95\%}$ as functions of initial energy, for damped VI responses initiated on VI IOs over a wide energy range of the FEP. The system parameters used for these simulations are $\rho = 0.7$, $\lambda = 0.005\lambda_{crit}$ and $\varepsilon = \sigma = 0.1$. As expected,

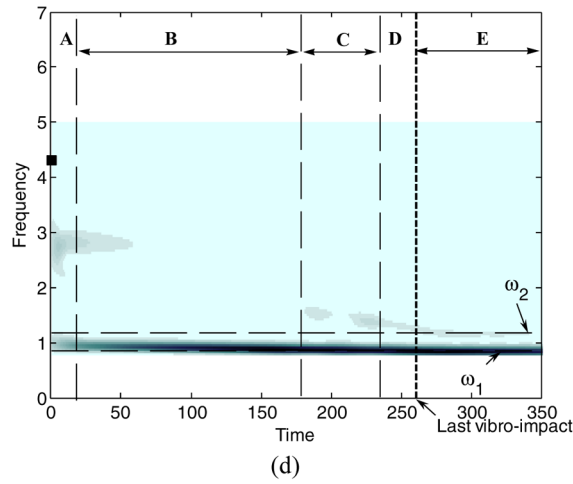
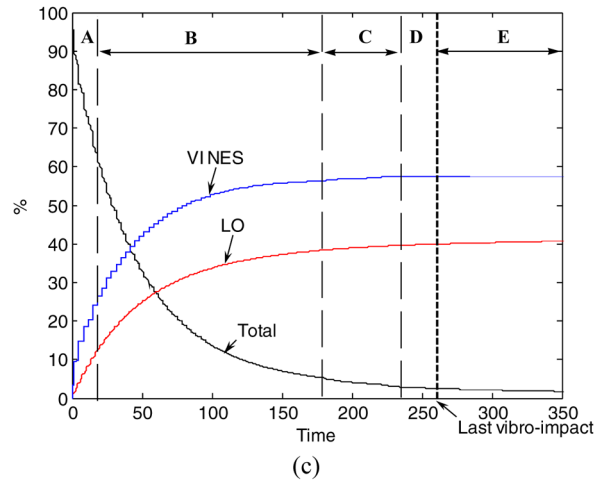


Fig. 7.35 Damped transition initiated on a VI IO in regime IV: (c) percentages of total energy dissipated by the LO and the VINES; (d) WT spectrum of the relative response $x_2 - x_1$.

with increasing energy more vibro-impacts occur, as indicated by the increase of the normalized time measure ξ_{LI} with increasing energy in Figure 7.37a. Judging from the dependence of the energy measure E_{VINES} on energy (see Figure 7.37a), we conclude that most efficient VI TET is realized when VI IOs are excited in Regimes III and IV of the FEP (the highest VI TET efficiency is above 65% for this series of simulations). Moreover, VI TET in Regimes III and IV occurs at a relatively fast time scale, as indicated by the relatively small values of the normalized time measure $\xi_{95\%}$ in the corresponding energy ranges (see Figure 7.37a).

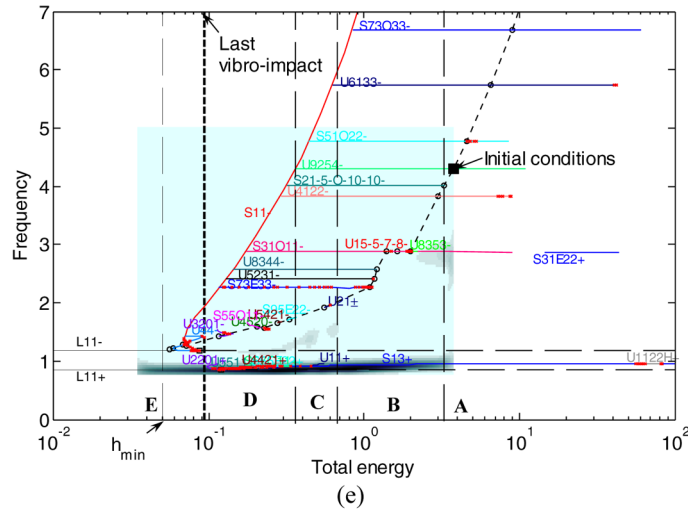


Fig. 7.35 Damped transition initiated on a VI IO in regime IV: (e) WT spectrum of the relative response superimposed to the FEP.

Focusing now on the average rates depicted in Figure 7.37b, we deduce again that the most efficient rates of the overall energy dissipation measure $95/\xi_{95\%}$, are realized in Regimes III and IV, although the highest rates of energy dissipated by the VI NES during vibro-impacts, $E_{VI\ NES}/\xi_{LI}$, are realized in the lower energy Regimes I and II. We conclude that, although in these Regimes there occurs strong TET from the LO to the VI NES as long as vibro-impacts last (i.e., there is more efficient energy dissipation per vibro-impact), the overall duration of vibro-impacts is small (due to the small level of overall energy), as reflected by the relatively small values of the corresponding overall TET efficiency rates $95/\xi_{95\%}$.

In an additional series of numerical simulations we computed the previous measures for simulations corresponding to excitations of VI IOs at varying energies and restitution coefficients, and the fixed viscous damping coefficient $\lambda = 0.005\lambda_{crit} = 0.01$. This study identified the regimes of efficient VI TET when both the energy of the excited VI IO and the coefficient of restitution of vibro-impacts are varied. The results are presented in Figures 7.38 and 7.39, from which we conclude that the most efficient TET takes place when highly-energetic VI IOs are excited (in Regimes III and IV of the FEP), and for smaller restitution coefficients, i.e., for highly inelastic vibro-impacts. This last result is not as obvious as it might seem from a first reading; indeed, although it is clear that the average rate $E_{VI\ NES}/\xi_{LI}$ is favored when the restitution coefficient increases (as this results in increased dissipated energy per vibro-impact), this does not necessarily imply that the overall TET efficiency as measured by the average rate $95/\xi_{95\%}$ is also favored (for example, refer to the average rates depicted in the plot of Figure 7.37b).

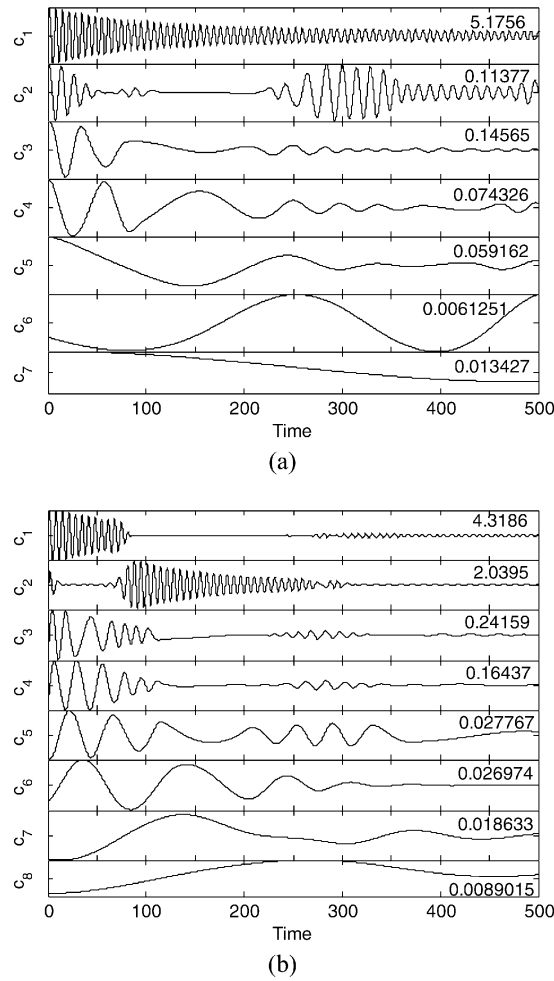


Fig. 7.36 Results of EMD analysis of the damped transition of Figure 7.28: (a) IMFs of the VI NES response (maximum amplitudes indicated); (b) IMFs of the LO response.

In conclusion, we showed that a SDOF primary LO with an attached VI NES possesses very complicated dynamics. In the absence of energy dissipation, vibro-impacts give rise to a variety of periodic (and quasi-periodic) motions, which when represented in the FEP yield a quite complex topology of periodic and quasi-periodic orbits. In the limit of zero clearance the entire complex VI FEP degenerates to just two linear (in- and out-of-phase) modes. By superimposing WT spectra of weakly damped responses to the Hamiltonian FEP we were able to study complicated transitions, and deduce the different mechanisms for passive TET from the LO to the VI NES. As in the case of smooth stiffness nonlinearity (the ‘smooth’ NES), both fundamental and subharmonic TET can be realized by the VI NES. The most

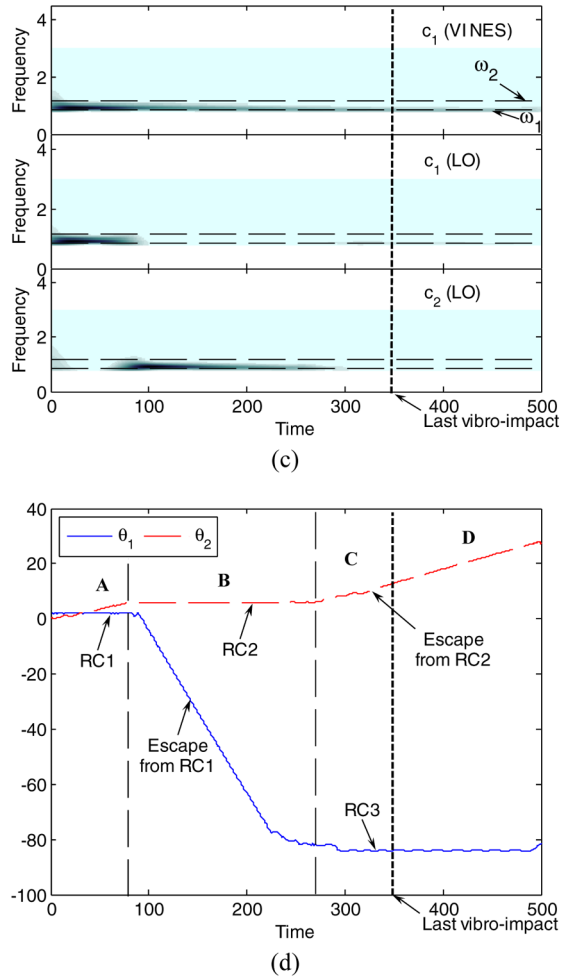
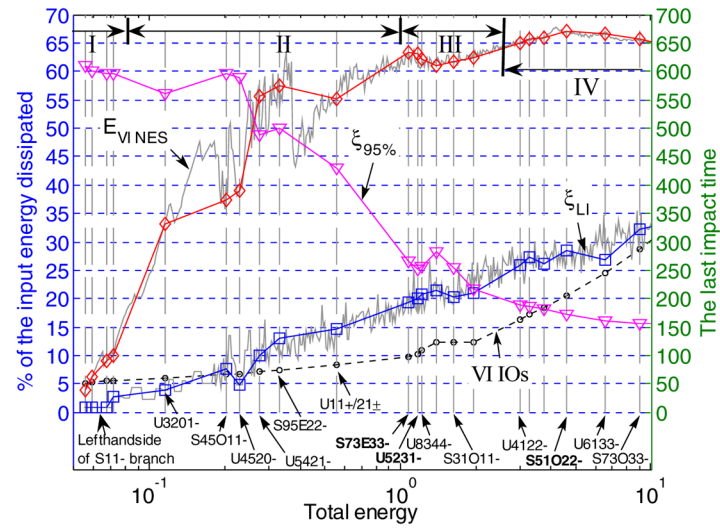
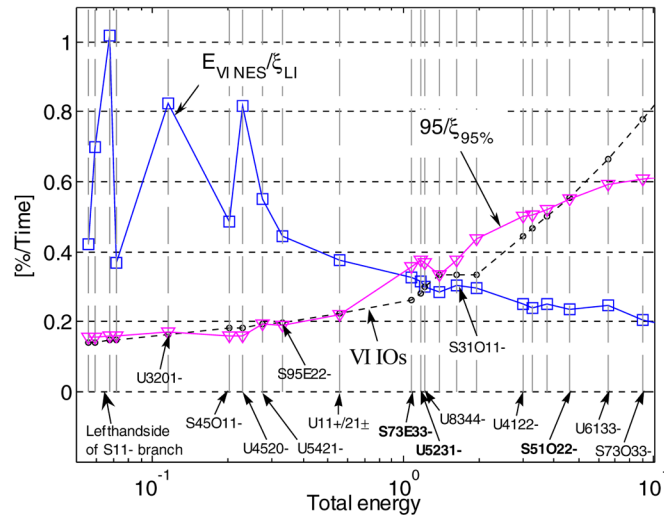


Fig. 7.36 Results of EMD analysis of the damped transition of Figure 7.28: (c) WT spectra of the dominant IMFs; (d) evolutions of the phase differences θ_1 and θ_2 indicating the occurrence of TRCs in the dynamics.

efficient mechanism for TET, however, is through the excitation of highly-energetic VI IOs, in similarity to the case of smooth nonlinearity. In contrast to NESs with smooth essential nonlinearities, however, VI NESs are capable of passively absorbing and locally dissipating significant portions of the energy of the primary systems to which they are attached, at sufficiently fast time scales; this renders them especially suitable for applications where rapid energy dissipation is required, such as, passive seismic mitigation, where shock elimination in the early, highly energetic regime of the structural response is a critical requirement. The application of



(a)



(b)

Fig. 7.37 Study of efficiency of TET in the VI system for excitation of VI IOs: (a) measures ξ_{LI} , $\xi_{95\%}$ and $E_{VI NES}$ as functions of total energy; (b) average rates $E_{VI NES}/\xi_{LI}$ and $95/\xi_{95\%}$ as functions of total energy.

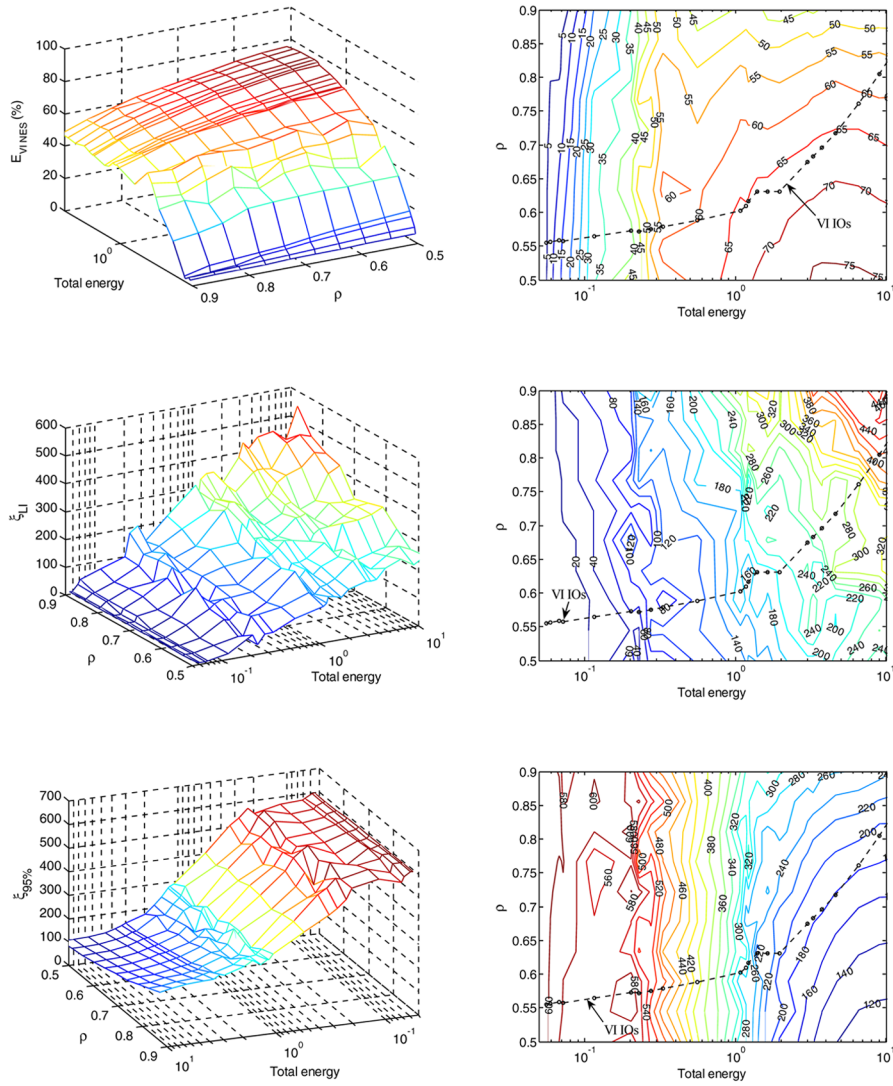


Fig. 7.38 Efficiency of TET in the VI system for excitation of VI IOs: left column, average rates $E_{VI\ NES}$, ξ_{LI} and $\xi_{95\%}$ as functions of total energy and restitution coefficient for $\lambda = 0.01$; right column, corresponding projections in the total energy-restitution coefficient plane.

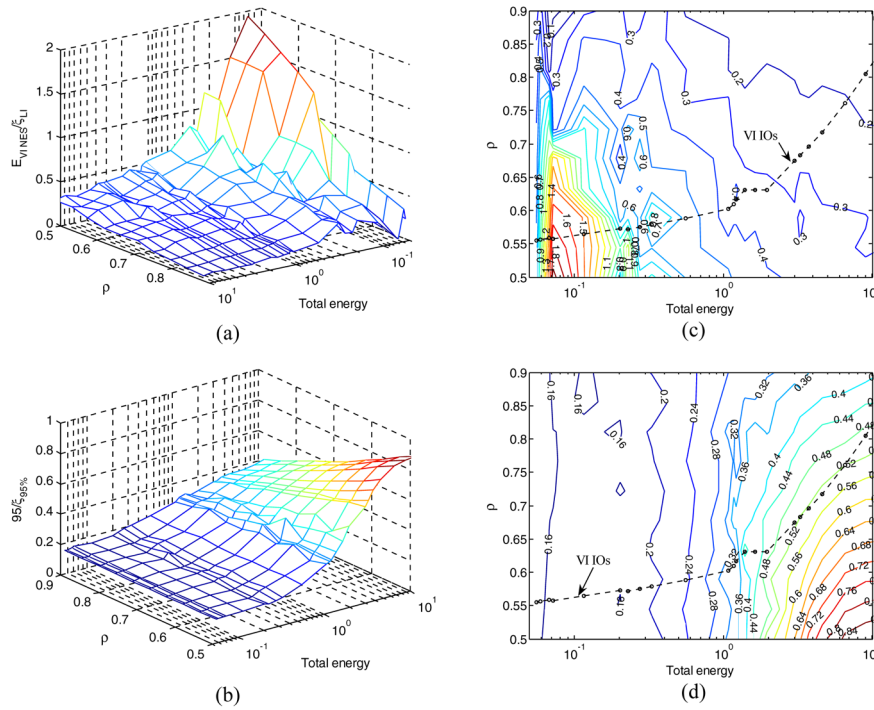


Fig. 7.39 Efficiency of TET in the VI system for excitation of VI IOs: left column, average rates $E_{VI\ NES}/\xi_{LI}$ and $95/\xi_{95\%}$ as functions of total energy and restitution coefficient for $\lambda = 0.01$; right column, corresponding projections in the total energy–restitution coefficient plane.

combinations of NESs with smooth and non-smooth stiffness characteristics to the problem of seismic mitigation will be examined in detail in Chapter 10.

References

*ReferencesReferencesReferences

Awjrejcwicz, J., Lamarque, C.-H., *Bifurcation and Chaos in Non-Smooth Mechanical Systems*, World Scientific, Singapore, 2003.

Azeez, M.F.A., Vakakis, A.F., Proper orthogonal decomposition (POD) of a class of vibro-impact oscillations, *J. Sound Vib.* **240**(5), 859–889, 2001.

Azeez, M.F.A., Vakakis, A.F., Manevitch, L.I., Exact solutions of the problem of the vibro-impact oscillations of a discrete system with two degrees-of-freedom, *J. Appl. Math. Mech. (PMM)* **63**(4), 527–530, 1999.

Babitsky, V.I., *Theory of Vibro-Impact Systems*, Springer Verlag, Berlin/New York, 1998.

Babitsky, V.I., Krupenin, V.L., *Vibration of Strongly Nonlinear Discontinuous Systems*, Springer Verlag, Berlin/New York, 2001.

Blazejczyk-Okolewska, B., Analysis of an impact damper of vibration, *Chaos Solit. Fract.* **12**, 1983–1988, 2001.

- Brogliato, B., *Non-Smooth Mechanics*, Springer Verlag, Berlin/New York, 1999.
- Czolczynski, K., Kapitaniak, T., On the existence of a stable periodic solution of two impacting oscillators with damping, *Int. J. Bif. Chaos* **14**(11), 3931–3947, 2004.
- Dupac, M., Marghitu, D.B., Nonlinear dynamics of a flexible mechanism with impact, *J. Sound Vib.* **289**, 952–966, 2006.
- Emaci, E., Nayfeh, T.A., Vakakis, A.F., Numerical and experimental study of nonlinear localization in a flexible structure with vibro-impacts, *ZAMM* **77**(7), 527–541, 1997.
- Filippov, A.F., *Differential Equations with Discontinuous Righthand Sides*, Kluwer Academic Publishers, 1988.
- Gendelman, O.V., Modeling of inelastic impacts with the help of smooth functions, *Chaos Solit. Fract.* **28**, 522–526, 2006.
- Georgiades, F., *Nonlinear Localization and Targeted Energy Transfer Phenomena in Vibrating Systems with Smooth and Non-Smooth Stiffness Nonlinearities*, PhD Thesis, National Technical University of Athens, Athens, Greece, 2006.
- Georgiades, F., Vakakis, A.F., McFarland, D.M., Bergman, L.A., Shock isolation through passive energy pumping caused by non-smooth nonlinearities, *Int. J. Bif. Chaos* (Special Issue on ‘Non-Smooth Dynamical Systems: Recent Trends and Perspectives’) **15**(6), 1–13, 2005.
- Glocker, C., *Set-valued Force Laws*, Springer Verlag, New York/Berlin, 2001.
- Gorelyshev, I.V., Neishtadt, A.I., On the adiabatic perturbation theory for systems with impacts, *J. Appl. Math. Mech. (PMM)* **70**, 4–17, 2006.
- Halse, C.K., Wilson, R.E., di Bernardo, M., Homer, M.E., Coexisting solutions and bifurcations in mechanical oscillators with backlash, *J. Sound Vib.* **305**, 854–885, 2007.
- Hu, B., Schiehlen, W., Multi-time scale simulation for impacting systems: From wave propagation to rigid-body motion, *Arch. Appl. Mech.* **72**, 885–898, 2003.
- Ivanov, A.P., Analytical methods in the theory of vibro-impact systems, *J. Appl. Meth. Mech. (PMM)* **57**(2), 5–21, 1993.
- Ivanov, A.P., Singularities in the dynamics of systems with non-ideal constraints, *J. Appl. Math. Mech. (PMM)* **67**(2), 185–192, 2003.
- Ivanov, A.P., The properties of solutions of the fundamental problem of dynamics in systems with non-ideal constraints, *J. Appl. Math. Mech. (PMM)* **69**, 338–350, 2004.
- Karayannis, I., Vakakis, A.F., Georgiades, F., Vibro-impact attachments as shock absorbers, *Proc. Inst. Mech. Eng. C: J. Mech. Eng. Sci.* (Special Issue on ‘Vibro-Impact Systems’, V. Babitsky Ed.), 2008 (in press).
- Kerschen, G., Vakakis, A.F., Lee, Y.S., McFarland, D.M., Kowtko, J., Bergman, L.A., Energy transfers in a system of two coupled oscillators with essential nonlinearity: 1:1 resonance manifold and transient bridging orbits, *Nonl. Dyn.* **42**(3), 283–303, 2005.
- Kerschen, G., Lee, Y.S., Vakakis, A.F., McFarland, D.M., Bergman, L.A., Irreversible passive energy transfer in coupled oscillators with essential nonlinearity, *SIAM J. Appl. Math.* **66**(2), 648–679, 2006.
- Kerschen, G., Gendelman, O., Vakakis, A.F., Bergman, L.A., McFarland, D.M., Impulsive periodic and quasi-periodic orbits of coupled oscillators with essential stiffness nonlinearity, *Comm. Nonlinear Sc. Num. Sim.*, 2008a (in press).
- Kerschen, G., Vakakis, A.F., Lee, Y.S., McFarland, D.M., Bergman, L.A., Toward a fundamental understanding of the Hilbert–Huang Transform in nonlinear structural dynamics, *J. Vib. Control* **14**, 77–105, 2008b.
- Kryzhevich, S.G., Pliss, V.A., Chaotic modes of oscillation of a vibro-impact system, *J. Appl. Math. Mech. (PMM)* **69**, 13–26, 2005.
- Lancioni, G., Lenci, S., Forced nonlinear oscillations of a semi-infinite beam resting on a unilateral elastic soil: Analytical and numerical solutions, *J. Comp. Nonlinear Dyn.* **2**, 155, 2007.
- Lee, Y.S., Kerschen, G., Vakakis, A.F., Panagopoulos, P.N., Bergman, L.A., McFarland, D.M., Complicated dynamics of a linear oscillator with an essentially nonlinear local attachment, *Physica D* **204**, 41–69, 2005.
- Lee, Y.S., Nucera, F., Vakakis, A.F., L.A. Bergman, D.M. McFarland, Periodic orbits and damped transitions of vibro-impact dynamics, *Physica D*, 2008 (submitted).

- Leine, R.I., Bifurcations of equilibria in non-smooth continuous systems, *Physica D* **223**, 121–137, 2006.
- Leine, R.I., Nijmeijer, H., *Dynamics and Bifurcations in Non-Smooth Mechanical Systems*, Springer-Verlag, Berlin/New York, 2004.
- Leine, R.I., Van Campen, D.H., Van de Vrande, B.L., Bifurcations in nonlinear discontinuous systems, *Nonl. Dyn.* **23**, 105–164, 2000.
- Li, K., Darby, A.P., Experiments on the effect of an impact damper on a MDOF system, *J. Vib. Control* **12**(5), 445–464, 2006.
- Lin, W., Ni Q., Huang Y., Bifurcations and chaos in a forced cantilever system with impacts, *J. Sound Vib.* **296**, 1068–1078, 2006.
- Luo, G.W., Zhang, Y.L., Chu, Y.D., Zhang, J.G., Co-dimension-two bifurcations of fixed points in a class of vibratory systems with symmetrical rigid stops, *Nonl. Analysis* **8**, 1272–1292, 2007.
- Manevitch, L.I., Mikhlin, Yu.V., Pilipchuk, V.N., *The Method of Normal Modes for Essentially Nonlinear Systems*, Nauka, Moscow, 1989 [in Russian].
- Masri, S.F., Ibrahim, A.M., Response of the impact damper to nonstationary random excitation, *J. Acoust. Soc. Am.* **53**(1), 200–211, 1973.
- Masri, S.F., Caughey, T.K., On the stability of the impact damper, *J. Appl. Mech.* **33**(3), 586–592, 1966.
- Meimukhlin, D., Gendelman, O.V., Response regimes of integrable damped strongly nonlinear oscillator under impact periodic forcing, *Chaos Solit. Fract.* **32**(2), 405–414, 2007.
- Mikhlin, Yu.V., Vakakis, A.V., Salenger, G., Direct and inverse problems encountered in vibro-impact oscillations of a discrete system, *J. Sound Vib.* **216**(2), 227–250, 1998.
- Murphy, K.D., Morrison, T.M., Grazing instabilities and post-bifurcation behavior in an impacting string, *J. Acoust. Soc. Am.* **111**(2), 884–892, 2002.
- Namachchivaya, S., Park, J.H., Stochastic dynamics of impact oscillators, *J. Appl. Mech.* **72**, 862–870, 2005.
- Nayeri, R.D., Masri, S.F., Caffrey, J.P., Studies of the performance of multi-unit impact dampers under stochastic excitation, *J. Vib. Acoust.* **129**, 239–251, 2007.
- Nucera, F., Vakakis, A.F., McFarland, D.M., Bergman, L.A., Kerschen G., Targeted energy transfers in vibro-impact oscillators for seismic mitigation, *Nonl. Dyn.* (Special Issue on ‘Discontinuous Dynamical Systems’) **50**, 651–677, 2007.
- Nucera, F., McFarland, D.M., Bergman, L.A., Vakakis, A.F., Application of broadband nonlinear targeted energy transfers for seismic mitigation of a shear frame: Part I. Computational results, *J. Sound Vib.* 2008a (in press).
- Nucera, F., Lo Iacono, F., McFarland, D.M., Bergman, L.A., Vakakis, A.F., Application of broadband nonlinear targeted energy transfers for seismic mitigation of a shear frame: Part II. Experimental results, *J. Sound Vib.* 2008b, (in press).
- Persson, B.N.J., *Sliding Friction*, Springer Verlag, Berlin/New York, 1998.
- Peterka, F., Blazejczyk-Okolewska, B., Some aspects of the dynamical behavior of the impact damper, *J. Vib. Control* **11**, 459–479, 2005.
- Pfeiffer, F., Glocker, C., Contacts in multibody systems, *J. Appl. Math. Mech. (PMM)* **64**(5), 773–782, 2000.
- Pilipchuk, V.N., The calculation of strongly nonlinear systems close to vibration-impact systems, *Prikl. Mat. Mech. (PMM)* **49**, 572–578, 1985.
- Pilipchuk, V.N., A transformation for vibrating systems based on a non-smooth periodic pair of functions, *Dokl. AN Ukr. SSR Ser. A* **4**, 37–40, 1988 [in Russian].
- Pilipchuk, V.N., Analytic study of vibrating systems with strong nonlinearities by employing sawtooth time transformations, *J. Sound Vib.* **192**(1), 43–64, 1996.
- Pilipchuk, V.N., Impact modes in discrete vibrating systems with rigid barriers, *Int. J. Nonlinear Mech.* **36**, 999–1012, 2001.
- Pilipchuk, V.N., Some remarks on non-smooth transformations of space and time for vibrating systems with rigid barriers, *J. Appl. Math. Mech. (PMM)* **66**, 31–37, 2002.
- Pilipchuk, V.N., Vakakis, A.F., Azeez, M.A.F., Study of a class of subharmonic motions using a non-smooth temporal transformation, *Physica D* **100**, 145–164, 1997.

- Pilipchuk, V.N., Vakakis, A.F., Azeez, M.A.F., Sensitive dependence on initial conditions of strongly nonlinear periodic orbits of the forced pendulum, *Nonl. Dyn.* **16**, 223–237, 1998.
- Pinnington, R.J., Energy dissipation prediction in a line of colliding oscillators, *J. Sound Vib.* **268**, 361–384, 2003.
- Quinn, D.D., The dynamics of two parametrically excited pendula with impacts, *Int. J. Bif. Chaos* **15**(6), 1975–1988, 2005.
- Salapaka, S., Dahleh, M., Mezic, I., On the dynamics of a harmonic oscillator undergoing impacts with a vibrating platform, *Nonl. Dyn.* **24**, 333–358, 2001.
- Salenger, G.D., Vakakis, A.F., Localized and periodic waves with discreteness effects, *Mech. Res. Comm.* **25**(1), 97–104, 1998.
- Sampaio, R., Soize, C., On measures of nonlinearity effects for uncertain dynamical systems – Application to a vibro-impact system, *J. Sound Vib.* **303**, 659–674, 2007.
- Shaw, S.W., The dynamics of a harmonically excited system having rigid amplitude constraints. I: Subharmonic motions and local bifurcations. II: Chaotic motions and global bifurcations, *J. Appl. Mech.* **52**(2), 453–464, 1985.
- Shaw, S.W., Holmes, P., Periodically forced linear oscillator with impacts – Chaos and long term motions, *Phys. Rev. Lett.* **51**, 623–626, 1982.
- Shaw, S.W., Holmes, P., A periodically forced piecewise linear oscillator, *J. Sound Vib.* **90**(1), 129–155, 1983.
- Shaw, J., Shaw, S.W., The onset of chaos in a two-DOF impacting system, *J. Appl. Mech.* **56**, 168–174, 1989.
- Shaw, S.W., Pierre, C., The dynamic response of tuned impact absorbers for rotating flexible structures, *J. Comp. Nonl. Dyn.* **1**, 13–24, 2006.
- Shaw, S.W., Rand, R.H., The transition to chaos in a simple mechanical system, *Int. J. Nonl. Mech.* **24**, 41–56, 1989.
- Sun, J.Q., Luo, A., *Bifurcation and Chaos in Complex Systems*, Elsevier, 2006.
- Thomsen, J.J., Fidler, A., Near elastic vibro-impact analysis by discontinuous transformations and averaging, *J. Sound Vib.*, DOI: 10.1016/j.jsv.2007.09.007, 2007
- Thota, P., Dankowicz, H., Continuous and discontinuous grazing bifurcations in impacting oscillators, *Physica D* **214**, 187–197, 2006.
- Thota, P., Zhao, X., Dankowicz, H., Co-dimension-two grazing bifurcations in single-degree-of-freedom impact oscillators, *J. Comp. Nonl. Dyn.* **1**, 328–335, 2006.
- Vakakis, A.F., Manevitch, L.I., Mikhlin, Y.V., Pilipchuk, V.N., Zevin, A.A., *Normal Modes and Localization in Nonlinear Systems*, Wiley Interscience, New York, 1996.
- Valente X.A.C.N., McClamroch, N.H., Mezic I., Hybrid dynamics of two coupled oscillators that can impact a fixed stop, *Int. J. Nonl. Mech.* **38**, 677–689, 2003.
- Vedenova, Ye., Manevitch, L.I., Periodic and localized waves in vibro-impact systems of regular configuration, *Mashinovedenie* **4**, 21–32, 1981 [in Russian].
- Vedenova, Ye., Manevitch, L.I., Pilipchuk, V.N., The normal vibrations of a string with concentrated masses on nonlinearly elastic supports, *J. Appl. Math. Mech. (PMM)* **49**(2), 203–211, 1985.
- Veprik, A.M., Babitsky, V.I., Nonlinear correction of vibration protection system containing tuned dynamic absorber, *J. Sound Vib.* **239**(2), 335–356, 2001.
- Wagg, D.J., A note on coefficient of restitution models including the effects of impact induced vibration, *J. Sound Vib.* **300**, 1071–1078, 2007.
- Wen, G., Xie, J., Xu, D., Onset of degenerate Hopf bifurcation of a vibro-impact oscillator, *J. Appl. Mech.* **71**, 579–581, 2004.
- Wiercigroch, M., de Kraker, B., *Applied Nonlinear Dynamics and Chaos of Mechanical Systems with Discontinuities*, World Scientific, Singapore, 2000.
- Zhao, X., Dankowicz, H., Unfolding degenerate grazing dynamics in impact actuators, *Nonlinearity* **19**, 399–418, 2006.

Zhuravlev, V.F., A method of analyzing vibro-impact systems using special functions, *Izv. Akad. Nauk. SSSR, MTT* **2**, 30–34, 1976 [in Russian].

Zhuravlev, V.F., Investigation of some vibro-impact systems by the method of non-smooth transformations, *Izv. Akad. Nauk. SSSR, MTT* **6**, 24–28, 1977 [in Russian].

Chapter 8

Experimental Verification of Targeted Energy Transfer

Experimental verification of TET will be carried out in this chapter. Some preliminary experimental results concerning TET from a two-DOF linear primary system to an attached ungrounded SDOF NES (of Configuration II – see Section 3.1) were already presented in Section 3.5.1.3, where experimental verification of resonance capture cascades (RCCs) was also performed. In this chapter we focus on some basic experimental tests that confirm in a systematic way certain of the previous theoretical predictions related to TET from linear primary systems to grounded or ungrounded NESs (i.e., NES Configurations I and II – see Sections 2.6 and 3.1). All experimental results were carried out in the Linear and Nonlinear Dynamics and Vibrations Laboratory of the University of Illinois, Urbana–Champaign. Further experimental studies of TET will be presented in Chapter 9, in our study of aeroelastic instability suppression of in-flow wings through the use of SDOF NESs with essential cubic nonlinearities; and in Chapter 10, in our study of TET-based passive seismic mitigation designs for seismically forced structures with essentially nonlinear and/or vibro-impact NESs.

8.1 TET to Ungrounded SDOF NES (Configuration II)

The first experimental study of TET is carried out with the fixture depicted in Figure 2.27, consisting of a SDOF linear oscillator (LO) with an attached ungrounded NES of Configuration II (according to the notation introduced in Section 3.1 – refer to the NES configuration depicted in Figure 3.2). The experimental results of this work are fully discussed in McFarland et al. (2005b), and here only a summary of the main findings is provided.

Assuming that the LO is forced by an external excitation, the experimental fixture is modeled by the following two-DOF system:

$$M\ddot{x} + \varepsilon\lambda_1\dot{x} + \varepsilon\lambda_2(\dot{x} - \dot{v}) + kx + C(x - v)^3 = p(t)$$

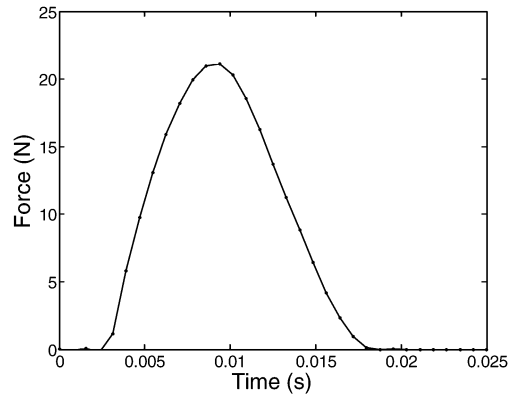


Fig. 8.1 Experimental impulsive force.

$$\varepsilon \ddot{v} + \varepsilon \lambda_2 (\dot{v} - \dot{x}) + C(v - x)^3 = 0 \quad (8.1)$$

From Section 2.6 we recall that the essential cubic nonlinearity of the NES is realized by means of wires with nearly no pretension that are connected to the LO using clamps. In the described experiment, the wire span was adjusted to 12 in, and further details about the construction of the essential nonlinearity can be found in McFarland et al. (2005a, b).

A long-stroke shaker provided a controlled (and repeatable) short impulse to the LO; a representative input (broadband) force is depicted in Figure 8.1. The response of both oscillators was then measured using accelerometers. Estimates of the corresponding velocity and displacement time series were obtained by numerically integrating the measured acceleration time series. The resulting signals were then high-pass filtered to remove the spurious components introduced by the numerical integration procedure.

8.1.1 System Identification

The first stage of the experimental study concerns the system identification of the various parameters of the model. This is needed in order to perform comparisons of the experimental results with theoretical predictions (using discrete models), and thus identify the experimentally measured nonlinear dynamics. The goal of system identification is to exploit input and output measurements performed on the structure using vibration sensing devices in order to estimate all the parameters governing the equations of motion. Prior to system identification, the LO and the NES were weighed as $M = 1.266$ kg and $\varepsilon = 0.140$ kg, respectively, which implies a mass ratio $\varepsilon/M = 0.11$.

Table 8.1 Parameters of model (8.1) identified through experimental modal analysis, and the restoring force surface method.

Parameter	Estimated Value
M	1.266 kg
ε	0.140 kg
k	1143 N/m
$\varepsilon\lambda_1$	0.155 Ns/m
$\varepsilon\lambda_2$	0.4 Ns/m
C	1.85×10^6 N/m ^{2.8}
α	2.8

System identification was carried out in two separate steps. First, the LO was disconnected from the NES, and modal analysis was performed on the disconnected LO employing the stochastic subspace identification method (Van Overschee and De Moor, 1996). This yielded natural frequency and the critical viscous damping ratio estimates equaling 4.78 Hz and 0.2%, respectively. Because the mass of the LO was known, the stiffness and the damping parameters were easily deduced from this modal analysis, and their values are listed in Table 8.1.

In the second step of the system identification, the LO was clamped, and an impulsive force was applied to the NES using an instrumented modal hammer. Both the NES acceleration and applied force were measured, and the restoring force surface method (Masri and Caughey, 1979) was employed to estimate the nonlinearity C and the damping coefficient $\varepsilon\lambda_2$ from these measurements. In essence, Newton's second law is applied to estimate the nonlinear stiffness force by the following relation:

$$f_{\text{NL}}(v, \dot{v}, x, \dot{x}) = p - \varepsilon\ddot{v} \quad (8.2)$$

where $f_{\text{NL}}(v, \dot{v}, x, \dot{x})$ is the restoring force and p the external force [for simplicity, the temporal dependences are omitted from (8.2)]. Hence, the time history of the restoring force can be estimated directly from the measurement of the acceleration and the external force and from the knowledge of the mass ε . This is illustrated for the 21 N force level in Figure 8.2a. The representation of the restoring force in terms of the relative displacement ($v-x$) is depicted in Figure 8.2b, and demonstrates that indeed the linear component of the nonlinear stiffness is negligible; in other words, the experimental wire assembly behaved as an essential nonlinearity (as predicted).

The model,

$$f_{\text{NL}}(v, \dot{v}, x, \dot{x}) = \varepsilon\lambda_2(\dot{v} - \dot{x}) + C(v - x)^3 \quad (8.3)$$

could then be fitted to the measured estimate of the restoring force, and least-squares parameter estimation could be used to obtain the values of coefficients C and $\varepsilon\lambda_2$. For greater flexibility, the functional form of the nonlinear stiffness was replaced by the more general expression,

$$f_{\text{NL}}(v, \dot{v}, x, \dot{x}) = \varepsilon\lambda_2(\dot{v} - \dot{x}) + C|v - x|^\alpha \text{sign}(v - x) \quad (8.4)$$

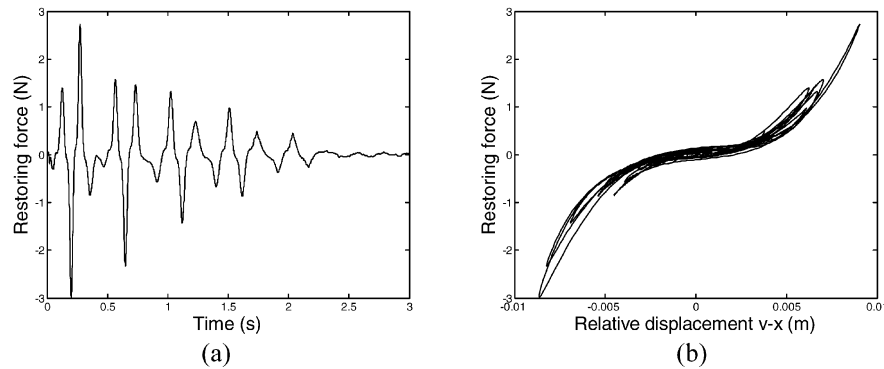


Fig. 8.2 Measured restoring force represented as a function of (a) time and (b) relative displacement ($v - x$).

The three unknown parameters in (8.4), namely the nonlinear coefficient, the exponent of the nonlinearity and the dashpot constant, were estimated by following the same procedure as in Kerschen et al. (2001); i.e., one seeks the minimum of the normalized mean-square error between the measured and predicted restoring forces as a function of the exponent of the nonlinearity. The resulting parameters are listed in Table 8.1. The best results were obtained using an exponent equal to 2.8, which is not far from the theoretical value of 3.

8.1.2 Experimental Measurements

Two series of experimental tests were performed in both of which the LO was impulsively loaded. In the first series of tests, the damping in the NES was kept relatively weak in order to highlight the different mechanisms for targeted energy transfer (TET). Additional tests were performed to investigate whether TET could still be realized when the viscous damping of the NES was increased.

8.1.2.1 Weak Damping Case

In the weak damping case, several force levels ranging from 21–55 N were considered, but for conciseness, only the results for the lowest and highest force levels are displayed in Figures 8.3 and 8.4. At the 21 N forcing level, the acceleration and displacement of the NES are higher than those of the LO, which indicates targeted transfer of vibration energy to the NES. The percentage of instantaneous total energy carried by the NES depicted in Figure 8.3c illustrates that strong energy exchanges between the LO and the NES take place, and that this channeling of energy to the NES is not irreversible. Indeed, after 0.23 s, as much as 88% of the

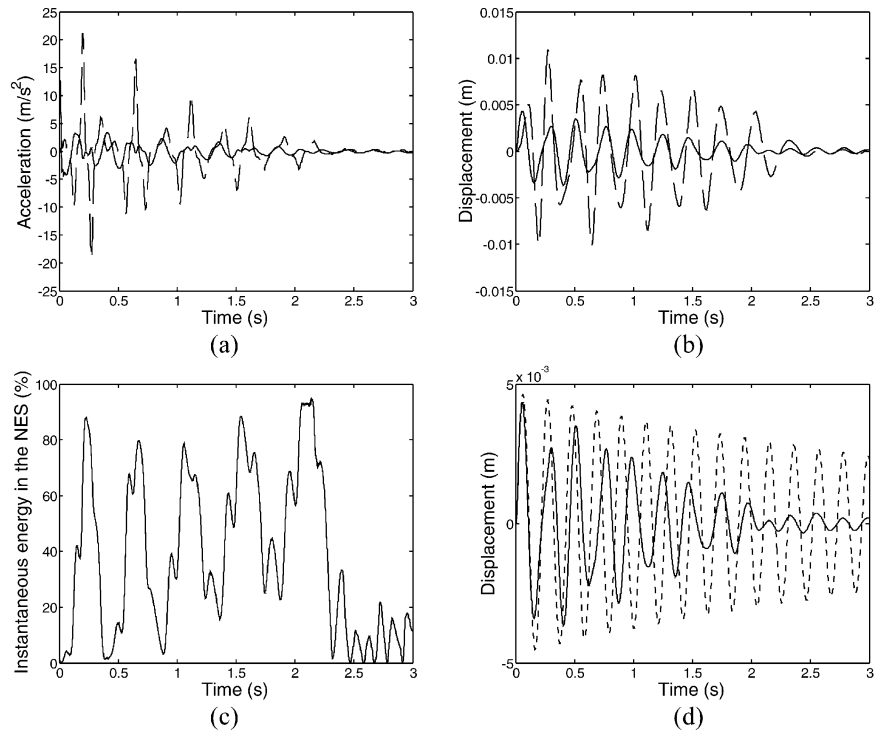


Fig. 8.3 Experimental results for low damping (21 N force level): (a) measured accelerations (solid line: LO; dashed line: NES); (b) measured displacements (solid line: LO; dashed line: NES); (c) percentage of instantaneous total energy in the NES, and (d) LO displacement (solid line: with NES attached; dashed line: with only grounded dashpot).

total instantaneous energy is present in the NES, but this level drops down to 1.5% immediately thereafter. Hence, in this case, energy rapidly flows back and forth between the two oscillators, which is characteristic of a nonlinear beat phenomenon. Another indication that nonlinear beating occurs is that the envelope of the NES response undergoes large modulations in this case.

At the 55 N forcing level, the nonlinear beat phenomenon still dominates the early regime of the motion. A less vigorous but faster energy exchange is now observed as 63% of the total energy is transferred to the NES after 0.12 s. These quantities also hold for the intermediate force levels listed in Table 8.2. These observations are in close agreement with the numerical studies in Section 3.2; indeed, in this case due to the excitation of IOs there is smaller transfer of energy from the LO to the NES, but in a faster fashion as the force level increases.

The main qualitative difference from the case of the lowest force level is that there exists now a second regime of motion. Indeed, after approximately $t = 2.5$ s, the motion is captured in the domain of attraction of the 1:1 resonant manifold, as

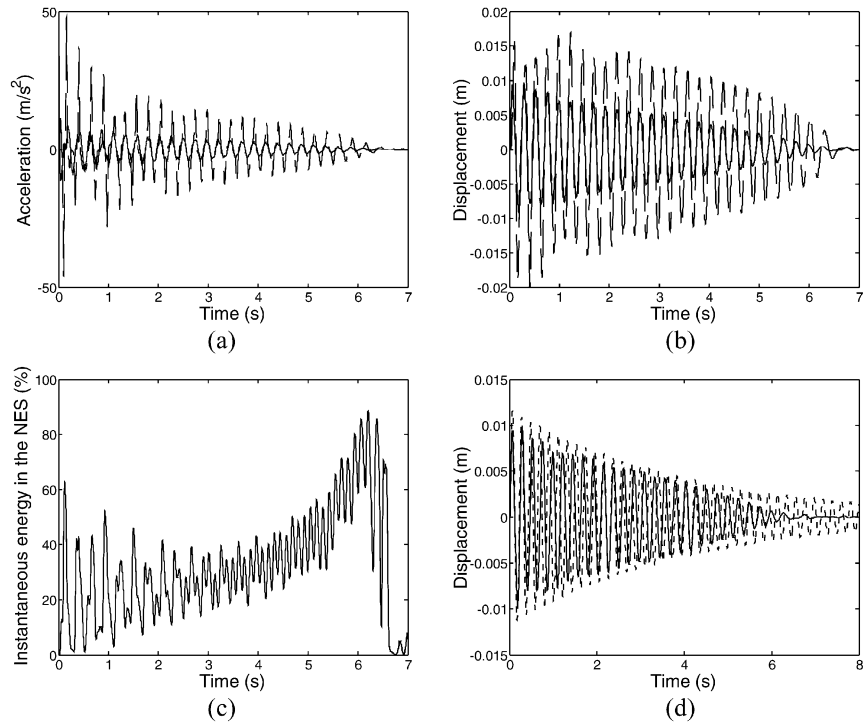


Fig. 8.4 Experimental results for low damping (55 N force level): (a) measured accelerations (solid line: LO; dashed line: NES); (b) measured displacements (solid line: LO; dashed line: NES); (c) percentage of instantaneous total energy in the NES, and (d) LO displacement (solid line: with NES attached; dashed line: with only grounded dashpot).

Table 8.2 Nonlinear beating phenomenon: energy transferred from the LO to the NES, and corresponding transfer time.

Excitation level (N)	Energy transferred to the NES (%)	Transfer time (s)
21	88	0.23
29	72	0.20
34	67	0.19
45	64	0.13
55	63	0.12

clearly evidenced in Figure 8.5c. This graph also demonstrates the irreversibility of the energy transfer in this case, at least until escape from resonance capture occurs around $t = 6.2$ s. Another manifestation of 1:1 resonance capture is that the envelopes of the displacement and acceleration time series decrease almost monotonically during this regime, and no envelope modulation is observed. The system is capable of sustaining the resonance capture during a significant interval of the mo-

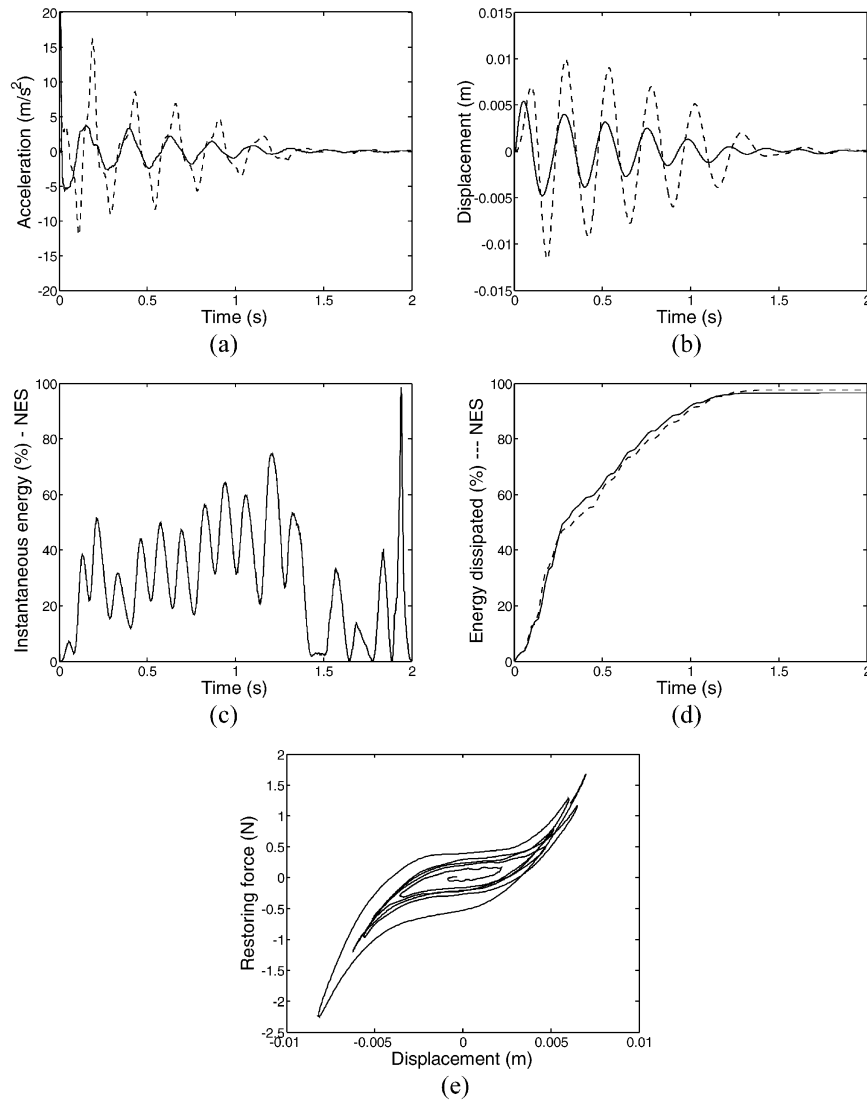


Fig. 8.5 Experimental results for high damping (31 N force level): (a) measured accelerations (solid line: LO; dashed line: NES); (b) measured displacements (solid line: LO; dashed line: NES); (c) percentage of instantaneous total energy in the NES; (d) energy dissipated in the NES (solid line: measurements; dashed line: simulations), and (e) restoring coupling force.

tion (i.e., in the interval $2.5 < t < 6.2$ s). Hence, experimental confirmation of TET from the LO to the NES is established in this case.

A qualitative way to assess the efficiency of energy dissipation by the NES is to compare the responses of the LO in the following two cases: (a) when the NES

is attached to the LO (which corresponds to the presented results); and (b) when the NES is disconnected and replaced by a dashpot installed between the LO and ground. This later configuration corresponds to a SDOF LO with just added damping. Case (b) was not realized in the laboratory, but the system dynamics was studied using numerical simulation. Figures 8.3d and 8.4d compare the corresponding displacements of the LO for the aforementioned two different system configurations. It can be observed that the NES performs much better than the grounded dashpot for the 21 N forcing level, but this is less obvious for the 55 N forcing level. This might mean that for weak damping (when the nonlinear beat phenomenon is capable of transferring a significant portion of the total energy to the NES), nonlinear beating might be a more useful mechanism for energy dissipation compared to resonance capture leading to irreversible energy transfer.

8.1.2.2 Strong Damping Case

We now consider the experimental response of a system with strong damping. Several force levels in the range 31–75 N are considered in this case, but only the results for the 31 N level are presented herein. The damping constant λ_2 in the coupling element was identified as 1.48 Ns/m, which means that the damping element that couples the two oscillators (and is situated in parallel to the essential stiffness nonlinearity) can no longer be considered as being of order ε . The increase in damping is also reflected in the measured restoring coupling force depicted in Figure 8.5e.

The experimental system response shown in Figures 8.5a, b is almost entirely damped out after about 5 to 6 cycles of oscillation. The NES acceleration and displacement are still higher than the corresponding responses of the LO, which means that TET may also occur in the presence of stronger damping. The percentage of instantaneous total energy in the NES in Figure 8.5c never reaches values close to 100% as in the previous case, but we conjecture that this is due to the faster decay of the response due to strong damping; as soon as energy is transferred to the NES, it is almost immediately dissipated by the dashpot, and irreversible TET takes place. This is fully compatible with the theoretical results.

A quantitative measure of energy dissipation is available through the computation of the energy dissipation measure (EDM), i.e., of the energy dissipated in the NES normalized by the total input energy:

$$E_{\text{diss.NES, \%}}(t) = 100 \frac{\varepsilon \lambda_2 \int_0^t [\dot{v}(\tau) - \dot{x}(\tau)]^2 d\tau}{\int_0^t p(\tau) \dot{x}(\tau) d\tau} \quad (8.5)$$

Experimental and simulated estimates of the EDM are depicted in Figure 8.5d. This demonstrates that as much as 96% of the total input energy is dissipated by the NES, which indicates high TET efficiency by the NES. Moreover, there is satisfactory agreement between theoretical predictions and experimental measurements,

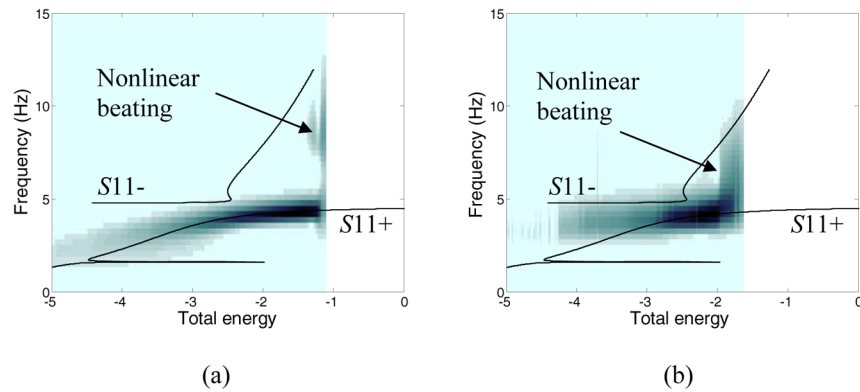


Fig. 8.6 Superposition of the WT spectrum of the relative displacement across the nonlinearity and the backbone of the frequency energy plot: (a) forcing amplitude 55 N, system with low damping; (b) forcing amplitude 31 N, system with high damping.

validating the mathematical analysis and the corresponding models developed in Chapter 3.

8.1.2.3 Post Processing Results and Additional Experiments

To study further the nonlinear mechanisms governing energy transfers in the experimental system, we applied the numerical wavelet transform (WT) to selected time series for systems with weak and strong damping. In Figure 8.6, we depict the Morlet WT spectra of the relative displacements $v(t) - x(t)$ of the systems with (a) weak damping and forcing amplitude 55 N (Figure 8.6a) and (b) strong damping and forcing amplitude 31 N (Figure 8.6b). Superimposed to the WT spectra are the backbone curves of the frequency energy plot (FEP) of the model (8.1), represented by solid line. We recall that the shading of the WT spectra denotes the relative amplitude of the dominant harmonic components of the corresponding damped motions, as computed through the WT.

Based on the experimental WT spectra depicted in Figure 8.6 we deduce that the dynamics of the system is indeed nonlinear. A strong indication of this fact is that the predominant frequency component of the NES varies with energy; moreover, there appear strong harmonic components during the initial nonlinear beating phenomena in these responses. Once these harmonic components disappear, fundamental TET due to 1:1 transient resonance capture is triggered, as the transient dynamics traces approximately the in-phase backbone branch $S11+$. Hence, the experimental results confirm the theoretical finding that the formation of initial nonlinear beats provides the ‘bridging dynamics’ for triggering fundamental (or subharmonic) TET in the two-DOF system (8.1).

Another remark regarding the experimental results concerns the fact that, in the weakly damped system (see Figure 8.6a) the predominant harmonic component of the NES traces the backbone branch for most of the duration of the time series. This is not so apparent in the heavily damped response of Figure 8.6b, and validates our theoretical finding that the weakly damped, transient dynamics can be interpreted and understood in terms of the topological structure of periodic orbits (NNMs) of the underlying Hamiltonian system in the FEP.

Additional measurements were performed for a system with stiffer stiffness nonlinearity by shortening the span of the wire from 12 in to 10 in and increasing the wire diameter from 0.010 in to 0.020 in; this yields a nonlinear coefficient of $C = 1.65 \times 10^7 \text{ N/m}^3$. Inspection of the accelerations and displacements shown in Figures 8.7a, b reveals that the NES is no longer vibrating symmetrically with respect to its equilibrium position, particularly in the time interval $1 < t < 3 \text{ s}$. Interestingly enough, as can be judged from the results depicted in Figures 8.7c, d, there is an almost pointwise agreement between the experimental accelerations and those predicted by the theoretical model (8.1).

A better understanding of this particular regime of the motion can be gained from a snapshot of the configuration space depicted in Figure 8.7e. Apparently, the transient dynamics is captured in the domain of attraction of a subharmonic tongue in the FEP, with the corresponding motion not being symmetric with respect to the origin of the configuration space. Indeed, it turns out that in this case the motion takes the form of a closed loop (Lissajous curve), which might mean that an unsymmetric U -branch is excited. However, due to the existence of a countable infinity of tongues, and due to the presence of damping, it is difficult to identify with certainty the specific subharmonic tongue that is excited in this particular experimental run. Nonetheless, this result provides further evidence of the complex dynamical behavior that this two-DOF system with essential nonlinearity can possess, in full agreement with the theoretical predictions of Chapter 3; moreover, it provides further experimental evidence of the intricate relationship between the Hamiltonian and weakly damped dynamics. Finally, Figure 8.7f illustrates that a nonlinear beating occurs during this particular regime, with the resulting energy exchanges being not so vigorous, since less than 40% of vibration energy gets transferred at any given time of the beating cycle from the LO to the NES.

8.2 TET to Grounded SDOF NES (Configuration I)

We now proceed to discuss a second series of experimental results regarding TET from a linear primary system to a grounded NES of Configuration I according to the notation introduced in Section 3.1 (with configuration depicted in Figure 3.1). Our exposition follows closely (McFarland et al., 2005a).

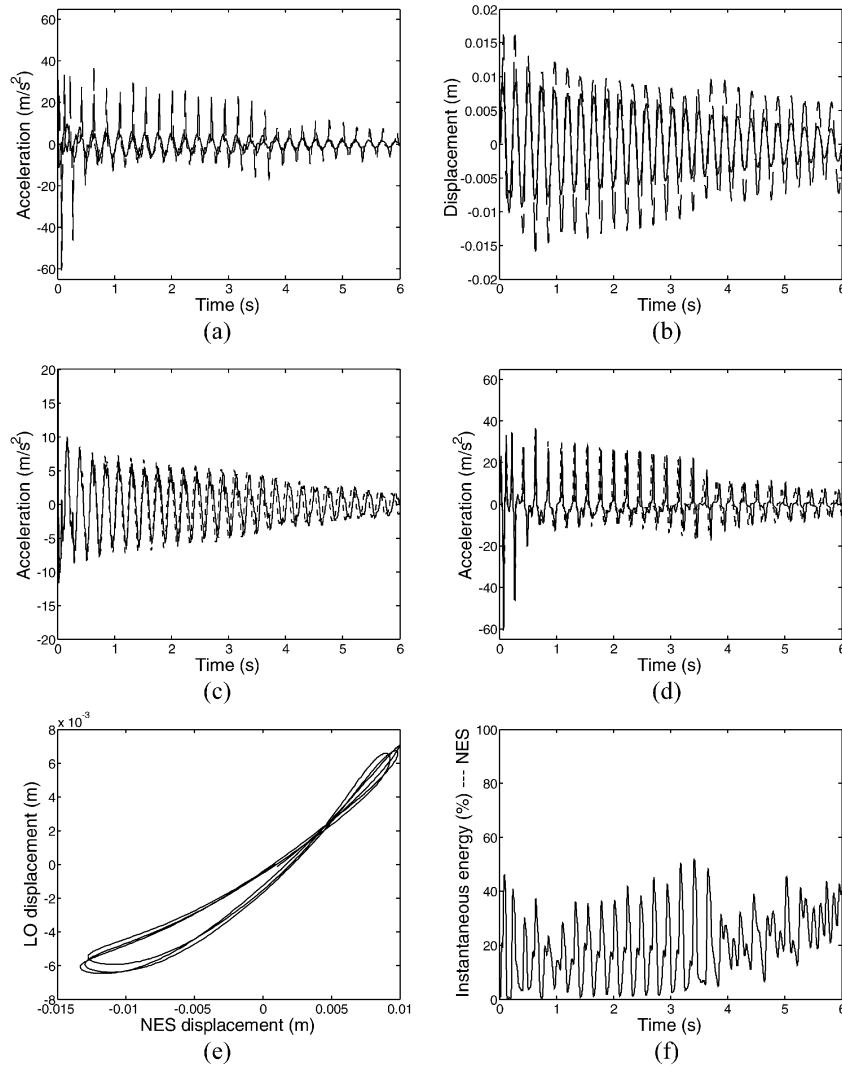


Fig. 8.7 Case of increased stiffness nonlinearity: (a) measured accelerations (solid line: LO; dashed line: NES); (b) measured displacements (solid line: LO; dashed line: NES); comparison between predicted (dashed line) and measured (solid line) accelerations: (c) LO; (d) NES; (e) motion in the configuration plane, and (f) percentage of instantaneous total energy contained in the NES.

8.2.1 Experimental Fixture

The experimental fixture employed for this study is depicted in Figure 2.26. It consists of two SDOF oscillators (the linear primary system and the NES) connected by means of a linear coupling stiffness. The left oscillator (the linear subsystem) is grounded by means of a linear spring, whereas the right one (the nonlinear energy sink – NES) is grounded by means of a nonlinear spring with essential cubic nonlinearity. To dissipate the transferred energy, a grounded viscous damper exists in parallel with the NES. Transient (shock) excitation of the linear primary system is provided by means of a rod that impacts elastically with the left mass. More details regarding the experimental fixture and the realization of the essential cubic stiffness nonlinearity by means of wires with no pretension can be found in Section 2.6.

The two-DOF system model of the experimental fixture is governed by the equations of motion

$$\begin{aligned} M\ddot{y} + Ky + \varepsilon\lambda\dot{y} + \varepsilon(y - v) &= F(t) \\ m\ddot{v} + \varepsilon c\dot{v} + Cv^3 - \varepsilon(y - v) &= 0 \end{aligned} \quad (8.6)$$

for zero initial conditions. Weak coupling between the linear primary system and the NES is assumed by requiring that $\varepsilon \ll K$. Assuming that $F(t)$ is an impulsive (broadband) excitation of finite duration, we aim to show experimentally that broadband energy initially imparted to the linear subsystem is passively transferred to the NES in an irreversible (on the average) way, where this energy is confined and dissipated without ‘spreading back’ to the linear primary system.

The eigenfrequency of the linear subsystem, and the viscous damping factors of both subsystems, were estimated by performing experimental modal analysis tests using an instrumented modal hammer manufactured by *PCB Piezotronics, Inc.* to provide the necessary excitation. Data analysis was performed using the *Diamond* modal analysis package developed at Los Alamos National Laboratory. The modal parameters of the linear primary system were estimated to be

$$M = 0.834 \text{ kg}, \quad K = 993 \text{ N/m}, \quad \varepsilon\lambda = 0.129 \text{ Ns/m}$$

corresponding to the eigenfrequency $\omega_0 = 35.63 \text{ rad/s}$, and the viscous damping ratio $\zeta = 2.3 \times 10^{-3}$; hence, the linear oscillator is lightly damped. The mass and damping parameters of the NES, and the linear coupling stiffness connecting the primary system and the NES, were estimated by performing experimental modal analysis of the linear SDOF oscillator which results when the coupling stiffness is grounded and the nonlinear spring is disconnected. The system parameters were estimated as

$$m = 0.393 \text{ kg}, \quad \varepsilon = 114 \text{ N/m}, \quad \varepsilon c = 0.454 \text{ Ns/m}$$

The stiffness characteristic of the nonlinear spring of the NES was identified by performing a series of static tests, wherein known displacements were imposed

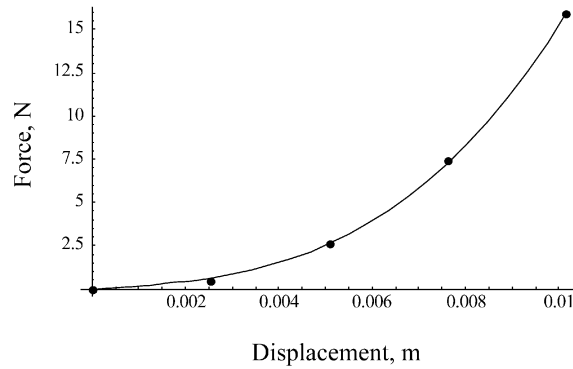


Fig. 8.8 Identified stiffness characteristic of the essentially nonlinear spring of the NES: • experimental measurement, — fitted cubic polynomial.

to the NES mass and the corresponding restoring forces created by the wire were measured. A cubic polynomial was then fitted to the experimental measurements, yielding the following nonlinear force-displacement relationship:

$$f(x) = 166x + 1.36 \times 10^7 x^3 \quad (8.7)$$

Hence, a small (undesirable) linear term is identified in the stiffness of the NES which, however, is negligible for the characteristic displacements of interest in our experiment. In Figure 8.8, the fitted model of the essential stiffness nonlinearity of the NES is compared to experimental measurements.

Experimental data collected included the input (broadband) force, the acceleration of each mass, and the force associated with the nonlinear stiffness. These signals were digitized using two Tektronix 2630 spectrum analyzers. One of these ran at a sampling rate which allowed it to store 8 s of time-history data, which was deemed adequate to capture all of the significant TET phenomena realized in the experimental fixture. The other analyzer acquired input force and the acceleration of the linear subsystem at a much higher rate, allowing the reconstruction of these short signals in adequate detail. The discrete signals thus acquired were first transferred to Matlab[®] for post-processing, including correcting biases and synchronization of the time data. All signals were shifted to start at time $t = 0$, and the processed time histories were imported to *Mathematica* for all further manipulations, during which the experimental signals were commonly interpolated by cubic spline approximations for simplicity.

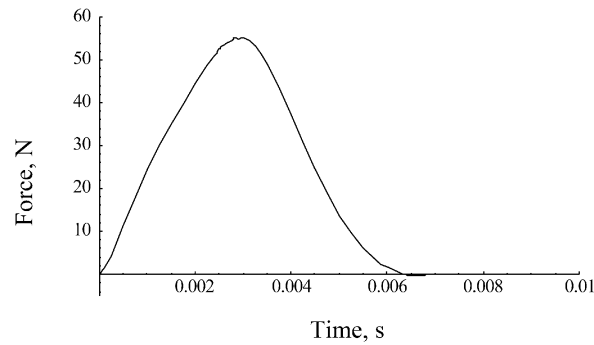


Fig. 8.9 Strong experimental impulsive force for inducing nonlinear TET in the experimental fixture.

8.2.2 Results and Discussion

Two series of experimental tests were performed. In the first series of tests, consisting of eight trials (labeled ep1 through ep8), the input force was strong enough to produce significant nonlinear effects, including TET. Four additional trials (labeled NOEP1 through noep4) were performed with the input force reduced to where the system response was practically linear and no TET occurred. The aforementioned sets of experiments were dictated by the theoretical prediction (see Chapter 3), that passive TET in the considered system of coupled oscillators can only be realized if the imparted energy gets above a critical threshold. As shown below, the experimental results fully validate this theoretical prediction. In what follows, typical results from each of the two trial sets are provided.

First, experimental results for the case EP2 (when TET is realized) will be presented, corresponding to the experimentally produced impulsive force depicted in Figure 8.9. This force is applied to the linear primary system with the entire system being initially at rest, and is approximately 6.25 ms in duration; this forcing level is typical of the strong excitation required for inducing nonlinear passive TET in the experimental fixture. To perform comparisons between measured results and theoretical predictions, we carried out an additional independent numerical simulation of the transient response of system (8.6) subjected to the experimentally measured force and zero initial conditions. In Figure 8.10 a comparison between the experimental and theoretical acceleration time series of the two subsystems is depicted, from which very good agreement is noted. Such agreement is typical of what was observed in all experimental trials. Nonlinear TET is noted, especially at the early stage of the dynamics ($0 < t < 4$ s) when the energy of the system is relatively high and the nonlinear effects are more pronounced. Moreover, by studying the experimental time series of Figure 8.10, one notes that during this early TET regime the NES oscillates with a dominant ‘fast’ frequency that is approximately equal to the eigenfrequency of the linear subsystem, i.e., a 1:1 TRC takes place.

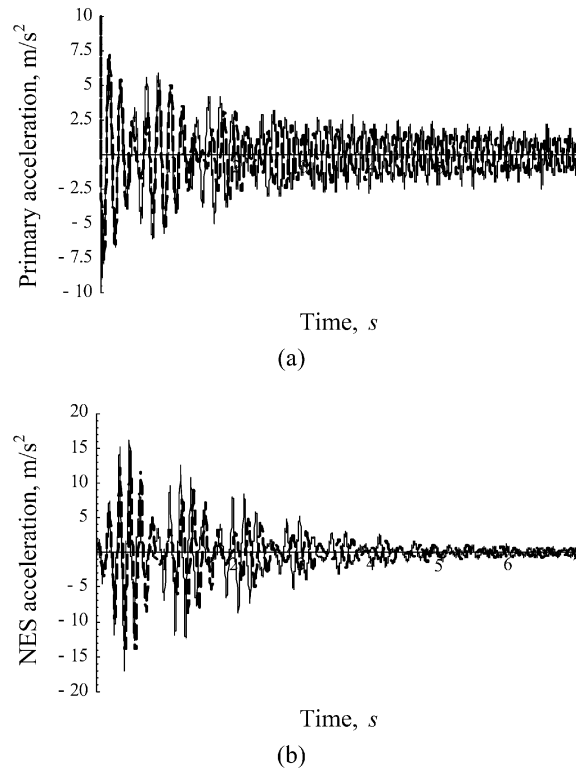


Fig. 8.10 Case when passive TET from the linear primary system to the NES occurs: experimental — and numerical --- acceleration time series of (a) the linear (directly excited) primary system, and (b) the NES.

A quantitative measure of passive TET in the system is performed by computing the energy dissipation measure (EDM),

$$E_{\text{NES}}(t) = \frac{\varepsilon c}{E_i(T)} \int_0^t \dot{v}^2(\tau) d\tau \quad (8.8)$$

representing the instantaneous portion of the input energy $E_i(t)$ dissipated by the viscous damper of the NES, where T is the duration of the external impulse. The input energy measure is computed from the following expression:

$$E_i(t) = \int_0^t F(\tau) \dot{y}(\tau) d\tau \quad 0 < t \leq T \quad (8.9)$$

Regarding the experimental estimation of the input energy measure (8.9), the acceleration record of the linear subsystem shown in Figure 8.10 was integrated starting from zero initial velocity to obtain the velocity signal. Despite high-pass filtering

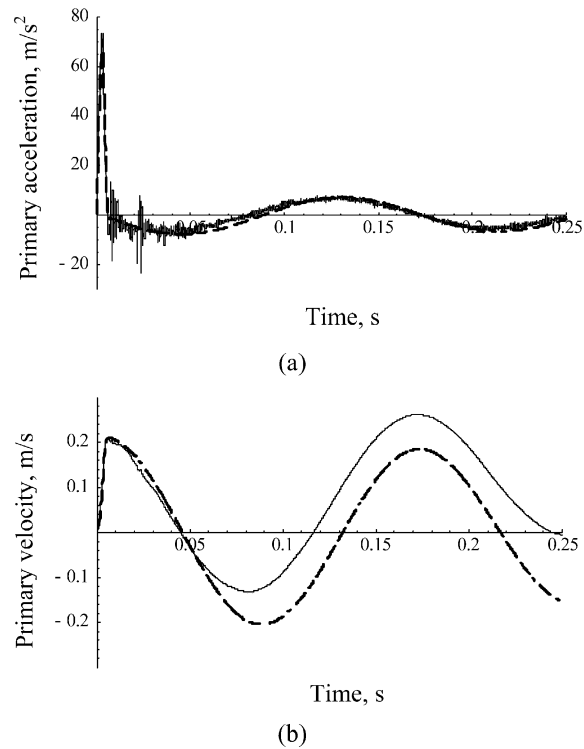


Fig. 8.11 Acceleration (a), and velocity (b), of the linear primary system during and immediately after application of the external impulsive load; experimental data —, numerical data ---.

of the experimental data, it was found that it was very difficult to obtain a stable velocity signal in this way (see Figure 8.11); fortunately, this limitation is of less importance in the total energy calculation (8.9), because of the short duration over which the applied force acts. In general, however, noise in the data constitutes a limitation when numerically integrating experimental acceleration signals. The NES velocity necessary for computing the EDM (8.8) was obtained in the same way, but while no obvious error was visible in the result, computing the energy dissipated in the NES over several seconds proved to be less reliable than the total input energy computation.

The energy input $E_i(t)$ is plotted in Figure 8.12a; both experimental and simulated measurements are provided, with good agreement between them. In Figure 8.12b experimental and simulated estimates of the energy measure $E_{\text{NES}}(t)$ (energy portion dissipated at the NES) are depicted, again with good agreement between them (indeed, there is a small error between the experimental and numerical limiting values of these plots for $t \gg 1$; as noted below, this error varies significantly among the various runs). From these results it is determined that, eventually, 88.5% of the total input energy is absorbed and dissipated by the NES; this estimate

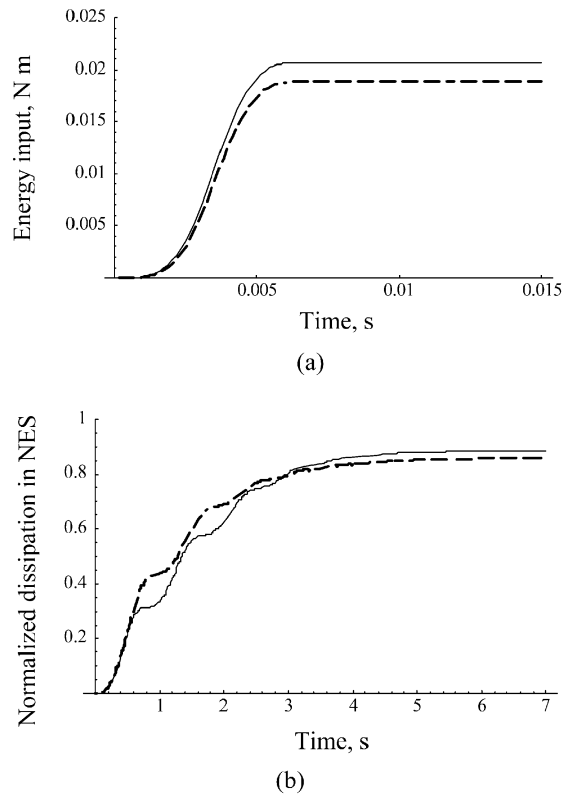
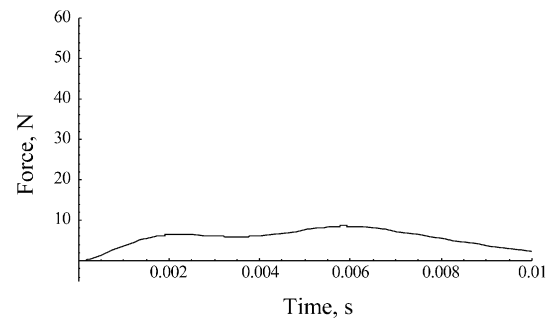


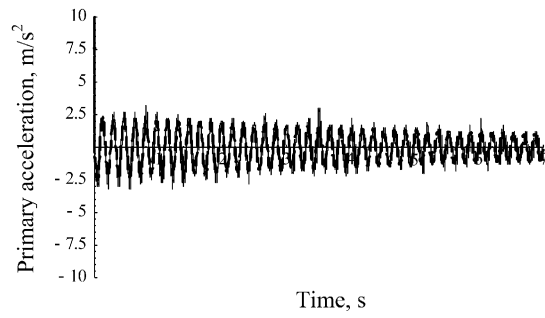
Fig. 8.12 Case when TET occurs: (a) instantaneous input energy and (b) energy dissipated at the NES; experimental data —, numerical data ----.

was obtained by considering the asymptotic limit of $E_{NES}(t)$ for $t \gg 1$. This experimental result demonstrates that the NES is an effective mechanism for passively absorbing and dissipating a significant portion of impulsively generated vibration energy of the structure to which it is attached.

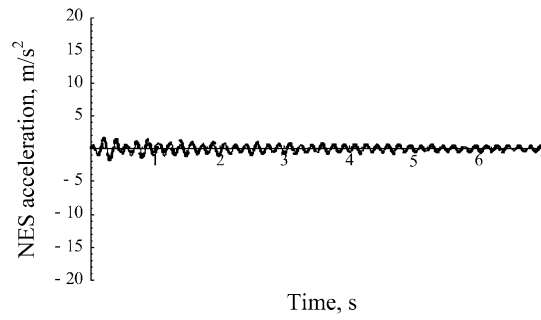
To verify experimentally the theoretical prediction that nonlinear TET in the two-DOF system under examination can not be realized for sufficiently low external excitations, the case NOEP1 is now considered, corresponding to the small impulsive force depicted in Figure 8.13a. From the acceleration time series plots of Figures 8.13b, c it is concluded that in this case no significant energy transfer occurs from the linear subsystem to the attached NES, a fact that is confirmed by the energy measures presented in Figure 8.14. Indeed, in this case the experimental and simulated estimates of the total portion of the input energy eventually dissipated at the NES are equal to 25.09% and 39.02%, respectively. These results confirm experimentally the lack of TET in the system when excited by a weak impulsive force.



(a)



(b)



(c)

Fig. 8.13 Case when no TET occurs: (a) weak impulsive force, (b) acceleration of the directly excited primary system, (c) acceleration of the NES; experimental —, numerical ---.

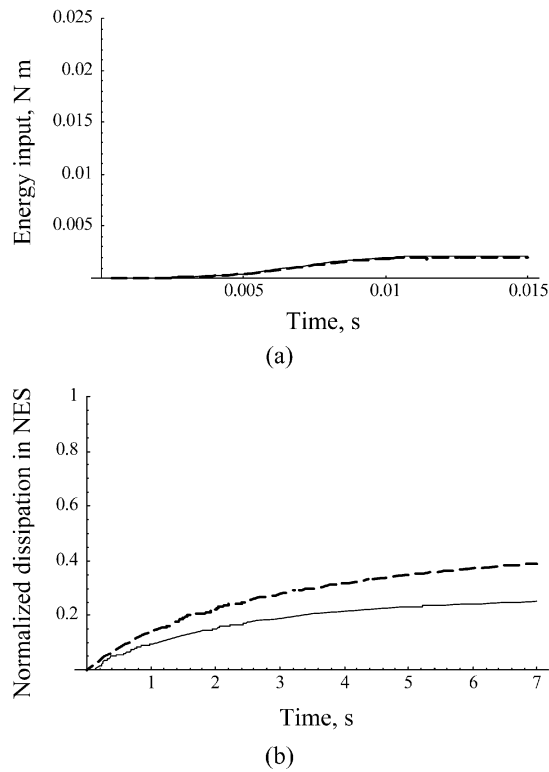
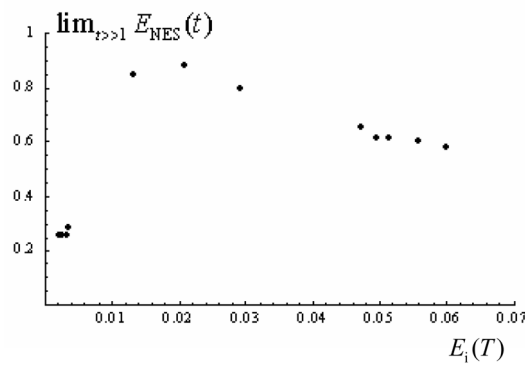


Fig. 8.14 Case when no TET occurs: (a) instantaneous input energy (N/m) and (b) energy dissipated by the NES (N/m); experimental data —, numerical data ---.

In Table 8.3 experimental and simulated estimates of the asymptotic EDM limit are presented for all tests performed. In that Table, the two series of experimental tests corresponding to relatively strong and weak impulsive excitations, respectively, are clearly distinguished. In runs with relatively strong impulsive excitations consistent TET from the primary system to the NES is noted; whereas for weak impulses TET is consistently small. There are variations between theoretical and experimental estimates but, more significantly, also between experimental estimates derived from different experimental runs. Besides unpredictable experimental factors that are not fully captured by the two-DOF theoretical model (8.6), the differences between experimental and theoretical estimates can be attributed, in part, to the transient and strongly nonlinear nature of the experiments yielding the previously discussed difficulties in the accurate computation of the transient experimental velocities (especially those of the NES) from post-processing of measured acceleration time series. The dependence of TET on the level of input energy, however, is clearly discerned in the experimental results, confirming the dependence on energy of the transient, strongly nonlinear dynamics governing TET. This dependence is clearly depicted in

Table 8.3 Asymptotic limit of the EDM (8.8) [$\lim_{t \gg 1} E_{\text{NES}}(t)$].

Test	Measured	Simulated
EP1	0.799	0.862
EP2	0.885	0.860
EP3	0.658	0.814
EP4	0.583	0.775
EP5	0.848	0.737
EP6	0.617	0.804
EP7	0.599	0.787
EP8	0.616	0.798
NOEP1	0.251	0.390
NOEP2	0.258	0.402
NOEP3	0.283	0.404
NOEP4	0.258	0.397

**Fig. 8.15** Experimental estimate of the asymptotic limit of the EDM (8.8) as function of the level of input energy.

the plot of Figure 8.15, where the limiting value of the EDM is plotted for varying energy input $E_i(T)$ (this plot corresponds to the experimental results listed in Table 8.3). Moreover, the experimental results reveal that there exists an ‘optimal’ energy input for which the portion of energy dissipated by the NES is a maximum. This result, which is of significance for the implementation of TET in practical designs, is in full agreement with the theoretical findings of Chapter 3.

8.3 Experimental Demonstration of 1:1 TRCs Leading to TET

In this section we provide an experimental demonstration of 1:1 TRC leading to TET in the two-DOF system with grounded NES (Configuration I) studied in Section 8.2. We will perform this task (Kerschen et al., 2007) by showing that during

TRC the primary linear oscillator (LO) and the NES are in a state of transient 1:1 resonance (the frequency of which varies with time), leading to nonlinear TET. In addition, by applying numerical Hilbert transform and EMD to the measured transient time series we show that 1:1 TRC is associated with non-time-like behavior of the (slowly varying) phase difference between the two oscillators. These results are in agreement with the theoretical findings reported in Chapter 3.

8.3.1 Experimental Fixture

The two-DOF system considered for this study (Kerschen et al., 2007) possesses a slightly different configuration than the one considered in Section 8.2. The schematic of the experimental fixture is depicted in Figure 2.26b, and is similar to the one employed in Section 8.2; its details are shown in Figure 8.16. The fixture is composed of a linear oscillator – LO (designated as the primary system) that is linearly coupled to a grounded NES. The corresponding mathematical model is given by:

$$\begin{aligned} M\ddot{y} + Ky + \varepsilon\lambda\dot{y} + \varepsilon(y - v) + \varepsilon\lambda_1(\dot{y} - \dot{v}) &= F(t) \\ m\ddot{v} + \varepsilon c\dot{v} + Cv^3 - \varepsilon(y - v) - \varepsilon\lambda_1(\dot{y} - \dot{v}) &= 0 \end{aligned} \quad (8.10)$$

Both linear and nonlinear subsystems are realized in the form of cars made of aluminum angle stock oscillating on an air-track in order to eliminate as much as possible the effects of friction forces from the measured dynamics. Comparing this model to the similar model (8.6), we note the addition of weak viscous damping $\varepsilon\lambda_1$ in the coupling element; this was experimentally achieved by adding viscoelastic tape to the coupling leaf spring (Figure 8.16c). As in the previous section, however, weak coupling is assumed by requiring that $\varepsilon \ll K$.

In addition, Teflon coating was attached to the undersides of the cars to reduce any friction that might occur while the cars were in motion. As a result, in (8.10) the damping constants $\varepsilon\lambda$ and εc were much smaller than the damping coefficient $\varepsilon\lambda_1$ of the coupling element. A long-stroke electrodynamic shaker provided a controlled and repeatable short force pulse to the primary linear system (i.e., the left car in Figure 8.16a), with a typical broadband input force being depicted in Figure 8.17. The response of both oscillators was measured using accelerometers, and estimates of the corresponding velocities and displacements were obtained by numerically integrating the measured acceleration time series. The resulting signals were then high-pass filtered to remove spurious components introduced by noise in the integration procedure.

System identification of the model (8.10) was performed following the procedures and applying the techniques discussed in the two previous sections. A detailed description of the system identification procedure can be found in Kerschen et al. (2007). The nonlinear grounding force applied to the NES through the wire system was identified employing the restoring force method (Masri and Caughey, 1979) as

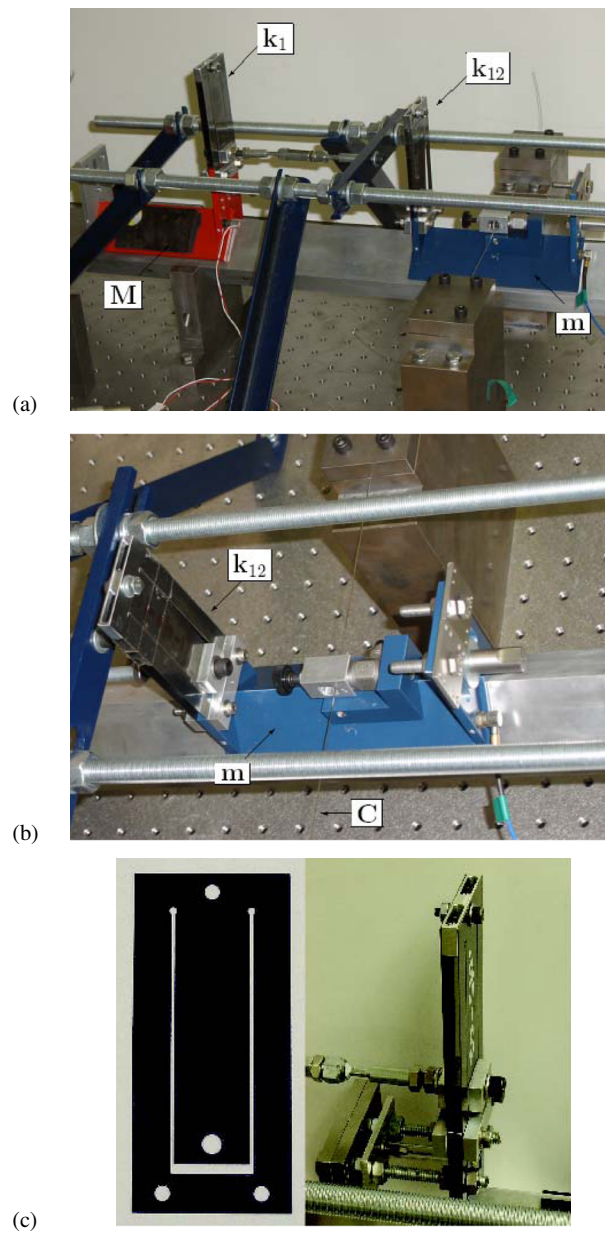


Fig. 8.16 Details of the experimental fixture: (a) linear primary system with attached NES, (b) NES, (c) leaf spring.

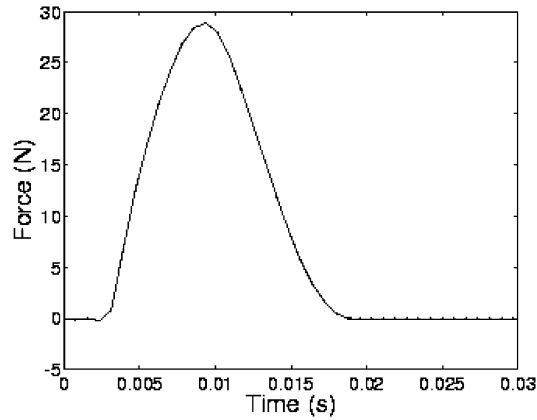


Fig. 8.17 Typical input force applied to the linear primary system by the long-stroke shaker.

Table 8.4 Parameters of model (8.10) identified through experimental modal analysis, and the restoring force surface method.

Parameter	Estimated Value
M	0.7348
m	0.4734
K	942
ε	151
$\varepsilon\lambda$	0.09
εc	0.11
$\varepsilon\lambda_1$	0.4
C	1.83×10^7
C_{lin}	11.3

$$f_{\text{NES}}(v, \dot{v}) = \varepsilon c \dot{v} + C_{\text{lin}} v + C v^3 \quad (8.11)$$

where the coefficients and the other identified parameters of the model (8.10) are listed in Table 8.4. The small linear stiffness component in (8.11) (caused by the small pretension in the wires that realize the essential stiffness nonlinearity of the NES) was small enough to not affect our study of TRCs in the system considered.

8.3.2 Experimental TRCs

Three excitation levels were considered in this specific set of experiments, corresponding to force peak amplitudes of 7, 13 and 18 N, respectively. Figure 8.18 displays the responses (displacements) of the primary LO and the NES, from which we note that the dynamics of the system at the 7 N level is qualitatively different

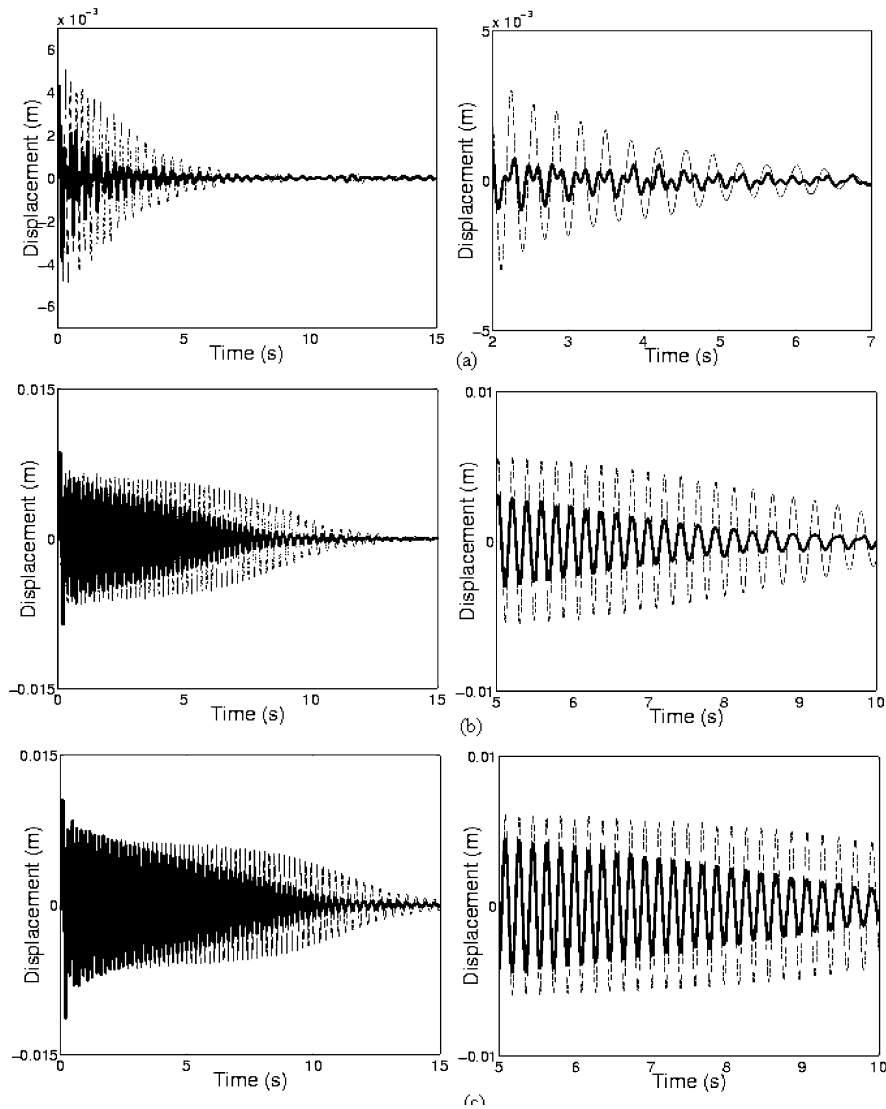


Fig. 8.18 Experimentally measured displacements (left column: entire record; right column: close-up): (a) 7 N peak force; (b) 13 N peak force; (c) 18 N peak force; LO response —, NES response - -.

than that at the other two levels. Indeed, at the 7 N level the response of the LO possesses at least two significant frequency components, whereas the responses at the 13 N and 18 N levels are in the form of a fast frequency modulated by a slowly varying envelope. Hence, at the higher energy levels slow-fast decomposition of the transient dynamics is noted.

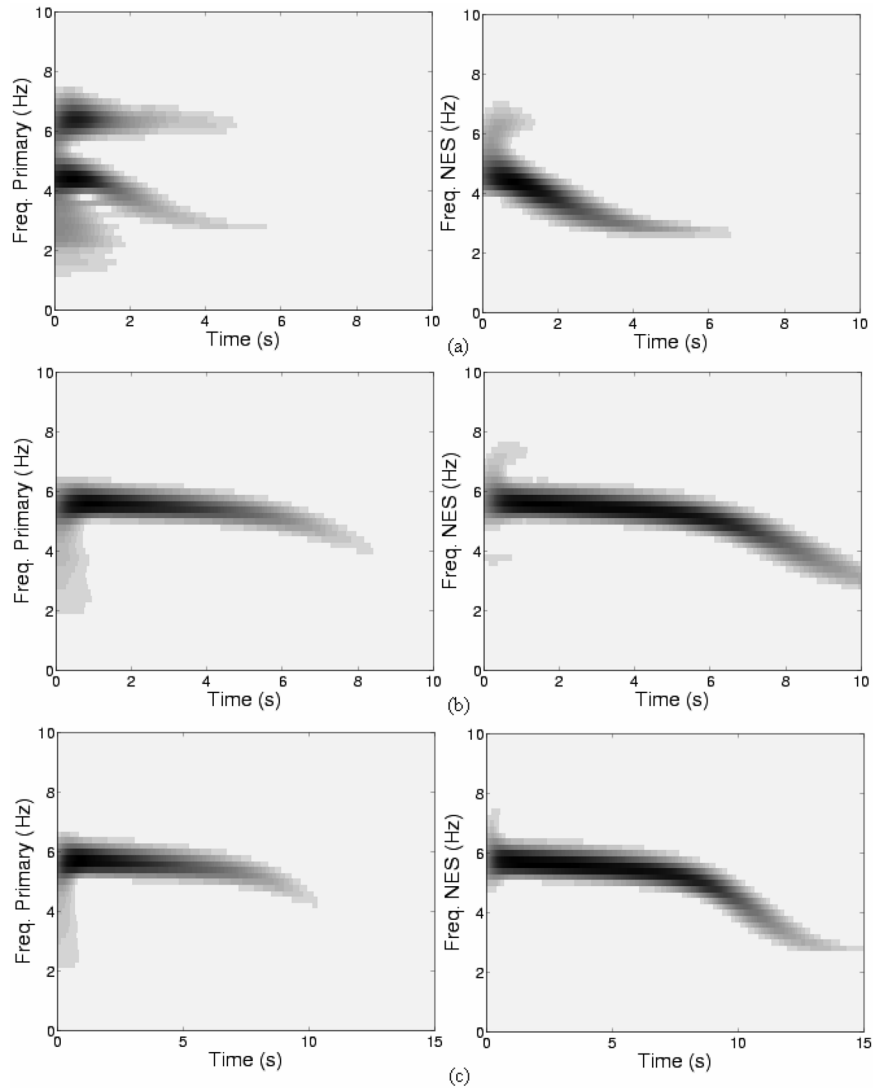


Fig. 8.19 WT spectra of the experimental responses of Figure 8.18 (left column: primary LO; right column: NES): (a) 7 N peak force; (b) 13 N peak force; (c) 18 N peak force.

From these results it is evident that at the higher energy levels fundamental TET takes place from the directly forced primary LO to the NES; moreover, in the fundamental TET regimes both oscillators perform in-phase oscillations with the same apparent frequency, i.e., 1:1 TRCs occur. The transient nature of these resonance captures in the TET regimes is not fully clarified by these plots but it is clearly deduced from the following post-processing study of the experimental measurements.

Further evidence of 1:1 TRCs in the transient dynamics is provided in Figure 8.19, which depicts the instantaneous dominant frequencies (wavelet transform spectra) of the experimentally measured displacements of Figure 8.18. As in our previous studies in this monograph, heavily shaded areas correspond to regions where the amplitudes of the wavelet transform spectra are high, revealing the presence of dominant harmonic components in the corresponding transient responses. In addition to verifying the occurrence of 1:1 TRCs in the fundamental TET dynamics, these results indicate that during resonance captures the (common) dominant frequency of the two oscillators shifts downward (due to the hardening characteristic of the stiffness nonlinearity of the system) as the total energy decreases due to viscous dissipation. Hence, at the beginning of the 1:1 TRCs, this frequency is close to 5.7 Hz (i.e., the eigenfrequency of the LO), whereas at the end of the TRC this decreases to as low as 3.3 Hz, respectively.

As discussed in previous chapters, 1:1 TRCs can be accurately studied by considering the evolution of the relative phase of the slow flow (modulation) dynamics governing the high-energy responses. In particular, in the neighborhood of the 1:1 resonance manifold, non-time-like behavior of this phase is anticipated, which prevents direct averaging of the equations of motion over this angle variable. Hence, the slow evolution of the relative phase signifies the occurrence of the corresponding resonance capture. To this end, the relative phase of the dynamics of the two oscillators is computed directly from the experimental responses using either directly the Hilbert transform (if the responses possess a single dominant-fast-frequency), or empirical mode decomposition – EMD (see Section 2.5.2) followed by Hilbert transform (for responses with multiple dominant frequencies).

In Figure 8.20 we depict the temporal evolution of the relative phase $\phi_{yv} = \phi_y - \phi_v$ between the LO and the NES for the energetically high measurements (i.e., the experimental responses depicted in Figures 8.18b, c and 8.19b, c). In both cases 1:1 TRCs occur (leading to TET), and the transient responses of the LO and the NES possess a single fast frequency component (Feldman, 1994). It follows that by applying Hilbert transform to the time series of Figures 8.18b, c, these responses can be decomposed in terms of slow and fast components as follows:

$$\begin{aligned} y(t) &= A_y(t) \cos \varphi_y(t) \\ v(t) &= A_v(t) \cos \varphi_v(t) \end{aligned} \quad (8.12)$$

where $A_y(t)$, $A_v(t)$ and φ_y , φ_v are slowly varying amplitudes and phases, respectively. In 1:1 TRC regimes non-time-like behavior of the phase difference ϕ_{yv} is observed in both cases, followed by escape from resonance capture as noted by the corresponding time-like behavior of the phase difference. Clearly, we may not apply Hilbert Transform directly to the transient responses of the low-energy case (see Figures 8.18a and 8.19a), as these possess two dominant frequency components (and no TET is realized).

To study resonance interactions in the energetically low responses (Figures 8.18a and 8.19a) we first analyze them by means of EMD, thus decomposing them in terms of their intrinsic mode functions (IMFs) $c_{yi}(t)$, $c_{vp}(t)$, $i, p = 1, 2, \dots$; as discussed

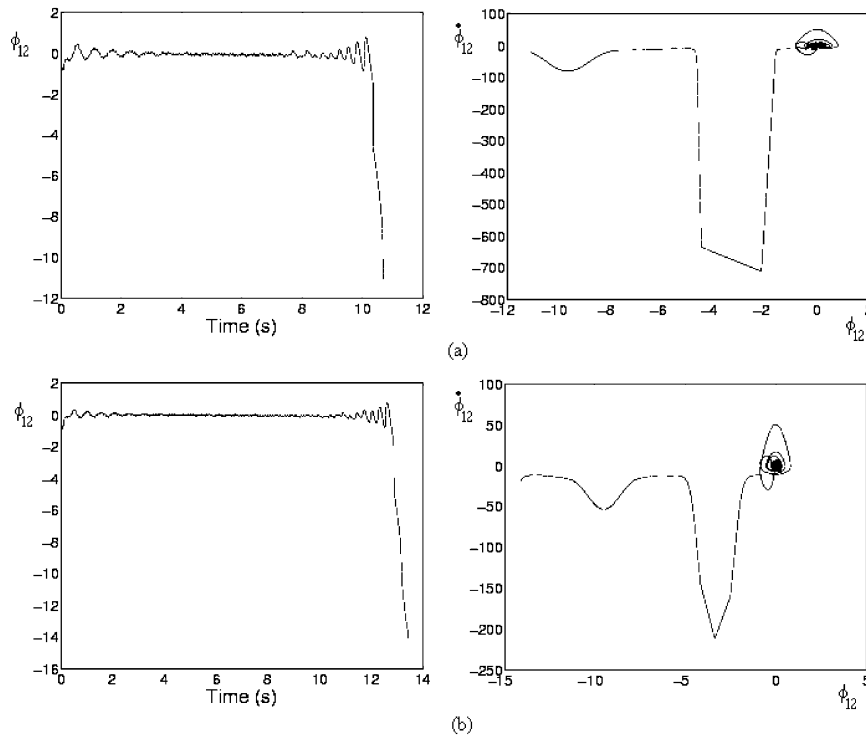


Fig. 8.20 Time series (left column) and trajectory in phase plane (right column) of the phase difference ϕ_{yv} : (a) 13 N peak force; (b) 18 N peak force.

in Section 2.5.2 the IMFs are oscillatory modes embedded in the time series and can be analyzed individually by the Hilbert transform. Then, the transient responses are expressed as

$$y(t) = \sum_i c_{yi}(t) \quad \text{and} \quad v(t) = \sum_p c_{yp}(t) \quad (8.13)$$

Figure 8.21 depicts the first two IMFs of the experimental displacement of the oscillators depicted in Figure 8.18a; additional higher-order IMFs were also computed but were omitted from further consideration as they had negligible participation in the transient responses. For the response of the primary LO (see Figure 8.21a) the two IMFs have approximately similar contributions to the response, which indicates that two terms must be taken into account in the series expression for $y(t)$ in (8.13). On the other hand, the second IMF of the NES displacement (see Figure 8.21b) can be neglected when compared to the first IMF, so $v(t)$ in (8.13) may be approximated solely by its first IMF.

Decomposing these dominant IMFs in terms of their instantaneous amplitudes and phases, the transient responses of Figure 8.18a are approximated as follows:

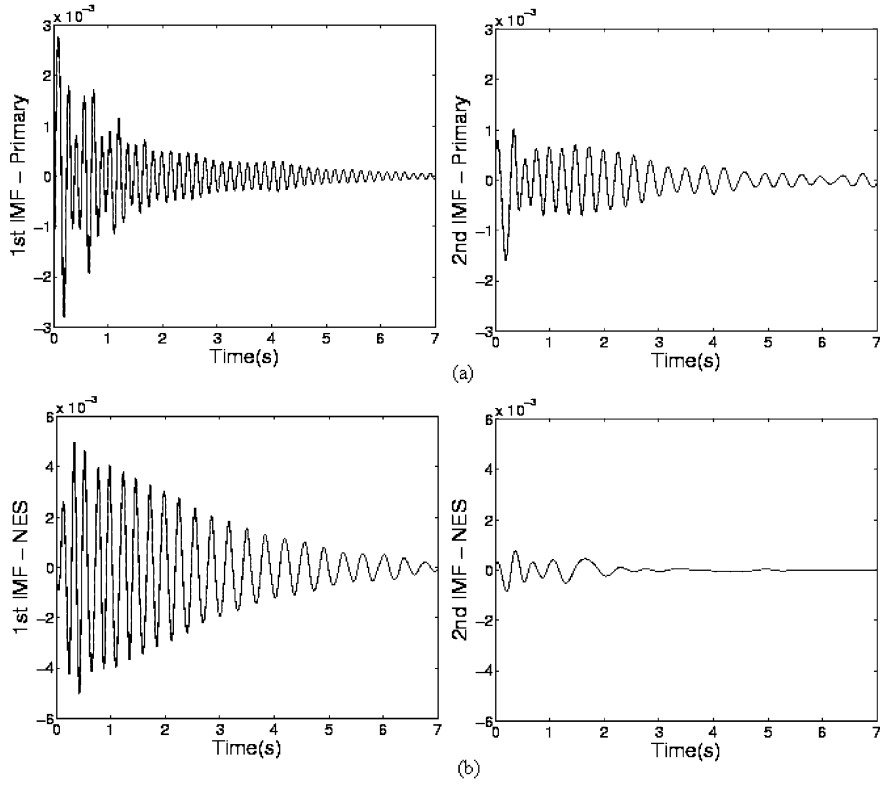


Fig. 8.21 IMFs resulting from EMD of the experimental responses depicted in Figure 8.18a \tilde{U} -7 N peak force (left column: 1st IMF; right column: 2nd IMF): (a) primary LO; (b) NES.

$$\begin{aligned}
 y(t) &\approx A_{y1}(t) \cos \phi_{y1}(t) + A_{y2}(t) \cos \phi_{y2}(t) \\
 v(t) &\approx A_{v1}(t) \cos \phi_{v1}(t)
 \end{aligned}
 \tag{8.14}$$

where $A_{y1}(t)$, $A_{y2}(t)$, $A_{v1}(t)$ and $\phi_{y1}(t)$, $\phi_{y2}(t)$, $\phi_{v1}(t)$ are slowly-varying amplitudes and phases of the dominant IMFs, respectively. Moreover, a careful examination of the IMFs depicted in Figure 8.21 reveals that the second IMF, $c_{y2}(t)$ of the displacement of LO, and the first IMF $c_{v1}(t)$ of the NES displacement, possess nearly identical fast frequencies over the time interval $1 < t < 5$ s; this becomes apparent when we examine the corresponding phase difference, $\phi_{y2}(t) - \phi_{v1}(t)$ depicted in Figure 8.22. These IMFs, therefore, are engaged in 1:1 TRC on the mentioned time interval. Note that no such resonance capture occurs involving the participation of the first IMF of the response of the LO, which explains why no TRC can be discerned in the original time series corresponding to the low forcing level.

A study of the energy dissipation measure of the NES, i.e., of the percentage of total energy dissipated by the damper of the NES in time, is presented in Figure 8.23.

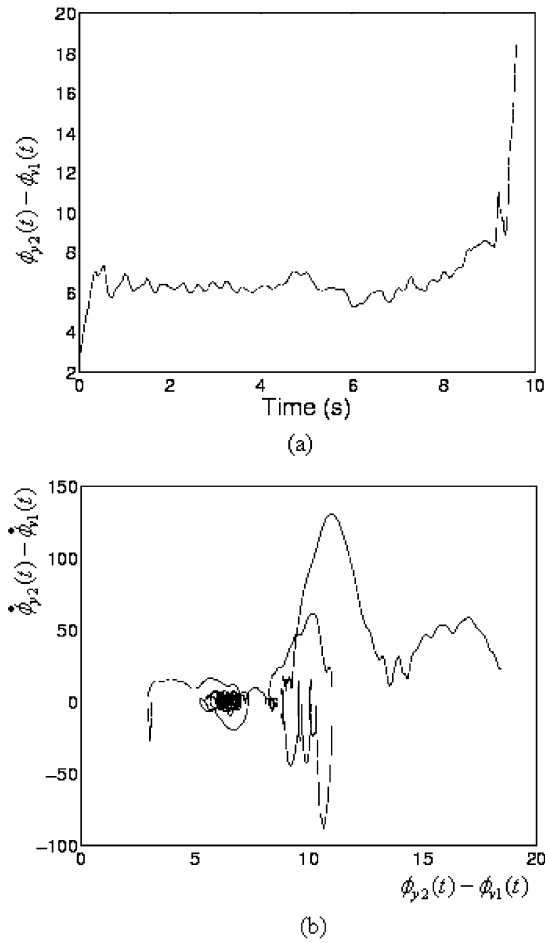


Fig. 8.22 Phase difference $\phi_{y_2}(t) - \phi_{v_1}(t)$ between the 2nd IMF of the response of the primary LO and the 1st IMF of the response of the NES – 7 N peak force: (a) time series, (b) trajectory in the phase plane.

At the lowest energy level (Figure 8.23a – for which previous results indicated that TRC is not realized), a single regime is realized during which strong nonlinear beat phenomena exist and energy quickly flows back and forth between the LO and the NES. After 0.35s, as much as 98.2% of the total energy is transferred from the impulsively excited primary LO to the NES, but this number drops to 18% immediately thereafter (during an energetically lower regime).

At the other two energy levels (Figures 8.23b, c), for which 1:1 TRCs are realized, three Regimes, labeled I, II and III, exist during the motion. During Regime I, a nonlinear beat phenomenon can also be observed during the first few cycles (though this is weaker than the one realized at the lower energy level). Although this Regime

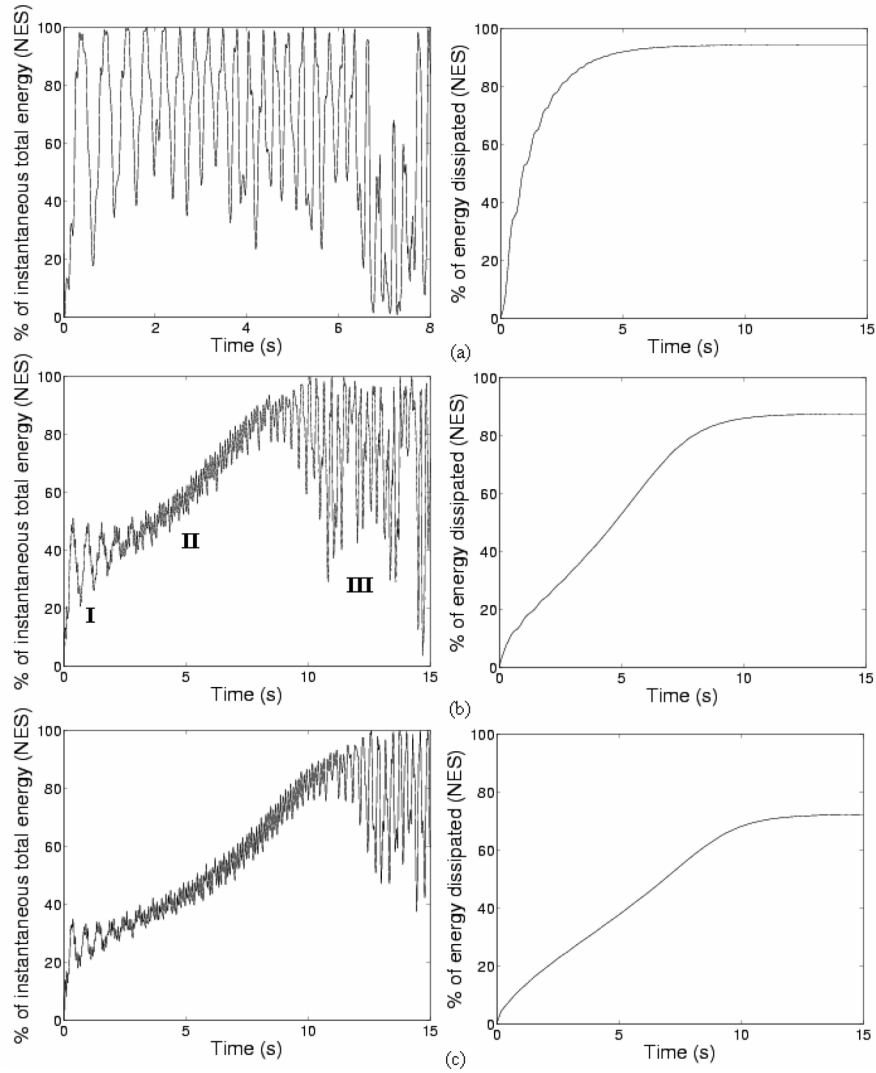


Fig. 8.23 Energy exchange and dissipation in the system [left column: percentage of instantaneous total energy in the NES; right column: EDM (8.15)]: (a) 7 N peak force; (b) 13 N peak force; (c) 18 N peak force.

could not be clearly observed in the responses of Figures 8.18 and 8.19 (except for the presence of small harmonic components in Figures 8.18b and 8.18c), it plays a very important role in the dynamics since it ‘drives’ the motion into the domain of attraction of the 1:1 resonance manifold (and, thus to 1:1 TRC); this is performed by the transfer of a certain amount of energy from the LO to the NES during the nonlinear beats. The system is then capable of sustaining a 1:1 TRC during a sig-

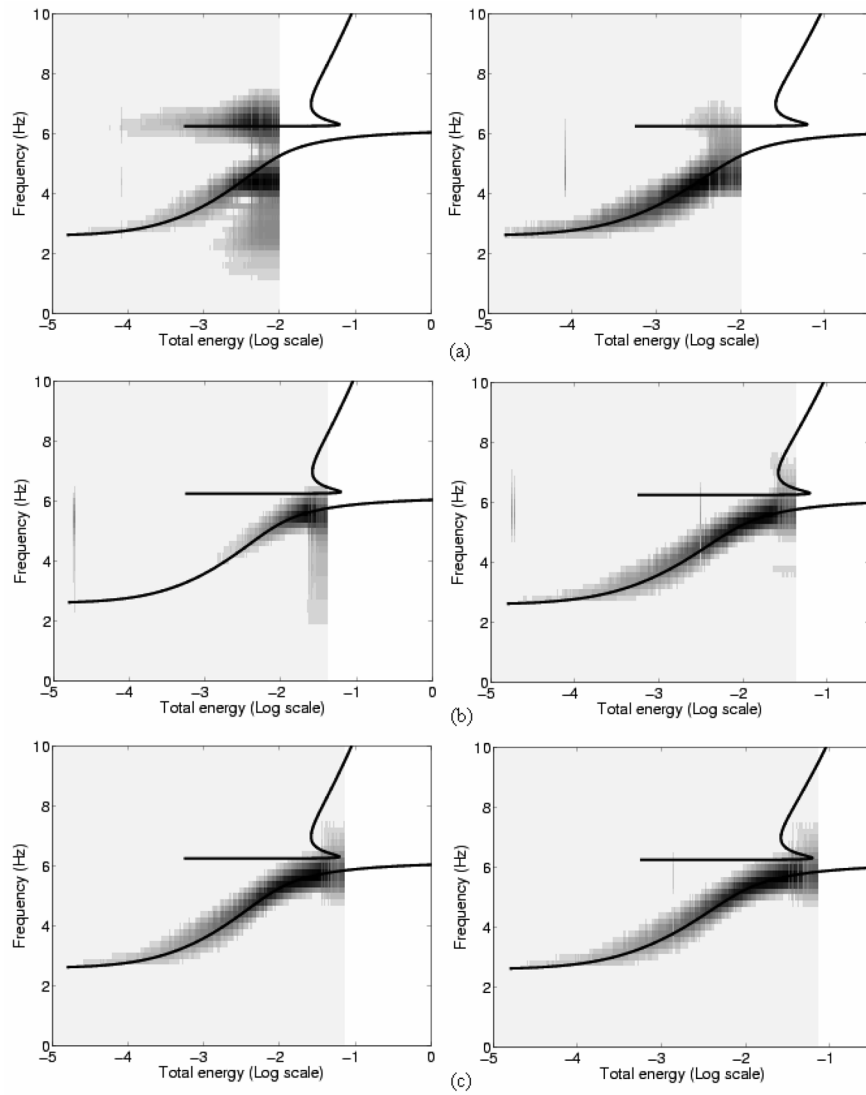


Fig. 8.24 Wavelet transform spectra of experimental displacements superimposed to the Hamiltonian frequency-energy plot of system (8.10) (left column: primary LO; right column: NES): (a) 7 N peak force; (b) 13 N peak force; (c) 18 N peak force.

nificant part of the motion, namely, during Regime II. At the beginning of Regime III, the NES carries almost all the instantaneous energy of the system; then escape from the regime of 1:1 TRC resonance capture occurs, and energy is released from the NES back to the primary system, though at an energetically lower regime, after most of the energy of the system has been dissipated by the dampers of the system.

This is inferred from the EDM plots depicted in Figure 8.23. In this case the EDM is computed as

$$E_{\text{NES}}(t) = \frac{\varepsilon c \int_0^t \dot{v}^2(\tau) d\tau + \varepsilon \lambda_2 \int_0^t [\dot{v}(\tau) - \dot{y}(\tau)]^2 d\tau}{E_i(T)} \quad (8.15)$$

where $E_i(T)$ is the total energy input to the system by the impulsive excitation.

In Figure 8.24, the backbone curve of the frequency-energy plot (FEP) of the underlying Hamiltonian system (8.10), represented by a solid line, is superposed on the wavelet transform spectra of the displacements. As mentioned in Chapter 3 this plot can only be used for descriptive purposes as it superposes wavelet transform spectra of damped responses to branches of undamped periodic orbits; however, it is useful for depicting the relation between the damped and undamped dynamics. We notice that for all three excitation levels, the predominant frequency components follow the in-phase backbone branch $S11+$ for most of the duration of the motion. This validates the similar theoretical findings in Chapter 3. Moreover, it is established that the dynamics of system (8.10) is strongly nonlinear, as the predominant frequency components undergo significant variations in frequency content with energy. In addition, we conclude that during a 1:1 TRC (i.e., at the 13 and 18 N peak force levels), the displacements of both oscillators possess mainly a single (fast) frequency component which closely tracks the lower part of the backbone branch (see Figures 8.24b, c). At the 7 N peak force level, however, a strong nonlinear beat phenomenon is observed, and there exist two (fast) frequency components in the transient responses, one of which closely traces (approximately) the linearized out-of-phase subbranch of $S11-$, while the other follows the lower backbone in-phase branch $S11+$.

In general, satisfactory agreement was obtained between theoretical predictions and experimental measurements throughout this study, in spite of the transient and strongly nonlinear nature of the dynamics. For illustration of this fact, a comparison between experimentally measured and predicted displacements resulting from direct numerical integrations of the model (8.10) at the 13 N peak force level is presented in Figure 8.25.

8.4 Steady State TET Under Harmonic Excitation

In our final experimental study we consider steady state TET in a two-DOF system possessing a grounded NES (of Configuration I). This system was examined in detail in Jiang et al. (2003) where systems with both weak and strong coupling were considered. In Chapter 6 we studied different mechanisms for steady state TET in periodically forced oscillators, namely, time-periodic TET, or TET in the form of strongly modulated responses (SMRs). The experimental study in this section is concerned with time-periodic TET, whereas for experimental verification of TET through SMRs we refer to Gourdon et al. (2005).

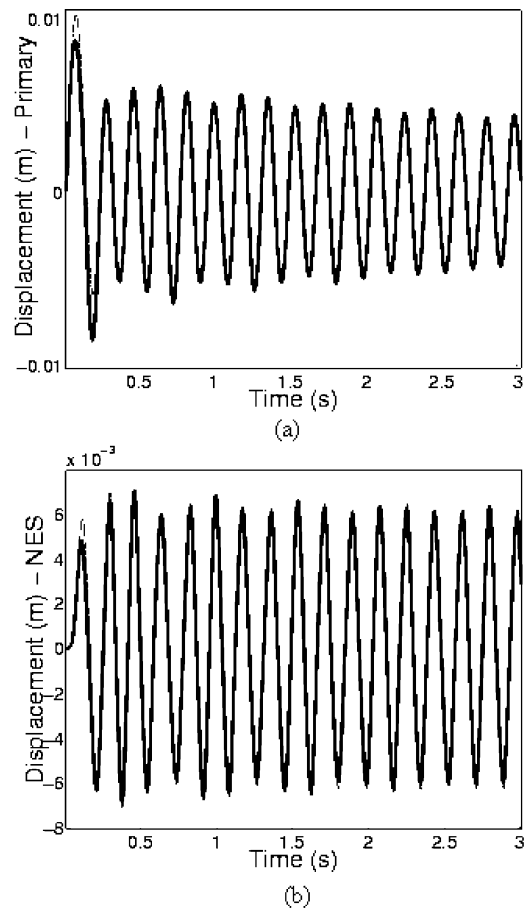


Fig. 8.25 Comparison between experimentally measured and predicted displacements (13 N peak force level): (a) LO, (b) NES; prediction —, experiment —.

We find that, in contrast to the classical linear vibration absorber, the NES is capable of absorbing steady state vibration energy from the linear oscillator over a relatively broad frequency range. This results in localization of the steady state vibration to the NES. Both forward and backward frequency sweeps are considered and generation or elimination of localized steady state responses through sudden transitions (jumps) are detected, leading to nonlinear hysteresis phenomena.

8.4.1 System Configuration and Theoretical Analysis

We consider a SDOF oscillator weakly coupled to a grounded NES (Configuration I) with governing equations given by,

$$\begin{aligned} m_1 \ddot{y}(t) + c_1 \dot{y}(t) + k_1 y(t) + \varepsilon k [y(t) - v(t)] &= F \sin \omega t \\ m_2 \ddot{v}(t) + c_2 \dot{v}(t) + k_2 v_2^3(t) + \varepsilon k [v(t) - y(t)] &= 0 \end{aligned} \quad (8.16)$$

where $|\varepsilon| \ll 1$. In Jiang et al. (2003) the steady state responses of this system were analyzed by applying the CX-A technique; these results are not reproduced here, and we will summarize only the main results that are necessary for the experimental study that follows.

To give an indication of the dynamics of system (8.16), in Figure 8.26 we depict the steady state amplitudes of the responses of the system with parameters $m_1 = 2.800$ kg, $m_2 = 0.400$ kg, $k_1 = 8005.300$ N/m, $k_2 = 4000000$ N/m³, $c_1 = 219.663$ N/m/s, $c_2 = 0.808$ N/m/s, $\varepsilon k = 130$ N/m, and $F = 30$ N. The steady responses of the system were computed for constant forcing amplitude F and varying forcing frequency ω ; due to the essential nonlinearity of the system there exist frequency ranges where multiple coexisting stable steady state solutions are realized. Referring to the plot of Figure 8.26 we note that linear resonance in branch 1 (at $\omega \approx k_1/m_1$) is completely suppressed due to the heavy damping considered and, instead, the steady state response is dominated by the localized part of branch 1, corresponding to motions confined to the NES. Indeed, we note that close to the point of the jump from branch 1 to branch 3, the steady state amplitude of the nonlinear attachment is nearly 4.3 times greater than that of the directly forced linear oscillator. Moreover, we note that the nonlinear attachment is capable of localizing steady state energy over a relatively broad frequency range (20–38 rad/s); moreover, the localization becomes increasingly more profound with increasing frequency. After the jump to branch 3 the dynamics settles to a low-amplitude linearized steady state vibration.

It is shown in Jiang et al. (2003) that these analytical results are in agreement with direct numerical simulations of the governing nonlinear equations of motion. As an indication of the agreement between analysis and numerical simulation, in Figure 8.27 we depict transitions (jumps) between stable steady state branches when the system is perturbed by impulses. To this end, a series of direct numerical simulations of the equations of motion (8.16) was performed as follows: (i) first, we let the system reach a steady state motion at frequency ω ; (ii) then, keeping the harmonic force running we apply an impulse of constant magnitude to the linear oscillator for a duration of half cycle of the harmonic response, $T = \pi/\omega$. It was found that the proper timing of this impulse depended upon which transition was to be induced: a shift from branch 1 to branch 3 was readily initiated by an impulse timed with the motion of the linear oscillator, while a jump from branch 3 to branch 1 was more easily produced by a pulse in-phase with the motion of the nonlinear attachment. By appropriately selecting the magnitude of the impulse we were able

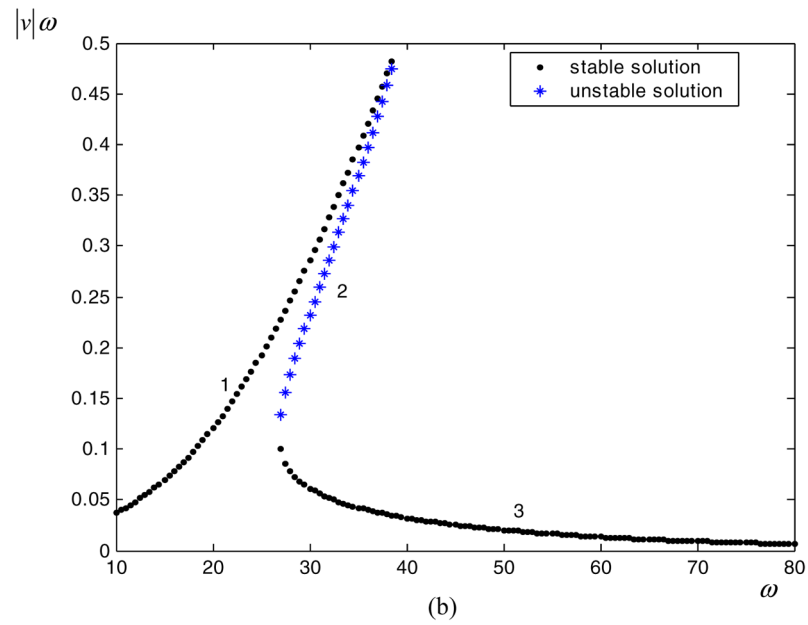
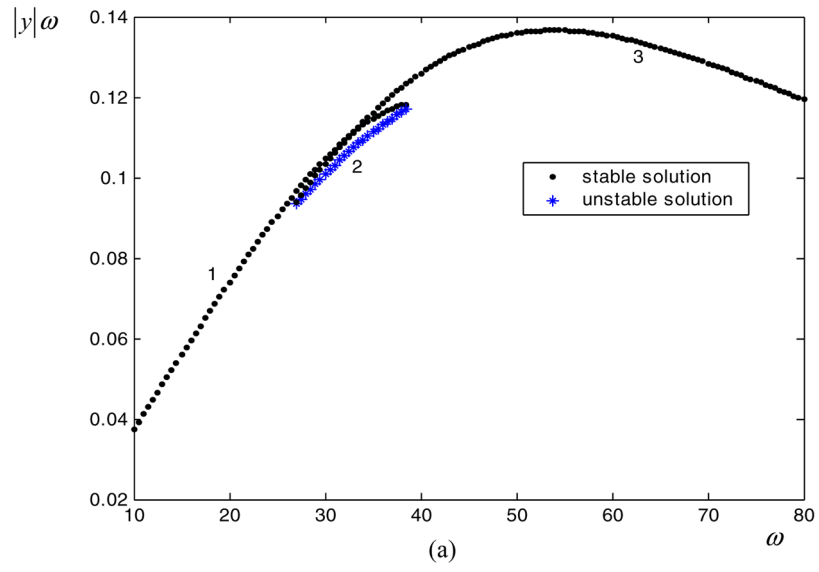


Fig. 8.26 Steady state amplitudes of system (8.16) computed by the CX-A method: (a) linear oscillator, and (b) nonlinear attachment.

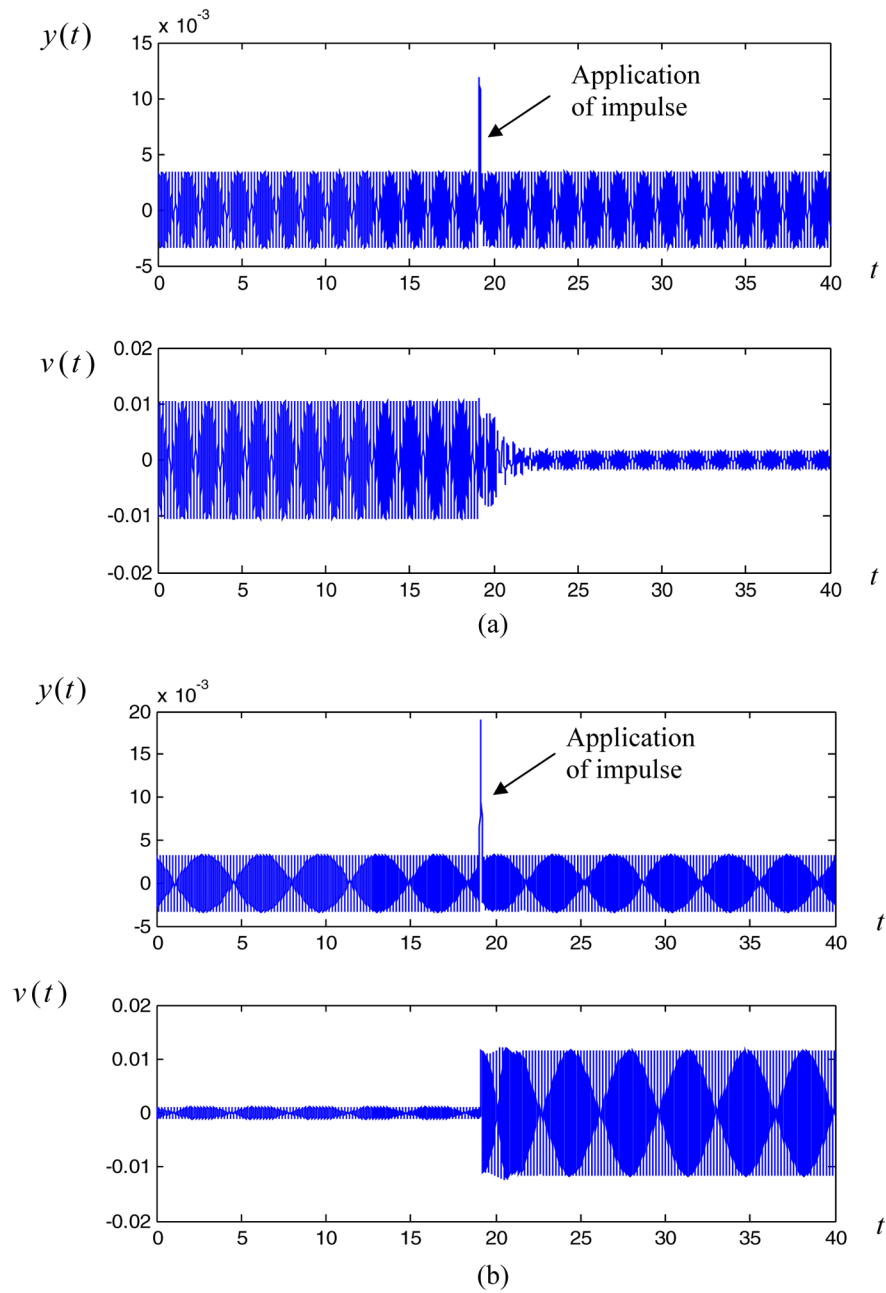


Fig. 8.27 Transitions between stable steady state branches induced by an impulse in system (8.16): (a) transition from branch 1 to branch 3 at $\omega = 32 \text{ rad/sec}$ for an impulse of magnitude 85 N; (b) transition from branch 3 to branch 1 at $\omega = 35 \text{ rad/sec}$ for an impulse of magnitude 135 N.

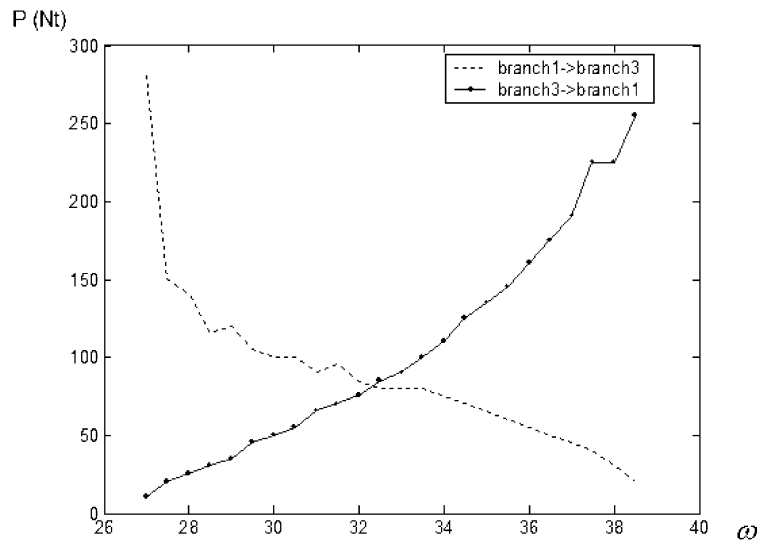


Fig. 8.28 Minimum impulse magnitude required for inducing transitions between stable steady state branches in system (8.16).

to induce transitions between branches 1 and 3, as shown in Figure 8.27. Moreover, the numerical simulations indicated that there was a certain minimum pulse level that was required for inducing the transitions between the stable branches, and once that minimum was exceeded a transition between branches could always be realized. We found that this minimum pulse level was frequency-dependent, and, in addition, depended on the specific transition considered (that is, from branch 1 to 3 or *vice versa*). The minimum impulse magnitudes required for initiating the two transitions in the range of co-existing steady states of the heavily damped system are depicted in Figure 8.28.

In the next section experimental work is performed to validate the theoretical predictions. The experimental system is composed of the armature of a shaker weakly coupled to an attachment with essential stiffness nonlinearity. By performing a series of frequency sweeps we aim to verify the existence of the theoretically predicted steady state TET phenomena.

8.4.2 Experimental Study

The experimental fixture is depicted in Figure 8.29a and its schematic representation is presented in Figure 8.29b. The linear oscillator was built around a long-stroke electrodynamic shaker (Electro-Seis Model 400, APS Dynamics Inc.), with an armature mass of 2.8 kg. Because this mass was large compared to any components

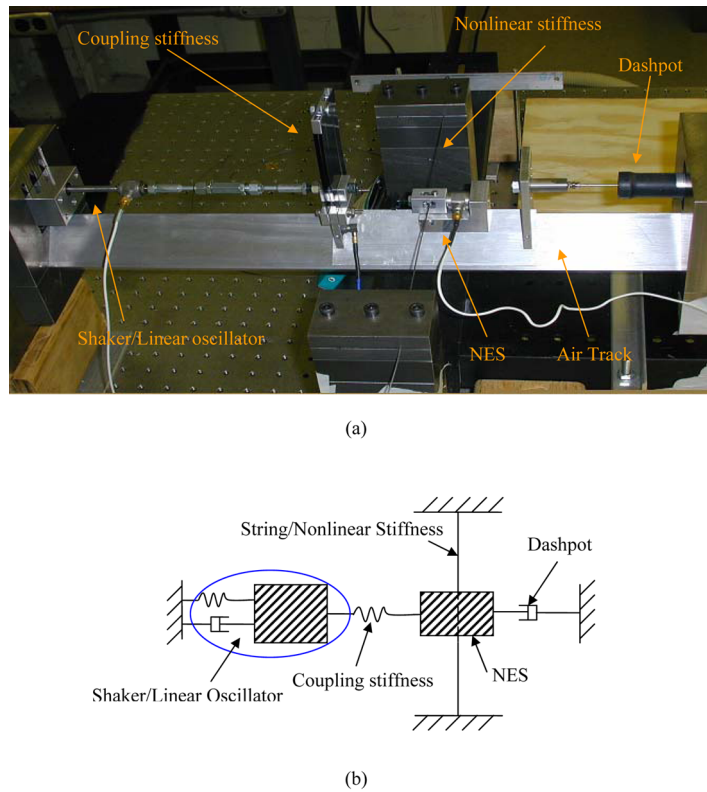


Fig. 8.29 The experimental fixture: (a) setup, (b) schematic representation.

that might have been directly attached to it in this experiment, the armature itself was arranged to function as the mass m_1 of the theoretical model (8.16). Modal analysis of the shaker as an single degree-of-freedom (SDOF) linear system, using a white noise signal as input, provided its inherent linear stiffness $k_1 = 649.89$ N/m with damping $c_1 = 11.57$ Ns/m. The external harmonic force $F \sin \omega t$ of the theoretical model was provided by the electromagnetic force between the armature and the frame of the shaker. The dual mode power amplifier driving the shaker (Model 144, APS Dynamics Inc.) was operated in current-feedback mode, with the result that the current supplied to the shaker (and thus the force on the armature) was nearly independent of frequency, and the structural dynamic response was measured for a specified amplitude of the voltage signal input to the amplifier. This current was monitored on an oscilloscope and its waveform compared to that of the sinusoidal driving voltage. Thus, the requirement that the applied force possesses a fixed magnitude during the forward and backward experimental sine sweeps was experimentally satisfied.

The shaker armature was attached to a weak coupling spring of stiffness $\epsilon k = 130$ N/m by means of a horizontal stinger which ran in a linear bearing (visible at the

left edge of the photo in Figure 8.29a). The bearing aligned the stinger with an air track on which rode the mass m_2 of the nonlinear attachment (the NES). This coupling spring was a vertical double cantilever of thin spring steel, capable of remaining linear during the large relative displacements encountered in this experiment. The base of this spring was attached to the NES mass; this was a $50 \times 50 \times 3$ mm aluminum angle stock supported in operation by air emitted through a series of small holes in the upper surfaces of the air track, itself a box beam of length 77 cm supported rigidly at each end. The NES mass was connected to ground by a viscous damper (an air dashpot with an adjustable orifice) and by an essentially nonlinear, cubic-hardening spring. As mentioned in previous sections, the essential nonlinearity was experimentally realized by the transverse deflection of a piece of piano wire with no pretension; horizontal deflection of its midpoint produced axial stretching of each half-span with the desired (geometric) nonlinearity following from the geometry of the deformed shape. This essentially nonlinear spring was calibrated under static loads for a range of spans and wire sizes. In the present study two diameters of wire were used, namely, 0.79 mm and 1.04 mm with elastic modulus 200 GPa and wire half span equal to 133.2 mm; these correspond, respectively, to the ‘thin-wire’ and ‘thick-wire’ cases discussed below. The remaining system parameters of the NES subsystem were identified by considering it as a linear SDOF structure with the nonlinear spring removed and the stinger fixed to ground, and conducting a hammer modal test on this configuration. Hence, the following system parameters were identified for the experimental fixture [based on the notation of system (8.16)]:

$$\begin{aligned} m_1 &= 2.8 \text{ kg}, \quad m_2 = 0.4 \text{ kg}, \quad k_1 = 649.89 \text{ N/m}, \\ k_2 &= 4 \times 10^7 \text{ N/m}^3 \quad (\text{thin wire}), \quad k_2 = 7.1 \times 10^7 \text{ N/m}^3 \quad (\text{thick wire}), \\ c_1 &= 11.570 \text{ Ns/m}, \quad c_2 = 0.808 \text{ Ns/m}, \quad \varepsilon k = 130 \text{ N/m}, \quad F = 5 \text{ N} \end{aligned}$$

With the linear oscillator and NES connected as shown in Figure 8.29, a harmonic force was applied to the shaker armature. The responses of both masses, the armature and the sink, were measured using miniature piezoelectric accelerometers. In addition, the force between the two degrees of freedom (that is, the force transmitted by the coupling spring εk), and the restoring force provided by the nonlinear spring were measured with piezoelectric load cells. All of these signals were recorded using a Tektronix 2630 Spectrum Analyzer and exported to Matlab[®] for post-processing. The experimental displacement values given herein were obtained by integrating the measured acceleration records.

In Figures 8.30 and 8.31 we present the comparisons between the numerical simulations [derived by numerically integrating the model (8.16) with the aforementioned identified parameters] and the experimental frequency response plots for a constant applied force level equal to $F = 5$ N. As mentioned previously two wire thicknesses were used to realize the nonlinearity of the NES, yielding nonlinear stiffness characteristics equal to 4×10^7 and 7.1×10^7 N/m³, respectively. Figure 8.30 displays the steady state dynamics of the thin wire case, while Figure 8.31 the steady state dynamics corresponding to the thick wire case. The experimental

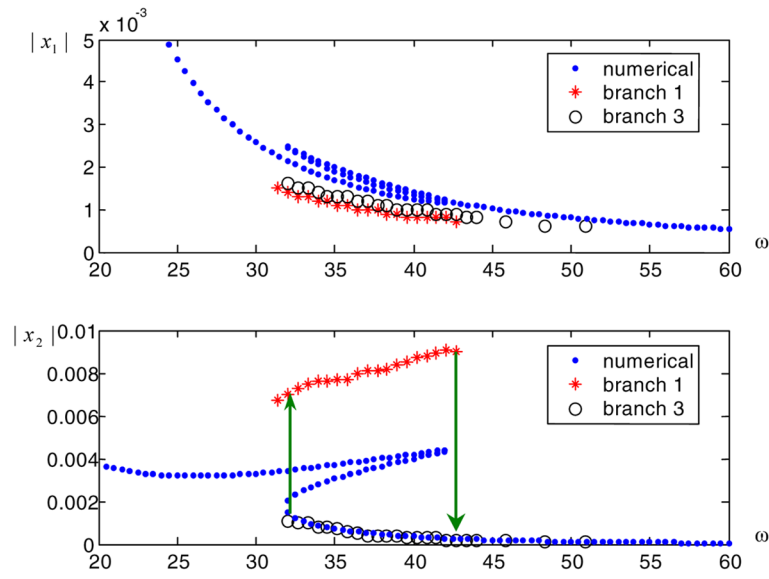


Fig. 8.30 Theoretical and experimental frequency responses for thin-wire stiffness nonlinearity.

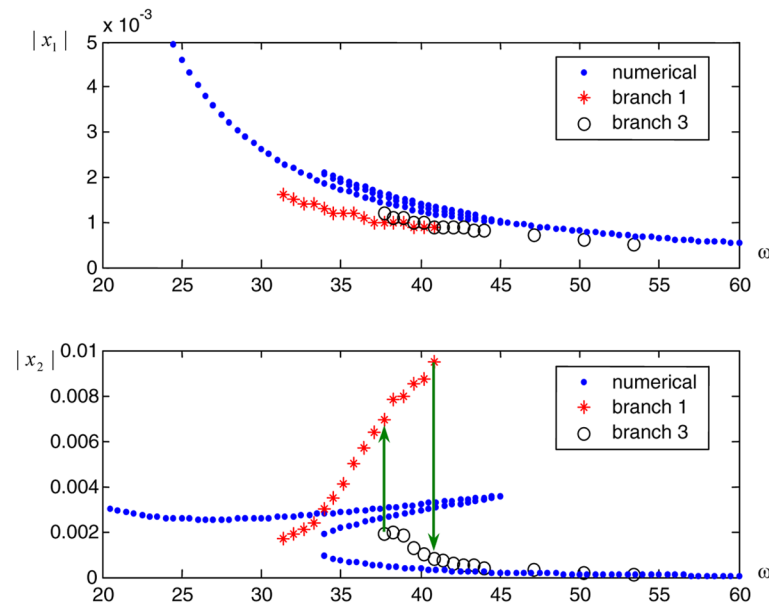


Fig. 8.31 Theoretical and experimental frequency responses for thick-wire stiffness nonlinearity.

results confirm the qualitative features of the nonlinear dynamics predicted by the theoretical analysis. Steady state TET from the linear oscillator to the NES is observed in the range 30–42 rad/s for the thin-wire and 37–41 rad/s for the thick-wire configuration, leading to confinement of the steady state motion to the nonlinear attachment. Moreover, in these frequency ranges the co-existence of the two types of the steady state solutions predicted by theory is confirmed, as well as the two sudden transitions (jumps) for increasing or decreasing excitation frequency and the realization of the nonlinear hysteresis phenomenon. We note that just before the forward jump (from high to low NES motion), the amplitude of the NES is nearly nine times (for both thin and thick wires) that of the linear oscillator, which represents an even better nonlinear motion confinement than that predicted by theory.

It is interesting to note that the experimental transition band is close to that predicted from numerical simulations – the theoretical transition ranges were 32–42 rad/s for the thin-wire configuration and 34–45 rad/s for the thick-wire one. The thin-wire case presented a better match between the experimental data and the numerical simulations, since the essential cubic stiffness was realized with more accuracy in that case; indeed, it is easier to clamp a thin wire rigidly, without introducing any initial pretension (as the theoretical model requires). Moreover, the experimental responses of the primary (shaker armature) match very well that of the numerical result. Note that we arrived at the conclusion that branch 1 and branch 3 are very close to each other from both the experimental result and numerical result of the shaker armature response, and both experimental and numerical results for the response of the shaker armature have similar trends; that is, the response decreases gradually for gradual increases of the forcing frequency.

However, we also note that there is fairly large disagreement in the magnitude of the responses for the NES compared with the experimental measurements. This discrepancy is attributed mainly to the uncertain characterization of the nonlinear stiffness of the NES. We recall that in deriving the theoretical cubic approximation for the essential stiffness nonlinearity of the NES we omitted higher-order nonlinearities of odd degree that might affect the response at relatively high resonance amplitudes (in fact, the experimental response for the low-amplitude branch matches very well that of the numerical result). Moreover, the theoretical modeling of the nonlinear stiffness was based on clamped boundary conditions of the piano wire, which can be realized only approximately in an experimental setup; in fact, a certain amount of slipping of the wire at the boundaries is unavoidable during the experiment. This uncertainty in the boundary conditions might also affect the nonlinear performance of the wire configuration. Nevertheless, there is satisfactory qualitative agreement between theory and experiment, and, more importantly, the spatial confinement property predicted by the numerical simulations is fully verified by the experimental results.

References

*ReferencesReferencesReferences

- Feldman, M., Non-linear system vibration analysis using Hilbert Transform – I. Free vibration analysis method ‘Freevib’, *Mech. Syst. Signal Proc.* **8**, 119–127, 1994.
- Gourdon, E., Coutel, S., Lamarque, C.H., Pernot, S., Nonlinear energy pumping with strongly nonlinear coupling: Identification of resonance captures in numerical and experimental results, in *Proceedings of the 20th ASME Biennial Conference on Mechanical Vibration and Noise*, Long Beach, CA, USA, Sept. 24–28, 2005.
- Jiang, X., McFarland, D.M., Bergman, L.A., Vakakis, A.F., Steady state passive nonlinear energy pumping in coupled oscillators: Theoretical and experimental results, *Nonl. Dyn.* **33**, 87–102, 2003.
- Kerschen, G., Lenaerts, V., Marchesiello, S., Fasana, A., A frequency domain vs. a time domain identification technique for nonlinear parameters applied to wire rope isolators, *J. Dyn. Syst. Meas. Control* **123**, 645–650, 2001.
- Kerschen, G., McFarland, D.M., Kowtko, J., Lee, Y.S., Bergman, L.A., Vakakis, A.F., Experimental demonstration of transient resonance capture in a system of two coupled oscillators with essential stiffness nonlinearity, *J. Sound Vib.* **299**(4–5), 822–838, 2007.
- Masri, S.F., Caughey, T.K., A nonparametric identification technique for nonlinear dynamic systems, *J. Appl. Mech.* **46**, 433–441, 1979.
- McFarland, D.M., Bergman, L.A., Vakakis, A.F., Experimental study of non-linear energy pumping occurring at a single fast frequency, *Int. J. Nonlinear Mech.* **40**, 891–899, 2005a.
- McFarland, D.M., Kerschen, G., Kowtko, J.J., Lee, Y.S., Bergman, L.A., Vakakis, A.F., Experimental investigation of targeted energy transfer in strongly and nonlinearly coupled oscillators, *J. Acoust. Soc. Am.* **118**, 791–799, 2005b.
- Van Overschee, P., De Moor B., *Subspace Identification For Linear Systems: Theory, Implementation, Applications*, Kluwer Academic Publishers, Boston, 1996.

Chapter 9

Suppression of Aeroelastic Instabilities through Passive Targeted Energy Transfer

The first practical application of TET concerns passive suppression of aeroelastic instabilities in rigid in-flow wings. We show that the capacity of the essentially nonlinear NES to passively absorb vibration energy from a primary structure in a broadband fashion, paves the way for robust partial or complete suppression of limit cycle oscillations (LCOs) developing in in-flow wings. Our systematic study of this passive instability suppression commences with a simplified model, the van der Pol oscillator, which can be considered as the prototypical system exhibiting an LCO instability. Then we discuss the nonlinear dynamics causing instability in a two-DOF model of an in-flow rigid wing, by means of a reduced-order technique based on slow-fast decomposition of its dynamics. Quasi-steady flow is assumed in the particular model used in this study. Then, we demonstrate that the addition of a lightweight SDOF NES affects drastically the dynamics of the wing, resulting in new dynamical phenomena that, under certain conditions, lead to partial or even complete LCO suppression. An extensive experimental program undertaken with wind tunnel tests fully confirms the theoretical predictions and validates the TET-based design. We conclude this section by performing bifurcation analysis of the dynamics of the integrated wing-NES system; by demonstrating that the use of alternative NES configurations, such as, MDOF NESs enhances the robustness of LCO suppression; and by providing some preliminary results on the efficacy of the NES to suppress instabilities in wings in unsteady flow.

9.1 Suppression of Limit-Cycle Oscillations in the van der Pol Oscillator

The term ‘van der Pol oscillator’ originally referred to an electrical circuit consisting of resistors, inductance coils, a capacitor, and a triode with two DC power sources. When power is supplied, the current exhibits steady state periodic oscillations; namely, limit cycle oscillations (LCOs) (Nayfeh and Mook, 1995). The van der Pol (VDP) oscillator can be derived via a coordinate transformation from a me-

chanically analogous system, the Rayleigh oscillator, which possesses a damping force of the form $\varepsilon(\dot{u} - \dot{u}^3)$ where u is a displacement variable (analogous to the current variable in the electric circuit) and ε is a parameter; in this case, the displacement u exhibits LCOs. In nonlinear aeroelastic problems, similar types of equations were employed in phenomenological descriptions of nonlinear motions of in-flow bluff bodies possessing LCOs (Skop and Griffin, 1973; Griffin and Skop, 1973; Dowell, 1981).

Regarding suppression of self-excited vibrations, some progress has been reported in the literature. For example, under parametric or autoparametric excitation, full vibration cancellation was observed for some system parameter ranges (Tondl et al., 2000; Fatimah and Verhulst, 2003). Another paradigm (Ko et al., 1997; Friedmann et al., 1997) utilized adaptive control to suppress LCOs developing in a wing due to aeroelastic effects. All these suppression strategies require an active control input, that is, they need external energy for their realization. Note that, for the case of LCO elimination through parametric excitation, the secondary subsystem is effective only at narrow frequency bands of the primary system.

On the other hand, in recent works it was reported that it is possible to apply passive (i.e., requiring no external energy source) broadband vibration control to eliminate self-excited oscillations, by means of grounded or ungrounded local nonlinear energy sinks (NESs) (Lee et al., 2004, 2005), inducing TET (Vakakis and Gendelman, 2001; Vakakis et al., 2003; Kerschen et al., 2006a). For some parameter domains, one can obtain complete elimination of LCOs, and the robustness of suppression turns out to depend on the bifurcation structure of the steady state dynamics. The LCO suppression or elimination is realized through one-way, irreversible transfer of energy from the primary system (the VDP oscillator) to the nonlinear attachment (the NES). Ungrounded NESs are more practical, since they can be applied to structural components such as aircraft wings far from the ground; they also turn out to possess richer dynamics and be more effective as their masses decrease, a feature which makes them very attractive from a practical design point of view. For grounded NES configurations, the reverse holds; that is, they become more effective as their masses increase [see Lee et al. (2005a) and the discussion in Section 3.1].

In this study, we consider a mechanical VDP oscillator and regard it as the representative aeroelastic system possessing LCOs above some critical parameter values. We show that by adding an NES we can efficiently suppress or even completely eliminate these LCOs. We also perform steady state bifurcation analyses of steady state motions by means of numerical continuation utilizing both the MATCONT Matlab® package, developed by Dhooge et al. (2003), and Kubíček's method (1976), in order to gain an understanding of the dynamical mechanisms that govern LCO suppression. Moreover, we wish to relate the topology of bifurcations of the steady state dynamics to the robustness of LCO suppression in this system. We end up this application with some concluding remarks. The analysis follows closely (Lee et al., 2006).

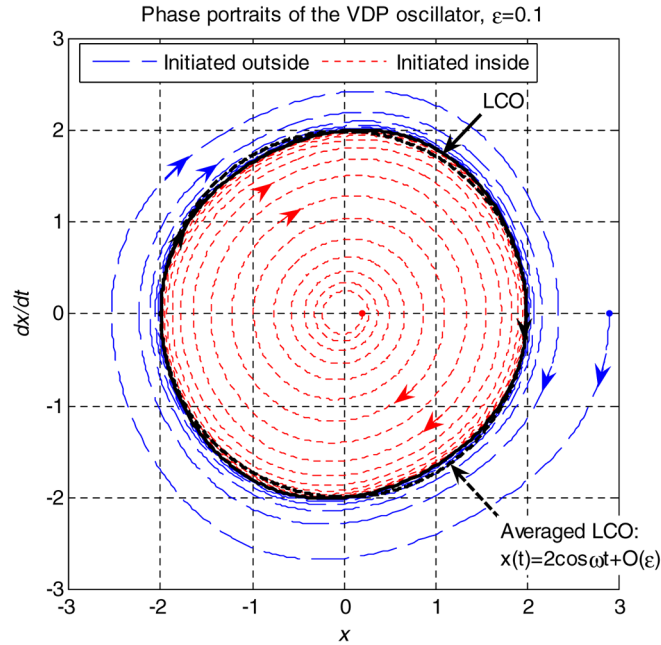


Fig. 9.1 Phase portraits for the van der Pol oscillator ($\varepsilon = 0.1$).

9.1.1 VDP Oscillator and NES Configurations

We consider the VDP oscillator,

$$\ddot{x} - \varepsilon \dot{x}(1 - x^2) + x = 0, \quad \varepsilon > 0$$

For $0 < \varepsilon \ll 1$, the equilibrium point $(0,0)$ is always an unstable spiral. There exists a stable ω -limit set (or limit cycle) on which the solution can be approximated by averaging in the form, $x(t) = 2 \cos \omega t + O(\varepsilon)$, where the frequency is given by $\omega = 1 - \varepsilon^2/16 + O(\varepsilon^3)$ (Guckenheimer and Holmes, 1983). Figure 9.1 depicts the LCO of the VDP oscillator in the phase plane when $\varepsilon = 0.1$, and shows that there is small deviation between the original and averaged solutions [of $O(\varepsilon)$]. We wish to study the suppression of the LCO of the VDP oscillator by adding a lightweight NES to it. Throughout this study we will assume that ε is the small parameter of the problems considered, and assign it the value $\varepsilon = 0.01 \ll 1$.

We will consider two alternative NES attachments, namely, grounded and ungrounded NESs, as depicted in Figure 9.2. We designate the corresponding configurations of VDP oscillators with grounded and ungrounded NESs as VDPNES₁ and VDPNES₂, respectively. The grounded NES (labeled as NES₁) is linearly coupled to the VDP oscillator, whereas the ungrounded NES (NES₂) is coupled to the VDP

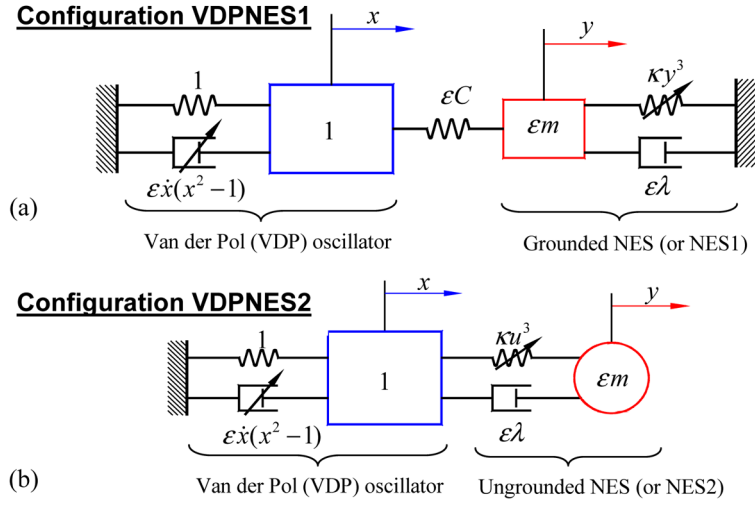


Fig. 9.2 System configuration with (a) grounded (VDPNES₁) and (b) ungrounded NES (VDPNES₂).

oscillator through essentially nonlinear stiffness in parallel to a viscous damping element.

The equations of motion for configuration VDPNES₁ (Figure 9.2a – Configuration I in the notation of Section 3.1) are expressed as

$$\begin{aligned}\ddot{x} - \varepsilon\dot{x}(1 - x^2) + x + \varepsilon C(x - y) &= 0 \\ \varepsilon m\ddot{y} + \varepsilon\lambda\dot{y} + \kappa y^3 + \varepsilon C(y - x) &= 0\end{aligned}\quad (9.1)$$

where x and y are the displacements of the VDP and NES masses, respectively; εm is the ratio of the NES and VDP masses, $\varepsilon\lambda$ the damping coefficient, εC , the linear coupling stiffness, and κ the nonlinear stiffness coefficient.

The equations of motion for configuration VDPNES₂ (Figure 9.2b – Configuration II in the notation of Section 3.1) are given by

$$\begin{aligned}\ddot{x} - \varepsilon\dot{x}(1 - x^2) + x + \varepsilon\lambda(\dot{x} - \dot{y}) + \kappa(x - y)^3 &= 0 \\ \varepsilon m\ddot{y} + \varepsilon\lambda(\dot{y} - \dot{x}) + \kappa(y - x)^3 &= 0\end{aligned}\quad (9.2)$$

where similar definitions for the parameters hold. The underlying Hamiltonian dynamics, as well as the transient damped dynamics of NESs connected to single degree-of-freedom linear oscillators were studied in Vakakis and Gendelman (2001) and Vakakis et al. (2003) for NES₁, and in Kerschen et al. (2006a) and Lee et al. (2005) for NES₂. Moreover, the dynamics of these NES configurations have been studied extensively in previous chapters of this monograph.

First, we perform computational parametric studies of systems (9.1) and (9.2) to identify parameter subsets where the LCO of the VDP oscillator can be suppressed or even completely eliminated. For this purpose, we restrict the NES parameters to the ranges, $0.01 \leq \varepsilon m \leq 0.5$, $0.01 \leq \kappa \leq 1.0$, and $0.01 \leq \varepsilon \lambda \leq 0.3$ for NES₁ and $0.01 \leq \varepsilon \lambda \leq 0.1$ for NES₂. For configuration VDPNES₁, two cases of linear coupling stiffness are considered: $\varepsilon C = 1.0$ (weaker) and $\varepsilon C = 10.0$ (stronger). We select initial conditions for the numerical simulations outside the LCO of the uncoupled VDP oscillator [specifically, $(x(0), y(0), \dot{x}(0), \dot{y}(0)) = (3.5, 0, 0, 0)$], and integrate the equations of motion (9.1a) and (9.1b) for sufficiently long time to ensure that the initial transients die out. Then we compute the root-mean-square (r.m.s.) amplitude of the corresponding steady state response. Since the LCO response of the uncoupled VDP oscillator possesses an r.m.s. amplitude equal to $\sqrt{2}$, steady state responses with r.m.s. amplitudes less than $\sqrt{2}$ imply suppression of the LCO.

Figures 9.3 and 9.4 depict contour plots of VDP r.m.s. amplitudes on the minimum parameter planes, and on the sections corresponding to mass ratio of 5% and nonlinear stiffness of 0.2 for configurations VDPNES₁ and VDPNES₂, respectively. In both cases, we observe that very small damping (e.g., 1%) causes complicated (or non-uniform) steady state amplitudes of the VDP oscillator. For the grounded NES configuration (Figure 9.3), the steady state amplitudes of the VDP oscillator vary relatively uniformly on the parameter plane whether the linear coupling is weak or strong. For example, on the plane corresponding to $\varepsilon m = 5\%$ ($\kappa = 0.2$), the steady state amplitudes become smaller as the damping increases; that is, they seem to be independent of the nonlinear stiffness (the mass ratio). It is generally observed that strong damping leads to better suppression results for the grounded NES. On the other hand, we do not observe uniform behavior of steady state r.m.s. amplitudes for the ungrounded NES (Figure 9.4). Instead, a larger mass ratio, stronger damping and sufficiently weaker nonlinear coupling tend to produce a larger degree of suppression. *A general conclusion drawn from these plots, however, is that the addition of light passive (but essentially nonlinear) NESs may completely eliminate the LCOs of the VDP oscillator over relatively wide parameter ranges.* More systematic studies of the effects of the parameters will be provided later utilizing the method of numerical continuation.

In Figure 9.5, we show that an NES with an even small mass ratio can passively eliminate the LCO of the VDP oscillator. Evidently, the grounded NES₁ appears to be more effective in eliminating the LCO in a shorter period compared to the ungrounded NES₂; however, such isolated simulations cannot be used to draw general conclusions regarding the relative effectiveness of the two NES configurations in suppressing LCOs. Indeed, this relative performance ought to be evaluated by considering aspects such as robustness of LCO suppression over wide NES parameter ranges, as well as issues of applicability of these NES configurations to practical designs.

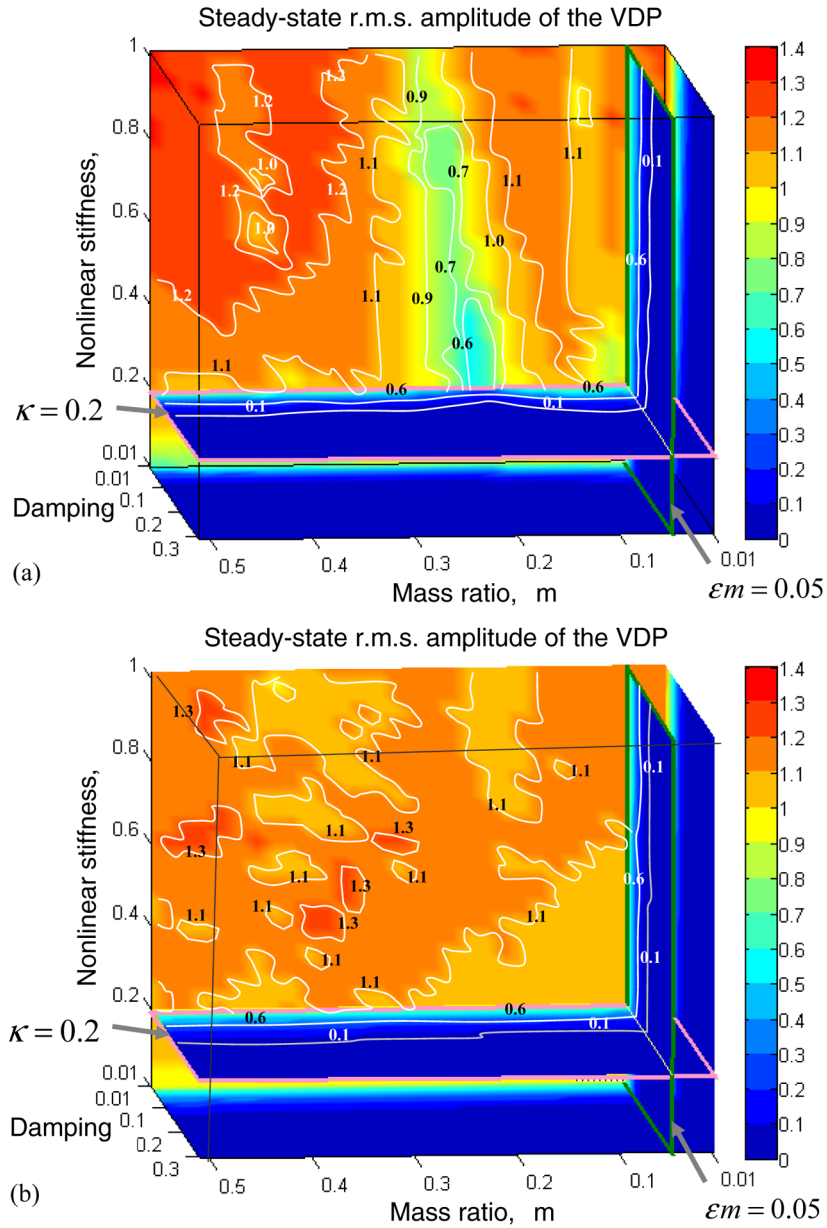


Fig. 9.3 Contour plots of steady state r.m.s. amplitudes of (grounded) configuration VDPNES₁ with respect to mass, damping, and nonlinear stiffness coefficient of the NES: (a) weaker linear coupling ($\epsilon C = 1.0$); (b) stronger linear coupling ($\epsilon C = 10.0$).

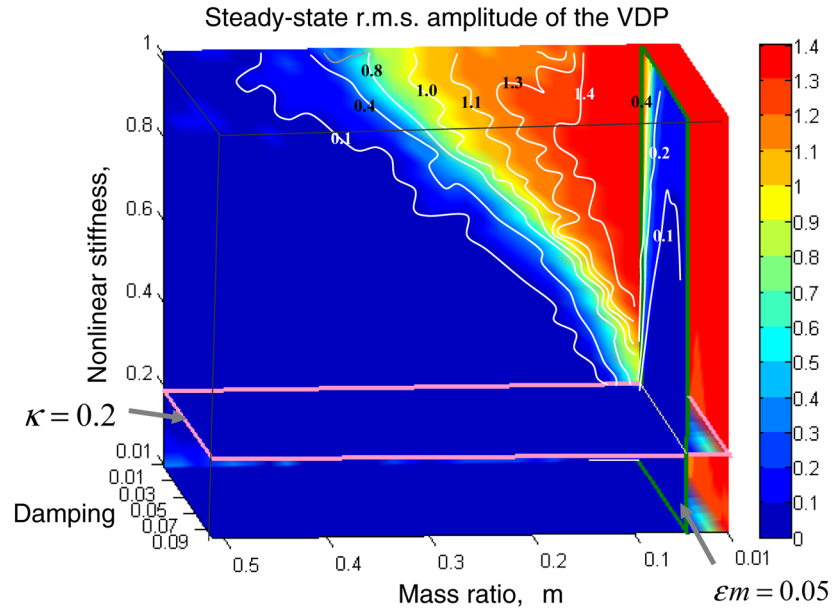


Fig. 9.4 Contour plots of steady state r.m.s. amplitudes of (ungrounded) configuration VDPNES₂ with respect to mass, damping, and nonlinear stiffness coefficient of the NES.

9.1.2 Transient Dynamics

In this section, we construct slow flow dynamical models in order to analytically study the transient and steady state motions of the VDP oscillator with attached NES. This is achieved by applying the complexification-averaging technique (CX-A) of Manevitch (2001). The analytical study of the transient dynamics will reveal the dynamical mechanism responsible for LCO suppression, whereas the study of the steady state dynamics will address issues of robustness of LCO suppression.

9.1.2.1 Slow Flow Model

Following the CX-A technique, we introduce at this point the new complex variables $\psi_1 = \dot{y} + jy$ and $\psi_2 = \dot{x} + jx$ where $j^2 = -1$, and substitute them into the equations of motion (9.1a, b) through the relations

$$\begin{aligned} y &= \frac{1}{2j}(\psi_1 - \psi_1^*), & \dot{y} &= \frac{1}{2}(\psi_1 + \psi_1^*), & \ddot{y} &= \dot{\psi}_1 - \frac{j}{2}(\psi_1 + \psi_1^*) \\ x &= \frac{1}{2j}(\psi_2 - \psi_2^*), & \dot{x} &= \frac{1}{2}(\psi_2 + \psi_2^*), & \ddot{x} &= \dot{\psi}_2 - \frac{j}{2}(\psi_2 + \psi_2^*) \end{aligned} \quad (9.3)$$

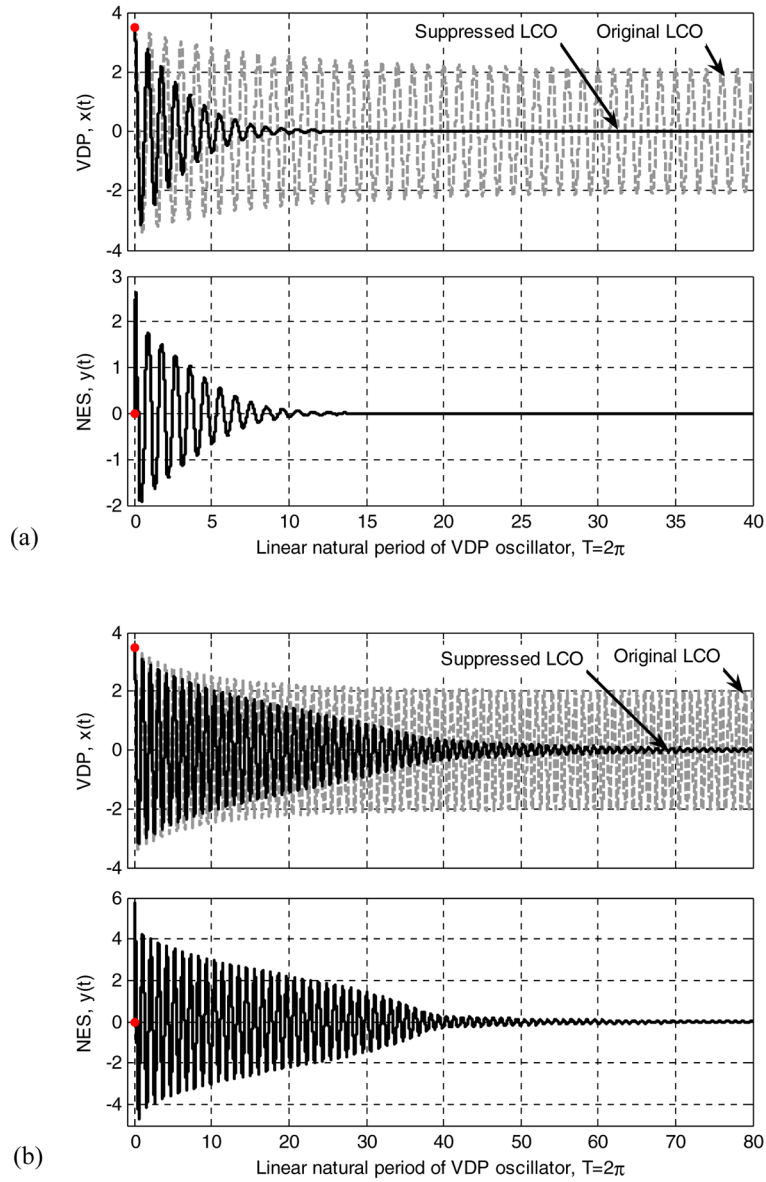


Fig. 9.5 Transient responses depicting LCO elimination for initial conditions $(x(0), y(0), \dot{x}(0), \dot{y}(0)) = (3.5, 0, 0, 0)$: (a) configuration $VDPNES_1$, $\epsilon_m = 5\%$, $\epsilon_\lambda = 15\%$, $\kappa = 0.2$, $\epsilon_C = 1.0$; (b) configuration $VPDNES_2$, $\epsilon_m = 5\%$, $\epsilon_\lambda = 5\%$, $\kappa = 0.2$.

where as usual, the asterisk denotes complex conjugate. Then, we express the complex variables in polar form:

$$\psi_1(t) = \varphi_1(t)e^{jt}, \quad \psi_2(t) = \varphi_2(t)e^{jt} \quad (9.4)$$

where $\varphi_i(t)$, $i = 1, 2$, represent the slowly-varying complex amplitudes, and e^{jt} the fast-varying components at the (linearized) natural frequency of the VDP oscillator. By expressions (9.3) we partition the transient dynamics into slow and fast components, that is, we make the assumption that the transient responses of systems (9.1) and (9.2) are composed of fast oscillations that are modulated by slowly-varying envelopes.

Averaging out all fast-frequency components with frequencies higher than unity, we obtain a set of two complex-valued modulation equations that govern the slow flow dynamics. For configuration VDPNES₁, the slow flow dynamical model is expressed as

$$\begin{aligned} \dot{\varphi}_1 &= -\frac{1}{2} \left[\frac{\lambda}{m} + j \left(1 - \frac{C}{m} \right) \right] \varphi_1 - j \frac{C}{2m} \varphi_2 + j \frac{3\kappa}{8\epsilon m} \varphi_1 |\varphi_1|^2 \\ \dot{\varphi}_2 &= -j \frac{\epsilon C}{2} \varphi_1 + \frac{1}{2} (\epsilon + j\epsilon C) \varphi_2 - \epsilon \frac{1}{8} \varphi_2 |\varphi_2|^2 \end{aligned} \quad (9.5)$$

whereas for VDPNES₂ it reads

$$\begin{aligned} \dot{\varphi}_1 &= \frac{1}{2} \left(j + \frac{\lambda}{m} \right) \varphi_1 + \frac{\lambda}{2m} \varphi_2 + j \frac{3\kappa}{8\epsilon m} (\varphi_1 - \varphi_2) |\varphi_1 - \varphi_2|^2 \\ \dot{\varphi}_2 &= \frac{\epsilon\lambda}{2} \varphi_1 + \frac{\epsilon}{2} (1 - \lambda) \varphi_2 - \frac{\epsilon}{8} \varphi_2 |\varphi_2|^2 - j \frac{3\kappa}{8} (\varphi_1 - \varphi_2) |\varphi_1 - \varphi_2|^2 \end{aligned} \quad (9.6)$$

These represent the averaged slow flows of the corresponding VDP-NES configurations.

In Figures 9.6 and 9.7, we examine the validities of the averaged systems by comparing the averaged responses to the (numerically) exact solutions. Validation is demonstrated both in cases when the LCO survives the addition of the NES, and also in cases when it is suppressed. Although the systems under consideration do not necessarily possess weak nonlinear terms, we may recall from the classical averaging theorem that an $O(\epsilon)$ approximation for stable dynamics of vector fields is guaranteed up to a time scale of $O(1/\epsilon)$ (Sanders and Verhulst, 1985). From the comparisons depicted in Figures 9.6 and 9.7 we verify that the averaged systems (9.5) and (9.6) provide satisfactory approximations to the original dynamics. The only small deviation can be found in the case when the LCO is sustained in configuration VDPNES₁ (Figure 9.6a). In this case the exact NES response possesses an additional fast, high-frequency component, e^{3jt} , which is filtered out in our averaging process. For a more precise approximation we need to include this high-frequency term, yielding a two-frequency averaged slow dynamical system (see, for example the CX-A analysis carried out in Sections 3.3.2.2 and 3.3.2.3); however, this will not

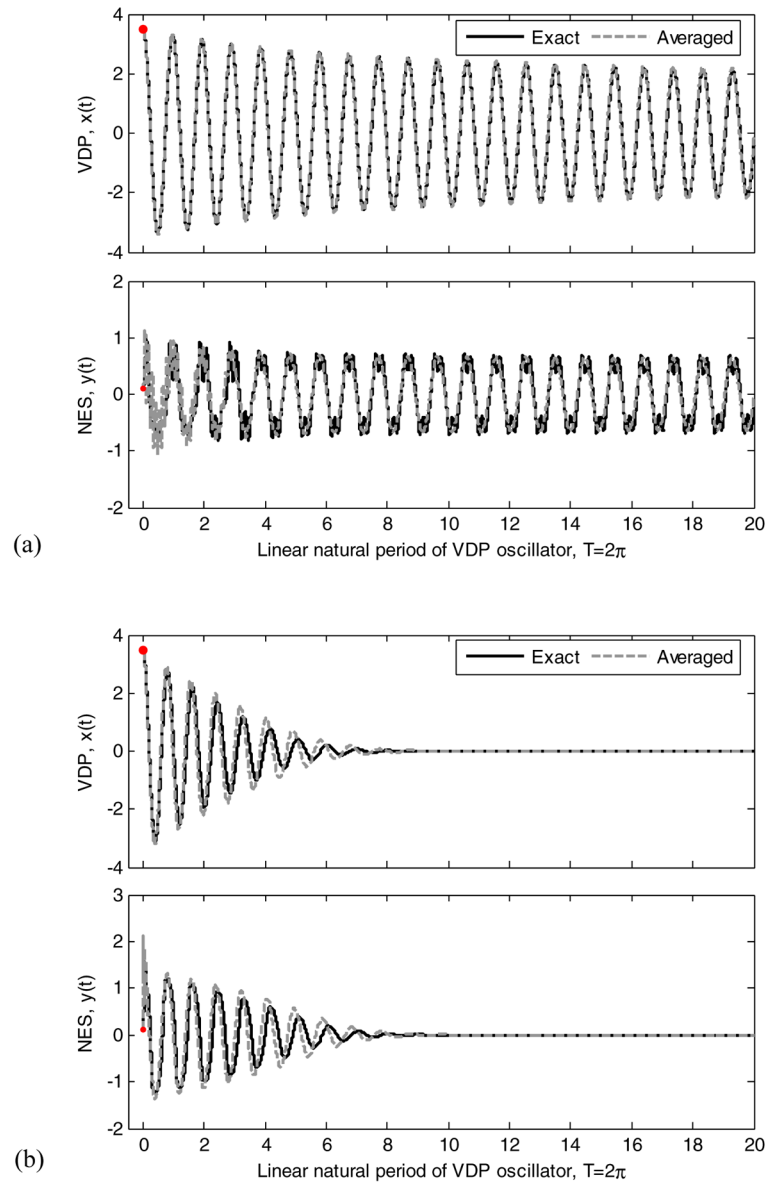


Fig. 9.6 Validity of the averaged slow dynamics model for configuration VPDNES₁, (a) when the LCO survives ($\varepsilon m = 5\%$, $\kappa = 1.0$, $\varepsilon \lambda = 1\%$, $\varepsilon C = 0.1$), and (b) when the LCO is eliminated ($\varepsilon m = 5\%$, $\kappa = 1.0$, $\varepsilon \lambda = 30\%$, $\varepsilon C = 1.0$); initial conditions are given by $(x(0), y(0), \dot{x}(0), \dot{y}(0)) = (3.5, 0.1, 0, 0)$.

be considered in this study. Instead, we will examine this high-frequency component via numerical wavelet transformations later in this section.

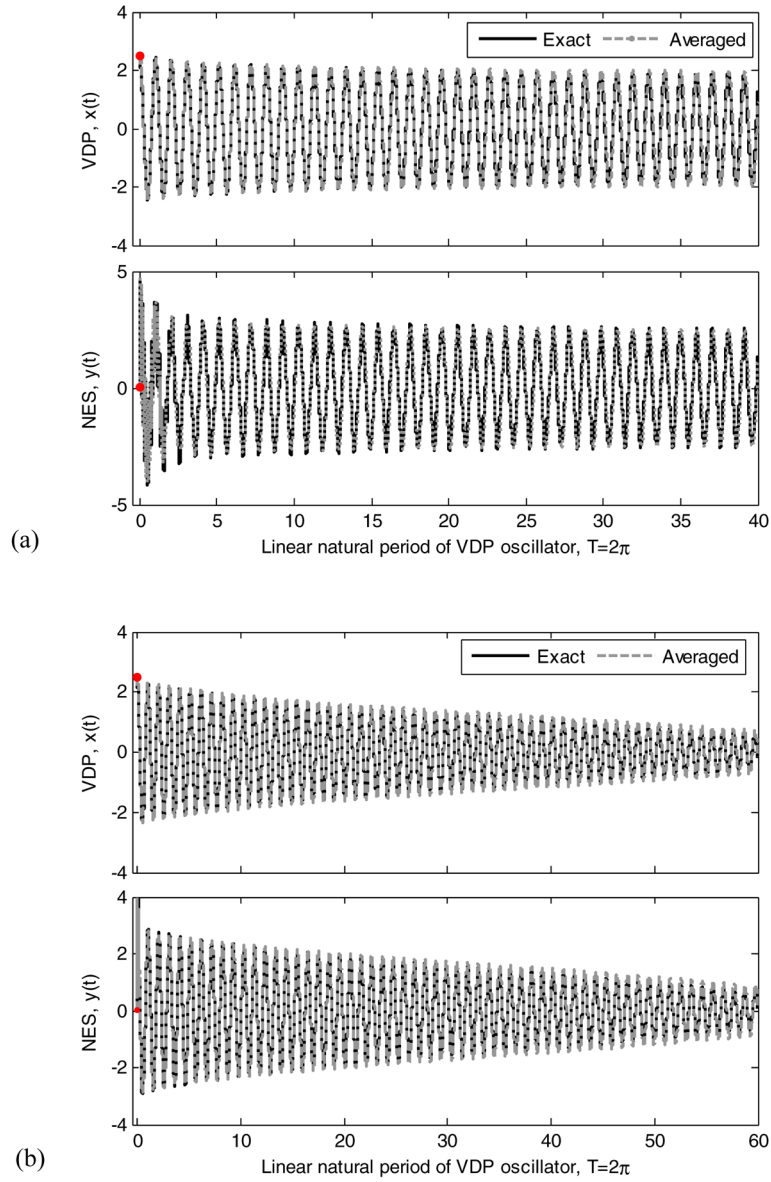


Fig. 9.7 Validity of the averaged slow dynamics model for configuration VPDNES₂, (a) when the LCO survives ($\epsilon m = 5\%$, $\kappa = 1.0$, $\epsilon \lambda = 1\%$), and (b) when the LCO is eliminated ($\epsilon m = 5\%$, $\kappa = 1.0$, $\epsilon \lambda = 10\%$); initial conditions are given by $(x(0), y(0), \dot{x}(0), \dot{y}(0)) = (2.5, 0.01, 0, 0)$.

Returning now to the complex modulation equations (9.5) and (9.6), we express the slowly-varying complex amplitudes in polar form

$$\varphi_i(t) = \alpha_i(t)e^{j\beta_i(t)}, \quad \alpha_i, \beta_i \in R, \quad i = 1, 2 \quad (9.7)$$

where $\alpha_i(t)$ and $\beta_i(t)$ represent the slowly-varying amplitude and phase of each degree of freedom, respectively. Substituting into the averaged systems (9.5) and (9.6), and setting separately equal to zero the real and imaginary parts, we obtain two sets of real modulation equations. For configuration VDPNES₁, these are written as

$$\begin{aligned} \dot{\alpha}_1 &= -\frac{\lambda}{2m}\alpha_1 - \frac{C}{2m}\alpha_1 \sin \phi \\ \dot{\alpha}_2 &= \frac{\varepsilon}{8}(4 - \alpha_2^2)\alpha_2 + \frac{\varepsilon C}{2}\alpha_1 \sin \phi \\ \alpha_1\alpha_2\dot{\phi} &= \frac{1}{2}\left(\frac{C}{m} - 1 - \varepsilon C\right)\alpha_1\alpha_2 + \frac{3\kappa}{8\varepsilon m}(\varepsilon m\alpha_1^2 - \alpha_2^2)\cos \phi \end{aligned} \quad (9.8)$$

whereas, for VDPNES₂, they are given by

$$\begin{aligned} \dot{\alpha}_1 &= -\frac{\lambda}{2m}\alpha_1 + \frac{\lambda}{2m}\alpha_2 \cos \phi - \frac{3C}{8\varepsilon m}\alpha_2(\alpha_1^2 + \alpha_2^2)\sin \phi + \frac{3C}{8\varepsilon m}\alpha_1\alpha_2^2 \sin 2\phi \\ \dot{\alpha}_2 &= \frac{\varepsilon\lambda}{2}\alpha_1 \cos \phi + \frac{\varepsilon}{2}(1 - \lambda)\alpha_2 - \frac{\varepsilon}{8}\alpha_2^3 \\ &\quad + \frac{3C}{8}\alpha_1(\alpha_1^2 + \alpha_2^2)\sin \phi - \frac{3C}{8}\alpha_1^2\alpha_2 \sin 2\phi \\ \alpha_1\alpha_2\dot{\phi} &= -\frac{1}{2}\alpha_1\alpha_2 + \frac{3C}{8\varepsilon m}\alpha_1\alpha_2(\alpha_1^2 + 2\alpha_2^2) - \frac{3C}{8}\alpha_1\alpha_2(2\alpha_1^2 + \alpha_2^2) \\ &\quad - \frac{\lambda}{2m}(\varepsilon m\alpha_1^2 + \alpha_2^2)\sin \phi + \frac{3C}{8\varepsilon m}\left[\varepsilon m\alpha_1^4 - \alpha_2^4 - 3(1 - \varepsilon m)\alpha_1^2\alpha_2^2\right]\cos \phi \\ &\quad - \frac{3C}{8\varepsilon m}\alpha_1\alpha_2(\varepsilon m\alpha_1^2 - \alpha_2^2)\cos 2\phi \end{aligned} \quad (9.9)$$

In the relations above, α_1 and α_2 are the envelopes of the amplitude of the NES and VDP oscillator, respectively, and $\phi \equiv \beta_1 - \beta_2$, the phase difference between the oscillations of the VDP oscillator and the NES.

The slow dynamical models (9.8) and (9.9) approximate the transient dynamics of the two NES configurations considered, and can be used to study the LCO suppression mechanism based on passive TET from the VDP oscillator to the NES.

9.1.2.2 LCO Suppression Mechanism

The LCO suppression mechanism is now explored by directly studying the transient dynamics. We consider two cases: (i) when the LCO either survives the action of the NES or is not effectively suppressed, and (ii) when the LCO is completely eliminated through TET from the VDP oscillator to the NES. As a first step, the transient responses of the system for initial conditions chosen outside or inside the LCO of the uncoupled VDP oscillator are plotted, and their amplitude and frequency contents are compared.

In addition, by studying the dynamics of the slow flows (9.8) or (9.9) with prescribed initial conditions, we can examine the behavior of orbits in the slow flow phase space $(\alpha_1, \alpha_2, \phi)$, and examine the possible existence of transient or permanent resonance captures (RCs) in the dynamics. If a resonance capture occurs, the phase variable ϕ exhibits *non-time-like* (but rather oscillatory) behavior (as discussed in Section 9.3, and also in Bosley and Kevorkian, 1992), and the corresponding trajectory in the $(\phi, \dot{\phi})$ plane appears in the form of a spiral. Specifically, when a 1:1 resonance capture occurs at a specific time instant $t = t_0$, the slow phase difference ϕ becomes small, and the frequencies of the VDP oscillator and the NES become ‘locked’ in an approximately 1:1 relationship up to times $t - t_0 = O(1)$. As discussed in Section 2.3, we distinguish between two types of resonance capture. *Transient resonance capture* (TRC) refers to the case when the resonance capture persists for a certain period of time [i.e., on the time scale $O(1/\varepsilon)$], followed by an escape from the resonance capture regime and subsequent time-like behavior of the slow phase difference ϕ . By contrast, *sustained resonance capture* (SRC) occurs when the resonance capture is permanent. We note that, since the slow flow models (9.8) and (9.9) are based on the assumption of a single fast frequency (identical for both the VDP oscillator and the NES), only 1:1 resonance captures can be modeled by the outlined slow flow analysis (higher-order RCs can be studied by including multiple fast frequency components in the derived slow flow models).

As shown in previous sections, another way for examining the transient dynamics is through application of numerical wavelet transforms (WTs). Moreover, WT spectra can be superimposed to appropriately defined frequency-energy plots (FEPs) to provide a clear interpretation of the damped dynamics in terms of the underlying Hamiltonian ones. As discussed previously, the purpose of superimposing the transient damped dynamics on FEPs is to show that for weak damping (negative for the VDP oscillator and positive for the NES) the evolutions of the transient responses of the damped systems in the frequency-energy plane follow closely branches of periodic orbits of the underlying Hamiltonian systems. To this end we need to evaluate the total instantaneous energy of both considered configurations, as outlined below.

The initial total energy for configuration VDPNES₁ is given by

$$E(0) = \frac{1}{2}(\dot{x}(0)^2 + \varepsilon m \dot{y}(0)^2) + \frac{1}{2}x(0)^2 + \frac{\varepsilon C}{2}(x(0) - y(0))^2 + \frac{\kappa}{4}y(0)^4 \equiv E_0 \quad (9.10)$$

whereas for VDPNES₂ it is given by

$$E(0) = \frac{1}{2}(\dot{x}(0)^2 + \varepsilon m \dot{y}(0)^2) + \frac{1}{2}x(0)^2 + \frac{\kappa}{4}(x(0) - y(0))^4 \equiv E_0 \quad (9.11)$$

For both NES configurations, we can numerically compute the energy generated or dissipated by the nonlinear damper in the VDP oscillator as

$$E_d^{\text{VDP}}(t) = \varepsilon \int_0^t \dot{x}(\tau)^2 (x(\tau)^2 - 1) d\tau \quad (9.12)$$

The energy dissipated by the NES can be expressed, for VDPNES₁, as

$$E_d^{\text{NES}}(t) = \varepsilon \lambda \int_0^t \dot{y}(\tau)^2 d\tau \quad (9.13)$$

and for VDPNES₂ as:

$$E_d^{\text{NES}}(t) = \varepsilon \lambda \int_0^t (\dot{x}(\tau) - \dot{y}(\tau))^2 d\tau \quad (9.14)$$

Thus, we express the total energy in the following way:

$$E^{\text{total}}(t) = E(0) - E_d^{\text{VDP}}(t) - E_d^{\text{NES}}(t) \quad (9.15)$$

for both configurations.

We then consider the energy exchange between the VDP oscillator and the NES, which is basically a competition between the nonlinear damping in the VDP oscillator (which either dissipates energy or feeds energy to the system) and the positive damping in the NES (which only dissipates energy). For this purpose, we define the energy components $E^{\text{VDP}}(t)$ and $E^{\text{NES}}(t)$ for each subsystem as

$$E^{\text{VDP}}(t) \equiv E_0^{\text{VDP}} - E_d^{\text{VDP}}(t), \quad E^{\text{NES}}(t) \equiv E_0^{\text{NES}} - E_d^{\text{NES}}(t) \quad (9.16)$$

where E_0^{VDP} or E_0^{NES} represents the initial energy imposed by the initial conditions, with the initial potential energy stored in the coupling stiffness shared equally by both degrees of freedom.

Figure 9.8 depicts the transient dynamics of configuration VDPNES₁ (with parameters $\varepsilon m = 5\%$, $\kappa = 1.0$, $\varepsilon \lambda = 1\%$, $\varepsilon C = 0.1$) for initial conditions outside the LCO of the uncoupled VDP oscillator given by $(x(0), y(0), \dot{x}(0), \dot{y}(0)) = (3.5, 0.01, 0, 0)$. All results are exact, resulting from numerical integration of system (9.1) with the exception of the plot of Figure 9.8b which depicts the dynamics of the averaged system (9.8). The time series depicted in Figure 9.8a indicate that the LCO of the VDP oscillator survives the presence of the NES. From the phase portrait $(\phi, \dot{\phi})$ depicted in Figure 9.8b, computed from the averaged system (9.8) with identical initial conditions, we can predict that a 1:1 SRC occurs when the LCO is retained. However, the WT analysis of the response (Figure 9.8c) indicates that the steady state LCO dynamics is captured into a 3:1 SRC. In order to study such subharmonic resonance captures, we would need to employ at least a two fast frequency slow dynamics model, however, this will not be considered in this study.

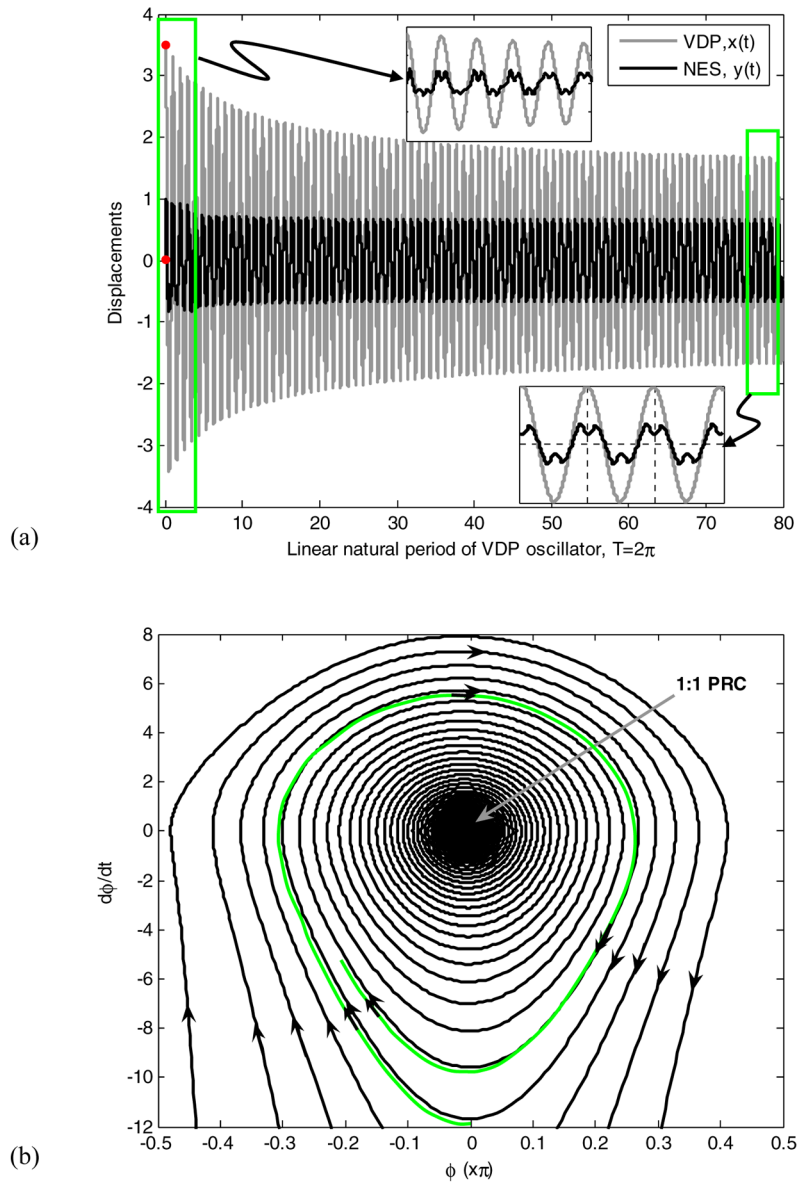


Fig. 9.8 Transient dynamics of configuration VDPNES₁ when the LCO survives, case of 3:1 SRC as total energy decreases: (a) time series; (b) motion on the plane $(\phi, \dot{\phi})$ for the averaged system (9.8); (c) instantaneous frequencies; (d) WT spectrum on the FEP; (e) energy exchange measures.

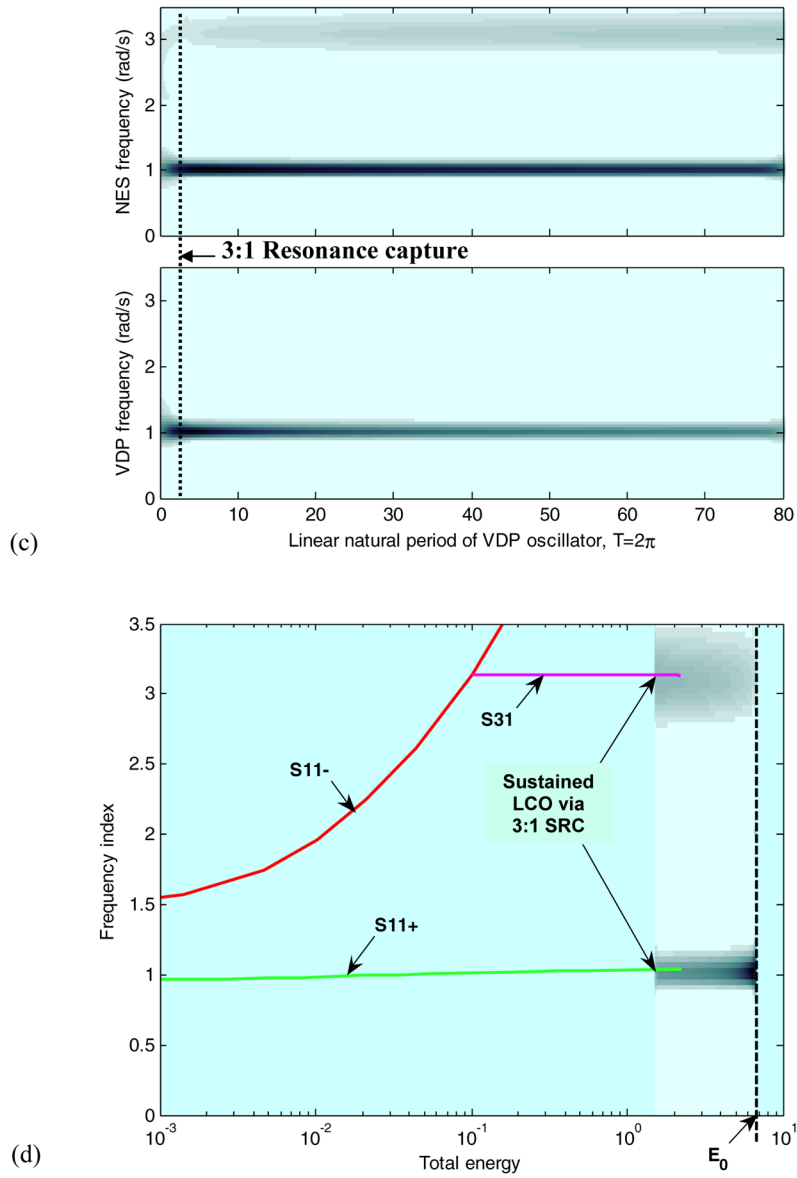


Fig. 9.8 Transient dynamics of configuration VDPNES₁ when the LCO survives, case of 3:1 SRC as total energy decreases: (c) instantaneous frequencies; (d) WT spectrum on the FEP.

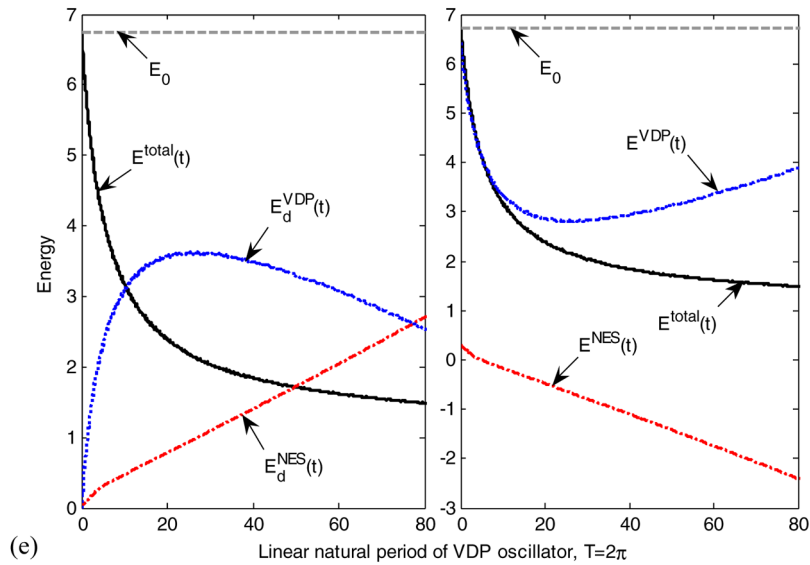


Fig. 9.8 Transient dynamics of configuration VDPNES₁ when the LCO survives, case of 3:1 SRC as total energy decreases: (e) energy exchange measures.

The 3:1 SRC becomes clearer if we superimpose the WT spectrum of the transient response on the FEP of the underlying Hamiltonian system which is derived by eliminating the damping terms from system (9.1); this is performed in Figure 9.8d where the WT spectrum of the relative displacement $x(t) - y(t)$ is plotted against the total instantaneous energy of the system. The initial state of the system is away from any periodic solutions of the underlying Hamiltonian system, but the response approaches the vicinity of and is finally captured in a 3:1 internal resonance manifold as the total energy decreases to reach the steady state LCO. This proves conclusively that the surviving LCO is the product of a 3:1 SRC.

We then compare the energy exchanges between the components of the system in Figure 9.8e. Since the motion is initiated outside the LCO of the uncoupled VDP oscillator, the total energy decreases until it reaches the steady state value corresponding to the surviving LCO. The energy dissipation by the NES is monotonically increasing with time. On the other hand, the nonlinear damper of the VDP oscillator initially dissipates energy up to time $20T$, where $T = 2\pi$ is the linear natural period of the VDP oscillator; afterwards it feeds energy into the system, decreasing monotonically. As a result, the energy fed by the VDP oscillator and the energy dissipated by the NES reach a balance to produce the surviving LCO. This type of sustained LCO is similar to vortex-induced resonant vibrations of a circular cylinder, where the fluid-structure interaction yielding LCOs of the cylinder immersed in the fluid flow, exhibits synchronization and lock-in between the vortex and vibration frequencies (Skop and Griffin, 1973; Griffin and Skop, 1973).

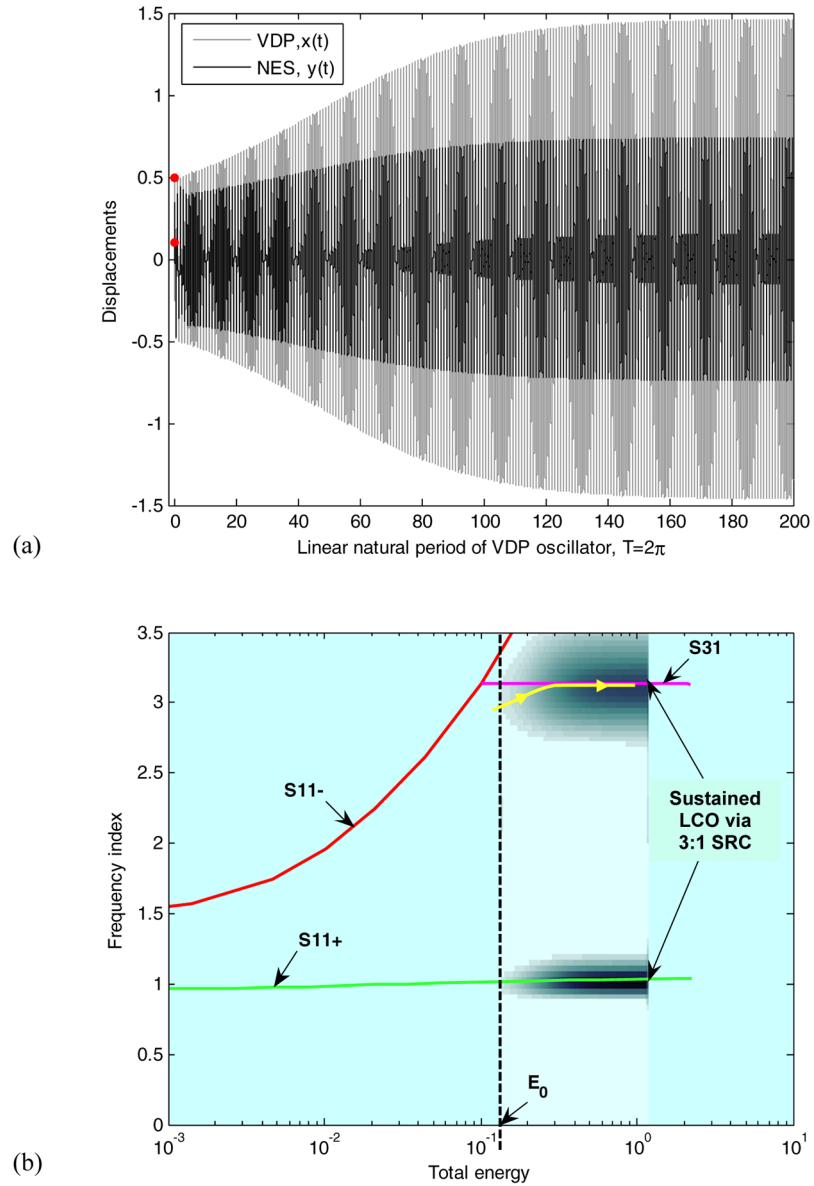


Fig. 9.9 Transient dynamics of configuration VDPNES₁ when the LCO survives, case of 3:1 SRC as total energy increases: (a) time series; (b) WT spectrum on the FEP.

Figure 9.9 depicts another possible case of the dynamics of $VDPNES_1$ with the LCO surviving the action of the NES, for motion initiated inside the LCO of the uncoupled VDP oscillator; in this case, only the time series and FEP are considered, for system parameters identical to the previous case. We note that the dynamics is captured by the 3:1 resonance manifold as the total energy increases.

We now examine the transient dynamics of configuration $VDPNES_1$ when the LCO is completely eliminated by the action of the NES. The only difference in parameters from the ones used for the simulations of Figure 9.8 is the damping of the NES, which in this case is taken equal to $\varepsilon\lambda = 0.1$. In Figure 9.10 we depict the exact transient dynamics of the system resulting from numerical integration of system (9.1), except for Figure 9.10b where the averaged dynamics [system (9.8)] is considered. The time series of Figure 9.10a indicates an initial 3:1 transient resonance capture (the NES possesses two frequency components equal to unity and three), which becomes a 1:1 resonance capture at the late stage of LCO suppression. This behavior is clearer when one inspects the WT analysis results depicted in Figure 9.10c. The slow flow model (9.8) predicts a 1:1 TRC as time increases (see Figure 9.10b), and, as discussed previously, it is not capable of modeling the initial 3:1 TRC. By studying the transient response superimposed on the FEP (Figure 9.10d) the TRCs and the associated transitions in the dynamics become clear. Initially the dynamics is captured close to the 3:1 resonance manifold of the underlying Hamiltonian system, and the resulting TRC is sustained for a certain period of time as the total energy decreases. As the energy reaches the value where the S_{31} –branch meets the S_{11} –branch, the dynamics escapes from 3:1 TRC and engages in 1:1 TRC. As energy decreases further and the LCO is completely eliminated, the dynamics escapes from 1:1 resonance capture at the later stage of the motion.

Examining the corresponding energy exchanges of Figure 9.10e, we clearly identify the reasons for LCO elimination. Contrary to the case when the LCO survives (Figure 9.8e), the energy dissipation by the NES counterbalances the energy supply provided by the nonlinear (negative) damping of the VDP oscillator. *It is interesting to note that the NES passively adjusts the rate of energy dissipation so to precisely counterbalance the energy input fed by the VDP oscillator.* Moreover, in this case the rates of energy dissipation or generation asymptotically reach steady state values, whereas the corresponding ones of Figure 9.8e are almost linearly increasing or decreasing as the LCO is retained. Therefore, for LCO elimination it is necessary that TET from the VDP oscillator to the NES should occur at a sufficiently fast time scale and be strong enough to overcome the energy fed by the nonlinear damper of the VDP oscillator.

Similar studies were performed for configuration $VDPNES_2$ with a mass ratio $\varepsilon m = 0.05$ and coefficient of essentially-nonlinear coupling stiffness equal to $\kappa = 1.0$. The damping values $\varepsilon\lambda = 1\%$ and $\varepsilon\lambda = 10\%$ were considered for the cases when the LCO survives or is eliminated by the action of the NES. Initial conditions were equal to $(x(0), y(0), \dot{x}(0), \dot{y}(0)) = (3.5, 0.1, 0, 0)$ for motions initiated outside the unperturbed LCO, and $(1.0, 1.0, 0, 0)$ for those initiated inside the unperturbed LCO. *Contrary to the configuration with grounded NES, in this case the underlying Hamiltonian system possesses a very complicated structure of periodic*

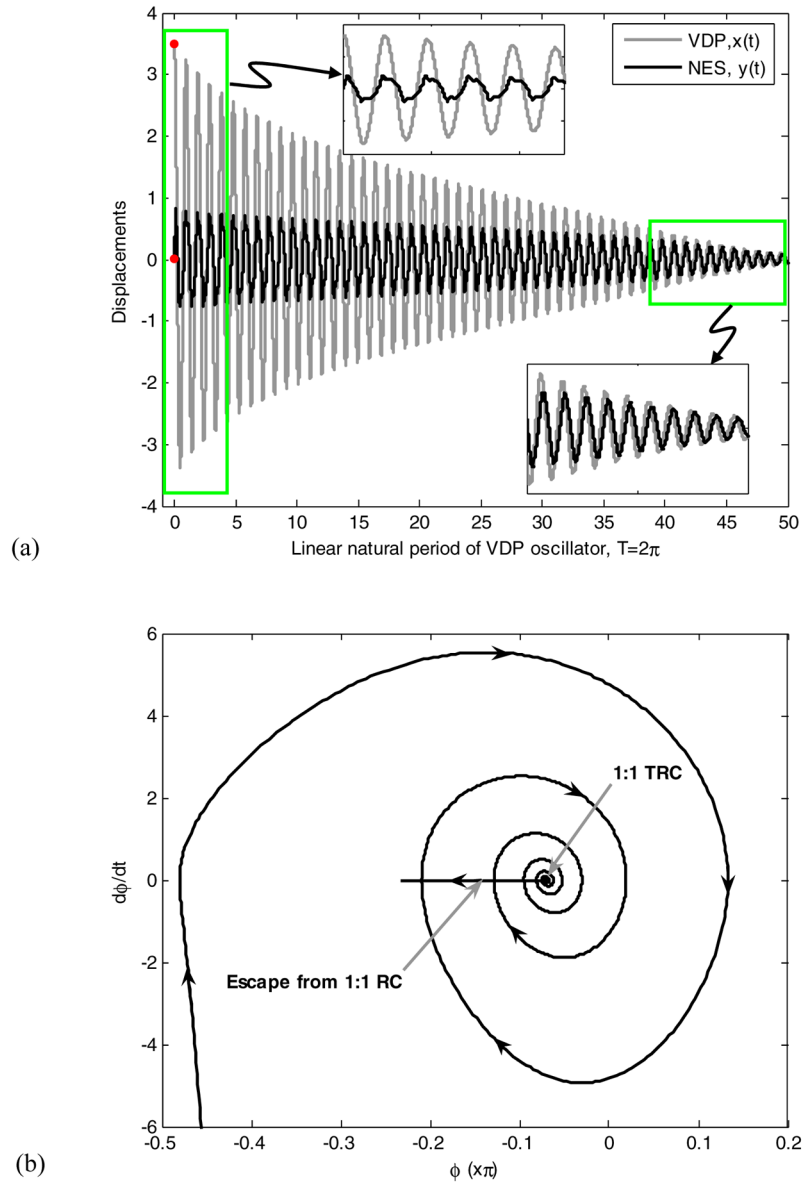


Fig. 9.10 Transient dynamics of configuration VDPNES₁ when the LCO is eliminated, case of initial 3:1 TRC and subsequent 1:1 TRC as total energy decreases: (a) time series; (b) motion on the plane $(\phi, \dot{\phi})$ of the averaged system (9.8).

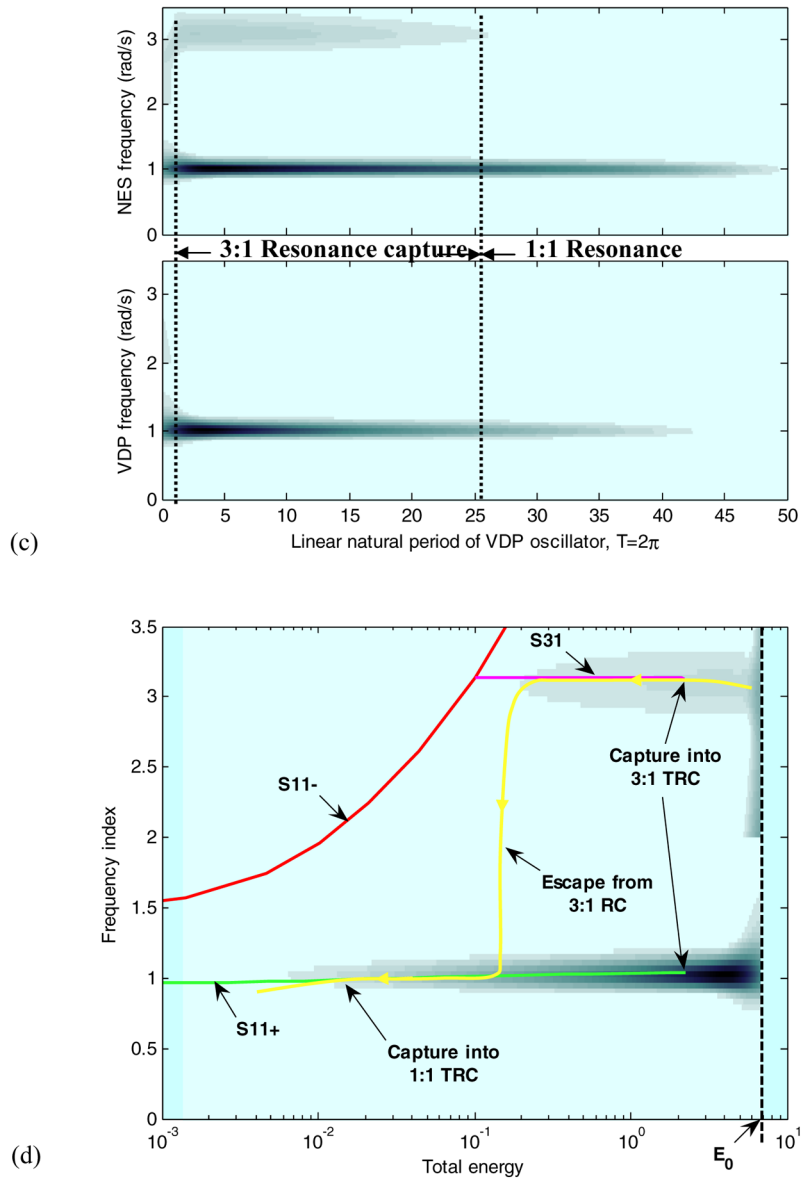


Fig. 9.10 Transient dynamics of configuration $VDPNES_1$ when the LCO is eliminated, case of initial 3:1 TRC and subsequent 1:1 TRC as total energy decreases: (c) instantaneous frequencies; (d) WT spectrum on the FEP.

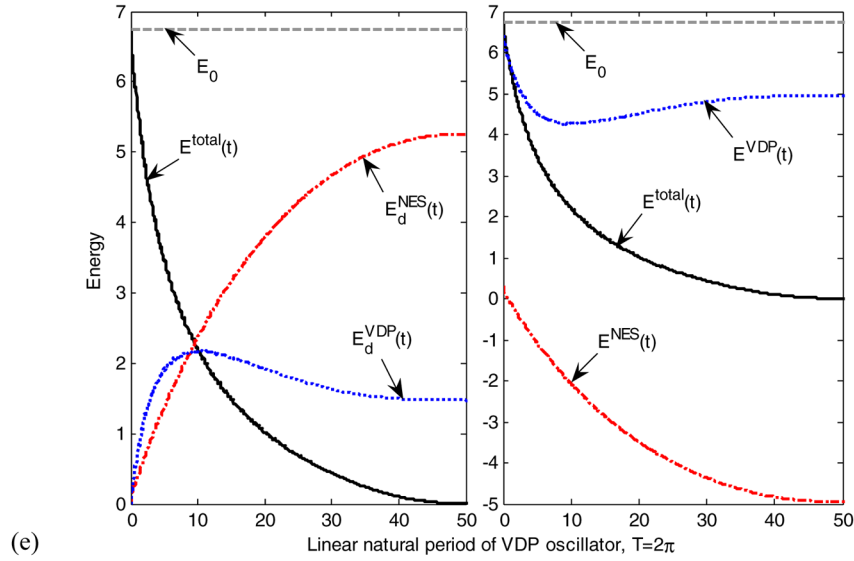


Fig. 9.10 Transient dynamics of configuration VDPNES₁ when the LCO is eliminated, case of initial 3:1 TRC and subsequent 1:1 TRC as total energy decreases: (e) energy exchange measures.

solution branches (as shown in the corresponding FEP), which suggests a higher possibility for strong resonance interactions between the VDP oscillator and the NES.

Mostly, similar conclusions as for VDPNES₁ can be drawn, except for the following. Regardless of whether the motion is initiated outside or inside the unperturbed LCO, when the LCO survives, the resulting TRCs on the FEP of the relative displacement $x(t) - y(t)$ [describing the structure of periodic orbits of the Hamiltonian system resulting by eliminating damping terms from system (9.2)] are generally more complex – although the dominant frequency contents lock into a 1:1 frequency ratio; the complex, underlying Hamiltonian dynamics may be responsible for this. Also, the initial energy exchanges between the VDP oscillator and the NES now occur on a fast scale (i.e., within a few linearized natural periods).

A general conclusion of the previous transient simulations is that, in order to achieve complete elimination of the LCO, the NES must be designed to cause an overall continuous reduction of the instantaneous total energy of the system; that is, it must stimulate energy flow in the system towards a path from superharmonic to subharmonic resonance captures on the FEP. This goal does not merely imply an increase in damping (although this is definitely beneficial in certain cases), but rather, a careful selection of the system parameters (such as mass ratio and coupling stiffness) that influence the underlying Hamiltonian dynamics. In accordance to results reported in previous Chapters, the topology of the branches of periodic solutions of the underlying Hamiltonian influences to a great extent the TRCs and the sudden

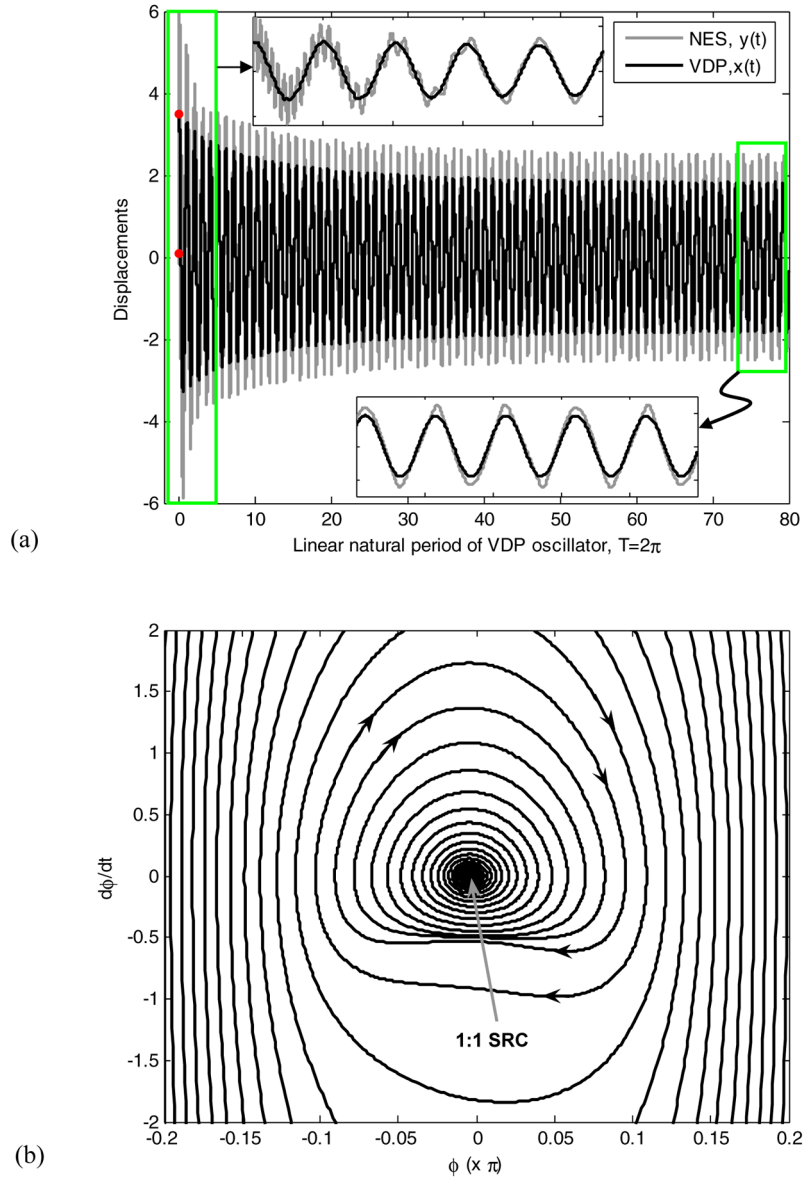


Fig. 9.11 Transient dynamics of configuration VDPNES₂ when the LCO survives ($\epsilon m = 5\%$, $\kappa = 1.0$, $\epsilon \lambda = 1\%$), for initial conditions $(x(0), y(0), \dot{x}(0), \dot{y}(0)) = (3.5, 0.1, 0, 0)$: (a) time series; (b) motion on the plane $(\phi, \dot{\phi})$ of the averaged system (9.9).

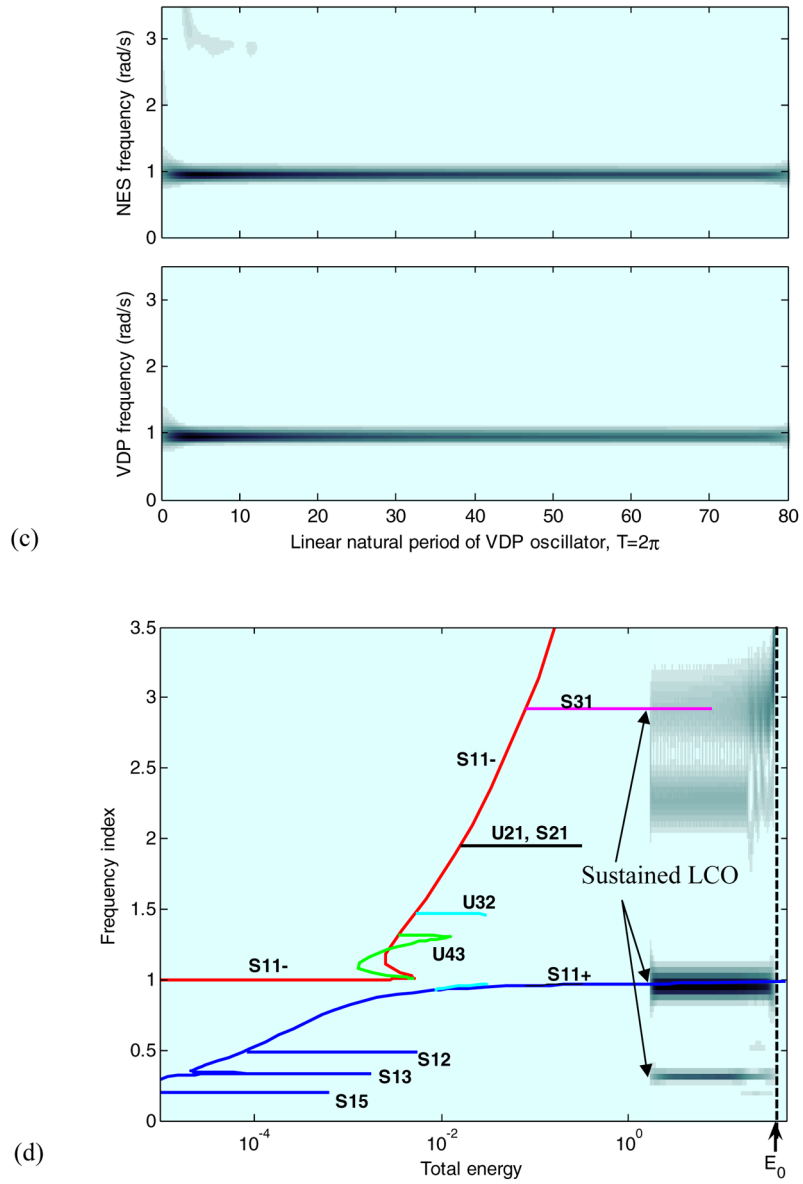


Fig. 9.11 Transient dynamics of configuration VDPNES₂ when the LCO survives ($\epsilon m = 5\%$, $\kappa = 1.0$, $\epsilon \lambda = 1\%$), for initial conditions $(x(0), y(0), \dot{x}(0), \dot{y}(0)) = (3.5, 0.1, 0, 0)$: (c) instantaneous frequencies; (d) WT spectrum on the FEP.

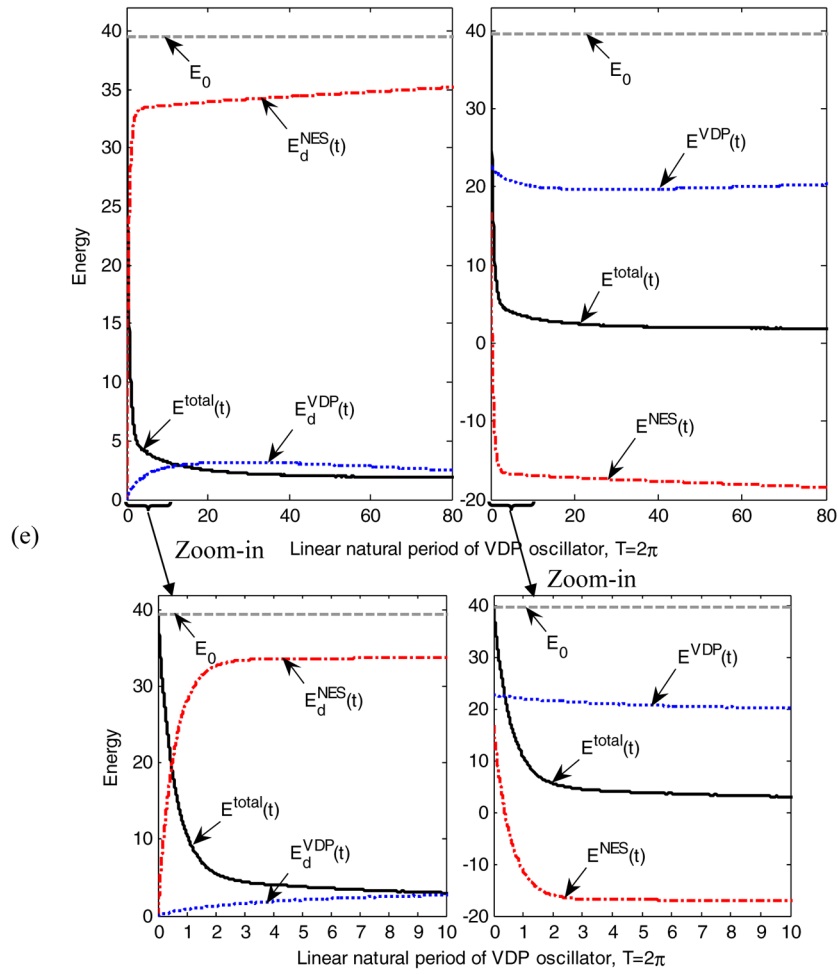


Fig. 9.11 Transient dynamics of configuration VDPNES₂ when the LCO survives ($\varepsilon m = 5\%$, $\kappa = 1.0$, $\varepsilon \lambda = 1\%$), for initial conditions $(x(0), y(0), \dot{x}(0), \dot{y}(0)) = (3.5, 0.1, 0, 0)$: (e) energy exchange measures.

transitions (jumps) in the transient damped dynamics. For example, reducing (increasing) the mass ratio for configuration VDPNES₂, shifts the entire FEP towards lower (higher) energies. Hence, an optimization study is required to achieve robust passive LCO suppression, a topic that is addressed in the next section.

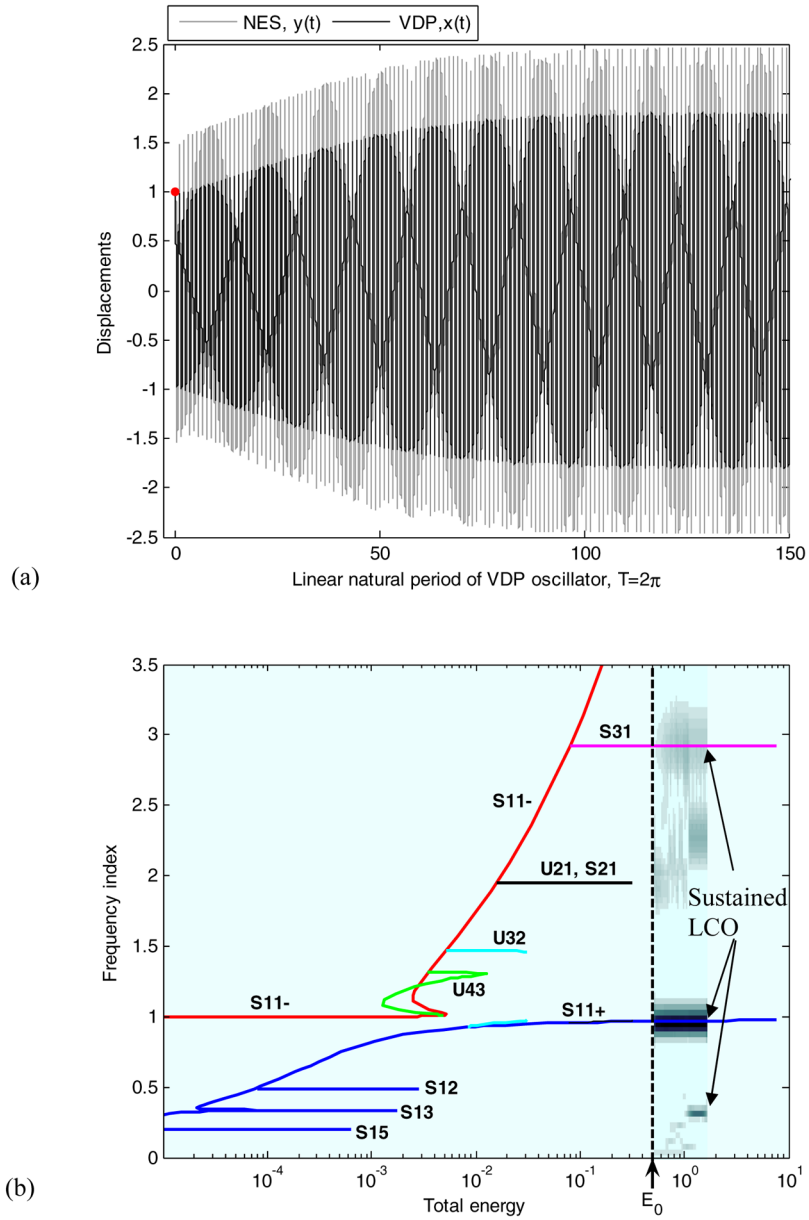


Fig. 9.12 Transient dynamics of configuration VDPNES₂ when the LCO survives ($\epsilon m = 5\%$, $\kappa = 1.0$, $\epsilon \lambda = 1\%$), for initial conditions $(x(0), y(0), \dot{x}(0), \dot{y}(0)) = (1.0, 1.0, 0, 0)$: (a) time series; (b) WT spectrum on the FEP.

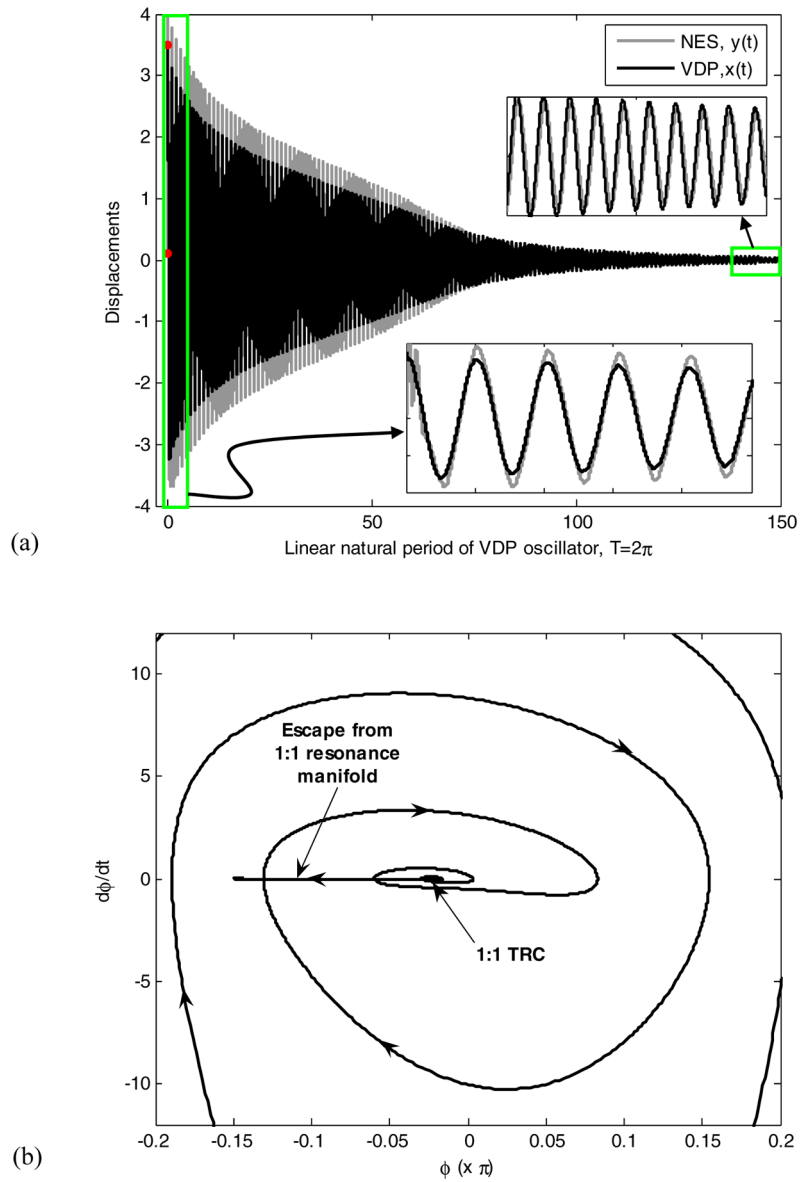


Fig. 9.13 Transient dynamics of configuration VDPNES₂ when the LCO survives ($\epsilon m = 5\%$, $\kappa = 1.0$, $\epsilon \lambda = 10\%$), for initial conditions $(x(0), y(0), \dot{x}(0), \dot{y}(0)) = (3.5, 0.1, 0, 0)$: (a) time series; (b) motion on the plane $(\phi, \dot{\phi})$ of the averaged system (9.9).

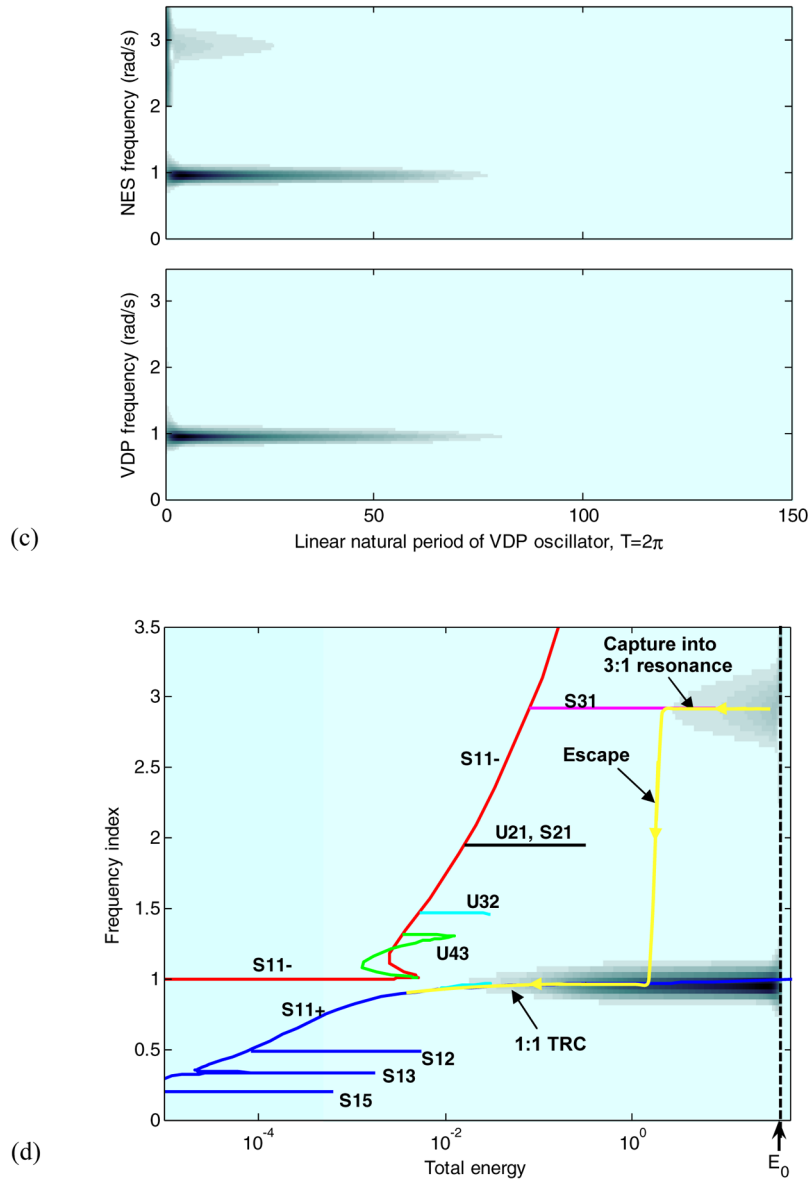


Fig. 9.13 Transient dynamics of configuration VDPNES₂ when the LCO survives ($\epsilon m = 5\%$, $\kappa = 1.0$, $\epsilon \lambda = 10\%$), for initial conditions $(x(0), y(0), \dot{x}(0), \dot{y}(0)) = (3.5, 0.1, 0, 0)$: (c) instantaneous frequencies; (d) WT spectrum on the FEP.

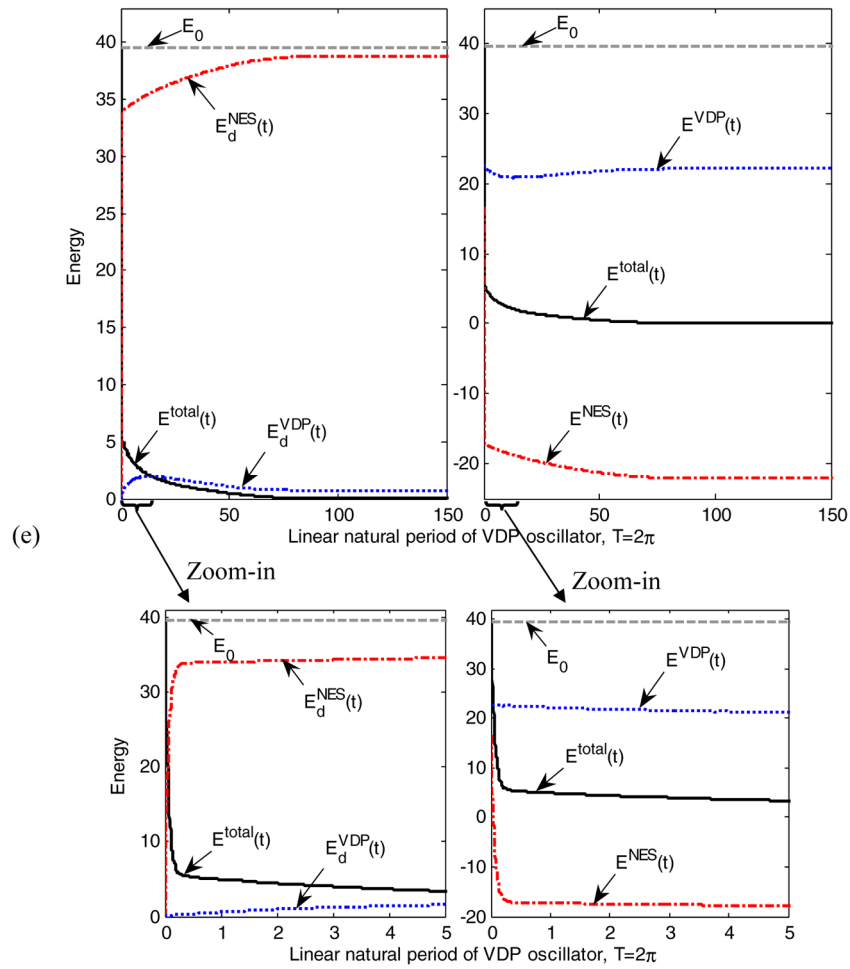


Fig. 9.13 Transient dynamics of configuration VDPNES₂ when the LCO survives ($\varepsilon m = 5\%$, $\kappa = 1.0$, $\varepsilon \lambda = 10\%$), for initial conditions $(x(0), y(0), \dot{x}(0), \dot{y}(0)) = (3.5, 0.1, 0, 0)$: (e) energy exchange measures.

9.1.3 Steady State Dynamics and Bifurcation Analysis

In this section, we will explore the steady state dynamics of the system by utilizing the method of numerical continuation, and relate LCO suppression to the bifurcation structure of the steady state solutions. The results will provide optimal design parameters for the NES, guaranteeing robustness of LCO elimination.

9.1.3.1 Study of Robustness of LCO Elimination

We now show numerically that LCO elimination due to the action of the NES is the result of a Hopf bifurcation. The steady state solutions of the full equations of motion (9.1) and (9.2) are computed through numerical continuation performed using the package MATCONT in Matlab[®] (Dhooge et al., 2003).

We consider the configuration VDPNES₁ first, with the linear coupling stiffness εC regarded as a control parameter, and fixing the other NES parameters to the values $\kappa = 1.0$, $\varepsilon\lambda = 3\%$. We consider two mass ratios, namely, $\varepsilon m = 10\%$ where supercritical LCOs exist, and $\varepsilon m = 50\%$ where only subcritical LCOs exist. We remark that the Hopf bifurcation in the steady state dynamics proves to be subcritical, i.e., to involve a subcritical LCO near the bifurcation point. By *subcritical* we denote that the LCO occurs below the critical parameter value.

In Figure 9.14 we present the bifurcation structure of steady state amplitudes of configuration VDPNES₁, governed by system (9.1). At the bifurcation plots, the notation BPC denotes a *branch point of cycles*, a point LPC, a *limit point cycle*, and a point NS, a *Neimark–Sacker* bifurcation (Golubitsky and Schaeffer, 1985). From these results it is clear that the LCOs are eliminated through a Hopf bifurcation that occurs at $\varepsilon C = 0.0415$ for $\varepsilon m = 10\%$, and $\varepsilon C = 0.2579$ for $\varepsilon m = 50\%$. We note that all non-trivial curves in the bifurcation diagram represent periodic oscillations of the system, that is, LCOs.

The first case ($\varepsilon m = 10\%$) is regarded as a case of ‘malign’ system nonlinearities (as far as LCO suppression is concerned) because, although the trivial equilibrium is stable after the bifurcation point, the solution may jump onto coexisting stable LCOs if sufficiently strong perturbations are imposed; hence, the LCO suppression cannot be characterized as robust in this case. On the other hand, the latter case ($\varepsilon m = 50\%$) provides *robust elimination of LCOs*, since the stable trivial solution that results after the Hopf bifurcation is a global attractor of the dynamics (this is a case of ‘benign’ system nonlinearities). We also remark that, when the system exhibits malign nonlinearities, it possesses a complicated bifurcation structure. For example, considering the bifurcation diagram of Figure 9.14a, there exist LPC bifurcations (or equivalently, saddle-node bifurcations of equilibria), BPC bifurcations (or pitchfork bifurcations of equilibria), and NS bifurcations (or Hopf bifurcation of equilibrium positions) (Golubitsky and Schaeffer, 1985); it follows that the steady state dynamics of the system can assume complex forms such as higher-dimensional periodic or quasi-periodic orbits on two-tori generated at points of NS bifurcations.

Similar bifurcation studies were performed for the configuration VDPNES₂ governed by system (9.2), with mass ratio εm as the control parameter. Similar results were obtained, such as sub- and supercritical LCOs; however, the system with an ungrounded NES does not possess a complex bifurcation structure even in the case of malign system nonlinearities (there simply exist two LPC points in the bifurcation diagram). Although the detailed results are not discussed at this point, we will reexamine these behaviors utilizing the averaged system later in this section.

Finally, we remark that the existence of a Hopf bifurcation in the steady state dynamics can be proven theoretically, employing the method of Lyapunov–Schmidt

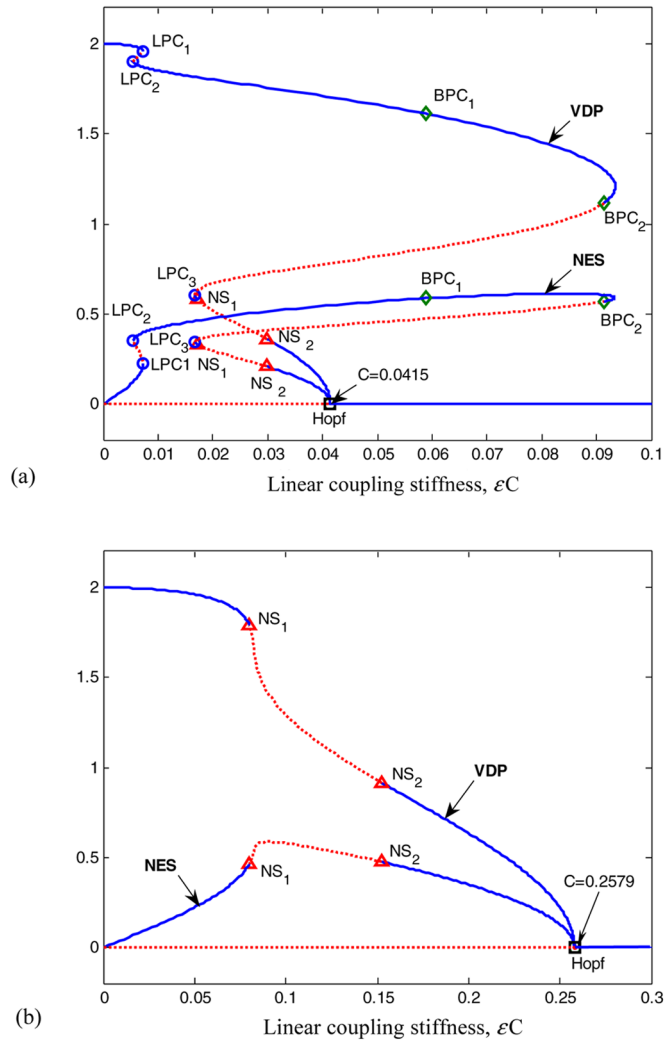


Fig. 9.14 Bifurcation diagrams of steady state amplitudes of configuration VDPNES₁ ($\kappa = 1.0$, $\varepsilon\lambda = 3\%$), stable (unstable) branches are marked by solid (dotted) lines: (a) case when supercritical LCOs exist (malign nonlinearity), $\varepsilon m = 10\%$; (b) case when subcritical LCOs exist (benign nonlinearity), $\varepsilon m = 50\%$.

reduction (LSR) (Golubitsky and Schaeffer, 1985). By this methodology, singularities are removed by projecting the complement of the null space of the linearized system operator and the null space itself, onto the range and its complement space, respectively. Then, the generalized implicit function theorem is invoked. Hence, LSR can be directly applied to the full equations of motion (9.1) and (9.2); alternatively, LSR can be applied to the slow flow models (9.8) and (9.9), to show that their

equilibrium positions exhibit pitchfork bifurcations. More details are not included in this study, but are left as future work.

9.1.3.2 Analytical Study

We now examine analytically the steady state dynamics of both configurations VDPNES₁ and VDPNES₂, utilizing the slow flow dynamics models (9.8) and (9.9). In so doing we demonstrate the capacity of these models to accurately capture the steady state dynamics and their bifurcations of systems (9.1) and (9.2), respectively. We will analyze each NES configuration separately.

Starting from Configuration VDPNES₁, we express the slow flow model (9.8) in the following compact form:

$$\begin{aligned}\dot{\alpha}_1 &= f_1(\alpha_1, \alpha_2, \phi) \\ \dot{\alpha}_2 &= f_2(\alpha_1, \alpha_2, \phi) \\ \alpha_1 \alpha_2 \dot{\phi} &= g(\alpha_1, \alpha_2, \phi)\end{aligned}\quad (9.17)$$

Then, the steady state amplitudes α_1 , α_2 and the phase difference ϕ are obtained by solving the set of homogeneous nonlinear algebraic equations

$$f_1(\alpha_1, \alpha_2, \phi) = f_2(\alpha_1, \alpha_2, \phi) = g(\alpha_1, \alpha_2, \phi) = 0$$

where trivial solutions are excluded. It turns out that in this case we can find the analytical solutions in explicit form. Indeed, taking into account the analytical expression for f_1 , we can solve explicitly for amplitude α_1

$$f_1(\alpha_1, \alpha_2, \phi) = 0 \Rightarrow \alpha_1 = -\frac{C}{\lambda} \alpha_2 \sin \phi \quad (9.18)$$

which, when plugged into the relation $f_2(\alpha_1, \alpha_2, \phi) = 0$ yields

$$\alpha_2^2 = 4 \left(1 - \frac{C^2}{\lambda} \sin^2 \phi \right) \quad (9.19)$$

Since $\alpha_2^2 > 0$, the parenthesis on the right-hand side must be positive, so that

$$\lambda > C^2 \sin^2 \phi \Rightarrow \sin^2 \phi < \frac{\lambda}{C^2} \equiv \Phi_{\text{crit}}, \quad \text{or} \quad |\sin \phi| < \sqrt{\Phi_{\text{crit}}} \quad (9.20)$$

and thus

$$\begin{aligned}\phi \in & \left(-\pi, -\pi + \sin^{-1} \sqrt{\Phi_{\text{crit}}} \right) \cup \left(-\sin^{-1} \sqrt{\Phi_{\text{crit}}}, \sin^{-1} \sqrt{\Phi_{\text{crit}}} \right) \\ & \cup \left(\pi - \sin^{-1} \sqrt{\Phi_{\text{crit}}}, \pi \right)\end{aligned}\quad (9.21)$$

In the expressions above ϕ is considered to be in the interval $\phi \in (-\pi, \pi)$. Note that the trivial solution can exist only when the condition $\lambda \leq C^2 \sin^2 \phi$ is met.

Substituting (9.19) and (9.20) into the relation $g(\alpha_1, \alpha_2, \phi) = 0$, we obtain,

$$\begin{aligned} & \left(\frac{\varepsilon m C^2}{\lambda^2} \sin^2 \phi - 1 \right) \cos \phi \\ &= \frac{1}{\lambda} (C - m - \varepsilon m C) \sin \phi + 3 \frac{\kappa C^2}{\varepsilon \lambda^3} \left(1 - \frac{C^2}{\lambda} \sin^2 \phi \right) \sin^3 \phi \end{aligned} \quad (9.22)$$

where the phase variable ϕ is the only unknown in the above transcendental equation. Squaring both sides of (9.23), and designating $\sin^2 \phi \equiv \Phi$, we obtain the following fifth-order polynomial equation in terms of Φ :

$$\sum_{n=0}^5 a_n \Phi^n = 0, \quad 0 < \Phi < \Phi_{\text{crit}} \quad (9.23)$$

where the coefficients a_n , $n = 1, \dots, 5$, are explicitly given by:

$$\begin{aligned} a_5 &= 9\kappa^2 C^8, & a_4 &= -18\lambda\kappa^2 C_6, & a_0 &= -3\varepsilon^2 \lambda^8 \\ a_3 &= \lambda^2 \kappa^2 C^4 \{9\kappa^2 + 6\varepsilon\kappa(m - C + \varepsilon m C)\lambda + \varepsilon^4 m^2 \lambda^2\} \\ a_2 &= -\varepsilon \lambda^4 C^2 \{6\kappa C(\varepsilon m - 1) + \varepsilon^2 m^2 C^2 + 2m(3\kappa + \varepsilon^2 \lambda^2)\} \\ a_1 &= \varepsilon^2 \lambda^6 \{2mC(\varepsilon m - 1) + m^2 + C^2(\varepsilon^2 m^2 + 1) + \lambda^2\} \end{aligned} \quad (9.24)$$

Once we compute a solution Φ from (9.24), there correspond two phase differences given by:

$$\begin{cases} \phi_{1,3} = \sin^{-1} \sqrt{\Phi} \text{ and } \pi - \sin^{-1} \sqrt{\Phi}, & \text{for } 0 < \phi < \pi \\ \phi_{2,4} = -\sin^{-1} \sqrt{\Phi} \text{ and } -\pi + \sin^{-1} \sqrt{\Phi}, & \text{for } -\pi < \phi < 0 \end{cases} \quad (9.25)$$

Then, by (9.19) and (9.20) we compute the corresponding steady state amplitudes as follows:

$$\alpha_2 = \pm 2 \sqrt{1 - \frac{\sin^2 \phi_k}{\Phi_{\text{crit}}}} \quad (9.26)$$

$$\alpha_2 = \mp 2 \frac{C}{\lambda} \sqrt{1 - \frac{\sin^2 \phi_k}{\Phi_{\text{crit}}}} \sin \phi_k \quad (9.27)$$

where $k = 1, \dots, 4$. Note that the pairs of phases (ϕ_1, ϕ_3) and (ϕ_2, ϕ_4) yield identical amplitudes, being either out-of-phase or in-phase, respectively. After the non-trivial equilibrium solutions are determined we can study their stability using the eigenvalues of the corresponding Jacobian matrix of system (9.18) evaluated at each solution. The stability of the trivial solution requires the expression of the slow flow

model (9.5) in Cartesian coordinates [instead of equations (9.8) with variables in polar form], followed by similar linearized stability analysis.

We examine the non-trivial steady state motions with respect to the coupling stiffness and mass ratio by varying damping and nonlinear stiffness. Figures 9.15 and 9.16 show the steady state amplitudes of each oscillator with respect to the mass ratio and the coupling stiffness by different (fixed) damping and nonlinear stiffness values. Stability results are not included in these plots, but these will be discussed when we apply the numerical continuation of equilibria, which turns out to be the same as depicted in Figure 9.14. Regardless of other parameter values, the steady state amplitudes approach asymptotic limits when the coupling stiffness approaches zero, i.e., when the two oscillators become decoupled as their amplitudes reach the limits $|\alpha_1| \rightarrow 0$ and $|\alpha_2| \rightarrow 2$ when $C \rightarrow 0$.

Considering the effect of mass ratio on the steady state response, we remark that subcritical LCOs (as benign nonlinearities) occur for higher mass ratios. This suggests that *the grounded NES is more effective in robustly eliminating the LCO at higher mass ratios*. Higher damping seems to limit the generation of supercritical LCOs (corresponding to malign system nonlinearities), in which case the system possesses only subcritical LCOs which are susceptible to robust LCO suppression. Moreover, at higher damping values, the bifurcation points tend to occur at lower coupling stiffness values (see Figure 9.15). Regarding the effects of the NES nonlinearity, the stronger nonlinearity seems to induce more complicated steady state dynamics; that is, as the nonlinear stiffness grows stronger, supercritical LCOs develop over broader parameter spaces, a result which does not favor robust LCO suppression (see the plots depicted in Figure 9.16).

Finally, we apply Kubíček's method (Kubíček, 1976), which provides an algorithm for computing the dependence of the steady state equilibria of the averaged system (9.8) on a system parameter (configuration VDPNES₁). To this end, we write the steady state conditions for the averaged system in the following compact form:

$$\mathbf{f}(\mathbf{x}; \mu) = \mathbf{0} \quad (9.28)$$

where $\mathbf{x} = (x_1, x_2, x_3)^T$, $\mathbf{f} = (f_1, f_2, f_3)^T$, $f_3 \equiv g$, $x_1 = \alpha_1$, $x_2 = \alpha_2$, $x_3 = \phi$ and $\mu = \varepsilon C$ is the control parameter. That is, we aim to examine the parametric dependence of the steady state solutions on the linear coupling stiffness εC . We make this choice since we already know the asymptotic values of the solutions as the coupling approaches zero, which can serve as initial conditions for the algorithm.

Let s denote the arc-length parameter of the solution curve. From (9.29) we derive

$$\frac{d\mathbf{f}}{ds} = \sum_{j=1}^3 \frac{\partial \mathbf{f}}{\partial x_j} \frac{dx_j}{ds} + \frac{\partial \mathbf{f}}{\partial \mu} \frac{d\mu}{ds} = \mathbf{0} \quad (9.29)$$

with an additional equation:

$$\sum_{j=1}^3 \left(\frac{dx_j}{ds} \right)^2 + \left(\frac{d\mu}{ds} \right)^2 = 1 \quad (9.30)$$

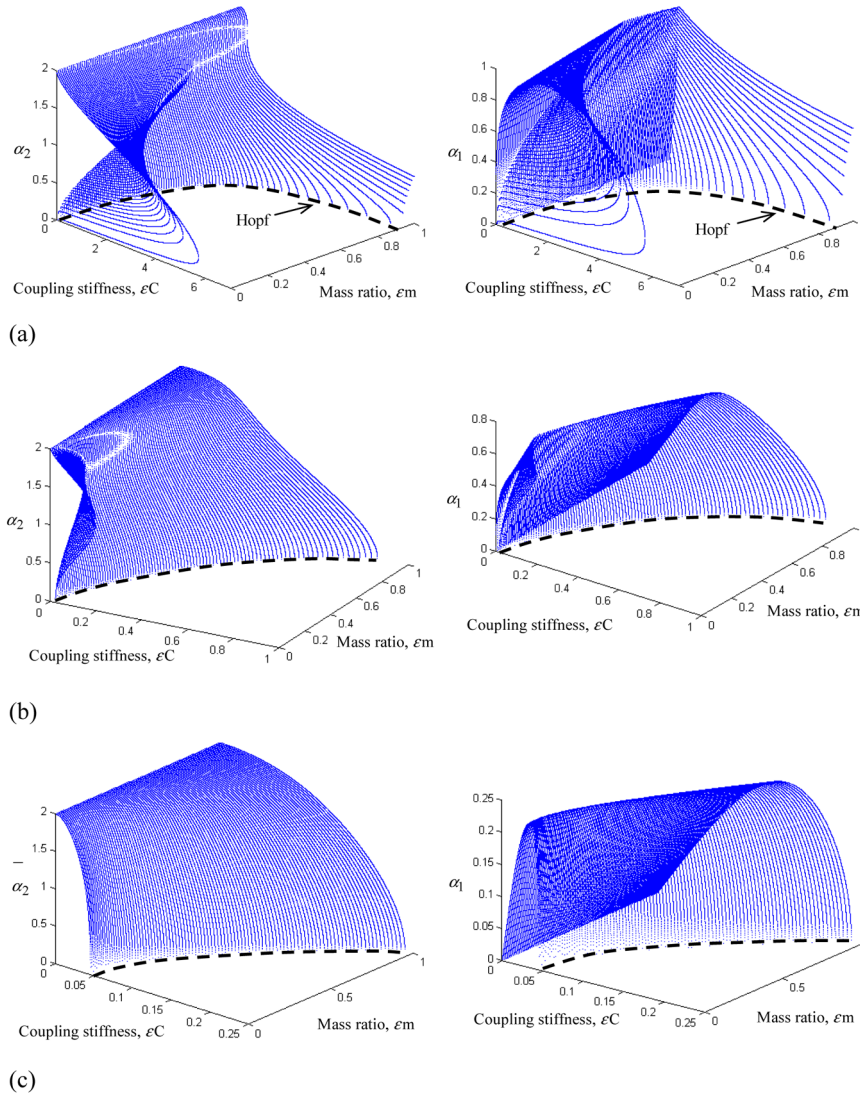


Fig. 9.15 steady state amplitudes of configuration VDPNES₁ for $\kappa = 1.0$, and (a) $\varepsilon\lambda = 1\%$; (b) $\varepsilon\lambda = 3\%$; (c) $\varepsilon\lambda = 20\%$; Hopf bifurcations responsible for LCO elimination occur along dashed lines.

which imposes the parametrizing condition of a unit tangential vector along the solution curve. We denote $x_4 = \mu$ for notational convenience, and rewrite (9.30) in the following matrix form:

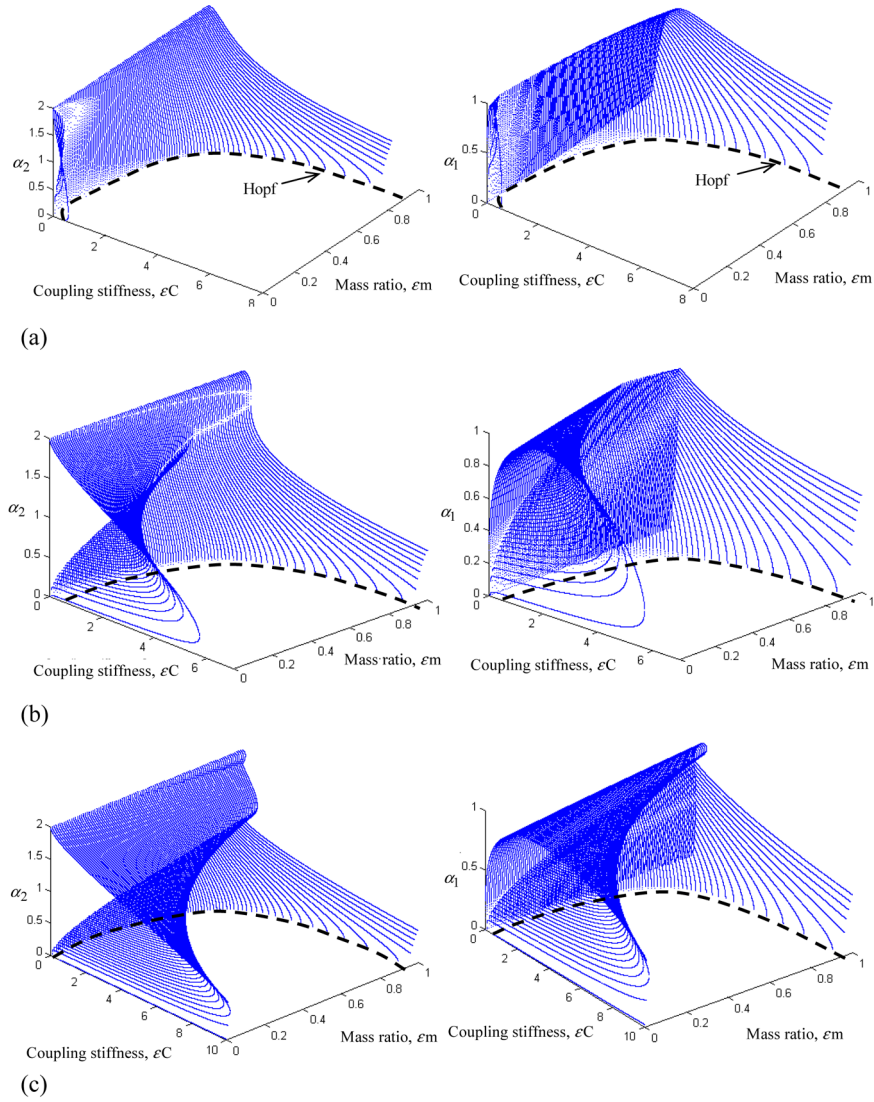


Fig. 9.16 steady state amplitudes of configuration VDPNES₁ for $\varepsilon\lambda = 1\%$, and (a) $\kappa = 0.1$; (b) $\kappa = 1.0$; (c) $\kappa = 2.0$; Hopf bifurcations responsible for LCO elimination occur along dashed lines.

$$\begin{bmatrix} \frac{\partial f_1}{\partial x_1} & \cdots & \frac{\partial f_1}{\partial x_{k-1}} & \frac{\partial f_1}{\partial x_{k+1}} & \cdots & \frac{\partial f_1}{\partial x_{n+1}} \\ \frac{\partial f_2}{\partial x_1} & \cdots & & & & \frac{\partial f_2}{\partial x_{n+1}} \\ \vdots & \vdots & & & & \vdots \\ \frac{\partial f_n}{\partial x_1} & \cdots & \frac{\partial f_n}{\partial x_{k-1}} & \frac{\partial f_n}{\partial x_{k+1}} & \cdots & \frac{\partial f_n}{\partial x_{n+1}} \end{bmatrix} \begin{Bmatrix} x'_1 \\ \vdots \\ x'_{k-1} \\ x'_{k+1} \\ \vdots \\ x'_{n+1} \end{Bmatrix} = -x'_k \begin{Bmatrix} \frac{df_1}{dx_k} \\ \frac{df_2}{dx_k} \\ \vdots \\ \frac{df_n}{dx_k} \end{Bmatrix} \quad (9.31)$$

where primes denote differentiation with respect to the arc length s of the solution branch. The matrix on the left-hand side is regular for certain values of s and k such that $1 \leq k \leq n + 1$, and $n = 3$ in this problem.

By the following relation (9.32) we express each of the unknown variables, $x'_1, \dots, x'_{k-1}, x'_{k+1}, \dots, x'_{n+1}$ in terms of x'_k :

$$x'_i = \beta_i x'_k, \quad i = 1, \dots, k-1, k+1, \dots, n+1 \quad (9.32)$$

where the coefficients β_i can be determined by applying Gaussian elimination, for example. Using (9.31), we express the derivative squared $x_k'^2$ in the following form:

$$x_k'^2 = \left[1 + \sum_{i=1, i \neq k}^{n+1} \beta_i^2 \right]^{-1} \quad (9.33)$$

where the sign of x'_k is determined by the orientation of the arc-length s along the solution branch. Then, the remaining derivatives x'_i are determined by the relations (9.33) for the following initial conditions:

$$x_i = x_{i0} \quad \text{at } s = 0, \quad i = 1, \dots, k-1, k+1, \dots, n+1 \quad (9.34)$$

The next step includes numerical integration of x'_i . For more detailed control of the solution, we can apply an iterative method such as the Newton's method; hence, for the variables $\bar{\mathbf{x}} = (x_1, \dots, x_{k-1}, x_{k+1}, \dots, x_{n+1})^T$ we improve the calculated profile through

$$\bar{\mathbf{x}}_{\text{new}} - \bar{\mathbf{x}}_{\text{old}} = -\mathbf{\Gamma}_k \mathbf{f} \quad (9.35)$$

where $\mathbf{\Gamma}_k$ denotes the Jacobian matrix in (9.32). Note that the solvability condition requires that the matrix $\mathbf{\Gamma}_k$ is non-singular. Finally, the stability of each equilibrium obtained above can be determined from the eigenvalues of the Jacobian matrix of equation (9.8) evaluated at the equilibrium point.

Typical numerical bifurcation diagrams of the slow flow dynamics (9.8) are shown in Figure 9.17 for supercritical LCOs, and Figure 9.18 for subcritical LCOs. A comparison of the results with those obtained by considering the full equations of motion was performed for the same parameter conditions, and the agreement is satisfactory. By applying Kubíček's method to the averaged system, we clearly observe the dependence and bifurcations of the steady state amplitudes as well as their phase difference (either in-phase or out-of-phase) on the chosen parameter, in this case the linear coupling stiffness.

We now consider Configuration VDPNES₂. Since the slow flow equations (9.6) and (9.9) are not solvable by hand, we directly apply Kubíček's method to examine the parameter dependence of the steady state solutions. In this case, the asymptotic relations for the amplitudes, $|\alpha_1| \rightarrow 2$ and $|\alpha_2| \rightarrow 2$ are satisfied as $\varepsilon m \rightarrow 0$, which can be used as initial conditions for solving the differential equations (9.34) in this case. In the following results we consider the parameter dependence of the steady state solutions on the mass ratio, $\mu = \varepsilon m$.

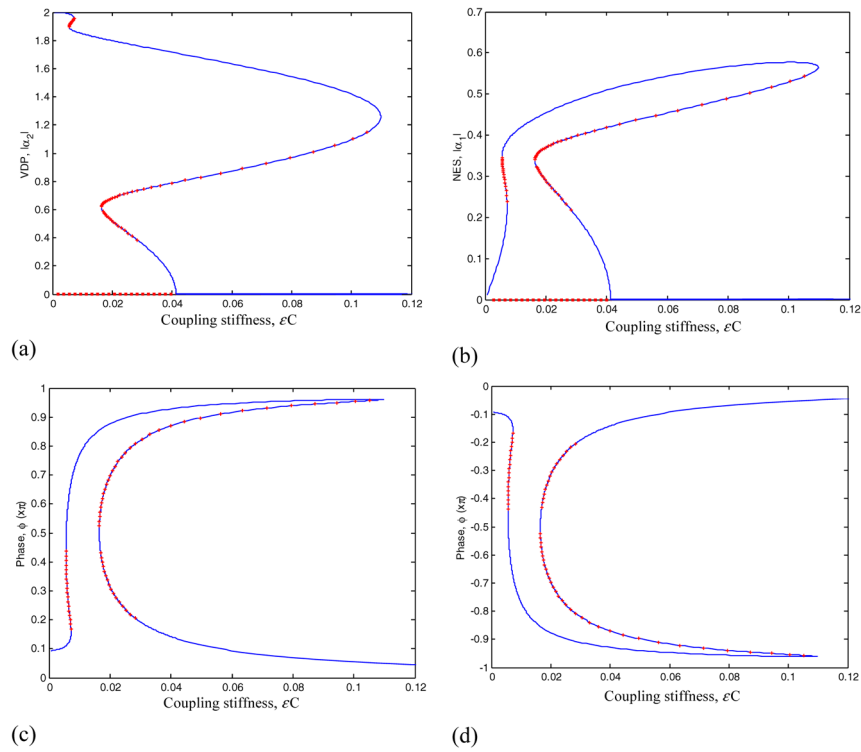


Fig. 9.17 Bifurcation diagram with respect to the linear coupling stiffness obtained by applying Kubíček's method to the averaged system (9.8) of VDPNES₁ with the system parameters same as for Figure 9.14a: (a) steady state amplitude of VDP oscillator; (b) steady state amplitude of NES; (c) phase difference (in-phase solution); (d) phase difference (out-of-phase solution); instability is marked by crosses.

The existence of supercritical LCOs is concluded from the bifurcation diagrams of Figure 9.19, corresponding to $\kappa = 2$, $\varepsilon\lambda = 2\%$, and mass ratio in the range 0–100%. Compared to Configuration VDPNES₁, the stability behavior of the steady state solutions is now simpler; that is, there exist only two LPC bifurcations at points A and B, and one Hopf bifurcation at point C. Thus, jump phenomena are possible at points A and B.

Figure 9.20 depicts schematically the types of steady state responses realized in each of the three possible Regions of the bifurcation diagrams. Supercritical LCOs exist in Region II, where the system possesses two stable and one unstable LCOs, and one unstable trivial equilibrium; in this Region, robustness of LCO elimination is questionable, as the steady state response of the system depends on whether its initial conditions bring the dynamics into the domain of attraction of either one of the co-existing stable LCO solutions. Similarly, in Region I, there exists only one stable LCO (which can be regarded as 'retained' from the unperturbed VDP oscil-

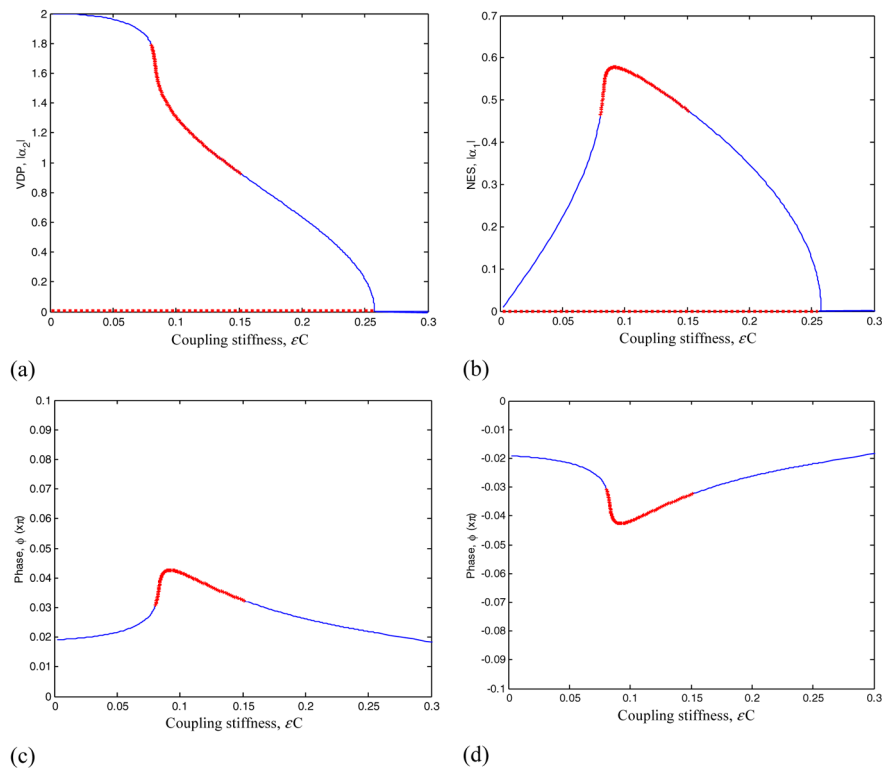


Fig. 9.18 Bifurcation diagram with respect to the linear coupling stiffness by applying Kubíček’s method to the averaged system (9.8) of VDPNES₁ with the system parameters same as in Figure 9.14b: (a) steady state amplitude of VDP oscillator; (b) steady state amplitude of NES; (c) phase difference (in-phase solution); (d) phase difference (out-of-phase solution); instability is marked by crosses.

lator), and an unstable trivial equilibrium point; hence, again robustness of LCO elimination is hindered. Finally, there exists a *single stable trivial equilibrium* in Region III, where complete and robust elimination of the LCO is indeed possible. In order to show sensitive dependence on initial conditions in Region II, we performed two different numerical simulations, depicted in Figure 9.21, for a system with $\varepsilon m = 3\%$, $\kappa = 2$, $\varepsilon \lambda = 2\%$, and initial conditions on either side of branch 2. These results clearly show why supercritical LCOs in this case are hindering robust LCO elimination.

Finally, Figure 9.22 depicts the dependence of the steady state motions on two system parameters. In contrast to Configuration VDPNES₁ where higher mass ratios favored robustness of LCO suppression, in this case the appearance of super- or subcritical LCOs turns out to be independent of the mass ratio. Indeed, for fixed nonlinear coupling stiffness (see Figures 9.22a–c), larger damping values tend to reduce the possibility of occurrence of supercritical LCOs, and, eventually for sufficiently

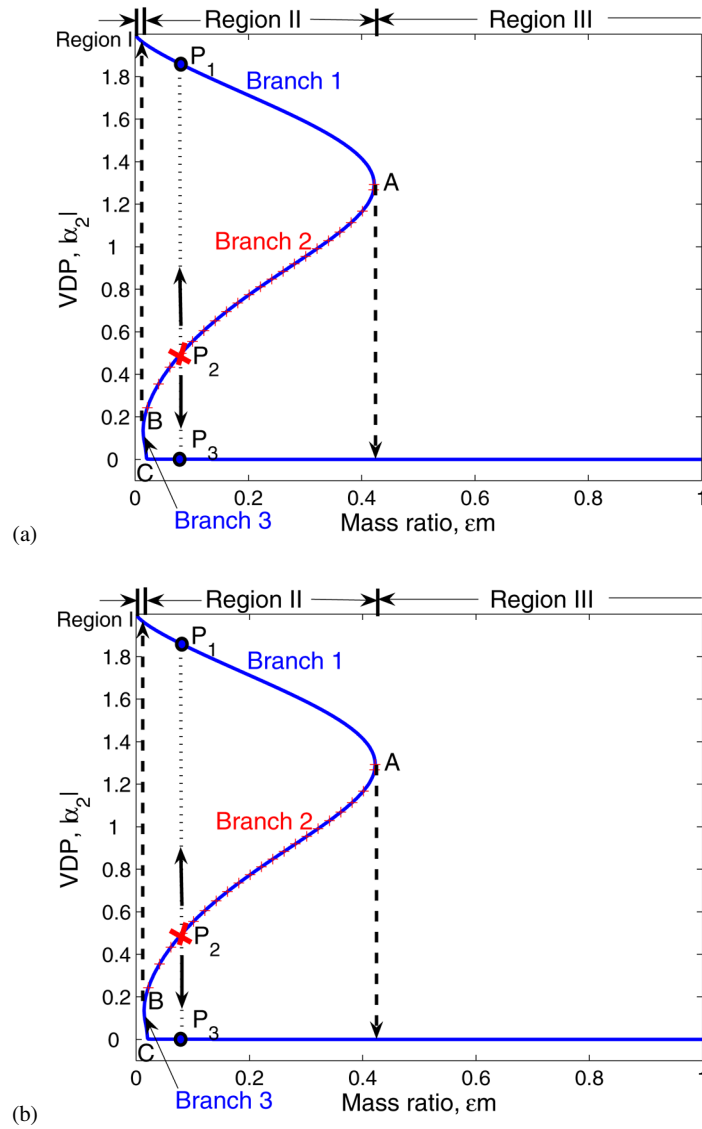


Fig. 9.19 Bifurcation diagrams obtained by applying Kubiček's method to the averaged system (9.9) of VDPNES₂, parameters $\kappa = 2$, $\varepsilon\lambda = 2\%$: (c) phase difference; (d) eigenvalue variation with respect to mass ratio; only branch 2 is unstable.

large damping one may completely and robustly eliminate the LCOs even with relatively small mass attachments, i.e., 3–5%. On the other hand, for fixed damping (see Figures 9.22d–f), and sufficiently weak nonlinear coupling, one may again perform robust and complete elimination of LCOs. These results strongly support the

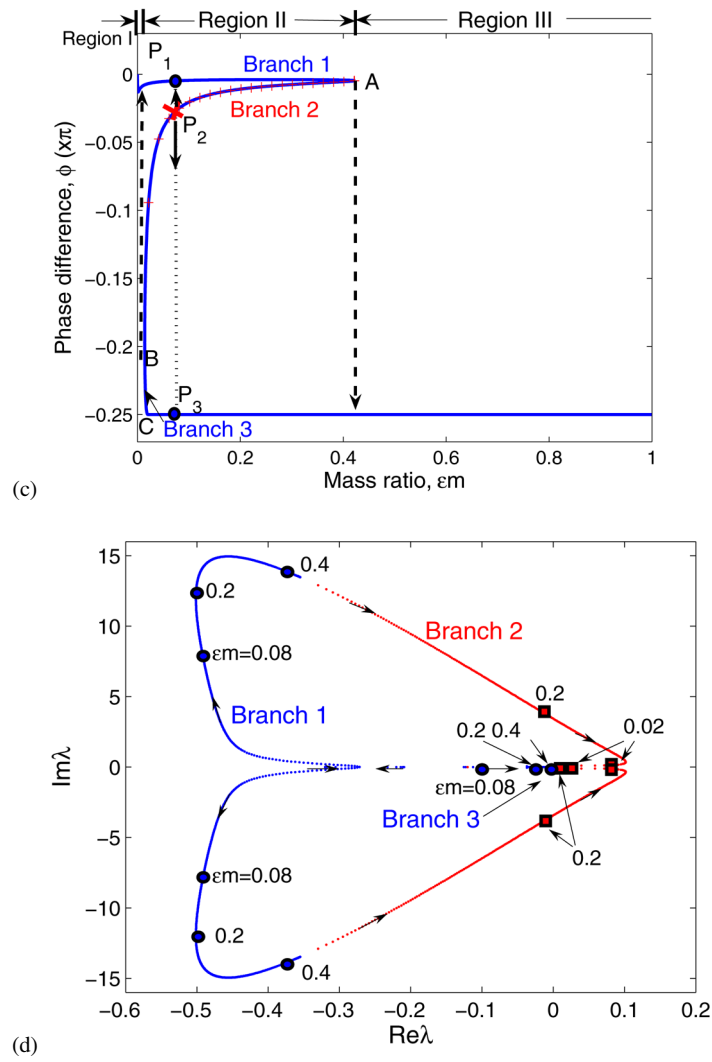


Fig. 9.19 Bifurcation diagrams obtained by applying Kubíček’s method to the averaged system (9.9) of VDPNES₂, parameters $\kappa = 2$, $\epsilon\lambda = 2\%$: (c) phase difference; (d) eigenvalue variation with respect to mass ratio; only branch 2 is unstable.

argument that the ungrounded NES configuration is more suitable for practical applications compared to the grounded one.

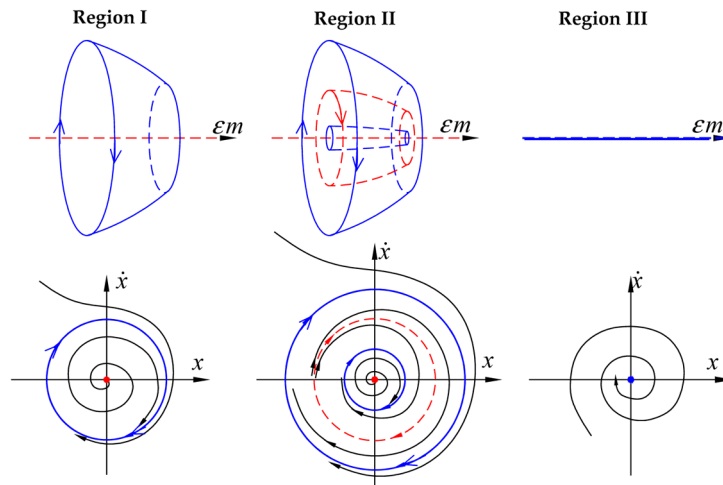


Fig. 9.20 Schematic of steady state responses in the three regions of Figure 9.19; solid (dashed) lines indicate stable (unstable) LCOs or equilibrium positions.

9.1.4 Summary of Results

We studied suppression and even complete elimination of the LCO of the VDP oscillator, utilizing grounded and ungrounded nonlinear energy sink (NES) configurations. Computational parameter studies proved the efficacy of LCO elimination by means of passive nonlinear TET from the VDP oscillator to appropriately designed NESs.

The numerical study of the transient damped dynamics of the system showed that the dynamical mechanism for LCO suppression is a series of 1:1 and 1:3 transient resonance captures (TRCs), with the damped transient dynamics being captured in neighborhoods of resonant manifolds of the underlying Hamiltonian systems. It is through these TRCs that energy gets transferred from the VDP oscillator to the NES, thus causing LCO suppression. By performing an additional bifurcation analysis of the steady state responses through numerical continuation, we examined the parameter dependence and bifurcations of the steady state solutions, and proved that a Hopf bifurcation is the global dynamical mechanism for generation of the LCOs in the NES configurations considered. The bifurcation analysis revealed that it is possible to design grounded or ungrounded NESs that robustly and completely eliminate the LCO instability of the system. This was possible when the system parameters are chosen so that subcritical Hopf bifurcation occurs, thus assuring the existence of a unique global trivial attractor of the dynamics in the parameter ranges of interest.

The preliminary results reported in this section indicate that passive TET to appropriately designed SDOF NESs can robustly suppress the LCO of the VDP oscillator. Motivated by these results, we will proceed to investigate LCO suppression

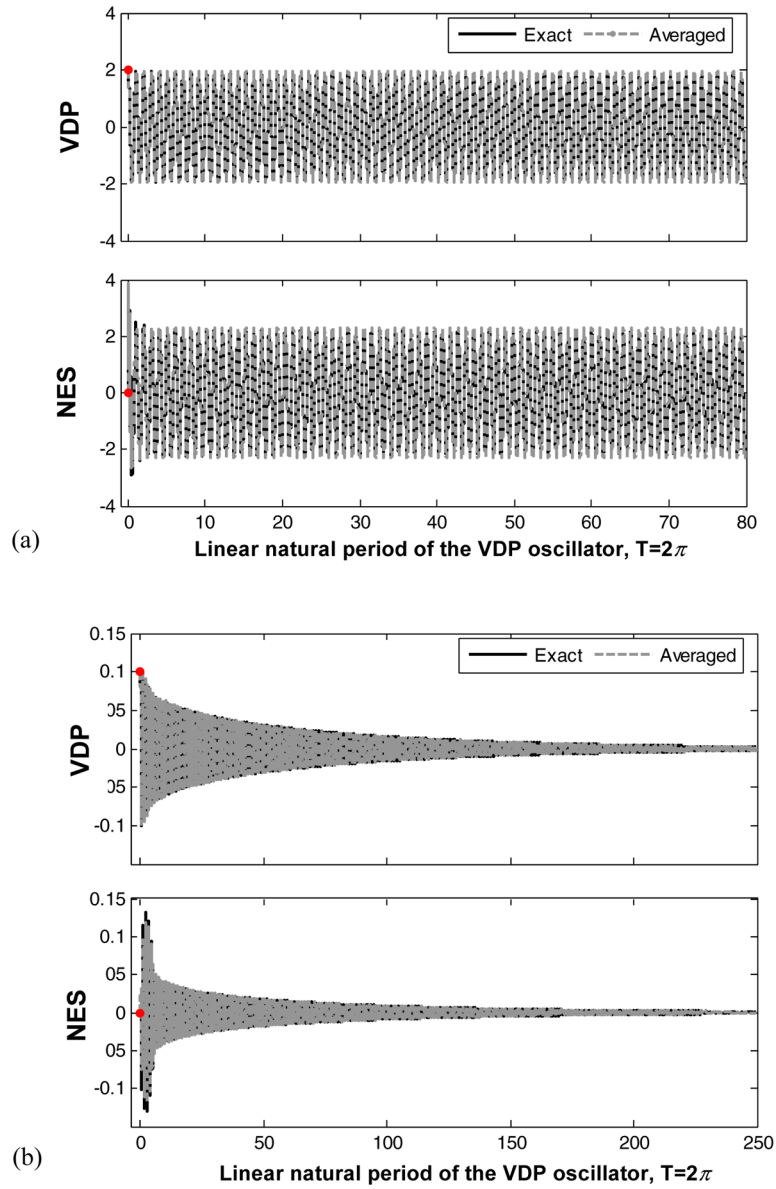


Fig. 9.21 Two different stable LCOs (denoted by points P_1 and P_3 in Figure 9.19) of configuration VDPNES₂ with $\epsilon m = 3\%$, $\kappa = 2$, $\epsilon \lambda = 2\%$, and zero initial conditions, but for (a) $x(0) = 2.0$, (b) $x(0) = 0.1$.

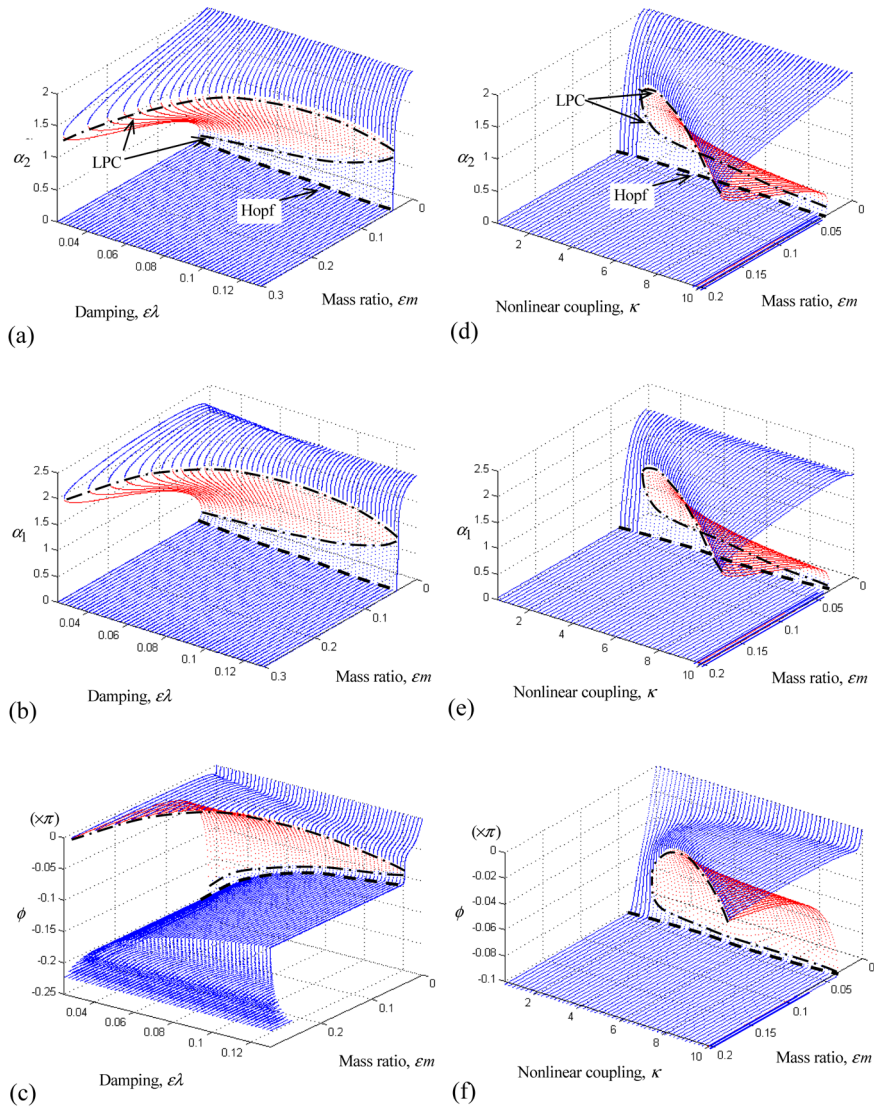


Fig. 9.22 Bifurcations of steady state motions of configuration VDPNES₂ with respect to two parameters: (a–c) dependence on the mass ratio and damping for fixed nonlinear stiffness $\kappa = 2$; (d–f) dependence on the mass ratio and nonlinear stiffness for fixed damping $\varepsilon\lambda = 10\%$; solid-dot lines are stability boundaries indicating LPC bifurcations between which motions are unstable; dashed lines imply parameter values where Hopf bifurcations occur.

in more realistic in-flow rigid wing models with attached (SDOF or MDOF) NESs. This study will be a first attempt towards applying TET to the important problem of robust aeroelastic instability suppression in realistic wing (or wing-store) configurations. A preliminary step towards addressing this task is to identify the dynamical (triggering) mechanism that generates this instability, and this is performed in the next section.

9.2 Triggering Mechanism for Aeroelastic Instability of an In-Flow Wing

In this section we study the triggering mechanism generating limit cycle oscillations (LCOs) due to aeroelastic instability in a two-dimensional, two-degree-of-freedom (DOF) wing model with cubic stiffness nonlinearities in both structural modes (i.e., heave and pitch), under the assumptions of subsonic flight and quasi-steady aerodynamics (Lee et al., 2005b). The fundamentals of flutter analysis for the underlying linear model are well understood [see, for example, Fung (1955) and Dowell et al. (1995)], i.e., the aeroelastic instability due to Hopf bifurcation at the flutter speed leading to diverging responses. However, when structural or damping nonlinearities are added to the model, such divergence in the linearized model reaches bounded limits, so that, eventually, the nonlinear system attains self-sustaining responses in the form of LCOs (Nayfeh and Mook, 1995).

The development of divergent flutter, leading to immediate structural failure, is rare, but sustained LCOs can cause structural damage, including fatigue. In addition, the need to avoid flight conditions (speeds, attitudes, and aircraft configurations) conducive to instability leads to onerous restrictions on operations and increased pilot workload. The establishment of safe flight envelopes often requires extensive and costly flight-test programs, which must be repeated for each change in aircraft configuration (i.e., the introduction of a new type of external store). It follows that dynamical analysis providing predictive capacity of aeroelastic instability in parameter space is needed.

LCOs are known to be a persistent problem in fighter aircraft such as the F-16 and F/A-18 at high subsonic and transonic speeds (Bunton and Denegri, 2000). Denegri (2000) observed limit cycle oscillations in flight tests of F-16 and F/A-18 aircraft when certain wing-mounted stores were present, and Croft (2001) discussed limit cycle oscillations in the elevators of several Airbus passenger airplanes. The interaction between wing and store of a parametric F-16 wing was studied numerically by combining the finite element method and computational fluid mechanics (Cattarius, 1999). Flight tests were performed to measure actual LCOs of these fighters (Denegri, 2000). Lee and LeBlanc (1986) numerically examined the effects of cubic nonlinear stiffness on the flutter behavior of a two-dimensional airfoil. They established that when the system possessed softening stiffness, it exhibited the potential of subcritical LCOs which occurred below the linear flutter speed, indicating dependence on initial conditions; for a hardening spring, however, such dependence

on initial conditions disappeared, and a single LCO was obtained for a single value of the flow speed.

Lee and Desrochers (1987) considered different kinds of structural nonlinearities, such as free play (i.e., dead-zone nonlinearity) for flutter analysis. The existence of LCOs in prototypical aeroelastic wing sections with torsional nonlinearity including asymmetry was studied using the describing function method, and it was shown that the amplitude of a pitching LCO does not always increase with flow speed for certain elastic axis positions (Singh and Brenner, 2003). Computational and experimental studies of LCOs in nonlinear aeroelastic systems were also performed (O'Neil and Strganac, 1998; Sheta et al., 2002). In particular, Sheta et al. (2002) employed a multidisciplinary analysis to compare numerical with experimental data, suggesting the importance of modeling both the fluid and structural nonlinearities for accurate prediction of the onset and the magnitudes of LCOs. Normal form theory was utilized to investigate and unfold the subcritical/supercritical nature of the flutter Hopf bifurcation (Coller and Chamara, 2004); and a higher-order harmonic balance method was considered to study the secondary Hopf bifurcation of aeroelastic responses (Liu and Dowell, 2004). Gilliatt et al. (2003) studied the possibility of internal resonance in an aeroelastic system (a stall model) under nonlinear aerodynamic loads; and Lind et al. (2001) utilized numerical wavelet transform to model structural nonlinearities from flight data, and used its results to predict the onset of LCOs.

Many studies have attempted to analyze flutter behavior and the resulting LCOs; however, no works have focused on the modeling and physical understanding of the LCO triggering mechanism itself. The classical and prevailing notion of flutter from linear analysis is that '*... lift inputs energy into heave and pitch lags by 90°; flutter is a combination of the pitch and heave modes with phase and amplitude that extracts energy from the flow when either mode acting alone would be stable ...*' (Fung, 1955). Thus, the main objective of the study undertaken in this section is to understand the LCO triggering mechanism considering the simplest adequate model; i.e., to perform a study of the dynamics of how the LCOs are triggered and then developed in a wing model containing cubic nonlinear structural stiffness in both heave and pitch modes.

We start by reviewing the results of linear flutter analysis which can be found in references such as Dowell et al. (1995). Then, we formulate a theoretical framework for analyzing the dynamics of aeroelastic instability, by first examining the dominant frequency components in the transient responses via fast Fourier transforms (FFTs), and characterizing the instantaneous variations of their harmonic contents via wavelet transforms (WTs) as a reduced velocity varies. Next, we develop a slow flow model based on system identification of the dynamics, which will help us establish a multi-phase averaged system with three dominant fast frequency components utilizing the complexification-averaging (CX-A) technique [see Manevitch (2001), and also a similar analysis carried out in Sections 3.3 and 3.4]. Then, we present steady state bifurcation analysis utilizing the package MATCONT in Matlab[®] (Dhooge et al., 2003).

Based on this strong theoretical framework, and after reviewing some useful definitions and theories, we numerically study the LCO triggering mechanism using

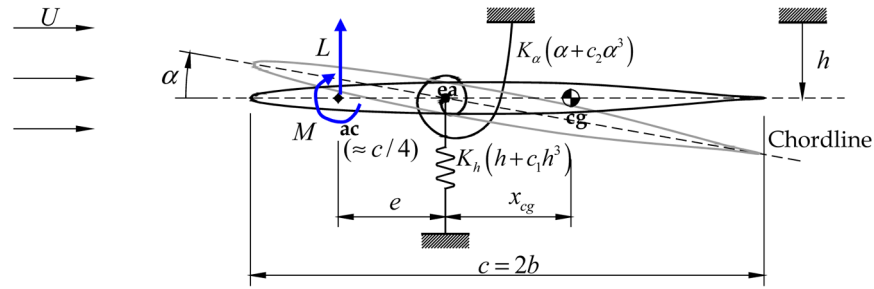


Fig. 9.23 Two-dimensional, two-DOF wing model.

the slow flow dynamics model, and demonstrate that it is composed of a series of *transient and sustained resonance captures* (Vakakis and Gendelman, 2001 – see also Section 2.4), through which energy transfers between the flow and aeroelastic modes occur. Eventually, energy balance is reached, leading to steady state periodic motions, or LCOs. Then, the partially-averaged systems derived at each stage constitute reliable analytical models that are used to study resonance capture phenomena that accompany *frequency shifting* (Zniber and Quinn, 2003) in the response due to fluid-structure interaction with increasing input energy. Finally, this section ends by presenting some concluding remarks.

9.2.1 The Two-DOF Aeroelastic Model

Consider an in-flow two-dimensional rigid wing model with two degrees of freedom, namely heave and pitch modes. Referring to the model presented in Figure 9.24, we denote by ac the aerodynamic center (usually assumed to be located at a quarter-chord); by ea , the elastic axis; by cg , the center of gravity; by h and α , the heave (positive downward) and pitch (positive clockwise) degrees of freedom, respectively; by $c = 2b$, the chord length; by e , the location of ac measured from the ea (positive forward of ea); by x_{cg} , the location of the cg measured from the ea (positive aft of the ea); by K_h and K_α , the linear bending and twist stiffness coefficients, respectively; by c_1 and c_2 , the nonlinear bending and twist stiffness factors, respectively; by U , the (constant and uniform) flow speed around the wing; by L and M , the lift and aerodynamic moments, respectively, acting at the ac so that equivalent aerodynamic forces acting at the ea can be computed as $L_{ea} = L$, $M_{ea} = M + eL \approx eL$ under the assumption of small angles.

Referring to Dowell et al. (1995), the equations of motion of the two-DOF aeroelastic model can be expressed as follows:

$$m\ddot{h} + S_\alpha\ddot{\alpha} + K_h(h + c_1 h^3) + q S C_{L,a} \left(\alpha + \frac{\dot{h}}{U} \right) = 0$$

$$I_\alpha \ddot{\alpha} + S_\alpha \dot{h} + K_\alpha (\alpha + c_2 \alpha^3) - q S e C_{L,\alpha} \left(\alpha + \frac{\dot{h}}{U} \right) = 0 \quad (9.36)$$

where m is the mass of the airfoil; S_α , the mass unbalance; I_α , the mass moment of inertia with respect to ea ; q , the dynamic pressure; $C_{L,\alpha} = \partial C_L / \partial \alpha|_{\alpha=0}$ the lift curve slope and C_L the lift coefficient for the airfoil; and S , the almost invariable platform area of the wing. The differentiation indicated by the over-dot is with respect to time t . *Quasi-steady aerodynamics* is assumed so the expression for the lift force is given by $L = q S (\partial C_L / \partial \alpha) (\alpha + \dot{h}/U)$.

Considering the fluid-structure interaction model that determines the fluid forces in (9.36), we note that *steady aerodynamic theory* assumes that the angle of twist of a wing is always equal to the angle of attack so that the relative velocity incident to the wing is exactly the same as the freestream velocity U , and that there are no time derivatives of h and α in the expression of the lift force. *Quasi-steady aerodynamic theory* considers the fluid force on the structure to be determined solely by the instantaneous relative velocity (i.e., by including terms associated with \dot{h} and $\dot{\alpha}$ in the expression of the lift), so that the fluid forces can be measured in wind-tunnel test on stationary models held at various angles. The quasi-steady assumption is valid only if the frequencies of the harmonic components of the fluid force, associated with vortex shedding or time-lag effects, are well above the frequencies of the structural modes of the wing, and this requirement is often met at higher reduced velocities (Blevins, 1990; Fung, 1955). Later in this chapter we will briefly consider the extension of the in-flow wing model for *unsteady aerodynamic theory*.

In non-dimensional form the equations of motion are rewritten as

$$\begin{aligned} y'' + x_\alpha \alpha'' + \mu C_{L,\alpha} \Theta y' + \Omega^2 y + \xi_y y^3 + \mu C_{L,\alpha} \Theta^2 \alpha &= 0, \\ r_\alpha^2 \alpha'' + x_\alpha y'' - \mu \gamma C_{L,\alpha} \Theta y' + (r_\alpha^2 - \mu \gamma C_{L,\alpha} \Theta^2) \alpha + \xi_\alpha \alpha^3 &= 0 \end{aligned} \quad (9.37)$$

where $y = h/b$ is the non-dimensional heave motion; $x_\alpha = S_\alpha / (mb) = x_{cg}/b$, the non-dimensional static unbalance; $\Omega = \omega_h / \omega_\alpha$, the ratio of uncoupled linear natural frequencies $\omega_h = \sqrt{K_h/m}$ and $\omega_\alpha = \sqrt{K_\alpha/I_\alpha}$; $\mu = \rho_\infty b S / (2m)$, the density ratio; $C_{L,\alpha} = \partial C_L / \partial \alpha$, the slope of the lift coefficient at zero angle of attack; $\Theta = U / (b\omega_\alpha)$, the reduced speed of the flow; r_α , the radius of gyration of the cross section of the wing; $\gamma = e/b$, the non-dimensional distance of the ea from the ac ; and ξ_y and ξ_α , the respective coefficients for the nonlinear stiffness terms. All dependent variables in (9.37), as well as their differentiations are with respect to the non-dimensional time $\tau = \omega_\alpha t$.

First, we perform a linearized analysis of (9.37) by seeking responses in the form, $y = e^{p\tau} \bar{y}$, $\alpha = e^{p\tau} \bar{\alpha}$ and considering only linear terms (i.e., setting $c_1 = c_2 \equiv 0$); this yields the following linearized eigenvalue problem:

$$\begin{bmatrix} p^2 + \mu C_{L,\alpha} \Theta p + \Omega^2 & x_\alpha p^2 + \mu C_{L,\alpha} \Theta^2 \\ x_\alpha p^2 - \mu \gamma C_{L,\alpha} \Theta p & r_\alpha^2 p^2 + r_\alpha^2 - \mu \gamma C_{L,\alpha} \Theta^2 \end{bmatrix} \begin{pmatrix} \bar{y} \\ \bar{\alpha} \end{pmatrix} = \begin{pmatrix} 0 \\ 0 \end{pmatrix} \quad (9.38)$$

The linearized solvability condition for the complex frequency equation becomes

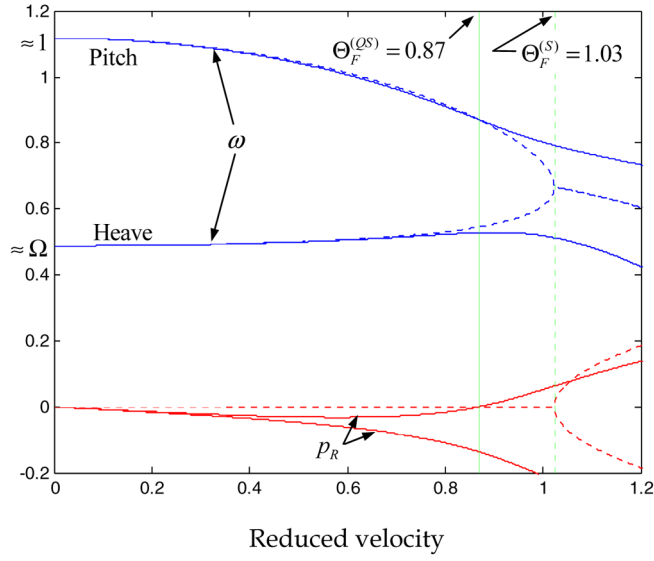


Fig. 9.24 Real and imaginary parts of the solutions of the eigenvalue problem (9.38) with respect to the reduced velocity; solid and dashed lines correspond to eigenvalues computed by using quasi-steady (QS) and steady (S) aerodynamics, respectively.

$$A_4 p^4 + A_3 p^3 + A_2 p^2 + A_1 p + A_0 = 0 \quad (9.39)$$

where

$$\begin{aligned} A_4 &= r_\alpha^2 - x_\alpha^2, & A_3 &= \mu C_{L,\alpha} \Theta (r_\alpha^2 + \gamma x_\alpha) \\ A_2 &= r_\alpha^2 (1 + \Omega^2) - \mu C_{L,\alpha} (x_\alpha + \gamma) \Theta^2 \\ A_1 &= \mu r_\alpha^2 C_{L,\alpha} \Theta, & A_0 &= \Omega^2 (r_\alpha^2 - \mu \gamma C_{L,\alpha} \Theta^2) \end{aligned} \quad (9.40)$$

Using the following numerical values for the parameters as defined by Dowell et al. (1995):

$$\begin{aligned} x_\alpha &= 0.2, & r_\alpha &= 0.5, & \gamma &= 0.4, & \Omega &= 0.5, \\ \mu &= (10\pi)^{-1}, & C_{L,\alpha} &= 2\pi, & \xi_y &= \xi_\alpha \equiv 1 \end{aligned} \quad (9.41)$$

we perform linearized flutter analysis to compute the reduced flutter speed $\Theta = \Theta_F$ at which divergent responses are predicted.

Figure 9.24 depicts the real and imaginary parts of the solution $p = p_R + j\omega$, $p_R, \omega \in \mathcal{R}$, $j = (-1)^{1/2}$ of (9.38). The real part p_R determines the stability of the trivial equilibrium; if $p_R > 0$, the solution is unstable, which implies divergent response of the wing. For comparison, we depict the results predicted from both steady aerodynamics and quasi-steady aerodynamics. The model based of steady aerody-

namics (S) predicts that the typical section model is neutrally stable for $\Theta < \Theta_F^S$ (that is, that all eigenvalues are purely imaginary); when $\Theta = \Theta_F^S$, the bending (heave) and torsion (pitch) frequencies merge in a phenomenon called *coalescence or merging frequency flutter* (Dowell et al., 1995). If $\Theta > \Theta_F^S$, the dynamics becomes unstable, and the responses diverge. On the other hand, the model based on quasi-steady aerodynamics (QS) predicts flutter at a lower value of the reduced velocity, $\Theta_F^{(QS)} < \Theta_F^{(S)}$, where the real parts of the complex pair of eigenvalues change sign from negative to positive (see Figure 9.24). We note that in the quasi-steady case there exists a tendency for the frequencies to merge but complete merging does not occur (Dowell et al., 1995).

For the above numerical parameter values, we obtain a flutter speed equal to $\Theta_F^{(QS)} \equiv \Theta_F = 0.87$. Note that steady aerodynamics predicts a higher flutter speed than quasi-steady theory (i.e., $\Theta_F^{(S)} = 1.03$), and also a higher coalescence frequency at the flutter speed for the steady flow condition.

Now we include nonlinear stiffnesses in both degrees of freedom of the model. Clearly, stability behavior of the trivial solution $y = \alpha \equiv 0$ will follow the linear analysis since the trivial solution is a hyperbolic equilibrium point, so we can invoke the *Hartman–Grobman Theorem* and claim topological conjugacy between the linear and nonlinear local vector fields sufficiently close to the hyperbolic equilibrium (Guckenheimer and Holmes, 1983). Also, due to the hardening nature of the nonlinearities of the system, which are expected to limit the amplitudes of the responses, the nonlinear system may possess LCOs at supercritical speeds (i.e., for $\Theta > \Theta_F$).

In Figure 9.25 we depict typical responses at subcritical and supercritical speeds of the linearized and nonlinear systems, respectively. We see that the linearized system predicts divergent responses, which, clearly, are not realistic, whereas, in actuality the nonlinearities restrict the growth of the diverging wing responses so that LCOs are developed instead. It follows that the development of LCOs is a direct product of aeroelastic instability in the system.

9.2.2 *Slow Flow Dynamics*

We now construct a slow flow model of the dynamics of system (9.37), based on slow-fast partition of the dynamics, and valid for response regimes both before and after flutter instability has occurred. For the construction of the model we separate the important (slow flow) from the secondary or unessential (fast flow) dynamics and utilize ideas from the CX-A methodology discussed in previous chapters.

9.2.2.1 **Dominant (Fast) Frequencies in the Responses**

To establish an accurate slow flow dynamical model capturing reliably and robustly the full nonlinear response of system (9.37), we need to consider the dominant fre-

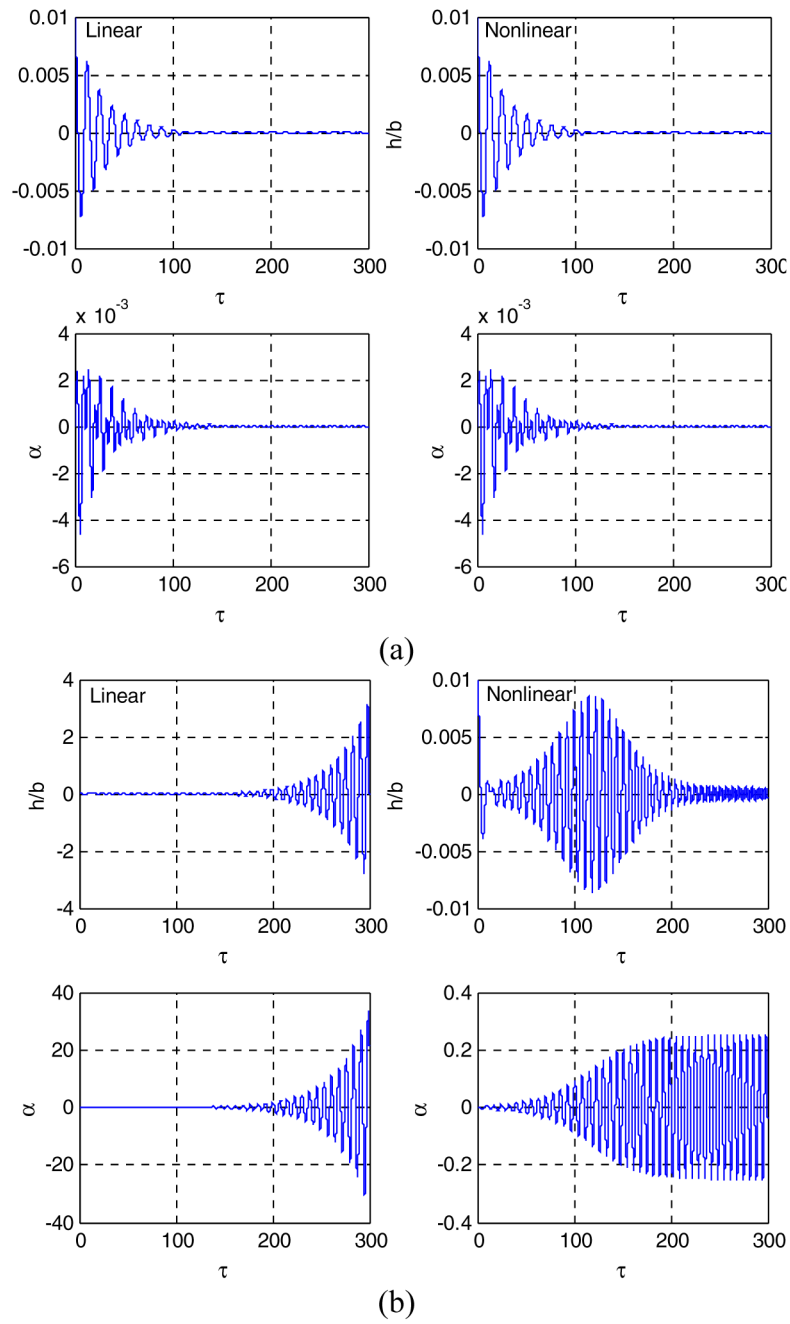


Fig. 9.25 Time responses at (a) subcritical ($\Theta = 0.5$) and (b) supercritical ($\Theta = 0.95$) reduced velocities in the linear and nonlinear models; initial conditions are given by $(y(0), \alpha(0), y'(0), \alpha'(0)) = (0.01, 0, 0, 0)$.

quency components of the dynamics in the different stages of the motion. These will be regarded as the ‘fast’ frequencies in the dynamics, in terms of which (‘slow’) modulation equations will be developed. This procedure will establish also the dimensionality of the slow flow of the transient nonlinear dynamics.

First, we examine the dominant frequency components in the transient responses for varying reduced velocity Θ . Figure 9.26 depicts power (FFT) spectra of the responses of the heave and pitch modes normalized with respect to their respective maxima at each value of the reduced velocity. For subcritical reduced speeds (i.e., $\Theta < \Theta_F$), there are only two dominant frequency components, ω_{heave} and ω_{pitch} , related to the two linearized natural frequencies for the heave and pitch (in terms of the non-dimensional frequencies defined previously the two dominant components are Ω and unity, respectively).

When the reduced velocity exceeds the flutter speed (i.e., $\Theta > \Theta_F$), there appear two dominant frequency components, ω_{pitch} and $3\omega_{\text{pitch}}$, for the heave mode, and one dominant frequency component, ω_{pitch} , for the pitch mode. This clearly shows that both below and above the flutter speed, the aeroelastic response of the wing contains at most three dominant frequency components, related to the two linear natural frequencies of the linear flutter model. That is, the lowest component corresponds to the heave mode $\omega_{\text{heave}} \approx \Omega = 0.5$, the middle one to the pitch mode, $\omega_{\text{pitch}} \approx 1$, and the highest one to approximately three times that of the pitch mode, $3\omega_{\text{pitch}} \approx 3$. In the following exposition we will refer to these three dominant frequencies by LF, MF, and HF (low, middle, and high frequency), respectively.

The FFT analysis provides an averaged (static) view of the frequency content of the transient nonlinear signals. Since the phenomena studied in this work are essentially nonlinear and transient, we resort instead to frequency decompositions based on numerical wavelet transforms (WTs), which provide information on the temporal evolutions of the dominant harmonic components of the subcritical or supercritical transient responses of the wing. This will enable us to clearly establish and study dynamical transitions occurring between different regimes of the transient motions. We perform WT analysis for two specific reduced velocities, namely, $\Theta = 0.5$ and $\Theta = 0.95$, corresponding to subcritical and supercritical wing responses, respectively, and depicted in Figures 9.27 and 9.28. However, the results presented herein can be similarly extended to other subcritical or supercritical reduced speeds.

Considering the plots of the WT spectra depicted in Figures 9.27 and 9.28, we note that when the flow speed is less than the flutter speed (in a subcritical regime – see Figure 9.27) the linearized natural frequency of the heave mode appears as the main frequency component in heave response, and that of the pitch mode as the minor. On the other hand, the pitching response possesses both heave and pitch harmonics with the pitch harmonic being the dominant one. Apparently, there exists a frequency relation of $\omega_{\text{pitch}} \approx 2\omega_{\text{heave}}$ as we may expect from the relation satisfied by the two linearized natural frequencies, i.e., a 1:2 internal resonance occurs in the transient dynamics of the wing when a flow speed is less than the flutter speed. In addition, we can deduce the existence of a non-negligible frequency component at the linearized heave natural frequency ($\Omega = 0.5$) in the pitch mode, so that the lowest likewise frequency components both in heave and pitch modes appear to

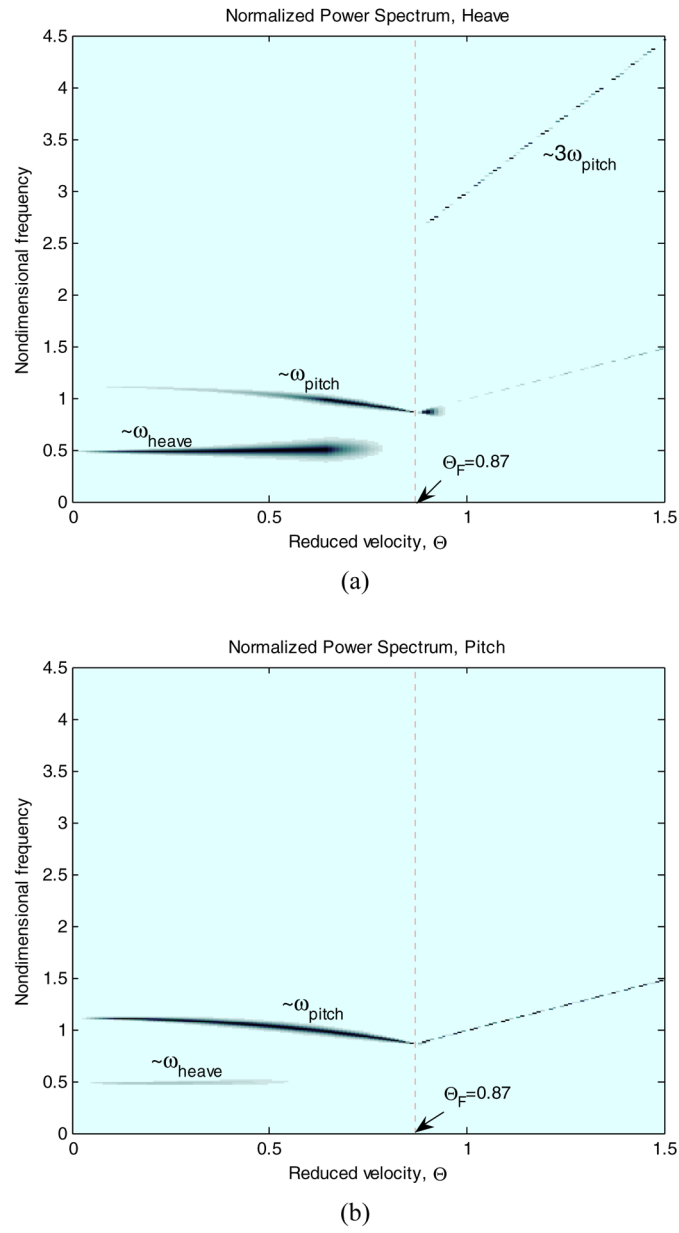
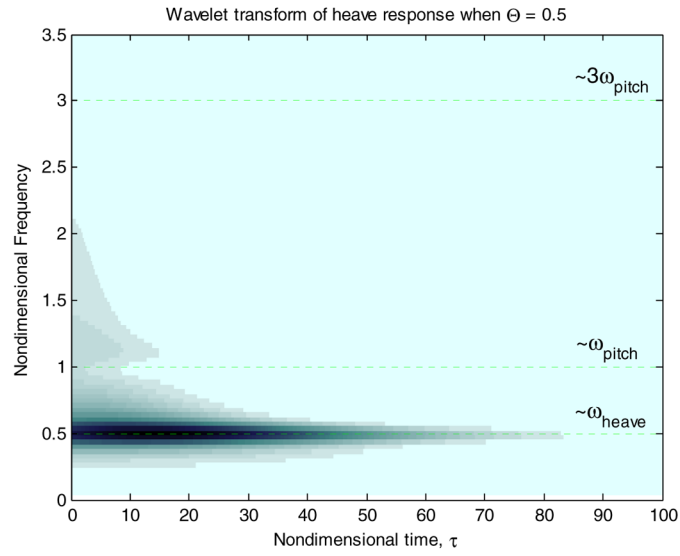
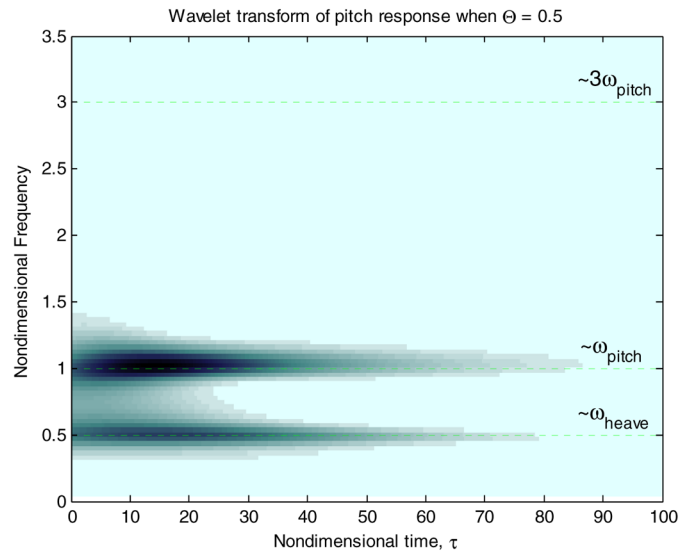


Fig. 9.26 Normalized power spectrum with respect to the reduced velocity; (a) heave mode, (b) pitch mode; heave ω_{heave} and pitch ω_{pitch} denote frequency components close to the linear natural frequencies of heave and pitch, respectively ($\omega_{\text{heave}} \approx \Omega = 0.5$ and $\omega_{\text{pitch}} \approx 1$); initial conditions are $(y(0), \alpha(0), y'(0), \alpha'(0)) = (0.01, 0, 0, 0)$.

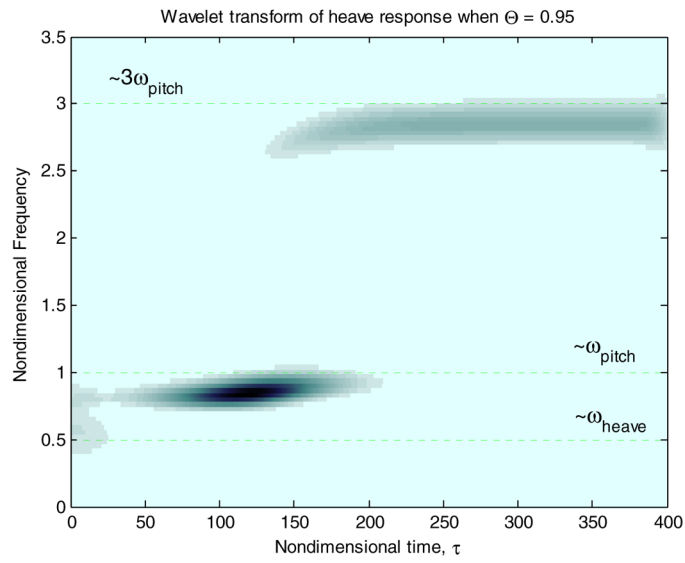


(a)

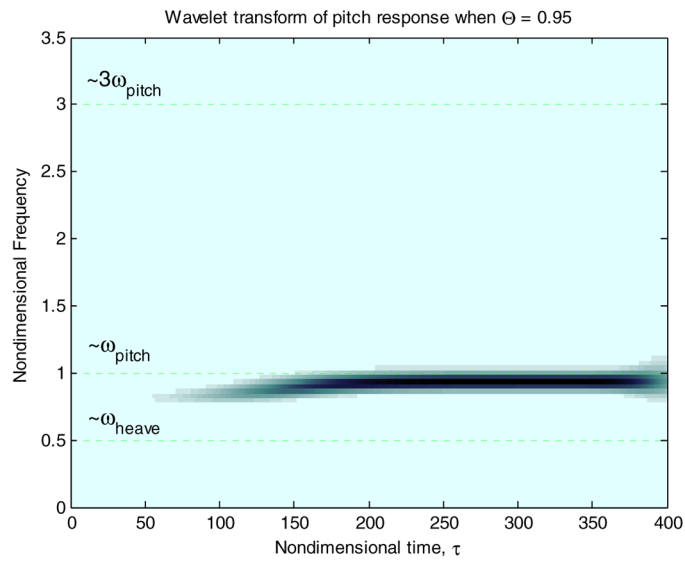


(b)

Fig. 9.27 WT spectra of transient responses at a subcritical speed ($\Theta = 0.5$); (a) heave mode, (b) pitch mode; initial conditions are given by $(y(0), \alpha(0), y'(0), \alpha'(0)) = (0.01, 0, 0, 0)$.



(a)



(b)

Fig. 9.28 WT spectra of transient responses at a supercritical speed ($\Theta = 0.95$); (a) heave mode, (b) pitch mode; initial conditions are given by $(y(0), \alpha(0), y'(0), \alpha'(0)) = (0.01, 0, 0, 0)$.

interact with each other up to $\tau \approx 80$. Later we will show numerically that this transient dynamics is also captured in a 1:1 resonance manifold (Quinn, 1997a; Vakakis and Gendelman, 2001), so that a 1:1 TRC occurs in the dynamics as well. Clearly, below the critical flutter velocity the energy extracted from the flow is being channeled and then exchanged between the nonlinear modes through resonance captures (as discussed below).

In the supercritical regime, however, a qualitative change in the dynamics occurs, since a sudden transition (jump) between frequency components takes place (see Figure 9.28). To understand this transition we will need to partition the dynamics into three separate phases: (i) an initial transient period, where likewise frequency components are likely to match each other leading to 1:1 TRC; (ii) a transition or escape from TRC into new frequency or resonance relations, where the basic heave harmonic gradually triggers the pitch mode at its dominant harmonic and then dies out, whereas at the same time a higher frequency component develops nearly at three times the linearized frequency of the pitch mode (i.e., a 3:1 superharmonic component); and finally, (iii) the generation of an LCO as a steady state response develops, where the resulting dominant harmonics are a 3:1 superharmonic component in heave mode, and a component at the pitch linearized frequency in pitch mode, resulting in a 3:1 sustained resonance capture (SRC). We will explore each one of these phases of the dynamics in detail, since they constitute the *triggering mechanism for LCOs* in the in-flow rigid wing.

9.2.2.2 Multi-Phase Averaging

Before proceeding to analyzing the different regimes of the previously outlined LCO triggering mechanism, it will be necessary to develop a slow flow model of the dynamics through multi-phase averaging, taking into account the previous WT-based frequency analysis. To this end, we reconsider the equations of motion (9.37), and through a linear coordinate transformation express them in the following inertially decoupled form:

$$\begin{aligned} y'' + \zeta_1 y' + k_{11}y + k_{12}\alpha + n_{11}y^3 + n_{12}\alpha^3 &= 0 \\ \alpha'' + \zeta_2 \alpha' + k_{21}y + k_{22}\alpha + n_{21}y^3 + n_{22}\alpha^3 &= 0 \end{aligned} \quad (9.42)$$

where the coefficients are defined as follows:

$$\begin{aligned} \zeta_1 &\equiv \mu C_{L,\alpha} \Theta (r_\alpha^2 + \gamma x_\alpha) / D, & \zeta_2 &\equiv -\mu C_{L,\alpha} \Theta (\gamma + x_\alpha) / D \\ k_{11} &\equiv r_\alpha^2 \Omega^2 / D, & k_{12} &\equiv \{ \mu C_{L,\alpha} \Theta^2 (r_\alpha^2 + \gamma x_\alpha) - r_\alpha^2 x_\alpha \} / D \\ k_{21} &\equiv -x_\alpha \Omega^2 / D, & k_{22} &\equiv \{ r_\alpha^2 - \mu C_{L,\alpha} \Theta^2 (\gamma + x_\alpha) \} / D \\ n_{11} &\equiv r_\alpha^2 \xi_y / D, & n_{12} &\equiv -x_\alpha \xi_\alpha / D, & n_{21} &\equiv -x_\alpha \xi_y / D, & n_{22} &\equiv \xi_\alpha / D \end{aligned} \quad (9.43)$$

and it holds that $D = r_\alpha^2 - x_\alpha^2 > 0$ for any mass distribution of the rigid wing. Note that only the coefficients $\zeta_1, \zeta_2, k_{12}, k_{22}$ are functions of the reduced velocity Θ . Moreover, the condition $k_{12} \equiv 0$ that results from the previous linearized eigenvalue analysis provides the following analytical (linearized) approximation for the flutter speed:

$$\Theta_F \equiv \sqrt{\frac{r_\alpha^2 x_\alpha}{\mu C_{L,\alpha}(r_\alpha^2 + \gamma x_\alpha)}} \quad (9.44)$$

It follows that $k_{12} < 0$ implies that $\Theta < \Theta_F$, so that no flutter occurs.

Motivated by our previous numerical analysis and the fact that there exist at most three dominant (fast) frequency components in the subcritical and supercritical in-flow wing responses, we decompose the heave and pitch transient responses in terms of the following three dominant frequency components:

$$\begin{aligned} y(\tau) &= y_1(\tau) + y_2(\tau) + y_3(\tau) \\ \alpha(\tau) &= \alpha_1(\tau) + \alpha_2(\tau) + \alpha_3(\tau) \end{aligned} \quad (9.45)$$

The subscripts 1, 2, and 3 denote terms possessing three distinct dominant (fast) frequencies, proportional to $e^{j\Omega\tau}$, $e^{j\tau}$, and $e^{3j\tau}$, respectively. This representation is similar to our previous theoretical analyses of transient responses possessing multiple fast frequency components (for example, see Sections 3.3 and 3.4).

Now, following the CX-A methodology (Manevitch, 2001) we introduce the following new complex variables:

$$\begin{aligned} \psi_1 &= y'_1 + j\Omega y_1, & \psi_3 &= y'_2 + jy_2, & \psi_5 &= y'_3 + 3jy_3 \\ \psi_2 &= \alpha'_1 + j\Omega\alpha_1, & \psi_4 &= \alpha'_2 + j\alpha_2, & \psi_6 &= \alpha'_3 + 3j\alpha_3 \end{aligned} \quad (9.46)$$

where $j^2 = -1$. Then, we may express the original real variables in (9.37) in terms of the new complex ones as follows:

$$\begin{aligned} y &= \frac{1}{2j\Omega}(\psi_1 - \psi_1^*) + \frac{1}{2j}(\psi_3 - \psi_3^*) + \frac{1}{6j}(\psi_5 - \psi_5^*) \\ \alpha &= \frac{1}{2j\Omega}(\psi_2 - \psi_2^*) + \frac{1}{2j}(\psi_4 - \psi_4^*) + \frac{1}{6j}(\psi_6 - \psi_6^*) \\ y' &= \frac{1}{2}(\psi_1 + \psi_1^* + \psi_3 + \psi_3^* + \psi_5 + \psi_5^*) \\ \alpha' &= \frac{1}{2}(\psi_2 + \psi_2^* + \psi_4 + \psi_4^* + \psi_6 + \psi_6^*) \\ y'' &= \psi'_1 + \psi'_3 + \psi'_5 - \frac{j\Omega}{2}(\psi_1 + \psi_1^*) - \frac{j}{2}(\psi_3 + \psi_3^*) - \frac{3j}{2}(\psi_5 + \psi_5^*) \\ \alpha'' &= \psi'_2 + \psi'_4 + \psi'_6 - \frac{j\Omega}{2}(\psi_2 + \psi_2^*) - \frac{j}{2}(\psi_4 + \psi_4^*) - \frac{3j}{2}(\psi_6 + \psi_6^*) \end{aligned} \quad (9.47)$$

At this point we introduce a slow-fast partition of the dynamics, by partitioning the complex responses into slow and fast parts,

$$\begin{aligned}\psi_1(\tau) &= \varphi_1(\tau) e^{j\Omega\tau}, \psi_3(\tau) = \varphi_3(\tau) e^{j\tau}, \psi_5(\tau) = \varphi_5(\tau) e^{3j\tau} \\ \psi_2(\tau) &= \varphi_2(\tau) e^{j\Omega\tau}, \psi_4(\tau) = \varphi_4(\tau) e^{j\tau}, \psi_6(\tau) = \varphi_6(\tau) e^{3j\tau}\end{aligned}\quad (9.48)$$

where $\varphi_k(\tau)$, $k = 1, 2, \dots, 6$ represent slowly-varying, complex-valued amplitude modulations. In expressing the variables according to (9.48) we assume that the transient responses are composed of ‘fast’ oscillations [represented by the complex exponentials in (9.48)] modulated by ‘slow’ envelopes [represented by the complex amplitudes $\varphi_k(\tau)$]. These partitions are fully compatible with the results of numerical simulations. It should be clear that the (slow) temporal evolutions of the modulations $\varphi_k(\tau)$ govern the important (essential) dynamics of system (9.37) in an appropriately defined slow flow phase space. Interestingly enough, the dimensionality of the slow flow phase space – in this case this space is 12-dimensional – exceeds the dimensionality of the phase space of the original system (9.37) – which is four-dimensional; this is due to the fact that the dimensionality of the slow flow phase space depends on the number of dominant harmonics that govern the transient dynamics – in this case three.

Substituting (9.47) and (9.48) into (9.37) and applying multi-phase averaging (Lochak and Meunier, 1988) over the frequency components $e^{j\Omega\tau}$, $e^{j\tau}$, and $e^{3j\tau}$ we obtain six complex-valued, ordinary differential equations governing the slow evolutions of the modulations, in the compact form

$$\varphi' + F(\varphi; \Theta) = 0, \quad F, \varphi \in C^6, \quad \Theta \in R \quad (9.49)$$

where the reduced velocity Θ is regarded as the independent parameter of the problem. The detailed form of the slow flow (9.49) is given below:

$$\begin{aligned}\varphi_1' + \frac{1}{2} \left[\zeta_1 + j \left(\Omega - \frac{k_{11}}{\Omega} \right) \right] \varphi_1 - \frac{jk_{12}}{2\Omega} \varphi_2 - \frac{3j}{8\Omega^3} (n_{11}\varphi_1|\varphi_1|^2 + n_{12}\varphi_2|\varphi_2|^2) \\ - \frac{3j}{4\Omega} (n_{11}\varphi_1|\varphi_3|^2 + n_{12}\varphi_2|\varphi_4|^2) - \frac{j}{12\Omega} (n_{11}\varphi_1|\varphi_5|^2 + n_{12}\varphi_2|\varphi_6|^2) = 0 \\ \varphi_2' + \frac{1}{2} \left(\zeta_2 - j \frac{k_{21}}{\Omega} \right) \varphi_1 + \frac{j}{2} \left(\Omega - \frac{k_{22}}{\Omega} \right) \varphi_2 - \frac{3j}{8\Omega^3} (n_{21}\varphi_1|\varphi_1|^2 + n_{22}\varphi_2|\varphi_2|^2) \\ - \frac{3j}{4\Omega} (n_{21}\varphi_1|\varphi_3|^2 + n_{22}\varphi_2|\varphi_4|^2) - \frac{j}{12} (n_{21}\varphi_1|\varphi_5|^2 + n_{22}\varphi_2|\varphi_6|^2) = 0 \\ \varphi_3' + \frac{1}{2} [\zeta_1 + j(1 - k_{11})] \varphi_3 - \frac{jk_{12}}{2} \varphi_4 - \frac{3j}{4\Omega^2} (n_{11}\varphi_3|\varphi_1|^2 + n_{12}\varphi_4|\varphi_2|^2) \\ - \frac{3j}{8} (n_{11}\varphi_3|\varphi_3|^2 + n_{12}\varphi_4|\varphi_4|^2) - \frac{j}{12} (n_{11}\varphi_3|\varphi_5|^2 + n_{12}\varphi_4|\varphi_6|^2) \\ + \frac{j}{8} (n_{11}\varphi_3^{*2}\varphi_5 + n_{12}\varphi_4^{*2}\varphi_6) = 0\end{aligned}$$

$$\begin{aligned}
& \varphi_4' + \frac{1}{2}(\zeta_2 - jk_{21})\varphi_3 + \frac{j}{2}(1 - k_{22})\varphi_4 - \frac{3j}{4\Omega^2}(n_{21}\varphi_3|\varphi_1|^2 + n_{22}\varphi_4|\varphi_2|^2) \\
& - \frac{3j}{8}(n_{21}\varphi_3|\varphi_3|^2 + n_{22}\varphi_4|\varphi_4|^2) - \frac{j}{12}(n_{21}\varphi_3|\varphi_5|^2 + n_{22}\varphi_4|\varphi_6|^2) \\
& + \frac{j}{8}(n_{21}\varphi_3^{*2}\varphi_5 + n_{22}\varphi_4^{*2}\varphi_6) = 0 \\
& \varphi_5' + \frac{1}{2}\left[\xi_1 + j\left(3 - \frac{k_{11}}{3}\right)\right]\varphi_5 - \frac{jk_{12}}{6}\varphi_6 - \frac{j}{4\Omega^2}(n_{11}\varphi_5|\varphi_1|^2 + n_{12}\varphi_6|\varphi_2|^2) \\
& - \frac{j}{4}(n_{11}\varphi_5|\varphi_3|^2 + n_{12}\varphi_6|\varphi_4|^2) - \frac{j}{72}(n_{11}\varphi_5|\varphi_5|^2 + n_{12}\varphi_6|\varphi_6|^2) \\
& + \frac{j}{8}(n_{11}\varphi_3^3 + n_{12}\varphi_4^3) = 0 \\
& \varphi_6' + \frac{1}{2}\left(\zeta_2 - j\frac{k_{21}}{3}\right)\varphi_5 + \frac{j}{2}\left(3 - \frac{k_{22}}{3}\right)\varphi_6 - \frac{j}{4\Omega^2}(n_{21}\varphi_5|\varphi_1|^2 + n_{22}\varphi_6|\varphi_2|^2) \\
& - \frac{j}{4}(n_{21}\varphi_5|\varphi_3|^2 + n_{22}\varphi_6|\varphi_4|^2) - \frac{j}{72}(n_{21}\varphi_5|\varphi_5|^2 + n_{22}\varphi_6|\varphi_6|^2) \\
& + \frac{j}{8}(n_{21}\varphi_3^3 + n_{22}\varphi_4^3) = 0
\end{aligned} \tag{9.50}$$

The plots presented in Figures 9.29 and 9.30 demonstrate the validity of the averaged system with ‘optimally’ determined initial conditions (see below) compared to the (numerically) exact solutions for both subcritical and supercritical reduced velocities. Our careful numerical study (not fully shown herein) indicates that the three-harmonic slow flow model (9.49) approximates well the original dynamics at the entire range of reduced speeds, i.e., the averaged system is valid for accurately modeling the nonlinear dynamics over the entire subsonic fluid-structure interaction regime.

We note that each of the dominant harmonic components in the model (9.45) can be recovered from the averaged system (9.49), according to the following expressions:

$$\begin{aligned}
y_1(\tau) &= \frac{1}{\Omega}\text{Im}[\varphi_1(\tau)e^{j\Omega\tau}], & \alpha_1(\tau) &= \frac{1}{\Omega}\text{Im}[\varphi_2(\tau)e^{j\Omega\tau}] \\
y_2(\tau) &= \text{Im}[\varphi_3(\tau)e^{j\tau}], & \alpha_2(\tau) &= \text{Im}[\varphi_4(\tau)e^{j\tau}] \\
y_3(\tau) &= \frac{1}{3}\text{Im}[\varphi_5(\tau)e^{3j\tau}], & \alpha_3(\tau) &= \frac{1}{3}\text{Im}[\varphi_6(\tau)e^{3j\tau}]
\end{aligned} \tag{9.51}$$

so we may reconstruct the heave and pitch responses directly from the decompositions (9.45).

An interesting point now discussed concerns the choice of initial conditions of the averaged set of equations (9.50). Because we need twelve initial conditions for the averaged system, and we possess only four available initial conditions for the full

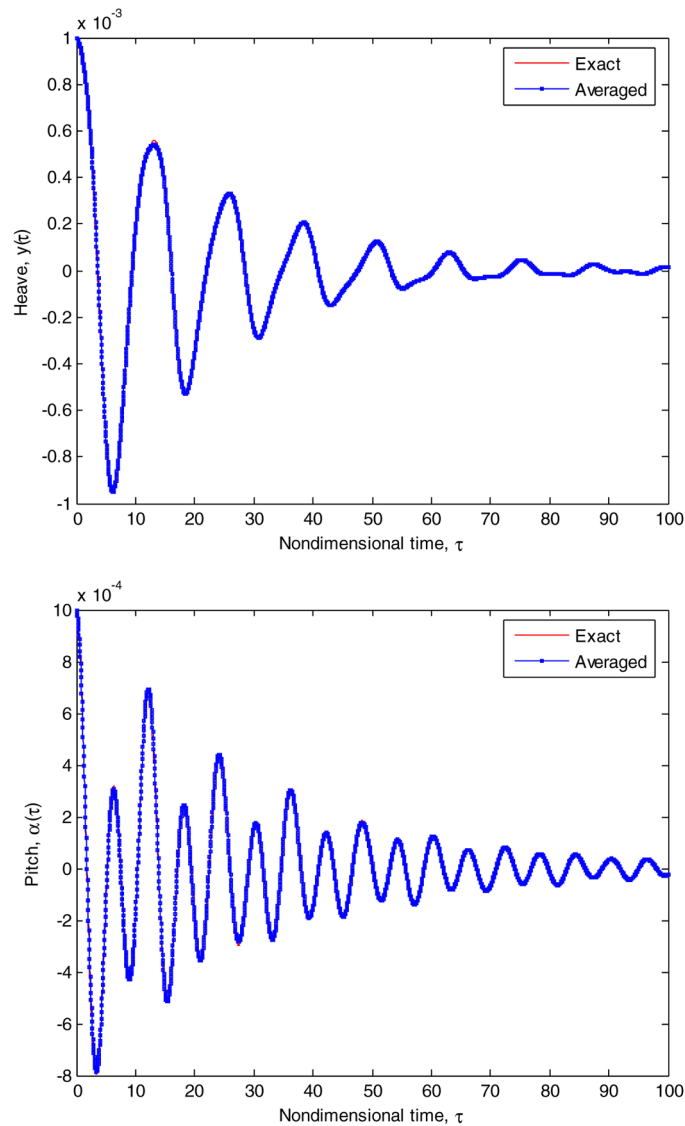


Fig. 9.29 Validation of the averaged system (9.50) for a subcritical reduced velocity ($\Theta = 0.5$), with initial conditions $(y(0), \alpha(0), y'(0), \alpha'(0)) = (10^{-3}, 10^{-3}, 0, 0)$.

system (9.37), the problem of determining the appropriate initial conditions of the slow flow model becomes indeterminate. This problem also arose in Section 3.4.2.2, where the analytical study of subharmonic TET in a two-DOF system was carried out.

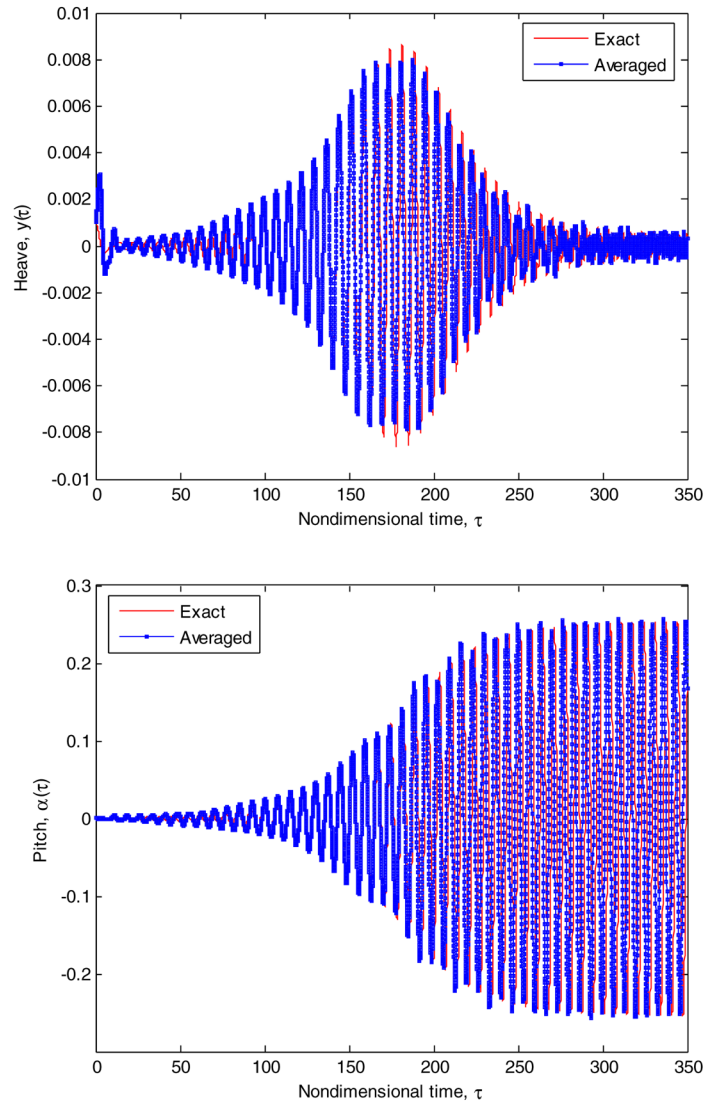


Fig. 9.30 Validation of the averaged system (9.50) for a supercritical reduced velocity ($\Theta = 0.95$), with initial conditions $(y(0), \alpha(0), y'(0), \alpha'(0)) = 10^{-3}, 10^{-3}, 0, 0$.

Returning to the problem of determining the initial conditions of the slow flow (9.50), we may express the initial conditions directly from the decomposition (9.45),

$$\begin{aligned}
 y(0) &= y_1(0) + y_2(0) + y_3(0), & \alpha(0) &= \alpha_1(0) + \alpha_2(0) + \alpha_3(0) \\
 y'(0) &= y'_1(0) + y'_2(0) + y'_3(0), & \alpha'(0) &= \alpha'_1(0) + \alpha'_2(0) + \alpha'_3(0) \quad (9.52)
 \end{aligned}$$

which leads to the expressions

$$\begin{aligned}\varphi_1(0) &= y'_1(0) + j\Omega y_1(0), & \varphi_2(0) &= \alpha'_1(0) + j\Omega\alpha_1(0) \\ \varphi_3(0) &= y'_2(0) + jy_2(0), & \varphi_4(0) &= \alpha'_2(0) + j\alpha_2(0) \\ \varphi_5(0) &= y'_3(0) + 3jy_3(0), & \varphi_6(0) &= \alpha'_3(0) + 3j\alpha_3(0)\end{aligned}\quad (9.53)$$

under the restrictions:

$$\begin{aligned}\operatorname{Im} \varphi_3(0) &= y(0) - \left[\frac{1}{\Omega} \operatorname{Im} \varphi_1(0) + \frac{1}{3} \operatorname{Im} \varphi_5(0) \right] \\ \operatorname{Im} \varphi_4(0) &= \alpha(0) - \left[\frac{1}{\Omega} \operatorname{Im} \varphi_2(0) + \frac{1}{3} \operatorname{Im} \varphi_6(0) \right] \\ \operatorname{Re} \varphi_3(0) &= y'(0) - [\operatorname{Re} \varphi_1(0) + \operatorname{Re} \varphi_5(0)] \\ \operatorname{Re} \varphi_4(0) &= \alpha'(0) - [\operatorname{Re} \varphi_2(0) + \operatorname{Re} \varphi_6(0)]\end{aligned}\quad (9.54)$$

The determination of the initial conditions for the averaged system (9.50) is thus converted to the optimization problem of computing the minimum of the normalized mean square error,

$$E[\|x - x_a\|^2] / E[\|x - E[x]\|^2]$$

in the time interval $0 < \tau < \hat{\tau}$ for some $\hat{\tau}$, where the quantity to be minimized is regarded as function of the six sought initial conditions $\{\varphi_1(0), \dots, \varphi_6(0)\}$; $E[\cdot]$ denotes the mean value, and $\|\cdot\|$ the norm based on the standard inner product; moreover, $x(\tau) \equiv (y(\tau), \alpha(\tau))^T$ and $x_a(\tau) \equiv (y_a(\tau), \alpha_a(\tau))^T$ are the response vectors of the exact and averaged systems, respectively. Note that the solution of this optimization problem may not be unique, since it depends on the topological properties and singularities of the solution manifold in the corresponding space (for example, the solution manifold may have several local minima so that the ‘optimal’ solution can be computed as any one of them).

We may avoid this lack of uniqueness by expressing the solutions of the optimization problem in Taylor series

$$\varphi_i(\tau) = \sum_{j=0}^N \varphi_{ij} \tau^j + O(\tau^{N+1}) \quad (9.55)$$

where $\varphi_{ij} \in \mathbb{C}$, $i = 1, \dots, 6$ as $\tau \rightarrow 0$ (hence, we assume that $|\hat{\tau}| \ll 1$), and matching the series with the exact solutions at a specified matching time instant to determine uniquely each of the Taylor coefficients. Then we can construct the normal equation and find the so-called Moore-Penrose least squares solution which should be unique in terms of the *Fredholm Alternative Theorem* (i.e., see Keener, 2000). However, this kind of matching – in spite of uniqueness – may not provide good long-term results, particularly for higher-order approximations or multi-phase averaging. For example, Keener (1977) studied the validity of the two-timing method

(method of multiple scales, or, equivalently, first-order averaging method) for limit cycles for large times; he showed that the approximate solution, which is *pointwise valid* only for times of order $O(1/\varepsilon)$, is *orbitally valid* for large times in the sense that the approximate solution (although not necessarily pointwise valid for all times) approaches a valid approximation of a stable limit cycle.

Therefore, in this work we consider approximate solutions in the sense of orbital validity by way of the ‘optimal’ initial conditions, instead of pointwise accuracy which is guaranteed only up to a small time scale and may provide inaccurate results in the long run.

Considering the analysis of the slow flow (9.49–9.50), two different formulations for analyzing the slow flow dynamics can be followed, by expressing the complex quantities in Cartesian or polar coordinates. Let us first consider the slow flow equations in Cartesian coordinates. Expressing $\varphi_k(\tau) = z_{2k-1}(\tau) + j z_{2k}(\tau)$, $k = 1, \dots, 6$, where $z_i \in R$, $\forall i$ into (9.50), we obtain twelve (real-valued) slow flow modulation equations:

$$Z' = G(Z; \Theta), \quad Z = (z_1, \dots, z_2) \in R^{12}, \quad \Theta \in R \quad (\text{Cartesian coordinates}) \quad (9.56)$$

Alternatively, expressing the complex quantities in polar-form, we express $\varphi_k(\tau) = a_k(\tau) e^{j\beta_k(\tau)}$, $a_k \in R^+$, $\beta_k \in S^1$, $k = 1, \dots, 6$, which when substituted into (9.50), and upon separation of real and imaginary parts, leads again to a set of 12 slow flow equations in the form:

$$a'_k = \tilde{f}_k(a, \beta; \Theta) \quad \text{and} \quad a_k \beta'_k = \tilde{g}_k(a, \beta; \Theta) \quad (9.57)$$

The exact form of these equations is given below:

$$\begin{aligned} a'_1 + \frac{\xi_1}{2} a_1 - \frac{a_2}{2\Omega} \sin(\beta_1 - \beta_2) \left(k_{12} + \frac{3n_{12}}{4\Omega^2} a_2^2 + \frac{3n_{12}}{2} a_4^2 + \frac{n_{12}}{6} a_6^2 \right) &= 0 \\ a'_2 + \frac{\xi_2}{2} a_1 \cos(\beta_1 - \beta_2) & \\ + \frac{a_1}{2\Omega} \sin(\beta_1 - \beta_2) \left(k_{21} + \frac{3n_{21}}{4\Omega^2} a_1^2 + \frac{3n_{21}}{2} a_3^2 + \frac{n_{21}}{6} a_5^2 \right) &= 0 \\ a'_3 + \frac{\xi_1}{2} a_3 - \frac{a_4}{2} \sin(\beta_3 - \beta_4) \left(k_{12} + \frac{3n_{12}}{2\Omega^2} a_2^2 + \frac{3n_{12}}{4} a_4^2 + \frac{n_{12}}{6} a_6^2 \right) & \\ + \frac{n_{11}}{8} a_3^2 a_5 \sin(3\beta_3 - \beta_5) + \frac{n_{12}}{8} a_4^2 a_6 \sin(\beta_3 + 2\beta_4 - \beta_6) &= 0 \\ a'_4 + \frac{\xi_2}{2} a_3 \cos(\beta_3 - \beta_4) + \frac{a_3}{2} \sin(\beta_3 - \beta_4) \left(k_{21} + \frac{3n_{21}}{2\Omega^2} a_1^2 + \frac{3n_{21}}{4} a_3^2 + \frac{n_{21}}{6} a_5^2 \right) & \\ + \frac{n_{22}}{8} a_4^2 a_6 \sin(3\beta_4 - \beta_6) + \frac{n_{21}}{8} a_3^2 a_5 \sin(2\beta_3 + \beta_4 - \beta_5) &= 0 \end{aligned}$$

$$\begin{aligned}
& a_5' + \frac{\zeta_1}{2} a_5 - \frac{a_6}{6} \sin(\beta_5 - \beta_6) \left(k_{12} + \frac{3n_{12}}{2\Omega^2} a_2^2 + \frac{3n_{12}}{2} a_4^2 + \frac{n_{12}}{12} a_6^2 \right) \\
& \quad - \frac{n_{11}}{8} a_3^3 \sin(3\beta_3 - \beta_5) - \frac{n_{12}}{8} a_4^3 \sin(3\beta_4 - \beta_5) = 0 \\
& a_6' + \frac{\zeta_2}{2} a_5 \cos(\beta_5 - \beta_6) + \frac{a_5}{6} \sin(\beta_5 - \beta_6) \left(k_{21} + \frac{3n_{21}}{2\Omega^2} a_1^2 + \frac{3n_{21}}{2} a_3^2 + \frac{n_{21}}{12} a_5^2 \right) \\
& \quad - \frac{n_{22}}{8} a_4^3 \sin(3\beta_4 - \beta_6) - \frac{n_{21}}{8} a_3^3 \sin(3\beta_3 - \beta_6) = 0 \\
& a_1 \beta_1' + \frac{a_1}{2\Omega} \left(\Omega^2 - k_{11} - \frac{3n_{11}}{4\Omega^2} a_1^2 - \frac{3n_{11}}{2} a_3^2 - \frac{n_{11}}{6} a_5^2 \right) \\
& \quad - \frac{a_2}{2\Omega} \cos(\beta_1 - \beta_2) \left(k_{12} + \frac{3n_{12}}{4\Omega^2} a_2^2 + \frac{3n_{12}}{2} a_4^2 + \frac{n_{12}}{6} a_6^2 \right) = 0 \\
& a_2 \beta_2' + \frac{a_2}{2\Omega} \left(\Omega^2 - k_{22} - \frac{3n_{22}}{4\Omega^2} a_2^2 - \frac{3n_{22}}{2} a_4^2 - \frac{n_{22}}{6} a_6^2 \right) + \frac{\zeta_1}{2} a_1 \sin(\beta_1 - \beta_2) \\
& \quad - \frac{a_1}{2\Omega} \cos(\beta_1 - \beta_2) \left(k_{21} + \frac{3n_{21}}{4\Omega^2} a_1^2 + \frac{3n_{21}}{2} a_3^2 + \frac{n_{21}}{6} a_5^2 \right) = 0 \\
& a_3 \beta_3' + \frac{a_3}{2} \left(1 - k_{11} - \frac{3n_{11}}{2\Omega^2} a_1^2 - \frac{3n_{11}}{4} a_3^2 - \frac{n_{11}}{6} a_5^2 \right) \\
& \quad - \frac{a_4}{2} \cos(\beta_3 - \beta_4) \left(k_{12} + \frac{3n_{12}}{2\Omega^2} a_2^2 + \frac{3n_{12}}{4} a_4^2 + \frac{n_{12}}{6} a_6^2 \right) \\
& \quad + \frac{n_{11}}{8} a_3^2 a_5 \cos(3\beta_3 - \beta_5) + \frac{n_{12}}{8} a_4^2 a_6 \cos(\beta_3 + 2\beta_4 - \beta_6) = 0 \\
& a_4 \beta_4' + \frac{a_4}{2} \left(1 - k_{22} - \frac{3n_{22}}{2\Omega^2} a_2^2 - \frac{3n_{22}}{4} a_4^2 - \frac{n_{22}}{6} a_6^2 \right) + \frac{\zeta_2}{2} a_3 \sin(\beta_3 - \beta_4) \\
& \quad - \frac{a_3}{2} \cos(\beta_3 - \beta_4) \left(k_{21} + \frac{3n_{21}}{2\Omega^2} a_1^2 + \frac{3n_{21}}{4} a_3^2 + \frac{n_{21}}{6} a_5^2 \right) \\
& \quad + \frac{n_{22}}{8} a_4^2 a_6 \cos(3\beta_4 - \beta_6) + \frac{n_{21}}{8} a_3^2 a_5 \cos(2\beta_3 + \beta_4 - \beta_5) = 0 \\
& a_5 \beta_5' + \frac{a_5}{6} \left(9 - k_{11} - \frac{3n_{11}}{2\Omega^2} a_1^2 - \frac{3n_{11}}{2} a_3^2 - \frac{n_{11}}{12} a_5^2 \right) \\
& \quad - \frac{a_6}{6} \cos(\beta_5 - \beta_6) \left(k_{12} + \frac{3n_{12}}{2\Omega^2} a_2^2 + \frac{3n_{12}}{2} a_4^2 + \frac{n_{12}}{12} a_6^2 \right) \\
& \quad + \frac{n_{11}}{8} a_3^3 \cos(3\beta_3 - \beta_5) + \frac{n_{12}}{8} a_4^3 \cos(3\beta_4 - \beta_5) = 0 \\
& a_6 \beta_6' + \frac{a_6}{6} \left(9 - k_{22} - \frac{3n_{22}}{2\Omega^2} a_2^2 - \frac{3n_{22}}{2} a_4^2 - \frac{n_{22}}{12} a_6^2 \right) + \frac{\zeta_2}{2} a_5 \sin(\beta_5 - \beta_6)
\end{aligned}$$

$$\begin{aligned}
& -\frac{a_5}{6} \cos(\beta_5 - \beta_6) \left(k_{21} + \frac{3n_{21}}{2\Omega^2} a_1^2 + \frac{3n_{21}}{2} a_3^2 + \frac{n_{21}}{12} a_5^2 \right) \\
& + \frac{n_{22}}{8} a_4^3 \cos(3\beta_4 - \beta_6) + \frac{n_{21}}{8} a_3^3 \cos(3\beta_3 - \beta_6) = 0
\end{aligned} \tag{9.58}$$

By combining these equations we derive the following alternative autonomous set of slow flow modulation equations:

$$a'_k = f_k(a, \phi; \Theta), \quad a_i a_p \phi'_{ip} = g_n(a, \phi; \Theta) \quad (\text{polar coordinates}) \tag{9.59}$$

where $k = 1, \dots, 6$, $\phi_{ip} \equiv \beta_i - \beta_p$ and $(n; i, p) = (1; 1, 2), (2; 3, 5), (3; 3, 6), (4; 4, 5), (5; 4, 6)$. There are only five independent phase relations in (9.60) representing five phase differences between components of the solution with the following physical meanings: ϕ_{12} represents the interaction between LF heave and LF pitch; ϕ_{35} represents the interaction between MF heave and HF heave; ϕ_{36} represents the interaction between MF heave and HF pitch; ϕ_{45} represents the interaction between MF pitch and HF heave; and ϕ_{46} represents the interaction between MF pitch and HF pitch. It can be shown that all other possible phase differences arising in (9.60) can be expressed in terms of these five independent phase variables; for example, the phase interaction between MF heave and MF pitch can be expressed as

$$\phi_{34} = \frac{1}{3} (\phi_{35} - \phi_{45}) \quad \text{or} \quad \frac{1}{3} (\phi_{36} - \phi_{46}).$$

Although the modulation sets (9.57) and (9.58) are equivalent, in the following analysis we will be using the modulation equations in the polar form, equations (9.58) or in autonomous form, equations (9.60), since they provide direct information for the amplitudes of the components of the solution, as well as, for the phases representing the nonlinear interactions between these components. A well recognized mathematical deficiency, however, of the equations in polar form relates to the mathematical singularity of the polar transformation at the origin, which renders the set (9.58) invalid for analyzing the dynamics when some of the components have zero (or nearly zero) amplitudes. In that case the modulation equations in Cartesian form, (9.57), should be used instead.

9.2.2.3 Bifurcation Analysis of Steady State Dynamics

Before we employ the slow flow model to study the LCO triggering mechanism, we perform a steady state bifurcation analysis of the dynamics utilizing MATCONT in Matlab[®] (Dhooge et al., 2003), in conjunction with the algorithm introduced in Kubíček (1976) utilizing parameterization with respect to the arc length of equilibrium loci (see Section 9.1.3).

To this end, we consider the original equations of motion (9.42), and express them in the following first-order form:

$$x' = X(x; \Theta) \quad \text{where} \quad x = (y, \alpha, y', \alpha')^T, \quad \Theta \in R \quad (9.60)$$

Direct application of MATCONT on these first-order differential equations provides bifurcation diagrams that yield information on the global dynamics of the full system at steady state, as depicted in Figure 9.39. As we discussed in Section 9.2.1, the (stable) trivial equilibrium $x = 0$ undergoes a Hopf bifurcation at the flutter speed $\Theta_F = 0.87$, and changes its stability with simultaneous generation of a stable LCO. When the reduced velocity reaches the divergence flutter speed $\Theta_D = 1.767$, two unstable non-trivial equilibrium points are computed. The solution curve for heave appears to be almost vertical at Θ_D , while that for pitch this does not hold. The physical interpretation is that, for reduced velocities higher than the divergence flutter speed, almost every heave position can be an equilibrium position whereas the pitch mode attains a specific equilibrium position. We note that, if we zoom out the vertical axis in Figure 9.31a to the same order as in Figure 9.31b, then the heave equilibrium curve also looks like a parabola; but this understanding may not be physically meaningful. In any case, these nontrivial equilibrium points are unstable so that they are not physically realizable. The divergence due to flutter represents a ‘static’ instability from a dynamics point of view (Blevins, 1990) and the corresponding reduced speed can be computed from static balance as

$$\Theta_D \equiv \sqrt{r_\alpha^2 / (\gamma \mu C_{L,\alpha})} \quad (9.61)$$

Since the above results provide only global information regarding to where and what type of bifurcations occur, and how large the LCO amplitudes are, they will not help us understand the nonlinear modal interactions that generate the fluid-structure instabilities that eventually act as LCO triggering mechanisms. To address this issue it is necessary to perform bifurcation analysis of the averaged system (9.57) for the trivial equilibrium via MATCONT, and for (9.60) for the nontrivial LCOs utilizing Kubíček’s method (1976). The reason for using two different approaches is dictated by the possible singularities built in (9.60) when one of the amplitudes becomes zero; then, the set degenerates to a set of differential-algebraic equations and becomes unsolvable using MATCONT since this package only solves differential equations of the standard form $x' = X(x; \sigma)$ where $x \in R^n$, $\sigma \in R^k$.

Figure 9.32 depicts the numerical continuation results for steady state amplitudes and phase differences for the multi-phase averaged system (9.60). We note that after the speed exceeds the critical value of flutter the HF heave and MF pitch components are dominant at steady state, a result that is consistent with numerical simulations. These steady state results will be revisited in a later section where analytical study of the LCO triggering mechanism is carried out.

Because our wing model assumes small oscillations, $|\alpha| < 10^\circ \approx 0.1745$ rad, the numerical solutions at higher supercritical speeds may deviate from physical observations. In addition, we may not observe the secondary Hopf bifurcation by our slow flow analysis, since at least five dominant harmonics are required for its computation (Liu and Dowell, 2004). Moreover, only supercritical LCOs will be obtained due to the specific parameter choices used in our numerical study.

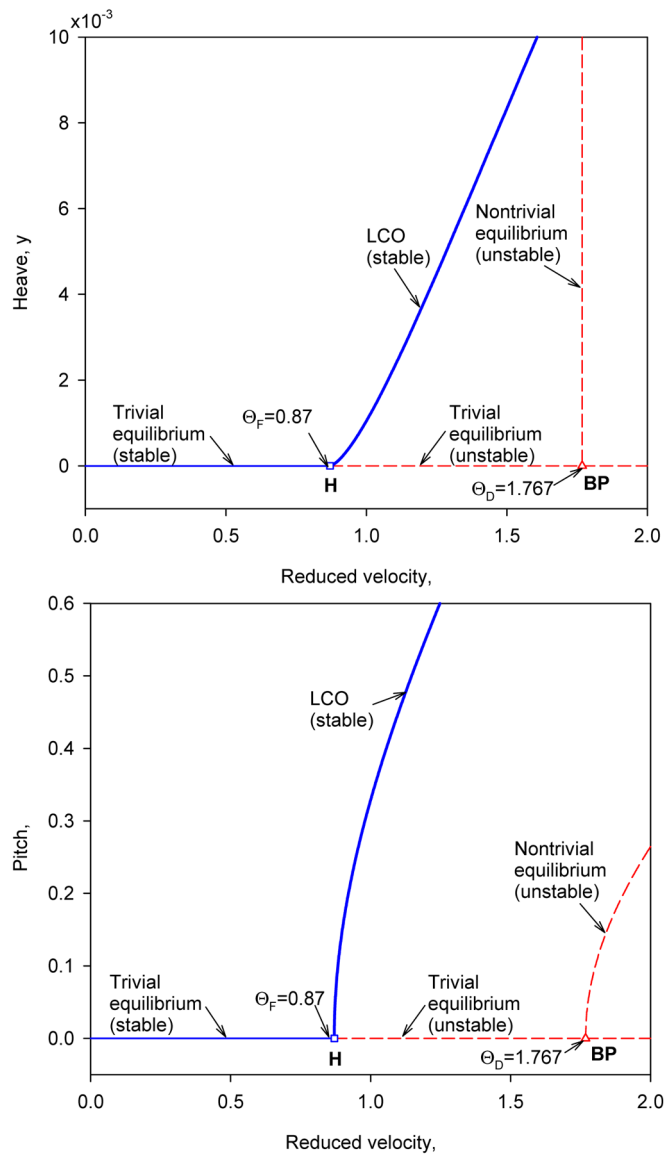


Fig. 9.31 Bifurcation analysis of the steady state dynamics of system (9.42): ‘H’ and ‘BP’ stand for Hopf bifurcation point and branching point, respectively; stable (unstable) motion is represented by a solid (dashed) line.

We now examine the possible existence of other equilibrium solutions of the slow flow equations (9.60). In fact, there exist many other non-trivial but degenerate equilibrium solutions; Figure 9.33 presents one of these computed by numerical

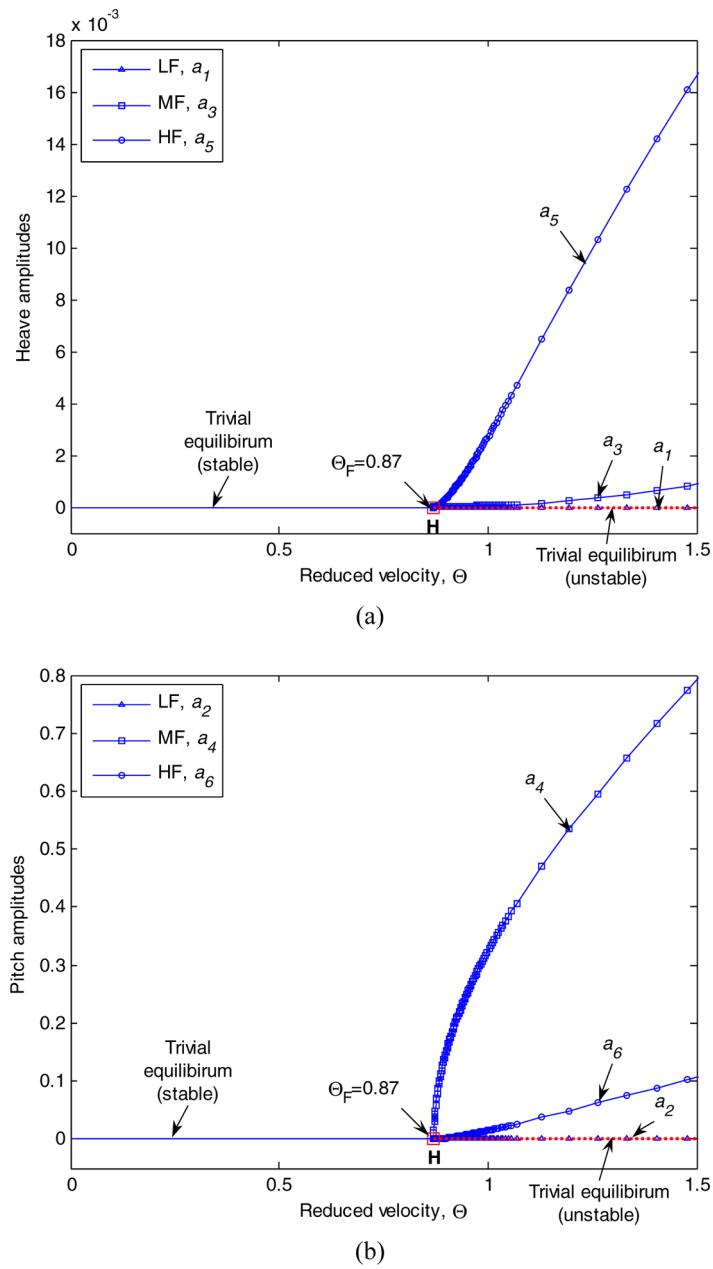
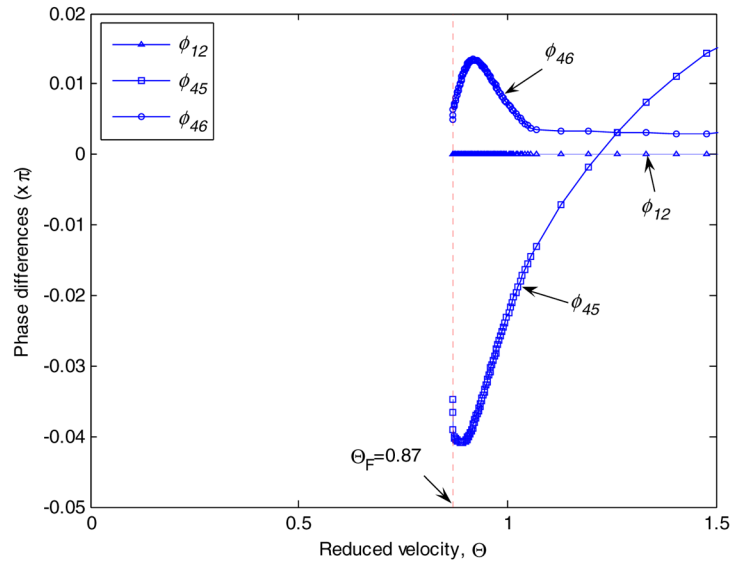
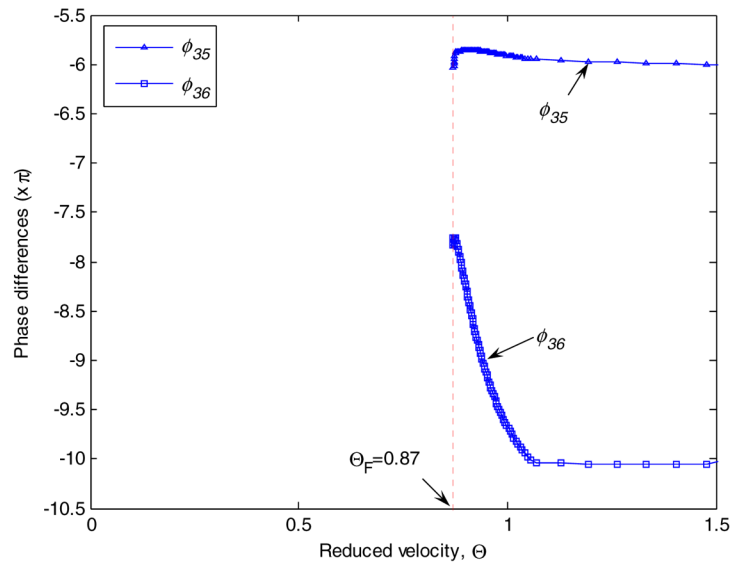


Fig. 9.32 Steady state LCO amplitudes and phase differences from the averaged system (9.60); (a) heave amplitudes, (b) pitch amplitudes.



(c)



(d)

Fig. 9.32 Steady state LCO amplitudes and phase differences from the averaged system (9.60); (c, d) phase differences.

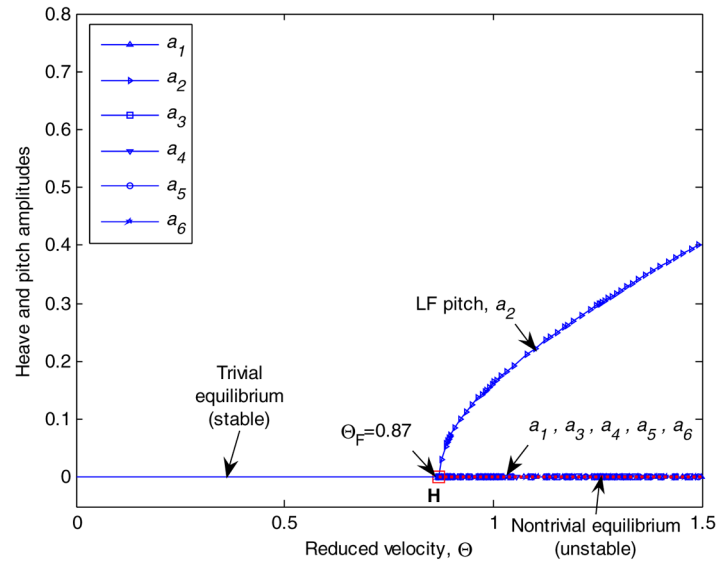
continuation of equilibrium positions, corresponding to near-trivial values for all amplitudes except for the LF pitch a_2 .

The LF pitch amplitude a_2 in Figure 9.33a is estimated as, $a_2 = \Omega a_4 = 0.5a_4$ where a_4 is the MF pitch amplitude in Figure 9.32b. Although this relation can be obtained analytically as shown below, we may intuitively guess it by examining the expression of the amplitudes in (9.51) and noting that at a specific reduced speed all amplitudes except LF or MF pitch are almost trivial, and that the contribution of the heave mode to the total energy at steady state is rather negligible. Then, $\alpha \approx a_4$ when only MF pitch is dominant, and if only LF pitch is dominant, then we may approximately compute $\alpha \approx a_2/\Omega = a_4$ by (9.51).

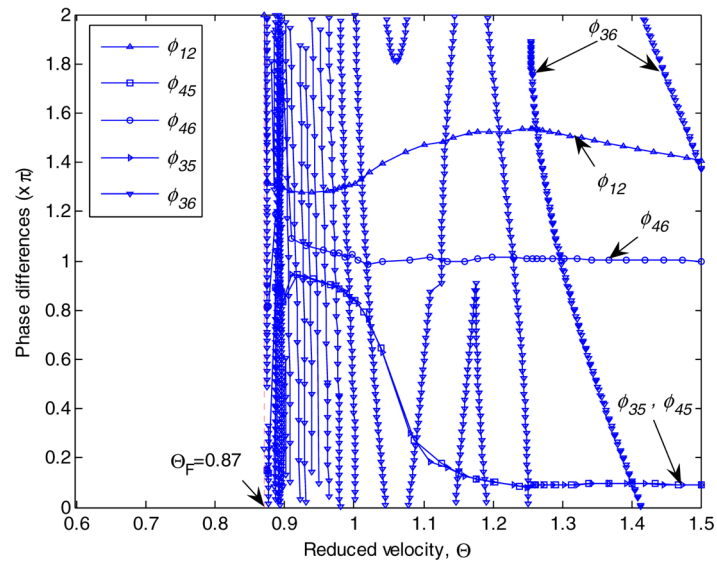
Figures 9.34 and 9.35 depict heave and pitch responses corresponding to the steady state motions for $\Theta = 0.95$ in the plots of Figures 9.32 and 9.33, respectively. Both cases correspond to identical initial conditions, $(y(0), \alpha(0), y'(0), \alpha'(0)) = (10^{-3}, 10^{-3}, 0, 0)$. However, the corresponding initial conditions used for integrating the slow flow equations (9.60) are different. For example, the initial conditions used for performing the numerical simulations depicted in Figure 9.34 are selected to be ‘optimal’ in the sense discussed in Section 9.2.2.2 (where the overdeterminacy of the problem of selecting the initial conditions of the slow flow was discussed), in order to accurately approximate the exact solutions which will be used later in the study of LCO triggering mechanism; whereas, the initial conditions utilized for the numerical simulations of Figure 9.35 are slightly different. Since numerical studies can be made only for stable motions, it turns out that the prediction depicted in Figure 9.35 is not meaningful in our study of the LCO triggering mechanism because it is based on a degenerate equilibrium of the slow flow modulation equations, and does not provide any information on the HF heave component which is observable in actuality.

It turns out that the degenerate equilibrium solutions presented in Figure 9.33 can be derived analytically from a subsystem of the slow flow model (9.60), namely, from the multi-phase averaged system with two dominant frequencies corresponding to LF and MF components; this subsystem will be called the *two-frequency averaged system* hereafter. For this subsystem, we neglect HF terms $y_3(\tau)$ and $\alpha_3(\tau)$ in (9.45), or, equivalently, the corresponding complex variables ψ_5 and ψ_6 , so the resulting complex-valued slow flow equations (9.49) contain only the complex modulations $\varphi_1, \dots, \varphi_4 \in C^4$. Then, we obtain the following reduced two-frequency averaged system in polar form:

$$\begin{aligned} a_1' + \frac{\xi_1}{2}a_1 - \frac{a_2}{2\Omega} \sin \phi_{12} \left(k_{12} + \frac{3n_{12}}{4\Omega^2}a_2^2 + \frac{3n_{12}}{2}a_4^2 \right) &= 0 \\ a_2' + \frac{\xi_2}{2}a_1 \cos \phi_{12} + \frac{a_1}{2\Omega} \sin \phi_{12} \left(k_{21} + \frac{3n_{21}}{4\Omega^2}a_1^2 + \frac{3n_{21}}{2}a_3^2 \right) &= 0 \\ a_3' + \frac{\xi_1}{2}a_3 - \frac{a_4}{2} \sin \phi_{34} \left(k_{12} + \frac{3n_{12}}{2\Omega^2}a_2^2 + \frac{3n_{12}}{4}a_4^2 \right) &= 0 \\ a_4' + \frac{\xi_2}{2}a_3 \cos \phi_{34} + \frac{a_3}{2} \sin \phi_{34} \left(k_{21} + \frac{3n_{21}}{2\Omega^2}a_1^2 + \frac{3n_{21}}{4}a_3^2 \right) &= 0 \end{aligned}$$



(a)



(b)

Fig. 9.33 Additional steady state LCO solution, amplitudes and phase differences predicted by the averaged system (9.60); (a) amplitudes, (b) phase differences (mod 2π was applied for the plot of ϕ_{36}).

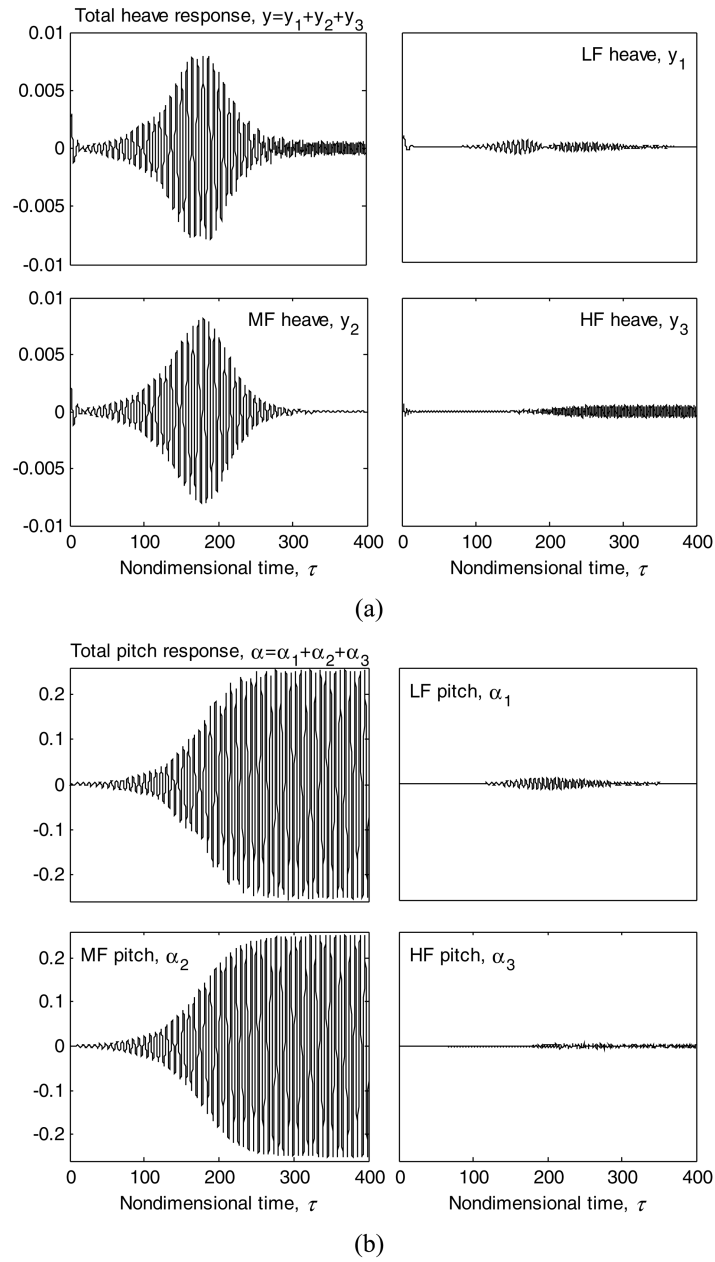


Fig. 9.34 Total and component responses for steady state solutions corresponding to amplitudes and phases depicted in Figure 9.32 for $\Theta = 0.95$; (a) heave mode response and (b) pitch mode response.

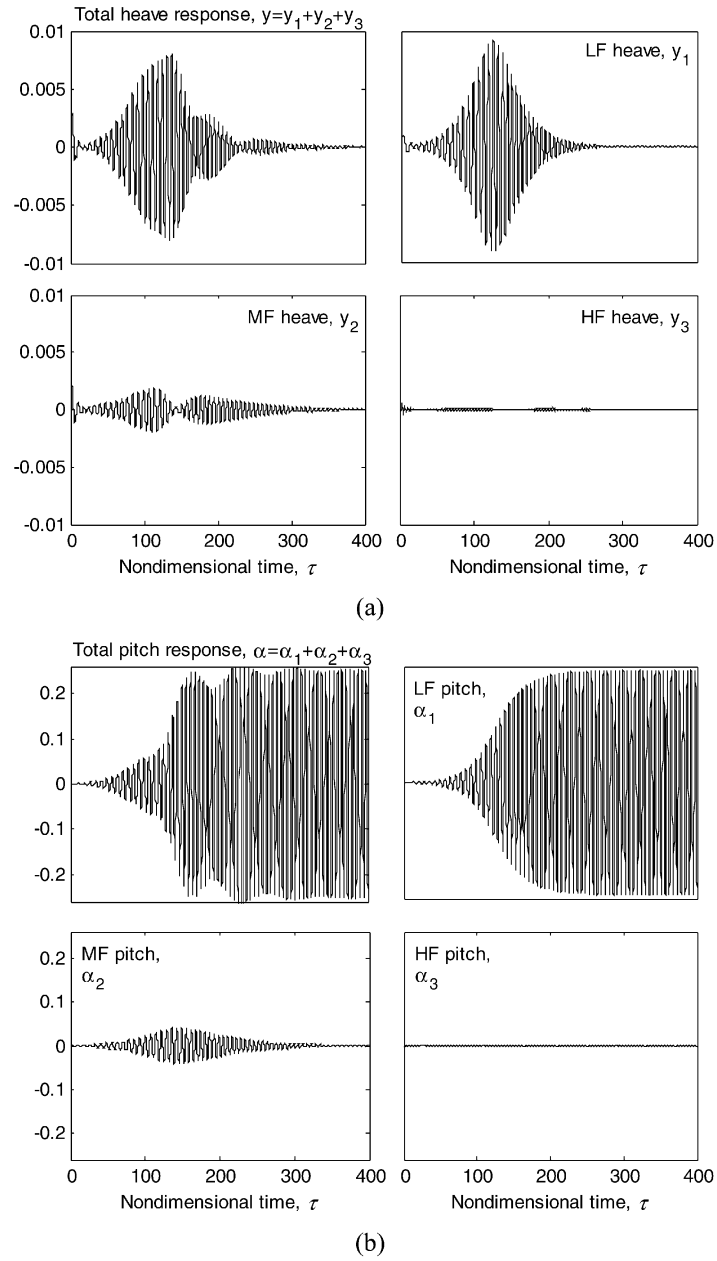
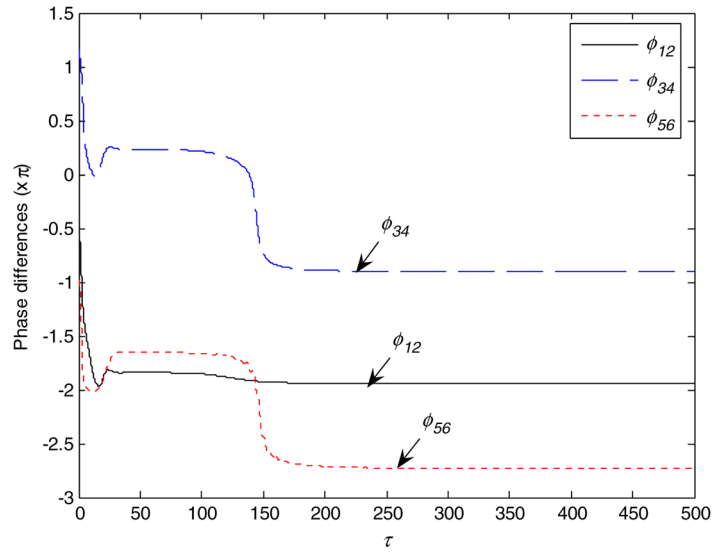
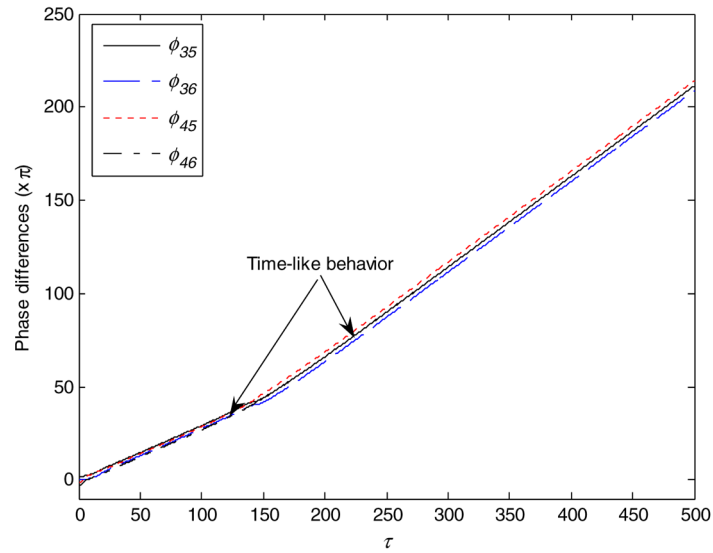


Fig. 9.35 Total and component responses corresponding to steady state solutions of the averaged system depicted in Figure 9.33 for $\Theta = 0.95$; (a) heave, (b) pitch.



(c)



(d)

Fig. 9.35 Total and component responses corresponding to steady state solutions of the averaged system depicted in Figure 9.33 for $\Theta = 0.95$; (c, d) phase differences.

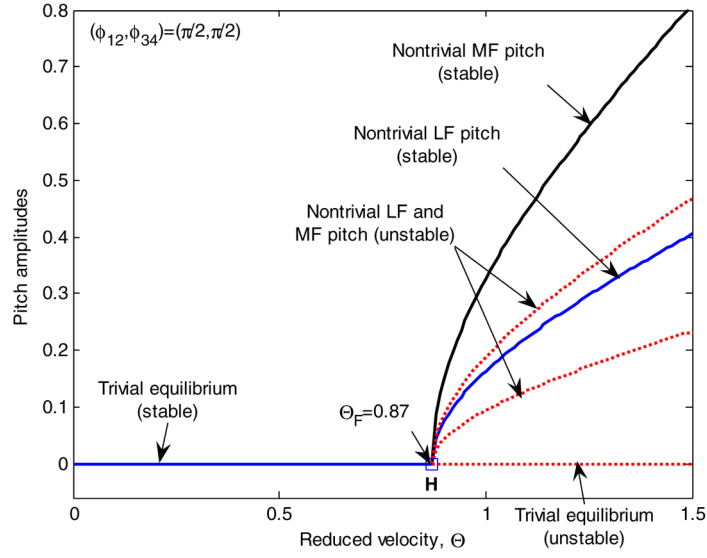


Fig. 9.36 Analytical steady state pitch amplitudes and their stability when $(\phi_{12}, \phi_{34}) = (\pi/2, \pi/2)$, computed from the two-frequency averaged system (9.63).

$$\begin{aligned}
 & a_1 a_2 \phi'_{12} + \frac{a_1 a_2}{2\Omega} \left(k_{22} - k_{11} - \frac{3n_{11}}{4\Omega^2} a_1^2 - \frac{3n_{11}}{2} a_3^2 + \frac{3n_{22}}{4\Omega^2} a_2^2 + \frac{3n_{22}}{2} a_4^2 \right) - \frac{\zeta_1}{2} a_1^2 \sin \phi_{12} \\
 & - \frac{1}{2\Omega} \cos \phi_{12} \left[a_2^2 \left(k_{12} + \frac{3n_{12}}{4\Omega^2} a_2^2 + \frac{3n_{12}}{2} a_4^2 \right) - a_1^2 \left(k_{21} + \frac{3n_{21}}{4\Omega^2} a_1^2 + \frac{3n_{21}}{2} a_3^2 \right) \right] = 0 \\
 & a_3 a_4 \phi'_{34} + \frac{a_3 a_4}{2} \left(k_{22} - k_{11} - \frac{3n_{11}}{2\Omega^2} a_1^2 - \frac{3n_{11}}{4} a_3^2 + \frac{3n_{22}}{2\Omega^2} a_2^2 + \frac{3n_{22}}{4} a_4^2 \right) - \frac{\zeta_2}{2} a_3^2 \sin \phi_{34} \\
 & - \frac{1}{2} \cos \phi_{34} \left[a_4^2 \left(k_{12} + \frac{3n_{12}}{2\Omega^2} a_2^2 + \frac{3n_{12}}{4} a_4^2 \right) - a_3^2 \left(k_{21} + \frac{3n_{21}}{2\Omega^2} a_1^2 + \frac{3n_{21}}{4} a_3^2 \right) \right] = 0
 \end{aligned} \tag{9.62}$$

In this case there appear only two phase expressions, related to phase interactions between the LF heave and LF pitch modes, $\phi_{12} = \beta_1 - \beta_2$, and also between MF heave and MF pitch modes, $\phi_{34} = \beta_3 - \beta_4$.

For steady state solutions, we set $a'_1 = \dots = a'_4 = \phi'_{12} = \phi'_{34} = 0$ in (9.63), and obtain a set of six algebraic equations, from which the equilibrium solutions can be computed. First we consider the case where $(\phi_{12}, \phi_{34}) = (m\pi, n\pi)$ and $m, n \in \mathbb{Z}$, and substitute $\sin \phi_{12} = \sin \phi_{34} \equiv 0$, $\cos \phi_{12} = \cos \phi_{34} \equiv \pm 1$ into (9.63) to obtain $a_1 = a_3 = 0$, i.e., only trivial solutions for the heave mode. Then we obtain the following two relations satisfied by the corresponding non-trivial amplitudes:

$$a_2^2 \left(k_{12} + \frac{3n_{12}}{4\Omega^2} a_2^2 + \frac{3n_{12}}{4} a_4^2 \right) = 0 \tag{9.63}$$

$$a_4^2 \left(k_{12} + \frac{3n_{12}}{2\Omega^2} a_2^2 + \frac{3n_{12}}{4} a_4^2 \right) = 0 \quad (9.64)$$

The solutions of (9.66) and (9.67) yield the following four cases:

- (i) $a_2 = a_4 \equiv 0$: trivial solutions
- (ii) $a_4 \equiv 0$ but $a_2 \neq 0$: non-trivial LF pitch mode,

$$a_2 = 2\Omega \sqrt{-k_{12}/(3n_{12})} \quad \text{if } k_{12}/n_{12} < 0$$

- (iii) $a_2 \equiv 0$ but $a_4 \neq 0$: non-trivial MF pitch mode,

$$a_4 = 2\sqrt{-k_{12}/(3n_{12})} \quad \text{if } k_{12}/n_{12} < 0 \text{ (or } \Theta > \Theta_F)$$

- (iv) $a_2 \neq 0$ and $a_4 \neq 0$: non-trivial LF and MF pitch modes,

$$a_2 = \frac{2}{3}\Omega \sqrt{-k_{12}/n_{12}}, \quad a_4 = \frac{2}{3}\sqrt{-k_{12}/n_{12}} \quad \text{if } k_{12}/n_{12} < 0 \quad (9.65)$$

Similarly, for the following combinations of phase differences, $(\phi_{12}, \phi_{34}) = (m\pi, (2n+1)\pi/2)$, $((2m+1)\pi/2, n\pi)$, $((2m+1)\pi/2, (2n+1)\pi/2)$, where $m, n \in N$, we can also compute the same equilibrium solutions as in (9.67). Furthermore, we can evaluate their stability analytically (Lee et al., 2005b). Figure 9.37 depicts one specific set of steady state amplitudes corresponding to $(\phi_{12}, \phi_{34}) = (\pi/2, \pi/2)$; these steady state solutions for the two-frequency averaged system can be regarded as a degenerate subset of the three-frequency averaged system (9.49).

Using the slow flow models developed in this section we are in the position to study the dynamical mechanism that ‘triggers’ aeroelastic instabilities (LCOs) in the two-DOF in-flow wing (9.37) or (9.42). We will prove that these instabilities are caused by series of transient and sustained resonance captures which ultimately direct energy from the flow to the pitch mode. The identification of the LCO triggering mechanism will be key to the passive LCO mitigation designs and strategies developed in later sections.

9.2.3 LCO Triggering Mechanism

In this section, we show numerically and analytically that series resonance captures are responsible for the triggering and development of LCOs in the in-flow rigid wing. We start by presenting some motivating numerical results.

9.2.3.1 Numerical Results

Considering the slow flow equations (9.49) with ‘optimal’ initial conditions (see Section 9.2.2.2), we examine first the dynamics of the system at subcritical reduced speeds. Figure 9.37a depicts the heave and pitch responses at a subcritical reduced

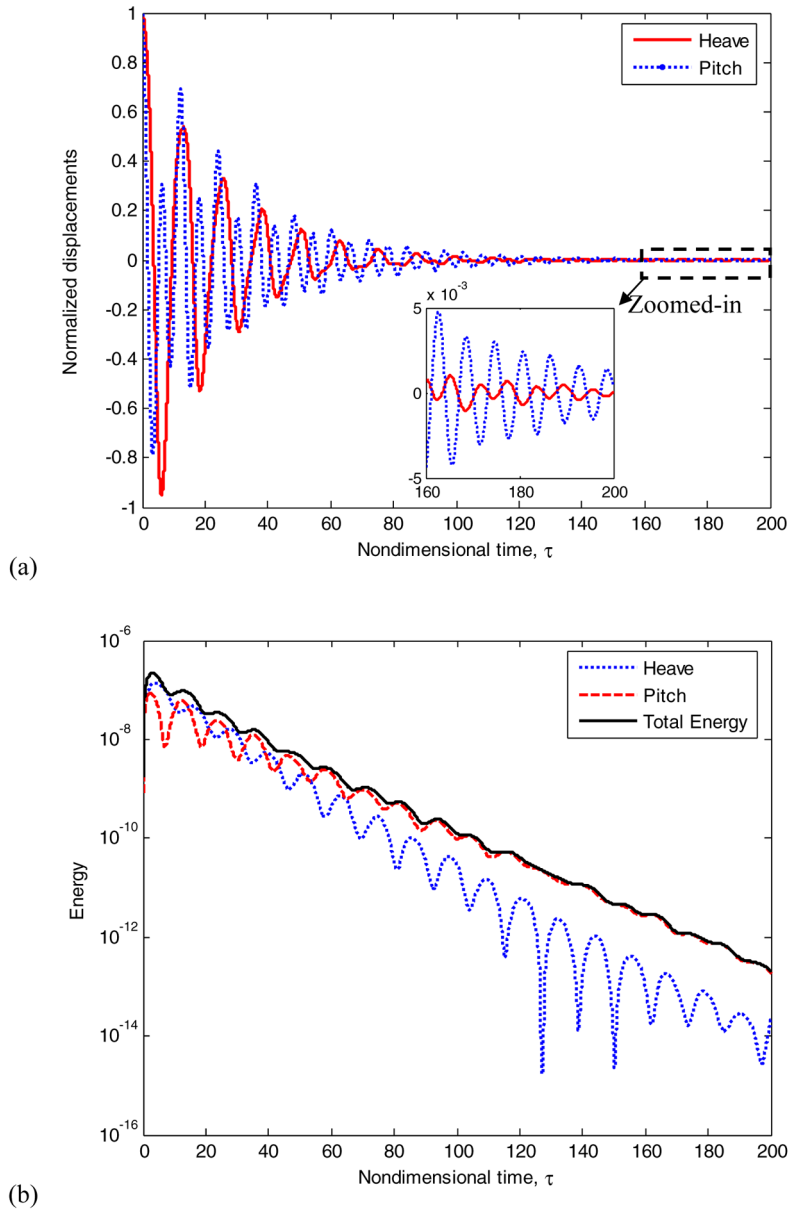


Fig. 9.37 Response of the slow flow (9.49) at a subcritical speed ($\Theta = 0.5$): (a) normalized heave and pitch responses; (b) energy variations with respect to time; initial conditions correspond to $(y(0), \alpha(0), y'(0), \alpha'(0)) = (10^{-3}, 10^{-3}, 0, 0)$.

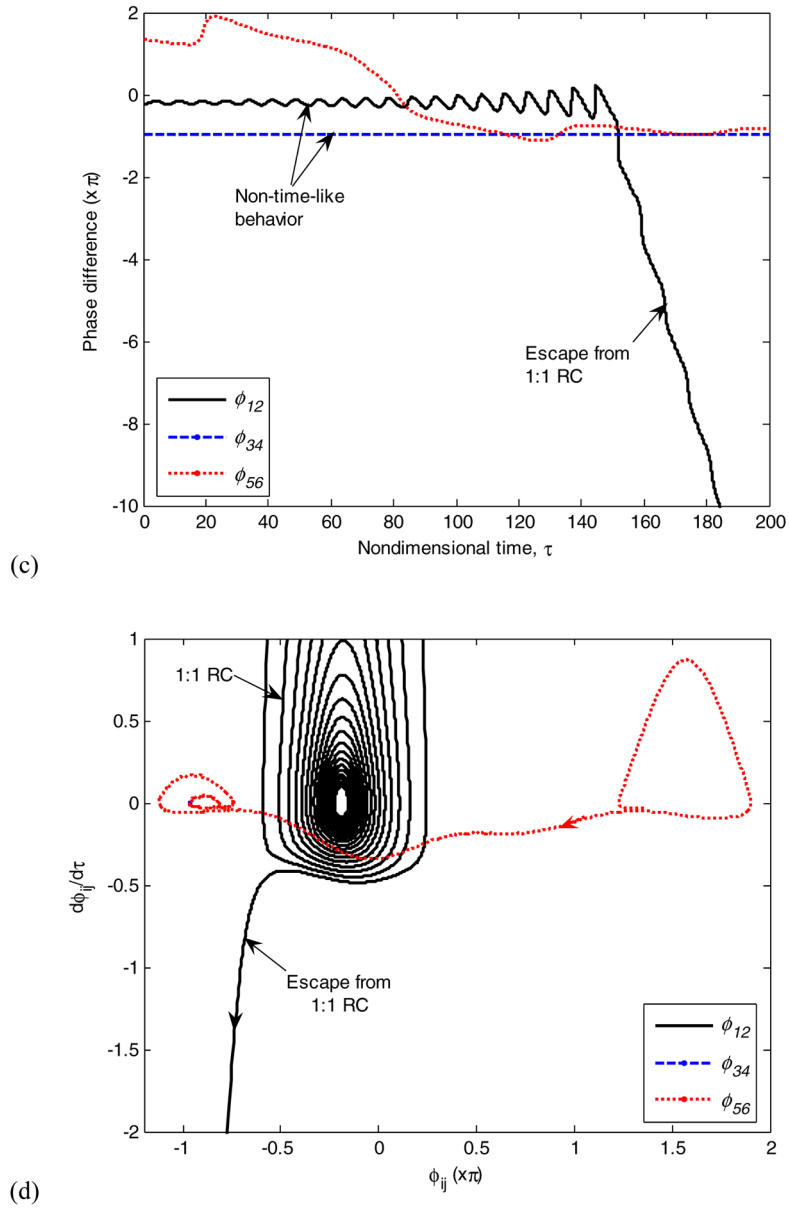


Fig. 9.37 Response of the slow flow (9.49) at a subcritical speed ($\Theta = 0.5$): (c) phase differences in time; (d) phase differences in their phase planes; initial conditions correspond to $(y(0), \alpha(0), y'(0), \alpha'(0)) = (10^{-3}, 10^{-3}, 0, 0)$.

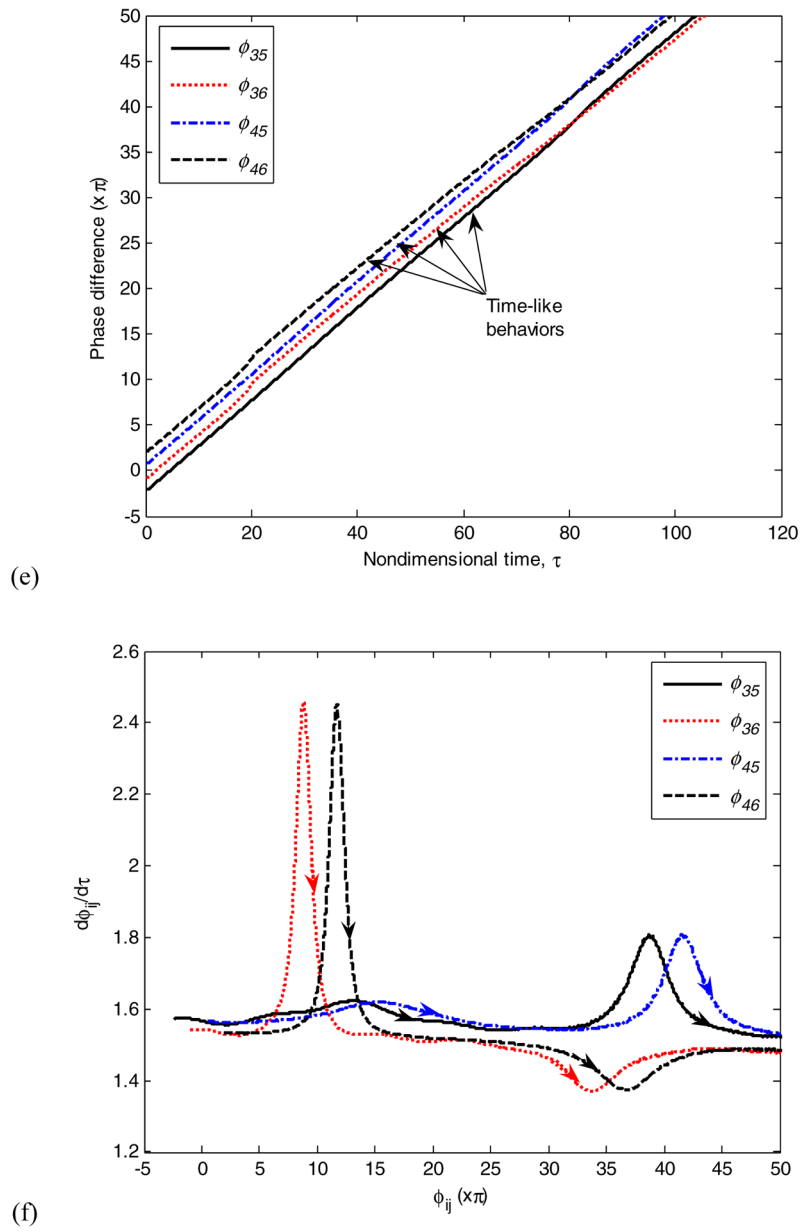


Fig. 9.37 Response of the slow flow (9.49) at a subcritical speed ($\Theta = 0.5$): (e, f) phase interactions between different frequency components in time and phase plane; initial conditions correspond to $(y(0), \alpha(0), y'(0), \alpha'(0)) = (10^{-3}, 10^{-3}, 0, 0)$.

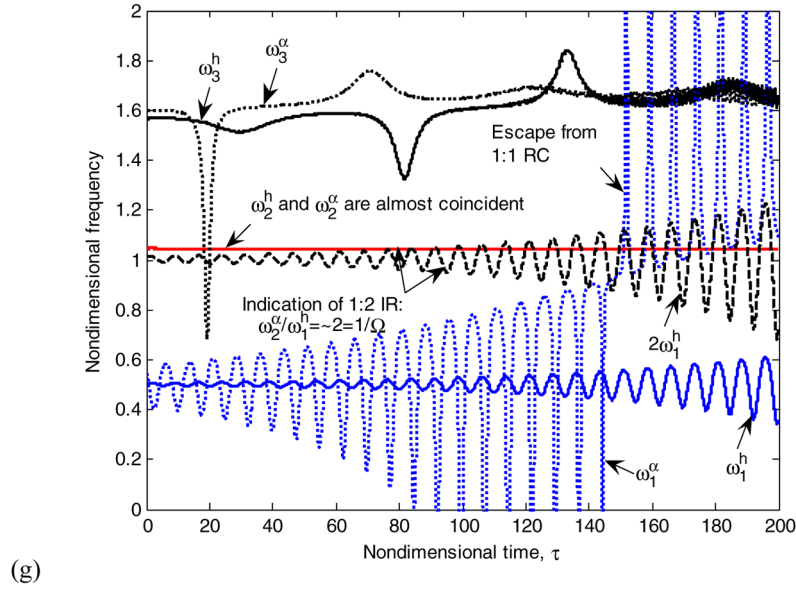


Fig. 9.37 Response of the slow flow (9.49) at a subcritical speed ($\Theta = 0.5$): (g) instantaneous frequencies; initial conditions correspond to $(y(0), \alpha(0), y'(0), \alpha'(0)) = (10^{-3}, 10^{-3}, 0, 0)$.

speed ($\Theta = 0.5$), normalized by their respective maximum amplitudes in order to compare their frequency contents. The existence of a 1:2 internal resonance between the heave and pitch modes (i.e., $\omega_{\text{pitch}} \approx 2\omega_{\text{heave}}$) was already mentioned in Section 9.2.2.1 from the wavelet transform analysis (Figure 9.27). In addition, the possible occurrence of 1:1 TRCs was also suggested. One may deduce the occurrence of these two types of resonance interactions directly from the plot of Figure 9.37a. Indeed, considering the dominant frequencies in each response up to $\tau \approx 100$, we approximately compute the frequency ratio of heave to pitch modes as 1:2; moreover, at later times the frequency ratio of these two modal responses becomes 1:1, and the modal responses become out-of-phase as shown in the zoomed plot.

The existence of a 1:1 TRC in the transient responses can be verified by the phase analysis depicted in Figures 9.37c–f. We note the lack of phase interactions involving the HF components, which underlines the fact that no such resonance interactions involving these components occur at subcritical speeds (this is in accordance to the WT results of Figure 9.27 which indicate that there are no HF components in the modal responses). Note the wandering behavior of the phase difference ϕ_{56} in Figure 9.37c, and the time-like behaviors of the phase interactions of the MF components with HF components in Figures 9.37e–f. If we examine the phase interaction ϕ_{12} between the LF heave and LF pitch components, and the phase interaction ϕ_{34} between the MF heave and MF pitch components, we clearly establish their non-time-like behaviors (see Figure 9.37c); this is also revealed in the form of spirals

in the appropriate phase planes (see Figure 9.37d). We conclude that these phase differences cannot be regarded as ‘fast’ angles so they may not be averaged out of the dynamics, which indicates that the corresponding components are involved in internal resonance or resonance capture. The fact that the LF heave and LF pitch components are involved in 1:1 TRC (instead of 1:1 internal resonance) is indicated by the clear escape from the resonance capture regime, as evidenced from the plot of the phase difference ϕ_{12} at $\tau \approx 150$.

The utilization of these phase interactions as evidence for internal resonances or resonance captures is confirmed by the instantaneous frequencies depicted in Figure 9.37g, computed by the following relations [recall the decompositions (9.45–9.48) together with the polar coordinate transformations $\varphi_k(\tau) = a_k(\tau)e^{j\beta_k(\tau)}$],

$$\begin{aligned}\omega_1^h(\tau) &= \Omega = \beta_1'(\tau), & \omega_2^h(\tau) &= 1 + \beta_3'(\tau), & \omega_3^h(\tau) &= 3 + \beta_5'(\tau) \\ \omega_1^\alpha(\tau) &= \Omega = \beta_2'(\tau), & \omega_2^\alpha(\tau) &= 1 + \beta_4'(\tau), & \omega_3^\alpha(\tau) &= 3 + \beta_6'(\tau)\end{aligned}\quad (9.66)$$

where $\beta_k = \tan^{-1}(\text{Im } \varphi_k / \text{Re } \varphi_k)$, $k = 1, \dots, 6$, and their derivatives are regarded as slow frequency corrections to the fast dominant values (Zniber and Quinn, 2003).

For the 1:2 internal resonance between the heave and pitch modes, the frequency $\omega_2^\alpha(\tau)$ is compared to $2\omega_1^h(\tau)$. Then, we check that the frequency relation, $\omega_2^\alpha - 2\omega_1^h \approx 0$, persists in the entire time interval, which clearly implies the occurrence of 1:2 internal resonance throughout the transient response. We remark that this internal resonance is possible only because of our choice of the specific ratio between natural frequencies, i.e., $\Omega = 0.5$. On the other hand, comparing $\omega_1^h(\tau)$ and $\omega_1^\alpha(\tau)$, and $\omega_2^h(\tau)$ and $\omega_2^\alpha(\tau)$, we clearly verify that 1:1 TRC and escape from resonance capture between likewise LF components occur in the response. Then, it is natural to expect the occurrence of energy exchanges between the heave and pitch modes, similar to those occurring between modes in internal resonance in systems with dissipation [see Figure 9.37b, (Greenlee and Snow, 1975)].

Next, we apply similar arguments to explore the triggering mechanism that gives rise to LCOs at supercritical flow speeds. Basically, the LCO triggering mechanism is composed of three main stages as discussed in the wavelet transform (WT) analysis of Section 9.2.2.1. This classification is established by studying the corresponding energy exchanges between the heave and pitch modes (see Figure 9.38b), the phase interactions between dominant frequency components of these modes (see Figure 9.38c-f), and the corresponding instantaneous modal frequencies (see Figure 9.38g). We refer to these three stages as Stages I, II, and III, with main corresponding features, 1:1 TRC, escape from 1:1 TRC, and finally 3:1 SRC, respectively. Each of these regimes occurring for a supercritical reduced speed $\Theta = 0.95$ is considered in detail below.

Starting from Stage I, initial transients (up to $\tau \approx 20$) involve a 1:2 internal resonance (see Figure 9.38g) which may initially cause strong energy exchanges between the heave and pitch modes (as shown in Figure 9.38b). Then, a 1:1 TRC is realized in the dynamics. Indeed, comparing the time responses of Figure 9.38a, we find that the amplitudes of both modes (and thus their respective energies) increase

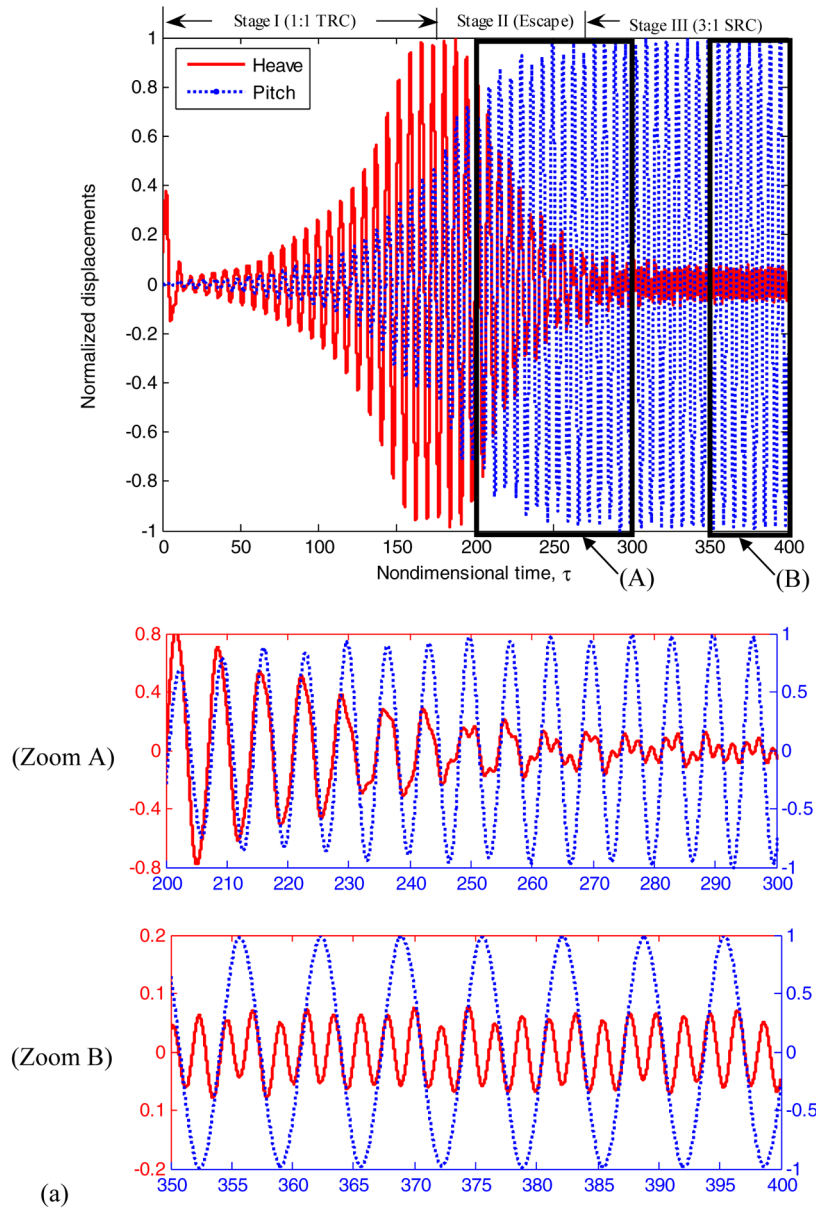


Fig. 9.38 Response of the slow flow (9.48) at a supercritical speed ($\Theta = 0.95$): (a) normalized heave and pitch responses; initial conditions correspond to $(y(0), \alpha(0), y'(0), \alpha'(0)) = (10^{-3}, 10^{-3}, 0, 0)$.

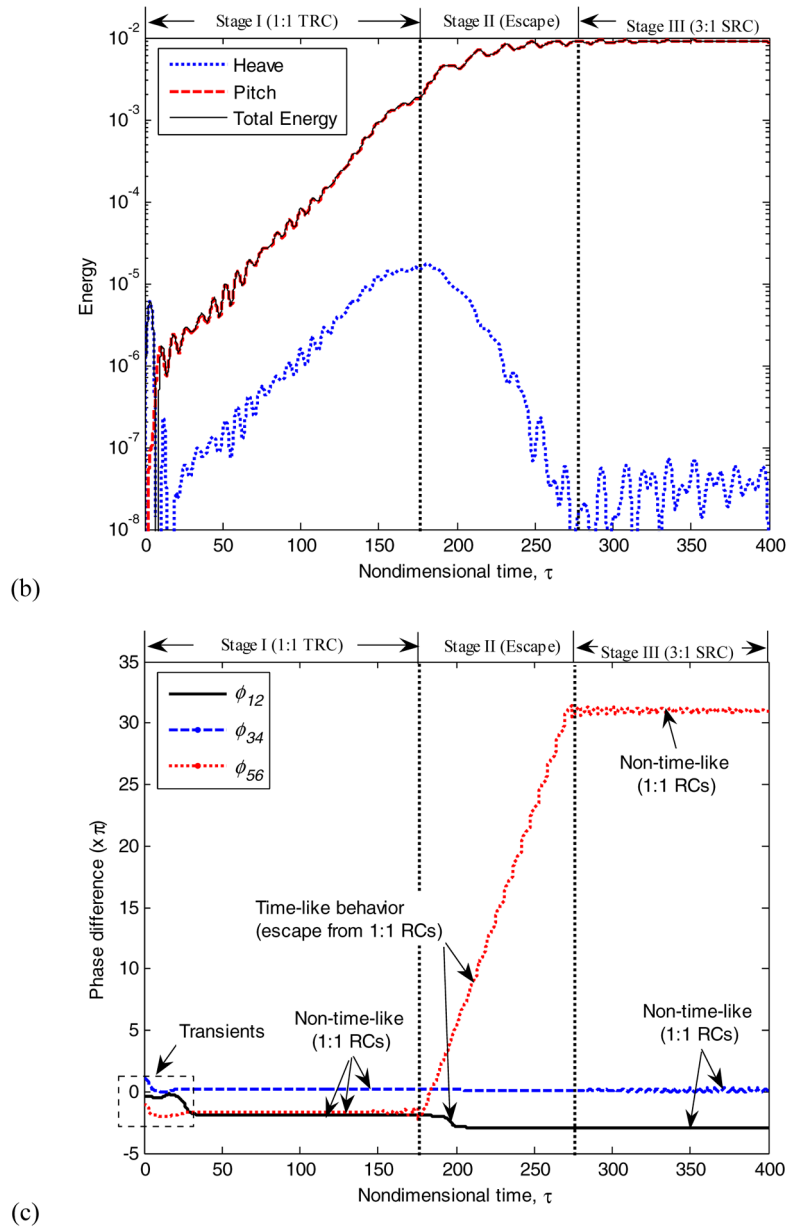


Fig. 9.38 Response of the slow flow (9.48) at a supercritical speed ($\Theta = 0.95$): (b) energy variations with respect to time; (c) phase differences in time; initial conditions correspond to $(y(0), \alpha(0), y'(0), \alpha'(0)) = (10^{-3}, 10^{-3}, 0, 0)$.

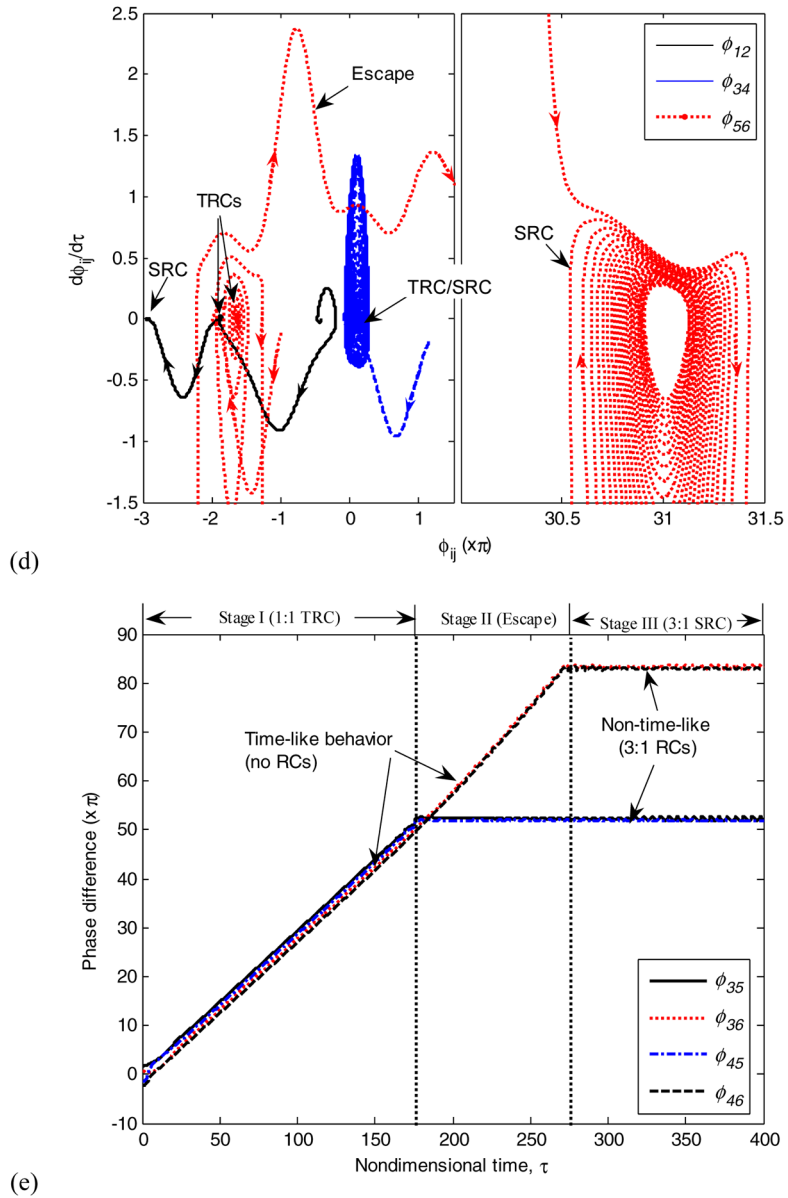


Fig. 9.38 Response of the slow flow (9.48) at a supercritical speed ($\Theta = 0.95$): (d) phase differences in their phase planes; (e) phase interactions between different frequency components in time and phase plane; initial conditions correspond to $(y(0), \alpha(0), y'(0), \alpha'(0)) = (10^{-3}, 10^{-3}, 0, 0)$.

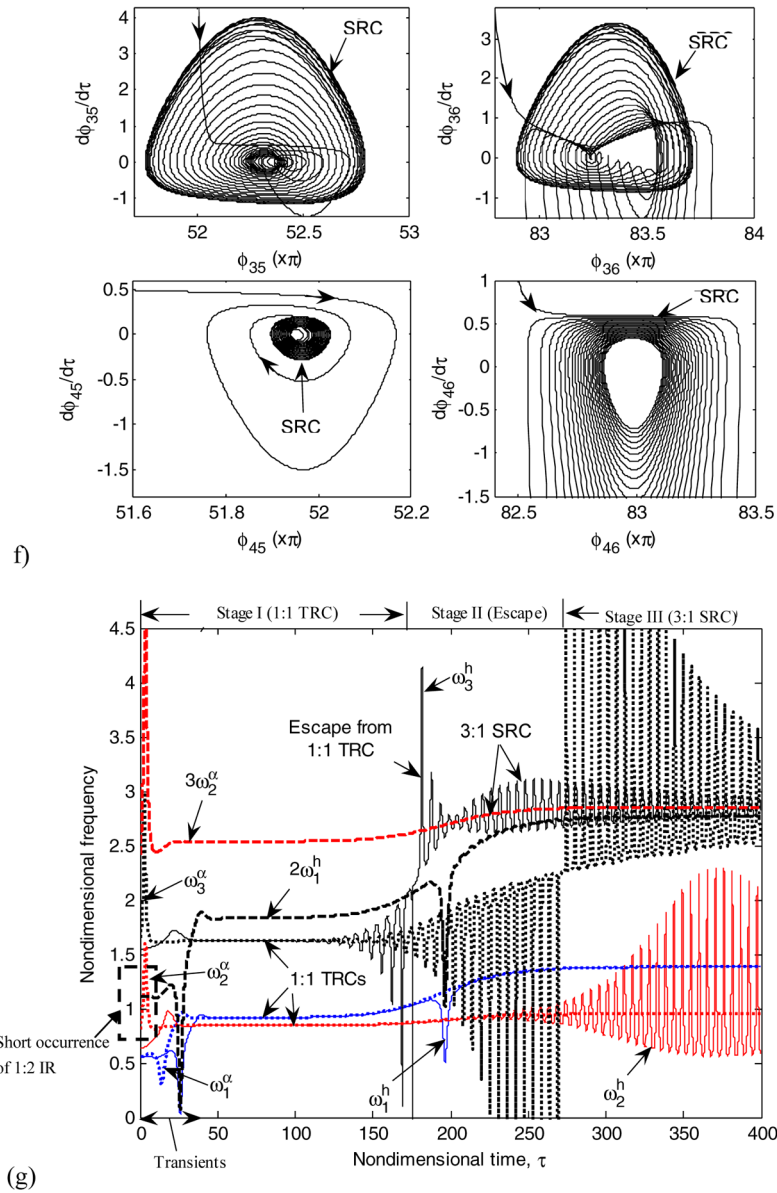


Fig. 9.38 Response of the slow flow (9.48) at a supercritical speed ($\Theta = 0.95$): (f) phase interactions between different frequency components in time and phase plane; (g) instantaneous frequencies; initial conditions correspond to $(y(0), \alpha(0), y'(0), \alpha'(0)) = (10^{-3}, 10^{-3}, 0, 0)$.

during this initial 1:1 TRC, until the energy of the heave mode reaches its maximum at the end of the Stage I.

In Chapter 3 we found that in-phase 1:1 TRC is the underlying mechanism for fundamental TET from a SDOF LO to an essentially nonlinear SDOF attachment (the NES). In analogy, *in the case of the in-flow rigid wing, the pitch mode can be regarded as the primary system, and the heave mode as the NES to which vibration energy is irreversibly transferred during Stage I.* Our aeroelastic model possesses a positive damping component in the heave mode and a negative damping component in the pitch mode. Thus, unlike the usual nonlinear TET phenomenon, energies in both heave and pitch modes increase during 1:1 TRCs as energy from the flow feeds directly to both modes. Besides, energy dissipation by the heave mode (as for the NES) plays no significant role in the competition between the two damping mechanisms. This also explains the viewpoint that *the initial excitation of the heave mode acts or triggers initiation and development of the pitch mode.*

It is remarkable that the nonlinear beating phenomenon which is caused by 1:2 internal resonance between heave and pitch was reported in Section 3.4.2 as the most efficient mechanism to transfer or initiate TET (corresponding to TET through nonlinear beats – see Section 3.4.2.3). Hence, it seems that *energy exchange between heave and pitch during Stage I occurs in the most efficient way from a TET point of view.* That is why the initial short occurrence of 1:2 internal resonance makes possible maximum energy transfer. The occurrence of 1:1 TRCs are verified by the non-time-like behaviors of the phase differences between likewise frequency components (see Figure 9.38c), and by spirals formed in the corresponding projections of the phase space (see Figure 9.38d). In particular, the instantaneous frequencies shown in Figure 9.38g indicate the occurrence of 1:1 TRCs, since the frequencies of likewise frequency components lie, on average, very close to each other, following straight lines, whereas in later times some of the components show *frequency shifting* (Zniber and Quinn, 2003) with increasing energy.

We now consider Stage II of the transient dynamics. Once the heave mode reaches its maximum amplitude, escapes from 1:1 TRCs occur. Superimposed time responses show the corresponding transitions in the dynamics (refer to Zoom A in Figure 9.38a); the in-phase 1:1 TRCs of Stage I turn to 3:1 TRCs gradually as the heave amplitude decreases and pitch amplitude increases. Thus the energy exchanges between the two modes (see Figure 9.38b) follow the typical behavior of escape from resonance capture (Kerschen et al., 2005, 2006a); in particular, time-like behaviors of likewise phase differences (with ϕ_{56} being the most prominent – see Figure 9.38c), and escapes from spirals in projected phase planes (see Figure 9.38d) confirm escape from the in-phase 1:1 TRCs of Stage I. In the meanwhile, the phase differences between MF heave and HF heave and between MF pitch and HF heave do not exhibit time-like behaviors anymore, which are precursors for the occurrence of 3:1 SRCs (Figure 9.38e). These observations are confirmed also in terms of the plots of instantaneous frequencies depicted in Figure 9.38g.

Finally, we discuss Stage III, during which the LCO fully develops and the steady state aeroelastic instability is reached. As a result of the escapes from TRCs in Stage II, the steady state dynamics finally settles into a series of 3:1 SRCs. Examining the

zoomed-in plots of the responses depicted in Figure 9.38a, we can establish the frequency relation between the two modes as nearly 3:1, and the occurrence of in-phase modal oscillations. The energy exchanges between heave and pitch modes become balanced, on average, with most energy being imparted to the pitch mode (see Figure 9.38b). The occurrence of SRCs can be verified in a way similar to Stages I and II, i.e., by the occurrence of non-time-like phase behaviors and of spirals in the corresponding phase planes, or, more directly, in terms of plots of instantaneous frequencies. In particular, comparing the instantaneous frequencies $3\omega_2^\alpha(\tau)$ and $\omega_3^h(\tau)$ in this stage, we can find a good alignment between them on average, i.e., $3\omega_2^\alpha - \omega_3^h \approx 0$ (see Figure 9.38g).

An interesting note concerns the fact that the HF heave (or the steady state resonance frequency component) undergoes upward frequency shift so that 3:1 SRC to MF pitch is made possible, as energy is continuously fed from the flow into the system. It is also remarkable that the likewise phase differences in Figures 9.38c, d in this stage imply the existence of 1:1 SRCs.

9.2.3.2 Analytical Proof of the LCO Triggering Mechanism

In the previous section we analyzed numerical simulations to study the LCO triggering mechanism. The numerical findings can be confirmed analytically employing partial averaging, which is a local analysis. Specifically, we will perform averaging only for non-resonant (fast) phase angles possessing time-like behavior in order to remove the unessential dynamics and derive a reduced-order slow flow model (Zniber and Quinn, 2003).

In an effort to confirm that an internal resonance and a series of resonance captures are responsible for the LCO triggering mechanism, we study the resonance captures that occur in the slow flow at each stage of the response. Then, the order of approximation and its validity on the corresponding time scales can be verified when escapes from resonance captures occur. For example, in order to prove the existence of SRCs in Stage III of the LCO triggering mechanism, the existence of steady state equilibrium points of the slow flow model will serve as the necessary (but not sufficient) condition (Quinn, 1997; Zniber and Quinn, 2003).

Since the averaged system possesses sensitive dependence on initial conditions (due to the fact that the problem of assigning initial conditions to the slow flow is indeterminate – see discussion in Section 9.2.2.2), ‘optimal’ initial conditions for the slow flow modulation equations in polar form (9.60) will be utilized in the following analysis. As a result, we may deduce different phase behaviors and different steady states (see Figures 9.39c,d) than the ones in the corresponding plots of Figure 9.38 which were computed using the ‘optimal’ initial conditions for the complex-valued modulation equations (9.49).

Figures 9.39a, b depict envelopes of the responses of the heave and pitch components, respectively. We may expect that the dominant contribution to the initial triggering of LCOs comes from the MF heave component, so that it develops the likewise counterpart, MF pitch in Stage I. Then, from Stage II until the dynamics

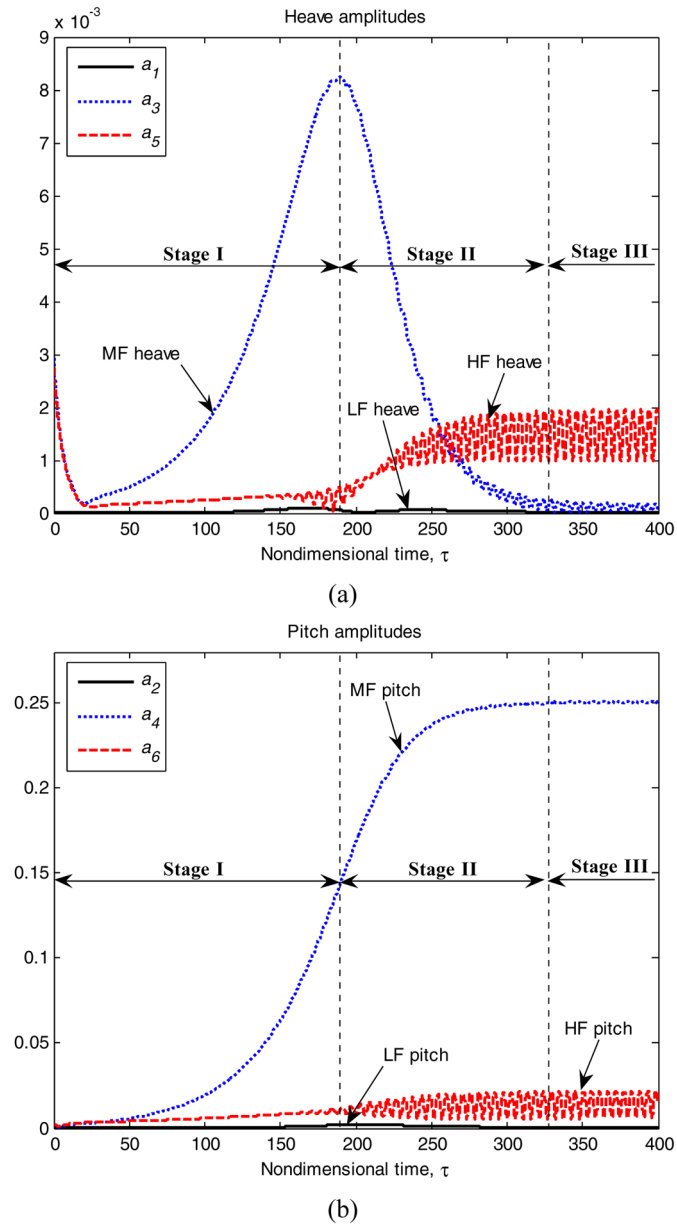
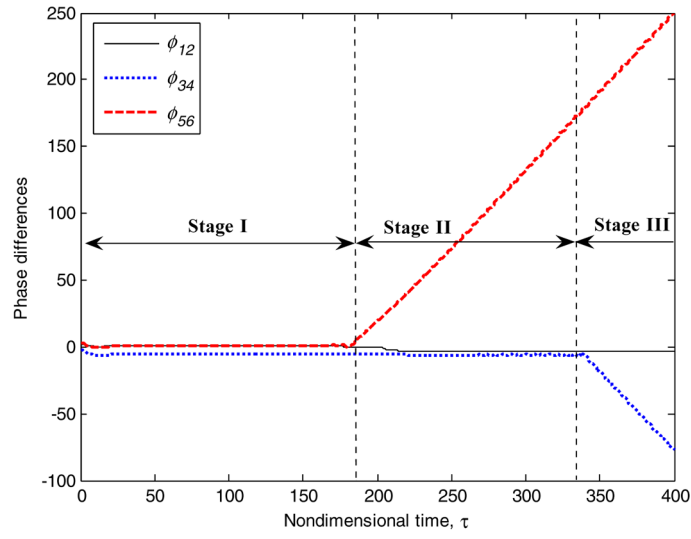
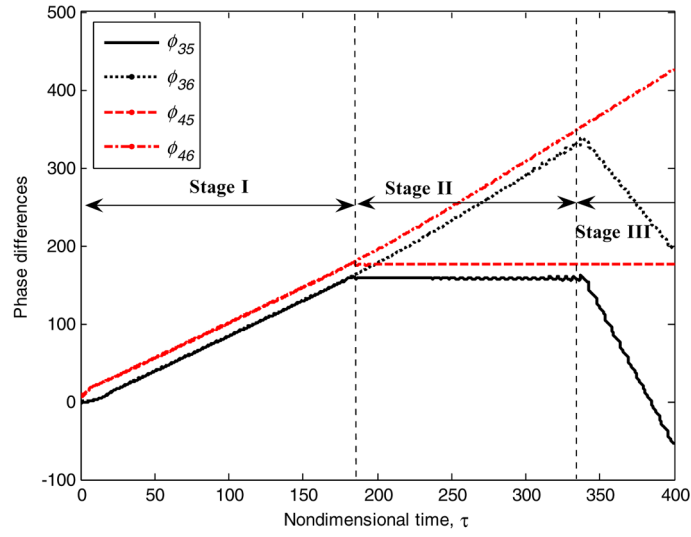


Fig. 9.39 Amplitude and phase responses computed with the averaged slow flow (9.60) for a supercritical reduced velocity ($\Theta = 0.95$); initial conditions correspond to $(y(0), \alpha(0), y'(0), \alpha'(0)) = (10^{-3}, 10^{-3}, 0, 0)$.

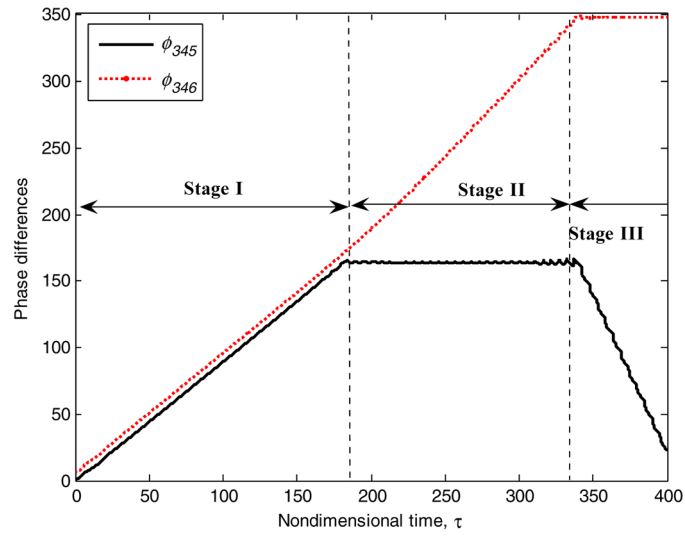


(c)

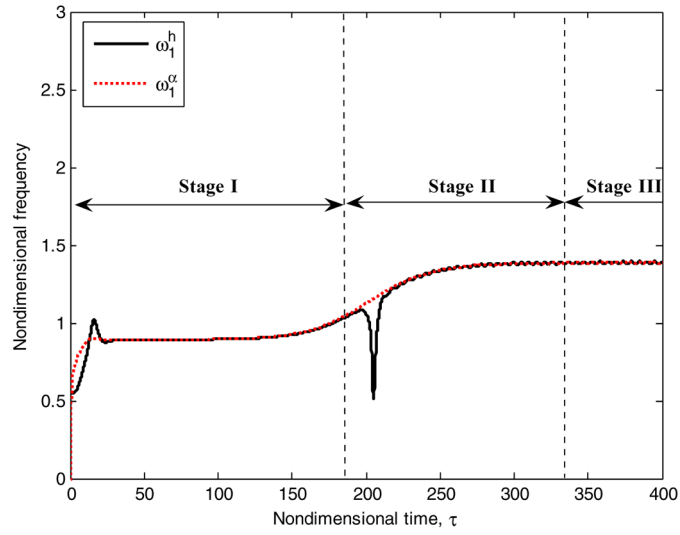


(d)

Fig. 9.39 Continued.

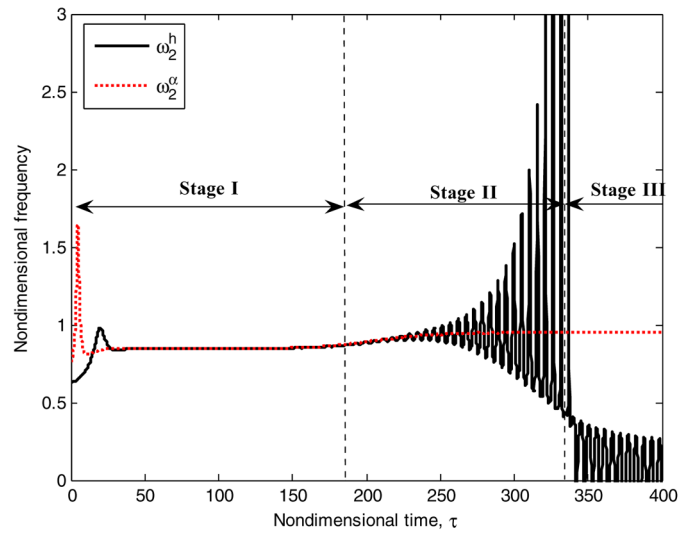


(e)

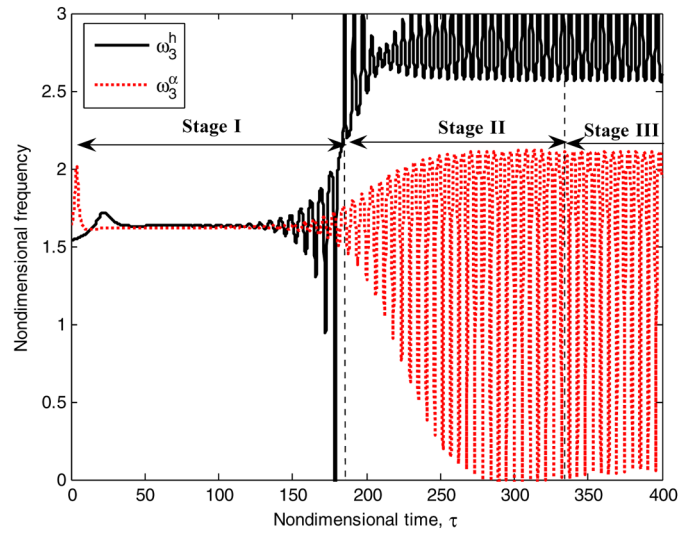


(f)

Fig. 9.39 Continued.



(g)



(h)

Fig. 9.39 Continued.

reaches its steady state, MF pitch together with MF heave act as the driving mechanism to further raise the amplitude of the HF heave response. This intuition is visualized in the phase responses.

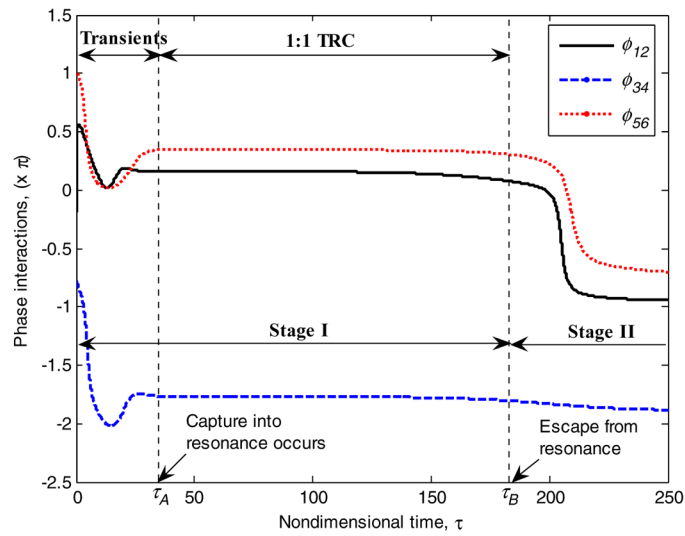
The initial triggering of the LCO corresponds to non-time-like behaviors of the likewise phase differences (and thus by the existence of 1:1 TRCs) in Stage I (see Figure 9.39c). On the other hand, time-like responses of the other phase differences imply that no other effective triggering mechanisms exist during this initial stage. In Stage II, however, escape from 1:1 TRCs of likewise HF components occurs while the other likewise frequency components remain still ‘locked’ in the regime of 1:1 TRCs. Non-time-like behaviors of the phase interactions between MF heave and HF heave (corresponding to the phase difference ϕ_{35}) and between MF pitch and HF heave (phase difference ϕ_{45}) support the previous argument. At steady state when the fully developed LCO is realized during Stage III, only the phase difference between LF heave and LF pitch indicates capture of these components into 1:1 SRC, while the other phase differences escape from 1:1 TRCs. Indeed only the phase interaction between MF pitch and HF heave exhibits non-time-like behavior, which coincides with the numerical simulations of the previous sections [where the original dynamical system (9.37) or (9.42) was used, before averaging is applied].

In Figures 9.39f, h the instantaneous frequency of each harmonic component is plotted by means of relations (9.69); however, this time the slowly varying frequency corrections β'_k , $k = 1, \dots, 6$ are directly computed from the slow flow equations (9.60). Frequency locking between the LF components persists almost during the entire time interval, and, in addition, the steady state resonance frequencies show upward frequency shift along with increasing energy input from the flow. The frequencies of the MF components are kept locked in 1:1 resonance capture, on average, and become unlocked only after Stage II, whereas those of the HF components are unlocked just at the end of Stage I. In particular, the frequency shift in HF heave engages into another locking at three times the frequency of the MF pitch, as we already observed in the previous section.

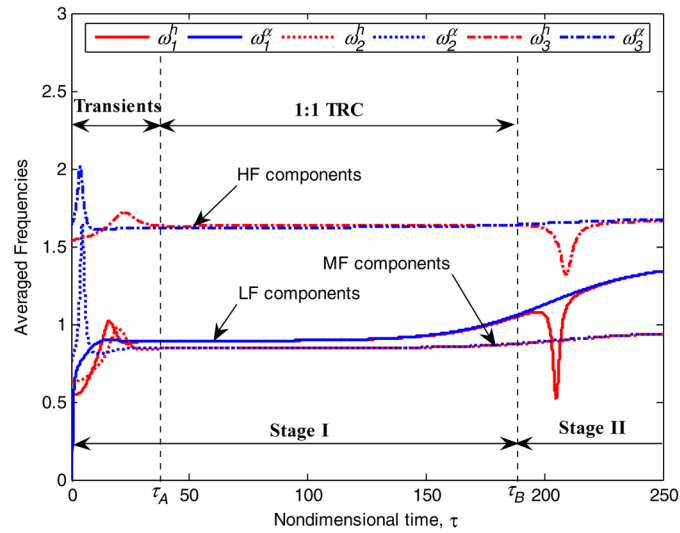
Examining the slow dynamics in each stage separately, in Stage I we perform partial averaging over all time-like phase variables except the phases $\psi_I = (\phi_{12}, \phi_{34}, \phi_{56})$, and construct the following reduced-order model describing 1:1 TRCs between surviving components in the form:

$$a' = f_I(a; \psi_I), \quad \psi'_I = g_I(a; \psi_I) \quad (9.67)$$

where $a \in R^6$ and $\psi_I \in T^3 = S^1 \times S^1 \times S^1$. It is sufficient to show that there occur escapes from 1:1 TRCs after some time interval of frequency locking. When solving the reduced-order model (9.70), we use ‘optimal’ initial conditions which are the same to those used for the slow flow equations (9.60). This leads to the phase interactions depicted in Figures 9.40a, b where τ_A and τ_B refer to the approximate time instants when the dynamics is captured into, and escape from resonance capture, respectively. Hence, we analytically verify that there exist 1:1 TRCs during Stage I. When transition to escape occurs at time instant τ_B , the partially-averaged system (9.70) loses validity since the assumptions upon which it is derived are no



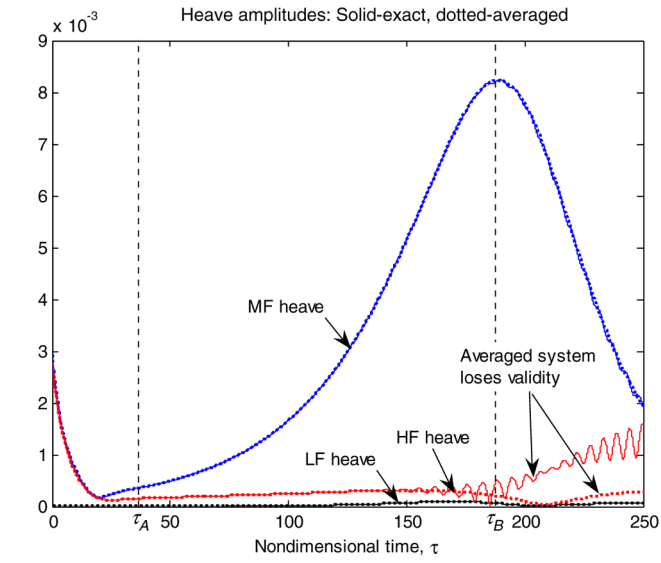
(a)



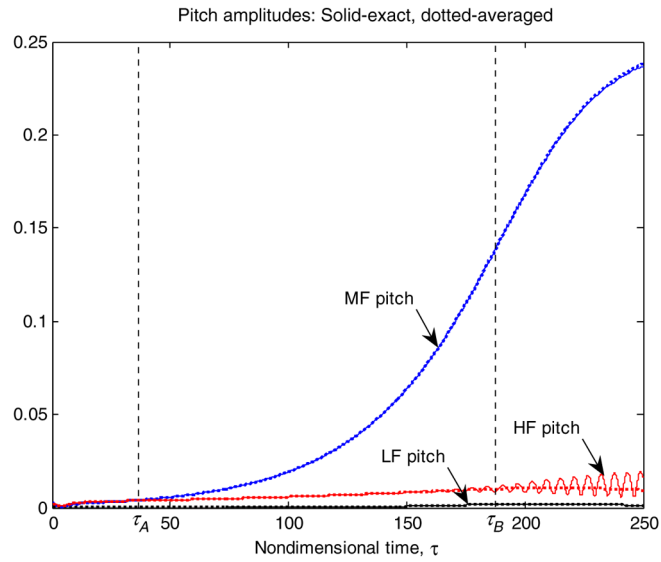
(b)

Fig. 9.40 Analytical study of 1:1 TRCs at Stage I for $\Theta = 0.95$: (a) phase interactions; (b) frequency shiftings; initial conditions correspond to $(y(0), \alpha(0), y'(0), \alpha'(0)) = (10^{-3}, 10^{-3}, 0, 0)$.

longer valid. This becomes clear when one compares the exact and averaged HF heave responses in Figure 9.40d.



(c)



(d)

Fig. 9.40 Analytical study of 1:1 TRCs at Stage I for $\Theta = 0.95$: (c) heave amplitude components; (d) pitch amplitude components; initial conditions correspond to $(y(0), \alpha(0), y'(0), \alpha'(0)) = (10^{-3}, 10^{-3}, 0, 0)$.

For Stage II we perform a similar analysis as in Stage I. Taking into account the resonance interactions between heave and pitch components in this stage of the dynamics, we define the non-time-like variables of the problem as $\psi_{II} = (\phi_{12}, \phi_{34}, \phi_{35}, \phi_{45}, \phi_{345}) \in T^5$ and construct a slow flow model in the form:

$$a' = f_{II}(a; \psi_{II}), \quad \psi'_{II} = g_{II}(a; \psi_{II}) \quad (9.68)$$

We note that in this case there exist only three phases as independent variables. As for the initial conditions for (9.71), we use the state of the dynamics at instant τ_B when the system enters Stage II, starting from the ‘optimal’ initial conditions for (9.60). From the results depicted in Figure 9.41 it is evident that the dynamics is settling down into a steady state motion at time instant τ_C . In particular, the (resonant) frequencies of the HF components shift upward to their original values close to a value equal to three, so that the system can sustain 3:1 resonance captures. Note that the high-frequency modulations disappear through the previous partial averaging.

Finally, in Stage III we derive a slow flow model with non-time-like phase variables $\psi_{III} = (\phi_{12}, \phi_{45}, \phi_{346})$, yielding:

$$a' = f_{III}(a; \psi_{III}), \quad \psi'_{III} = g_{III}(a; \psi_{III}) \quad (9.69)$$

When solving this reduced-order model, we perform a similar analysis with Stage II, and find that there exist equilibrium points in the slow flow, which is proof of existence of SRCs. Recall that in this case the time derivatives of the phase variables, β'_k , $k = 1, \dots, 6$ in (9.27) act as effective detuning frequency components. Therefore, instead of finding equilibrium conditions for detuning parameters as in Zniber and Quinn (2003), we focus on finding such conditions that $\beta'_i \approx \beta'_{i+1}$, $i = 1, 3, 5$ for 1:1 resonance captures, and $3\beta'_4 \approx \beta'_5$ for 3:1 resonance captures. In this way, we may define the intervals where frequency lockings occur as evidence for resonance captures.

In Figure 9.42 we depict the steady state response of the slow flow (9.72) that prove the occurrence of 3:1 SRCs, or equivalently the development of the LCO instability. Since it is not feasible to explicitly compute the equilibrium points of the slow flow (9.72), we may instead verify implicitly their existence, for example, by examining the plots of Figures 9.42a–d we regard to convergence of the slow dynamics at steady state values as proof of existence of the corresponding equilibrium points. Besides, we have already computed some of these steady state solutions by way of numerical continuation in Section 9.2.2.3. Hence, we may conclude that in Stage III 3:1 resonance captures are sustained permanently in time, i.e., that 3:1 SRCs are realized in the dynamics.

9.2.4 Concluding Remarks

We investigated the LCO triggering mechanisms in a two-DOF in-flow rigid wing model in subsonic flow by employing quasi-steady aerodynamics. Reviewing fun-

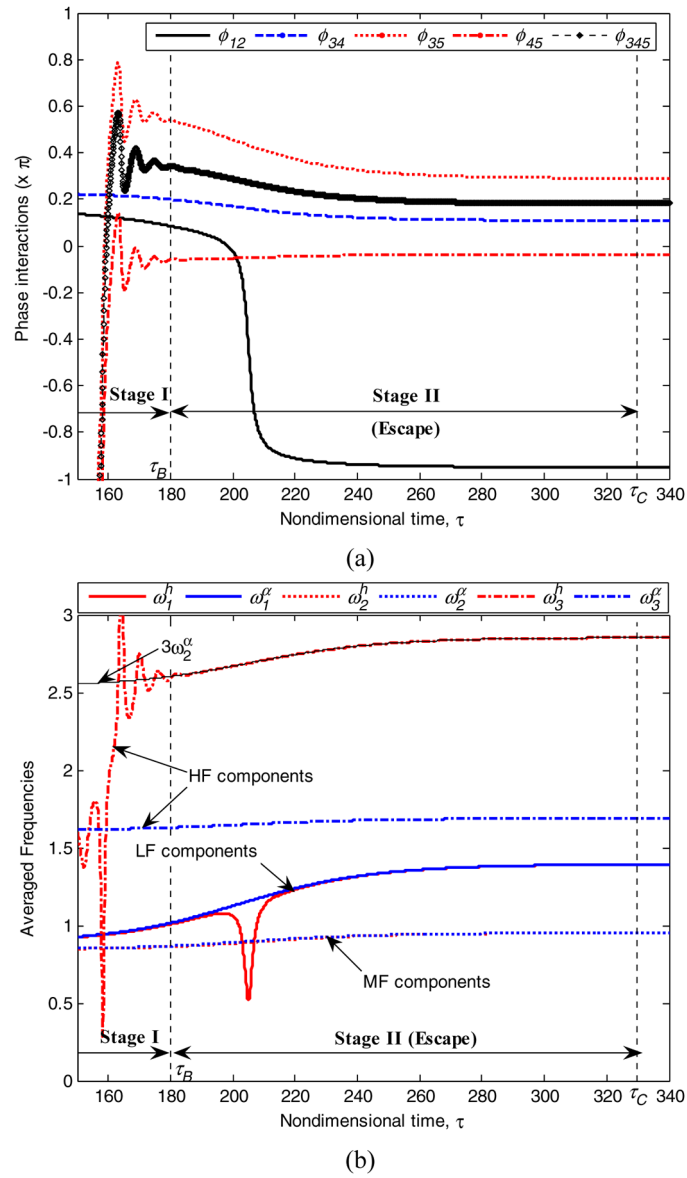
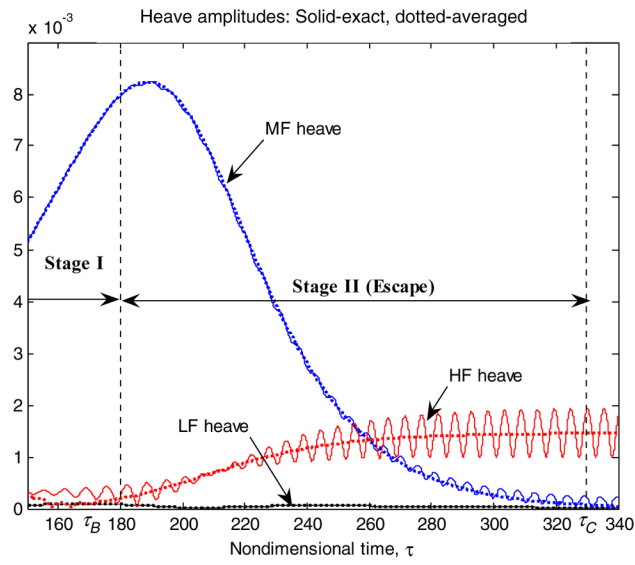
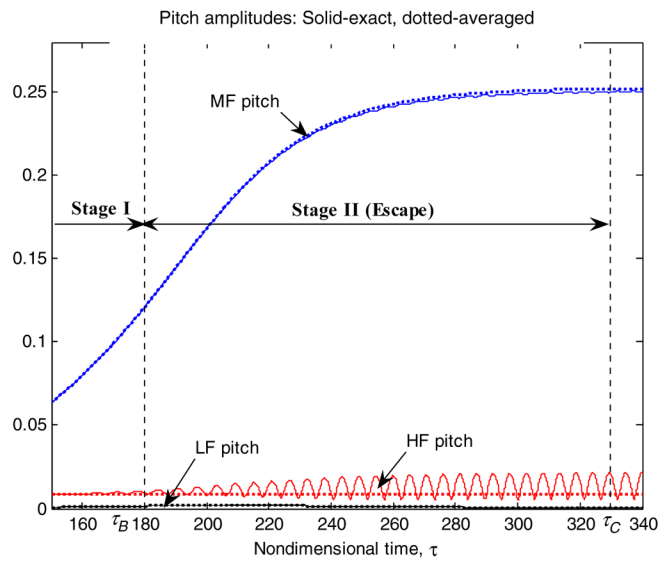


Fig. 9.41 Analytical study of the transient dynamics at Stage II for $\Theta = 0.95$: (a) phase interactions; (b) frequency shiftings.

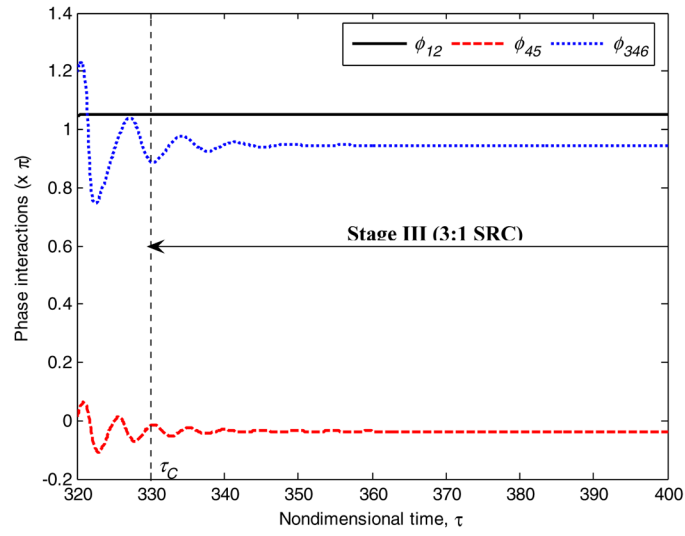


(c)

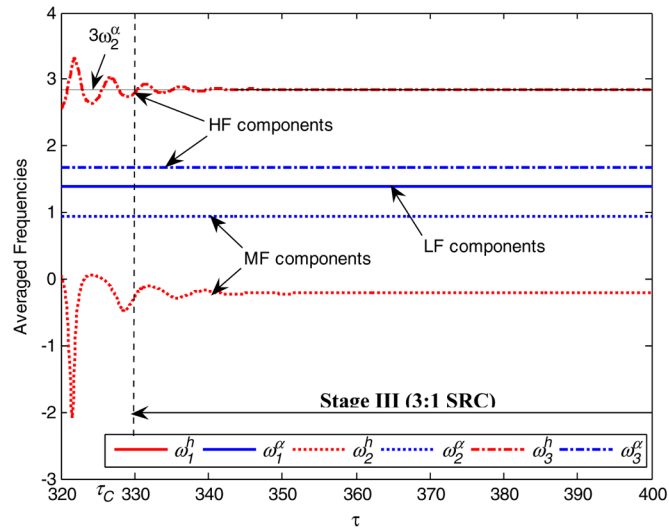


(d)

Fig. 9.41 Analytical study of the transient dynamics at Stage II for $\Theta = 0.95$: (c) heave amplitude components; (d) pitch amplitude components.

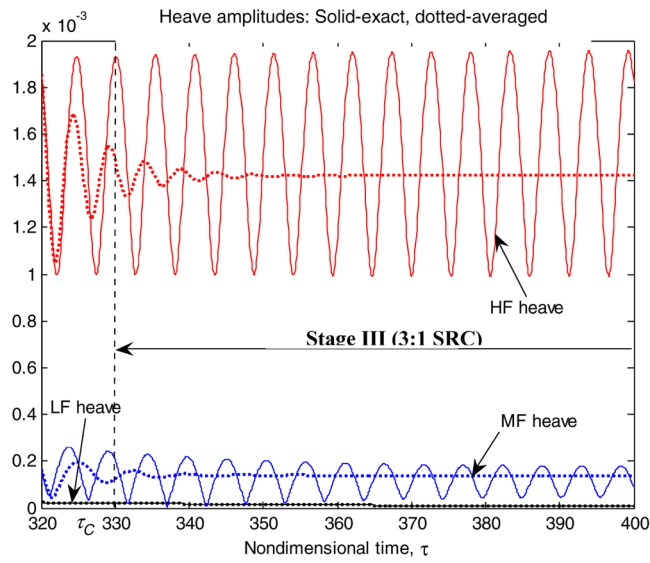


(a)

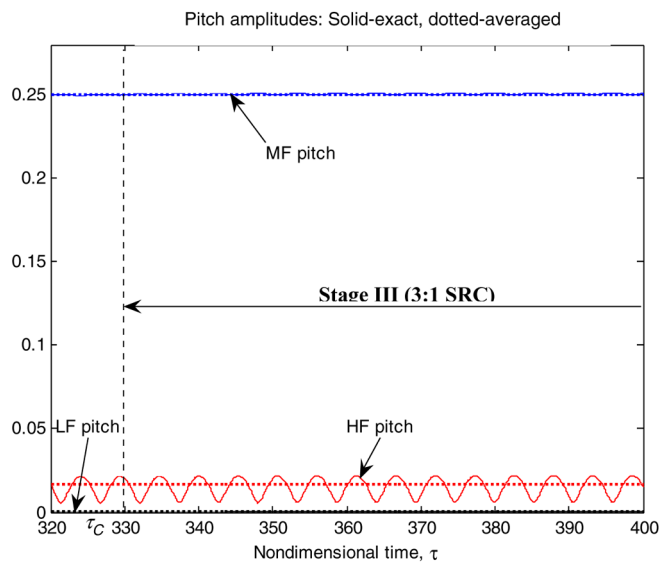


(b)

Fig. 9.42 Analytical study of 3:1 SRCs at Stage III for $\Theta = 0.95$: (a) phase interactions; (b) frequency shiftings; initial conditions correspond to $(y(0), \alpha(0), y'(0), \alpha'(0)) = (10^{-3}, 10^{-3}, 0, 0)$.



(c)



(d)

Fig. 9.42 Analytical study of 3:1 SRCs at Stage III for $\Theta = 0.95$: (c) heave amplitude components; (d) pitch amplitude components; initial conditions correspond to $(y(0), \alpha(0), y'(0), \alpha'(0)) = (10^{-3}, 10^{-3}, 0, 0)$.

damental aspects of linear flutter theory, we established a slow flow system based on multi-phase averaging which exhibits good agreement with the original dynamics. Through the method of numerical continuation we analyzed the steady state dynamics of the slow flow. The slow flow system showed sensitive dependence on initial conditions due to the resulting complexity of the dynamics in phase space and the indeterminacy of the problem of computing initial conditions from the exact system. Hence, the initial conditions for the slow flow were determined through an optimization process.

It is interesting to note that even at subcritical speeds 1:1 transient resonance captures occur between heave and pitch harmonic components, which are responsible for strong energy exchanges between aeroelastic modes. We also found that the LCO triggering mechanism is composed of a series of dynamical phenomena, starting with a 1:1 transient resonance capture, followed by escape from resonance capture, and then a final 3:1 sustained resonance capture between the heave and pitch modes. After exploring the triggering mechanism numerically at each of the aforementioned stages of the dynamics, we proved our claims analytically by means of partial averaging and by studying the resulting slow flow models.

The identification of the dynamical mechanism generating LCOs in system (9.37) or (9.42) provides the necessary framework for developing strategies and techniques for their passive suppression. Indeed, based on a purely phenomenological view of the problem of LCO formation, one might arrive to the conclusion that the problem of LCO suppression can be formulated as a problem of suppressing a steady state oscillation. Instead, as shown in this section, the problem of LCO triggering and development is a problem involving series of transient and sustained resonance captures between heave and pitch harmonic components, i.e., it is a problem of *transient modal interactions*. *The premise adopted in this work, therefore, is that by eliminating the triggering mechanism for LCOs, one would be to eliminate the aeroelastic instability at the early stage of its development, before it reaches steady state*. Hence, the problem of LCO suppression is converted to the problem of suppressing the transient triggering mechanism, i.e., to a problem formulated in the transient domain.

Definitely, dealing with a strongly nonlinear problem in the transient (instead of steady state) domain is a challenging undertaking, yet the TET-based designs based on transient directed energy transfers developed in this work offer a solution with the potential to address the present problem. This is due to the fact that, as shown in previous chapters, essentially nonlinear attachments of the type considered in this work are capable of passively absorbing and locally dissipating broadband vibration energy from primary structures in a one way irreversible fashion; this renders such attachments suitable candidates for suppressing aeroelastic instabilities of the in-flow rigid wing. This issue is addressed in the following sections.

9.3 Suppressing Aeroelastic Instability of an In-Flow Wing Using a SDOF NES

The triggering mechanism of limit cycle oscillation (LCO) of a wing due to aeroelastic instability was studied in the previous section, where it was shown that a cascade of resonance captures constitutes the LCO triggering mechanism in the form of (i) initial attraction into 1:1 TRC, (ii) escape from this capture and finally, and (iii) entrapment of the dynamics in 3:1 SRC leading to full development of the LCO. Alternatively, an initial excitation by the flow of the heave mode acts as the triggering mechanism for the eventual activation of the pitch mode through transient nonlinear modal interactions involving the aforementioned resonance captures and escapes; the eventual excitation of the pitch mode signifies the appearance of an LCO of the in-flow wing in flow.

In general, efforts have been made to control LCOs by means of active control schemes (Ko et al., 1997; Friedman et al., 1997) or by inducing autoparametric resonances (Fatimah and Verhulst, 2003; Tondl et al., 2000). In this section we study the efficacy of passively suppressing aeroelastic instabilities (LCOs) in the two-DOF in-flow rigid wing model (9.37) or (9.42) by attaching a SDOF NES. In the process we will provide an application of TET to an engineering problem of practical significance. First, we perform computational parametric studies that clearly demonstrate (at least) three fundamental mechanisms of LCO suppression by means of TET from the in-flow wing to the NES. Then, we further investigate the numerically detected LCO suppression mechanisms by performing numerically time-frequency analysis by means of WTs and EMD, and applying the CX-A technique performing multi-phase averaging.

By computing appropriately defined measures of energy dissipated by the NES, we explore the energetic transactions associated with each LCO suppression mechanism in terms of transient modal interactions. Furthermore, we prove that LCO suppression is due to TRCs between heave and pitch harmonic components and the NES, during which strong TET from the wing to the NES take place. Then, we address the issue of robustness of LCO suppression by performing bifurcation analysis in order to detect stable co-existing stable attractors in the steady state dynamics which can have either a beneficial or an inadverse effect regarding LCO suppression. In the process we describe how the three LCO suppression mechanisms are related to the bifurcation picture of the steady state dynamics. The following exposition follows the work reported in Lee et al. (2007a).

9.3.1 Preliminary Numerical Study

We examine the two-DOF rigid in-flow wing model of Figure 9.23 with an attached SDOF NES (see Figure 9.43). Assuming small motions and using the principle of virtual work (Dowell et al., 1995), we derive the equations of motion of the wing-

NES assembly as follows:

$$\begin{aligned}
& m\ddot{h} + S_\alpha\ddot{\alpha} + K_h(h + c_1h^3) + qSC_{L,\alpha}(\alpha + \dot{h}/U) \\
& \quad + c_s(\dot{h} - d\dot{\alpha} - \dot{z}) + k_s(h - d\alpha - z)^3 = 0 \\
& I_\alpha\ddot{\alpha} + S_\alpha\ddot{h} + K_\alpha(\alpha + c_2\alpha^3) - qeSC_{L,\alpha}(\alpha + \dot{h}/U) \\
& \quad + dc_s(d\dot{\alpha} + \dot{z} - \dot{h}) + dk_s(d\alpha + z - h)^3 = 0 \\
& m_s\ddot{z} + c_s(\dot{z} + d\dot{\alpha} - \dot{h}) + k_s(z + d\alpha - h)^3 = 0
\end{aligned} \tag{9.70}$$

or in non-dimensional form

$$\begin{aligned}
& y'' + x_\alpha\alpha'' + \Omega^2y + \xi_y y^3 + \mu C_{L,\alpha}\Theta(y' + \Theta\alpha) \\
& \quad + \varepsilon\lambda(y' - \delta\alpha' - v') + C(y - \delta\alpha - v)^3 = 0 \\
& r_\alpha^2\alpha'' + x_\alpha y'' + r_\alpha^2\alpha + \xi_\alpha\alpha^3 - \gamma\mu C_{L,\alpha}\Theta(y' + \Theta\alpha) \\
& \quad + \delta\varepsilon\lambda(\delta\alpha' + v' - y') + \delta C(\delta\alpha + v - y)^3 = 0 \\
& \varepsilon v'' + \varepsilon\lambda(v' + \delta\alpha' - y') + C(v + \delta\alpha - y)^3 = 0
\end{aligned} \tag{9.71}$$

where the notation of the previous section applies for (9.73), and the normalized parameters in (9.74) are defined as follows:

$$\begin{aligned}
& y = h/b, \quad v = z/b, \quad C = b^2k_s/m\omega_a^2, \quad \delta = d/b, \quad \gamma = e/b, \quad r_\alpha = \sqrt{I_a/(mb^2)}, \\
& x_\alpha = x_{cg}/b, \quad \tau = \omega_a t, \quad \varepsilon = m_s/m, \quad \lambda = c_s/m_s\omega_a, \quad \xi_y = c_1b^2\Omega^2, \\
& \xi_\alpha = c_2r_\alpha^2, \quad \Omega = \omega_h/\omega_a, \quad \omega_h = \sqrt{K_h/m}, \quad \omega_a = \sqrt{K_a/I_a}
\end{aligned}$$

The quantities ω_h and ω_a are the linearized frequencies of the heave and pitch modes, respectively, primes denote differentiation with respect to the normalized time τ , $\mu = \rho_\infty bS/2m$ is the density ratio and $\Theta = U/(b\omega_a)$ the reduced fluid velocity. Note that through the offset d (or δ) from the elastic axis, the NES (with corresponding response z or v) interacts with both the heave (response h or y) and pitch (angle α) modes.

We now perform computational parametric studies of the dynamics of system (9.75) to identify parameter subsets where LCOs of the wing can be suppressed or even completely eliminated. Initial conditions close to the trivial equilibrium position are considered; i.e., we set all initial conditions equal to zero except for the initial velocity $y'(0) = 0.01$. Regarding the wing parameters, we take these to be identical to the ones utilized in Section 9.2 where the LCO triggering mechanism was studied,

$$\begin{aligned}
& x_\alpha = 0.2, \quad r_\alpha = 0.5, \quad y = 0.4, \quad \Omega = 0.5, \\
& \mu = (10\pi)^{-1}, \quad C_{L,\alpha} = 2\pi, \quad \xi_y = \xi_\alpha = 1
\end{aligned} \tag{9.72}$$

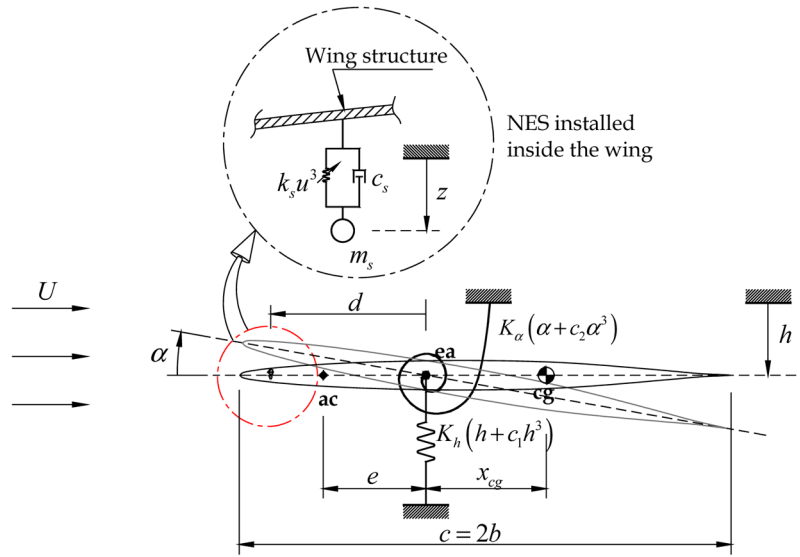


Fig. 9.43 Two-DOF rigid wing model with an attached SDOF NES.

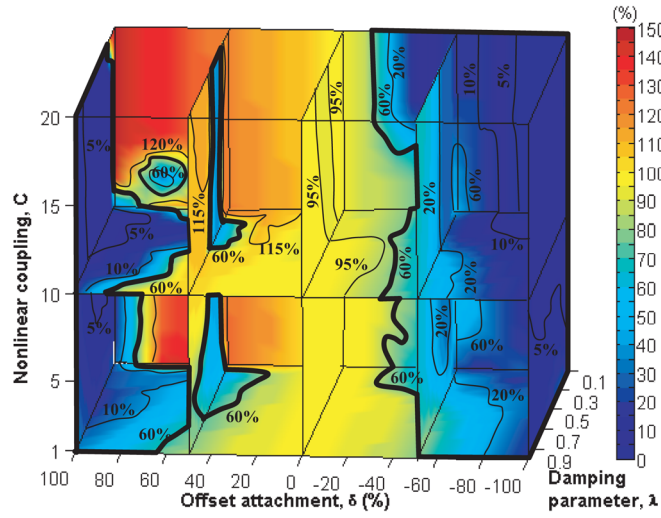
which gives a flutter speed equal to $\Theta_F = 0.87$ (see Figure 9.24).

There are four control parameters for the NES, namely, the mass ratio of the NES and the wing, ε ; the normalized damping coefficient, λ ; the normalized coefficient of the essentially-nonlinear stiffness, C ; and the normalized offset attachment, δ . In the numerical study, we will consider parameter variations in the ranges, $0.01 \leq \varepsilon \leq 0.1$ (i.e., for practical reasons we consider as small as possible mass ratios), $0.1 \leq \lambda \leq 1$, $1 \leq C \leq 20$, and $-1 \leq \delta \leq 1$.

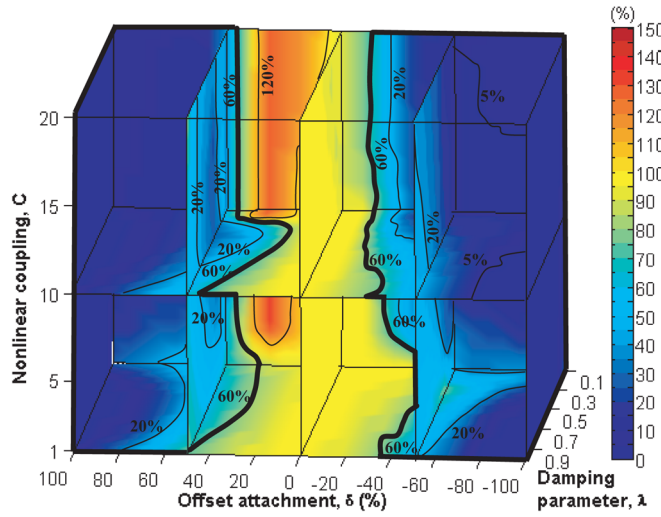
Our methodology for performing the computational parametric study is as follows. Using the aforementioned initial conditions and parameter sets, we integrate the equations of motion (9.75) for sufficiently long time to assure that initial transients die out. Then we compute the root-mean-square (r.m.s.) amplitude of the resulting steady state response. Comparing the steady state pitch (or heave) amplitudes in r.m.s. with and without NES attached, we may infer partial or complete LCO suppression. *Partial LCO suppression* can be inferred by computing the amplitude ratio (in the pitch mode) for systems with and without NES attached, which should be less than unity. *Complete LCO suppression* is inferred when this amplitude ratio tends to zero as the steady state of the system is approached. More specifically, we introduce the following definition for the amplitude ratio in the pitch mode,

$$\Delta^\alpha = \frac{\text{Steady state pitch amplitude (rms) with NES}}{\text{Steady state pitch amplitude (rms) without NES}} \times 100\% \quad (9.73)$$

and a similar expression for the heave mode Δ^y .



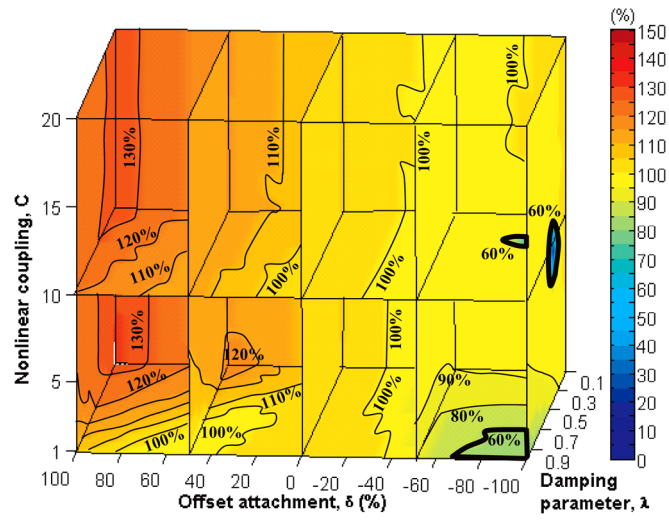
(a) $\Theta = 0.9, \varepsilon = 0.01$



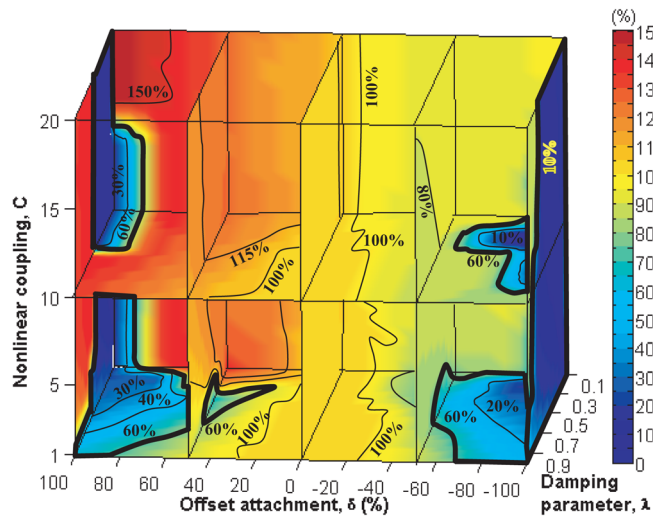
(b) $\Theta = 0.9, \varepsilon = 0.02$

Fig. 9.44 Steady state amplitude ratio in the pitch mode, Δ^α for various mass ratios and reduced speeds; the areas enclosed by the thick curves indicate parameter domains where $\Delta^\alpha < 60\%$; the r.m.s. steady state pitch amplitude for the system with no NES is 0.11 rad for $\Theta = 0.9$, and 0.17 rad for $\Theta = 0.95$; initial conditions are all zero except for $y'(0) = 0.01$.

Figure 9.44 depicts the steady state amplitude ratio in the pitch mode Δ^α for mass ratios equal to $\varepsilon = 0.01$ and 0.02 , and reduced speeds $\Theta = 0.9$ and 0.95 . Here we only consider the reduction in the amplitude of the pitch mode because this is the dominant mode during the aeroelastic instability (actually, the overall amplitude



(c) $\Theta = 0.95, \varepsilon = 0.01$



(d) $\Theta = 0.95, \varepsilon = 0.02$

Fig. 9.44 Continued

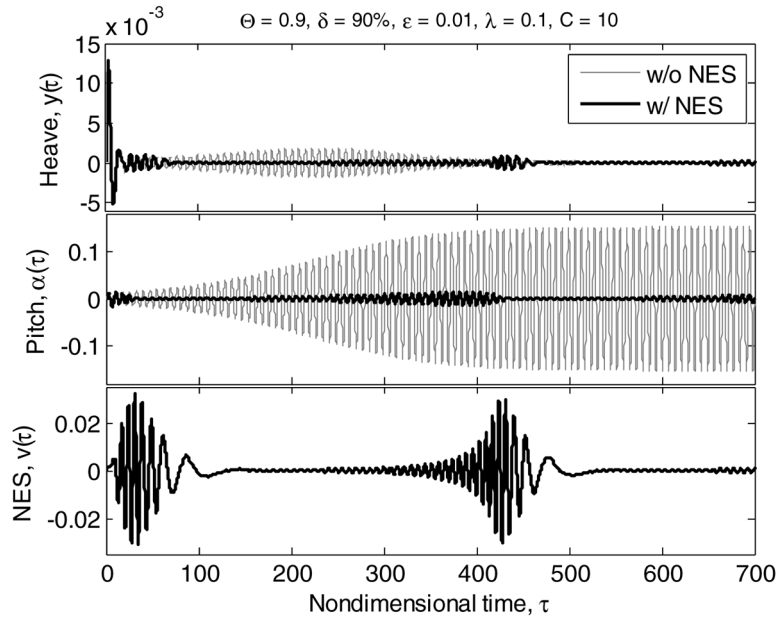


Fig. 9.45 The first LCO suppression mechanism for $\Theta = 0.9$, $\delta = 90\%$, $\varepsilon = 1\%$, $\lambda = 0.1$, and $C = 10$; zero initial conditions are used except for $y'(0) = 0.01$.

of the NES is similar to that of the pitch mode). From these numerical computations we conclude that *LCO suppression is more probable when the NES is attached far from the elastic axis of the wing*; a possible reason for this is that, for relatively large offsets, the NES interacts efficiently with both heave and pitch modes, which permits nonlinear energy exchanges between both modes and the NES.

Moreover, it appears that by *attaching the NES aft of the elastic axis (i.e., for $\delta < 0$) more effective LCO suppression is realized*. This can be inferred heuristically by examining the system (9.74); indeed energy dissipation by the NES due to the damping term $\varepsilon\lambda(y' - \delta\alpha' - v')$ is maximized if the NES interacts with both heave and pitch modes under condition of 1:1 resonance capture, and δ is negative. This will be revisited in a later section where bifurcation analysis of the steady state dynamics will be performed.

In addition, we note that if the aim is to achieve good suppression results for increased flow speeds, we might need to consider higher mass ratios of the NES; for example, most of the regions where instability is suppressed by about 40% for $\varepsilon = 0.01$ and $\Theta = 0.9$ (the area enclosed by thick curves in Figure 9.44a) disappear when the same mass ratio is used but the reduced speed is increased to $\Theta = 0.95$ (see Figure 9.44c). Finally, we remark that this computational parametric study provides simple comparison of r.m.s. steady state amplitude reduction (more precisely, of average power reduction) under a specific set of initial conditions. Hence, the results depicted in Figure 9.44 can be only indicative of the capacity of NES for

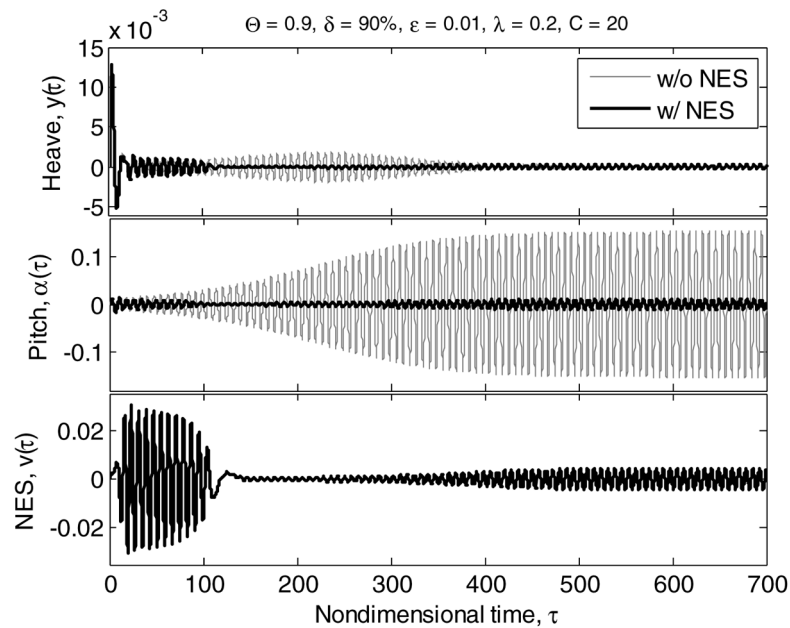


Fig. 9.46 The second LCO suppression mechanism for $\Theta = 0.9$, $\delta = 90\%$, $\varepsilon = 1\%$, $\lambda = 0.2$, and $C = 20$; zero initial conditions are used except for $y'(0) = 0.01$.

LCO suppression, and in order to draw conclusions of a more general nature a more detailed study should be performed addressing the issue of possible co-existing attractors of the steady state dynamics; this is performed in a later section.

From this preliminary computational parametric study, we deduce the existence of three dynamical mechanisms for LCO suppression, as depicted in Figures 9.45–9.47; moreover, Figure 9.48 presents the case where the NES fails to suppress the aeroelastic instability. By studying these preliminary numerical results, some general conclusions can be drawn regarding the nonlinear dynamics of LCO suppression by the NES. In the first suppression mechanism (Figure 9.45) the action of the NES yields repeated burst-outs and eliminations of aeroelastic instabilities, eventually leading to complete LCO suppression; the second mechanism (Figure 9.46) results again in partial LCO suppression, but with no instability burst-outs; whereas, the third mechanism (Figure 9.47) results in complete LCO suppression.

Apart from the phenomenological differences in the action of the NES in the three mentioned LCO suppression mechanisms, there appear to be some common features in the dynamics. First, the nonlinear dynamics of the NES-wing interaction involves broadband energy exchanges in the transient (as opposed to steady state) domain; second, it appears that the essential stiffness nonlinearity of the NES initially prevents the aeroelastic instability from growing above a certain amplitude; at a later phase of the response, conditions for resonance capture between the aeroelas-

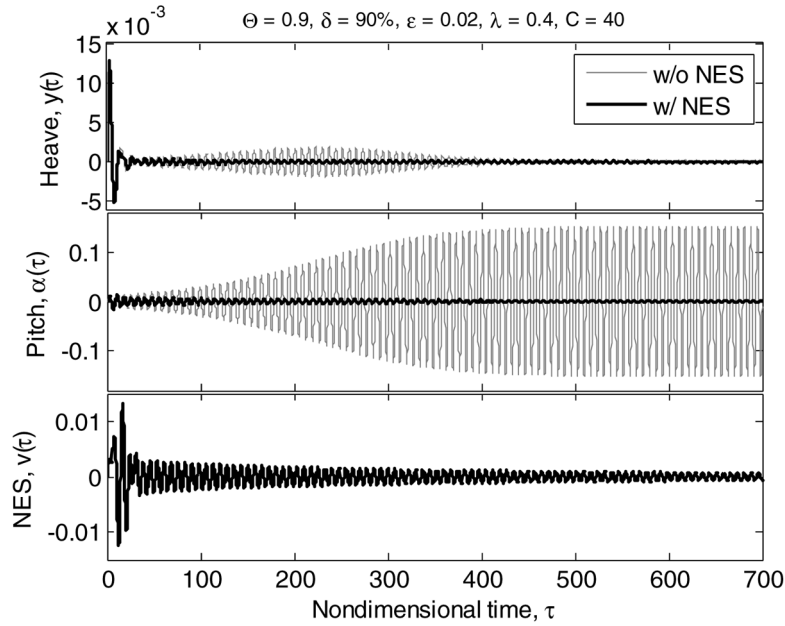


Fig. 9.47 The third LCO suppression mechanism for $\Theta = 0.9$, $\delta = 90\%$, $\varepsilon = 1\%$, $\lambda = 0.4$, and $C = 40$; zero initial conditions are used except for $y'(0) = 0.01$.

tic modes of the wing and the NES are fulfilled and passive targeted energy transfers (TETs) from the wing to the NES take place leading to further LCO suppression.

Below we discuss separately the aforementioned three LCO suppression mechanisms, by post-processing the corresponding numerical time series, focusing only in the main dynamical features, and leaving the discussion of further details to a following section.

9.3.1.1 The First LCO Suppression Mechanism

This mechanism is characterized by *a recurrent series of suppressed burst-outs of the heave and pitch modes of the wing, leading eventually to complete suppression of the aeroelastic instabilities*. In the initial phase of transient burst-outs, a series of developing instabilities of predominantly the heave mode is effectively suppressed by proper transient ‘activation’ of the NES, which passively tunes itself¹ to the fast frequency of the developing aeroelastic instability; as a result, the NES engages

¹ Because an NES possesses no preferential resonance frequency (due to its essential stiffness nonlinearity), the NES can resonantly interact with any mode of the primary system to which it is attached. By locally dissipating the absorbed energy by means of its viscous damper, it can exhibit an escape from one resonance capture to another, engaging in resonance capture cascades (see Section 3.5 and Kerschen et al., 2006a).

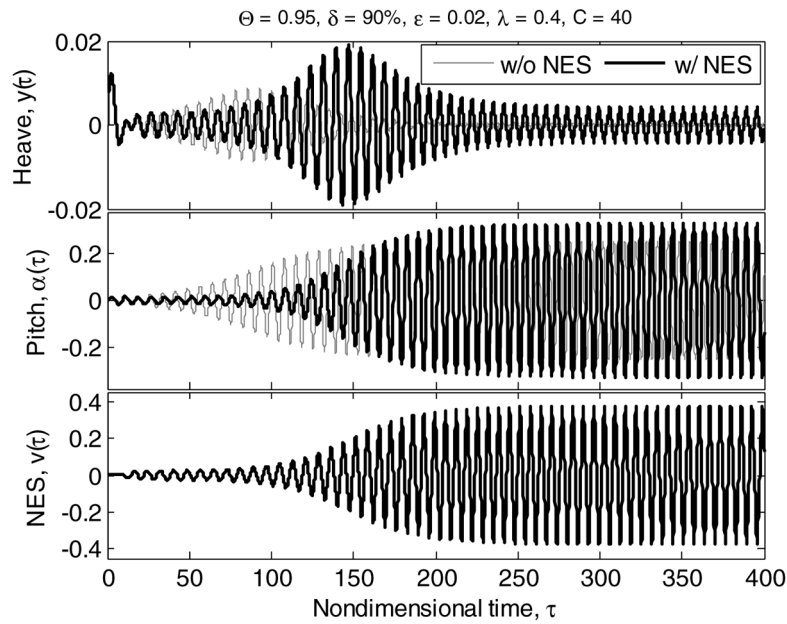


Fig. 9.48 Case of no LCO suppression for $\Theta = 0.9$, $\delta = 90\%$, $\varepsilon = 2\%$, $\lambda = 0.4$, and $C = 40$; zero initial conditions are used except for $y'(0) = 0.01$.

in 1:1 TRC with the heave mode, passively absorbing broadband energy from the wing, thus eliminating the burst-out. In the latter phase of the dynamics, the energy fed by the flow does not appear to directly excite the heave and pitch modes of the wing, but, instead, it seems to get transferred directly to the NES until the wing is entirely at rest and complete LCO suppression is achieved.

At the initial stage of the recurrent burst-outs, at time instants when the pitching LCO is nearly eliminated, most of the energy induced by the flow to the wing is absorbed directly by the NES with only a small amount of energy being transferred to the heave mode, so that both the NES and the heave mode reach their maximum amplitude modulations. This is followed by suppression of the burst-out, and this process is repeated until at a later stage of the dynamics complete suppression of the aeroelastic instability is reached. It will be shown in a later section that the beating-like (quasi-periodic) modal interactions observed during the recurrent burst-outs turn out to be associated with Neimark–Sacker bifurcations (Kuznetsov, 1995) of a periodic solution of system (9.74), and to be critical for determining domains of robust LCO suppression.

9.3.1.2 The Second LCO Suppression Mechanism

This mechanism is characterized by *intermediate or partial suppression of LCOs*. The initial action of the NES is the same as in the first suppression mechanism. Targeted energy transfer to the NES then follows under conditions of 1:1 TRC, followed by conditions of 1:1 SRC where both heave and pitch modes attain constant (but non-zero) steady state amplitudes. We note that the heave mode response can grow larger than in the corresponding system with no NES attached (exhibiting an LCO), at the expense of suppressing the pitch mode. We also note that, in contrast to the first suppression mechanism, the action of the NES is non-recurring in this case, as the NES acts only during the early phase of the motion stabilizing the wing and suppressing the developing LCO.

9.3.1.3 The Third LCO Suppression Mechanism

This mechanism is the most effective for suppressing the aeroelastic instabilities, as it results in *complete and permanent elimination of LCOs*. The dynamics of the wing-NES interaction resembles the second suppression mechanism (at least in a phenomenological way), leading, however, to asymptotic suppression of the LCO and possessing radically different underlying dynamics (as discussed later). Again, transient TET from the aeroelastic modes of the wing to the NES is caused by non-linear modal interactions during 1:1 TRCs. Both heave and pitch modes, as well as the NES exhibit exponentially decaying responses resulting in attraction of the dynamics to a trivial attractor. In general, for increasing reduced speeds larger NES masses are required for the realization of this suppression mechanism and complete elimination of LCOs.

9.3.1.4 Case of No LCO Suppression

The action of the NES is not always beneficial to the objective of LCO suppression. Indeed, for certain combinations of system parameters, initial conditions and reduced flow speeds the transient dynamics of system (9.74) may be attracted to non-trivial attractors that *enhance* the aeroelastic instability. This underlines the need for a robustness study of the proposed NES designs.

It follows that the NES might have an inadverse effect on the dynamics when it does not act as an efficient energy absorber of the oscillating wing undergoing aeroelastic excitation. In some cases, as the representative result of Figure 9.48 shows, *the steady state amplitudes of LCOs may grow even larger compared to the corresponding system with no NES attached*. Depending on the particulars of the cases examined (system parameters, initial conditions, flow speeds) the steady state dynamics of system (9.74) may result in superharmonic frequency relations between aeroelastic modes. Then, similarly to the behavior observed in the LCO triggering mechanism in the in-flow wing with no NES attached (see Section 9.2),

the dynamics might undergo a transition from 1:1 to 3:1 locking of frequency ratios between the heave and pitch modes; this implies the possibility of occurrence of an initial 1:1 TRC followed by a transition to a 3:1 SRC between the heave and pitch modes of the wing, and the generation of aeroelastic instability.

This observation suggests that *in order to effectively suppress the aeroelastic instabilities, the NES must interact with both heave and pitch modes in a way as to prevent direct energy transfer from the flow to the wing modes through subharmonic and superharmonic resonance captures* (similar conclusions were drawn in Section 9.1 where LCO suppression in the van der Pol oscillator was studied).

9.3.2 Study of LCO Suppression Mechanisms

In this section, we investigate numerically and analytically the three LCO suppression mechanisms mentioned previously. First, we numerically post-process the transient responses of the wing-NES system (9.74) in order to determine the dominant harmonic components and the underlying nonlinear resonant interactions that give rise to TET and result in aeroelastic instability suppression. The post-processing techniques that are employed include numerical wavelet transforms (WTs) and empirical mode decompositions (EMDs) combined with Hilbert transforms (see Section 2.5). Based on these numerical post-processing results, in the following section we analytically study the corresponding nonlinear modal interactions by performing fast-slow partitions of the transient dynamics employing complexification and multi-frequency averaging; the resulting reduced-order slow flow model fully capture the wing-NES nonlinear interactions, and provide a full understanding and modeling of the three instability suppression mechanisms. Through this systematic plan of study we aim to formulate a new paradigm for passive TET-based LCO mitigation.

9.3.2.1 Numerical Study

We first explore the nonlinear dynamics and energetic interactions governing each suppression mechanism by numerically computing the instantaneous energy exchanges between the aeroelastic modes and the attached NES of the self-excited system (9.74). To this end, we need to define certain energy measures.

The instantaneous total energy of the wing-NES system can be expressed as a sum of the instantaneous kinetic and potential energies of the wing and the NES as follows:

$$E^{\text{Total}}(\tau) = \left[\frac{1}{2}y'(\tau)^2 + \frac{1}{2}r_\alpha^2\alpha'(\tau)^2 + x_\alpha y'(\tau)\alpha'(\tau) + \frac{1}{2}\varepsilon v'(\tau)^2 \right] \\ + \left[\frac{1}{2}\Omega^2 y(\tau)^2 + \frac{1}{2}r_\alpha^2(\tau)^2 + \frac{1}{4}\xi_y y(\tau)^4 + \frac{1}{4}\xi_\alpha \alpha(\tau)^4 \right]$$

$$+ \left[\frac{1}{4} C (y(\tau) - \delta\alpha(\tau) - v(\tau))^4 \right] \quad (9.74)$$

The energy dissipated by the viscous damper of the NES is computed by the following expression:

$$E_d^{\text{NES}}(\tau) = \varepsilon\lambda \int_0^\tau [v'(s) + \delta\alpha'(s) - y'(s)]^2 ds \quad (9.75)$$

whereas the energy input to the system is the sum of the initial energy provided by the initial conditions and the non-conservative work performed by the flow

$$E_d^{\text{Input}}(\tau) = E^{\text{Total}}(0) + W_{nc}^y(\tau) + W_{nc}^\alpha(\tau) \quad (9.76)$$

where

$$\begin{aligned} W_{nc}^y(\tau) &= \mu C_{L,\alpha} \Theta \int_0^\tau [y'(s) + \Theta\alpha(s)] y'(s) ds \\ W_{nc}^\alpha(\tau) &= -\gamma \mu C_{L,\alpha} \Theta \int_0^\tau [y'(s) + \Theta\alpha(s)] \alpha'(s) ds \end{aligned} \quad (9.77)$$

As a result, at any time instant the following instantaneous energy balance should hold:

$$E^{\text{Total}}(\tau) = E^{\text{Input}}(\tau) - E_d^{\text{NES}}(\tau) \quad (9.78)$$

Figure 9.49 depicts the instantaneous energy exchanges between the two aeroelastic modes (pitch and heave) and the NES (upper parts), and the relation between the energy input fed from the flow to the system in time and the corresponding energy dissipation by the NES (lower part), for each of the three LCO suppression mechanisms. For comparison, the case where the LCO survives the action of the NES (case of no suppression) is also provided. Note that the depicted partition of total energy into each wing mode assumes that the contribution to the potential energy of the essentially nonlinear coupling is assigned entirely to the NES part.

The instantaneous energy exchanges depicted in Figure 9.49 demonstrate the transient and broadband nature of the nonlinear modal interaction between the inflow wing and the NES. A study of these plots indicates that the first suppression mechanism exhibits the most vivid transient energy interactions, especially between the pitch mode and the NES (see Figure 9.49a). The form of these modal interactions is quite similar to the corresponding energy exchanges studied in Section 3.4, where the targeted energy transfer (TET) mechanisms were investigated for a two-DOF system with essential stiffness nonlinearity (specifically, TET initiated by nonlinear beat phenomena-resonance captures will be discussed later).

In a later section, we will interpret this nonlinear beating behavior in terms of the study of steady state bifurcations, whereby it will be shown that the first LCO suppression mechanism is due to a Neimark–Sacker bifurcation of a stable LCO (which is analogous to a Hopf bifurcation in a codimension-one bifurcation prob-

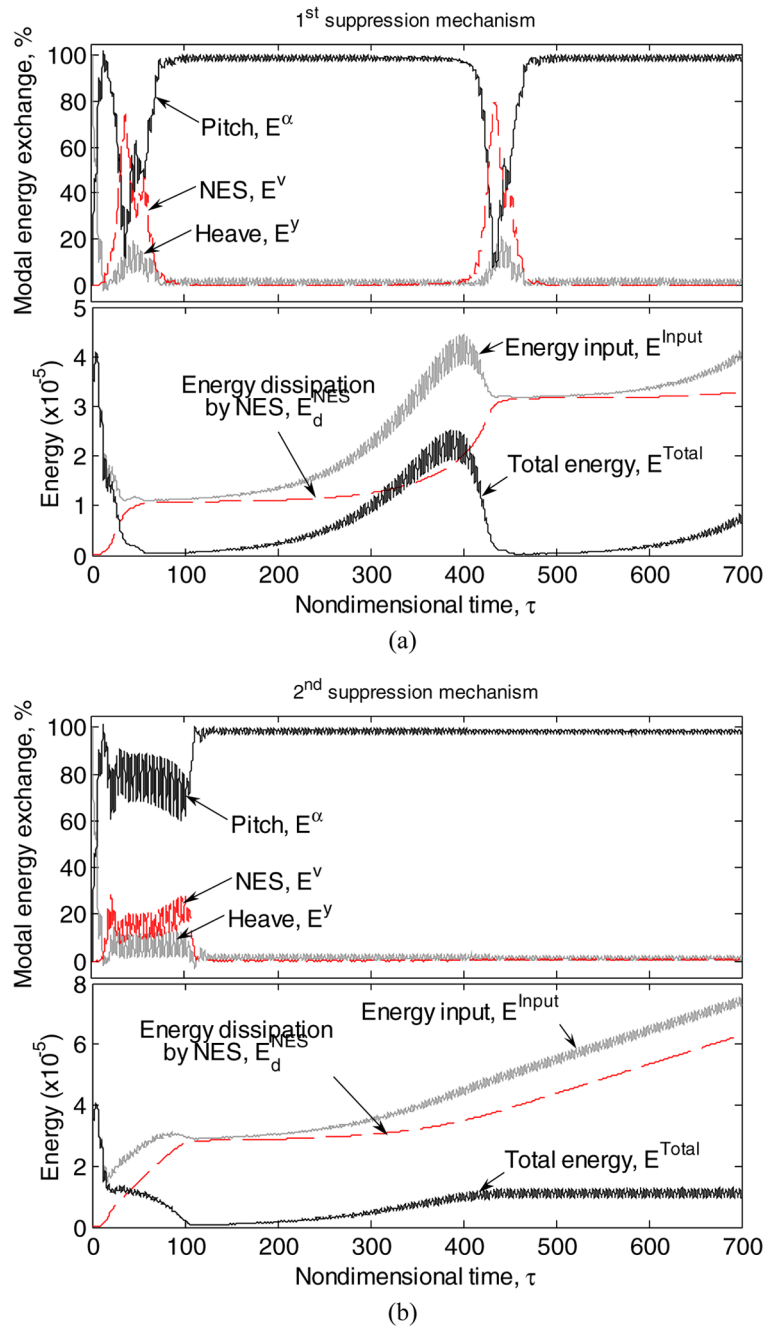
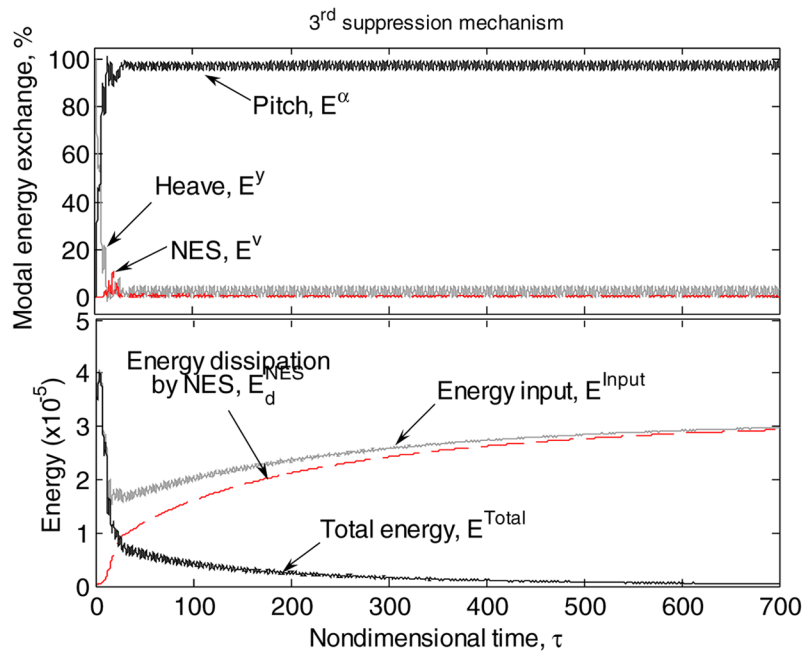
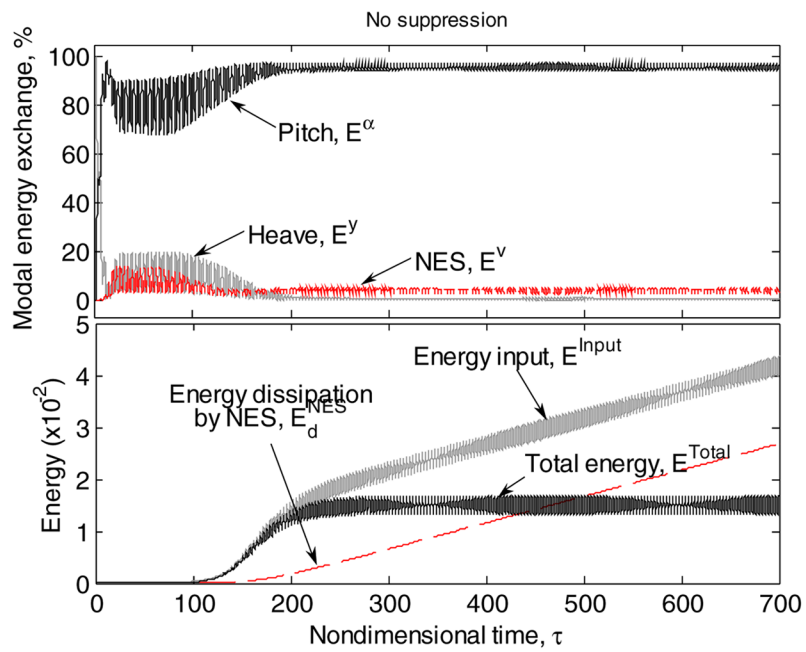


Fig. 9.49 Instantaneous energy exchanges (upper), and comparison of input energy to the system fed from flow in time and corresponding energy dissipation by the NES (lower), for the three LCO suppression mechanisms (a–c) and the case of no suppression (d); the simulations correspond to those depicted in Figures 9.45–9.48.



(c)



(d)

Fig. 9.49 Continued.

lem; see Guckenheimer and Holmes, 1983), yielding quasi-periodic solutions by adding an additional dominant harmonic component in the steady state response. Hence, variation of the total energy shows repeated burst-outs followed by suppressions; eventually, the energy input from the flow to the wing E^{Input} continuously increases nearly at the same rate with the energy dissipated by the NES, E_d^{NES} . At the time instant where a complete balance between E^{Input} and E_d^{NES} occurs, the total energy balance becomes zero; however, small disturbances from that totally balanced energetic state lead to recurring excitations of aeroelastic instabilities, and, as a result, the alternating series of suppressions and instability burst-outs is continuously repeated. Note that, although the aeroelastic instabilities cannot be completely removed by this suppression mechanism, their corresponding amplitudes are greatly reduced compared to those developed when the NES is absent (see Figure 9.45).

The second suppression mechanism involves initial strong modal interactions so that a balance between energy input and dissipation of energy by the NES is quickly reached at the initial early stage of the motion (see Figure 9.49b). This vigorous initial energy exchange behavior resembles the mechanism of fundamental TET mechanism (due to in-phase 1:1 resonance capture) discussed in Section 3.4.2.1. Again, in this case small disturbances can lead to the reappearance of instabilities but with much smaller amplitudes (see Figure 9.46). The (increasing) rates of energy input and energy dissipation by the NES become identical when an energy balance is reached, i.e., when the averaged trends in the energy input and NES energy dissipation follow parallel but non-coinciding paths; the nearly constant steady state difference between these energy rates makes possible the survival of aeroelastic instability in this case, in the form of reduced-amplitude LCOs.

In a later section we will establish that this partial LCO suppression mechanism is related to the generation of stable LCOs that bifurcate from a stable trivial equilibrium in a supercritical Hopf bifurcation; however, the Hopf bifurcation point, i.e., the flutter speed, occurs above that of the corresponding system with no NES attached. Moreover, we will show that the robustness of the second suppression mechanism depends on the global bifurcation structure of the steady state dynamics of system (9.74), and that this mechanism can be destroyed under sufficiently large disturbances to yield LCOs with amplitudes greater than those realized in the wing with no NES attached.

As for the third LCO suppression mechanism (see Figure 9.49c), most of the total energy of the motion apparently remains confined in the pitch mode so that the erroneous conclusion might be drawn that the NES does not perform efficiently in this case. However, comparing the energy input fed by the flow to the energy dissipated by the NES, we conclude that E_d^{NES} increases in a manner that energy balancing can occur only asymptotically for increasing time, thus preventing reappearance of LCOs in the long term. In this case we can obtain complete elimination of LCOs in a robust way, depending on the global bifurcation structure of the steady state dynamics, as discussed later.

Figure 9.49d depicts the energy exchanges for a case where the LCO survives the action of the NES. Initially, there occur vigorous modal energy exchanges, but these involve predominantly interactions between the heave and pitch modes, with only

secondary involvement of the NES. This means that the action of the NES is not as effective as in the previous three cases; as a result, the NES fails to prevent energy interactions between the heave and pitch modes. Moreover, the energy dissipation by the NES is not sufficiently strong to balance the energy input fed from the flow, which ‘feeds’ directly into the modes of the wing inducing aeroelastic instability. As a result, the LCOs are not only retained in this case, but their amplitudes become even larger than those realized in the wing with no NES attached (see Figure 9.48). Note that at steady state the NES continuously dissipates energy at a constant rate, which is nearly equal to the average rate of increase of the energy input from the flow. This behavior is similar to the second suppression mechanism except for the magnitude of the uniform differences between the two averaged dissipation rates.

We now examine the time-frequency behavior of the transient responses by utilizing the numerical wavelet transform (WT). In Figure 9.50 we present the WT spectra corresponding to the transient responses of Figures 9.45–9.48, i.e., the three instability suppression mechanisms and the additional case of no suppression. Comparing the evolutions of the dominant instantaneous frequencies of the heave and pitch mode responses and of the NES response, provides an additional (direct) way to verify the occurrence of resonance captures in the transient dynamics.

First, we focus in cases where partial or complete instability suppression is realized, corresponding to Figures 9.45–9.47. The WT spectra depicted in Figures 9.50a–c indicate that primarily there occur 1:1 TRCs between the NES and the heave mode; in addition, there occur 1:1 TRCs followed by transitions to subharmonic resonance captures between the NES and the pitch mode. Moreover, there exists a common strong harmonic component in these plots at a frequency near the natural frequency of the pitch mode $\omega \approx 1$. Indirectly, the WT spectra suggest that in the study of all three suppression mechanisms one may utilize a reduced-order averaged model possessing two fast frequencies, since at most two dominant frequency components appear in the transient responses governing the resonance interactions between modes; that is, in all cases considered, the responses are dominated by two frequency components with frequencies $\omega_h \approx \Omega = 0.5$ and $\omega_\alpha \approx 1$ (i.e., the linearized eigenfrequencies of the heave and pitch modes, respectively). We will make use of this important finding in the next section, in our analytical study of the LCO suppression mechanisms.

Focusing now on Figures 9.48 and 9.50d where no LCO suppression takes place, we make the additional remark that when the LCO survives the action of the NES, the interaction between the heave and pitch modes completely resembles the behavior of the LCO triggering mechanism studied in Section 9.2. That is, there occurs a transition from an initial 1:1 TRC to a 3:1 SRC. Moreover, in this case, the NES possesses a higher superharmonic component, so that its dynamic interaction with the pitch mode also involves a transition from a 1:1 TRC to 3:1 SRC. It follows that in this case the resonance interactions between the various modes of the wing-NES assembly are qualitatively different than those taking place in the three cases where LCO suppression is realized.

Combining the results of Figures 9.49 and 9.50, we may construct the frequency-energy plot (FEP) of the transient dynamics of system (9.74), which, as shown in

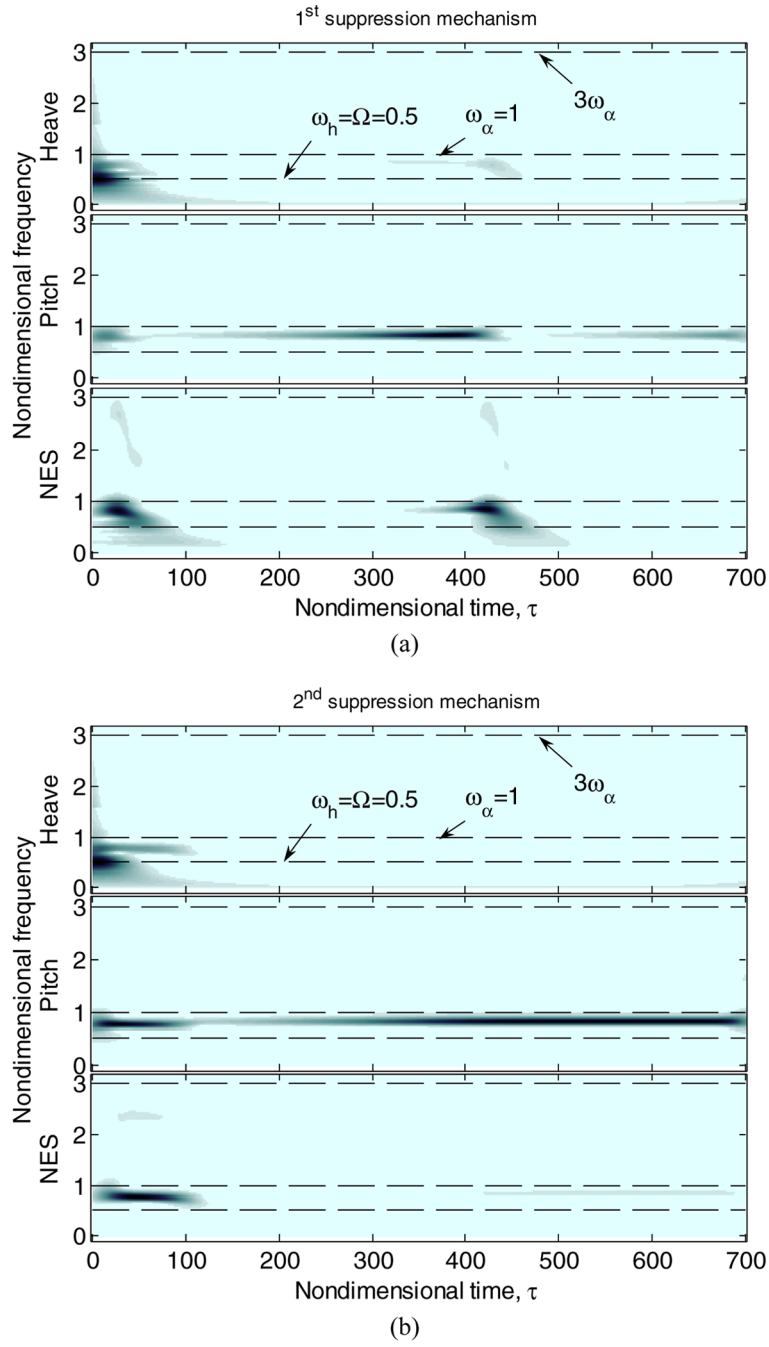


Fig. 9.50 Wavelet transform spectra of transient responses: (a–c) the three suppression mechanisms depicted in Figures 9.45–9.47, respectively; (d) the case of no suppression depicted in Figure 9.48.

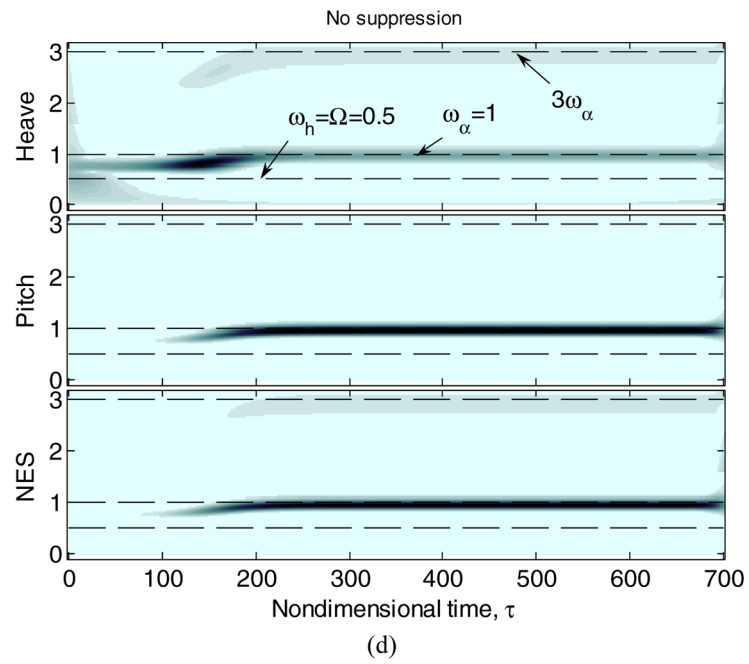
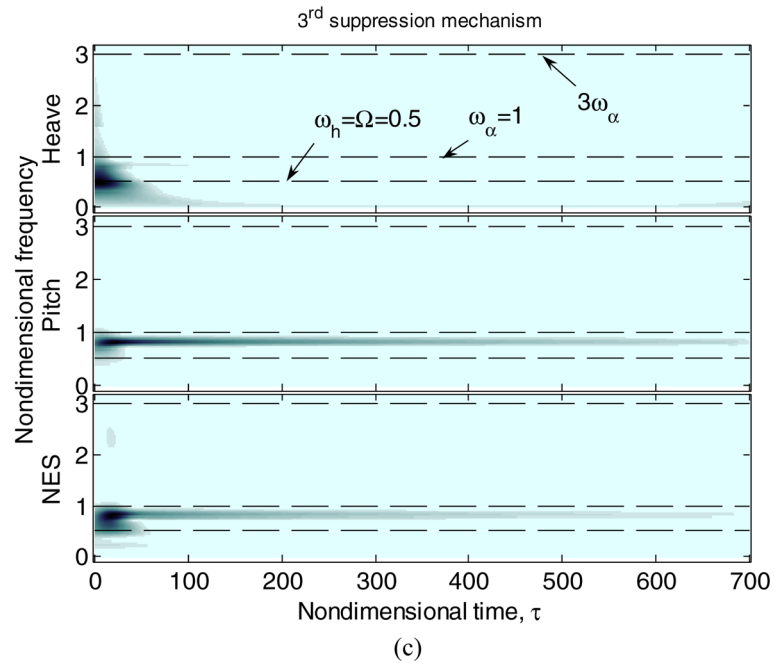


Fig. 9.50 Continued.

previous chapters, can be a useful tool for identifying the essential nonlinear modal interactions and presenting the damped transitions that occur in the dynamics (including 1:1 TRCs, subharmonic and superharmonic TRCs, and escapes from these regimes). In Section 3.3 the FEP for a Hamiltonian system composed of a SDOF linear oscillator with an essentially nonlinear lightweight attachment was computed, and it was shown that such a simple system possesses very complicated dynamics, including a countable infinity of subharmonic tongues. For the corresponding weakly damped system the Hamiltonian FEP was also utilized in conjunction with WT spectra of damped transient responses to study alternative mechanisms for TET (see Section 3.4). Similar use of the FEP was made in other chapters of this monograph for MDOF linear oscillators with SDOF or MDOF essentially nonlinear attachments, as well as for the case of a self-excited system, namely, the van der Pol oscillator with an attached NES (see Section 9.1).

However, unlike the above-mentioned cases, the definition of an FEP describing the topological structure of the periodic or quasi-periodic orbits of the underlying Hamiltonian system becomes difficult in the current problem (9.74). This is mainly due to the aeroelastic terms that provide non-conservative work to the system and change the intrinsic eigenfrequencies (and the total energy of the system) of the system when the flow speed varies. Hence, *we propose an alternative way of constructing the FEP for aeroelastic systems based on the bifurcation structures of their steady state LCO solutions*, obtained either numerically (utilizing a numerical continuation technique) or analytically (employing multi-phase averaging or harmonic balance).

We demonstrate the construction of the FEP for system (9.74) by considering the steady state LCOs for parameters $\delta = 90\%$, $\varepsilon = 1\%$, $\lambda = 0.1$, and $C = 10.0$ (corresponding to transient responses shown in Figure 9.45). In Figure 9.51a we depict the bifurcation diagrams of system (9.74) with respect to the reduced velocity Θ . The stable LCOs generated at $\Theta = \Theta^H$ become unstable at $\Theta = \Theta^{NS}$, yielding new periodic components that amount to quasi-periodic motions realized on two-tori in phase space. *The resulting branch of quasi-periodic motions is closely associated with the first LCO suppression mechanism* (see Figure 9.45). In addition, the periods of the LCOs, T_{LCO} , are computed when performing the numerical continuation of the branches of LCOs (these are depicted as functions of Θ in the upper plot of Figure 9.51b); it follows that the corresponding frequencies of these LCOs can be computed as $\omega_{LCO} = 2\pi/T_{LCO}$, and are depicted as functions of Θ in the lower plot of Figure 9.51b. It is noted that this numerical method may not provide information regarding the existence of multiple frequencies in the computed responses, if any, since it only provides the dominant frequency of the LCO. On the other hand, we already practiced computing the total energy of the system; in Figure 9.51c we depict the mean value of the total energy of the system as function of reduced speed Θ . We note that the instantaneous total energy of the system is expected to oscillate about this mean value due to nonlinear modal interactions (resonance captures – see Figure 9.49). Finally, combining the lower plot of Figure 9.51b with the plot of Figure 9.51c we compute the FEP shown in Figure 9.51d. By construction, the FEP is parameterized by the reduced speed Θ , and represents the averaged dominant

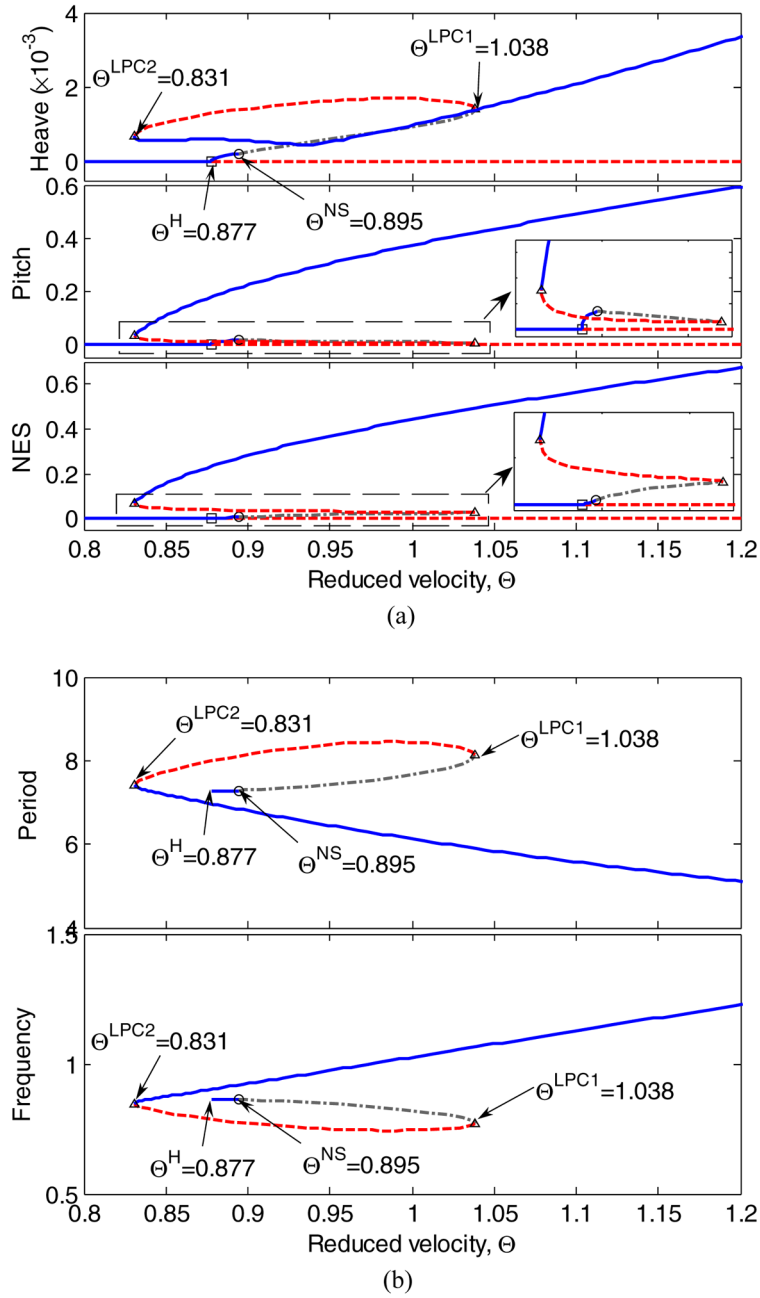
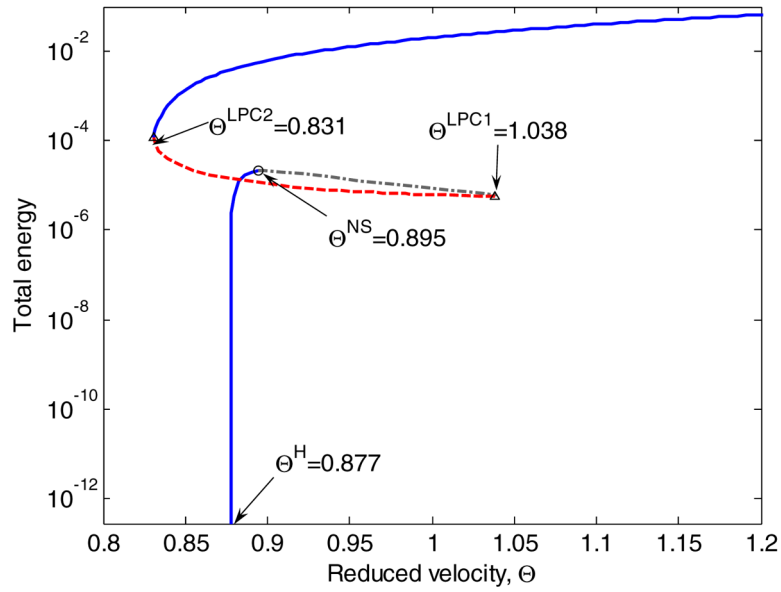
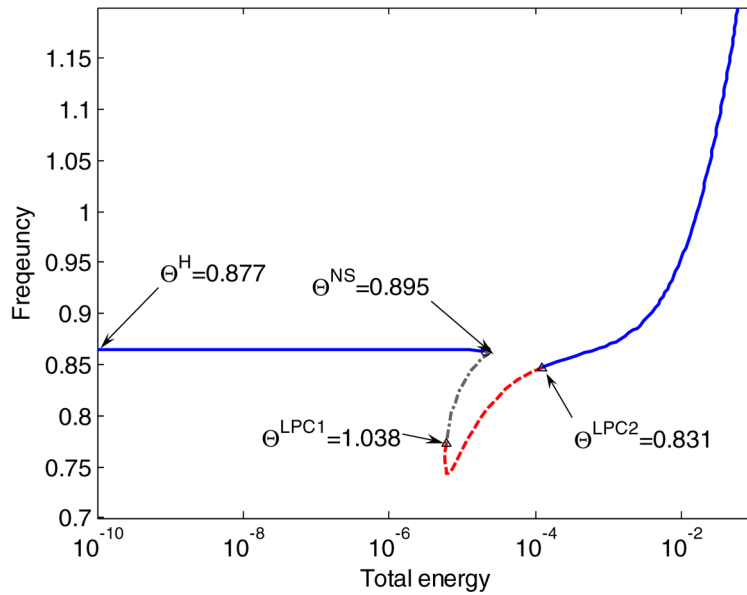


Fig. 9.51 Construction of the frequency-energy plot (FEP) of LCOs of system (9.74) for $\delta = 0.9$, $\varepsilon = 0.01$, $\lambda = 0.1$, and $C = 10$: (a) bifurcation diagrams of LCO amplitudes with respect to Θ ; (b) LCO periods and frequencies as functions of Θ ; H, NS, and LPC denote Hopf, Neimark-Sacker, and Limit Point Cycle bifurcations, respectively; solid line indicates stability, dashed line indicates instability, and dash-dotted quasi-periodic solutions.



(c)



(d)

Fig. 9.51 Construction of the frequency-energy plot (FEP) of LCOs of system (9.74) for $\delta = 0.9$, $\varepsilon = 0.01$, $\lambda = 0.1$, and $C = 10$: (c) total energies of the system when LCOs occur as functions of Θ ; (d) FEP for LCO solutions; H, NS, and LPC denote Hopf, Neimark–Sacker, and Limit Point Cycle bifurcations, respectively; solid line indicates stability, dashed line instability, and dash-dotted quasi-periodic solutions.

frequencies of LCOs as functions of the corresponding total energies of the system (9.74).

We are now in a position to examine the three LCO suppression mechanisms by means of representations of the dynamics on appropriately defined FEPs, as depicted in the plots of Figure 9.52. To this end, the instantaneous frequencies of the modal responses were computed by applying numerical Hilbert transforms to the transient responses corresponding to the three LCO suppression mechanisms represented in Figures 9.45–9.47. In addition we apply numerical wavelet transform to the transient responses for the case when the LCO survives the action of the NES, as depicted in Figure 9.48. The traces of the instantaneous frequencies are then plotted against the corresponding instantaneous total energies of the system, with time being the parametrizing variable. Finally, these traces are superimposed to the FEP corresponding to the system parameters of the specific case considered. In computing the instantaneous frequencies, we applied the Savitzky–Golay polynomial smoothing filter in order to remove high-frequency noise caused by numerical differentiation of the phase variable.

A general conclusion is that nonlinear modal interactions between the heave and pitch modes are realized mainly through 1:1 resonance captures whether or not LCO suppression is realized. The first LCO suppression mechanism (depicted in Figure 9.52a and corresponding to the numerical simulation depicted in Figure 9.45) is characterized by repeated loops of the instantaneous frequencies with time, corresponding to the recurrent burst-outs and suppressions of aeroelastic instability; these loops consist of transitions from 1:1 to subharmonic TRCs (suppression stage), and then reversals back to 1:1 TRCs (burst-out stage). Reflecting the intrinsic LCO solutions depicted in the FEP, we find the following interesting behavior influencing the first suppression mechanism: Once the dynamics exceeds the Neimark–Sacker (NS) bifurcation point $\Theta^{NS} = 0.89$ (note that the instantaneous frequency plot of Figure 9.52a corresponds to the flow speed $\Theta = 0.9 > \Theta^{NS}$) the only choice for the dynamics is to follow the unstable LCO branches which might yield either periodic or quasi-periodic steady state motions, as the heave and pitch modes are in 1:1 TRC (see Figure 9.51d). Hence, the dynamics can only be captured into loops that lead to transitions into subharmonic resonances. These repetitions (bursting outs and consequent suppressions) characterize the first suppression mechanism.

In the second LCO suppression mechanism depicted in Figure 9.52b intermediate (partial) suppression of the LCO occurs, and the dynamics on the FEP forms a single loop involving a *single* transition from 1:1 to subharmonic resonance capture, with a final reversal back to 1:1 SRC when the steady state dynamics is reached. The plots of Figure 9.52b correspond to the transient responses and system parameters of the plots of Figure 9.46, again for flow speed $\Theta = 0.9 > \Theta^{NS}$. On the contrary, complete LCO elimination (the third suppression mechanism – Figure 9.47) involves 1:1 TRCs before the dynamics escapes from resonance, at which point the NES has completely exhausted the energy input fed by the flow to the wing (see Figure 9.52c).

Finally, we note a transition from 1:1 to superharmonic resonance capture between the NES and the aeroelastic modes when the LCOs survive the action of the

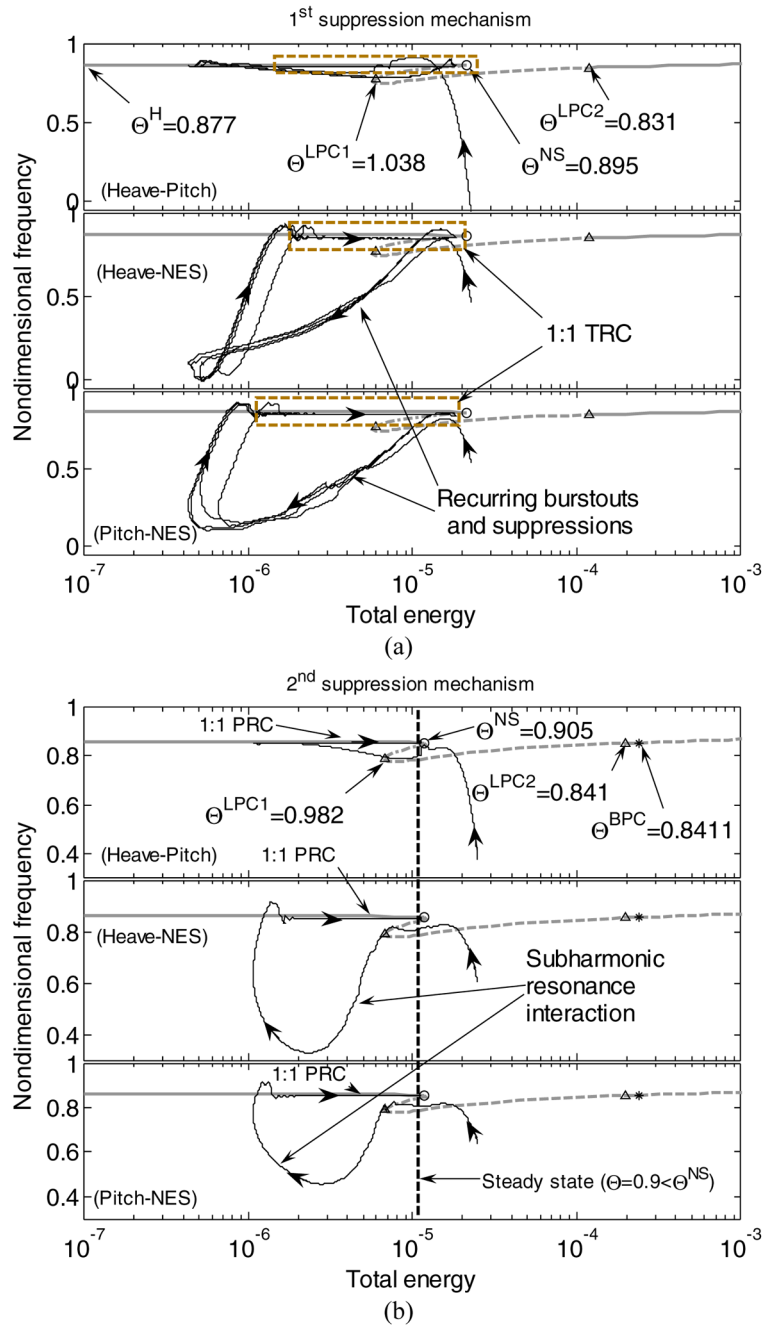


Fig. 9.52 Instantaneous frequencies superimposed to FEPs of LCOs of the corresponding systems: (a, b) LCO suppression mechanisms corresponding to Figures 9.45–9.47 (thin solid lines); H, NS, and LPC denote Hopf, Neimark–Sacker, and Limit Point Cycle bifurcations, respectively, of the FEPs of LCOs; bold solid line indicates stable LCOs, dashed line unstable LCOs, and dash-dotted line quasi-periodic solutions.

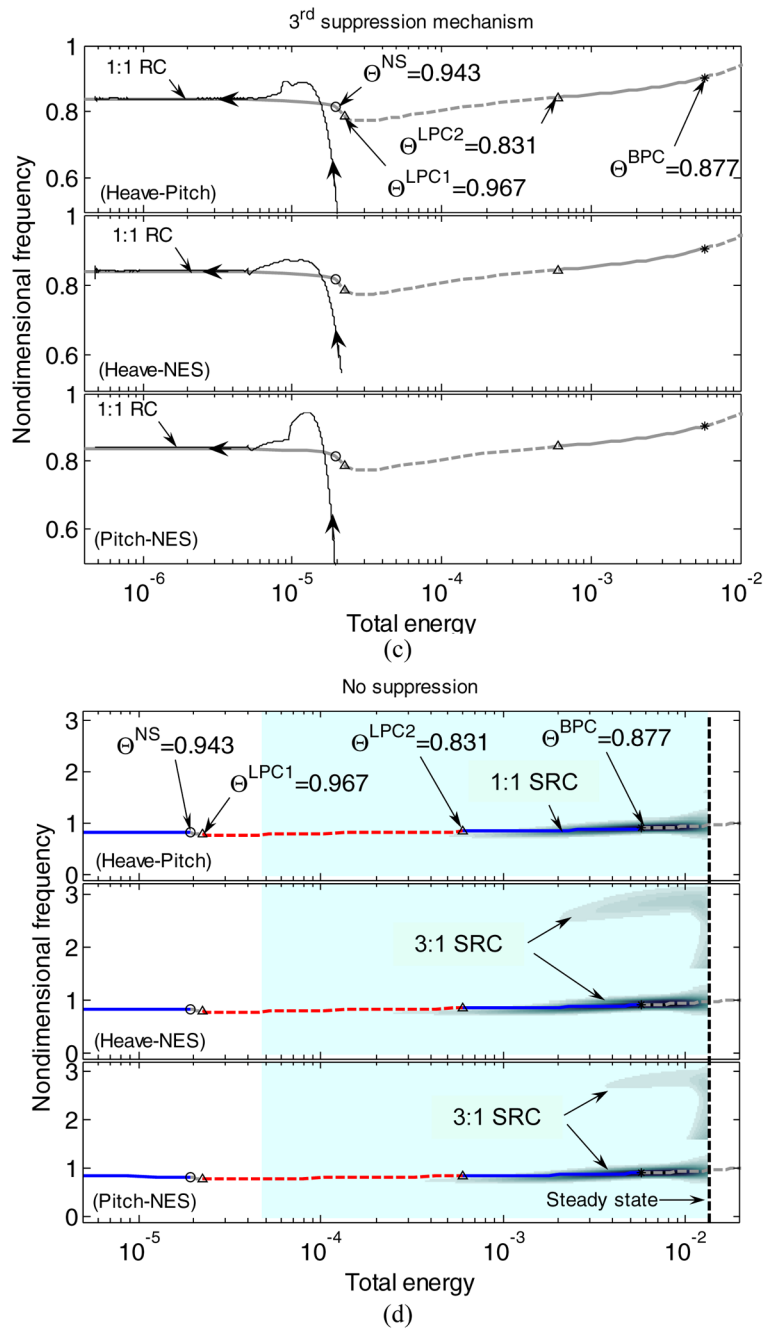


Fig. 9.52 Instantaneous frequencies superimposed to FEPs of LCOs of the corresponding systems: (c) LCO suppression mechanisms corresponding to Figures 9.45–9.47 (thin solid lines); (d) no suppression corresponding to Figure 9.48 (WT spectra); H, NS, and LPC denote Hopf, Neimark–Sacker, and Limit Point Cycle bifurcations, respectively, of the FEPs of LCOs; bold solid line indicates stable LCOs, dashed line unstable LCOs, and dash-dotted line quasi-periodic solutions.

NES (Figure 9.52d – the plot corresponds to the time responses and system parameters depicted in Figure 9.47). Comparing the plots of Figures 9.52c and 9.52d (corresponding to the same system parameters but different NES mass ratios), we conclude that *whether or not the LCOs are suppressed depends on the state of the dynamics of the system when 1:1 resonance capture occurs*. That is, in Figure 9.52c where complete LCO suppression occurs, the dynamics is captured into the domain of attraction of the stable LCO branch at a lower energy regime; whereas, in Figure 9.52d where LCO suppression fails, the dynamics is entrapped in the domain of attraction of the stable LCO branch formed at a higher energy regime and involving superharmonic SRCs between the NES and the aeroelastic modes that yield large-amplitude LCOs.

In conclusion, we studied frequency-energy representations of the transient dynamics of system (9.74) superimposed on appropriately defined FEPs of LCOs. The first LCO suppression mechanism exhibits escapes near the NS bifurcation point that drives the dynamics into regimes of quasi-periodic responses; the second suppression mechanism drives the dynamics to a stable steady state (LCO) corresponding to the reduced velocity (and energy) of the system (i.e., $\Theta = 0.9 \leq \Theta^{\text{NS}} = 0.905$ in Figure 9.52b). Moreover, the same system parameter values (i.e., the same underlying FEP of LCOs) can yield drastically different LCO suppression results, depending on the specific energy values (or reduced flow speeds) where the resonant interaction phenomena between the flow and the wing modes occur; this last observation raises the issue of robustness of LCO suppression which will be addressed in a later section. These concluding remarks underline the importance of designing the initial entrainment of the wing – NES dynamics into the proper resonance manifolds in order to achieve efficient and robust LCO suppression.

To numerically prove that the basic underlying dynamical mechanism for TET-based aeroelastic instability suppression is a series of resonance captures of the wing – NES dynamics, we analyze the dynamics by empirical mode decomposition (EMD). By computing the IMFs of the transient responses we express the heave, pitch, and NES responses as,

$$y(t) = \sum_{i=1}^{N_1} c_i(\tau), \quad \alpha(t) = \sum_{i=1}^{N_2} c_i(\tau), \quad v(t) = \sum_{i=1}^{N_3} c_i(\tau) \quad (9.79)$$

where the i -th (complex) IMF, $c_i(\tau)$, for each response is Hilbert-transformed and expressed in polar form as, $c_i(\tau) = a_i(\tau)e^{j\theta_i(\tau)}$. The amplitude $a_i(\tau)$ and phase $\theta_i(\tau)$ can be computed from the analytic signal, $z_i(\tau) = c_i(\tau) + j \text{HT}[c_i(\tau)]$, where $\text{HT}[c_i(\tau)]$ denotes the Hilbert transform of $c_i(\tau)$:

$$a_i(\tau) = \sqrt{c_i(\tau)^2 + \text{HT}[c_i(\tau)]^2} \quad (9.80)$$

$$\theta_i(\tau) = \tan^{-1} \frac{\text{HT}[c_i(\tau)]}{c_i(\tau)} \quad (9.81)$$

It follows that the instantaneous frequency of the i -th IMF can be computed by the expression:

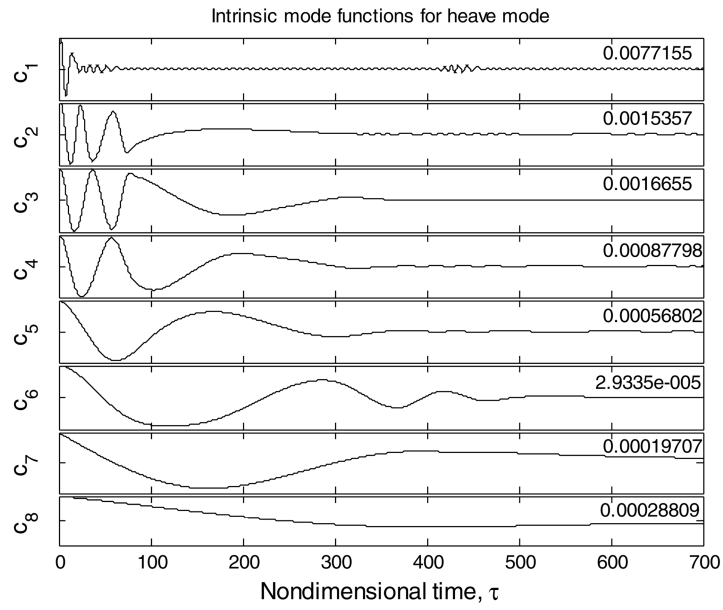
$$\omega_i(\tau) = \frac{d\theta_i(\tau)}{d\tau} \quad (9.82)$$

To demonstrate the application of EMD in the problem of identification of the nonlinear modal interactions in the in-flow wing-NES dynamics, we will consider only the first LCO suppression mechanism studied in Figures 9.45, 9.49a, 9.50a and 9.52a. We wish to numerically prove that this mechanism is governed by a recurrent series of resonance captures, escapes and transitions to recaptures. In the next section, these numerical results will be compared to, and verified with analytical models. The other two LCO suppression mechanisms can be analyzed by applying a similar methodology so they will not be considered herein.

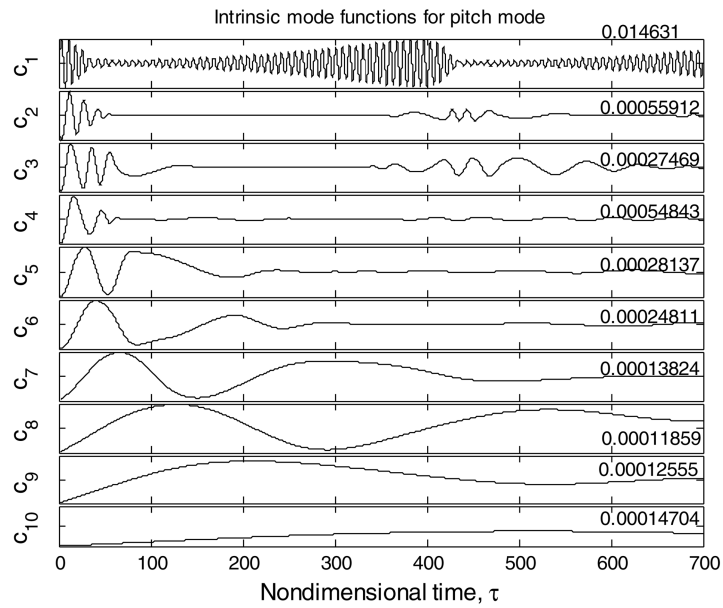
Figure 9.53 depicts the IMFs of the heave, pitch and NES transient responses shown in Figure 9.45. The value on the upper right part of each plot represents the maximum amplitude of the corresponding IMF, so we conclude that the leading-order IMF of each of the analyzed responses is the dominant oscillatory component in that specific time series. The plots of Figure 9.54a depict a comparison of the three leading-order (dominant) IMFs of each response with the corresponding exact time series from Figure 9.45. We observe satisfactory match between them, except for an initial period where the end effects of the EMD process pollute the data, and for some lower-frequency intervals where higher-order IMFs may possess enhanced contributions in the responses. This confirms that the leading-order IMFs in Figure 9.53 are dominant and capture the essential dynamics of the transient interactions.

Let θ_i , $i = 1, 2, 3$, [computed by relation (??) Author, no eq. (9.81) in original manuscript, what should correct eq. number be? Author] be the phases of the three aforementioned dominant IMFs of the heave and pitch modes, and the NES, respectively. Then, $\theta_{12} \equiv \theta_1 - \theta_2$ denotes the corresponding phase difference between the heave and pitch modes; $\theta_{13} \equiv \theta_1 - \theta_3$, the phase difference between the heave mode and the NES; and $\theta_{23} \equiv \theta_2 - \theta_3$, the phase difference between the pitch mode and the NES. Figure 9.54b depicts the temporal evolutions of the instantaneous phase differences, θ_{12} , θ_{13} , θ_{23} . If a phase difference exhibits monotonically increasing or decreasing temporal behavior, it is considered to be *time-like*; otherwise, it is regarded as *non-time-like* phase difference. For example, a constant or oscillatory phase difference with zero mean is considered to be non-time-like.

Following the averaging arguments discussed in Section 2.4, if a phase difference is time-like, it can be considered to be a ‘fast’ phase of the dynamics, and, as a result, it may be removed from the dynamics (as non-essential) by simply averaging it out of the problem; in other words, this phase difference will negligibly influence the slow flow dynamics of the system after averaging and its contribution will not be considered as essential in the corresponding time window of the dynamics. On the other hand, if a phase difference is non-time-like, it may not be averaged out of the dynamics (as it cannot be regarded as ‘fast’ phase), and is expected to influence the slow (essential) dynamics of the system in the specific time interval of the analysis. In the latter case there occurs resonance capture and TET, as the dynamics is cap-



(a) Heave



(b) Pitch

Fig. 9.53 Intrinsic mode functions (IMFs) of the transient responses depicted in Figure 9.45 (first LCO suppression mechanism) computed by EMD: (a) heave mode; (b) pitch mode; the value shown on the upper right of each IMF plot indicates the maximum amplitude of that IMF.

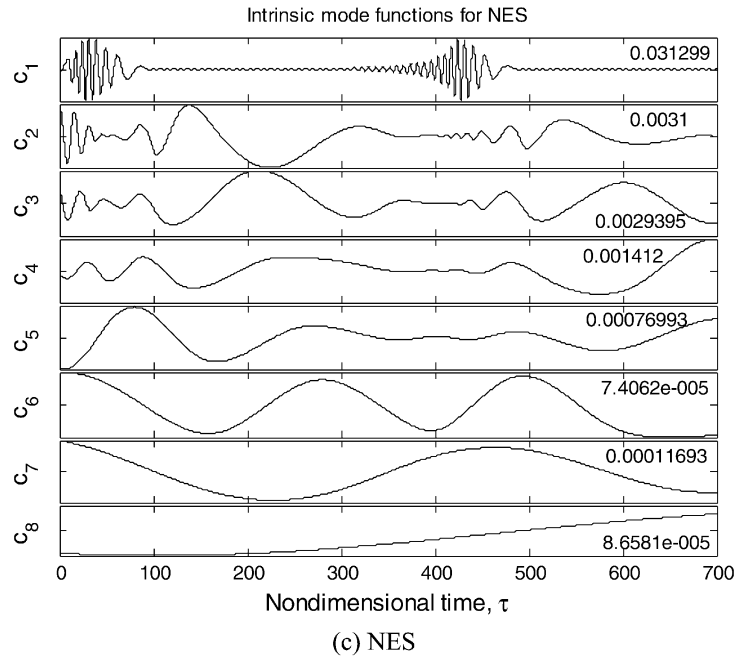
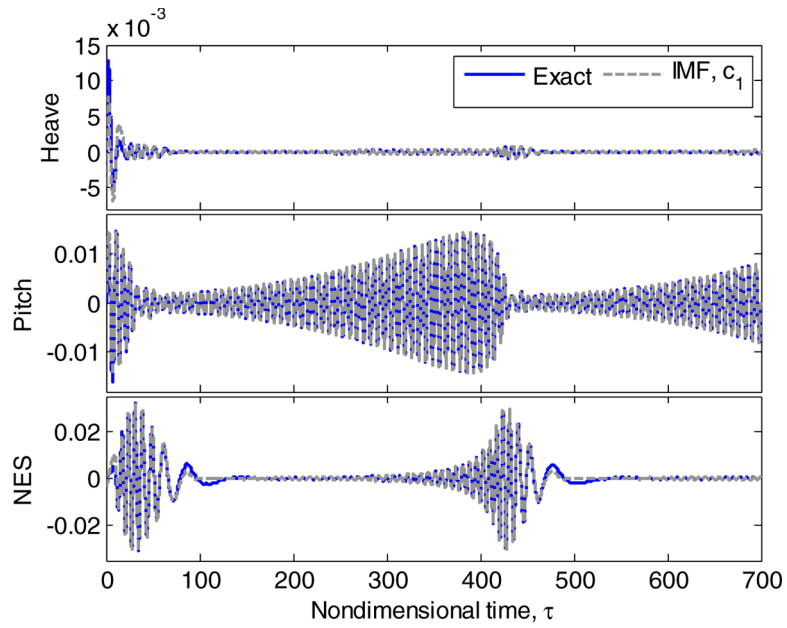


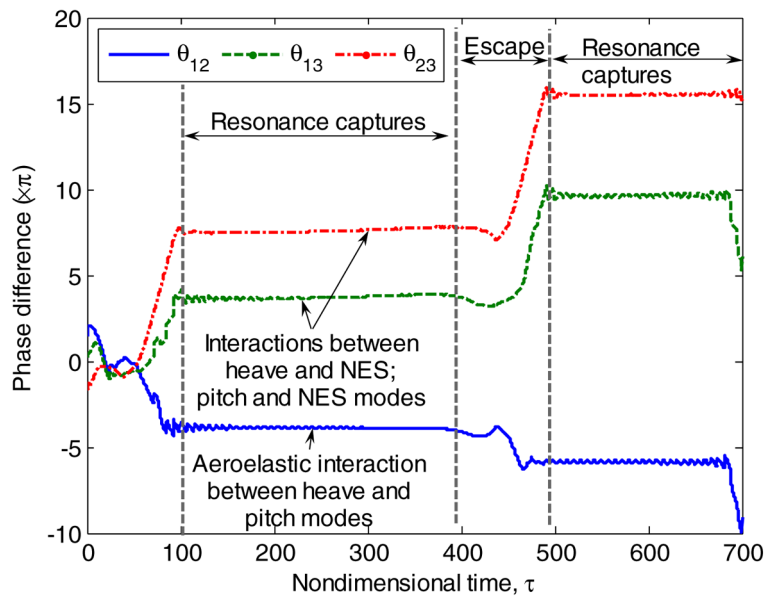
Fig. 9.53 Intrinsic mode functions (IMFs) of the transient responses depicted in Figure 9.45 (first LCO suppression mechanism) computed by EMD: (c) NES; the value shown on the upper right of each IMF plot indicates the maximum amplitude of that IMF.

tured transiently in the corresponding resonance manifold (Arnold, 1988) defined by an integral relation between the instantaneous frequencies of the corresponding IMFs.

From Figures 9.54b, c, we note that there exist three time intervals where non-time-like behavior of certain phase differences occurs, namely, for $\tau \in [20, 60]$, $\tau \in [110, 400]$ and $\tau \in [490, 700]$. In these time intervals 1:1 TRCs occur (as evidenced by the instantaneous frequency plots, θ'_i , $i = 1, 2, 3$, of Figure 9.54d), appearing as spirals in the corresponding phase portraits of Figure 9.54c. We note that not only do 1:1 TRCs occur between the heave mode and the NES, and between the pitch mode and the NES, but also between the heave and pitch modes, exactly as in the case of the LCO triggering mechanism (see Section 9.2). In between these recurring 1:1 TRCs the dynamics engage in subharmonic TRCs, which correspond to the loops in the FEPs depicted in Figure 9.52a. These results confirm the conclusions drawn earlier regarding the dynamics governing the first LCO suppression mechanism. Moreover, this analysis can be extended to the other two suppression mechanisms discussed previously.



(a)



(b)

Fig. 9.54 EMD analysis of the transient responses of Figure 9.45 (first LCO) suppression mechanism: (a) dominant IMFs compared to the exact responses; (b) phase differences between the dominant IMFs of the NES and aeroelastic mode responses.

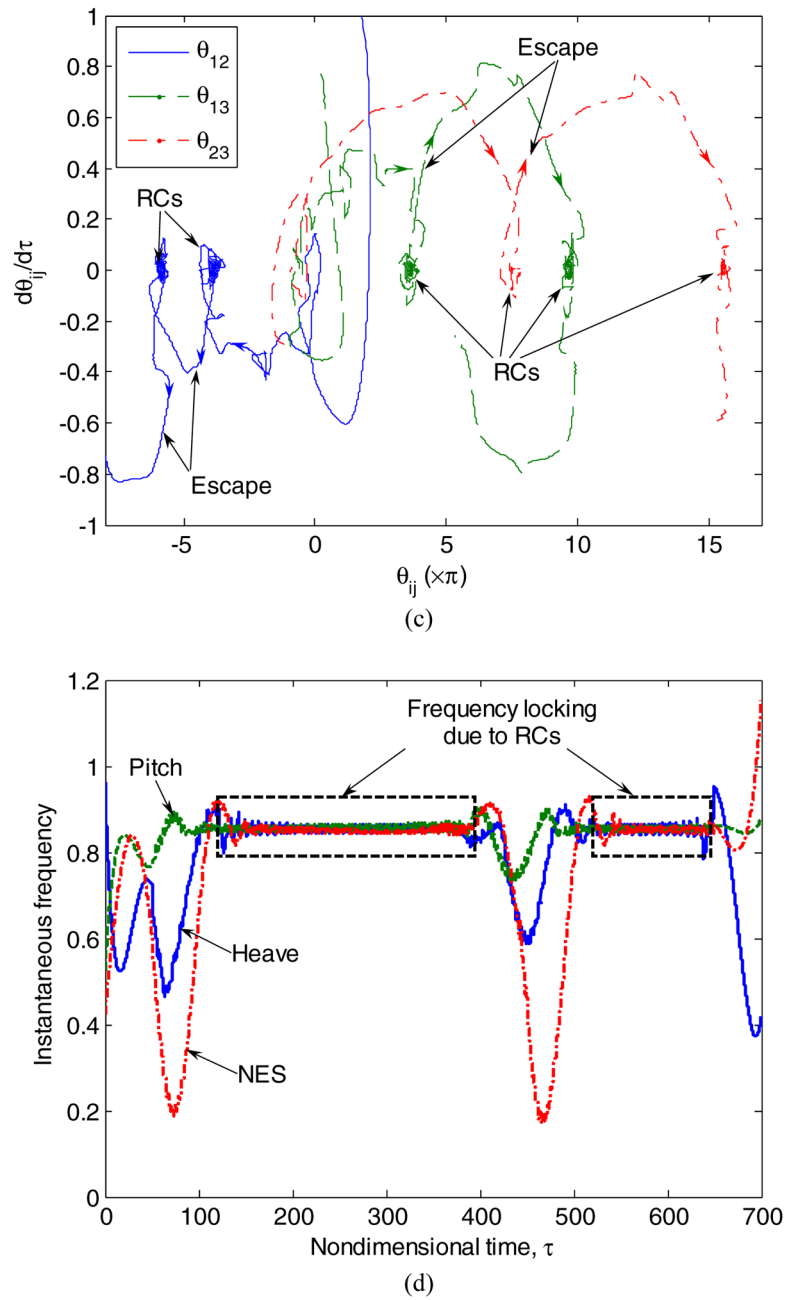


Fig. 9.54 EMD analysis of the transient responses of Figure 9.45 (first LCO) suppression mechanism: (c) phase differences between the dominant IMFs of the NES and aeroelastic mode responses; (d) corresponding instantaneous frequencies of the dominant IMFs.

9.3.2.2 Analytical Study

In the previous section, we found numerically that LCO suppression in the wing under consideration is due to a series of 1:1 or subharmonic resonance captures between the pitch and heave modes and the attached NES. In this section, we analytically prove this result by constructing and analyzing slow flow analytical models using the CX-A technique (see Section 2.4). We will focus only in the first LCO suppression mechanism, as the analysis can be extended similarly to study the other two suppression mechanisms.

Based on the WT spectra depicted in Figure 9.50a, we conclude that there exist two dominant ('fast') frequencies in the dynamics at normalized frequencies equal to unity and $\Omega = 0.5$, corresponding to the two normalized linearized eigenfrequencies ω_h and ω_a of the pitch and heave modes, respectively. For notational convenience we designate these components as LF (lower-frequency) and MF (middle-frequency) components, respectively, since this is consistent to the notation introduced in previous sections. There are some additional superharmonic frequency components (realized in between the recurrent 1:1 TRCs), but these will be neglected from the model as non-dominant.

Accordingly, following the multi-frequency CX-A methodology we will express the heave, pitch and NES transient responses as follows:

$$\begin{aligned} y(\tau) &= y_1(\tau) + y_2(\tau) \\ a(\tau) &= a_1(\tau) + a_2(\tau) \\ v(\tau) &= v_1(\tau) + v_2(\tau) \end{aligned} \quad (9.83)$$

where the notation of the previous sections was employed, and the components with subscripts 1 and 2 correspond to slowly varying modulations of the fast frequency components $e^{j\Omega\tau}$ and $e^{j\tau}$, respectively. In essence, these representations are slow-fast, multi-frequency decompositions of the transient responses, with the fast frequencies determined by the dominant harmonic components identified by the WT spectra of Figure 9.50a (in this case two fast frequencies).

Introducing the new complex variables,

$$\begin{aligned} \psi_1 &= y'_1 + j\Omega y_1 \equiv \varphi_1 e^{j\Omega\tau}, & \psi_3 &= y'_2 + j y_2 \equiv \varphi_3 e^{j\tau} \\ \psi_2 &= \alpha'_1 + j\Omega \alpha_1 \equiv \varphi_2 e^{j\Omega\tau}, & \psi_4 &= \alpha'_2 + j \alpha_2 \equiv \varphi_4 e^{j\tau} \\ \psi_5 &= v'_1 + j\Omega v_1 \equiv \varphi_5 e^{j\Omega\tau}, & \psi_6 &= v'_2 + j v_2 \equiv \varphi_6 e^{j\tau} \end{aligned} \quad (9.84)$$

expressing the normalized equations of motion (9.74) in terms of the complex variables, and applying two-frequency averaging over the two fast components $e^{j\Omega\tau}$ and $e^{j\tau}$, we obtain a set of six complex-valued modulation equations governing the slow flow dynamics,

$$\underline{\varphi}' = \underline{F}(\underline{\varphi}) \quad (9.85)$$

where $\underline{\varphi} \in C^6$ and the complex-valued vector $\underline{F}(\underline{\varphi})$ is quite involved and is not explicitly reproduced here.

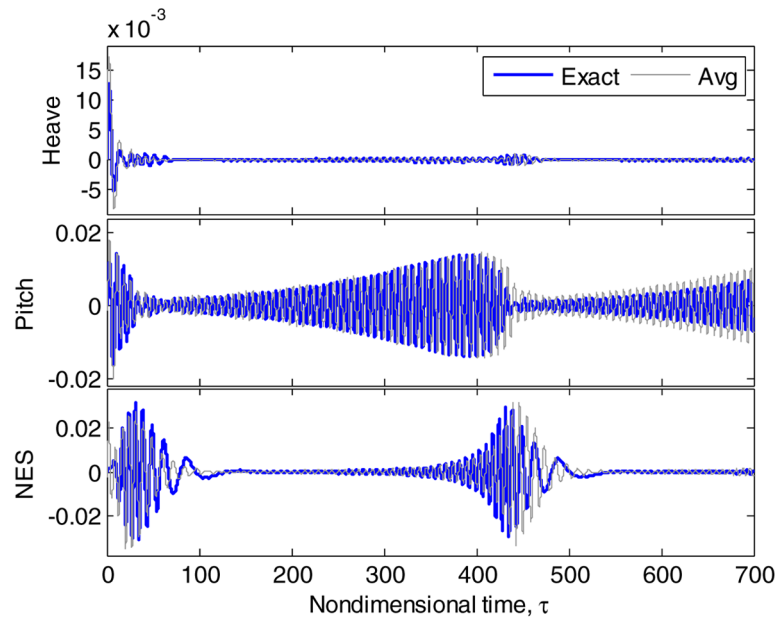
Introducing the polar form decompositions of the slow modulations, $\varphi_i(\tau) = a_i(\tau) e^{j b_i(\tau)}$, $a_i(\tau), b_i(\tau) \in R$, $i = 1, \dots, 6$, we express (9.85) as a set of 12 (real-valued) autonomous modulation equations governing the slow evolutions of the amplitudes and phases,

$$\underline{a}' = \underline{f}(\underline{a}, \underline{\phi}), \quad \underline{\phi}' = \underline{g}(\underline{a}, \underline{\phi}) \quad (9.86)$$

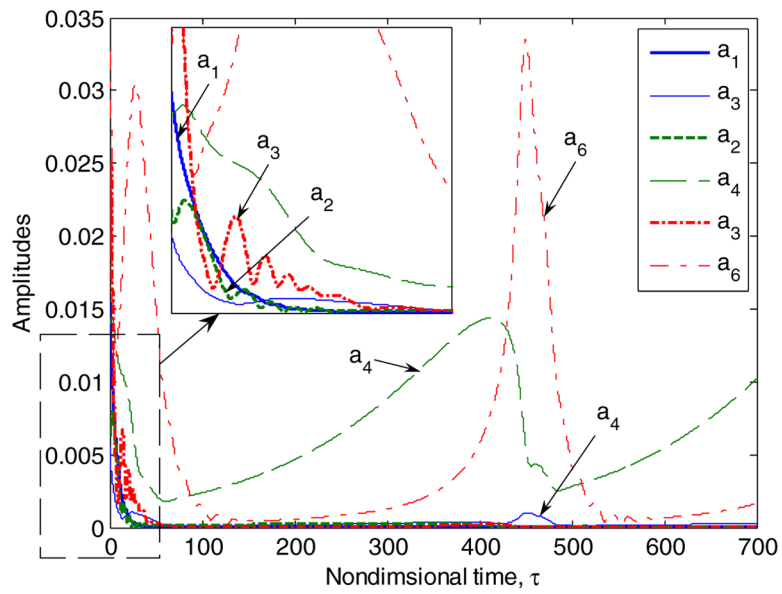
where $\underline{a} \in R^{+6}$ and $\underline{\phi} \in S^6$. The slowly-varying amplitudes a_1 and a_3 (a_2 and a_4 ; a_5 and a_6) are LF and MF slowly varying amplitudes, respectively, of the heave (pitch; NES) mode. The phase angle vector $\underline{\phi}$ in (9.86) possesses the components, $\phi_{12} \equiv b_1 - b_2$ (phase difference between LF heave and LF pitch), $\phi_{34} \equiv b_3 - b_4$ (MF heave – MF pitch), $\phi_{15} \equiv b_1 - b_5$ (LF heave – LF NES), $\phi_{25} \equiv b_2 - b_5$ (LF pitch – LF NES), $\phi_{36} \equiv b_3 - b_6$ (MF heave – MF NES) and $\phi_{46} \equiv b_4 - b_6$ (MF pitch – MF NES). We note that all independent phase interactions occur between same frequency components (LF-LF or MF-MF), and that all other phase interactions can be expressed in terms of the aforementioned six independent phase differences.

Comparisons of the transient responses predicted by the slow flow (9.85–9.86) and the exact responses resulting by direct numerical simulations of system (9.74) are depicted in Figure 9.55a, and demonstrate the validity of the slow flow model. Except for very low-frequency variations in the NES response, the slow flow model shows good overall match with the exact transient dynamics. The discrepancies may be improved if we employ additional fast frequency components in the *ansatz* (9.83–9.84). That is, recalling that the dominant instantaneous normalized frequency in Figure 9.54d is approximately equal to $\omega \approx 0.85$ in the regimes of 1:1 TRCs, we conjecture that single-frequency averaging with respect to that ‘fast’ frequency might be sufficient to capture the important (slow flow) dynamics of the system; nonetheless, special care must be taken when applying single-frequency averaging as the fast frequencies are expected to vary with respect to the flow speed. In fact, some efforts have been made recently to establish sufficiently reasonable slow flow models by utilizing EMD and WTs, showing that multi-frequency averaging is basically equivalent to applying EMD (Kerschen et al., 2006b).

From the evolutions of the amplitude components in Figure 9.55b, we verify that the MF components are the dominant ones in the first LCO suppression mechanism; this result is consistent with the WT results depicted in Figure 9.50a. Moreover, similar resonance captures followed by escapes to the ones depicted in Figures 9.55c, d were observed in the numerical EMD results presented in Figures 9.54b–d. An additional interesting remark regarding the first LCO suppression mechanism is that the resonance captures between the heave and pitch modes (characterized by the phase angles ϕ_{12} and ϕ_{34}) occur ahead of those between the heave mode and the NES (phase angles ϕ_{15} and ϕ_{36}), or those between the pitch mode and the NES (phase angles ϕ_{25} and ϕ_{46}). This implies that *in the first LCO suppression mechanism there occur nonlinear modal energy exchanges between the heave and pitch modes (i.e., the triggering mechanism for the LCO is activated – see Section 9.2)*

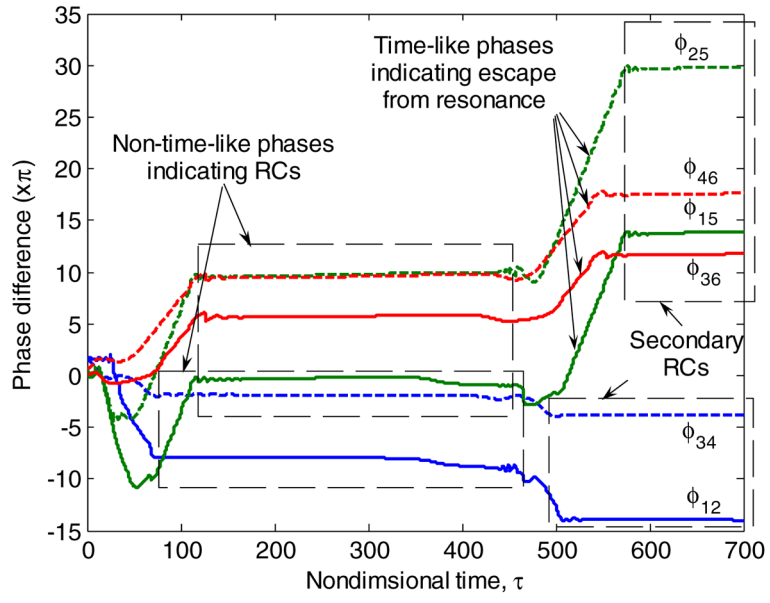


(a)

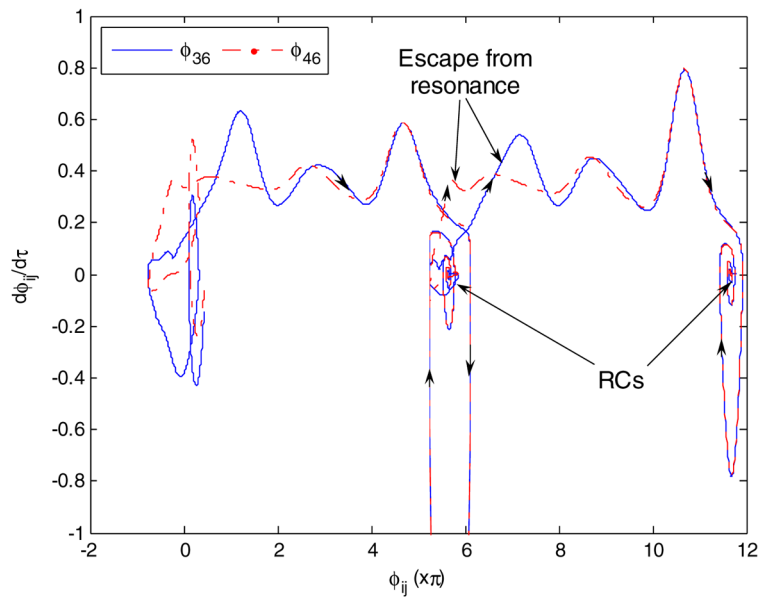


(b)

Fig. 9.55 CX-A analysis of the first LCO suppression mechanism shown in Figure 9.45: (a) comparison of analytical and numerical responses; (b–d) instantaneous amplitudes and phase interactions of the slow flow model (9.86).



(c)



(d)

Fig. 9.55 Continued

before TET from the aeroelastic modes to the NES (with the ensuing instability suppression) occurs; this early occurrence of RCs between the heave and pitch modes ‘activating’ the LCO triggering mechanism makes the repetition of suppressions and burst-outs in the first suppression mechanism possible. Moreover, this suggests that for more efficient (and robust) suppression of LCOs, the NES should interact with the aeroelastic modes before energy transfers between these modes are realized, thus preventing the activation of the triggering mechanism for LCO instability.

The results of Figure 9.56 depicting the phase interactions of the transient responses of Figure 9.47 corresponding to the third LCO suppression mechanism (resulting in complete LCO elimination) support this argument. Note that in this case the energy transfer from the pitch mode to the NES occurs almost simultaneously with the triggering of the pitch from the heave mode, leading to complete elimination of the aeroelastic instability.

9.3.3 Robustness of LCO Suppression

We now investigate the robustness, i.e., the dependence on initial conditions and changes on flow speeds, of the identified aeroelastic instability suppression mechanisms. We will perform this study by means of steady state bifurcation analysis of the dynamics of system (9.74) utilizing the method of numerical continuation of equilibrium and periodic solutions. This bifurcation analysis will examine the possibility of co-existence of stable attractors in the dynamics and will determine the parameter ranges where the dynamics of the system is attracted to steady state solutions that are favorable to the LCO suppression objective. In the process we will explore the effect of offset distance δ on LCO suppression, and confirm the numerical finding that negative offsets generally appear to cause more robust and effective LCO suppression results. From here on, by ‘positive’ or ‘negative’ attachment, we will mean that the NES is connected to the wing ahead or aft of the elastic axis, respectively (that is, closer to the nose or tail of the in-flow wing). *The global bifurcation structure of the dynamics will eventually reveal how the previously discussed three LCO suppression mechanisms are related to bifurcations of steady state solutions.* This study will provide hints for NES designs that result in efficient and robust aeroelastic suppression.

The results depicted in Figure 9.57 indicate that in some cases strong disturbances may eliminate LCO suppression, that is, LCO suppression may be achieved at certain energy levels but not at others. Indeed, as shown in Figure 9.57 by increasing the non-zero initial condition $y'(0)$ by a factor of ten compared to the value used for demonstrating the first LCO suppression mechanism in Figure 9.45, we may completely eliminate this LCO suppression mechanism yielding larger-amplitude LCO compared to the system with no NES attached. Hence, the issue of robustness of LCO suppression is raised with respect to the effects of changes in initial conditions or the flow speed with the other system parameters remaining fixed.

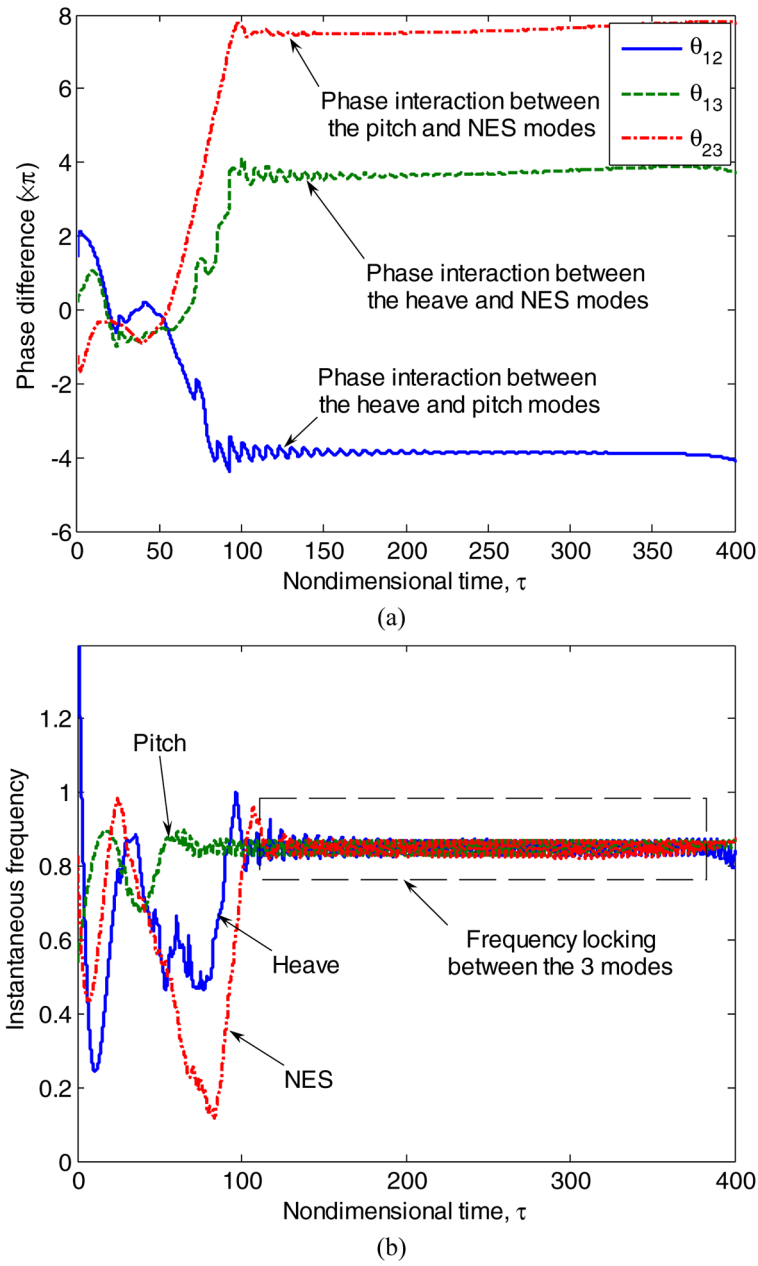


Fig. 9.56 EMD analysis of the third suppression mechanism shown in Figure 9.47: (a) phase interactions $\theta_{ij} \equiv \theta_i - \theta_j$ computed by the Hilbert transform of the dominant IMFs; (b) instantaneous frequencies θ'_i .

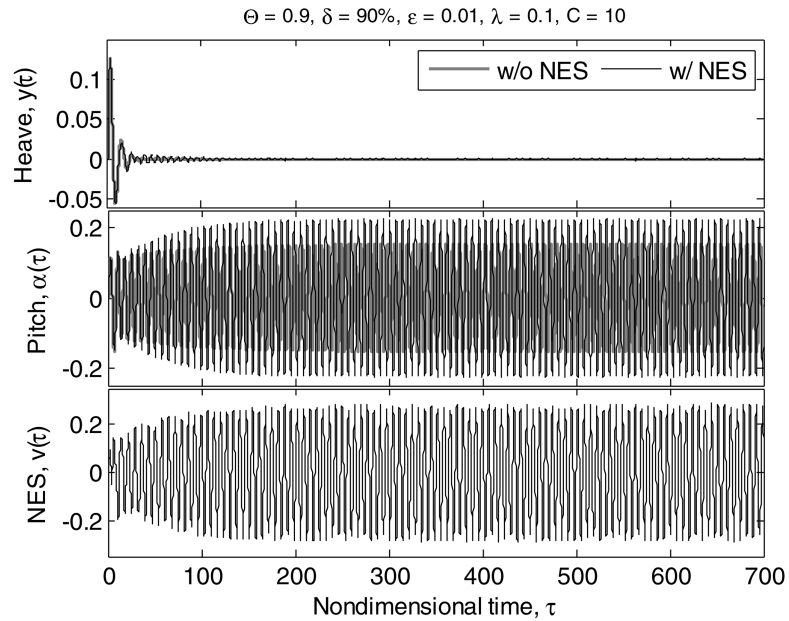


Fig. 9.57 Breakdown of the first suppression mechanism to form a larger amplitude LCO compared to the system with no NES attached; system parameters and initial conditions are identical to those used for the plots of Figure 9.45, except for $y'(0) = 0.1$.

In Figure 9.58 the reduction in the steady state r.m.s. pitch amplitude Δ^α [defined by relation (9.76)] with respect to the set of initial conditions $\{y(0) = 0, \alpha(0) = 0, y'(0) \in [0, 0.1], \alpha'(0) \in [0, 0.1]\}$ and various values of the system parameters is computed. For these computations we performed direct numerical simulations of the normalized equations of motion (9.74). Generally, it appears that the reduction of the steady state pitch amplitude due to the action of the NES does not depend in an essential way on the initial pitching velocity. Moreover, for a fixed flow speed increasing the mass ratio and damping broadens the domain of initial conditions where complete elimination or significant reduction of the amplitudes of LCOs occurs. On the contrary, for fixed mass ratio and damping increasing the flow speed can eliminate or significantly reduce the domain where LCO suppression occurs. It will turn out in the later part of this section that *robustness of LCO suppression with respect to the initial conditions is highly dependent on the global bifurcation structure of the steady state dynamics of the system.*

Robustness of LCO suppression with respect to variations of the flow speed also depends on the global features of the steady state dynamics. Figure 9.59 depicts bifurcation diagrams of peak-to-peak steady state amplitudes of system (9.74) against the reduced flow speed Θ , when the flow speed increases slowly with acceleration rate $\Theta'(\tau) = 10^{-5}$. For fixed mass ratio, damping and nonlinear coupling stiffness, the effects of positive or negative offsets δ are compared in Figures 9.59a, b. For a

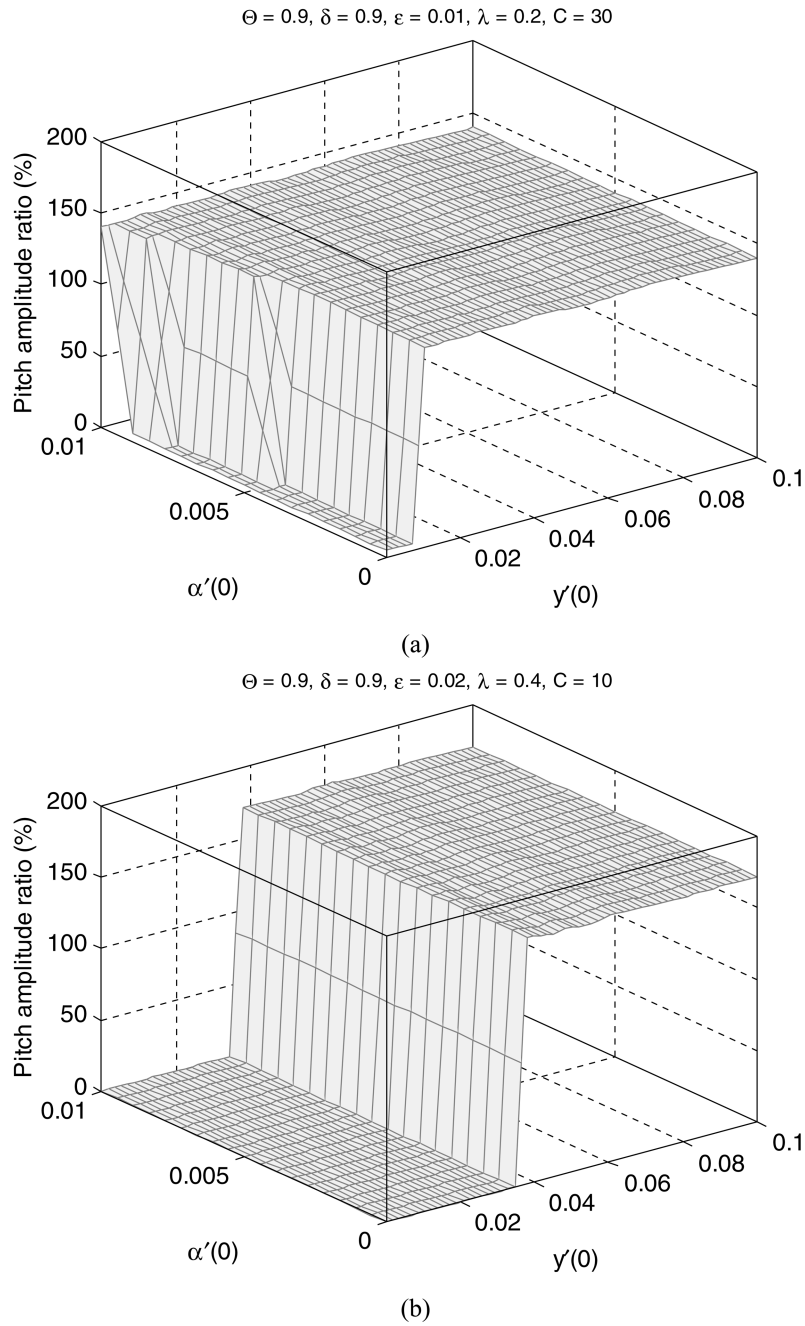


Fig. 9.58 The steady state r.m.s. pitch amplitude ratio Δ^α , with respect to the set of initial conditions $\{y(0) = 0, \alpha(0) = 0, y'(0) \in [0, 0.1], \alpha'(0) \in [0, 0.1]\}$, $\delta = 0.9$ and: (a) $\Theta = 0.9, \varepsilon = 0.01, \lambda = 0.2$, and $C = 30$; (b) $\Theta = 0.9, \varepsilon = 0.02, \lambda = 0.4$, and $C = 10$.

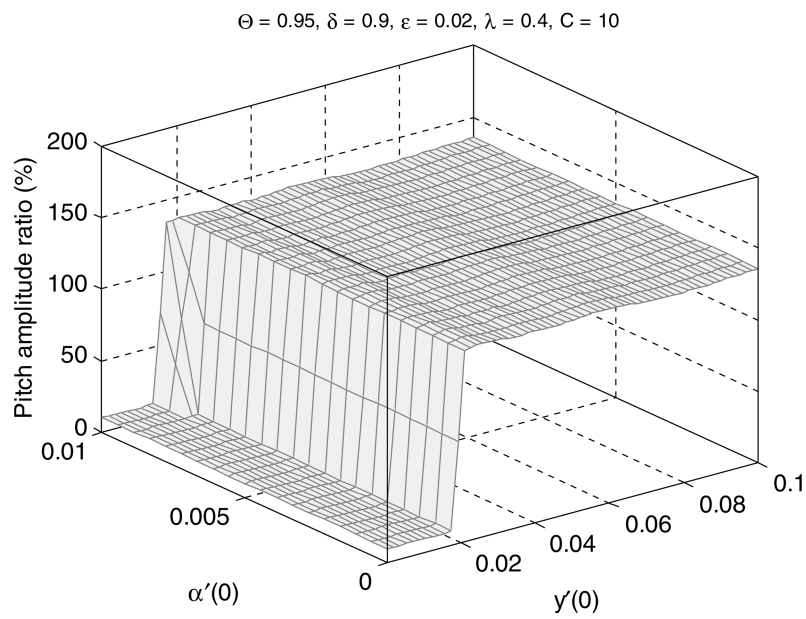
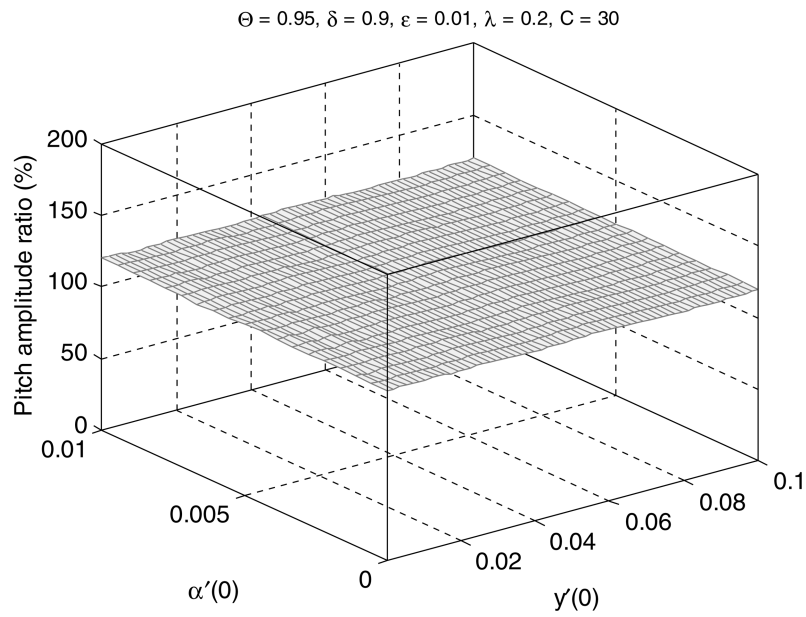


Fig. 9.58 The steady state r.m.s. pitch amplitude ratio Δ^α , with respect to the set of initial conditions $\{y(0) = 0, \alpha(0) = 0, y'(0) \in [0, 0.1], \alpha'(0) \in [0, 0.1]\}$, $\delta = 0.9$ and: (c) $\Theta = 0.95, \varepsilon = 0.01, \lambda = 0.2$, and $C = 30$; (d) $\Theta = 0.95, \varepsilon = 0.02, \lambda = 0.4$, and $C = 10$.

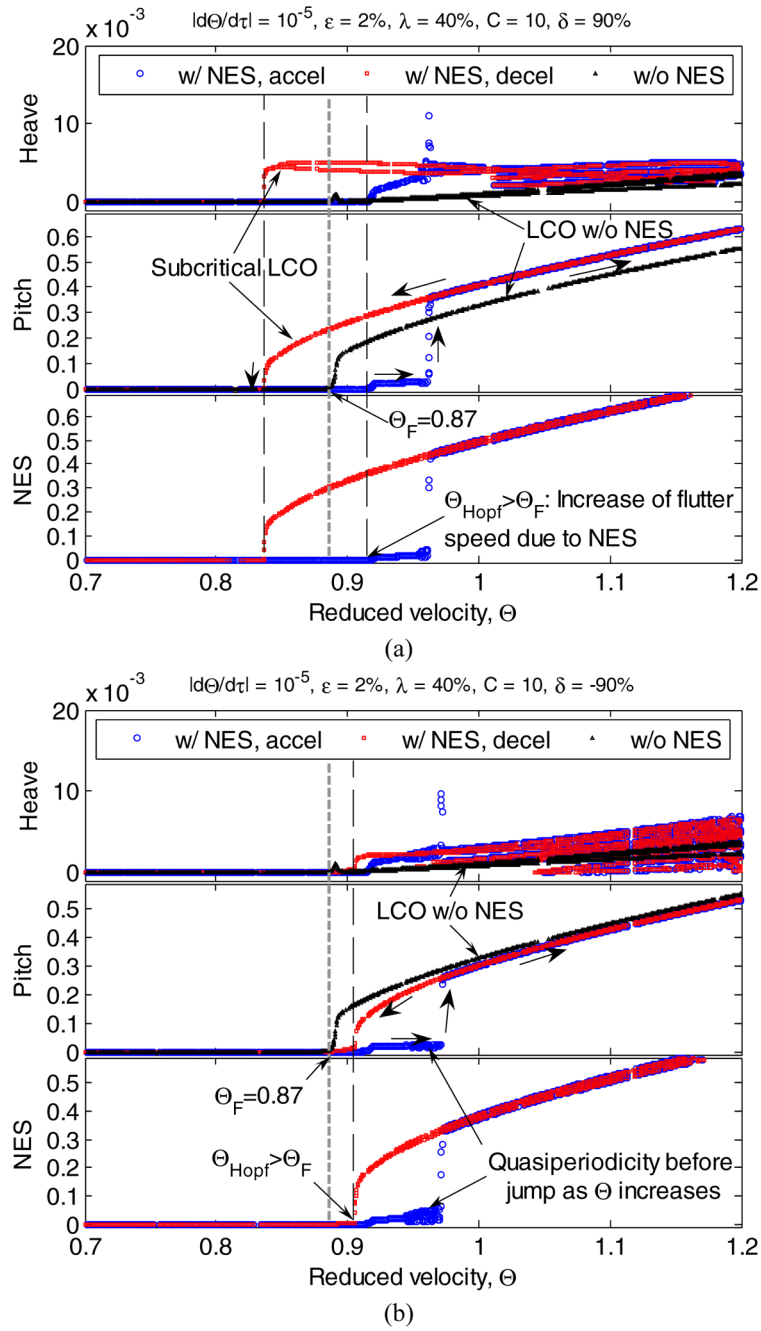


Fig. 9.59 Bifurcation diagrams depicting peak-to-peak steady state amplitudes with respect to the reduced speed Θ , for a slowly accelerating flow, $d\Theta/d\tau = 10^{-5}$ and $\varepsilon = 0.02$, $\lambda = 0.4$, $C = 10$: (a) $\delta = 0.9$ and (b) $\delta = -0.9$.

specific value of reduced flow speed Θ , a single point in a bifurcation plot implies either a stable trivial equilibrium or a stable LCO; and multiple points in a bifurcation plot imply a quasi-periodic orbit or an unstable LCO. Basically, this methodology is analogous to a frequency-sweeping method when performing modal testing of a structure. We note that although system (9.74) is derived under the assumption of fixed reduced flow speed Θ , the bifurcation results for slowly varying Θ are still expected to approximate the true dynamics of the system for $|\Theta'| \ll 1$.

In general, increasing the flow speed Θ delays the occurrence of the Hopf bifurcation that generates the aeroelastic instability (the stable LCOs), for both ‘positive’ and ‘negative’ attachments. An increase of Θ causes a sudden transition of the dynamics to a stable LCO, which implies that there exists a LPC (limit point cycle) bifurcation at the point of transition; the LPC bifurcation is analogous to the saddle-node bifurcation of equilibrium points. We note that for a ‘negative’ attachment ($\delta = -90\%$, Figure 9.59b) quasi-periodicity occurs before the transition. Later, we will verify that this quasi-periodicity is generated through a NS (Neimark–Sacker) bifurcation of a periodic solution which is analogous to the Hopf bifurcation of an equilibrium point. For a ‘positive’ NES attachment ($\delta = 90\%$, Figure 9.59a), the LCOs after the transition from the stable equilibrium possess larger amplitudes compared to the system with no NES attached.

Decreasing the reduced flow speed reveals the clear difference in the steady state dynamics for systems with ‘positive’ and ‘negative’ attachments. In both cases there exist branches of unstable periodic solutions connecting the upper and lower branches of steady state solutions; in addition, jumps to stable equilibrium positions occur, implying that there exist ‘inverse’ LPC bifurcations. Whereas the ‘negative’ attachment induces a transition of the steady state dynamics close to the Hopf bifurcation point (but above the critical flutter speed Θ_F of the system with no NES attached), the ‘positive’ attachment induces a similar transition at a flow speed even less than the flutter speed Θ_F . In the latter case the NES clearly introduces additional instability to the system, since small disturbances may generate large-amplitude LCOs at flow speeds in ranges of Θ where only stable trivial equilibrium points exist in the system with no NES attached.

To perform a further study of robustness of LCO suppression by means of the bifurcation structure of the steady state dynamics of system (9.74) we employ a numerical continuation method based on MATCONT (Dhooge et al., 2003). Figure 9.60 presents bifurcation diagrams depicting the steady state pitch amplitude $|\alpha|$ against damping λ and offset δ , for fixed mass ratios $\varepsilon = 0.01, 0.02$, and fixed reduced flow speed $\Theta = 0.9$ and nonlinear coefficient $C = 10$. The contour plots for Δ^α extracted from Figure 9.44 are incorporated into the bifurcation diagrams to help the visualization of the steady state amplitudes. We note that by the definition of the normalized offset, only the range $-1 \leq \delta \leq 1$ is permissible, although in order to provide a complete picture of the steady state dynamics we allowed values of δ outside this range.

Figure 9.60a depicts the bifurcation structure of steady state dynamics for the smaller mass ratio $\varepsilon = 0.01$; the corresponding bifurcation diagrams for two specific damping values are depicted in Figure 9.61a (these may be regarded as two-

dimensional ‘slices’ for fixed damping of the three-dimensional bifurcation diagram of Figure 9.60a). Note that, due to the required computational complexity of the bifurcation study, the stable large-amplitude LCOs (which are comparable to the corresponding LCOs of the system with no NES attached) are not displayed in these plots. The Hopf bifurcation curves are realized at offsets with absolute values greater than unity, which suggests that we cannot achieve complete elimination of aeroelastic instabilities (the third LCO suppression mechanism) within the ranges of system parameters considered in these diagrams. Moreover, the presence of stable large-amplitude LCOs implies that *it is not possible to achieve robust suppression of LCOs in this case*. However, the first and second LCO suppression mechanisms can be realized in the ‘permissible’ range $-1 \leq \delta \leq 1$, although a disturbance can eliminate LCO suppression and give rise to the stable large-amplitude LCOs and aeroelastic instability. Moreover, weaker damping tends to induce more complicated dynamics (see, for example, the lower plot of Figure 9.61a).

The steady state bifurcation structure for the larger mass ratio $\varepsilon = 0.02$ is presented in Figure 9.60b and two ‘slices’ corresponding to fixed damping values are depicted in Figure 9.61b. As in the case of smaller mass ratio, larger damping values tend to eliminate complicated dynamic behavior. Using these bifurcation diagrams we are in the position to explain the three LCO suppression mechanisms; we will discuss this only for the case of ‘positive’ attachment, since similar arguments hold for ‘negative’ attachments.

Studying the bifurcation diagrams of Figures 9.60b and 9.61b we conclude that for the larger mass ratio and for a certain range of damping the third LCO suppression mechanism (complete elimination of LCOs) can be realized for offsets greater in magnitude than the offsets corresponding to the Hopf bifurcation points but less than unity; moreover, *in this case the complete suppression of the LCO is robust*, since the bifurcation diagrams in this case provide information on the *global dynamics* of system (9.74) (that is, in contrast to the plots of Figures 9.60a and 9.61a they include also the large-amplitude LCOs), so there are no other stable attractors to ‘compete’ with the ones depicted in the bifurcation diagrams. For example, the third LCO mechanism is realized in the intervals $\Lambda 1$ and $\Lambda 2$ in the upper plot of Figure 9.61b for the system with $\varepsilon = 0.02$.

At offset values where the only attractors of the steady state dynamics are quasi-periodic LCOs the second LCO suppression mechanism is realized, which is also robust in this case; this holds, for example in the offset intervals $\Sigma 1$ and $\Sigma 2$ in the lower plot of Figure 9.61b. Noting that the NS bifurcation implies the generation of a new periodic solution (LCO), one can draw the conclusion that quasi-periodic behavior is the norm in the first suppression mechanism, interrupted, however, by instances of periodic motions when the frequency of the new periodic solution is in rational relation to the frequency of the pre-existing periodic orbit. Decreasing damping tends to increase the interval where the first LCO suppression mechanism is realized. For sufficiently large values of damping, one cannot observe the occurrence of the first suppression mechanism due to the strong dissipation effects in the steady state dynamics. Clearly, at offset intervals where stable LCOs exist, either the second LCO mechanism is realized (for low-amplitude LCOs), or no suppression is

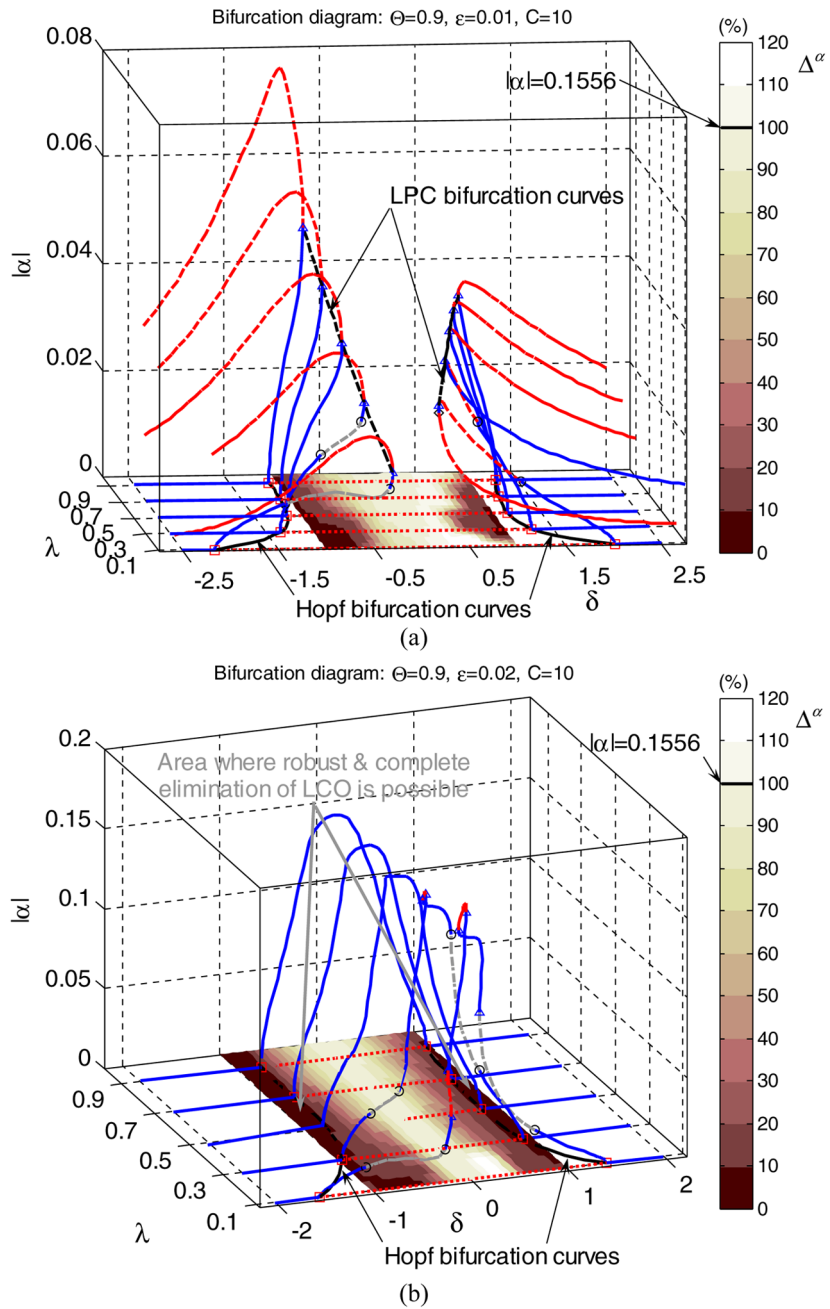


Fig. 9.60 Steady state bifurcation diagrams with respect to δ and λ for $\Theta = 0.9$ and $C = 10$: (a) $\epsilon = 0.01$ and (b) $\epsilon = 0.02$; solid lines indicate stable trivial equilibrium points or LCOs, dotted lines unstable trivial equilibrium points; dashed lines, unstable LCOs; and dash-dotted lines quasi-periodic LCOs; squares indicate Hopf bifurcations, triangles for LPCs, circles for NS (Neimark-Sacker) bifurcations, and diamonds neutral-saddle bifurcations.

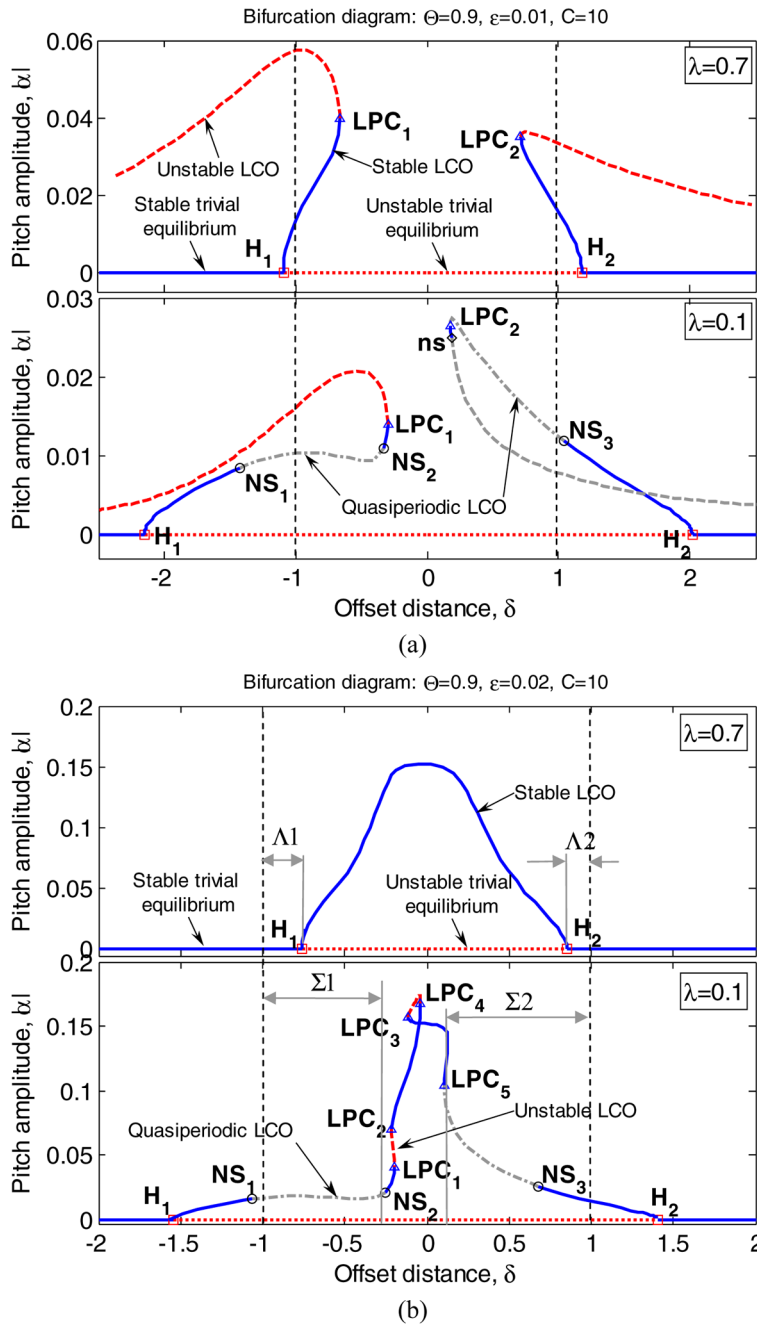


Fig. 9.61 Two-dimensional ‘slices’ of the three-dimensional bifurcation diagrams of Figure 9.60 for fixed damping values λ : (a) $\epsilon = 0.01$ and (b) $\epsilon = 0.02$; the branches of stable large-amplitude LCOs comparable to the LCOs of the system with no NES attached are not depicted; thin dashed lines depict the permissible range of the offset, $-1 \leq \delta \leq 1$.

possible at all (when the amplitudes of LCOs are comparable to the LCOs of the system with no NES attached).

The first LCO suppression mechanism examined in Figure 9.45 is re-examined in Figure 9.62 for the negative offset distance $\delta = -0.9$. One evident result is that more energy transfer from the aeroelastic modes to the NES occurs in this case. Moreover, it appears that a ‘negative’ nonlinear attachment extracts more energy from the heave mode, and the duration of the nonlinear resonant interactions between modes lasts longer than in the case of ‘positive’ attachment.

In a previous section we briefly raised the issue of maximizing the energy dissipation by the NES, which is proportional to $(y' - \delta\alpha' - v')^2$. Examining the responses under condition of 1:1 resonance captures, we can approximate each response roughly as, $y'(\tau) \approx Y \sin \omega\tau$, $\alpha'(\tau) \approx A \sin \omega\tau$ and $v'(\tau) \approx V \cos \omega\tau$, where the amplitudes Y , A and V are assumed to be positive and ω is the frequency where resonance captures occur. Then, we derive the approximation, $y' - \delta\alpha' - v' \approx (Y - \delta A) \sin \omega\tau - V \cos \omega\tau = X \sin(\omega\tau - \theta)$, where $X^2 = (Y - \delta A)^2 + V^2$ and $\theta = \tan^{-1}[V/(Y - \delta A)]$. Clearly, in order to maximize the quantity $(y' - \delta\alpha' - v')^2$, the value of X should be maximum, and negative values of the offset δ provide larger values for X . Although this may not be a mathematically rigorous argument, it helps to get a rough understanding of why negative offsets lead to better and more robust instability suppression compared to positive ones.

Finally, we provide an alternative view of the bifurcation structure of the steady state dynamics of system (9.74) by plotting the steady state pitch amplitude as function of the offset δ and the reduced flow speed Θ ; this is performed in Figure 9.63. Since the qualitative features of the steady state dynamics are similar in the two plots corresponding to positive and negative offsets, we focus only in the case of ‘positive’ attachment ($\delta > 0$). We note that for zero offset the bifurcation behavior is that of the system with no NES attached, as the NES is incapable of affecting the dynamics of the wing. For large reduced flow speeds branch point cycle (BPC) bifurcations of large-amplitude periodic solutions (LCOs) occur (denoted by asterisks in the bifurcation diagrams of Figures 9.63 and 9.64); a BPC bifurcation of a periodic solution is similar to a pitchfork or transcritical bifurcation of an equilibrium point, and leads to exchanges of stability and generation of new branches of large-amplitude LCOs.

For positive offset values $\delta > 0$ the occurrence of the Hopf bifurcation is delayed for an increase of the flow speed; moreover, the intervals where quasi-periodic responses occur (and the first LCO suppression mechanism is realized) widen, as do the intervals between the two LPC bifurcation points. In this case, the BPC bifurcation point converges to the lower-amplitude LPC bifurcation point, and the Hopf bifurcation curves are almost symmetric with respect to the plane $\delta = 0$. Typical two-dimensional ‘slices’ of the three-dimensional bifurcation structure of Figure 9.63 are depicted in Figure 9.64; these results reaffirm the quantitative differences between the dynamics of steady state systems with ‘positive’ and ‘negative’ attachments, discussed in our previous bifurcation study. ‘Positive’ attachments generally lead to LCOs of larger amplitudes compared to those of the system with no NES attached, whereas ‘negative’ attachments yield smaller-amplitude LCOs. In terms of the three

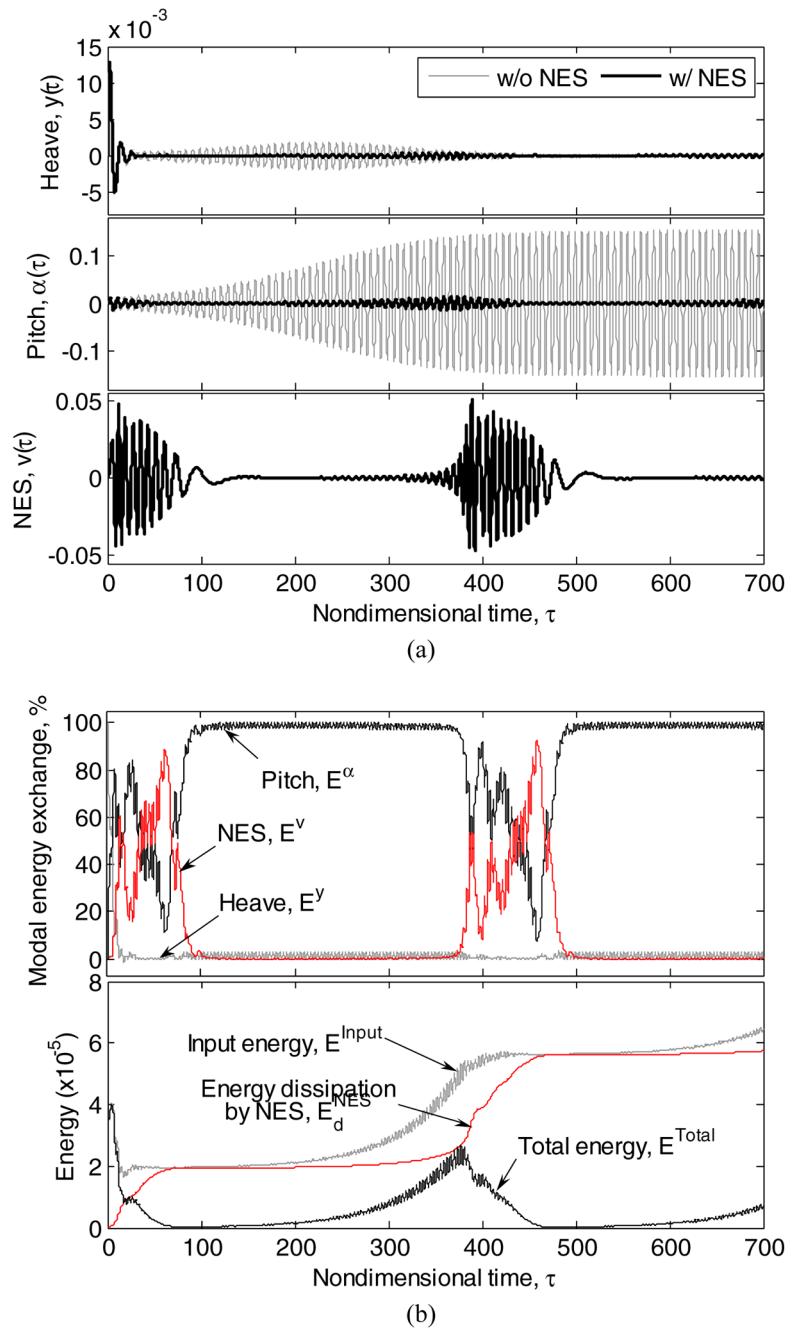


Fig. 9.62 The first LCO suppression mechanism realized in the system with identical parameters to that corresponding to the responses of Figure 9.45, except for the negative offset distance $\delta = -0.9$: (a) transient responses, (b) instantaneous energy exchanges between the NES and the aeroelastic modes.

LCO suppression mechanisms, we observe the transition from the third to the first LCO suppression mechanism when the flow speed increases. Further increase of the flow speed above the bifurcation point LPC1 produces a sudden transition of the dynamics to LCOs with larger amplitudes, and yields increased aeroelastic instability in the system.

Based on our previous discussion we conclude that an in-flow wing-NES system with a bifurcation structure of steady state dynamics similar to that depicted in Figure 9.64b is a configuration suitable for practical applications. Indeed, considering this bifurcation diagram we note that LCOs can be completely and robustly suppressed for reduced flow speeds below the speed Θ_H corresponding to the Hopf bifurcation (i.e., a robust third LCO suppression mechanism is realized). For reduced speeds in the range $\Theta_H < \Theta < \Theta_{NS1}$ robust partial LCO suppression is achieved, as a low-amplitude LCO survives the action of the NES (robust second LCO suppression mechanism). For $\Theta_{NS1} < \Theta < \Theta_{LPC1}$ there is co-existence of the first and second LCO suppression mechanisms, but, of course, neither of these is robust. Which of the two LCO suppression mechanism is eventually realized depends on the initial state of the problem, as the dynamics may be attracted either by the quasi-periodic LCO (non-robust first suppression mechanism) or by the low-amplitude stable LCO (non-robust second suppression mechanism), both of which co-exist in the intervals $\Theta_{NS2} < \Theta < \Theta_{LPC1}$ and $\Theta_{LPC2} < \Theta < \Theta_{BPC}$. Of course, for $\Theta > \Theta_{BPC}$ the case of no LCO suppression becomes possible, and for $\Theta > \Theta_{LPC1}$ LCO suppression is unfeasible as the steady state dynamics is attracted by the large-amplitude LCOs generated after the BPC bifurcation.

9.3.4 Concluding Remarks

In this section we investigated passive suppression of aeroelastic instabilities in a two-DOF in-flow rigid wing system by means of passive, broadband, nonlinear targeted energy transfers. The physical mechanism for inducing these transfers was a lightweight, essentially nonlinear SDOF oscillator attachment which acted as nonlinear energy sink. Through numerical parametric studies we found that there exist three suppression mechanisms for suppressing aeroelastic instabilities in this system.

We investigated these mechanisms both numerically and analytically, and proved that the underlying dynamics were series of resonance captures, i.e., of transient resonances either between the NES and the heave and/or pitch aeroelastic modes, or between the wing modes themselves. We explored these LCO suppression mechanisms in terms of steady state bifurcation analysis, which also addressed the issue of the robustness of suppression, i.e., of the dependence of LCO suppression on the initial conditions and the parameters of the problem. We found that *NESs attached at negative offsets can provide robust aeroelastic instability suppression within relatively wide ranges of system parameters*; on the contrary, NESs at positive offsets do not provide robust suppression, as explained by the associated series of bifur-

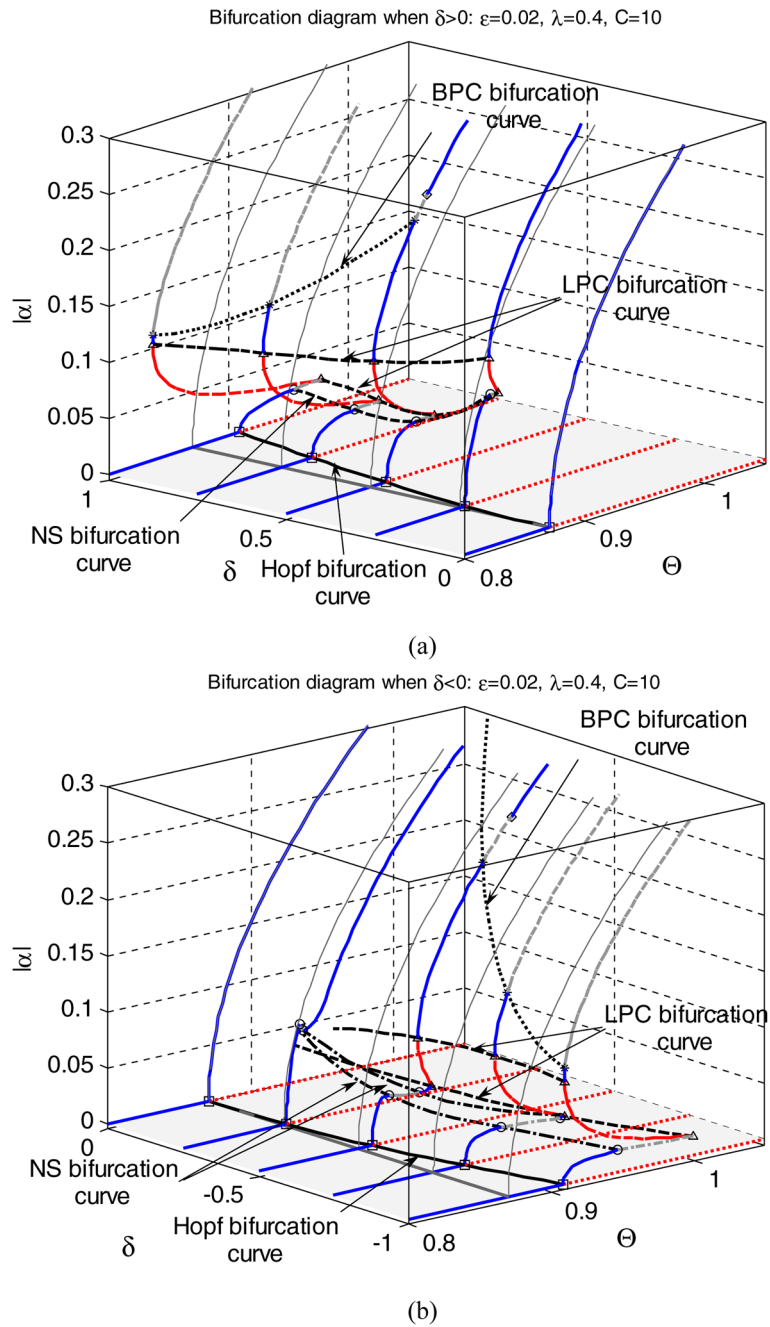


Fig. 9.63 Bifurcation diagrams of steady state dynamics for varying reduced flow speed Θ and offset δ , and $\varepsilon = 0.02$, $\lambda = 0.4$, and $C = 10$: (a) case of positive offset ($\delta > 0$), and (b) case of negative offset ($\delta < 0$); the notation of Figure 9.60 applies, and the asterisk denotes a branch point cycle (BPC) bifurcation.

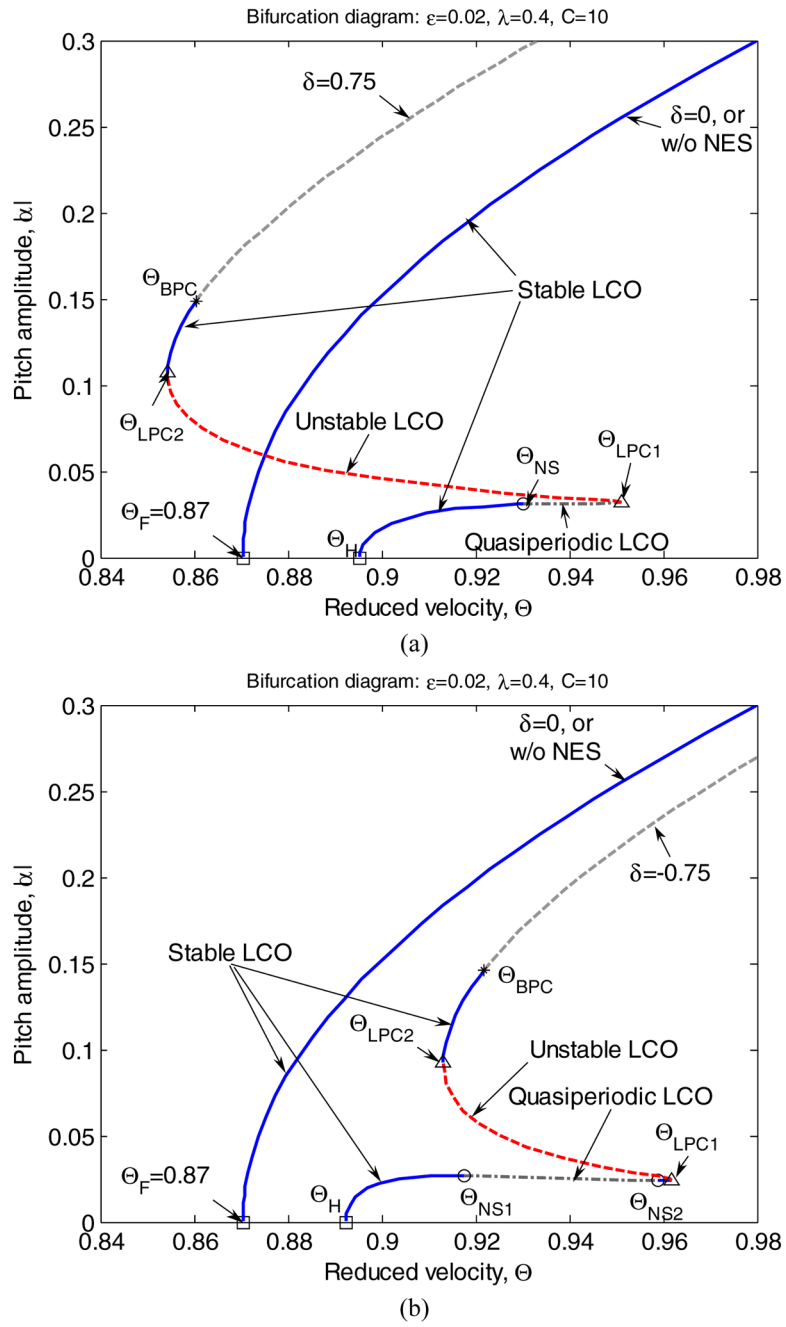


Fig. 9.64 Two-dimensional ‘slices’ of the three-dimensional bifurcation diagrams of Figure 9.63 for fixed offsets δ : (a) $\delta = 0.75$ and (b) $\delta = -0.75$.

cations of steady state dynamics that occur in this case. It follows that lightweight NESs with negative offsets can form the basis of practical, economical, robust and realistic designs for LCO suppression in the in-flow wing under consideration.

In the following section we provide experimental verification of these theoretical findings by presenting results of a series of wind tunnel tests of a practical in-flow wing with an attached SDOF NES. In a later section we discuss the issue of extending robustness of TET-based passive LCO suppression, by investigating the dynamics of wings with more complicated NES configurations, namely MDOF NESs. We show that such configurations improve the robustness of LCO suppression compared to the results presented in this section.

9.4 Experimental Validation of TET-Based, Passive LCO Suppression

In this section we examine experimental validation of LCO suppression using the SDOF NES design discussed previously. The exposition follows the work by Lee et al. (2007b) where more details of the experimental methodology and results can be found. The potentially unstable aeroelastic structure considered herein is a rigid airfoil in a low-speed wind tunnel located at Texas A&M University. This wing was mounted on separately adjustable springs restraining its motion in heave (plunge) and pitch. The apparatus has been used by Strganac and co-workers in several experiments on passive and active aeroelastic control (Block and Strganac, 1998; Ko et al., 1999; Platanitis and Strganac, 2004), in the course of which it has been very thoroughly studied, modeled and dynamically characterized.

In the absence of any corrective measures, this wing has a critical speed of approximately 9.5 m/s. When the flow speed in the wind tunnel exceeds this value, LCOs can readily be induced by a small initial displacement in the heave degree of freedom. A SDOF NES with the configuration examined in the previous section (Configuration II – Section 3.1) was designed to be coupled to the heave mode of the airfoil, with the goal of increasing the critical speed of the combined system above that of the wing without NES attached. The assessment of the LCO suppression capacity of the NES is studied by comparing measured responses of the wing and the integrated wing-NES system configurations to predictions from analysis and simulation in an effort to both quantify the performance improvement due to the action of the NES, and verify our theoretical analysis of the underlying dynamics.

9.4.1 Experimental Apparatus and Procedures

The hardware used in the tests reported below is broadly divisible into (i) the wind tunnel, the model wing, and its supporting structure; (ii) the nonlinear energy sink and its support; and (iii) the equipment used to measure the response of both sub-

structures (Lee et al., 2007b). The nonlinear aeroelastic test apparatus (NATA) at Texas A&M University was developed to experimentally test linear and nonlinear aeroelastic behavior. The device consists of a rigid NACA 0015 wing section capable of movement with two degrees-of-freedom, pitch, and heave, as shown schematically in Figure 9.65a. Stiffness nonlinearity can be introduced to either degree of freedom. The device is mounted in a 0.61×0.91 m low-speed wind tunnel capable of speeds up to 45 m/s.

Each degree of freedom of the NATA wing is supported by its own set of springs. Heave motion, which mimics out-of-plane bending of the wing, is provided by mounting the wing on a carriage which can slide from side to side on shafts mounted under the wind tunnel. The motion of the carriage is restricted by springs stretching from the rigid frame of the wind tunnel to a rotating cam. The carriage is attached to the same cam such that its movement is resisted by the springs, as shown in Figure 9.65b. The wing section stands vertically in the wind tunnel, spanning the entire tunnel from top to bottom, as shown in Figure 9.65c. The wing is attached to a shaft that exits through the tunnel floor and mounts via rotational bearings to the plunge carriage beneath the tunnel. These bearings allow the wing to pitch (rotate), simulating torsion of the wing. Each of the pitch springs has one ends rigidly fixed to the plunge carriage, whereas its other end wraps around a cam on the pitch shaft.

Hence, the set of equations of motion of the NATA may be expressed as follows:

$$\underline{M} \ddot{\underline{x}} + \underline{C} \dot{\underline{x}} + \underline{K} \underline{x} = \underline{F}_c + \underline{F}_a \quad (9.87)$$

where $\underline{x}(t) = [h(t), \alpha(t)]^T$, with $h(t)$ and $\alpha(t)$ being the responses of the heave and pitch modes, respectively; \underline{F}_c the $(2 \ 1)$ vector of Coulomb friction forces, and $\underline{F}_a = [-L, M]^T$ the $(2 \ 1)$ vector of aerodynamic forces and moments (see Figure 9.65a). Moreover, in equation (9.87) \underline{M} , \underline{C} and \underline{K} denote the $(2 \ 2)$ mass, viscous damping and stiffness matrices of the system, respectively. These matrices are expressed in terms of the physical parameters of the NATA (Lee et al., 2007b) which are listed in Table 9.1. We only note here that the only nonlinear structural element in NATA is the torsional stiffness in pitch, which is a nonlinear function of the response $\alpha(t)$ as depicted in Figure 9.66 and listed in Table 9.1.

Experiments using the NATA are conducted at very low speeds and very low reduced frequencies. The wing section spans the entire wind tunnel, so the flow can be considered as being approximately two-dimensional. For this tame flow environment, lift and drag can be modeled with quasi-steady aerodynamics. This type of aerodynamic model has provided very good agreement with NATA experimental results in the past. However, an element that has not been considered in the theoretical analysis of Section 9.3 is dry friction. Friction has a significant effect on the dynamic behavior of the NATA system, so both viscous damping and Coulomb friction are expected to appear in equations (9.87).

For the first proof-of-concept experiments with an NES in an aerodynamic application, the design goals were similar to what would be desired of flight hardware, tempered by the realities of the laboratory environment and the scale of the test program. It was desired to design a lightweight, passive, self-contained, essentially

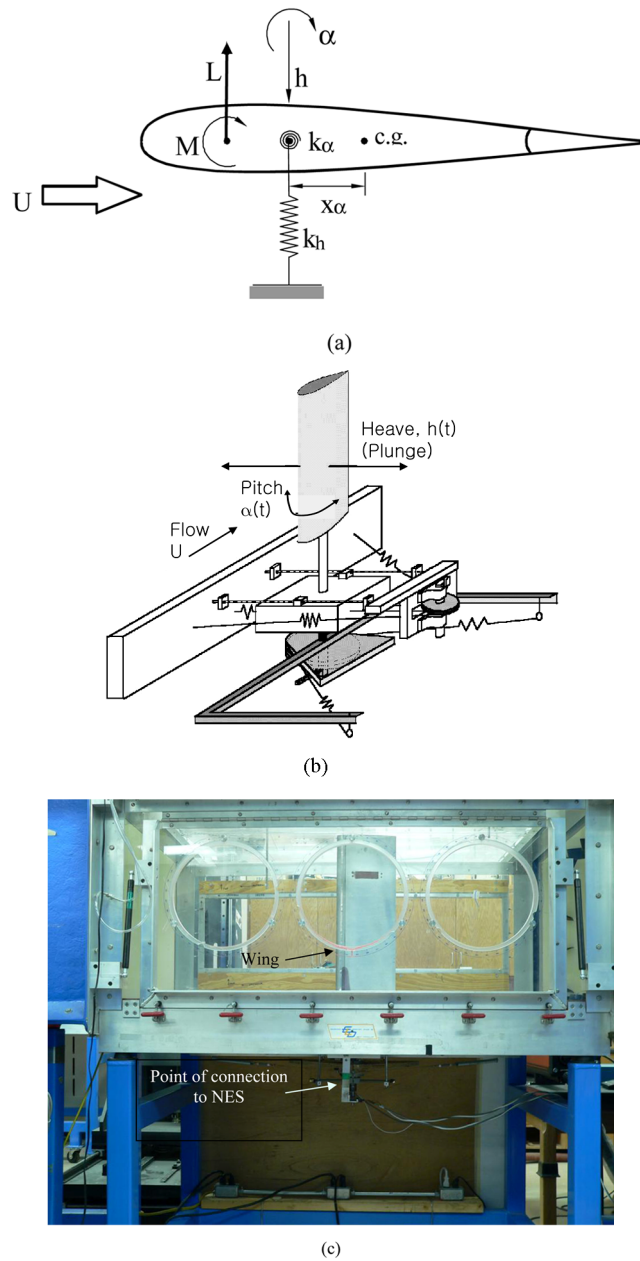


Fig. 9.65 Experimental apparatus: (a) schematic of wing with heave and pitch degrees-of-freedom; (b) schematic of the nonlinear aeroelastic test apparatus (NATA); (c) picture of the NATA, air flow is from left to right, the plunge carriage and pitch cam are visible beneath the tunnel.

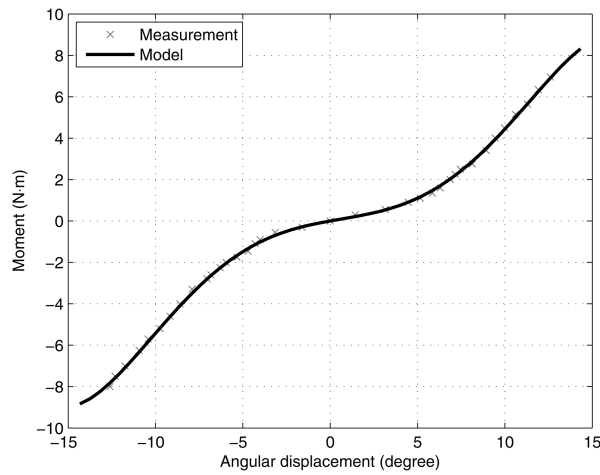


Fig. 9.66 Measured and modeled torsional stiffness in pitch.

Table 9.1 NATA parameter values.

Parameter	Value
Wing mass, m_w	1.645 kg
Pitch cam mass, m_c	0.714 kg
Total plunging mass, m_T	12.1 kg
Total pitching inertia, I_α	$0.04561 + m_w r_{cg}^2$ kg m ²
Wing mass offset, r_{cg}	$-b(1 + 0.18)$ m
Wing section semichord, b	0.1064 m
Non-dimensional elastic axis location, a	-0.4 m
Pitch cam mass offset, r_c	0.127 m
Viscous plunge damping coefficient, c_h	5.0747 kg/s
Viscous pitch damping coefficient, c_α	0.015 kg m ² /s
Plunge spring stiffness, k_h	2537.2 N/m
Pitch spring stiffness, $k_\alpha(\alpha)$	$8.6031 - 27.67\alpha + 867.15\alpha^2$ $+ 376.64\alpha^3 - 7294.6\alpha^4$ Nm/rad
Wing section span, s	0.6 m

nonlinear SDOF attachment of Configuration II (see Section 2.6 – Figure 2.27, and Section 3.1 – Figure 3.2) that would significantly improve the dynamic response of the NATA under typical operating conditions. In the present context, the characterization ‘lightweight’ should be construed as a requirement that the NES mass should be small with respect to the total translational mass of the NATA. When the structure supporting the wing section was taken into account, it was found that the NATA mass equaled approximately $m_I \approx 12$ kg. To make the best use of available hardware, it was convenient to fix the mass of the NES at $m_s \approx 1.2$ kg, corresponding to a mass ratio, in heave, of $m_s/m_I \approx 0.1$. Because of the manner in which the wing is supported in the NATA, it was possible to regard the NES as interacting

directly with only the heave degree of freedom of the wing (i.e., it was assumed that the NES was effectively mounted at the elastic axis of the NATA wing). Indeed, the analysis of Section 9.3 suggests that, in general, it would in be preferable to attach the NES away from the wing's elastic axis, but to achieve this with the NATA would require much more extensive structural modifications so it was not attempted in the experimental work reported herein.

With the mass fixed, preliminary design of the NES was reduced to the specification of the linear viscous damping coefficient c_s and the coefficient k_s of the essentially nonlinear stiffness that couples the NES mass m_s to the NATA plunge displacement $h(t)$. The ranges of values of these two parameters that could be readily produced with an existing NES had been established in earlier experiments on other (non-aerodynamic) NES applications (some of which are discussed in other sections of this work), and data were available relating nonlinear stiffness and coupling efficiency at low structural frequencies. On this basis, preliminary values for the NES stiffness and damping were selected, and then refined through a series of numerical simulations carried out in Matlab[®].

With the addition of the SDOF NES the equations of motion of the integrated wing-NES system are given by

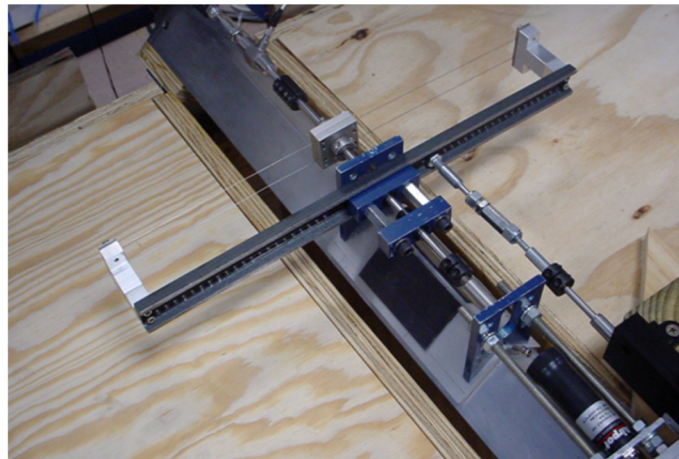
$$\begin{bmatrix} M & 0 \\ 0 & m_s \end{bmatrix} \begin{Bmatrix} \ddot{x} \\ \ddot{v} \end{Bmatrix} + \begin{bmatrix} C & 0 \\ 0 & c_s \end{bmatrix} \begin{Bmatrix} \dot{x} \\ \dot{v} \end{Bmatrix} + \begin{bmatrix} K & 0 \\ 0 & k_s \end{bmatrix} \begin{Bmatrix} x \\ v \end{Bmatrix} = \begin{Bmatrix} F_c \\ 0 \end{Bmatrix} + \begin{Bmatrix} F_a \\ 0 \end{Bmatrix} + \begin{Bmatrix} F_s \\ -f_s \end{Bmatrix} \quad (9.88)$$

where the previously introduced notation holds, $v(t)$ denotes the absolute response of the NES, and $\underline{F}_s = [-f_s \ 0]^T$ the force exerted on the NATA by the NES. This force was experimentally identified as follows:

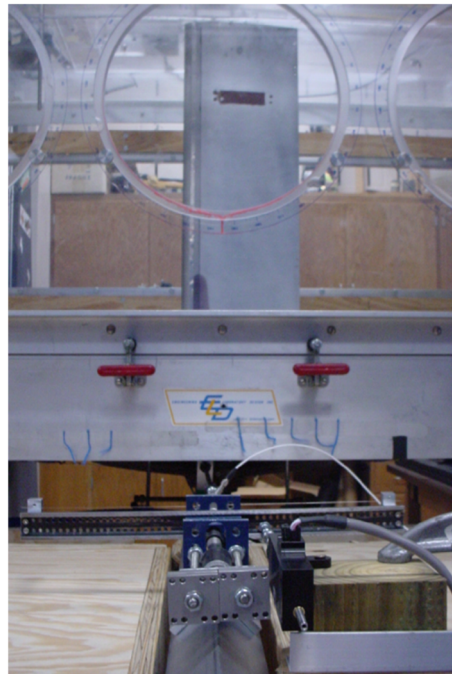
$$f_s = c_s(\dot{v} - \dot{h}) + k_s|v - h|^\gamma \text{sgn}(v - h) \quad (9.89)$$

where the exponent of the essential stiffness nonlinearity was identified as, $\gamma = 2.8 \approx 3$, and is typical of the values experimentally identified for the (theoretically purely cubic) coupling stiffness.

The results of simulations indicated that good NES performance could be achieved over a range of damping values. As shown in Chapter 3, the viscous damping coefficient c_s is not expected to significantly affect the rate and efficiency of TET in the integrated system, and this was confirmed by the fact that the simulations were relatively insensitive to this parameter; so a value of $c_s = 0.40$ Ns/m was chosen, which was typical of damping levels identified in previous experiments. Additional simulations indicated that values of k_s in the range $[1 \times 10^6, 2 \times 10^6]$ N/m^{2.8} led to effective TET, with larger values in this range to be preferred for practical reasons, such as smaller relative displacements during testing. Hence, the value $k_s = 1.6 \times 10^6$ N/m^{2.8} was selected for the preliminary NES design. The aforementioned parameter values for the NES can be considered as nominal NES parameters, since actual values were identified and adjusted accordingly during the experimental testing.



(a)



(b)

Fig. 9.67 NATA-NES configuration: (a) the NES at rest on the air track, with the connecting rod to the NATA visible at the top (wing heave and NES motion are parallel to the track); (b) the NES and air track structure mounted to the windtunnel frame of the NATA (wing heave and NES motion are orthogonal to the picture).

The NES used for the experiments described here consisted of a small ‘car’ made of aluminum angle stock. The car was supported on an air track to reduce sliding friction in the NES system, and was connected to the NATA through the essentially nonlinear spring in parallel to a viscous damper. The nonlinear spring was created by securing a pair of thin wires perpendicular to the relative movement of the NATA and the NES (i.e., to the heave motion of the NATA) as shown in Figure 9.67a. The wires were mounted with no initial tension and hence their spring force had no linear component (see Section 2.6). This arrangement of wires ensured that when the NATA moved with respect to the NES, tension was created in the wires, ideally providing a nearly pure cubic restoring force between the two subsystems. The entire NES assembly was attached to the NATA plunge carriage through a rod. Figure 9.67b shows the NES installed on the NATA in line with the plunge carriage.

Considering the data acquisition system, the pitch and plunge motions of the aeroelastic system were measured with optical angular encoders attached to the cams of the NATA, whereas the NES response was monitored using an accelerometer, and then integrated numerically to obtain velocity and displacement time series as needed. The force developed between the NES and NATA was sensed by a piezoelectric force transducer, and this signal was used only during some of the system identification procedures [for example, for identifying the nonlinear force (9.89)]. Freestream velocity inside the wind tunnel was determined using a Pitot probe and an electronic pressure transducer. All of these signals were sent to a data acquisition board for recording and post-processing.

9.4.2 *Results and Discussion*

The first step in performing experiments with the integrated NATA-NES system was to set the wind tunnel to the desired freestream velocity. Next, the initial conditions were imposed by manually displacing the NATA plunge carriage (and thus the NES) and waiting until equilibrium was established. The system was then released and the responses measured. In all the experiments conducted with the NATA with NES attached, the dynamic behavior of the system was initiated by such a static heave displacement. As a consequence of the kinematics of the NATA, these initial conditions produced no aerodynamic moment on the wing, and when the NES was attached its initial displacement was equal to that of the plunge carriage, h_0 .

Considering the wing without NES attached, when the flow speed in the wind tunnel exceeded the NATA’s flutter speed, approximately 9.5 m/s, an LCO could be reliably induced by releasing the wing from an initial heave displacement h_0 , with all other initial conditions (pitch angle and pitch and heave rates) being zero. Because of the presence of Coulomb friction in the system, very small values of h_0 (up to a few millimeters) could not trigger the wing’s LCO, but for all larger values of h_0 the development of the LCO was very consistent.

The various combinations of flow speed, initial plunge displacement, and NES characteristics tested are summarized as follows: freestream speed $U = 9\text{--}13$ m/s;

initial heave displacement $h(0) = h_0 = 1.27 \times 10^{-2}$ and 1.91×10^{-2} m; NES mass $m_s = 1.2$ and 1.5 kg; NES nonlinear stiffness coefficient $k_s = 1.6 \times 10^6$ and 2.0×10^6 N/m^{2.8}; NES damping $c_s = 0.015$ and 0.040 Ns/m (where the leading values represent baseline values). The mass of the NES was determined by means of a laboratory static balance test, while the stiffness of the essentially nonlinear coupling spring and the associated viscous damping coefficient were identified using the restoring force surface method (Masri and Caughey, 1979). The damping force produced by the motion of the NES car on the air track was by comparison very small, and so has been neglected throughout this work. The ratios of the two NES mass values, (1.2 and 1.5 kg) to the translational mass of the NATA were equal to 10 and 12.5%, respectively. Although these may represent unrealistically large values for flight hardware, they were deemed not to be unreasonable for purposes of validating the theoretical results of Section 9.3 (see also Lee et al., 2007a). The results presented there indicate that TET from the wing to the NES will not be degraded as the NES mass is made smaller.

Time histories of the heave and pitch responses of the various wing-NES configurations at several flow speeds are shown in insets within Figures 9.68–9.70. In each case, the corresponding response of the NATA with no NES attached is shown for reference and comparison. On these are superimposed responses with the NES attached, which experimentally verify the three LCO suppression mechanisms discussed in Section 9.3, namely: (i) recurring LCO burst out and suppression; (ii) intermediate (partial) LCO suppression; and (iii) complete LCO elimination. The steady state amplitudes of the LCOs, if they survive TET to the NES, are plotted in these Figures as discrete points for each flow speed at which tests were conducted (namely, 9, 10, 11, 12, and 13 m/s). When the amplitude of a ‘surviving’ LCO exhibited amplitude modulation (i.e., for the first LCO suppression mechanism), a pair of points has been plotted to indicate the range of the response envelope.

It is clear from these results that, with no NES attached, the NATA does not exhibit aeroelastic instability at a flow speed of 9 m/s. At this speed, the heave and pitch responses following an initial heave displacement of either $h(0) = 1.27 \times 10^{-2}$ m or 1.91×10^{-2} m (with all other initial conditions zero) decay to the original trivial equilibrium position. When the flow speed is increased to $U \geq 10$ m/s or higher, the response of NATA exhibits a highly consistent LCO, with amplitude and frequency depending on the flow speed U . These findings are consistent with the estimate of $U = 9.5$ m/s for the flutter speed of the NATA reported in previous works. The precise flutter speed is of limited interest here, as it is sufficient to show that robust LCOs exist for $U \geq 10$ m/s in the wing with no NES attached.

Concerning the LCO triggering mechanism (see Section 9.2) in the NATA, we noted that there occurred a nonlinear interaction between the two aeroelastic modes (heave and pitch) through a 1:1 resonance capture. Although the experimental dynamics did not involve a stage of superharmonic resonance capture for the particular parameters (i.e., frequency ratio) of the NATA as configured for these tests, it did display a phase-locked frequency shift with time (and thus with increased energy fed into the system from the freestream).

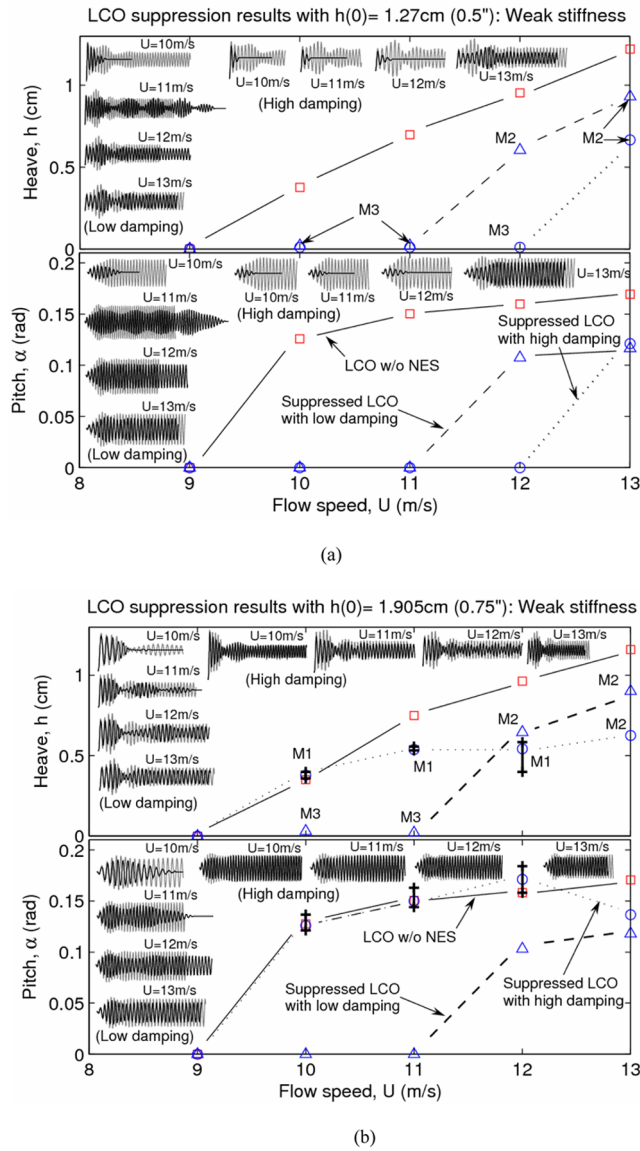


Fig. 9.68 Experimental responses (gray – without NES; black – with NES) obtained for the lighter NES mass ($m_s = 1.2$ kg) and weaker nonlinear coupling stiffness ($k_s = 1.6 \times 10^6$ N/m^{2.8}): (a) initial heave $h(0) = 1.27 \times 10^{-2}$ m; (b) $h(0) = 1.91 \times 10^{-2}$ m; steady state amplitudes are indicated by squares (□) for NATA without NES, triangles (Δ) for NATA and NES with lower damping ($c_s = 0.015$ Ns/m), and circles (○) for NATA and NES with higher damping ($c_s = 0.04$ Ns/m); minimum and maximum values of modulated amplitudes are indicated by bars (‡); M1, M2, and M3 indicate the type suppression mechanism at work.

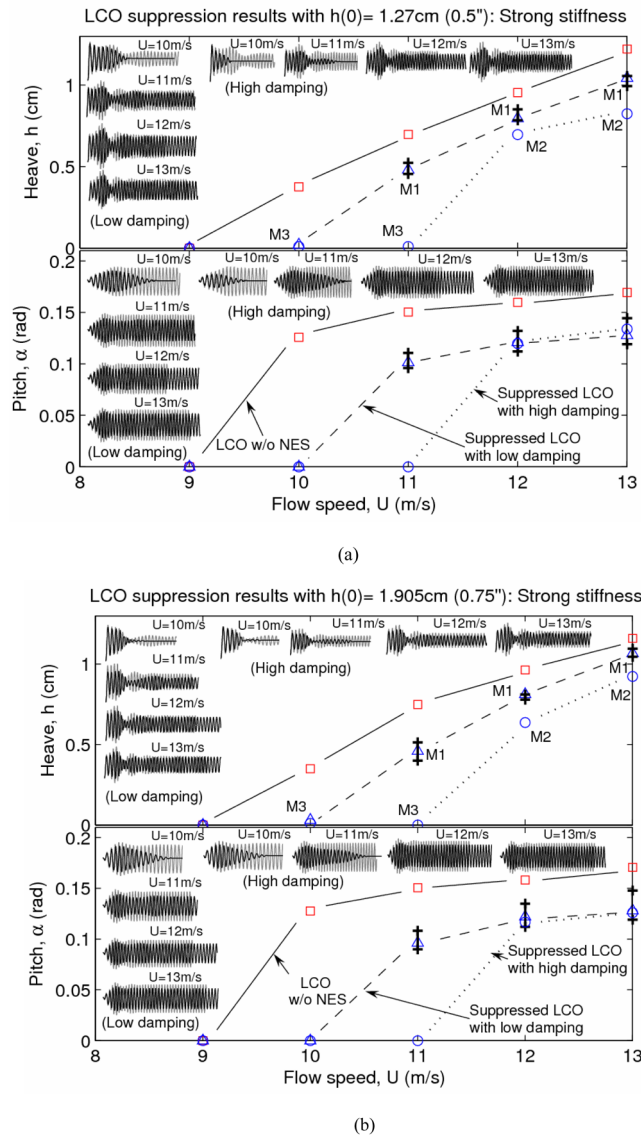


Fig. 9.69 Experimental responses (gray – without NES; black – with NES) obtained for the lighter NES mass ($m_s = 1.2$ kg) and stronger nonlinear coupling stiffness ($k_s = 2.0 \times 10^6$ N/m^{2.8}): (a) initial heave $h(0) = 1.27 \times 10^{-2}$ m; (b) $h(0) = 1.91 \times 10^{-2}$ m; steady state amplitudes are indicated by squares (\square) for NATA without NES, triangles (Δ) for NATA and NES with lower damping ($c_s = 0.015$ Ns/m), and circles (\circ) for NATA and NES with higher damping ($c_s = 0.04$ Ns/m); minimum and maximum values of modulated amplitudes are indicated by bars (\ddagger); M1, M2, and M3 indicate the type suppression mechanism at work.

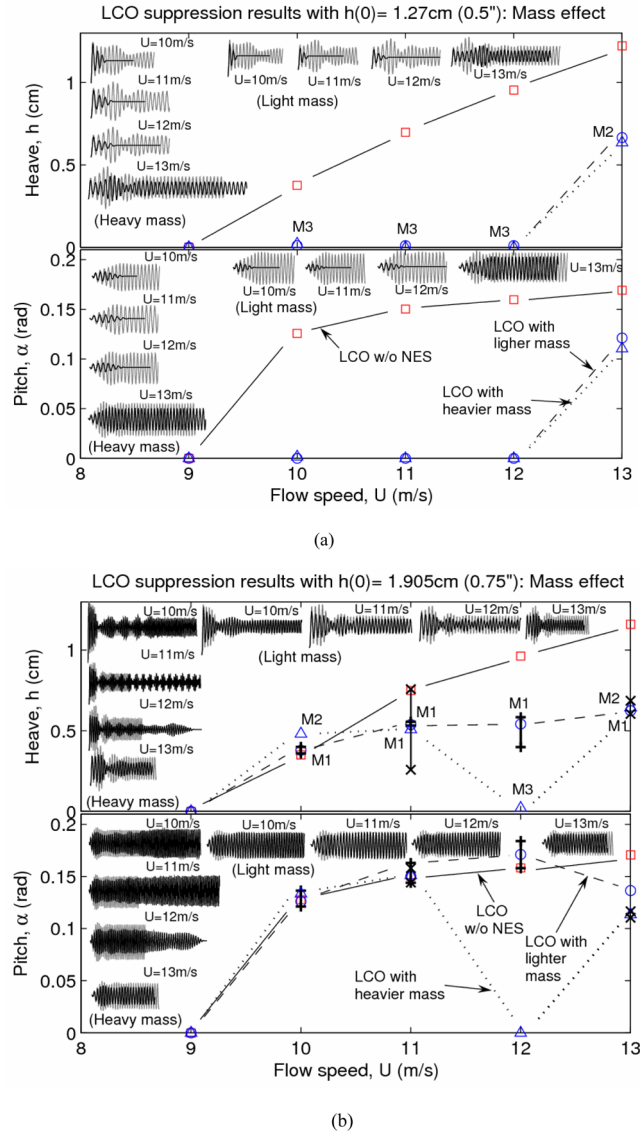


Fig. 9.70 Experimental responses (gray – without NES; black – with NES) obtained for the heavier NES mass ($m_s = 1.5$ kg) and weaker nonlinear coupling stiffness ($k_s = 1.6 \times 10^6$ N/m^{2.8}): (a) initial heave $h(0) = 1.27 \times 10^{-2}$ m; (b) $h(0) = 1.91 \times 10^{-2}$ m; steady state amplitudes are indicated by squares (\square) for NATA without NES, triangles (Δ) for NATA and NES with lower damping ($c_s = 0.015$ Ns/m), and circles (\circ) for NATA and NES with higher damping ($c_s = 0.04$ Ns/m); minimum and maximum values of modulated amplitudes are indicated by bars (\ddagger); M1, M2, and M3 indicate the type suppression mechanism at work.

The dashed lines in Figure 9.68 connect points representing the LCO amplitudes computed for the NATA with of an attached NES with parameters equal to the baseline values mentioned previously. This configuration corresponds to the smaller mass, weaker coupling nonlinear stiffness, and smaller damping coefficient of the values tested for the NES. From the results depicted in that figure, we note significant improvement in flutter speed, from 9 to 11 m/s, irrespective of the initial heave displacement considered. Beyond the flutter speed there is a transition from complete LCO suppression (third suppression mechanism) to partial suppression (i.e., ‘surviving’ LCOs with amplitudes less than those in the NATA with no NES attached – second suppression mechanism). We also note that while the LCO amplitude decays almost exponentially when $U = 10$ m/s, the decay becomes slower and the dynamics more complicated as the limit $U = 11$ m/s of the third suppression mechanism is approached, although complete LCO suppression is still achieved in the process.

The effects of varying the initial conditions or NES parameters on the response of the integrated system NATA-NES system (depicted in the results of Figures 9.68–9.70) are generally in agreement with theoretical predictions, namely, that increasing the NES mass and decreasing its damping or nonlinear stiffness tend to simplify the bifurcation behavior of the steady state dynamics, and thus, enhance the robustness of LCO suppression. However, it is difficult to formulate definitive rules describing these influences because of the high dimensionality of the phase space of the system, and the possible presence of subcritical LCOs, as discussed in Section 9.3 (see also Lee et al., 2007a). Still, based on the results depicted in Figures 9.68–9.70 we arrive at the following conclusions: Stronger nonlinear coupling stiffness k_s reduces the dependence of LCO suppression on the amplitude of the initial displacement; weaker nonlinear coupling stiffness can result in higher flutter speeds (i.e., it extends the range of validity of the third suppression mechanism, yielding complete LCO suppression at higher flow speeds); heavier NES damping usually produces better LCO suppression results, although this may come at the expense of increased sensitivity to initial conditions; and finally, larger NES mass improves its TET performance for the smaller initial heave displacement, but yields more complex dynamics (and generally inferior NES performance) for the larger initial condition. This later remark is consistent with our earlier theoretical finding that ungrounded NESs of the type considered in this application (i.e., Configuration II – see Sections 2.6 and 3.1) display better TET performance for small mass ratios, and suggests that the mass of the NES used in this study was rather large compared to the actual optimum value. Of course, because of the complexity of the bifurcation structure of the steady state dynamics introduced by the NES the afore-mentioned conclusions may not apply under different operating conditions or different NES parameters than those tested in this work.

Apart from the experimental affirmation of enhancement of flutter speed in the wing with NES attached, *a major result of the experimental work is the verification of the three LCO suppression mechanisms* that were theoretically predicted in Section 9.3. Figure 9.71 depicts the experimentally realized first LCO suppression mechanism for $U = 11$ m/s, the NES with heavier mass, weaker nonlinear cou-

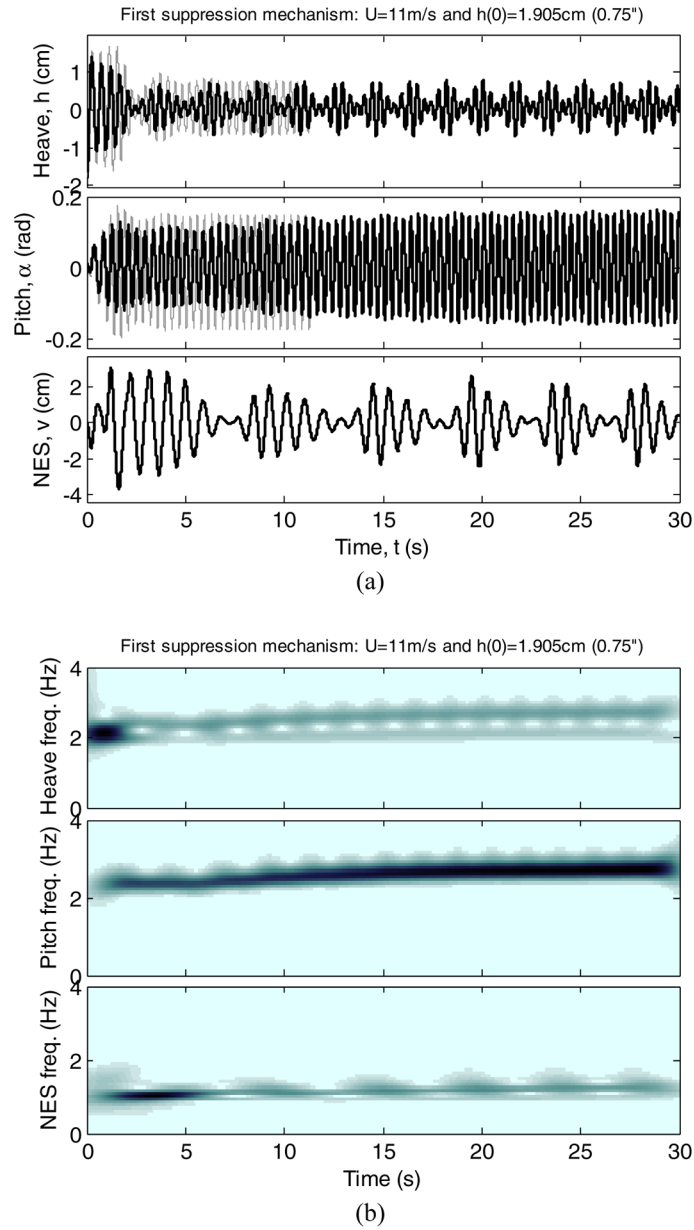


Fig. 9.71 Experimentally realized first LCO suppression mechanism, for flow speed $U = 11$ m/s, NES with heavier mass, weaker nonlinear coupling, heavier damping, and $h(0) = 1.91 \times 10^{-2}$ m: (a) transient responses, and (b) wavelet transform spectra; these results correspond to data points in Figure 9.70b.

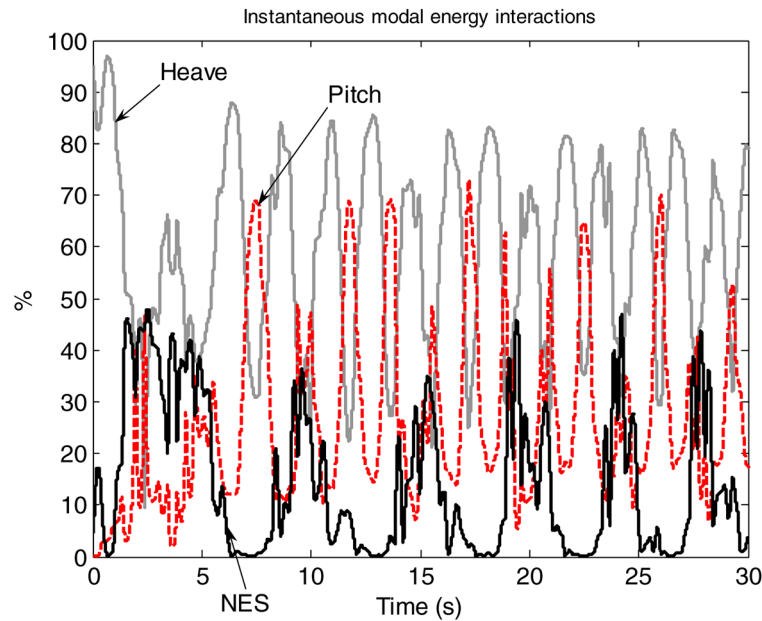


Fig. 9.72 Normalized energy exchanges between the aeroelastic modes and the NES during the first LCO suppression mechanism depicted in Figure 9.71.

pling stiffness and heavier damping, and the larger heave initial condition (these results correspond to the data points in Figure 9.70b). In agreement with theory, both aeroelastic modes and the NES response exhibit nonlinear beating, that is, a recurring bursting out of aeroelastic instability followed by suppression. The frequencies of the aeroelastic modes indicate the occurrence of an initial 1:1 transient resonance capture (TRC) around 2 Hz, and later a sustained resonance capture (SRC) at about 3 Hz. The ratio between the NES frequency and that of the heave mode, and the corresponding ratio between the NES and the pitch mode, are nearly 1:2, which suggests that this suppression mechanism consists primarily of recurring transient subharmonic resonance captures between the NES and the aeroelastic modes, while the two aeroelastic modes remain continuously locked in 1:1 SRC.

The results depicted in Figure 9.72 indicate that strong energy exchanges between the aeroelastic modes and the NES take place in this case. The instantaneous energies shown in that plot were normalized by the total instantaneous energy of the system. Initially, the triggering mechanism for aeroelastic instability is that discussed in Section 9.2 (see also Lee et al., 2005b), that is, energy from the flow is fed directly into the heave mode, which then excites the pitch mode. After the initial development of instability the NES interacts transiently with the heave mode on the onset of the pitch response ($0 < t < 7$ s) thus preventing full development of the LCO. Almost half of the total instantaneous energy of the system is transferred to

the NES within 2 s. Noting that subharmonic resonance capture is generally less efficient than 1:1 resonance capture as far as targeted energy transfer is concerned (see discussion in Sections 3.4.2.1–3.4.2.3), we conjecture that in the responses considered in Figure 9.72 the 1:2 subharmonic resonance captures between the NES and the aeroelastic modes were not sufficient to eliminate the 1:1 internal resonance between these modes (i.e., the triggering of the LCO) and thus prevent the recurrent bursting out of aeroelastic instability.

Figure 9.73 depicts the experimentally realized second LCO suppression mechanism, leading to partial LCO suppression; these simulations correspond to flow velocity $U = 13$ m/s, the NES with lighter mass, weaker nonlinear coupling stiffness and heavier damping, and the smaller initial heave displacement (these results correspond to the data points in Figure 9.68a). After the decay of the initial transients this system exhibits a steady state LCO of reduced amplitude compared to the NATA with no NES attached. Again, there exists strong nonlinear interaction between the heave and pitch modes through 1:1 resonance capture, and the dynamics of the dynamics of the NES undergoes 1:2 subharmonic resonance capture with both aeroelastic modes.

The experimentally realized third LCO suppression mechanism corresponding to complete elimination of the LCO, is shown in Figure 9.74 for a flow speed of $U = 10$ m/s, the NES with smaller mass, stronger nonlinear coupling and higher damping, and the smaller initial heave displacement. This response is characterized by rapid and complete elimination of the aeroelastic instability. From the WT spectrum depicted in Figure 9.74b, it can be seen that while the aeroelastic modes are again in 1:1 TRC and the NES interacts with these modes in 1:2 subharmonic resonance (as in the previous LCO suppression mechanisms), the NES develops an additional 1:1 resonance interaction with the heave mode. This 1:1 TRC is sufficient to eliminate the aeroelastic instability in this case.

Finally, Figure 9.75 depicts another experimental example of complete LCO suppression, i.e., the third LCO suppression mechanism. In this case the flow speed is increased to $U = 11$ m/s, and the coupling stiffness between the wing and the NES is reduced to its smaller value; as a result, complete LCO suppression is achieved, but only after a modulated initial transient response, which superficially resembles the characteristic LCO bursting and suppression of the first suppression mechanism. However, when the frequency contents of the transient responses are examined, it is found that the NES resonantly interacts with both aeroelastic modes, ultimately overcoming the 1:1 TRC between the heave and pitch modes (i.e., eliminating the LCO triggering mechanism) to stabilize the dynamics.

In conclusion, the experiments reported in this section successfully validate the theoretical results of Section 9.3. The experimental results confirm that key to achieving complete LCO suppression by means of passive TET, is the design of the NES to resonantly interact with both aeroelastic modes through 1:1 resonance captures. Moreover, increasing the mass of the NES and decreasing its damping and essentially nonlinear stiffness tend, in general, to simplify the bifurcation structure of the steady state dynamics, and thus, to enhance the robustness of LCO suppression. The presented results show that passive TET from the wing to the NES signif-

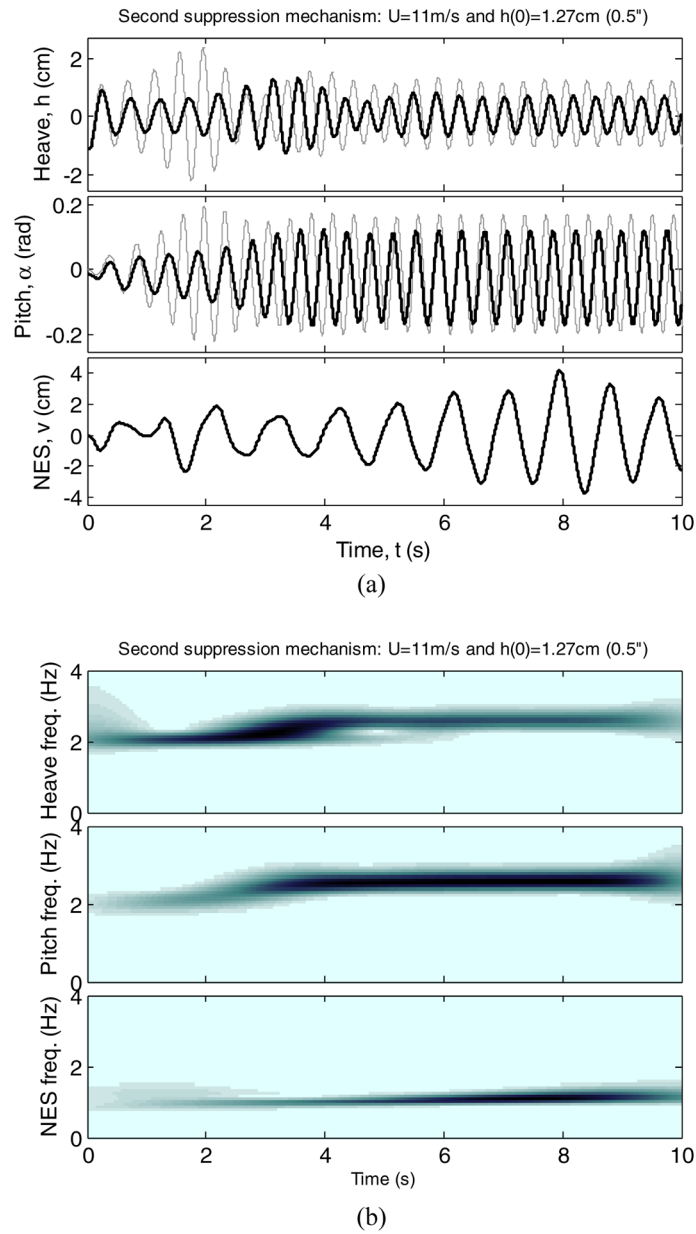


Fig. 9.73 Experimentally realized second LCO suppression mechanism, for flow speed $U = 13$ m/s, NES with lighter mass, weaker nonlinear coupling, heavier damping, and $h(0) = 1.27 \times 10^{-2}$ m: (a) transient responses and (b) wavelet transform spectra; these results correspond to data points in Figure 9.68a.

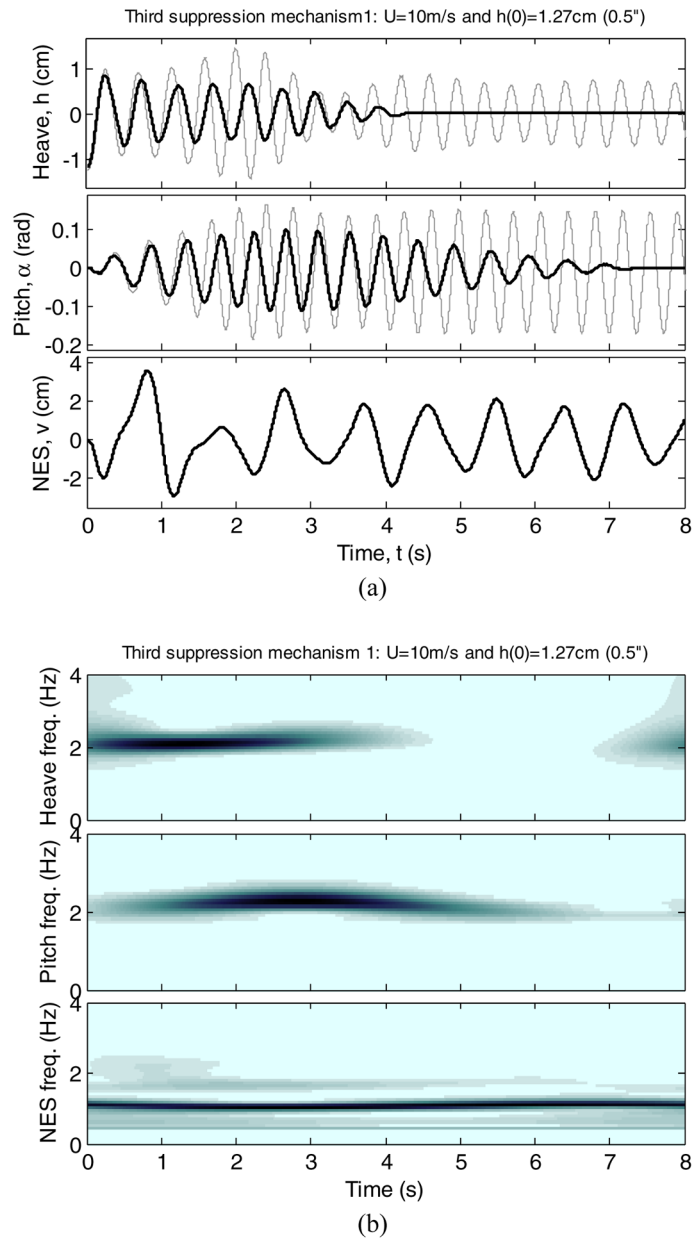


Fig. 9.74 Experimentally realized third LCO suppression mechanism, for flow speed $U = 10$ m/s, NES with lighter mass, stronger nonlinear coupling, weaker damping, and $h(0) = 1.27 \times 10^{-2}$ m: (a) transient responses and (b) wavelet transform spectra; these results correspond to data points in Figure 9.69a.

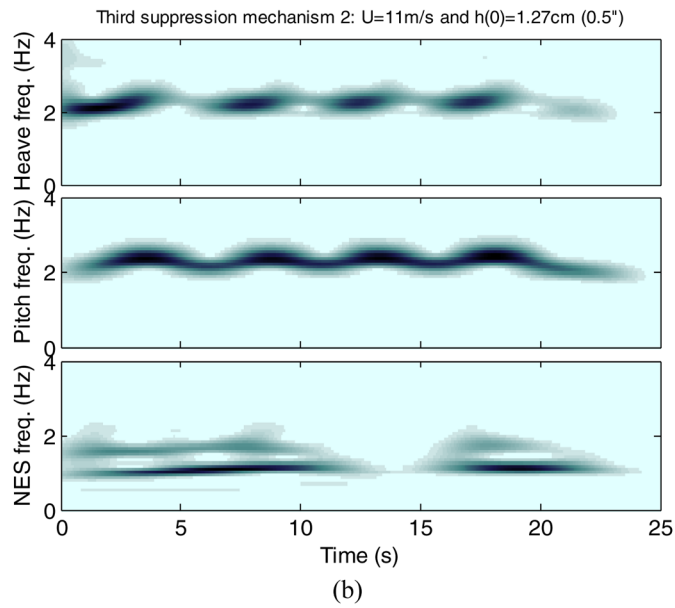
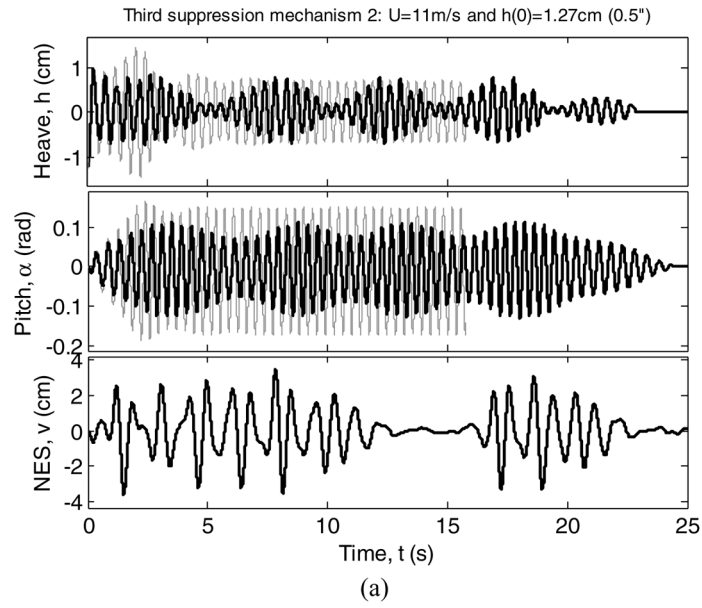


Fig. 9.75 Experimentally realized third LCO suppression mechanism, for flow speed $U = 11$ m/s, NES with lighter mass, weaker nonlinear coupling, weaker damping, and $h(0) = 1.27 \times 10^{-2}$ m: (a) transient responses and (b) wavelet transform spectra; these results correspond to data points in Figure 9.68a.

icantly improves the stability envelope of the NATA wing, preventing the formation of LCOs for flow speeds up to $U = 12$ m/s, compared to the flutter speed of 9.5 m/s of the NATA with no NES attached.

9.5 Suppressing Aeroelastic Instability of an In-Flow Wing Using a MDOF NES

In this section we consider an alternative design for LCO suppression based on the use of MDOF NESs. We show that simultaneous multi-modal broadband TET from the in-flow wing to the nonlinear normal modes (NNMs) of the MDOF NES improves significantly the robustness of passive aeroelastic instability suppression in this case. In particular, numerical bifurcation analysis of the LCOs of the integrated wing-MDOF NES configuration indicates that the action of the MDOF NES can result in more robust LCO suppression, compared to a SDOF NES of equal total mass. Moreover, compared to the SDOF case, LCO suppression is achieved for lower total mass of the MDOF NES, which from a practical point of view represents an added benefit of the proposed MDOF NES design. In this section we investigate also the nonlinear modal interactions that occur between the aeroelastic modes and the MDOF NES, in an effort to gain a physical understanding of the mechanisms governing aeroelastic instability suppression in this complicated MDOF strongly nonlinear system.

Since the issue of robustness of LCO suppression is the main focus of the discussion of this section, we start by revisiting the SDOF NES design of Section 9.3 in order to explore in greater detail its limitations regarding robustness of LCO elimination. This task will be performed by examining the dependence of the bifurcation structure of steady state dynamics on variations of NES parameters, and by relating certain topological features of LCO bifurcations to robustness of instability suppression. Following this preliminary discussion we will be in the position to better assess the benefits in robustness gained by the proposed alternative MDOF NES design.

9.5.1 *Revisiting the SDOF NES Design*

We start by revisiting the SDOF NES aeroelastic suppression design discussed in Section 9.3, and refer to the normalized governing equations of motion (9.74). We recall that the computational study carried out in that section revealed the existence of (at least) three passive LCO suppression mechanisms, resulting in recurring LCO bursting out followed by suppression (mechanism 1), partial LCO suppression (mechanism 2), or complete LCO elimination (mechanism 3). Robustness of LCO suppression can be studied according to whether the three aforementioned TET-based suppression mechanisms can be sustained in the presence of disturbances in parameters and/or initial conditions. In Figure 9.58 we provided a numerical robust-

ness study by considering the effects on LCO suppression of variations in initial conditions for a system with positive NES offset ($\delta = 0.9$). In Figure 9.76 we depict the results of a similar study for a SDOF NES with negative offset ($\delta = -0.9$), from which we deduce that for the same mass ratio ε , complete elimination of aeroelastic instability can be achieved for a wider set of initial conditions compared to the case of positive offset. Indeed, as Figure 9.76b indicates complete LCO elimination may be possible over the entire domain of initial conditions considered in the present study.

As discussed in Section 9.3.3, the problem of robustness of LCO suppression is closely linked to the bifurcation structure of the steady state nonlinear dynamics of the integrated wing-NES configuration. To remind ourselves of the results reported in Section 9.3.3, in Figure 9.77 we provide an example demonstrating the link between robustness of LCO suppression and bifurcations of steady state dynamics. In particular, in Figure 9.77a we depict the bifurcation diagrams of systems with positive and negative offsets, utilizing the reduced flow speed Θ as bifurcation parameter. These diagrams illustrate clearly the NES configurations that lead to more robust suppression of instability. For example, we note that an NES with either positive or negative offset causes a delay of the occurrence of LCOs by shifting the Hopf bifurcation point Θ_H (indicated by squares in Figure 9.77a) to higher reduced speeds. This, however, in itself does not necessarily imply enhancement of robustness of LCO suppression for both NES configurations. Indeed, considering the system with positive offset, the LPC bifurcation point close to pitch amplitude 0.1 (indicated by a triangle in Figure 9.77a) occurs before the Hopf bifurcation, $\Theta_{LPC2} < \Theta_H$. It follows that for reduced speeds in the range $\Theta_{LPC2} < \Theta < \Theta_{BPC} < \Theta_H$ the stable trivial equilibrium coexists with a stable large-amplitude LCO, thus preventing robust LCO suppression; whereas, in the range $\Theta_{BPC} < \Theta < \Theta_H$ the LCO suppression is robust since the trivial equilibrium is the only stable attractor of the dynamics. On the contrary, for the system with negative offset it is possible to achieve robust and complete LCO suppression in the range $\Theta < \Theta_H$, as the stable trivial equilibrium is a global attractor of the dynamics in this range; in addition, in the range $\Theta_H < \Theta < \Theta_{LPC2}$ partial LCO suppression is robust as well, as there exists global attraction of the dynamics by a stable, low-amplitude LCO.

In Figure 9.77b we demonstrate non-robustness and destruction of the first LCO suppression mechanism for the system with negative offset and reduced speed $\Theta = 0.95$, by applying an impulsive disturbance to the heave mode. This result can be understood by considering the respective ‘slice’ of the bifurcation diagram of Figure 9.77a corresponding to $\Theta = 0.95$. We deduce that the quasi-periodic LCO (which is responsible for the repeated LCO burst-outs and suppressions before the external disturbance is applied) coexists with an unstable low-amplitude LCO and a stable large-amplitude LCO resulting from a branch point cycle bifurcation (i.e., for $\Theta > \Theta_{BPC}$). It follows that by applying disturbances to the initial conditions it is possible to drive the dynamics out of the domain of attraction of the quasi-periodic LCO (i.e., to eliminate the first suppression mechanism), and into the domain of attraction of the stable large-amplitude LCO. This yields the reappearance of strong aeroelastic instability in the system, in spite of the action of the NES.

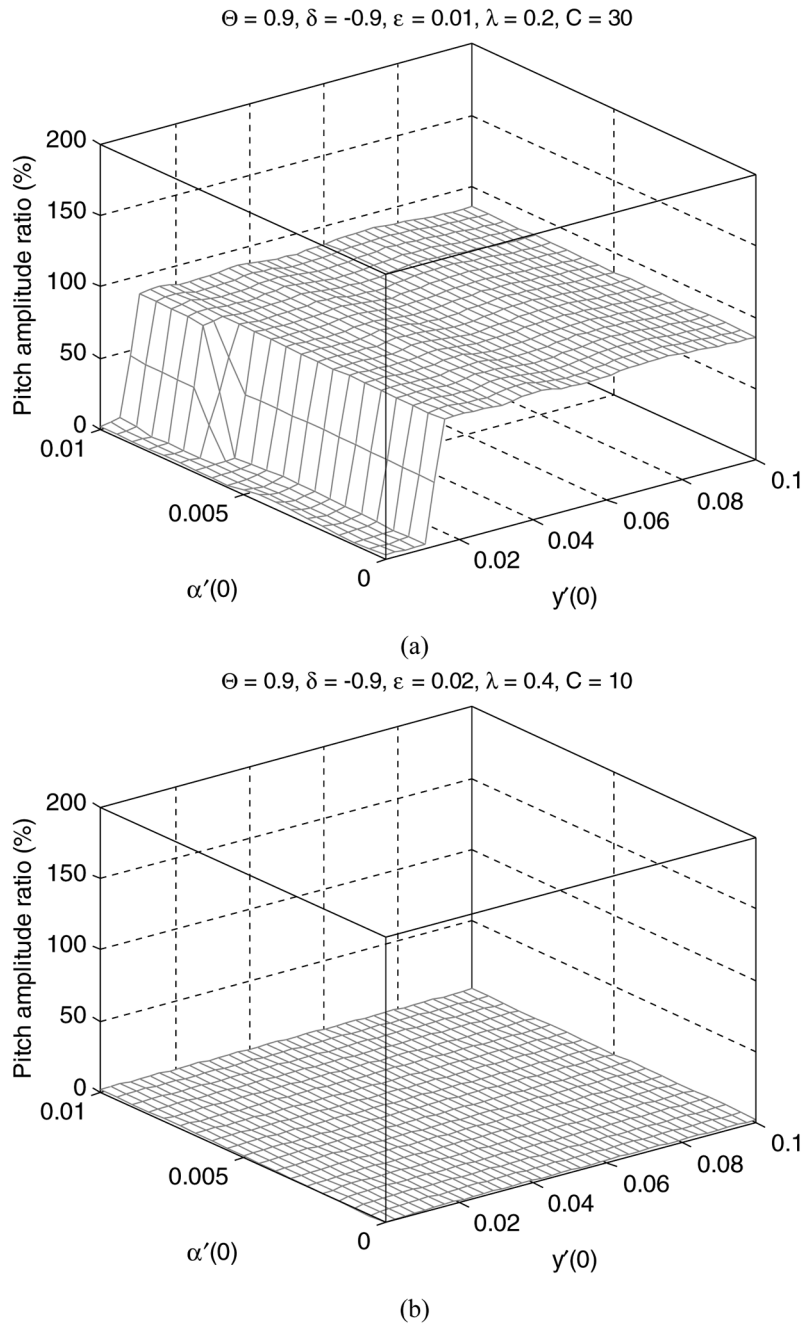


Fig. 9.76 SDOF NES design, steady-state r.m.s. pitch amplitude ratio Δ^α , with respect to the set of initial conditions $\{y(0) = 0, \alpha(0) = 0, y'(0) \in [0, 0.1], \alpha' \in [0, 0.1]\}$, $\delta = -0.9$ and $\Theta = 0.9$: (a) $\varepsilon = 0.01$, $\lambda = 0.2$, and $C = 30$; (b) $\varepsilon = 0.02$, $\lambda = 0.4$, and $C = 1$.

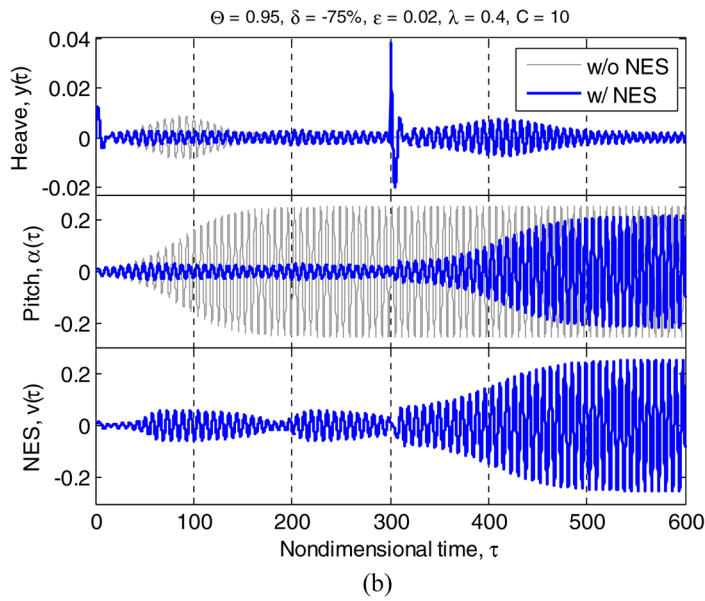
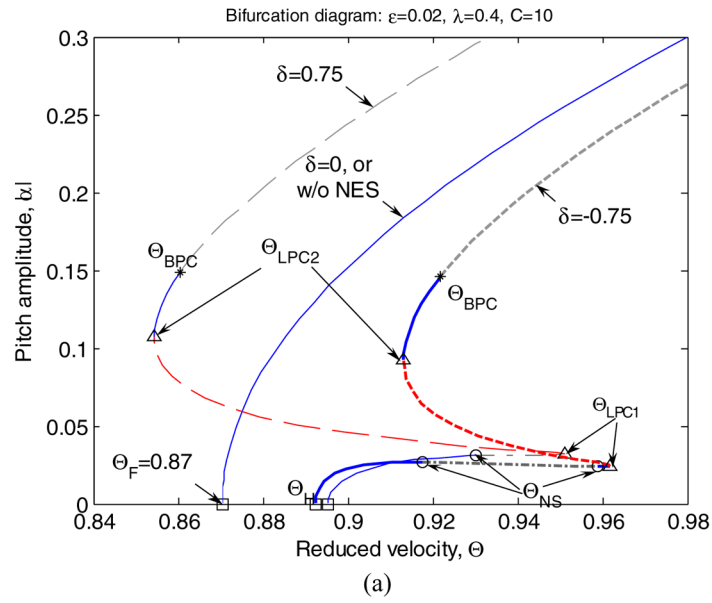


Fig. 9.77 SDOF NES design, robustness study for $\varepsilon = 0.02, \lambda = 0.4, C = 10.0$: (a) (incomplete) bifurcation diagrams for systems with offsets $\delta = \pm 0.75$, solid (dashed, dash-dotted) lines indicate stable (unstable, quasi-periodic) LCOs, and squares (circles, triangles, asterisks) indicate Hopf (Neimark–Sacker, LPC, BPC) bifurcation points; (b) effect of an impulsive disturbance on the heave mode applied at $\tau = 300$ for the system with $\Theta = 0.95$ and $\delta = -0.75$.

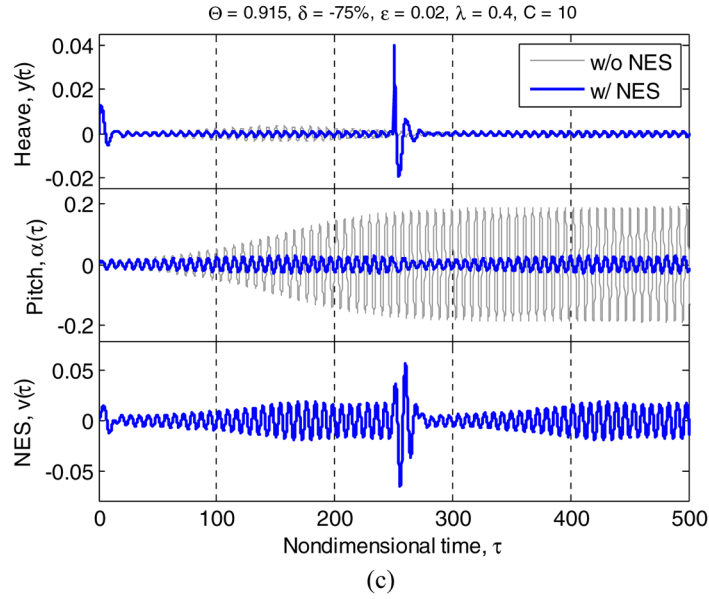


Fig. 9.77 SDOF NES design, robustness study for $\varepsilon = 0.02$, $\lambda = 0.4$, $C = 10.0$: (c) effect of an impulsive disturbance on the heave mode applied at $\tau = 250$ for the system with $\Theta = 0.915$ and $\delta = -0.75$.

A different scenario is provided in Figure 9.77c, where robustness of the second LCO suppression mechanism is demonstrated for the system with negative offset and reduced speed $\Theta = 0.915$. In this case we note that after the application of the impulsive external disturbance to the heave mode the system returns to its prior state, i.e., to a small-amplitude LCO. Again, this result may be interpreted by examining the ‘slice’ $\Theta = 0.915$ of the corresponding bifurcation diagram of Figure 9.77a. Indeed, we note that for that value of the reduced speed the stable LCO generated after the Hopf bifurcation is the only attractor of the dynamics, as it only co-exists with the unstable trivial equilibrium. It follows that the small-amplitude LCO is the only possible stable steady state solution of the dynamics for that particular reduced flow speed.

These results demonstrate that the bifurcation structure of LCOs (and the corresponding nonlinear resonant interactions between the aeroelastic modes and the NES) affects the robustness of instability suppression in the system with the SDOF NES. We recall from Section 9.3.3 that a Hopf bifurcation point signifies the generation of stable LCOs from the trivial equilibrium point. Since in the wing with no NES attached a Hopf bifurcation signifies the generation of aeroelastic instability, it follows that by comparing the relative placement of this point with respect to the corresponding point of the system with NES attached we can obtain a first quantitative measure of the stabilizing effect on the dynamics of the action of the

NES. On the other hand the LPC bifurcation occurring at $\Theta = \Theta_{\text{LPC1}}$ represents the critical point above which no LCO suppression is possible by the action of the SDOF NES. As mentioned in the previous example, the location of the other LPC bifurcation point $\Theta = \Theta_{\text{LPC2}}$ relative to the Hopf bifurcation point $\Theta = \Theta_H$ affects the robustness of instability suppression in the system with SDOF NES attached. Being interested in the location of this LPC bifurcation point relative to the Hopf bifurcation point, in the following exposition we extend the bifurcation analysis of Section 9.3.3 to three-dimensional parameter spaces.

On the other hand, a NS bifurcation point generates quasi-periodicity in the dynamics, and is responsible for the recurrent burst-outs and suppressions of aeroelastic instability (i.e., for the first LCO mechanism). In general, a NS bifurcation occurs between a Hopf bifurcation and the higher-speed LPC bifurcation at $\Theta = \Theta_{\text{LPC1}}$. Finally, the BPC bifurcation (which is a codimension-2 bifurcation of an LCO) generally occurs at higher fluid velocities than the first LPC bifurcation at $\Theta = \Theta_{\text{LPC2}}$ and introduces a destabilizing effect in the dynamics, as it gives rise to stable, large-amplitude LCOs. Again, in the following analysis we will be interested in the variations of all these bifurcation points as the parameters of the SDOF NES vary.

In Figures 9.78a–c we present bifurcation sets of steady state dynamics of the inflow wing with a SDOF NES attached in the three-dimensional parameter spaces $(\varepsilon, \delta, \Theta)$, $(\lambda, \delta, \Theta)$ and (C, δ, Θ) , respectively. These bifurcation diagrams can be understood in the following way. We recall that in the bifurcation diagram of Figure 9.77a, the NES parameters were fixed to the values $\varepsilon = 0.02$, $\lambda = 0.4$ and $C = 10.0$. Considering the two-dimensional ‘slice’ $\varepsilon = 0.02$ of the three-dimensional bifurcation structure of Figure 9.78a, we obtain the bifurcation diagrams of Figure 9.79, where three curves can be identified resulting from the intersection of the plane of constant mass ratio ε with the three two-dimensional surfaces corresponding to the Hopf and the two LPC bifurcations. If we are interested in studying the bifurcation structure of the dynamics when the SDOF NES is attached at offsets $\delta = \pm 0.75$, additional two-dimensional ‘slices’ (planes) corresponding to constant offsets should be imposed, as depicted in Figures 9.79a and 9.79b, respectively.

Once these two planes (‘slices’) are constructed in the three-dimensional bifurcation diagrams, we can add vertical axes (depicted with solid lines in Figures 9.79a, b) starting at the Hopf bifurcation points $\Theta = \Theta_H$ and being orthogonal to the plane $\varepsilon = 0.02$; on these axes we may represent steady state LCO amplitudes, in which case the bifurcation diagram of Figure 9.77a can be drawn for $\delta = \pm 0.75$. Moreover, the two dashed vertical lines passing through $\Theta = \Theta_{\text{LPC1}}$ and $\Theta = \Theta_{\text{LPC2}}$ in Figures 9.79a, b correspond to points $A_{1,2}$ and $B_{1,2}$, respectively. Points $A_{1,2}$ ($B_{1,2}$) are obtained as intersections of the planes $\varepsilon = 0.02$, $\delta = \pm 0.75$, and the LPC1 (LPC2) two-dimensional bifurcation surface. With these constructions, compact information regarding the bifurcation behavior of the dynamics on the three-dimensional parameter spaces of Figures 9.78a–c can be displayed.

Note that, in order to clarify the robustness features of the SDOF NES design, the NS and BPC bifurcation surfaces are not included in these diagrams, and neither are additional bifurcations of co-dimension two or of higher co-dimension. Recall

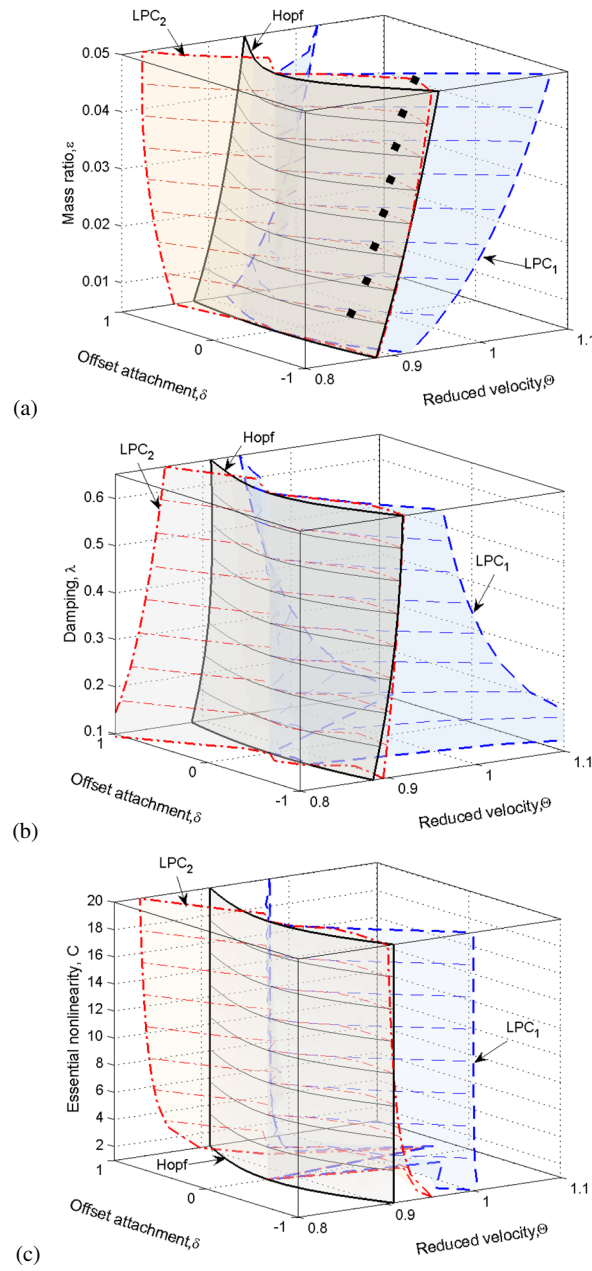


Fig. 9.78 Bifurcation diagrams of steady state dynamics of the in-flow wing with an attached SDOF NES: (a) effect of varying the mass ratio ε for $\lambda = 0.4$ and $C = 10.0$ (diamonds on the LPC2 bifurcation surface imply optimal offset locations for enhancing robustness of LCO suppression); (b) effect of varying damping λ for $\varepsilon = 0.02$ and $C = 10.0$; (c) effect of varying the coefficient of the essential nonlinearity C for $\varepsilon = 0.02$ and $\lambda = 0.4$.

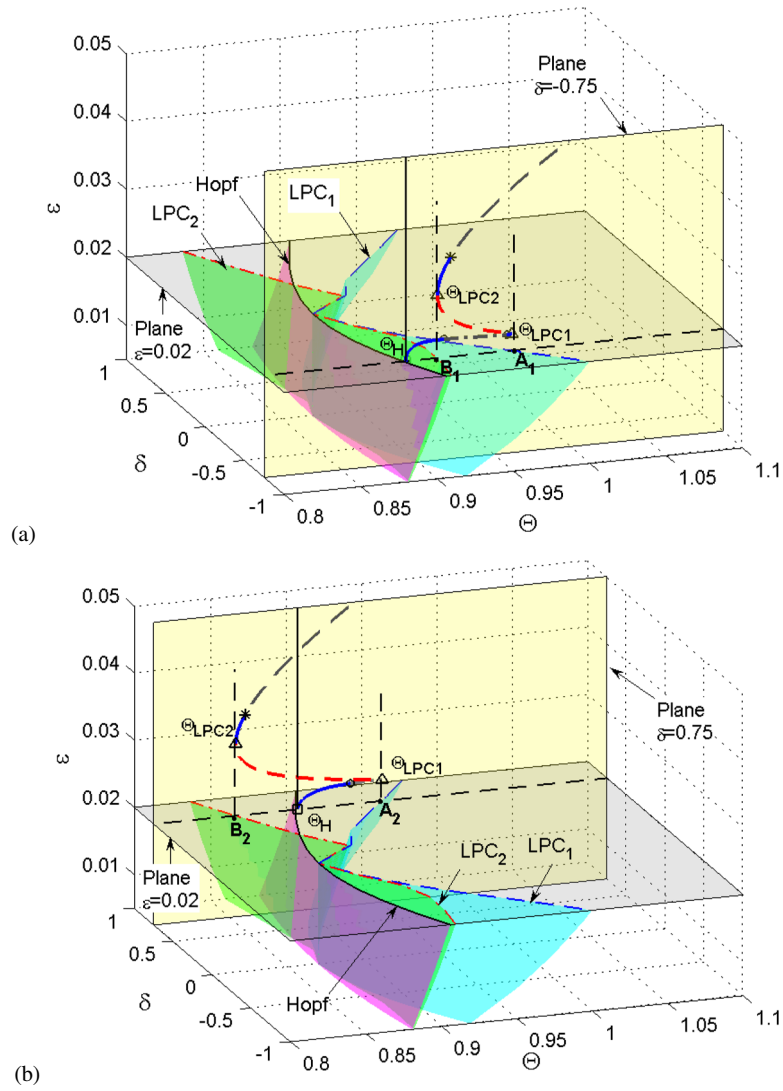


Fig. 9.79 In-flow wing with SDOF attached, understanding the three-dimensional bifurcation sets for $\varepsilon = 0.02$ and (a) $\delta = -0.75$, (b) $\delta = 0.75$.

that, in the SDOF NES design, a zero offset ($\delta = 0$) does not affect the aeroelastic responses, since in that case the bifurcation structure coincides with that of the wing with no NES attached. This can be inferred also from the bifurcation results of Figures 9.78a–c, since as $\delta \rightarrow 0$ the two LPC bifurcation surfaces tend to coalesce with the Hopf bifurcation surface.

In the following, we provide some remarks regarding the effects of varying the NES mass ratio (ε), damping (λ), and essential nonlinearity (C) on LCO suppression, for fixed offset δ and reduced fluid velocity Θ . Focusing first on the effect of varying the NES mass ratio ε , and referring to Figure 9.78a, we note that this ratio contributes significantly to the shift of the Hopf bifurcation point towards higher reduced velocities (this is contrary to the common view that damping has a greater influence towards that effect). In addition, as the NES mass ratio ε increases along with the offset δ away from the elastic axis, the Hopf and LPC bifurcation points exhibit a monotonic shift towards higher reduced velocities. In terms of robustness of LCO suppression (which depends on the location of the bifurcation point LPC2 relatively to the Hopf bifurcation point), an optimal interval of offset values exists for each mass ratio. That is, if the SDOF NES is attached too far away from the elastic axis, the bifurcation point LPC2 may be realized very close to the Hopf bifurcation point for negative offsets. Even worse from the point of view of robustness, for positive offsets the point LPC2 can be realized at smaller reduced velocities than the Hopf bifurcation point. As was conjectured in Section 9.3 if the NES possesses larger mass, the robustness of LCO suppression may improve within the optimal offset interval. The points denoted by diamonds in Figure 9.78a indicate optimal offsets from the point of view of optimally enhanced robustness of aeroelastic instability suppression.

The above-mentioned conclusions are confirmed by the series of bifurcation diagrams presented in Figure 9.80 which depict the steady state amplitude of the pitch mode as function of NES parameters for six values of the mass ratio ε . We note that as the mass ratio increases, the LPC bifurcation curves are realized at increasingly higher pitch amplitudes. This observation indirectly explains why robust suppression of LCO instability is barely observed for very small values of NES mass. Indeed, for small NES masses (see Figure 9.80a) the Hopf bifurcation curve appears to be nearly flat and to lie parallel to the offset axis; this indicates that in this case the offset of the SDOF NES does not significantly affect the critical reduced speed of Hopf bifurcation. Moreover, for small NES masses partially-suppressed LCO branches exist (corresponding to the second LCO suppression mechanism), but they are realized over small intervals of reduced velocities; in addition, small-amplitude LCOs on those branches are vulnerable to disturbances, after which the dynamics may undergo transitions to large-amplitude LCOs, rendering the LCO suppression non-robust. Finally, regarding the overall topology of the LCO branches of Figure 9.80a, we note that, apart for the LCO branches leading to partial instability suppression (second LCO suppression mechanism) or recurring burst-outs and suppressions of instability (first LCO suppression mechanism), it resembles the topology of the bifurcation diagram of the system with no NES attached.

Although not as significant as the effect of the mass ratio, increasing the NES damping coefficient λ improves the flutter speed (see Figure 9.78b). The overall robustness behavior of LCO suppression seems to be similar to that obtained when increasing the mass ratio. That is, there exist optimal intervals of the offset for which enhanced robustness of LCO suppression is realized, with negative offsets resulting in improved LCO suppression performance. As depicted in Figure 9.81, when

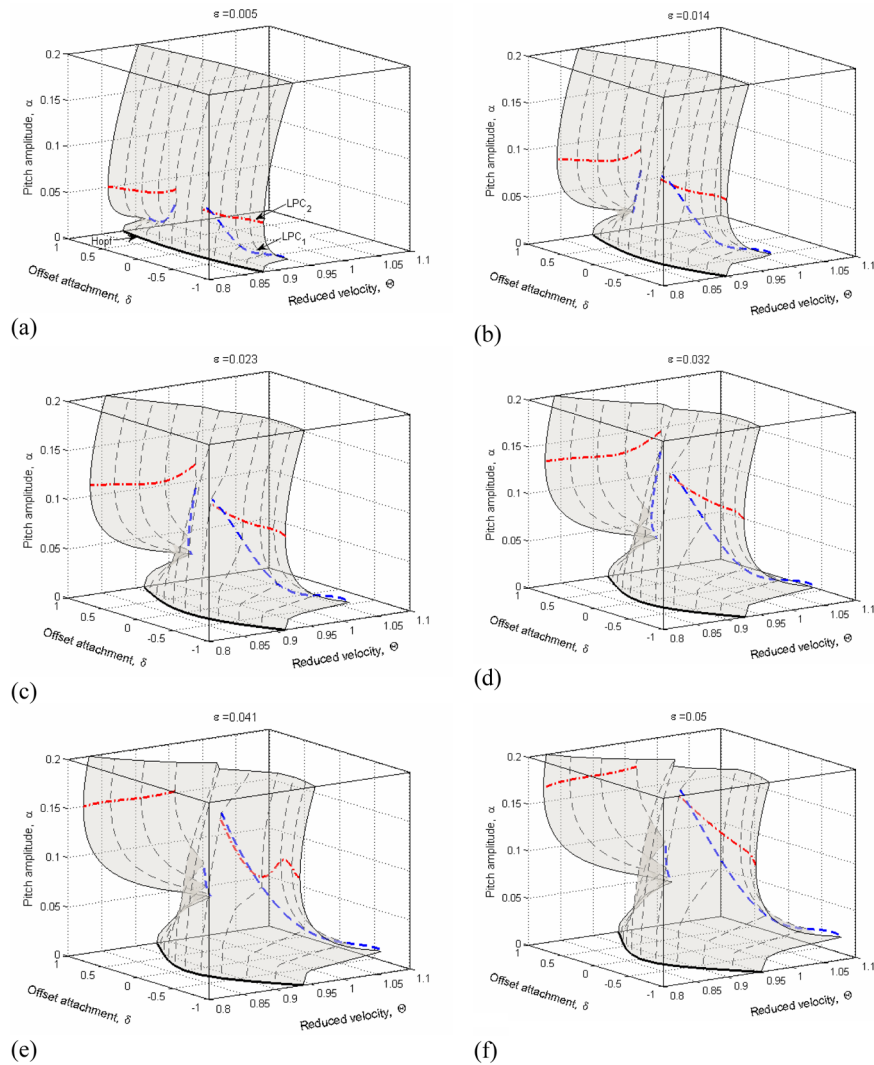


Fig. 9.80 In-flow wing with SDOF NES attached, bifurcation plots of steady state dynamics for varying mass ratio ϵ and $\lambda = 0.4$, $C = 10.0$: (a) $\epsilon = 0.005$, (b) $\epsilon = 0.014$, (c) $\epsilon = 0.023$, (d) $\epsilon = 0.032$, (e) $\epsilon = 0.041$, (f) $\epsilon = 0.05$; bold solid (dashed, dash-dotted) line denotes a Hopf (LPC1, LPC2) bifurcation curve.

damping is increased the LPC bifurcation curves shift towards higher LCO amplitudes. Moreover, low NES damping (see Figure 9.81a) results in inefficient energy dissipation of the energy transferred from the wing to the NES, which tends to yield non-robust LCO suppression over the reduced fluid velocities of interest.

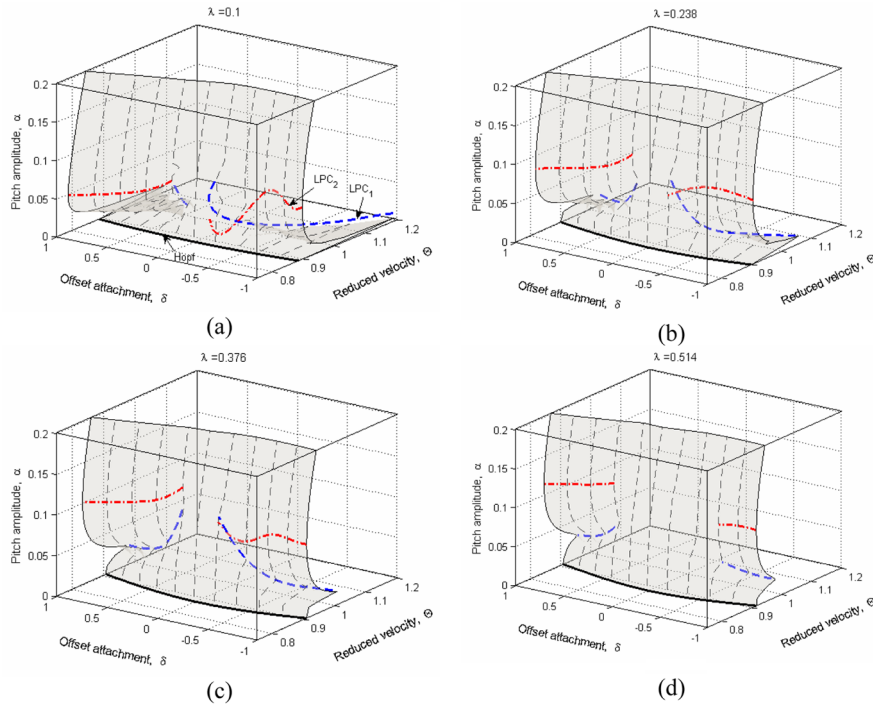


Fig. 9.81 In-flow wing with SDOF NES attached, bifurcation plots of steady state dynamics for varying damping λ and $\varepsilon = 0.02$, $C = 10.0$: (a) $\lambda = 0.1$, (b) $\lambda = 0.238$, (c) $\lambda = 0.376$, (d) $\lambda = 0.514$; bold solid (dashed, dash-dotted) line denotes a Hopf (LPC1, LPC2) bifurcation curve.

Considering the effect of varying the coefficient C of the essential stiffness nonlinearity (see Figure 9.78c), we note that the Hopf and LPC bifurcation manifolds seem to be nearly insensitive to variations of this coefficient. It follows that the robustness of LCO instability suppression is not significantly affected by the coefficient of the essential nonlinearity, provided that this coefficient is sufficiently large. In fact, the main role of the essential nonlinearity is to induce broadband nonlinear resonance interaction between the wing and SDOF NES. This conclusion is supported by the bifurcation diagrams of Figure 9.82, where the topologies of all bifurcation diagrams appear to be similar, with the possible exception of the diagram corresponding to small C ($C = 1$ – see Figure 9.82a). A minor distinction between the bifurcation diagrams is that the LPC bifurcation curves are suppressed to lower pitch amplitudes as C increases.

The previous results identify clearly certain limitations of the SDOF NES design from the point of view of robustness of LCO suppression. As a way to enhance robustness we will consider an alternative design based on the use of MDOF NESs, which as shown in Chapters 4 and 5 have the potential to yield enhanced and broadband TET performance. In the next section we will perform a numerical study of the

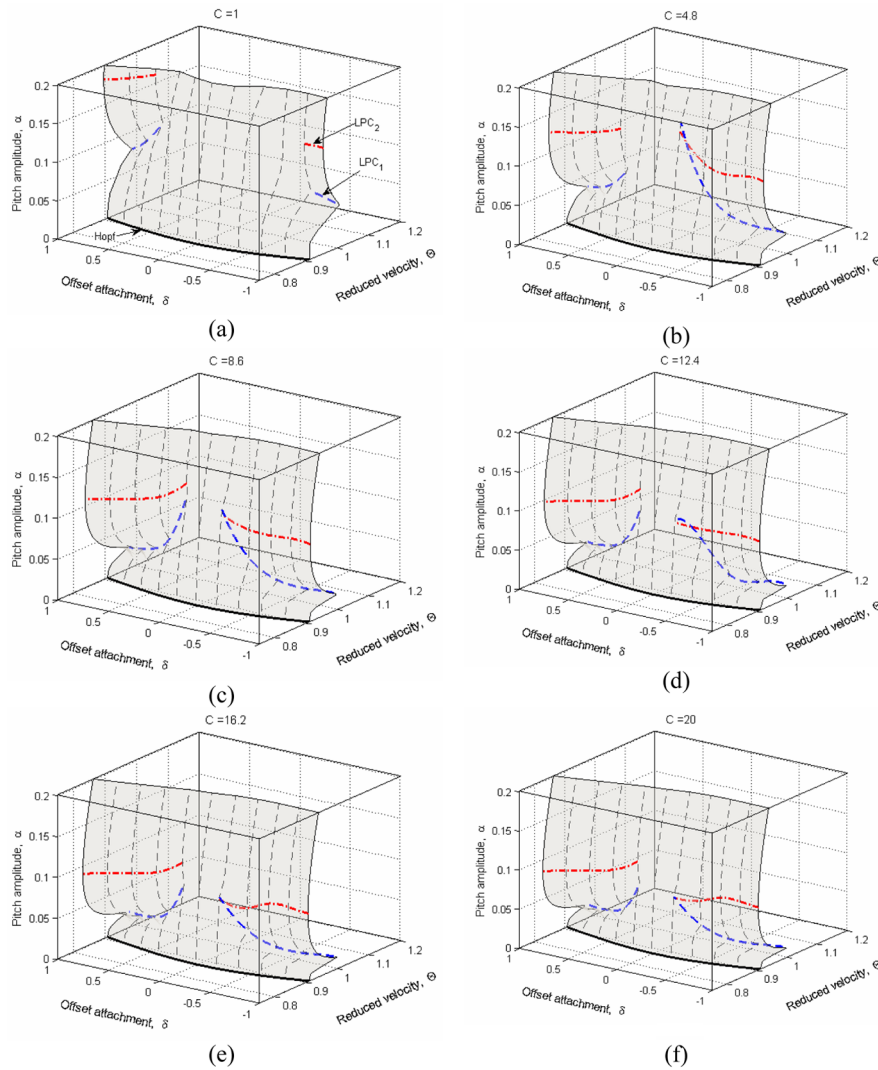


Fig. 9.82 In-flow wing with SDOF NES attached, bifurcation plots of steady state dynamics for varying essential nonlinearity C and $\varepsilon = 0.02$, $\lambda = 0.4$: (a) $C = 1.0$, (b) $C = 4.8$, (c) $C = 8.6$, (d) $C = 12.4$, (e) $C = 16.2$, (f) $C = 20.0$; bold solid (dashed, dash-dotted) line denotes a Hopf (LPC1, LPC2) bifurcation curve.

bifurcation structures of the steady state dynamics of an integrated wing – MDOF NES system, in an effort to demonstrate that the MDOF NES can yield considerable improvement of LCO suppression robustness, as a direct result of enhanced passive broadband TET.

9.5.2 Configuration of a Wing with an Attached MDOF NES

The alternative MDOF NES configuration attached to the in-flow wing is depicted in Figure 9.83 (Lee et al., 2008). The MDOF NES consists of three particles coupled in series by essentially nonlinear stiffnesses lying in parallel to viscous dampers; moreover, the NES is coupled to the wing through a linear coupling stiffness. This configuration is identical to the MDOF NES design studied in detail in Chapter 4. Recalling the results of that study we anticipate that the highly degenerate structure of the MDOF NES dynamics will introduce additional features in the dynamics of the integrated wing-NES system, some of which will end up being beneficial to the task of robust passive LCO suppression.

Assuming small motions and quasi-steady fluid-structure interaction the equations of motion of this system are expressed in the following form:

$$\begin{aligned}
m\ddot{h} + S_\alpha\ddot{\alpha} + K_h(h + c_1h^3) + qSC_{L,\alpha}(\alpha + \dot{h}/U) + k(h - d\alpha - z_1) &= 0 \\
I_\alpha\ddot{\alpha} + S_\alpha\ddot{h} + K_\alpha(\alpha + c_2\alpha^3) - qeSC_{L,\alpha}(\alpha + \dot{h}/U) + dk(d\alpha + z_1 - h) &= 0 \\
(m_s/3)\ddot{z}_1 + c_s(\dot{z}_1 - \dot{z}_2) + k(z_1 + d\alpha - h) + k_s(z_1 - z_2)^3 &= 0 \\
(m_s/3)\ddot{z}_2 + c_s(\dot{z}_2 - \dot{z}_1) + c_s(\dot{z}_2 - \dot{z}_3) + (k_s/50)(z_2 - z_3)^3 + k_s(z_2 - z_1)^3 &= 0 \\
(m_s/3)\ddot{z}_3 + c_s(\dot{z}_3 - \dot{z}_2) + (k_s/50)(z_3 - z_2)^3 &= 0
\end{aligned} \tag{9.90}$$

or in non-dimensional form,

$$\begin{aligned}
y'' + x_\alpha\alpha'' + \Omega^2y + \xi_y y^3 + \mu C_{L,\alpha}\Theta(y' + \Theta\alpha) + C_1(y - \delta\alpha - v_1) &= 0 \\
r_\alpha^2\alpha'' + x_\alpha y'' + r_\alpha^2\alpha + \xi_\alpha\alpha^3 - \gamma\mu C_{L,\alpha}\Theta(y' + \Theta\alpha) + \delta C_1(\delta\alpha + v_1 - y) &= 0 \\
(\varepsilon/3)v_1'' + \varepsilon\lambda(v_1' - v_2') + C_1(v_1 + \delta\alpha - y) + C(v_1 - v_2)^3 &= 0 \\
(\varepsilon/3)v_2'' + \varepsilon\lambda(v_2' - v_1') + \varepsilon\lambda(v_2' - v_3') + C(v_2 - v_1)^3 + (C/50)(v_2 - v_3)^3 &= 0 \\
(\varepsilon/3)v_3'' + \varepsilon\lambda(v_3' - v_2') + (C/50)(v_3 - v_2)^3 &= 0
\end{aligned} \tag{9.91}$$

where the notation of Sections 9.2 and 9.3 applies for (9.90) and (9.91), and the additional new normalized parameters are defined as follows:

$$C_1 = k/m\omega_a^2, \quad v_1 = z_1/b, \quad v_2 = z_2/b, \quad v_3 = z_3/b$$

Some interesting features of the MDOF NES design are now discussed. First, we note that the total mass of the MDOF NES is set to be identical to the SDOF NES considered in previous section; that is, in the new design the single normalized mass ε of the SDOF NES is divided into the three masses equal to $\varepsilon/3$ in the MDOF NES. This allows us to make direct comparisons of the LCO suppression capacities of the two designs without any mass-added effects. Second, there exists a linear coupling stiffness between the wing structure and the first mass of the NES; as discussed

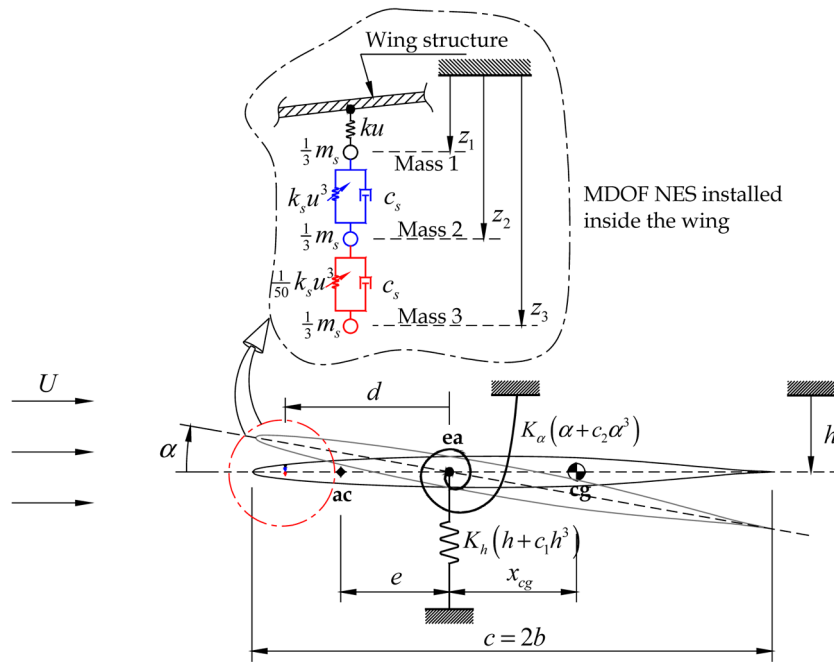


Fig. 9.83 Two-DOF rigid wing model with an attached MDOF NES.

in Chapter 4 weaker linear coupling facilitates broadband TET from the primary structure (in this case, the wing) to the MDOF NES, and it would be interesting to examine if this enhanced TET yields enhanced and more robust LCO suppression compared to the SDOF NES design. Finally, we make the remark that the upper essentially-nonlinear stiffness (which couples the first and second masses) of the NES is chosen to be much stiffer than the lower nonlinear stiffness (which connects the second and third NES masses). This relative scaling is motivated by the results presented in Chapter 4, where it was found that a stiffer upper nonlinear spring enables enhanced nonlinear resonance (modal) interactions between the MDOF NES and the modes of the primary structure, whereas a weaker lower nonlinear spring yields large-amplitude relative motions between the second and the third masses of the NES, and thus, facilitates strong dissipation of the energy transferred to the NES from the primary structure through TET.

An indication of the improvement in robustness of LCO suppression achieved by the action of the MDOF NES is obtained when considering the preliminary numerical results depicted in Figure 9.84 where the steady state r.m.s. pitch amplitude ratio Δ^α is computed for various combinations of initial conditions and system parameters. These results should be compared to similar results for the SDOF NES design depicted in Figures 9.58 and 9.76. We note that when using the MDOF NES the domain of initial conditions where complete LCO suppression is realized expands,

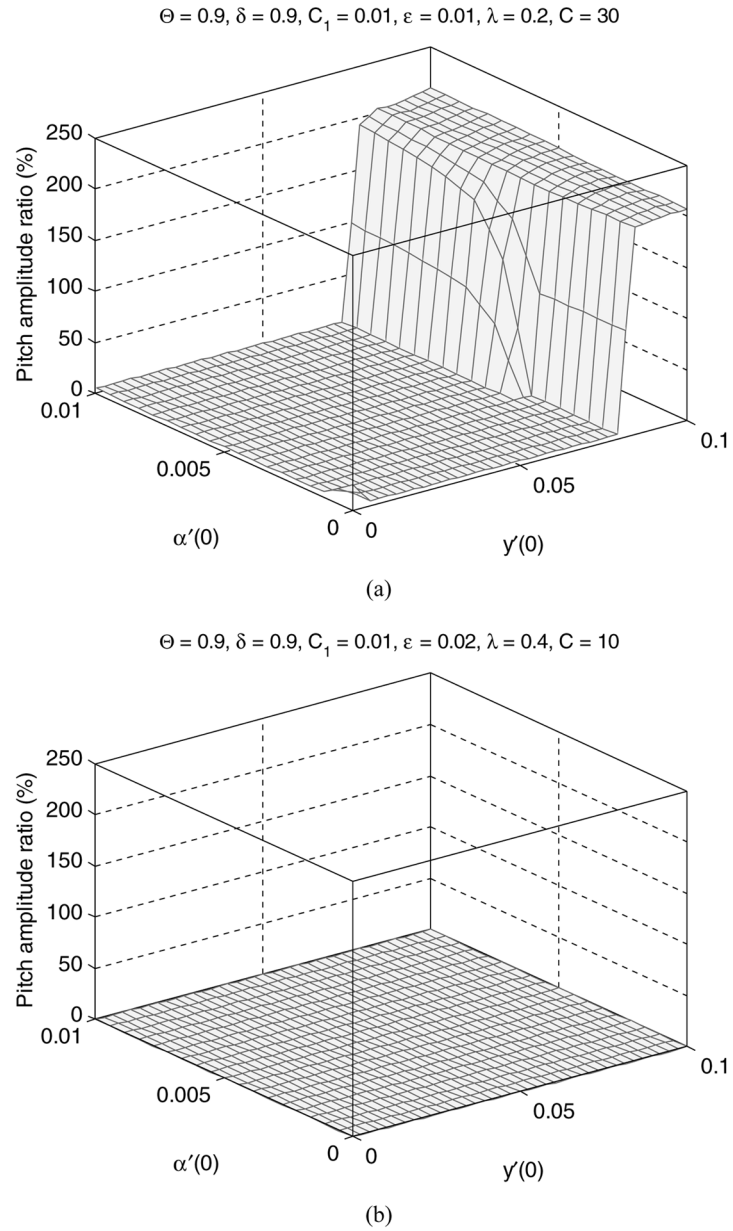


Fig. 9.84 MDOF NES design, steady state r.m.s. pitch amplitude ratio Δ^α , with respect to the set of initial conditions $\{y(0) = 0, \alpha(0) = 0, y'(0) \in [0, 0.1], \alpha'(0) \in [0, 0.1]\}$, $\delta = 0.9, C_1 = 0.01$: (a) $\Theta = 0.9, \varepsilon = 0.01, \lambda = 0.02, C = 30.0$; (b) $\Theta = 0.9, \varepsilon = 0.02, \lambda = 0.4, C = 10.0$.

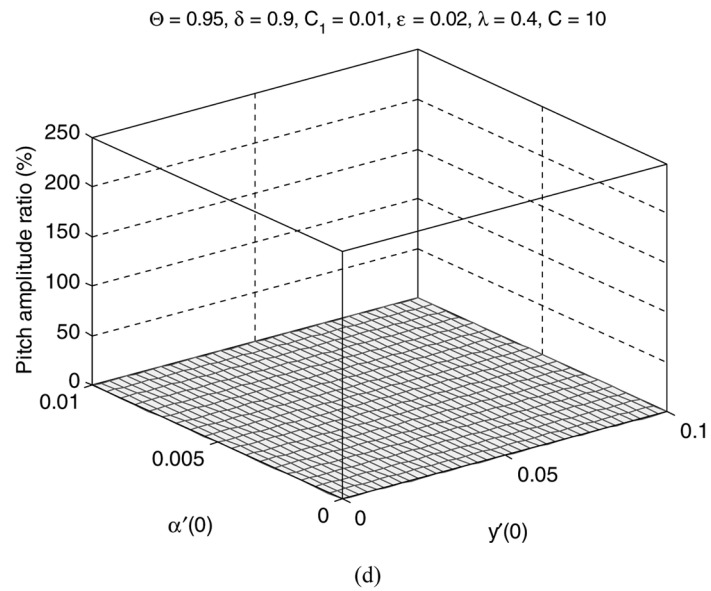
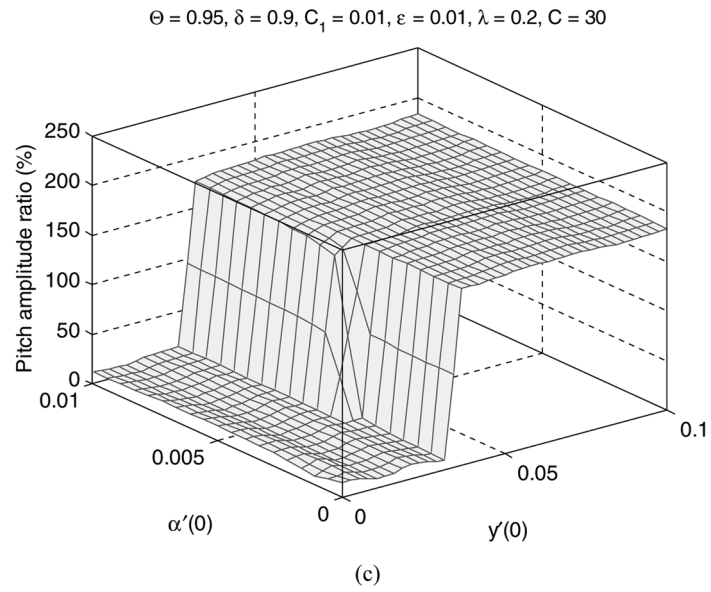


Fig. 9.84 MDOF NES design, steady state r.m.s. pitch amplitude ratio Δ^α , with respect to the set of initial conditions $\{y(0) = 0, \alpha(0) = 0, y'(0) \in [0, 0.1], \alpha'(0) \in [0, 0.1]\}$, $\delta = 0.9, C_1 = 0.01$: (c) $\Theta = 0.95, \varepsilon = 0.01, \lambda = 0.2, C = 30.0$; (d) $\Theta = 0.95, \varepsilon = 0.02, \lambda = 0.4, C = 10.0$.

even for small total NES mass. For example, the simulations of Figure 9.84a correspond to $\varepsilon = 0.01$, i.e., for NES mass equaling 1% of the total wing mass. Moreover, for a mass ratio $\varepsilon = 0.02$ (see Figure 9.84d) the action of the MDOF NES can completely eliminate aeroelastic instability over the entire domain of initial conditions of interest, even for the reduced velocity $\Theta = 0.95$ which is a relatively high flow speed that produces large-amplitude LCOs (above 0.25 rad in the pitch mode) in the wing without NES.

The three LCO suppression mechanisms identified in the SDOF NES design can be detected in the MDOF NES design as well. However, as it will become apparent from the following bifurcation analysis, the action of the MDOF NES tends to suppress the occurrence of Neimark–Sacker (NS) bifurcations which lead to quasi-periodic LCOs. As a result, the first LCO suppression mechanism (corresponding to recurrent series of LCO burst-outs and suppressions) is rarely realized in this case. In fact, we conjecture that the MDOF NES renders the NS bifurcation highly degenerate; for example, neutral-saddle singularities (Kuznetsov, 1995) may occur instead, for which the numerical continuation method may fail to accurately compute the resulting bifurcating LCO branches. The rare occurrence of the first LCO suppression mechanism implies that partial or complete suppression of aeroelastic instabilities (i.e., the second and third suppression mechanisms, respectively) will be the main LCO suppression mechanisms observed in the MDOF NES design.

9.5.3 Robustness of LCO Suppression – Bifurcation Analysis

The MATCONT numerical continuation technique (Dhooge et al., 2003) was utilized to construct bifurcation diagrams of steady state dynamics (LCOs) of the system (9.91). As discussed in previous sections these diagrams are important for assessing the robustness of LCO suppression due to the action of the MDOF NES, and for comparing the relative performances of the SDOF and MDOF NES designs. In the following numerical bifurcation study we consider two cases of linear coupling stiffness between the wing and the MDOF NES, namely, $C_1 = 0.1$ (designated as strong coupling) and $C_1 = 0.01$ (designated as weak coupling). In addition, the overall MDOF NES parameters are chosen to be identical to those of the SDOF NES considered in Section 9.5.1, so that direct comparisons between the two NES designs make sense and can be performed.

9.5.3.1 Case of Strong Coupling

In Figures 9.85a–c we depict the two-dimensional manifolds of Hopf and LPC bifurcations for the system with strong linear coupling between the wing and the MDOF NES. These diagrams are constructed with respect to the total NES mass ratio ε , the damping coefficient λ , and the coefficient C of the essential nonlinearity, respec-

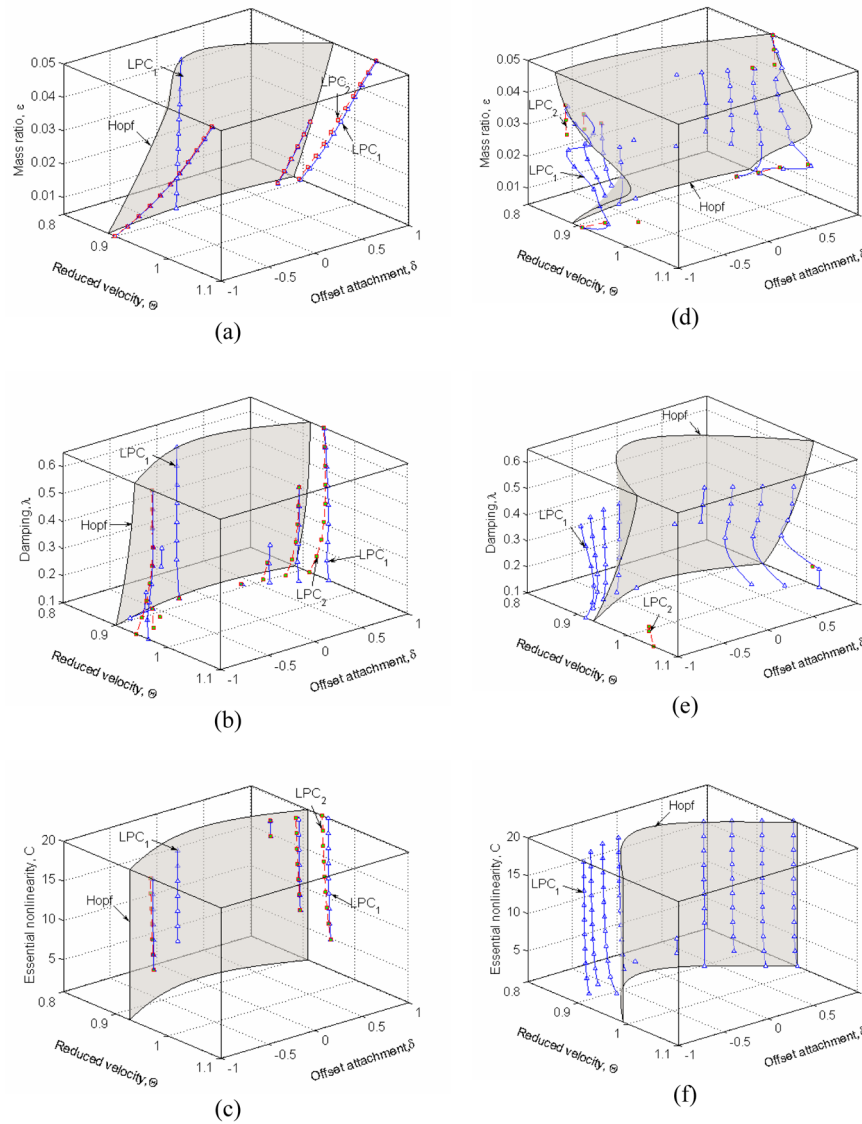


Fig. 9.85 MDOF NES design, sets of Hopf and LPC bifurcations for (a–c) strong linear coupling ($C_1 = 0.1$), and (d–f) weak linear coupling ($C_1 = 0.01$): (a, d) effect of mass ratio ϵ for $\lambda = 0.4$, $C = 10.0$; (b, e) effect of damping λ for $\epsilon = 0.02$, $C = 10.0$; (c, f) effect of essential nonlinearity C for $\epsilon = 0.02$, $\lambda = 0.4$; bifurcation points LPC1 are denoted by triangles (connected by solid line), and bifurcation points LPC2 by squares (connected by dashed line).

tively. The corresponding branches of steady state dynamics (LCOs) for selected parameters are depicted in Figures 9.86–9.88.

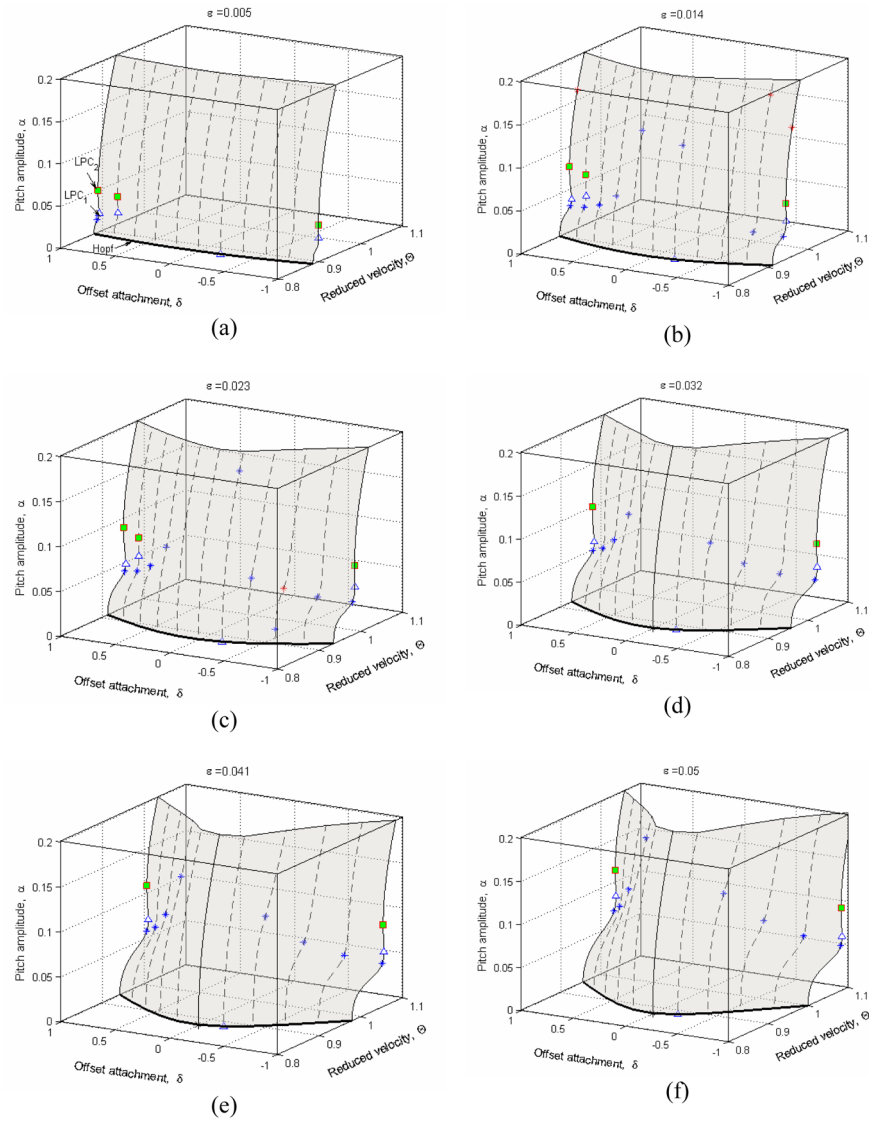


Fig. 9.86 MDOF NES design, branches of steady state dynamics (LCOs) with respect to the mass ratio ε for strong linear coupling $C_1 = 0.1$ and $\lambda = 0.4$, $C = 10.0$: (a) $\varepsilon = 0.005$; (b) $\varepsilon = 0.014$; (c) $\varepsilon = 0.023$; (d) $\varepsilon = 0.032$; (e) $\varepsilon = 0.041$; (f) $\varepsilon = 0.05$; bold solid line denotes Hopf bifurcations curve, triangles (squares) LPC1 (LPC2) bifurcations, and asterisks degenerate bifurcation points such as ‘neutral-saddles’ or ‘generalized Hopf bifurcations’ (Kuznetsov, 1995).

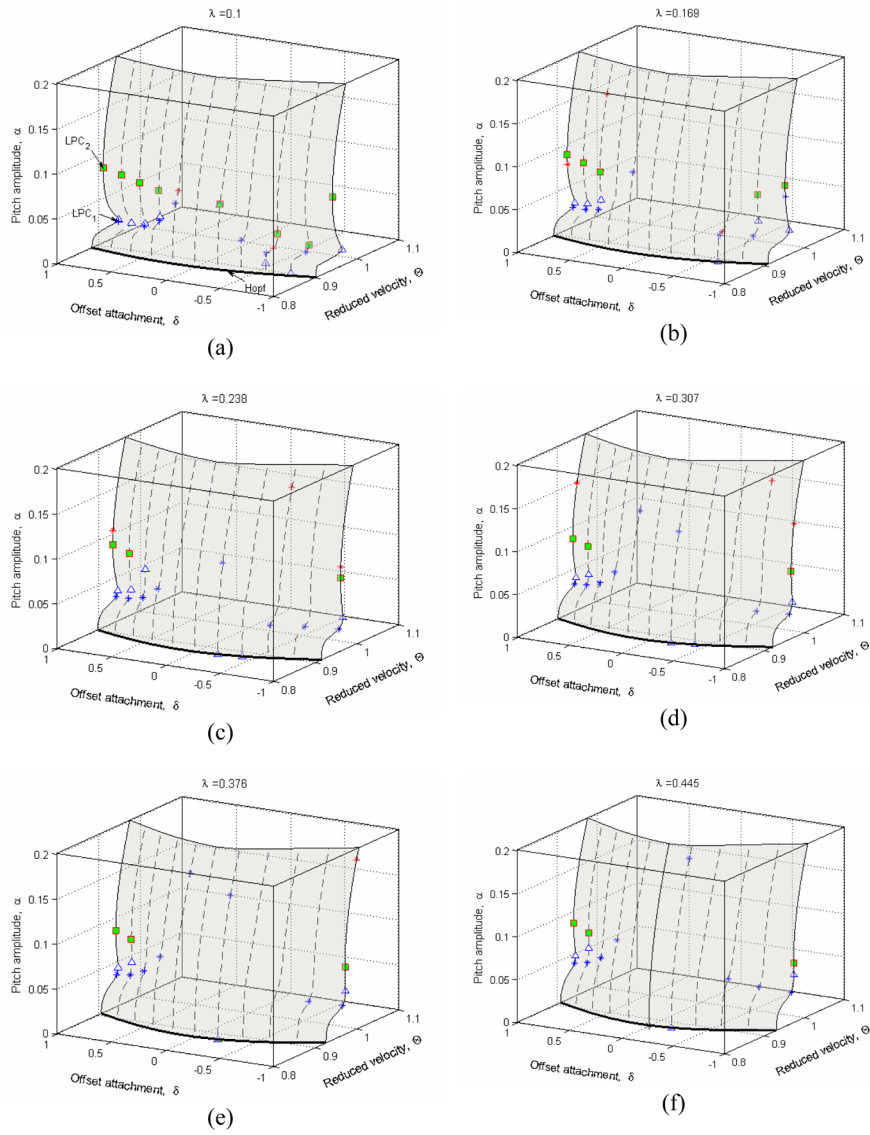


Fig. 9.87 MDOF NES design, branches of steady state dynamics (LCOs) with respect to the viscous damping coefficient λ for strong linear coupling $C_1 = 0.1$ and $\varepsilon = 0.02$, $C = 10.0$: (a) $\lambda = 0.1$; (b) $\lambda = 0.169$; (c) $\lambda = 0.238$; (d) $\lambda = 0.307$; (e) $\lambda = 0.376$; (f) $\lambda = 0.445$; bold solid line denotes Hopf bifurcations curve, triangles (squares) LPC1 (LPC2) bifurcations, and asterisks degenerate bifurcation points such as ‘neutral-saddles’ or ‘generalized Hopf bifurcations’ (Kuznetsov, 1995).

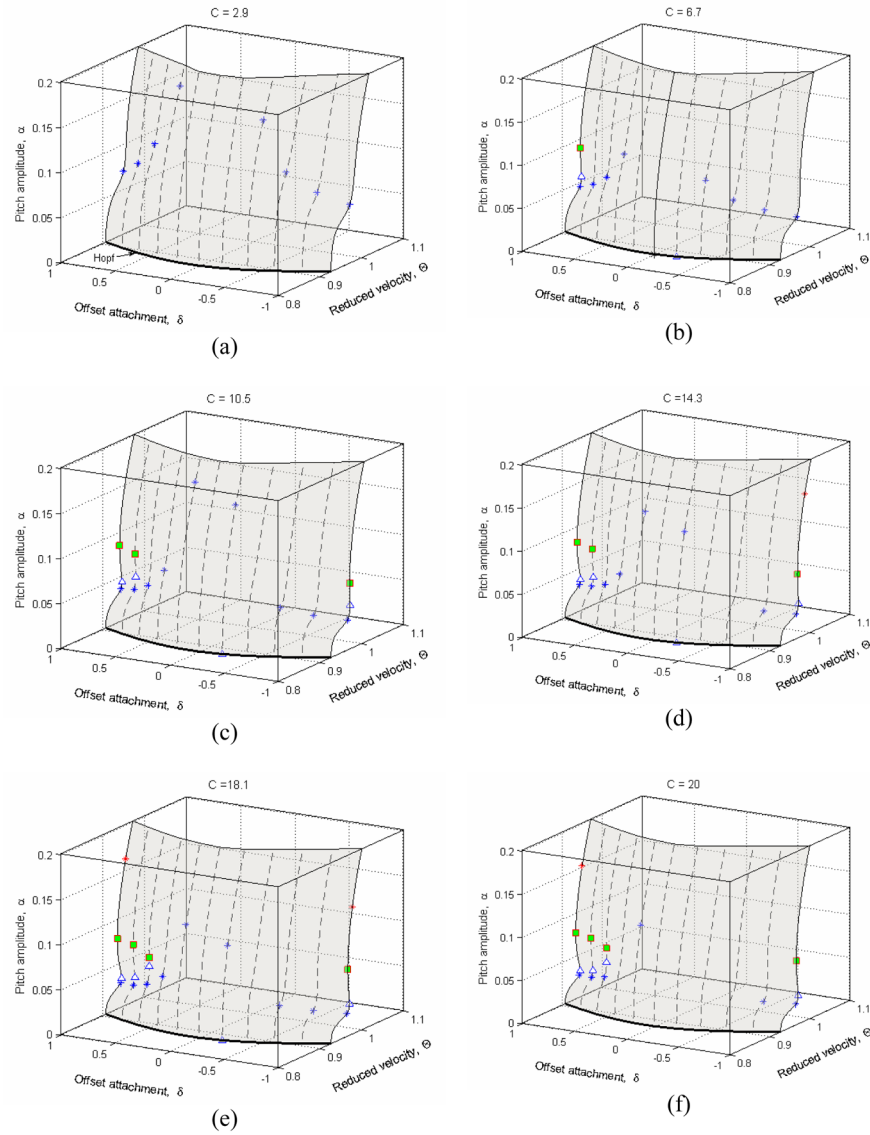


Fig. 9.88 MDOF NES design, branches of steady state dynamics (LCOs) with respect to the coefficient of the essential nonlinearity C for strong linear coupling $C_1 = 0.1$ and $\varepsilon = 0.02$, $\lambda = 0.4$: (a) $C = 2.9$; (b) $C = 6.7$; (c) $C = 10.5$; (d) $C = 14.3$; (e) $C = 18.1$; (f) $C = 20.0$; bold solid line denotes Hopf bifurcations curve, triangles (squares) LPC1 (LPC2) bifurcations, and asterisks degenerate bifurcation points such as 'neutral-saddles' or 'generalized Hopf bifurcations' (Kuznetsov, 1995).

We note that the manifolds of Hopf bifurcations for the system with MDOF NES with strong linear coupling stiffness, appear to have similar topological structures for varying NES mass ratio, damping and essential nonlinearity to those of the case of SDOF NES. That is, for fixed offset the critical reduced velocity for Hopf bifurcation (i.e., the flutter speed) increases monotonically with increasing NES mass ratio ε , and seems to be nearly insensitive to variations of damping and essential nonlinearity. This is due to the fact that for strong linear coupling stiffness the upper mass of the MDOF NES is almost rigidly connected to the wing. We note that strong linear coupling may facilitate strong linear resonant interactions between the wing modes and the MDOF NES, and, it causes stronger shift of the point of Hopf bifurcation towards higher reduced speeds compared to the SDOF design, even when zero offset is considered.

The fact that the Hopf bifurcation points increase monotonically with increasing NES mass ratio ε simply means that a larger NES mass provides better suppression of aeroelastic instability in the strongly coupled MDOF NES configuration (see Figure 9.85a). Moreover, for large offsets the curves of LPC1 and LPC2 bifurcations are closely spaced and are realized at higher reduced velocities than the flutter speeds (i.e., the Hopf bifurcation points). This implies that the unstable LCO branches between the two LPC points exist over short intervals of the reduced velocity, so that the manifolds of LCOs in Figure 9.86 appear as surfaces with no turning points (see Figure 9.86).

In addition, as the mass ratio increases the bifurcation point LPC2 is realized at higher fluid speeds than the Hopf bifurcation point (the flutter speed). The interval between these two bifurcation points corresponds to the range of reduced velocities where robust suppression of aeroelastic instability occurs. We note, however, that the nearly linear monotonic increase of the speed for Hopf bifurcation with respect to the mass ratio may not be attractive for practical applications since we generally require light weightiness for the NES.

Hopf bifurcations are mostly of the supercritical type (Guckenheimer and Holmes, 1983), that is, stable LCOs are generated after the Hopf bifurcations, below which there exist only stable trivial equilibrium points (see Figure 9.86). However, Hopf bifurcations near the point of zero offset are of the subcritical type in short intervals of reduced velocities (for example, at $\delta = -0.2$ in Figures 9.85a–c). The LPC1 bifurcation points are aligned almost vertically for all NES parameters near that range of offset values, and they hardly affect the overall robustness of instability suppression. The branches of LCOs depicted in Figure 9.86 support the above arguments. For example, similarly to the SDOF NES, the LPC bifurcations occur at higher amplitudes as the mass ratio increases. Furthermore, the LPC bifurcation points tend to move away from the line of zero offset as the mass ratio increases.

Higher damping values shift the LPC bifurcation points to larger offsets (see Figure 9.87). High damping also suppresses the occurrence of bifurcations of LCOs and makes the LCO branches smoother. That is, the two LPC bifurcation points merge at larger offsets as damping increases. Thus, optimal offset intervals for robust instability suppression can be identified for smaller damping coefficients. Figure 9.85b depicts the bifurcation sets in the $(\Theta, \delta, \lambda)$ parameter space. As in the case of the

SDOF NES, the manifold of points of Hopf bifurcation exhibits less dependence on the damping value compared to its dependence on the total mass ratio ε .

Whereas the manifold of Hopf bifurcations still exhibits insensitivity to changes in the coefficient of the essential nonlinearity C (see Figure 9.85c), the manifolds of LPC bifurcations become separated from each other for large offsets as C increases. In fact, larger values of C induce two LPC bifurcation points at lower LCO amplitudes (see Figure 9.88). Similar to the SDOF NES design, negative offsets provide better LCO suppression capacity for the MDOF NES design with strong coupling stiffness; moreover, the LCO suppression is robust in that case.

9.5.3.2 Case of Weak Coupling

Weak coupling stiffness between the MDOF NES and the wing removes the monotonic dependence of the position of the Hopf bifurcation point on the mass ratio ε , and shifts the points of Hopf bifurcations (i.e., the points of generation of LCOs) to higher reduced velocities (see Figure 9.85d). An optimal mass ratio can be found near the value $\varepsilon = 0.02$, shifting the point of generation of LCOs to the highest values of reduced speed. Then, the locations of the LPC bifurcation points relative to the Hopf bifurcation points provide an indication of the robustness of instability suppression. A single LPC bifurcation point at lower reduced flow velocity than the Hopf bifurcation point implies that the Hopf bifurcation is of the subcritical type.

It is interesting to note that for negative offsets and in the vicinity of the aforementioned optimal mass ratio, most of LPC bifurcations occur at lower reduced fluid velocities than the Hopf bifurcation points; and at higher reduced velocities, for positive offsets. This behavior appears for varying values of damping and essential nonlinearity, and most LPC bifurcations occur at reduced speeds lower (higher) than the Hopf bifurcation points for negative (positive) offsets. Moreover, the distance between the LPC1 and LPC2 bifurcation points is maximized near the mass ratio where optimal shift to higher fluid velocity of the Hopf bifurcation point is achieved. This means that the robustness of instability suppression may not be optimally enhanced at the optimal mass ratio.

Figure 9.89 depicts the branches of steady state dynamics (LCO surfaces) for selective values of the mass ratio of the MDOF NES with weak linear coupling stiffness. Comparing the manifolds of Hopf bifurcations for $\varepsilon = 0.014$ and $\varepsilon = 0.023$ (Figures 9.89b and 9.89c, respectively), we conclude that the value of $\varepsilon = 0.023$ is optimal in terms of shifting the points of Hopf bifurcation at higher reduced velocities. However, these Hopf bifurcations are of the subcritical type, as indicated by the fact that the LPC bifurcation points are realized at lower reduced velocities. On the other hand, the mass ratio $\varepsilon = 0.014$ shifts the Hopf bifurcation points by lesser amounts, but these Hopf bifurcations are supercritical, with the LPC bifurcation points occurring at higher reduced velocities. This is more desirable from a practical point of view, as less NES mass is seen to yield better performance in terms of robustness of instability suppression.

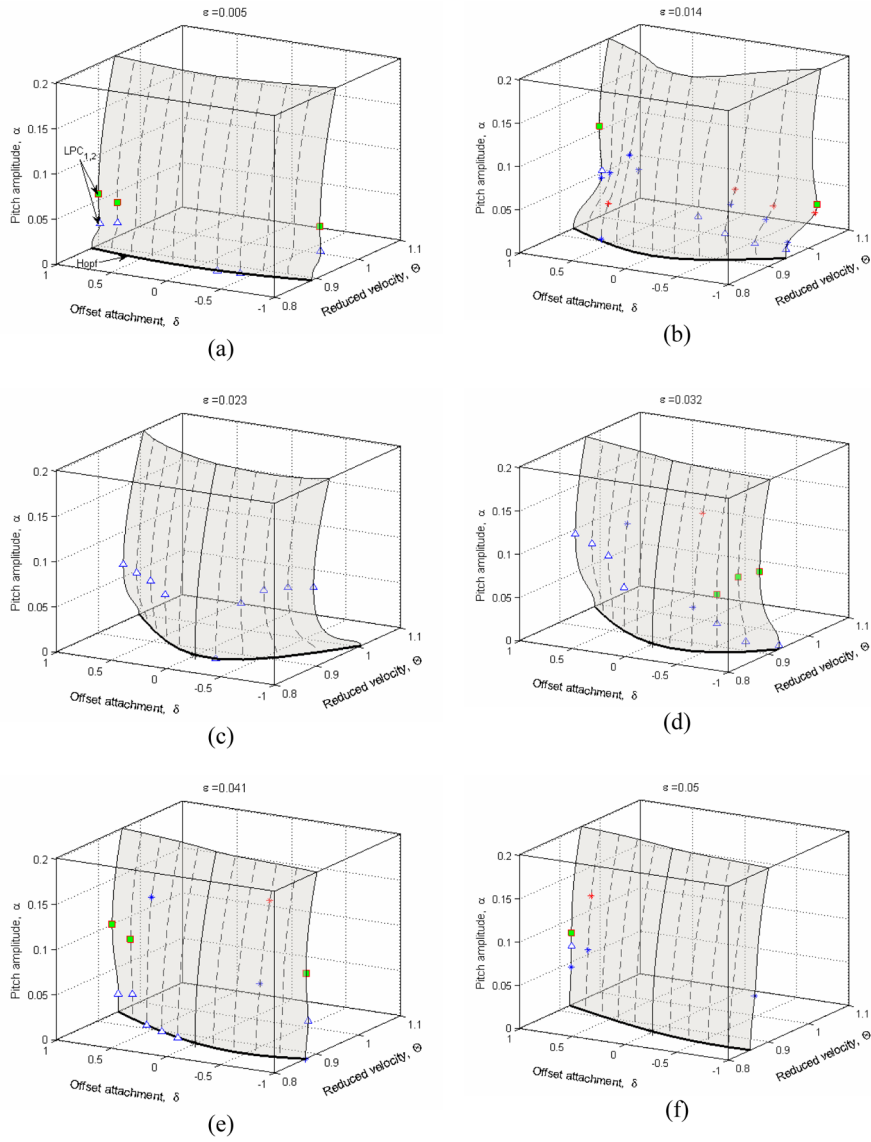


Fig. 9.89 MDOF NES design, branches of steady state dynamics (LCOs) with respect to the mass ratio ε for weak linear coupling $C_1 = 0.01$ and $\lambda = 0.4$, $C = 10.0$: (a) $\varepsilon = 0.005$; (b) $\varepsilon = 0.014$; (c) $\varepsilon = 0.023$; (d) $\varepsilon = 0.032$; (e) $\varepsilon = 0.041$; (f) $\varepsilon = 0.05$; bold solid line denotes Hopf bifurcations curve, triangles (squares) LPC1 (LPC2) bifurcations, and asterisks degenerate bifurcation points such as ‘neutral-saddles’ or ‘generalized Hopf bifurcations’ (Kuznetsov, 1995).

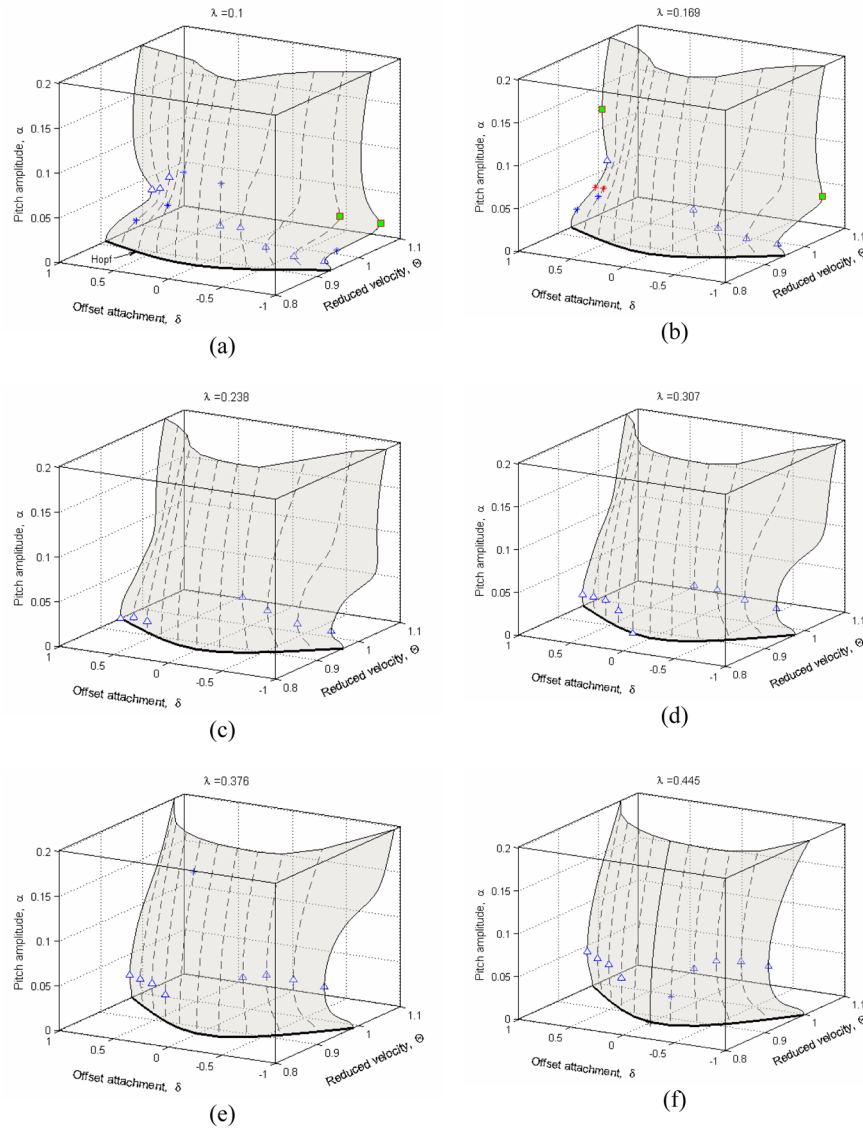


Fig. 9.90 MDOF NES design, branches of steady state dynamics (LCOs) with respect to the viscous damping coefficient $\ddot{\epsilon}$ for weak linear coupling $C_1 = 0.01$ and $\epsilon = 0.02$, $C = 10.0$: (a) $\lambda = 0.1$; (b) $\lambda = 0.169$; (c) $\lambda = 0.238$; (d) $\lambda = 0.307$; (e) $\lambda = 0.376$; (f) $\lambda = 0.445$; bold solid line denotes Hopf bifurcations curve, triangles (squares) LPC1 (LPC2) bifurcations, and asterisks degenerate bifurcation points such as ‘neutral-saddles’ or ‘generalized Hopf bifurcations’ (Kuznetsov, 1995).

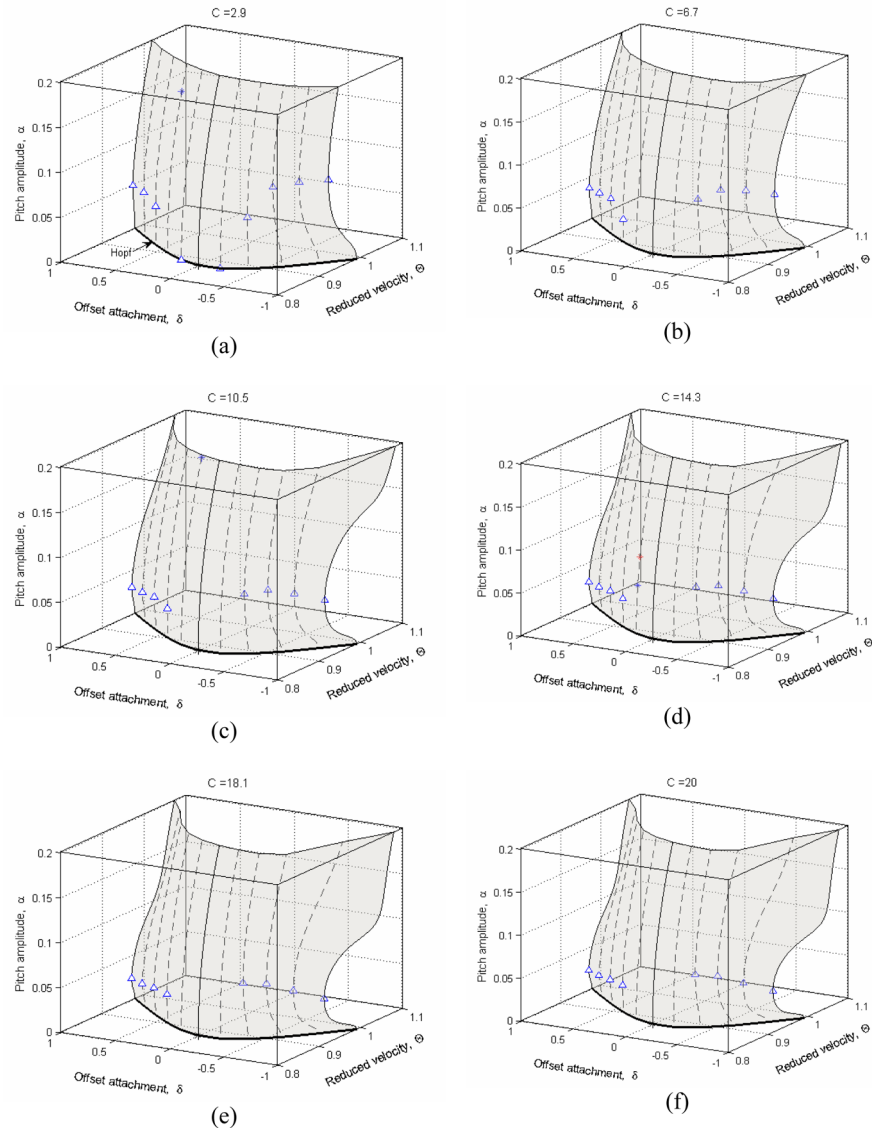


Fig. 9.91 MDOF NES design, branches of steady state dynamics (LCOs) with respect to the coefficient of the essential nonlinearity C for weak linear coupling $C_1 = 0.01$ and $\varepsilon = 0.02$, $\lambda = 0.4$: (a) $C = 2.9$; (b) $C = 6.7$; (c) $C = 10.5$; (d) $C = 14.3$; (e) $C = 18.1$; (f) $C = 20.0$; bold solid line denotes Hopf bifurcations curve, triangles (squares) LPC1 (LPC2) bifurcations, and asterisks degenerate bifurcation points such as ‘neutral-saddles’ or ‘generalized Hopf bifurcations’ (Kuznetsov, 1995).

Whereas the manifold of Hopf bifurcations still exhibits near independence with respect to the coefficient of the essential nonlinearity (see Figure 9.85f), it becomes more dependent on the damping coefficient as noted from the plot of Figure 9.85e. Referring to the variation of the LCO branches with respect to damping and essential nonlinearity (see Figures 9.90 and 9.91), we note that for positive offsets the LPC bifurcations occur either at higher reduced velocities or close to the Hopf bifurcation points; this indicates that the Hopf bifurcations are mainly of the supercritical type, and if they are subcritical their effect on robustness is negligible. For negative offsets the LPC bifurcations occur at much lower reduced velocities. Subcritical LCOs become more prevalent for higher values of damping and essential nonlinearity.

9.5.3.3 Robustness Enhancement

From the previous bifurcation analysis we conclude that the MDOF NES with strong linear coupling (whose dynamics is discussed in Section 9.5.3.1) behaves similarly to a SDOF NES, with the exception of improved performance in terms of aeroelastic instability suppression. Regarding the MDOF NES with weak linear coupling, when appropriately optimized (in terms of offset, stiffness and mass parameters), it may yield efficient and robust passive LCO suppression even when it is lightweight.

In this section, we demonstrate the enhancement in robustness of instability suppression achieved by the MDOF NES design with weak coupling, by comparing its performance to the SDOF NES design with corresponding parameters. Furthermore, we analyze the underlying dynamic mechanisms governing TET from wing modes to the MDOF NES, as well as the resulting nonlinear modal energy exchanges between these subsystems.

In Figure 9.92 we provide a direct comparison of the bifurcation diagrams of systems with MDOF and SDOF NESs for various parameter sets. These diagrams examine the dependence of the steady state pitch amplitude of the wing on the reduced fluid velocity Θ , when (i) no NES is attached; (ii) a SDOF NES with mass ratio $\varepsilon = 0.02$ and offset $\delta = -1$ is attached; and (iii) a MDOF NESs with varying total mass ratio ε and offsets $\delta = \pm 1$ is attached. In these bifurcation diagrams all other NES parameters such as damping, essential nonlinearity, and weak linear coupling stiffness are kept fixed to the values $\lambda = 0.4$, $C = 10.0$ and $C_1 = 0.01$.

The SDOF NES with $\varepsilon = 0.02$ (i.e., 2% ratio of the NES mass with respect to the wing mass) and $\delta = -1$ exhibits good performance in suppressing the aeroelastic instability. Moreover, it yields robust suppression up to the reduced velocity $\Theta \approx 0.91$. However, the MDOF NES with even smaller total mass ratio $\varepsilon = 0.005$ (0.5% overall mass ratio – see Figure 9.92a) provides similar or slightly better suppression results. If the total mass of the MDOF NES increases to $\varepsilon = 0.095$ (i.e., slightly below 1% of the wing mass), the robustness enhancement (as denoted by the interval Θ_{RE} in Figure 9.92b) becomes pronounced, extending the regime of robust LCO suppression up to $\Theta \approx 0.94$ for $\delta = 1$, and $\Theta \approx 0.96$ for $\delta = -1$. Finally, by increasing the total mass ratio of the MDOF NES to $\varepsilon = 0.014$ (see Figure 9.92c – still less than the SDOF NES mass ratio of 2%), robustness enhancement

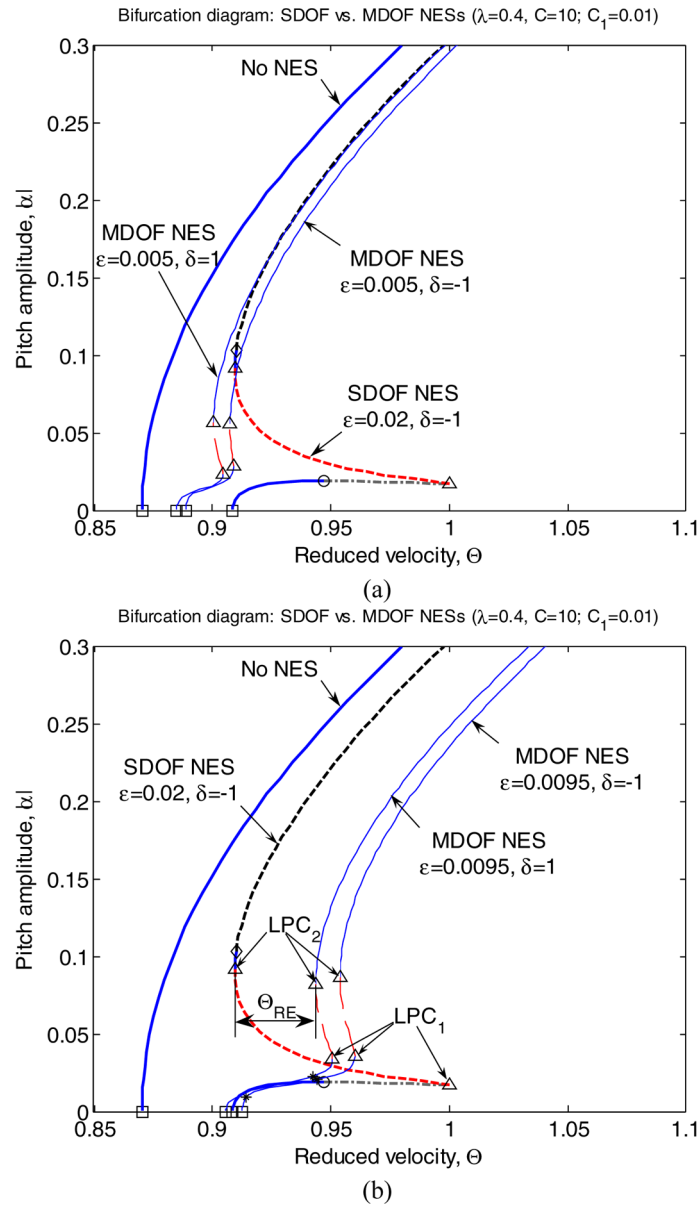


Fig. 9.92 Bifurcation diagrams of the wing with SDOF and MDOF NESs (with weak linear coupling) for $\lambda = 0.4$, $C = 10.0$, $C_1 = 0.01$, and varying offsets and mass ratios: the SDOF NES is considered for mass ratio $\varepsilon = 0.02$ and offset $\delta = -1$; the MDOF NES is considered for varying total mass ratios and offsets, (a) $\varepsilon = 0.005$, $\delta = \pm 1$, (b) $\varepsilon = 0.0095$, $\delta = \pm 1$; dashed lines indicate unstable LCO branches, and squares (circles, triangles, diamond, asterisks) indicate Hopf (Neimark–Sacker, LPC, BPC, neutral-saddle) bifurcation points; the intervals indicated by Θ_{RE} provide measures of enhancement of robustness of LCO suppression.

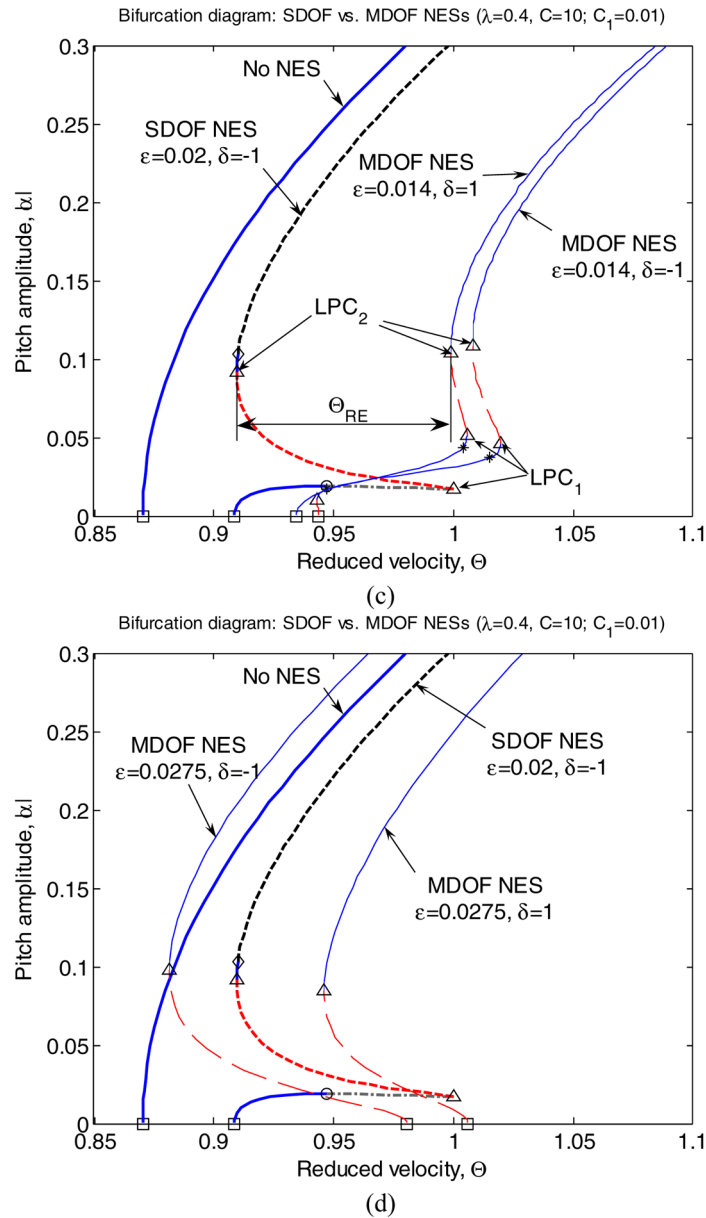


Fig. 9.92 Bifurcation diagrams of the wing with SDOF and MDOF NESs (with weak linear coupling) for $\lambda = 0.4$, $C = 10.0$, $C_1 = 0.01$, and varying offsets and mass ratios: the SDOF NES is considered for mass ratio $\varepsilon = 0.02$ and offset $\delta = -1$; the MDOF NES is considered for varying total mass ratios and offsets, (c) $\varepsilon = 0.014$, $\delta = \pm 1$, (d) $\varepsilon = 0.0274$, $\delta = \pm 1$; dashed lines indicate unstable LCO branches, and squares (circles, triangles, diamond, asterisks) indicate Hopf (Neimark–Sacker, LPC, BPC, neutral-saddle) bifurcation points; the intervals indicated by Θ_{RE} provide measures of enhancement of robustness of LCO suppression.

becomes optimal, with the region of robust suppression extending up to $\Theta \approx 1.0$ for $\delta = 1$, and up to $\Theta \approx 1.01$ for $\delta = -1$. We note that for these values of reduced velocities the results are out of the realm of the current aeroelastic model (based on quasi-steady approximation of fluid-structure interaction), since the amplitudes of the uncontrolled aeroelastic responses are in violation of the initial assumption of small motions. However, these results can be interpreted as being indicative (i.e., as providing trends) of improvement of LCO suppression achieved with the light-weight MDOF NES design.

It is interesting to note that if the total mass ratio of the MDOF NES becomes greater than that of the SDOF NES (see Figure 9.92d), robustness of LCO suppression by the MDOF NES deteriorates compared to the SDOF NES case, even though the generation of LCOs from the trivial equilibrium position is significantly shifted to higher reduced fluid velocities. In conclusion, *optimally designed light-weight MDOF NESs can provide improved and more robust LCO suppression performance, compared to optimally designed SDOF NESs.*

Figure 9.93 demonstrates by means of numerical simulations of the enhancement in robustness of LCO suppression achieved using the MDOF NES design, compared to the SDOF one. Considering a SDOF NES with 2% mass ratio, we assess its LCO suppression capacity at reduced velocity $\Theta = 0.98$, and compare it to the case of a MDOF NES with 1.4% total mass ratio. Considering the time series of Figure 9.93a, for small initial conditions we note that the SDOF NES can suppress the aeroelastic instability through recurrent burst outs and suppressions, i.e., the first suppression mechanism is activated, corresponding to excitation of a quasi-periodic LCO on a branch between two NS bifurcation points. However, an impulsive disturbance applied to the heave mode at $\tau = 200$ destroys this LCO suppression, as it induces a transition of the dynamics to a branch of stable large-amplitude LCOs, thus reviving the triggering mechanism of LCO formation (see Section 9.2). Hence, lack of robustness of LCO suppression is established in the SDOF NES design.

On the contrary, as it can be deduced from the results of Figure 9.93b under the same flow conditions an MDOF NES with even smaller mass ratio maintains robustness of LCO suppression even after an identical impulsive disturbance has been applied to the heave mode of the wing. Moreover, the suppression of the developing instability caused by the impulsive disturbance is achieved due to the capacity of the MDOF NES to efficiently and rapidly absorb the (broadband) energy of the disturbance through TET.

Now, we briefly examine the underlying dynamics that make robustness enhancement possible in the MDOF NES design. We will study the dynamics by analyzing the computed times series of the wing and NES responses by means of wavelet transforms (WTs), and by examining the dominant transient resonant interactions (TRCs) between the aeroelastic modes and the masses of the MDOF NES. In addition, instantaneous modal energy exchanges and measures of energy dissipation by the MDOF NES will be computed, in an effort to relate TET to the enhanced capacity of the MDOF NES to robustly suppress aeroelastic instabilities over certain ranges of reduced fluid velocities.

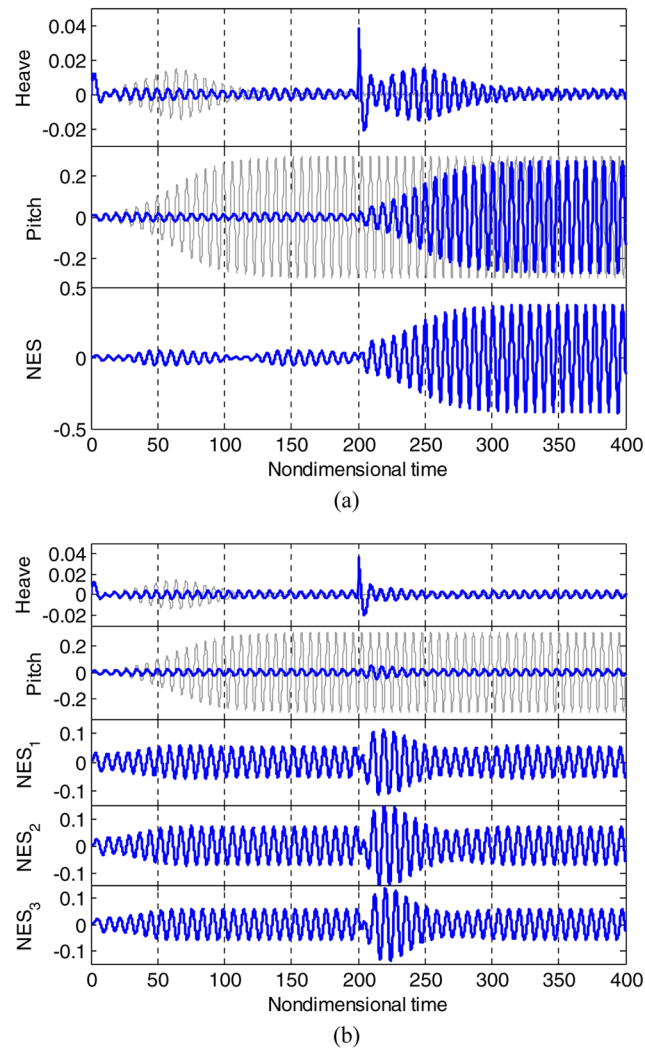


Fig. 9.93 Demonstration of robustness enhancement of LCO suppression, when an impulsive disturbance is applied to the heave mode at $\tau = 200$, for $\Theta = 0.98$, $\delta = -1$, $\lambda = 0.4$, $C = 10.0$ and $C_1 = 0.01$: (a) when a SDOF NES of mass ratio $\varepsilon = 0.02$ is attached, and (b) when a MDOF NES of total mass ratio $\varepsilon = 0.014$ is attached; thicker (thinner) lines indicate controlled (uncontrolled) responses.

To this end, the instantaneous kinetic energy $\bar{T}(\tau)$, and potential energy $\bar{V}(\tau)$, of the integrated wing – MDOF NES system in normalized form (9.91), are computed as follows:

$$\begin{aligned}
\bar{T}(\tau) &= (1/2)y'^2(\tau) + x_a y'(\tau) \alpha'(\tau) + (1/2)\alpha'^2(\tau) \\
&\quad + (1/3) \left[v_1'^2(\tau) + v_2'^2(\tau) + v_3'^2(\tau) \right] \\
\bar{V}(\tau) &= (\Omega^2/2)y^2(\tau) + (r_a^2/2)\alpha^2(\tau) + (\xi_y/4)y^4(\tau) + (\xi_a/4)\alpha^4(\tau) \\
&\quad + (C/4) [v_1(\tau) - v_2(\tau)]^4 + (C/200) [v_2(\tau) - v_3(\tau)]^4 \\
&\quad + (C_1/2) [y(\tau) - \delta\alpha(\tau) - v_1(\tau)]^2
\end{aligned} \tag{9.92}$$

Hence, the total instantaneous energy of the system is computed as

$$E^{\text{Total}}(\tau) = \bar{T}(\tau) + \bar{V}(\tau) \tag{9.93}$$

The instantaneous energy input in the integrated wing-NES system is computed as the summation of the energy provided by the initial conditions and the non-conservative work performed by the flow. This is expressed as follows:

$$E^{\text{Input}}(\tau) = E^{\text{Total}}(0) + W_{nc}^y(\tau) + W_{nc}^\alpha(\tau) \tag{9.94}$$

where

$$\begin{aligned}
W_{nc}^y(\tau) &= \mu C_{L,\alpha} \Theta \int_0^\tau \{y'(s) + \Theta\alpha(s)\} y'(s) ds \\
W_{nc}^\alpha(\tau) &= -\gamma \mu C_{L,\alpha} \Theta \int_0^\tau \{y'(s) + \Theta\alpha(s)\} \alpha'(s) ds
\end{aligned}$$

Each of the above expressions represents the instantaneous non-conservative work performed by the heave or pitch mode of the in-flow wing.

To assess the efficiency of TET from the aeroelastic modes to the MDOF NES, and relate it to the capacity of the NES for LCO suppression we also compute the following energy dissipation measure (EDM), which represents the total energy dissipated by the two damping elements of the NES (see Figure 9.83) up to time τ :

$$\begin{aligned}
E_d^{\text{NES}}(\tau) &= E_d^{\text{NES1}}(\tau) + E_d^{\text{NES2}}(\tau) \\
&= \varepsilon\lambda \int_0^\tau [v_1'(s) - v_2'(s)]^2 ds + \varepsilon\lambda \int_0^\tau [v_2'(s) - v_3'(s)]^2 ds
\end{aligned} \tag{9.95}$$

Combining the previous energy measures we may formulate the following instantaneous total energy balance for the integrated wing-NES system:

$$E^{\text{Total}}(\tau) = E^{\text{Input}}(\tau) - E_d^{\text{NES}}(\tau) \tag{9.96}$$

We consider the dynamics of the integrated system for reduced fluid velocity $\Theta = 0.92$, when complete and robust elimination of aeroelastic instability is realized by the action of the MDOF NES with parameters $\varepsilon = 0.014$, $\lambda = 0.4$, $C = 10.0$, $C_1 = 0.01$ (i.e., weak coupling stiffness is considered) and $\delta = \pm 1$; moreover,

zero initial conditions are considered, except for the heave velocity. The bifurcation diagrams for $\delta = \pm 1$ are depicted in Figure 9.92c, together with the comparison to the bifurcation diagram of the system with a heavier SDOF NES.

In Figures 9.94a and 9.94b we depict the transient responses of the integrated wing-NES system for initial condition $y'(0) = 0.02$ (i.e., for a relatively small initial energy input to the heave mode) and $\delta = \pm 1$, respectively; whereas in Figures 9.94c and 9.94d, we depict the corresponding responses for initial condition $y'(0) = 0.1$ (i.e., for a relatively large initial energy input to the heave mode) and $\delta = \pm 1$, respectively. We note that in both cases of relatively small or large initial input energies the developing aeroelastic instabilities are completely eliminated by the action of the MDOF NES (i.e., the third LCO suppression mechanism is activated), due to TET from the developing instabilities in the aeroelastic modes to the MDOF NES, where the energy is locally dissipated without being ‘fed back’ to the instability. Moreover, it is interesting to note, that *the developing LCO instability is eliminated on a faster time scale when stronger disturbances are applied to the heave mode* (see Figures 9.94c, d); it is also of interest to note that for the particular case of negative offset $\delta = -1$ (see Figure 9.94d) there occur initial nonlinear beat phenomena between the pitch mode and the three masses of the NES, which facilitate energetically-rich modal energy exchanges and transfers from the pitch mode to the NES.

We recall from the exposition in Chapter 3 that the excitation of nonlinear beats through excitation of impulsive orbits (IOs) provides the most efficient mechanism for TET; in that context, the specific excitation of the heave mode considered in the simulations of Figure 9.94 amounts to excitation of IOs of the integrated wing-NES system. In addition, we recall from the results of Chapter 3 that broadband TET from primary systems to SDOF and MDOF NESs is enhanced when energy exceeds certain energy thresholds. We conjecture that this dynamic phenomenon is also observed in the numerical simulations of Figure 9.94, where the NES is observed to perform better at an increased energy level (i.e., for the case of stronger impulsive disturbance).

The WT spectra of the transient responses of Figure 9.94 are depicted in Figure 9.95. Similar to (but in a more efficient way than) the SDOF NES design, subharmonic transient resonant captures (TRCs) between the heave and pitch modes take place, thus replacing (and effectively prohibiting) 1:1 TRCs between the same modes that trigger aeroelastic instabilities (LCOs) in the wing without NES. However, the nonlinear interactions between the pitch mode and the masses of the NES occur through 1:1 TRCs; in addition, the nonlinear beat phenomena occurring between the pitch mode and the NES masses for the case of relatively strong disturbance and offset $\delta = -1$ become apparent by the presence of the two closely spaced harmonics close to the unit normalized frequency in the WT spectra of Figure 9.95d.

Finally, in Figure 9.96 we depict the nonlinear modal energy exchanges corresponding to the time responses of Figure 9.94. Since the action of the MDOF NES yields complete elimination of the aeroelastic instability, eventual zero energy balance between the input energy and the energy dissipated by the NES is achieved at all cases considered. Moreover, the state of zero balance is achieved faster in cases

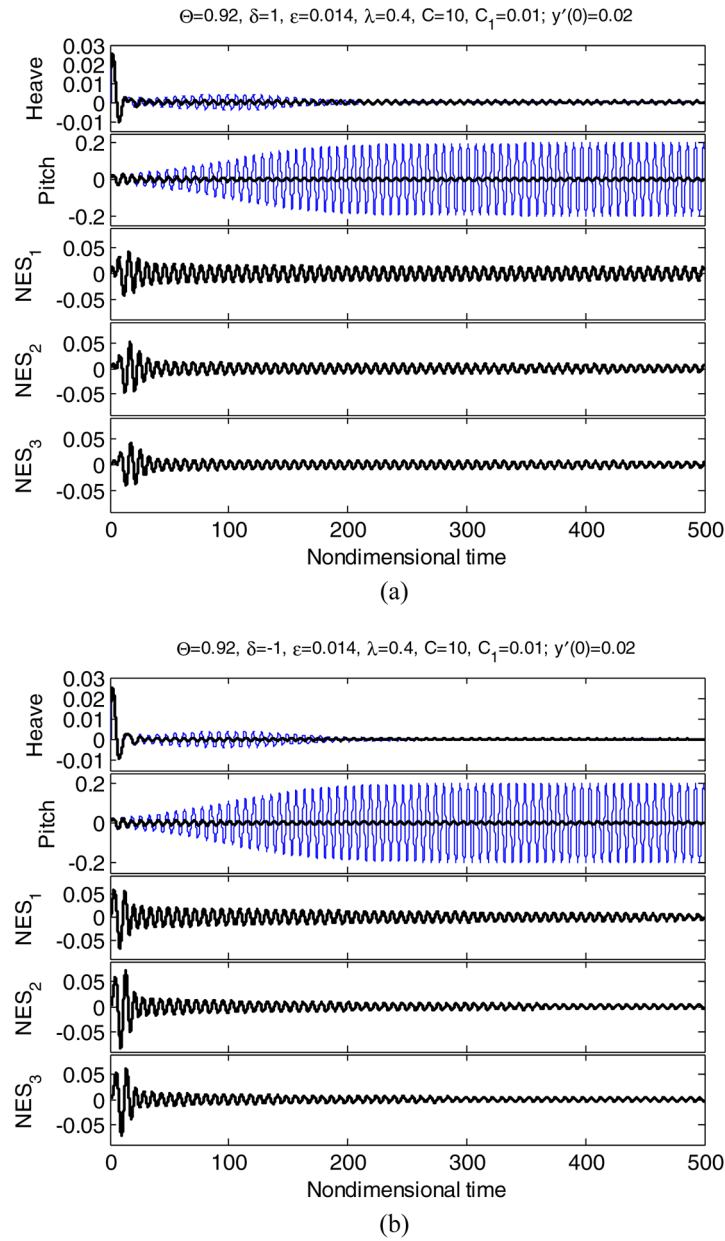
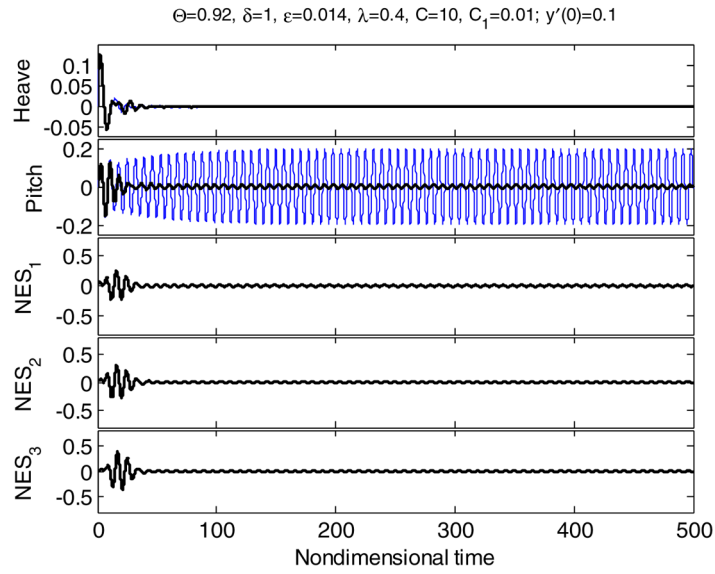
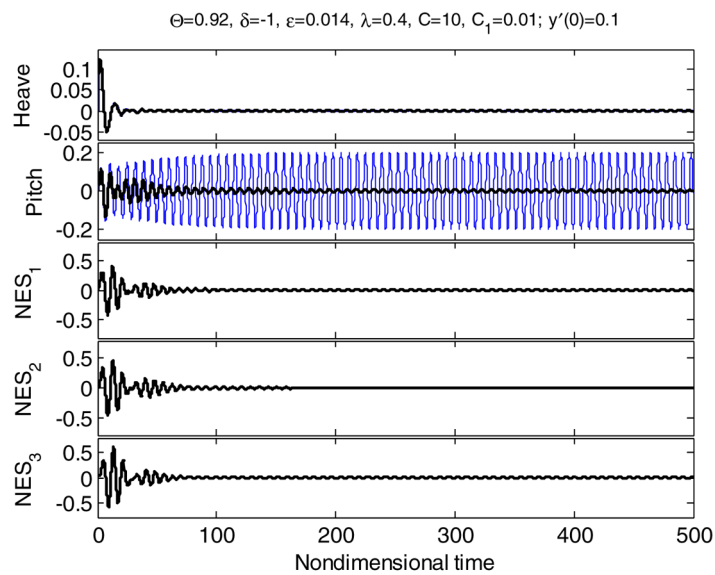


Fig. 9.94 Transient responses of the integrated in-flow wing-MDOF NES system for initial impulse applied to the heave mode, and system parameters $\Theta = 0.92$, $\varepsilon = 0.014$, $\lambda = 0.4$, $C = 10.0$ and $C_1 = 0.01$: (a) $y'(0) = 0.02$, $\delta = 1$; (b) $y'(0) = 0.02$, $\delta = -1$; by the notation NES1–3 we denote the three masses in the MDOF NES, respectively, and thicker (thinner) line indicates controlled (uncontrolled) responses.

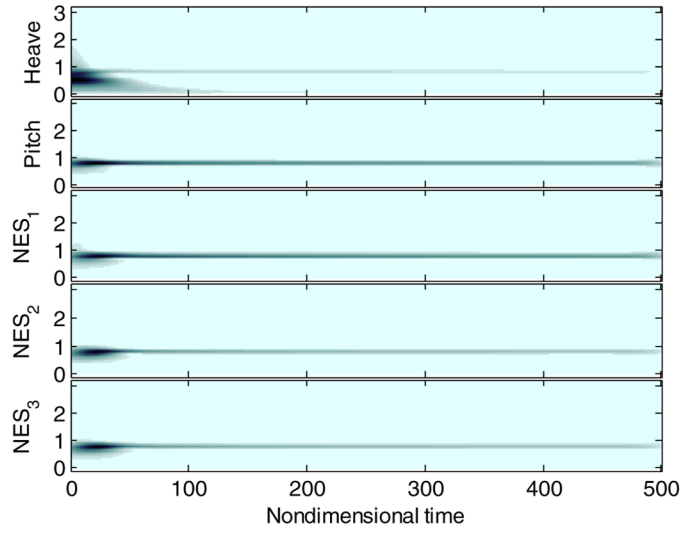


(c)

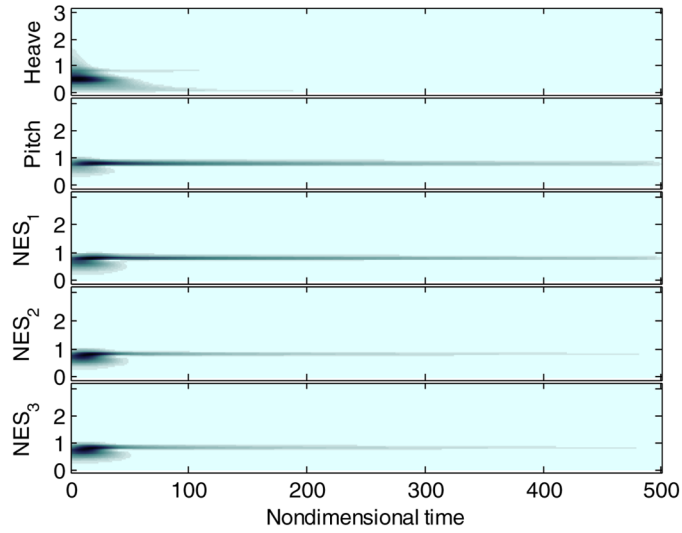


(d)

Fig. 9.94 Transient responses of the integrated in-flow wing-MDOF NES system for initial impulse applied to the heave mode, and system parameters $\Theta = 0.92$, $\varepsilon = 0.014$, $\lambda = 0.4$, $C = 10.0$ and $C_1 = 0.01$: (c) $y'(0) = 0.1$, $\delta = 1$; (d) $y'(0) = 0.1$, $\delta = -1$; by the notation NES1–3 we denote the three masses in the MDOF NES, respectively, and thicker (thinner) line indicates controlled (uncontrolled) responses.



(a)

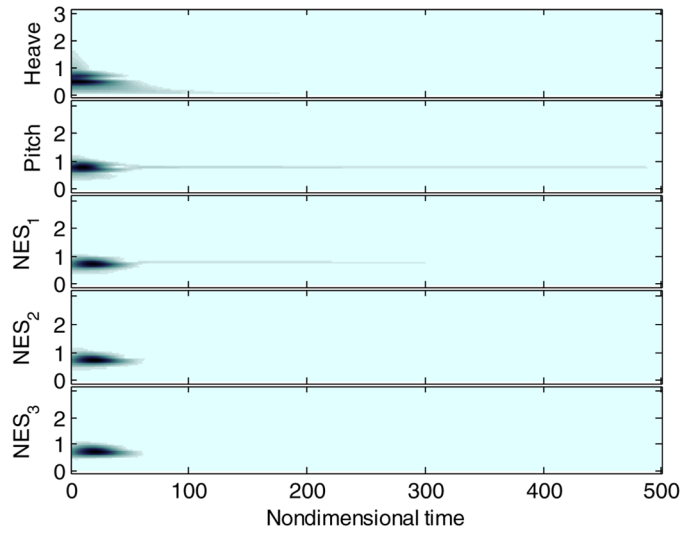


(b)

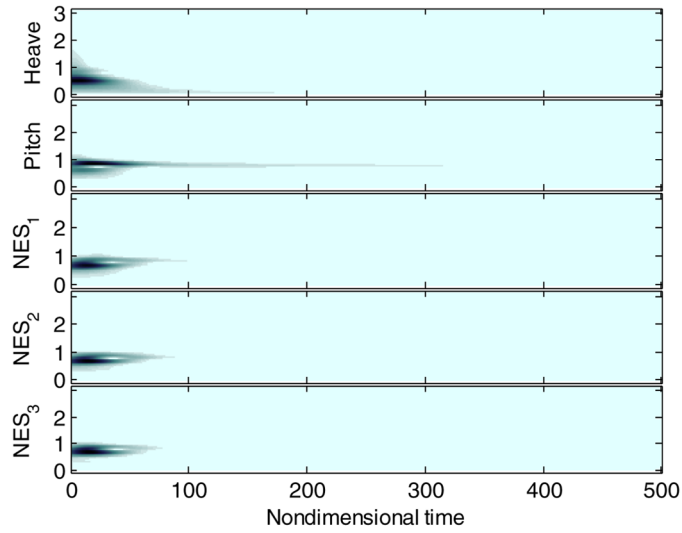
Fig. 9.95 Wavelet transform spectra of the transient responses of Figure 9.94.

where stronger heave disturbances are applied, which confirms the more efficient LCO suppression performance of the MDOF NES at the higher energy level.

All four simulations depicted in Figures 9.94–9.96 display strong initial nonlinear interactions between the aeroelastic modes and the NES. That is, the energy



(c)



(d)

Fig. 9.95 Continued.

applied to the heave mode by the impulsive disturbance is initially absorbed by the MDOF NES, with its upper mass acting as the main absorber of energy as evidenced by the instantaneous energy plots of Figure 9.96 (with the instantaneous energy levels of the upper mass reaching levels of more than 50% of input energy for strong applied impulses). Also, consistent with the previous bifurcation analysis, weaker

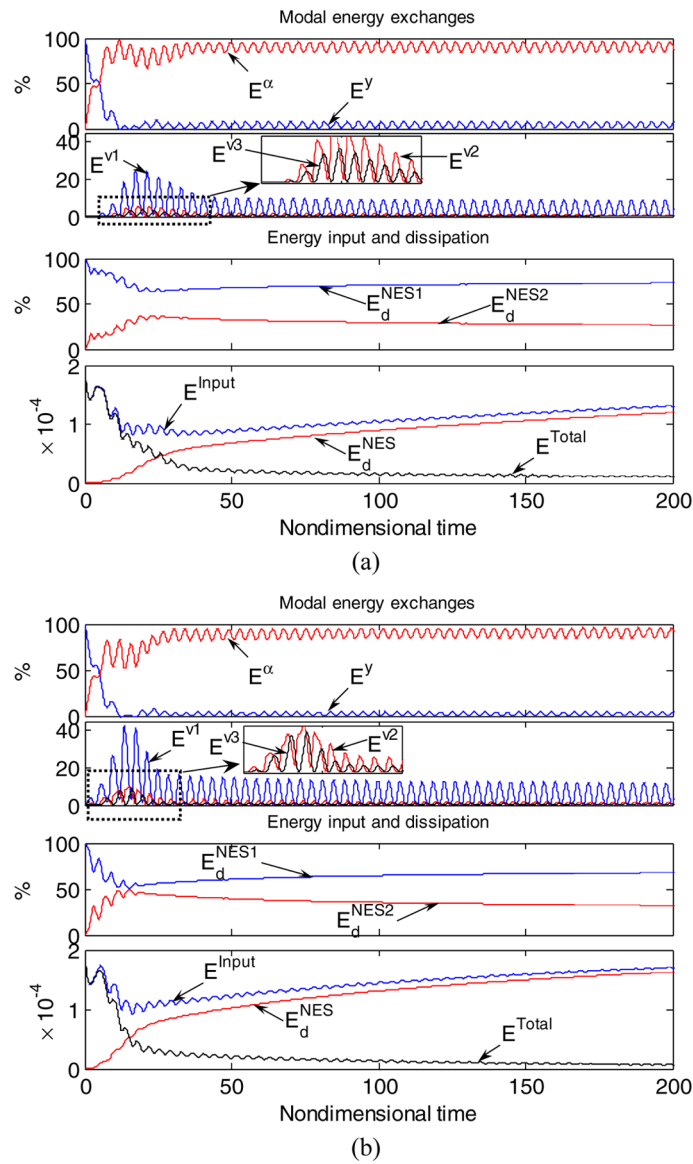
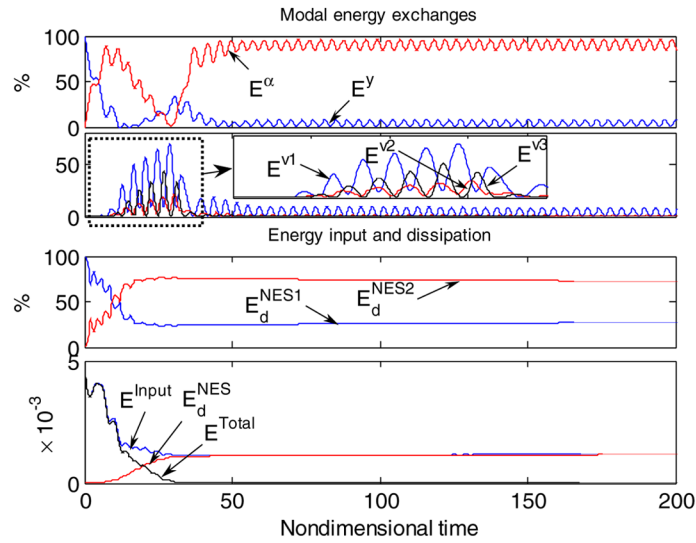
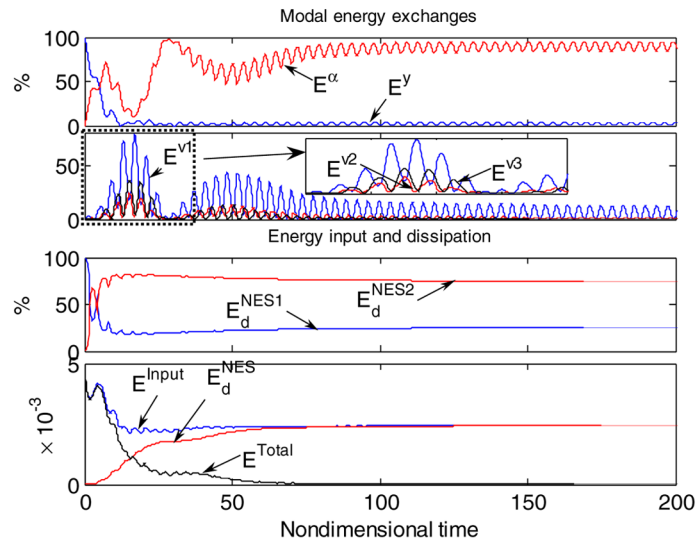


Fig. 9.96 Nonlinear modal energy exchanges corresponding to the responses depicted in Figure 9.94; E^a and E^y denote the percentages of total instantaneous energy stored in the pitch and heave modes, respectively; and E^{v1} , E^{v2} and E^{v3} denote the percentages of total instantaneous energy stored in the first, second and third mass of the NES, respectively.

linear coupling stiffness provides less resistance to this energy transfer from the wing modes to the upper mass of the NES. Considering the energy dissipation ca-



(c)



(d)

Fig. 9.96 Continued.

capacity of the MDOF NES, it is noted that for strong applied impulses it holds that, $E_d^{NES2} > E_d^{NES1}$, i.e., the weakly coupled pair of masses dissipates a bigger portion of the transferred energy from the wing modes compared to the strongly coupled pair; the opposite holds for the case of weak applied impulse. This implies that, for

efficient suppression of aeroelastic instabilities by means of the MDOF NES, the strongly coupled pair of masses of the NES (the one closest to the point of attachment to the wing) should act as effective nonlinear energy absorber, whereas, the weakly coupled pair of masses of the NES (the one farthest from the wing) should act as efficient energy dissipater of this transferred energy. This remark is consistent with the results derived in Chapter 4.

In conclusion, the bifurcation analysis of the dynamics of the integrated wing – MDOF NES system indicates that the placement of the lower LPC bifurcation point at reduced fluid speeds above the Hopf bifurcation point is crucial to enhancing robustness of LCO suppression. Moreover, we demonstrated that the proposed MDOF NES design not only enhances the robustness of LCO suppression against strong impulsive disturbances, but also achieves better (or at least comparable) LCO suppression performance than the SDOF NES design, with smaller total mass.

These results, when viewed in conjunction with previous theoretical and experimental results concerning the SDOF NES design, indicate that appropriately designed lightweight passive nonlinear absorbers with essential stiffness nonlinearities can passively suppress, effectively and robustly, LCO instabilities by means of broadband TET. The dynamical mechanisms governing passive LCO suppression is a series of transient resonance captures occurring between the wing aeroelastic modes and multiple nonlinear normal modes (NNMs) of the MDOF NES, resulting in passive broadband TET of unwanted vibration energy from the wing to the NES, where this energy is spatially confined and passively dissipated. However, open issues that require further investigation include the study of the complex and highly degenerate structure of the dynamics of the integrated wing – MDOF NES system, as well as the study of the performance of the proposed NES designs under conditions of unsteady fluid-structure interaction. We will provide some preliminary results regarding the later topic in the following section.

9.6 Preliminary Results on LCO Suppression in a Wing in Unsteady Flow

Having established effective and robust LCO suppression in a rigid wing by means of passive TET and based on the assumption of quasi-steady aerodynamic theory, one may ask whether a similar passive approach will still be effective when a different aeroelastic model is adopted based on more realistic aerodynamic modeling and yielding unsteady lift force and pitching moment. The purpose of this section is to provide a preliminary answer to this question.

A two-DOF rigid wing with nonlinear structural support, coupled to a SDOF NES with an offset from the elastic axis will be considered, and, contrary to our previous studies, unsteady aerodynamic theory will be employed to model the fluid-structure interaction. After summarizing the system configuration and certain of its dynamical features a numerical continuation technique will be utilized to examine

the dynamical mechanisms governing LCO suppression in this system, and to assess their robustness.

Hence, we reconsider the two-DOF rigid wing coupled to a SDOF NES with an offset from the aeroelastic axis (see Figure 9.43); in contrast, however, to the analysis of Section 9.3 (which was based on quasi-steady flow), we now consider unsteady flow-structure interaction. In this case, the non-dimensional equations of motion for the integrated wing-NES system can be expressed as follows:

$$\begin{aligned}
& y'' + x_\alpha \alpha'' + (\Omega/\Theta)^2 (y + \xi_y y^3) + (\varepsilon\lambda/\Theta)(y' - \delta\alpha' \cos \alpha - v') \\
& + (C/\Theta)(y - \delta \sin \alpha - v)^3 = -(\mu/\pi) C_L(\tau) \\
& \alpha'' + (x_\alpha/r_\alpha^2)y'' + (1/\Theta)^2(\alpha + \xi_\alpha \alpha^3) + (\delta\varepsilon\lambda/\Theta r_\alpha^2)(\delta\alpha' \cos \alpha + v' - y') \\
& + (\delta C/\Theta^2 r_\alpha)(\delta \sin \alpha + v - y)^3 = (2\mu/\pi r_\alpha^2) C_M(\tau) \\
& \varepsilon v'' + (\varepsilon\lambda/\Theta)(v' + \delta\alpha' \cos \alpha - y') + (C/\Theta^2)(v + \delta \sin \alpha - y)^3 = 0 \quad (9.97)
\end{aligned}$$

where an identical notation to Section 9.3 is employed, with the exception of the normalized time which in this case is defined as $\tau = Ut/b$. The unsteady lift force $C_L(\tau)$ and pitching moment $C_M(\tau)$ for incompressible flow are expressed as follows:

$$\begin{aligned}
C_L(\tau) &= \pi[y''(\tau) - \alpha_h \alpha''(\tau) + \alpha'(\tau)] \\
&+ 2\pi[\alpha(0) + y'(0) + (0.5 - \alpha_h)\alpha'(0)]\phi(\tau) \\
&+ 2\pi \int_0^\tau \phi(\tau - s)[\alpha'(s) + y''(s) + (0.5 - \alpha_h)\alpha''(s)] ds \\
C_M(\tau) &= \pi(0.5 + \alpha_h)[\alpha(0) + y'(0) + (0.5 - \alpha_h)\alpha'(0)]\phi(\tau) \\
&+ \pi(0.5 + \alpha_h) \int_0^\tau \phi(\tau - s)[\alpha'(s) + y''(s) + (0.5 - \alpha_h)\alpha''(s)] ds \\
&+ (\pi/2)\alpha_h[y''(\tau) - \alpha_h \alpha''(\tau)] - (\pi/2)(0.5 - \alpha_h)\alpha'(\tau) - (\pi/16)\alpha''(\tau)
\end{aligned} \quad (9.98)$$

The Wagner function $\phi(\tau)$ in (9.98) can be expressed by Jones' approximation (Jones, 1940) as

$$\phi(\tau) = 1 - \psi_1 e^{-\varepsilon_1 \tau} - \psi_2 e^{-\varepsilon_2 \tau} \quad (9.99)$$

where $\psi_1 = 0.165$, $\psi_2 = 0.335$, $\varepsilon_1 = 0.0455$ and $\varepsilon_2 = 0.3$, and α_h denotes the normalized distance over b of the elastic axis ea from the midpoint of the chord length $c = 2b$ (with positive values indicating that the midpoint is on the right of the elastic axis – see Figure 9.43). We note that if we set $\psi_1 = \psi_2 = 0$ quasi-steady aerodynamic theory is recovered, but the secondary bifurcation occurring after the Hopf bifurcation is not observed (Liu and Dowell, 2004).

In order to avoid dealing with a set of integro-differential equations resulting due to the unsteady aerodynamic force and moment, the following new variables (Lee et al., 1997) are introduced:

$$\begin{aligned} w_1(\tau) &= \int_0^\tau e^{-\varepsilon_1(\tau-s)} \alpha(s) ds, & w_2(\tau) &= \int_0^\tau e^{-\varepsilon_2(\tau-s)} \alpha(s) ds \\ w_3(\tau) &= \int_0^\tau e^{-\varepsilon_1(\tau-s)} y(s) ds, & w_4(\tau) &= \int_0^\tau e^{-\varepsilon_2(\tau-s)} y(s) ds \end{aligned} \quad (9.100)$$

Then, the equations of motion (9.97) can be expressed by adopting a state-vector formulation as follows,

$$\underline{\dot{x}}(\tau) = \underline{f}(\underline{x}, \tau) \quad (9.101)$$

where the 10-dimensional state vector of dependent variables is defined as $\underline{x} = t[\alpha \ \alpha' \ y \ y' \ w_1 \ w_2 \ w_3 \ w_4 \ v \ v']^T \in R^{10}$.

As in Section 9.3, in this model structural nonlinearity exists only in the pitch mode (i.e., the plunge support is linear). Hence, we set $\xi_a = 80$ and $\xi_y = 0$, and assume that there is no viscous damping in the wing structure. In addition, we consider the following numerical values for the system parameters, $\mu = 100$, $r_a = 0.5$ and $a_h = -0.5$. As for the static unbalance and frequency ratio, the following two different parameter sets are considered: (i) $x_a = 0.25$, $\Omega = 0.2$, with the aeroelastic instability occurring due to a supercritical Hopf bifurcation at $\Theta_F = 6.2851$ (Set I); and (ii) $x_a = 0.10$, $\Omega = 1.2$ with the aeroelastic instability occurring due to a subcritical Hopf bifurcation at $\Theta_F = 2.951$ (Set II). Finally, the following study will be performed for the following parameters for the SDOF NES, $\varepsilon = 0.02, 0.05$, $\lambda = 0.05$, $C = 10.0$, and $\delta \in [-1, 1]$. That is, the NES mass will be assumed to be at most 5% of the wing mass, and to possess light damping; moreover, the offset of the NES will be allowed to cover almost the entire wing span, that is, from the leading to the trailing edge.

The numerical method MATCONT realized through a Matlab[®] package is utilized to investigate the steady state bifurcation structure of LCOs in the unsteady flow model (9.97), and to study the robustness of LCO suppression by means of TET to the attached NES. Figure 9.97 depicts the bifurcation diagram for the wing parameter Set I, and an NES with 5% mass ratio. Unlike the case with the quasi-steady results reported in Section 9.3, it is interesting to note that the suppressed LCOs exhibit subcritical behavior, whereas the original aeroelastic system undergoes a supercritical Hopf bifurcation. In addition, the shift of the Hopf bifurcations due to the action of the NES is quite insignificant, which is also not coincident with our earlier observations in Section 9.3. However, we conjecture that better results can be obtained once an optimization of NES parameters is performed following the methodologies described previously. Apart from the subcritical LCO branches near the Hopf bifurcation points, we note that the amplitudes of the suppressed LCOs when the NES is attached at the leading edge of the wing (i.e., $\delta = 1.0$) are smaller than the original LCOs, although this reduction involves a series of very complicated

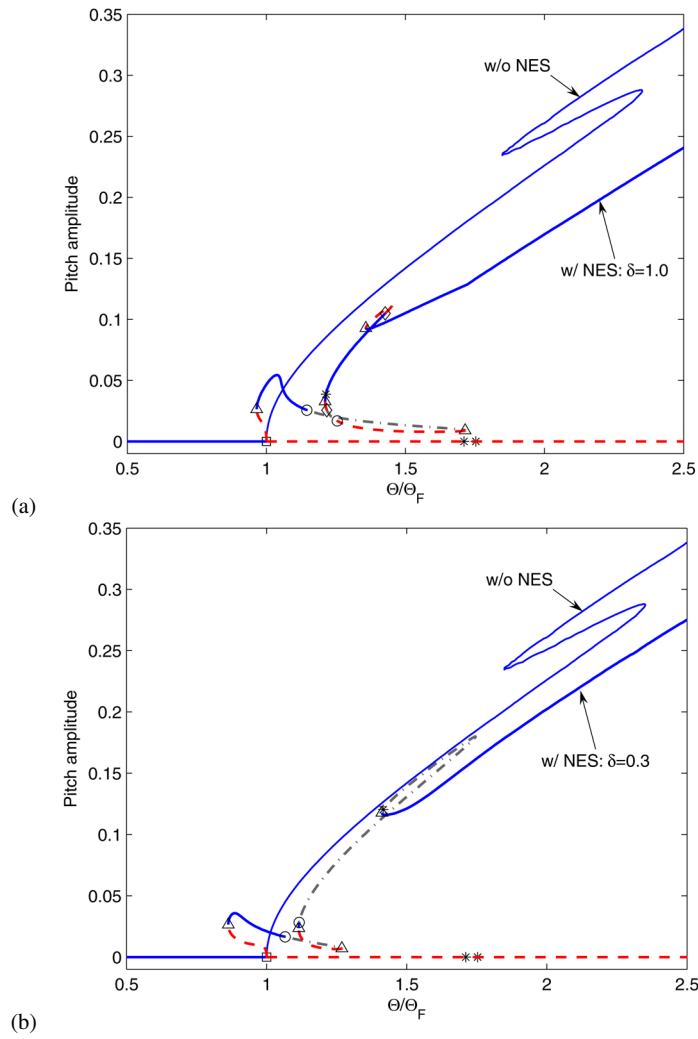


Fig. 9.97 Bifurcation diagram of the pitch response for the wing parameter Set I with respect to the reduced velocity for NES parameters $\varepsilon = 0.05$, $\lambda = 0.05$, $C = 10.0$: (a) $\delta = 1.0$, (b) $\delta = 0.3$; solid (dashed) line indicates a stable (unstable) LCO branch, dash-dotted line a quasi-periodic LCO, and squares (triangles, circles, asterisks, diamonds) Hopf (Saddle-node, Neimark–Sacker, neutral saddle, branch point cycle) bifurcation points.

codimension-1 (Hopf, Saddle-node, Neimark–Sacker) and codimension-2 (Neutral Saddle, Branch Point Cycle) bifurcations.

If, however, our aim is to suppress subcritical LCOs (as for the case of wing parameter Set II), this can be performed by suitably selecting the NES parameters so that supercritical Hopf bifurcations are realized. In particular, focusing in the bifurcation diagrams depicted in Figure 9.98, robust LCO elimination can be achieved

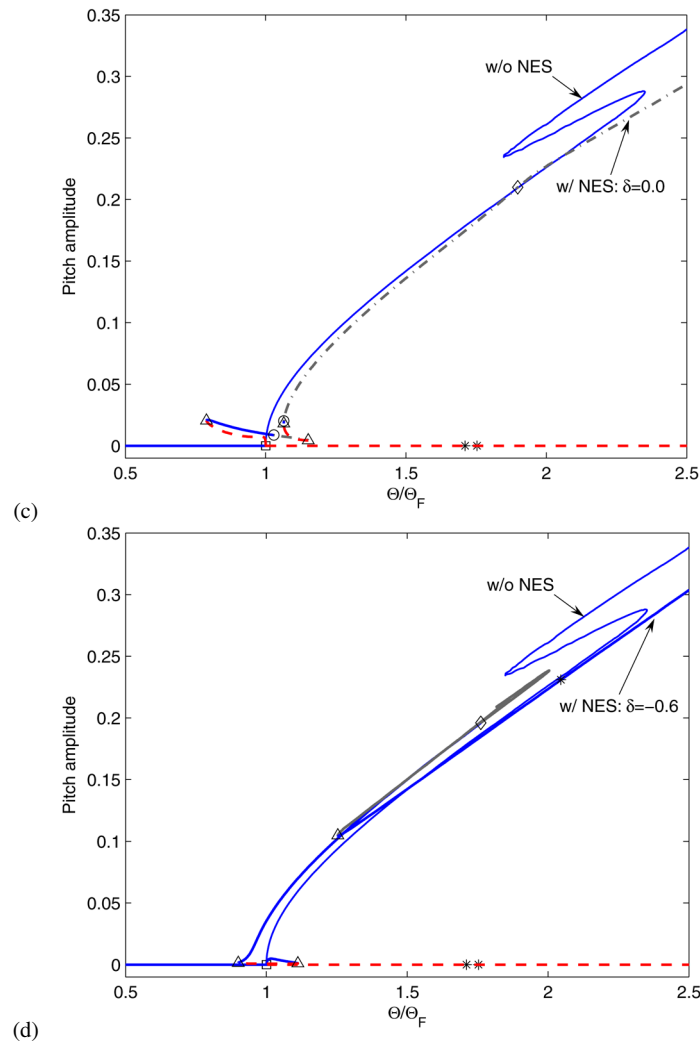


Fig. 9.97 Bifurcation diagram of the pitch response for the wing parameter Set I with respect to the reduced velocity for NES parameters $\varepsilon = 0.05$, $\lambda = 0.05$, $C = 10.0$: (c) $\delta = 0.0$, (d) $\delta = 0.6$; solid (dashed) line indicates a stable (unstable) LCO branch, dash-dotted line a quasi-periodic LCO, and squares (triangles, circles, asterisks, diamonds) Hopf (Saddle-node, Neimark–Sacker, neutral saddle, branch point cycle) bifurcation points.

up to about 5% higher reduced speeds than the linear flutter speed when a 2% NES mass ratio is utilized. If a 5% NES mass ratio is used instead, this robust LCO elimination can be achieved even up to 112% of the linear flutter speed; moreover, robust suppression of aeroelastic instability can be guaranteed up to 130% of the linear flutter speed.

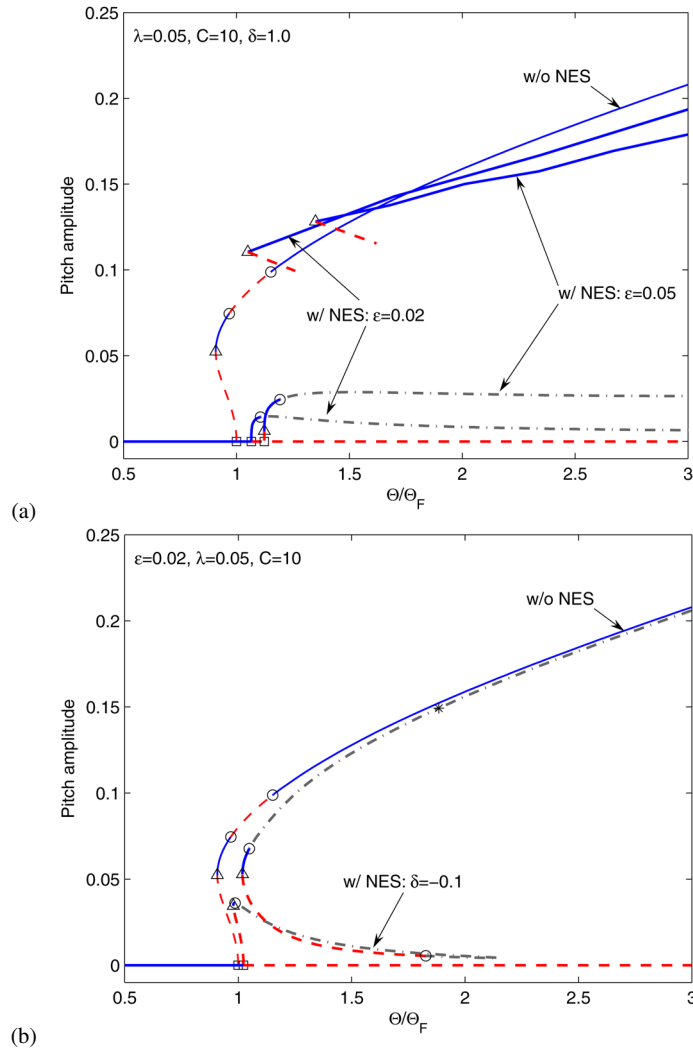


Fig. 9.98 Bifurcation diagram of the pitch response for the wing parameter Set II with respect to the reduced velocity for NES parameters $\varepsilon = 0.02$, $\lambda = 0.05$, $C = 10.0$: (a) $\delta = 1.0$ (the LCO branch for $\varepsilon = 0.05$ is superimposed for the purpose of comparison), (b) $\delta = 0.1$; solid (dashed) line indicates a stable (unstable) LCO branch, dash-dotted line a quasi-periodic LCO, and squares (triangles, circles, asterisks, diamonds) Hopf (Saddle-node, Neimark–Sacker, neutral saddle, branch point cycle) bifurcation points.

Figure 9.99 demonstrates the suppressed aeroelastic responses due to the action of the SDOF NES for the following cases: (a) complete elimination at 112% of U_L^* , and (b) recurring burst-out and suppression of aeroelastic instability at 130% of U_L^* . The wavelet transforms of the aeroelastic responses depicted in Figure 9.100 clearly demonstrate that the underlying dynamic mechanisms for passive LCO suppressions

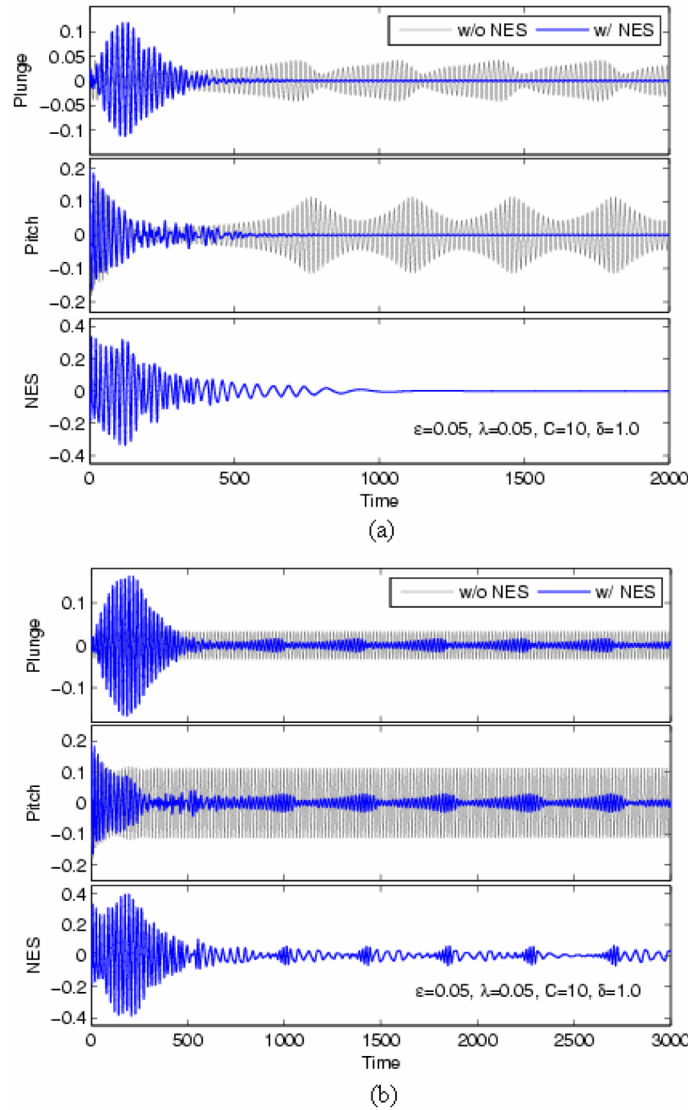


Fig. 9.99 Suppressed aeroelastic responses for parameter Set II and NES parameters $\epsilon = 0.05$, $\lambda = 0.05$, $C = 10.0$ and $\delta = 1.0$: (a) $\Theta/\Theta_F = 1.12$ (third suppression mechanism – complete elimination of aeroelastic instability); (b) $\Theta/\Theta_F = 1.30$ (first suppression mechanism – recurring burst-out and suppression of aeroelastic instability).

is a series of 1:1 to subharmonic transient resonance captures (TRCs), which was also the case in our previous results reported of this chapter.

The three LCO suppression mechanisms identified in our previous studies of the quasi-steady aerodynamic model are also realized in the unsteady aeroelastic model

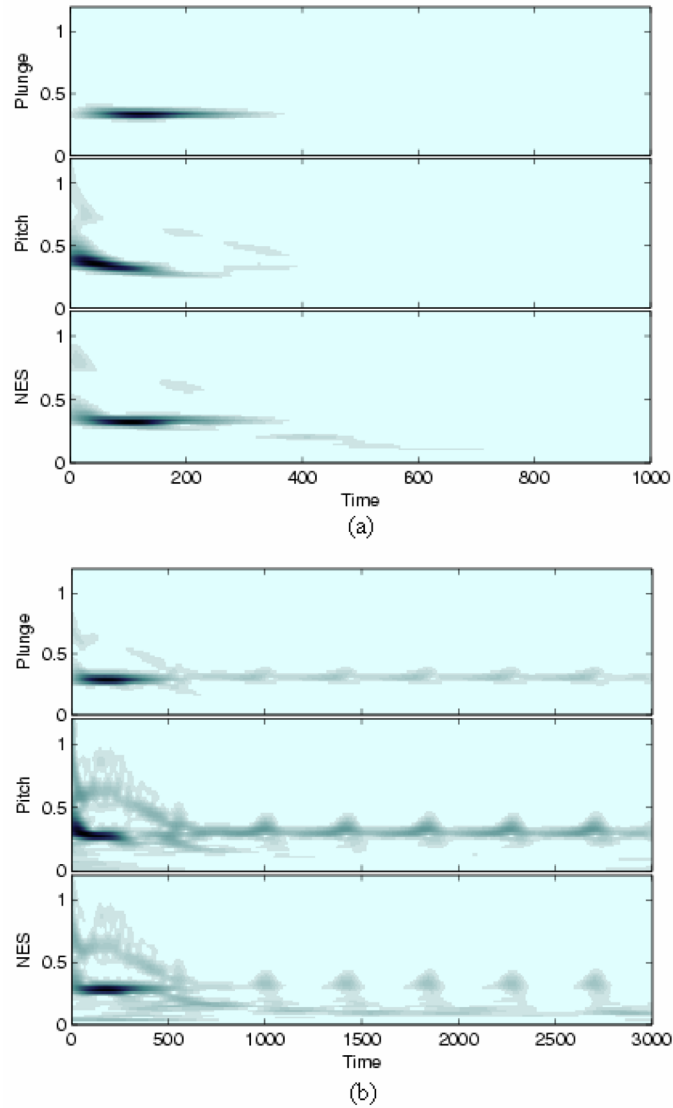


Fig. 9.100 Wavelet transform spectra of the transient responses depicted in Figure 9.99.

(9.97). Although feasibility of TET-based LCO suppression can be demonstrated by the preliminary results reported in this section, further (analytical and numerical) investigation should be performed in order to gain better understanding of the non-linear modal interactions that lead to LCO suppression in the unsteady model, and to perform optimization of the considered NES design.

References

*ReferencesReferencesReferences

- Arnold, V.I., *Dynamical Systems III*, Encyclopaedia of Mathematical Sciences Vol. 3, Springer Verlag, Berlin/New York, 1988.
- Bakhtin, V.I., Averaging in multi-frequency systems, *Funct. Anal. Appl.* **20**, 83–88, 1986 (English translation from *Funkts. Anal. Prilozh.* **20**, 1–7, 1986).
- Blevins, R., *Flow-Induced Vibration*, Van Nostrand Reinhold, New York, 1990.
- Block, J.J., Strganac, T.W., Applied active control for a nonlinear aeroelastic structure, *AIAA J. Guid. Control Dyn.* **21**(6), 838–845, 1998.
- Bunton, R., Denegri Jr., C., Limit cycle oscillation characteristics of fighter aircraft, *AIAA J. Aircraft* **37**, 916–918, 2000.
- Cattarius, J., *Numerical Wing/Store Interaction Analysis of a Parametric F16 Wing*, PhD Thesis, Virginia Polytechnic Institute and State University, 1999.
- Chen, P.C., Sarhaddi, D., Liu, D.D., Limit cycle oscillation studies of a fighter with external stores, AIAA Paper 98-1727, 1998.
- Coller, B.D., Chamara, P.A., Structural non-linearities and the nature of the classic flutter instability, *J. Sound Vib.* **277**, 711–739, 2004.
- Croft, J., Airbus elevator flutter: Annoying or dangerous? *Av. Week Space Tech.* **155**(9), 41, 2001.
- Cunningham, Jr., A.M., The role of non-linear aerodynamics in fluid-structure interaction, AIAA Paper 98-2423, 1998.
- Denegri Jr., C., Limit cycle oscillation flight test results of a fighter with external stores, *AIAA J. Aircraft* **37**, 761–769, 2000.
- Dhooge, A., Govaerts, W., Kuznetsov, Y.A., MATCONT: A Matlab package for numerical bifurcation analysis of ODEs, *ACM Trans. Math. Software* **29**, 141–164, 2003.
- Dowell, E.H., Non-linear oscillator models in bluff body aeroelasticity, *J. Sound Vib.* **75**, 251–264, 1981.
- Dowell, E.H., Crawley, E.E., Curtiss Jr., H.C., Peters, D.A., Scanlan, R.H., Sisto, F., *A Modern Course in Aeroelasticity*. Kluwer, Dordrecht, The Netherlands, 1995.
- Dowell, E.H., Edwards, J., Strganac, T.W., Nonlinear aeroelasticity, *AIAA J. Aircraft* **40**(5), 857–874, 2003.
- Fatimah, S., Verhulst, F., Suppressing flow-induced vibrations by parametric excitation, *Nonl. Dyn.* **23**, 275–297, 2003.
- Friedmann, P.P., Guillot, D., Presente, E., Adaptive control of aeroelastic instabilities in transonic flow and its scaling, *AIAA J. Guid. Control Dyn.* **20**, 1190–1199, 1997.
- Fung, Y., *An Introduction to the Theory of Aeroelasticity*, John Wiley & Sons, New York, 1955.
- Gendelman, O., Transition of energy to a nonlinear localized mode in a highly asymmetric system of two oscillators, *Nonl. Dyn.* **25**(1–3), 237–253, 2001.
- Gendelman, O., Manevitch, L.I., Vakakis, A.F., M'Closkey, R., Energy pumping in nonlinear mechanical oscillators: Part 1 – Dynamics of the underlying Hamiltonian systems, *J. Appl. Mech.* **68**, 34–41, 2001.
- Gilliatt, H., Strganac, T., Kurdila, A., An investigation of internal resonance in aeroelastic systems, *Nonl. Dyn.* **31**, 1–22, 2003.
- Golubitsky, M., Schaeffer, D.G., *Singularities and Groups in Bifurcation Theory I*, Springer-Verlag, Berlin/New York, 1985.
- Govaerts, W.J.F., *Numerical Methods for Bifurcations of Dynamical Equilibria*, SIAM, Philadelphia, PA, 2000.
- Greenlee W., Snow, R., Two-timing on the half line for damped oscillation equations, *J. Math. An. Appl.* **51**, 394–428, 1975.
- Griffin, O.M., Skop, R.A., The vortex-excited resonant vibrations of circular cylinders, *J. Sound Vib.* **27**, 235–249, 1973.
- Guckenheimer, J., Holmes, P., *Nonlinear Oscillations, Dynamical Systems, and Bifurcations of Vector Fields*, Springer-Verlag, Berlin/New York, 1983.

- Hartwich, P.M., Dobbs, S.K., Arslan, A.E., Kim, S.C., Navier–Stokes computations of limit cycle oscillations for a B-1-like configuration, AIAA Paper 2000-2338, 2000.
- Huang, N., Shen, Z., Long, S., Wu, M., Shih, H., Zheng, Q., Yen, N.-C., Tung, C., Liu, H., The empirical mode decomposition and the Hilbert spectrum for nonlinear and non-stationary time series analysis, *Proc. Royal Soc. London A* **454**(1971), 903–995, 1998.
- Jones, R.T., The unsteady lift of a wing of finite aspect ratio, NACA Report 681, 1940.
- Keener, J., *On the validity of the two-timing method for large times*, *SIAM J. Math. An.* **8**, 1067–1091, 1977.
- Keener, J., *Principles of Applied Mathematics: Transformation and Approximation*, Westview Press, Boulder, CO, 2000.
- Kerschen, G., Vakakis, A.F., Lee, Y.S., McFarland, D.M., Kowtko, J.J., Bergman, L.A., Energy transfers in a system of two coupled oscillators with essential nonlinearity: 1:1 resonance manifold and transient bridging orbits, *Nonl. Dyn.* **42**, 282–303, 2005.
- Kerschen, G., Lee, Y.S., Vakakis, A.F., McFarland, D.M., Bergman, L.A., Irreversible passive energy transfer in coupled oscillators with essential nonlinearity, *SIAM J. Appl. Math.* **66**(2), 648–679, 2006a.
- Kerschen, G., Vakakis, A., Lee, Y.S., McFarland, D.M., Bergman, L.A., Toward a fundamental understanding of the Hilbert–Huang transform, in *Proc. Int. Modal An. Conf. (IMAC) 24*, Paper 31, Society for Experimental Mechanics, Bethel, CT, 2006b.
- Kerschen, G., Kowtko, J.J., McFarland, D.M., Bergman, L.A., Vakakis, A.F., Theoretical and experimental study of multi-modal targeted energy transfer in a system of coupled oscillators, *Nonl. Dyn.* **47**(1–3), 285–309, 2007a.
- Kerschen, G., McFarland, D.M., Kowtko, J.J., Lee, Y.S., Bergman, L.A., Vakakis, A.F., Experimental demonstration of transient resonance capture in a system of two coupled oscillators with essential stiffness nonlinearity, *J. Sound Vib.* **299**(4–5), 822–838, 2007b.
- Ko, J., Kurdila, A., Strganac, T., Nonlinear control of a prototypical wing section with torsional nonlinearity, *AIAA J. Guid. Control Dyn.* **20**, 1181–1189, 1997.
- Ko, J., Strganac, T.W., Kurdila, A.J., Adaptive linearization for the control of a typical wing section with torsional nonlinearity, *Nonl. Dyn.* **18**(3), 289–301, 1999.
- Kubíček, M., Dependence of solution of nonlinear systems on a parameter, *ACM Trans. Math. Software* **2**, 98–107, 1976.
- Kuznetsov, Y., *Elements of Applied Bifurcation Theory*, Springer Verlag, Berlin/New York, 1995.
- Lee, B.H.K., Desrochers, J., Flutter analysis of a two-dimensional airfoil containing structural nonlinearities, National Aeronautical Establishment, Aeronautical Report LR-618, National Research Council (Canada), No. 27833, Ottawa, PQ, Canada, 1987.
- Lee, B.H.K., Gong, L., Wong, Y., Analysis and computation of nonlinear dynamic response of a two-degree-of-freedom system and its application in aeroelasticity, *J. Fluids Str.* **11**, 225–246, 1997.
- Lee, B.H.K., LeBlanc, P., Flutter analysis of a two-dimensional airfoil with cubic nonlinear restoring force, National Aeronautical Establishment, Aeronautical Note 36, National Research Council (Canada) No. 25438, Ottawa, PQ, Canada, 1986.
- Lee, Y.S., Kerschen, G., Vakakis, A.F., Panagopoulos, P., Bergman, L.A., McFarland, D.M., Complicated dynamics of a linear oscillator with a light, essentially nonlinear attachment, *Physica D* **204**, 41–69, 2005a.
- Lee, Y.S., Vakakis, A.F., Bergman, L.A., McFarland, D.M., Kerschen, G., Triggering mechanisms of limit cycle oscillations in a two-degree-of-freedom wing flutter model, *J. Fluids Str.* **21**(5–7), 485–529, 2005b.
- Lee, Y.S., Vakakis, A., Bergman, L., McFarland, D.M., *Suppression of limit cycle oscillations in the van der Pol oscillator by means of passive nonlinear energy sinks (NESs)*, *Struct. Control Health Mon.* **13**(1), 41–75, 2006.
- Lee, Y.S., Vakakis, A., Bergman, L., McFarland, D.M., Kerschen, G., Suppression of aeroelastic instability using broadband passive targeted energy transfers I: Theory, *AIAA J.* **45**(3), 693–711, 2007a.

- Lee, Y.S., Kerschen, G., McFarland, D.M., Hill, W.J., Nickkawde, C., Strganac, T.W., Bergman, L.A., Vakakis, A.F., Suppression of aeroelastic instability by means of broadband passive targeted energy transfers II: experiments, *AIAA J.* **45**(12), 2391–2400, 2007b.
- Lee, Y.S., Vakakis, A.F., Bergman, L.A., McFarland, D.M., Kerschen, G., Enhancing robustness of aeroelastic instability suppression using multi-degree-of-freedom nonlinear energy sinks, *AIAA J.*, 2008 (in press).
- Lind, R., Snyder, K., Brenner, M., Wavelet analysis to characterise non-linearities and predict limit cycles of an aeroelastic system, *Mech. Syst. Signal Proc.* **15**, 337–356, 2001.
- Liu, L., Dowell, E., The secondary bifurcation of an aeroelastic airfoil motion: Effect of high harmonics, *Nonl. Dyn.* **37**, 31–49, 2004.
- Manevitch, L., The description of localized normal modes in a chain of nonlinear coupled oscillators using complex variables, *Nonl. Dyn.* **25**, 95–109, 2001.
- Masri, S.F., Caughey, T.K., Nonparametric identification technique for nonlinear dynamic systems, *J. Appl. Mech.* **46**, 433–447, 1979.
- McFarland, D.M., Bergman, L.A., Vakakis, A.F., Experimental study of nonlinear energy pumping occurring at a single fast frequency, *Int. J. Nonl. Mech.* **40**(6), 891–899, 2005a.
- McFarland, D.M., Kerschen, G., Kowtko, J.J., Bergman, L.A., Vakakis, A.F., Experimental investigation of targeted energy transfers in strongly and nonlinearly coupled oscillators, *J. Acoust. Soc. Am.* **118**(2), 791–799, 2005b.
- Nayfeh, A.H., Mook, D.T., *Nonlinear Oscillations*, Wiley Interscience, New York, 1995.
- O'Neil, T., Nonlinear aeroelastic response – Analyses and experiments, AIAA Paper 96-0014, 1996.
- O'Neil, T., Gilliatt, H., and Strganac, T. W., Investigations of aeroelastic response for a system with continuous structural nonlinearities, AIAA Paper 96-1390, 1996.
- O'Neil, T., Strganac, T., Aeroelastic response of a rigid wing supported by nonlinear springs, *AIAA J. Aircraft* **35**, 616–622, 1998.
- Panagopoulos, P., Vakakis, A., Tsakirtzis, S., Transient resonant interactions of finite linear chains with essentially nonlinear end attachments leading to passive energy pumping, *Int. J. Solids Str.* **41**(22–23), 6505–6528, 2004.
- Platanitis, G., Strganac, T.W., Control of a nonlinear wing section using leading- and trailing-edge surfaces, *AIAA J. Guid. Control Dyn.* **27**(1), 52–58, 2004.
- Quinn, D., Resonance capture in a three degree-of-freedom mechanical system, *Nonl. Dyn.* **14**, 309–333, 2007.
- Rilling, G., Flandrin, P., Gonçalves, P., On empirical mode decomposition and its algorithms, IEEE-Eurasip Workshop on Nonlinear Signal and Image Processing (NSIP-03), Grado, Italy, 2003.
- Sheta, E.F., Harrand, V.J., Thompson, D.E., Strganac, T.W., Computational and experimental investigation of limit cycle oscillations in nonlinear aeroelastic systems, AIAA Paper 2000-1399, 2000.
- Sheta, E.F., Harrand, V.J., Thompson, D.E., Strganac, T.W., Computational and experimental investigation of limit cycle oscillations of nonlinear aeroelastic systems, *AIAA J. Aircraft* **39**, 133–141, 2002.
- Singh, S., Brenner, M., Limit cycle oscillation and orbital stability in aeroelastic systems with torsional nonlinearity, *Nonl. Dyn.* **31**, 435–450, 2003.
- Skop, R.A., Griffin, O.M., A model for the vortex-excited resonant response of bluff cylinders, *J. Sound Vib.* **27**, 225–233, 1973.
- Tang, D., Dowell, E., Experimental and theoretical study on aeroelastic response of high-aspect-ratio wings, *AIAA J.* **39**(8), 1430–1441, 2001.
- Thompson, Jr., D.E., Strganac, T.W., Store-induced limit cycle oscillations and internal resonances in aeroelastic systems, AIAA Paper 2000-1413, 2000.
- Tondl, A., Ruijgrok, M., Verhulst, F., Nabergoj, R., *Autoparametric Resonance in Mechanical Systems*, Cambridge University Press, New York, 2000.

- Tsakirtzis, S., Panagopoulos, P., Kerschen, G., Gendelman, O., Vakakis, A., Bergman, L., Complex dynamics and targeted energy transfers in linear oscillators coupled to multi-degree-of-freedom essentially nonlinear attachments, *Nonl. Dyn.* **48**(3), 285–318, 2007.
- Vakakis, A.F., Gendelman, O., Energy pumping in nonlinear mechanical oscillators Part II: Resonance capture, *J. Appl. Mech.* **68**, 42–48, 2001.
- Vakakis, A.F., Manevitch, L.I., Gendelman, O., Bergman, L.A., Dynamics of linear discrete systems connected to a local essentially nonlinear attachment, *J. Sound Vib.* **264**, 559–577, 2003.
- Vakakis, A.F., Manevitch, L.I., Mikhlin, Y.V., Pilipchuk, V.N., Zevin, A.A., *Normal Modes and Localization in Nonlinear Systems*, J. Wiley & Sons, New York, 1996.
- Vakakis, A.F., McFarland, D.M., Bergman, L.A., Manevitch, L.I., Gendelman, O., Isolated resonance captures and resonance capture cascades leading to single-or multi-mode passive energy pumping in damped coupled oscillators, *J. Vib. Acoust.* **126**(2), 235–244, 2004.
- Zniber, A., Quinn, D., Frequency shifting in nonlinear resonant systems with damping, Proceedings of ASME Design Engineering Technical Conferences and Computers and Information in Engineering Conference, DETC2003 /VIB-48444, Chicago, Illinois, 2003.

Chapter 10

Seismic Mitigation by Targeted Energy Transfer

In this chapter we examine the application of NESs to the problem of seismic protection of frame structures, though other infrastructural systems such as towers, bridges, and so forth will likely benefit from this technology. As has often been noted, infrastructure in the United States alone constitutes a societal investment counted in the trillions of dollars. While the fraction of infrastructure vulnerable to large-scale earthquakes is relatively limited by geography (i.e., the west coast, midwest and southeast, in addition to Alaska and Hawaii, are historically the most vulnerable areas), seismic activity capable of causing property damage has been recorded throughout the country and around the world. This provides the impetus to develop effective strategies to protect not only new construction but also existing structures likely to be subjected to seismic effects.

Various passive methods for mitigating the effects of earthquakes have been applied to large scale structures, including auxiliary dampers, base isolation systems, tuned mass dampers, as well as active, semi-active and hybrid systems. Detailed descriptions and a comparison of the performance and limitations of each of these are beyond the scope of this chapter. Rather, the interested reader should refer to several excellent monographs, including Soong and Constantinou (1994), Soong (1990), Skinner et al. (1993), Chu et al. (2005), and recent review articles (Housner et al., 1997; Spencer and Sain, 1997; Soong and Spencer, 2002; Spencer and Nagarajaiah, 2003), as well as references therein for details. It seems clear, given the recent extensive body of literature and burgeoning number of isolated structures,¹ that the need exists for a fully passive isolation strategy, lightweight and inexpensive but capable of high performance over an extensive range of earthquakes of different properties.

The aim of this chapter, then, is to demonstrate through several case studies that it is possible to design and implement one or more NESs in a primary linear system with multiple degrees of freedom (DOF) that will passively absorb and dissipate seismic energy drawn from the primary system as well as advantageously redistrib-

¹ According to Spencer and Nagarajaiah (2003), by 2003 more than 40 buildings and 10 bridges were constructed with integral active or hybrid seismic isolation systems. This does not include statistics for passive base isolation systems employing laminated rubber bearings, which for low-rise buildings have become ubiquitous in seismically-active regions.

ute seismic energy within the modes of the primary system, thus enhancing its reliability and enabling performance under widely varying seismic conditions. For an example of an earlier implementation of configurations of linear springs exhibiting geometric nonlinearities for passive seismic attenuation we refer to DeSalvo (2007) and references therein.

Building upon the theoretical underpinnings presented in earlier chapters, we now demonstrate the application of TET to the seismic protection of flexible structures. In the first section, we continue the discussion of the two-DOF linear primary system examined in Chapter 7, assessing through simulation and optimization the capability of the nonlinear energy sink concept for seismic protection. Evaluation procedures, including the choice of historic earthquakes and system performance criteria to be employed throughout this chapter, are defined. Finally, the ability of a single VI NES to mitigate seismic effects is assessed.

In the next section, we examine a more relevant problem: seismic protection of a model three-story, single-bay, two-dimensional steel frame structure using, first, a single VI NES at the top floor and, second, a VI NES at the first floor and a smooth NES at the top floor. The design and optimization of each protective system configuration are discussed, and its performance is assessed both computationally and experimentally.

The final section provides a brief evaluation of protective system performance and offers some insights concerning possible full-scale implementation of the NES concept for seismic protection of civil infrastructural systems.

10.1 The Two-DOF Linear Primary System with VI NES

10.1.1 System Description

The efficacy of TET for reduction of the seismic response of a primary structure depends on the ability of one or more attached NESs to passively absorb and dissipate a significant portion of the seismic energy at a sufficiently fast time scale. This ensures that the response of the primary structure is significantly reduced during the crucial initial few cycles of the strong motion. Thus, we will first perform a study of the proposed concept by considering a simple linear primary system and developing an optimization procedure for choosing the parameters of the protective system so that its action is compatible with our design objectives. For this, we employ a two degree of freedom linear primary system attached to an ungrounded VI NES. This type of NES, using clearances and impact to achieve the essential nonlinearity, promotes strongly nonlinear behavior of the full system (Georgiades, 2006; Karayannis et al., 2008; Lee et al., 2008).

Following Nucera (2005) and Nucera et al. (2007), the integrated system consisting of the linear primary structure connected to the VI NES is shown in Figure 10.1. The NES mass m_3 is connected to the primary structure through a weak

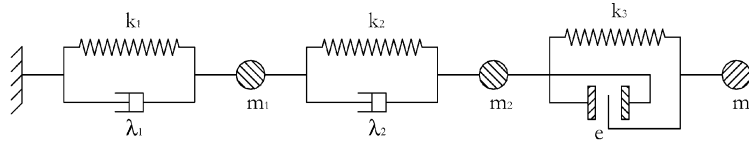


Fig. 10.1 Two-DOF linear system with VI NES.

linear spring² k_3 . Two rigid stops constrain the relative displacement between m_2 and m_3 to be less than or equal to the specified clearance e .

For simplicity, let the primary two degree of freedom linear system be proportionally damped, and let ζ_1 and ζ_2 be the assumed (small) viscous damping ratios. In modal coordinates, the diagonal damping matrix will have the form

$$\hat{C} = \begin{bmatrix} 2\zeta_1\omega_1 & 0 \\ 0 & 2\zeta_2\omega_2 \end{bmatrix} \quad (10.1)$$

and, in physical coordinates,

$$C = M\Phi\hat{C}\Phi^{-1} = M\Phi\hat{C}\Phi^T M \quad (10.2)$$

where M is the mass matrix and Φ is the normalized modal matrix.

Within the NES, the relation for the absolute velocities, with respect to a fixed reference frame, of the colliding masses before and after each impact is given by the expression

$$v'_2 - v'_3 = rc(v_3 - v_2) \quad (10.3)$$

where $v_i = \dot{u}_{ai}$ is the absolute velocity of mass m_i ($i = 2, 3$) before impact, the prime denotes 'after impact', and rc is the coefficient of restitution. While energy is not conserved through each impact due to the required condition $rc < 1$, momentum is conserved. Thus,

$$m_2v_2 + m_3v_3 = m_2v'_2 + m_3v'_3 \quad (10.4)$$

The equations of motion of the system depicted in Figure 10.1 are given by

$$M\ddot{u} + C\dot{u} + Ku = -MI_0\ddot{u}_g \quad (10.5)$$

where M , C , and K are, respectively, the mass, damping and stiffness matrices given by

$$M = \begin{bmatrix} m_1 & 0 & 0 \\ 0 & m_2 & 0 \\ 0 & 0 & m_3 \end{bmatrix}, \quad C = \begin{bmatrix} \lambda_1 + \lambda_2 & -\lambda_2 & 0 \\ -\lambda_2 & \lambda_2 & 0 \\ 0 & 0 & 0 \end{bmatrix},$$

² The weak linear spring functions strictly as a centering device for the VI NES. The interpretation of essential nonlinearity in this case should be modified to include 'nearly' essential nonlinearity.

$$K = \begin{bmatrix} k_1 + k_2 & -k_2 & 0 \\ -k_2 & k_2 + k_3 & -k_3 \\ 0 & -k_3 & k_3 \end{bmatrix}$$

The displacement vector, relative to ground, is $u = [u_1 \ u_2 \ u_3]^T$, \ddot{u}_g is the specified ground acceleration, and $I_0 = [1 \ 1 \ 1]^T$ is a distribution vector.

In all of the simulations to follow in this section, we will assume that $m_1 = m_2 = 2.9 \times 10^6$ kg, $k_1 = k_2 = 2.5 \times 10^7$ N/m, $\zeta_1 = \zeta_2 = 0.01$, $\lambda_1 = 7.62 \times 10^4$ N-sec/m, and $\lambda_2 = 1.52 \times 10^5$ N-sec/m.

10.1.2 Simulation and Optimization

An extensive series of simulations employing Matlab[®] as the computational engine was completed. The simulation code determined precisely when impacts occurred in the VI NES and solved a series of linear problems between them, accounting for dissipation due to inelastic impacts between masses m_2 and m_3 . The response of the full system, including the VI NES, was determined for four historic earthquakes as the excitation source. These included:

- El Centro, N-S component – May 18, 1940;
- Hachinohe, N-S component – May 16, 1968;
- Kobe, N-S component – January 17, 1995; and
- Northridge, N-S component – January 16, 1994.

As discussed in significant detail in Nucera (2005) and Nucera et al. (2007), these four were chosen as representative of two distinct classes of earthquakes. The first, containing the El Centro and Hachinohe records, are characterized by longer effective ground motion duration and smaller peak ground acceleration and velocity, while the second, containing Kobe and Northridge, exhibit shorter duration but larger peak ground acceleration and velocity. As noted in the references, Kobe has the highest energy content and destructive capacity of the four records.

The design space for the system optimization encompassed three VI NES parameters: mass m_3 , weak linear stiffness coefficient k_3 , and clearance e . The eight evaluation criteria, J_i , $i = 1, \dots, 8$, employed to assign quantitative measures of performance to the computed seismic response of the system, were those introduced by Spencer et al. (1998a, b) in the context of a moderated benchmark control problem for a seismically excited structure.

$$J_1 = \max_{\text{earthquakes}} \left\{ \frac{\max_{i \in \eta} |u_i(t)|}{u^{\max}} \right\} \quad (10.6)$$

The first criterion (10.6) is a non-dimensional measure of the displacement relative to ground motion. Here, η represents the set of computed relative displacements,

and u^{\max} is maximum relative displacement for the uncontrolled (no NES) linear structure.

$$J_2 = \max_{\text{earthquakes}} \left\{ \frac{\max_{t,i} \frac{|d_i(t)|}{h_i}}{d_n^{\max}} \right\} \quad (10.7)$$

The second criterion (10.7) is a normalized interstory drift ratio, where $d_i(t) = u_i(t) - u_{i-1}(t)$ is the time history of the i -th interstory drift, h_i is the i -th interstory height, and d_n^{\max} is the maximum interstory drift for the uncontrolled structure.

$$J_3 = \max_{\text{earthquakes}} \left\{ \frac{\max_{t, i \in \eta} |\ddot{u}_{ai}(t)|}{\ddot{u}_a^{\max}} \right\} \quad (10.8)$$

The third criterion (10.8) is a normalized maximum absolute acceleration. Here, $\ddot{u}_{ai}(t)$ is the time history of absolute acceleration for the i -th degree of freedom, and \ddot{u}_a^{\max} is the maximum acceleration over all degrees of freedom for the uncontrolled structure.

$$J_4 = \max_{\text{earthquakes}} \left\{ \frac{\max_t \sum_{i \in \eta} m_i \ddot{u}_{ai}(t)}{F_b^{\max}} \right\} \quad (10.9)$$

The fourth criterion (10.9) is a normalized inertial force ratio, where F_b^{\max} is the maximum base shear force for the uncontrolled structure.

$$J_5 = \max_{\text{earthquakes}} \left\{ \frac{\max_{i \in \eta} \|u_i(t)\|}{\|u^{\max}\|} \right\} \quad (10.10)$$

The fifth criterion (10.10) is the L_2 -normed measure of structural response. Here,

$$\|u_i(t)\| = \left\{ \int_0^{t_f} u_i^t(t) dt \right\}^{1/2}$$

t_f is a sufficiently large time permitting the response of the structure to attenuate to less than 0.1% of its maximum value, and $\|u^{\max}\| = \max_{i \in \eta} \|u_i(t)\|$ is the maximum normed uncontrolled displacement.

$$J_6 = \max_{\text{earthquakes}} \left\{ \frac{\max_{i,j} \frac{\|d_i(t)\|}{h_i}}{\|d_n^{\max}\|} \right\} \quad (10.11)$$

The sixth criterion (10.11) is a normed interstory drift ratio, where $\|d_n^{\max}\|$ is the maximum normed interstory drift for the uncontrolled structure.

$$J_7 = \max_{\text{earthquakes}} \left\{ \frac{\max_{i \in \eta} \|\ddot{u}_{ai}(t)\|}{\|\ddot{u}_a^{\max}\|} \right\} \quad (10.12)$$

The seventh criterion (10.12) is the normed absolute acceleration ratio, where $\|\ddot{u}_a^{\max}\|$ is the maximum normed absolute acceleration of the uncontrolled structure.

$$J_8 = \max_{\text{earthquakes}} \left\{ \frac{\sum_{i \in \eta} m_i \ddot{u}_{a\eta i}(t)}{\|F_b^{\max}\|} \right\} \quad (10.13)$$

The final criterion (10.13) is a normed inertial force ratio, where $\|F_b^{\max}\|$ is the maximum normed base shear force for the uncontrolled structure. We note here that all of the criteria are applied over the array of four historic earthquakes.

The method employed to optimize the parameters of the VI NES is *Differential Evolution* (Storn and Price, 1997), a global evolutionary procedure. In all of the analyses performed, the weak linear spring associated with the VI NES was fixed at $k_3 = 0.02k_1$. While each of the afore-mentioned criteria was evaluated over the array of four historic earthquakes, sufficient additional computations were completed to facilitate the determination of an optimal solution corresponding to each historic earthquake. Following Nucera (2005), a series of Pareto optimizations were performed utilizing the objective function

$$\text{OF} = J_1 + J_2 + J_5 + J_6 \quad (10.14)$$

10.1.3 Computational Results

In results that follow, a subset of cases considered most significant are given. Table 10.1 summarizes the optimal clearance values over the earthquake array, mass ratio, and coefficient of restitution, and Tables 10.2 through 10.5 provide numerical values of the evaluation criteria corresponding to the computed optimal clearances.

Evaluation of the ability of the system to effectively dissipate energy was accomplished through an energy balance. Components considered included the seismic energy input to the system, the kinetic and strain energies, the energy dissipated in the linear primary structure, and the energy dissipated by the NES through vibro-impacts. The last of these is a consequence of two effects: (i) transient resonance capture, during which significant dissipation occurs due to repeated strong inelastic impacts (as discussed in Chapter 7); and (ii) energy spreading from high amplitude, low frequency modes of the system to low amplitude, high frequency modes, where

Table 10.1 Optimal VI NES clearances (m), two-DOF system.

Earthquake	Mass ratio %	Coefficient of restitution			
		0.5	0.6	0.7	0.8
El Centro	10	0.20	0.14	0.17	0.14
	15	0.15	0.14	0.13	0.15
	20	0.10	0.10	0.11	0.19
Hachinohe	10	0.31	0.31	0.33	0.35
	15	0.31	0.30	0.31	0.32
	20	0.22	0.21	0.22	0.31
Kobe	10	0.32	0.37	0.38	0.39
	15	0.33	0.33	0.34	0.37
	20	0.32	0.29	0.33	0.37
Northridge	10	0.80	0.81	0.80	0.85
	15	0.70	0.70	0.72	0.75
	20	0.59	0.63	0.66	0.69

Table 10.2 El Centro earthquake evaluation criteria, two-DOF system.

Coefficient of restitution	Mass ratio %	J ₁	J ₂	J ₃	J ₄	J ₅	J ₆	J ₇	J ₈
		0.5	10	0.68	0.60	0.93	0.59	0.50	0.50
15	0.63		0.60	0.99	0.55	0.47	0.46	0.55	0.46
20	0.63		0.62	0.99	0.56	0.47	0.46	0.63	0.45
0.6	10	0.69	0.71	0.96	0.70	0.51	0.51	0.71	0.50
	15	0.63	0.61	1.04	0.57	0.46	0.46	0.66	0.46
	20	0.62	0.62	1.00	0.59	0.49	0.48	0.68	0.48
0.7	10	0.72	0.66	0.96	0.65	0.50	0.51	0.82	0.51
	15	0.63	0.63	1.02	0.62	0.47	0.48	0.78	0.47
	20	0.62	0.62	1.02	0.58	0.51	0.50	0.75	0.49
0.8	10	0.69	0.75	0.97	0.74	0.60	0.59	0.78	0.59
	15	0.62	0.60	1.03	0.59	0.58	0.57	0.73	0.57
	20	0.56	0.56	1.04	0.58	0.50	0.52	0.79	0.52

it is more readily dissipated by viscous effects. Both of these are beneficial effects in the seismic environment, particularly for strong motion earthquakes.

Of interest here is the energy ratio E_{SS}/E_I , where E_{SS} is the energy dissipated by the NES through both vibro-impacts and viscous dissipation and E_I is the total input seismic energy. This ratio must be computed at each vibro-impact. We first compute the total input energy less the energy dissipated by the NES relative to the fixed frame, given by

$$E_{I-S} = E_K + E_D + E_P \tag{10.15}$$

Letting $u_a, \dot{u}_a, \ddot{u}_a$ be the absolute displacement, velocity and acceleration vectors and u, \dot{u}, \ddot{u} the displacement, velocity and acceleration vectors relative to ground,

$$E_{I-S} = \int_0^t [(M\ddot{u}_a)^T + (C\dot{u} + Ku)^T] \dot{u}_a dt \tag{10.16}$$

The energy dissipated by the VI NES for each impact is given by

Table 10.3 Hachinohe earthquake evaluation criteria, two-DOF system.

Coefficient of restitution	Mass ratio %	J ₁	J ₂	J ₃	J ₄	J ₅	J ₆	J ₇	J ₈
0.5	10	0.50	0.46	0.56	0.46	0.35	0.34	0.42	0.33
	15	0.47	0.46	0.51	0.46	0.36	0.36	0.45	0.36
	20	0.44	0.46	0.57	0.47	0.29	0.28	0.37	0.29
0.6	10	0.50	0.46	0.55	0.46	0.32	0.31	0.40	0.30
	15	0.46	0.46	0.51	0.46	0.32	0.31	0.39	0.31
	20	0.43	0.46	0.57	0.46	0.29	0.29	0.39	0.29
0.7	10	0.49	0.46	0.53	0.46	0.33	0.32	0.41	0.31
	15	0.45	0.46	0.49	0.46	0.32	0.32	0.42	0.32
	20	0.44	0.46	0.63	0.46	0.30	0.30	0.45	0.30
0.8	10	0.50	0.46	0.62	0.46	0.33	0.32	0.39	0.31
	15	0.44	0.46	0.57	0.46	0.33	0.33	0.52	0.33
	20	0.43	0.46	0.58	0.46	0.32	0.33	0.56	0.33

Table 10.4 Kobe earthquake evaluation criteria, two-DOF system.

Coefficient of restitution	Mass ratio %	J ₁	J ₂	J ₃	J ₄	J ₅	J ₆	J ₇	J ₈
0.5	10	0.78	0.76	0.66	0.81	1.00	0.79	0.68	0.88
	15	0.81	0.85	0.59	0.94	0.99	0.75	0.52	0.83
	20	0.82	0.86	0.59	0.94	0.94	0.74	0.62	0.82
0.6	10	0.79	0.65	0.59	0.68	1.00	0.76	0.54	0.84
	15	0.77	0.63	0.54	0.68	0.99	0.73	0.43	0.81
	20	0.75	0.63	0.54	0.68	1.06	0.78	0.49	0.87
0.7	10	0.79	0.65	0.58	0.69	1.14	0.84	0.48	0.93
	15	0.77	0.63	0.54	0.68	1.13	0.83	0.47	0.93
	20	0.78	0.63	0.54	0.68	1.02	0.76	0.56	0.85
0.8	10	0.79	0.64	0.66	0.71	1.33	0.97	0.51	1.08
	15	0.82	0.63	0.60	0.68	1.28	0.93	0.49	1.03
	20	0.82	0.65	0.54	0.71	1.18	0.87	0.50	0.97

$$E_S = \frac{1}{2}(m_2 v_2^2 + m_3 v_3^2) - \frac{1}{2}(m_2 v_2'^2 + m_3 v_3'^2) \quad (10.17)$$

Thus, $E_{SS} = E_S + E_D$, with $E_I = E_{I-S} + E_S$ evaluated immediately after each impact.

The responses of the system with the VI NES compared to those without the VI NES, the relative motion between mass m_2 and the VI NES m_3 , and the energy ratio E_{SS}/E_I are shown in Figures 10.2 through 10.4, for three specific cases sampled from Table 10.1. In general, over the range of cases examined, we noted that the optimal clearance decreases with increasing mass ratio. Furthermore, at each mass ratio, the optimal clearance appeared to be not sensitive to the coefficient of restitution but, rather, to the inherent characteristics of the individual historic earthquakes.

As noted in Chapter 7, there are two fundamental dynamic mechanisms that govern the interaction between the seismically excited primary structure and VI NES. The first of these is targeted energy transfer (TET), which leads to dissipation of a significant portion of input energy early in the regime of strong motion. This is due to a 1:1 transient resonance capture, and as shown earlier there is a time window dur-

Table 10.5 Northridge earthquake evaluation criteria, two-DOF system.

Coefficient of restitution	Mass ratio %	J_1	J_2	J_3	J_4	J_5	J_6	J_7	J_8
0.5	10	0.77	0.73	0.83	0.66	0.40	0.38	0.56	0.37
	15	0.72	0.66	0.75	0.66	0.34	0.31	0.40	0.31
	20	0.66	0.64	0.67	0.66	0.33	0.31	0.45	0.31
0.6	10	0.77	0.77	0.83	0.66	0.44	0.43	0.61	0.41
	15	0.71	0.65	0.74	0.66	0.37	0.34	0.42	0.33
	20	0.67	0.64	0.67	0.66	0.34	0.31	0.38	0.31
0.7	10	0.81	0.74	0.81	0.66	0.50	0.47	0.54	0.46
	15	0.72	0.67	0.74	0.66	0.40	0.39	0.54	0.38
	20	0.67	0.64	0.67	0.66	0.36	0.34	0.45	0.34
0.8	10	0.83	0.85	0.93	0.66	0.53	0.50	0.61	0.48
	15	0.74	0.75	0.78	0.73	0.46	0.43	0.53	0.42
	20	0.68	0.75	0.72	0.72	0.38	0.39	0.68	0.37

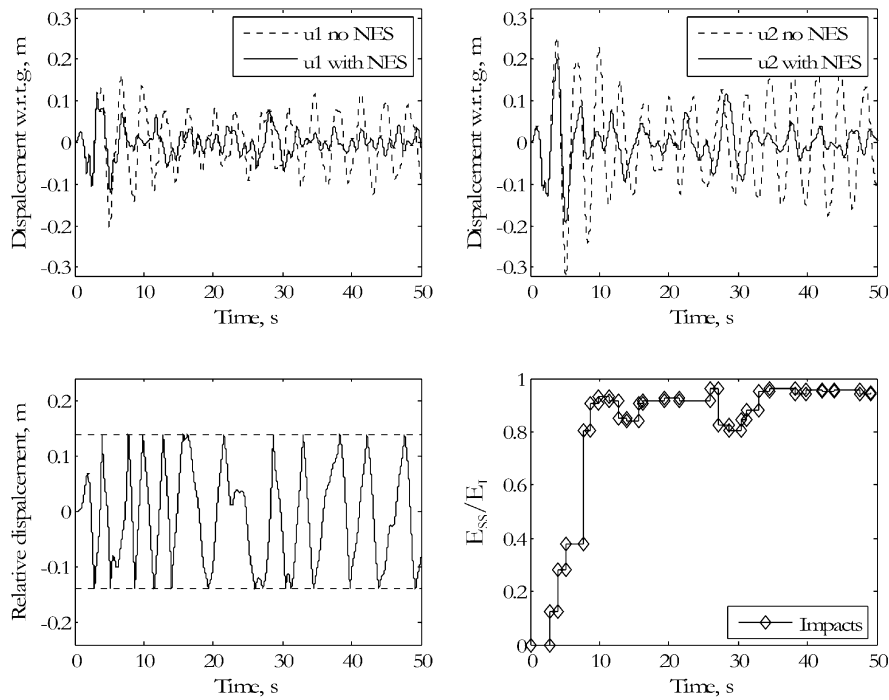


Fig. 10.2 Responses of the two-DOF system with VI NES to the El Centro earthquake: controlled and uncontrolled relative displacements (top); relative displacement of the NES and energy dissipation due to vibro-impacts (bottom).

ing which the VI NES oscillates with frequency approximately equal to one of the modes of the primary structure until a sufficient fraction of energy is dissipated, and escape from capture occurs. In fact, the fast scale of the VI NES dynamics enables the absorption and dissipation through inelastic impacts during the initial phase of

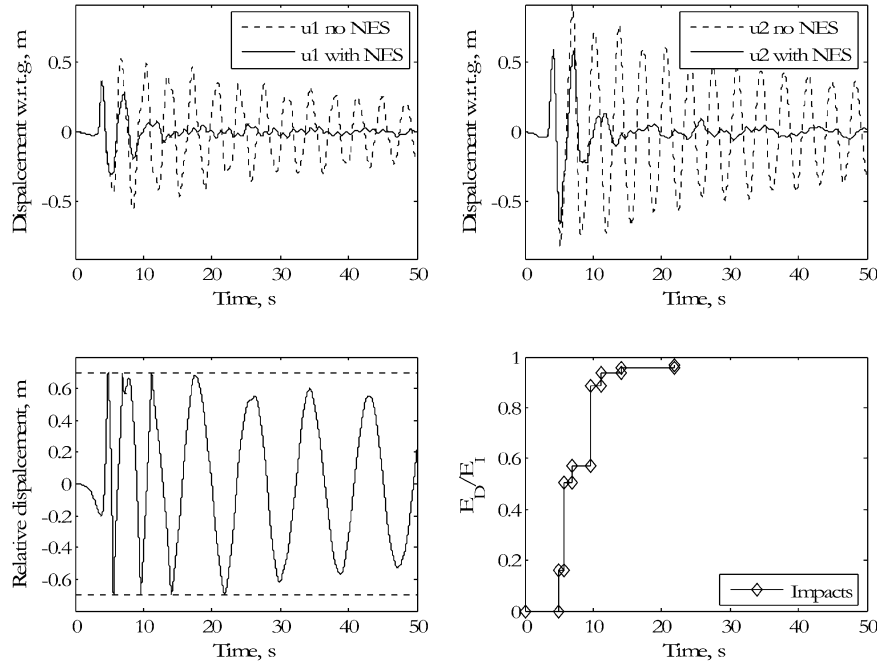


Fig. 10.3 Responses of the two-DOF system with VI NES to the Northridge earthquake: controlled and uncontrolled relative displacements (top); relative displacement of the NES and energy dissipation due to vibro-impacts (bottom).

the high-energy strong ground motion, the critical first few cycles of seismic response. This results in a significant reduction of the maximum levels of seismic response of the primary structure, which is a necessary condition for prevention of catastrophic failure in, for example, connections between floor beams and columns of the structure. These fast scales cannot be realized with smooth (i.e., continuous) nonlinearities; thus, the discontinuous nature of the VI NES is key to the successful application of TET to seismic mitigation in large structures.

The second mechanism acting between the primary system and VI NES is energy redistribution from the lower modes of the integrated system to the higher modes due to vibro-impacts in the VI NES. The consequence of this energy transfer from high-amplitude, low-frequency to low-amplitude, high-frequency modes is more effective dissipation due to viscous damping. While this effect is likely to be more pronounced in large scale systems with many degrees of freedom, it is also visible in the energy balance previously discussed.

An examination of the performance of the system, as shown in Figures 10.2 through 10.4, reveals that a significant amount of energy is dissipated within the first five vibro-impacts. These vibro-impacts involve sudden changes in velocity and, hence, often result in large accelerations. Thus, the passively controlled accelerations, reflected in evaluation criteria J_3 , J_4 , J_7 and J_8 , were not included in

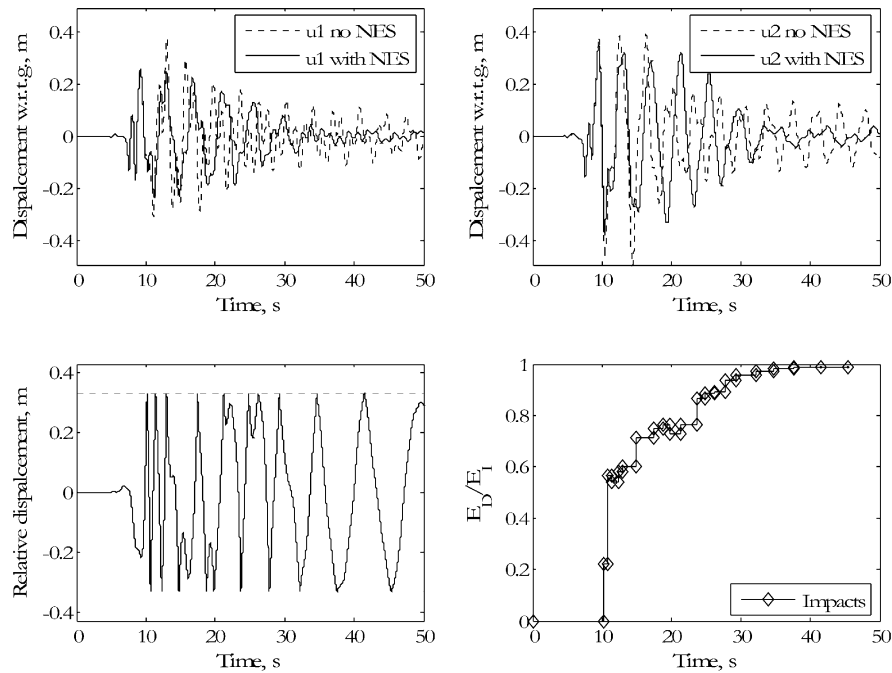


Fig. 10.4 Responses of the two-DOF system with VI NES to the Kobe earthquake: controlled and uncontrolled relative displacements (top); relative displacement of the NES and energy dissipation due to vibro-impacts (bottom).

the objective function. However, the remarkably short reaction time of the VI NES, affecting the amplitude of even the first cycle of response of the primary system, makes it a valuable protective component. As demonstrated in Tables 10.2 through 10.5, use of the VI NES provided reductions in maximum displacement (J_1) and maximum interstory drift (J_2) of 40% and 50%, respectively, for both the El Centro and Hachinohe earthquakes. For the most severe historic earthquake studied, the Kobe, the figures were 25% and 37%; and for the Northridge, 34% and 36%.

10.2 Scaled Three-Story Steel Frame Structure with NESs

In this section we examine the application of TET to a scaled three-story frame structure, subjected to the same four historic earthquakes introduced in Section 10.1. The structure was designed and built in the Linear and Nonlinear Dynamics and Vibrations Laboratory (LNDVL) at the University of Illinois at Urbana-Champaign. The problem was motivated by a recent series of benchmarks designed to challenge the structural control community (Spencer et al., 1998a, b, c; Ohtori et al., 2004),

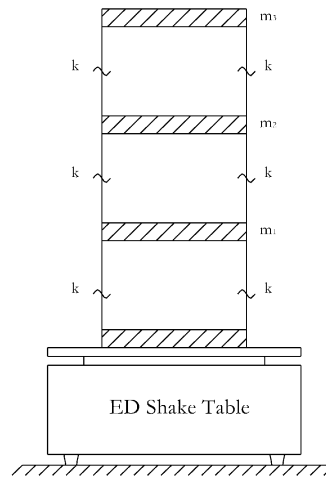


Fig. 10.5 Sketch of the three-story, one-bay steel and polypropylene frame structure shown mounted to an electromechanical shake table.

though we were unable to duplicate and test any of those structures in our laboratory due to physical limitations in our shake table capability. The design and characterization of the structure was accomplished through a combination of finite element computations and experimental modal analysis. Once the model was complete, several protective system configurations employing NESs were designed, optimized, and verified experimentally. One configuration in particular was shown to provide a significant level of protection for all four earthquakes examined, remarkable in view of the fully passive design. The mechanics of the system will be discussed in what follows.

10.2.1 Characterization of the Three-Story Linear Frame Structure

Following Nucera (2005) and Nucera et al. (2008a, b), the structure (i.e., the linear primary system), shown in Figure 10.5, is a three-story, one-bay structure with spring steel columns and polypropylene floor slabs, approximately 60 cm tall, 20 cm wide and 10 cm deep. The floor slabs are bolted directly to the columns, through small aluminum plates to increase rigidity, using 4 cap screws per connection. The foundation, also polypropylene, was bolted directly to a mechanical shake table (Figure 10.6) through which the historic earthquake time histories were applied. The floor slabs were sufficiently thick in dimension to ensure adequate rigidity against bending; thus, the frame was designed to respond as a shear beam, with each column modeled as a clamped-clamped Euler–Bernoulli beam with lateral stiffness $k = 12EI/h^3$. Here, E is Young’s modulus for spring steel, I is the area moment

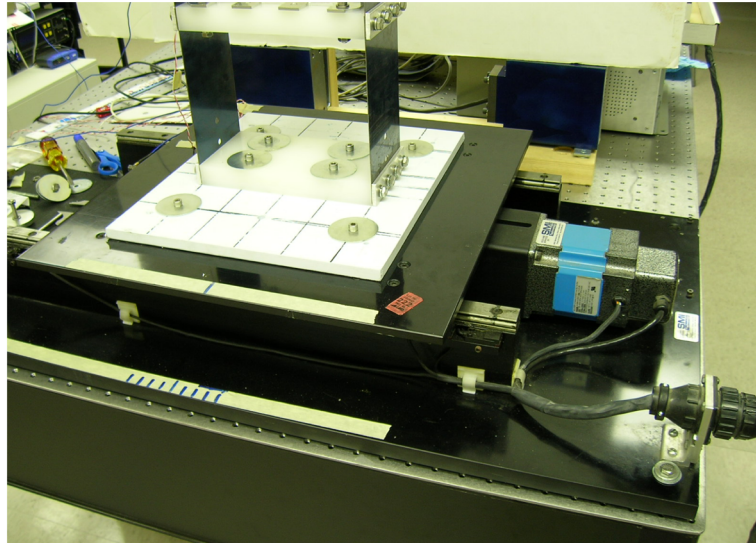


Fig. 10.6 Detail showing mounting of the steel frame to the locked-down shake table.

of inertia of the column about its bending axis, and h is the effective column length of a story. The resulting floor masses are assumed to be equal to 1.127 kg, and the column stiffnesses, also assumed equal, are rounded off to 5000 N/m.

The frame is governed by the equation of motion

$$M\ddot{u} + C\dot{u} + Ku = -MI_0\ddot{u}_g \quad (10.18)$$

where the mass and stiffness matrices, displacement vector relative to ground motion, and distribution vector are given, respectively, by

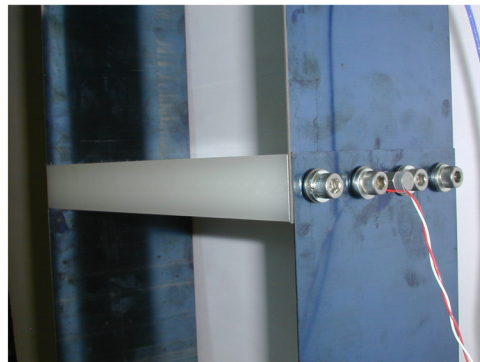
$$M = \begin{bmatrix} m_1 & 0 & 0 \\ 0 & m_2 & 0 \\ 0 & 0 & m_3 \end{bmatrix}, \quad K = \begin{bmatrix} 2k & -k & 0 \\ -k & 2k & -k \\ 0 & -k & k \end{bmatrix},$$

$$I_0 = \begin{bmatrix} 1 \\ 1 \\ 2 \end{bmatrix}, \quad u(t) = \begin{bmatrix} u_1 \\ u_2 \\ u_3 \end{bmatrix}$$

and $\ddot{u}_g(t)$ is the ground acceleration. We considered the case where the system is proportionally damped and determined the modal damping factors from an experimental modal analysis of the structure. Here, the mechanical shaker was locked down, and an impact hammer with an integral piezoelectric force transducer was employed to provide the necessary impulsive excitation at each story; responses were measured using a piezoelectric accelerometer at each story, as shown in Figure 10.7. All transducers used were manufactured by PCB Piezotronics, Inc. Data



(a)



(b)

Fig. 10.7 The three-story uncontrolled frame undergoing modal testing using an impact hammer to determine its eigenspectrum and modal damping factors: (a) excitation using a modal hammer; (b) typical accelerometer installation.

was subsequently acquired through a SigLab system, and both impulsive responses and complex frequency responses were saved for further analysis.

The experimental modal analysis was performed in the time domain using the Ibrahim Time Domain (ITD) method (Ibrahim and Pappa, 1982; Kerschen, 2002)

and frequency domain using the Rational Fraction Polynomial (RFP) method, the latter implemented in the Diamond software package made available by the Los Alamos National Laboratory (Doebbling et al., 1997). The average of the two methods gave natural frequencies of 4.6, 12.8, and 18.3 Hz, compared with computational values of 4.7, 13.2, and 19.1 Hz, resulting in a consistently high error ranging from 2 to 4% , which we attribute to arithmetic round-off and, perhaps, to compliance in the ball-screw mechanism of the shaker. However, the close agreement in natural frequency makes the damping estimates, again the average of ITD and RFP results, credible; the modal damping factors were found to be 0.00275, 0.00313, and 0.00236 for modes one through three, respectively. The modal damping matrix \hat{C} was then determined, from which the viscous damping matrix was computed from (10.2). This completed the determination of the linear portion of the simulation model.

10.2.2 Simulation and Optimization of the Frame-Single VI NES System

A VI NES was attached to the top (third) floor of the primary system in order to utilize the large building displacements at that height to maximize its authority, as shown in the schematic of Figure 10.8. Development of the equations of motion followed that of Section 10.1, where the NES degree of freedom was added to the equations of the primary system. Thus, (10.18) applies with

$$M = \begin{bmatrix} m_1 & 0 & 0 & 0 \\ 0 & m_2 & 0 & 0 \\ 0 & 0 & m_3 & 0 \\ 0 & 0 & 0 & m_4 \end{bmatrix}, \quad C = \begin{bmatrix} \lambda_1 + \lambda_2 & -\lambda_2 & 0 & 0 \\ -\lambda_2 & \lambda_2 + \lambda_3 & -\lambda_3 & 0 \\ 0 & -\lambda_3 & \lambda_3 & 0 \\ 0 & 0 & 0 & 0 \end{bmatrix}$$

and

$$K = \begin{bmatrix} 2k & -k & 0 & 0 \\ -k & 2k & -k & 0 \\ 0 & -k & k + k_{\text{NES}} & -k_{\text{NES}} \\ 0 & 0 & -k_{\text{NES}} & k_{\text{NES}} \end{bmatrix}, \quad I_0 = \begin{bmatrix} 1 \\ 1 \\ 1 \\ 1 \end{bmatrix}, \quad u(t) = \begin{bmatrix} u_1 \\ u_2 \\ u_3 \\ u_{\text{NES}} \end{bmatrix}$$

As before, k_{NES} is small compared with k .

As noted earlier, adding the VI NES makes the combined system piecewise linear; i.e., between any two consecutive impacts of m_{NES} the system is linear. Hence, the numerical integration of the equations of motion requires the solution of a sequence of linear initial value problems, each of which is bounded by successive vibro-impacts of the NES. The precise computation of the times at which vibro-impacts occur is necessary for accurate simulation of the transient dynamics of the system, as they determine the temporal boundaries of the linear computations. When a vibro-impact occurs, the computation is halted, the initial conditions are modified

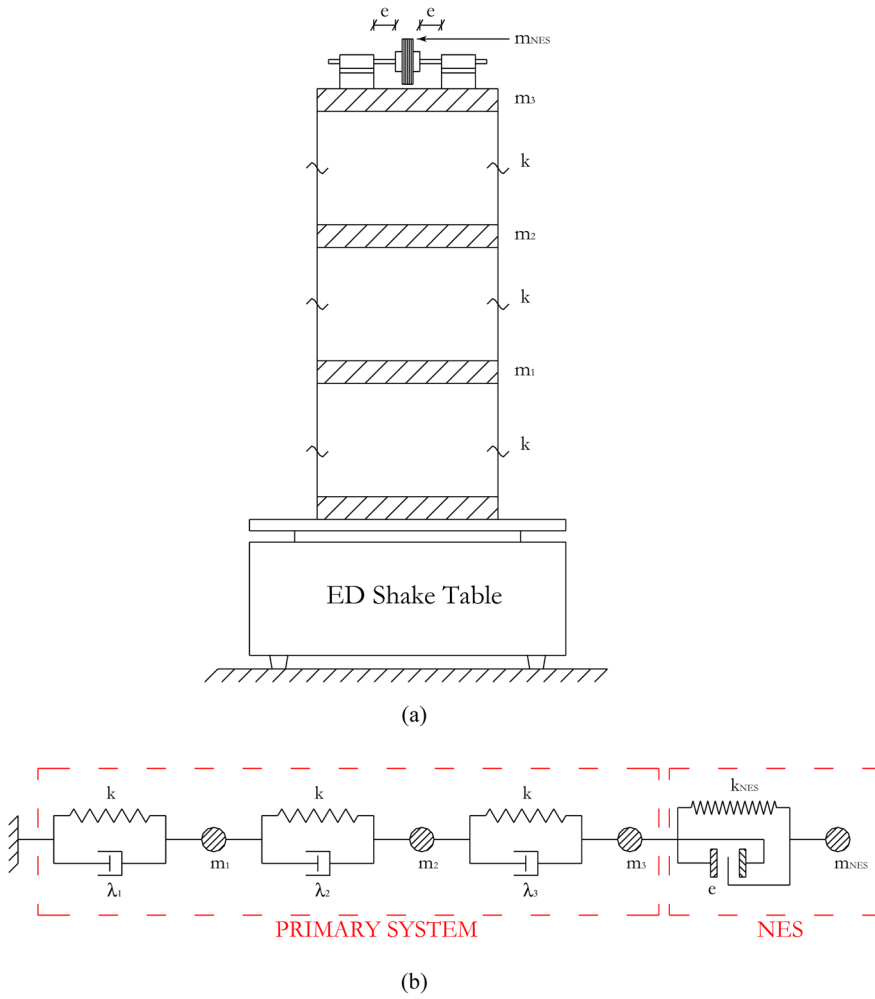


Fig. 10.8 Sketch (a) and schematic (b) of the three-story, one-bay steel and polypropylene frame structure with a single VI NES attached to the third floor.

to account for the state of the system post-impact, and the computation then resumes. The relation for the velocities of the affected masses before and after impact is

$$v'_3 - v'_{NES} = rc(v_{NES} - v_3) \tag{10.19}$$

and, as before, while energy is not conserved through the inelastic impact, momentum is conserved leading to

$$m_3 v_3 + m_{NES} v_{NES} = m_3 v'_3 + m_{NES} v'_{NES} \tag{10.20}$$

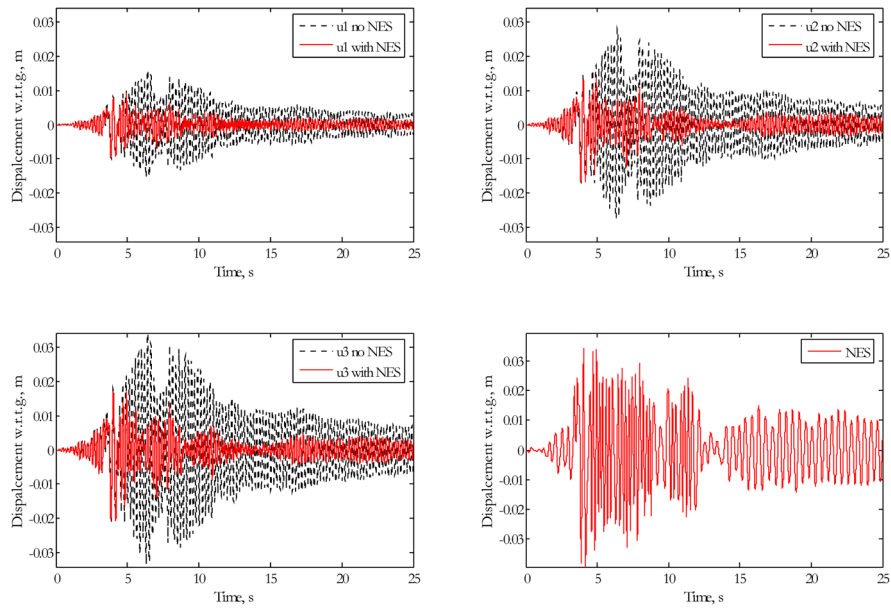


Fig. 10.9 Comparison of uncontrolled and controlled floor displacements relative to the ground and the VI NES displacement relative to the ground for the system optimized for and subjected to the Northridge earthquake.

The system of equations was reduced to state-space form and integrated using function ODE45 in Matlab[®], taking advantage of its adaptive time-stepping to achieve the required accuracy in the vicinity of each impact.

The optimization parameters were those of the VI NES; i.e., m_{NES} , k_{NES} , e , and rc , and the evaluation criteria, objective function, and procedure were identical to those employed in Section 10.1. The optimization was again performed over the array of four historic earthquakes named earlier, with an optimal solution determined for each particular earthquake. Both the Northridge and Kobe results will be discussed further as they represent the more severe case within each class.

10.2.2.1 Optimization Design for the Northridge Earthquake

Prior to initiating the study, examination of the Fourier spectrum of the Northridge acceleration record revealed that a mismatch existed between the frequency bandwidth of maximum energy content and the eigenspectrum of the three story structure. In order to place the maximum energy of the earthquake in a frequency band consistent with the eigenspectrum of the structure, the duration of the earthquake was scaled by a factor of one half to 25 seconds from its original 50, thus doubling

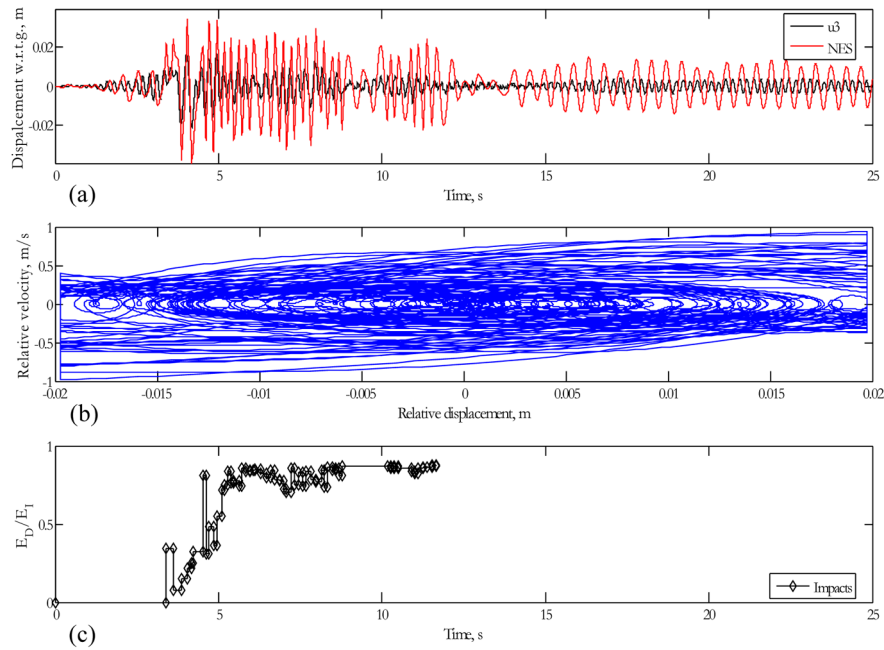


Fig. 10.10 Performance of the VI NES optimized for and subjected to the Northridge earthquake; (a) comparison between absolute displacements of the third floor and NES; (b) phase plot of relative velocity versus relative displacement between the third floor and NES; and (c) energy dissipation by the VI NES showing the portion of instantaneous seismic energy dissipated during each vibro-impact.

its effective bandwidth and ensuring that the computed response represents the most severe condition. The acceleration amplitude, however, was left unscaled.

It was observed throughout the ensuing simulations that during the strong motion portion of the earthquake, the VI NES was able to respond quickly resulting in vibro-impacts that dissipate a significant portion of the input energy. This is a signal advantage of the VI NES over the smooth NES, which acts more slowly and is unable to affect structural response during the first few critical cycles of strong motion. The optimal VI NES parameters for the Northridge record were determined to be: m_{NES} equal to 4% of the total mass of the primary system; $k_{\text{NES}} = 0.005k$; $rc = 0.40$; and $e = 0.02$ m. The natural frequencies of the system including the VI NES were computed to be 2.2, 4.6, 12.8, and 18.3 Hz, reflecting the addition of the new, low-frequency mode due to the weakly coupled NES mass at the top floor.

Figure 10.9 provides a comparison between the controlled and uncontrolled (no NES) relative displacements with respect to ground of each floor of the frame, while Figure 10.10 compares the absolute displacement of the third floor with that of the NES and gives the phase plot of the response of the NES relative to the third floor as well as the instantaneous total energy dissipated at each vibro-impact and the

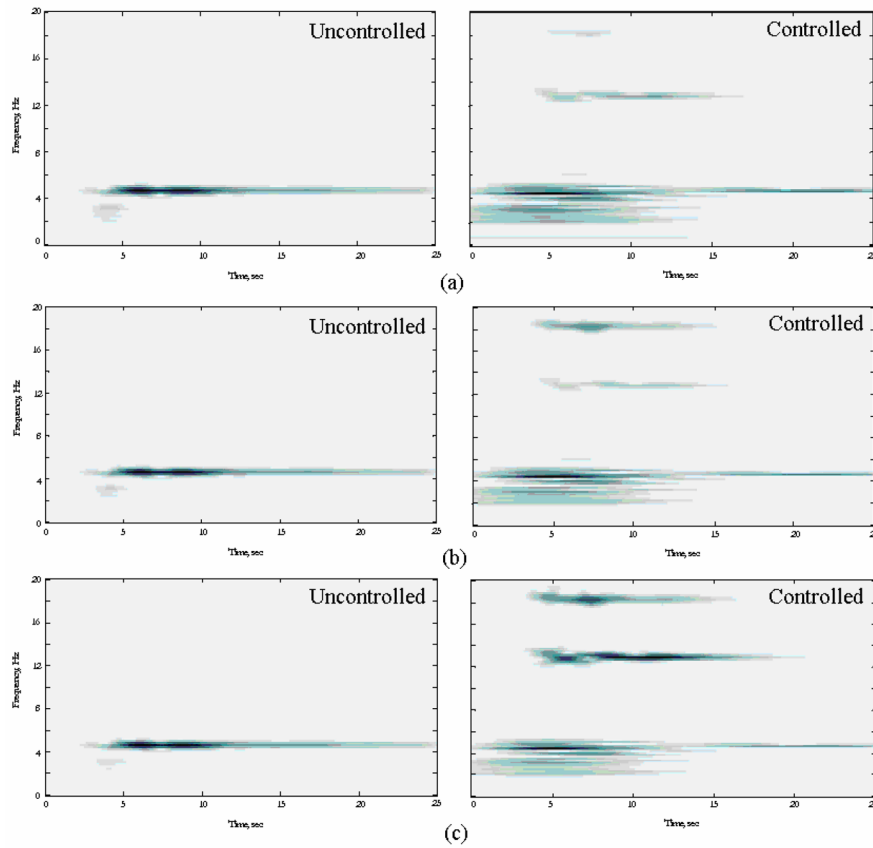


Fig. 10.11 Comparison between the wavelet spectra of controlled and uncontrolled relative displacements for a primary system with Northridge-optimized VI NES attached to the third floor and Northridge seismic excitation: (a) $u_1(t) - u_g(t)$, (b) $u_2(t) - u_1(t)$, (c) $u_3(t) - u_2(t)$.

vibro-impact time history. The last of these provides a measure of the severity of vibro-impacts, indicating whether there is sufficient interaction between the primary system and NES.

Wavelet spectra of the relative displacements between the first floor and ground, the second and first floors, and the third and second floors are shown in Figure 10.11, clearly depicting the scattering of energy to all structural modes due to vibro-impacts of the NES. We note that the uncontrolled structure responds primarily at its first mode of 4.6 Hz, which leads to large relative displacements. In the presence of the NES, however, seismic energy is spread to as many as four linear modes, with the spreading becoming more pronounced at the higher floors. This is a two-fold advantage from the mitigation standpoint and explains the reduced levels of structural response observed with the NES in place. First, due to the vibro-impacts, seismic energy is transferred from the low frequency, high amplitude first structural mode

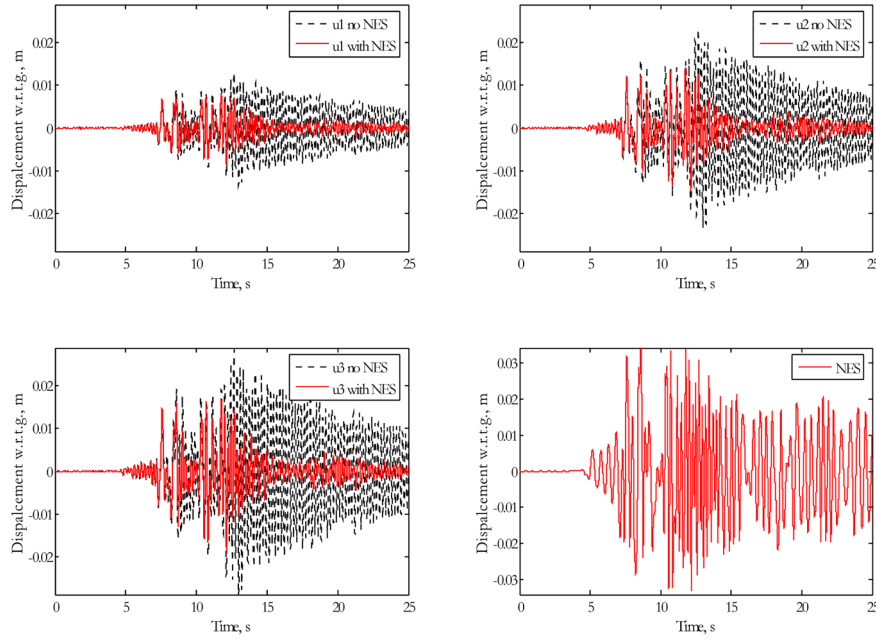


Fig. 10.12 Comparison of uncontrolled and controlled floor displacements relative to the ground and the VI NES displacement relative to the ground for the system optimized for and subjected to the Kobe earthquake.

to the lower amplitude, higher frequency structural modes where it is more readily dissipated by internal damping effects; second, energy ‘leaking’ to the lowest mode at 2.2 Hz results in even greater mitigation as that mode is localized to the NES.

The performance of the optimized system can be visualized through the evaluation criteria $(J_1, J_2, \dots, J_8) = (0.61, 0.59, 0.80, 0.58, 0.37, 0.39, 0.57, 0.39)$. Thus, a 39% reduction in maximum displacement and a 41% reduction in maximum interstory drift are realized compared with the uncontrolled system, with the normed criteria reduced even more.

Examination of the controlled responses of Figures 10.9 and 10.10 reveals three distinct phases. During the first three seconds, the relative motion between the NES and third floor is less than the clearance so that no vibro-impacts occur and the system is linear. In the second phase, from three to eight and a half seconds, strong vibro-impacts occur due to a 1:1 transient resonance capture between the first structural mode and the VI NES, resulting in dissipation of approximately 87% of the input seismic energy. The final phase occurs after escape from resonance capture; however, a series of vibro-impacts occurs between 10 and 12 seconds, though efficient energy dissipation is not achieved since the earthquake has released nearly all of its energy by eight seconds. This confirms that the VI NES is effective from the first cycle of response and is able to dissipate seismic energy at a sufficiently fast

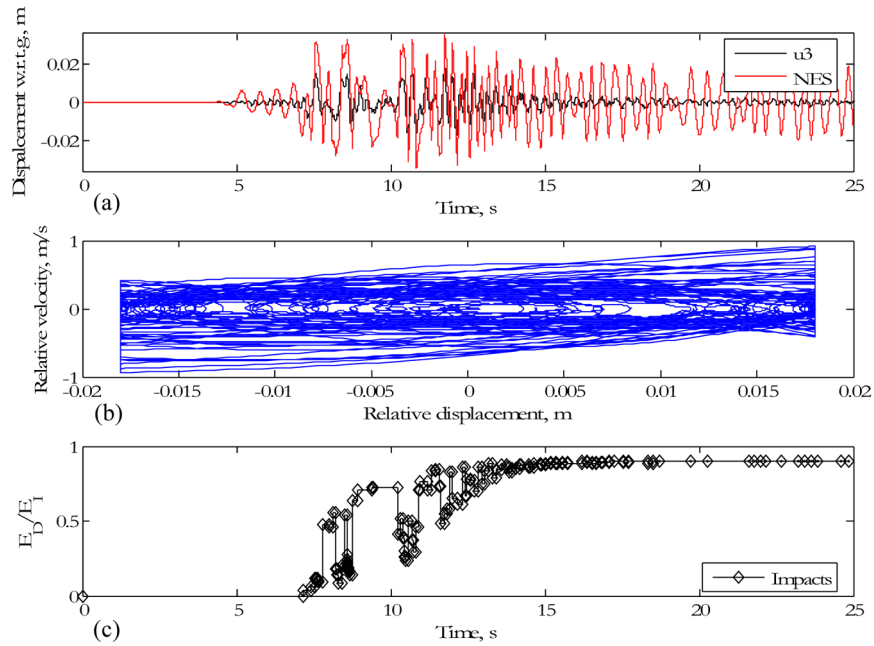


Fig. 10.13 Performance of the VI NES optimized for and subjected to the Kobe earthquake: (a) comparison between absolute displacements of the third floor and the NES; (b) phase plot of relative velocity versus relative displacement between the third floor and NES; and (c) energy dissipation by the VI NES showing the portion of instantaneous seismic energy dissipated during each vibro-impact.

time scale to mitigate large responses at early time typical of near-field events. This fundamental mechanism, in conjunction with the spreading phenomenon already discussed, provides an effective mitigation strategy for large scale structures.

10.2.2.2 Optimization Design for the Kobe Earthquake

Optimization of the VI NES system for the Kobe earthquake followed that of the Northridge earthquake, just discussed. Again, in order to tune the earthquake record to the eigenspectrum of the structure, the record was scaled to 25 seconds from the original duration of 50 seconds, doubling its frequency bandwidth; acceleration amplitude was not scaled. The optimal VI NES parameters for the Kobe record were determined to be: m_{NES} equal to 4.5% of the total mass of the primary system; $k_{\text{NES}} = 0.004k$; $rc = 0.40$; and $e = 0.018$ m. The natural frequencies of the system including the VI NES were computed to be 1.7, 4.6, 12.8, and 18.3 Hz, reflecting the addition of the new, low-frequency mode due to the weakly coupled NES mass at the top floor.

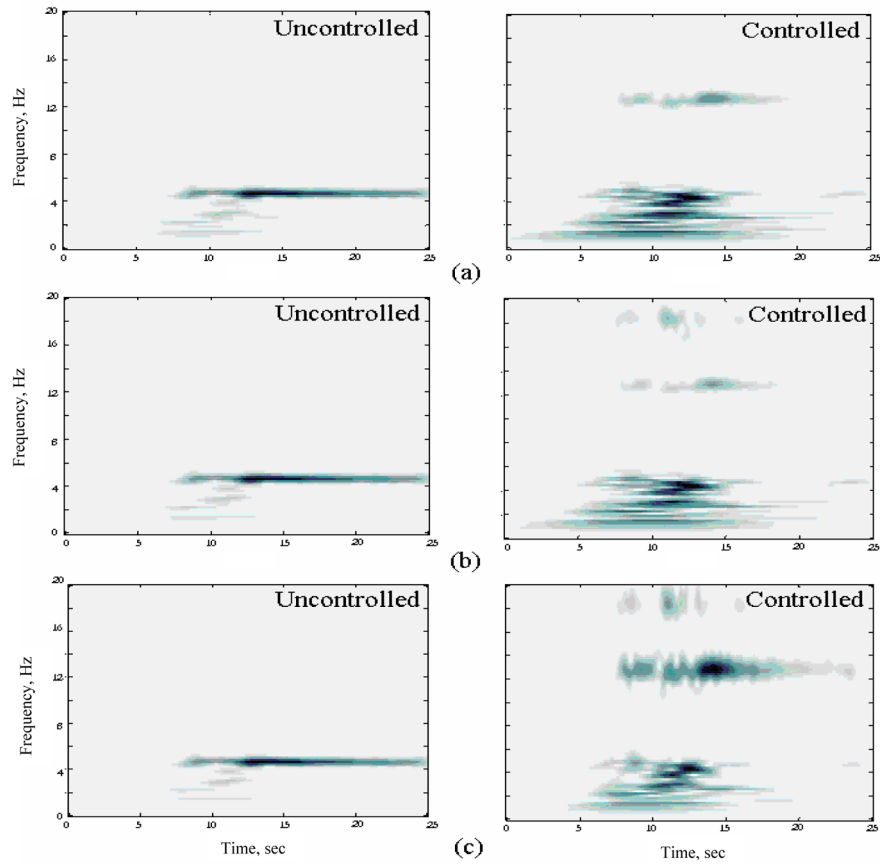


Fig. 10.14 Comparison between the wavelet spectra of controlled and uncontrolled relative displacements for a primary system with Kobe-optimized VI NES attached to the third floor, and Kobe seismic excitation: (a) $u_1(t) - u_g(t)$, (b) $u_2(t) - u_1(t)$, (c) $u_3(t) - u_2(t)$.

Figure 10.12 provides a comparison between the controlled and uncontrolled (no NES) relative displacements with respect to ground of each floor of the frame, while Figure 10.13 compares the absolute displacement of the third floor with that of the NES and gives the phase plot of the response of the NES relative to the third floor as well as the instantaneous total energy dissipated at each vibro-impact and the vibro-impact time history. The last of these provides a measure of the severity of vibro-impacts, indicating whether there is sufficient interaction between the primary system and NES.

Wavelet spectra of the relative displacements between the first floor and ground, the second and first floors, and the third and second floors are shown in Figure 10.14, again depicting the scattering of energy to all structural modes due to vibro-impacts

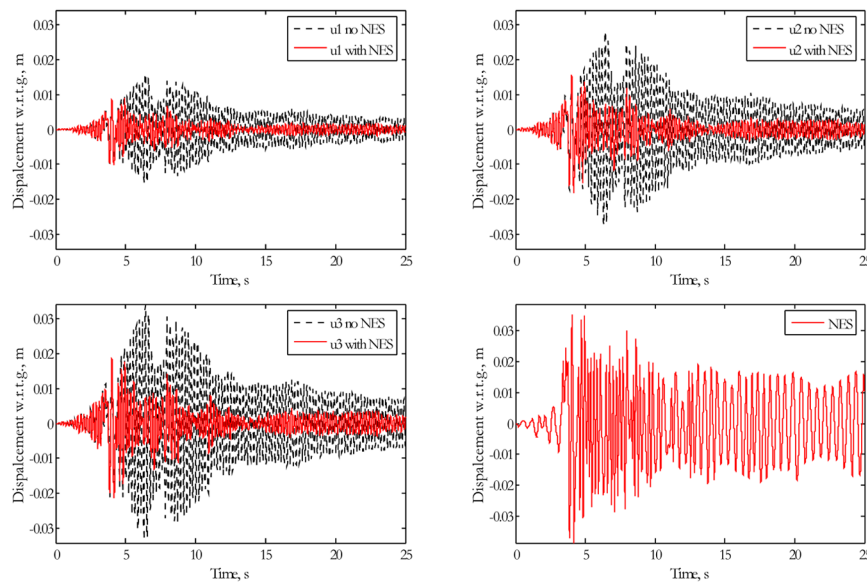


Fig. 10.15 Uncontrolled and controlled displacements relative to the ground when a Kobe-optimized VI NES is attached to the third floor of the frame, subjected to the Northridge excitation.

of the NES. In the presence of the VI NES, seismic energy is spread to the linear modes as before, resulting in dissipation and reduction in response.

It would be desirable if a protective system designed and optimized specifically for a particular, severe historic earthquake acting on a known structure functioned in near-optimal fashion for a range of historic earthquakes. Thus, we examined the system resulting from the Kobe analysis in terms of its performance under the El Centro, Hachinohe and Northridge records. Both the El Centro and Hachinohe acceleration records were scaled in time to 50% of their original length, with the amplitude left unscaled. Comparisons of controlled and uncontrolled displacements relative to ground, and the NES displacement relative to ground, for the El Centro, Hachinohe and Northridge earthquake records are given in Figures 10.15, 10.16 and 10.17, respectively. That there is a dramatic reduction in response for all three systems is clear from the plots.

The eight evaluation criteria for the Kobe-designed system subjected to all four historic earthquake records are given in Table 10.6. Reductions in maximum displacement and maximum interstory drift were 36% and 38%, respectively, for Kobe, 36% and 36% for Northridge, 50% and 51% for El Centro, and 39% and 42% for Hachinohe. In all cases, reductions in the normed criteria were equally impressive.

This cursory study demonstrates that the VI NES can be an efficacious element of a control strategy for seismic protection of shear beam structures. We noted in the course of this study, however, that the VI NES functions most effectively during the strong motion segment of the earthquake, losing its ability to undergo vibro-

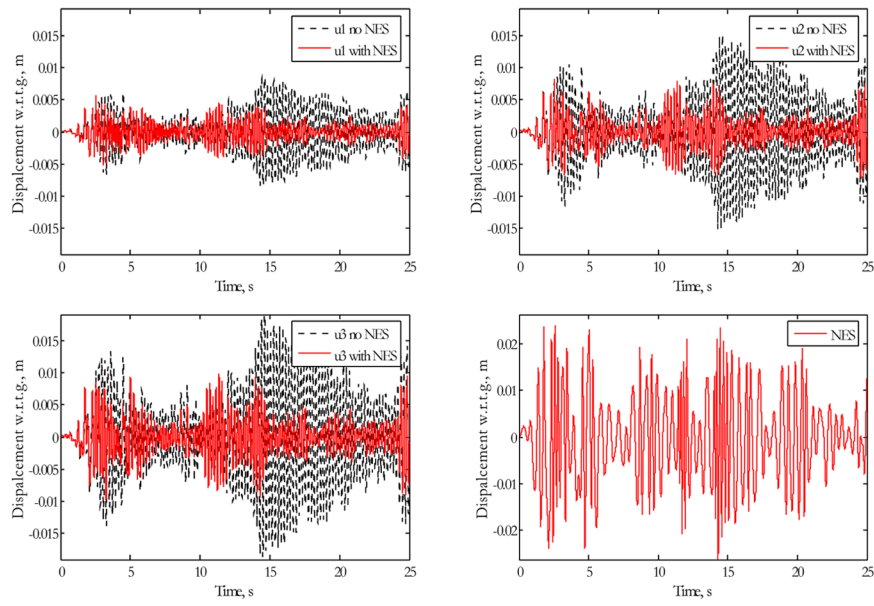


Fig. 10.16 Uncontrolled and controlled displacements relative to the ground when a Kobe-optimized VI NES is attached to the third floor of the frame, subjected to the El Centro excitation.

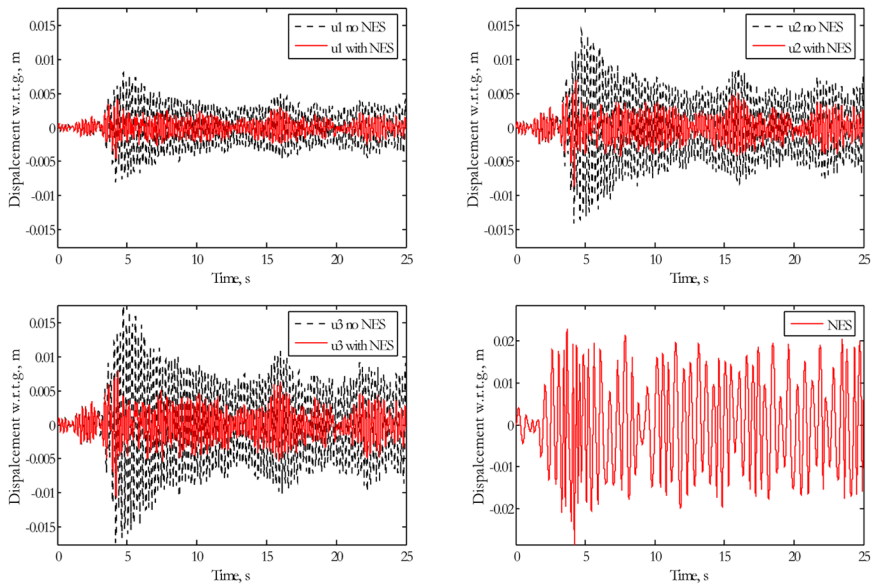


Fig. 10.17 Uncontrolled and controlled displacements relative to the ground when a Kobe-optimized VI NES is attached to the third floor of the frame, subjected to the Hachinohe excitation.

Table 10.6 Evaluation criteria for four historic earthquakes; linear frame with Kobe-designed single-VI NES at floor 3.

Earthquake	J ₁	J ₂	J ₃	J ₄	J ₅	J ₆	J ₇	J ₈
Kobe	0.64	0.62	0.98	0.62	0.42	0.45	0.61	0.45
Northridge	0.64	0.64	0.92	0.65	0.39	0.40	0.51	0.40
El Centro	0.50	0.69	1.00	0.69	0.38	0.43	0.78	0.43
Hachinohe	0.61	0.58	1.00	0.57	0.39	0.41	0.51	0.41

impacts as the input energy decreases and, in the limit, reaching a no-impact condition where it becomes ineffective. This condition will be exacerbated for the case of earthquakes of low-to-moderate intensity, with seismic energy well below that of the design earthquake. Thus, we now consider a second, alternate design based upon the combined utilization of a VI NES and a smooth NES, in order to extend the useful range of the TET strategy for seismic protection of structures.

10.2.3 Simulation and Optimization of the Frame-VI NES-Smooth NES System

We now attach a smooth NES incorporating an essentially nonlinear cubic spring to the top (third) floor of the primary structure and a VI NES to the first floor, as shown in Figure 10.18. The intent of this design is to combine a lightweight smooth NES design which will perform adequately for moderate-to-severe earthquakes and a relatively heavy VI NES for protection from severe, possibly near field, events. As the more massive VI NES is positioned lower in the structure, its effect upon the structural design will be minimized; the smooth NES at the top floor will continue to function even as the available seismic energy input becomes relatively small.

The equations of motion are now given by

$$M\ddot{u} + C\dot{u} + Ku = -MI_0\ddot{u}_g + f \quad (10.21)$$

where, following the previous section, the mass, damping and stiffness matrices and displacement vector relative to ground are given by

$$M = \begin{bmatrix} m_1 & 0 & 0 & 0 & 0 \\ 0 & m_2 & 0 & 0 & 0 \\ 0 & 0 & m_3 & 0 & 0 \\ 0 & 0 & 0 & m_{\text{NES}_1} & 0 \\ 0 & 0 & 0 & 0 & m_{\text{NES}_2} \end{bmatrix},$$

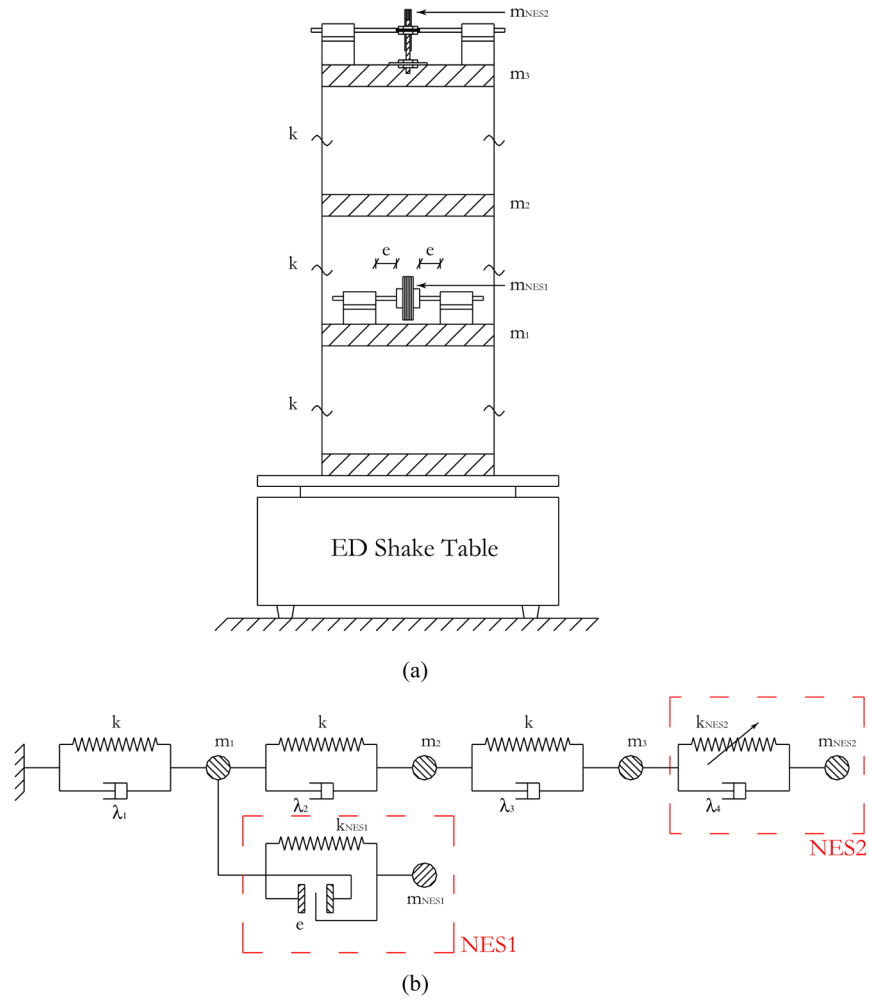


Fig. 10.18 Sketch (a) and schematic (b) of the three-story, one-bay steel and polypropylene frame structure with a single-VI NES attached to the first floor and a smooth NES attached to the third floor.

$$C = \begin{bmatrix} \lambda_1 + \lambda_2 & -\lambda_2 & 0 & 0 & 0 \\ -\lambda_2 & \lambda_2 + \lambda_3 & -\lambda_3 & 0 & 0 \\ 0 & -\lambda_3 & \lambda_3 + \lambda_4 & 0 & -\lambda_4 \\ 0 & 0 & 0 & 0 & 0 \\ 0 & 0 & -\lambda_4 & 0 & \lambda_4 \end{bmatrix}$$

and

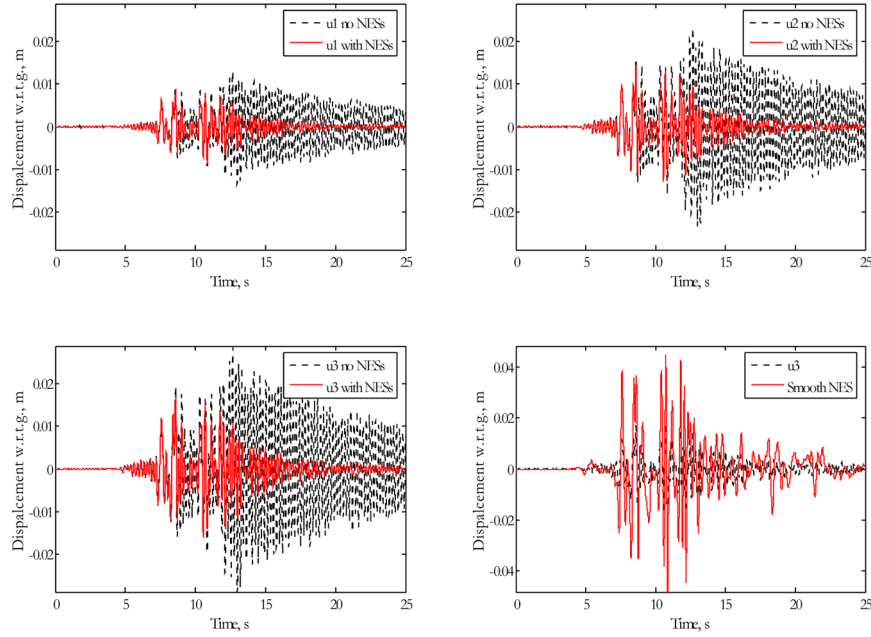


Fig. 10.19 Uncontrolled and controlled displacement relative to the ground when a Kobe-optimized VI NES is attached to the first floor and a smooth NES is attached to the third floor of the frame, for the Kobe excitation.

$$K = \begin{bmatrix} 2k + k_{\text{NES}_1} & -k & 0 & -k_{\text{NES}_1} & 0 \\ -k & 2k & -k & 0 & 0 \\ 0 & -k & k & 0 & 0 \\ -k_{\text{NES}_1} & 0 & 0 & k_{\text{NES}_1} & 0 \\ 0 & 0 & 0 & 0 & 7 \end{bmatrix}, \quad u = \begin{Bmatrix} u_1 \\ u_2 \\ u_3 \\ u_{\text{NES}_1} \\ u_{\text{NES}_2} \end{Bmatrix}$$

and f represents the restoring force vector associated with the essentially nonlinear, cubically-varying stiffness of the smooth NES,

$$f = \begin{Bmatrix} 0 \\ 0 \\ -k_{\text{NES}_2}(u_3 - u_5)^3 \\ 0 \\ -k_{\text{NES}_2}(u_5 - u_3) \end{Bmatrix}$$

Clearly, NES_1 and NES_2 refer to the VI NES and smooth NES, respectively; as before, \ddot{u}_g is the ground acceleration and I_0 is the distribution vector.

As in the previous section, simulation was performed within Matlab[®] where now, however, the system is strongly nonlinear between impacts of NES_1 . Precise calculation of the times at which vibro-impacts occur remains a critical part of the

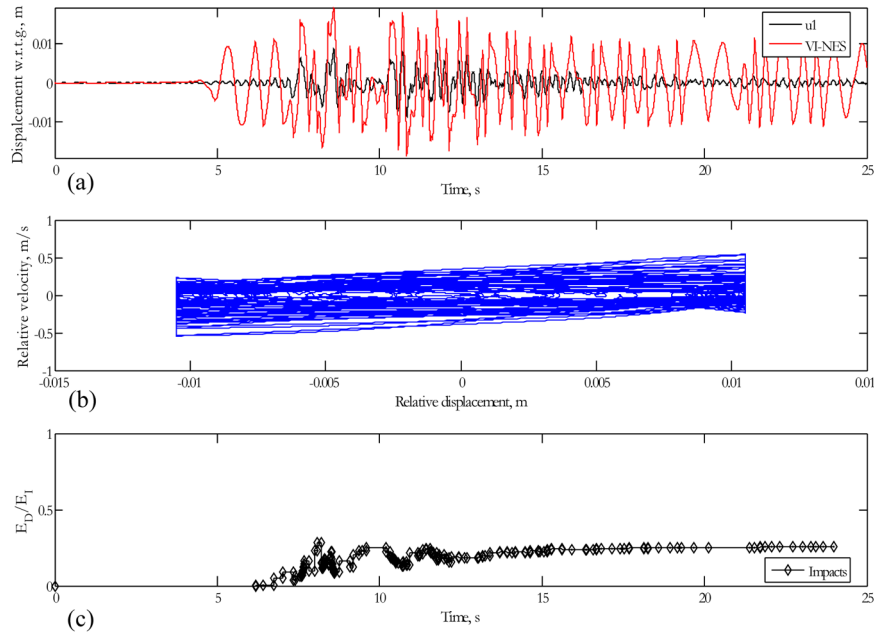


Fig. 10.20 Performance of the VI NES optimized for the Kobe earthquake: (a) comparison between absolute displacements of the first floor and the NES; (b) phase plot of relative velocity versus relative displacement between the first floor and NES; and (c) energy dissipation by the VI NES showing the portion of instantaneous seismic energy dissipated during each vibro-impact.

algorithm, though the problem is no longer piecewise linear. Optimization of this system proceeded in precisely the same way as the previous one, although the number of optimization parameters expanded due to the addition of the smooth NES; i.e., m_{NES} , k_{NES} , e , and rc for NES_1 and m_{NES_2} , k_{NES_2} , and λ_4 for NES_2 .

For this system, the optimization study was completed for the Kobe record alone, with the additional constraint that neither NES mass could exceed 2.5% of the total mass of the linear primary structure. The optimal parameters were determined to be: m_{NES_1} equal to 2.4% of the total mass of the linear primary structure, $e = 0.011$ m, $rc = 0.426$, $k_{NES_1} = 0.001k$; m_{NES_2} equal to 2% of the total mass of the linear primary structure, $k_{NES_2}/k = 19 \text{ m}^{-2}$, and $\lambda_4 = 3.277\lambda_3$.

Figure 10.19 provides a comparison between the controlled and uncontrolled relative displacements with respect to ground of each floor of the frame along with the absolute displacements of the third floor and of NES_2 . Figure 10.20 depicts the absolute displacement of the first floor and that of NES_1 and gives the phase plot of the response of NES_1 relative to the first floor as well as the instantaneous total energy dissipated at each vibro-impact and the vibro-impact time history.

The frame-dual NES system, optimized for the Kobe record, was also subjected to the Northridge earthquake in order to examine the robustness of the protective system, with the results shown in Figures 10.21 and 10.22. From these, we observe

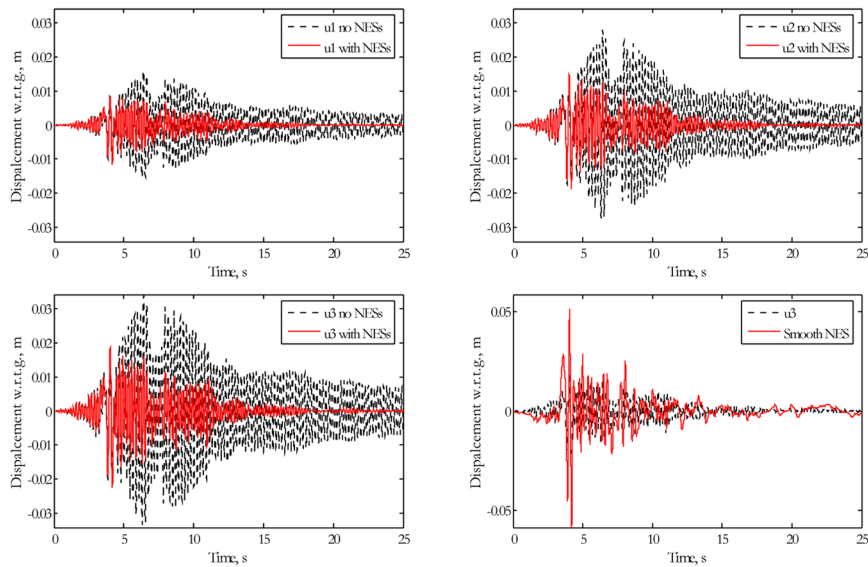


Fig. 10.21 Uncontrolled and controlled displacement relative to the ground when a Kobe-optimized VI NES is attached to the first floor and a smooth NES is attached to the third floor of the frame, for the Northridge excitation.

that the portion of seismic energy dissipated by the VI NES (NES_2) is on the order of 25–30%. While smaller than the dissipation realized in the single-VI NES design, it should be noted that here the mass ratio is smaller, and the device is located at the first floor where frame velocity, and consequently momentum exchange, is also smaller.

The eight evaluation criteria for the Kobe-designed dual-NES system subjected to all four historic earthquakes are given in Table 10.7. For the Kobe record, the dual-NES system clearly outperforms the single-NES system in terms of all eight criteria, while for the Northridge record there is improvement in the third and seventh criteria but deterioration in the first, though still satisfactory. The situation for the El Centro and Hachinohe records appears somewhat less impressive, with improvements noted only in the normed criteria. Note, however, that these earthquakes are less energetic than the Kobe and Northridge and, consequently, the opportunity for transient resonance capture, which requires exceedance of an energy threshold in order to occur, is reduced with the VI NES located at the first floor and at a reduced mass ratio.

These conjectures are confirmed by Figures 10.23 and 10.24, the wavelet spectra of the floor displacements relative to ground, showing that scattering toward higher modes of the system is less pronounced in the dual-NES design. However, reductions in the normed criteria demonstrate that the smooth NES continues to operate in low energy regimes, long after the VI NES becomes ineffective. In Figures 10.25 and 10.26, the wavelet spectra of the relative displacements between NES_1 and the

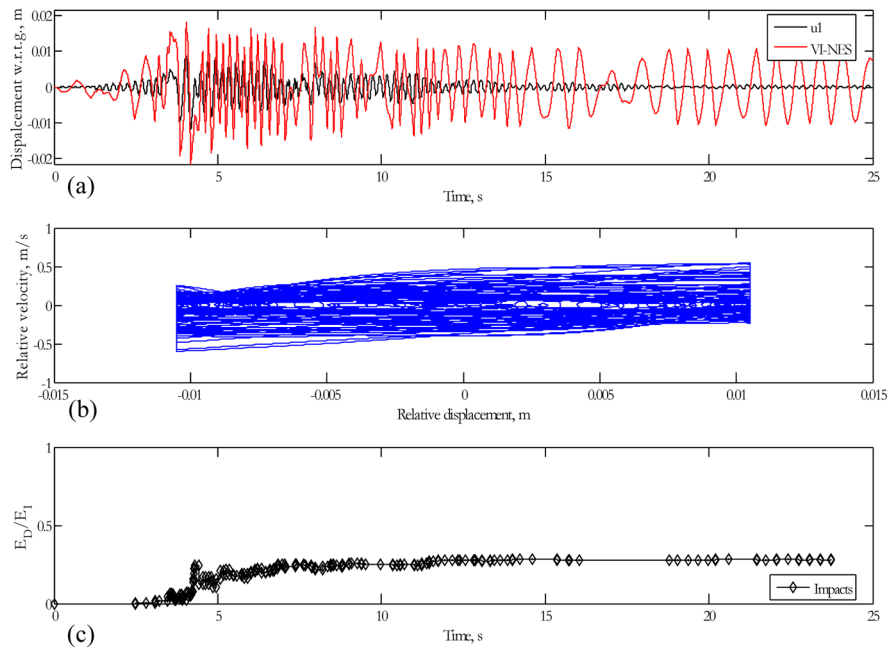


Fig. 10.22 Performance of the VI NES optimized for the Kobe earthquake, subjected to the Northridge earthquake: (a) comparison between absolute displacements of the first floor and the NES; (b) phase plot of relative velocity versus relative displacement between the first floor and NES; and (c) energy dissipation by the VI NES showing the portion of instantaneous seismic energy dissipated during each vibro-impact.

Table 10.7 Evaluation criteria for four historic earthquakes; linear frame with Kobe-designed single-VI NES at floor 1 and smooth NES at floor 3.

Earthquake	J_1	J_2	J_3	J_4	J_5	J_6	J_7	J_8
Kobe	0.58	0.62	0.65	0.69	0.39	0.40	0.42	0.43
Northridge	0.63	0.70	0.76	0.66	0.39	0.41	0.42	0.41
El Centro	0.53	0.60	0.68	0.62	0.40	0.40	0.52	0.50
Hachinohe	0.80	0.87	0.86	0.87	0.38	0.39	0.45	0.42

first floor and between NES₂ and the third floor, it is clear that seismic energy is pumped more vigorously from the first mode, particularly for the Northridge record. The high amplitude of the wavelet spectrum in this case indicates the occurrence of a transient resonance capture accompanied by TET at the first linearized natural frequency of the system. The capture and resulting TET persists for several seconds, after which escape occurs.

The result of this effort, then, is a functional, fully passive, lightweight and inexpensive protective system that can be designed for peak performance when exposed to highly energetic earthquakes in the near field but that will also perform well for less energetic earthquakes or those that occur at some distance from the structure.

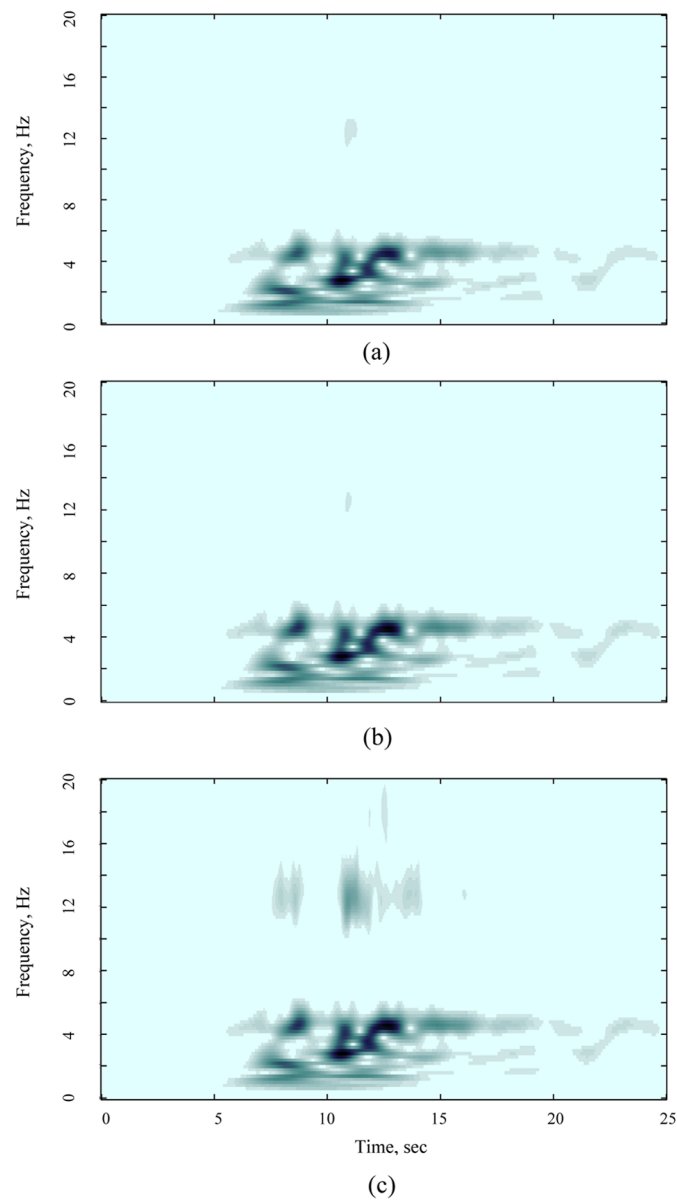


Fig. 10.23 Wavelet spectra of controlled relative displacements for the frame with Kobe-optimized VI NES attached to the first floor, smooth NES at the top floor, and Kobe excitation: (a) $u_1(t) - u_g(t)$, (b) $u_2(t) - u_1(t)$, (c) $u_3(t) - u_2(t)$.

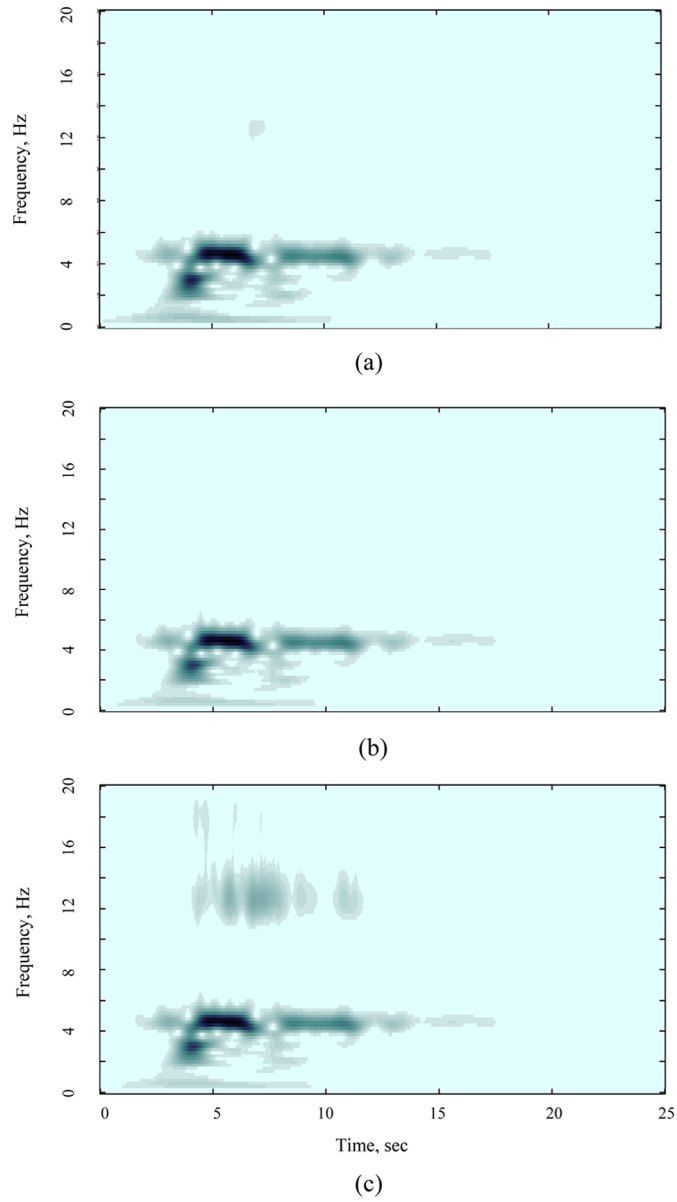


Fig. 10.24 Wavelet spectra of controlled relative displacements for the frame with Kobe-optimized VI NES attached to the first floor, smooth NES at the top floor, and Northridge excitation: (a) $u_1(t) - u_g(t)$, (b) $u_2(t) - u_1(t)$, (c) $u_3(t) - u_2(t)$.

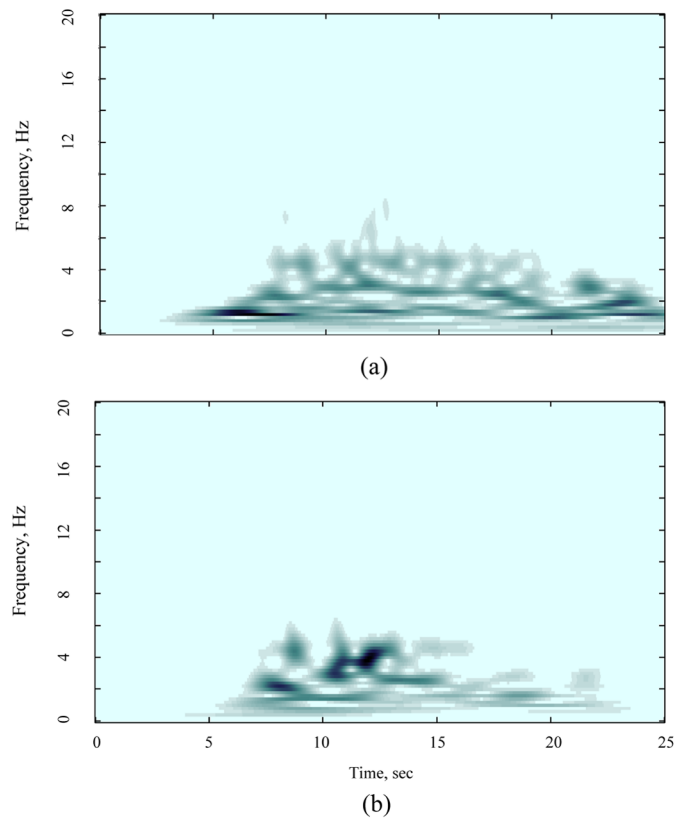


Fig. 10.25 Wavelet spectra of controlled relative displacements for the frame with optimized VI NES attached to the first floor, smooth NES at the top floor, and Kobe seismic excitation: (a) $u_{NES_1}(t) - u_1(t)$, (b) $u_{NES_2}(t) - u_3(t)$.

The results of several experiments, to follow, will confirm the capability of both single-NES and dual-NES systems.

10.3 Experimental Verification

The single-VI NES and dual-NES systems were built and tested in the Linear and Nonlinear Dynamics and Vibrations Laboratory (LNDVL) at the University of Illinois at Urbana–Champaign. The laboratory is jointly managed by the departments of aerospace engineering and mechanical science and engineering.

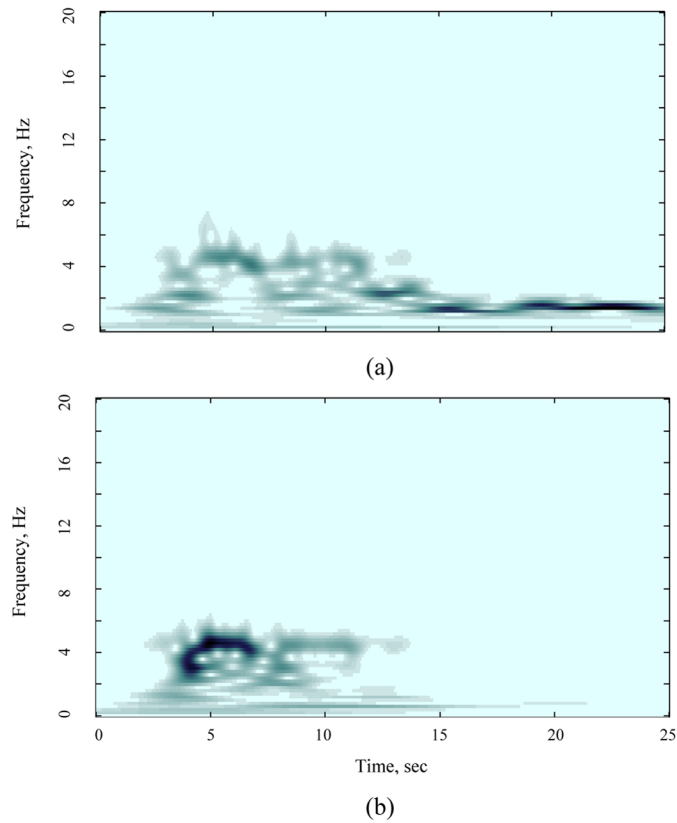


Fig. 10.26 Wavelet spectra of controlled relative displacements for the frame with optimized VI NES attached to the first floor, smooth NES at the top floor, and Northridge seismic excitation: (a) $u_{\text{NES}_1}(t) - u_1(t)$, (b) $u_{\text{NES}_2}(t) - u_3(t)$.

The three-story frame was mounted to an electromechanical shake table, basically a servomotor-driven ball-screw device³ that provided sufficient authority for open-loop application of the Kobe and Northridge earthquake records at full amplitude (and scaled by 50% in time as discussed previously) to the frame and protective system. Figures 10.27 and 10.28 illustrate the displacements with respect to ground, at floors one, two and three, for the Kobe and Northridge earthquake records obtained from double integrating the measured accelerations, from which the severity of the response to the Kobe compared with the Northridge is apparent. Henceforth, these will be denoted the uncontrolled responses.

³ The authors are indebted to Professor Bill Spencer of the civil and environmental engineering department at UIUC for the long-term loan of his shake table and associated electronics.

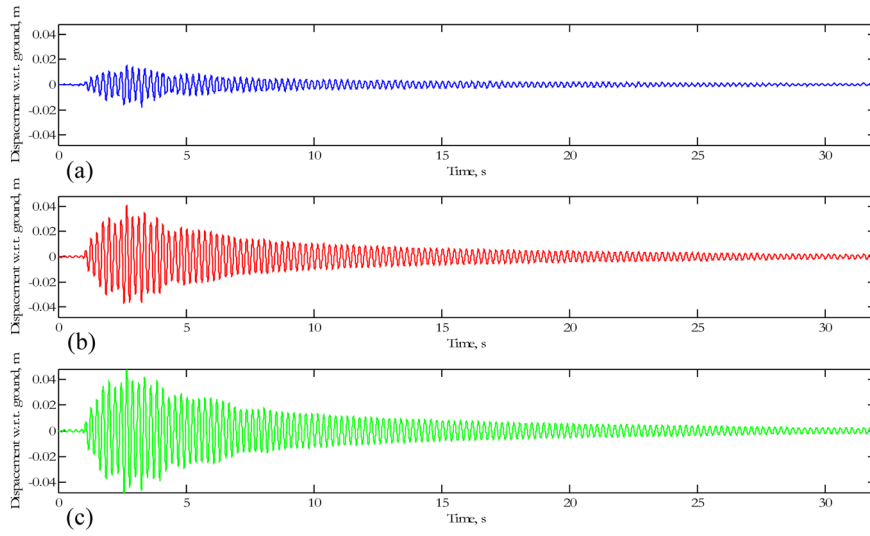


Fig. 10.27 Experimentally obtained uncontrolled response to the Kobe earthquake, displacements with respect to the ground of the shear frame: (a) top floor 1, (b) middle floor 2, (c) bottom floor 3.

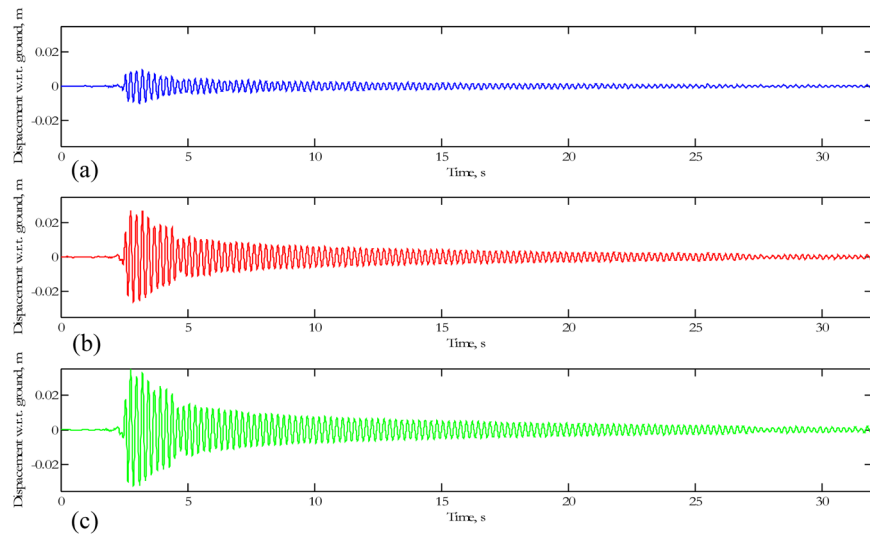


Fig. 10.28 Experimentally obtained uncontrolled response to the Northridge earthquake, displacements with respect to ground of the shear frame: (a) top floor 1, (b) middle floor 2, (c) bottom floor 3.

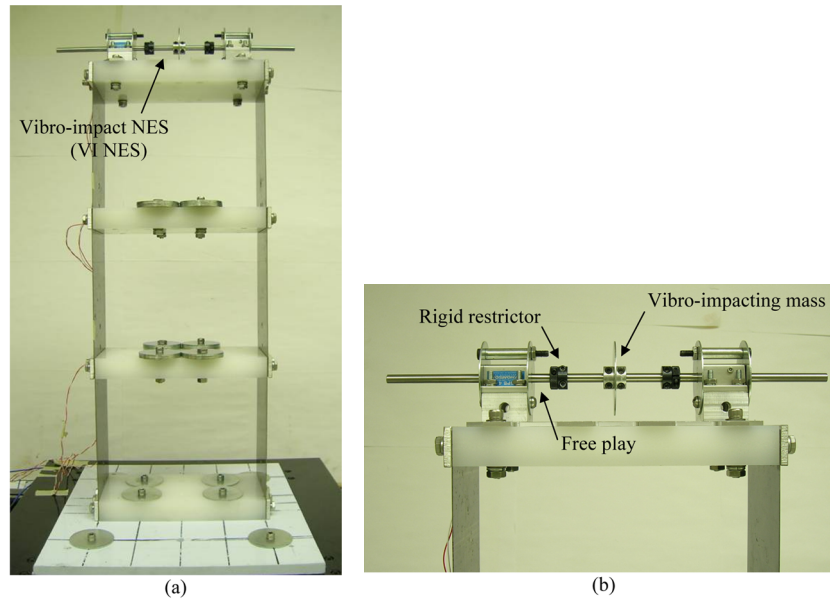


Fig. 10.29 Frame-single VI NES system: (a) the full system mounted on the shake table; and (b) a detail of the VI NES.

10.3.1 System Incorporating the Single-VI NES

The single-VI NES was attached to the third story of the frame, as shown in Figure 10.29. As can be seen in the figure, the NES consists of a small mass clamped to a shaft that is free to move horizontally in linear bearings until either of the two restrictors inelastically impacts its respective bearing housing. Note that consists of the washer, collars, shaft and restrictors, while the bearings and bearing housings are included in m_3 . Two discrete values, 2.5% and 3.5%, were placed on the ratio of NES mass to the total mass of the frame in an effort to make the design realistic, and the design optimization was repeated for the Kobe earthquake employing the identical evaluation criteria and algorithm used previously. The optimal solutions, corresponding to the two mass ratios, are:

$$\text{System 1: } m_{\text{NES}}/m_{\text{TF}} = 0.025, \quad k_{\text{NES}}/k = 0.004, \quad e = 0.024 \text{ m}, \quad rc = 0.43$$

$$\text{System 2: } m_{\text{NES}}/m_{\text{TF}} = 0.035, \quad k_{\text{NES}}/k = 0.005, \quad e = 0.016 \text{ m}, \quad rc = 0.42$$

Figures 10.30 and 10.31 show the relative displacements obtained experimentally for Systems 1 and 2, respectively, when subjected to the Kobe record. In System 1, reductions of 31% in maximum displacement relative to ground and 30% in maximum interstory drift are realized, while in System 2, the reductions are 46% and 37%, respectively.

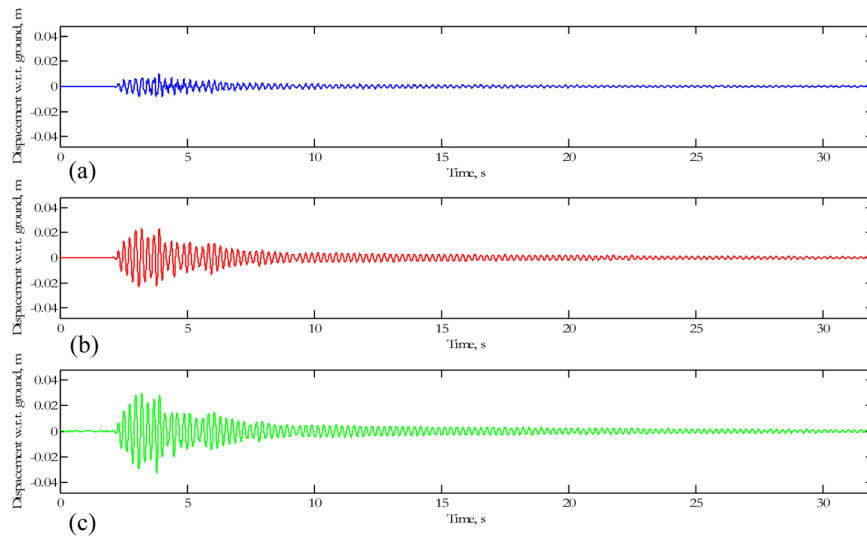


Fig. 10.30 Experimentally obtained response of the Kobe-optimized, frame-single VINES system with mass ratio of 2.5% to the Kobe earthquake: displacements with respect to ground of the shear frame, (a) top floor 1, (b) middle floor 2, (c) bottom floor 3.

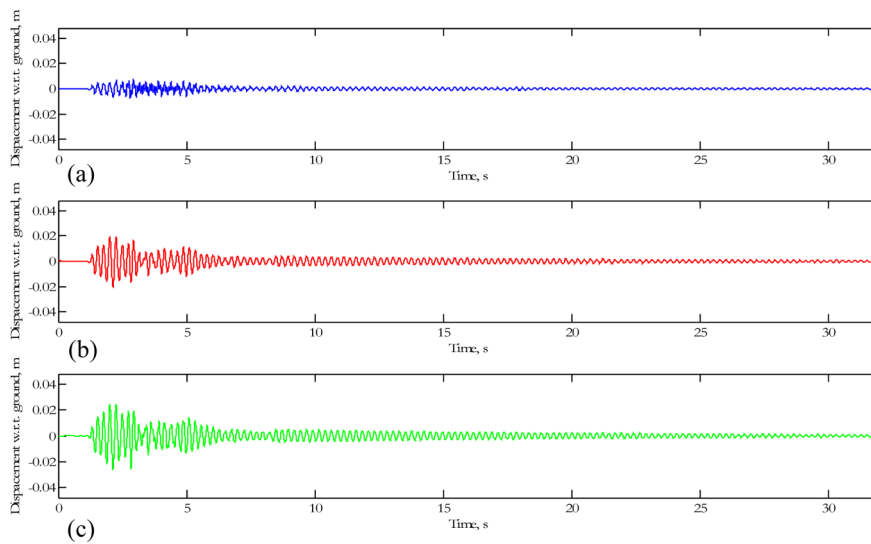


Fig. 10.31 Experimentally obtained response of the Kobe-optimized, frame-single VINES system with mass ratio of 3.5% to the Kobe earthquake: displacements with respect to ground of the shear frame, (a) top floor 1, (b) middle floor 2, (c) bottom floor 3.

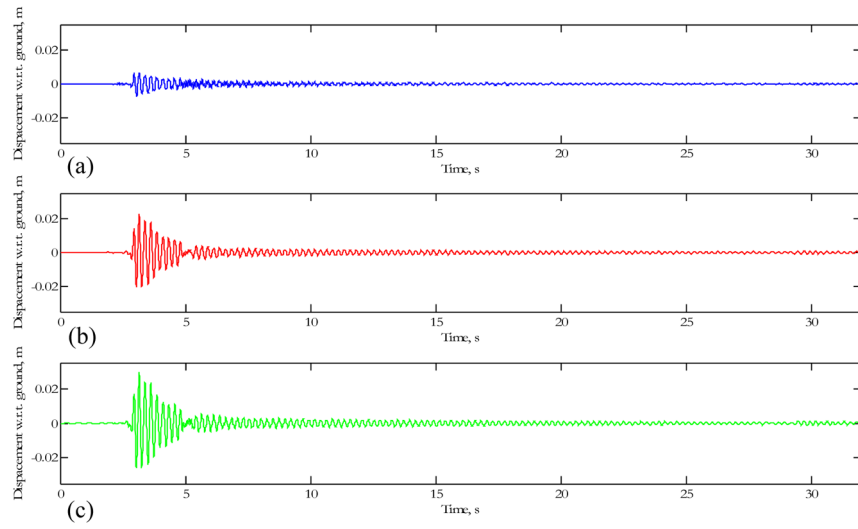


Fig. 10.32 Experimentally obtained response of the Kobe-optimized, frame-single VINES system with mass ratio of 2.5% to the Northridge earthquake: displacements with respect to ground of the shear frame, (a) top floor 1, (b) middle floor 2, (c) bottom floor 3.

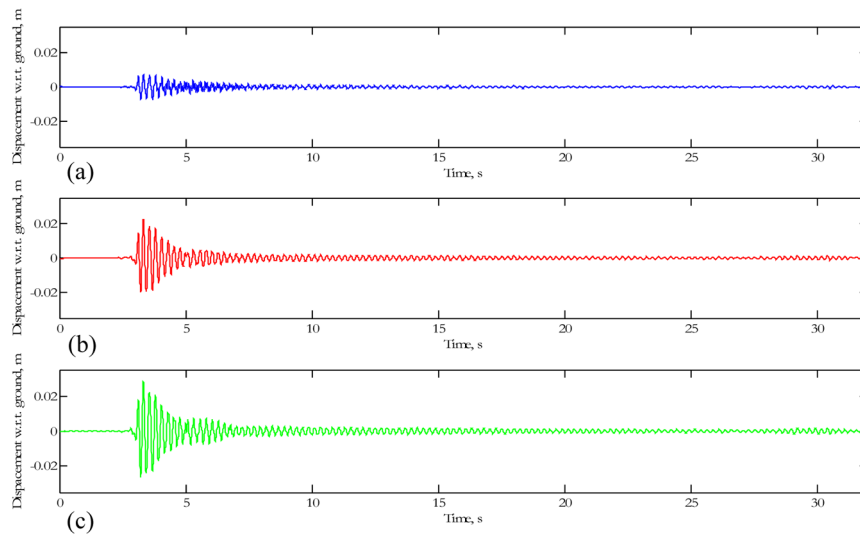


Fig. 10.33 Experimentally obtained response of the Kobe-optimized, frame-single VINES system with mass ratio of 3.5% to the Northridge earthquake: displacements with respect to ground of the shear frame, (a) top floor 1, (b) middle floor 2, (c) bottom floor 3.

The Kobe-designed system was also subjected to the consistently scaled Northridge earthquake. Figures 10.32 and 10.33 show the relative displacements obtained

Table 10.8 Experimental evaluation criteria; linear frame with Kobe-designed single-VI NES at floor 3.

Earthquake	mass ratio %	J ₁	J ₂	J ₃	J ₄	J ₅	J ₆	J ₇	J ₈
Kobe	2.5	0.69	0.70	0.89	0.66	0.49	0.50	0.55	0.50
	3.5	0.54	0.63	0.81	0.57	0.40	0.41	0.54	0.42
Northridge	2.5	0.84	0.87	0.92	0.82	0.54	0.57	0.67	0.57
	3.5	0.80	0.84	0.88	0.83	0.53	0.56	0.73	0.56

experimentally for Systems 1 and 2, respectively, for this input record. As expected, the results were not as impressive as for the Kobe, for reasons explained earlier. The computed evaluation criteria corresponding to the two systems for each of the two earthquake records are summarized in Table 10.8.

The spreading of seismic energy due to vibro-impacts, predicted in our earlier analyses, was verified in the experimental results. Figures 10.34 and 10.35 show the wavelet spectra of the interstory displacements $RD_1 = u_1$, $RD_2 = u_2 - u_1$, $RD_3 = u_3 - u_2$ of the uncontrolled frame structure subjected to the Kobe and Northridge records, respectively. Examination of these plots reveals that the response is limited nearly completely to the first linear mode of the structure. Significantly different results are obtained when the larger of the two VI NESs (System 2) is installed at the third floor, as indicated in Figures 10.36 and 10.37. Here we see that, for the Kobe earthquake, significant levels of seismic energy are spread from the first to the second and third linearized modes of the system while, for the Northridge record, spreading occurs mainly from the first to the second linearized mode. From these plots we see clearly that the VI NES acts at a sufficiently fast time scale to affect early time response, thus limiting peak values that are major sources of damage. We also note that the effect of the NES is negligible once the seismic energy is reduced to the point that vibro-impacts occur infrequently or not at all.

10.3.2 System Incorporating both VI and Smooth NESs

A VI NES (NES₁) was attached to the first floor and a smooth NES (NES₂) was bolted to the third floor of the frame as shown in Figure 10.38. NES₁ was described previously; however, now the mass of the bearing housings is added to that of the first floor, m_1 . From the figure, we see that NES₂ consists of a mass fixed to a shaft supported on bearings, connected to an extension of the third floor of the primary structure through a pair of thin wires without pretension, providing a geometrically nonlinear force-displacement characteristic. Further details of this construction may be found in McFarland et al. (2005a, b) and Kerschen et al. (2007). The force exerted by the mass-wire assembly on the frame is essentially nonlinear due to the absence of pretension and has been shown to be approximately cubic.

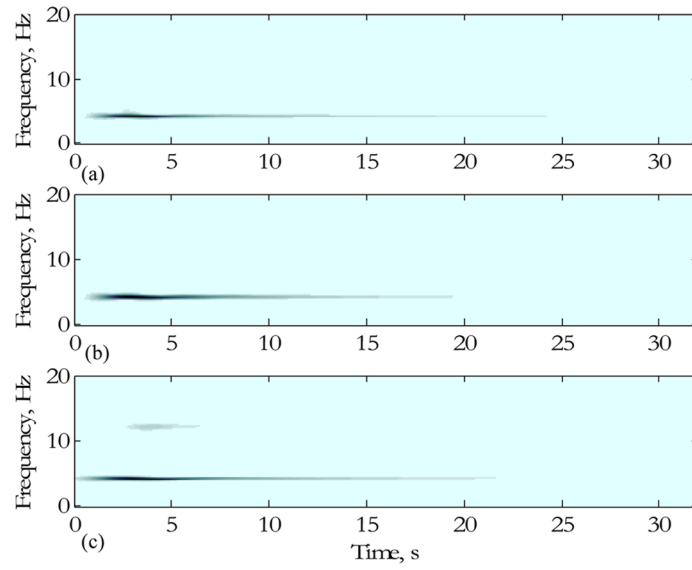


Fig. 10.34 Experimentally derived wavelet spectra of interstory displacements of the uncontrolled shear frame subjected to the Kobe earthquake: (a) RD_1 , (b) RD_2 , (c) RD_3 .

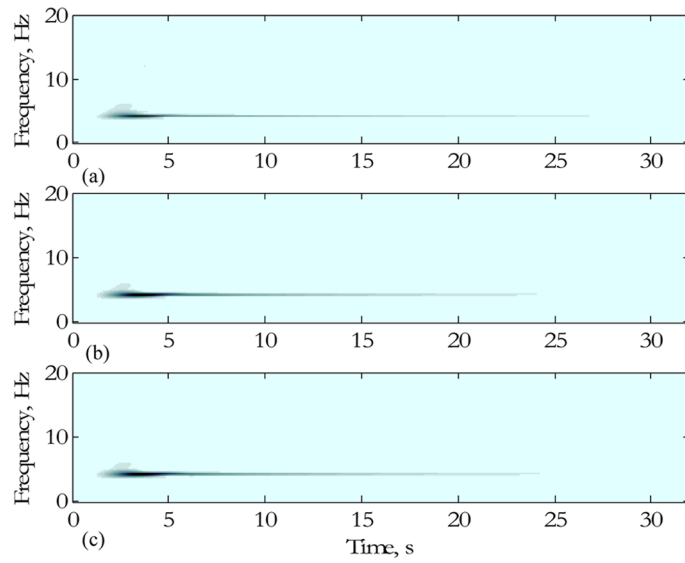


Fig. 10.35 Experimentally derived wavelet spectra of interstory displacements of the uncontrolled shear frame subjected to the Northridge earthquake: (a) RD_1 , (b) RD_2 , (c) RD_3 .

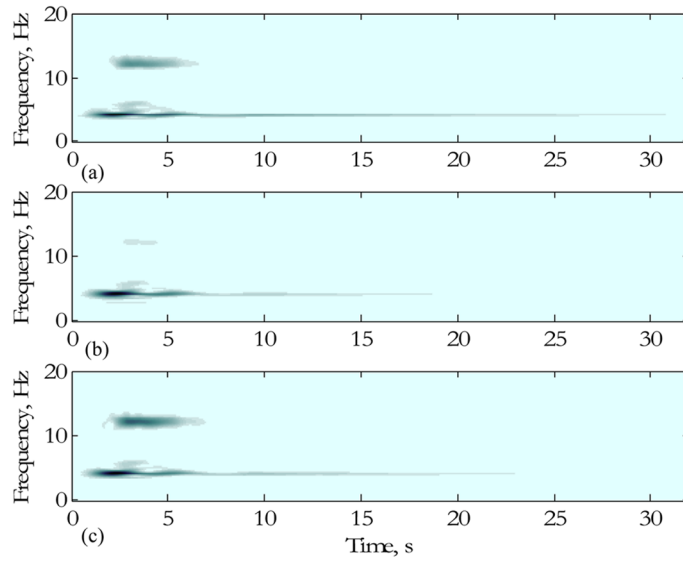


Fig. 10.36 Experimentally derived wavelet spectra of interstory displacements of the Kobe-optimized, frame-single VI NES system with 3.5% mass ratio subjected to the Kobe earthquake: (a) RD_1 , (b) RD_2 , (c) RD_3 .

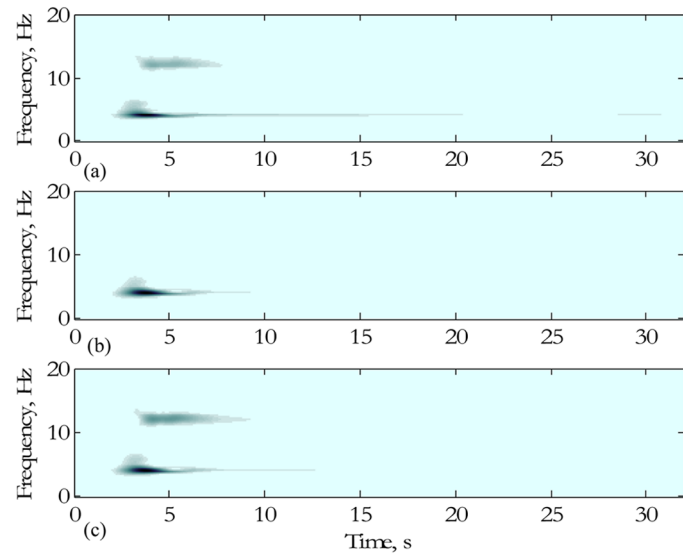


Fig. 10.37 Experimentally derived wavelet spectra of interstory displacements of the Kobe-optimized, frame-single VI NES system with 3.5% mass ratio subjected to the Northridge earthquake: (a) RD_1 , (b) RD_2 , (c) RD_3 .

Table 10.9 Experimental evaluation criteria; linear frame with Kobe-designed VI-NES at floor 1 and smooth NES at floor 3, both with 2.5% mass ratios.

Earthquake	J_1	J_2	J_3	J_4	J_5	J_6	J_7	J_8
Kobe	0.56	0.62	0.51	0.55	0.38	0.39	0.37	0.34
Northridge	0.73	0.82	0.85	0.81	0.53	0.57	0.64	0.56

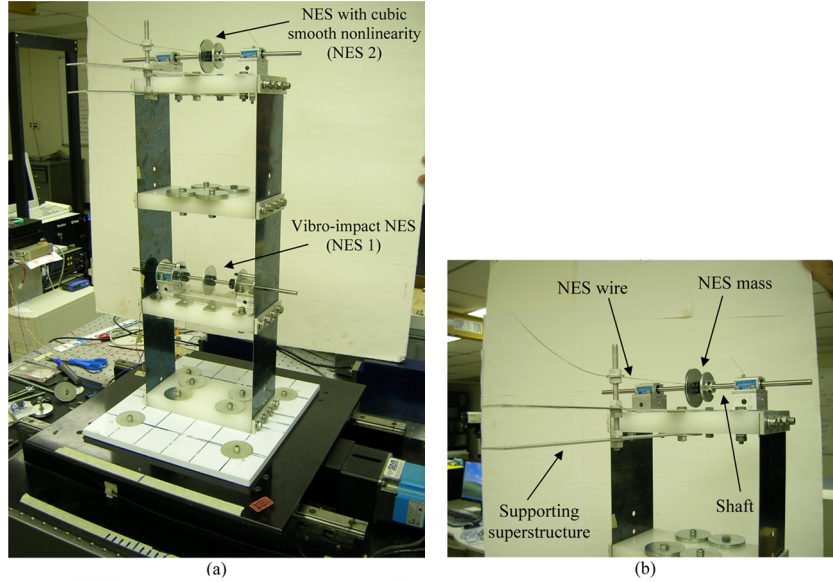


Fig. 10.38 Frame-dual NES system with the VI NES attached to floor 1 and the smooth NES attached to floor 3: (a) the full system mounted on the shake table; and (b) a detail of the smooth NES.

Fixing each of the two NES mass ratios at 2.5% of the total mass of the frame, the system optimization was repeated employing the Kobe earthquake as input. The optimal parameters for NES₁ and NES₂ were found to be: $m_{\text{NES}_1}/M_{\text{TF}} = m_{\text{NES}_2}/m_{\text{TF}} = 0.025$, $k_{\text{NES}_1}/k = 0.003$, $e = 0.012$ m, $rc = 0.43$, $k_{\text{NES}_2}/k = 16$ m⁻², and $\lambda_4/\lambda_3 = 2.8$. Displacements with respect to ground of the frame are given by Figures 10.39 and 10.40 for the Kobe and Northridge earthquakes, respectively, and a summary of the eight mitigation criteria for both records is given in Table 10.9.

Examination of the Kobe responses reveals dramatic reductions at early time during the strong motion portion of the earthquake and later, around 15 seconds, after which nearly all of the seismic energy has been released by the ground motion. Reductions of 41% and 38% are realized for maximum displacement (J_1) and maximum interstory drift (J_2), respectively. Comparison of the dual-NES and single-VI NES systems during the latter stage of response show that, while the maximum displacement is slightly higher, the normed criteria are made uniformly and markedly

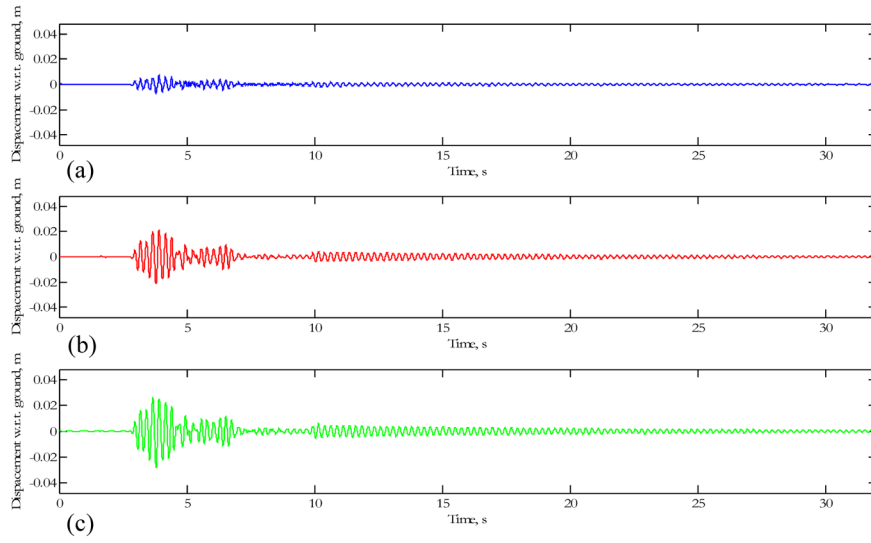


Fig. 10.39 Experimentally obtained responses of the Kobe-optimized, frame-dual NES system with a mass ratio of 2.5% subjected to the Kobe earthquake: displacements with respect to ground of the shear frame, (a) top floor 1, (b) middle floor 2, (c) bottom floor 3.

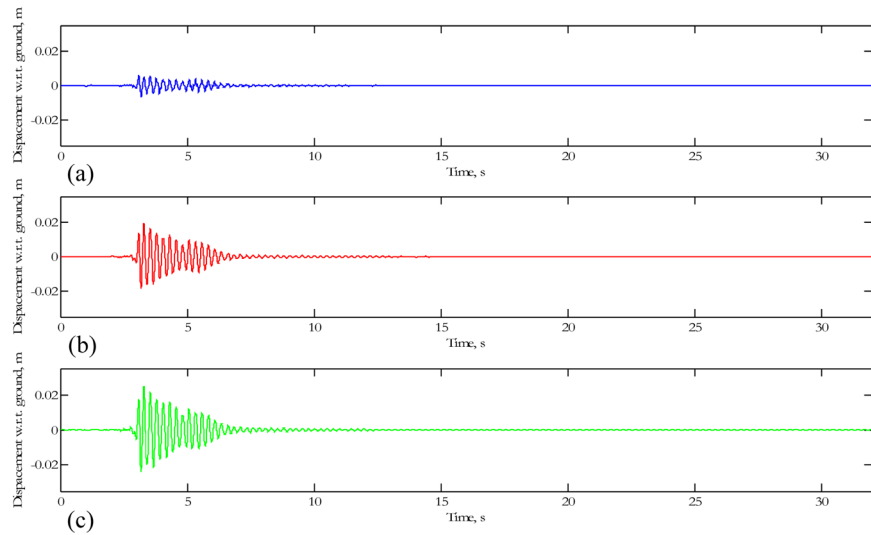


Fig. 10.40 Experimentally obtained responses of the Kobe-optimized, frame-dual NES system with a mass ratio of 2.5% subjected to the Northridge earthquake: displacements with respect to ground of the shear frame, (a) top floor 1, (b) middle floor 2, (c) bottom floor 3.

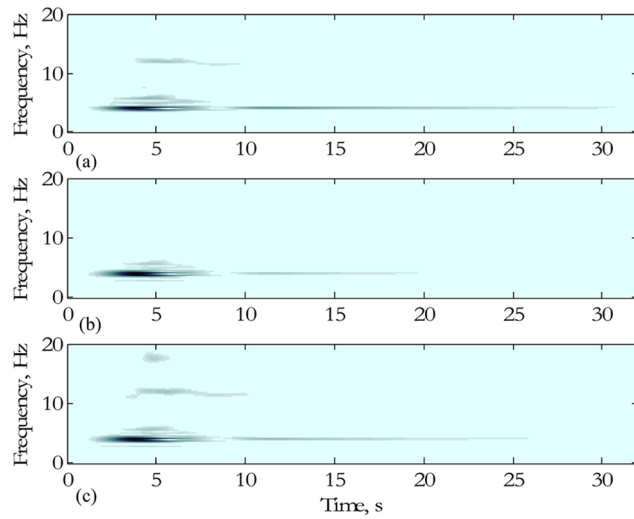


Fig. 10.41 Experimentally derived wavelet spectra of the interstory displacements of the Kobe-optimized, frame-dual NES system with mass ratios of 2.5% subjected to the Kobe earthquake: (a) RD_1 , (b) RD_2 , (c) RD_3 .

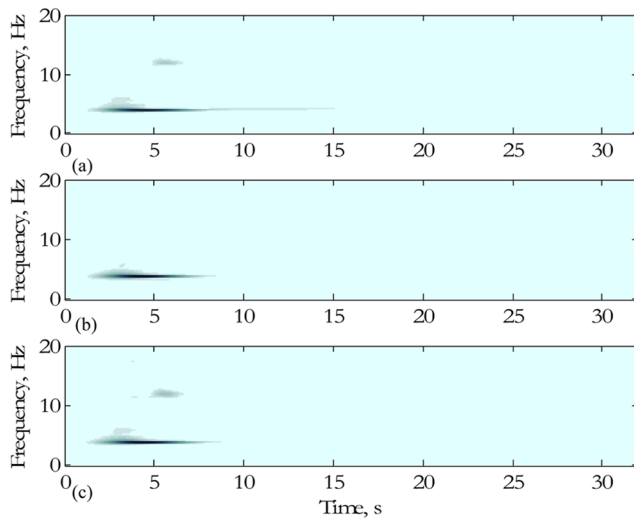


Fig. 10.42 Experimentally derived wavelet spectra of the interstory displacements of the Kobe-optimized, frame-dual NES system with mass ratios of 2.5% subjected to the Northridge earthquake: (a) RD_1 , (b) RD_2 , (c) RD_3 .

lower by the presence of NES_2 . Furthermore, the wavelet spectra of Figures 10.41 and 10.42 clearly show that spreading of seismic energy to the higher linearized modes of the system is significantly enhanced in the dual-NES design.

10.4 Observations, Summary and Conclusions

That seismic protection of buildings and other civil infrastructure will become an imperative in this century seems obvious. Construction costs associated with repair and replacement, insurance premiums, and the potential for loss of life will jointly drive the development of technologies needed to achieve cost- and performance-effective mitigation. The necessary technologies are available; however, certain of them, particularly those involving active and hybrid systems, are not viable for reasons including reliability, maintainability, cost, and energy requirements, all of which are well-documented in the literature. Passive systems, then, are most likely to gain broad acceptance, especially if performance can be made competitive with that realized by the active and hybrid systems.

Structural designers have long been wary of nonlinearity because of its association with damage. Currently, however, there is general understanding that damping in structural systems, much of it derived from friction and hysteresis occurring at many scales, is desirable, though difficult to model and accurately predict. Because of this, the constructive use of strongly nonlinear passive systems to achieve necessary levels of performance and reliability needed for effective mitigation is more likely to be accepted by the community at this time.

The case studies presented in this chapter fully demonstrate the ability of targeted energy transfer (TET), implemented through the use of nonlinear energy sinks (NESs), to mitigate seismic effects in frame structures. Efficacious design ensures that the mitigation system performs effectively over a wide range of earthquakes and under conditions of peak input acceleration ranging from extreme to moderate. The protective systems are relatively lightweight, inexpensive to fabricate and maintain, and fully passive; and unlike classical tuned mass dampers they are broadband devices that do not require frequency tuning.

We have demonstrated, in the case of the three-story frame, that multiple NESs can be deployed throughout the structure and that, with judicious design of the system, mitigation levels consistent with those reported in the literature using active and hybrid systems can be achieved passively. Furthermore, there are no scalability issues associated with passive TET; thus, application to full-scale structures should offer no significant challenges beyond those already addressed.

References

*ReferencesReferencesReferences

- Chu, S.Y., Soong, T.T., Reinhorn, A.M., *Active, Hybrid, and Semi-active Structural Control: A Design and Implementation Handbook*, Wiley, Hoboken, NJ, USA, 2005.
- DeSalvo, R., Passive, nonlinear, mechanical structures for seismic attenuation, *J. Comp. Nonlinear Dyn.* **2**, 290–298, 2007.
- Doebling, S.W., Farrar, C.R., Cornwell, P.J., A computer toolbox for damage identification based on changes in vibration characteristics, in *Structural Health Monitoring: Current Status and Perspectives*, F-K. Chang (Ed.), Technomic Publishing Co., Lancaster, PA, USA, pp. 241–254, 1997.

- Georgiades, F., *Nonlinear Localization and Targeted Energy Transfer Phenomena in Vibrating Systems with Smooth and Non-smooth Stiffness Nonlinearities*, Ph.D. Thesis, National Technical University of Athens, Athens, Greece, 2006.
- Housner, G.W., Bergman, L.A., Caughey, T.K., Chassiakos, A.G., Claus, R.O., Masri, S.F., Skelton, R.E., Soong, T.T., Spencer, B.F., Yao, J.T.P., Structural control: Past, present, and future, *ASCE J. Engrg. Mech.* **123**(9), 897–971, 1997.
- Ibrahim, S.R., Pappa, R.S., Large modal survey testing using the Ibrahim Time Domain identification technique, *AIAA J. Spacecraft Rockets* **19**(5), 459–465, 1982.
- Karayannis, I., Vakakis, A.F., Georgiades, F., Vibro-impact attachments as shock absorbers, *Proc. IME C J. Mech. Eng. Sci.* (Special Issue on ‘Vibro-impact Systems’, V. Babitsky, editor), 2008 (in press).
- Kerschen G., *On the Model Validation in Non-linear Structural Dynamics*. Ph.D. Dissertation, University of Liege, Department of Aerospace, Mechanics and Materials Engineering, 2002.
- Kerschen, G., McFarland, D.M., Kowtko, J., Sup Lee, Y., Bergman, L.A., and Vakakis, A.F., Experimental demonstration of transient resonance capture in a system of two coupled oscillators with essential stiffness nonlinearity, *J. Sound Vib.* **299**(4–5), 822–838, 2007.
- Lee, Y.S., Nucera, F., Vakakis, A.F., L.A. Bergman, D.M. McFarland, Periodic orbits and damped transitions of vibro-impact dynamics, *Physica D*, 2008 (submitted).
- McFarland, D.M., Bergman, L.A., Vakakis, A.F., Experimental study of nonlinear energy pumping occurring at a single fast frequency, *Int. J. Non-lin. Mech.* **40**(6), 891–899, 2005a.
- McFarland, D.M., Kerschen, G., Kowtko, J., Bergman, L.A., and Vakakis, A.F., Experimental investigation of targeted energy transfers in strongly and nonlinearly coupled oscillators, *J. Acoust. Soc. Amer.* **118**(2), 791–799, 2005b.
- Nucera F., *Nonlinear Energy Pumping as a Strategy for Seismic Protection*, Ph.D. Thesis, University of Calabria at Arcavacata of Rende, Cosenza, Italy, 2005.
- Nucera, F., Vakakis, A.F., McFarland, D.M., Bergman, L.A., Kerschen G., Targeted energy transfers in vibro-impact oscillators for seismic mitigation, *Nonlin. Dyn.* (Special Issue on ‘Discontinuous Dynamical Systems’) **50**, 651–677, 2007.
- Nucera, F., McFarland, D.M., Bergman, L.A., Vakakis, A.F., Application of broadband nonlinear targeted energy transfers for seismic mitigation of a shear frame: Part I. Computational results, *J. Sound Vib.*, 2008a (in press).
- Nucera, F., Lo Iacono, F., McFarland, D.M., Bergman, L.A., Vakakis, A.F., Application of broadband nonlinear targeted energy transfers for seismic mitigation of a shear frame: Part II. Experimental results, *J. Sound Vib.*, 2008b (in press).
- Ohtori, Y., Christenson, R.E., Spencer, Jr., B.F., Dyke, S.J., Benchmark control problems for seismically excited nonlinear buildings, *J. Eng. Mech.* (Special Issue on ‘Benchmark Control Problems’) **130**(4), 366–385, 2004.
- Skinner, R.I., Robinson, W.H., McVerry, G.H., *An Introduction to Seismic Isolation*, Chichester/Wiley, New York, 1993.
- Soong, T.T., *Active Structural Control: Theory and Practice*, Longman Scientific/Wiley, New York, 1990.
- Soong, T.T., Constantino, M.C., *Passive and Active Structural Vibration Control in Civil Engineering*, Springer-Verlag, New York, 1994.
- Soong, T.T., Spencer, Jr., B.F., Supplemental energy dissipation: State-of-the-art and state-of-the-practice, *Eng. Struct.* **24**, 243–259, 2002.
- Spencer, Jr., B.F., Dyke, S.J., Deoskar, H.S., Benchmark problems in structural control: Part I – Active mass driver system, *Earthquake Eng. Struct. Dynam.* (Special Issue on ‘Benchmark Structural Control Comparison’) **27**, 1127–1139, 1998a.
- Spencer, Jr., B.F., Dyke, S.J., Deoskar, H.S., Benchmark problems in structural control: Part II – Active Tendon system, *Earthquake Engineering and Structural Dynamics* (Special Issue on the Benchmark Structural Control Comparison) **27**, 1141–1147, 1998b.
- Spencer, Jr., B.F., Christenson, R.E., Dyke, S.J., Next Generation benchmark control problem for seismically excited buildings, in *Proceedings of the Second World Conference on Structural Control*, Kyoto, Japan, pp. 1351–1360, 1998c.

- Spencer, Jr., B.F., Nagarajaiah, S., State of the art of structural control, *ASCE J. Struct. Eng.* **129**(7), 845–856, 2003.
- Spencer, Jr., B.F., Sain, M.K., Controlling buildings: A new frontier in feedback, *IEEE Contr. Systems Mag.* (Special Issue on ‘Emerging Technology’) **17**(6), 19–35, 1997.
- Storn, R., Price K., Differential evolution – A simple and efficient adaptive scheme for global optimization over continuous spaces, *J. Global Optimiz.* **11**, 341–359, 1997.

Chapter 11

Suppression of Instabilities in Drilling Operations through Targeted Energy Transfer

Our final demonstration of application of TET to engineering problems concerns instability suppression in models of deep drilling of oil and gas wells. In particular, in deep-drilling operations it can be difficult to maintain a smooth cutting process at bit-rock interfaces. Among other disturbances and uncertainties in such operations, we mention the non-homogeneity of rock, the unavoidable friction effects (which are further complicated by fluid flow), and the spatially asymmetric, time-varying character of forces introduced during ‘steering’ of the drill into the well bore. All these effects interact with the drill string, which itself can be several thousand meters long (and, hence, very flexible), to produce a dynamic environment which makes the operation susceptible to instabilities.

In this chapter we address the problem of stabilizing the dynamics of a model of the drill-string system by means of nonlinear passive targeted energy transfer (TET), i.e., by adding a passive, local nonlinear energy sink (NES) to an existing configuration. In the particular application considered herein the NES takes the form of a discrete torsional oscillator consisting of a disk coupled to the drill string system through an essentially nonlinear spring and a viscous damper.

Following a precise statement of the problem to be studied, we will review some of the distinct numerical challenges associated with the study of the drill-string model. Most of these arise from the need to efficiently compute the dynamics of this model in the presence of friction and related non-smooth effects. A bifurcation diagram depicting the different qualitative dynamics of the system over a realistic range of inputs will be produced, and will be used to assess the influence of the NES parameters on the dynamics of the integrated system. A numerical study and the resulting NES design will be described next. Finally, a detailed analysis of the integrated system composed of the drill string system and the attached NES will be presented, including some remarks on the robustness of the passive control of instabilities achieved with this device. The results presented in this chapter follow closely the work by Vigué et al. (2008).

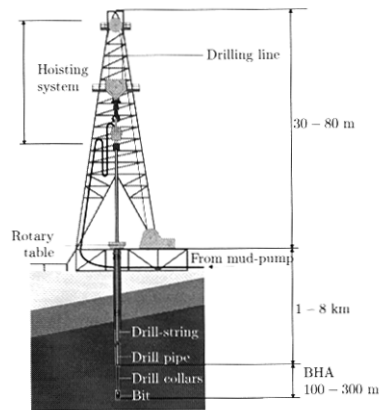


Fig. 11.1 Schematic view of the drill-string structure (Mihajlovic, 2005).

11.1 Problem Description

Deep wells for the exploration and production of oil and gas are drilled with a rotary drilling system (see Figure 11.1). A rotary drilling system creates a borehole by means of a rock-cutting tool, called the bit. The torque driving the bit is generated at the surface by a motor with a mechanical transmission box. Via the transmission, the motor drives the rotary table that consists of a large disk acting as a kinetic energy storage unit. The medium used to transport mechanical energy from the surface to the bit is a drill-string, mainly consisting of drill pipes. The drill-string is a long elastic medium, reaching in some cases up to 8 km long. The lowest part of the drill-string is the bottom-hole-assembly (BHA) consisting of drill collars and the bit.

This structure undergoes different types of vibrations during the drilling operation, including torsional (rotational) vibrations caused by the interaction between the bit and the rock, or the drill-string and the borehole wall; bending (lateral) vibrations often caused by pipe eccentricity and yielding centripetal forces during rotation; axial (longitudinal) vibrations during the rock cutting process (an extreme form of such axial vibrations is called bit bouncing); and hydraulic vibrations taking place in the circulation system, coming from pump pulsations. In addition, there exist coupling effects between torsional, lateral and longitudinal vibrations, as highlighted in Mihajlovic (2005). In this study, our efforts are only devoted towards vibration mitigation of torsional vibrations.

Numerous studies were undertaken to gain knowledge of the origins of those vibrations (Brett, 1992; Cunningham, 1968; Jansen and van den Steen, 1995; Kreuzer and Kust, 1996; Leine et al., 2002; van den Steen, 1997). It was established that a possible mechanism for torsional vibration is the stick-slip phenomenon generated by the friction force between the bit and the well (Jansen and van den Steen, 1995;

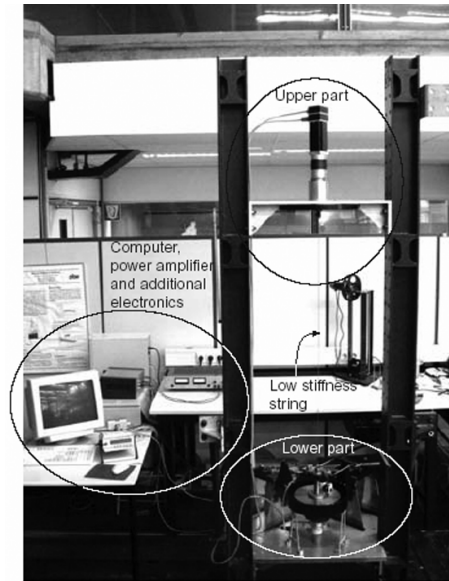


Fig. 11.2 Experimental fixture of a drill-string set-up (Mihajlovic, 2005).

Leine et al., 2002; van den Steen, 1997). Other studies showed that the cause of torsional vibrations is velocity weakening in the friction force (i.e., the Stribeck effect) due to the contact between the bit and the borehole (Brett, 1992; Kreuzer and Kust, 1996). In Richard et al. (2004) and Germaý et al. (2007) it was shown that this velocity weakening effect originates from the coupling between the torsional and axial dynamics through the bit/rock interaction. Ultimately, the velocity weakening effect plays a very important role in the occurrence of (unstable) limit cycle oscillations (LCOs) in drill-string systems (Mihajlovic et al., 2006).

To examine this instability, a prototypical drill-string system was built at the Technische Universiteit Eindhoven (Mihajlovic, 2005; Mihajlovic et al., 2006). Figure 11.2 depicts the experimental set-up, whereas Figure 11.3 presents its schematic representation. The system consists of two discs that model the inertia effects created by the rotating components in the upper (i.e., the rotary table) and lower (i.e., the BHA) parts of the system. For further details about the experimental fixture, the interested reader may refer to Mihajlovic (2005) and Mihajlovic et al. (2006).

Because the focus of this study is in the steady state torsional vibration of the drill-string system, it will be assumed that lateral movements of this system are restrained so they can be neglected from further consideration. This results in a reduced-order two-DOF analytical model, the equations of motion of which are given by

$$\begin{aligned} J_u \dot{\omega}_u - k_\theta \alpha + T_{fu}(\omega_u) &= k_m u_c \\ J_l (\ddot{\alpha} + \dot{\omega}_u) + k_\theta \alpha + T_{fl}(\omega_u + \dot{\alpha}) &= 0 \end{aligned} \quad (11.1)$$

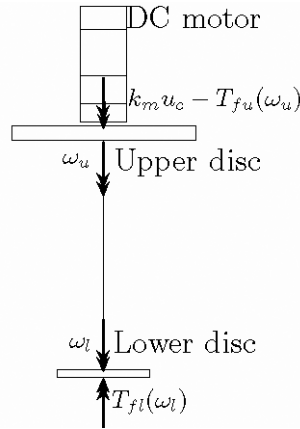


Fig. 11.3 Schematic view of the drill-string set-up (Mihajlovic, 2005).

Table 11.1 Definitions

ω_u	Velocity of the upper disk
ω_l	Velocity of the lower disk
J_u, J_l	Moment of inertia of the disks
k_m	Motor constant
T_{fu}, T_{fl}	Friction torque at the upper and lower disks
k_θ	Torsional spring stiffness
θ_u, θ_l	Angular displacements
$\alpha = \theta_l - \theta_u$	Relative angular displacement
u_c	Input voltage at the DC-motor

where the definition of the parameters in these equations is given in Table 11.1. The model consists of two linearly coupled disks, with the upper disk driven by a DC-motor, and both disks being affected by friction effects. Modeling of friction is an important issue in this problem, so we will discuss it in detail.

In order to model friction in the set-up, either static or dynamic friction models can be considered. Because the main objective of the present study is the analysis of the steady state dynamical behavior, a detailed modeling of friction for small (initial) angular velocities is not necessary. Therefore, a static friction model will be adopted for our study.

Both disks of the system are subject to friction torques that originate from different sources. On the upper disc, the applied friction torque T_{fu} is due to friction in the bearings, as well as, electro-magnetic effects in the driving DC-motor. At the lower disc, the friction torque T_{fl} is due to friction in the bearings, as well as, due to a brake mechanism that aims to reproduce the Stribeck effect. It follows that both disks are subject to a torque which results from the combination of static friction (denoted by T_{su} for the upper disk and T_{sl} for the lower) and viscous friction (applied through the viscous damping coefficients b_u and b_l for the upper and lower disks, respectively). Moreover, at the lower disk the presence of the

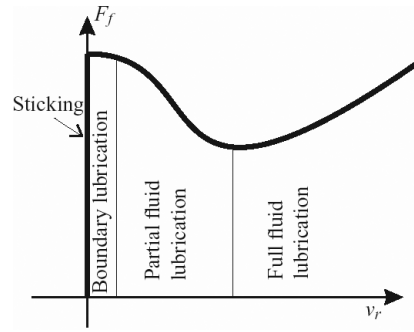


Fig. 11.4 Different regimes in the plot of the friction force F_f as a function of the relative velocity v_r .

Stribeck effect imposes the combination of the previous contributions in a Stribeck model. This model introduces new parameters, such as, the Stribeck velocity ω_{sl} , the Stribeck shape parameter δ_{sl} , and the Coulomb friction coefficient T_c . The resulting combined friction effect is depicted in Figure 11.4, which presents the plot of the dependence of friction force on relative velocity. This plot can be divided into four different regimes: sticking, boundary lubrication, partial fluid lubrication and full fluid lubrication. All these regimes, as well as further details about this friction model, are discussed in Armstrong-Helouvry (1991), Canudas de Wit et al. (1995), Olsson (1996), Hensen (2002), Mihajlovic (2005) and Viguié (2006).

Summarizing, the friction torques acting on the upper and lower disks can be expressed by the following set-valued force laws:

$$T_{fu}(\omega_u) = \begin{cases} T_{cu}(\omega_u) \operatorname{sgn}(\omega_u), & \text{for } \omega_u \neq 0 \\ [-T_{su}, T_{su}], & \text{for } \omega_u = 0 \end{cases} \quad (11.2)$$

$$T_{fl}(\omega_l) = \begin{cases} T_{cl}(\omega_l) \operatorname{sgn}(\omega_l), & \text{for } \omega_l \neq 0 \\ [-T_{cl}(0^-), T_{cl}(0^+)], & \text{for } \omega_l = 0 \end{cases} \quad (11.3)$$

where subscripts u and l refer to upper and lower parts of the set-up depicted in Figure 11.3, respectively. In these relations the terms $T_{cu}(\omega_u)$ and $T_{cl}(\omega_l)$ express the velocity dependencies of the friction torques acting on the upper and lower disks, respectively, and are defined by the following expressions:

$$T_{cu}(\omega_u) = T_{su} + b_u |\omega_u| \quad (11.4)$$

$$T_{cl}(\omega_l) = T_{cbl} + (T_{sl} - T_{cbl}) \exp(-|\omega_l/\omega_{sl}|^{\delta_{sl}}) + b_l |\omega_l| \quad (11.5)$$

where T_{sl} and T_{cbl} refer, respectively, to the static friction and Coulomb friction torque acting on the lower disk, and similar notation is used for the upper disk. Figures 11.5 and 11.6 depict the combined friction torques acting on the upper and lower disks as functions of the corresponding angular velocities.

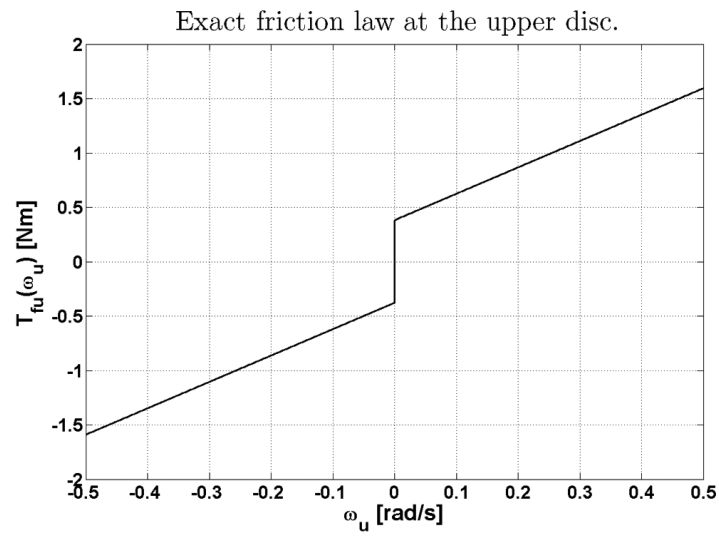


Fig. 11.5 Friction torque acting on the upper disk.

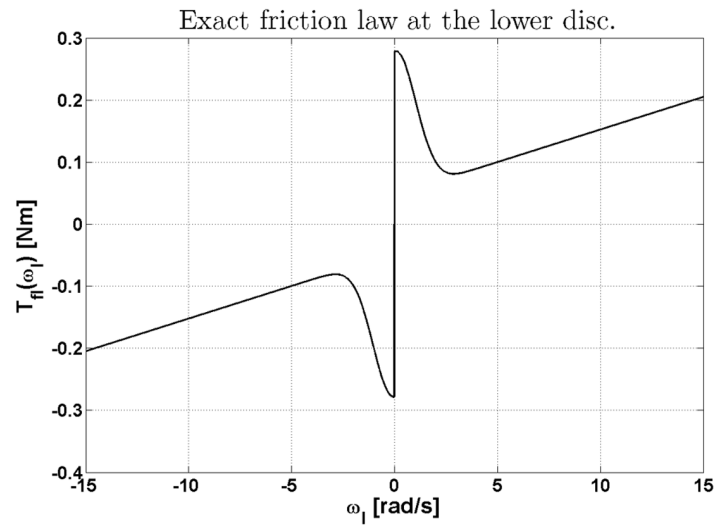


Fig. 11.6 Friction torque acting on the lower disk.

The present study focuses on numerical simulations of the two-DOF reduced-order model (11.1). The numerical values of the parameters of this model, however, are taken to be identical to the corresponding system parameters identified in the experimental fixture developed by Mihajlovic (2005); the numerical values of the parameters of the model are listed in Table 11.2. Hence, the computational results

Table 11.2 Parameters of the two-DOF drill-string system for the bifurcation diagram presented in Figure 11.7.

J_u	0.4765 kg·m ² /rad
k_m	4.3228 N·m/V
T_{su}	0.37975 N·m
b_u	2.4245 N·m·s/rad
k_θ	0.0775 N·m/rad
J_l	0.0414 kg·m ² /rad
T_{sl}	0.2781 N·m
c_{sl}	0.0473 N·m
ω_{sl}	1.4302 rad/s
δ_{sl}	2.0575
b_l	0.0105 N·m·s/rad

presented in this chapter should be directly comparable to the experimental results reported in the above-mentioned work by Mihajlovic.

11.2 Instability in the Drill-String Model

The objective of this section is to study the steady state behavior of the reduced two-DOF drill-string model for constant input voltage u_c . The steady state behavior is of particular interest, since this system is typically driven by a constant torque while aiming at a constant velocity at the lower part of the set-up. The presence of friction and related discontinuities in the equations of motion dictate the use of appropriate numerical algorithms to efficiently compute the dynamical responses.

In this study, the so-called *switch model* is used. It aims in approximating a differential inclusion by sets of ordinary differential equations. This concept is explained in great detail in Leine and Nijmeijer (2004), and its application to the drill-string system is described in Vigié et al. (2008). The numerical integration process provides the possible steady state solutions of the dynamics, such as equilibrium points, and periodic or quasi-periodic orbits. Typically, these solutions are presented in bifurcation plots using selected system parameters as bifurcation parameters. We now proceed to construct the bifurcation plot of steady state responses of the two-DOF drill-string model considering the input voltage u_c as bifurcation parameter; the numerical values of the remaining parameters are listed in Table 11.2. In order to obtain accurate approximations of these solutions and their related stability, specific numerical methods and stability analysis techniques must be considered.

Stable equilibrium points can be easily computed using numerical simulations, but a more general method consists of the resolution of the algebraic inclusion of the discontinuous system. Moreover, the related stability (local and global) can be determined using Lyapunov's indirect and direct methods. For the computation of stable and unstable periodic solutions, a shooting method is used in this study (Keller, 1976). This method relies on an iterative process and requires an initial guess. The

local stability of the periodic solutions is determined using Floquet theory. The association of the previous methods with the arc length continuation method enables us to compute the bifurcation diagrams of the system for varying values of the constant input voltage u_c .

Throughout this study, we adopt the same terminology for the bifurcation diagrams. The periodic solutions leading to limit cycle oscillations (LCOs) are denoted by ‘ p ’, whereas the branches of equilibrium positions by ‘ e ’. Solid and dotted lines refer to stable and unstable branches, respectively. The bifurcation diagram of the steady state dynamics of system (11.1–11.5) is depicted in Figure 11.7.

The following remarks concern the structure of the branches of equilibrium points of the system. For input voltages below a critical value $u_c \leq u_A$ (bifurcation point A in Figure 11.7b) there is a single branch of asymptotically stable (trivial) equilibrium points e_1 , and therefore the operation of the drill-string is stable. For input voltages in the range $u_A \leq u_c \leq u_{h1}$ the trivial branch becomes unstable, and gives rise to the branch of asymptotically stable (non-trivial) equilibrium points e_2 . This branch loses stability in the interval $u_{h1} \leq u_c \leq u_{h2}$ and appears as a branch of unstable equilibrium points denoted by e_3 in the bifurcation diagram. Finally, for relatively high voltages, $u_c > u_{h2}$ this branch of equilibrium points regains asymptotic stability and appears as branch e_4 in the bifurcation diagram. Hence, there occur two main bifurcations corresponding to points B and C in the bifurcation plots of Figure 11.7, associated with exchanges of stability of the branch of stable equilibrium positions $e_2 - e_4$. As shown below, these bifurcations give rise to stable LCOs which inadvertently affect the stability of the operation of the drill-string; however, for sufficiently high voltages ($u_c > u_E$ in Figure 11.7a) branch e_4 is the only stable steady state solution of the system.

In this system LCOs are generated due to a steady state balance between the ‘stabilizing’ effect of viscous friction (at higher velocities) and the ‘destabilizing’ effect of the Stribeck effect (at lower velocities). Considering the bifurcation plots of Figure 11.7 we note that for input voltages higher than u_{h1} (i.e., above point B in Figure 11.7b), in addition to the branch e_3 of unstable equilibrium points, there exists the branch p_1 of periodic solutions consisting of unstable LCOs without stick-slip. It follows that point B is a subcritical Hopf bifurcation point. The branch of unstable LCOs p_1 is connected to branch p_2 of stable LCOs at point D (see Figure 11.7b). The branch p_2 consists of LCOs during which the drill-string undergoes torsional vibration with stick-slip, so that D is a point of (discontinuous) saddle-node (SN) bifurcation. Moreover, at point C a subcritical Hopf bifurcation takes place that generates the branch p_3 of unstable LCOs. This unstable LCO branch merges with the stable LCO branch p_2 at point E, in a SN bifurcation of LCOs (see Figure 11.7a). For voltages $u_c > u_E$ no LCOs are possible in the drill-string model. To illustrate some of the above-mentioned steady state solutions, in Figure 11.8 we present direct numerical integrations of the system on a branch of stable LCOs, as well as, a case of attraction of the dynamics by a stable equilibrium position.

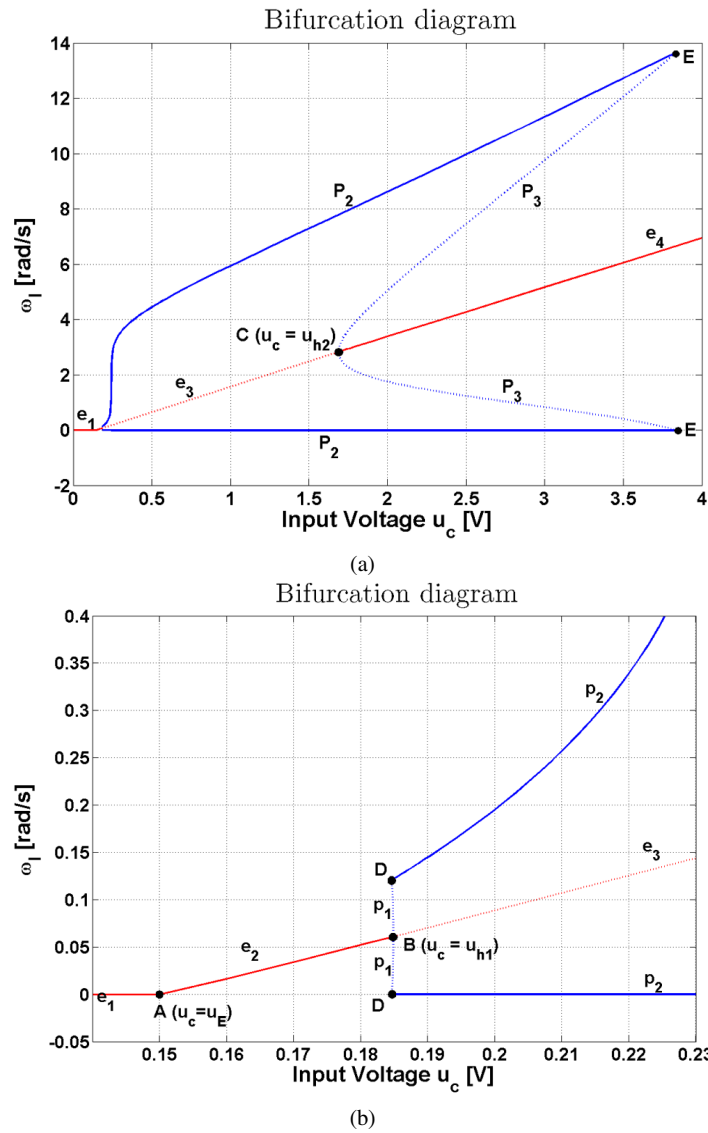


Fig. 11.7 Steady state dynamics of the two-DOF drill-string model for varying voltage u_c : (a) bifurcation diagram, (b) zoom in the low voltage range; solid lines correspond to stable solutions and dotted lines to unstable ones.

11.3 Suppression of Friction-Induced Limit Cycles by TET

We now study passive suppression of destabilizing LCOs in the drill-string model through TET. To this end, we attach an essentially nonlinear, passive torsional non-

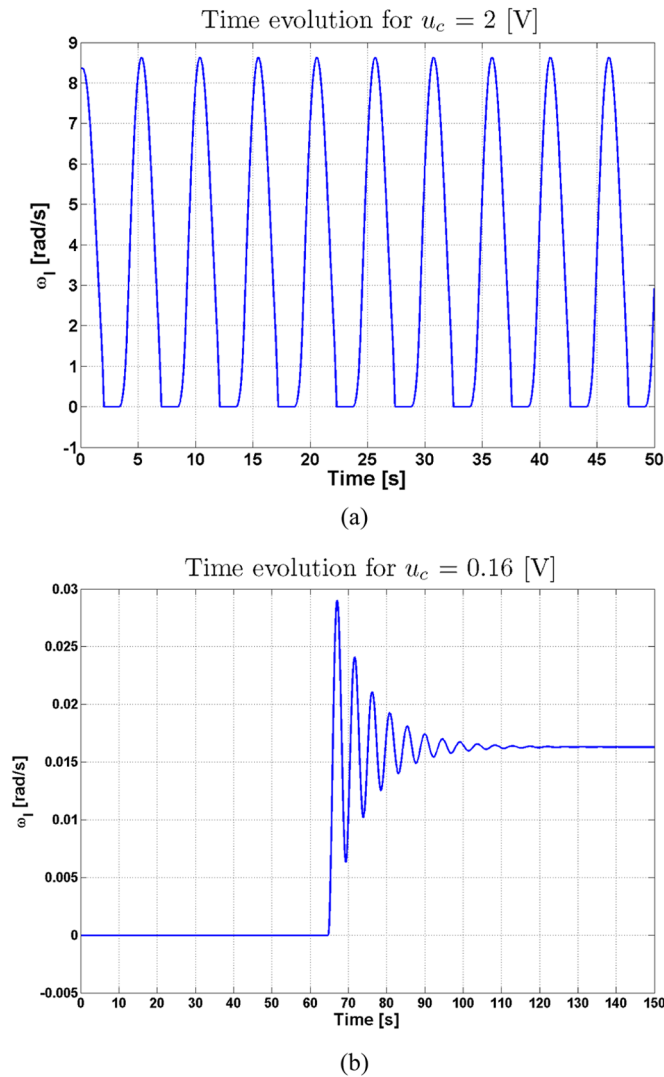


Fig. 11.8 Direct numerical simulation of the drill-string model: (a) stable LCO with stick-slip on branch p_2 ($u_c = 2$ V); (b) transition of the dynamics to a stable equilibrium point on branch e_2 ($u_c = 0.16$ V).

linear energy sink (NES) to the lower disk and study its effect on the dynamics. From previous applications it has been shown that appropriately designed NESs are capable of absorbing and locally dissipating significant portions of vibration energy from the systems to which they are attached; moreover, this type of passive devices are capable of absorbing energy at extended frequency ranges through transient or sustained resonance captures with multiple structural modes. Additional advantages

of the proposed design is that it brings only relatively minor structural modification to the drill-string system, and that it does not require any external energy supply for its operation.

11.3.1 Addition of an NES to the Drill-String System

As discussed in previous chapters, the tuned mass damper (TMD) is a simple and efficient device, but it is only effective when it is precisely tuned to the frequency of a vibration mode of the structure to which it is attached. In the drill-string problem under consideration, the nonlinear primary system possesses a single vibration mode, but the LCOs during operation have frequencies that vary with the input voltage u_c . It follows, that in this case, the TMD would have to be tuned to a particular frequency (i.e., on a specific LCO of the system), which would clearly limit its efficiency and robustness.

To overcome the limitations of the TMD, an essentially nonlinear attachment (characterized by the absence of a linear term in the force-displacement relation) is added to the system, and designed to act as a nonlinear energy sink (NES) and local dissipater of undesired vibrations. As shown in previous chapters an NES possesses certain important properties. Indeed, since the NES does not possess any preferential resonant frequency, it is capable of engaging in resonance capture with any structural mode of the system to which it is attached, irrespective of the frequency range where that mode lies (as long, of course, as the mode has no node close to the point of attachment of the NES). For instance, an NES may resonate with, and extract energy through TET from any mode of a primary structure through either isolated transient resonance captures (TRCs) or resonance capture cascades (RCCs). This versatility of the NES makes it particularly suitable for passive elimination of the stick-slip LCOs described in the previous section, whose frequencies vary with varying input voltage (the passive elimination of a different type of aeroelastic LCOs through passive TET was already demonstrated in Chapter 9).

The use of an NES therefore seems promising for vibration mitigation of nonlinear primary systems such as a drill-string system, since passive TET from the drill-string to the NES may reduce the amplitude of vibration, or even completely eliminate the LCO instabilities. However, the increased complexity of the dynamical behavior of the integrated system with the attached NES, dictates that the dynamics be carefully studied, and the robustness of the proposed design to changes of initial conditions be addressed.

The addition of the NES yields an additional degree-of-freedom in the system; the NES consists of a disk with moment of inertia J_{add} , coupled to the lower disc of the drill-string by a cubic stiffness, $k_{\theta nl}$, which lies in parallel to a dashpot with damping coefficient c_a (see Figure 11.9). The only degree-of-freedom of this disk is its rotation θ_a about its geometric center, whereas any lateral motion is assumed to be negligible. Hence, the equations of motions of the three-DOF integrated system with NES attached are given by

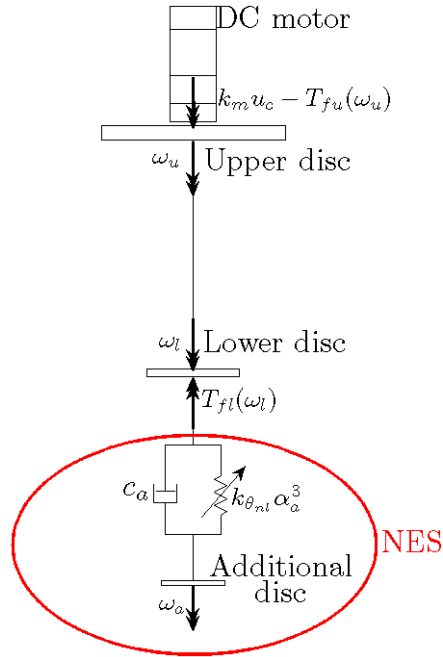


Fig. 11.9 Integrated drill-string system with torsional NES attached.

$$\begin{aligned}
 J_u(\dot{\omega}_u - \ddot{\alpha}) - k_\theta \alpha + T_{fu}(\omega_l + \dot{\alpha}) &= k_m u \\
 J_l(\dot{\omega}_l + k_\theta \alpha - k_{\theta nl}(\alpha_a)^3 - c_a \dot{\alpha}_a + T_{fl}(\omega_l)) &= 0 \\
 J_u(\dot{\omega}_l + \ddot{\alpha}_a) + k_{\theta nl}(\alpha_a)^3 + c_a \dot{\alpha}_a &= 0
 \end{aligned} \tag{11.6}$$

where $\alpha_a = \theta_a - \theta_l$.

A parametric study of the dynamics of the integrated system was performed to study the effect of the NES on the steady state responses. In particular, of significant practical interest is to investigate the efficacy of reducing or even completely eliminating the domain of existence of unwanted stable LCOs through passive TET from the drill-string to the NES, as this would stabilize the operation of the integrated system and enhance its performance.

11.3.2 Parametric Study for Determining the NES Parameters

In the parametric design we performed a study on the effect of the NES parameters, namely the nonlinear stiffness $k_{\theta nl}$, the moment of inertia J_{add} , and the damping coefficient c_a , on TET and drill-string stabilization. This study provided a set of values for these parameters; we mention at this point that the design objective was not to

Table 11.3 Initial set of NES parameters.

J_{add}	0.025895 kg·m ² /rad
c_a	0.0105 N·m·s/rad
$k_{\theta nl}$	0.0025 N·m/rad ³

determine the optimal set of values for the NES parameters, but rather to establish the efficacy of using an NES in order to extend the range of working input voltages for which stick-slip LCOs in the integrated system could be avoided. Therefore, an initial set of parameter values was utilized, and then adapted to obtain the largest range of input voltages leading to stable equilibrium solutions and avoidance of stick-slip limit cycling (i.e., of periodic solutions).

For obvious practical reasons, we selected the mass ratio between the NES and the drill-string system to be as small as possible, and followed the same design rules as those considered in our previous applications. To this end, the NES inertia was initially set equal to 5% of the total inertia of the system. In practice, this value may seem to be large, but the focus of our study was on the new dynamics introduced by the addition of the NES to the nonlinear (discontinuous) primary structure, instead of providing an NES design that could be directly applied to practical applications. As the inertia of the additional NES disk was close to that of the lower disk, the NES dashpot was chosen so that its viscous damping coefficient be of value close to that of the lower disk b_1 . Finally, the determination of the nonlinear (cubic) stiffness was based on the linear stiffness of the string of the primary system. The aim was to find a value of the nonlinear stiffness that creates an elastic torque of the same order of magnitude to that in the primary system. Based on this rationale, the selected initial set of NES parameters is listed in Table 11.3.

A series of numerical simulations was carried out by varying a single parameter of the initial set in order to assess the impact of the nonlinear structural modification on the dynamical behavior of the integrated system; this impact was studied through bifurcation diagrams. The results related to these numerical experiments are available in Vigiúé (2006), and are summarized in Tables 11.4–11.6 for modifications of nonlinear stiffness $k_{\theta nl}$, moment of inertia J_{add} and viscous coefficient c_a , respectively. Depending on the selected parameter values, the existence of periodic solutions is restricted to wider or narrower ranges of input voltage. For instance, the selection of the nonlinear stiffness coefficient is crucial, as judged from the results listed in Table 11.4; indeed, for some values of the nonlinear stiffness coefficient time-periodic solutions (LCOs) are realized up to 3.5 V, whereas for others values of this parameter LCOs exist only up to 1.7 V. The parametric study in Vigiúé (2006) showed that the sets of parameters in Table 11.7 provide interesting results regarding LCO suppression in the drill-string system.

An illustrative example of the effect of the NES on the dynamics is presented in Figure 11.10; the results clearly show that the effect of the NES is to stabilize the operation of the drill-string system for an input voltage equal to 2 V. It is worth mentioning that the equilibrium of the system without NES, $\omega_l = \omega_u = \omega_{\text{eq}}$ and

Table 11.4 Changes in the bifurcation diagram for variation of the nonlinear stiffness $k_{\theta nl}$.

$k_{\theta nl}$ (Nm/rad ³)	$k_{\theta nl}$ ($n \times k_{\theta nl \text{ init}}$)	Stable equilibria (range)	Other solutions (range)	Other solutions (type)
0.0025	1	[1.7 →] V	[0.3 → 1.7] V	Periodic solutions
1	4×10^2	[3.5 →] V	[0.3 → 3.5] V	Periodic solutions
1×10^{-2}	4	[2.9 →] V	[0.3 → 2.9] V	Periodic solutions
1×10^{-3}	4×10^{-1}	[2.1 →] V	[0.3 → 2.1] V	Periodic solutions
1×10^{-7}	4×10^{-5}	[2.6 →] V	[0.3 → 2.6] V	Periodic solutions

Table 11.5 Changes in the bifurcation diagram for variation of the inertia J_{add} .

J_{add} (kg·m ²)	J_{add} (% of J_{tot})	Stable equilibria (range)	Other solutions (range)	Other solutions (type)
0.25895	50	[2.5 →] V	[0.3 → 2.5] V	Periodic solutions
0.05179	10	[2.1 →] V	[0.3 → 2.1] V	Periodic solutions
0.03107	6	[1.9 →] V	[0.3 → 1.9] V	Periodic solutions
0.02072	4	[1.6 →] V	[0.3 → 1.6] V	Periodic solutions
0.01294	2.5	[2.8 →] V	[0.3 → 2.8] V	Periodic solutions
0.00259	0.5	[3.6 →] V	[0.3 → 3.6] V	Periodic solutions

Table 11.6 Changes in the bifurcation diagram for variation of the damping coefficient c_a .

c_a (Nms/rad)	c_a ($n \times c_{a, \text{init}}$)	Stable equilibria (range)	Other solutions (range)	Other solutions (type)
0.1050	10	[2.8 →] V	[0.3 → 2.8] V	Periodic solutions
0.0210	2	[1.7 →] V	[0.3 → 1.7] V	Periodic solutions
0.00525	0.5	[2.1 →] V	[0.3 → 2.1] V	Periodic solutions
0.00105	0.1	[3.5 →] V	[0.3 → 3.5] V	Periodic solutions

Table 11.7 Selected NES parameters.

Set	$k_{\theta nl}$ (Nm/rad ³)	J_{add} (kg·m ²)	c_a (Nms/rad)
#1	0.002515	0.025895	0.0105
#2	0.002515	0.020716	0.0105
#3	0.002515	0.025895	0.0210

$\alpha = \alpha_{\text{eq}}$, is preserved also in the system with NES attached as the new equilibrium $\omega_l = \omega_u = \omega_a = \omega_{\text{eq}}$ and $\alpha = \alpha_{\text{eq}}$. We note that the new equilibrium solution provided by the NES (and depicted in Figure 11.10b) might not be the only possible steady state solution at this particular value of the voltage. This issue is addressed by a detailed study of the topology of the steady state solutions of the integrated system performed in the next section.

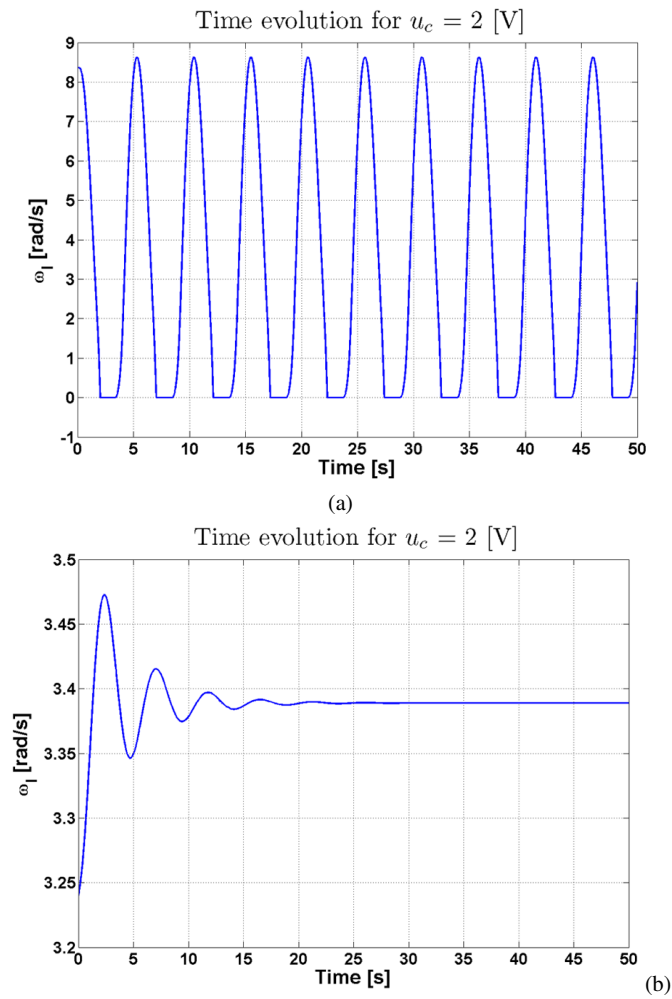


Fig. 11.10 Direct numerical simulation of the drill-string system for input voltage $u_c = 2$ V: (a) without NES; (b) with NES (parameter set 1).

11.4 Detailed Analysis of the Drill-String with NES Attached

We now carry out a detailed analysis of the nonlinear dynamics of the drill-string system coupled to the NES. The main result of this analysis consists of bifurcation diagrams of the integrated system for the three sets of NES parameters listed in Table 11.7. Moreover, the basins of attraction of the stable solutions (for given input voltages) are presented. The purpose of the study is to investigate the NES efficacy and robustness together with the complexity of the resulting dynamical behavior. Finally, the wavelet transform is applied to the resulting time series in order to iden-

tify TRCs between the drill-string system and the NES. As discussed in previous chapters, this type of transient resonance interactions is responsible for passive TET in the integrated system.

11.4.1 NES Efficacy

To examine the efficacy of using an NES to stabilize the drill-string system, in Figure 11.11 we depict the comparison of bifurcation diagrams of the steady state dynamics of the system with and without NES attached. In these diagrams we adopt the notation of Figure 11.7 to denote the branches of equilibrium points and periodic orbits. These results clearly demonstrate the uniform improvement of the steady state dynamical behavior brought by the addition of the NES, for all three parameter sets considered (see Table 11.7).

In particular, we note the following: (i) the ranges of input voltages corresponding to stable equilibrium points (i.e., the nominal behavior of the drill-string system) increase; (ii) the LCOs of the drill-string system can be completely eliminated in certain voltage ranges; and (iii) the addition of the NES can result in partial LCO suppression, i.e., it can reduce the amplitude of the surviving LCOs in the regions where complete elimination is not possible (mainly for voltages below 1.8 V). Moreover, a comparison of the bifurcation diagrams presented in Figure 11.11 reveals that, depending on the NES parameters the dynamics of the system in regions of partial LCO suppression can be either relatively simple (e.g., parameter set 3 – Figure 11.11d), or more complicated (e.g., parameter set 1 – Figure 11.11b).

For the quantitative assessment of NES efficacy, three different criteria are considered: (i) the percentile reduction of the range of voltages leading to unstable equilibrium points and their stabilization to asymptotically stable equilibrium points; (ii) the percentage of the voltage range leading to stable equilibrium points in the range [0, 3.38 V]; and (iii) the percentage of the input voltage range [1.69 V, 3.83 V] for which locally stable equilibrium solutions are transformed to globally stable equilibrium solutions (or equivalently, complete LCO suppression by the NES).

The numerical values related to these criteria are listed in Table 11.8, and show that the NES parameter set 3 (see Table 11.7) provides a wider range of voltages leading to globally stable equilibrium solutions; hence, for this parameter set better stabilization of the drill-string operation results. Only NES parameter sets 1 and 3 are considered in detail in this study, as their respective bifurcation diagrams present clear differences due to the differences of the corresponding damping coefficients. Another advantage of using the NES parameter set 3 is that it leads to a less complex bifurcation diagram, as seen from the plots depicted in Figure 11.11.

A complete characterization of the different bifurcation diagrams is beyond the scope of this work. However, we note that transitions between different branches may be realized through discontinuous SN bifurcations and subcritical Hopf bifurcations.

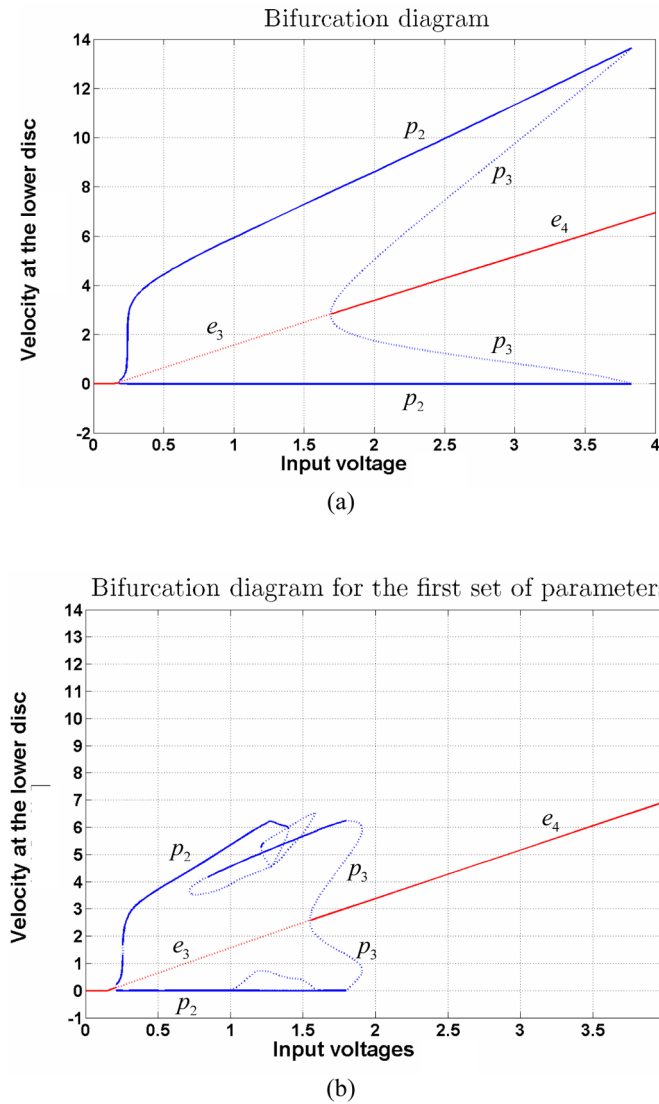


Fig. 11.11 Bifurcation diagrams of steady state solutions for the system with (a) no NES attached; (b) NES with parameter set 1 (see Table 11.7); solid lines correspond to stable solutions and dotted lines to unstable ones.

An additional aim of the passive vibration mitigation design is to structurally perturb the primary (drill-string) system to the lowest possible extent. Accordingly, the NES was kept as light as possible. The second parameter set in Table 11.7 corresponds to rotating inertia for the NES equal to 4% of the total rotating inertia, instead of 5% used for parameter sets 1 and 3. Comparing the bifurcation diagrams

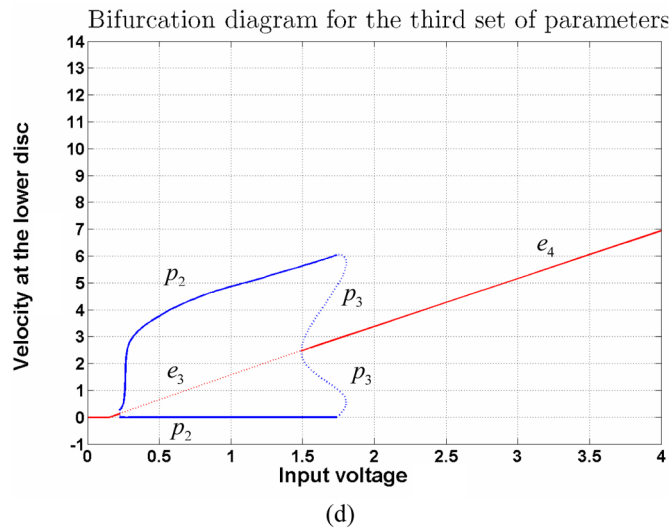
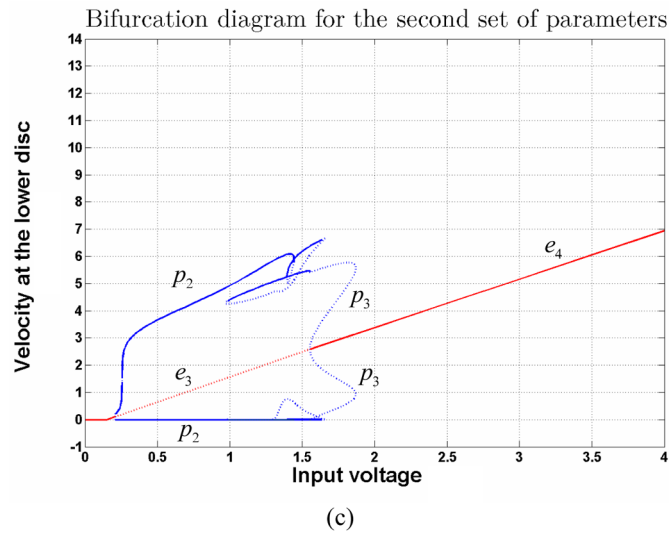


Fig. 11.11 Bifurcation diagrams of steady state solutions for the system with (c) NES with parameter set 2; (d) NES with parameter set 3; solid lines correspond to stable solutions and dotted lines to unstable ones.

corresponding to NES parameter sets 1 and 2 (which differ only slightly by the NES mass moment of inertia – depicted in Figures 11.11b and 11.11c, respectively), we note that, although the corresponding global topologies of the branches of steady state solutions appear to be similar, the slightly larger rotating inertia introduces added complexity to the steady state dynamics in the local range [0.7 V, 1.7 V].

Table 11.8 Stabilization of the drill-string system (quantitative assessment).

Criterion	Set 1 (%)	Set 3 (%)	Difference (%)
(i)	11.04	15.89	4.85
(ii)	65.04	66.95	1.91
(iii)	94.95	97.66	2.71

This confirms the added complexity of the dynamics of the integrated system, due to the strongly nonlinear stiffness characteristic of the attached NES.

11.4.2 Robustness of LCO Suppression

The previous parametric study indicated that there are ranges of input voltages at which multiple stable and unstable steady state solutions co-exist. Indeed, a key feature of nonlinear dynamical responses is that multiple periodic, quasi-periodic, equilibrium or even chaotic solutions may coexist in certain parameter ranges. For instance, in the drill-string system a stable LCO may coexist with a stable equilibrium point in certain ranges of input voltage. What determines the attraction of the dynamics to either one of these co-existing steady state solutions is the specific set of initial conditions of the system, which places the dynamics in the domain of attraction of either one of the stable attractors. Therefore, to study the robustness of the passive vibration control realized by the addition of the NES, it is meaningful to study the basins of attraction of each of the computed co-existing steady state solutions.

The integrated system (11.6) consisting of the drill-string and the attached NES possesses a five-dimensional phase space, meaning that the corresponding basins of attraction of its stable solutions are five-dimensional. It follows that for graphical representation of the basins of attraction, only two phase variables will be varied, namely the velocity of the lower disc ω_1 and the deformation of the string of the primary system α . All other phase variables will be assumed to possess zero initial values.

The basins of attraction of the attractors of the integrated system for input voltages $u_c = 2$ V and $u_c = 1.65$ V are depicted in Figures 11.12 and 11.13, respectively; these plots enable us to get insight into the variations of the basins of attraction when the NES is added to the drill-string system. Circles and stars refer to initial conditions leading to stable LCOs and stable equilibrium points, respectively. It is noted that for an input voltage $u_c = 2$ V (see Figure 11.12), the transformation of locally stable equilibrium points into globally stable equilibrium points due to the action of the NES, is evident for the three parameter sets considered in this study. For an input voltage of $u_c = 1.65$ V (see Figure 11.13) we note the complicated dynamics introduced by the NES for parameter set 1; this does not hold, however, for parameter set 3. These diagrams confirm that the LCOs originally present in

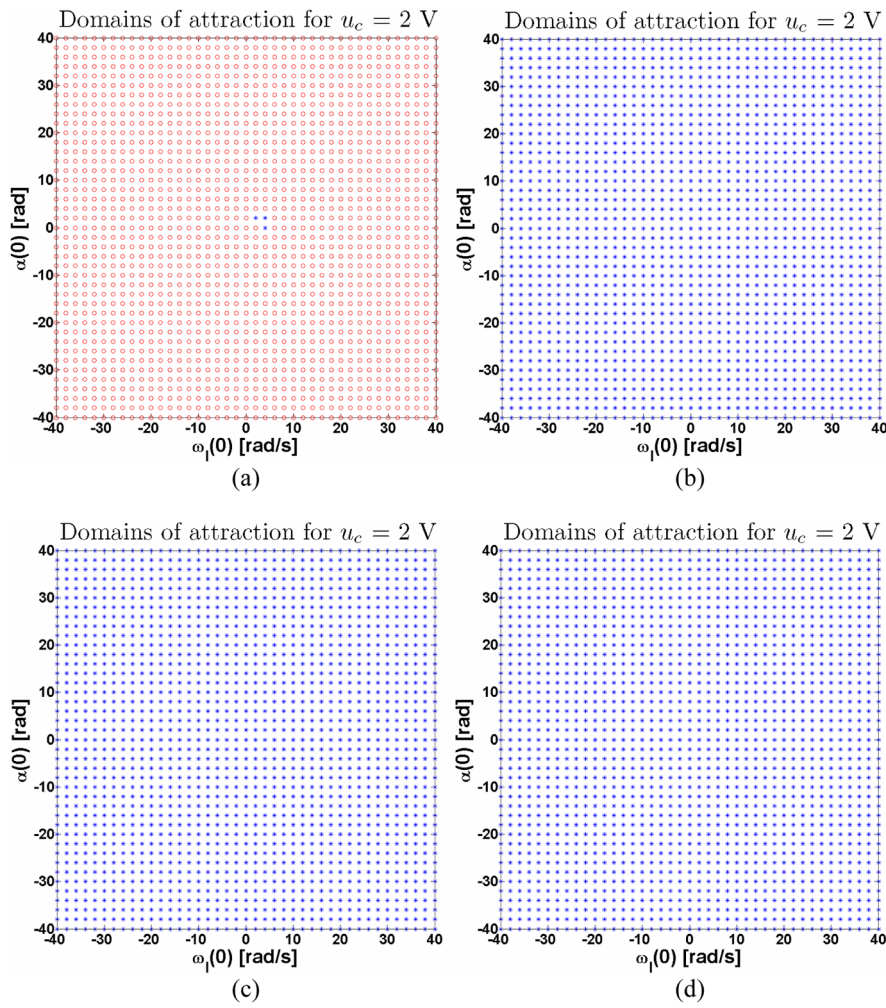


Fig. 11.12 Domains of attraction of the dynamics of the integrated system for input voltage $u_c = 2$ V, system with (a) no NES attached; (b) NES parameter set 1; (c) NES parameter set 2; (d) NES parameter set 3; circles denote attraction by stable periodic solutions and stars denote attraction by stable equilibrium points.

the drill-string system without NES attached, have been transformed into locally asymptotically stable equilibrium points in the integrated system.

A final remark is that these numerical results confirm that the branch e_4 of stable equilibrium points of the bifurcation diagrams in Figures 11.11b and 11.11d consists indeed of locally (for $u_c = 1.65$ V) or globally (for $u_c = 2$ V) asymptotically stable equilibrium points.

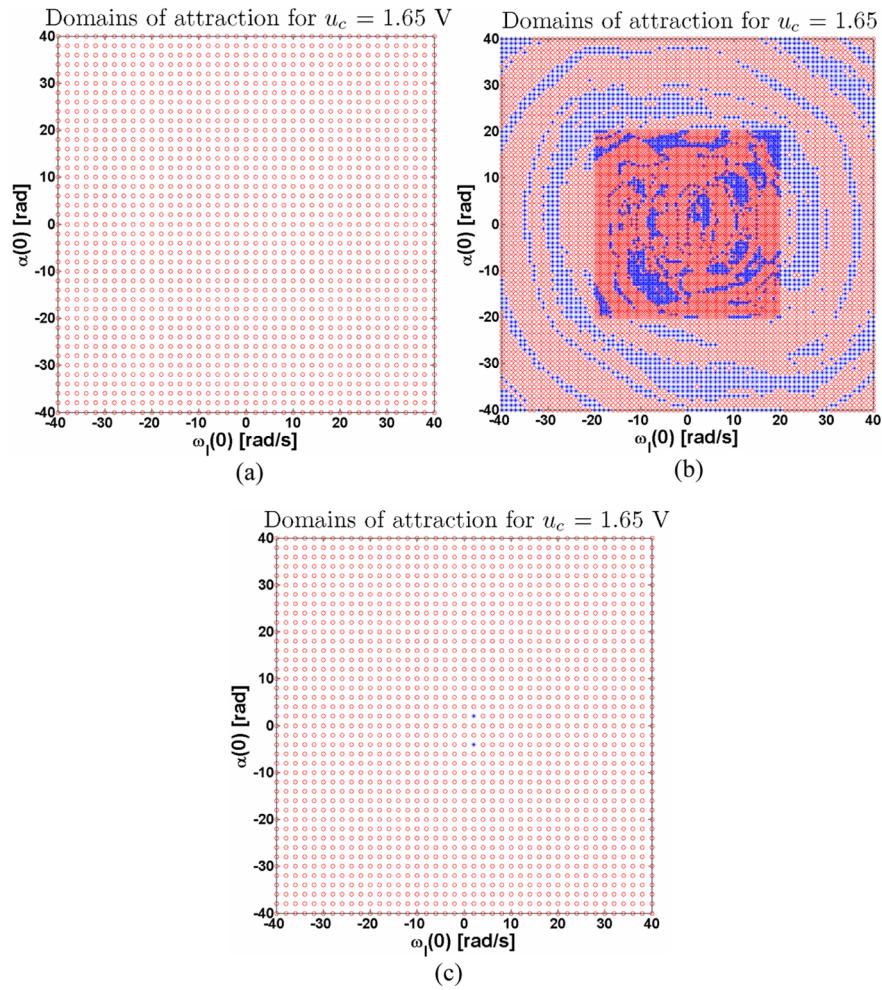


Fig. 11.13 Domains of attraction of the dynamics of the integrated system for input voltage $u_c = 1.65$ V, system with (a) no NES attached; (b) NES parameter set 1; (c) NES parameter set 2; (d) NES parameter set 3; circles denote attraction by stable periodic solutions and stars denote attraction by stable equilibrium points.

11.4.3 Transient Resonance Captures

The purpose of this section is to study the dynamical mechanisms that govern LCO suppression in the integrated drill-string-NES system. In particular, motivated by similar studies carried out in previous chapters we are interested to identify possible TRCs in the dynamics leading to TET from the drill-string to the NES. To address this issue we apply the wavelet transform (WT) to the time series of the responses of

the integrated system, as this will help us reveal the possible TRCs that occur in the transient dynamics. As shown in previous chapters, the WT is a suitable technique for analyzing the temporal evolution of the dominant frequency components of nonlinear signals. The comparison of the instantaneous frequencies of the velocities of the lower disk of the drill-string and the NES provides a robust means for verifying the occurrence of TRCs (or frequency locking) in the transient dynamics.

Figures 11.14 and 11.15 depict the instantaneous frequencies of the velocities of the lower disk (ω_1) and the NES (ω_a) for input voltages leading to attraction of the dynamics to either a stable equilibrium point (for $u_c = 2$ V – Figure 11.14), or a stable periodic solution ($u_c = 1.5$ V – Figure 11.15), respectively. These Figures confirm that 1:1 transient or sustained resonance captures leading to fundamental TET from the drill-string to the NES are responsible for the beneficial action of the NES, leading to enhanced instability mitigation.

In the results depicted in Figure 11.14 there occurs a 1:1 TRC at frequency ≈ 0.13 Hz in the initial stage of the dynamics, after which the dynamics settles to a stable equilibrium (complete LCO suppression); during the initial 1:1 TRC the NES resonantly interacts with the developing LCO instability of the drill-string and suppresses it by means of TET. In Figure 11.15 there occurs a 1:1 SRC at a frequency $f \approx 0.175$ Hz as the dynamics settles into a stable LCO, albeit of smaller amplitude compared to the LCO of the drill-string with no NES attached; in this case the NES is capable of only partially suppressing the developing LCO instability. These numerical results confirm once more that, since the essentially nonlinear NES possesses no preferential resonant frequency, it is capable of passively tuning itself to (and transiently resonating at) the frequency of the developing drill-string instability irrespective of the characteristic frequency of this instability; hence, *the NES passively ‘tracks’ the varying frequency of the developing instability*. This is demonstrated by the fact that the described 1:1 resonance captures occur at different frequencies in the WT plots of Figures 11.14 and 11.15. In accordance to the applications discussed in previous chapters, these resonance interactions lead to TET from the drill-string system to the NES, where the energy is confined and locally dissipated.

11.5 Concluding Remarks

Self-sustained vibrations may appear in mechanical systems for various reasons and often limit the performance of such systems or even cause damage and system failure. In this chapter, the focus was on friction-induced vibrations in drill-string systems. As a benchmark we considered a rotor-dynamic system with (set-valued) friction and flexibilities. We investigated the possibility of passively mitigating these friction-induced vibrations using a nonlinear absorber or NES, characterized by essential stiffness nonlinearity. The motivation for using an NES is its absence of preferential resonance frequency, which enables it to resonate with and extract energy from the drill-string system at arbitrary frequency ranges. Indeed it is this *passive*

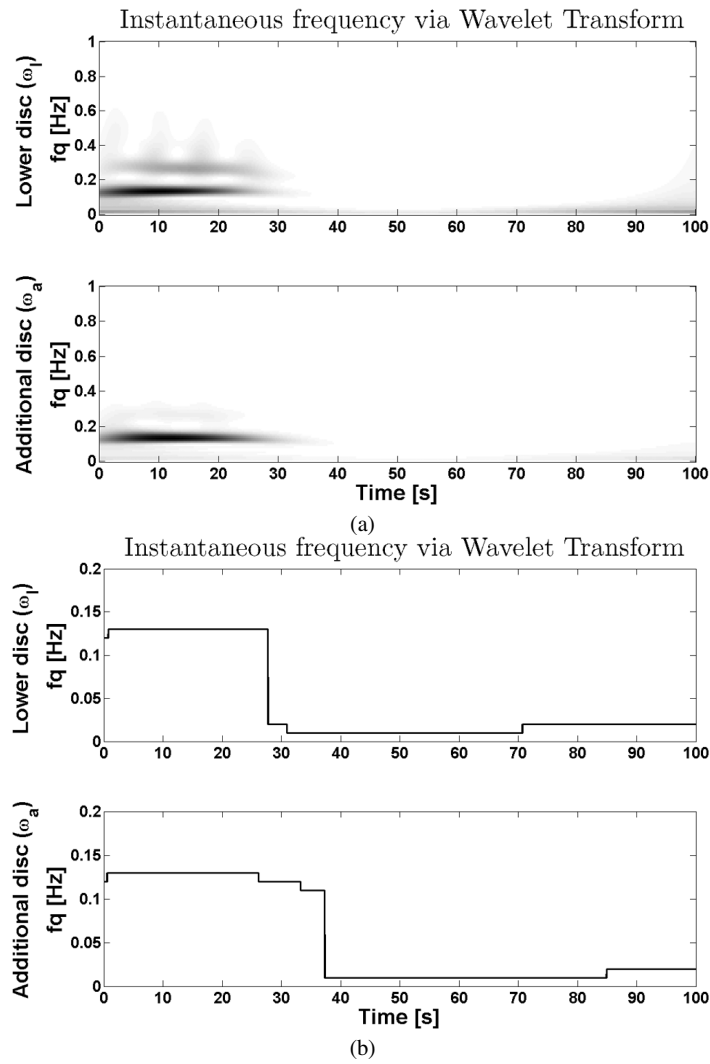


Fig. 11.14 Instantaneous frequencies of the responses of the integrated system via WT, for $u_c = 2$ V and NES parameter set 1: (a) WT spectra; (b) plot of local frequency maxima.

adaptive (self-tuning) capacity of the NES that makes it suitable for suppressing time-varying instabilities in a wide range of applications. This was demonstrated not only in the application considered in this chapter, but also in the applications involving vibration and shock isolation, aeroelastic LCO suppression and seismic mitigation considered in previous chapters.

The parametric study demonstrated that the NES can completely eliminate LCO instabilities over a relatively wide range of parameters. In other parameter ranges, the action of the NES results in only partial LCO suppression; i.e., in a mere reduc-

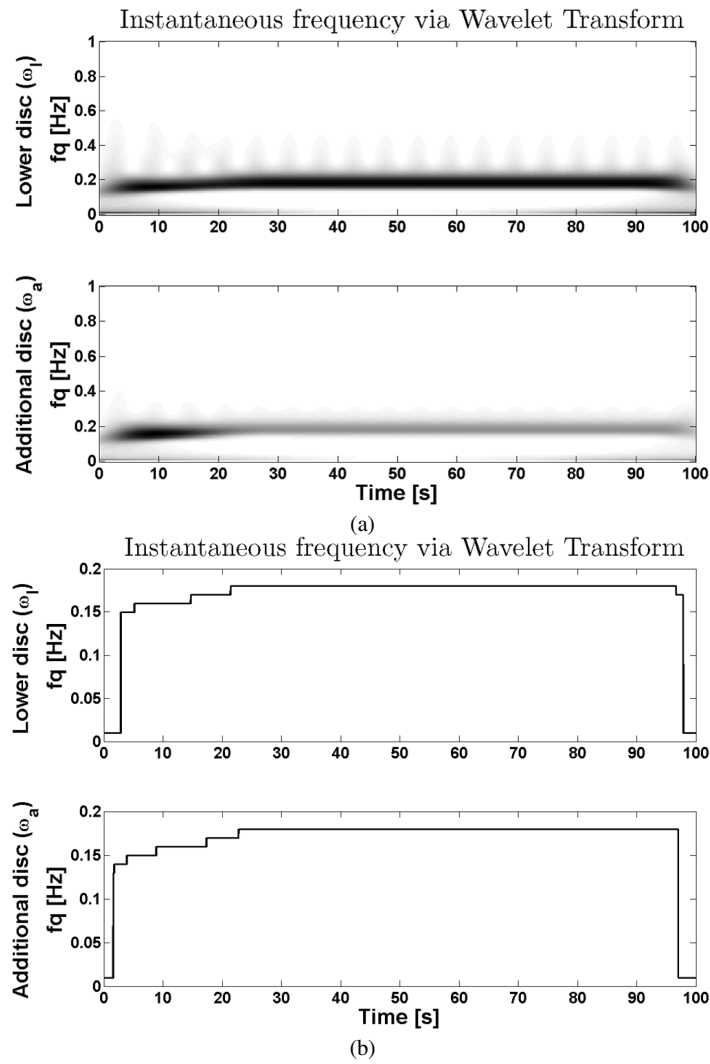


Fig. 11.15 Instantaneous frequencies of the responses of the integrated system via WT, for $u_c = 1.5$ V and NES parameter set 2: (a) WT spectra; (b) plot of local frequency maxima.

tion of the amplitudes of the surviving LCOs in parameter ranges where complete LCO elimination is not possible. As a general conclusion, however, the addition of an NES to a drill-string system has the potential to improve the global dynamical behavior of the system, and to substantially extend its domain of stable operation. Further optimization studies have to be carried out in order to not only improve the vibration mitigation action of the NES, but also to ensure the robustness and effectiveness of the NES-based passive vibration mitigation design to changes in initial conditions and system parameters.

References

*ReferencesReferencesReferences

- Armstrong-Helouvry, B., *Control of Machines with Friction*, Kluwer Academic Publisher, Boston, 1991.
- Brett, J.F., Genesis of torsional drill-string vibrations, *SPE Drilling Eng.* **7**(3), 168–174, 1992.
- Canudas de Wit, C., Olsson, H., Aström, K.J., Lischinsky, P., A new model for control of systems with friction, *IEEE Trans. Aut. Control* **40**(3), 419–425, 1995.
- Cunningham, R.A., Analysis of downhole measurements of drill string forces and motions, *J. Eng. Ind.* **90**, 208–216, 1968.
- Germay, C., van de Wouw, N., Nijmeijer, H., Sepulchre, R., Nonlinear drill string dynamics analysis, *SIAM J. Appl. Dyn. Syst.*, 2007 (in press).
- Hensen, R.H.A., *Controlled Mechanical Systems with Friction*, PhD Thesis, Eindhoven University of Technology, the Netherlands, 2002.
- Jansen, J.D., van den Steen, L., Active damping of self-excited torsional vibrations in oil well drill-string, *J. Sound Vib.* **179**, 647–668, 1995.
- Keller, H.B., *Numerical Solution of Two-Point Boundary Value Problems*, Society of Industrial and Applied Mathematics, Philadelphia, 1976.
- Kreuzer, E., Kust, O., Analyse selbsterregter Drehschwingungen in Torsionsstäben, *ZAMM – J. Appl. Math. Mech.* **76**(10), 547–557, 1996.
- Leine, R.I., Nijmeijer, H., *Dynamics and Bifurcations of Non-Smooth Mechanical Systems*, Springer Verlag, Berlin/New York, 2004.
- Leine, R.I., van Campen, D.H., Keultjes, W.J.G., Stick-slip whirl interaction in drill-string dynamics, *J. Vib. Acoust.* **124**, 209–220, 2002.
- Mihajlovic, N., *Torsional and Lateral Vibrations in Flexible Rotors Systems with Friction*, PhD Thesis, Technische Universiteit Eindhoven, the Netherlands, 2005.
- Mihajlovic, N., van de Wouw, N., Hendriks, M.P.M., Nijmeijer, H., Friction-induced limit cycling in flexible rotor systems and experimental drill-string set-up, *Nonl. Dyn.* **46**, 273–291, 2006.
- Olsson, H., *Control Systems with Friction*, PhD Thesis, Lund Institute of Technology, Sweden, 1996.
- Richard, T., Germay, C., Detournay, E., Self-excited stick-slip oscillations of drill bits, *Com. Rendus Méc.* **332**, 619–626, 2004.
- Van den Steen, L., *Suppressing Stick-Slip-Induced Drill-String Oscillations: A Hyper Stability Approach*, PhD Thesis, University of Twente, the Netherlands, 1997.
- Viguié, R., *Passive Vibration Mitigation in Rotor Systems Using Nonlinear Energy Sinks*, M.Sc. Thesis, University of Liège, Belgium, 2006.
- Viguié, R., Kerschen, G., Golinval, J.C., McFarland, D.M., Bergman, L.A., Vakakis, A.F., van de Wouw, N., Using passive nonlinear targeted energy transfer to stabilize drill-string systems, *Mech. Syst. Signal Proc.*, 2008 (in press).

Chapter 12

Postscript

For more than a century, beginning with the pioneering work of Lord Rayleigh, a fundamental issue addressed in the field of vibration engineering has been the protection of critical systems subjected to destructive input forces and/or motions. Much of this effort has been directed toward narrow-band excitations, that is, harmonic or at least periodic in nature, thus facilitating the development of classical passive vibration isolation and vibration absorption strategies. In the former case, a compliant suspension was integrated in the system to be protected thus reducing its natural frequencies well below the lowest frequency component of the excitation. The greater this difference, the greater the attenuation of the response of the system achieved by the vibration isolation design. In the latter case, an additional degree of freedom, a vibration absorber, was attached to the primary system and tuned to one of its natural frequencies. Input forces and motions at or near that frequency were attenuated to a degree defined by the inherent damping of the absorber, resulting in localization of vibration to the absorber.

In general, neither of these approaches provides a solution for the case of broad-band excitations. The difficulty arises when the bandwidth of the excitation encompasses one or more natural frequencies of the primary system, resulting in a resonant condition. This is typical for, say, stationary white noise input, which renders both vibration isolation and vibration absorption strategies ineffective; the former due to magnification of the response of the integrated system over a frequency band defined by the damping of the isolation system; and the latter due to magnification at side-bands formed at the new added natural frequencies of the integrated system. The situation is made even more challenging when the wide-band excitation is transient in nature, such as the case of impulsive excitation, since initial conditions become the predominant factor in determining the magnitude of the peak response which is nearly insensitive to damping. While tremendous strides have been made in the field of vibration engineering over the past one hundred years, the analyst and designer of protective systems are still largely constrained to reducing steady-state responses to narrow-band excitations.

Within the past 30 years, there has been a synthesis of control engineering, materials engineering, and vibration engineering, resulting in active vibration control

systems often employing smart materials. These systems can provide significant advantages in performance due to their ability to provide optimal and adaptive solutions to a wide range of problems, including those involving wide-band and transient excitations. However, the price paid for flexibility and performance is cost, weight, maintenance and reliability. For these reasons, most vibration engineers prefer a passive to an active solution, if necessary performance can be achieved.

In this monograph, the authors have attempted to document the genesis and subsequent development of a different, yet still fully passive, paradigm for protecting critical systems from destructive force and motion inputs: *targeted energy transfer* (TET). The novelty of this approach, though, is its applicability to wide-band and transient inputs, as well as the usual narrow-band and steady state excitations. The method represents a new and unique application of strong nonlinearity, the *nonlinear energy sink* (NES), a local, simple, lightweight subsystem capable of completely altering the global behavior of the primary system to which it is attached. The underlying mechanism, a series of transient resonance captures and escapes, combined with nonlinear beating phenomena associated with excitation of special impulsive orbits which comprise the bridges to TET, provides an entirely different approach to quickly, efficiently, and nearly irreversibly moving vibrational energy through a preferred, *a priori* selected direction from the primary system to an NES where it can be harmlessly dissipated.

The application of TET through the use of both smooth and discontinuous NESs has been demonstrated herein for shock and vibration isolation, passive aeroelastic instability control, seismic hazard mitigation, and stabilization of long, slender drill strings. Additional applications of the technology currently under investigation by the authors, their colleagues, and others include vibration control of bluff bodies in flow, protection of complex structures from large magnitude shocks, vibration reduction in gear sets, broadband acoustic attenuation, and broadband vibration amplification for energy harvesting.

Moreover, we envision that the generality of the methods discussed herein may also lead to fruitful applications of TET in diverse fields of science and engineering. In the field of acoustics, TET can be employed in designing acoustic NESs for passively reducing engine noise or improving the acoustic performance of closed chambers and halls. In biomedical applications, electromagnetic TET could be applied to non-intrusive detection of abnormalities, such as cancers. In electronics, TET could find application in wireless energy/power transfer in portable devices. Moreover, TET-based designs can find application in micro/nano devices for enhanced passive vibration mitigation of sensitive components or for achieving directed energy transfers between components, favorable to the design objectives. Additional potential applications of nonlinear TET could be in the fields of solid state physics (e.g., studying the dynamics of lattices or superlattices with local nonlinear defects), sensing technology (e.g., developing sensors with enhanced sensitivity towards ambient energy variations), turbulence modeling and chaotic dynamical systems (that is, studying targeted energy transfers between temporal or spatial scales and relating these to bifurcations and complexity), bioengineering (understanding, for example,

the role of TET in stiff/soft dynamical interactions in cell dynamics leading to complex dynamic phenomena such as relaxation oscillations) and in other areas.

It should also be stated that despite the amount of work already devoted to the development of a theory for nonlinear TET, some of it reported in this monograph and some included in references herein, certain challenging issues still remain unresolved or at least not completely resolved. Among important open issues one should mention the need for designing practical, essentially nonlinear NESs suitable for engineering applications; current designs, some of which are reported in this work, are sufficient under laboratory conditions but are hardly applicable to engineering practice. Another challenge is the need to extend low-dimensional analytical models of TET-related phenomena so that they are applicable to realistic high-dimensional problems. The authors can only hope that this monograph will assist those interested in applying TET in their own work and, in the mean time, hopefully raise awareness of the potential benefits to be gained through intentional, constructive and careful application of nonlinearity in applications in science and engineering.

Index

- Absorber
 - linear
 - nonlinear
 - shock
 - tuned
 - vibration
 - broadband
 - frequency independent
 - linear
 - narrowband
 - nonlinear
- Action-angle variable
- Acoustics
- Adiabatic
- Aeroelastic
 - excitation
 - instability
 - mode
 - response
- Asymptotic
 - expansion
 - limit
 - method
 - stability
- Attenuation zone
- Attraction
 - domain of –
- Attractor
- Averaging
 - method of –
 - multi-phase
 - simple
- Backbone curve
- Beam
- Beat
 - nonlinear
- Bifurcation
 - branch point cycle
 - co-dimension 1
 - global
 - high co-dimensional
 - Hopf
 - limit point cycle
 - manifold
 - Neimark–Sacker
 - neutrally stable
 - pitchfork
 - saddle-node
- Boundary value problem
 - nonlinear
- Chaotic dynamics
- Clearance nonlinearity
- Configuration
 - plane
 - space
- Complexification-averaging method
- Confinement
 - energy
 - motion
 - passive
- Continuation
 - analytic
 - numerical
- Continuum
 - approximation
 - limit
- Coupling
 - strong
 - weak
- Cutting
- Damping

- inherent
 - radiation
 - structural
 - viscous
- Differential evolution
- Dissipative systems
- Duffing oscillator
- Earthquake
- Empirical mode decomposition
- Energy
 - absorber
 - dissipater
 - dissipation measure
 - flow of –
 - harvesting
 - targeted-transfer
 - broadband
 - experimental
 - fundamental
 - multi-frequency
 - narrowband
 - subharmonic
 - threshold
 - transaction measure
- Equilibrium
 - stable
 - unstable
- Experimental
 - TET
 - TRC
- Fast dynamics
- Fluid-structure interaction
- Fluorescence
- Floquet multiplier
- Flutter
 - low frequency
 - merging frequency
- Frequency
 - component
 - instantaneous
 - response
- Frequency-energy plot
- Friction
- Fundamental
 - resonance capture
 - TET
- Hamiltonian
 - dynamics
 - perturbation
 - system
- Harmonic balance
- Heat transport
- Heave mode
- Heteroclinic orbit
- Homoclinic loop, orbit
- Impulsive
 - excitation
 - orbit
 - manifold of
 - periodic
 - quasi-periodic
- Instability
 - aeroelastic
 - drill-string
- Integrability
 - non-
- Interaction
 - modal
 - nonlinear
 - phase
- Internal resonance
- Intrinsic mode function
- Invariant
 - manifold
 - slow-
 - damped NNM-
 - torus
- Isolation
 - vibration
 - seismic
 - shock
- KAM theory
- Limit cycle oscillation
 - generation of –
 - suppression of –
- Localization
- Map
 - one-dimensional
 - Poincaré
- Mitigation
 - seismic
 - shock
 - vibration
- Modal
 - function
 - relation
- Mode
 - empirical-decomposition
 - localized
 - nonlinear normal
 - normal

structural	singular
Modulation	Pitch mode
equation	Plate
Multiple scales	Propagation zone
NATA	Reduced-order model
Nonlinear beat	Resonance
Nonlinear energy sink	:1
Configuration I (grounded) –	band
Configuration II (ungrounded) –	fundamental
MDOF	interaction
piecewise-linear	internal
SDOF	manifold
vibro-impact	nonlinear
Nonlinear modal interactions	passage through –
Nonlinear normal mode	scattering by –
damped	subharmonic
Nonlinearity	superharmonic
clearance	Resonance capture
essential	cascade
geometrical	escape from –
non-smooth	permanent
smooth	sustained
vibro-impact	transient
Oil-drilling	Response
Optimal	co-existence of –
condition	frequency diagram of –
parameter	modulated
range	periodic
TET	quasi-periodic
Orbit	strongly modulated
fine structure of –	transient
impulsive	vibro-impact
quasi-periodic	Robustness
periodic	of LCO suppression
symmetric	of TET
unsymmetric	Rod
Oscillation	Shock
chaotic	absorber
periodic	isolation
quasi-periodic	mitigation
limit cycle –	spectrum
friction induced	Sifting process
subcritical	Signal processing
supercritical	Slow-fast partition
suppression of –	Slow dynamics
relaxation	Slow Invariant Manifold
sustained	Soliton
transient	Stability
Perturbation	asymptotic
non-smooth	orbital
regular	Steady state
	bifurcation analysis

- response
 - TET
- Stirbeck effect
- Subharmonic
 - resonance capture
 - TET
 - tongue
- Superharmonic
- Suppression mechanism
 - LCO –
- Switch model
- System identification

- Transversality
- Transform
 - Fast Fourier
 - Hilbert
 - integral
 - wavelet
- Transformation
 - non-smooth coordinate –
- Transient
 - response
 - TET
- Transition
 - damped
 - multi-frequency
 - multi-modal
- Triggering
- Tuned mass damper
- Turbine blade
- Twist

- Van der Pol oscillator
- Vibro-impact
 - NES
 - oscillation
 - seismic mitigation
 - TET
- Vortex shedding

- Wave
 - backscattering of –
 - localized
 - solitary
 - standing
 - traveling
- Wavelet
 - transform
 - Cauchy
 - Morlet
 - spectrum
- Windowing
- Wing